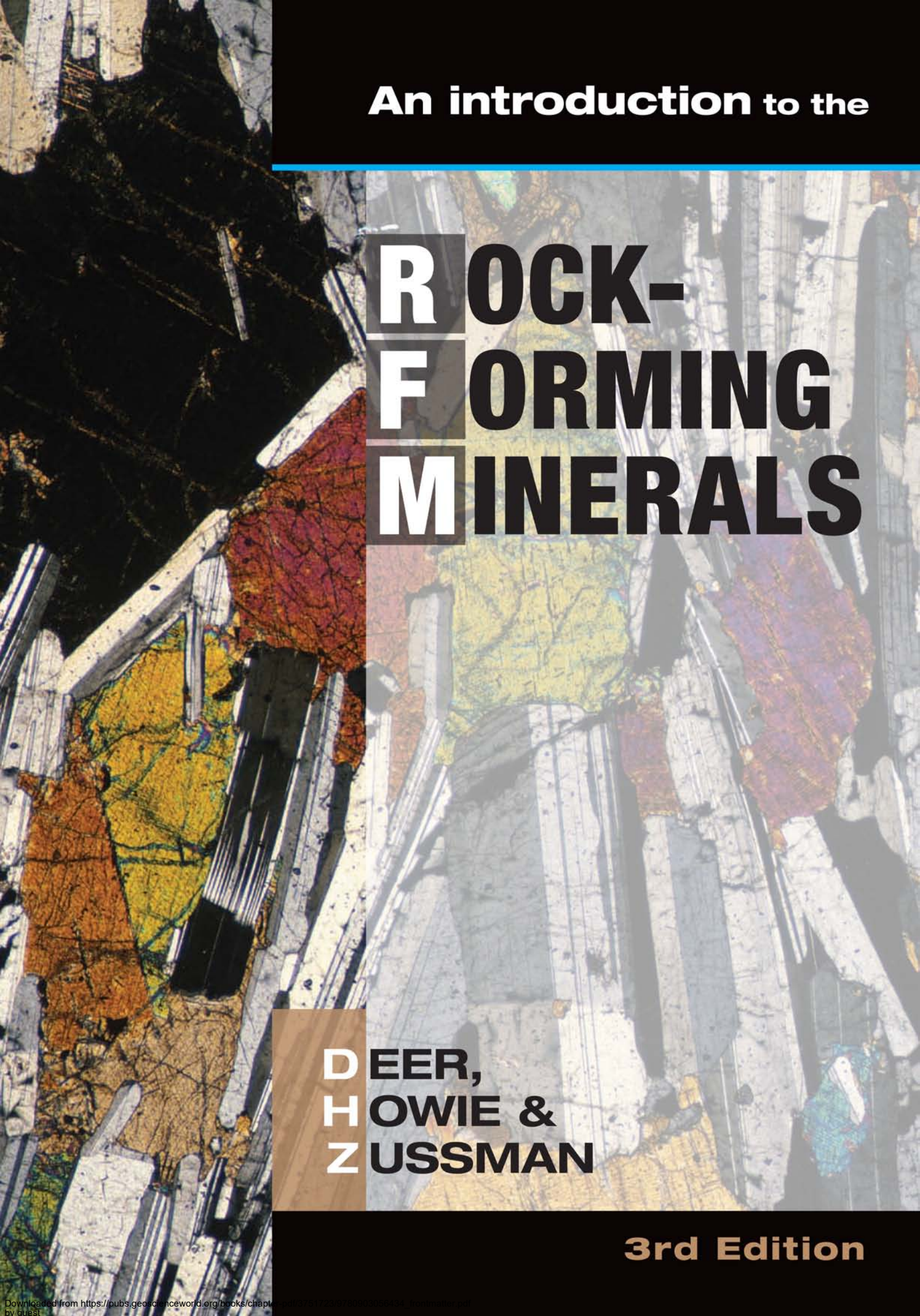


Downloaded from https://pubs.geoscienceworld.org/books/chapter-pdf/3791793/9781780650654.fm.pdf
by guest

An Introduction to the Rock-Forming Minerals

Third Edition

W. A. DEER†, FRS
Emeritus Professor of Mineralogy & Petrology,
University of Cambridge

R. A. HOWIE†
Emeritus Professor of Mineralogy,
University of London

J. ZUSSMAN
Emeritus Professor of Geology,
University of Manchester

† *Sadly, Professors Deer and Howie died while this edition was in preparation*

The Mineralogical Society
London

Downloaded from https://pubs.geoscienceworld.org/books/chapter-pdf/3751723/9780903056434_frontmatter.pdf
by guest

The Mineralogical Society

First published 1966
Second edition 1992
Third edition 2013

© W. A. Deer, R. A. Howie and J. Zussman 1966
Second edition © W. A. Deer, R. A. Howie and J. Zussman 1992
This edition © W. A. Deer, R. A. Howie and J. Zussman 2013

All rights reserved; no part of this publication may be reproduced, stored in a retrieval system, or transmitted in any form or by any means, electronic, mechanical, photocopying, recording, or otherwise without either the prior written permission of the Publishers or a licence permitting restricted copying in the United Kingdom issued by the Copyright Licensing Agency Ltd, 90 Tottenham Court Road, London W1P 9HE.

First published 1966
Second edition 1992
Third edition 2013

British Library Cataloguing in Publication Data
Deer, W. A.
An introduction to the rock-forming minerals. – 3rd ed.
I. Title II. Howie, R. A. III. Zussman, J.
549

ISBN 978-0903056-33-5

Library of Congress Cataloging-in-Publication Data
Deer, W. A. (William Alexander)
An introduction to the rock-forming minerals/W. A. Deer, R. A. Howie, J. Zussman. – 3rd ed.
p. cm.
Includes bibliographical references and index.
ISBN ISBN 978-0903056-33-5
1. Silicate minerals. 2. Mineralogy. 3. Rocks. I. Howie R. A. (Robert Andrew) II. Zussman, J. (Jack) III. Title.
2013
549-dc23

Typeset by Almaroca Ltd., West Kirby, Wirral, UK
Printed by Berforts Information Press, Stevenage, Hertfordshire, UK

Downloaded from https://pubs.geoscienceworld.org/books/chapter-pdf/3751723/9780903056434_frontmatter.pdf
by guest

Contents

Preface to Third Edition v
Preface to Second Edition vii
Preface to First Edition viii
Acknowledgements ix
Abbreviations and Symbols x

Key to optical sketches and data 1

Ortho-, Di- and Ring Silicates

Olivine 4
Zircon 12
Titanite (sphene) 15
Garnet group 18
Vesuvianite (idocrase) 28
Sillimanite 30
Andalusite 33
Kyanite 36
Staurolite 39
Topaz 44
Chloritoid 47
Epidote group 52–64
Zoisite, Clinozoisite, Epidote, Piemontite, Allanite 53
Lawsonite 65
Pumpellyite 68
Melilite group 72–75
Gehlenite, Melilite, Åkermanite 72
Beryl 76
Cordierite 80
Tourmaline group 86–92
Dravite–Fluor-dravite, Schorl–Fluor-schorl, Elbaite–Fluor-elbaite, Olenite–Fluor-olenite, Uvite–Fluor-uvite 86

Chain Silicates

Pyroxene group 94–131
Enstatite–Ferrosilite, Pigeonite, Diopside–Hedenbergite, Johannsenite, Augite–Ferroaugite, Omphacite, Jadeite, Kosmochlor, Aegirine, Aegirine-augite, Spodumene 102
Wollastonite 132
Amphibole group 137–171
Anthophyllite–Gedrite, Cummingtonite–Grunerite, Tremolite–Ferro-actinolite, Hornblendes, Kaersutite, Glaucophane, Riebeckite, Richterite–Ferrorichterite, Magnesiokatophorite–Katophorite, Eckermannite–Arfvedsonite 144

Layered Silicates

Mica group 174–180
Muscovite, Paragonite, Glauconite, Phlogopite–Biotite, Lepidolite, Zinnwaldite 181
Stilpnomelane 199
Pyrophyllite 202
Talc 204
Chlorite Group 208–215
Clinochlore, chamosite 208
Serpentine 216
Clay Minerals 224–227
Kaolinite group, Illite group, Smectite group, Vermiculite 226
Prehnite 244

Framework Silicates

Feldspar group 248–309
Alkali feldspars, Barium feldspars Plagioclase feldspars 253
Silica minerals
Quartz, Tridymite, Cristobalite 311
Feldspathoids 325–354
Nepheline and Kalsilite, Leucite, Sodalite Group, Cancrinite–Vishnevite, Scapolite 325
Zeolite group 355–379
Analcime, Natrolite, Phillipsite–Harmotome series, Laumontite, Heulandite series, Chabazite series, Mordenite 363

Non-silicates

Oxides 382
Periclase, Cassiterite, Corundum, Hematite, Ilmenite, Rutile, Anatase, Brookite, Perovskite 382
Spinel group 402
Al hydroxides and oxyhydroxides 409
Brucite, Gibbsite, Diaspore, Boehmite 409
Fe oxyhydroxides 417
Goethite, Lepidocrocite, Ferrihydrite 418
Sulphides 423
Pyrite, Pyrrhotite, Chalcopyrite, Sphalerite, Galena 424
Sulphates 441
Baryte, Celestine, Gypsum, Anhydrite 441
Carbonates 451
Calcite, Magnesite, Siderite, Dolomite, Aragonite, Strontianite 453
Phosphates 473
Apatite, Monazite 473
Halides 480
Fluorite, Halite 480

Appendix 1: *Calculation of a chemical formula from a mineral analysis* 485
Appendix 2: *Atomic and molecular weights for use in calculations of mineral formulae from chemical analyses* 487
Appendix 3: *End-member (Mol%) calculations* 488
Appendix 4: *Use of optical identification tables* 490
Table 4A: Birefringences and Michel-Levy colours 491
Table 4B: Optical properties of common minerals 492
Index 495

Downloaded from https://pubs.geoscienceworld.org/books/chapter-pdf/3751723/9780903056434_frontmatter.pdf
by guest

Downloaded from https://pubs.geoscienceworld.org/books/chapter-pdf/3751723/9780903056434_frontmatter.pdf
by guest

Preface to Third Edition

In this edition most of the commonly occurring minerals of igneous, metamorphic and sedimentary rocks are discussed in terms of structure, chemistry, optical and other physical properties, distinguishing features and paragenesis. Important correlations between these aspects of mineralogy are emphasized wherever possible, and the content of each section has been updated where needed in the light of published research over the 21 years between editions. The text on each mineral now opens with a brief highlighted introduction on its nature and occurrence, and where appropriate, following the last in a group of closely related minerals, a panel gives a very brief summary of their basic similarities and differences. Tables of over 200 chemical analyses and formulae are included and a number of older entries have been replaced by more recent examples. The rather small selection of references listed previously has been replaced by a more extensive reading list, including many recent publications and major reviews.

Treatment of several mineral groups has been moderately expanded, and the zeolites more so, their general introduction now being followed by separate sections for six of the main zeolite sub-groups. Still more expanded is the treatment of the feldspar minerals, comprising a comprehensive, more integrated, and updated account of this very complex mineral group, most of it generously provided by Ian Parsons. In order to help limit the size and price of this volume, however, we have omitted previous brief sections on some of the less common minerals.

This edition makes extensive use of colour, both in the optical orientation sketches and in the many photomicrographs of minerals in thin section. As well as adding colour to earlier crystal structure diagrams, many entirely new views are presented, and a 'CrystalViewer' interactive CD containing more than 100 crystal structures is provided.

While our text continues to be primarily concerned with the understanding of the properties and formation of minerals rather than the use of properties as a means of identification, the latter purpose is also addressed in several ways. The tabulated data and optical orientation sketches at the head of each mineral section are now accompanied by a guide to their use. One new appendix has a chart showing appropriate interference colours for most of the main minerals dealt with in this volume, and another has an Identification Table based on birefringence and other properties. The sections on 'Distinguishing Features' for each main mineral are particularly useful in helping to discriminate between one mineral and others with which it is most likely to be confused, and in addition over 60 photomicrographs are presented illustrating typical features of minerals as seen under the petrological microscope. The electron probe and other analytical instruments have become more widely employed, but in our view this does not diminish the importance of the petrological polarizing microscope which provides an overview of the minerals and their relationships as they occur in rocks before they are given individual attention using the powerful but generally more complex equipment now available.

It is intended that this book dealing with the basic nature and properties of the principal rock-forming minerals, while being particularly useful to undergraduate and postgraduate students of mineralogy, petrology and geochemistry at various levels, will also help those coming to these subjects for the first time from other disciplines such as Materials Science and Chemistry, for whom it may serve as a condensed version of the more extensive volumes of the DHZ series, *Rock-Forming Minerals*, 2nd edition.

We wish to express our thanks to many people. To Kevin Murphy (Executive Director) and members of the publications committee of the Mineralogical Society of Great Britain and Ireland, for their very helpful suggested improvements. We are grateful to Pearson Education for allowing use of a selection of the late W.S. MacKenzie's photomicrographs, and to Mrs Anne MacKenzie for making the original transparencies available to us; we also thank Giles Droop for supplying us with photomicrographs from his teaching collection.

Enclosed inside the back cover of this third edition is an interactive CD "CrystalViewer 8.3" containing a set of crystal structures of the more common minerals. These were created using "CrystalMaker" software (www.crystalmaker.com) and the authors and The Mineralogical Society are very grateful to Dr David Palmer for supplying this CD and for helping in the construction of many of the new crystal structure images seen throughout the volume.

We owe thanks also to Mark Welch, for generously preparing for us many other coloured illustrations of crystal structures, and our thanks are due to Takenori Kato, Nagoya University, for his help and agreement to our use of his synthesized sequence of interference colours in our birefringence chart.

We have benefited also from help and advice from Manchester University colleagues including John Bowles, Kate Brodie, Giles Droop, Alexander Edwards, Richard Hartley, Mike Henderson, Cathy Hollis, Christopher Horsfall, Richard Pattrick, Alison Pawley and David Vaughan, all of The School of Earth,

Downloaded from https://pubs.geoscienceworld.org/books/chapter-pdf/3751723/9780903056434_frontmatter.pdf
by guest

Atmospheric and Environmental Sciences. We are grateful to the many other Earth Scientists (listed below) who responded to our request for comments on specific mineral sections, and David Green for his many valuable improvements to the accuracy and clarity of the text as a whole. We wish to thank Ian Parsons for his contribution of a large part of the feldspar text and figures, as mentioned above, enabling us to present an authoritative treatise on these complex minerals.

Robert Preston has had the difficult task of putting the book together for us and we thank him for his consistent help and patience over an extended period, and Cathy Preston for valuable help with checking final proofs. Having thanked the above for their involvement we accept nevertheless responsibility for errors and omissions.

We wish to record our indebtedness to the late Professor W.A. Deer for the initial concept of this compact volume and for his extensive and authoritative contributions to our succession of co-authored volumes.

R. A. Howie
J. Zussman
January 2012

My good friend and colleague Bob Howie was noted nationally and internationally for his many contributions to Mineralogy throughout his working life, by his university research and teaching, by his activities within the Mineralogical Society of Great Britain and Ireland, and by his prodigious work, year after year, as editor of *Mineralogical Abstracts*. Alongside these he managed also to share fully in the continuous preparation of the various volumes and editions of *Rock-Forming Minerals* and *Introduction to Rock-Forming Minerals*. Unfortunately as we were approaching the completion of the latter's 3rd edition, his health deteriorated. Bob continued writing, with increasing difficulty, until very close to his passing away in March 2012. He would have liked so much to see this volume's publication, but that was not to be. I see it, however, as dedicated to his memory.

Jack Zussman
February 2013

Thomas Armbruster
Etienne Balan
Geoff Bromiley
Fernando Cámara
Michael A. Carpenter
Petr Černý
Bernardo Cesare
Christian Chopin
Giancarlo Della Ventura
Harald G. Dill
Colin H. Donaldson
Bernard W. Evans
Adrian Finch
Godfrey Fitton
Gerhard Franz
Charles A. Geiger
Nurit Goldman
Ed Grew
Joel D. Grice
Steve Guggenheim
Simon Harley
Dan Harlov
Frank Hawthorne
Karen Hudson-Edwards
Bernard Leake
Juhn G. Liou
Walter Maresch
Roger H. Mitchell
Enver Murad
Mariko Nagashima
Fabrizio Nestola
Phil Neuhoff
Roberta Oberti
Richard Pattrick
Simon A.T. Redfern
Mark Welch
M. Jeff Wilson
Bruce Yardley

Downloaded from https://pubs.geoscienceworld.org/books/chapter-pdf/3751723/9780903056434_frontmatter.pdf
by guest

Preface to Second Edition

This major revision takes place some 25 years after the publication of the first edition. The intervening years have seen great changes in all aspects of the Earth Sciences, including mineralogy. There have been many improved and new techniques for investigating minerals, producing a new body of data and often a better understanding of their nature, properties and relationships. Such changes are evident in each section under which we treat each major mineral.

Crystal structures are far better known through the development of automatic X-ray diffraction methods supplemented by spectroscopic studies (infrared, X-ray, Mössbauer, etc.) of site preferences, and high-resolution electron microscopy revealing fine-scale departures from regularity of structure.

The chemical variations in minerals are better appreciated through the development of electron-probe microanalysis which is rapid and is done without separation of minerals from the rock. New techniques have greatly extended the range of pressure and temperature at which phase transformations can be studied in the laboratory. Geothermometry has been developed considerably as has the use of fluid inclusions to give information on temperatures of crystallization and genetic sequences.

Whereas we are now not so dependent on optical properties for determining chemical composition, light microscopy remains the basic general tool underpinning all other methods, and the study of sub-microscopic features (e.g. habits and intergrowths) is enhanced by the use of scanning or transmission electron microscopy. The increased attention given to opaque minerals by both students and researchers is recognized and we now give data on properties in reflected light. In the new edition we include some plates showing a selection of interesting microscopic features, but recommend the more comprehensive set of micrographs in the *Atlas of Rock-Forming Minerals* (W.S. MacKenzie & C. Guildford, Longman), a useful companion volume.

In the paragenesis sections of our new edition we are able to relate the occurrences of some minerals to their environments in terms of the modern concepts of plate tectonics. We are also able to include the Moon as a mineral locality.

Although our text was, and still is, primarily intended for university students, it has gained use also as a reference book for researchers, albeit at a less detailed level than the original five volumes from which it was derived, or their replacement editions. We have tried to recognize this by, for example, adding cell parameters to the tabulated mineral data; also our selection of references includes not only examples of different approaches to the study of minerals but also some wider 'review-type' publications on particular mineral groups, e.g. clay minerals, feldspars and zeolites.

We have attempted to restrict the work to a similar size, and although some expansion has been felt necessary for some major groups such as olivine and nepheline, the balance has been maintained by omitting coverage of datolite, rosenbuschite, lävenite, catapleiite and the helvite group.

W. A. DEER
R. A. HOWIE
J. ZUSSMAN
January 1991

Downloaded from https://pubs.geoscienceworld.org/books/chapter-pdf/3751723/9780903056434_frontmatter.pdf
by guest

Preface to First edition

The authors began about ten years ago to write a text book for university students, but this aim was gradually relinquished as the text grew into the five volumes of *Rock-Forming Minerals.* We have now reverted to our original purpose by condensing the latter work into this single volume, which is intended to provide a short account of the more important minerals encountered in many undergraduate courses in mineralogy and petrology. We have attempted to present the basic data which are essential to the understanding of minerals, especially in relation to the environment of their formation.

The study of minerals is commonly presented largely as a listing of optical and physical properties which can be used for mineral identification. While this is without doubt an essential aspect of the subject, the study of minerals, particularly in relation to petrology, requires also the detailed consideration of crystal structure, chemistry and paragenesis, and we make no apologies for the prominence we have given these topics.

To those familiar with the five volumes of *Rock-Forming Minerals* the present volume will be seen to be based essentially on the pattern of the earlier work. Thus the more common minerals are each considered under the headings: Structure, Chemistry, Optical and Physical Properties, Distinguishing Features and Paragenesis. Sections on chemistry show typical compositions and illustrate the major atomic replacements which occur in the various minerals. In the sections on optical and physical properties, the variations of these properties with chemistry are discussed and are in many cases presented graphically.

We have tried to make the text useful also as a laboratory manual by giving tabulated data and optic orientation sketches at the head of each mineral section, and by including the paragraphs on distinguishing features.

Selected references are given for most minerals, and have been chosen, not so much in order to augment the data presented, but rather to draw attention to the various types of information available relating to particular minerals. Moreover, by drawing the attention of the student to some of the original data on which this work is based, it is hoped to stimulate a deeper interest in the study of minerals.

Minerals of lesser importance are given a shorter treatment. All the minerals dealt with in *Rock-Forming Minerals* are included in the present work, and in addition mullite, some of the rarer but typical minerals of caic-silicate rocks, and the accessory minerals of nepheline-syenites and related rocks have been included.

The earlier spelling of felspar has been changed to feldspar in accordancc with the 1962 recommendation of the New Minerals and Mineral Names Commission of the International Mineralogical Association.

A description of the method of calculating structural formulae from mineral analyses is given in Appendix 1

W. A. DEER
R. A. HOWIE
J. ZUSSMAN
October 1965

Downloaded from https://pubs.geoscienceworld.org/books/chapter-pdf/3751723/9780903056434_frontmatter.pdf
by guest

Acknowledgements

We are indebted to the following for permission to reproduce copyright material. Full details of publication are included in relevant figure captions.

Akademische Verlagsgesellschaft, Munich for figures from *Mineralogische Tabellen* (2nd ed.)

Cambridge University Press for figures from *Crystal Chemistry*; *Introduction to Crystal Chemistry*

Carnegie Institute of Washington for figures from *Carnegie Institute of Washington, Annual Report of the Director, Geophysical Laboratory*

The Clay Minerals Society for figures from *Clays and Clay Minerals*

Cornell University Press for figures from *Atomic Structure of Minerals*

Elsevier for figures from *Earth Science Reviews*; *Geochimica et Cosmochimica Acta*; *Journal of Solid State Chemistry*; *Lithos*

The Geological Society of America for figures from *Bulletin of the Geological Society of America*; *Memoirs of the Geological Society of America*

Geological Society of London for figures from *Rock-Forming Minerals*

International Union of Crystallography for figures from *Acta Crystallographica*

Japan Association of Mineralogical Sciences for figures from *Mineralogical Journal*

John Wiley & Sons for figures from *Journal of Metamorphic Geology*; *Manual of Mineralogy*; *Physics and Chemistry of Minerals and Rocks*

Longman/Pearson Education for figures from *An Introduction to the Rock-Forming Minerals*; photomicrographs from the W.S. MacKenzie collection

The McGraw-Hill Companies for figures from *Igneous Petrology*; *Microscopic Identification of Minerals*; *Encyclopedia of Science and Technology*

Mineralogical Association of Canada for figures from *The Canadian Mineralogist*

The Mineralogical Record for figures from *Mineralogical Record*

Mineralogical Society of America for figures from *American Mineralogist*; *Special Paper* **2**; *Reviews in Mineralogy*

Mineralogical Society of Great Britain and Ireland for figures from *Mineralogical Magazine*; *Clay Minerals*

Oldenbourg Wissenschaftsverlag Leipzig for figures from *Zeitschrift für Kristallographie*

Oxford University Press for figures from *Journal of Petrology*

NASA for a photomicrograph

National Institute for Metallurgy, Johannesburg for figures from *Minerals Science and Engineering*

The Royal Society of London for figures from *Proceedings of the Royal Society*; *Philosophical Transations of the Royal Society*

The Russell Society for figures from *Journal of the Russell Society*

Scandinavian University Press for figures from *Norsk Geologisk Tidsskrift*

E. Schweizerbart'sche Verlagsbuchhandlung for figures from *Neues Jahrbuch für Mineralogie*, *European Journal of Mineralogy*; *Fortschritte der Mineralogie*

SEPM Society for Sedimentary Geology for figures from *Journal of Sedimentary Research*

Society of Economic Geologists for figures from *Economic Geology*

Springer-Verlag GmbH for figures from *Feldspar Minerals*; *Sedimentary Carbonate Minerals*; *Contributions to Mineralogy and Petrology*; *Physics and Chemistry of Minerals*

Swiss Society of Mineralogy and Petrology for figures from *Schweizer Mineralogische und Petrographische Mitteilungen*

University of Chicago Press for figures from *Journal of Geology*

Yale University (Kline Geology Laboratory) for figures from *American Journal of Science*

D.H.M. Alderton for a photomicrograph

R.A. Berner for figures from *Principles of Chemical Sedimentology*

R.M.F. Preston for a photograph

D.J. Vaughan for figures from *Mineral Chemistry of Metal Sulphides*

F.J. Wicks for photomicrographs

Downloaded from https://pubs.geoscienceworld.org/books/chapter-pdf/3751723/9780903056434_frontmatter.pdf
by guest

Abbreviations and symbols

Å (= 10 nm)	Ångstrom units (10^{-8} cm)
a	cell edge in the *x* direction
a	activity (of substance indicated by subscript)
atom %	atoms per cent, percentage on an atomic basis
b	cell edge in the *y* direction
Bx_a	acute bisectrix
c	cell edge in the *z* direction
calc.	calculated
D	density (g/cm^3)
d	interplanar spacing
DTA	differential thermal analysis
Eh	redox potential
EPMA	electron probe microanalysis
f	fugacity (of substance indicated by subscript)
Fe*	total Fe^{2+} + Fe^{3+}
H	hardness (Mohs' scale)
H_2O-	absorbed water
H_2O+	water derived from mineral breakdown
hex (subscript)	hexagonal
IR	infrared spectroscopy
K_D	distribution coefficient
LA-ICP-MS	Laser ablation inductively coupled plasma mass spectrometry
M	mol/litre
M	generalized cation site
Ma	million years
meq., μeq.	milliequivalents, microequivalents
mol%	molecules per cent, percentage on a molecular basis
n	refractive index (for a cubic mineral)
nm	nanometre (10^{-9} m)
NMR	nuclear magnetic resonance
O.A.P.	optic axial plane
P	pressure (see note below on units of pressure)
pfu	per formula unit
pH	−log (H^+) concentration
ppm	parts per million
‰	parts per mille (parts per thousand)
R	generalized symbol for group of metal ions
R	reflectance
RE, *REE*	rare earth, rare earth element
$r < v$ (or $r > v$)	optic axial angle in red light is less than (or greater than) that in violet light
rh (subscript)	rhombohedral
SEM	scanning electron microscopy
SIMS	Secondary ion mass spectrometry
TEM	transmission electron microscopy
HRTEM	high resolution transmission electron microscopy
T	temperature. Also 'tetrahedral site'
tr.	trace
VHN_{100}	microindentation hardness, Vickers Hardness Number at 100 g load
wt.%	percentage on a weight basis
XRD	X-ray diffraction
x, *y*, *z*	crystallographic axes
Z	number of formula units per unit cell
2V	optic axial angle
α, β, γ	least, intermediate and greatest refractive indices; the vibration direction of the rays; also the rays themselves.
α, β, γ	angles between the positive directions of the *y* and *z*, *x* and *z*, and *x* and *y* crystal axes
δ	birefringence
ε	extraordinary ray, refractive index (uniaxial)
ω	ordinary ray, refractive index (uniaxial)
□	vacant site in crystal structure

Buffers

FMQ	fayalite + oxygen ⇌ magnetite + quartz
HM	hematite−magnetite
IW	iron + oxygen ⇌ wüstite
MH	magnetite + oxygen ⇌ hematite
MI	magnetite ⇌ iron + oxygen
MW	magnetite ⇌ wüstite + oxygen
NNO	nickel + oxygen ⇌ nickel oxide
QFM	quartz–fayalite–rnagnetite
WM	wüstite–magnetite

Units of Pressure

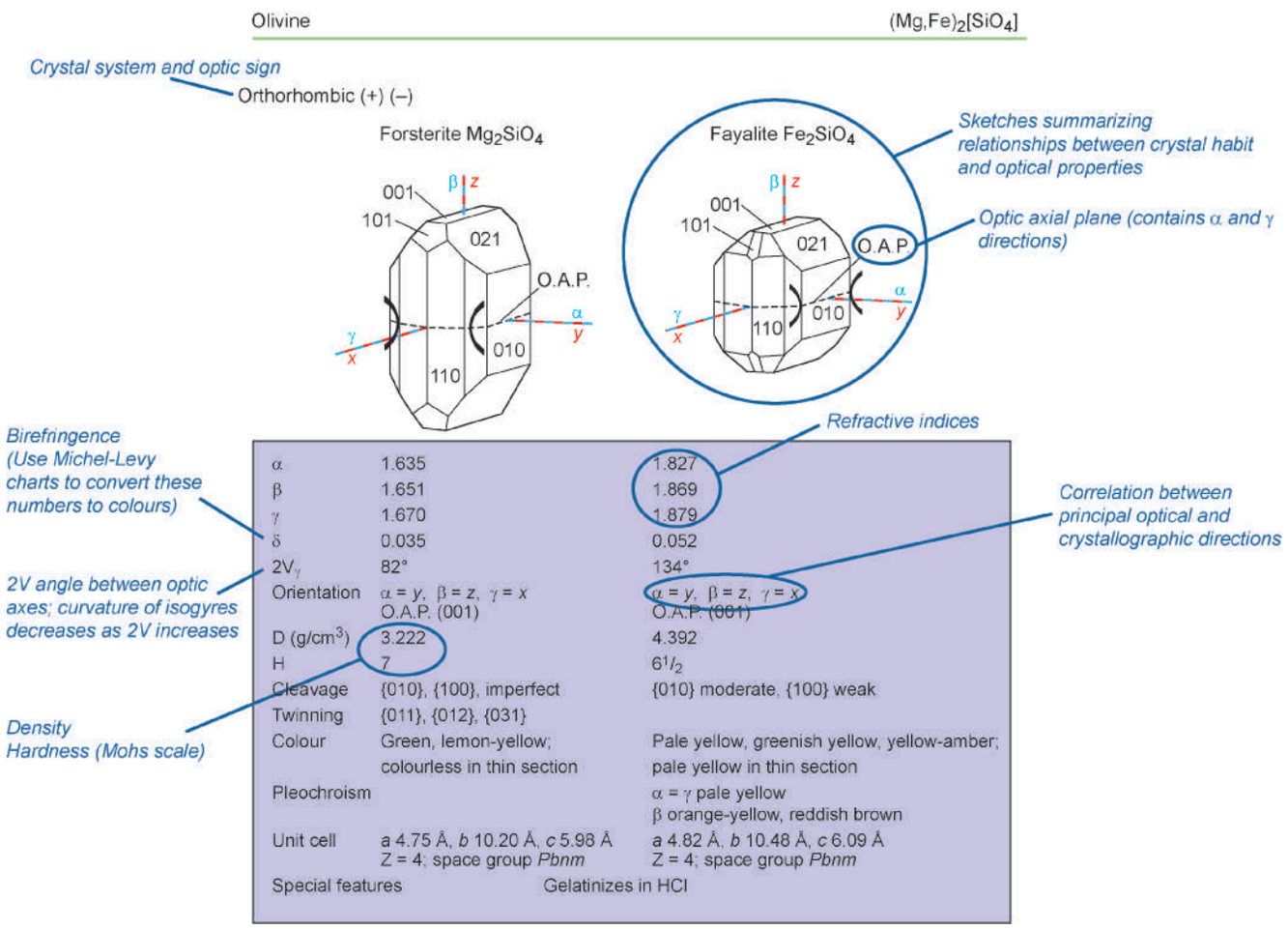
Various units for pressure are found in geological literature. In older publications, bar or atm. (atmosphere), kilobar (kbar) and megabar (Mbar), and more recently, the IS units: pascal (Pa), megapascal (MPa) and Gigapascal (GPa). Their relationships are as follows:

1 bar = 10^5 N(newtons)/m^2
1 atm. = 1.0133 bar
1 kbar = 1000 bar
1 Pa = 1 N/m^2
1 MPa = 10^6 Pa = 10 bar
1 GPa = 10^9 Pa = 10 kbar

Thus to convert pressure in kbar to pressure in GPa, or pressure in bars to pressure in MPa, divide by 10.

Downloaded from https://pubs.geoscienceworld.org/books/chapter-pdf/3751723/9780903056434_frontmatter.pdf
by guest

Key to optical sketches and data



Downloaded from https://pubs.geoscienceworld.org/books/chapter-pdf/3751723/9780903056434_frontmatter.pdf
by guest

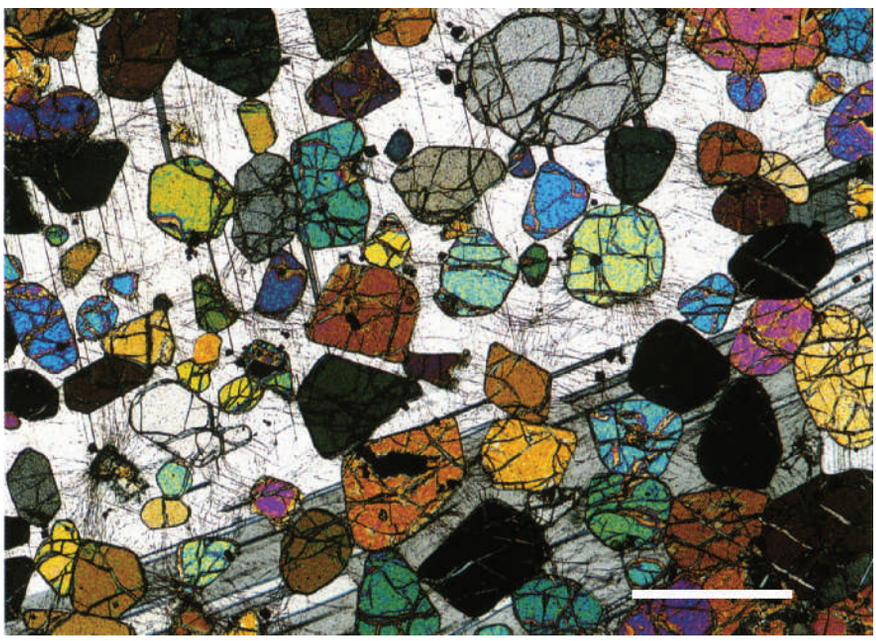
Downloaded from https://pubs.geoscienceworld.org/books/chapter-pdf/3751723/9780903056434_frontmatter.pdf
by guest

Olivine Group

The members of the olivine group crystallize with orthorhombic symmetry, the structures consisting of independent SiO_4 tetrahedra linked by divalent cations in six-fold coordination. In the (Mg,Fe)-olivines there is complete solid solution between Mg_2SiO_4 (forsterite) and Fe_2SiO_4 (fayalite); similarly the (Fe,Mn)-olivines form a continuous series. Olivine is a major constituent of ultrabasic plutonic rocks and olivines of metamorphic origin occur principally in rocks of ultramafic composition, in impure carbonates and in iron-rich sediments.

The $CaMgSiO_4$ orthosilicate (monticellite) does not show any appreciable variation from the ideal composition. The (Ca,Fe)-olivine kirschsteinite, ideally $CaFeSiO_4$, is commonly found in industrial slag but is relatively rare in nature. Monticellite is a relatively common mineral which crystallizes during the progressive metamorphism of siliceous and magnesian limestones and in skarns. It also occurs in ultrabasic rocks such as kimberlite and alnöite.

The minerals of the humite group (which include norbergite, $Mg(OH,F)_2{\cdot}Mg_2[SiO_4]$; chondrodite, $Mg(OH,F)_2{\cdot}2Mg_2[SiO_4]$; humite, $Mg(OH,F)_2{\cdot}3Mg_2[SiO_4]$; clinohumite, $Mg(OH,F)_2{\cdot}4Mg_2[SiO_4]$) have closely related structures. Although their structures have much in common with that of olivine, the replacement of Mg by Fe^{2+} is considerably smaller in amount; some chondrodites and clinohumites have a high content of titanium and other members of the group have high manganese contents. The refractive indices and densities of the humite-group minerals increase progressively from norbergite to clinohumite; they are restricted mainly to metamorphosed and metasomatized limestones and dolomites, and to skarns associated with ore deposits at contacts with acid plutonic rocks.

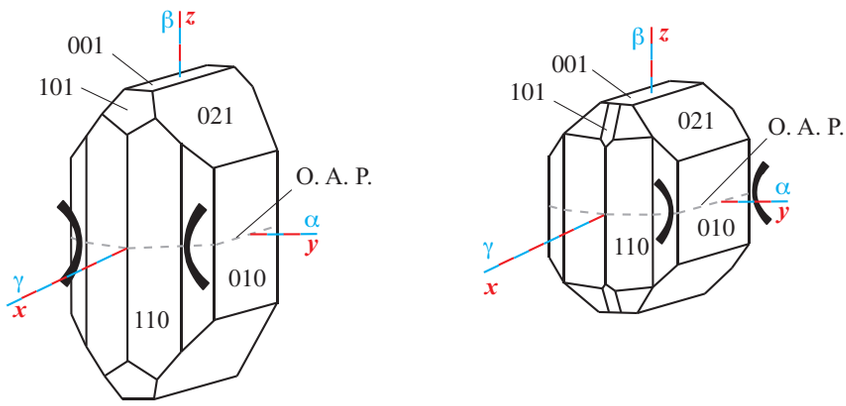


Subhedral olivine crystals enclosed poikilitically in a single large plagioclase crystal, feldspar peridotite, Rum, NW Scotland (crossed polars, scale bar 1 mm) (W.S. MacKenzie collection, courtesy of Pearson Education).

Downloaded from https://pubs.geoscienceworld.org/books/chapter-pdf/3751728/9780903056434_ch01.pdf
by guest

Orthorhombic (+)(−)

Forsterite Mg_2SiO_4 **Fayalite Fe_2SiO_4**



α[a]	1.635	1.827
β	1.651	1.869
γ	1.670	1.879
δ	0.035	0.052
$2V_\gamma$	82°	134°
Orientation	$\alpha = y$, $\beta = z$, $\gamma = x$ O.A.P. (001)	$\alpha = y$, $\beta = z$, $\gamma = x$ O.A.P. (001)
D (g/cm^3)	3.222	4.392
H	7	6½
Cleavage	{010}, {100}, imperfect	{010} moderate, {100} weak
Twinning	{011}, {012}, {031}	
Colour	Green, lemon-yellow; colourless in thin section	Pale yellow, greenish yellow, yellow-amber; pale yellow in thin section
Pleochroism		$\alpha = \gamma$ pale yellow β orange-yellow, reddish brown
Unit cell	*a* 4.75 Å, *b* 10.20 Å, *c* 5.98 Å Z = 4; space group *Pbnm*	*a* 4.82 Å, *b* 10.48 Å, *c* 6.09 Å Z = 4; space group *Pbnm*
Special features	Gelatinizes in HCl	

Olivine is a major constituent of many ultramafic and mafic igneous rocks and its Mg/Fe ratio decreases in the more evolved gabbros and basalts. In metamorphic rocks, both Mg-rich (forsterite) and iron-rich (fayalite) compositions occur, and it is found also in the progressive metamorphism of serpentinites. Its high relief, high birefringence and absence of a well developed cleavage are characteristic.

[a] Values of refractive indices, birefringence and 2V refer to end-members forsterite (Fo) and fayalite (Fa), between which there is continuous variation.

Downloaded from https://pubs.geoscienceworld.org/books/chapter-pdf/3751728/9780903056434_ch01.pdf
by guest

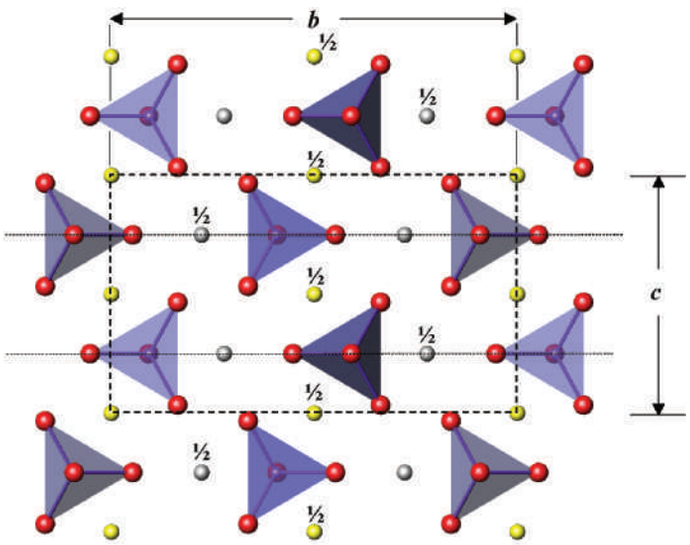


Fig. 1. Projection of the structure of olivine on the (100) plane. The Si atoms at the centres of tetrahedra are not shown (based on data from Bragg, W.L. & Brown, G.B., 1926, *Z. Krist*., **63**, 538–56. Fig. produced by M.D. Welch). Red: oxygens; blue: independent SiO_4 tetrahedra; gold: *M*1 cations at centres of symmetry; silver: *M*2 atoms on mirror planes.

Structure

The olivine structure is based on sheets of oxygen atoms parallel to (100) in a quasi hexagonal-close-packed arrangement and sequence ...ABABAB... (Fig. 1). The interstitial sites between the oxygen sheets are of two kinds such that the atoms occupying them are in either octahedral or tetrahedral coordination. In olivine, half of the available octahedral sites are occupied by M atoms (Mg,Fe) and one eighth of the tetrahedral sites by Si atoms. Each oxygen is bonded to one silicon and three (Mg,Fe) atoms. The M atoms do not occupy a single set of equivalent sites: half are located at centres of symmetry (*M*1) and half (*M*2) on mirror planes. A perspective view of the structure (Fig. 2) shows that approximately straight rows of edge-sharing (*M*1) octahedra lie parallel to *z*, and these are linked laterally by zigzag rows of (*M*2) octahedra and by isolated single Si tetrahedra, a feature which defines olivine as an ortho-silicate. It is worth noting here that very many silicate structures, when viewed in the appropriate direction, are seen to be based on quasi hexagonal- or cubic-close-packed layers of oxygen atoms, similar to those of Fig. 1, but with different partial occupation of the tetrahedral and octahedral interstices. The same applies to many oxides, and, with a change of anion, to sulphides and minerals with layers of other large anions.

The distribution of Mg^{2+} and Fe^{2+} in *M*1 and *M*2 sites shows varying degrees of ordering with Fe^{2+} cations commonly showing a slight preference for the smaller *M*1 site.

Cell parameters vary linearly with composition and olivine compositions are readily determined from X-ray powder diffraction data. The olivine series, perhaps better than any other rock-forming mineral series, approximates to an ideal binary solid solution.

At higher pressures, olivines adopt the denser structure of a spinel. For Mg_2SiO_4 the transformation to a disordered β-phase occurs at ~14.0 GPa at a temperature of 1000ºC. The transformation of the β-phase to a spinel-type structure (γ) occurs at ~17.0 GPa at the same temperature. The α–β transition is restricted to compositions with Mg/(Mg + Fe) ratios greater than 0.85. The effect of high pressure on more iron-rich olivine solid solutions is shown in Fig. 3.

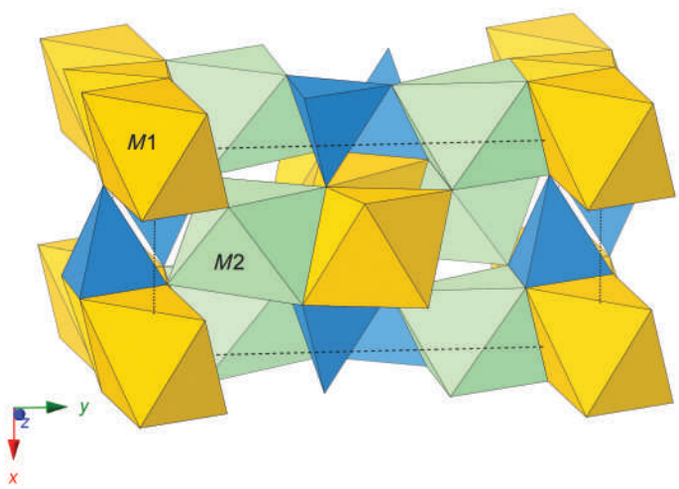


Fig. 2. Polyhedral model of the structure of olivine. Vertices of polyhedra represent oxygens, and polyhedra have at their centres: *M*1 (yellow), *M*2 (green) and Si (blue) sites (CrystalMaker image).

Downloaded from https://pubs.geoscienceworld.org/books/chapter-pdf/3751728/9780903056434_ch01.pdf
by guest

Phase changes in olivine-group minerals are of particular importance at the temperatures and pressures in the transition zone of the Earth's mantle, where they produce seismic discontinuities.

Chemistry

Olivines vary in composition from Mg_2SiO_4 (forsterite) to Fe_2SiO_4 (fayalite), there being complete solid solution between Mg^{2+} and Fe^{2+} in the structure (Table 1). The names forsterite and fayalite were at one time restricted by petrogaphers to the near end-member compositions Fo_{100-90} and Fo_{0-10}, and other names (chrysolite, hyalosiderite, hortonolite and ferrohortonolite) were used for intermediate compositions. These are now considered to be obsolete and modern texts use the 50% rule which defines forsterite as Fo_{100-50} and fayalite as Fo_{0-50}. In many natural crystals and particularly in more iron-rich olivines there is a little replacement of (Mg,Fe) by Mn and Ca. Nickel and chromium are commonly present in Mg-rich olivines, but the chromium occurs most commonly in minute exsolved plates of chromite. Some Fe^{3+} is usually present and similarly may be related to small exsolved grains of magnetite or more commonly to an oxidation product formed by alteration of the olivine. Relatively small amounts of calcium are present in the majority of olivines, the normal range being 0.0–1.0 wt.% CaO. Phosphorus in trace amounts (up to 400 ppm) occurs in some olivines, the charge balance being maintained by octahedral site vacancies.

The melting point of forsterite is 1890±20ºC. The melting point of forsterite under anhydrous conditions increases with pressure, and under water-saturated conditions decreases with pressure (Fig. 4a,b). The mineral, in addition to its occurrence in many experimental systems, has been synthesized in boules up to 3 cm in length, from stoichiometric mixtures of its oxides in the presence of water at temperatures as low as 500ºC and pressures between 0.013 and 0.266 GPa, and by solid-state reactions between MgO and SiO_2 at temperatures between 1100 and 1400ºC.

In the system Mg_2SiO_4–SiO_2 at atmospheric pressure (~0.1 MPa), forsterite reacts with the liquid to form protoenstatite at the peritectic point at about 1560ºC (Fig. 5). At higher pressure, enstatite melts congruently and forsterite and enstatite have a eutectic relationship; the eutectic liquids become less SiO_2-rich as the pressure increases. The pressure at which the peritectic reaction is replaced by a eutectic relationship cannot be applied directly to natural magmas since iron in olivine reduces and aluminium in enstatite increases the pressure.

The Mg–Fe olivines form a complete solid-solution series. The thermal behaviour of the series illustrates the effect on melting temperature in a solid-solution series of replacing an ion of smaller radius by one of larger radius. The cation–oxygen bonds are weaker for the larger cation of the same charge and as more of the larger cations enter the structure there is a progressive reduction in the melting points of intermediate compositions. Thus the first olivines to separate from a liquid of given composition are richer in Mg than those of later crystallization, and in consequence the larger Fe^{2+} ions are concentrated in the residual liquids. The heats of solution for forsterite and fayalite are a linear function of the molar composition, indicating a zero heat of isomorphous mixing and the maintenance of perfect thermal equilibrium during the replacement of Mg by Fe^{2+}.

Fayalite occurs as a stable phase in many synthetic systems, and has also been produced as large colourless crystals using ferrosilicon alloys or ferrous chloride and ethylorthosilicate as starting mixtures. Fayalite melts incongruently at 1205ºC at atmospheric pressure to a liquid plus iron.

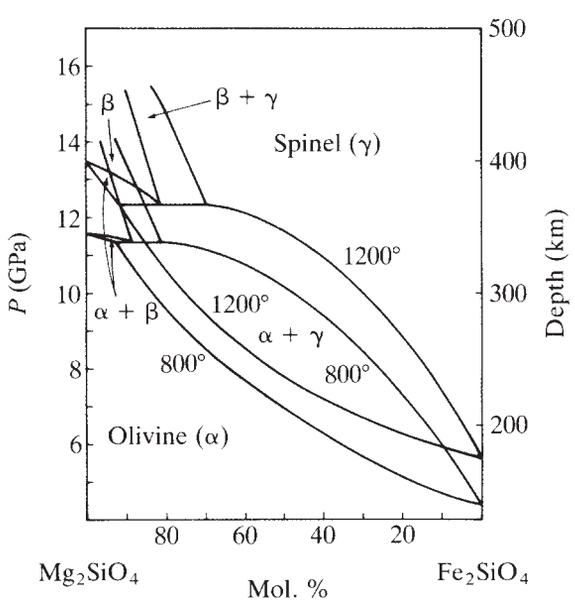


Fig. 3. The olivine–spinel transformation in the system Mg_2SiO_4–Fe_2SiO_4 at 800ºC and 1200ºC (after Akimoto, S. *et al*., 1976, Pp. 327–63 in *Physics and Chemistry of Minerals and Rocks*. R.G.J. Strens, editor, 327–63).

Downloaded from https://pubs.geoscienceworld.org/books/chapter-pdf/3751728/9780903056434_ch01.pdf
by guest

Table 1. Olivine group analyses.

	1		2		3		4		5		6	
SiO_2	41.85		32.47		30.09		31.50		29.27		36.63	
TiO_2	0.07		0.34		–		0.00		–		0.00	
Al_2O_3	0.00		0.02		0.00		0.04		–		0.07	
Fe_2O_3	–		0.18		–		–		–		–	
FeO	2.05		53.14		69.42		40.33		1.20		8.59	
MnO	0.21		0.73		0.28		26.09		65.23		0.44	
MgO	56.17		13.22		0.91		1.59		1.98		19.69	
CaO	0.00		0.00		0.08		0.05		2.32		34.17	
Total	100.35		100.10		100.78		99.66		100.00		99.61	
Numbers of ions on the basis of 4 O												
Si	0.988		0.997		1.003		1.038		0.974		0.997	
Al	0.000		0.001		0.000		0.001		–		0.002	
Ti	0.001		0.007		–		0.000		–		0.000	
Fe^{3+}	–		0.004		–		–		–		–	
Mg	1.976	2.02	0.602	2.00	0.046	1.99	0.078	1.92	0.098	2.05	0.815	2.02
Fe^{2+}	0.040		1.363		1.937		1.112		0.033		0.196	
Mn	0.004		0.018		0.008		0.728		1.838		0.010	
Ca	0.000		0.000		0.003		0.001		0.083		0.997	
Atomic percentages												
Mg	98.0		30.3		2.3		4.0		5.0		74.9	
Fe	2.0		68.7		97.3		58.0		1.7		19.2	
Mn	0.0		1.0		0.4		38.0		93.3		0.9	

1 Forsterite, serpentinite, Douglas Creek, South Island, New Zealand (Cooper, A.F., 1976, *J. Geol. Geophys. New Zealand*, **19**, 603–23).
2 Hortonolite, ferrodiorite, upper zone a, Skaergaard intrusion, East Greenland (Vincent, E.A., 1964, *Amer. Min.*, **49**, 805–6).
3 Fayalite, Gunflint Iron Formation, Minnesota-Ontario, USA (Floran, R.J. & Papike, J.J., 1978, *J. Petrol.*, **19**, 215–88).
4 Knebelite, metasomatized limestone, Blue Bell Mine, British Columbia, Canada (Mossman, D.J. & Pawson, D.J., 1976, *Can. Min.*, **14**, 479–86). Total Fe as FeO. Total includes K_2O 0.01, H_2O 0.05.
5 Tephroite, Benallt Mine, Caernarvonshire, Wales, UK (Smith, W.C. *et al.*, 1944, *Mineral. Mag.*, **27**, 33–46). Analysis recalculated.
6 Monticellite, alnöite, Talnakh, Russia (Nikishov, K.N. *et al.*, 1978, *Abstracts IMA XI Meeting, Novosibirsk*, 56–7). Total includes Cr_2O_3 0.02; average of five microprobe analyses.

Olivine is very susceptible to hydrothermal alteration, to the effects of weathering and to low-grade metamorphism. The products of alteration are varied, including serpentine-group minerals with or without nanograins of clays, iron oxides and chlorite-group minerals. If these minerals formed optically homogeneous, submicroscopic intergrowths, they were historically described using terms including "iddingsite", "bowlingite" and "chlorophaeite'.

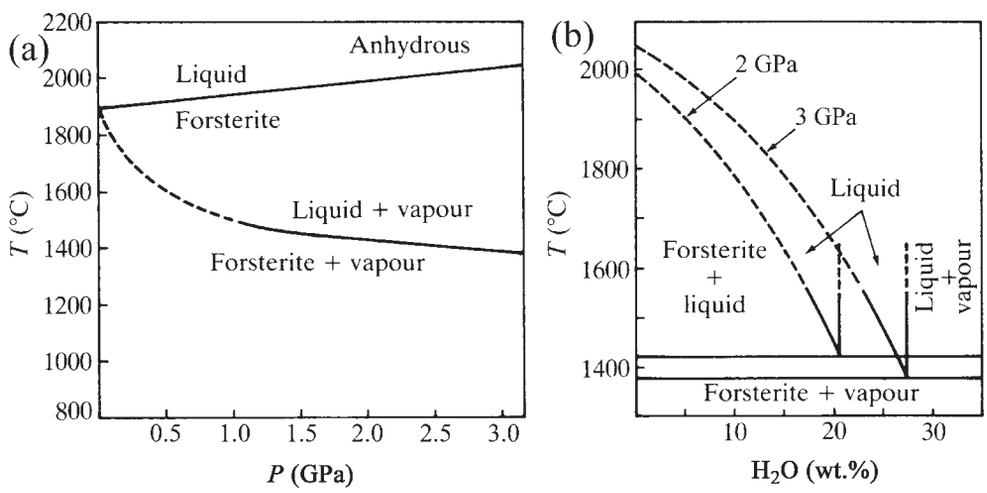


Fig. 4. (a) Melting curve of forsterite under anhydrous and water-saturated conditions (after Kushiro, I. & Yoder, H.S., 1969, *Carnegie Inst. Washington, Ann. Rept. Dir. Geophys. Lab., 1967–68*, 153). (b) Phase relations in the system Mg_2SiO_4–H_2O at 2 and 3 GPa (after Hodge, F.N., 1973, 1974, *ibid*, 1972–73, 495).

Downloaded from https://pubs.geoscienceworld.org/books/chapter-pdf/3751728/9780903056434_ch01.pdf
by guest

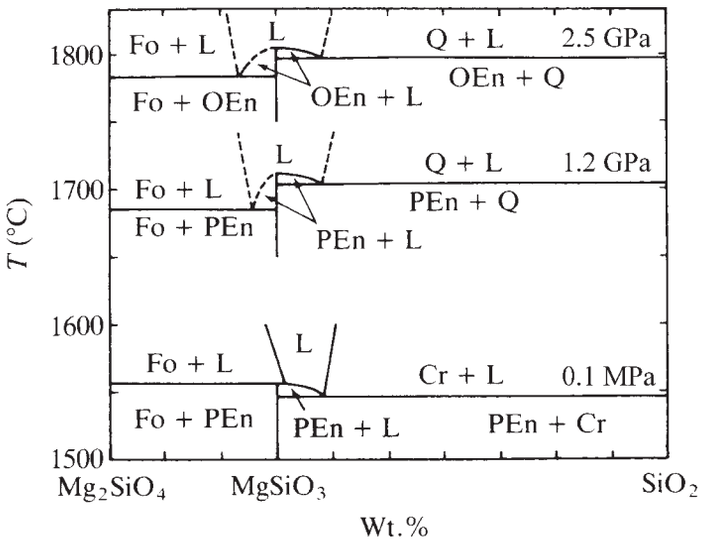


Fig. 5. Temperature-composition sections at 0.1 MPa, 1.2 and 2.5 GPa for the system Mg_2SiO_4–SiO_2 (after Chen, C.H. & Presnall, D.G., 1975, *Amer. Min.*, **60**, 398–406). Fo: forsterite; OEn: orthoenstatite; PEn: protoenstatite; Q: high quartz; Cr: cristobalite; L: liquid.

Iddingsite is reddish brown (R.I. ~1.76–1.89), and consists of smectite, chlorite and goethite/hematite. The alteration mechanism involves the diffusion of hydrogen ions into the olivine structure where their temporary attachment to oxygen ions releases Mg, Fe^{2+} and Si, thus permitting their replacement by Fe^{3+}, Al and Ca. Bowlingite is a green alteration product and consists of smectite-chlorite together with serpentine-group minerals and minor amounts of talc, mica and quartz. The relationship between iddingsite and bowlingite is essentially dependent on the oxidation state of iron (the green alteration product can be converted to brown by heating in air at 600ºC). Chlorophaeite does not differ greatly from iddingsite, it is more variable in colour, contains less Fe^{3+} and more Fe^{2+} and has a lower refractive index. It contains chlorite, smectite, goethite and calcite.

Serpentinization is the most widespread form of olivine alteration and the most common process of metamorphism in olivine-rich rocks (dunite and peridotite). The main alteration products, particularly of Mg-rich olivine, are the three serpentine polymorphs, lizardite, chrysotile and antigorite, together with brucite, talc and carbonates. Serpentinization may be expressed by the reactions:

$$\underset{\text{forsterite}}{2\,Mg_2SiO_4} + 3\,H_2O \rightleftharpoons \underset{\text{serpentine}}{Mg_3Si_2O_5(OH)_4} + \underset{\text{brucite}}{Mg(OH)_2} \quad (1)$$

$$3\,Mg_2SiO_4 + 4\,H_2O + SiO_2 \rightleftharpoons 2\,Mg_3Si_2O_5(OH)_4 \quad (2)$$

The reversibility of the first reaction has been demonstrated experimentally; P–T coordinates are approximately 375 and 425ºC at 0.2 and 0.6 GPa, respectively. In the presence of CO_2, talc and magnesite may also be formed:

$$\underset{\text{serpentine}}{2\,Mg_3Si_2O_5(OH)_4} + 3\,CO_2 \rightarrow \underset{\text{talc}}{Mg_3Si_4O_{10}(OH)_2} + \underset{\text{magnesite}}{3\,MgCO_3} + 3\,H_2O \quad (3)$$

and a further serpentinization reaction may be:

$$6\,Mg_2SiO_4 + Mg_3Si_4O_{10}(OH)_2 + 9\,H_2O \rightarrow 5\,Mg_3Si_2O_5(OH)_4 \quad (4)$$

The effect of Mg–Fe replacement on the equilibrium curve for reaction (1) is illustrated by the P–T curves defining the minimum thermal stability of Fo_{100} and Fo_{93} (Fig. 6).

Optical and physical properties

The refractive indices vary linearly with composition, both α and γ indices increasing by about 0.002 per mol% Fe_2SiO_4 (Fig. 7). The optic axial angle likewise varies systematically from $2V_\gamma$ 82º for Mg_2SiO_4 to $2V_\gamma$ 134º for Fe_2SiO_4, the sign changing at about Fa_{13}. Zoned olivines with less iron-rich cores and more iron-rich margins are common in some basic volcanic and hypabyssal rocks (compositional range Fa_{30}–Fa_{87} is reported). Zoning may be detected by differences in extinction angles in sections approximately perpendicular to an optic axis, i.e. sections showing low birefringence. Because of the rapid change in the partial birefringences γ–β and β–α, strongly zoned crystals display a marked variation in polarization colours. Olivines exhibit a number of different habits (equant, tabular, acicular and dendritic) that can in general be related to the inferred rate of cooling of the liquid during crystallization. The formation of elongated and dendritic olivines is displayed in komatiites and produces a spinifex texture in these remarkable volcanic rocks. Olivines, particularly in ultrabasic rocks, commonly display undulose extinction, faint translation lamellae (slip bands) and kink bands (due to inhomogeneous translation gliding).

Distinguishing features

Magnesium-rich olivine is distinguished from diopside by its poor cleavage, large optic axial angle and higher birefringence (Fig. 8). Chondrodite has lower refractive

Downloaded from https://pubs.geoscienceworld.org/books/chapter-pdf/3751728/9780903056434_ch01.pdf
by guest

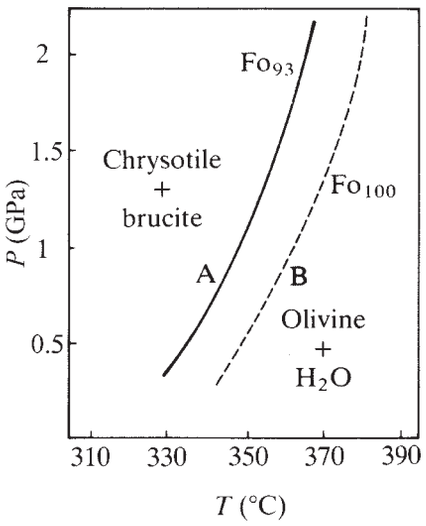


Fig. 6. Reaction curves (A) for $10\,(Mg_{1.86}Fe_{0.14})SiO_4 + 14.2\,H_2O = 5\,Mg_3Si_2O_5(OH)_4 + 3.8\,(Mg_{0.95}Fe_{0.05})(OH)_2 + 0.4\,Fe_3O_4 + 0.4\,H_2$ (after Moody, J.B., 1976, *Can. Min.*, **14**, 462–78) determined with iron–magnetite buffer and (B) for $2\,Mg_2SiO_4 + 3\,H_2O = Mg_3Si_2O_5(OH)_4 + Mg(OH)_2$ (after Johannes, W., 1968, *Contrib. Mineral. Petrol.*, **19**, 309–15).

indices, birefringence and oblique extinction; humite has a lower birefringence and optic axial angle. The optic axial plane in humite and clinohumite is parallel to the cleavage; monticellite has lower refractive indices and birefringence. Fayalite is distinguished from epidote by the yellow–green pleochroism, larger optic axial angle and oblique extinction of the latter.

Paragenesis

Olivine is a major constituent of dunite and peridotite and in these ultrabasic rocks varies in composition between Fo_{96} and Fo_{87} although it may be as iron-rich as Fo_{82} in some spinel lherzolites and garnet peridotites. In the ultramafic nodules in basalts and kimberlites, olivine compositions range between Fo_{91} and Fo_{86}. Olivines in the compositional range Fo_{80}–Fo_{50} are common constituents of gabbroic rocks. More iron-rich olivines occur in basic rocks but in general are restricted to ferrodiorites and mangerites, the olivines of which may extend to fayalitic compositions. Olivine occurs in a wide variety of volcanic rocks, both as phenocrysts and as a groundmass constituent. The most magnesium-rich compositions (Fo_{94}–Fo_{85}) occur in komatiite lavas, though olivine microphenocrysts, $Fo_{98.5}$ in composition, occur in the Kilbeinsay basalt on the extension of the Mid-Atlantic ridge between Iceland and Jan Mayen. The extremely low Fa content of this olivine is probably related to the very high oxidation state of the magmas at the time of primary crystallization, which resulted in depletion of Fe^{2+} in the liquid.

Iron-rich olivines occur in both alkaline and acid plutonic and hypabyssal rocks; they are relatively common and are usually associated with hedenbergite and arfvedsonitic amphiboles, in quartz syenites. Fayalite is present in arfvedsonite-fayalite-hedenbergite granites and in small amounts in many acid and alkaline

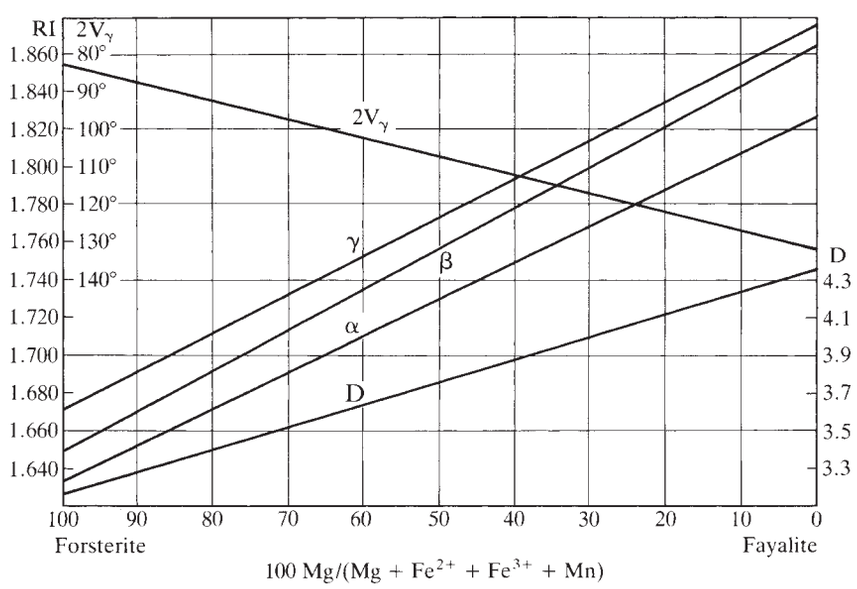


Fig. 7. Variation of optical properties and density with chemical composition in the (Mg,Fe)-olivines.

.

Downloaded from https://pubs.geoscienceworld.org/books/chapter-pdf/3751728/9780903056434_ch01.pdf
by guest

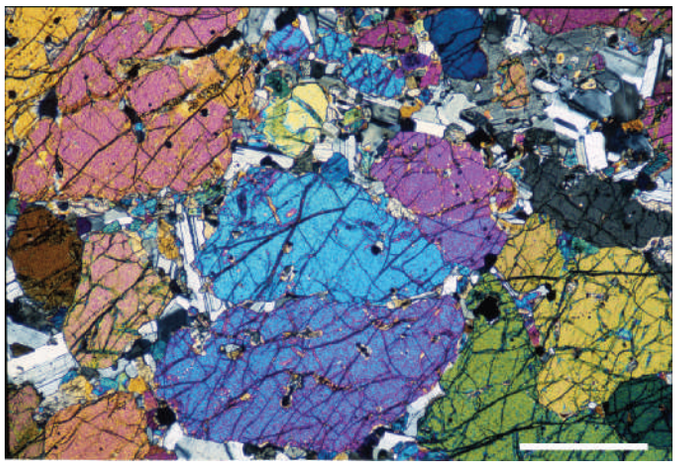


Fig. 8. Olivine in gabbro from the Skaergaard intrusion, East Greenland (crossed polars, scale bar 1 mm), showing mostly second order interference colours. The high relief and cracks in the crystals are characteristic (W.S. MacKenzie collection, courtesy of Pearson Education).

volcanic rocks, e.g. obsidians, rhyolites, trachytes and phonolites.

Olivines of metamorphic origin occur principally in rocks of ultramafic composition, in impure carbonates and in iron-rich sediments. Most of these olivines are either highly magnesium- or iron-rich. The most extensive development of olivine is found in the various mineral assemblages formed during the progressive metamorphism of serpentinites, by reactions such as:

$$\underset{\text{serpentine}}{5\,Mg_3Si_2O_5(OH)_4} + \underset{\text{diopside}}{2\,CaMgSi_2O_6} \rightarrow \underset{\text{forsterite}}{6\,Mg_2SiO_4} + \underset{\text{tremolite}}{Ca_2Mg_5Si_8O_{22}(OH)_2} + 9\,H_2O \quad (5)$$

$$\underset{\text{serpentine}}{5\,Mg_3Si_2O_5(OH)_4} \rightarrow \underset{\text{forsterite}}{6\,Mg_2SiO_4} + \underset{\text{talc}}{Mg_3Si_4O_{10}(OH)_2} + 9\,H_2O \quad (6)$$

$$\underset{\text{serpentine}}{Mg_3Si_2O_5(OH)_4} + \underset{\text{brucite}}{Mg(OH)_2} \rightarrow 2\,\underset{\text{forsterite}}{Mg_2SiO_4} + 3\,H_2O \quad (7)$$

An equilibrium temperature of about 485ºC has been calculated for reaction (5) at $P_{H_2O} = P_{total} = 0.2$ GPa. The formation of magnesium-rich olivines in metamorphosed impure carbonate sediments under anhydrous conditions is illustrated by the reaction:

$$2\,CaMg(CO_3)_2 + SiO_2 \rightarrow Mg_2SiO_4 + 2\,CaCO_3 + 2\,CO_2 \quad (8)$$

Under more hydrous conditions in which tremolite appears as a product of the metamorphism, olivine is formed by a reaction between the amphibole and dolomite:

$$Ca_2Mg_5Si_8O_{22}(OH)_2 + 11\,CaMg(CO_3)_2 \rightarrow 8\,Mg_2SiO_4 + 13\,CaCO_3 + 9\,CO_2 + H_2O \quad (9)$$

Fayalite, often associated with ferroan augite and grunerite, occurs in medium-grade thermally metamorphosed iron-rich sediments, and in rocks of more cherty composition. It is formed by the reaction:

$$2\,FeCO_3 + SiO_2 \rightarrow Fe_2SiO_4 + 2\,CO_2 \quad (10)$$

In many basic igneous rocks in high-grade metamorphic terranes, the olivine is surrounded by a number of successive shells consisting of various combinations of orthopyroxene, clinopyroxene, spinel, amphibole and garnet. Described as coronas, reaction rims, corrosion mantles and kelyphitic borders, these shells formed during cooling from subsolidus igneous temperatures at relatively high pressures.

Further reading

Boyd, F.R. and Nixon, P.H. (1978) Ultramafic nodules from the Kimberley pipes, South Africa. *Geochimica et Cosmochimica Acta*, **42**, 1367–1382.

Donaldson, C.H. (1976) An experimental investigation of olivine morphology. *Contributions to Mineralogy and Petrology*, **57**, 187–213.

Falloon, T.J., Ariskin, A., Green, D.H. and Ford, C.E. (2007) The application of olivine geothermometry to infer crystallization temperatures of parental liquids: implications for the temperature of MORB magmas. *Chemical Geology*, **241**, 207–233.

Faure, F., Schiano, P., Nicollet, C., Trolliard, G. and Soulestin, B. (2007) Textural evolution of polyhedral olivine experiencing rapid cooling rates. *Contributions to Mineralogy and Petrology*, **153**, 405–416.

Libourel, G., Boivin, P. and Biggar, G.M. (1989) The univariant curve liquid = forsterite + anorthite + diopside in the system CMAS at 1 bar, solid solutions and melt structure. *Contributions to Mineralogy and Petrology*, **102**, 406–421.

Morey, G.B., Papike, J.J., Smith, R.W. and Weiblen, P.W. (1972) Observations on the contact metamorphism of the Biwabik Iron-Formation, East Mesabi district, Minnesota. *Memoir of the Geological Society of America*, 225–264.

O'Driscoll, B., Donaldson, C.H., Troll, V.R., Jerram, D.A. and Emeleus, C.H. (2007) An origin for harrisite and granular olivine in the Rum Layered Suite, a crystal distribution study. *Journal of Petrology*, **48**, 253–270.

Downloaded from https://pubs.geoscienceworld.org/books/chapter-pdf/3751728/9780903056434_ch01.pdf
by guest

Tetragonal (+)

ω	1.922[a]–1.960
ε	1.961[a]–2.015
δ	0.042[a]–0.065
D (g/cm^3)	4.6[a]–4.7
H	7½
Cleavage	{110} imperfect, {111} poor
Twinning	Rare, on {111}; some zoning may occur
Colour	Reddish brown, yellow, grey, green or colourless; in thin section colourless to pale brown
Pleochroism	Very weak; in thick sections may show absorption ω < ε
Unit cell	*a* 6.62 Å, *c* 6.02 Å Z = 4; space group $I4_1/amd$
Special features	Slowly attacked by hot concentrated H_2SO_4

Zircon is a common accessory mineral in igneous rocks. Its hardness and poor cleavage make it an important detrital mineral in sedimentary rocks, commonly surviving more than one cycle of weathering and sedimentation. It can incorporate many elements (e.g. Nb, Hf, Ti, U, Pb and *REE*) in trace amounts and is the pre-eminent geochronometer using the radioactive decay of uranium to lead. Consideration of the Y and *REE* amounts and oxygen isotope composition can assist in the reconstruction of magmatic histories and assessments of the contribution of sediments and crust to magma sources.

Structure

In the zircon structure each silicon atom is tetrahedrally coordinated by four oxygen atoms at a distance of 1.62 Å, and each zirconium atom is coordinated by four oxygen atoms at 2.13 Å and four at a distance of 2.27 Å. The principal structural unit is a chain of alternating edge-sharing SiO_4 tetrahedra and ZrO_8 triangular dodecahedra extending parallel to the *z* axis (Fig. 9). This configuration leads to the prismatic habit and {110} cleavage of zircon and its extreme birefringence and optically positive character. Radiation produced by the small amounts of uranium and thorium that are commonly present in zircon causes breakdown of the crystal structure, which expands during amorphization.

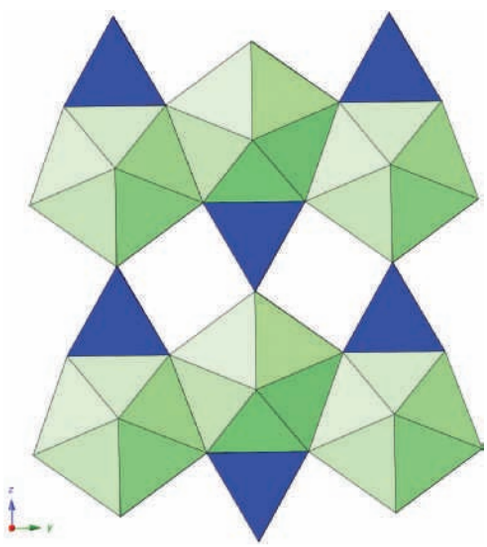


Fig. 9. Part of the structure of zircon projected on (100) with *z* vertical, showing chains of alternating edge-sharing SiO_4 tetrahedra (blue) and ZrO_8 dodecahedra (green) linked laterally by edge-sharing dodecahedra (CrystalMaker image).

[a] These values are for relatively fresh material; metamict zircon may have properties outside this range.

Downloaded from https://pubs.geoscienceworld.org/books/chapter-pdf/3752289/9780903056434_ch02.pdf
by guest

Chemistry

Zircon always contains some hafnium; the content normally being about 1 wt.% and the Hf/Zr ratio is around 0.02–0.04. This ratio tends to increase from around 0.015 for zircons in nepheline syenites to 0.04 for those in granites. Hafnium becomes increasingly enriched with increasing differentiation of the granite; hafnian zircon has been reported from pegmatites, and zoned crystals have been recognized in Mozambique, ranging from hafnian zircon to zirconian hafnon to end-member hafnon ($HfSiO_4$). Reidite is a high-pressure polymorph of zircon and has the scheelite ($CaWO_4$) structure; it occurs associated with shock-metamorphosed zircon in impactites, and in subducted slabs. Experimentally, the phase boundary between reidite and zircon at temperatures of 1000–1900 K occurs at ~9 GPa.

Analyses of zircons are quoted in Table 2. Phosphorus may be present in some varieties, probably replacing Si, the structure maintaining charge balance by the entry of rare earths (in zircon, the latter are dominantly of the yttrium group). Many zircons contain appreciable U and Th. For age determinations the Th/U ratio or the ratios of the various lead isotopes to each other or to isotopes of uranium or thorium are determined. There are many problems connected with the interpretation of discordant U/Pb data, one of them being chemical reactions involving migration of Pb and U. The capability of the ion microprobe to obtain age data from micrometre-size areas of a single grain of zircon in a thin section or grain mount can avoid areas with cracks or inclusions and make interpretation of the results more useful.

Zircon can be synthesized by sintering ZrO_2 and SiO_2 in air at high temperatures. The hydrothermal synthesis of zircon over the range 150–700ºC by heating gelatinous ZrO_2 and SiO_2 with water in steel pressure vessels has been reported. Metamict varieties of zircon can be converted to crystalline zircon by heating to 1000–1450ºC in many cases.

Optical and physical properties

The optical properties and density of zircon vary with the amount of iron and similar elements which may enter the structure and with the degree of amorphization. The reduction in birefringence is approximately proportional to the intensity of radioactivity (see Table 3). The metamict variety may show an appreciably biaxial character.

Zircon may be colourless or of varying shades of brown, yellow, green or even blue (usually after heat treatment), but in thin section it is typically colourless to pale brown, and may be weakly pleochroic in very thick sections. The dispersion is high and only slightly less than that of diamond. Gem varieties have received various names, jargoon being the colourless, slightly smoky or pale yellow zircon, and hyacinth the orange and reddish brown transparent variety. Metamict zircon is typically leaf-green to olive or brownish green in colour.

Table 2. Zircon analyses.

	1	2	3		Numbers of ions on the basis of 16 O 1	2	3
SiO_2	32.51	31.45	27.13	Si	4.013	4.000[a]	4.000[c]
ZrO_2	67.02	64.03	51.68	Zr + Hf	3.941	3.896	3.241
HfO_2		1.18		Al	0.030	0.081	0.016
TiO_2	–	0.04	tr.	Fe^{3+}	0.007	0.008	0.044
Al_2O_3	0.21	1.36	0.48	Mg	–	0.007	–
Fe_2O_3	0.08	0.09	0.45	Ca	0.030	0.017	–
RE_2O_3	0.04	1.18	10.51				
MgO	0.01	0.04	tr.	ω	1.950	1.922	–
CaO	0.22	0.13	tr.	ε	2.008	1.970	–
ThO_2	–	0.01	1.03	D	4.658	4.61	3.957
P_2O_5	–	–	3.37				
H_2O+	0.03	–	3.12				
H_2O-	–	0.17	0.32				
Total	100.12	99.81	99.84				

(4.01 = 0.030 + 0.007 + 0.030 + 0.017; 4.10[b] = 0.081 + 0.008 + 0.007 + 0.017; 4.10[d] = 0.016 + 0.044)

1 Dark red-brown zircon, North Burgess, Ontario, Canada (Palache, C. & Ellsworth, H.V., 1928, *Amer. Min.*, **13**, 384–9).
2 Zircon, China (Su, H-T. & Pan, T-M., 1973, *Geochimica*, **93**, 102). Includes Na_2O 0.13.
3 Greyish green to brown zircon, with allanite, fergusonite and thorogummite in pegmatite, Hayamadake, Fukishima Pref., Japan (Hasegawa, S., 1957, *Sci. Rept. Tohoku Univ.*, ser. 3, **5**, 345–71). Includes UO_2 1.75; $RE_2O_3 = Ce_2O_3$ 0.37, Y_2O_3 10.14.

[a] Includes Al 0.117.
[b] Includes Ti 0.004, *REE* 0.055, Na 0.031.
[c] Includes Al 0.058, P 0.375.
[d] Includes U^{4+} 0.058, Y 0.710, Ce 0.018, Th 0.031.

Downloaded from https://pubs.geoscienceworld.org/books/chapter-pdf/3752289/9780903056434_ch02.pdf
by guest

Table 3. Optical and physical properties of zircon.

	D (g/cm^3)	ω	ε	δ	Radioactivity
Normal zircon	4.6–4.7	1.924–1.934	1.970–1.977	0.036–0.053	Low
Intermediate	4.2–4.6	1.903–1.927	1.921–1.970	0.017–0.043	Medium
Metamict zircon	3.9–4.2	1.782–1.864	1.827–1.872	0–0.008	High

Distinguishing features

The straight extinction, high refractive indices and high birefringence of zircon are fairly characteristic and the commonly observable tetragonal form is an additional aid to identification. Cassiterite and rutile have higher refractive indices and birefringence, and are more typically reddish brown in thin section or in grains.

Paragenesis

Zircon is a common accessory mineral of igneous rocks, particularly in the plutonic rocks and especially those that are relatively rich in sodium. It is generally present as small early-formed crystals commonly enclosed in later minerals, but may form large well-developed crystals in granite pegmatites and particularly in those of nepheline syenites. If zircon is enclosed by biotite or amphibole or other coloured silicates, it may give rise to pleochroic haloes due to its content of radioactive elements. The size and morphological character of zircons, particularly their length/breadth ratio, may be closely similar throughout a body of magmatic granite, and it has been suggested that lack of such a relationship may indicate that an intrusion is complex. A study of zircon crystal habits has also revealed, however, that some rounding of zircon can take place in igneous rocks by magmatic resorption and that appreciable corrosion of the grains may be due to metasomatism.

Zircon is a common accessory mineral in many sediments, often surviving more than one cycle of weathering and sedimentation. It may be of use in correlating sandstones by their heavy mineral content. Zircon is also found, though less commonly, in rocks of hydrothermal origin.

Further reading

Correia Neves, J.M., Lopes Nunes, J.E. and Sahama, Th.G. (1974) High hafnium members of the zircon–hafnon series from the granite pegmatites of Zambezia. *Contributions to Mineralogy and Petrology*, **48**, 73–80.

Glass, S.P., Liu, S. and Leavens, P.B. (2002) Reidite: an impact-produced high pressure polymorph of zircon found in marine sediments. *American Mineralogist,* **87,** 562–565.

Hanchar, J.M. and Hoskin, P.W.O. (editors) (2003) *Zircon.* Reviews in Mineralogy & Geochemistry, **53**, Mineralogical Society of America and Geochemical Society, Washington, D.C., 500 pp.

Harley, S.L. and Kelly, N.M. (2007) Zircon: tiny but timely. *Elements*, **3**, 13–18 [This paper introduces six others on zircon in this issue].

Hoskin, P.W.O. (2005) Trace-element composition of hydrothermal zircon and the alteration of Hadean zircon from the Jack Hills, Australia. *Geochimica et Cosmochimica Acta*, **69**, 637–648.

Krogh, T.E. (1973) A low contamination method for hydrothermal decomposition of zircon and extraction of U and Pb for isotopic age determinations. *Geochimica et Cosmochimica Acta*, **37**, 485–494.

Mitchell, R.S. (1973) Metamict minerals: a review. *Mineralogical Record*, **4**, 177–182; 214–223.

Ono, S., Funakashi, K., Nakajima, Y., Tange, Y. and Katsura, T. (2004) Phase transition of zircon at high P–T conditions. *Contributions to Mineralogy and Petrology*, **147**, 505–509.

Robinson, K., Gibbs, G.V. and Ribbe, P.H. (1971) The structure of zircon: a comparison with garnet. *American Mineralogist*, **56**, 782–790.

Wang, X. and Griffen, W.L. (2004) Unusual Hf contents in metamorphic zircon from coesite-bearing eclogites of the Dabie Mountains, east-central China: implications for the dating of ultrahigh pressure metamorphism. *Journal of Metamorphic Geology*, **22**, 629–637.

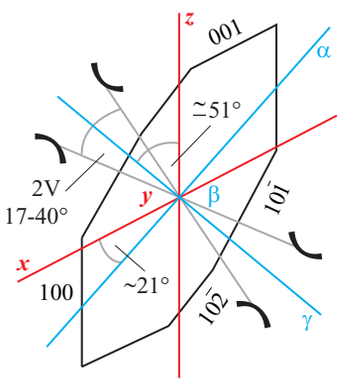
Whitehouse, M.J. (2003) Rare earth elements in zircon: a review of application and case studies from the Outer Hebridean Lewisian Complex, NW Scotland. Pp. 49–64 in: *Geochronology: Linking the Isotopic Record with Petrology and Textures* (D. Vance, W. Muller and I. Villa, editors). Special Publications, **220**. The Geological Society, London.

Downloaded from https://pubs.geoscienceworld.org/books/chapter-pdf/3752289/9780903056434_ch02.pdf
by guest

Titanite (Sphene) $CaTi[SiO_4](O,OH,F)$

Monoclinic (+)

α	1.843–1.950
β	1.870–2.034
γ	1.943–2.110
δ	0.100–0.192
$2V_\gamma$	17–40°
Orientation	γ:*z* ~ 51°, O.A.P. (010)
D (g/cm^3)	3.48–3.60
H	5
Cleavage	{110} good
Twinning	Single twins with twin plane {100}; occasional lamellar twinning on {221}
Colour	Colourless, yellow, green, brown, or black; colourless, yellow or typically brown in thin section
Pleochroism	Coloured varieties may be moderately pleochroic, e.g. α pale yellow, β brownish yellow, γ orange-brown
Unit cell[a]	*a* 7.07 Å, *b* 8.72 Å, *c* 6.57 Å, β 113.85° Z = 4; space group $P2_1/a$.
Special features	Decomposed by H_2SO_4.



Titanite is a widespread accessory mineral in igneous rocks, particularly those with an alkaline composition. It is common in Alpine-type veins, in gneisses and schists, and in calc-silicate rocks and skarns. Its sphenoidal crystal shape is characteristic; it is variable in colour but commonly black in hand specimen and brown with moderate pleochroism in thin section.

Structure

The dominant structural units in titanite are chains of corner-sharing TiO_6 octahedra running parallel to the *x* axis[a] (Fig. 10); these chains are cross-linked by SiO_4 tetrahedra sharing the remaining four oxygens. This produces a $[TiOSiO_4]^{2-}$ framework with large cavities enclosing Ca atoms in irregular seven-coordinated polyhedra. The polyhedra around the three different cations share edges and corners but not faces: an SiO_4 tetrahedron thus shares one of its edges with a CaO_7 polyhedron, and a TiO_6 octahedron shares four of its edges with CaO_7 polyhedra. The 20 oxygen atoms per unit cell occupy three different sites: one of these, O(1), is not bound in any of the SiO_4 groups and can be replaced by (OH,F). The substitution of $(Al + Fe^{3+})$ appears to favour a domain structure, the average

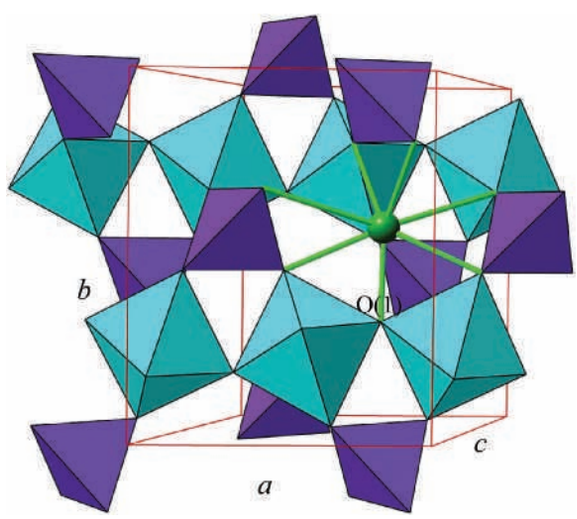


Fig. 10. The structure of titanite in perspective view, showing zigzag chains of Ti–O octahedra parallel to *x*, cross-linked by isolated Si–O tetrahedra. One of the Ca cations (green) is shown in its seven-coordinated site (CrystalMaker image).

[a] In this cell chosen for structure description *x* corresponds with *z* of the cell for morphology and optics.

Downloaded from https://pubs.geoscienceworld.org/books/chapter-pdf/3752334/9780903056434_ch03.pdf
by guest

symmetry of which becomes *A*2/*a*. Pure $CaTiSiO_5$ also changes to *A*2/*a* symmetry at ~220ºC, and there is a transition to *A*2/*a* at high pressure.

The tin silicate malayaite ($CaSnSiO_5$) is isostructural with titanite. For metamict titanite, the structure is normally fully restored after heating for several hours at 800ºC.

Chemistry

Recent analyses of titanite indicate that the chemical substitutions of primary importance are $(Al,Fe^{3+}) + (F,OH)^- \leftrightarrow Ti^{4+} + O^{2-}$. The total of $Al + Fe^{3+}$ is less than 30 mol%, usually with Al predominant. Detailed structural refinement of analysed specimens indicates that Al and Fe^{3+} occupy octahedral sites in natural titanites and that the rare earths substitute for Ca. The titanite analyses quoted in Table 4 have been recalculated on the basis of 4 Si in the unit cell, rather than on the more usual number of (O,OH,F) ions. The tetrahedral sites are filled with Si and after assigning Ti, Al and Fe^{3+} to fill the octahedral sites, excess Fe (as Fe^{2+}) is placed with Ca, Mg, Na, K, in the seven-coordinated site. The grothite variety of titanite contains appreciable iron and aluminium, whereas those varieties containing appreciable rare earths have been termed keilhauite or yttrotitanite. Titanites are commonly rich in trace elements, particularly those from late-stage granites and pegmatites: considerable amounts of niobium, tantalum and vanadium have been recorded. The occurrence of traces of the radioactive elements Th and U in titanite allows such samples to be used for age determinations; it may also lead to the development of metamict varieties.

Titanite has been prepared artificially by fusing its component oxides; it melts congruently at 1382ºC. In the system $CaAl_2Si_2O_8$–$CaTiSiO_5$ the eutectic composition is at 63% titanite, and the eutectic temperature is 1301ºC. The subsolidus relations of the $CaTiSiO_5$ (titanite)–$CaSnSiO_5$ (malayaite) join show complete solid solution at 700ºC and 0.1 GPa.

Alteration products of titanite include anatase, often together with quartz, or occasionally rutile.

Optical and physical properties

Data are insufficient to allow the relationship between optical properties and chemical composition to be fully determined, but in general a decrease in Ti causes the refractive indices and birefringence to decrease and 2V to increase; thus the grothite varieties, containing Fe^{3+}

Table 4. Titanite analyses.

	1	2	3		Numbers of ions on the basis of 4 Si 1		2		3	
SiO_2	30.44	31.28	29.32	Si	4.000		4.000		4.000	
TiO_2	39.66	33.33	35.26	Al	–		0.596		0.164	
RE_2O_3	0.37	1.06	4.51	Fe^{3+}	–		0.186	3.99	0.138	3.92
Al_2O_3	0.00	3.95	1.02	Ti	3.919		3.205		3.618	
Fe_2O_3	0.00	1.93	1.34	Mg	–		0.008		0.073	
FeO	0.14	–	1.05	Fe^{2+}	0.016		–		0.120	
MnO	0.05	0.00	0.03	Mn	0.005		–		0.003	
MgO	0.00	0.04	0.36	Na	0.094	4.02[a]	0.010	3.84	0.037	4.24[b]
CaO	27.20	27.85	25.72	*REE*	0.018		–		0.231	
Na_2O	0.37	0.04	0.14	Ca	3.829		3.816		3.760	
K_2O	0.00	0.03	0.07	K	–		0.005		0.012	
F	0.61	–	–	F	0.253		–		–	
H_2O+	0.56	1.31	0.64	OH	0.491		–		0.582	
H_2O-	0.08	–	0.18	O	19.83		19.83		20.02	
	'100.26'	100.82	99.74							
$-O \equiv F$	0.26	–	–							
Total	100.00	100.82	99.74							

1 Light reddish brown titanite, nepheline syenite, Kola Peninsula, Russia (Sahama, Th. G., 1946, *Bull. Comm. géol Finlande*, **24**, 88–120). Includes ZrO_2 0.11, Nb_2O_5 0.34, Ta_2O_5 0.01, SrO 0.32, V_2O_s 0.10; *REE* are La_2O_3 0.04, Ce_2O_3 0.12, Pr_2O_3 0.02, Nd_2O_3 0.08, Sm_2O_3 0.02 Gd_2O_3 0.02, $Dy_2O_3 < 0.01$, $Er_2O_3 < 0.01$, Y_2O_3 0.05.

2 Grothite, pumpellyite-actinolite-facies schists, Taveyanne formation, near Loèche, Valais, Switzerland (Coombs, D.S. *et al*., 1976, *J. Petrol*., **17**, 440–71).

3 Black titanite, pegmatite, Quoscescer, north-east of Harar, Ethiopia (Morgante, S., 1943, *Periodico Min*., *Roma*, **14**, 13–33). Includes ZrO_2 tr., P_2O_s 0.06, BaO 0.04; *RE* are Ce_2O_3 2.98, Y_2O_3 1.53.

[a] Includes Zr 0.007, Nb 0.020, Sr 0.024, V 0.008.
[b] Includes Ba 0.002.

Downloaded from https://pubs.geoscienceworld.org/books/chapter-pdf/3752334/9780903056434_ch03.pdf
by guest

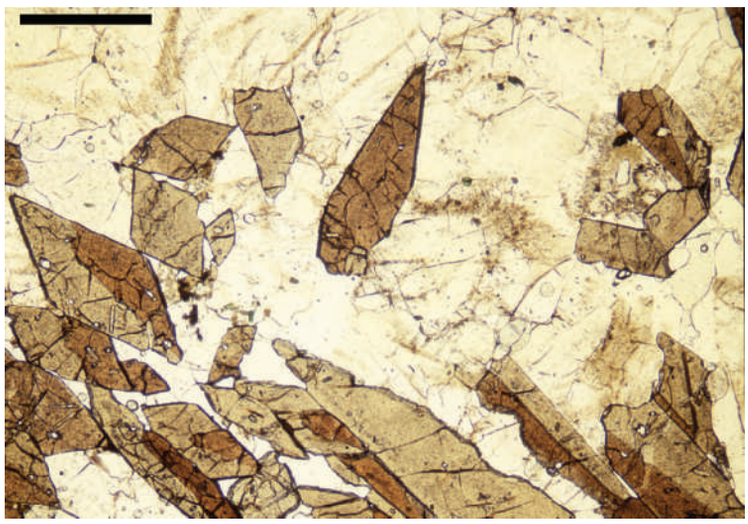


Fig. 11. Titanite in syenite, Kola Peninsula, Russia, (ppl, scale bar 1 mm), showing brownish crystals with high relief and characteristic sphenoidal shape. The crystals are pleochroic; simple twinning (e.g. mid-left and bottom right of figure) is common (W.S. MacKenzie collection, courtesy of Pearson Education).

and Al, usually have lower refractive indices and higher values of 2V. In general the colour can be correlated with the iron content: the green and yellow varieties contain little iron whereas the brown or black titanites may carry 1% or more Fe_2O_3; rare earths may cause an orange hue, though this is often masked by the iron coloration. The more usual yellow, brown or dark brown titanites are pleochroic in the greenish yellow to orange-brown range, with absorption $\alpha < \beta < \gamma$, though the pleochroism is commonly weak (Fig. 11).

Distinguishing features

The rhombic or sphenoidal cross-section of titanite is very characteristic. Its extreme refringence, birefringence and dispersion distinguish it from monazite and its monoclinic symmetry enables it to be distinguished from cassiterite.

Paragenesis

Titanite is a widespread accessory mineral in igneous rocks, and in many intermediate and acid plutonic rocks it is the dominant titanium-bearing mineral; it may be particularly abundant in some nepheline syenites (e.g. Table 4, analysis 1). It also occurs in low-temperature Alpine-type veins where it may be associated with adularia, albite and epidote. In metamorphic rocks it occurs chiefly in gneisses and schists rich in ferromagnesian minerals (Table 4, analysis 2), and it is fairly common in metamorphosed impure calc-silicate rocks and in skarns. In some sedimentary rocks titanite is found as detrital grains; where it is abundant it is possibly of authigenic origin. Malayaite, the tin analogue of titanite, typically occurs in skarns where Fe or Mg are low.

Further reading

Frost, B.R., Chamberlain, L.R. and Schumacher, J.C. (2001) Titanite (sphene) phase relations and role as a geochronometer. *Chemical Geology*, **172**, 131–148.

Higgins, J. and Ribbe, P.H. (1976) The crystal chemistry and space groups of natural and synthetic titanites. *American Mineralogist*, **61**, 878–888.

Kunz, M., Arlt, T. and Stolz, J. (2000) In situ powder diffraction study of titanite ($CaTiOSiO_4$) at high pressure and high temperature. *American Mineralogist*, **85**, 1465–1473.

Liou, J.G. and Bird, D.K. (1993) Al-Fe^{3+} and F-OH substitutions in titanite and constraints on their P-T dependence. *European Journal of Mineralogy*, **5**, 219–231.

Prowatke, S. and Klemme, S. (2005) Effect of melt composition on the partitioning of trace elements between titanite and silicate melt. *Geochimica et Cosmochimica Acta*, **69**, 695–709.

Tiepolo, M., Oberti, R. and Vanucci, R. (2002) Trace element incorporation in titanite: constraints from experimentally determined solid/liquid partition coefficients. *Chemical Geology*, **191**, 105–119.

Tropper, P., Manning, C.E. and Essene, E.J. (2001) The substitution of Al and F in titanite at high pressure and temperature: phase relations and solid solution properties. *Journal of Petrology*, **43**, 1787–1814.

Downloaded from https://pubs.geoscienceworld.org/books/chapter-pdf/3752334/9780903056434_ch03.pdf
by guest

Garnet Group

Cubic

	n[a]	D (g/cm^3)	a (Å)	
Pyrope	1.714	3.58	11.46	$Mg_3Al_2Si_3O_{12}$
Almandine	1.830	4.32	11.53	$Fe^{2+}_3Al_2Si_3O_{12}$
Spessartine	1.800	4.19	11.62	$Mn_3Al_2Si_3O_{12}$
Grossular	1.734	3.59	11.85	$Ca_3Al_2Si_3O_{12}$
Andradite	1.887	3.86	12.06	$Ca_3(Fe^{3+},Ti)_2Si_3O_{12}$
Uvarovite	1.865	3.83[b]	12.00	$Ca_3Cr_2Si_3O_{12}$
Hydrogrossular	1.734–1.675	3.59–3.13	11.85–12.16	$Ca_3Al_2Si_2O_8(SiO_4)_{1-x}(OH)_{4x}$

H	6–7½
Cleavage	None; {110} parting sometimes present; subconchoidal fracture
Twinning	Complex and sector twinning, and zoning, may be visible in birefringent varieties
Colour	Red, brown, black, green, yellow, pink or white; colourless, pink, yellow or brown in thin section
Unit cell	Z = 8; space group *Ia3d*
Special features	Soluble with difficulty in HF; hydrogrossular soluble in HCl or HNO_3

The minerals of the garnet group (general formula $X_3Y_2Si_3O_{12}$, major compositions within the group are listed above) are particularly characteristic of metamorphic rocks but are also found in some igneous types and as detrital grains in sediments. The group is subdivided into the species listed above, which represent the end-members of isomorphous series. A garnet corresponding in composition with any one end-member is rare, however, and names are assigned according to the dominant 'molecular' type present. The principal garnets can be sub-divided into two sets: the Ca garnets (grossular, andradite and uvarovite) and the (Mg,Fe,Mn) garnets (pyrope, almandine and spessartine). Experimental work has established that within each sub-group, pairs can show complete solid solution at moderate to high temperatures and pressures, and that across sub-groups, pairs such as grossular–pyrope, grossular–almandine and spessartine–uvarovite also show complete solid solution, but at higher pressures and temperatures. Hydrogrossular has been taken as the name for members of the series $Ca_3Al_2Si_3O_{12}$–$Ca_3Al_2(OH)_{12}$ with a composition between grossular and hibschite, $Ca_3Al_2(SiO_4)_{3-x}(OH)_{4x}$, with $x = 0.2–1.5$.

Structure

The unit cell of garnet contains eight $X_3Y_2Z_3O_{12}$ formula units where X and Y are di- and trivalent cations, respectively. The structure consists of alternating ZO_4 tetrahedra and YO_6 octahedra which share corners to form a three-dimensional network (Fig. 12). Within this, there are cavities that can be described as distorted cubes of eight oxygens which contain the X ions.

[a] Grossular, spessartine, andradite and uvarovite may show appreciable birefringence.
[b] With this exception the values tabulated are those obtained for pure synthetic end-member garnets.

The length of the cell edge within the garnet group is of considerable use as a diagnostic feature and one which is readily obtained. If it is assumed that the cell edge is an additive function of the molecular proportions of the end-members of the garnet group, formulae may be constructed enabling the cell edge to be related to the number and type of metal ions in the particular garnet 'molecule'. A combined form of equation covering the five main garnet molecules is given by

$$a\ (\text{Å}) = 9.04 + 1.61\,r(\text{X}) + 1.89\,r(\text{Y})$$

where r(X) and r(Y) are the mean radii of the X and Y cations.

Cell parameters for garnets with a wide range of r(X) and r(Y) values provide information on the role and size

Downloaded from https://pubs.geoscienceworld.org/books/chapter-pdf/3752401/9780903056434_ch04.pdf
by guest

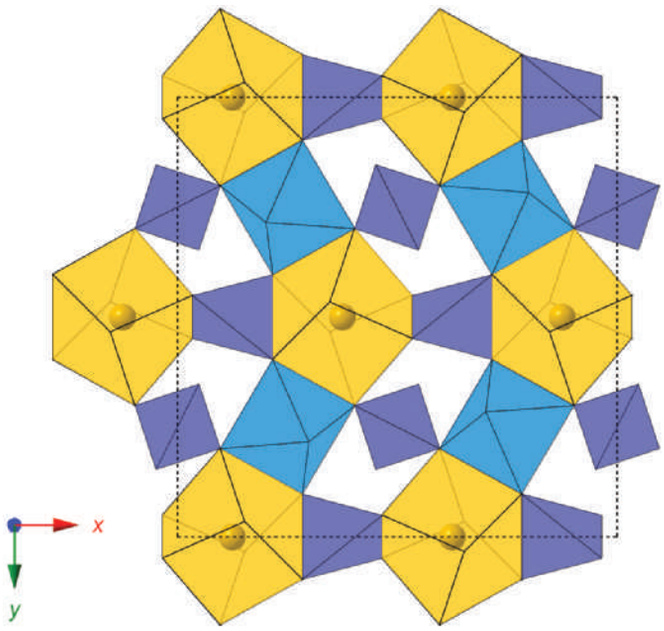


Fig. 12. A simplified version of an (001) slice of the garnet structure which has a framework of alternating tetrahedra (purple), octahedra (blue) and dodecahedra (approximating to distorted cubes; yellow), containing at their centres, (Si), trivalent (Y) and divalent (X) cations respectively. Shared oxygens (not shown) are at the corners of polyhedra, and links within and between successive slices form a three-dimensional framework. Tetrahedra are not linked directly to one another; thus garnet is an orthosilicate (CrystalMaker Image).

of the non-tetrahedral cations in determining structural 'stability'. Thus, making certain assumptions as to Si–O bond length (<1.66 Å), O–O distances of unshared octahedral edges (>2.68 Å) and the sizes of the octahedral and dodecahedral cavities, the 'stability' field for which compatible combinations of cations occur can be delineated (Fig. 13).

Chemistry

Although there are only six common garnet species, it is theoretically possible to have a total of 16 such species, each of the divalent metals Ca, Mg, Fe and Mn combining with trivalent Al, Fe, Mn and Cr (all with Si dominant in the tetrahedral position). Some of these have been described, though others would appear to be unlikely to occur in nature on geochemical grounds. Compositions containing $Mg_3Cr_2Si_3O_{12}$ (knorringite) are now recognized as an important constituent in some kimberlitic garnets. Substitutions which may take place in the garnet structure include Si by P and Al or Fe^{3+} by Ti. Pyrope garnets of ultra-high-pressure rocks (mainly garnet peridotites) may show small amounts of Al substitution by (Mg,Fe). In the hydrogarnets there is replacement of SiO_2 by $2\,H_2O$, with vacant Si spaces in the structure. Chemical analyses of six garnets are given in Table 5, their formulae are calculated on the basis of 24 O and also given as molecular proportions of their end-member components.

Pyrope garnets containing more than about 80% of the pyrope component are rare; the typical pyrope of high-grade metamorphic rocks contains around 40–70% of this molecule, the other components being chiefly almandine and subsidiary grossular. Pyrope garnets with Cr_2O_3 contents of 3–8% are common. Many such garnets have a characteristic greenish violet or purple hue and their common association with diamond-bearing kimberlites is considered to justify the name chrome-pyrope for this variety.

Direct synthesis of euhedral pyrope in the presence of water is possible at ~2.5 GPa and 1000ºC (the starting

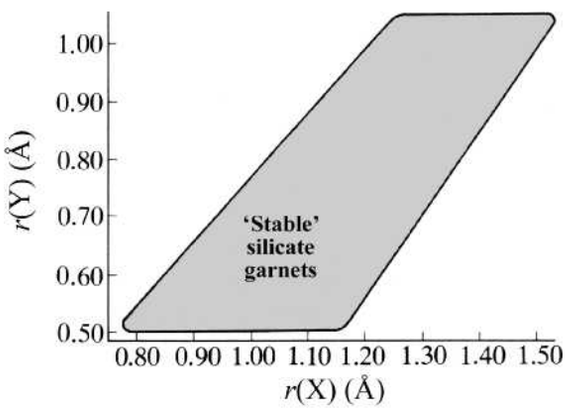


Fig. 13. Stability field for garnets from *r*(X) and *r*(Y) values (after Novak, G.A. and Gibbs, G.V., 1971, *Amer. Min.*, **56**, 791–825).

Downloaded from https://pubs.geoscienceworld.org/books/chapter-pdf/3752401/9780903056434_ch04.pdf
by guest

Table 5. Garnet analyses.

	1		2		3		4		5		6	
SiO_2	41.33		36.7		36.34		39.04		36.48		36.77	
TiO_2	0.28		0.75		0.10		0.12		0.50		–	
Al_2O_3	21.83		21.4		20.25		20.43		6.80		8.36	
Cr_2O_3	1.73		–		–		–		–		13.72	
Fe_2O_3	1.44		–		0.92		3.29		21.94		5.85	
FeO	9.00		29.9		7.30		1.81		3.33		–	
MnO	0.44		1.14		34.51		0.34		0.56		0.22	
MgO	19.60		0.90		tr.		0.73		0.00		0.27	
CaO	4.40		9.02		0.44		34.29		30.22		34.56	
Total	100.05		99.81		99.86		100.05		99.83		99.75	
Numbers of ions on the basis of 24 O												
Si	5.919	6.00	5.882	8.00	5.981	8.00	5.877	6.00	5.986	6.00	5.923	6.00
Al	0.081		0.118		0.019		0.123		0.014		0.077	
Al	3.604	3.99	3.925	4.02	3.909	4.04	3.502	3.89	1.311	4.08	1.510	3.97
Cr	0.196		–		–		–		–		1.747	
Fe^{3+}	0.155		–		0.114		0.373		2.709		0.709	
Ti	0.030		0.090		0.012		0.014		0.062		–	
Mg	4.184	5.99	0.215	5.93	–	5.89	0.164	5.97	–	5.85	0.065	6.06
Fe^{2+}	1.078		4.008		1.005		0.228		0.457		–	
Mn	0.053		0.155		4.811		0.043		0.078		0.030	
Ca	0.675		1.549		0.078		5.531		5.313		5.965	
Mol per cent end-members												
Almandine	17.4		67.4		17.1		3.8		7.8		–	
Andradite	3.4		–		1.3		9.4		69.5		18.0	
Grossular	2.5		26.3		–		81.6		21.4		36.2	
Pyrope	70.4		3.7		–		2.7		–		1.1	
Schorlomite	0.5		–		–		[a]		–		–	
Spessartine	0.9		2.6		81.6		0.7		1.3		0.5	
Uvarovite	4.9		–		–		–		–		44.2	

1 Pyrope, garnet-peridotite xenolith in kimberlite pipe, Matsoku, Lesotho, southern Africa (Carswell, D.A. & Dawson, J.B., 1970, *Contrib. Mineral. Petrol*., **25**, 163–84).

2 Almandine, chlorite-phengite-biotite-garnet-albite-quartz schist, Dora-Maira massif, western Italian Alps (Chatterjee, N.D., 1971, *Neues Jahrb. Min., Abhdl*., **114**, 181–215).

3 Spessartine, single crystal in green mica, Benson no. 4 Pegmatite, north Mtoko region, Zimbabwe (Hornung, G. & Knorring, O. von, 1962, *Trans. Geol. Soc. South Africa*, **65**, 153–80).

4 Cinnamon coloured grossular crystal, rodingite, altered gabbro, Hunting Hill quarry, Montgomery County, Maryland (Larrabee, D.M., 1969, *Bull. US Geol. Surv*., **1283**, 34 pp). Includes H_2O+ 0.36.

5 Andradite, hedenbergite-garnet-epidote-plagioclase skarn, Hallinmäki borehole, Virtasalmi area, eastern Finland (Hyvärinen, L., 1969, *Bull. Comm. géol. Finlande*, **240**, 82 pp). Includes Na_2O 0.03, K_2O 0.02, H_2O 0.06.

6 Uvarovite, quartz–albite–prehnite–uvarovite–pyrrhotite, contact zone with nordmarkite, Kalkoven, Grua, north of Oslo, Norway (Prestvik, T., 1974, *Norsk. Geol. Tidsskr*., **54**, 177–82).

[a] 1.7 hydrogrossular

material being the low-pressure assemblage cordierite + spinel + forsterite crystallized from a glass of pyrope composition at atmospheric pressure [0.1 MPa]).

Retrograde changes affecting pyrope may cause its breakdown to a mixture of hornblende, plagioclase and magnetite, sometimes in the form of a light green kelyphitic intergrowth.

Almandine is the most common species in the garnet group. Almandine garnets generally contain appreciable amounts of both the pyrope and spessartine end-members and may have important amounts of the grossular end-member; a typical composition for the garnet of garnet-mica schist of regional metamorphism might be $Alm_{66}Gro_{25}Py_5Sp_4$. It is now recognized that many uniformly coloured and isotropic almandines are nevertheless chemically zoned: for example, almandines of regional metamorphism may show an antipathetic relationship between Fe and Mn, the normal zoning pattern showing a manganese-rich core and an iron-rich rim. In other cases the cores may be rich in Ca and Mn and the rims richer in Fe and Mg. Garnets in rocks that have not experienced temperatures higher than about 600ºC may preserve growth zoning, generally characterized by increasing Mg/(Mg+Fe) from core to rim. In high-grade metamorphic rocks, diffusion can result in compositional homogenization and hence obliteration of growth zoning and, in slowly cooled rocks, the development of retrograde zoning at garnet rims in which Mg/(Mg+Fe) decreases rim-wards. A common alteration product of almandine is chlorite.

Downloaded from https://pubs.geoscienceworld.org/books/chapter-pdf/3752401/9780903056434_ch04.pdf
by guest

Spessartines have a wide range of composition; the main substituent is almandine but spessartines with an appreciable grossular component also occur, and it is evident that at moderate pressures there is virtually complete miscibility between these two end-members. The geochemical association of yttrium with manganese gives rise to occasional yttrian spessartines which may contain >2% Y_2O_3. The alteration and surface oxidation of spessartine gives rise to a mixture of black manganese oxides and hydroxides.

Synthetic spessartine is readily produced in the range 410−900ºC at 0.05−0.3 GPa P_{H_2O}, but at temperatures <600ºC it becomes increasingly hydrated. It melts at 1205ºC. Calderite, the Fe^{3+} analogue, $Mn_3Fe_2^{3+}Si_3O_{12}$, appears to be stable only at high pressures (>3 GPa).

Grossular very close to the end-member composition can occur; otherwise the predominant substitutional molecule is andradite, with which it forms a continuous series. Many garnets coloured green by chromium have been termed uvarovites when in reality their chromium content is relatively small and they are chromian grossulars. Despite the existence of the grossular–hydrogrossular series there is no evidence that the grossular typical of thermal metamorphism contains appreciable amounts of water.

Anhydrous grossular can be synthesized from glass of an appropriate composition at 800ºC and at water-vapour pressures as low as 0.2 GPa. In the system grossular–3 $CaO.Al_2O_3.6\,H_2O$, anhydrous grossular has been produced at 500ºC; at 0.1 GPa and above 850ºC it breaks down to wollastonite + gehlenite + anorthite.

Andradite containing more than 90% of the andradite 'molecule' is fairly common. The main solid-solution series, however, is that of andradite−grossular; many andradites in skarns show compositional (and colour) zoning, the alternating zones varying between nearly pure andradite and $And_{50}Gro_{50}$. Garnets intermediate between andradite and spessartine are also known. Andradites of primary origin in alkaline igneous rocks may contain appreciable amounts of titanium. Structural and experimental evidence indicates that the Ti is mainly in the octahedral site replacing Fe^{3+}, as the relative preference for the tetrahedral site (partially substituting for Si) must be in the order Al ⩾ Fe > Ti. Thus the name melanite is used for those titanian varieties of andradite with Fe^{3+} > Ti in the octahedral site whereas those with Fe^{3+} < Ti in this site are described as schorlomite (this division occurs at ~15 wt.% TiO_2).

Garnets containing vanadium as a major component have been reported; the vanadium analogue of grossular and andradite is goldmanite, $Ca_3V_2^{3+}Si_3O_{12}$. Zirconium occurs as a minor constituent in some titanian andradites. A garnet with Zr as a major component has been named kimzeyite; its ideal formula is $Ca_3Zr_2(Al_2Si)O_{12}$ with some Ti replacing Zr, and Fe^{3+} replacing Al.

Andradite has been synthesized from glasses and from its powdered components. It is stable above 550ºC (below this temperature a member of the andradite–hydroandradite solid solution may occur) and breaks down at above 1137ºC to pseudowollastonite and hematite. The mineral pair andradite−hedenbergite limit the range of oxygen fugacity (f_{O_2}) possible for their joint production under equilibrium conditions (Fig. 14).

Uvarovite is a member of the ugrandite series but garnets with uvarovite as the dominant molecule are relatively rare. It is chiefly the grossular molecule, with smaller amounts of andradite, which enters into solid solution with uvarovite (Table 5, analysis 6). It can be synthesized from its component oxides at 525ºC and 11 MPa and is stable up to 1370ºC. There is a complete solid solution with grossular below 855±5ºC at atmospheric (total) pressure.

Hydrogrossular has been taken as the name for members of the series $Ca_3Al_2Si_3O_{12}$–$Ca_3Al_2(OH)_{12}$ with a composition between grossular and hibschite $Ca_3Al_2(SiO_4)_{3-x}(OH)_{4x}$ where x is 0.2−1.5. Minerals in this compositional range have also been called hydrogarnet and katoite, the latter being more broadly defined to conform with the general formula $Ca_3Al_2(SiO_4)_{3-x}(OH)_{4x}$,

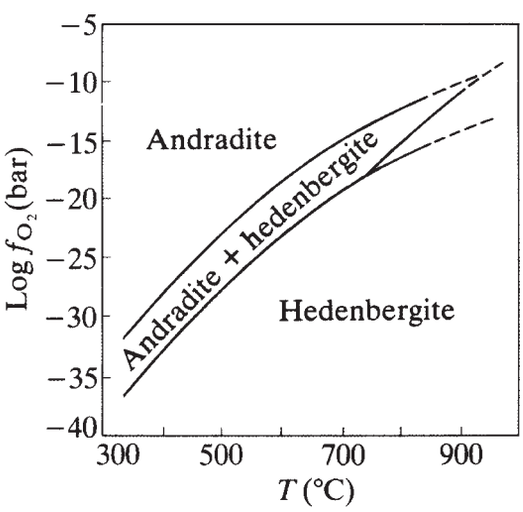


Fig. 14. Projections of log f_{O_2}−T stability range of pure andradite and pure hedenbergite at 0.2 GPa fluid pressure (after Gustafson, W.I., 1974, *J. Petrol.*, **15**, 455−96).

Downloaded from https://pubs.geoscienceworld.org/books/chapter-pdf/3752401/9780903056434_ch04.pdf
by guest

where $1.5 < x < 3.0$. Hydrogrossular is chemically less resistant than grossular, and is slowly soluble in HCl or HNO_3.

The complete series from grossular to $3\,CaO.Al_2O_3.6\,H_2O$ can be synthesized by the hydrothermal treatment of glasses of appropriate composition below 500ºC and 0.2 GPa.

Optical and physical properties

The synthesis of the major end-member garnet compositions has enabled the refractive indices, densities and cell edges to be established, and various diagrams have been constructed relating variation in physical properties with change in composition within the garnet group. Of the three common parameters (D, *n*, *a*), the density (D) is the least reliable because of the common occurrence of small inclusions of quartz or other minerals. The use of such diagrams is based on the assumption that the physical properties represented are linear additive functions of the molecular proportions of the end-members, and that components other than the five common end-member garnet molecules are relatively insignificant. In addition other data such as MnO or FeO content or a knowledge of the mineral associations or paragenesis may be necessary to estimate more completely and less ambiguously the composition of the garnet. Microprobe analysis is normally the most efficient method of determining the composition of a garnet.

Garnet is often thought of as the isotropic mineral *par excellence*, but although almandine and pyrope are usually isotropic (Fig. 15), spessartine may be weakly anisotropic and the ugrandite-series garnets commonly show marked optical anisotropy. Small crystals of andradite, grossular and uvarovite may be isotropic but weak birefringence is rather characteristic of large crystals of these species, all of which may also show a complex series of twins due probably to internal strain in the crystals. The type of twinning varies, commonly appearing as sector twins composed of 6, 12 or 24 pyramids with vertices meeting at the centre of the crystal; these sectors are commonly slightly biaxial. In the ugrandite series, zoning may also be visible; zoning and twinning are shown particularly well in the andradite of some contact metamorphic skarn deposits and examples are known with a 2V of 90º and a birefringence of 0.008. The temperature to which birefringent varieties of garnet have to be heated to lose the birefringence has been used as an indication of their crystallization temperature.

The garnets generally show well developed crystal forms, those occurring most commonly being rhombic dodecahedra or trapezohedra. A study of the relationship between morphology and composition is depicted in Fig. 16.

The colour of garnets is extremely variable, it is mainly controlled by the amounts of Fe, Mn (and Cr) present. Pyrope is typically pinkish red ranging from an almost crimson colour to a purplish shade (with the chrome-pyrope variety having a greenish violet to purplish hue). Almandine is commonly deep red to brownish black, and in thin section is colourless to pinkish red. Spessartine ranges from black to red, brown and orange. The hand-specimen colour of grossular is determined largely by the amount of Fe and Mn present; colourless, pink or yellowish green varieties are not uncommon. Hessonite is a name used for yellowish and brownish varieties; appreciable Cr imparts a vivid green colour to the mineral. Andradite ranges from yellowish to dark brown but the Ti-bearing varieties (melanite, schorlomite) are black in hand specimen and brown in thin section. Demantoid is a transparent yellow-green variety and topazolite is honey-yellow. Uvarovite is typically dark green to a vivid emerald green and is

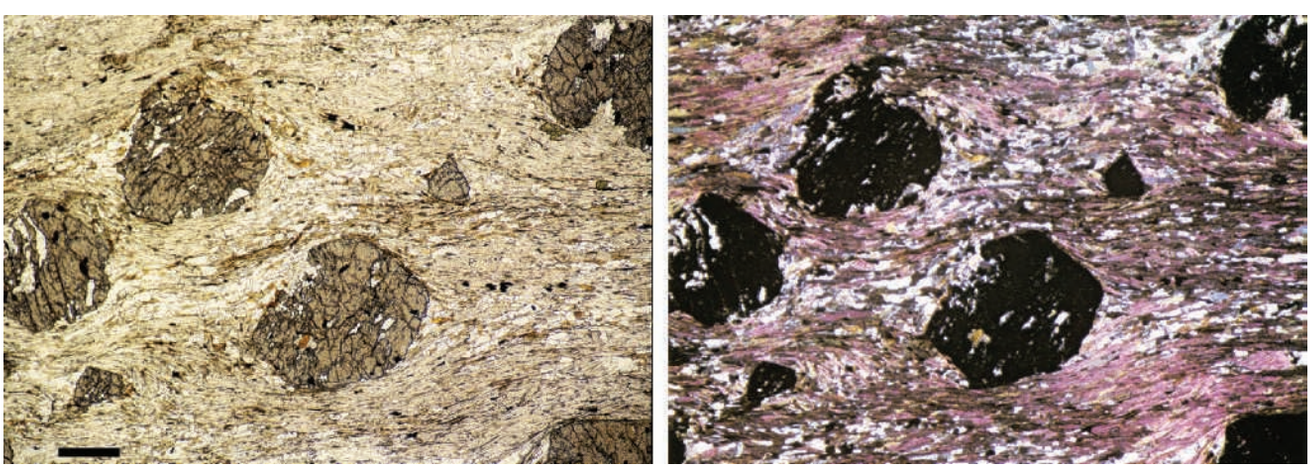


Fig. 15. (*left*) Subhedral brownish crystals of a garnet of the almandine series from Pitlochry, Scotland, showing high relief and abundant inclusions of the groundmass minerals (ppl, scale bar 1 mm). (*right*) Same view under crossed polars, showing this garnet to be isotropic with weakly birefringent inclusions (these are very common in garnets and must be avoided in analytical work) (W.S. MacKenzie collection, courtesy of Pearson Education).

Downloaded from https://pubs.geoscienceworld.org/books/chapter-pdf/3752401/9780903056434_ch04.pdf
by guest

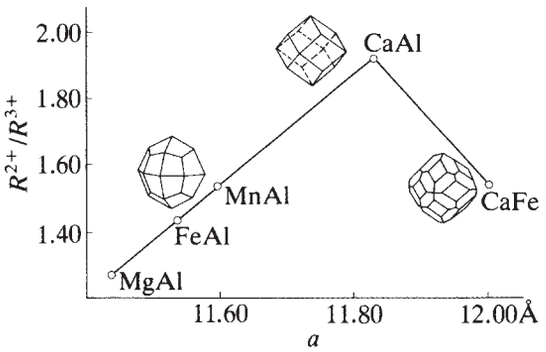


Fig. 16. Variation in habit of garnet crystals in relation to the cation ratio and cubic cell edge (after Kostov, I., 1968, *Mineralogy*, Oliver & Boyd).

green in thin section. Transparent garnets are commonly used as gemstones.

Distinguishing features

The high relief and isotropic or weakly birefringent nature of garnet is characteristic, with, in the birefringent varieties, zoning or sector twinning. Minerals of this group generally are less strongly coloured in thin section than the spinels, and lack the {111} cleavage seen in the latter. Within the garnet group the various species are best distinguished by their refractive indices, densities and cell edges, in conjunction, if possible, with partial chemical data, e.g. for FeO or MnO. Hydrogrossular has a lower refractive index than any of the natural anhydrous garnets.

Paragenesis

Garnet is especially characteristic of a wide variety of metamorphic rocks and is also found in some granites and pegmatites, acid volcanic rocks and kimberlites. As it is fairly resistant to weathering, it is commonly found in sediments; the commonest detrital varieties are almandine and pyrope, reflecting the abundance of these species in metamorphic (and igneous) rocks.

Pyrope garnet is the characteristic aluminous mineral of peridotites that have crystallized at high pressures, equivalent to upper mantle depths, and occurs in many orogenic peridotites and peridotite xenoliths in kimberlite. The well known Bohemian garnets of gem quality are pyrope and occur in the debris of a basaltic breccia derived from a peridotite. Pyrope is one of the most diagnostic tracer minerals used in prospecting for kimberlite. The garnets typically occur not as primary kimberlite minerals but as rounded isolated megacrysts within the kimberlite matrix and in blocks or xenoliths of garnet peridotites, garnet pyroxenites and eclogites.

In eclogites, which have garnet as an essential constituent, the pyrope content of the garnets has been used to distinguish three groups (Fig. 17). Inclusions of fassaite eclogite containing pyrope occur in basic breccia–nephelinite pipes at Delegate, New South Wales, and are considered to have crystallized in the range 0.7–1.5 GPa, 700–1200ºC, i.e. uppermost mantle or lowermost part of the crust.

Pyrope is a characteristic constituent of Mg,Al-rich metasediments of high metamorphic grade, where it coexists with minerals including sapphirine, spinel, orthopyroxene, cordierite, corundum, sillimanite, gedrite and biotite. The garnet is typically almandine–pyrope (e.g. $Alm_{46}Pyr_{54}$).

Virtually pure pyrope (Pyr_{90-98}), locally containing relict inclusions of the dense silica polymorph coesite,

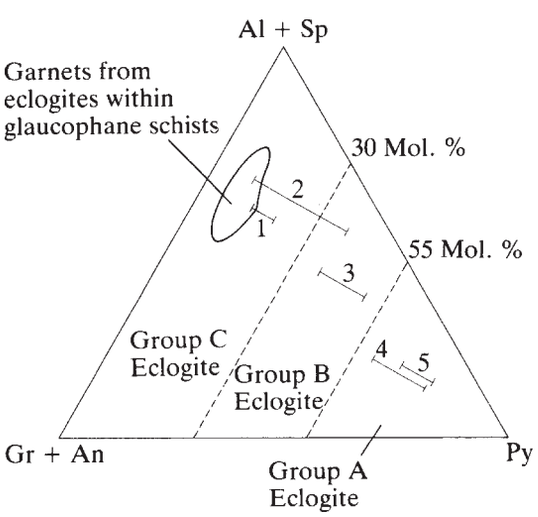


Fig. 17. The relative proportions of end-member 'molecules' for garnets in eclogites and related rock types. Dotted lines represent the range for the average garnets from: (1) amphibolites, (2) charnockites and granulites, (3) eclogites in gneisses or migmatitic terrain, (4) eclogites associated with kimberlite pipes, (5) eclogites within ultramafic rocks such as dunite and peridotite (after Coleman, R.G. *et al*., 1965, *Bull. Geol. Soc. Amer.*, **76**, 483–580).

Downloaded from https://pubs.geoscienceworld.org/books/chapter-pdf/3752401/9780903056434_ch04.pdf
by guest

Garnet geothermometry

The partitioning of elements between coexisting minerals when adequately calibrated can be of considerable use in geothermometry and for measuring the degree of chemical equilibrium. Thus the distribution of Mg and Fe between coexisting garnet and biotite can be considered in terms of equilibrium for the reaction:

$$\underset{\text{almandine}}{Fe_3Al_2Si_3O_{12}} + \underset{\text{phlogopite}}{KMg_3AlSi_3O_{10}(OH)_2} \rightleftharpoons \underset{\text{pyrope}}{Mg_3Al_2Si_3O_{12}} + \underset{\text{annite}}{KFe_3AlSi_3O_{10}(OH)_2}$$

The variation in the equilibrium constant $K_D{}^{\text{Gt/Bi}}_{\text{Mg/Fe}}$ for different metamorphic grades is shown in Fig. 18. Another useful mineral pair in this regard is garnet–clinopyroxene: the pressure–temperature dependence of the Fe–Mg distribution coefficient for this pair has been determined experimentally and can be expressed as:

$$T(\text{K}) = [3686 + 283.5P(\text{GPa})]/(\ln K_D + 2.33)$$

Later work developed this relationship to take account of the effect of Ca (see Nakamura, D., 2009).

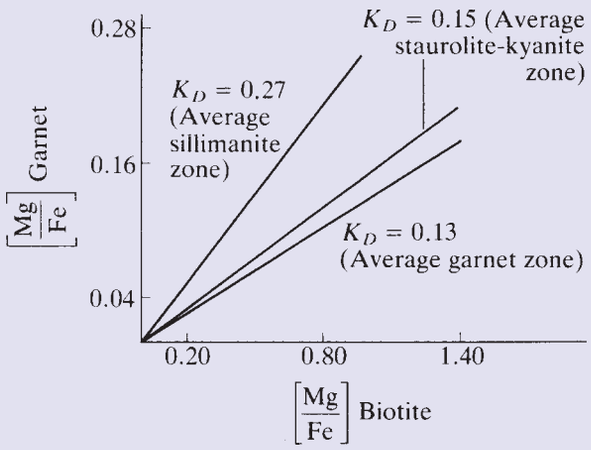


Fig. 18. Distribution of Mg/Fe^{2+} for garnet–biotite pairs from different metamorphic zones (after Baltatzis, E., 1979, *Mineral. Mag.*, **43**, 155–157).

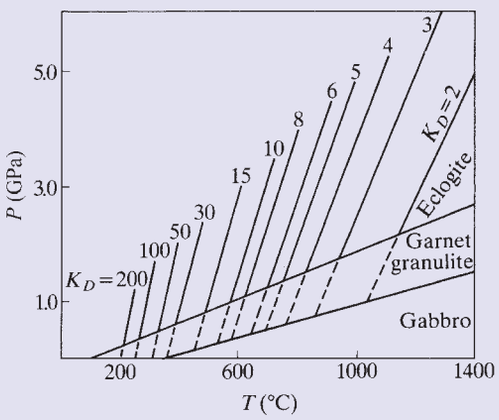


Fig. 19. $K_{D\text{Mg/Fe}}^{\text{Gt/Cpx}}$ as a function of pressure and temperature (after Råheim, A. & Green, D.H., 1974, *Contrib. Mineral. Petrol.*, **48**, 179–203).

The temperature of crystallization can thus be obtained from Fig. 19, if the K_D value is known and a pressure estimate can be made.

Many reactions involving garnet end-members are sensitive to pressure, particularly if low-density minerals such as anorthite or cordierite dominate the opposite side of the reaction, and many such equilibria have been calibrated as geobarometers. Examples applicable to metapelites include:

$$\underset{\text{in garnet}}{Ca_3Al_2Si_3O_{12}} + \underset{\text{sillimanite}}{Al_2SiO_5} + \underset{\text{quartz}}{SiO_2} \rightleftharpoons \underset{\text{in plagioclase}}{3\,CaAl_2Si_2O_8}$$

and:

$$\underset{\text{in garnet}}{2\,Fe_3Al_2Si_3O_{12}} + \underset{\text{sillimanite}}{4\,Al_2SiO_5} + \underset{\text{quartz}}{5\,SiO_2} \rightleftharpoons \underset{\text{in cordierite}}{3\,Fe_2Al_4Si_5O_{18}}$$

$$5\,\text{almandine} \rightleftharpoons 2\,\text{iron-cordierite} + 5\,\text{fayalite} + \text{hercynite}$$

Downloaded from https://pubs.geoscienceworld.org/books/chapter-pdf/3752401/9780903056434_ch04.pdf
by guest

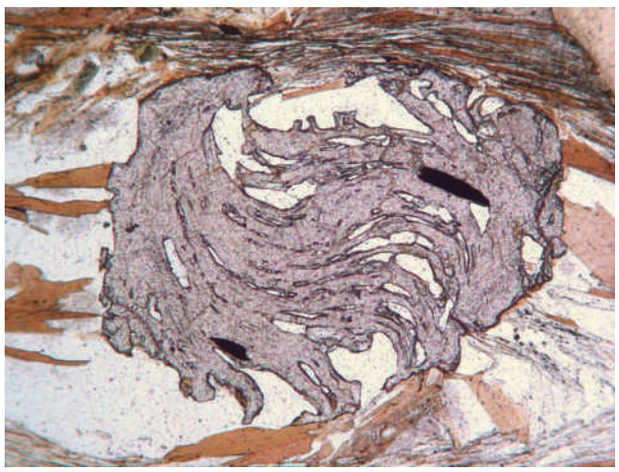


Fig. 20. Syn-tectonic garnet porphyroblast in a mica-schist. Note S-shaped trails of aligned elongated quartz and ilmenite inclusions, indicating rotation of the porphyroblast relative to its schistose matrix during growth. Field of view 2 mm across. Garnet-mica-schist, Perthshire, Scotland (courtesy of G.T.R. Droop).

coexists with kyanite, talc and phengite in a magnesian schist in orthogneiss of the Dora Maira Massif, Western Alps. This unusual occurrence is ascribed to a combination of metamorphism at ultra-high pressure ($\geqslant$3 GPa) and a protolith with a composition high in Mg and low in Fe (probably a sheared and metasomatically altered granitoid rock).

Chrome-pyrope is found in kimberlites and peridotitic xenoliths in peridotite and is also one of the two characteristic types of garnet found as inclusions in diamonds, leading to the recognition of a paragenetic relationship between diamonds and kimberlites and their peridotitic xenoliths.

Almandine is the typical garnet of the garnetiferous schists resulting from the regional metamorphism of argillaceous sediments and basic igneous rocks, and as such it is used as a zonal mineral in regions of progressive metamorphism of these rocks. In metapelites it commonly develops at the top of the biotite zone where it may be produced by reaction with chlorite, but in higher grades it may also be produced by the breakdown of mica to give garnet and K-feldspar and by the reaction of staurolite with quartz to give garnet together with kyanite or sillimanite. For Ca-poor garnets there appears to be a continuous variation of (FeO + MgO) against (CaO + MnO) with metamorphic grade. The increase in (FeO + MnO)/(CaO + MnO) is a useful indicator of increase in grade as also is the progressive decrease in cell edge of garnet. Euhedral almandine megacrysts commonly occur in the leucosomes of migmatites, and have been interpreted as the solid products of incongruent melting reactions. Porphyroblasts of garnet in metamorphic rocks may show inclusion trails of various shapes (e.g. straight, bowed, S-shaped, helicitic), allowing the relative timing of porphyroblast growth and plastic deformation to be determined (Fig. 20).

In rocks of the granulite facies, the garnets are typically almandine or more rarely almandine–pyrope. In Precambrian granulite terranes, a garnetiferous enderbite is probably the most common rock type, the garnets having the composition $Alm_{66-70}Pyr_{30-5}Gro + And_{5-20}Sp_{1-5}$. The Lewisian rocks of the Outer Hebrides include garnet granulites for which the application of activity–composition relations combined with thermodynamic data on three equilibria reactions gave an intersection (Fig. 21) indicating conditions of crystallization at 825ºC and 1.3 GPa; the equilibria involve the two assemblages indicated and

$$\underset{\text{clinopyroxene}}{3\,CaFeSi_2O_6} + \underset{\text{garnet}}{Mg_3Al_2Si_3O_{12}} \rightleftharpoons \underset{\text{garnet}}{Fe_3Al_2Si_3O_{12}} + \underset{\text{clinopyroxene}}{3\,CaMgSi_2O_6}$$

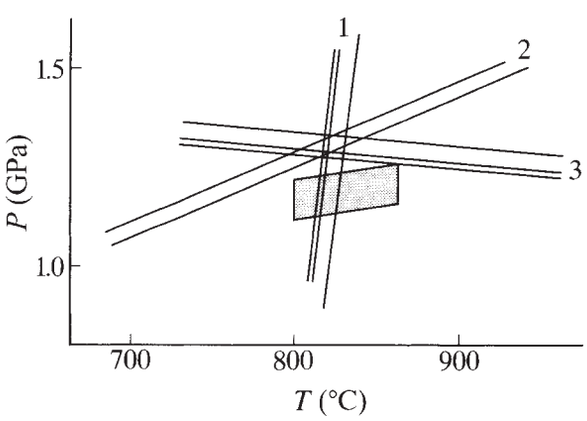


Fig. 21. Thermodynamic data for natural equilibrium assemblages from pyroxene granulites of South Harris, Scotland, derived from (1) Fe-Mg distribution between garnet and clinopyroxene; (2) the activity coefficient for the $Ca_3Al_2Si_3O_{12}$ component in garnet using the equilibrium $3\,CaAl_2Si_2O_8$ (plagioclase) $\rightleftharpoons$ $Ca_3Al_2Si_3O_{12} + 2\,Al_2SiO_5 + SiO_2$; (3) the activity coefficient for the equilibrium $CaAl_2Si_2O_8 \rightleftharpoons CaAl_2SiO_6$ (clinopyroxene) + SiO_2. The shaded area is the apparent region of 'bracketing' of metamorphic pressure and temperature derived from other equilibria (after Wood, B.J., 1975, *Earth Planet. Sci. Letters*, **26**, 299–31 and Wood, B.J., 1977, *Phil. Trans. Roy. Soc. London, A.*, **286**, 331–42).

Downloaded from https://pubs.geoscienceworld.org/books/chapter-pdf/3752401/9780903056434_ch04.pdf
by guest

The regional metamorphism of Precambrian banded iron formations in granulite facies conditions typically gives rise to an iron-rich silicate assemblage as in the eulysites of Sweden or collobrièrites of southern France. A banded iron formation with almandine-hedenbergite quartzites and rhodonite-garnet rock is associated with the Pb–Zn orebodies of Broken Hill, Australia. Here there are marked compositional variations in the original garnet compositions from one crystal to the next on a scale of 1–2 mm, and it is considered that these garnets have preserved for 1800 million years an original pattern of chemical banding.

In many blueschists the garnets which accompany glaucophane, epidote and lawsonite are typically calcic almandine–pyrope. In eclogites of groups A and B (Fig. 17) the garnet is in the almandine–pyrope range, typically near $Alm_{60}Py_{40}$. Although most garnets in inclusions in diamonds are chrome-pyrope, a group of them have compositions near $Alm_{40}Py_{35}Gro_{25}$.

Almandine may occur as a product of thermal metamorphism of pelitic rocks, but tends to be restricted to those aureoles which contain white mica rather than K-feldspar. Such almandines may have an appreciable spessartine component as well as pyrope (e.g. $Alm_{78}Py_{15}Sp_4Gro_3$). A typical assemblage might be a garnet-cordierite-orthopyroxene-plagioclase hornfels.

The presence of almandine garnets in igneous rocks is by no means rare. They occur in three different parageneses: late-stage minerals found in granitic aplites and pegmatites (generally an almandine–spessartine), accidental xenocrysts due to contamination by pelitic material, and as primary equilibrium phases in some calc-alkali granites and rhyolites (e.g. $Alm_{65}Py_{20}Gro_{10}Sp_5$).

Spessartine is less common than many of the garnet species. Although the spessartine component is present in significant amounts in the almandine found in granites and rhyolites and metamorphic rocks, it is rarely dominant in such environments. Garnets in which spessartine is the dominant component are found in some skarn deposits; they commonly occur in manganese-rich assemblages with rhodonite, pyroxmangite and tephroite of metasomatic origin associated either with adjacent igneous intrusions or with a more widespread regional metamorphism. In igneous rocks, spessartine is found mainly in granite pegmatites and aplites (e.g. Table 5, analysis 3).

Grossular is especially characteristic of both thermally and regionally metamorphosed impure calcareous rocks, and also occurs in rocks which have undergone calcium metasomatism. In contact metamorphism, for example, it occurs in metamorphosed marls or calcareous shales and is found in abundance in some skarns (though here the more typical garnet is andradite). Grossular is also known from zeolite-bearing vesicles in metamorphosed basaltic lavas and is sometimes found with diopside or scapolite resulting from pneumatolysis associated with granite pegmatites.

The occurrence of grossular as the result of regional metamorphism of impure limestone is less common than from contact metamorphism but it has been recorded in the almandine zone of metamorphism. In regional metamorphism grossular may be associated with vesuvianite + diopside. It is also found in serpentinites and in some rodingites.

Andradite typically occurs in contact or thermally metamorphosed impure calcareous rocks and particularly in the metasomatic skarn deposits often associated with such metamorphism. This involves the introduction of Fe_2O_3 ($\pm SiO_2$):

$$3\,CaCO_3 + Fe_2O_3 + 3\,SiO_2 \rightarrow Ca_3Fe_2Si_3O_{12} + 3\,CO_2$$

If FeO also is introduced, hedenbergite may form in addition to andradite, but if insufficient silica is present magnetite may form:

$$2\,Fe_2O_3 + 2\,FeO + 5\,SiO_2 + 4\,CaCO_3 \rightarrow Ca_3Fe_2Si_3O_{12} + CaFeSi_2O_6 + Fe_3O_4 + 4\,CO_2$$

giving the typical andradite-hedenbergite-magnetite skarn assemblage (Table 5, analysis 5). If SiO_2:Fe_2O_3 >3, wollastonite and andradite are produced.

Andradite also occurs as a result of metasomatism related to the thermal metamorphism of calcic igneous rocks such as andesites. The topazolite and demantoid varieties occur mainly in serpentinites and chlorite schists.

The titanian andradites melanite and schorlomite typically occur in an entirely different paragenesis, being found principally in alkaline igneous rocks such as nepheline syenite and ijolite and their volcanic equivalents phonolite and nephelinite. They are also known from skarn deposits.

Uvarovite is the rarest of the six common (anhydrous) species of the garnet group, and although the uvarovite molecule is known in association with grossular, the garnets with uvarovite as the dominant molecule are of restricted occurrence and are found chiefly in serpentinite, often in association with chromite, and in metamorphosed limestones and skarns. In such calcareous rocks the production of uvarovite appears to depend on the metasomatic introduction of Cr from basic or ultrabasic igneous rocks.

Hydrogrossular may be more common than has been realized; many of the garnets described as grossular may belong to this series. It occurs in metamorphosed marls and in altered gabbroic rocks and rodingites where a redistribution of calcium has taken place. It is also found in jade-like massive bands where metasomatic introduction of Ca has occurred, as in feldspar-bearing pyroxenite horizons in the Bushveld complex.

Further reading

Chmielova, M., Martinec, P. and Weiss, Z. (1997) Almandine-pyrope-grossular garnets: a method for estimating their composition using their X-ray powder diffraction patterns. *European Journal of Mineralogy*, **9**, 463–469.

Downloaded from https://pubs.geoscienceworld.org/books/chapter-pdf/3752401/9780903056434_ch04.pdf
by guest

Chopin, C. (1984) Coesite and pure pyrope in high grade blueschists of the Western Alps: a first record and some consequences. *Contributions to Mineralogy and Petrology*, **86,** 107–118.

Geiger, C.A. (2008) Silicate garnet. A micro- to macroscopic (re)view. *American Mineralogist*, **93**, 360–372.

Nakamura, D. (2009) A new formulation of garnet–clinopyroxene geothermometer based on accumulation and statistical analysis of a large experimental data set. *Journal of Metamorphic Geology*, 2009, **27**, 495–508.

Orlando, A. and Borrini, D. (2001) Solubility of Ti in andradite in upper mantle conditions: preliminary result. *Periodico Mineralogia, Roma*, **70**, 99–110.

Rodeorst, U., Geiger, C.A. and Armbruster, T. (2002) The crystal structure of grossular and spessartine between 100 and 600 K and the crystal chemistry of grossular–spessartine solid solutions. *American Mineralogist*, **87**, 542–549.

Stahl, G. and Rossman, G.R. (2000) Single crystal and UV/VIS-spectroscopic measurements on transition metal bearing pyrope: the incorporation of hydroxide in garnet. *European Journal of Mineralogy*, **12**, 259–271.

Stanton, R.L. and Williams, K.L. (1978) Garnet compositions at Broken Hill, New South Wales, as indicators of metamorphic processes. *Journal of Petrology*, **19**, 514–529.

Woodland, A.B., Droop, G. and O'Neill, H.St.C. (1995) Almandine-rich garnet from near Collobrières, southern France, and its petrology. *European Journal of Mineralogy*, **7**, 187–194.

Downloaded from https://pubs.geoscienceworld.org/books/chapter-pdf/3752401/9780903056434_ch04.pdf
by guest

Vesuvianite (Idocrase) $Ca_{19}(Al,Fe)_{10}(Mg,Fe)_3[Si_2O_7]_4[SiO_4]_{10}(O,OH,F)_{10}$

Tetragonal (−)

ε	1.700−1.746
ω	1.703−1.752
δ	0.001−0.009
D (g/cm^3)	3.32−3.34
H	6−7
Cleavage	{110} poor, {100} and {001} very poor
Colour	Yellow, green, brown, more rarely red or blue; colourless to pale yellow, green, brown or pinkish brown in thin section
Pleochroism	Coloured varieties may show weak pleochroism, e.g. brownish yellow to yellowish brown
Unit cell	*a* 15.4−15.6 Å, *c* 11.8 Å Z = 2; space group *P4/nnc*
Special features	Varieties with low birefringence may show anomalous interference colours in brilliant blues or brown. Optically positive and biaxial varieties are also known.

Brown or green vesuvianite is a common mineral in skarns and contact metamorphosed limestones, where it may occur with garnet and diopside. Its composition and structure resemble those of grossular–andradite. Recent work has shown it to have a complex phase chemistry.

The structure of vesuvianite is somewhat similar to that of grossular garnet: the *c* lattice parameter of vesuvianite is approximately equal to the *a* lattice parameter of grossular and certain structural elements are common to both minerals. In vesuvianite eight of the 18 Si atoms in the formula unit form Si_2O_7 groups, and the other ten form independent SiO_4 tetrahedra.

Chemical analyses, X-ray diffraction and data on the thermal stability of vesuvianite indicate a formula based on 78 anions per formula unit. In addition to the major elements, appreciable Ti and Mn are commonly present and minor amounts of Be, Cu, Zn or B have been recorded. The hydrothermal synthesis of vesuvianite shows that it is stable at temperatures as low as 360ºC at 50 MPa and remains stable up to 800ºC and 1 GPa (Fig. 22). At lower temperatures, hydrogrossular and hydrated calc-silicates such as xonotlite are the stable phases, at higher temperatures, diopside. Grossular may appear at the high-temperature boundary ± wollasonite, monticellite and melilite.

The refractive indices of vesuvianite in general increase with increasing amounts of titanium and iron. The birefringence falls with increase in (OH) content. In some vesuvianites the decrease in birefringence (and in the ε index) is sufficient to make them virtually isotropic or even optically positive as in the variety wiluite. Vesuvianite with such low birefringence may be optically positive at one wavelength and negative at another, and in white light may exhibit anomalous birefringence colours; an intense 'Berlin' blue is commonly seen which is quite distinct from the blue of Newton's scale. The colour of vesuvianite appears to be controlled mainly by the amount and state of oxidation of the iron or titanium present; the Cu-bearing variety cyprine is blue or greenish blue. A compact olive-green variety has been termed californite and some so-called 'Transvaal-jade' has been shown to be vesuvianite rather than hydrogrossular.

The tetragonal form, high relief and low refringence of vesuvianite are characteristic, though the distinction from grossular or hydrogrossular may be difficult.

The principal mode of occurrence of vesuvianite is in contact metamorphosed limestones, where it is commonly associated with garnet, diopside and wollastonite; it is common in skarns. It is also found in regionally metamorphosed impure limestones and appears to be stable over a wide range of metamorphic temperatures (Fig. 22). Vesuvianite is also found in nepheline-syenites and in veins associated with mafic rocks and serpentinites and in garnetized gabbros (rodingites).

Downloaded from https://pubs.geoscienceworld.org/books/chapter-pdf/3752918/9780903056434_ch05.pdf
by guest

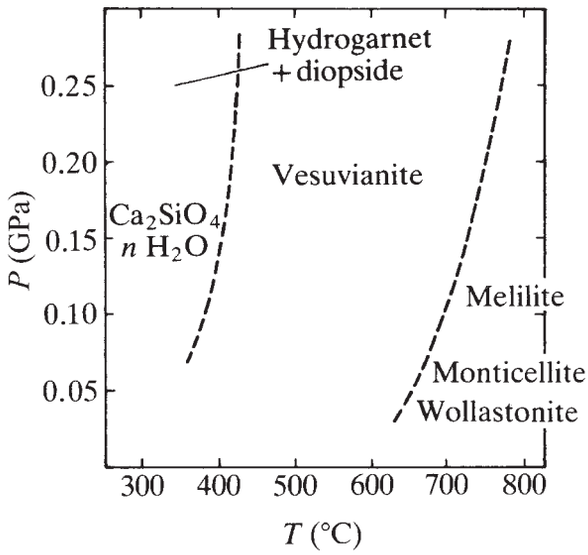


Fig. 22. The pressure–temperature diagram for synthetic vesuvianite in pure water and an alkali-free environment (after Ito, J. & Arem, J.E., 1970, *Amer. Min*., **55**, 880–921).

Further reading

Armbruster, T. and Gnos, E. (2000) 'Rod' type polytypism in vesuvianite: crystal structure of a low-temperature *P*4*nc* vesuvianite with pronounced octahedral cation ordering. *Schweizerische Mineralogische und Petrographische Mitteilungen*, **80**, 109–116.

Ahmed-Said, Y. and Leake, B.E. (1996) The conditions of metamorphism of a grossular-vesuvianite skarn from the Omey granite, Connemara, western Ireland with special reference to the chemistry of vesuvianite. *Mineralogical Magazine*, **60**, 541–550.

Galuskin, E.V., Armbruster, T., Malsy, A., Galuskina, I.O. and Sitarz, M. (2003) Morphology, composition and structure of low-temperature *P*4/*nnc* high-fluorine vesuvianite whiskers from Polar Yakutia, Russia. *The Canadian Mineralogist*, **41**, 843–856.

Groat, L.A., Hawthorne, F.C., Ercit, T.S. and Grice, J.D. (1998) Wiluite, $Ca_{19}(Al,Mg,Fe,Ti)_{13}(B,Al,\square)_5Si_{18}O_{68}(O,OH)_{10}$, a new mineral species isostructural with vesuvianite, from the Sakha Republic, Russian Federation. *The Canadian Mineralogist*, **36**, 1301–1304.

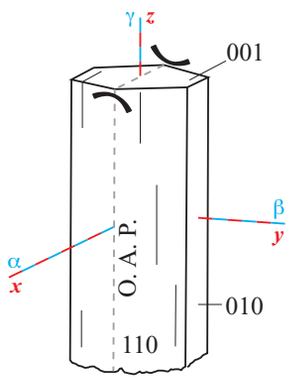
Pavese, A., Prencipe, M., Tribaudino, M. and Aagard, S.S. (1998) X-ray and neutron single-crystal study of *P*4/*n* vesuvianite. *The Canadian Mineralogist*, **36**, 1029–1037.

Tanaka, T., Akizuki, M. and Kudoh, Y. (2002) Optical properties and crystal structure of triclinic growth sectors in vesuvianite. *Mineralogical Magazine*, **66**, 261–274.

Downloaded from https://pubs.geoscienceworld.org/books/chapter-pdf/3752918/9780903056434_ch05.pdf
by guest

Orthorhombic (+)

α	1.653–1.661
β	1.657–1.662
γ	1.672–1.683
δ	0.018–0.022
$2V_\gamma$	21–30°
Orientation	α = *x*, β = y, γ = z; O.A.P. (010) $Bx_a \perp$ (001)
D (g/cm^3)	3.23–3.27
H	6½–7½
Cleavage	{010} good, uneven transverse fractures
Colour	Normally colourless or white, also yellow, brown, greyish green, bluish green; colourless in thin section
Pleochroism	In thick sections coloured varieties may be pleochroic with α pale brown or pale yellow, β brown or greenish, γ dark brown or blue
Unit cell	*a* 7.48 Å, *b* 7.67 Å, *c* 5.77 Å; *V* 331 $Å^3$ Z = 4; space group *Pbnm*



Sillimanite is a high-temperature polymorph of Al_2SiO_5 and occurs as colourless or white acicular to fibrous crystals in high grade metamorphosed pelitic rocks. It has high relief and straight extinction.

Structure

Sillimanite has a structure consisting of chains of edge-sharing aluminium–oxygen octahedra parallel to the *z* axis (Fig. 23). The lateral linkage between octahedral chains is made by a double chain containing alternate Si and Al in tetrahedral coordination. The Al in sillimanite is thus half in octahedral coordination with an Al–O distance of 1.91 Å, and half in tetrahedral coordination with an Al–O distance of 1.77 Å. The Si–O tetrahedra do not share oxygens with other Si–O tetrahedra. The arrangements of chains of octahedra in the three Al_2SiO_5 polymorphs are illustrated in Fig. 24.

Chemistry

The composition is fairly constant and relatively close to pure Al_2SiO_5. The most common ion replacing Al in the structure is Fe^{3+} (Table 7, p. 37); the small amounts of other elements that have been reported probably represent impurities. Small amounts of absorbed and entrapped water are commonly found in the fibrous mass of crystals developed in the variety fibrolite.

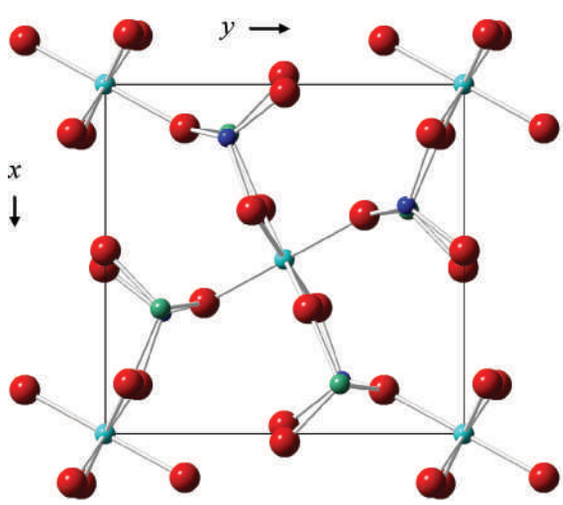


Fig. 23. Projection on (001) of the structure of sillimanite showing end view of chains of edge-sharing octahedra at corners and centre of unit cell, linked by chains of alternating Si–O and Al–O tetrahedra (CrystalMaker image). Dark blue: Si; pale green: Al in tetrahedral coordination; light blue: Al in octahedral coordination; red: oxygen.

Downloaded from https://pubs.geoscienceworld.org/books/chapter-pdf/3752920/9780903056434_ch06.pdf
by guest

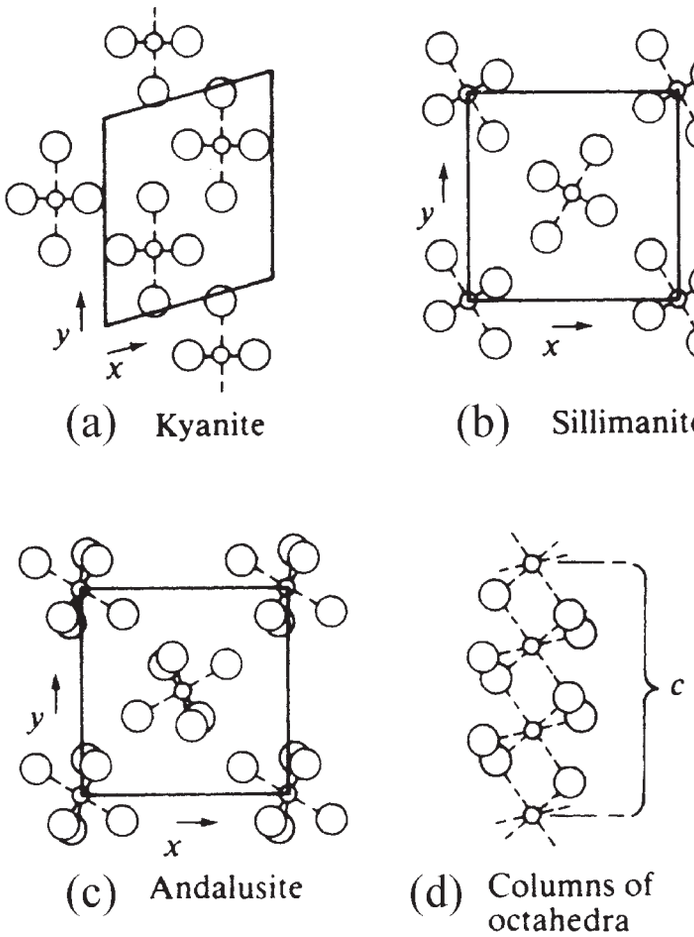


Fig. 24. The chains of octahedral groups in the three forms of Al_2SiO_5. (a), (b) and (c) viewed down the *z* axis; (d) viewed perpendicular to *z* (after Hey, J.S. & Taylor, W.H., 1931, *Z. Krist*., **80**, 428).

Sillimanite can be synthesized from its component oxides at high temperatures and pressures; the phase diagram for Al_2SiO_5 (Fig. 27, p. 34) shows the triple point between andalusite, sillimanite and kyanite to lie at about 530±20ºC and 0.42±0.03 GPa. On heating above about 1000ºC sillimanite is unstable and alters to mullite and quartz. Other alteration products include muscovite and sericite, pyrophyllite, kaolinite and montmorillonite. Under conditions of stress or rising pressure it may be converted to kyanite; the conversion to andalusite with falling temperature is very sluggish.

Optical and physical properties

Sillimanite commonly occurs as long prismatic crystals or as fibrous mats of fine crystalline material, which are commonly described as fibrolite; more equidimensional crystals are also known. The relief is moderately high and the refractive indices vary only slightly; the birefringence is comparatively large, though the normal retardation is not always observed in finely fibrous material. The {010} cleavage is not always noticeable in thin section. In cross-sections showing the dominant {110} form the extinction is symmetrical with respect to the crystal boundaries (Fig. 25).

Distinguishing features

The positive (length-slow) elongation and higher birefringence distinguish sillimanite from andalusite. Apatite is length-fast and has weaker birefringence, and kyanite has higher refractive indices and a greater 2V. The distinction of sillimanite from mullite is difficult (see below).

Paragenesis

Sillimanite is the high-temperature polymorph of Al_2SiO_5 and is found both in the higher grades of thermally metamorphosed argillaceous rocks, as in sillimanite-cordierite gneiss and biotite-sillimanite hornfels (where it is often derived from the breakdown of biotite or from earlier-formed andalusite), and in the highest grade of regional metamorphism of similar rocks, as in micaceous sillimanite schist or the coarser quartz-sillimanite gneiss. Much of the sillimanite of regional metamorphism is derived from the breakdown of muscovite and biotite but it may also be produced by reaction between staurolite and quartz. The polymorphic transition of kyanite to sillimanite appears to be sluggish and local persistence of kyanite in the sillimanite zone

Downloaded from https://pubs.geoscienceworld.org/books/chapter-pdf/3752920/9780903056434_ch06.pdf
by guest

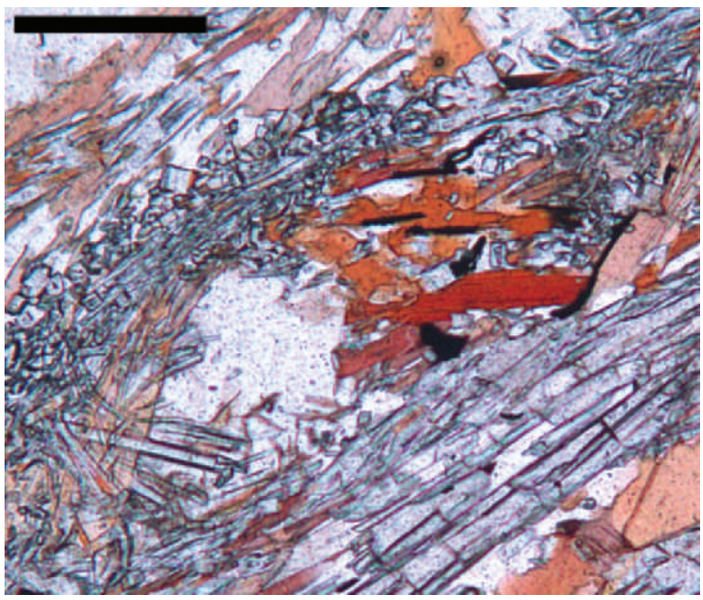


Fig. 25. Sillimanite (blueish-grey; more commonly grey) and mica (red) in high-grade metamorphosed pelitic schist (ppl, scale bar 0.3 mm) (courtesy of G.T.R. Droop).

of metamorphism is not uncommon. Where regional metamorphism of pelitic rocks has been followed by thermal metamorphism, sillimanite and andalusite may be found in oriented intergrowth, as in the sillimanite gneiss enclosed in the Ross of Mull granite.

The high-temperature aluminosilicate mullite resembles sillimanite in many of its properties, and is best distinguished using single-crystal XRD, IR absorption spectroscopy or EPMA. Compositionally, it is deficient in silica compared to sillimanite. It is rare in nature, being found typically in pelitic xenoliths (buchites) in basic igneous rocks. The type occurrence on the island of Mull is in a fused xenolith of Jurassic shale in the tholeiitic portion of a composite sill. Iron-bearing mullite occurs in thermally metamorphosed lateritic rocks. It is a common refractory phase in ceramic products.

Further reading

Ashworth, J.R. (1975) The sillimanite zones of the Huntly–Portsoy area in the northeast Dalradian, Scotland. *Geological Magazine*, **112**, 113–136.

Burt, J.B., Ross, N.L., Angel, R.J. and Koch, M. (2006) Equations of state and structures of andalusite to 9.8 GPa and sillimanite to 8.5 GPa. *American Mineralogist*, **91**, 319–326.

Cesare, B., Gomez-Pugnaire, M.T., Sanchez-Navas, A. and Grobety, B. (2002) Andalusite-sillimanite replacement (Mazarrón, SE Spain): a microstructural and TEM study. *American Mineralogist*, **87**, 433–449.

Grambling, J.A. (1981) Kyanite, andalusite, sillimanite and related mineral assemblages in the Truchas Peaks region, New Mexico. *American Mineralogist*, **66**, 702–722.

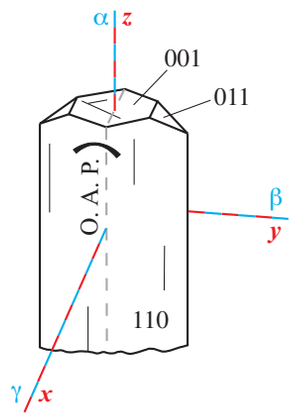
Moecher, D.P. and Brearley, A.J. (2004) Mineralogy and petrology of a mullite-bearing pseudotachylyte: constraints on the coseismic frictional fusion. *American Mineralogist*, **89**, 1486–1495.

Yardley, B.W.D. (1977) The nature and significance of the mechanism of sillimanite growth in the Connemara schists, Ireland. *Contributions to Mineralogy and Petrology*, **65**, 53–58.

Downloaded from https://pubs.geoscienceworld.org/books/chapter-pdf/3752920/9780903056434_ch06.pdf
by guest

Orthorhombic (−)

α	1.633−1.642[a]
β	1.639−1.644
γ	1.644−1.650
δ	0.009−0.012
$2V_\alpha$	73−86°
D (g/cm^3)	3.14−3.16[a]
H	6½−7½
Orientation	α = *z*, β = *y*, γ = *x*; O.A.P. (010)
Cleavage	{110} good, {100} poor; (110): (1$\bar{1}$0) = 89°
Colour	Usually pink, but may be white or rose-red; also grey, violet, yellow, green or clouded with inclusions; in thin section normally colourless, but may be pink or green
Pleochroism	In coloured varieties weak, with α rose-pink, β and γ greenish yellow
Twinning	Rare on {101}
Unit cell	*a* 7.79 Å, *b* 7.90 Å, *c* 5.55 Å; *V* 342 Å^3 Z = 4. Space group *Pnnm*



Andalusite, the low-temperature, low-pressure polymorph of Al_2SiO_5, is commonly found associated with cordierite in argillaceous rocks in contact aureoles. It has high relief and low birefringence. Included carbonaceous material may produce the variety chiastolite.

Structure

Andalusite has chains of edge-sharing distorted Al−O octahedra parallel to *z*, linked laterally by chains of Si−O tetrahedra alternating with five-coordinated distorted Al−O trigonal bipyramids (Fig. 26). The Si−O tetrahedra do not share oxygens with other Si−O tetrahedra. Andalusite, with a volume of 17.1 Å^3 per oxygen ion, has the largest specific volume of the three polymorphs and is thus favoured by lowest pressure conditions.

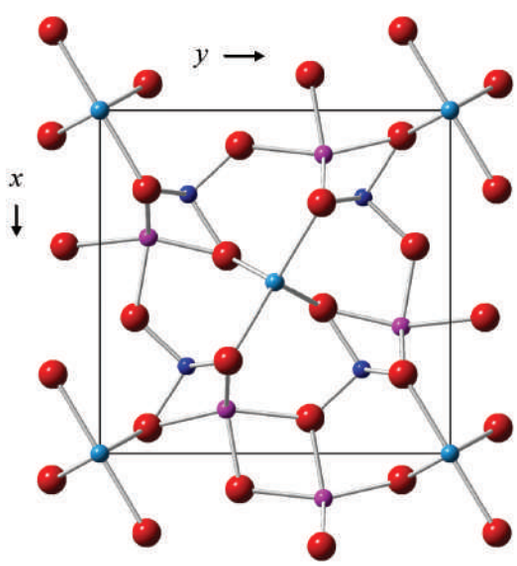


Fig. 26. Projection on (001) of the structure of andalusite showing end view of chains of edge-sharing octahedra at corners and centre of unit cell, linked by Si−O tetrahedra and pairs of Al−O polyhedra. (CrystalMaker image). Dark blue: Si; light blue: tetrahedral Al; purple: Al in five-fold coordination (but the fifth oxygen is obscured in this projection); red: oxygen.

Chemistry

The composition of andalusite is typically near to Al_2SiO_5, the only substituents that have been reported in significant amounts are ferric iron and manganese; the replacement of Al by Fe^{3+} is generally small and in

[a] Viridine has higher values.

Downloaded from https://pubs.geoscienceworld.org/books/chapter-pdf/3753007/9780903056434_ch07.pdf
by guest

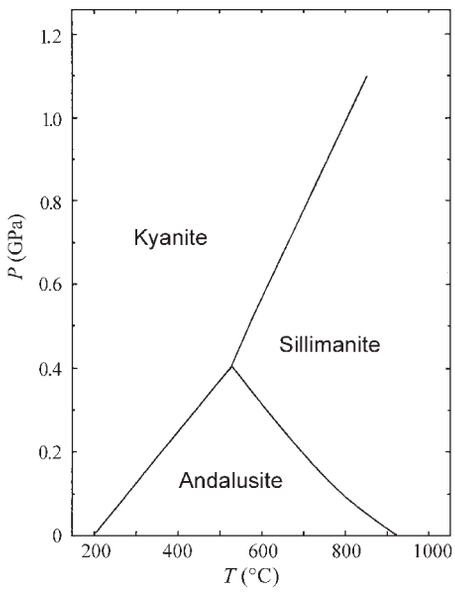


Fig. 27. Phase diagram for kyanite–andalusite and andalusite–sillimanite (after Bohlen, S.R., Montana, A. & Kerrick, D.M., 1991, *Amer. Min.*, **76**, 677–680).

most andalusites Fe_2O_3 is less than 2%. The manganese-rich variety of andalusite, viridine, contains appreciable ferric iron and manganese (e.g. Table 7, p. 37, analysis 3) and viridine with up to 4.8% of Fe_2O_3 and 19.6% Mn_2O_3 is known. A phase containing 32.2% Mn_2O_3 has been described, leading to the formula $(Mn^{3+},Al)AlSiO_5$, and the name kanonaite has been given to the ideal end-member composition $Mn^{3+}AlSiO_5$. Andalusite can be synthesized from kaolinite, or from $A1_2O_3$ + SiO_2, at 450–650ºC at a water-vapour pressure between 0.06 and 0.2 GPa. The phase diagram for the Al_2SiO_5 composition (Fig. 27) shows the triple point between andalusite, sillimanite and kyanite to lie at ~530±20ºC and 0.42±0.03 GPa. Andalusite may alter rather easily to sericite, the variety chiastolite being particularly susceptible to this type of alteration along the lines of carbonaceous inclusions. Other alteration products include sillimanite and kyanite (by inversion with rising temperature or pressure), e.g. the 'chiastolite' hornfels of the English Lake District where the andalusite has been replaced by brush-like aggregates of kyanite or pseudomorphs of kyanite and 'shimmer aggregate', pinite, corundum, spinel and feldspar.

Optical and physical properties

The refractive indices and density of andalusite are increased by the entry of ferric iron and manganese into the structure. The colour and pleochroism are related chiefly to the Fe and Mn contents, the pink and red varieties containing Fe whereas the green crystals contain Mn. For the green variety viridine the optic sign becomes positive and the pleochroism may become marked and vary from yellow to emerald green. The variety chiastolite has a regular arrangement of carbonaceous impurities, often forming a cruciform

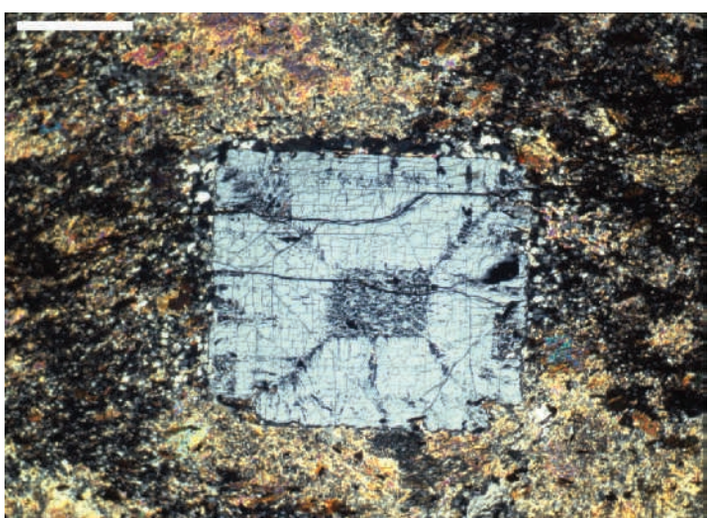


Fig. 28. The chiastolite variety of andalusite, in chiastolite hornfels, English Lake District, showing two cleavages at approximately right angles, with a central area full of inclusions radiating towards the corners of the crystal, giving a characteristic cruciform pattern (crossed polars, scale bar 0.5 mm) (W.S. MacKenzie collection, courtesy of Pearson Education).

Downloaded from https://pubs.geoscienceworld.org/books/chapter-pdf/3753007/9780903056434_ch07.pdf
by guest

pattern when viewed in cross-section (Fig. 28). The impurities may be concentrated at the centre of each crystal, representing the initial growth stage, and along the diagonals, representing the trace of the prism edges as the crystal grew, the foreign matter being brushed to the edges by the crystal growth which was most effective in directions perpendicular to the prism faces. On heating to between 1450 and 1500ºC andalusite is converted to mullite; this reaction is used in the manufacture of refractories.

Distinguishing features

The almost-square cross-section, high relief, low birefringence and length-fast prismatic crystals are characteristic. The pleochroic varieties may be distinguished from orthopyroxenes by the length-slow character and higher birefringence of the latter minerals.

Paragenesis

Andalusite is found typically in metamorphosed pelitic rocks surrounding igneous intrusions, where it is commonly associated with cordierite. In the early stages of such metamorphism it occurs as anhedral grains but acquires a prismatic outline, pushing aside enclosed foreign matter to form the chiastolite pattern: in a more advanced grade the andalusite becomes clear of inclusions. Under conditions of higher temperature and pressure it may become unstable and alter to its polymorphs sillimanite or kyanite (see Fig. 27). Andalusite and cordierite schists are found occasionally in regionally metamorphosed areas where there appears to have been a deficiency or relaxation of shearing stress, as in the Banff area of north-east Scotland. Andalusite is of rare occurrence in granites, probably having been formed as a result of contamination, although the occurrence of pseudomorphs of andalusite in quartz veins in pegmatites has been taken to suggest a pegmatitic or hydrothermal origin for this mineral. Manganian andalusite (viridine) occurs typically in low-grade regionally metamorphosed Mn-rich pelitic rocks, where it may be associated with piemontite, spessartine, chlorite or hematite. Andalusite is a fairly common detrital mineral in some sandstones.

Further reading

Abs-Wurmbach, I., Langer, K., Seifert, F. and Tillmans, E. (1981) The crystal chemistry of Mn^{3+}, Fe^{3+}-substituted andalusites (viridines and kanonaite) $(Al_{1-x-y}Mn^{3+}_{x}Fe^{3+}_{y})_2(O|SiO_4)$: crystal structure refinements, Mössbauer and polarized optical absorption spectra. *Zeitschrift für Kristallographie*, **155**, 81–113.

Bohlen, S.R., Montana, A. and Kerrick, D.M. (1991) Precise determination of the equilibria kyanite ⇌ sillimanite and kyanite ⇌ andalusite and a revised triple point for Al_2SiO_5 polymorphs. *American Mineralogist*, **76**, 677–680.

Burt, J.B., Ross, N.L., Angel, R.J. and Koch, M. (2006) Equation of state and stucture of andalusite to 9.8 GPa and sillimanite to 8.5 GPa. *American Mineralogist*, **91**, 319–326.

Garcia, C.A. and Rios, C.A. (2004) Occuirrence and significance of the polymorphs of Al_2SiO_5 in metamorphic rocks of the Santander Massif, Eastern Cordillera (Colombian Andes). *Boletin de Geologia*, **26**, 23–38.

Gunter, M. and Bloss, F.D. (1982) Andalusite–kanonaite series: lattice and optical parameters. *American Mineralogist*, **67**, 1218–1228.

Holdaway, M.J. (1971) Stability of andalusite and the aluminum silicate phase diagram. *American Journal of Science*, **271**, 97–131.

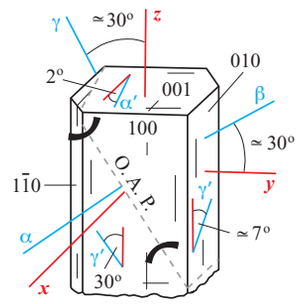
Pattison, D.R.M. and Vogl, J.J. (2005) Contrasting sequences of metapelitic mineral-assemblages in the aureole of the tilted Nelson batholith, British Columbia: implications for phase equilibria and pressure determination in andalusite-sillimanite settings. *The Canadian Mineralogist*, **43**, 51–88.

Ralph, R.I., Finger, I.W., Hazen, R.M. and Ghose, S. (1984) Compressibility and crystal structure of andalusite at high pressures. *American Mineralogist*, **69**, 513–519.

Downloaded from https://pubs.geoscienceworld.org/books/chapter-pdf/3753007/9780903056434_ch07.pdf
by guest

Triclinic (−)

α	1.710−1.718
β	1.719−1.724
γ	1.724−1.734
δ	0.012−0.016
$2V_\alpha$	78−83º
Orientation	γ′:*z* on (100) = 27−32º, on (010) = 5−8º α′:*x* on (001) = 0−3º; Bx_a nearly ⊥(100)
D (g/cm^3)	3.53−3.65
H	5½−7, variable
Cleavage	{100} perfect, {010} good, {001} parting; (001):*z* = 85º
Twinning	Lamellar on (100), twin axis ⊥(100) or ‖ *y* or *z*; multiple on {001}
Colour	Blue to white, also grey, green, yellow, pink or black; colourless to pale blue in thin section
Pleochroism	Weak; in thick sections α colourless, β violet-blue, γ cobalt-blue
Unit cell	*a* 7.12 Å, *b* 7.85 Å, *c* 5.57 Å, α 89.98º, β 101.12º, γ 106.01º; *V* 293 Å^3 Z = 4; space group $P\bar{1}$



Kyanite is the high-pressure polymorph of Al_2SiO_5 and occurs mainly in regionally metamorphosed pelitic rocks. Pale blue or white in hand specimen and colourless with high relief in thin section, it shows good cleavage and variable extinction angle depending on orientation.

Structure

Kyanite has a structure in which the oxygen atoms are arranged in a slightly distorted close-packed cubic array. As in andalusite and sillimanite, there are chains of Al−O octahedra (Al coloured green in Fig. 29) and these are linked together by the remaining Si, Al and O atoms, Si being coordinated by four oxygen atoms, and Al by six oxygen atoms. The Si−O tetrahedra do not share corners with other Si−O tetrahedra, although they may appear to do so because of overlap in projection. The volumes of the unit cell of the three Al_2SiO_5 polymorphs and their molar volumes are as listed in Table 6, confirming that kyanite has the lowest specific volume and will thus be the polymorph favoured by highest pressure conditions.

Chemistry

Like the other aluminosilicates, kyanite approximates closely to Al_2SiO_5 (Table 7) with apparently only a very limited amount of Fe^{3+} able to enter the structure: Cr can be present in moderate amounts. The small amounts of Ti reported may be due to inclusions of rutile which are commonly present in kyanite. Recent work has shown that in pure material the alkali content never exceeds 0.06%. Kyanite can be synthesized at 900ºC and 1−4 GPa. The phase diagram for the Al_2SiO_5 composition (Fig. 27, p. 34) shows the triple point between kyanite, andalusite and sillimanite to lie at about 530±20ºC and 0.42±0.03 GPa. On heating to about 1300ºC kyanite is converted to mullite and a glass. Alteration products include pyrophyllite, muscovite and sericite. It may also

Table 6. Molar volumes of Al_2SiO_5 polymorphs.

	V at 25ºC	
	Å^3	(cm^3/mol)
Andalusite	342	51.5
Sillimanite	331	49.9
Kyanite	293	44.1

Downloaded from https://pubs.geoscienceworld.org/books/chapter-pdf/3753012/9780903056434_ch08.pdf
by guest

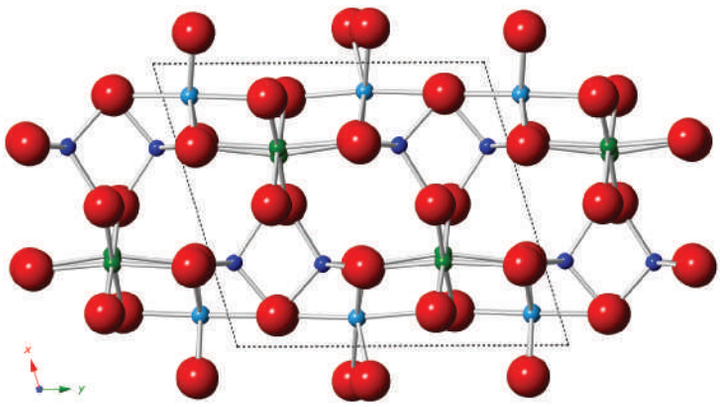


Fig. 29. Projection parallel to *z* of the structure of kyanite showing cation–anion bonds (based on data from Burnham, C.W., 1963, *Z. Krist*., **118**, 337–60). Dark blue: Si; green: Al in chains of octahedra parallel to *z*; light blue: other octahedral Al; red: oxygen.

invert to sillimanite or andalusite by a change in the pressure–temperature conditions, the kyanite of regional metamorphism, for instance, being converted to andalusite within the aureole of a late granite. Kyanite when calcined is used in refractory products and is the most economically important of the aluminosilicates as it occurs in relatively large workable deposits.

Optical and physical properties

The relief is high for a mineral which is normally colourless in thin section, whereas the birefringence is moderate giving rise to higher first-order colours for sections of normal thickness. The optic axial plane is almost perpendicular to (100), and is inclined at

Table 7. Sillimanite, andalusite, kyanite and mullite analyses.

	1	2	3	4	5
SiO_2	37.05	36.65	35.41	37.46	27.77
TiO_2	–	0.04	–	0.03	0.90
Al_2O_3	62.33	61.7	46.95	61.52	69.37
Fe_2O_3	0.60	1.75	0.82	0.71	1.87
FeO	–	–	–	–	–
Mn_2O_3	–	–	16.75	0.006	–
MgO	–	0.03	–	0.03	0.30
CaO	–	–	–	0.02	–
Na_2O	–	–	–	0.03	–
K_2O	–	–	–	0.01	–
H_2O+	–	–	–	0.05	–
H_2O-	–	–	–		–
Total	99.98	100.19	99.96	99.87	100.21
Numbers of ions on the basis of 20 O (6 cations for mullite)					
Si	4.005	3.973	4.072	4.057	1.487
Al	7.944	7.884	6.365	7.855	4.378
Fe^{3+}	0.048	0.142	0.071	0.058	0.075
Mg	–	0.005	–	0.005	0.024
Ti	–	0.003	–	0.003	0.036
Mn^{3+}	–	–	1.466	–	–
Na	–	–	–	0.006	–
Ca	–	–	–	0.002	–
K	–	–	–	0.001	–
	7.99	8.04[a]	7.90[b]	7.93	4.51

1 Sillimanite, enstatite-sillimanite-cordierite rock, pyroxene-granulite facies terrain, north-east of Beitbridge, Zimbabwe (Chinner, G.A. & Sweatman, T.R., 1968, *Mineral. Mag*., **36**, 1052–60). Microprobe analysis.
2 Colourless andalusite, andalusite-sillimanite hornfels, Steinach, Bavaria (Okrush, M. & Evans, B.W., 1970, *Lithos*, **3**, 261–68). Includes Cr_2O_3 0.01, V_2O_3 0.01.
3 Viridine, low-grade regionally metamorphosed chlorite-mica schist, Venn–Stavelot massif, Ardennes, Belgium (Kramm, U., 1973, *Contrib. Mineral. Petrol*., **69**, 143–50). Microprobe analysis, includes Cr_2O_3 0.03.
4 Light blue kyanite, kyanite quartzite, Hållsjöberget, Varmland, Sweden (Henriques, Å., 1957, *Arkiv. Min. Geol*., **2**, 271–74).
5 Mullite (pleochroic from lilac to colourless), spinel-mullite-pseudobrookite-glass buchite, Sithean Sluaigh, Argyllshire, Scotland, UK (Smith, D.G.W., 1965, *Amer. Min*., **50**, 1982–2022).

[a] Includes Cr 0.001, V 0.001.
[b] Includes Cr 0.003.

Downloaded from https://pubs.geoscienceworld.org/books/chapter-pdf/3753012/9780903056434_ch08.pdf
by guest

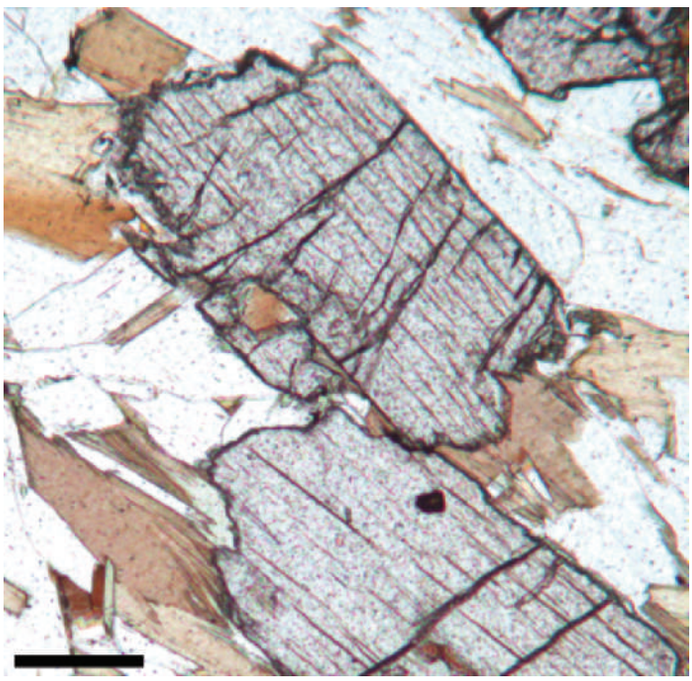


Fig. 30. Kyanite in large crystals showing high relief and notable cleavage (ppl, scale bar 0.2 mm) (courtesy of G.T.R. Droop).

approximately 30º to (010) and the *z* axis. The extinction position nearest to *z* corresponds with the slow ray, and the extinction angle varies from around 30º to zero: in basal sections it is almost zero. The colour is variable from colourless to blue, and is often unevenly distributed (Fig. 30). The hardness varies from face to face and according to crystallographic direction.

Distinguishing features

Kyanite has a higher relief than the other aluminosilicates: its birefringence is less than that of sillimanite but greater than that of andalusite and it differs from the latter in being length-slow. The maximum extinction angle of around 30º is distinctive and is obtained on sections giving a negative biaxial figure with a large 2V. In detrital grains kyanite may be recognized by the step-like features caused by its good cleavage.

Paragenesis

Kyanite is found in regionally metamorphosed pelitic rocks and, less commonly, in psammites. It is used as a zonal mineral in pelitic assemblages, kyanite developing after staurolite and before sillimanite with increasing grade of metamorphism. High-pressure kyanite-talc-quartz whiteschists are being increasingly recognized in such parageneses as the Dora Maira assemblages in the Western Alps and the Dabie Shan (China) coesite-bearing whiteschists, where the $P-T$ estimates range from 3.7 to 3.4 GPa at 700–750ºC. Kyanite may be derived also from pyrophyllite, from the dehydration of paragonite with the addition of quartz, and from the inversion of andalusite in areas where a regional metamorphism is superimposed on a normal thermal metamorphism. It has also been recorded in thermal aureoles, together with staurolite, where it may be due to an element of shear during the emplacement of the igneous body. Kyanite, in addition to its occurrence in metamorphosed pelitic rocks, has been reported from eclogites and kyanite amphibolites. It has also been recorded in some 'pegmatitic veins', though these are more probably quartz-kyanite segregation veins, and it is fairly common as a detrital mineral in sedimentary rocks.

Further reading

Hoschek, G. (2004) Comparison of calculated $P-T$ pseudosections for a kyanite eclogite from the Tauern window, Eastern Alps, Austria. *European Journal of Mineralogy*, **16**, 59–72.

Kerrick, D.M. (Editor) (1990) *The Al_2SiO_5 Polymorphs*. Reviews in Mineralogy, **22**, Mineralogical Society of America, Washington, D.C., 405 pp.

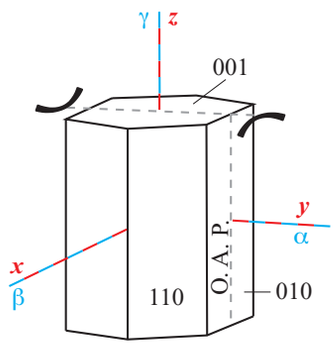
O'Brien, P.J. (2006) Type locality granulites: high-pressure rocks formed at eclogite facies conditions. *Mineralogy and Petrology*, **86**, 161–175.

Schreyer, W. (1979) Whiteschists: their composition and pressure-temperature regime based on experimental, field, and petrographic evidence. *Tectonophysics*, **43**, 127–144.

Downloaded from https://pubs.geoscienceworld.org/books/chapter-pdf/3753012/9780903056434_ch08.pdf
by guest

Monoclinic (pseudo-orthorhombic) (+)

α	1.736–1.747
β	1.742–1.753
γ	1.748–1.761
δ	0.011–0.014
$2V_\gamma$	80–90º
Orientation	α = *y*, β = *x* γ = *z*; O.A.P. (100)
D (g/cm^3)	3.74–3.83
H	7
Cleavage	{010} moderate
Twinning	{023}, {232} interpenetration, rarely seen in thin section
Colour	Dark brown, reddish brown, yellow-brown; pale golden yellow in thin section
Pleochroism	α colourless, β pale yellow, γ golden yellow
Unit cell	*a* 7.85–7.90 Å, *b* 16.60–16.65 Å, *c* 5.65–5.67 Å, β ~ 90º Z = 2; space group *C*2/*m*
Special features	Slowly attacked by H_2SO_4, insoluble in cold HF



Staurolite typically occurs in medium-grade regionally metamorphosed pelitic schists, generally preceding the appearance of kyanite and being replaced at higher grade by kyanite and almandine. It is rusty brown in hand specimen and yellow with weak pleochroism, high relief and straight extinction in thin section. It has a complex crystal chemistry.

Structure

The staurolite structure is based upon an approximately cubic close packed array of oxygens with mainly (Al,Fe,Mg) in its octahedral and (Si,Al,Fe) in its tetrahedral interstices. It can be described also in terms of (010) slabs of the kyanite (Al_2SiO_5) structure alternating with layers of cations in octahedral and tetrahedral coordination with basic composition $AlFe_2O_3(OH)$, but capable of exhibiting a wide range of cation substitutions (see below). The two components are labelled K and S, respectively, in Fig. 31. In the S layer the Al octahedra share edges forming chains parallel to the *z* axis. The ideal overall formula for staurolite is $H_2Fe_4^{2+}Al_{18}Si_8O_{48}$ but analysed staurolites contain between 2 and 4 hydrogens per formula unit. This would result in a net positive charge, but it is balanced by substitutions such as Al for Si, or Mg,Fe^{2+} for Al and also by only partial occupation of some cation sites. A different view of the staurolite structure is that given by the polyhedral model shown in perspective in Fig 32.

Staurolites have been reported to have orthorhombic symmetry, but the majority are monoclinic (pseudo-orthorhombic) with β = 90–90.68º. The pseudo-symmetry, wide variety of cations and available sites (some partially filled and with partially ordered occupation) and variable H content, all contribute to the complexity of staurolite crystal chemistry well beyond that presented here (see Further reading list).

Chemistry

Following Hawthorne *et al.* (1993c), a good way to understand the complex chemistry of staurolite is to consider the general formula, which can be written $A_4B_4C_{16}D_4T_8O_{40}X_8$, where:

	Sites
A = Fe^{2+}, Mg, □ (□ ⩾ 2 pfu)	*M*4*A*, *M*4*B*
B = Fe^{2+}, Zn, Co, Mg, Li, Al, Mn^{2+}, Fe^{3+}(?),□	*T*(2)
C = Al, Fe^{3+}, Cr, V, Mg, Ti	*M*1*A*, *M*1*B*, *M*(2)
D = Al, Mg, □ (□ ⩾ 2 pfu)	*M*3*A*, *M*3*B*
T = Si, Al	*T*(1)
X = OH, F, O^{2-}	

□ denotes vacant or partially filled sites.

Downloaded from https://pubs.geoscienceworld.org/books/chapter-pdf/3753084/9780903056434_ch09.pdf
by guest

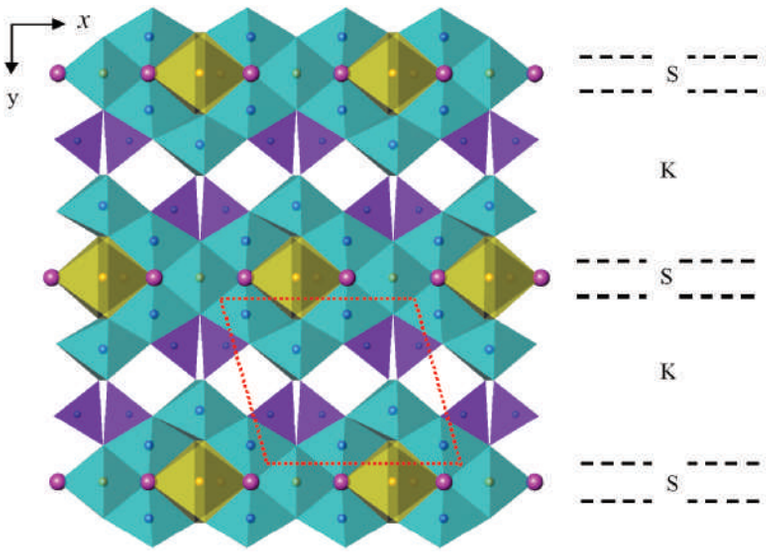


Fig. 31. The structure of staurolite projected on (001) showing two unit cells. The kyanite part of the structure is outlined by the red broken lines (CrystalMaker image). Yellow, Fe; blue, Al; purple, Si; pink: (OH).

This shows that a wide variety of chemical elements can substitute into different sites in the crystal structure (these are labelled in Fig. 32). In the majority of staurolites, Fe^{2+} is the dominant cation, but Mg-rich varieties are not uncommon. Zinc is present in many staurolites (Table 8, analysis 3); in the cobaltian staurolite variety, lusakite, almost half (1.8 Co atoms per formula unit) the divalent tetrahedral cations are cobalt. Chromian staurolite may contain up to 0.45 Cr^{3+}, atoms per formula unit (Cr_2O_3 2.0%). Lithium, probably located in the *T*2 sites is a significant substituent at up to 1.3 wt.% Li_2O in some samples. The relatively large lithium content is related to its preferential entry into staurolite in comparison with the common coexisting ferromagnesian minerals cordierite, biotite, muscovite and garnet.

The variation in the reported content of hydrogen in staurolite is in part related to the fact that all the structural water is not evolved at 1000ºC and not all adsorbed water removed at 110ºC. Recent determination of hydrogen using H-isotope extraction-line and ion microprobe techniques indicate that the content is probably related to the physical conditions of metamorphism. Thus staurolites occurring with or in the absence of garnet and biotite contain 1.4–1.8 and 2.25% H_2O, respectively (2.7–3.4 and 4H ions per 48-oxygen formula unit).

In calculating the numbers of ions in the formula unit on the basis of 48(O,OH), Fe^{3+}, Ti and Cr are assigned to octahedral sites; where a deficiency exists Mg is assumed to occupy some of these sites. The remaining Mg, plus Fe^{2+} and Zn, are assigned to the tetrahedral site that is usually dominated by Fe^{2+}.

The stability field of the assemblage staurolite + magnetite + quartz at 650ºC in the presence of a pure water vapour phase and a vapour phase consisting of 50% H_2O based on experimental and theoretical data is shown in Fig. 33a. The field is wedge-shaped,

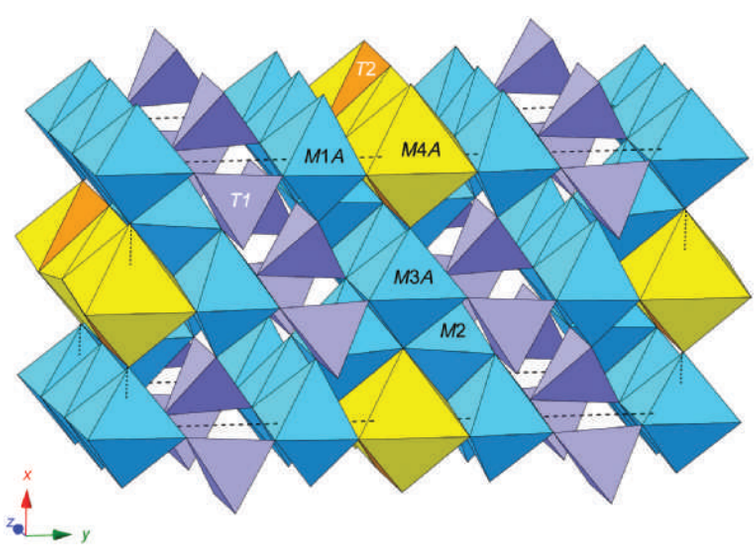


Fig. 32. Perspective view of a polyhedral model of the structure of staurolite showing rows of octahedra parallel to *z* linked by individual tetrahedra, with labelling as indicated in the Chemistry section. The A and B sites listed there are pseudo-equivalent but only A sites are labelled in this image (CrystalMaker image).

Downloaded from https://pubs.geoscienceworld.org/books/chapter-pdf/3753084/9780903056434_ch09.pdf
by guest

Table 8. Staurolite analyses.

	1	2	3		Numbers of ions on the basis of 48 (O,OH)[b] 1	2	3
SiO_2	27.22	26.62	28.64	Si	7.539 } 8.00	7.232 } 8.00	8.000 } 8.00
TiO_2	0.56	1.67	0.56	Al	0.461	0.768	0.000
Al_2O_3	54.16	55.15	50.14	Al	17.226	16.890	16.602
Fe_2O_3	1.47	–	0.84	Ti	0.116 } 18.00	0.340 } 18.00	0.118 } 18.00[d]
FeO	12.31	9.75[a]	7.18	Fe^{3+}	0.306	–	0.179
ZnO	–	–	7.44	Mg	0.352	0.770	1.058
MnO	0.23	0.03	0.16	Mg	0.613	1.380	0.381
MgO	2.34	5.31	3.44	Fe^{2+}	2.851 } 3.52	2.216 } 3.61[c]	1.686 } 3.69[e]
CaO	–	0.00	–	Mn	0.053	0.008	0.039
H_2O+	1.98	–	1.92	Ca	–	0.000	–
Total	100.27	98.55	100.32	OH	3.659	–	3.598

1 Staurolite, staurolite-mica schist, Windham, Maine, USA (Juurinen, A., 1956, *Ann. Acad. Sci. Fennicae, ser. A*, III, **47**, 1–53).
2 Staurolite, sapphirine-garnet-gedrite-spinel-corundum-phlogopite rock (Schreyer, W. *et al*., 1984, *Contrib. Mineral. Petrol*., **86**, 200–07). Microprobe analysis, includes Na_2O 0.02.
3 Zincian staurolite, with chalcocite and quartz, Cherokee County, Georgia, USA (Juurinen, A., 1956, *Ann. Acad. Sci. Fennicae, ser. A*, III, **47**, 1–53).

[a] Total iron as FeO.
[b] No. 2 on the basis of 46O.
[c] Includes Na 0.008.
[d] Includes Si 0.043.
[e] Includes Zn 1.586.

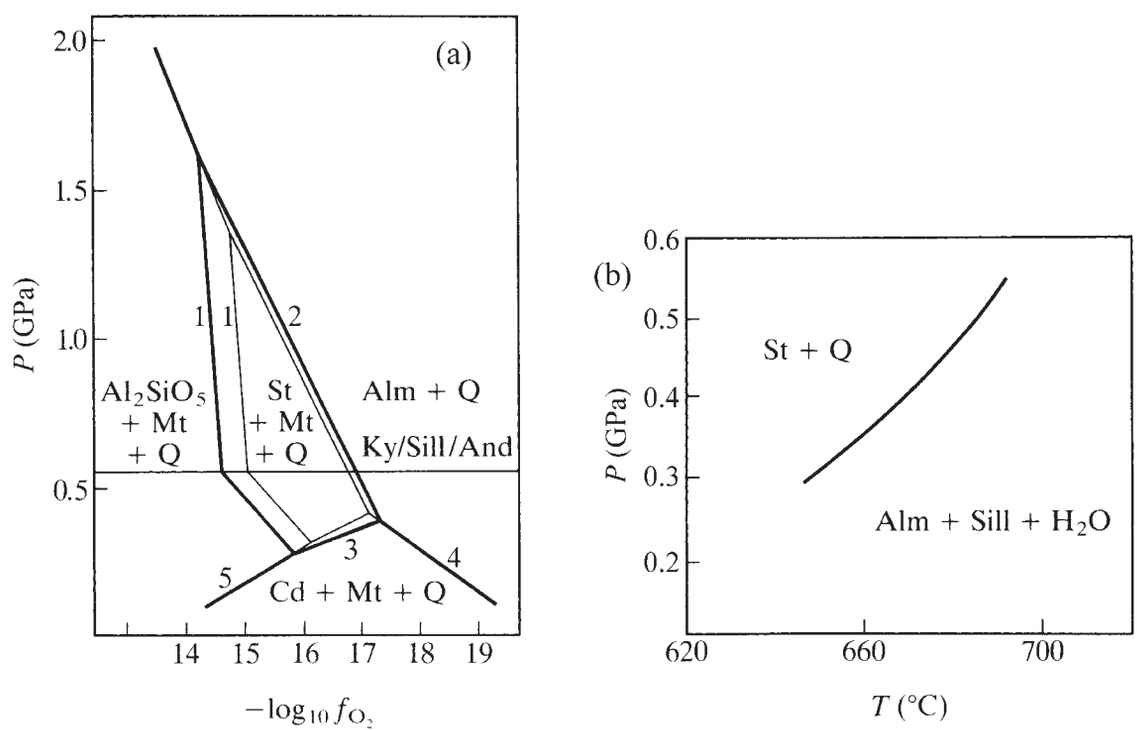


Fig. 33. (a) Pressure–log f_{O_2} diagram showing stability field of staurolite + magnetite + quartz at 620ºC, and divariant equilibria stable in the presence of excess silica (after Ganguly, J., 1972, *J. Petrol*., **13**, 335–65). Heavy lines, vapour phase pure water; light lines, vapour phase 50 per cent H_2O. St: staurolite; Ky: kyanite; Sill: sillimanite; And: andalusite; Alm: almandine; Mt: magnetite; Q: quartz, (b) The thermal equilibrium for the reaction Fe-staurolite + quartz ⇌ almandine + sillimanite + andalusite H_2O (after Dutrow, B.L. & Holdaway, M.J., 1989, *J. Petrol*., **30**, 229–48).

Downloaded from https://pubs.geoscienceworld.org/books/chapter-pdf/3753084/9780903056434_ch09.pdf
by guest

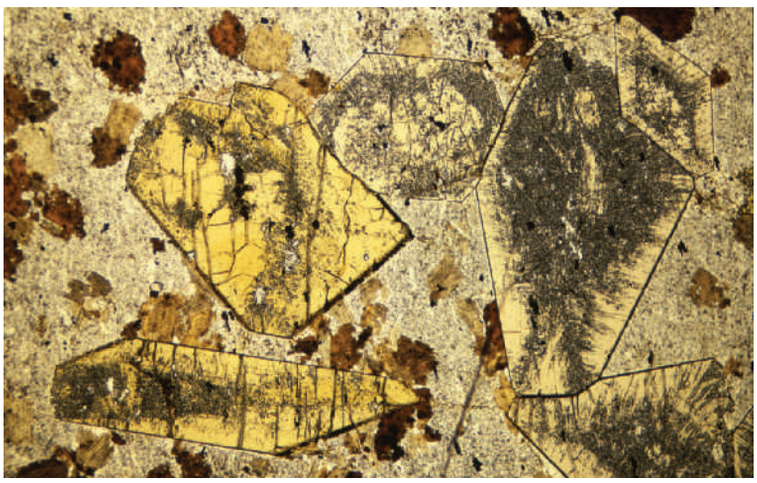


Fig. 34. Staurolite in staurolite schist, Waddy Lake, Saskatchewan, Canada (ppl, scale bar 1 mm), showing high relief and weak pleochroism (W.S. MacKenzie collection, courtesy of Pearson Education).

terminating at about 1.6 GPa and truncated at about 0.4 GPa by the assemblage cordierite + magnetite + quartz. The thermal equilibrium for the reaction

$$\text{Fe-staurolite} + \text{quartz} \rightleftharpoons \text{almandine} + \text{sillimanite} + H_2O$$

between 0.3 and 0.5 GPa is shown in Fig. 33b.

Optical and physical properties

Corresponding with the variations in chemical composition, staurolites show minor changes in their range of optical properties. The refractive indices of synthetic magnesiostaurolite are, however, substantially lower at α 1.703, γ 1.710, than the range α ~1.740, γ ~1.755 of the common ferroan staurolites. Staurolite crystals are prismatic in habit and show six-sided basal sections bounded by the forms {110} and {010}. The well formed porphyroblasts are sometimes bent and rotated and this provides evidence of crystallization during late or post-deformational metamorphism or of syn-tectonic growth. Zoning, including sector zoning, is not uncommon and is sometimes defined by a chiastolite-like arrangement of inclusions. Inclusions, particularly of quartz, are very common and the mineral then has a sponge-like appearance. Staurolite sometimes occurs in parallel growth with kyanite with St(010)||Ky(100). The colour intensity appears to be directly related to the content of titanium (Fig. 34).

Distinguishing features

The colourless to golden yellow pleochroism, straight extinction, high refringence and moderate birefringence generally are sufficient to distinguish staurolite from other minerals having a yellow colour in thin section: vesuvianite is uniaxial and has a lower birefringence (often anomalous). Melanite garnet is isotropic, and fayalite has higher refringence and birefringence and a negative sign and these last minerals are found in different geological environments.

Paragenesis

Staurolite is a characteristic mineral in medium-grade metamorphosed pelitic schists and gives its name to a regional metamorphic zone. The staurolite-almandine garnet-kyanite assemblage is typical of Barrovian-type metamorphic terranes, and the staurolite-cordierite-andalusite/sillimanite assemblage results from the lower-pressure Buchan-type metamorphism. During the progressive metamorphism of rocks of pelitic composition staurolite develops earlier than kyanite, then together with kyanite before being replaced by kyanite and almandine or, less commonly, by sillimanite and almandine according to the reaction:

$$\text{staurolite} + \text{muscovite} + \text{quartz} \rightarrow \text{almandine} + Al_2SiO_5 + \text{biotite} + H_2O$$

The staurolites are generally iron-rich {Mg/(Mg + Fe) = $X_{Mg} < 0.3$}; the metamorphic conditions indicate that their formation lies within the stability field for Fe-staurolite + quartz determined experimentally, i.e. $P > 0.15$ GPa, T 500–700ºC. The rare magnesiostaurolites are stable only in the absence of quartz and are restricted to high-P–T parageneses such as eclogites and sapphirine-bearing rocks.

Staurolite is formed also at somewhat lower metamorphic grade and in this paragenesis is often associated with chloritoid. Although chloritoid decreases and staurolite increases with increasing metamorphic grade, there is little textural evidence of the direct formation of staurolite from chloritoid. The P–T coordinates of the breakdown of chloritoid to staurolite + magnetite + quartz + H_2O have been determined experimentally (see Fig. 38, p. 49).

Many staurolite-bearing rocks have a high aluminium content; staurolite formation, however, is not restricted to pelitic rocks and this mineral occurs in some quartzofeldspathic schists. Associated with kyanite, corundum and magnetite, it is present in emeries (metabauxites).

Staurolite is affected by retrograde metamorphism resulting in its mantling and partial replacement by

Downloaded from https://pubs.geoscienceworld.org/books/chapter-pdf/3753084/9780903056434_ch09.pdf
by guest

chlorite in rocks of the staurolite zone. Staurolite, due to its resistance to chemical weathering, occurs in clastic sediments and it is a common constituent of heavy-mineral assemblages.

Further reading

Cesare, B. and Grobety, B. (1995) Epitaxial replacement of kyanite by staurolite: a TEM study of the microstructures. *American Mineralogist*, **80**, 77–86.

Dutrow, B.L. and Holdaway, M.J. (1989) Experimental determination of the upper temperature of Fe-staurolite + quartz at medium pressures. *Journal of Petrology*, **30**, 229–248.

Grevel, K.-D., Navrotsky, A., Fockenberg, T. and Majzlan, J. (2002) The enthalpy of formation and internally consistent thermodynamic data of Mg-staurolite. *American Mineralogist*, **87**, 397–404.

Hawthorne, F.C., Ungaretti, L., Oberti, R., Caucia, F. and Callegari, A. (1993a) The crystal chemistry of staurolite. I. Crystal structure and site populations. *The Canadian Mineralogist*, **31**, 551–582.

Hawthorne, F.C., Ungaretti, L., Oberti, R., Caucia, F. and Callegari, A. (1993b) The crystal chemistry of staurolite. II. Order–disorder and the monoclinic–orthorhombic phase transition. *The Canadian Mineralogist*, **31**, 583–595.

Hawthorne, F.C., Ungaretti, L., Oberti, R., Caucia, F. and Callegari, A. (1993c). The crystal chemistry of staurolite. III. Local order and chemical composition. *The Canadian Mineralogist*, **31**, 597–616.

Holdaway, M.J., Dutrow, B.L., Borthwick, J., Shore, P., Harmon, R.S. and Hinton, R.W. (1986) H content of staurolite as determined by H extraction line and ion microprobe. *American Mineralogist*, **71**, 1135–1141.

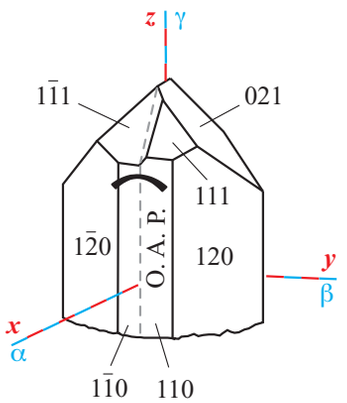
Oberti, R., Hawthorne, F.C., Zanetti, A. and Ottolini, L. (1996) Crystal structure refinement of a highly ordered staurolite. *The Canadian Mineralogist*, **34**, 1051–1057.

Ståhl, K. and Legros, J.-P. (1990) On the crystal structure of staurolite. The X-ray crystal structure of staurolite from the Pyrenees and Brittany. *Acta Crystallographica B*, **46**, 292–301.

Downloaded from https://pubs.geoscienceworld.org/books/chapter-pdf/3753084/9780903056434_ch09.pdf
by guest

Orthorhombic (+)

α	1.606–1.634
β	1.609–1.637
γ	1.616–1.644
δ	0.008–0.011
$2V_\gamma$	48–68º
Orientation	$x = \alpha$, $y = \beta$, $z = \gamma$; O.A.P. (010)
D (g/cm^3)	3.49–3.57
H	8
Cleavage	{001} perfect
Colour	Variable: colourless, white, yellow, light shades of grey, green, red or blue; colourless in thin section
Pleochroism	Coloured varieties may show pleochroism in thick sections, e.g. α yellow, γ pink.
Unit cell	*a* 4.65 Å, *b* 8.80 Å, *c* 8.39 Å[a] Z = 4; space group *Pbnm*
Special features	Attacked only slightly by H_2SO_4



Topaz is found mainly in acid igneous rocks such as granites, granite pegmatites and rhyolites. In thin section it is colourless with a moderate relief and straight extinction. Its optical properties vary with the F/OH ratio.

Structure

The structure of topaz contains chains (parallel to *y*) of edge-sharing Al–(O,F,OH) octahedra and SiO_4 tetrahedra (Fig. 35): four of the six anions around each Al are oxygens shared with the SiO_4 tetrahedra, the others being fluorine or hydroxyl ions. In topaz Si–O tetrahedra do not share oxygens with other tetrahedra; it is thus classified as an orthosilicate.

Chemistry

The composition of topaz is fairly constant, the only major variation being in the ratio of fluorine to hydroxyl ions. Several analyses (e.g. Table 9, analysis 1) show a fluorine content close to the theoretical maximum of 20.7%. The replacement of F by (OH), however, is generally small and analysis 3 shows one of the highest (OH) values reported.

[a] Morphological data refer to a cell with halved *c* dimension.

Topaz has been synthesized by the thermal hydrolysis of AlF_3 and SiO_2, where it crystallizes between 750 and 850ºC. It has also been produced by heating a mixture of Na_2SiF_6, amorphous Al_2O_3 and water to 500ºC for nine days at a pressure of 0.4 GPa. Topaz liberates fluorine on heating to 850–900ºC and mullite is

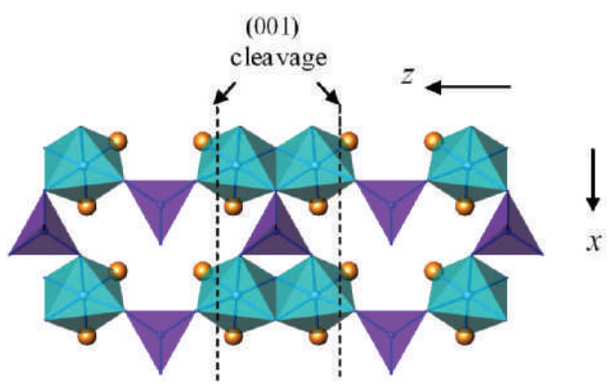


Fig. 35. The key structural unit of topaz, showing chains of edge-sharing $AlO_4(F,OH)_2$ octahedra and downward-pointing corner-sharing SiO_4 tetrahedra cross-linked in the *x* direction by upward-pointing SiO_4 tetrahedra (CrystalMaker image). Purple, Si; blue: Al; gold: (F,OH).

Downloaded from https://pubs.geoscienceworld.org/books/chapter-pdf/3753391/9780903056434_ch10.pdf
by guest

Table 9. Topaz analyses.

	1	2	3		Numbers of ions on the basis of 24 (O,OH,F) 1	2	3
SiO_2	31.93	31.94	33.00	Si	3.905 } 4.00	3.922 } 4.00	4.037
Al_2O_3	56.26	55.80	56.76	Al	0.095 }	0.078 }	–
Fe_2O_3	–	0.32	tr.	Al	8.017	7.980	8.180
FeO	–	0.07	–	Fe^{3+}	–	0.029	–
MgO	–	0.07	–	Fe^{2+}	–	0.007 } 8.04	–
CaO	–	0.13	tr.	Mg	–	0.014	–
F	20.37	17.24	13.23	Ca	–	0.014	–
H_2O+	0.19	1.57	2.67	F	7.884 } 8.04	6.688 } 7.97	5.122 } 7.30
H_2O-	–	0.03	0.04	OH	0.156 }	1.281 }	2.178 }
	108.75	107.18	105.70				
$-O \equiv F$	8.58	7.27	5.57				
Total	100.17	99.91	100.13				
α	1.6072	1.616	1.629				
β	1.6104	1.618	1.631				
γ	1.6176	1.625	1.638				
$2V_\gamma$	67°	61°	48°				
D	3.565	3.55	3.509				

1 Colourless topaz, rhyolite, Thomas Range, Utah, USA (Penfield, S.L. & Minor, J.C., Jr., 1894, *Amer. J. Sci.*, ser. 3, **137**, 389–96).
2 Colourless topaz, topaz-quartz rock, Belowda Beacon, Roche, Cornwall, UK (Chaudhry, M.N. & Howie, R.A., 1970, *Mineral. Mag.*, **37**, 717–20). Includes TiO_2 0.01.
3 Fine-grained topaz in quartz vein, near granite, Chesterfield Co., South Carolina, USA (Pardee, J.T. *et al.*, 1937, *Amer. Min.*, **22**, 1058–64).

produced. Natural alteration products include fluorite, kaolinite, sericite and hydromuscovite.

Optical and physical properties

As the optic axial plane is parallel to (010) and the positive acute bisectrix is normal to (001), the plane of the cleavage, an interference figure is obtainable on cleavage flakes. The optic axial angle decreases with increasing replacement of F by (OH), as does the density, whereas the refractive indices increase with increasing (OH); see Fig. 36.

The colour of topaz is very variable, ranging from water-clear colourless crystals through yellow and delicate shades of wine-red, light blue and light green. The rose-coloured variety (Brazilian 'ruby') is rare but can be produced by careful heating of yellow topaz. Microscopic cavities are sometimes found in topaz, usually filled with a liquid: one such liquid, first described as brewsterlinite, has a refractive index of 1.13 and is liquid CO_2.

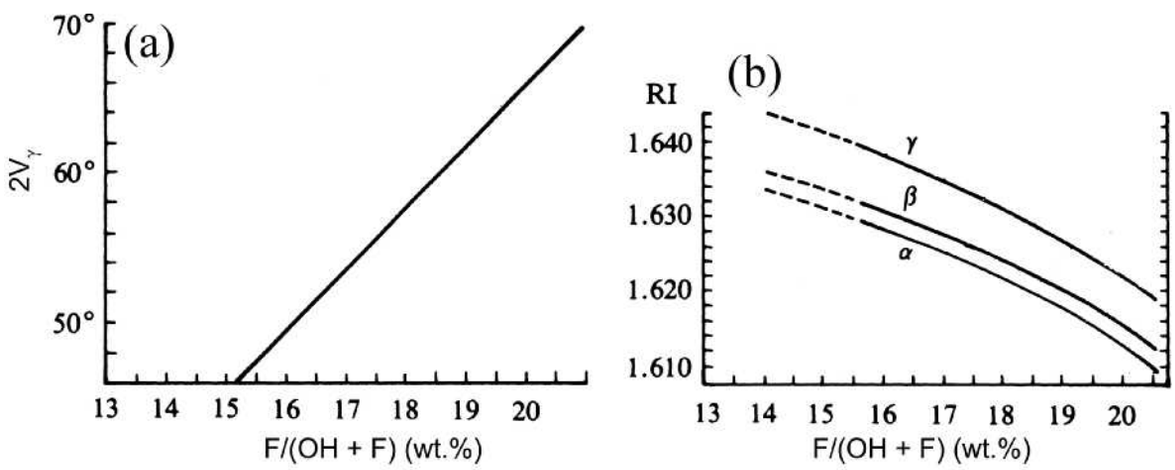


Fig. 36. (a) Optic axial angle $2V_\gamma$ plotted against F content for natural topazes; (b) refractive indices plotted against F content (after Ribbe, P.H. & Rosenberg, P.E., 1971, *Amer. Min.*, **56**, 1812–21).

Downloaded from https://pubs.geoscienceworld.org/books/chapter-pdf/3753391/9780903056434_ch10.pdf
by guest

Distinguishing features

The hardness and the perfect basal cleavage are useful diagnostic features in hand specimens and the high relief together with the weak birefringence, positive optic sign, prismatic form and moderate 2V are characteristic in thin section. Topaz may be distinguished from andalusite by its smaller 2V and by its different orientation in that $\gamma = z$ and the cleavage traces (001) are parallel to the fast ray, whereas andalusite is length-fast, $\alpha = z$. It has higher birefringence than melilite or vesuvianite, and although cleavage flakes of topaz may show very weak birefringence they yield a biaxial figure. It may resemble quartz and feldspar in colour and birefringence but the high relief is distinctive. Hand specimens feel relatively heavy for their size.

Paragenesis

Topaz occurs chiefly in acid igneous rocks, such as granites, granite pegmatites, and rhyolites, and is often found in veins and cavities in such rocks (Table 9, analyses 1, 3). It is usually associated with late-stage pneumatolytic action and is a common constituent of greisen. Associated minerals may include quartz (particularly in topaz-quartz rock or topazfels: e.g. Table 9, analysis 2), fluorite, tourmaline, beryl, cassiterite, and muscovite or zinnwaldite. It may be found as a heavy mineral in detrital sediments near areas of acid intrusive rocks and is known also from emery deposits produced by the metamorphism of bauxite.

Further reading

Akizuki, M., Hampar, M. and Zussman, J. (1979) An explanation of anomalous optical properties of topaz. *Mineralogical Magazine*, **43**, 37–41.

Albertico, A., Ferrando, S., Ivaldi, G. and Ferraris, G. (2003) X-ray single-crystal structure refinement of an OH-rich topaz from Sulu UHP terrane (eastern China) – structural foundation of the correlation between cell parameters and fluorine content. *European Journal of Mineralogy*, **15**, 875–881.

Christiansen, E.H., Sheridan, M.F. and Burt, D.M. (1986) The geology and geochemistry of Cenozoic topaz rhyolites from the western United States. *Geological Society of America, Special Paper* **205**, 82 pp.

Foord, E.E., Jackson, L.L., Taggart, J.E., Crock, J.G. and King, T.V.V. (1995) Topaz: environment of crystallization, crystal chemistry, and infrared spectra. *Mineralogical Record*, **26**, 69–71.

Gatta, G.D., Nestola, F., Bromiley, G.D. and Loose, A. (2006) New insight into crystal chemistry of topaz: a multi-methodological study. *American Mineralogist*, **91**, 1839–1846.

Menzies, M.A. (1995) The mineralogy, geology and occurrence of topaz. *Mineralogical Record*, **26**, 5–53 [This is a special topaz issue.]

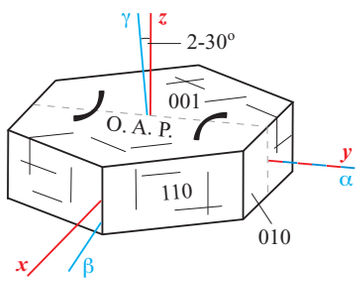
Ribbe, P.H. (1980) Topaz. Pp. 215–230 in: *Orthosilicates* (P.H. Ribbe, editor). Reviews in Mineralogy, **5**, Mineralogical Society of America, Washington, D.C.

Downloaded from https://pubs.geoscienceworld.org/books/chapter-pdf/3753391/9780903056434_ch10.pdf
by guest

Chloritoid $(Fe^{2+},Mg,Mn)_2(Al,Fe^{3+})(OH)_4Al_3O_2[SiO_4]_2$

Monoclinic, Triclinic (+) or (−)

α	1.705−1.730[a]
β	1.708−1.734
γ	1.712−1.740
δ	0.005−0.022
$2V_\gamma$	37−124° [b]
Orientation	*y*:*z* 2−30°; α = *y* or β = *y* (monoclinic polymorph)
Dispersion	*r* > *v* strong (anomalous interference colours)
D (g/cm^3)	3.46−3.80
H	6½
Cleavage	{001} perfect, {110} moderate, {010} parting
Twinning	{001} simple, ternary, lamellar, common
Colour	Dark green to black; colourless to green in thin section
Pleochroism	α pale grey green to green β slaty blue to indigo γ colourless to pale yellow
Unit cell	Monoclinic polytype: *a* 9.48 Å, *b* 5.48 Å, *c* 18.18 Å; β 101.74° Z = 4; space group *C*2/*c* Triclinic polytype: *a* 9.50 Å, *b* 5.48 Å, *c* 9.16 Å; α 96.88°, β 101.82°, γ 90.03° Z = 2; space group $C\bar{1}$
Special features	Soluble in H_2SO_4



Chloritoid is found in low to medium grades of regionally metamorphosed pelitic rocks: in the lower grades it may be associated with chlorite-group minerals and micas, whereas in the higher grades it may occur with staurolite and may be more magnesian at high pressure. It has a characteristic pleochroism, high relief and often displays lamellar twinning.

Structure

The structure of chloritoid consists essentially of two closely packed octahedral layers, L_1 and L_2, lying parallel to the (001) cleavage. L_1 is a trioctahedral brucite-type sheet with composition:

$$(Fe^{2+}Mn,Mg)_4Al_2O_4(OH)_8$$

and L_2 a corundum-type layer of composition $A1_6O_{16}$. These layers alternate in the direction perpendicular to (001) and are linked by individual SiO_4 tetrahedra (not sheets of linked tetrahedra) and by hydrogen bonds (Fig. 37). The corresponding ideal structural formula would be $(Fe^{2+},Mn,Mg)_2Al(OH)_4Al_3O_2[SiO_4]_2$, or to illustrate the linkage of the oxide and hydroxyl layers by Si atoms:

$$Al_3O_8Si_2(Fe^{2+},Mn,Mg)_2A1O_2(OH)_4$$

There are two distinct sets of cation sites in the octahedral L_1 layer (Fig. 37), (Fe^{2+},Mg,Mn) being statistically distributed over one set and Al and vacancies in the other. The L_2 layer contains only Al octahedra, each of which shares four edges with adjacent octahedra and three out of every four sites are occupied. Some twin laws shown by chloritoid are not consistent with the above structure. In addition, the optical properties of some chloritoids indicate departure from monoclinic symmetry and the existence of a triclinic structural type. The triclinic and monoclinic

[a] Mg-rich chloritoids have lower refractive indices and smaller cell parameters.
[b] 2V mainly in the range 45−70°

Downloaded from https://pubs.geoscienceworld.org/books/chapter-pdf/3753460/9780903056434_ch11.pdf
by guest

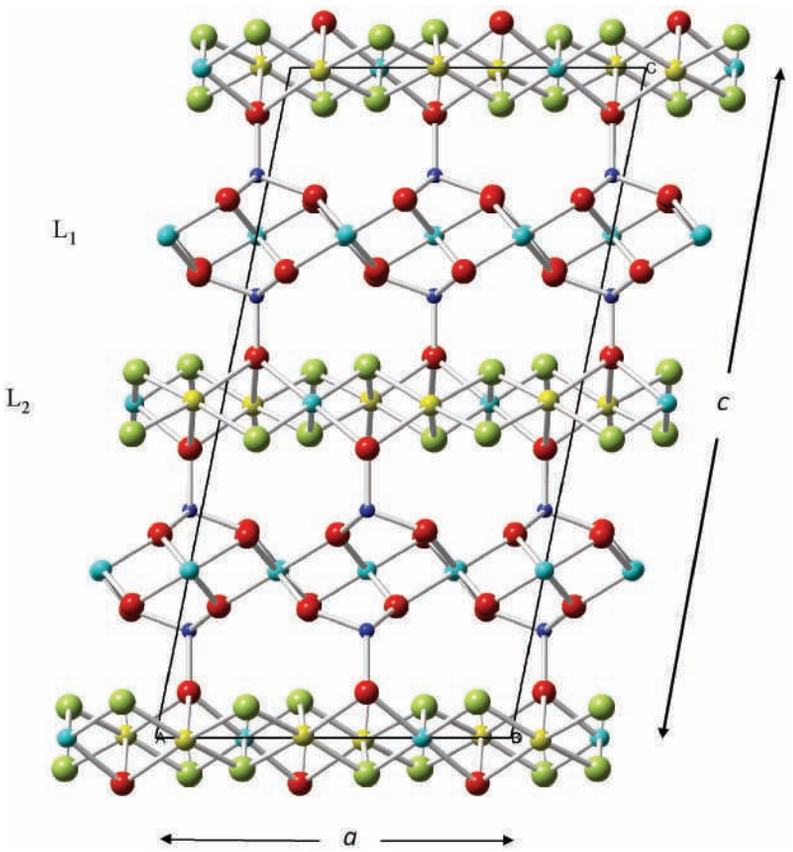


Fig. 37. The structure of chloritoid projected on (010) showing the two kinds of octahedral layer L_1 and L_2 (based on data from Brindley, G.W. & Harrison, F.W., 1952, *Acta Cryst*., **5**, 698–9. Fig. produced by M.D. Welch). Red: oxygen; green: (OH); light blue: Al; dark blue: Si; yellow: Mg.

polymorphs can be related by a twinning two-fold rotation or screw axis parallel to *y* operating on the triclinic space group $C\bar{1}$ to yield the space group *C*2/*c*. Other polymorphs (polytypes), one trigonal, have also been identified; the polymorphism can be described in terms of displacements across the L_1 layer and slight displacements in the L_2 layer.

Chemistry

The main compositional variations shown by chloritoid are related to the substitutions (Mg,Mn) ↔ Fe^{2+} and Fe^{3+} ↔ Al. The amount of substitution of Fe^{2+} by Mg and Mn generally ranges between 0 and 40 and 0 and 17 atom%, respectively. A considerable extension of this range, however, occurs in a small number of chloritoids and is as much as 97 atom% in the extremely Mg rich chloritoid (magnesiochloritoid) in high-pressure assemblages (Table 10, analysis 2). Mn-rich chloritoids (ottrelite) with Fe^{2+} ↔ Mn replacement as high as 96 atom% occur in schists from the Ardennes, Belgium. Manganese has a marked preference for chloritoid rather than coexisting chlorite in these rocks. Some substitution of Al by Fe^{3+} (or Cr^{3+} in a few Mg-rich chloritoids) occurs in the majority of chloritoids but usually amounts to less than 50% of the trivalent ions of the mixed octahedral layer. Most chloritoids do not have significantly less than the ideal 4 (OH) groups per formula unit. Those with an appreciably smaller amount of (OH) usually have above average contents of Fe^{3+}, and the hydroxyl deficiency may be due to oxidation of some ferrous iron.

At fluid pressures below 1 GPa and an oxygen fugacity of Ni–NiO and QFM buffers (Fig. 38), Fe-chloritoid is unstable above 550ºC at 0.1 GPa and above 575ºC at 0.2 GPa. It breaks down to hercynite$_{ss}$ + H_2O ± ferro-anthophyllite + staurolite, the amphibole being replaced by almandine at higher temperatures and pressures. In a detailed experimental study of chloritoid stability between 550 and 700ºC at 2.5 and 4.5 GPa (at various f_{O_2} conditions) it was found that at high pressures the Fe^{3+} contents of both chloritoid and almandine increase with pressure, amounting to 0.2 pfu $FeAl_2SiO_5(OH)_2$ in the chloritoid at above 3 GPa, in agreement with natural assemblages.

Optical and physical properties

The optical orientation of chloritoid shows considerable variation that may differ even between grains in the same specimen, and in individual grains adjacent lamellae may display alternating monoclinic and triclinic symmetry. In most chloritoids γ is the acute bisectrix and the majority are thus optically positive; α is the commonest vibration to lie in the (001) plane.

In monoclinic chloritoid either the α or the β vibration direction coincides with the *y* crystal axis, whereas the other two vibration directions have variable

Downloaded from https://pubs.geoscienceworld.org/books/chapter-pdf/3753460/9780903056434_ch11.pdf
by guest

Table 10. Chloritoid analyses.

	1	2	3		Numbers of ions on the basis of 14 (O,OH) 1		2		3	
SiO_2	23.91	26.01	24.24	Si	2.000		2.013		1.971	
TiO_2	0.20	0.00	–	Al	3.000		3.000		3.000	
Al_2O_3	40.12	43.57	41.31	Al	0.954	1.04	0.976	0.98	0.961	1.06
Fe_2O_3	1.23	–	1.70	Ti	0.013		–		–	
FeO	27.06	9.02	8.14	Fe^{3+}	0.077		–		0.103	
MnO	0.16	0.03	12.79	Mg	0.063	1.97	1.421	2.01	0.543	1.99
MgO	0.51	12.32	4.46	Fe^{2+}	1.892		0.584		0.553	
CaO	0.04	0.01	0.11	Mn	0.011		0.003		0.880	
Na_2O	0.00	0.01	–	Ca	0.004		0.001		0.010	
K_2O	tr.	0.00	–	Na	–		0.002		–	
H_2O+	7.03	–	7.26	OH	3.961[a]		–		3.941	
H_2O-	0.01	–	–							
Total	100.28	90.97	100.01							
				Atomic percentages						
				Fe	96		29		28	
				Mg	3		71		27.5	
				Mn	1		–		44.5	

1 Chloritoid, Natick, Rhode Island, USA (Halferdahl, L.B., 1961, *J. Petrol*., **2**, 49–135). Includes F 0.01.
2 Magnesiochloritoid, chloritoid–phengite–talc–chlorite–kyanite–quartz metapelite, Monte Rosa, Western Alps (Chopin, C. & Monié, P., 1984, *Contrib. Mineral. Petrol*., **87**, 388–98). Microprobe analysis. Number of ions on basis of 12 O.
3 Chloritoid (ottrelite), border of quartz vein cutting metamorphic slates. Ottré, Belgium (Fransolet, A.M., 1978, *Bull. Min*., **101**, 548–57).

[a] Includes F 0.003.

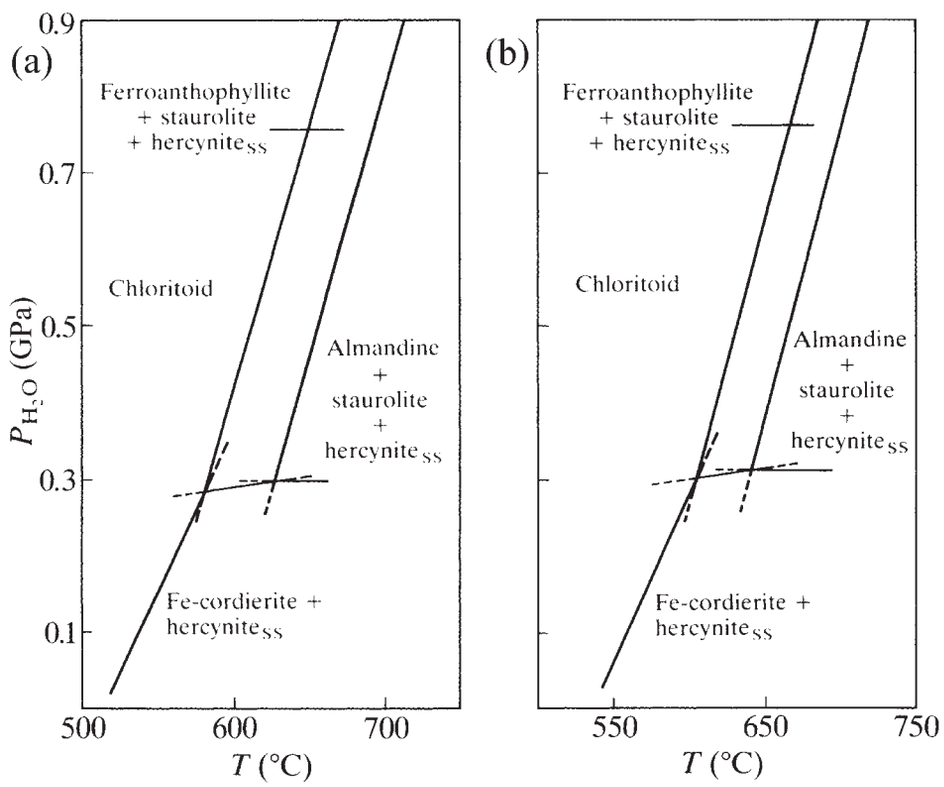


Fig. 38. P_{fluid}–T diagram for chloritoid + excess water: (a) oxygen fugacity defined by the Ni–NiO buffer; (b) oxygen fugacity defined by the quartz–fayalite–magnetite buffer (QFM) (after Grieve, R.A.F. & Fawcett, J.J., 1974, *J. Petrol*., **15**, 113–39).

Downloaded from https://pubs.geoscienceworld.org/books/chapter-pdf/3753460/9780903056434_ch11.pdf
by guest

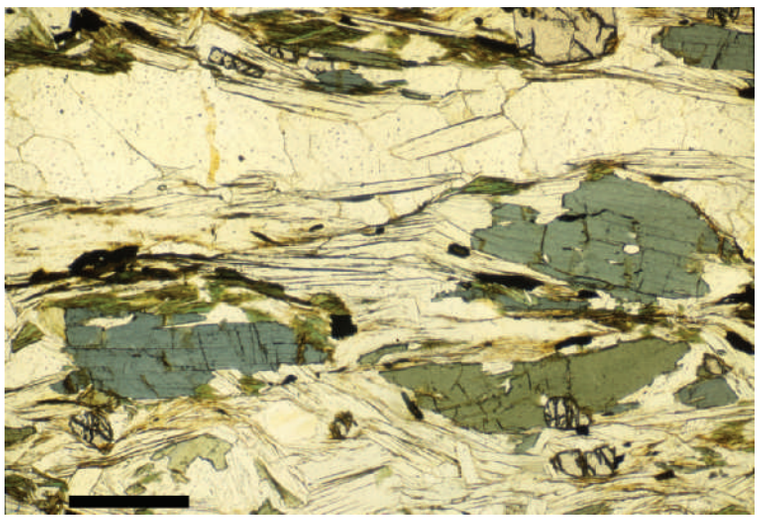


Fig. 39. Chloritoid in muscovite-garnet-quartz schist, Île de Groix, Brittany, France (ppl, scale bar 1 mm) in olive-green crystals with moderate relief (W.S. MacKenzie collection, courtesy of Pearson Education).

positions in the (010) plane; there is a wide range of extinction and optic axial angles. In the triclinic polymorph one or two vibration directions may lie in the (001) plane but neither necessarily is coincident with the *y* crystal axis, and the orientation of the optical indicatrix can be determined only by using universal stage methods. Chloritoid refractive indices show a limited correlation with $\Sigma(Fe^{2+} + Fe^{3+} + Mn)$ and are not a useful guide to chemical composition. Variations from the common greenish to bluish pleochroism occur in manganese-rich varieties (pale browns and browns); magnesium-rich chloritoids may be colourless or only faintly pleochroic (Fig. 39).

Many chloritoids show strong dispersion, $r > v$, and anomalous interference colours are a common feature. Zoning is sometimes present, including the development of hour-glass structure shown by slight colour differences or by the concentration of inclusions within the hour-glass. Repeated twinning is common with the composition plane parallel to {001}.

Distinguishing features

The chloritoid pleochroic scheme, high relief, common lamellar twinning, and strong dispersion are usually sufficiently diagnostic for its identification. Varieties with low birefringence and anomalous interference colours can be distinguished from chlorite by their higher refractive indices. Clintonite has a smaller optic axial angle and negative sign; green-coloured biotite and stilpnomelane both have a higher birefringence and single cleavage.

Paragenesis

Chloritoid is a relatively common constituent of low- to medium-grade regionally metamorphosed pelitic sediments, particularly those having a high content of aluminium and iron. In such rocks belonging to the low-grade greenschist facies, chloritoid is present in

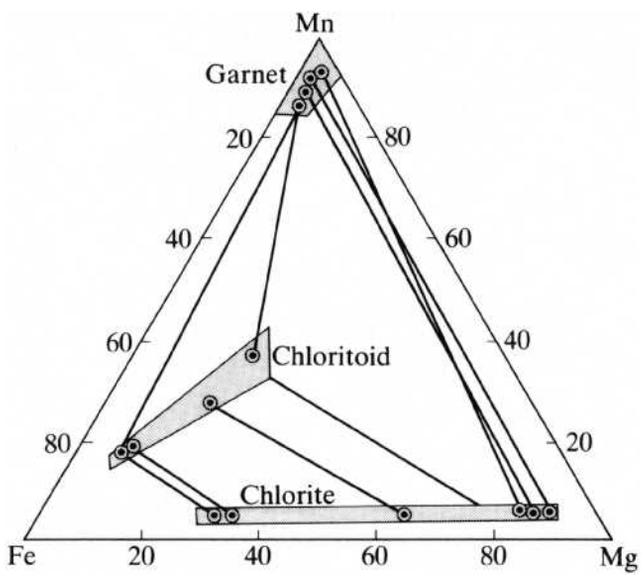


Fig. 40. Compositional fields (shaded) of chloritoid, chlorite and garnet in the isofacial assemblages chloritoid-phengite-paragonite-chlorite-garnet-quartz-hematite-rutile and phengite-paragonite-chlorite-garnet-quartz-hematite-rutile assemblages of the southern Venn–Stavelot massif, Ardennes (after Kramm, U., 1973, *Contrib. Mineral. Petrol.*, **41**, 171–96).

Downloaded from https://pubs.geoscienceworld.org/books/chapter-pdf/3753460/9780903056434_ch11.pdf
by guest

assemblages with chlorite, phengite and paragonite micas, garnet, hematite and rutile (Fig. 40). Both the monoclinic and triclinic polymorphs occur and the chloritoid typically has a high Mn content (up to 45 mol% of the ottrelite component). Some of these chloritoid-bearing rocks have bulk compositions resembling those of laterite, bauxite and ferruginous clays.

In rocks of medium grade, chloritoid-bearing assemblages not uncommonly include staurolite; the latter is derived in part from breakdown of the chloritoid resulting from the reaction:

$$\text{chloritoid} + \text{quartz} \rightarrow \text{staurolite} + \text{garnet} + H_2O$$

in iron-rich metapelites, and in more magnesium-rich metapelites to the reaction:

$$\text{chloritoid} + \text{chlorite} + \text{muscovite} \rightarrow \text{staurolite} + \text{biotite} + \text{quartz} + H_2O$$

Chloritoid is less common in rocks of higher grade than the lower amphibolite facies, but is present, with staurolite, garnet and kyanite, in some metapelites; it occasionally occurs in schists of the sillimanite zone. Coherent intergrowths of chloritoid with chlorite, stilpnomelane and paragonite occur in some garnet- and staurolite-grade metapelites; they probably formed by retrograde replacement of the chloritoid.

Chloritoid occurs in metasediments and metabasites in ophiolitic associations. Typical assemblages include glaucophane and garnet, but assemblages with stilpnomelane, lawsonite and pumpellyite also occur. Some chloritoid–glaucophane associations originate as the retrograde products of an eclogite assemblage, omphacite + garnet → chloritoid + glaucophane + epidote, the chloritoid and glaucophane later being replaced by paragonite + chlorite. Mg-rich chloritoid occurs with carpholite, $(Mg,Fe^{2+})Al_2[Si_2O_6](OH)_4$, in some pelitic blueschists.

Further reading

Chopin, C. and Schreyer, W. (1983) Magnesiocarpholite and magnesiochloritoid: two index minerals of pelitic blueschists and their preliminary phase relations in the model system $MgO–Al_2O_3–SiO_2–H_2O$. *American Journal of Science*, **283A**, 72–96.

Chopin, C., Seidel, E., Theye, T., Ferraris, G., Ivaldo, G. and Catti, M. (1993) Magnesiochloritoid and the Fe-Mg series in the chloritoid group. *European Journal of Mineralogy*, **4**, 67–76.

Gabriele, P., Ballèvre, M., Jaillard, E. and Hernandez, J. (2003) Garnet-chloritoid-kyanite metapelites from the Raspas complex (SW Ecuador): a key eclogite-facies assemblage. *European Journal of Mineralogy*, **15**, 977–989.

Ganguly, J. (1999) Chloritoid stability and related parageneses: theory, experiments and applications. *American Journal of Science*, **267**, 910–944.

Grieve, R.A.F. and Fawcett, J.J. (1974) The stability of chloritoid below 10 kb P_{H_2O}. *Journal of Petrology*, **15**, 113–139.

Koch-Müller, M., Abs-Wurmbach, L., Langer, K., Shaw, C., Wirth, R. and Gottschalk, M. (2000) Synthetic and natural Fe-Mg chloritoid: structural, spectroscopic and thermodynamic studies. *European Journal of Mineralogy*, **12**, 93–314.

Messiga, B., Scamburelli, M. and Picardo, G.B. (1995) Chloritoid bearing assemblages in mafic systems and eclogite-facies hydrated Alpine Mg-Fe metagabbros (Erro-Tabbio unit, Ligurian Western Alps). *European Journal of Mineralogy*, **7**, 1149–1167.

Okay, A. (2002) Jadeite-chloritoid-glaucophane-lawsonite blueschists in northwest Turkey: unusually high P/T ratios in continental crust. *Journal of Metamorphic Geology*, **20**, 757–768.

Rahn, M.K., Steinmann, M. and Frey, M. (2002) Chloritoid composition and formation in the eastern central Alps: a comparison between Penninic and Helvetic occurrences. *Schweizerische Mineralogische und Petrographische Mitteilungen*, **82**, 409–426.

Simon, G., Chopin, C. and Schenk, V. (2000) Near-end-member magnesiochloritoid in prograde-zoned pyrope, Dora-Maira massif, Western Alps. *Lithos*, **6**, 547–555.

Theye, T. and Fransolet, A.-M. (1994) Virtually pure ottrelite from the region of Ottré, Belgium. *European Journal of Mineralogy*, **6**, 547–555.

Vidal, O., Theye, T.H. and Chopin, C. (1984) Experimental study of chloritoid stability at high pressures and various f_{O_2} conditions. *Contributions to Mineralogy and Petrology*, **118**, 256–270.

Downloaded from https://pubs.geoscienceworld.org/books/chapter-pdf/3753460/9780903056434_ch11.pdf
by guest

Epidote Group

Introduction

All members of the epidote group have structures containing chains of edge-sharing octahedra parallel to the *y* axis and linked laterally by single [SiO_4] tetrahedra and double tetrahedral [Si_2O_7] groups. Relatively large cavities within this framework are occupied by larger cations, most commonly Ca, in seven- to nine-fold coordination by (O,OH) anions.

Members of the group have monoclinic symmetry, except for those in which the composition approximates to $Ca_2Al_3Si_3O_{12}(OH)$, which may have either orthorhombic (zoisite) or monoclinic (clinozoisite) symmetry. Compositional variations within the group are related mainly to the substitutions $Al \leftrightarrow Fe^{3+}$ and $Ca^{2+}+Fe^{3+} \leftrightarrow REE^{3+}+Fe^{2+}$. The compositions can be expressed by the general formula:

$$A_2M_3Z_3(O,OH,F)_{12}$$

in which A is most commonly Ca, but also Ce, Sr, Pb, La, Y, Th and Mn^{2+}; M is Al, Fe^{3+}, Mn^{3+}, Mn^{2+}, Fe^{2+}, Cr, V and Ti; and Z is Si.

A system of nomenclature for members of the epidote mineral group has been recommended by a subcommittee of the Commission on New Minerals Nomenclature and Classification of the International Mineralogical Association (Ambruster *et al*., 2006).

In terms of the crystal structures, there are two distinct *A* sites and three distinct *M* sites, and the major end-member compositions and site assignments within the main members of the epidote mineral group, are:

	*A*1	*A*2	*M*1	*M*2	*M*3
Clinozoisite (zoisite)	Ca	Ca	Al	Al	Al
Epidote	Ca	Ca	Al	Al	Fe^{3+}
Piemontite	Ca	Ca	Al	Al	Mn^{3+}
Allanite	Ca	$(REE)^{3+}$	Al	Al	Fe^{2+}

Epidote-group minerals with unusually high contents of chromium, vanadium, lead, strontium, cerium and fluorine have been described.

Epidote-group minerals occur in a wide variety of parageneses. Typically products of regional metamorphism, they also form under conditions of contact metamorphism and during crystallization of acid igneous rocks.

Further reading

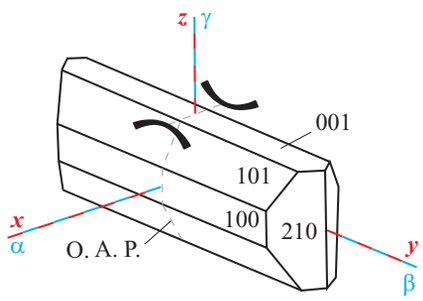
Armbruster, T., Bonazzi, P., Akasaka, M., Bermanec, V., Chopin, C., Gieré, R., Heuss-Assbichler, S., Liebscher, A., Menchetti, S., Pan, Y. and Pasero, M. (2006) Recommended nomenclature of epidote-group minerals. *European Journal of Mineralogy*, **18**, 551–567.

Liebscher, A. and Franz, G. (Editors) (2004) *Epidotes.* Reviews in Mineralogy & Geochemistry, **56**, Mineralogical Society of America and Geochemical Society, Washington, D.C., 368 pp.

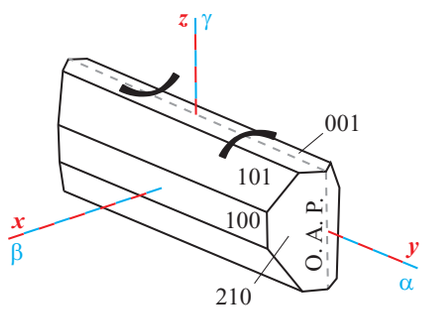
Downloaded from https://pubs.geoscienceworld.org/books/chapter-pdf/3753874/9780903056434_ch12.pdf
by guest

Orthorhombic (+)

Zoisite



Ferrian Zoisite



α	1.685–1.705	
β	1.688–1.710	
γ	1.697–1.725	
δ	0.003–0.008	
$2V_\gamma$	0–69°	
Orientation	$\alpha = x$, $\beta = y$, $\gamma = z$; O.A.P. (010)	$\alpha = y$, $\beta = x$, $\gamma = z$; O.A.P. (010)
D (g/cm^3)	3.15–3.37	
H	6–7	
Cleavage	{100} perfect, {001} imperfect	
Colour	Grey, green-brown (thulite, pink); colourless in thin section (thulite, pink-yellow)	
Pleochroism	*Thulite*: α pale pink (rose), dark pink β nearly colourless, bright pink γ pale yellow, yellow	
Unit cell	α ~ 16.2 Å, *b* ~ 5.55 Å, *c* ~ 10.04 Å Z = 4; space group *Pnma*	
Special features	Anomalous blue interference colours not uncommon	

Zoisite is the only orthorhombic member of the epidote group and is dimorphous with monoclinic clinozoisite. The *b* and *c* cell parameters of zoisite are similar to those for the monoclinic members of the epidote group, and the *a* dimension in orthorhombic zoisite corresponds with the 2*a* sinβ in monoclinic epidote. Zoisite is found commonly as a metamorphic product of calcareous shales in rocks of the epidote-amphibolite facies. It has low birefingence.

The structure of zoisite, like that of clinozoisite (Fig. 43, p. 57), is based upon chains of edge-sharing octahedra (*M*1,*M*2) linked laterally by isolated single SiO_4 and double Si_2O_7 tetrahedra. In zoisite, however, there is only one type of chain, not two, and this chain has additional octahedra (*M*3) attached on only one side along its length, rather than on both sides as in clinozoisite. The resulting framework contains sites of two kinds, *A*1 and *A*2, most commonly occupied by Ca in 7- and 8-fold coordination, respectively. The structure has orthorhombic symmetry and has been described as related to that of clinozoisite by a diagonal glide twin operation on the monoclinic cell. The result of this operation matches the structure of zoisite, but only qualitatively.

Zoisites show relatively minor compositional departures from $Ca_2Al_3Si_3O_{12}(OH)$ (Table 11, analysis 1, p. 58). Manganese is present in only small quantities even in the manganese-bearing variety, thulite; a green Cr-bearing variety, tawmawite and a V-bearing gem-

Downloaded from https://pubs.geoscienceworld.org/books/chapter-pdf/3753877/9780903056434_ch13.pdf
by guest

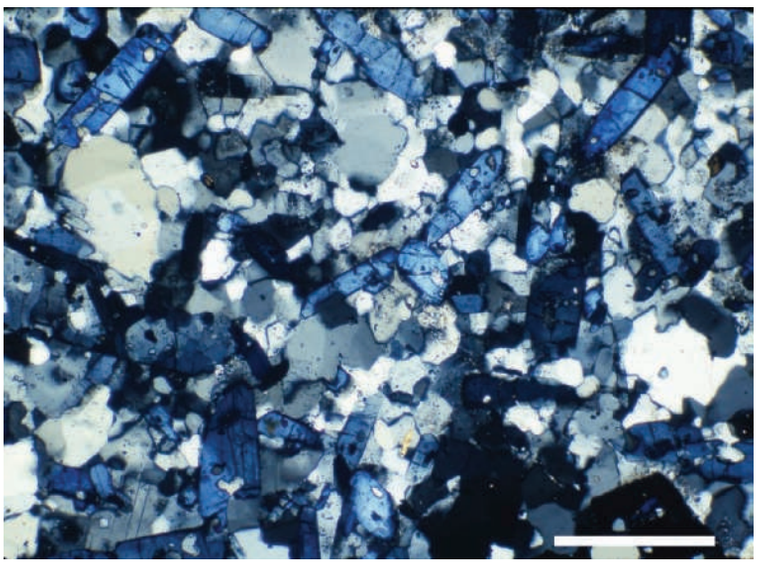


Fig. 41. Zoisite crystals in zoisite-quartz schist, Glen Roy, Inverness-shire, Scotland (crossed polars, scale bar 0.5 mm) showing high relief and anomalous blue interference colours. This is characteristic of both zoisite and clinozoisite, but zoisite shows straight extinction in all sections (W.S. MacKenzie collection, courtesy of Pearson Education).

variety, tanzanite are also known. Zoisite has been synthesized by a number of methods including its preparation by hydrothermal treatment of gel of requisite composition at 700ºC, P_{H_2O} 1.5 GPa. The same gel held at 470ºC, 2 GPa H_2O yields clinozoisite. Experiments have indicated that the transition from clinozoisite to zoisite occurs below 200ºC at pressures up to 1 GPa, and that in the system $CaO–Al_2O_3–SiO_2–H_2O$, zoisite is the stable polymorph up to temperatures above 1200ºC and pressures up to 7 GPa.

Zoisite occurs in two optical orientations that are related to the iron content. In zoisites with X_{Fe} [= $Fe^{3+}/(Fe^{3+} + Al)$] between 0 and ~0.05, the optic axial plane is (010); in zoisites with higher X_{Fe} values it is (100). Strong dispersion is common in most zoisites and is responsible for the anomalous blue interference colours of many specimens. Zoning, due to variations in X_{Fe}, is common and includes sector zoning. Colour banding in the thulite variety is correlated with variations in the Mn^{3+}/Mn^{2+} ratio and related to changes in f_{O_2} during growth.

Zoisite can be distinguished from clinozoisite by its parallel extinction, from other epidote-group minerals, except the thulite variety, by its lack of colour and weaker birefringence, from vesuvianite by its biaxial character, positive sign and perfect cleavage, from sillimanite by its weaker birefringence and from apatite by its biaxial character and positive sign. It may show anomalous blue interference colours between crossed polars in thin section (Fig. 41).

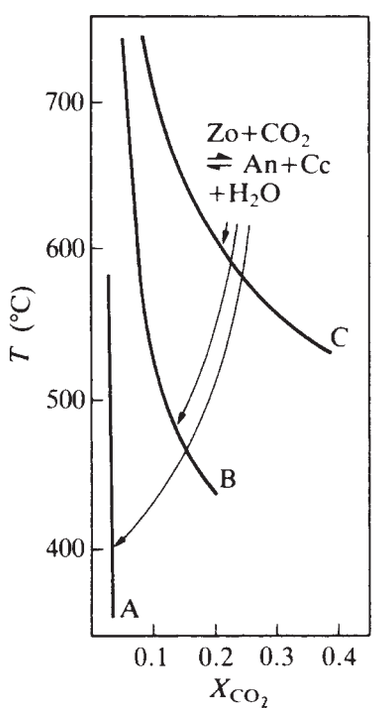


Fig. 42. $T–X_{CO_2}$ diagram showing equilibrium curves at pressures of 0.2 (A), 0.5 (B) and 0.7 (C) GPa for the reaction zoisite + $CO_2 \rightleftharpoons$ anorthite + calcite + H_2O (after Storre, B. *et al*., 1982, *Neues Jahrb. Min. Monat*., 395–406). Zo, zoisite; An, anorthite; Cc, calcite.

Downloaded from https://pubs.geoscienceworld.org/books/chapter-pdf/3753877/9780903056434_ch13.pdf
by guest

Zoisite is a relatively common constituent in epidote-amphibolite facies rocks derived from calcareous shales and sandstones, and in amphibolites derived from basic igneous rocks. At metamorphic grades higher than the amphibolite facies, zoisite is unstable and is commonly replaced by calcium-rich plagioclase. Experimentally determined equilibrium curves for the reaction:

$$2\,Ca_2Al_3Si_3O_{12}OH + CO_2 \rightleftharpoons 3\,CaAl_2Si_2O_8 + CaCO_3 + H_2O$$

at 0.2, 0.5 and 0.7 GPa are shown in Fig. 42. Other parageneses include its occurrence both as a primary and secondary phase in eclogites and blueschists.

Further reading

Allen, J.M. and Fawcett, J.J. (1982) Zoisite-anorthite-calcite stability relations in H_2O-CO_2 fluids at 5000 bars. An experimental and SEM study. *Journal of Petrology*, **23**, 215–239.

Brunsmann, A., Franz, G. and Heinrich, W. (2002) Experimental investigation of zoisite–clinozoisite phase equilibria in the system $CaO–Fe_2O_3–Al_2O_3–SiO_2–H_2O$. *Contributions to Mineralogy and Petrology*, **143**, 115–130.

Franz, G. and Liebscher, A. (2004) Physical and chemical properties of the epidote minerals – an introduction. Pp. 1–81 in: *Epidotes* (A. Liebscher and G. Franz, editors). Reviews in Mineralogy & Geochemistry, **56**, Mineralogical Society of America and Geochemical Society, Washington, D.C.

Poli, S. and Schmidt, M.W. (2004) Experimental subsolidus studies on epidote minerals. Pp. 171–195 in: *Epidotes* (A. Liebscher and G. Franz, editors). Reviews in Mineralogy & Geochemistry, **56**, Mineralogical Society of America and Geochemical Society, Washington, D.C.

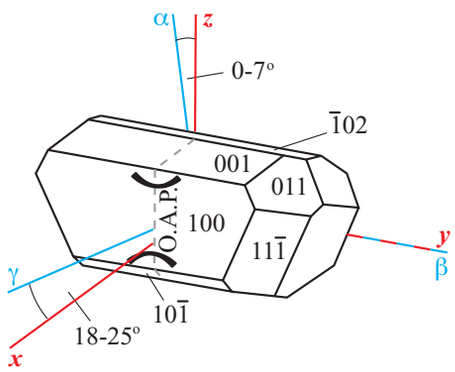
Prunier, A.R. and Hewitt, D.A. (1985) Experimental observations on coexisting zoisite–clinozoisite. *American Mineralogist*, **70**, 373–378.

Downloaded from https://pubs.geoscienceworld.org/books/chapter-pdf/3753877/9780903056434_ch13.pdf
by guest

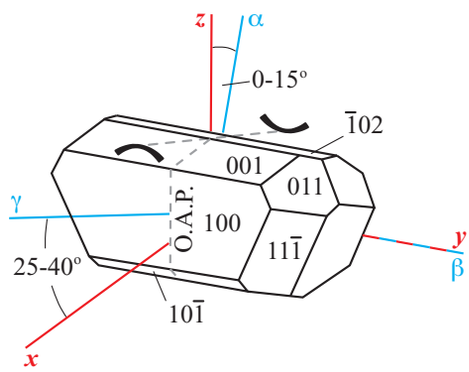
Clinozoisite $Ca_2Al_3[Si_2O_7][SiO_4]O(OH)$

Epidote $Ca_2Al_2Fe^{3+}[Si_2O_7][SiO_4]O(OH)$

Clinozoisite
Monoclinic (+)



Epidote
Monoclinic (−)



α	1.670–1.718	1.715–1.751
β	1.670–1.725	1.725–1.784
γ	1.690–1.734	1.734–1.797
δ	0.004–0.015	0.015–0.05
$2V_\gamma$	14–90°	90–116°
Orientation	α:*z* 0–7°, β = *y*; O.A.P. (010)	α:*z* 0–15°, β = *y*; O.A.P. (010)
D (g/cm^3)	3.21–3.38	3.38–3.49
H	6½	6
Cleavage	{001} perfect	{001} perfect
Twinning	{100} lamellar, not common	{100} lamellar, not common
Colour	Colourless, pale yellow, grey, green; colourless in thin section	Green, yellow, grey; yellow-green in thin section
Pleochroism	Usually non-pleochroic	α colourless, pale yellow, pale green β greenish yellow γ yellowish green
Unit cell	*a* ~ 8.86 Å, *b* ~ 5.58 Å, *c* ~ 10.14 Å, β ~ 115.5° Z = 2; space group $P2_1/m$	*a* 8.8–8.9 Å, *b* 5.59–5.65 Å, *c* 10.15–10.2 Å, β 115.4° Z = 2; space group $P2_1/m$
Special features	Insoluble in HC1 May show anomalous interference colours	Partially decomposed in HCl

Clinozoisite–epidote series minerals are characteristic of metamorphic rocks of the greenschist and epidote-amphibolite facies, and commonly occur in association with prehnite, pumpellyite, chlorite and actinolite. They have moderate to high refractive indices, notably in epidote, and range in colour from colourless in thin section (clinozoisite) to yellowish green (epidote). Clinozoisite may show anomalous interference colours.

Downloaded from https://pubs.geoscienceworld.org/books/chapter-pdf/3754121/9780903056434_ch14.pdf
by guest

Structure

The structure of clinozoisite is illustrated in Fig. 43. It contains chains, parallel to *y*, of edge-sharing octahedra of two kinds: one consists solely of edge-sharing *M*2−O,OH octahedra, whereas the other is a chain of *M*1−O octahedra with *M*3−O octahedra attached on alternate sides along its length. The *M*1 and *M*2 cation sites are centrosymmetric; *M*3 is non-centrosymmetric. Bridging the chains of octahedra laterally and sharing some of their oxygens are single tetrahedra [SiO_4] (labelled *Si*3) and corner-sharing pairs of Si tetrahedra [Si_2O_7] (labelled *Si*1 and *Si*2). The latter grouping places the epidotes as 'disilicates'. The framework so formed contains relatively large structural sites of two kinds, *A*1 and *A*2, most commonly occupied respectively by Ca in 7- and 8-fold coordination, in the almost Fe-free clinozoisites, and more generally by cations in 8- and 9-fold coordination

The *M*2 octahedra contain only Al and within the (*M*1,*M*3) chain the *M*3 site contains the most non-Al atoms (largely Fe^{3+} and Mn). The non-random octahedral site occupation results from the preference of Al for the (O,OH)-coordinated *M*2 site and the preference of the larger Fe,Mn atoms for the larger more distorted *M*3 site. The one H ion p.f.u. is associated with O_{10} of the *M*2 octahedron and hydrogen bonded to O_4 of the neighbouring *M*1 octahedron.

Cell parameters *a*, *b*, *c* and cell volume show an approximately linear relationship with increasing Fe,Mn content. A change in slope is observed, however, at X_{Fe} 0.6, associated with the preferential entry of Fe into the *M*3 site below, and into both *M*1 and *M*3 above, this discontinuity. The change at this composition is supported also by optical parameters and the site occupations by structure refinements and Mössbauer spectroscopy.

Chemistry

The great majority of the members of the clinozoisite–epidote series have compositions between $Ca_2Al_3Si_3O_{12}(OH)$ and $Ca_2Fe^{3+}Al_2Si_3O_{12}(OH)$; the latter [and in some cases $Ca_2Fe^{3+}_3Si_3(O,OH)_{12}$] were formerly described as the pistacite (Ps) end-member but epidote (Ep) is now preferred for the end-member $Ca_2Al_2Fe^{3+}Si_3(O,OH)_{12}$, even though the name is used also for the epidote group as a whole. The replacement of Ca by Fe^{2+},Mg,Mn rarely exceeds 0.15 atoms per formula unit. Rare earth elements are generally absent or present in trace quantities; a few epidotes, however, do contain appreciable amounts and show transitional characters towards allanite. Rare chromian (tawmawite), plumbian (hancockite) and vanadium-bearing (mukhinite) epidotes have been described.

At temperatures above ~730ºC there is continuous solid solution between clinozoisite and epidote (both Al/Fe^{3+} disordered), but with falling *T*, ordering and unmixing occur. On the basis of the compositions of natural specimens, and the results of laboratory experiments and calculation, two gaps occur at lower temperature (Fig. 44). Low-temperature epidotes with intermediate compositions have, however, been reported, and the effects of f_{O_2} as well as temperature need to be considered.

In addition to experiments on compositions within the binary clinozoisite–epidote system, there have been many others in the system $CaO–Al_2O_3–SiO_2–H_2O$, and in its extension by the inclusion of MgO, Fe_2O_3, Na_2O and/or K_2O (see Poli and Schmidt, 2004). Epidote is a stable mineral over a wide range of temperatures and pressures, including those of greenschist to epidote-amphibolite facies metamorphism. Experiments have shown epidote formation at *P*/*T* below these, with and without CO_2, and above them into blueschist- and

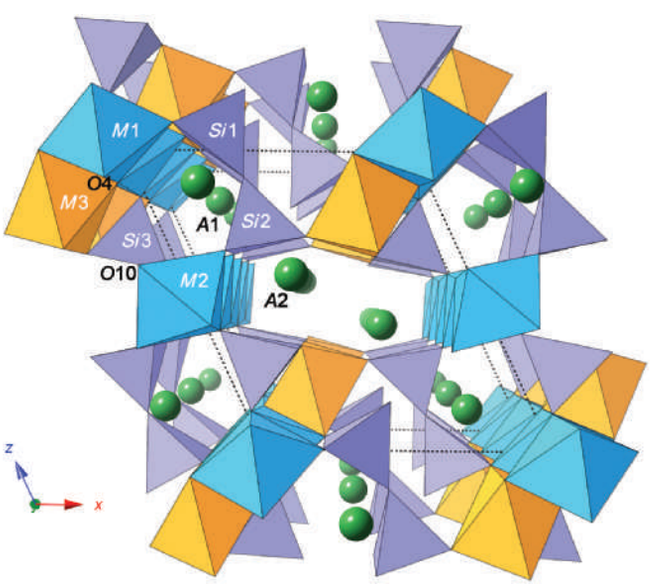


Fig. 43. The structure of clinozoisite. Perspective view from direction close to the *y* axis (CrystalMaker image). Lavender: Si−O tetrahedra; blue: *M*1 and *M*2 Al−O octahedra; yellow: *M*3 Al−O octahedra; green: Ca ions.

Downloaded from https://pubs.geoscienceworld.org/books/chapter-pdf/3754121/9780903056434_ch14.pdf
by guest

Table 11. Epidote-group analyses.

	1	2	3	4	5	6
SiO_2	41.64	39.50	38.44	36.96	37.06	30.82
TiO_2	0.02	0.13	0.15	0.50	0.24	0.71
Al_2O_3	33.38	31.78	30.91	16.08	21.86	14.83
Fe_2O_3	0.11	1.61	7.62	23.06	2.21	7.71
Mn_2O_3	–	–	–	–	15.44	–
Y_2O_3	–	–	–	–	–	1.03
Ce_2O_3	–	–	–	–	–	7.28
La_2O_3	–	–	–	–	–	11.43
FeO	–	0.35	–	–	–	9.11
MnO	0.05	0.03	0.11	0.10	–	5.16
MgO	0.00	0.34	0.06	0.03	0.05	0.45
CaO	23.97	23.78	23.73	22.02	21.73	8.83
Na_2O	0.45	0.10	0.02	0.02	0.02	–
K_2O	0.05	tr.	0.00	0.02	–	–
H_2O+	–	2.10	–	–	–	1.50
H_2O-	–		–	–	–	–
Total	99.67	99.72	101.04	98.79	98.61	98.86
	Numbers of ions on the basis of 12.5 O[a]					
Si	3.086 } 3.09	3.010 } 3.01	2.895 } 3.00	3.002 } 3.02	2.957 } 3.00	2.936 } 3.00
Al	0.000 }	0.000 }	0.105 }	0.000 }	0.043 }	0.064 }
Al	2.917 } 2.92	2.855 } 2.95	2.639 } 3.08	1.550 } 3.00	2.014 } 3.00	1.602 } 2.16
Fe^{3+}	0.006 }	0.092 }	0.432 }	1.419 }	0.133 }	0.553 }
Ti	0.001 }	0.007 }	0.008 }	0.031 }	0.014 }	0.051 } 0.84
Mn^{3+}	–	–	–	–	0.839 }	– }
Mg	0.000 } 1.98[b]	0.039 } 2.02[c]	0.007 } 1.93[d]	0.004 } 1.95[e]	0.006 } 1.97[f]	0.064 } 2.07[g]
Fe^{2+}	– }	0.022 }	– }	– }	– }	0.726 }
Mn^{2+}	0.003 }	0.002 }	0.007 }	0.007 }	– }	0.417 }
Y^{3+}	– }	– }	– }	– }	– }	0.052 }
Ca	1.904 }	1.941 }	1.915 }	1.929 }	1.858 }	0.901 }
Ce^{3+}	– }	– }	– }	– }	– }	0.243 }
La^{3+}	– }	– }	– }	– }	– }	0.404 }
OH	–	1.067	–	–	–	0.954

1 Zoisite, metagabbro, Feather River area, northern Sierra Nevada, California, USA (Hietanen, A., 1974, *Amer. Min.*, **69**, 22–40).
2 Clinozoisite, metamorphosed gabbro, Ala di Stura, Alpes piemontaises (Nicolas, A., 1966, *Fac. Sci. Nantes*, 299 pp).
3 Epidote, anorthosite, Sittampundi, Madras, India (Subramaniam, A.P., 1956, *Bull. Geol. Soc. Amer.*, **67**, 317–89). Includes Cl 0.07 less O ≡ Cl 0.02.
4 Epidote, granodiorite, Victoria Range, Smith Island, New Zealand (Tulloch, A.J., 1979, *Contrib. Mineral. Petrol.*, **69**, 105–17).
5 Piemontite, vein in manganiferous quartz-mica schist, Hidaka Mountains, Hokkaido, Japan (Grapes, R.H. & Hashimoto, S., 1978, *Contrib. Mineral. Petrol.*, **68**, 22–35). Microprobe analysis.
6 Manganoan allanite, migmatitic gneiss, Pietrosu valley, Sebes Mountains, southern Carpathia, Romania (Pavelescu, L. & Pavelescu, M., 1972, *Tschermaks Mineral. Petrol. Mitt.*, ser. 3, **17**, 208–14). Includes ThO_2 1.15.

[a] Numbers 2 and 6 on the basis of 13 (O,OH).
[b] Includes Na 0.065, K 0.005.
[c] Includes Na 0.015.
[d] Includes Na 0.003.
[e] Includes Na 0.003, K 0.002.
[f] Includes Mn^{3+} 0.099, Na 0.003.
[g] Includes Th^{4+} 0.052.

eclogite-facies conditions, and also at ultra-high pressures. Inconsistencies in results of some of these experiments have been attributed to factors such as slow reaction kinetics at the lower temperatures, variations in H_2O activity or availability, and high sensitivity to f_{O_2}. Experiments relating to magmatic epidote minerals were reviewed by Schmidt and Poli (2004).

Optical and physical properties

The refractive indices of the clinozoisite–epidote series of minerals show a moderate correlation with the replacement of Al by Fe^{3+}. The increase of γ with iron content is approximately linear for compositions up to 33 mol% $Ca_2Fe^{3+}_3Si_3O_{12}(OH)$. The variation in birefringence is less regular and there is a change in the rate of

Downloaded from https://pubs.geoscienceworld.org/books/chapter-pdf/3754121/9780903056434_ch14.pdf
by guest

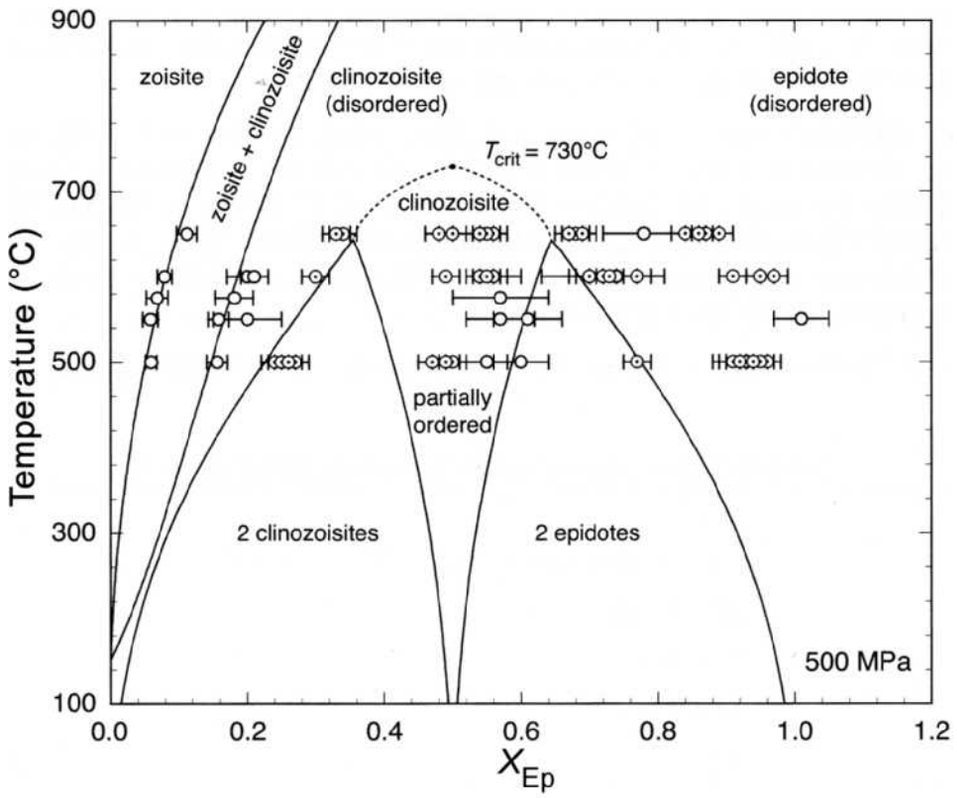


Fig. 44. *T–X* curves showing solid solution and two solvi for unmixing between clinozoisite and epidote. The variation of the zoisite/clinozoisite transformation temperature with composition X_{Ep} is also shown (after Gottschalk, M., 2004). Experimental results: circles with dots, Heuss-Aßbichler, S. & Fehr, K.T., 1997, *Neues Jahrb. Min., Abhdl.*, **172**, 69–70; open circles, Brunsmann, A. *et al.*, 2002, *Contrib. Mineral. Petrol.*, **143**, 115–130. Thermochemical calculations: Gottschalk M. (2004). $X_{Ep} = Fe^{3+}/(Fe^{3+} + Al - 2)$

increase at ~Ep_{45}. The optic axial angle increases from $2V_\gamma$ ~40º for clinozoisite to ~110º for compositions close to Ep_{100} but is irregular for the iron-poor members. The change from the optically positive clinozoisites to the optically negative epidotes occurs at ~Ep_{30} (6 wt.% Fe_2O_3). Pleochroism is also related to the degree of Al $\leftrightarrow$ Fe^{3+} substitution. The iron-poor clinozoisites display little pleochroism; the common epidote yellow–yellow-green pleochroism is usually associated with compositions more iron-rich than Ep_{57} and the strong green colours are characteristic of compositions close to Ep_{90}. Zoned epidotes are common; the zoning may be continuous or abrupt or reversed. Zoning from more to less iron-rich epidote is usually ascribed to crystallization of the aluminium-rich zone at higher metamorphic temperatures. Epidotes with an aluminium-rich inner zone and outer iron-rich margin may be correlated with an initial prograde metamorphism that was followed subsequently by a retrograde event.

Distinguishing features

Clinozoisite is distinguished from epidote by its lower birefringence, optically positive character and lack of pleochroism, from zoisite by its oblique extinction in prism zone sections, and from melilite and vesuvianite by its biaxial character. Epidote can be distinguished from hornblende by its greater birefringence and refractive indices and characteristic pleochroism, and from clinopyroxene by its single cleavage, negative optic sign and pleochroism (Fig. 45).

Paragenesis

Members of the clinozoisite-epidote series occur in a wide range of metamorphic parageneses but are particularly characteristic of rocks of the greenschist and epidote-amphibolite facies. Epidote occurs also in lower-grade rocks formed in some cases in pressure-temperature conditions as low as ~13 MPa, 320ºC. These epidotes are iron-rich, commonly approaching Ep_{100} in composition, and occur in association with chlorite, prehnite, albite and calcite. At a higher metamorphic grade epidote is found in associations that include pumpellyite. Its more extensive crystallization in these rocks takes place when the maximum pressure–temperature stability conditions for pumpellyite are reached at the transition from the prehnite-pumpellyite to the lower greenschist facies by the reaction:

$$2\,Ca_4Fe^{2+}Fe^{3+}Al_4Si_6O_{21}(OH)_7 + \tfrac{1}{2}\,O_2 \rightarrow \underset{\text{pumpellyite}}{} \quad \underset{\text{epidote}}{4\,Ca_2Fe^{3+}Al_2Si_3O_{12}(OH)} + 5\,H_2O$$

Downloaded from https://pubs.geoscienceworld.org/books/chapter-pdf/3754121/9780903056434_ch14.pdf
by guest

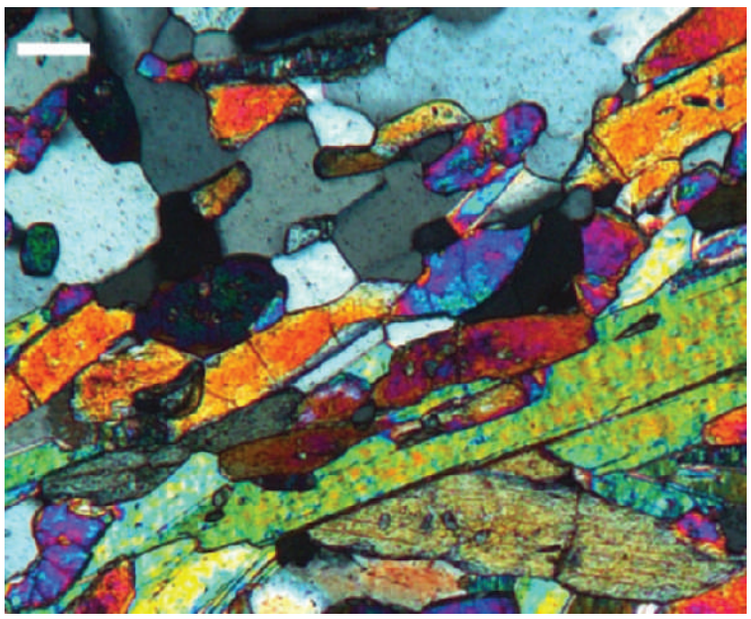


Fig. 45. Epidote in garnet-muscovite-epidote-glaucophane schist, Ward Creek, California (crossed polars, scale bar 0.1 mm), showing characteristically bright interference colours (courtesy of G.T.R. Droop).

In greenschist-facies rocks, epidote is characteristically associated with chlorite, actinolite, albite, quartz, and less commonly with white mica, biotite, stilpnomelane and garnet. In these assemblages the bulk rock oxidation ratio, the molar ratio $[(Fe_2O_3/(Fe_2O_3 + FeO)] \times 100$, has a marked influence on epidote composition. A progressive increase in Ep from 42 to 90 accompanying an oxidation ratio change from ~13.5 to 71 occurs in metabasic rocks and quartzofeldspathic schists of the Southern Alps, New Zealand. In rocks of the blueschist facies, epidote occurs variously in association with pumpellyite, glaucophane, garnet, lawsonite, riebeckite and omphacite; compositions vary between moderate to iron-rich members of the clinozoisite–epidote series.

In calc-schists, epidote is commonly associated with margarite, calcite and quartz and the coexisting phases are related by the reaction:

$$3\,\text{margarite} + 5\,\text{calcite} + 6\,\text{quartz} \rightleftharpoons 4\,\text{clinozoisite} + 5\,CO_2 + H_2O$$

Likewise epidote-bearing assemblages are present in the products of contact metamorphism, particularly of calcareous rocks. Here epidote occurs in assemblages with clinopyroxene, calcite, garnet, vesuvianite, scapolite, wollastonite and plagioclase. Epidote is a common gangue mineral and is not uncommon as an accessory constituent of acid igneous rocks, in which it occurs occasionally as an early product of magmatic crystallization.

Magmatic epidote is now recognized in intermediate plutonic rocks such as the tonalite-trondhjemite-granodiorite (TTG) series and in monzogranites; it also occurs in dacite and rhyodacite dykes. Experimental work has shown that epidote is stable above the wet granite solidus near 0.5 GPa at 680ºC, defining the pressure above which epidote may be present during melting processes. It also occurs as a product of the hydrothermal alteration (saussuritization) of plagioclase, and along joints and fissures and in amygdales and vugs.

Further reading

Brown, E.H. and Ghent, E.D. (1983) Mineralogy and phase relations in the blueschist facies of the Black Butte and Ball Rock areas, northern California Coast Ranges. *American Mineralogist*, **68**, 365–372.

Enami, M. and Banno, S. (1980) Zoisite–clinozoisite relations in low- to medium-grade high pressure metamorphic rocks and their implications. *Mineralogical Magazine*, **43**, 1005–1013.

Gottschalk, M. (2004) Thermodynamic properties of zoisite, clinozoisite and epidote. Pp. 83–124 in: *Epidotes* (A. Liebscher and G. Franz, editors). Reviews in Mineralogy & Geochemistry, **56**, Mineralogical Society of America and Geochemical Society, Washington, D.C.

Liou, J.G., Kim, H.S. and Maruyama, S. (1983) Prehnite–epidote equilibria and their petrologic applications. *Journal of Petrology*, **24**, 321–342.

Poli, S. and Schmidt, M.W. (2004) Experimental subsolidus studies on epidote minerals. Pp. 171–195 in: *Epidotes* (A. Liebscher and G. Franz, editors). Reviews in Mineralogy & Geochemistry, **56**, Mineralogical Society of America and Geochemical Society, Washington, D.C.

Raith, M. (1976) The Al–Fe(III) epidote miscibility gap in a metamorphic profile through the Penninic series of the Tauern window, Austria. *Contributions to Mineralogy and Petrology*, **57**, 99–117.

Schmidt, M.W. and Poli, S. (2004) Magmatic epidote. Pp. 199–430 in: *Epidotes* (A. Liebscher and G. Franz, editors). Reviews in Mineralogy & Geochemistry, **56**, Mineralogical Society of America and Geochemical Society, Washington, D.C.

Zen, E-an and Hammarstrum, J.M. (1984) Magmatic epidote and its petrologic significance. *Geology*, **12**, 515–518.

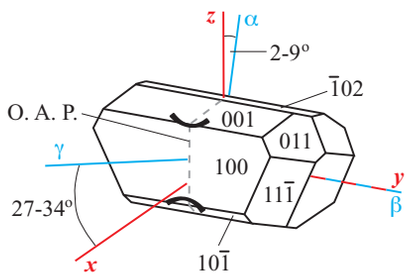
Downloaded from https://pubs.geoscienceworld.org/books/chapter-pdf/3754121/9780903056434_ch14.pdf
by guest

Piemontite

$Ca_2Al_2Mn^{3+}[Si_2O_7][SiO_4]O(OH)$

Monoclinic (+)

α	1.730–1.794[a]
β	1.740–1.807
γ	1.762–1.829
δ	0.025–0.073
$2V_\gamma$	64–106º
Orientation	α:*z* 2–9º, β = *y*; O.A.P. (010)
D (g/cm^3)	3.38–3.61
H	6
Cleavage	{001} perfect
Twinning	{100} lamellar, not common
Colour	Reddish brown, black; violet or pink in thin section
Pleochroism	α yellow, lemon-yellow, orange-yellow β pale pink, amethyst, violet-pink γ red, crimson, magenta
Unit cell	*a* 8.84–9.0 Å, *b* 5.58–5.70 Å, *c* 10.17–10.2 Å, β ~115.5º Z = 2; space group $P2_1/m$
Special features	Insoluble in HCl



Piemontite is the most common manganese-rich species in the epidote group and shows a characteristic and striking pleochroism, ranging from lemon yellow to amethystine and to carmine-red or magenta. It occurs in low-grade metamorphic rocks of the greenschist, blueschist and amphibolite facies and in hydrothermally altered rocks in association with manganese ore deposits.

The structure of piemontite is similar to that of epidote and other monoclinic members of the epidote group. The Mn is located mainly in *M*3 sites; an increase in the *b* and *c* cell parameters is associated with increasing substitution of Mn^{3+} + Fe^{3+} for Al.

Manganese-bearing members of the epidote group occupy a large compositional field which ranges from $Ca_2Fe^{3+}Al_2Si_3O_{12}(OH)$ and $Ca_2Mn^{3+}Al_2Si_3O_{12}(OH)$ towards $Ca_2Mn_2AlSi_3O_{12}(OH)$. Piemontite is readily synthesized between 500 and 600ºC and 0.1 and 0.8 GPa from oxide mixtures. At 0.2 GPa it is stable down to 408ºC and 575ºC under cuprite–tenorite and Cu–cuprite buffers respectively.

At lower temperatures it breaks down due to combination of a dehydration and oxidation–reduction reaction to a garnet solid solution + fluid:

$$Ca_2Mn^{3+}Al_2Si_3O_{12}(OH) \rightarrow Ca_2Mn^{3+}Al_2Si_3O_{12} + \tfrac{1}{2}H_2O + \tfrac{1}{4}O_2$$

Piemontites are strongly coloured and pleochroic in yellows, pinks and reds (Fig. 46); the low-manganese variety withamite is much paler in colour and is only weakly pleochroic.

Piemontite is distinguished from other epidote group minerals, except mukhinite (cations $Ca_2Al_2V^{3+}$) and members of the allanite subgroup, by its dark colour in hand specimens, yellow–red pleochroism and higher refractive indices. Allanite also has a distinctive paragenesis and is commonly metamict. The Mn-bearing zoisite (variety thulite) has a smaller optic axial angle and straight extinction.

Piemontite is predominantly a product of low-grade regional metamorphism and occurs in rocks ranging from greenschists and blueschists to amphibolites. It also occurs as a product of hydrothermal processes in association with manganese deposits. Its formation, however, does not depend solely on manganese-rich host-rock compositions; high oxygen fugacities also are important.

[a] Manganoan clinozoisite has lower values (e.g. α 1.714, β 1.724, γ 1.734), is much paler in colour and is only weakly pleochroic.

Downloaded from https://pubs.geoscienceworld.org/books/chapter-pdf/3754295/9780903056434_ch15.pdf
by guest

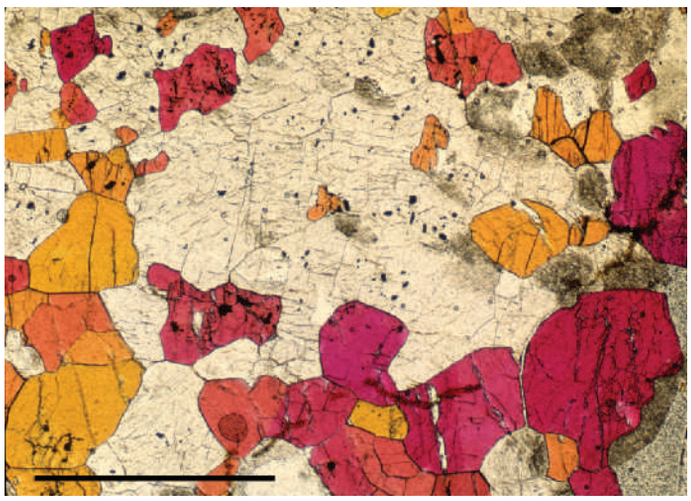


Fig. 46. Piemontite in piemontite-quartz rock, Mautia Hill, Tanzania (ppl, scale bar 1 mm), showing its spectacular pleochroic colours of yellow, carmine-red and violet or amethyst, set in a pale-coloured Mn-amphibole (W.S. MacKenzie collection, courtesy of Pearson Education).

Further reading

Bonazzi, P. and Menchetti, S. (2004) Manganese in monoclinic members of the epidote group: piemontite and related minerals. Pp. 495–552 in: *Epidotes* (A. Liebscher and G. Franz, editors). Reviews in Mineralogy & Geochemistry, **56**, Mineralogical Society of America and Geochemical Society, Washington, D.C.

Izadar, J. (2007) Multiple stages of piemontite formation in piemontite-quartz schists of the Sanbagawa metamorphic belt in central Shikoku, Japan. *GeoActa: an international Journal of Earth Sciences*, **6**, 47–58.

Kawachi, Y., Grapes, R.H., Coombs, D.S. and Dowse, M. (1983) Mineralogy and petrology of piemontite-bearing schist, western Otago, New Zealand. *Journal of Metamorphic Geology*, **1**, 353–372.

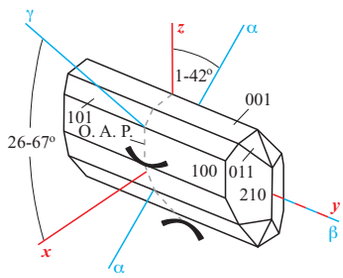
Keskinen, M. and Liou, J.G. (1979) Synthesis and stability relations of Mn-Al piemontite, $Ca_2MnAl_2Si_3O_{12}(OH)$. *American Mineralogist*, **64**, 317–328.

Reinecke, T. (1986) Crystal chemistry and reaction relations of piemontite and thulites from highly oxidized low grade metamorphic rocks at Vitali, Andros Island, Greece. *Contributions to Mineralogy and Petrology*, **93**, 56–76.

Downloaded from https://pubs.geoscienceworld.org/books/chapter-pdf/3754295/9780903056434_ch15.pdf
by guest

Monoclinic (−)(+)

α	1.690−1.813[a]
β	1.700−1.857
γ	1.706−1.891
δ	0.013−0.036
$2V_\alpha$	40−123°
Orientation	α:*z* 1−42°, β = *y*; O.A.P. (010)
D (g/cm^3)	3.4−4.2[b]
H	5−6½
Cleavage	{001} imperfect, {100}, {110} poor
Twinning	{100} not common, {001} rare
Colour	Light brown to black occasionally colourless but usually brownish yellow or brown in thin section
Pleochroism	α reddish brown β brownish yellow γ greenish brown to brownish red, reddish brown and dark reddish brown
Unit cell	*a* 8.9−9.0 Å, *b* 5.7−5.8 Å, *c* 10.15 Å, β ~115° Z = 2; space group $P2_1/m$
Special features	Gelatinizes with HCl



The allanite subgroup is made up of rare-earth bearing epidote-group minerals that commonly contain radioactive elements and are therefore subject to amorphization. Non-metamict allanite typically shows a rusty brown colour in thin section and moderate pleochroism, often showing dark cracks. It is a mineral of granitic rocks and is also found in some pegmatites and in skarns.

The structure of allanite is similar to that of the other monoclinic members of the epidote group. The coordination of Ca is less regular, and Ce and associated rare earth elements are located in the nine-coordinated *A*2 site. The unit cell is a little larger than those of the clinozoisite–epidote series. Cell parameters show a general increase with increasing contents of *REE*, Fe^{2+}, Fe^{3+}, Ti and Th but no simple relationship has been established.

The connection of allanite with the common $FeAl_2$-bearing epidotes may be expressed by the coupled substitution $Ca^{2+} + Fe^{3+} \leftrightarrow REE^{3+} + Fe^{2+}$, and allanite is the only member of the group in which Fe^{2+} is an essential constituent. Thorium and uranium, in amounts up to 5 ThO_2 and 0.5 U_3O_8 wt.% respectively, are present in the majority of allanites. Rare manganoan (Table 11, analysis 6, p. 58), beryllian, fluorian and phosphorian varieties have been described. Allanite often occurs in the metamict state due to the destruction of the crystalline structure by the bombardment of α particles emitted by the radioactive constituents. Amorphization lowers the stability and such allanites become more susceptible to alteration.

The wide variation in the optical properties and density of allanites is due to large differences in chemical composition and to the degree of crystallinity in individual minerals. Increasing metamictization is associated with a decrease in refractive index, to as low as 1.54, and in birefringence. The alteration and hydration are accompanied by expansion, and allanite is commonly surrounded by anastomosing cracks that radiate into the adjacent minerals (Fig. 47); brown haloes are sometimes observed in the surrounding rocks due to radiation damage.

[a] Some metamict allanites are isotropic with *n* 1.54 to 1.72.
[b] Density of metamict allanites may be as low as 2.8 g/cm^3.

Downloaded from https://pubs.geoscienceworld.org/books/chapter-pdf/3754500/9780903056434_ch16.pdf
by guest

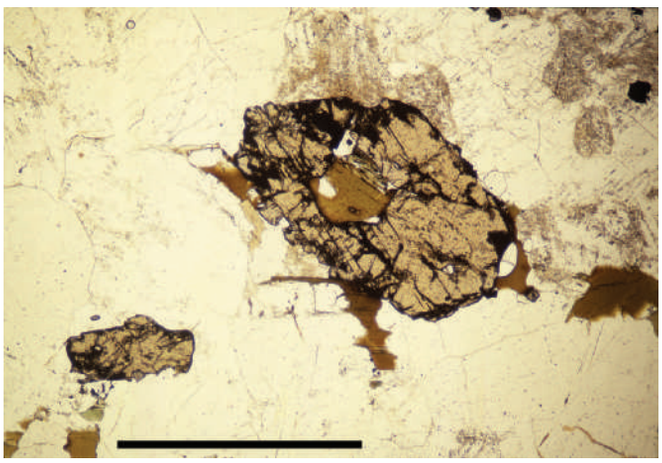


Fig. 47. Allanite in granite, near Mandalahy, Madagascar (ppl, scale bar 1 mm), showing the brown colour and characteristic dark cracks (W.S. MacKenzie collection, courtesy of Pearson Education).

The non-metamict allanites are distinguished from other epidotes by their brownish colour, the metamict specimens by their isotropic character and the presence of anastomosing cracks. Non-metamict allanite is distinguished from the brown amphiboles by its single cleavage and straight extinction in sections parallel to the elongation (i.e. parallel to the *y* axis). Isotropic varieties are distinguished from melanite garnet by their lower refractive index.

Allanite is a characteristic accessory mineral in many granites, granodiorites, monzonites and syenites; it occurs in larger amounts in some limestone skarns and in pegmatites.

Further reading

Gieré, R. and Sorensen, S.S. (2004) Allanite and other REE-rich epidote minerals. Pp. 431–493 in: *Epidotes* (A. Liebscher and G. Franz, editors). Reviews in Mineralogy & Geochemistry, **56**, American Mineralogical Society and Geochemical Society, Washington, D.C.

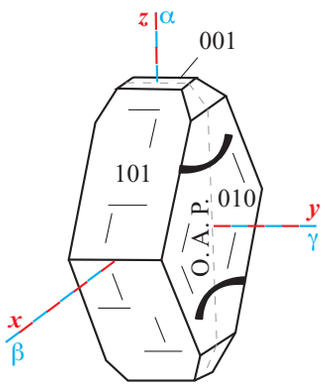
Rao, A.T., Rao, G.A. and Rao, P.P. (1979) Fluorian allanite from calc-granulite and pegmatite contacts at Garividi, Andhra Pradesh, India. *Mineralogical Magazine*, **43**, 312.

Downloaded from https://pubs.geoscienceworld.org/books/chapter-pdf/3754500/9780903056434_ch16.pdf
by guest

Lawsonite $CaAl_2[Si_2O_7](OH)_2.H_2O$

Orthorhombic (+)

α	1.663–1.665
β	1.672–1.675
γ	1.682–1.686
δ	0.019–0.021
$2V_\gamma$	76–87°
Orientation	$\gamma = y$; O.A.P. (100)
D (g/cm^3)	3.05–3.12
H	6
Cleavage	{100}, {010} perfect, {101} imperfect
Twinning	{101} simple, lamellar; common
Colour	Colourless, white, bluish, colourless to bluish green in thin section
Pleochroism	Usually non-pleochroic
Unit cell	*a* ~8.80 Å, *b* ~5.85 Å, *c* ~13.1 Å Z = 4; space group *Ccmm*



Lawsonite is a metamorphic mineral, which is most commonly found in basaltic and medium-grained immature clastic rocks that have been subjected to regional metamorphism. It is commonly associated with jadeite and glaucophane. Colourless or pale bluish green in thin section, it shows moderate relief and first or second order birefringence colours.

The structure of lawsonite includes chains of Al–O octahedra similar to those in epidote and pumpellyite. The chains run parallel to the *y* axis and are linked by Si_2O_7 groups. The framework is an open one and accommodates one Ca atom and one water molecule per formula unit; the latter occupies holes and not channels in the framework (Fig. 48).

Lawsonite does not depart significantly from the ideal composition, $CaAl_2Si_2O_7(OH)_2.H_2O$. Its chemical formula can also be expressed as $CaAl_2Si_2O_8.2H_2O$, i.e

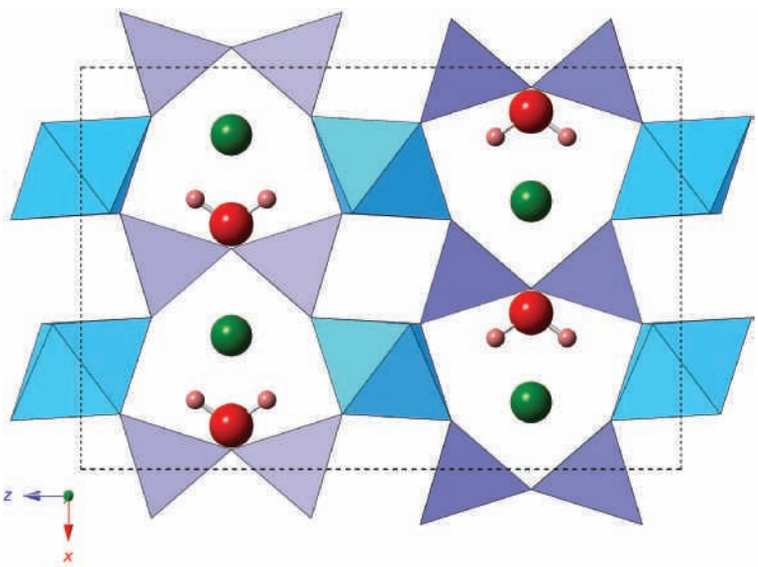


Fig. 48. The structure of lawsonite showing end-on view of chains of Al–O octahedra (pale blue) linked by double Si–O tetrahedra (lavender blue). Ca ions (green) and water molecules (red) occupy cavities in the structure. Hydrogens of OH anions are not shown (CrystalMaker image).

Downloaded from https://pubs.geoscienceworld.org/books/chapter-pdf/3754576/9780903056434_ch17.pdf
by guest

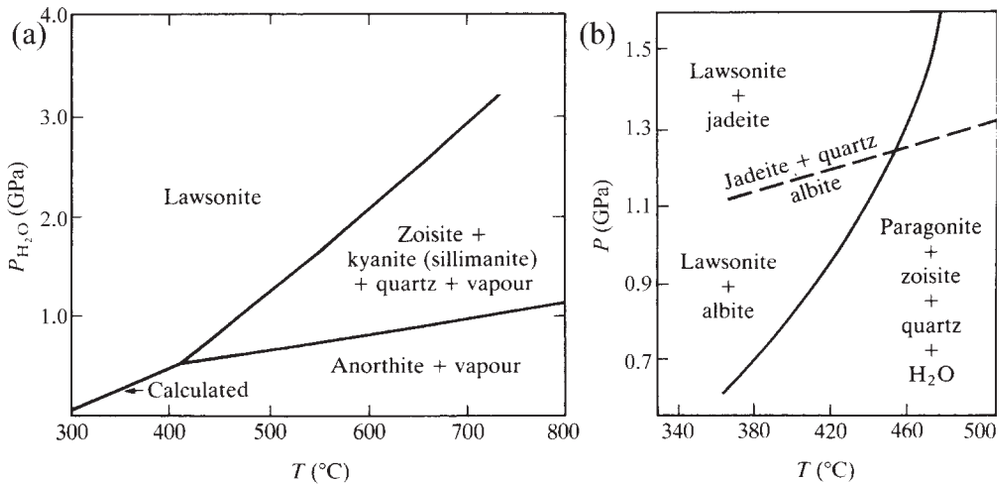


Fig. 49. (a) Equilibrium diagram of part of the system $CaAl_2Si_2O_8$–H_2O (after Newton, R.C. & Kennedy, G.C., 1963, *Journ. Geophys. Res.*, **68**, 2967–84). (b) P–T relations for the reactions 4 lawsonite + 1 albite ⇌ 1 paragonite + 2 zoisite + 2 quartz + 6 H_2O and 4 lawsonite + 1 jadeite ⇌ 1 paragonite + 2 zoisite + 1 quartz + 6 H_2O (after Heinrich, W. & Althaus, E., 1988, *Neues Jahrb. Min., Monat.*, 516–28).

as a hydrous analogue of anorthite. The equilibrium curve determined experimentally for the reaction:

$$4\,CaAl_2Si_2O_8.2\,H_2O \rightleftharpoons$$
lawsonite
$$2\,Ca_2Al_3Si_3O_{12}(OH) + Al_2SiO_5 + SiO_2 + 7\,H_2O$$
zoisite

is shown in Fig. 49a. The invariant point, lawsonite–zoisite–kyanite (sillimanite)–quartz–anorthite–vapour is located at 410ºC, 0.54 GPa. At pressures <0.3 GPa and temperatures <350ºC lawsonite is probably replaced by a zeolite or prehnite.

The optical properties show little variation. Lawsonite is distinguished from zoisite by its stronger birefringence, two perfect cleavages, common twinning and absence of anomalous interference colours, from prehnite by its lower birefringence, higher refringence and better cleavage, from scapolite by its biaxial character and from andalusite by its higher birefringence, refringence and positive optic sign. Although they are similar in chemical composition, lawsonite with Al in octahedral coordination has a higher density than anorthite with Al in tetrahedral coordination.

Lawsonite occurs almost exclusively in metamorphic terranes in situations in which fluid overpressure has

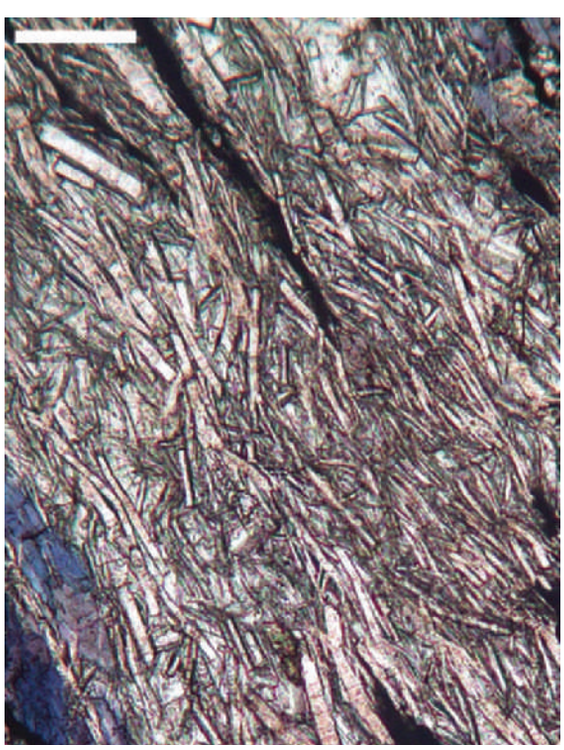


Fig. 50. Lawsonite, in glaucophane schist (ppl, scale bar 0.2 mm), Calabria, Italy, showing typical rectangular shapes, moderate relief and little or no colour (courtesy of G.T.R. Droop).

Downloaded from https://pubs.geoscienceworld.org/books/chapter-pdf/3754576/9780903056434_ch17.pdf
by guest

combined with a low thermal gradient. In high-pressure metabasites and metagreywackes the disappearance of lawsonite + albite is marked by reactions to paragonite + zoisite + quartz + H_2O (Fig. 49b). Lawsonite, with glaucophane, jadeitic pyroxene, aragonite, calcite and pumpellyite, is a critical constituent of the blueschist facies (Fig. 50).

The $P-T$ paths in subduction zones can be within the stability field of lawsonite from the crystallization conditions of blueschists and eclogites up to pressures of at least 10 GPa. The 11.5 wt.% H_2O contained in lawsonite may then be released and trigger partial melting of the slab or mantle or be incorporated in hydrous phases which may then transport H_2O to an even greater depth in the mantle (see Pawley, 1994).

Further reading

Baur, W.W. (1978) Crystal structure refinement of lawsonite. *American Mineralogist*, **63**, 311–315.

Black, P.M. (1977) Regional high-pressure metamorphism in New Caledonia phase equilibria in the Ouégou District. *Tectonophysics*, **43**, 89–107.

Brown, E.H. and Ghent, E.B. (1983) Mineralogy and phase relations in the blueschist facies of the Black Butte and Ball Rock areas, northern California Coast Range. *American Mineralogist*, **68**, 365–372.

Comodi, P. and Zanazzi, P.F. (1996) Effects of temperature and pressure on the structure of lawsonite *American Mineralogist*, **81**, 833–841.

Ghent, E.D., Erdmer, P., Archibald, D.A. and Stout, M.Z. (1996) Pressure–temperature and tectonic evolution of Triassic lawsonite-aragonite blueschists from Pinchi Lake, British Columbia. *Canadian Journal of Earth Sciences*, **33**, 800–810.

Okay, A.J. (2002) Jadeite–chloritoid–glaucophane–lawsonite blueschists in north-west Turkey: unusually high *P/T* ratios in continental crust. *Journal of Metamorphic Geology*, **20**, 757–768.

Pawley, A.R. (1994) The pressure and temperature stability limits of lawsonite: implications for H_2O recycling in subduction zones. *Contributions to Mineralogy and Petrology*, **118**, 98–108.

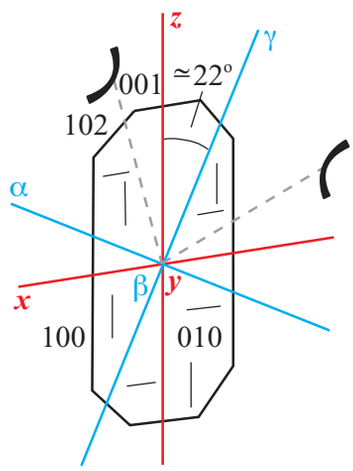
Perkins, D., Westrum, E.F. and Essene, E.J. (1980) The thermodynamic properties and phase relations in the system $CaO-Al_2O_3-SiO_2-H_2O$. *Geochimica et Cosmochimica Acta*, **44**, 61–84.

Schmidt, M.W. and Poli, S. (1994) The stabilities of lawsonite and zoisite at high pressures; experiments in CASH to 92 kbar and implications for the presence of hydrous phases in subducted lithosphere. *Earth and Planetary Sciences*, **124**, 105–118.

Downloaded from https://pubs.geoscienceworld.org/books/chapter-pdf/3754576/9780903056434_ch17.pdf
by guest

Monoclinic (+)(−)

α	1.665−1.710 (−1.776)[a]
β	1.670−1.720 (−1.814)[a]
γ	1.683−1.726 (−1.836)[a]
δ	0.010−0.020
$2V_\gamma$	7−110° (150°)[a]
Orientation	γ:z 4−32°, β = y; O.A.P. (010)
D (g/cm^3)	3.16−3.25
H	5−6
Cleavage	{001}, {100} moderate
Twinning	{001}, {100} common
Colour	Green, bluish green, brown; colourless, green, brown or yellow in thin section
Pleochroism	α colourless, pale blue green, pale yellowish brown, pale greenish yellow β colourless, bluish green, apple green, brownish yellow γ colourless, pale yellowish brown, brownish yellow, pinkish yellow, golden yellow
Unit cell	*a* ~ 8.8 Å, *b* ~ 5.9 Å, *c* ~ 19.1 Å, β 97.5° Z = 4; space group *A2/m*
Special features	Insoluble in HCl. Anomalous interference colours



The term pumpellyite is used here *sensu lato* to include all of the closely related members of the pumpellyite group of minerals. Pumpellyite typically occurs in low-grade metamorphic rocks, commonly associated with chlorite-group minerals and zeolites. In rocks of the pumpellyite-prehnite facies and the greenschist facies it may also be found with epidote. It occurs as colourless to bluish green crystals with a moderately high relief.

Structure

The structure of pumpellyite is related to that of epidote; chains of edge-sharing octahedra run parallel to *y* and are linked laterally by SiO_4 tetrahedra and Si_2O_7 groups. The whole or partial replacement of oxygens by (OH) ions is expressed by the presence of the $[Si_2(O,OH)_7]$ group in the formula.

A simplified general formula is $Ca_2XY_2Si_4O_{14-n}(OH)_n$ in which *X* and *Y* represent the two kinds of octahedral site, *X* (the larger) containing both divalent and trivalent, and *Y* only trivalent, cations. The value of *n* lies between 3 and 4. There are four *X* and two *Y* sites in the unit cell. Two independent seven-fold coordinated Ca atoms are present. Substitutions of cations of different valencies in *X* are balanced by replacements of some oxygens by 4(OH), if *X* is occupied only by divalent cations, and by 3(OH) if only by trivalent cations.

In the iron-rich pumpellyite jugoldite, *Y* sites are occupied solely by Fe^{3+} and more than half of the *X* sites are filled by Fe^{2+}. Chromium-rich and vanadium-rich pumpellyites have been described. The structure of the mineral sursassite, $(Mn^{2+})_2Al_3Si_3O_{11}(OH)_3$ does not have the pumpellyite structure and has symmetry $P2_1/m$. The two structures do, however, have similar layer features but with different modes of stacking. The mineral macfallite, $Ca_2Mn^{3+}_3Si_3O_{11}(OH)_3$, with Mn^{3+} in

[a] The range to higher value is restricted to Fe-, Mn- and Cr-rich varieties.

Downloaded from https://pubs.geoscienceworld.org/books/chapter-pdf/3754582/9780903056434_ch18.pdf
by guest

Table 12. Pumpellyite analyses.

	1	2	3		Numbers of ions on the basis of 14 (O,OH) 1		2		3	
SiO_2	39.60	35.75	34.0	Si	3.048		2.960		3.154	
TiO_2	0.00	0.12	0.1	Al	2.416		1.825		0.143	
Al_2O_3	26.30	18.70	1.3	Ti	0.000		0.007		0.007	
Fe_2O_3	–	11.10	29.6	Fe^{3+}	–	3.01	0.689	3.10	2.066	2.94
FeO	1.48	2.80	8.7	Mg	0.493		0.385		0.028	
MnO	0.05	0.05	0.2	Fe^{2+}	0.095		0.194		0.675	
MgO	4.30	3.12	0.2	Mn	0.003		0.003		0.016	
CaO	21.60	20.72	22.0	Na	0.009		0.071		–	
Na_2O	0.06	0.44	–	Ca	1.781	1.79	1.839	1.92	2.187	2.19
K_2O	0.04	0.06	–	K	0.004		0.006		–	
H_2O+	7.42	6.63	4.69	OH	3.908		3.672		2.902	
Total	100.85	99.49	100.79							

1 Pumpellyite, contact zone between country rocks and ultrabasic body of Luohusha ophiolite suite, Yalu Tsampo River drainage area, south Tibet (Huang *et al*., 1981, *Bull. Mineral*., **104**, 441–4). Includes P_2O_5 0.05, BaO 0.0006, NiO 0.0025, Cr_2O_3 0.006.
2 Pumpellyite, porphyrite, Gardena, Bolzano, Italy (Passaglia, E., 1972, *Periodico Min*., *Roma*, **41**, 273–80).
3 Julgoldite, Långban, Sweden (Moore, P.B., 1971, *Lithos*, **4**, 93–9). Includes BaO 0.1.

[a] Includes Ba 0.004.

Y sites has the same structure as sursassite. The nomenclature, cation distribution, and hydrogen bonding in pumpellyite and related minerals, are discussed by Nagashima *et al*. (2010).

Chemistry

Although most pumpellyites have a relatively restricted compositional range, some display substantial Al ↔ Fe^{3+} replacement (Table 12). Zoned pumpellyites with a content of Fe_2O_3 ranging from 2.9 to 15.7 wt.% are found in low-grade metamorphic rocks in the Tanzawa Mountains, Japan. The composition represented by the general formula $W_2XY_2Z_3(O,OH)_{14}$, where W = Ca,Na,K: X = Fe^{2+}, Fe^{3+}, V^{3+}, Cr^{3+}, Mg, Mn, Al; Y = Fe^{3+}, Al, Ti; Z = Si, illustrates the full substitutional range. In the iron pumpellyite, julgoldite, the *Y* position is occupied solely by Fe^{3+} and more than half the *X* positions are filled by Fe^{2+}. Chromium-rich pumpellyite with 1.9 Cr^{3+} and the related mineral sursassite with ~1.0 Mn^{2+} ions pfu have been described.

Equilibrium curves determined experimentally are shown in Fig. 51 for the reactions:

$$\underset{\text{chlorite}}{\tfrac{1}{2}\,Mg_4Al_4Si_2O_{10}(OH)_8} + 4\,\underset{\text{prehnite}}{Ca_2Al_2Si_3O_{10}(OH)_2} + H_2O \rightleftharpoons 2\,\underset{\text{pumpellyite}}{Ca_4MgAl_5O(OH)_3[Si_2O_7]_2[SiO_4]_2.2\,H_2O} + \underset{\text{quartz}}{SiO_2}$$

$$\text{pumpellyite} \rightleftharpoons \text{zoisite} + \text{grossular} + \text{chlorite} + \text{quartz} + \text{fluid}$$

The former is characteristic of the transition from the prehnite to the pumpellyite zone in the prehnite–pumpellyite facies, the latter corresponding with the lower boundary of the greenschist facies.

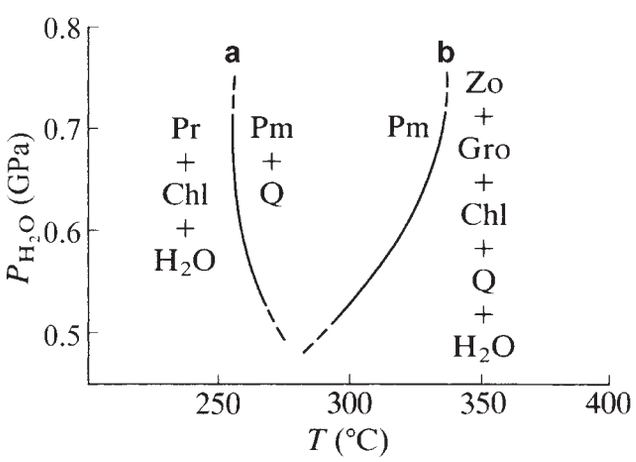


Fig. 51. (a) Equilibrium curve for the reaction prehnite + chlorite + H_2O ⇌ pumpellyite + quartz. (b) Equilibrium curve for the reaction pumpellyite ⇌ zoisite + grossular + chlorite + quartz + H_2O (after Hinrichsen, V.T. & Schurmann, K., 1969, *Neues Jahrb. Min*., *Monat*., 441–5).

Downloaded from https://pubs.geoscienceworld.org/books/chapter-pdf/3754582/9780903056434_ch18.pdf
by guest

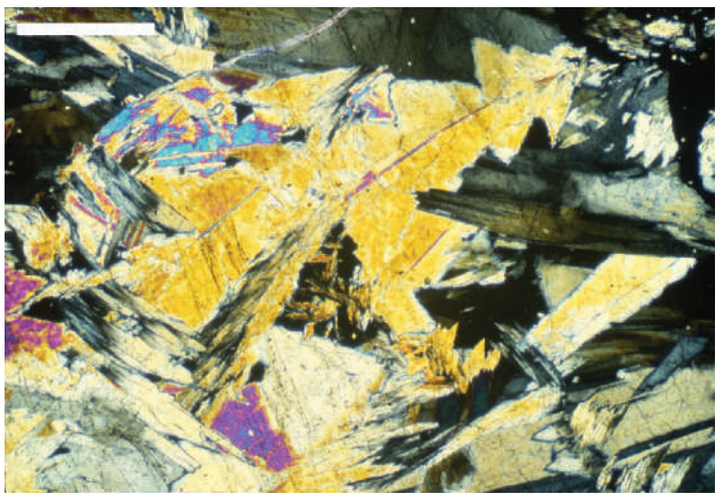


Fig. 52. Pumpellyite in blueschist, Tiburon Peninsula, California (crossed polars, scale bar 0.5 mm), showing up to second order interference colours and 'oak leaf' outline (W.S. MacKenzie collection, courtesy of Pearson Education).

Optical and physical properties

The optical properties of the pumpellyite series show a wide variation that is related to the iron content; thus refractive index γ ranges from 1.68 in iron-poor pumpellyite-series minerals to 1.83 in minerals of the julgoldite series. The increase in refringence is accompanied by an increase in optic axial angle ($2V_\gamma$ from <10 to 150°) and birefringence and the change from colourless or pale-coloured to dark green minerals. The 'oak leaf' habit (Fig. 52) is found mainly in vein occurrences, and is diagnostic if it is seen.

Distinguishing features

Weakly coloured pumpellyite is difficult to distinguish from clinozoisite, but has lower refractive indices and higher birefringence. The more coloured and iron-rich varieties of pumpellyite may be distinguished from epidote by their characteristic blue-green β absorption colour and positive optic axial angle. The refractive indices and birefringence are in general lower than those of epidote, but very strongly coloured and iron-rich pumpellyites have higher refractive indices and birefringence than the iron-poor epidotes; the latter may be distinguished, however, by their large optic axial angles. Pumpellyite is distinguished from zoisite by inclined extinction in (010) sections, from lawsonite by higher refractive indices, poorer cleavage and pleochroism, and from clinochlore by the lower birefringence of the latter. Pumpellyites showing anomalous interfence colours may be confused with chlorite but in general have considerably higher refractive indices.

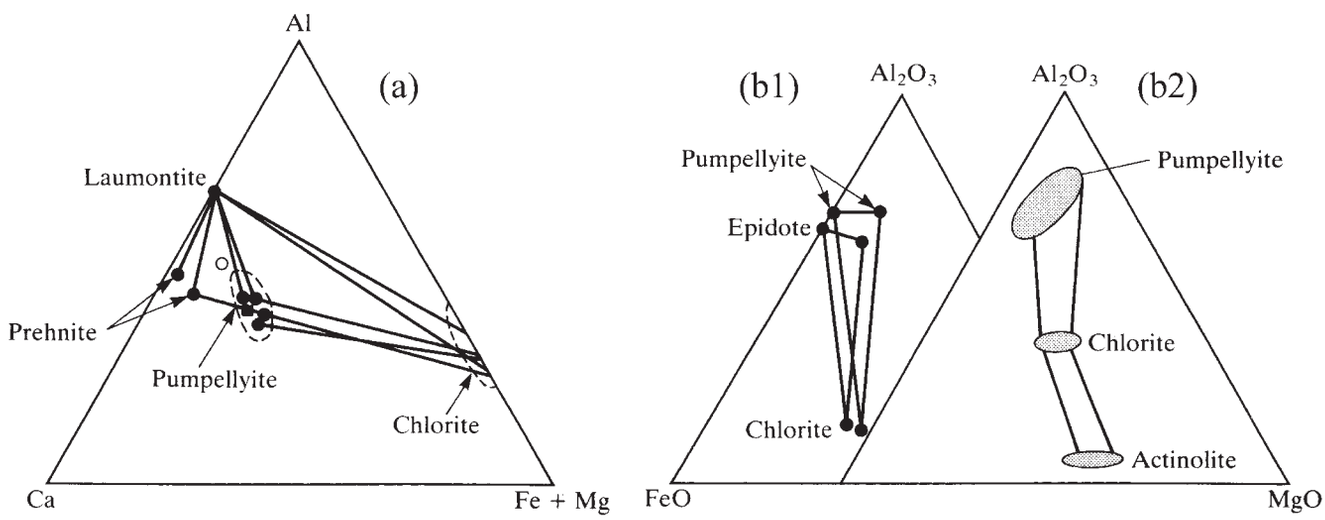


Fig. 53. (a) Compositions of zeolite facies minerals of the Murihiku group, South Island, New Zealand. ○: aluminous pumpellyite $Ca_4(MgFe^{2+})AlAl_4Si_6O_{21}(OH)_7$; ●: iron-rich pumpellyite $Ca_4(MgFe)_{2-x}Fe^{3+}_xAl_4Si_6O_{20+x}(OH)_{8-x}$ (after Boles, J.R. & Coombs, D.S., 1977, *Amer. J. Sci.*, **277**, 982–1012). (b1) Al_2O_3–FeO–MgO relations of major secondary phases in pumpellyite-prehnite facies lavas, Abitibi area, Quebec; lavas with pumpellyite and epidote (after Jolly, W.T., 1980, *J. Petrol.*, **21**, 323–64). (b2) Al–Fe–Mg diagram illustrating compositional fields of coexisting minerals from Taveyanne Formation, Loéche region, Valais, Switzerland (after Coombs, D.S. *et al.*, 1976, *J. Petrol.*, **17**, 440–71).

Downloaded from https://pubs.geoscienceworld.org/books/chapter-pdf/3754582/9780903056434_ch18.pdf
by guest

Paragenesis

Pumpellyite occurs in a wide range of metamorphic rocks of both igneous and sedimentary origin. In zeolite facies rocks, e.g. sandstones of andesitic parentage in the Southland syncline, New Zealand, where it partially replaces the chlorite-laumontite cement, pumpellyite is commonly associated also with calcite, clay minerals and prehnite (Fig. 53a). These pumpellyite-producing reactions are generally at metamorphic pressures between 50 and 10 MPa and temperatures between 50 and 150ºC. In rocks of the pumpellyite–prehnite facies, e.g. metabasalt lavas of the Abitibi area, Ontario and Quebec, Canada, pumpellyite, in addition to prehnite, is associated with chlorite and epidote (Fig. 53b1). With further increase in $P-T$, pumpellyite occurs with actinolite as well as with chlorite and epidote in typical greenschist-facies assemblages. A change from strongly coloured, iron-rich to pale-coloured, iron-poor pumpellyite in the assemblage is associated with the increase in grade between the zeolite and greenschist facies. This compositional trend is probably related to decreasing f_{O_2} with the loss of iron to coexisting chlorite and actinolite. The consequential compositional and phase effects that occurred in schists of the Taveyanne formation, Valais, Switzerland, are illustrated in Fig. 53b2.

Pumpellyite occurs commonly in rocks of blueschist metamorphic grade in assemblages with glaucophane, sodic amphiboles, aegirine, epidote and lawsonite. Its presence in these rocks is in some cases related to retrograde metamorphism and pumpellyite variously occurs replacing garnet, lawsonite and epidote. The composition of the mineral becomes more iron-rich as pressure and temperature decreases and in extreme cases pumpellyite occurs in association with stilpnomelane and hematite.

Further reading

Aldahan, A.A. (1989) The paragenesis of pumpellyite in granitic rocks of the Siljan area, central Sweden. *Neues Jahrbuch für Mineralogie, Monatshefte*, 367–383.

Artioli, G. and Geiger, C.A. (1994) The crystal chemistry of pumpellyite: an X-ray Rietveld refinement and ^{57}Fe Mössbauer study. *Physics and Chemistry of Minerals*, **20**, 443–453.

Brown E.H. and Ghent, E.D. (1983) Mineralogy and phase relations in the blueschist facies of the Black Butte and Ball Rock area, Northern California Coast Ranges. *American Mineralogist*, **68**, 365–372.

Nagashima, M., Armbruster, T. and Libowitzky, E. (2010) The hydrogen-bond system in pumpellyite. *European Journal of Mineralogy*, **22**, 333–342.

Nakajima, T., Banno, S. and Suzuki, Y. (1977) Reactions leading to the disappearance of pumpellyite in low-grade metamorphic rocks of the Sanbagawa metamorphic belt in central Shikoku, Japan. *Journal of Petrology*, **18**, 263–284.

Schiffman, F and Liou, J.G. (1983) Synthesis of Fe-pumpellyite and its stability relations with epidote. *Journal of Metamorphic Geology*, **1**, 91–101.

Downloaded from https://pubs.geoscienceworld.org/books/chapter-pdf/3754582/9780903056434_ch18.pdf
by guest

Melilite Group

Gehlenite — $Ca_2[Al_2SiO_7]$
Åkermanite — $Ca_2[MgSi_2O_7]$

	Gehlenite	Melilite	Åkermanite
	Tetragonal (−)	Tetragonal (+)(−)	Tetragonal (+)
ω	1.669	1.624−1.666	1.631
ε	1.658	1.616−1.661	1.639
δ	0.011	0.001−0.013	0.008
D (g/cm^3)	3.07	2.95−3.05	2.944
H	5−6	5−6	5−6
Cleavage	{001} moderate, {110} poor		
Colour	Colourless, greyish green, brown; colourless in thin section	Honey-yellow, brown, green-brown; colourless in thin section	Colourless, greyish green, brown; colourless in thin section
Pleochroism	–	In thick section: ω golden brown, ε colourless to faint yellow	–
Unit cell	*a* 7.69 Å, *c* 5.07 Å	*a* ~ 7.8 Å, *c* ~ 5.0 Å	*a* 7.84 Å, *c* 5.00 Å
		Z = 2; space group $P\bar{4}2_1m$	
Special features	Gelatinizes in HCl	Gelatinizes in cold, dilute HCl	Gelatinizes in HCl
	Melilite may show anomalous interference colours		

In modern nomenclature melilite is used as a group name. The most common minerals of the melilite group, gehlenite and akermanite, are found in high-temperature associations in thermally metamorphosed impure limestones, and in some highly silica-undersaturated basic volcanic rocks (melilitites). They are also common in feldspathoidal rocks formed by reactions between basic magmas and carbonate rocks, and are known from carbonatites. They are uniaxial and may show anomalous interference colours.

Structure

The structure of melilite-group minerals is based on a tetragonal lattice which has, in åkermanite, Mg (and in gehlenite Al) atoms located at the corners and face centres of the unit cell. The Mg or Al atoms are in tetrahedra of oxygens, all four of which are shared by adjacent SiO_4 tetrahedra which themselves are linked in pairs to form Si_2O_7 groups. The linkages of Mg (or Al) and Si tetrahedra form corrugated sheets parallel to (001), which are held together by Ca−O bonds. In åkermanite there is complete ordering with Mg in *T*1 tetrahedra and Si in *T*2 tetrahedra, but in gehlenite Si and Al are the only tetrahedral ions so there is the possibility of different ordering schemes as between the *T*1 and *T*2 sites (e.g. Al in *T*1 and ½Al, ½Si in *T*2). For a synthetic soda melilite, $CaNaAlSi_2O_7$, it has been shown that Al and Si atoms are ordered (A1 in *T*1 and Si in *T*2) whereas Ca and Na are disordered (Fig. 54).

There is a linear relationship between lattice parameters and composition, which is in agreement with the ordering scheme (Mg,Al) in *T*1 and (Si,Al) in *T*2. Most melilites from igneous rocks plot very close to the åkermanite–soda melilite join and their composition can be determined to within ±10% by a rapid X-ray diffraction method or from their cell parameters.

Downloaded from https://pubs.geoscienceworld.org/books/chapter-pdf/3754637/9780903056434_ch19.pdf
by guest

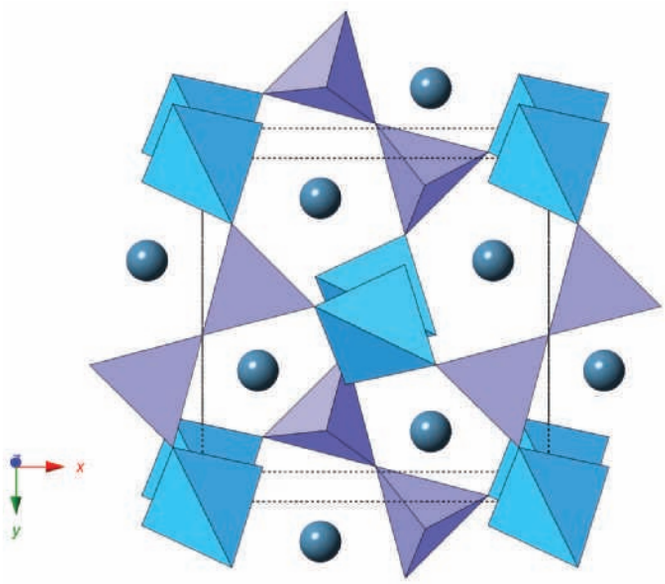


Fig. 54. Perspective view from direction near the *z* axis of the structure of a 'soda melilite', $CaNaAlSi_2O_7$ (CrystalMaker image). Blue: *T*1 tetrahedra; lavender: *T*2 tetrahedra; blue spheres: Ca,Na (random).

Chemistry

The composition of the melilites may be represented by the general formula $(Ca,Na,K)_2(Mg,Fe^{2+},Fe^{3+},Al,Si)_3O_7$ where $(Mg,Fe^{2+}) \leqslant 1.0$ and $Si \leqslant 2.0$.

In addition to the two principal end-member components, åkermanite and gehlenite, analyses of melilites typically show appreciable amounts of iron and sodium. The end-members of natural melilites can be taken to be:

Åkermanite	$Ca_2MgSi_2O_7$
Iron-åkermanite	$Ca_2Fe^{2+}Si_2O_7$
Gehlenite	$Ca_2Al_2SiO_7$
Iron-gehlenite	$Ca_2Fe_2{}^{3+}SiO_7$
Soda melilite	$CaNaAlSi_2O_7$

Thus in the åkermanite–iron-åkermanite–soda melilite series the iron is assumed to be present mainly as Fe^{2+} whereas in iron-gehlenite iron is substituting for Al and is present as Fe^{3+}.

Åkermanite and gehlenite melt congruently at 1451ºC and 1590ºC, respectively, and form a solid solution with a minimum melting temperature of 1385ºC at the composition $Åk_{72}Ge_{28}$. Crystallization thus proceeds from either åkermanite-rich or gehlenite-rich compositions to the minimum freezing point. Natural melilites, however, contain appreciable amounts of iron and sodium (Table 13); the replacement of (Ca,Mg,Al) by (Na,Fe^{2+},Fe^{3+}) causes a marked lowering of the melting temperature, and residual liquids of melilite crystallization become enriched in both iron and sodium.

Table 13. Melilite analyses.

	1	2	3		Numbers of ions on the basis of 14 O					
					1		2		3	
SiO_2	42.81	32.60	22.86	Si	3.921		2.991		2.115	
TiO_2	0.12	0.00	–	Al	0.711		1.957		3.499	
Al_2O_3	6.59	18.10	32.09	Ti	0.008		–		–	
Fe_2O_3	1.90	0.95	3.03	Fe^{3+}	0.131	6.03	0.006	6.03	0.211	5.94
FeO	3.06	0.92	–	Mg	1.021		0.944		0.117	
MnO	0.08	0.02	–	Fe^{2+}	0.234		0.070		–	
MgO	7.48	6.91	0.85	Mn	0.006		0.001		–	
CaO	33.27	40.08	41.25	Na	0.666		0.032		–	
Na_2O	3.75	0.18	–	Ca	3.265	3.97	3.940	4.00	4.08	
K_2O	0.33	0.21	–	K	0.038		0.024		–	
H_2O+	0.43	0.48	–							
H_2O-	0.00	0.00	–	ε	1.637		1.654		–	
Total	99.82	100.45	100.08	ω	1.630		1.656		–	

1 Melilite, melilite basalt, Hawaii (Neuvonen, K.J., 1952, *Bull. Comm. géol. Finlande*, **26**, no. 158, 50 pp).
2 Massive gehlenite, New Mexico, USA (Neuvonen, K.J., *ibid*).
3 Gehlenite, gehlenite–larnite–magnetite rock, chalk–dolerite contact, Carneal, Co. Antrim, Northern Ireland, UK (Sabine, P.A., Styles, M.T. & Young, B.R., 1982, *Rept. Inst. Geol. Sci.*, **82/1**, 61–3). Microprobe analysis.

Downloaded from https://pubs.geoscienceworld.org/books/chapter-pdf/3754637/9780903056434_ch19.pdf
by guest

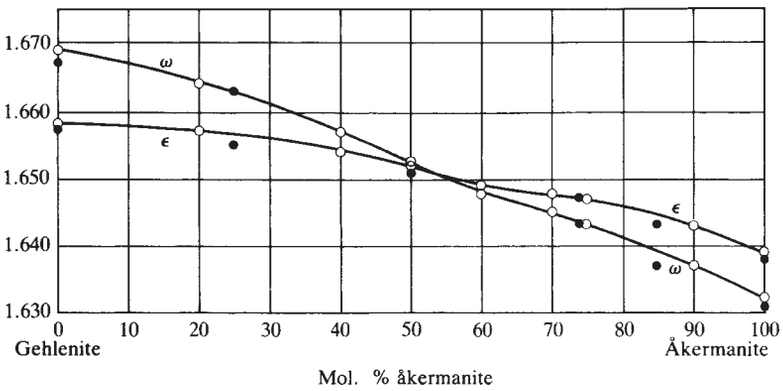


Fig. 55. Refractive indices of the synthetic åkermanite–gehlenite series (○: data from Ferguson. J.B. & Buddington, A.F., 1920, *Amer. J. Sci.*, 4th ser, **50**, 131–40; ●: data from Neuvonen, K.J., 1952, *Bull. Comm. géol. Finlande*, **26**, no. 158, 50 pp).

Experimental work has shown that ~50% $CaNaAlSi_2O_7$ will form melilite solid solutions with both gehlenite and åkermanite, but at 800ºC and 0.1 GPa P_{H_2O} the extent of solid solutions in the gehlenite–åkermanite–soda melilite series is very limited.

The melilites are unstable at temperatures below about 500ºC for åkermanite and 600ºC for gehlenite at water vapour pressures in the range 0.48–0.67 GPa. The decomposition products under these conditions are hydrogrossular, vesuvianite, diopside, ± clintonite and bicchulite, $Ca_2Al_2SiO_6(OH)_2$. Natural alteration products of melilite include garnet, calcite, vesuvianite, diopside and fibrous brown cebollite, $Ca_5Al_2Si_3O_{12}(OH)_4$.

Many natural melilites have small regions of blebs oriented parallel to the *z* axis, known as 'peg structure'. The blebs or pegs contain at least three phases, an SiO_2-rich mineral together with kalsilite and nepheline, and have been considered to be the result of alteration via a complex metasomatic process.

Optical and physical properties

The replacement of A1A1 by MgSi is accompanied by a decrease in both the ω and ε refractive indices. The rate of decrease of ω is much greater than that of ε, and the birefringence decreases from 0.011 for pure gehlenite to zero (ω = ε ~1.65) at approximately 52 mol% åkermanite; solid solutions of this composition are thus isotropic. Similar rates of decrease in the indices persist in the compositional range $Ge_{50}Åk_{50}$–$Åk_{100}$ and the åkermanite-rich members of the series are optically positive (Fig. 55). The replacement of Ca by Na, and to a smaller extent by K, in both gehlenite- and åkermanite-rich melilites results in a lowering of the refractive indices. Melilites are sometimes zoned and may show anomalous blue interference colours (Fig. 56); the minerals are commonly tabular in form with well developed {001} faces.

Distinguishing features

Gehlenite-rich melilites may be distinguished from åkermanite-rich varieties by the optic sign; small values for the birefringence indicate intermediate compositions. The melilites are distinguished from zoisite by their uniaxial optical character, from vesuvianite by their lower refractive indices, and from apatite by their simple tabular habit.

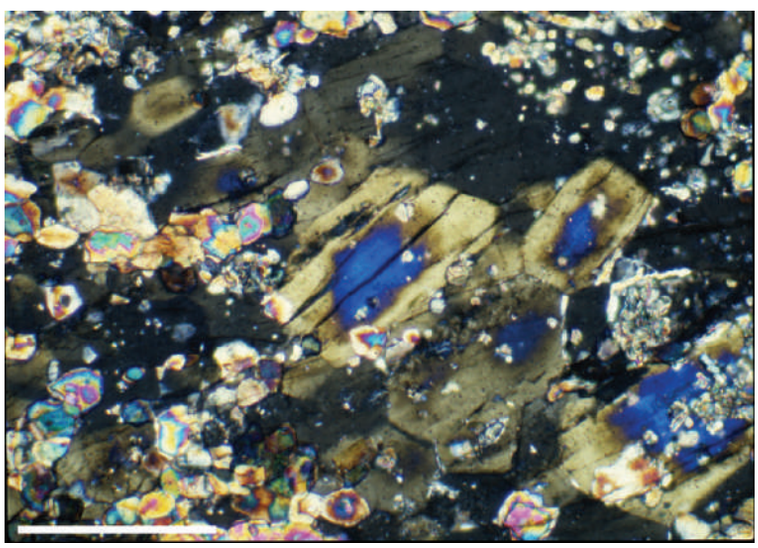


Fig. 56. Melilite, in melilite-phlogopite-clinopyroxene skarn, Carlingford, Ireland, (crossed polars, scale bar 0.5 mm) showing zoning from an anomalous blue to an anomalous brown birefringence colour (W.S. MacKenzie collection, courtesy of Pearson Education).

Downloaded from https://pubs.geoscienceworld.org/books/chapter-pdf/3754637/9780903056434_ch19.pdf
by guest

Paragenesis

Metamorphic rocks

Melilites are characteristic of high-temperature mineral associations in thermally metamorphosed impure limestones of contact zones and åkermanite is considered to be a critical index mineral of the sanidinite facies. The formation of åkermanite during the progressive metamorphism of siliceous limestones and dolomites is due to the reaction:

$$\underset{\text{diopside}}{CaMgSi_2O_6} + CaCO_3 \rightleftharpoons \underset{\text{åkermanite}}{Ca_2MgSi_2O_7} + CO_2$$

which occurs at a relatively high grade. At higher temperatures åkermanite becomes unstable in the presence of calcite and reacts with the carbonate to form merwinite:

$$\underset{\text{åkermanite}}{Ca_2MgSi_2O_7} + CaCO_3 \rightleftharpoons \underset{\text{merwinite}}{Ca_3MgSi_2O_8} + CO_2$$

In the highest grade of thermal metamorphism of such rocks åkermanite reacts with spurrite to give merwinite and larnite:

$$\underset{\text{åkermanite}}{Ca_2MgSi_2O_7} + 2\,\underset{\text{spurrite}}{Ca_2SiO_4.CaCO_3} \rightleftharpoons \underset{\text{merwinite}}{Ca_3MgSi_2O_6} + 2\,\underset{\text{larnite}}{Ca_2SiO_4} + CO_2$$

In many thermally metamorphosed impure limestones, Al and Si are both present, and the melilite is commonly closer in composition to gehlenite (Table 13, analysis 3). In the Hatrurim formation of Israel, both åkermanite and gehlenite occur associated with merwinite and larnite in a unique assemblage of high-temperature metamorphic minerals corresponding with the sanidinite and pyroxene-hornfels facies, produced not by an igneous intrusion but in a normal marine sedimentary sequence to which additional thermal energy was provided by combustion of bituminous organic matter.

Melilite is a common constituent of feldspathoidal rocks formed by the reaction of basic magmas with carbonate rocks. Thus in Northern Ireland, melilite is an abundant constituent of reaction zones between dolerite and chalk and occurs with titaniferous augite, aegirine-augite and nepheline in the hybrid rocks formed by assimilation of carbonate in dolerite magma.

Igneous rocks

Melilite is the dominant constituent of the plutonic ultramafic rock uncompahgrite or pyroxene melilitolite, and has also been reported from carbonatites. Extrusive ultramafic melilite-bearing rocks, or melilitites, contain melilite in the groundmass and occasionally also as phenocrysts. The melilite of these rocks has a relatively high content of sodium and iron, and not uncommonly has a 'peg structure' (see above). Melilite also occurs in melilite leucitites, melilite tuffs and, with olivine and monticellite, as an important constituent of some varieties of alnöites. Melilite nephelinites are common in many alkaline volcanic provinces. In igneous rocks in general, melilite is apparently incompatible with plagioclase and amphibole, though it can coexist with plagioclase in hybrid rocks. Melilite has been reported in chrondrules in several chondritic meteorites.

Further reading

Edgar, A.D. (1965) Lattice parameters of melilite solid solutions and a reconnaissance of phase relations in the system $Ca_3Al_2SiO_7$ (gehlenite)–$Ca_2MgSi_2O_7$ (åkermanite)–$NaCaAlSi_2O_7$ (soda melilite) at 1000 kg/m^2 water vapor pressure. *Canadian Journal of Earth Science*, **2**, 596–621.

Katona, I., Pascal, M.-L., Fonteiiles, M. and Verkaeren, J. (2003) The melilite (Gh_{50}) skarns of Oravita Banat, Romania: transition to gehlenite (Gh_{85}) and to vesuvianite. *The Canadian Mineralogist*, **41**, 1255–1270.

Louisnathan, S.J. (1970) The crystal structure of synthetic soda melilite $CaNaAlSi_2O_7$. *Zeitschrift für Kristallographie*, **131**, 314–321.

Yoder, H.S. (1973) Melilite stability and paragenesis. *Fortschrift für Mineralogie*, **50**, 140–173.

Downloaded from https://pubs.geoscienceworld.org/books/chapter-pdf/3754637/9780903056434_ch19.pdf
by guest

Beryl $Be_3Al_2[Si_6O_{18}]$

Hexagonal (−)

ε	1.565−1.599
ω	1.569−1.610
δ	0.004−0.009
D (g/cm^3)	2.66−2.92
H	7½−8
Cleavage	{0001} imperfect;
Twinning	Rare; on {31$\bar{4}$1}, {11$\bar{2}$0} and {40$\bar{4}$1}
Colour	Colourless, white, bluish green, greenish yellow, yellow, blue, rose; usually colourless in thin section
Pleochroism	In thick sections, weakly pleochroic: e.g. emerald may show ω yellowish green, ε sea-green
Unit cell	*a* 9.200−9.220 Å, *c* 9.187−9.249 Å Z = 2; space group *P*6/*mcc*

Beryl occurs typically in granitic rocks and pegmatites as white or bluish green hexagonal prisms often associated with lepidolite, topaz and tourmaline. It is known also from nepheline syenites and mica schists. Aquamarine is a pale blue gem variety, heliodor is a yellow gem variety and emerald is a deep green gem variety. The refractive indices and birefringence are low.

Structure

The dominant features in the beryl structure are the hexagonal rings of six Si−O tetrahedra (Fig. 57) forming hollow columns parallel to the *z* axis of the crystal. Within the rings two of the oxygen atoms in each SiO_4 group are shared by SiO_4 groups on either side, thus giving the ring silicate ratio Si:O = 1:3[a]. Between the rings lie the Al and Be atoms, each Al coordinated with an octahedral group of six oxygen atoms, and each Be surrounded by a distorted tetrahedron of four oxygen atoms. In these positions they link the oxygens of neighbouring Si_6O_{18} rings both laterally and vertically. The structure is thus like a honeycomb; no atomic centre is nearer than 2.55 Å to the centres of the open channels. Alkali beryls are known, however, with appreciable amounts of Na and Cs, and these larger ions occupy the otherwise vacant channels, the positive charges contributed by them being balanced by cation or (OH) substitution. The water commonly reported in beryl analyses is also located in these channels.

Two types of water may occur: the type I water molecule is oriented in the hollow channels with its diad axis perpendicular to the *z* axis of the beryl whereas the type II water molecule is rotated by 90º by the action of a nearby alkali ion on the molecule dipole and lies with its symmetry axis parallel to the hexagonal *z* axis (Fig. 58).

[a] It has been noted that Be and Si tetrahedra together form a 3-dimensional framework, so that beryl could also be classified as a 'framework silicate', and the formula written as $Al_2[Be_3Si_6O_{18}]$.

Chemistry

Although normally regarded as $Be_3Al_2Si_6O_{18}$, beryl usually contains some alkalis and in certain varieties the total alkali content may rise to about 7%. Although Li may substitute for Be, the larger ions Na and Cs, and less commonly Rb and K, are located in the hexagonal channel in the structure (see above). Analyses of four beryls are given in Table 14, where they have been listed in order of increasing number of metal ions. Possible substitution schemes in beryl include $3Be^{2+} \leftrightarrow 2Li^{+} + Si^{4+}$, $Si^{4+} \leftrightarrow Be^{2+} + 2R^{+}$, $Si^{4+} \leftrightarrow Al^{3+} + R^{+}$ and $Be^{2+} + Si^{4+} \leftrightarrow 2Al^{3+}$. The Al_2O_3 content of beryl varies considerably. The deficiency in Al is correlated with $\Sigma(Fe^{2+},Fe^{3+},Cr,V,Sc,Mn,Ti,Mg)$, indicating the mutual substitution of these ions in the octahedral sites ('octahedral' beryls). The Be shows an opposite trend with respect to Al, and there is a negative correlation between Be and Li, showing that Be is partially replaced by Li in the tetrahedral sites ('tetrahedral' beryls).

Three beryl series have been defined on the basis of the *c*/*a* ratio: (1) the 'octahedral' beryls, those where

Downloaded from https://pubs.geoscienceworld.org/books/chapter-pdf/3754661/9780903056434_ch20.pdf
by guest

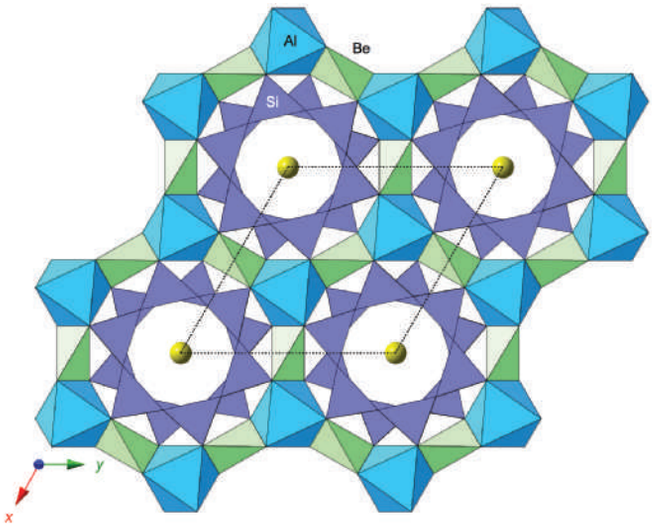


Fig. 57. Part of the structure of an (Na,Li,Cs) beryl projected on (0001) showing two overlapping rings of six Si−O tetrahedra (purple) sharing outer corners with Al octahedra (blue) and Be tetrahedra (green). Yellow circles represent alkali cations, water molecules and/or (OH) anions within structural channels (CrystalMaker image).

Al ↔ Me^{2+} is the main isomorphous replacement, characterized by *c/a* in the range 0.991−0.996; (2) the 'tetrahedral' beryls, with Be ↔ Li as the main substitution, with *c/a* 0.999−1.003; and (3) the 'normal' beryls with *c/a* 0.997−0.998, which include those where the two substitutions occur together, but only to a limited extent. There is a compositional gap between the 'octahedral' and 'tetrahedral' beryls.

Beryl can be synthesized hydrothermally from a mixture of SiO_2, Al_2O_3 and $BeCO_3$ at pressures varying from 0.04 to 0.15 GPa; at 400ºC beryl appears as a fine white powder, and at 600ºC transparent colourless crystals appear, together with minor amounts of phenakite (Be_2SiO_4) and chrysoberyl ($BeAl_2O_4$). Various methods have been used for producing synthetic emeralds, requiring minor Cr_2O_3 in addition to the major oxides, one of the most important being the Linde hydrothermal process using the relatively simple flux-melt method.

A common alteration product of beryl is kaolinite, sometimes together with a small amount of muscovite. Its alteration to bavenite, bertrandite, phenakite, epididymite and milarite is also known.

Optical and physical properties

The major factor affecting the optical properties of beryl is the alkali content of the mineral. An increase in the alkali content is accompanied by an increase in the refractive indices (Fig. 59) and a slight increase in the birefringence. The ω refractive index can be linked with

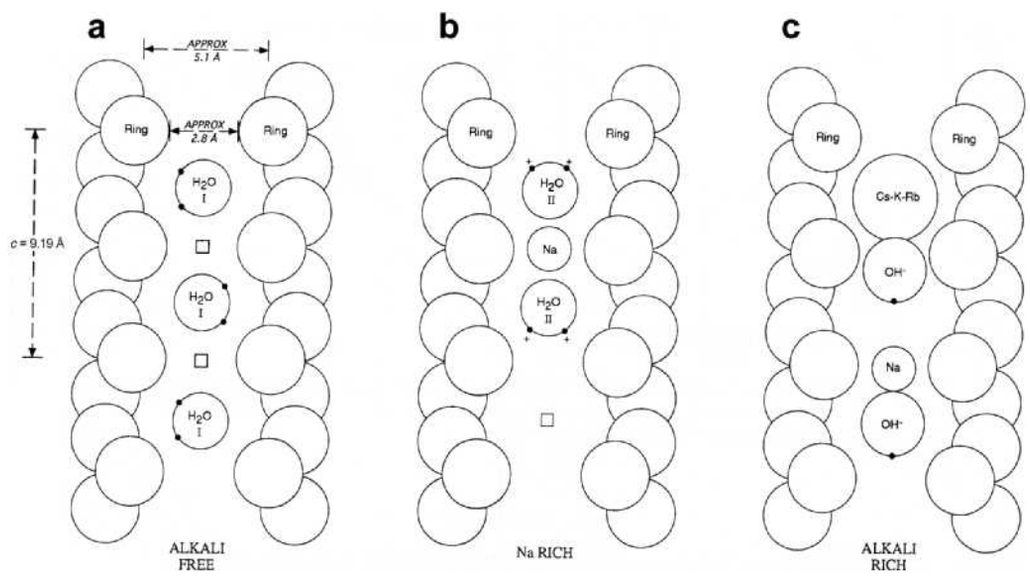


Fig. 58. (a) Side view of the channel of alkali-free beryl, showing the location and orientation of type 1 water molecules in relation to the Si_6O_{18} rings. (b) Channel occupation in Na-rich beryl showing location and orientation of type II water molecules, and Na cation. (c) Channel occupation in alkali-rich beryl showing, Na, (Cs,K,Rb) and (OH) ions (after Aurisicchio, C., Grubessi, O. & Zecchini, P., 1994, *Can. Min.*, **32**, 55−68, itself modified after Aimes, A.D. & Rossman,G.R., 1984, *Amer. Min.*, **69**, 319−327). □: vacant site.

Downloaded from https://pubs.geoscienceworld.org/books/chapter-pdf/3754661/9780903056434_ch20.pdf
by guest

Table 14. Beryl analyses.

	1	2	3	4		Numbers of ions on the basis of 36(O) 1	2	3	4
SiO_2	65.14	64.16	63.34	59.52	Si	11.997	11.865	12.04	11.965
TiO_2	0.06	–	–	0.05	Ti	0.008	–	–	0.008
Al_2O_3	18.20	18.73	17.80	10.63	Al	3.950	4.083	4.00	2.520
Cr_2O_3	–	–	–	0.09	Fe^{3+}	0.090	0.040	–	0.314
Fe_2O_3	0.65	0.28	–	2.08	Be	5.671	5.766	5.30	6.032
FeO	0.28	–	0.05	2.24	Mg	0.137	–	–	0.647
BeO	12.82	12.98	11.59	12.49	Li	–	0.060	0.65	0.186
MnO	–	–	–	0.29	Fe^{2+}	0.043	–	–	0.376
MgO	0.50	–	0.01	2.16	Na	0.144	0.456	0.424	0.452
CaO	tr.	–	–	0.11	Ca	–	–	–	0.024
Na_2O	0.40	1.27	1.15	1.16	K	0.012	0.098	–	0.041
K_2O	0.05	0.39	–	0.16	Cs	–	0.033	0.166	0.572
Li_2O	–	0.08	0.85	0.23	Σ^a	10.06	10.54	10.52	11.25[b]
Cs_2O	–	0.42	2.04	6.68					
H_2O+	1.98	1.44	1.70	1.62	ε	1.572	1.577	–	1.599
H_2O-	0.23	0.02	–	–	ω	1.577	1.583	–	1.608
Total	100.31	99.77	98.53	99.88	D	2.70	2.725	–	2.921

1 Pale green beryl, Charleston, New Zealand (Hutton, C.O. & Seelye, F.T., 1945, *Trans. Roy. Soc., New Zealand*, **75**, 160–68).
2 Clear vitreous beryl, Varuträsk pegmatite, Sweden (Quensel, P., 1937, *Geol. För. Förh. Stockholm*, **59**, 269–72).
3 Pink beryl (morganite), Minas Geraes, Brazil (Artioli *et al.*, 1993, *Amer. Min.*, **78**, 762–768). *a* 9.208, *c* 9.197 Å.
4 Bluish alkali beryl, pegmatite, Mohave Co., Arizona, USA (Schaller, W.T., Stevens, R.E. & Jahns, R.H., 1962, *Amer. Min.*, **47**, 672–94). Includes Sc_2O_3 0.10, P_2O_5 0.27.

[a] Σ = sum of metal ions other than Si.
[b] Includes Cr 0.014, Sc 0.017, Mn 0.049.

the variation in density of beryl as well as with the BeO percentage (Fig. 59).

The colour of beryl varies, the most common variety being white to pale green or yellow and generally opaque. Clear transparent types suitable for gems are classed as aquamarine if they are blue, heliodor if they are yellow, morganite if they are pink and emerald if they are vivid deep green. The green colour of emerald has long been attributed to its chromium content. It has been suggested that, gemmologically, no green beryl lacking chromium should be classed as an emerald, though either vanadium or chromium can also produce an emerald-green hue. The trace element contents of emeralds can be used to distinguish between natural and synthetic stones, and also to differentiate between the localities of natural emeralds. The clear pale blue to rich sky-blue colour of aquamarine is due to Fe^{2+} in the range 0.1–0.3% in an axial channel site; Fe^{3+} in the octahedral Al site gives heliodor the yellow or golden colour. In the rose or salmon-pink morganites the colour is attributed to a small amount of Mn^{3+}.

Distinguishing features

Beryl may be confused with quartz, but can be distinguished by having higher refractive indices, negative sign and length-fast orientation. Apatite has

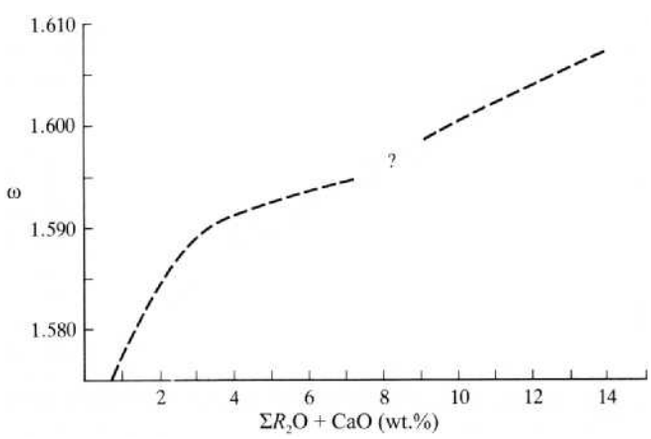


Fig. 59. Plot of ω refractive index *vs.* R_2O + CaO (wt.%) in (Na,Li) and (Na,Li,Cs)-rich pegmatitic beryls (after Černý, P. & Hawthorne, F.C., 1976, *Can. Min.*, **14**, 491–497). *R* = monovalent alkali ions.

Downloaded from https://pubs.geoscienceworld.org/books/chapter-pdf/3754661/9780903056434_ch20.pdf
by guest

considerably higher refractive indices and is less hard, being scratched by a knife. The glassy lustre of beryl is characteristic.

Paragenesis

Common beryl and aquamarine characteristically occur in vugs and druses in granite and granite pegmatites: associated minerals may include quartz, feldspar, muscovite, lepidolite, topaz, tourmaline, spodumene, cassiterite, columbite and tantalite. The occurrence of beryl in granite pegmatites is related to the small size of the Be ion, which, being too small to substitute in most silicate structures, is concentrated in the residual magmatic fluids. It has been suggested that it occurs in aluminium-rich rocks whereas helvite, $(Mn,Fe,Zn)_8Be_6Si_6O_{24}S_2$, is deposited in aluminium-poor rocks. Beryl also occurs in some nepheline syenites and in mica schists and marbles. Emeralds occur mainly in metamorphic rocks, typically in biotite schist, though an important source of emeralds, at Muzo, Colombia, is in calcite veins in bituminous limestone.

Further reading

Aurisicchio, C., Fioravanti, G., Grubessi, O. and Zanazzi, P.F. (1988) Reappraisal of the crystal chemistry of beryl. *American Mineralogist*, **73**, 826–837.

Aurisicchio, C., Grubessi, O. and Zecchini, P. (1994) Infrared spectroscopy and crystal chemistry of the beryl group. *The Canadian Mineralogist*, **32**, 55–68.

Černý, P. (2002). Mineralogy of beryllium in granite pegmatites. Pp. 405–444 in: *Beryllium: Mineralogy, Petrology, and Geochemistry,* (E.S. Grew, editor). Reviews in Mineralogy & Geochemistry, **50**. Mineralogical Society of America and Geochemical Society, Washington, D.C.

Černý, P. and Hawthorne, F.C. (1976) Refractive indices versus alkali contents in beryl: general limitations and applications to some pegmatitic types. *The Canadian Mineralogist*, **14**, 491–497.

Franz, G. and Morteani, G. (2002) Be-minerals: synthesis, stability and occurrence in metamorphic rocks. Pp. 551–590 in: *Beryllium: Mineralogy, Petrology, and Geochemistry* (E.S. Grew, editor). Reviews in Mineralogy & Geochemistry, **50**. Mineralogical Society of America and Geochemical Society, Washington, D.C.

Hawthorne, F.C. and Černý, P. (1977) The alkali metal position in Cs-Li beryl. *The Canadian Mineralogist*, **15**, 414–421.

Markl, G. and Schumacher, J.C. (1997) Beryl stability in local hydrothermal and chemical environments in a mineralized granite. *American Mineralogist*, **82,** 194–202.

Schrader, H.-W. (1983) Contributions to the study of the distinction of natural and synthetic emeralds. *Journal of Gemmology*, **18**, 530–543.

Sinkankas, J. (1981) *Emerald and Other Beryls*. Chilton Book Co., Radnor, Pennsylvania, USA, 665 pp.

Wood, D.L and Nassau, K. (1968) The characterization of beryl and emerald. by visible and infrared absorption spectroscopy. *American Mineralogist*, **53**, 777–800.

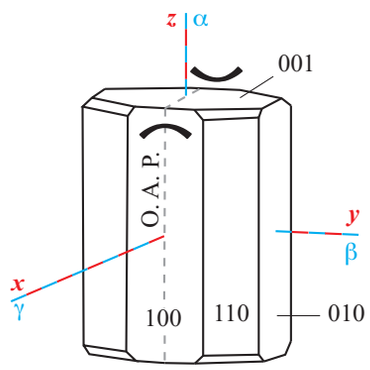
Zwaan, J.C. (2006) Gemmology, geology and origin of the Sandawana emerald deposits, Zimbabwe. *Scripta Geologica*, **131**, 1–211.

Downloaded from https://pubs.geoscienceworld.org/books/chapter-pdf/3754661/9780903056434_ch20.pdf
by guest

Cordierite $(Na,K)_{0-1}(Mg,Fe,Mn,Li)_2[Si_5Al_4O_{18}].n(H_2O,CO_2)$

Orthorhombic (pseudohexagonal) (−)(+)

α	1.527–1.560
β	1.532–1.574
γ	1.537–1.578
δ	0.008–0.018
$2V_\alpha$	35–106°
Orientation	α = *z*, β = *y*, γ = *x*; O.A.P. (010)
D (g/cm^3)	2.53–2.78
H	7
Cleavage	{100} moderate; {001}, {010} poor
Twinning	{110}, {310} simple, lamellar, cyclic, common
Colour	Greenish blue, lilac-blue, dark blue; colourless or very pale blue in thin section
Pleochroism	Mg-rich cordierite in thick section: α pale yellow or green, β violet or violet-blue, γ pale blue; pleochroic haloes common around zircon inclusions
Unit cell	α ~ 17.l Å, *b* ~ 9.7 Å, *c* ~ 9.3 Å Z = 4; space group *Cccm*



Cordierite is an aluminosilicate mineral that is most commonly found in metamorphic rocks. It is a characteristic phase in thermal aureoles in argillaceous rocks, commonly in association with andalusite, and is also found in regionally metamorphosed rocks, with garnet, staurolite and kyanite. It occurs in some basic igneous rocks, possibly due to contamination by argillaceous material. It has low relief and birefringence and may be confused with quartz.

Structure

Most natural specimens of cordierite are of the low-temperature polymorph which is orthorhombic but pseudo-hexagonal (as shown by the relationship $a \sim \sqrt{3}b$). The high-temperature polymorph, indialite, is truly hexagonal and is isostructural with beryl, $Al_2[Be_3Si_6O_{18}]$. Both structures contain six-membered rings of $(Si,Al)O_4$ tetrahedra and have therefore been regarded as 'ring silicates', but the rings are themselves linked laterally and vertically by additional (Al,Si) tetrahedra making cordierite strictly a 'framework silicate'. Small amounts of Fe^{2+} and even less Fe^{3+} have been reported as located in tetrahedral sites, in the latter case balanced by Na at the centre of the six-membered rings. Within the framework there are sites for (Mg,Fe) in octahedral coordination (Fig. 60). Water molecules and alkali ions occur to a variable extent in cordierite. Alkali ions are located in the narrower part of the channels formed by the six-membered rings; water molecules are of two kinds, one in a similar position and the other in the wider part of the channel. In indialite the ring tetrahedra are all equivalent and Si-rich whereas the non-ring tetrahedra are Al-rich. In cordierite there is a high degree of Si,Al order throughout the structure associated with its departure from hexagonality but the latter is also affected considerably by chemical substitutions. A first-order transition from hexagonal to orthorhombic Mg-cordierite occurs at about 1450°C. However, hexagonal cordierite may nucleate metastably below the transition temperature, and on further cooling undergo transformation to the orthorhombic form, and develope the characteristic twinning (see below).

Chemistry

In most cordierites the octahedrally coordinated positions in the structure are occupied predominantly by magnesium (Table 15), and cordierites containing more than one Fe^{2+} atom per formula unit are rare and

Downloaded from https://pubs.geoscienceworld.org/books/chapter-pdf/3754665/9780903056434_ch21.pdf
by guest

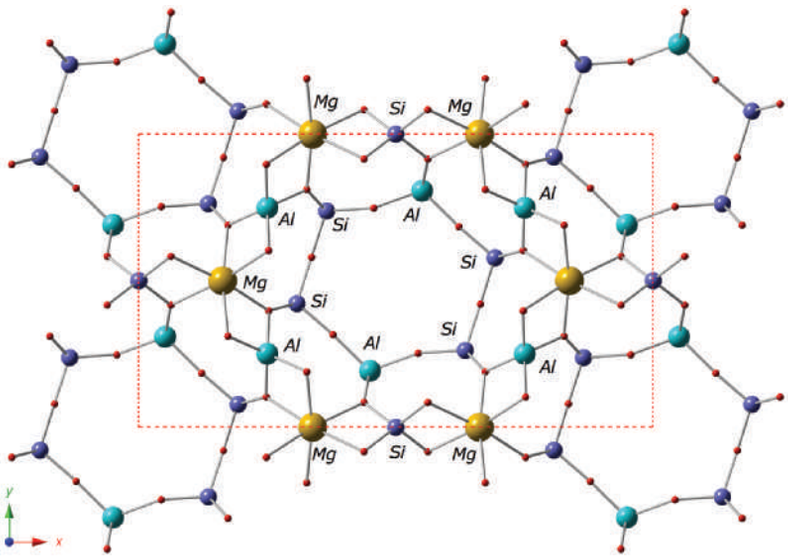


Fig. 60. Structure of a fully ordered cordierite projected on (001) (CrystalMaker image). Red: oxygen.

tend to be restricted to pegmatitic occurrences. Compared with associated ferromagnesian minerals, such as biotite, garnet, orthopyroxene and spinel, cordierites are preferentially enriched in magnesium relative to iron.

The Si:Al ratio does not vary much from 5:4, corresponding with an apparent structural requirement of 4 Si plus 2 Al within the six-membered rings and 1Si plus 2 Al outside them. Beryllium-rich cordierites (usually pegmatitic), however, have lower Al content, accompanied by higher Si and/or alkali ions, the latter located in the structural channels. The appreciable content of H_2O shown by many cordierite analyses is located in these channels which may also house CO_2, argon and other fluids. The maximum H_2O+ content shown by natural cordierite is about 2.8 wt.%, corresponding with about one molecule per formula unit.

Cordierite is commonly altered; the best known alteration product is greenish pinite which consists of a fine felty mixture of muscovite with some chlorite or serpentine mineral and iron oxides. The pinite alteration product may be colourless, or greenish, bluish or yellow.

Experimental work

Anhydrous magnesium cordierite melts incongruently at 1465ºC to mullite and a liquid. Sekaninaite, ideally, $Fe_2Al_4Si_5O_{18}$, the iron analogue, melts incongruently at 1210ºC to mullite, tridymite and a liquid.

Table 15. Cordierite analyses.

	1	2	3		Numbers of ions on the basis of 18 O (ignoring H_2O) 1		2		3	
SiO_2	50.2	47.69	44.64	Si	5.02	6.00	4.964	6.00	4.924	6.00
TiO_2	<0.01	tr.	–	Al	0.98		1.036		1.076	
Al_2O_3	33.5	32.52	29.96	Al	2.97	2.98	2.954	3.00	2.820	3.05
Fe_2O_3	0.14	0.63	2.72	Ti	–		–		–	
FeO	0.84	8.04	11.02	Fe^{3+}	0.01		0.048		0.225	
MnO	0.06	0.04	1.86	Mg	1.91	1.99	1.172	1.88	0.506	1.70
MgO	12.80	7.56	3.08	Fe^{2+}	0.07		0.700		1.017	
CaO	0.23	0.52	0.02	Mn	0.01		0.003		0.174	
Na_2O	0.26	0.53	2.05	Ca	0.02	0.07	0.106	0.22	0.002	0.55
K_2O	0.14	0.42	0.75	Na	0.03		0.058		0.437	
H_2O+	1.69	1.85	3.85	K	0.02		0.055		0.106	
H_2O-	0.12	0.55								
Total	99.98	100.35	99.95							
				Atomic percentages						
				X_{Mg}	92		61		26	

1 Cordierite, phlogopite schist, near White Well, Western Australia (Pryce, M.W., 1973, *Mineral. Mag.*, **39**, 241–43).
2 Cordierite, argillaceous hornfels, Sparcraigs, Belhelvie, Aberdeenshire, Scotland, UK (Stewart, F.H., 1942, *Mineral. Mag.*, **26**, 260–6).
3 Cordierite, pegmatite, Sugama, Fukushima, Japan (Iiyama, T., 1960, *Bull. Soc. franç. Min. Crist.*, **83**, 155–78).

X_{Mg} = 100 Mg/(Mg + Fe + Mn).

Downloaded from https://pubs.geoscienceworld.org/books/chapter-pdf/3754665/9780903056434_ch21.pdf
by guest

From laboratory experiments it has been deduced that the temperature for the transition from orthorhombic to hexagonal cordierite falls from 1450ºC for the Mg end-member to about 700ºC for an intermediate composition and rises to about 900ºC for Fe-cordierite.

Cordierite has been synthesized from anhydrous mixtures of its oxides, and hydrothermally from glasses of appropriate composition at temperatures as low as 450ºC.

Although anhydrous cordierite is stable to a high temperature it breaks down above about 0.6–0.8 GPa to enstatite + sillimanite (or at higher temperature, sapphirine) + quartz. Experimental work on the system $MgO-Al_2O_3-SiO_2-H_2O$ shows that the stable low-temperature breakdown assemblage from cordierite is andalusite (or kyanite) + quartz + chlorite (Fig. 61, curve 1), an assemblage commonly found in 'spotted slates'. At still lower temperatures and pressures pyrophyllite can occur rather than chlorite. At moderate $P-T$ conditions an important reaction producing cordierite in pelitic rocks is:

muscovite + chlorite + quartz → cordierite + biotite + H_2O

The iron-free version of this reaction is shown in Fig. 61 (curve 2), along with some other reactions involving cordierite.

Experiments in the $MgO-FeO-Al_2O_3-SiO_2-H_2O$ system at higher temperatures and/or pressures have also been made. Water content in synthetic sekaninaite. increases with increasing pressure and decreases slightly with increasing temperature. For compositions with excess aluminosilicate (below 1000ºC), cordierite breaks down according to the divariant reaction:

cordierite → garnet + sillimanite + quartz

for most values of the Mg/Fe ratio. The upper pressure limit for Mg-cordierite stability is about 0.6–1 GPa, depending upon temperature and H_2O content. The Mg/Fe ratios in coexisting cordierite and garnet in divariant equilibrium are functions of temperature and pressure and therefore are potentially useful as a geothermometer and geobarometer, though difficulties of calibration arise through metastable phases and the role of variable H_2O in cordierites. In these, and in other estimates of temperature by Mg/Fe distribution (cordierite with biotite, orthopyroxene or spinel), there is also the possibility that post-crystallization re-equilibration may have occurred.

In (K,Na)-bearing systems at moderately high temperatures the association mica + quartz is no longer stable and Mg,Fe-cordierites coexist with feldspar. Dehydration and partial melting experiments show the reaction:

quartz + biotite + plagioclase + aluminosilicate + vapour → cordierite + liquid

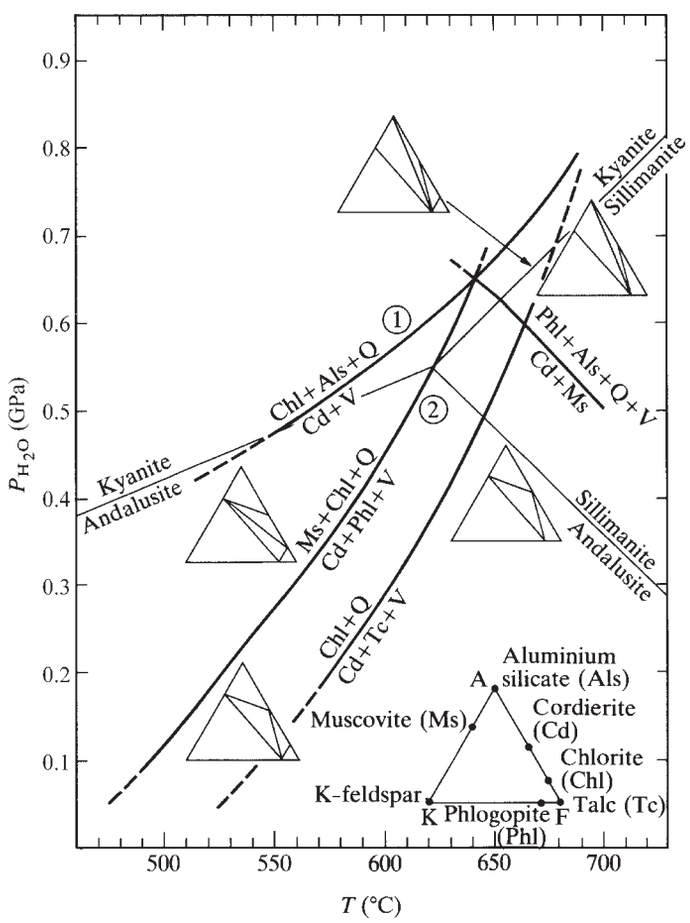


Fig. 61. $P-T$ diagram showing some important reactions in the system $K_2O-MgO-Al_2O_3-SiO_2-H_2O$ (after Seifert, F., 1970, *J. Petrol.*, **11**, 73–99).

Downloaded from https://pubs.geoscienceworld.org/books/chapter-pdf/3754665/9780903056434_ch21.pdf
by guest

taking place at about 660°C, and with P_{H_2O} ~ 0.3–0.6 GPa; with increasing temperature cordierite + garnet + liquid, then cordierite + orthopyroxene + liquid followed by orthopyroxene + liquid are the result. At lower pressures and temperatures, K-feldspar is an additional product in each of the last three cases.

Optical and physical properties

The majority of cordierites are optically negative, with $2V_\alpha$ ranging from 85° to 65° as (Fe + Mn) increases; values outside this range, however, are not uncommon. The value of $2V_\alpha$ may be lower because of above-average contents of Be, Na and H_2O, and higher than 85° (even becoming optically positive) for Mg-rich cordierites if these contents are unusually low and/or the CO_2 content is high. Submicroscopic twinning can also result in apparently low values of 2V.

The refractive indices of cordierite are affected principally by variations in iron and water content, both leading to increases, as also does the substitution of (Na + Be) for Al. Small crystals of zircon and apatite commonly occur as inclusions in cordierite, and they may be surrounded by an intense pleochroic halo (Fig. 63b), the outer part of which is deep yellow and the inner part less strongly coloured. Many other kinds of inclusion, such as biotite, chlorite, magnetite, hematite, quartz and feldspar, have been reported in cordierite. The blue colour and strong pleochroism of some cordierites is due to charge transfer between Fe^{3+} and Fe^{2+} in octahedral and tetrahedral sites respectively.

Cordierite is commonly twinned and the twinning may be simple, lamellar or cyclic. In the latter the composition planes radiate from a central point at intervals of 30°, 60° or 120°. In basal sections of (110) twins the angles between the β and γ vibration directions and the trace of the composition plane are 60° and 30° respectively; in similar sections of (310) twins the angles between the β and γ directions and the trace of the composition plane are respectively 30° and 60°. In concentric twins the twin lamellae are arranged parallel to or at angles of 30° and 60° to the hexagonal outline of the basal section (Fig. 62). The more complex twins are generally restricted to minerals of high-temperature paragenesis, and the more simply twinned cordierite to lower-temperature parageneses (Fig. 63a). The description of twinning as being on {110} and {310} is only approximately correct, as cordierite is pseudohexagonal and not strictly hexagonal.

An unusual property of cordierite is its very low volume coefficient of expansion (expansion parallel to *z* is actually negative near room temperatures).

Distinguishing features

Colourless and unaltered cordierite resembles quartz, but it can usually be distinguished by the large negative optic axial angle. Cordierite can also be distinguished from both quartz and feldspar by the characteristic dusting of the mineral by fine opaque material, by pleochroic haloes around included zircons (Fig. 63b) and apatites, and by the typical micaceous, pinitic, alteration products. Cordierite showing well developed lamellar twinning on {110} is difficult to distinguish from plagioclase, and in the absence of pleochroic haloes it may be necessary to use thick sections to display the pleochroism.

Paragenesis

Cordierite is pre-eminently a product of metamorphism, both contact and regional. It is particularly common in argillaceous rocks in which it forms at an early stage in the metamorphic process mainly at the expense of chlorite, and may be associated with aluminosilicate and biotite through the reaction:

muscovite + chlorite + quartz →
cordierite + Al-silicate + biotite + H_2O

The cordierite initially forms poorly defined and ovoid crystals crowded with inclusions of the recrystallized material of the original sediment.

In most thermal aureoles cordierite persists in the medium-grade hornfelses in which common associates are sillimanite, andalusite, feldspar and micas, and also in the higher grades with garnet, orthopyroxene, corundum or spinel. Examples of possible reactions are:

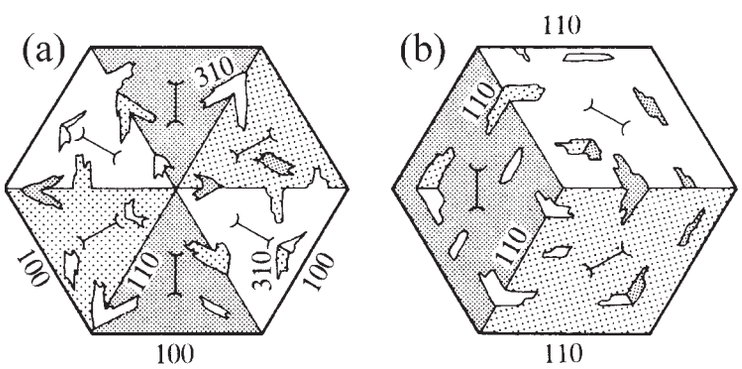


Fig. 62. Concentric twinning in cordierite. (a) Cross-triplet of {110} twins with {310} lamellae giving a star-shaped pattern, (b) Contact-triplet of {110} twins with {110} lamellae giving a concentric arrangement (after Strunz, H., Tennyson, Ch. & Uebel, P.J., 1971, *Min. Sci. Eng.*, **3**, 3–18).

Downloaded from https://pubs.geoscienceworld.org/books/chapter-pdf/3754665/9780903056434_ch21.pdf
by guest

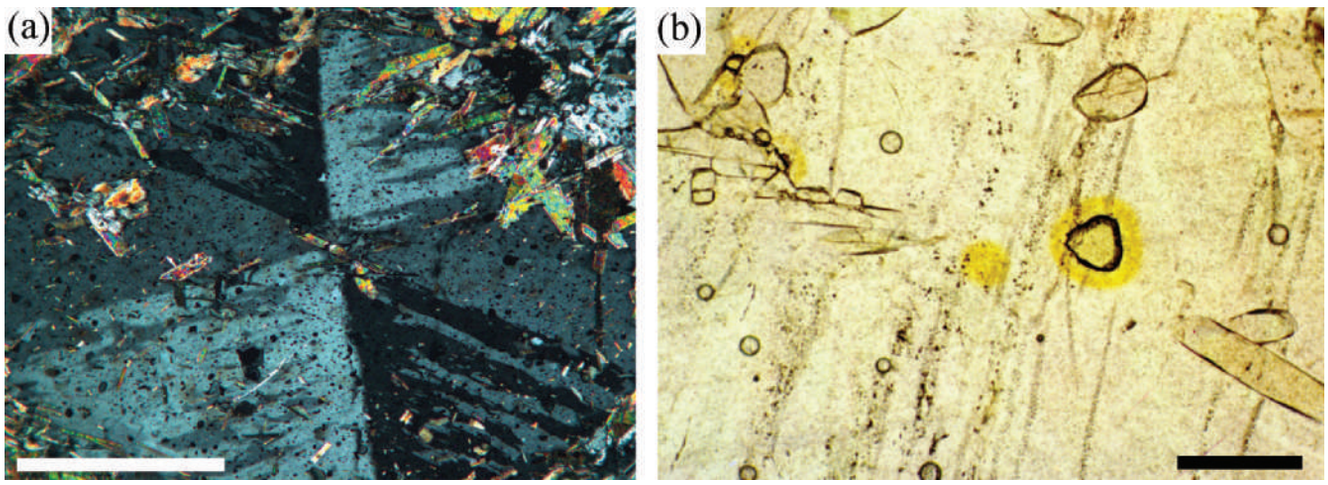


Fig. 63. (a) Cordierite in garnet-gedrite-cordierite-sillimanite hornfels, Huntly, NE Scotland (crossed polars, scale bar 0.5 mm), showing first order interference colours and classic sector twinning (courtesy of G.T.R. Droop). (b) Cordierite in cordierite-sillimanite gneiss, near Iboxy, Madagascar, with a pleochroic halo around an inclusion (ppl, scale bar 0.2 mm) (W.S. MacKenzie collection, courtesy of Pearson Education).

muscovite + biotite → K-feldspar + cordierite + garnet
biotite + Al-silicate → cordierite + spinel
biotite + Al-silicate → cordierite + garnet + orthopyroxene

Cordierite can be formed by the contact metamorphism of arenaceous as well as argillaceous sediments, as for example in cordierite-sillimanite buchites. Complete or partial melting may be involved and the high-temperature polymorph, indialite, may be produced.

Cordierite occurs in a wide variety of regionally metamorphosed paraschists and gneisses and develops over a wide range of $P-T$ conditions. In lower pressure and higher temperature conditions cordierite may be associated with andalusite and staurolite, and at higher pressures with kyanite. Typical gneiss assemblages include garnet and sillimanite, and in the higher-grade rocks transitional to granulite facies, K-feldspar and orthopyroxene are characteristic associated phases.

A possible reaction is:

biotite + garnet → cordierite + K-feldspar + orthopyroxene

An important reaction in the formation of cordierite-bearing gneisses is:

garnet + sillimanite + quartz → cordierite

and in the higher-grade gneisses:

biotite + sillimanite + quartz →
cordierite + garnet + K-feldspar + H_2O

Cordierite is a characteristic mineral in many granulitic rocks, occurring commonly in cordierite-garnet-orthopyroxene-quartz and cordierite-garnet-sillimanite-quartz assemblages; other typical phases include sapphirine, spinel and osumilite-group minerals as well as biotite and feldspar.

The occurrence of cordierite-bearing assemblages in high-grade migmatitic rocks may in some cases be related to the partial melting of metapelites. On removal of a partial (granitic) melt, the composition of the residue is appropriate to the crystallization of cordierite. The change in bulk composition necessary to produce the not-uncommon association of cordierite with anthophyllite (−gedrite) can be explained in a similar fashion, or alternatively by invoking metasomatic processes, or pre-metamorphic alteration of the parent rocks.

Cordierite is found in some igneous rocks. Cordierite-bearing norites are commonly considered to be derived from gabbroic magma contaminated by argillaceous material; in many such norites it is not xenocrystal in origin but crystallized directly from the contaminated magma. Likewise, in the cordierite granites, the cordierite is of both xenocrystal and pyrogenetic origin. Cordierite also occurs in some granite pegmatites; in this paragenesis it is commonly present in large, euhedral grains which are occasionally of gem quality. Micropegmatitic intergrowths of iron-rich cordierite and quartz occur in some pegmatites; these could have been formed by simultaneous crystallization, or by the metasomatic replacement of alkali feldspar by cordierite.

Further reading

Clarke, D.B. (1995) Cordierite in felsic igneous rocks: a synthesis. *Mineralogical Magazine*, **59**, 311−325.

Boberski, C. and Schreyer, W. (1990) Synthesis and water contents of Fe^{2+}-bearing cordierites. *European Journal of Mineralogy*, **2**, 565−584.

Geiger, C.A., Rager, H. and Czank, M. (2000) Cordierite III: the site occupation and concentration of Fe^{3+}. *Contributions to Mineralogy and Petrology*, **140**, 344−352.

Holdaway, M.J. and Lee, S.M. (1977) Fe-Mg cordierite stability in high-grade pelitic rocks based on experimental, theoretical and natural observations. *Contributions to Mineralogy and Petrology*, **63**, 175−198.

Kolesov, B.A. and Geiger, C.A. (2000) Cordierite II: the role of CO_2 and H_2O. *American Mineralogist*, **85**, 1265−1274.

Downloaded from https://pubs.geoscienceworld.org/books/chapter-pdf/3754665/9780903056434_ch21.pdf
by guest

Martignole, J. and Sisi, J.-C. (1981) Cordierite-garnet-H_2O equilibrium: a geological thermometer, barometer and water fugacity indicator. *Contributions to Mineralogy and Petrology*, **77**, 38–46.

Putnis, A. (1980) The distortion index in anhydrous Mg-cordierite. *Contributions to Mineralogy and Petrology*, **74**, 135–141.

Schreyer, W. (1985) Experimental studies on cation substitutions and fluid incorporation in cordierite. *Bulletin de Minéralogie*, **108**, 273–291.

Schreyer, W., Maresch, V.W., Daniels, P. and Wolfsdorff, P. (1990) Potassic cordierites: characteristic minerals for high-temperature, very low-pressure environments. *Contributions to Mineralogy and Petrology*, **105**, 162–172.

Selkregg, K.R. and Bloss, F.D. (1980) Cordierites: compositional controls of Δ, cell parameters and optical properties. *American Mineralogist*, **65**, 522–533.

Downloaded from https://pubs.geoscienceworld.org/books/chapter-pdf/3754665/9780903056434_ch21.pdf
by guest

Tourmaline Group

Trigonal (−)

Dravite–Fluor-dravite	$NaMg_3Al_6Si_6O_{18}(BO_3)_3(OH)_3(OH,F)$
Schorl–Fluor-schorl	$NaFe^{2+}_3Al_6Si_6O_{18}(BO_3)_3(OH)_3(OH,F)$
Elbaite–Fluor-elbaite	$Na(Li_{1.5},Al_{1.5})Al_6Si_6O_{18}(BO_3)_3(OH)_3(OH,F)$
Olenite–Fluor-olenite	$NaAl_3Al_6Si_6O_{18}(BO_3)_3(OH)_3(OH,F)$
Uvite–Fluor-uvite	$CaMg_3(Al_5Mg)Si_6O_{18}(BO_3)_3(OH)_3(OH,F)$

	Dravite	Schorl	Elbaite
ε	1.612−1.632	1.635−1.650	1.615−1.630
ω	1.634−1.661	1.660−1.671	1.633−1.651
δ	0.021−0.029	0.025−0.035	0.017−0.021
D (g/cm^3)	3.03−3.18	3.18−3.22	2.90−3.10
H	7		
Cleavage	{11$\bar{2}$0} and {10$\bar{1}$1}, very poor		
Twinning	Rare, on {10$\bar{1}$1} and {40$\bar{4}$1}		
Colour	*Dravite*: black to brown, yellow to colourless in thin section		
	Schorl: commonly black, blue to yellow in thin section		
	Elbaite: blue, green, yellow, red or colourless, colourless in thin section		
Pleochroism	Variable in intensity, normally very strong; absorption always ω > ε		
Unit cell	*a* 15.96 Å	15.98 Å	15.95 Å
	c 7.21 Å	7.16 Å	7.11 Å
	Z = 3; space group *R*3*m*		
Special features	Only slightly attacked by HF; decomposed by fusion with alkali carbonates or bisulphates. Crystals have polar symmetry and generally show strong pyro- and piezoelectric properties.		

Tourmaline is found characteristically in granitite pegmatites and veins in some granites. It occurs also in thermally metamorphosed argillaceous rocks as a product of boron metasomatism. It varies greatly in colour, generally showing strong pleochroism; schorl, the iron-bearing tourmaline is black in hand specimen, but blue to yellow in thin section, whereas dravite, the magnesium-bearing species, is black to brown and yellowish in thin section. The lithian elbaite varieties may be red, green or blue in hand specimen but are colourless in thin section.

Structure

The structure of tourmaline, general formula $XY_3Z_6[Si_6O_{18}](BO_3)_3(O,OH)_3(OH,F,O)$, is based on a rhombohedral lattice (*R*3*m*) and has trigonal symmetry. An (0001) projection of part of the structure is shown in Fig. 64. It contains Si−O tetrahedra which form six-member ditrigonal rings by each sharing two oxygens, thus defining tourmaline as a ring (or cyclo-) silicate. The Y cations (mainly Mg, Fe^{2+}, Mn, Al, Li) are octahedrally coordinated by oxygen and OH ions, and form a ring of three edge-sharing octahedra around the triad axis. Sharing edges with the *Y* octahedra are six (three pairs), of *Z* [mainly (Al,Fe^{3+},Mg)−(O,OH)] octahedra. The three boron (B) cations form BO_3 triangles, each triangle approximately perpendicular to *z* and sharing two corners with *Z* octahedra and the third corner with the large 9-coordinated *X* polyhedron, which lies on the triad axis and accommodates mainly Na, Ca,

Downloaded from https://pubs.geoscienceworld.org/books/chapter-pdf/3754743/9780903056434_ch22.pdf
by guest

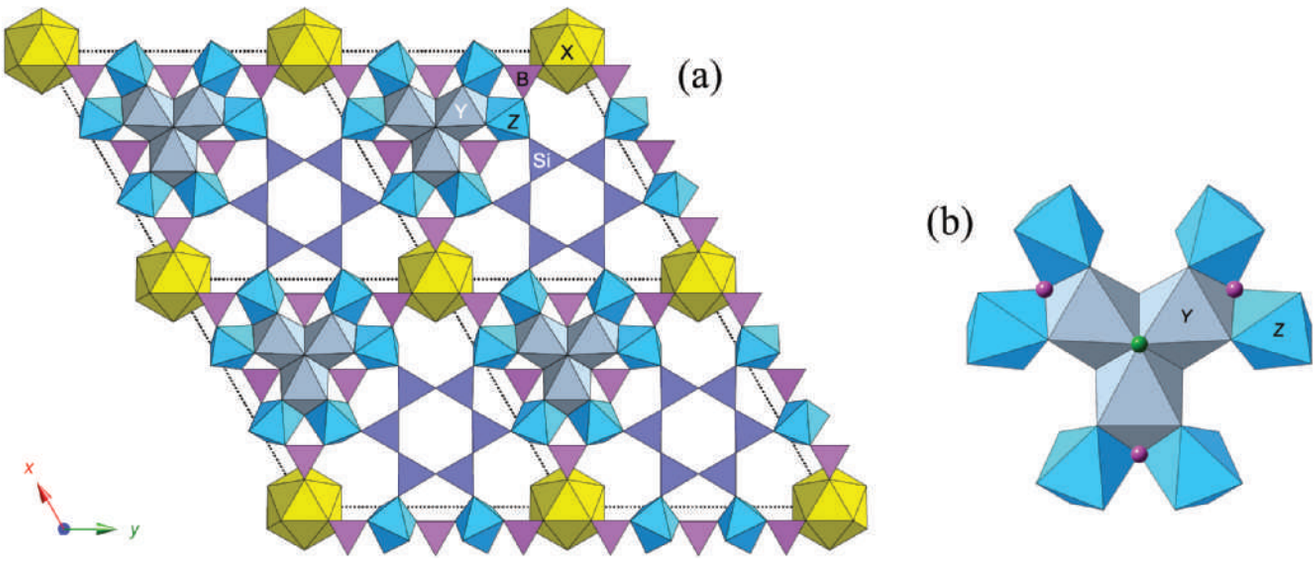


Fig. 64. (a) Projection on (0001) of part of the structure of tourmaline, showing the rings of six Si−O tetrahedra (and triangles of BO_3); two kinds of octahedra, *Y* and *Z*; and the large cation polyhedra *X*. These three elements are stacked above one another and linked laterally in the full structure but parts have been omitted here for greater clarity. (b) Detail showing the *W* (OH,F,O), green and *V* (OH,O), pink, anion sites (CrystalMaker image).

□ and K (□ indicates vacancies). The primary three-fold division of tourmaline species (see below) is based on the Na, Ca and vacancies assigned to the *X* site. Some tourmaline analyses show that minor Al and Fe^{3+} can replace Si, and some show boron content to be greater than three atoms pfu, indicating that, if accompanied by Si deficiency, B can partially replace Si in the structure.

With regard to anions, there are three symmetry related sites, *V*, (shared by one *Y* and two *Z* octahedra) the occupants of which are OH, and/or O, and one unique site, *W*, (shared by three *Y* octahedra) which lies on the triad axis and can be occupied by (OH), F or O (Fig. 64b). Because fluorine occurs only in the single W site, the anion formula is better given as containing

$$O_{27}(O,OH)_3(OH,F,O) \text{ rather than } O_{27}(OH,F,O)_4.$$

In the 3-D structure the elements described and illustrated above are stacked in the *z*-axis direction with the sequence: *Y* and *Z* octahedra and BO_3 triangles, followed by Si−O rings, all pointing in the same direction, and then *X* cations, and repeating in this fashion, thus giving the structure a polar character, and tourmaline its hemimorphic morphology and physical (e.g. pyro- and piezo-electric) properties.

Nearly all investigations have found the symmetry of tourmaline to be rhombohedral, but there have been some reports of specimens, or sectors within tourmalines, with orthorhombic, monoclinic or triclinic symmetry.

Correlations between chemical composition and cell parameters have been established for many minerals, but the task is unusually difficult for tourmalines, as so many chemical elements and different structural sites can be involved. Their constituents include the light elements H, B, F and Li, which are difficult to determine accurately, and also the Fe^{3+}/Fe^{2+} ratio is often somewhat uncertain. Furthermore the cation sites include two which are octahedral yet distinctly different; some of the major elements can be distributed between these two sites (with varying degrees of ordering) and there are several possibilities for coupled or multiple heterovalent as well as isovalent cation and anion substitutions. Nevertheless, when complete chemical analyses and site occupations are obtained*, correlations between them and with other properties (e.g. cell parameters, colour) can be established, and also indications provided of the physical and chemical conditions under which the mineral was formed. Many examples of such studies are reported in the tourmaline thematic issue of *The Canadian Mineralogist*, 2011, **49**, 1−405.

Chemistry and Nomenclature

Tourmaline is a borosilicate with the general chemical formula $XY_3Z_6(Si,Al)_6O_{18}(BO_3)_3V_3W$, with X: (Na,Ca,□), Y: (Fe^{2+},Mg,Mn,Al,Li,Fe^{3+},Cr), Z: (Al,Fe^{3+},Mg,Cr), V: (OH,O), W: (OH,F,O). The individual tourmaline species are defined by taking the dominant ion of the dominant valence state as the basis

* The collection of full data may require techniques such as Mössbauer, FTIR and NMR spectroscopy as well as full X-ray structure determination, and SIMS and LA ICP-MS as well as electron microprobe analysis.

Downloaded from https://pubs.geoscienceworld.org/books/chapter-pdf/3754743/9780903056434_ch22.pdf
by guest

for nomenclature (Henry *et al*., 2011). The primary tourmaline groups are defined by the occupancy of the *X* site, giving **alkali**, **calcic** and ***X*-vacant** groups (Fig. 65a). As cations of different charge are present, coupled heterovalent substitutions are required in order to relate compositions across the three primary groups, and also within each of these groups; the primary groups are therefore divided into sub-groups. The boundaries between the three primary groups are illustrated graphically in (Fig 65a), but boundary conditions can also be expressed numerically. For an alkali-group tourmaline: (Na+K) $\geqslant$ Ca and (Na+K) $\geqslant {}^{X}\square$, for the Ca-group: Ca $\geqslant$ (Na+K) and Ca $\geqslant {}^{X}\square$ and for *X*-vacant tourmalines: ${}^{X}\square \geqslant$ (Na+K) and ${}^{X}\square \geqslant$ Ca.

Another general division of tourmalines into hydroxyl-, fluor- or oxy-species expresses the occupation of the *W* anion site by (OH), F or O using the boundaries shown in Fig. 65b.

The recommended system for naming the more common individual tourmaline species, all with Al dominant in *Z* sites, OH dominant in *V* and *W* sites and (Fe^{2+},Mg) the dominant divalent cation in *Y*, is illustrated in Fig. 65c, d and e for alkali-, calcic and *X*-vacant species respectively. Variations from the above conditions are dealt with by the use of prefixes e.g. fluor-dravite and oxy-dravite if fluorine or oxygen rather than OH is dominant.

The names, compositions and site occupations of a number of recognized and hypothetical end-member tourmalines are listed below. All have in addition Si_6O_{18} and BO_3. Fluorine, when present, as in fluor-dravite, fluor-schorl, etc, substitutes for OH in the *W* site.

	X	*Y*	*Z*	*V*	*W*
Alkali tourmaline					
Dravite	Na	Mg_3	Al_6	$(OH)_3$	(OH)
Schorl	Na	Fe_3^{2+}	Al_6	$(OH)_3$	(OH)
Elbaite	Na	$Li_{1.5}Al_{1.5}$	Al_6	$(OH)_3$	(OH)
Olenite	Na	Al_3	Al_6	O_3	(OH)
Buergerite	Na	Fe_3^{3+}	Al_6	O_3	(O)
Povondraite	Na	$Fe_2^{3+}Mg$	$Fe_4^{3+}Mg_2$	$(OH)_3$	(O)
Ca tourmaline					
Uvite	Ca	Mg_3	Mg,Al_5	$(OH)_3$	(OH)
Liddicoatite	Ca	Li_2Al	Al_6	$(OH)_3$	(OH)
***X*-vacant tourmaline**					
Foitite	□	$Fe_2^{2+}Al$	Al_6	$(OH)_3$	(OH)
Rossmanite	□	$LiAl_2$	Al_6	$(OH)_3$	(OH)

Departures from the above formulae are many and varied in natural tourmalines, including simple isovalent, and heterovalent coupled, substitutions.

In the *X* site, substitution of K for Na appears to be very limited. Some replacement by Ca is very common but subject to charge balancing e.g. by Mg for Al in *Z*,

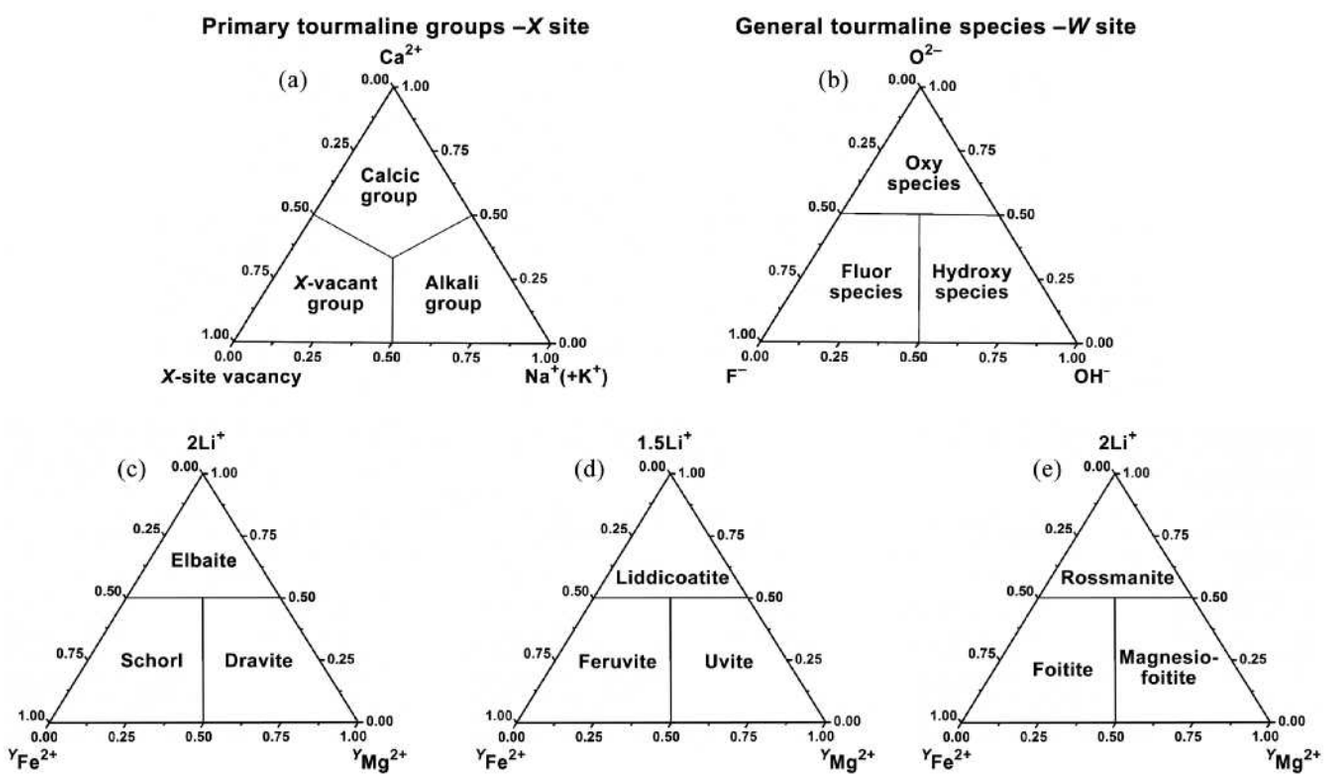


Fig. 65. Classification and nomenclature of tourmalines. (a) Primary tourmaline groups with *X* site: Na, Ca and vacant (□). (b) General tourmaline groups with *W* site: OH, F and O. (c) Alkali-group tourmaline species. (d) Calcic group tourmaline species. (e) 'X-vacant' group tourmaline species. All three have Al dominant in the *Z* site, OH dominant in the *W* and *V* sites and Fe^{2+} or Mg dominant R^{2+} cation in the *Y* site (adapted from Henry *et al*., 2011).

Downloaded from https://pubs.geoscienceworld.org/books/chapter-pdf/3754743/9780903056434_ch22.pdf
by guest

represented by $^{X}Na+^{Z}Al \leftrightarrow {}^{X}Ca+^{Z}Mg$, and also expressing the relationship between dravite and uvite.

The *X* site may also be involved in compensating for excess charge in *Y*, by having a proportion of sites vacant. One such substitution can be represented as $^{X}Na+^{Y}Mg_3 \leftrightarrow {}^{X}\square+^{Y}Al_2Li$, and another as $^{X}Ca+^{Y}Mg_3 \leftrightarrow {}^{X}\square+^{Y}Al_2Fe^{2+}$, expressing also the relationships between dravite and rossmanite, and dravite and foitite.

The *Y* site can be occupied predominantly by Fe^{2+} as in schorl, or Mg as in dravite, but other cations which may enter the site include Mn (up to 0.24 atoms pfu reported), Zn, Co, Ni and Cu. Trivalent cations, mainly Al or Fe^{3+} can enter *Y*, either accompanied by monovalent cations, e.g. Al+Li as in elbaite, or by compensating anion substitutions such as O for OH as in olenite and buergerite.

The *Z* sites are predominantly occupied by Al, but ferrian tourmalines with Fe^{3+} substituting for Al in *Z* are known, and limited substitution by Mg can occur there compensated by Ca in *X*, as referred to above. The Ti, Cr and V contents are very low (mostly < 0.1 atoms pfu) and these elements occur in octahedral coordination.

In general, *Y* and *Z* sites are occupied by divalent and trivalent cations, respectively, but disordered opposite substitutions can occur, in association with replacement of OH by O, particularly in the *W* site, as illustrated by the end-member povondraite.

With regard to the fluorine content in tourmalines, there is strong relationship between F and the cations of the *X* sites. F increases (maximum 1 atom pfu) with increases in the average charge of *X* cations; there is an opposite but weaker influence by the *Y* cations.

The compositions of several tourmalines together with their structural formulae on the basis of 31 (O,OH,F) are given in Table 16.

Because of the wide range of chemical elements in a variety of sites in the structure of tourmaline, there is scope for solid-solution series between some pairs (or more than two) of the principal species. The schorl–dravite (simple Mg–Fe) series shows complete solid solution, and the common black tourmalines of granites and pegmatites involve schorl–dravite–olenite–foitite solid solution. Dravite–uvite–schorl solid solution is exhibited, but to a more limited extent, by 'brown tourmalines'. Natural tourmalines show complete schorl–elbaite but not dravite–elbaite solid solution.

Depending upon the tourmaline species in question, some or all of a number of factors affect its synthesis and stability, including the B and F content of melt and fluid, the Al content of the melt, f_{O_2}, f_{H_2O}, the activities of *Y* cations and the pH of fluid. In the latter respect tourmaline formation is favoured by neutral to acid conditions; high alkalinity leads to the formation of albite and alkali amphiboles.

A variety of tourmalines have been synthesized hydrothermally, including dravite and elbaite (300–700ºC; 0.1–0.4 GPa), olenite (450–600ºC; 0.1 GPa) and uvite (400–700ºC; 0.2 GPa). A narrow range of tourmaline compositions synthesized in the system $MgO–Al_2O_3–SiO_2–B_2O_3–H_2O$ in the presence of excess silica, B_2O_3 and H_2O in the temperature range 400–800ºC and at a pressure of 0.1 GPa showed that alkali-site occupancy and $[Al]^4$ decrease with increasing temperature and protons are generally deficient. Tourmalines closely approaching the ideal defect end-member, $\square(Mg_2Al)Al_6B_3Si_6O_{27}(OH)_4$, were synthesized at 700–800ºC. Synthetic NaAl tourmalines approaching the ideal olenite end-member, $NaAl_3Al_6B_3Si_6O_{30}(OH)$, the Al analogue of buergerite, have also been produced between 450 and 600ºC at 0.1 GPa. In general, however, much further experimental work is needed to define the stability fields of tourmaline. Alteration products of tourmaline include muscovite, biotite or lepidolite micas, and also chlorite and cookeite, $LiAl_4(Si,Al)_4O_{10}(OH)_8$.

Optical and physical properties

The refractive indices, birefringence and density of tourmaline increase with increasing amounts of $(Fe^{2+}+Fe^{3+}+Mn+Ti)$; see Fig. 66.

Optical anomalies, eg. sector zoning, may be due to stress through defects and changes in composition. They may also be due to lowering of symmetry to biaxial orthorhombic or triclinic due to cation ordering, particularly at sites near the surface which are non-equivalent, but equivalent within the crystal.

The pleochroism is variable in intensity but is particularly strong for the iron-bearing tourmalines. The absorption is always $\omega > \varepsilon$ with the result that maximum absorption occurs when the *z* axis is lying perpendicular to the vibration direction of the polarizer. For schorl the contribution of the ω-ray to the transmitted intensity is $\leqslant 10\%$.

The colour of tourmaline is extremely variable but in general terms it can be related to the composition in so far as the iron-bearing tourmalines are black, while the elbaites tend to light shades of blue, green, pink or colourless, and the dravites vary from dark brown to pale yellow. The iron tourmalines typically show pleochroism from yellow, brown or blue to pale yellow or yellowish green. In the dravites the typical brown colour is related to the iron content, the golden brown varieties being relatively low in iron, whereas the black dravites have higher Fe contents. The colour of uvite is variable; the majority, like dravite, are brown. In the elbaites the colour range in hand specimen is particularly wide; the red or pink varieties have been termed rubellite, the green verdelite, and the blue indicolite. They are generally colourless in the ε direction and may show a paler shade of their body colour in the ω direction. Colour zoning is fairly common in all tourmalines and may be parallel to the prism faces, e.g. giving some elbaites rose-red cores with light green rims, or the colour banding may run parallel to the basal plane, often with a sharp discontinuity.

Downloaded from https://pubs.geoscienceworld.org/books/chapter-pdf/3754743/9780903056434_ch22.pdf
by guest

Distinguishing features

Tourmaline can be distinguished under the microscope by its marked pleochroism (Fig. 67): this differs from that of biotite or the common amphiboles in showing maximum absorption when the elongation of the crystal is perpendicular to the vibration plane of the polarizer. The straight extinction, uniaxial character, relatively high relief and moderate birefringence are also diagnostic. Distinction between different varieties of

Table 16. Tourmaline analyses.

	1	2	3	4	5	6
SiO_2	34.86	35.96	34.38	36.36	35.52	31.44
B_2O_3	10.21	11.49	10.12	10.30	10.61	15.25
Al_2O_3	22.54	26.80	31.76	40.48	37.90	46.53
TiO_2	1.57	0.62	0.17	tr.	0.05	0.02
FeO	6.67	0.41	13.15	3.64	0.14	0.05
Fe_2O_3	8.70	–	2.99	–	–	–
MgO	8.39	15.20	0.07	0.09	0.01	–
MnO	0.00	–	0.89	1.05	8.18	0.02
ZnO	0.00	–	0.12	–	0.02	0.09
Li_2O	0.00	0.00	–	1.27	0.73	0.56
K_2O	0.06	0.00	0.04	0.44	0.02	0.00
CaO	2.58	5.50	0.02	0.67	0.18	1.74
SrO	0.00	–	–	–	–	–
Na_2O	1.48	0.13	2.35	2.20	2.64	1.33
F	0.30	1.49	1.40	0.10	1.13	0.12
H_2O+	2.77	2.70	2.83	3.64	3.04	3.25
H_2O-	–	0.04	–	0.08	–	–
	100.13	100.34	100.30	100.32	100.17	100.45
$O \equiv F$	−0.14	−0.63	−0.59	−0.04	−0.48	−0.05
Total	99.99	99.71	99.71	100.28	99.69	100.20
	Numbers of ions on the basis of 31 (O,OH,F)					
Si	5.99	5.86	5.90	5.84	5.83	4.87
Al	0.01	0.14	0.10	0.16	0.17	0.05
B	–	–	–	–	–	1.08
ΣT	6.00	6.00	6.00	6.00	6.00	6.00
B	3.03	3.23	3.00	2.86	3.01	3.00
Al	4.57	5.15	5.59	6.00	6.00	6.00
Fe^{3+}	0.62	–	0.39	–	–	–
Mg	0.81	0.85	0.02	0.02	0.00	–
ΣZ	6.00	6.00	6.00	6.02	6.00	6.00
Mg	1.34	2.84	–	–	0.00	–
Al	0.00	–	0.73	1.66	1.17	2.41
Ti	0.20	0.08	0.02	–	0.01	–
Fe^{2+}	0.94	0.06	1.89	0.49	0.02	–
Fe^{3+}	0.49	–	0.39	0.00	–	–
Mn	0.00	–	0.13	0.14	1.14	–
Zn	0.00	–	0.02	–	0.00	–
Li	0.00	–	–	0.82	0.48	0.35
ΣY	2.97	2.98	3.18	3.11	2.82	2.76
Ca	0.48	0.96	–	0.11	0.03	0.29
K	0.01	–	0.01	0.09	0.00	0.00
Na	0.49	0.04	0.78	0.69	0.84	0.40
ΣX	0.98	1.00	0.79	0.89	0.87	0.69
F	0.18	0.77	0.76	0.05	0.59	0.06
OH	3.18	2.93	3.24	3.90	3.33	3.36
OH+F	3.36	3.70	4.00	3.95	3.92	3.42

1 Dravite, Madagascar (Camara, F. *et al*., 2002, *Amer. Min*., **87**, 1437–42). Electron microprobe data, except SIMS for B, Li, F and H.
2. Brown gem uvite, Sri Lanka (Dunn, P.J. *et al*., 1977, *Min. Rec*., **8**, 100–8).
3. Schorl, pegmatite, Grasstein, Trentino – South Tyrol, Italy (Ertl, A. *et al*., 2006, *Eur. J. Min*., **18**, 583–8). Includes 0.01 Cr_2O_3).
4. Light green elbaite, pegmatite vein in aplite, Meldon, Okehampton, Devon (Chaudhry, M.N. & Howie, R.A., 1976, *Mineral. Mag*., **40**, 747–51).
5 Mn-rich tourmaline, Eibenstein an der Thaya, Lower Austria. (Ertl, A. *et al*., 2003, *Amer. Min*., **88**, 1369–76). Electron microprobe data, except SIMS for B, Li, F and H.
6. Boron-rich olenite, granitic pegmatite, Stoffhütte, Koralpe, Austria (Hughes, J.M. *et al*., 2000, *Can. Min*., **38**, 861–8). Li_2O by SIMS.

Downloaded from https://pubs.geoscienceworld.org/books/chapter-pdf/3754743/9780903056434_ch22.pdf
by guest

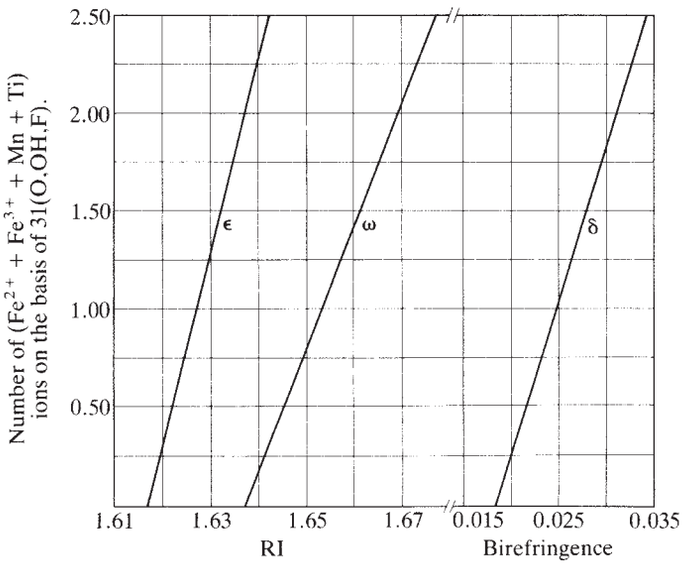


Fig. 66. Optical properties of tourmaline in relation to the number of (Fe^{2+} + Fe^{3+} + Mn + Ti) ions on the basis of 31 (O,OH,F).

tourmaline is easiest by reference to the refractive indices or birefringence to indicate the amount of the schorl molecule present, in conjunction with consideration of the colour or pleochroism to help distinguish between the elbaite and the dravite series.

Paragenesis

Tourmaline is typically a mineral of granite pegmatites, pneumatolytic veins, and of some granites: it is also commonly found in metamorphic rocks as a product of boron metasomatism or as the result of recrystallization of detrital grains from the original sediment. In granitic rocks the tourmalines belong to the schorl–elbaite series and are generally fairly iron-rich, the typical tourmaline-bearing granites of south-west England having black prismatic crystals visible in hand specimen and showing yellow or bluish-yellow pleochroic tourmaline in thin section. In certain pegmatites and late-stage granitic vein material, in which Li is commonly concentrated (sometimes accompanied by F), the lithium tourmalines are developed, often showing a variation in colour and composition corresponding with their position in the pegmatite. In the Varuträsk pegmatite both black and coloured tourmalines occur in the original zonal pegmatitic phase, whereas rubellite (Table 16, analysis 5) and the zoned tourmalines are mainly restricted to the sodium replacement unit in the so-called pneumatogenic stage.

In the pneumatolytic stage of alteration, tourmalinization may occur by the introduction of boron which attacks the normal granitic minerals. Thus the well known rock type luxullianite is regarded as the product of the arrested pneumatolytic modification by boric emanations from a porphyritic alkali granite: in this rock the biotite has been attacked first to give yellow tourmaline, and subsequently the feldspar has been replaced by a blue or blue-green tourmaline. Some yellow tourmaline may be primary in origin but, after a

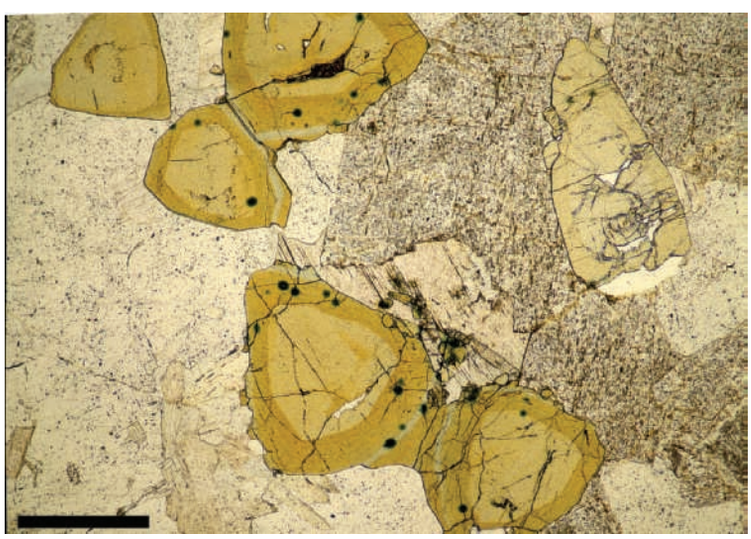


Fig. 67. Tourmaline, in topaz-tourmaline-quartz rock (ppl, scale bar 1 mm), Blackpool Clay Pit, Cornwall, England, showing trigonal cross-sections with zoning of the yellow absorption colours (W.S. MacKenzie collection, courtesy of Pearson Education)

Downloaded from https://pubs.geoscienceworld.org/books/chapter-pdf/3754743/9780903056434_ch22.pdf
by guest

period of corrosion, it serves as a nucleus for radially disposed acicular secondary tourmaline, giving the so-called tourmaline 'suns'. The quartz is not replaced and, if tourmalinization goes to completion, a tourmaline-quartz rock results. It has been suggested that in south-west England tourmalinization fluids have an ultimate source (particularly for boron) in the sediments of the country rocks which also, by assimilation, made a major contribution to the composition of the granites. In pneumatolytic igneous assemblages, minerals associated with tourmaline may include topaz, lepidolite, petalite, spodumene, cassiterite, fluorite, apatite and columbite.

The magnesian tourmalines or dravites are usually found in metamorphic or metasomatic assemblages. They are known from basic igneous rocks where they may be associated with axinite and datolite, the boron having been metasomatically introduced; they have been recorded, locally making up most of the rock, in spilosites and adinoles. Elsewhere in metamorphic rocks the tourmaline may represent the recrystallization of the detrital grains present in the original sediment, as in some Dalradian psammitic rocks. The small amount of boron found in argillaceous sedimentary rocks is not present as tourmaline but appears to have been derived from sea-water and to be held by adsorption. Brown magnesian tourmaline occurs as an important gangue mineral in several types of strata-bound ore deposits throughout the world. There is generally no evidence for an ancient evaporitic environment nearby, nor of associated granites or pegmatites, and it has been suggested that the abundance of such tourmaline in a metamorphic terrane is due to the occurrence of boron as an integral part of the hydrothermal system that deposited the ores and that the tourmaline indicates proximity to a former submarine fumarolic centre.

Uvite is probably more common than dravite; it has been suggested that most brown tourmaline associated with calcium minerals, as in metamorphosed limestones, is uvite whereas most brown tourmaline in schists or associated with non-pegmatitic micas is dravite.

Tourmaline is a common mineral in detrital sediments, different types being found depending on the source. Authigenic tourmaline is known from limestones and as secondary growths on well rounded detrital tourmaline grains in sandstones.

Associated borosilicates in contact metamorphosed and metasomatic rocks may include axinite (typically in lilac-brown axe-shaped crystals, colourless in thin section, with moderate relief and low birefringence) and dumortierite.

Further reading

Bernard, F., Mouton, P. and Pichavant, M. (1985) Phase relations of tourmaline leucogranites and the significance of tourmaline in silicic magmas. *Journal of Geology*, **93**, 271–291.

Bosi, F. and Lucchessi, S. (2007) Crystal chemical relationships in the tourmaline group: structural constraints on chemical variability. *American Mineralogist*, **92**, 1054–1063.

Charoy, B. (1982) Tourmalinization in Cornwall, England. Pp. 63–70 in: *Mineralization Associated with Acid Magmatism* (A.M. Evans, editor). Wiley, New York.

Ertl, A., Marschall, H.R., Giester, G., Henry, D.J., Schert, H.-P., Ntaflos, T., Luvitzotto, G.L., Nasdala, L. and Tillmanns, E. (2010) Metamorphic ultrahigh-pressure tourmaline: structure, chemistry and correlations to $P-T$ conditions. *American Mineralogist*, **95**, 1–10.

Foit, F.F. (1989) Crystal chemistry of alkali deficient schorl and tourmaline structural relationships. *American Mineralogist*, **74**, 422–431.

Grice, J.B. and Robinson, G.W. (1989) Feruvite, a new member of the tourmaline group, and its crystal structure. *The Canadian Mineralogist*, **27**, 199–203.

Hawthorne, F.C., Burns, P.C. and Grice, J.D. (1996) The crystal chemistry of boron. Pp. 41–115 in: *Boron: Mineralogy, Petrology and Geochemistry* (L.M. Anovitz and E.S. Grew, editors). Reviews in Mineralogy, **33**, Mineralogical Society of America, Washington, D.C.

Henry, D.J. and Guidotti, C.V. (1985) Tourmaline as a petrogenetic indicator mineral: an example from the staurolite grade metapelites of NW Maine. *American Mineralogist*, **70**, 1–15.

Henry, D.J. and Dutrow, B.L. (2011) The incorporation of fluorine in tourmaline: internal crystallographic controls or external environmental influences? *The Canadian Mineralogist*, **49**, 41–56.

Henry, D.J., Novak, M., Hawthorne, F.C., Ertl, A., Dutrow, B.L., Uher, P. and Pezzotta, F. (2011) Nomenclature of the tourmaline-supergroup minerals. *American Mineralogist*, **96**, 895–913.

Hinsberg, V.J., Henry, D.J. and Marschal, H.R. (2011) Tourmaline: an ideal indicator of its host environment. *The Canadian Mineralogist*, **49**, 1–16.

London, D. (2011) Experimental synthesis and stability of tourmaline: a historical overview. *The Canadian Mineralogist*, **49**, 117–136.

Rosenberg, P.E. and Foit, F.E. (1985) Tourmaline solid solutions in the system $MgO-Al_2O_3-SiO_2-B_2O_3-H_2O$. *American Mineralogist*, **70**, 1217–1223.

Selway, G.J.B., Novák, M., Hawthorne, F.C., Černý, P., Ottolini, L. and Kyser, T.K. (1998) Rossmanite $\square(LiAl_2)Al_6(Si_6O_{18})(BO_3)_3(OH)_4$, a new alkali deficient tourmaline: description and crystal structure. *American Mineralogist*, **83**, 896–900.

Taylor, R.E. and Slack, J.F. (1984) Tourmalines from Appalachian–Caledonian massive sulfide deposits: textural, chemical and isotopic relationships. *Economic Geology*, **79**, 1703–1726.

Downloaded from https://pubs.geoscienceworld.org/books/chapter-pdf/3754743/9780903056434_ch22.pdf
by guest

Pyroxene Group

Introduction

Pyroxenes are the most important group of rock-forming ferromagnesian silicates, and occur as stable phases in many different types of igneous rock. They are found in rocks of widely different compositions formed during regional and contact metamorphism.

The pyroxene group includes both orthorhombic and monoclinic minerals. The orthopyroxenes consist essentially of a simple chemical series of $(Mg,Fe)SiO_3$ minerals, in contrast with the larger group of monoclinic pyroxenes which have a very wide range of chemical composition. Many clinopyroxenes can be considered, to a first approximation, to be members of the four-component system $CaMgSi_2O_6$–$CaFeSi_2O_6$–$Mg_2Si_2O_6$–$Fe_2Si_2O_6$. The nomenclature used to describe these pyroxenes is illustrated in Fig. 68. The monoclinic series of $Mg_2Si_2O_6$–$Fe_2Si_2O_6$ (clinoenstatite–clinoferrosilite) pyroxenes is uncommon in terrestrial rocks and is considered here with the orthopyroxenes. Isomorphous substitutions in the clinopyroxenes are not restricted to the mutual replacement of divalent cations; the compositional fields of the great majority of pyroxenes in which monovalent and trivalent ions are important constituents are shown in Fig. 69.

The pyroxenes can be considered broadly in terms of three major subgroups: magnesium−iron pyroxenes in which other cations occupy less than 10% of the *M*1 and *M*2 sites in the general formula:

$$(M2)(M1)(Si,Al)_2O_6$$

calcium-rich pyroxenes in which Ca occupies more than two-thirds of the *M*2 sites, and the sodium-rich pyroxenes in which the *M*2 site is largely occupied by Na and the *M*1 site by Al, Fe^{3+} or Cr as in jadeite, aegirine and kosmochlor, respectively. There are, in addition, two minor subgroups, the calcium–sodium pyroxenes, represented by omphacite and aegirine-augite (the latter is treated here with aegirine), and the lithium pyroxenes, represented by spodumene ($LiAlSi_2O_6$).

Many other names have been used to describe individual members of the pyroxene group; most are obsolete. The names tabulated below are those accepted by the Commission on New Minerals and Mineral Names of the International Mineralogical Association.

For some pyroxenes, in order to indicate the presence of unusual amounts of a particular constituent it is convenient to use adjectival modifiers (e.g. chromian augite); the ending -ian is used for higher valency state (e.g. ferrian, titanian), the ending -oan for the lower valency state (e.g. ferroan, manganoan).

A wide variety of ionic substitutions occur in the pyroxenes and solid solution is complete between some subgroups, e.g. between diopside and hedenbergite; this pair also forms a continuous range of compositions with augite. Solid solution, however, is not complete between augite and pigeonite compositions and there is a miscibility gap (Fig. 75, p. 100) at subsolidus temperatures. The augite−pigeonite miscibility gap in natural systems does not extend to the Mg-free side of the pyroxene quadrilateral but terminates at about 87% Fe/(Fe + Mg). The tie-line of the limiting augite–pigeonite pair is referred to as the two-pyroxene boundary.

Although jadeite and aegirine commonly contain more than 90% of the $NaAlSi_2O_6$ and $NaFe^{3+}Si_2O_6$ components, respectively, both may show extensive solid solution with diopside, hedenbergite and augite, leading

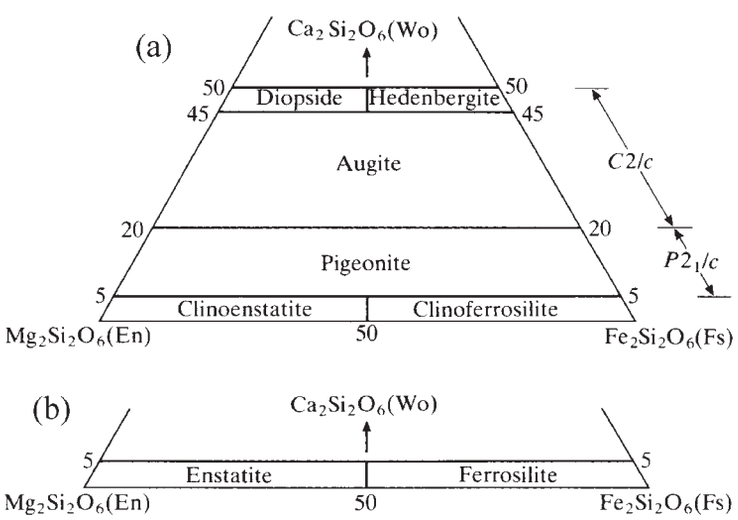


Fig. 68. Composition ranges and nomenclature of (a) the Ca−Mg−Fe clinopyroxenes, and (b) orthopyroxenes (after Morimoto, M., 1988, *Mineral. Mag.*, **52**, 535−50). Wo is the pyroxenoid wollastonite (see p. 132)

Downloaded from https://pubs.geoscienceworld.org/books/chapter-pdf/3754966/9780903056434_ch23.pdf
by guest

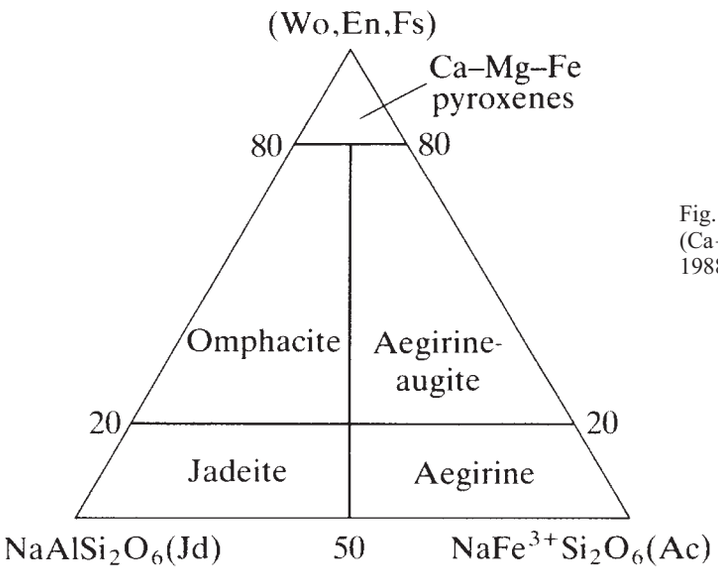


Fig. 69. Composition ranges and nomenclature of the common (Ca−Mg−Fe) and Na and Fe^{3+} pyroxenes (after Morimoto, M., 1988, *Mineral. Mag.*, **52**, 535−50).

Pyroxene chemistry

Common pyroxenes

Magnesium–iron pyroxenes

Orthopyroxenes (enstatite–ferrosilite)	$(Mg,Fe)_2Si_2O_6$
Clinoenstatite−clinoferrosilite	$(Mg,Fe)_2Si_2O_6$
Pigeonite	$(Mg,Fe^{2+},Ca)(Mg,Fe^{2+})Si_2O_6$

Calcium pyroxenes

Diopside–hedenbergite	$Ca(Mg,Fe)Si_2O_6$
Augite	$(Ca,Mg,Fe^{2+},Al)_2(Si,Al)_2O_6$

Calcium–sodium pyroxenes

Omphacite	$(Ca,Na)(Mg,Fe^{2+},Fe^{3+},Al)Si_2O_6$
Aegirine-augite	$(Ca,Na)(Mg,Fe^{2+},Fe^{3+})Si_2O_6$

Sodium pyroxenes

Jadeite	$NaAlSi_2O_6$
Kosmochlor	$NaCrSi_2O_6$
Aegirine	$NaFe^{3+}Si_2O_6$

Lithium pyroxenes

Spodumene	$LiAlSi_2O_6$

Rare pyroxenes

Donpeacorite $(Mn,Mg)MgSi_2O_6$
Esseneite $CaFe^{3+}AlSiO_6$
Grossmanite $CaTi^{3+}AlSiO_6$
Jervisite $NaScSi_2O_6$
Johannsenite $CaMn^{2+}Si_2O_6$
Kanoite $Mn^{2+}(Mg,Mn^{2+})Si_2O_6$
Kushiroite $CaAl[AlSiO_6]$
Petedunnite $CaZnSi_2O_6$
Namansilite $NaMn^{3+}Si_2O_6$
Natalyite $Na(V^{3+},Cr)Si_2O_6$

to omphacite or aegirine-augite compositions. The division between these two subgroups is illustrated in Fig. 69.

Structure

The essential feature of the pyroxene structure is the presence of chains of corner-sharing (Si,Al) tetrahedra (Fig. 70; blue), which have the composition $(Si,Al)O_3$. These chains repeat along their length at intervals of approximately 5.3 Å and this defines the *c* parameter of the unit cell. The apical oxygens of the tetrahedra are shared on each side of a ribbon of *M*−O octahedra

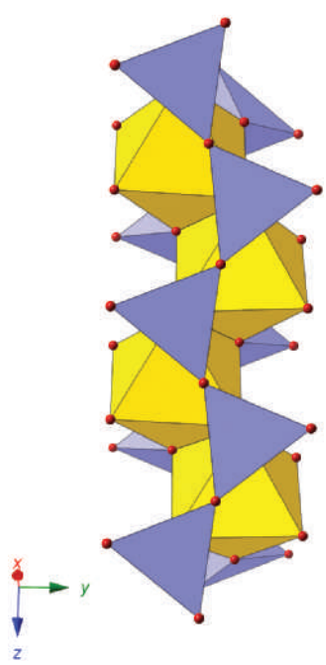


Fig. 70. Illustration of a single chain of Si−O corner-sharing tetrahedra (blue) linked by oxygens (red spheres) to a ribbon of Mg−O octahedra (yellow) as in the structure of the pyroxene diopside. (CrystalMaker image).

Downloaded from https://pubs.geoscienceworld.org/books/chapter-pdf/3754966/9780903056434_ch23.pdf
by guest

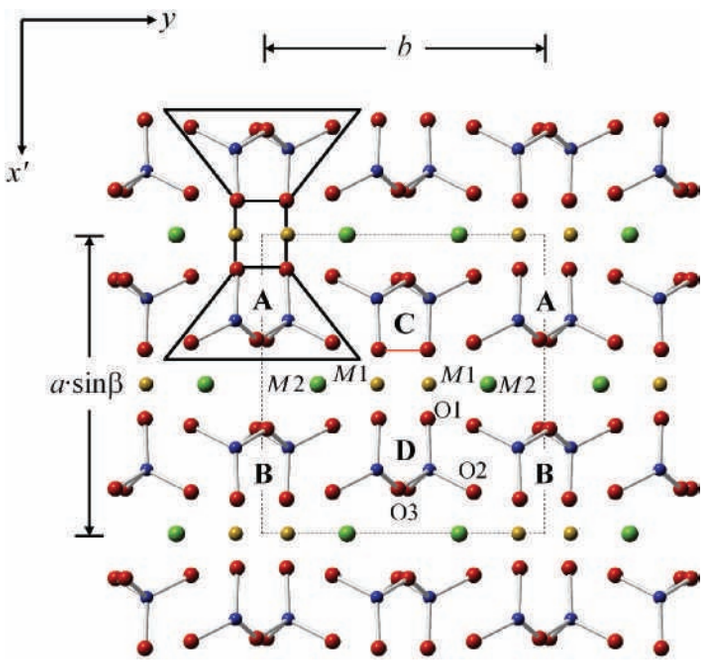


Fig. 71. Projection along z of an idealized pyroxene structure, showing the pyroxene chains and two distinct cation sites $M1$ and $M2$. The latter are in oxygen polyhedra which also form chains or bands parallel to z. In pyroxenes with space group $C2/c$, Si−O chains A, B, C and D are all equivalent. In those with space groups $P2_1/c$ and $Pbca$, C = A and D = B but A and B are non-equivalent. Areas such as that outlined (top left) are often referred to as I-beams and are used to simplify diagrams of pyroxene structures. Red: oxygen; blue: (Si,Al); yellow: Mg (in diopside); green: Ca (in diopside) (after Zussman, J., 1968, *Earth Sci. Rev.*, **4**, 39−67. Fig. produced by M.D. Welch).

(Fig. 70; yellow). The composite bands so formed are shown in Fig. 70 and also seen end-on in a projection down z in Fig. 71. The area outlined and others related by symmetry (sometimes referred to as I-beams), are linked laterally by 6−8-coordinated $M2$ cations as shown in Fig. 71. The $M1$ and $M2$ cations can also be seen as forming continuous sheets of M−O octahedra parallel to (100). A perspective view (partially polyhedral) of the structure of the pyroxene diopside is shown in Fig. 72. Strong bonding parallel to the T−O chains (z axis) and relatively weak lateral bonding between chains result in the good {110} cleavages intersecting at approximately 90º, characteristic of pyroxenes (Fig. 74).

The pyroxene group includes minerals with monoclinic and with orthorhombic space groups. The cell parameters of the monoclinic diopside (a 9.75 Å, b 8.92 Å, c 5.25 Å, β 105.83º) and the orthorhombic enstatite (a 18.22 Å, b 8.81 Å, c 5.17 Å) are typical of the two symmetry groups. The b and c parameters are similar and a (orthopyroxene) ~ $2a\sin\beta$ (clinopyroxene).

The M cations of the octahedral layer occupy two different sites, $M1$ and $M2$ (Figs 71 and 72). $M1$ atoms

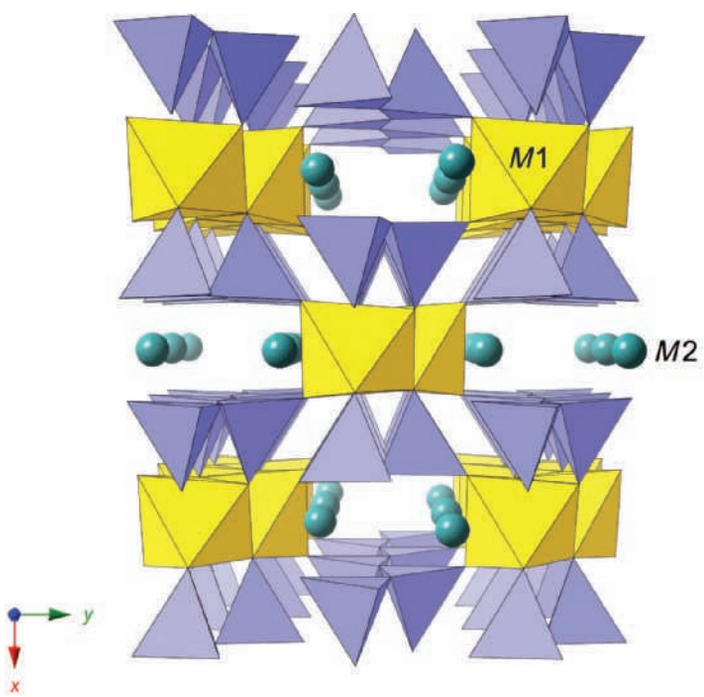


Fig. 72. A largely polyhedral model of the structure of the clinopyroxene diopside viewed from a direction close to the z axis. (CrystalMaker image). Green spheres: Ca; yellow: Mg−O octahedra; lavender: Si−O tetrahedra.

Downloaded from https://pubs.geoscienceworld.org/books/chapter-pdf/3754966/9780903056434_ch23.pdf
by guest

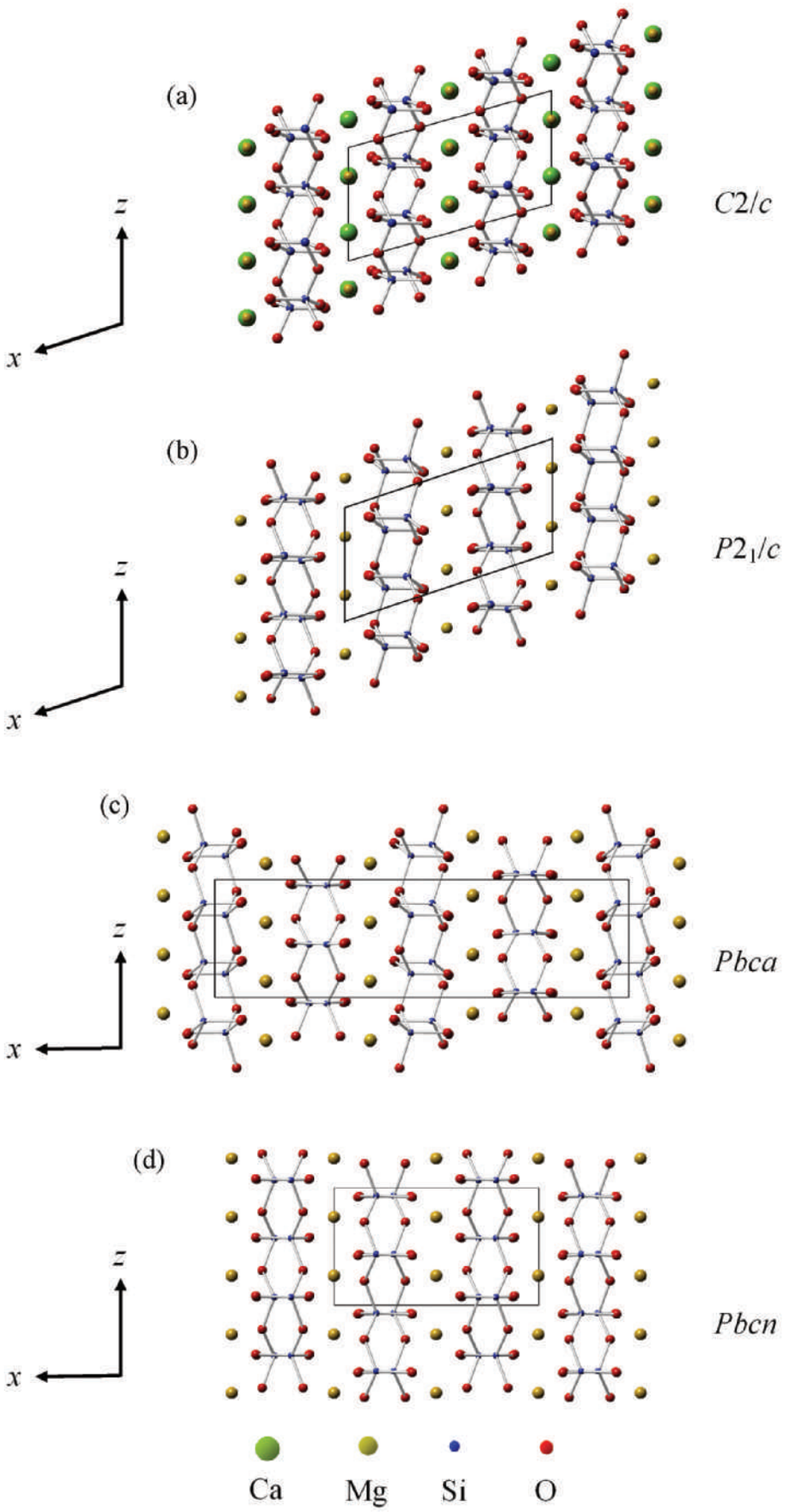


Fig. 73. Schematic illustrations of *y* axis projection of the structures of (a) diopside, (b) clinoenstatite, (c) enstatite, (d) protoenstatite (after Zussman, J., 1968, *Earth Sci. Rev.*, **4**, 39–67. Fig. produced by M.D. Welch).

Downloaded from https://pubs.geoscienceworld.org/books/chapter-pdf/3754966/9780903056434_ch23.pdf
by guest

lie principally between the apices of the SiO_3 chains, whereas M2 atoms lie principally between their bases. The *M*2 site is occupied by Ca in diopside and, in general, if a large ion (e.g. Ca,Na) is present it will occupy *M*2 rather than *M*1. The coordination of oxygen around *M*1 is nearly a regular octahedron, but the *M*2 site coordination is irregular and varies according to the atom present, six-fold for Mg, eight-fold for Ca and Na.

The oxygens (O1 and O2) coordinating *M*1 are all non-bridging (i.e. they belong to only one tetrahedron of the pyroxene chain); the M2 atom is coordinated partly by oxygens (O3) which are bridging (i.e. serving to link neighbouring tetrahedra). The projection along *z* of an idealized pyroxene structure (Fig. 71) shows that the $[SiO_3]$ chains lie back-to-back with no displacement in the *y* direction; it does not show how they are stacked

Table 17. Pyroxene analyses.

	1	2	3	4	5	6	7	8
SiO_2	57.10	50.00	51.47	54.66	46.71	48.81	52.70	48.18
TiO_2	0.17	0.49	0.29	–	0.95	0.01	0.34	0.70
Al_2O_3	0.70	0.47	1.56	0.07	0.93	0.74	1.84	1.06
Cr_2O_3	0.27	–	–	–	–	0.79	2.12	1.46
Fe_2O_3	0.60	0.56	1.42	0.68	0.59	1.54	5.42	26.08
FeO	5.21	33.83	21.72	0.07	31.48	22.58	0.16	0.53
MnO	0.17	0.84	0.52	0.02	0.26	2.29	15.15	3.52
MgO	34.52	11.51	21.68	18.78	0.14	21.87	21.58	18.90
CaO	0.62	1.74	1.45	25.85	18.75	0.07	0.49	0.23
Na_2O	0.07	0.20	0.07	–	0.26	0.02	0.01	0.04
K_2O	0.03	0.05	0.03	–	0.03	0.32	–	–
H_2O+	0.64	0.05	–	0.22	–	0.35	–	–
H_2O-	0.06	0.19	0.02	–	–	99.40	99.96	100.70
Total	100.20	100.37	100.23	100.35	100.10			
	Numbers of ions on the basis of 6 O							
Si	1.976	1.998	1.927	1.976	1.938	1.990	1.947	1.941
Al	0.024 } 2.00	0.002 } 2.00	0.067 } 2.00[b]	0.002 } 1.98[c]	0.047 } 1.99[d]	0.010 } 2.00	0.053 } 2.00	0.051 } 2.00[f]
Al	0.004	0.020	0.000	0.000	0.000	0.026	0.027	0.000
Cr	0.008	–	–	–	–	0.024	0.059	0.036
Fe^{3+}	0.016	0.017	0.034	0.000	0.002	0.000	0.009	0.021
Ti	0.004	0.031	0.009	–	0.031	0.139	0.834	0.211
Mg	1.780	0.686	1.210	1.012	0.007	0.053	0.167	0.879
Fe^{2+}	0.151	1.129	0.679	0.002	1.093	0.780	0.005	0.019
Mn	0.005	0.029	0.016	0.001	0.010	0.955	0.854	0.816
Ca	0.023	0.074	0.058	1.001	0.833	0.006	0.035	0.017
Na	0.004	0.014	0.004	–	0.020	0.001	0.000	0.002
K	0.002	0.002	0.000	–	0.002			
	2.00[a]	2.00	2.01	2.02	2.00	1.98	1.99[e]	2.00
	Atomic percentages and other compositional data							
Mg	90.3	35.5	60.4	49.8	0.4	–	43.2	10.7
ΣFe^{g}	8.5	60.7	36.7	1.0	57.1	–	12.5	47.8
Ca	1.2	3.8	2.9	49.2	42.5	–	44.3	41.5
X_{Mg}	91.2	36.9	62.4	98.6	0.1	14.0	79.3	18.4

1 Enstatite, peridotite, Dawros, Republic of Ireland (Rothstein, A.T.V., 1958, *Geol. Mag.*, **95**, 456–562. Includes NiO 0.04).
2 Ferrosilite, gabbro, Guadaloupe igneous complex, California, USA (Best, M.G., 1963, *J. Petrol.*, **4**, 223–59).
3 Inverted pigeonite, gabbro, Bushveld complex (Atkins, F.R., 1969, *J. Petrol.*, **10**, 222–49).
4 Diopside, limestone, Juva, Finland (Juurinen, A. & Hytönen, K., 1952, *Bull. Comm., géol. Finlande*, No. **157**, 145–6).
5 Ferrian hedenbergite, fayalite ferrodiorite, Skaergard, East Greenland (Brown, G.M. & Vincent, E.A., 1963, *J. Petrol.*, **4**, 175–97).
6 Johannsenite, Aravaipa mining district, Arizona, USA (Simons, F.S. & Munson, E., 1963, *Amer. Min.*, **48**, 1154–58. Includes P_2O_5 0.01).
7 Augite, pyroxene diorite, Feather River area, northern Sierra Nevada, USA (Hietanen, A., 1971, *Contrib. Mineral. Petrol.*, **30**, 161–76. Includes Cr_2O_3 0.10, V_2O_5 0.05).
8 Ferroan augite, ferrodiorite, Skaergard, East Greenland (Brown, G.M., 1960, *Amer. Min.*, **45**, 15–38).

[a] Includes Ni 0.001.
[b] Includes Fe^{3+} 0.006.
[c] Includes Fe^{3+} 0.018.
[d] Includes Fe^{3+} 0.015.
[e] Includes Cr 0.003.
[f] Includes Fe^{3+} 0.008.
[g] $\Sigma Fe = Fe^{2+} + Fe^{3+} + Mn$.
$X_{Mg} = 100\ Mg/(Mg + Fe^{2+} + Fe^{3+} + Mn)$.

Downloaded from https://pubs.geoscienceworld.org/books/chapter-pdf/3754966/9780903056434_ch23.pdf
by guest

with respect to one another parallel to their lengths and neither does it show any differences between chains. These two features are determined largely by the nature and proportions of the different cations present.

Pyroxene structures can vary in several ways:

(1) The substitution of different sizes of cations can give rise to proportionate expansion or contraction in one or more of the cell parameters but may result in little or no change in the basic structure. This is typified by the diopside–hedenbergite series in which *M*1 is occupied by (Mg,Fe) and *M*2 by Ca. The Mg-Fe substitution is accompanied by only minor changes in the Si−O chain configuration.

(2) Greater differences in the size of cations, e.g. in jadeite (Na,Al), may also be accommodated in the pyroxene structure by greater changes in the silicate chains, or in their relative positions, without a change in overall symmetry and the space group remains *C*2/*c*. In a pyroxene with space group *C*2/*c* there is only one kind of *M*1 and one kind of *M*2 site. Any mixture of atoms within either of these sites must thus be randomly distributed, e.g. (Mg,Fe) in *M*1 in the diopside–hedenbergite series, and the substitution should be one of ideal solid solution.

(3) If smaller atoms occupy the *M*2 sites, e.g. Mg in pigeonite or clinoenstatite, the departure of the

Table 17 (*contd.*)

	9	10	11	12	13	14	15
SiO_2	49.46	48.02	56.02	59.06	52.30	51.64	63.60
TiO_2	0.57	0.46	0.38	0.08	0.02	0.04	–
Al_2O_3	1.79	13.39	12.74	24.62	4.01	1.05	27.48
Fe_2O_3	1.65	2.09	0.88	0.41	–	32.98	0.04
FeO	25.51	3.11	1.64	0.18	0.91	0.14	–
MnO	0.81	0.07	0.00	0.03	0.04	0.26	0.14
MgO	10.94	8.18	8.01	0.17	0.55	0.38	<0.02
CaO	8.57	24.03	12.45	0.35	0.83	0.60	<0.02
Na_2O	0.23	0.31	7.05	14.95	13.30	12.21	0.22
K_2O	0.05	0.06	0.40	0.01	–	0.06	–
H_2O+	–	0.20	–	0.07	–	0.41	0.17
H_2O-	0.20	0.07	–	0.03	–	0.04	–
Total	99.78	99.99	99.57	99.96	99.6[h]	99.82	99.44
	Numbers of ions on the basis of 6 O						
Si	1.945 } 2.00	1.760 } 2.00	1.985 } 2.00	1.997 } 2.00	1.96 } 2.00	1.988 } 2.00	1.989 } 2.00
Al	0.055	0.240	0.015	0.003	0.04	0.012	0.011
Al	0.028	0.338	0.517	0.977	0.14	0.036	1.003
Fe^{3+}	0.049	0.058	0.023	0.010	–	0.954	0.001 } 1.00
Ti	0.017	0.012	0.010	0.002	0.001	0.001	–
Mg	0.641	0.447	0.423	0.008	0.030	0.022	0.000
Fe^{2+}	0.839 } 1.98	0.095 } 1.92	0.031 } 1.98	0.005 } 1.99	0.030 } 2.02[i]	0.004 } 1.96	–
Mn	0.027	0.002	0.000	0.001	0.001	0.008	0.004
Ca	0.361	0.944	0.473	0.012	0.030	0.025	0.000 } 1.00[j]
Na	0.018	0.022	0.484	0.978	0.970	0.912	0.013
K	0.003	0.002	0.018	0.000	–	0.002	0.000
	Atomic percentages and other compositional data						
Mg	33.5	–					
ΣFe	47.7	–					
Ca	18.8	–					
X_{Mg}	41.7	74.2					

9 Ferroan pigeonite, dolerite, Yamagata Prefecture, Japan (Aoki, K., 1962, *J. Japanese Assoc. Min. Petr., Econ. Geol.*, **47**, 41−5).
10 Aluminian diopside, eclogite, Knockormal, Ayrshire, Scotland, UK (Bloxam, T.W. & Allen, J.B., 1960, *Trans. Roy. Soc. Edinburgh*, **64**, 1−27).
11 Omphacite, eclogite, Puerto Cabello, Venezuela (Morgan, B.A., 1970, *J. Petrol.*, **11**, 101−46).
12 Jadeite, vein in albite-glaucophane-aegirine schist, New Idria district, California, USA. (Coleman, R.G., 1961, *J. Petrol.*, **2**, 209−47).
13 Kosmochlor, jadeite, jade mine region, Burma (Harlow, G.E. & Olds, E.P., 1987, *Amer. Min.*, **72**, 126−36. Probe analysis).
14 Aegirine, vein in iron formation, Cuyuna Range, Minnesota, USA (Grout, F.F., 1946, *Amer. Min.*, **31**, 125−30. Includes V_2O_3 0.01).
15 Spodumene (kunzite), Pala, San Diego, California, USA (Edgar, A.D., 1968, *Intern. Min. Assoc. Papers Proc. Fifth General Meeting, Cambridge*, 1966, 222−31. Includes Li_2O 7.79).

[h] Includes Cr_2O_3 27.6
[i] Includes Cr 0.82.
[j] Includes Li 0.980.

Downloaded from https://pubs.geoscienceworld.org/books/chapter-pdf/3754966/9780903056434_ch23.pdf
by guest

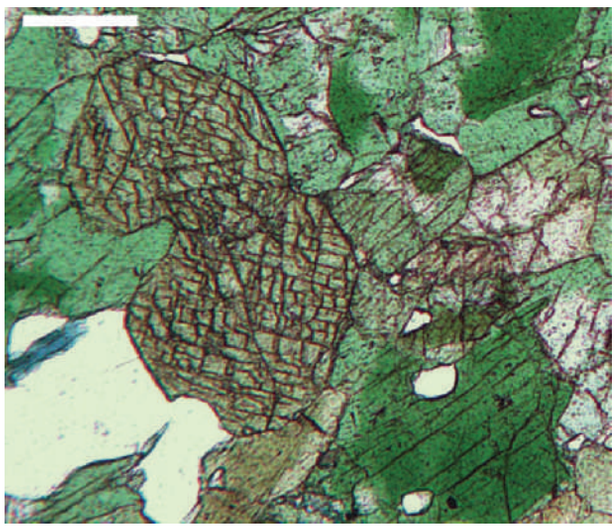


Fig. 74. Crystals of clinopyroxene (aegirine) showing high relief, two good {110} cleavages at ~90º, and crystal faces parallel to both cleavages (plane polarized light, scale bar 0.2 mm) (courtesy of G.T.R. Droop).

Si–O chains from a 'straight' configuration (kinking) becomes more pronounced and there is displacement parallel to z and the adoption of a different arrangement by the A and B chains. There is also displacement of the metal atoms from the diads and this loss of symmetry leads to space group $P2_1/c$ [compare (a) and (b) in Fig. 73]. At high temperatures the structures of these pyroxenes become more like that of diopside and a transformation to the $C2/c$ space group takes place.

(4) Polymorphism occurs in pyroxenes of the $MgSiO_3$–$FeSiO_3$ series, and there are grossly different stacking arrangements of the silicate chains in relation to each other and to the octahedral layers. Across the series there is a monoclinic polymorph, $P2_1/c$ (clinoenstatite–clinoferrosilite) and an orthorhombic polymorph, *Pbca* (orthoenstatite–orthoferrosilite). A further polymorph of $MgSiO_3$ (protoenstatite) is orthorhombic *Pbcn*. Some of the differences between $C2/c$ and $P2_1/c$ pyroxenes and the different chain-stacking arrangements are illustrated in Fig. 73.

(5) If the $M1$ sites are occupied by two groups of cations with significantly different radii and in approximately equal proportion [e.g. (Mg,Fe) and Al] an ordered replacement in two distinct kinds of $M1$ site can occur. Thus omphacite shows a polymorphic transition from high-temperature $C2/c$ to low-temperature $P2/n$ structure.

The most common pyroxenes are those of the Di–Hd–En–Fs quadrilateral. The more calcium-rich compositions have the $C2/c$ structure; the calcium-poor members have either the $P2_1/c$ or one of the orthorhombic structures at room temperature (Fig. 75), but at

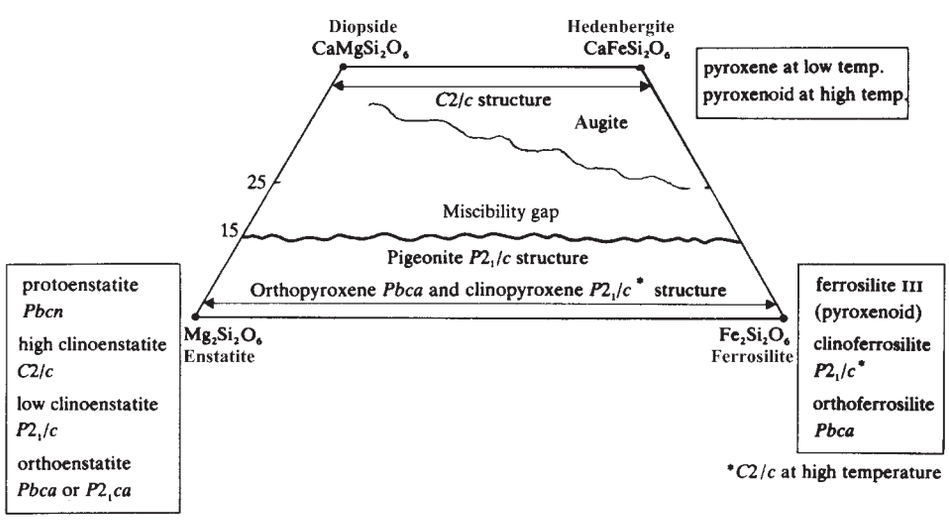


Fig. 75. Illustration of structural relationships among pyroxenes in the diopside–hedenbergite–enstatite–ferrosilite quadrilateral (modified after Zussman, J., 1968, *Earth Sci. Rev.*, **4**, 39–67).

Downloaded from https://pubs.geoscienceworld.org/books/chapter-pdf/3754966/9780903056434_ch23.pdf
by guest

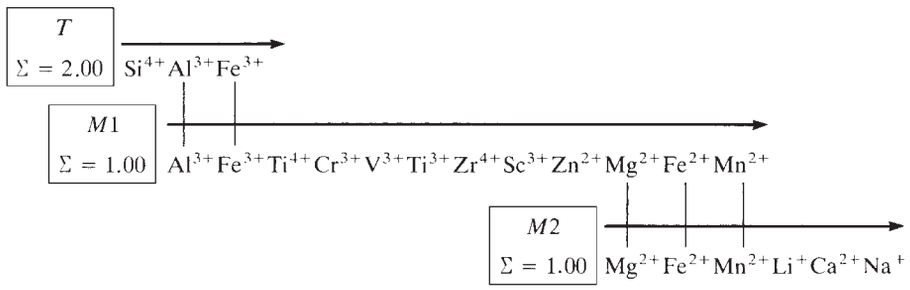


Fig. 76. Flow chart showing ideal site occupancy and order of assigning atoms to *T*, *M*1 and *M*2 sites of pyroxene structure (after Morimoto, M., 1988, *Mineral Mag*., **52**, 535–50).

higher temperature they too have *C*2/*c* symmetry. Although at near-liquidus temperature the Ca-rich and Ca-poor pyroxenes have the same space group, there is some evidence of a gap in the solid solution. At lower temperature miscibility is not complete and the gap widens with decreasing temperature of crystallization.

Chemistry

The pyroxene formula may, in structural terms, be expressed as $M2M1T_2O_6$, where M2 and M1 refer to cations in generally distorted and regular octahedral coordination, respectively, and T to tetrahedrally coordinated cations. The ideal cation occupancy among the *M*1, *M*2 and *T* sites and the generally accepted order of assigning atoms to sites is illustrated in Fig. 76. Compositions of many Mg–Fe and calcium pyroxenes can be represented by the formula:

$$M2(R^{2+})M1(R^{2+})T(2R^{4+})O_6$$

On the assumption that more than one R^{4+} cation is present in *T* sites, compositions of pyroxenes containing monovalent and trivalent cations can be described in terms of coupled substitutions:

(1) $M2(R^{+})M1(R^{3+})$, e.g. Na ↔ (Al,Fe^{3+},Cr), giving rise to jadeite, aegirine and kosmochlor end-members respectively;

(2) $M2(R^{+})M1(R^{2+}_{0.5}R^{4+}_{0.5})$; this substitution occurs in a small number of pyroxenes and leads to components such as $NaFe^{2+}_{0.5}Ti^{4+}_{0.5}Si_2O_6$;

(3) $M1(R^{3+})T(R^{3+})$ produces end-member compositions such as $CaAlAlSiO_6$ (commonly termed the 'Tschermak' component); in natural minerals the amount of Al in *T* sites is normally limited to ~0.5 but the pyroxene esseneite ($CaFe^{3+}[AlSiO_6]$) approaches closely the theoretical composition with Fe^{3+} in *M*1.

A number of pyroxene analyses are given in Table 17. They are calculated on the basis of six oxygens; deficiencies in the *T* sites are filled by adding the requisite amount of Al to Si to complete the ideal two tetrahedral site ions per formula unit. Pyroxenes commonly show more than one type of substitution. Reference to methods and procedures to determine the proportions of the various components are given in Appendix 3.

Further reading

Cameron, M. and Papike, J.J. (1981) Structural and chemical variations in pyroxenes. *American Mineralogist*, **66**, 1–50.

Hueber, J.S. and Turnock, A.C. (1980) The melting relations at 1 bar of pyroxenes composed largely of Ca-Mg and Fe-bearing components. *American Mineralogist*, **65**, 225–271.

Kogarko, L.N., Williams, C.T. and Woolley, A.R. (2006) Compositional evolution and cryptic variation in pyroxenes of the peralkaline Lovozero intrusion, Kola Peninsula, Russia. *Mineralogical Magazine*, **70**, 347–359.

Lindsley, D.H. (1983) Pyroxene thermometry. *American Mineralogist*, **68**, 477–493.

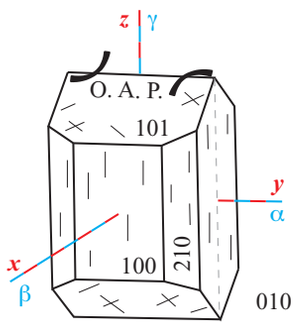
Melekhova, E., Schmidt, M.W., Ulmer, P. and Guggenbühl, E. (2006) The reaction talc + forsterite = enstatite + H_2O revised. Application of conventional and novel techniques and derivation of revised thermodynamic properties. *American Mineralogist*, **91**, 1081–1088.

Morimoto, N. (1988) Nomenclature of pyroxenes. *Mineralogical Magazine*, **52**, 535–550.

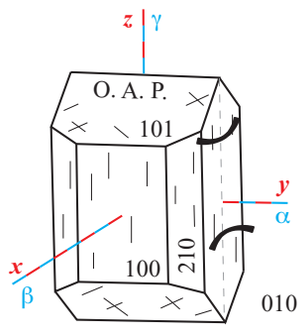
Downloaded from https://pubs.geoscienceworld.org/books/chapter-pdf/3754966/9780903056434_ch23.pdf
by guest

Orthorhombic (+)(−)

Enstatite (+)



$En_{50}Fs_{50}$ (−)



α	1.650–1.768
β	1.653–1.770
γ	1.658–1.788
δ	0.007–0.020
$2V_\alpha$	125–53–125°
Orientation	α = *y*, O.A.P. (100)
D (g/cm^3)	3.21–3.96
H	5–6
Cleavage	{210} good; {100}, {010} partings; (210):(2$\bar{1}$0) ~ 88°
Colour	Magnesium-rich members: colourless, grey, green, yellow, brown; colourless in thin section Iron-rich members: green or dark brown; reddish or greenish in thin section
Pleochroism	Enstatite none, other compositions variable weak to strong α pink, pale reddish brown, purple-violet, smoky brown β yellow, pale greenish brown, pale reddish yellow, pale brown γ green, pale green, smoky green
Unit cell	*a* 18.22–18.43 Å, *b* 8.81–9.08 Å, *c* 5.17–5.24 Å Z = 16; space group *Pbca*
Special features	Partially decomposed by HCl.

Minerals in the enstatite–ferrosilite solid solution are the only common orthopyroxenes. They show weak to moderate birefringence and straight extinction. In plutonic igneous rocks they are of major importance in ultramafic and mafic rocks and are essential components of norites; they occur also as phenocrysts in dolerites and andesites. In metamorphic rocks they are characteristic of the granulite facies.

Structure

Magnesium silicate, $MgSiO_3$, occurs in three well characterized polymorphs: enstatite (En) and protoenstatite (PEn) which have orthorhombic symmetry, and clinoenstatite (CEn) wich has monoclinic symmetry: details of cell dimensions and space groups are shown in Table 18 (see also Fig. 75, p. 100). The three polymorphic phases are stable at elevated (PEn), intermediate (En) and low (CEn) temperatures. The polymorphism is complex and there is some uncertainty regarding the relative stabilities of the three phases. Protoenstatite appears to be the stable form from about 1000°C to at least 1300°C and probably to the

Downloaded from https://pubs.geoscienceworld.org/books/chapter-pdf/3755101/9780903056434_ch24.pdf
by guest

Table 18. $MgSiO_3$ polymorphs – cell parameters.

Polymorph	Space group	*a* (Å)	*b* (Å)	*c* (Å)	β
Enstatite	*Pbca*	18.225	8.813	5.180	–
Protoenstatite	*Pbcn*	9.306	8.892	5.349	–
Clinoenstatite	$P2_1/c$	9.606	8.813	5.170	108.35°
'Ilmenite' type	*R*3	4.728	–	13.599	–

incongruent melting point at 1550ºC when it decomposes to forsterite + liquid; protoenstatite is unknown in nature. At temperatures <1000ºC, enstatite and members of the enstatite (En)–ferrosilite (Fs) series, with very few exceptions, are the polymorphic form that occurs in both igneous and metamorphic rocks. Clinoenstatite has been synthesized at a temperature below 566ºC, suggesting it is the stable low-temperature polymorph. It can also be produced by rapidly quenching protoenstatite or enstatite and by shear deformation of these phases. Members of the clinoenstatite–clinoferrosilite series are uncommon but occur in some igneous and metamorphic rocks, and in meteorites. The PEn → En transition is sluggish and time-dependent, and the En field increases in size with increasing pressure (Fig. 77). The structural differences between the three polymorphs reside mainly in the [100] stacking sequence of magnesium atoms. The inversions involve breaking Mg–O bonds and translations of the silicate chains parallel to *z* and thus are partially reconstructive and involve large activation energies.

Enstatite–ferrosilite forms a solid-solution series in which Mg and Fe^{2+} are mutually replaceable between $Mg_{100}Fe^{2+}_0$ and about $Mg_{10}Fe^{2+}_{90}$ at normal pressures. In the crystallographic orientation adopted here the largest dimension is taken as *a*; thus the optic axial plane is (100) and the prismatic cleavage {210}.

A high-temperature–high-pressure $(Mg,Fe)SiO_3$ phase with an ilmenite-type structure has been synthesized at pressure between 24 and 27 GPa at 1100–1400ºC. It is possible that this phase is an important constituent of the Earth's lower mantle.

Chemistry

Members of the enstatite–ferrosilite series are essentially metasilicates of magnesium and ferrous iron. Other elements including Al, Mn, Fe^{3+}, Ca, Ti, Cr and Ni are commonly present but in most (Mg,Fe) pyroxenes these constituents together do not exceed 10 mol%. Chromium and nickel occur mainly in the Mg-rich enstatites of metabasic and basic igneous rocks; high contents of manganese are generally restricted to ferrosilites in igneous rocks and contact metamorphosed iron formations. The manganese orthopyroxene, donpeacorite, has the composition $Mg_{1.4}Mn_{0.6}Si_2O_6$, and the Mn-rich member of the clinoenstatite–clinoferrosilite series, kanoite, contains 31.2 mol% MnO. Aluminium contents of up to 0.5 Al pfu occur in enstatites of high-grade metamorphic rocks, especially those in the granulite facies. The calcium content is generally small.

Experimental

In the system Mg_2SiO_4–SiO_2, protoenstatite melts incongruently at 1559ºC at atmospheric pressure (0.1 MPa) to forsterite + liquid; the peritectic point is at 60.6% SiO_2 (see Fig. 5, p. 9). This reaction disappears at about 0.13 GPa when $MgSiO_3$ melts congruently and forms a eutectic with forsterite. The pressure at which the peritectic reaction disappears cannot, however, be applied directly to consideration of natural magmas as the presence of iron reduces the

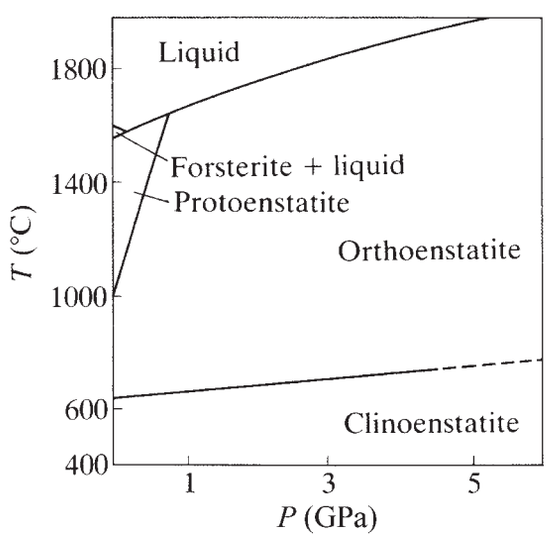


Fig. 77. Phase relations of $MgSiO_3$ polymorphs (after Boyd, F.R. *et al*., 1964, *J. Geophys. Res*., **69**, 2101–9).

Downloaded from https://pubs.geoscienceworld.org/books/chapter-pdf/3755101/9780903056434_ch24.pdf
by guest

Two-pyroxene geothermobarometry

Enstatite–ferrosilite and augitic compositions are sensitive to variations in pressure and temperature. The distribution of Mg and Fe between coexisting pyroxene pairs can be used to estimate conditions of equilibration. The distribution coefficient may be expressed by:

$$K_D^{Mg-Fe} = \frac{X_{MgSiO_3}}{(1 - X_{MgSiO_3})} \times \frac{(1 - X_{CaMgSi_2O_6})}{X_{CaMgSi_2O_6}}$$

where X_{MgSiO_3} and $X_{CaMgSi_2O_6}$ are mole fractions and the exchange equilibrium is:

$$FeSiO_3 + CaMgSi_2O_6 \rightleftharpoons MgSiO_3 + CaFeSi_2O_6$$

Systematic differences due to crystallization in the contrasted regimes of the granulite facies and igneous rocks are illustrated in Fig. 78. Experimental phase equilibrium data on compositions of coexisting ortho- and clino-pyroxenes have been used to construct Fig. 79 showing the relationship between X_{Fe} (the binary mole fraction Fe/(Fe + Mg) in orthopyroxene), K_D and temperature.

The increasing solubility of Al_2O_3 with increasing pressure in both ortho- and clinopyroxene, calibrated from experimental data, provides a two-pyroxene thermobarometer that is particularly applicable to natural ultrabasic assemblages. The partitioning of Fe and Mg between orthopyroxene and garnet according to the exchange reaction:

$$\underset{\text{enstatite}}{3\,MgSiO_3} + \underset{\text{almandine}}{Fe_3Al_2Si_3O_{12}} \rightleftharpoons \underset{\text{ferrosilite}}{3\,FeSiO_3} + \underset{\text{pyrope}}{Mg_3Al_2Si_3O_{12}}$$

may also be used as a geothermometer (see page 24).

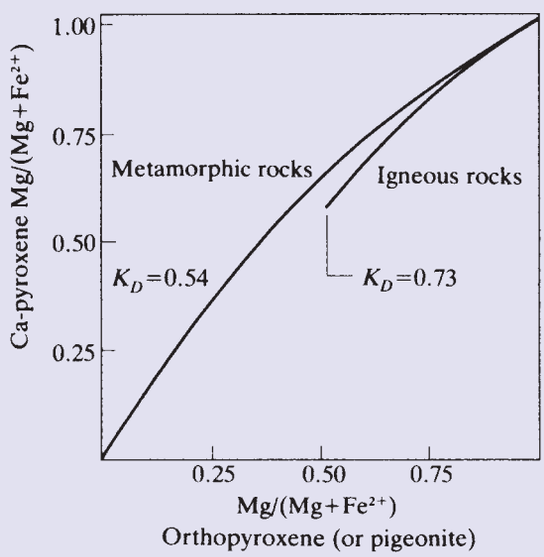


Fig. 78. Distribution of Mg and Fe^{2+} between coexisting orthopyroxene (or pigeonite) and Ca-pyroxene (after Saxena, S.K., 1968, *Neues Jahrb. Min., Abhdl.*, **108**, 292–323).

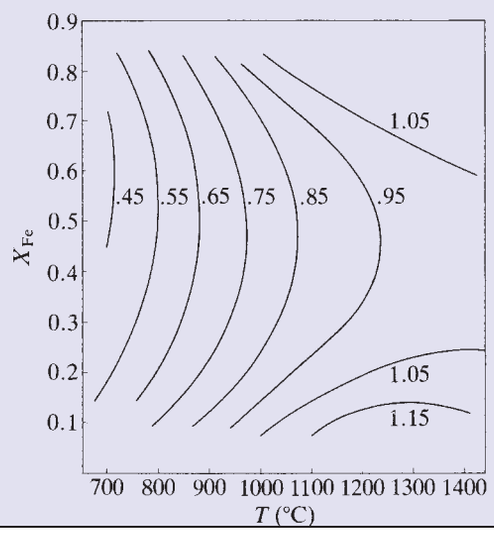


Fig. 79. Plot showing the relationship between X_{Fe} in orthopyroxene, temperature and K_D. K_D is also a function of X_{Ca} = Ca/(Ca+Mg+Fe) (after Saxena, S.K. *et al.*, 1986, *J. Petrol.*, **27**, 843–52).

Downloaded from https://pubs.geoscienceworld.org/books/chapter-pdf/3755101/9780903056434_ch24.pdf
by guest

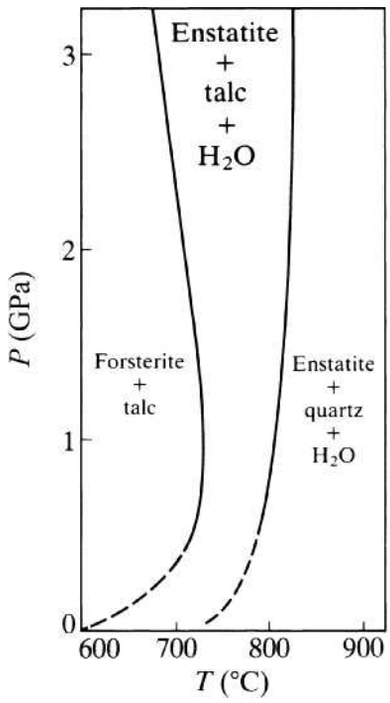


Fig 80. Phase equilibria in the system $MgO-SiO_2-H_2O$ (after Kitahara, S. *et al.*, 1966, *Amer. J. Sci.*, **264**, 223–33).

pressure whereas the solid solution of Al in enstatite increases the pressure at which the peritectic reaction is replaced by a eutectic relationship.

$P-T$ experiments in the system $MgO-SiO_2-H_2O$ have shown that enstatite crystallizes by the reaction:

$$\underset{\text{talc}}{Mg_3Si_4O_{10}(OH)_2} + \underset{\text{forsterite}}{Mg_2SiO_4} \rightarrow 5\,\underset{\text{enstatite}}{MgSiO_3} + H_2O$$

above 650 to 700ºC at low water-vapour pressure, but that increased pressure lowers this to approximately 570ºC at 2.0 GPa, see Fig. 80.

The subsolidus and liquidus phase relations in the system $MgSiO_3-CaMgSi_2O_6$ at 0.1 MPa are shown in Fig. 81. Protoenstatite is the liquidus pyroxene at high temperature along the enstatite end of the join. There is a reaction relationship between protoenstatite and

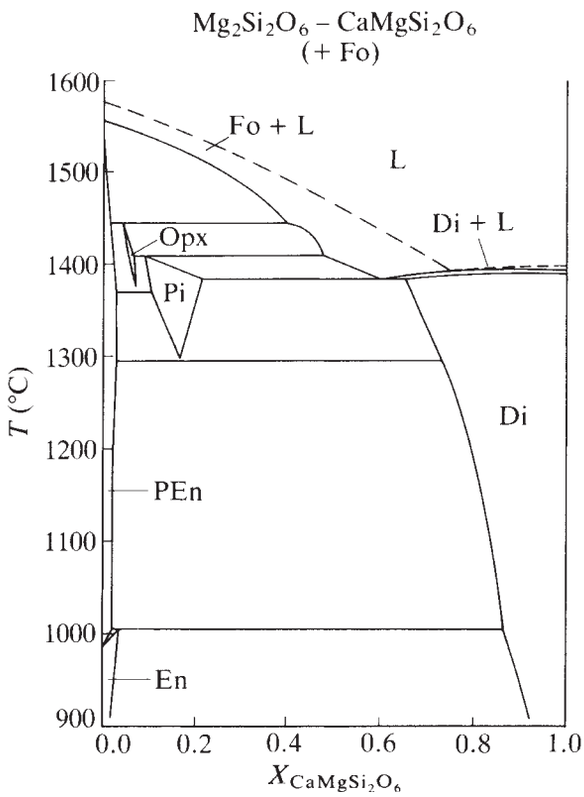


Fig. 81. Phase relations on the forsterite-saturated join $Mg_2Si_2O_6-CaMgSi_2O_6$ at atmospheric pressure (after Carlson, W.D., 1988, *Amer. Min.*, **73**, 232–41). Di: diopside; En: enstatite; Opx: orthopyroxene; PEn: protoenstatite; Pi: pigeonite; Fo: forsterite; L: liquid.

Downloaded from https://pubs.geoscienceworld.org/books/chapter-pdf/3755101/9780903056434_ch24.pdf
by guest

enstatite and between enstatite and pigeonite along their respective liquidus boundaries; all three phases melt incongruently to forsterite + liquid. The progression of the protoenstatite–enstatite–pigeonite liquidus fields is accompanied by an increasing diopside component in the melt. The amount of solid solution of $CaMgSi_2O_6$ in the three Ca-poor phases increases from less than 3 wt.% in protoenstatite to between 6 and 9 wt.% in enstatite and to between 10 and 25 wt.% in pigeonite; the field of the latter shrinks with decreasing temperature. The precise relationships between the Ca-poor phases are still uncertain because of the difficulty of achieving chemical equilibrium and the possible lack of identical structure over the whole enstatite temperature range. Clinoenstatite also may occur in the protoenstatite field and is regarded as the metastable inversion product of protoenstatite formed upon quenching. In natural systems the relationships are more complex owing to the presence of additional components, particularly Al_2O_3 and FeO.

A calcium-poor orthorhombic phase occurs at temperatures near 1400ºC; its optical properties and powder diffraction pattern are indistinguishable from those of enstatite stable below ~1000ºC at atmospheric pressure. It is uncertain if this high-temperature orthorhombic phase is the precise equivalent of enstatite or a distinct polymorph.

Enstatites, particularly the more magnesium-rich varieties, are sometimes altered to serpentine and talc and where alteration is complete the pseudomorphs display a characteristic bronze-like metallic lustre or schiller described as bastite. Alteration to a pale-green amphibole, usually referred to as uralite, is not uncommon.

The more Mg-rich orthopyroxenes of plutonic rocks commonly display a lamellar structure. The lamellae lie in the (100) plane of the host and have a higher birefringence; they consist of an exsolved Ca-rich monoclinic phase developed by preferential nucleation on lattice defects resulting from stresses induced during cooling from original magmatic temperatures. The lamellae form either parallel-sided continuous sheets resembling fine straight-ruled lines when the (010) plane of the crystal is observed between crossed polars (Fig. 82), or occur as rows of flattened blebs. Such orthopyroxenes are referred to as orthopyroxenes of the Bushveld type.

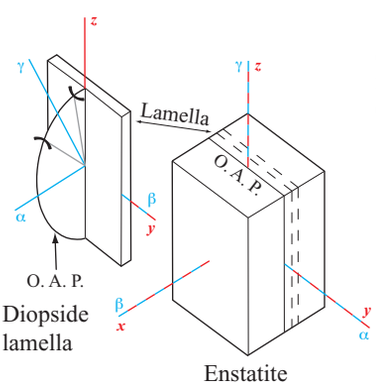


Fig. 82. The optical and crystallographic directions for enstatite and included diopside lamellae (after Hess, H.H., 1960, *Mem. Geol. Soc. Amer.*, **80**).

Similar lamellae occur in the more iron-rich (>Fs_{30}) orthopyroxenes of plutonic rocks. These pyroxenes are inverted pigeonites (see p. 110) and the exsolved plates consist of calcium-rich clinopyroxene that is oriented parallel to a plane which represents (001) of the original pigeonite. They are described as orthopyroxenes of the Stillwater type; their calcium content is ~4 wt.% CaO, about three times greater than that of the Bushveld-type orthopyroxenes. The formation of clinopyroxenes in orthopyroxenes and the relationship of orthopyroxenes to pigeonite and augite are discussed further in the pigeonite (p. 110) and augite (p. 117) sections.

Regular lamellae, parallel to the (100) plane, of exsolved calcic plagioclase occur in some aluminous orthopyroxenes; other exsolved phases in orthopyroxenes include rutile, spinel and ilmenite.

Optical and physical properties

The correlation between the optical properties and the Mg ↔ Fe replacement is almost ideal. The refractive indices vary linearly with ΣFe = (Fe^{2+} + Fe^{3+} + Mn), the γ index increasing ~0.00125 per atom% ΣFe. The rate of increase of the α index is less than that of the γ index, and the birefringence increases progressively with ΣFe (Fig. 83). Because most crushed fragments of orthopyroxene lie on a {210} cleavage plane the γ index can be measured with the greatest ease; this is the most accurate optical method of determining the En:Fs ratio. The α and β indices are most readily measured in grains showing a centred bisectrix figure extracted from a thin section.

The optic axial angles of the enstatite–ferrosilite series show a continuous and symmetrical variation with composition: $2V_\gamma$ for En_{100} is 55º, the same as the extrapolated value for Fs_{100}. There are two changes in optic sign; compositions between En_{100} and En_{88} and between En_{12} and En_0 are optically positive, compositions between En_{88} and En_{12} optically negative.

Many enstatites, particularly those containing moderate amounts of iron, display a characteristic α pinkish, γ greenish pleochroism (Fig. 84). The presence and intensity of the pleochroism is not simply related to the iron or aluminium content of individual minerals. Zoning is rare in plutonic and metamorphic but common in volcanic orthopyroxenes; the zoning is usually from more Mg-rich cores to Fe-rich margins; reversed zoning, however, is not uncommon.

The character and orientation of exsolution lamellae has been discussed above. Another lamellar structure, due to dislocation gliding in the (100) plane with glide direction [100], occurs in some orthopyroxenes; the lamellae are commonly about 1000 Å in width and a

Downloaded from https://pubs.geoscienceworld.org/books/chapter-pdf/3755101/9780903056434_ch24.pdf
by guest

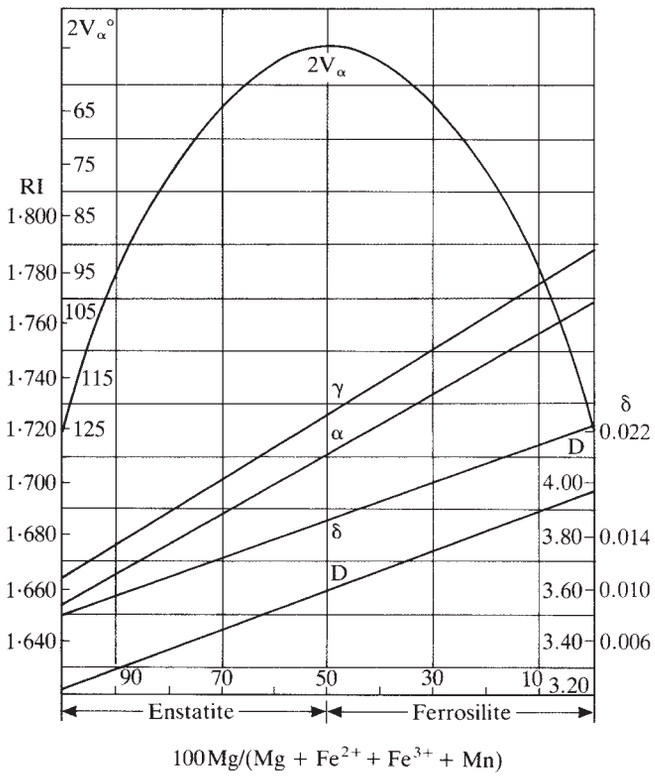


Fig. 83. The relationship of the optical properties and density D (g/cm^3) to the chemical composition of the orthorhombic pyroxenes (Deer *et al*., 1992, *An Introduction to the Rock-Forming Minerals*, Longman, UK).

few microns apart. Clinoenstatite lamellae have been recorded in experimentally deformed enstatite.

All members of the clinoenstatite–clinoferrosilite series are optically positive. Optic axial angles vary between 50º ($MgSiO_3$) and 23º ($FeSiO_3$); γ:z ~24º. The minerals characteristically show multiple twinning parallel to (100), usually attributed to inversion from protoenstatite. Crystals may show incomplete extinction due to (100) twinning on a fine scale down to nanometres in thickness.

Distinguishing features

Many enstatites can be distinguished from clinopyroxenes by their characteristic weak pink to green pleochroism. In the absence of pleochroism they are distinguished from clinopyroxenes by their lower birefringence and their straight extinction in all [001] zone sections. The negative optic sign is diagnostic for compositions between En_{88} and En_{12}. Orthopyroxenes are distinguished from sillimanite by the presence of

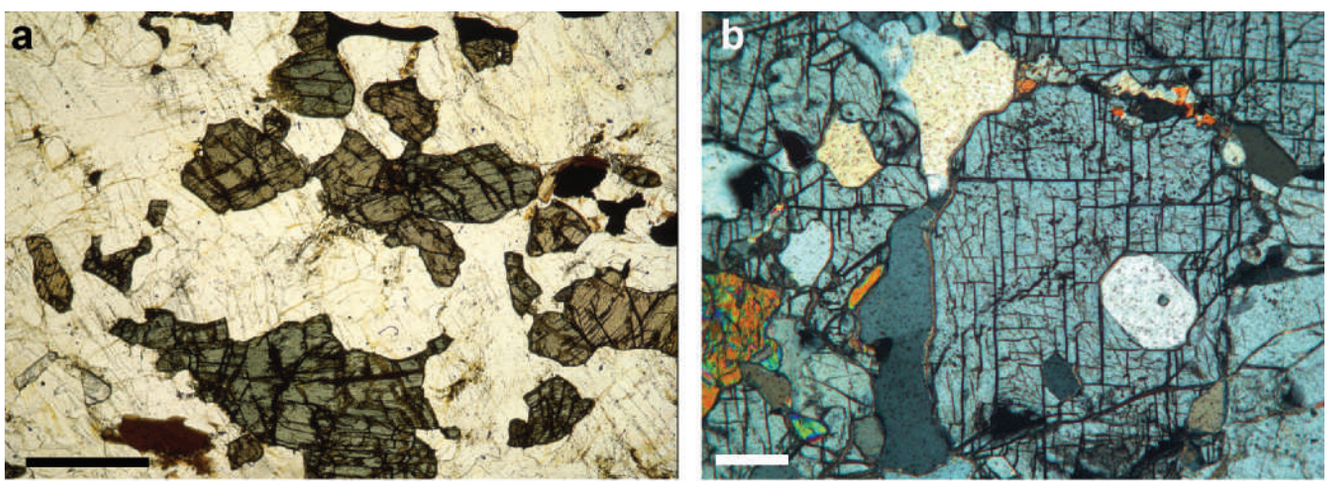


Fig. 84. (a) Orthopyroxene in charnockite, Madagascar (ppl, scale bar 1 mm), showing high relief and characteristic pleochroism from green to pink (W.S. MacKenzie collection, courtesy of Pearson Education). (b) Anhedral prisms of enstatite, in pyroxene granofels, Beitbridge, Zimbabwe (crossed polars, scale bar 0.25 mm), showing high relief, typical first-order interference colours, and 90º cleavages (courtesy of G.T.R. Droop).

Downloaded from https://pubs.geoscienceworld.org/books/chapter-pdf/3755101/9780903056434_ch24.pdf
by guest

{210} and the absence of (010) cleavage, as well as by the smaller optic axial angles of sillimanite; they are distinguished from andalusite by the positive sign of the magnesium-rich enstatite and the greater birefringence of the ferrosilites.

Paragenesis

Magnesium-rich enstatites (Fs_6–Fs_{13}), commonly associated with olivine, diopside and spinel, are important constituents of many ultrabasic and ultramafic rocks. In the ultramafic xenoliths in alkali basalts, enstatites often include varieties with relatively high contents of Al and Cr. Enstatite is present in the early differentiates of many layered intrusions; in the gabbros of the Skaergaard intrusion the composition of the calcium-poor pyroxenes varies from about $Ca_3Mg_{78}Fe_{19}$ to inverted pigeonite $Ca_9Mg_{45}Fe_{46}$ at the two-pyroxene boundary. In the layered sequence of the Bushveld complex the range is $Ca_3Mg_{85}Fe_{12}$ to $Ca_8Mg_{40}Fe_{52}$.

Enstatite is an essential constituent of norite, in which its formation is due to crystallization in basic magma contaminated by argillaceous material. Ferrosilites occur in some acid rocks, e.g. adamellites and granodiorites.

Enstatite phenocrysts are present in olivine tholeiites and tholeiitic andesites, and more iron-rich orthopyroxene (up to ~Fe_{50}) in some dacites and rhyolites. In the alkaline lavas hawaiite and basanite, orthopyroxene megacrysts are generally Al-rich. In some lavas, orthopyroxene together with magnetite occurs as reaction rims around olivine and may be due either to partial reaction of olivine with the liquid or to oxidation of olivine without reaction with the liquid.

Orthopyroxene is the most characteristic and important ferromagnesian mineral in rocks of the charnockite series and is a typical mineral of the granulite facies. In association with cordierite, orthopyroxene occurs in migmatitic rocks. In this paragenesis its formation may be related to the partial melting of pelitic sediments; the reaction albite + biotite + quartz + garnet + water vapour → orthopyroxene + cordierite has been demonstrated experimentally. In argillaceous hornfels orthopyroxene is derived from the breakdown of biotite:

$$K(Mg,Fe^{2+})_3AlSi_3O_{10}(OH)_2 + 3\,SiO_2 \rightarrow 3\,(Mg,Fe)SiO_3 + KAlSi_3O_8 + H_2O$$

Ferrosilites are characteristic constituents associated with fayalite, hedenbergite, grunerite and almandine-spessartine garnet in eulysite, a regionally metamorphosed iron-rich sediment.

Enstatite occurs in the norite and gabbroic anorthosite blocks of the lunar highlands. Members of the clinoenstatite–clinoferrosilite series are very rare in terrestrial rocks. A clinoenstatite is present in volcanic rocks, Cape Vogel, Papua New Guinea, and clinoferrosilite ($Fe_{0.95}Mn_{0.05}SiO_3$) in the lithophysae of obsidian, Lake Naivasha, Kenya. The manganese-rich member of the series kanoite, $(Mn^{2+},Mg)_2Si_2O_6$, associated with manganoan cummingtonite, occurs in Mn-rich seams in biotite–garnet gneiss.

Clinoenstatite, often intergrown with orthoenstatite, occurs in meteorites, in which environment its formation from the orthorhombic phase due to stress is indicated.

Enstatite partly converted to the monoclinic form occurs in granulite and a clinoferrosilite, $Wo_2En_{19}Fs_{79}$, containing exsolution lamellae of augite, $Wo_{40}En_{17}Fs_{43}$, derived from pigeonite, $Wo_{13}En_{17}Fs_{70}$, is the main constituent of eulysite in the Vredefort structure, South Africa.

Further reading

Carlson, W.D. (1988) Subsolidus phase equlibrium on the forsterite saturated join $Mg_2Si_2O_6$–$CaMgSi_2O_6$ at atmospheric pressure. *American Mineralogist*, **73**, 232–241.

Gasparik, T. (1984) Two pyroxene thermobarometry with new experimental data in the system CaO–MgO–Al_2O_3–SiO_2. *Contributions to Mineralgy and Petrology*, **87**, 87–97.

Jenner, G.A. and Green, D.H. (1983) Equilibria in the Mg-rich part of the pyroxene quadrilateral. *Mineralogical Magazine*, **47**, 153–160.

Saxena, S.K., Sykes, J. and Eriksson, G. (1986) Phase equilibria in the pyroxene quadrilateral. *Journal of Petrology*, **27**, 843–852.

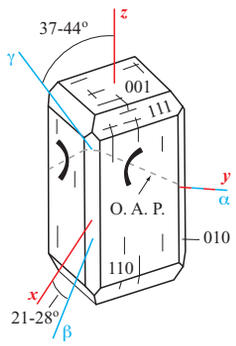
Tazzoli, V. and Domeneghetti, M.C. (1987) Crystal-chemistry of natural and heated aluminous orthopyroxenes. *Physics and Chemistry of Minerals*, **15**, 131–139.

Downloaded from https://pubs.geoscienceworld.org/books/chapter-pdf/3755101/9780903056434_ch24.pdf
by guest

Pigeonite $(Mg,Fe^{2+},Ca)(Mg,Fe^{2+})[Si_2O_6]$

Monoclinic (+)

α	1.682–1.732
β	1.684–1.732
γ	1.705–1.757
δ	0.023–0.029
$2V_\gamma$	0–30º
Orientation	γ:*z*, 37–44º, α = γ; O.A.P. ⊥ (010) more rarely β = γ; O.A.P. (010)
D (g/cm^3)	3.17–3.46
H	6
Cleavage	{110} good; {100}, {010} partings; (110):(1$\bar{1}$0) ~87º
Twinning	{100} or {001}, simple or lamellar, common
Colour	Brown, greenish brown, black; colourless, pale brownish, green, pale yellow-green in thin section
Pleochroism	Often absent but may be weak to moderate α colourless, pale green, yellowish green or smoky brown β pale brown, pale brownish green, brownish pink or smoky brown γ colourless, pale green or pale yellow
Unit cell	*a* ~ 9.7 Å, *b* ~ 8.95 Å, *c* ~ 5.24 Å, β ~ 108.5º Z = 4; space group $P2_1/c$
Special features	Insoluble in HCl



Pigeonites with their low 2V are characteristic of andesites and dacites; inverted pigeonite is a common cumulus phase in basic plutonic rocks

Chemistry

Although the name pigeonite remains valid, and is historically and petrologically useful, pigeonite can also be considered to be a calcium-rich clinoenstatite or calcium-rich clinoferrosilite. Pigeonites commonly contain about 10 mol% $CaSiO_3$, which is much more than can be accommodated by the orthorhombic enstatite–ferrosilite solid solution series. The Al content does not in general exceed 2% of the metal ions and may be insufficient to bring the (Si + Al) up to the ideal 2 atoms pfu; in such minerals it is probable that some tetrahedral sites are occupied by Fe^{3+}. Pigeonite is the monoclinic high-temperature form of Ca-poor pyroxene which inverts to orthopyroxene on cooling. The inversion temperature falls from about 1100ºC for Mg-rich to around 950ºC for Fe-rich pigeonites.

Pigeonites which crystallize early from saturated basaltic liquids have $Mg:Fe^{2+}$ ratios ~70:30; with fractional crystallization, pigeonites become progressively richer in iron to the two-pyroxene boundary (see p. 117) at $Mg:Fe^{2+}$ ratios that vary in different intrusions from ~45:55 to 20:80. Under slow-cooling plutonic conditions some calcium is exsolved as calcium-rich augite along planes parallel to (001)[a] (Fig. 85). At the monoclinic–orthorhombic inversion temperature, further exsolution occurs and gives rise to augite lamellae parallel to the (100) plane of the orthopyroxene. In rapidly quenched rocks the pigeonite does not display optically visible exsolution lamellae. Chemical homogeneity, however, cannot be assumed and some such crystals contain narrow lamellae less than 300 nm wide.

The subsolidus relations of iron-free pigeonite in the system enstatite–diopside at atmospheric pressure are

[a] Plane of exsolution is only approximately (001); see augite section (p. 118).

Downloaded from https://pubs.geoscienceworld.org/books/chapter-pdf/3755303/9780903056434_ch25.pdf
by guest

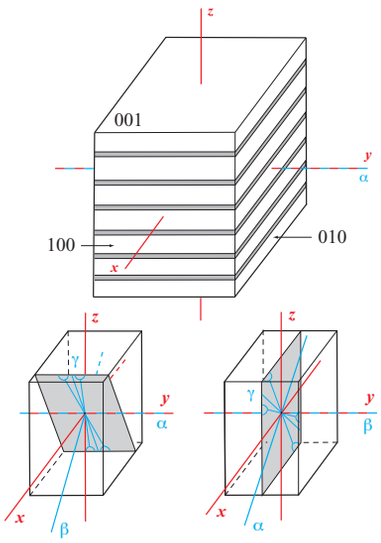


Fig. 85. Augite lamellae parallel to (001) in pigeonite (after Poldervaart, A. & Hess, H.H., 1951, *J. Geol.*, **59**, 472–489.

illustrated in Fig. 87a, p. 113. The amount of $CaMgSi_2O_6$ in the pigeonite solid solution decreases from the consolute temperature, ~450ºC, of the equilibrium solvus to a minimum mole fraction of about 0.2 $CaMgSi_2O_6$ at approximately 1315ºC. The corresponding subsolidus relations for the join hedenbergite–ferrosilite are shown in Fig. 87b.

Optical and physical properties

One of the most important optical properties of pigeonite is the low value of its optic axial angles. The optic axial plane may be either parallel with or (more commonly) perpendicular to (010). The effect of the replacement of Mg by Fe^{2+} on the β refractive index is shown in Fig. 94 (p. 119), from which the calcium content can also be estimated provided the optic axial angle and the β index are both measured. The precise location of the α, β and γ directions is difficult in pigeonites that are sensibly uniaxial.

Zoning is a common feature in pigeonites, and crystals in which the optic axial plane is perpendicular to (010) and parallel to (010) in the central area and outer zone, respectively, are not uncommon. Pleochroism is generally absent or weak but the more iron-rich varieties may show marked pleochroism in brownish tints.

Distinguishing features

Pigeonite is unlikely to be confused with minerals other than members of the pyroxene group, from which it is distinguished by the small (0–30º) value of the optic axial angle.

Pigeonite is distinguished from orthorhombic pyroxenes by the lower birefringence and straight extinction in all [001] zone sections of the latter minerals. In small grains pigeonite may be confused with olivine but the higher birefringence of the latter is usually sufficiently diagnostic. In plutonic rocks inverted pigeonites are

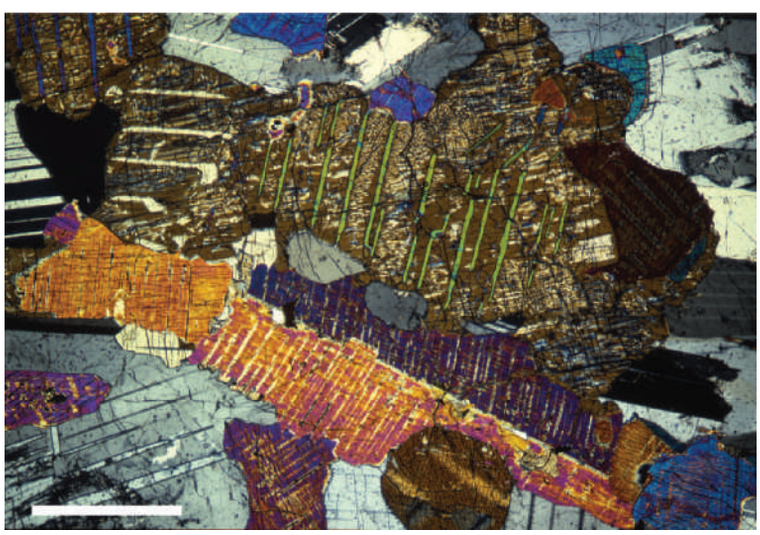


Fig. 86. Pyroxene intergrowths in norite, Bushveld intrusion, South Africa (crossed polars, scale bar 1 mm). The large crystal just above the centre was originally a pigeonite and has inverted to an orthopyroxene containing lamellae of clinopyroxene (green) parallel to (001) of the original pigeonite. The crystal with simple twinning on (100) in the lower part of the field of view is a clinopyroxene with exsolution lamellae of orthopyroxene or pigeonite (W.S. MacKenzie collection, courtesy of Pearson Education).

Downloaded from https://pubs.geoscienceworld.org/books/chapter-pdf/3755303/9780903056434_ch25.pdf
by guest

identified by the presence of augite lamellae located along the (001) plane of the original pigeonite and, in twinned crystals, by the herringbone pattern of the lamellae. (Fig. 86).

Paragenesis

Pigeonite is a particularly characteristic constituent of andesites and dacites. It is less common in basalts as magmatic temperatures of magnesium-rich liquids are in general higher than those of the orthorhombic inversion. With increasing fractionation and iron enrichment in magmatic liquids, pigeonite becomes the normal calcium-poor phase and, in many andesites, pigeonite phenocrysts (or microphenocrysts) coexist with augite.

Inverted pigeonite is a common cumulus phase in basic plutonic rocks with tholeiitic affinities. In these rocks the change from enstatite in the early cumulates to pigeonite in later differentiates occurs at compositions usually between Fs_{30} and Fs_{35}. In pigeonites of layered intrusions iron enrichment rarely exceeds Fs_{60}. Compositions of the most iron-rich pigeonite-augite pairs are about $Ca_8Mg_{16}Fe_{76}$ to $Ca_{32}Mg_{14}Fe_{54}$, respectively. Pigeonites ranging widely in composition, and enclosing exsolved augite lamellae, occur in both achondrite and eucritic meteorites.

Further reading

Domeneghetti, M.C., Zema, M. and Tazzoli, V. (2005) Kinetics of Fe^{2+}-Mg order-disorder in $P2_1/c$ pigeonite. *American Mineralogist*, **90**, 1816–1823.

Grove, T.L. and Juster, T.C. (1989) Experimental investigation of low-Ca pyroxene stability and olivine–pyroxene–liquid equilibria at 1 atm in natural basaltic and andesitic liquids. *Contributions to Mineralogy and Petrology*, **103**, 287–305.

Lindsley, D.H. (1981) The formation of pigeonite on the join hedenbergite–ferrosilite at 11.5 and 15 kbar: experiments and a solution model. *American Mineralogist*, **66**, 1175–1182.

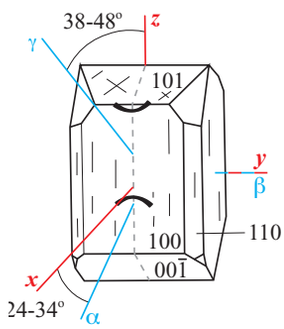
Ranson, W.A. (1986) Complex exsolution in inverted pigeonite: exsolution mechanisms and temperatures of exsolution. *American Mineralogist*, **71**, 1322–1366.

Turner, F.J. (1940) Note on determination of optic axial angle in pigeonite. *American Mineralogist*, **25**, 821–825.

Downloaded from https://pubs.geoscienceworld.org/books/chapter-pdf/3755303/9780903056434_ch25.pdf
by guest

Diopside–Hedenbergite — $Ca(Mg,Fe)[Si_2O_6]$
Johannsenite — $Ca(Mn,Fe)[Si_2O_6]$

Monoclinic (+)



	Diopside–Hedenbergite	Johannsenite
α	1.664–1.732	1.699–1.710
β	1.672–1.730	1.710–1.719
γ	1.694–1.755	1.725–1.738
δ	0.031–0.024	0.022–0.029
$2V_\gamma$	50–62°	58–72°
Orientation	γ:*z* 38–48° β = *y*; O.A.P. (010)	γ:*z* 46–55° β = *y*; O.A.P. (010)
D (g/cm^3)	3.22–3.56	3.27–3.54
H	5½–6½	
Cleavage	{110} good; {100}, {010} partings (110):(1$\bar{1}$0) ~ 87°	
Twinning	{100} or {001}, simple and multiple, common	
Colour	*Diopside*: white, pale green, dark green in hand specimen; colourless in thin section *Hedenbergite*: brownish green, dark green, black; pale green,yellow-green in hand specimen; brownish green in thin section *Johannsenite*: clove-brown, grey, green in hand specimen; colourless in thin section	
Pleochroism	More iron-rich members may show weak pleochroism in pale greens, greenish brown, bluish green and yellow-green.	
Unit cell	*a* ~ 9.75–9.85 Å *b* ~ 8.90–9.0 Å, *c* ~ 5.3 Å β ~ 105.8–104.8° Z = 4; space group *C*2/*c*	*a* ~ 9.8–10.0 Å *b* ~ 9.0–9.2 Å, *c* ~ 5.3 Å β ~ 105° Z = 4; space group *C*2/*c*
Special features	Insoluble in HCl	Decomposed by heating with HCl

Diopside may occur in some ultamafic and mafic igneous rocks and in olivine nodules in basalts. Both diopside and hedenbergite are found commonly in metamorphosed calcareous rocks, diopside being colourless or pale green whereas hedenbergite is usually brownish green. Johannsenite is rarer and is a typical skarn mineral with other Mn silicates.

Chemistry

The diopside–hedenbergite series forms a complete solid solution between $CaMgSi_2O_6$ and $CaFe^{2+}Si_2O_6$. Aluminium is present in most minerals throughout the series but the Si-for-Al replacement is typically <10%. Ferric iron in significant amounts ($\leqslant$0.25 Fe^{3+} pfu) is present in some diopsides and such compositions are qualified by the prefix ferrian. Chromium is characteristically present in diopside of basic and metabasic rocks; minerals in which there is appreciable solution of the $NaCrSi_2O_6$ (kosmochlor) or $CaCrAlSiO_6$ component are described as chromian diopside. The content of manga-

Downloaded from https://pubs.geoscienceworld.org/books/chapter-pdf/3755328/9780903056434_ch26.pdf
by guest

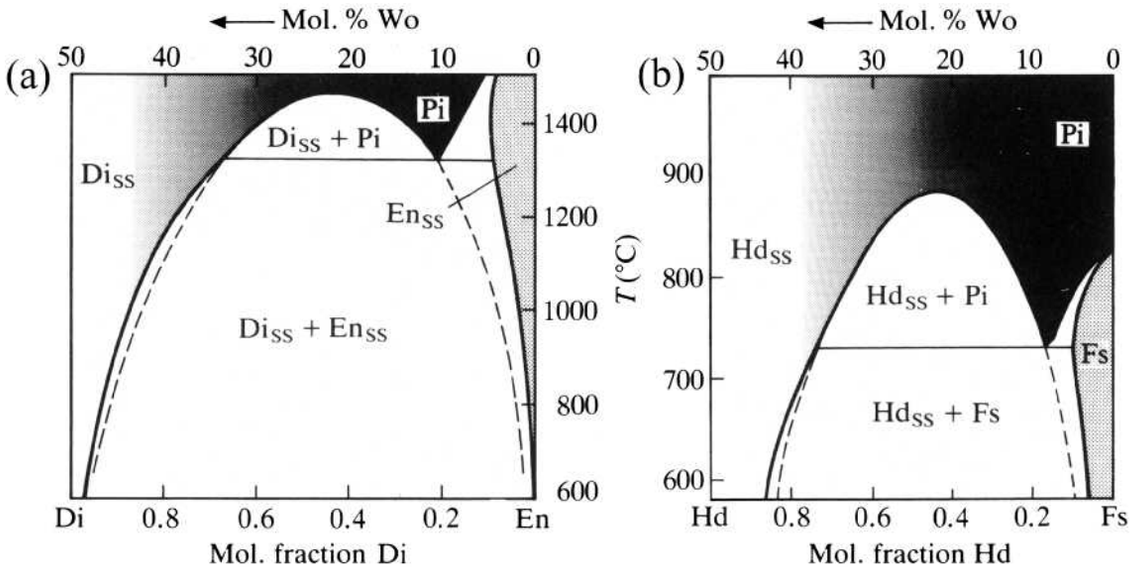


Fig. 87. (a) Phase relations (calculated) for the join diopside–enstatite at 0.1 MPa. (b) Phase relations (calculated) for the join hedenbergite–ferrosilite at 0.1 MPa (the pyroxene relationships are metastable with respect to olivine + silica + hedenbergite or ferrobustamite) [at high temperature some of the relations may be metastable with respect to liquid (with or without olivine) or to protopyroxene or both] (after Lindsley, D.H., 1983, *Amer. Min.*, **68**, 477–93).

nese is small (<0.25 wt.% MnO) in the magnesium-rich but greater in the more iron-rich members (hedenbergites contain up to 4 wt.% MnO). The replacement of (Mg,Fe) by Mn is much greater, with diopside–hedenbergite–johannsenite forming a complete solid-solution field. In the majority of johannsenites the manganese content varies between 0.8 and 0.95 Mn^{2+} pfu. Minerals with approximately equal amounts of manganese and iron occur; those with a composition closer to johannsenite than hedenbergite are described as ferroan johannsenite, those closer to hedenbergite as manganoan hedenbergite. The great majority of diopside–hedenbergite–johannsenite solid solutions contain negligible amounts of Zn, but zincian diopside and zincian hedenbergite with as much as 0.3 Zn pfu are known from Franklin, New Jersey. Zinc is the dominant cation in the *M*1 site of the pyroxene (0.37 Zn pfu) petedunnite.

At subsolidus temperatures there is a continuous series of clinopyroxenes between $CaMgSi_2O_6$ and $CaFe^{2+}Si_2O_6$ in composition. At liquidus temperatures, compositions between Di_{100} and $Di_{60}Hd_{40}$ form an essentially binary system. Compositions richer in the hedenbergite component exhibit more complex phase relations; between Hd_{80} and Hd_{100} a pyroxenoid ferrobustamite crystallizes at the liquidus. The diopside–hedenbergite join is not binary where liquid coexists with ferrobustamite; the latter contains more than 50 mol% $CaSiO_3$ and the liquid is enriched in $MgSiO_3$ and $FeSiO_3$. At subsolidus temperatures the ferrobustamite inverts to an iron-rich member of the diopside–hedenbergite series; for composition Hd_{100} the ferrobustamite–hedenbergite inversion occurs at 965ºC.

Solid solution along the join $CaMgSi_2O_6$–$Mg_2Si_2O_6$ is limited to about 30 mol% $MgSiO_3$ at atmospheric pressure (Fig. 87a) and increases with pressure (see orthopyroxene section, p. 103). The subsolidus relations on the join hedenbergite–ferrosilite are illustrated in Fig. 87b and show that the three pyroxene assemblage hedenbergite–pigeonite–orthoferrosilite is stable. At high pressure the hedenbergite$_{ss}$–pigeonite pair is replaced by a single clinopyroxene, and the distinction between the two phases disappears. The mole fraction of ferrosilite in solid solution with hedenbergite decreases with decreasing temperature to a minimum of about 0.25 at approximately 725ºC.

In the diopside–anorthite system the composition and temperature of the initial coprecipitation of the diopside solid solution and anorthite are very susceptible to pressure and P_{H_2O}. With increasing P and P_{H_2O} the eutectic composition becomes richer in anorthite, but the result of increase in pressure in the dry system is mainly a marked rise in the liquidus temperatures (Fig. 88). At atmospheric pressure diopside contains 3 wt.% of the $CaAl_2SiO_6$ component; the amount is increased by pressure due to the reaction:

$$CaMgSi_2O_6 + n\,CaAl_2Si_2O_8 \rightarrow CaMgSi_2O_6.nCaAl_2SiO_6 + n\,SiO_2$$

and the diopside solid solution becomes more Al-rich in composition (see augite section, p. 116). The enlargement of the primary field of diopside and contraction of the anorthite (and forsterite) field with increasing pressure in the diopside–anorthite–forsterite system is shown in Fig. 89. Johannsenite inverts to the triclinic polymorph, bustamite, at elevated temperatures. Johannsenite is very susceptible to oxidation, hydration and carbonization and commonly alters to rhodonite.

Downloaded from https://pubs.geoscienceworld.org/books/chapter-pdf/3755328/9780903056434_ch26.pdf
by guest

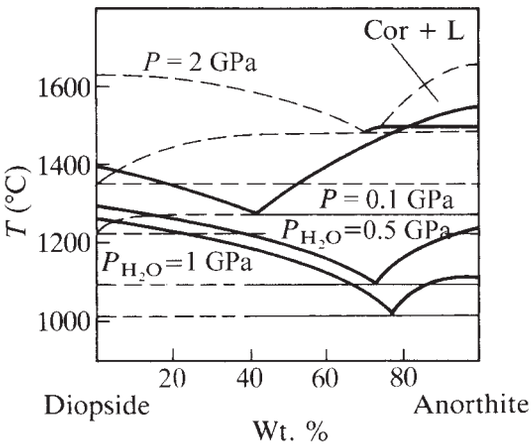


Fig. 88. Diopside–anorthite system at 0.1 GPa, 2 GPa, P_{H_2O} 0.5 GPa and 1 GPa (after Yoder, H.S., 1965, *Carnegie Inst. Washington, Ann. Rept. Dir. Geophys Lab.*, 1964–65, 82–9).

Optical and physical properties

The systematic increase in the α and γ refractive indices of synthetic members of the diopside–hedenbergite series as Mg is replaced by Fe^{2+} (see Fig. 94 p. 119) is in many natural minerals obscured by the effects of variable contents of Al and Fe^{3+}. There is little variation in the optic axial angles, the increase in γ:*z* from 38° in diopside to 48° in hedenbergite is erratic and extinction angles are of little practical value. Diopsides with a high content of the $CaCrAlSiO_6$ component are bluish and greenish in colour. This colour change results from the transformation of tetrahedrally coordinated low-spin Cr^{3+} to octahedrally coordinated high-spin Cr^{3+}. Sector zoning involving variations in Al, Ti, Fe^{3+} and Na as well as normal and reversed zoning is not uncommon in members of the series. Lamellar twinning parallel to (100), and to a lesser extent parallel to (001), occurs in diopsides from deformed basic and metamorphic rocks. Lamellae of orthopyroxene may be present in diopside, and in chromium-rich varieties narrow lamellae of spinel parallel to (010) may be present in addition to the broader orthopyroxene lamellae.

The optical properties of johannsenite and ferroan johannsenite are similar to those of hedenbergite and demonstrate that Mn^{2+} and Fe^{2+} do not differ greatly in their effect on the optical properties of pyroxenes of the diopside–hedenbergite series.

Distinguishing features

The members of the diopside–hedenbergite series cannot always be distinguished from clinopyroxenes of augitic composition (see p. 120), but in general the diopside–hedenbergite minerals have higher optic axial angles than those of augite with comparable refractive indices. Members of the diopside–hedenbergite series may be distinguished from the orthopyroxenes by their higher birefringence. Moreover, many orthopyroxenes display a characteristic pleochroism, and (except for the magnesium- and iron-rich members) their optic sign is negative; the extinction is straight in all sections of the [001] zone in orthopyroxenes. Diopside is distinguished from wollastonite by the presence of only two cleavages and by higher birefringence and refractive indices. Hedenbergite is distinguished from rhodonite by the higher birefringence, lower optic axial angle, and by the two cleavages of clinopyroxene.

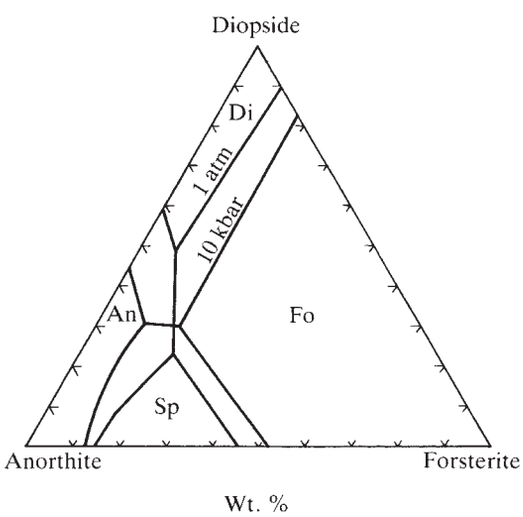


Fig. 89. Liquidus phase relations on the join $CaMgSi_2O_6$–$CaAl_2Si_2O_8$–Mg_2SiO_4 at 0.1 MPa and 1 GPa (after Presnall, D.C. *et al.*, 1978, *Contrib. Mineral. Petrol.*, **66**, 203–20).

Downloaded from https://pubs.geoscienceworld.org/books/chapter-pdf/3755328/9780903056434_ch26.pdf
by guest

Johannsenite is distinguished from diopside by higher refractive indices, optic axial angle and extinction angle, and from hedenbergite by lower refractive indices and high optic axial angle. The common fibrous and spherulitic habit is characteristic. It is distinguished from bustamite by its larger optic axial angle, weaker dispersion and higher refractive indices, from rhodonite by high birefringence and straight extinction in the [010] zone, and from pyroxmangite by its larger optic axial angle.

Paragenesis

Although many clinopyroxenes which crystallize early in basic magmas are augitic in composition, diopside is not an uncommon constituent of basic rocks, particularly those of alkali olivine basalt parentage (e.g. teschenite, theralite, picrite), and of ultramafic nodules found in alkali olivine basalts and kimberlites. Diopside also occurs in the more strongly alkaline rocks, e.g. in the potassium-rich lavas wyomingite, madupite and jumillite). Hedenbergite is a constituent of pulaskite, foyaite and quartz-bearing syenites, in which it is usually associated with fayalite.

Diopside and hedenbergite are typical minerals of many metamorphic rocks; they are particularly characteristic of contact-metamorphosed calcium-rich sediments. Although commonly preceded by tremolite or forsterite, diopside occurs relatively early in the sequence of increasing metamorphism of siliceous dolomites. Intermediates between diopside and hedenbergite occur in regionally metamorphosed calcium-rich sediments and basic igneous rocks in the higher grades of the amphibolite facies:

$$\underset{\text{hornblende}}{Ca_2(Mg,Fe^{2+})_3Al_4Si_6O_{22}(OH)_2} + 3\,\underset{\text{calcite}}{CaCO_3} + 4\,\underset{\text{quartz}}{SiO_2} \rightarrow 3\,\underset{\text{diopside}}{Ca(Mg,Fe^{2+})Si_2O_6} + 2\,\underset{\text{anorthite}}{CaAl_2Si_2O_8} + 3\,CO_2 + H_2O$$

Hedenbergite occurs in contact-metamorphosed iron-rich sediments. In regionally metamorphosed ironstones and eulysites it is associated with grunerite and fayalite. All members of the diopside–hedenbergite series occur in skarns; here associated phases include humite minerals, monticellite, vesuvianite, scapolite, garnet and bustamite.

Johannsenite, commonly associated with rhodonite and bustamite, occurs as a skarn mineral in metasomatized limestones.

Further reading

Capitani, G.C. and Mellini, M. (2000) The johannsenite–hedenbergite complete solid solution: clinopyroxenes frpm the Campiglia Marittima skarn. *European Journal of Mineralogy*, **12**, 1215–1227.

Huebner, J. and Turnock, C. (1980) The melting relations at 1 bar of pyroxenes composed largely of Ca-, Mg-, and Fe-bearing components. *American Mineralogist*, **65,** 225–271.

Lindsley, D.H. (1983). Pyroxene thermometry. *American Mineralogist*, **68**, 477–493.

Liu, T.-C. and Presnall, D.C. (1989) Diopside–tridymite liquidus boundary line in the system Mg_2SiO_4–$CaMgSi_2O_6$–SiO_2 at atmospheric pressure. *American Mineralogist*, **74**, 1032–1037.

Presnall, D.C., Dixon, S.A., Dixon, J.R., O'Donnell, T.H., Brenner, N.L., Schrock, R.L. and Dycus, D.W. (1978) Liquidus phase relations on the join diopside–forsterite–anorthite from 1 atm to 20 kbar: their bearing on the generation and crystallization of basaltic magma. *Contributions to Mineralogy and Petrology*, **66**, 203–220.

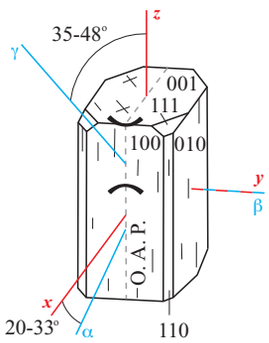
Tribaudino, M., Nestola, F. and Meneghini, C. (2005) Rietveld refinement of clinopyroxenes with intermediate Ca-content along the join diopside–enstatite. *The Canadian Mineralogist*, **43**, 1411–1421.

Weng, Y.-H. and Presnall, D.C. (2001) The system diopside–forsterite–enstatite at 5.1 GPa: a ternary model for melting of the mantle. *The Canadian Mineralogist*, **39**, 299–308.

Downloaded from https://pubs.geoscienceworld.org/books/chapter-pdf/3755328/9780903056434_ch26.pdf
by guest

Monoclinic (+)

α	1.671–1.735
β	1.672–1.741
γ	1.703–1.774
δ	0.018–0.033
$2V_\gamma$	25–61°
Orientation	γ:*z* 35–48°, β = *y*; O.A.P. (010)
D (g/cm^3)	3.19–3.56
H	5½–6
Cleavage	{110} good; {100}, {010} parting; (110):(1$\bar{1}$0) ~ 87°
Twinning	{100} simple, multiple, common; {001} multiple
Colour	Pale brown, brown, purplish brown, green, black; colourless, pale brown, pale purplish brown, pale greenish brown or pale green in thin section
Pleochroism	More strongly coloured varieties show weak to moderate pleochroism; titanian augite moderate to strong α pale greenish, pale brownish, green, greenish yellow, β pale brown, pale yellow–green, violet γ pale green, greyish green, violet
Unit cell	*a* ~9.8 Å, *b* ~9.0 Å, *c* ~5.25 Å, β ~105° Z = 4; space group *C*2/*c*
Special features	Insoluble in HCl



The term augite is much used by petrologists and is valid; however, clinopyroxenes with augitic compositions can also be considered to be a members of the diopside–hedenbergite series. Augites occur in a wide variety of igneous rocks, and are particularly characteristic constituents of gabbros, dolerites and basalts; they occur also, but less frequently, in ultrabasic and intermediate rocks. Augites are present in some granulites and charnockites and other high-grade metamorphic rocks. Iron-rich augites are largely restricted to highly differentiated ferrogabbros, iron-rich dolerites and their pegmatites, syenites, acid volcanic glasses and metamorphosed iron formations. The more calcium-poor augites are the characteristic clinopyroxene phases of quickly chilled basic magmas and occur almost exclusively in basalts and andesites. Titanian augites are the typical pyroxenes of basic alkaline rocks, e.g. teschenite, essexite and nepheline dolerite.

Augites range widely in composition and show a continuous extension of both chemical composition and optical properties from those of members of the diopside–hedenbergite series; the division is an arbitrary one (see Fig. 68, p. 94). Some Al, Fe^{3+} and Na are present in most augites and as their amount increases the compositional range is extended towards omphacite, $Ca(Mg,Fe^{2+}) \leftrightarrow NaAl$; aegirine, $Ca(Mg,Fe^{2+}) \leftrightarrow NaFe^{3+}$; and esseneite, $(Mg,Fe^{2+})Si \leftrightarrow AlFe^{3+}$. Clinopyroxenes with a high content of titanium and characterized by a violet-purple pleochroism are known as titanian augite.

Chemistry

The great majority of augitic pyroxenes contain between 2 and 4 wt.% Al_2O_3 (equivalent to between 0.1 and 0.2 Al atoms pfu), and in most of these minerals Si + Al is sufficient to satisfy the numerical requirement

Downloaded from https://pubs.geoscienceworld.org/books/chapter-pdf/3755373/9780903056434_ch27.pdf
by guest

of the *T* site. If Si + Al is insufficient to occupy fully the tetrahedral sites, Fe^{3+} rather than Ti is usually allotted to the *T* site. Augites generally contain relatively small amounts of Ti (0.5 to 0.8 TiO_2 wt.%) but in titanian augite typical contents range between 3 and 6 wt.% TiO_2, which is equivalent to about 1 in 10 of the *M*1 positions. Chromium is an important minor constituent in many Mg-rich augites; in contrast, the highest contents of Mn occur in Fe-rich augites. Alkalis, mainly sodium, generally amount to between 0.5 and 0.8 wt.% Na_2O. In the omphacitic pyroxenes, however, sodium is a major constituent and in omphacite (p. 123) sodium occupies approximately half the *M*2 sites. In the augitic pyroxenes a high proportion of the *M*1 sites are occupied by trivalent ions with the consequent major replacement of Si by Al (between 0.25 and 0.50 atoms per mol). In ferrian aluminium augites the main replacement may be expressed $(Mg,Fe^{2+})Si \leftrightarrow (Al,Fe^{3+})Al$, in contrast to the omphacite replacement $Ca(Mg,Fe^{2+}) \leftrightarrow Na(Fe^{3+},Al)$. In the Fe^{3+}-Al-rich pyroxene, esseneite, the composition is close to the ideal formula, $CaFe^{3+}AlSiO_6$.

The compositions of pyroxenes of basic rocks are closely related to their origin. The calcium-rich augites of the tholeiitic rock series show strong iron enrichment coupled initially with a decrease, and later with an increase, in calcium content. Until the later stage of magmatic fractionation, augites are associated with orthopyroxenes or pigeonites. In contrast, augites of the alkaline series show a more limited iron enrichment and a fractionation trend approximately parallel to the diopside–hedenbergite join.

These basaltic augites, as a first approximation, can be considered as members of the diopside–hedenbergite–clinoenstatite–clinoferrosilite system; the relationships of the four boundary pairs are known either from natural phases or experimental data. Solid solution extends from $Mg_2Si_2O_6$ to 88 wt.% $Fe_2Si_2O_6$ and is complete at subsolidus temperatures between diopside and hedenbergite. In the experimental system a ferrobustamite occurs as the liquidus phase for compositions more iron-rich than $Di_{25}Hd_{75}$. In the $CaMgSi_2O_6$–$Mg_2Si_2O_6$ system the solvus intersects the solidus between about 9 and 50 wt.% $CaMgSi_2O_6$ (see Fig. 87a p. 113) solid solution is not complete even at high temperatures.

The limit in the compositional field in which two pyroxenes (Ca-rich and Ca-poor) crystallize together is termed the two-pyroxene boundary, and is delineated by the join between iron-rich augite with minimum Ca content and the coexisting Ca-poor phase. The limits of the two-pyroxene field and the miscibility gap vary in individual intrusions (Fig. 90) and are probably related to the effects on the phase equilibria of different Al, Fe^{3+} and Na contents in the magma as well as H_2O vapour pressure and silica activity.

Exsolution lamellae of a calcium-poor phase, orthopyroxene/pigeonite singly or together, are a common feature of many plutonic augitic pyroxenes. The orthopyroxene lamellae are oriented approximately parallel to the (100) plane of the augite hosts (Fig. 91), with pigeonite lamellae parallel to the (001) plane. The more magnesium-rich augites crystallize below the pigeonite–orthopyroxene inversion temperature (pigeonite section, p. 110) and the lamellae in such augites consist of orthopyroxene. Augites more iron-rich than $Ca_{41}Mg_{44}Fe_{15}$ commonly crystallize above the pigeonite–orthopyroxene inversion temperature and the exsolved phase is pigeonite. The latter may subsequently invert to orthopyroxene on cooling through the monoclinic–orthorhombic inversion temperature. Thus a first set of lamellae are formed approximately parallel to (001) and a second set parallel to the (100) plane of the augite host.

The trend shown in Fig. 90 represents compositions of the pyroxene phases at solidus temperatures. The subsolidus trends, i.e. compositions of the augite sequence after exsolution of a Ca-poor phase, and of the orthopyroxene/pigeonite phase subsequent to the exsolution of a Ca-rich phase, together with the solidus trend for the pyroxenes of the Skaergaard intrusion, are shown in Fig. 92.

The phase equilibria for Ca-Mg-Fe pyroxenes have been determined experimentally over a range of pressures and temperatures. Isothermal phase relations showing variations in compositions of augite–orthopyroxene, augite–pigeonite and orthopyroxene–pigeonite

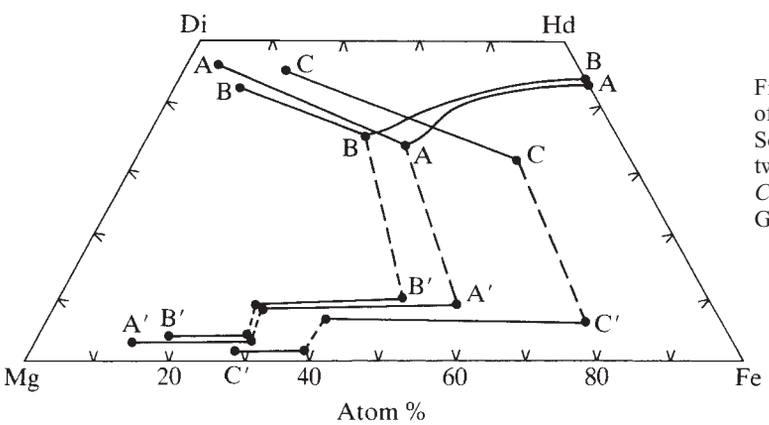


Fig. 90. Ca-rich and Ca-poor pyroxene fractionation trends of the Bushveld (AA′), Skaergaard (BB′) and Bjerkrem–Sogndal (CC′) intrusions. Broken lines: boundaries of the two-pyroxene field (after Deer, W.A. *et al.*, 1978, *Single-Chain Silicates*. Rock-Forming Minerals, 2nd Edn. **2A**, Geological Society, London. 668 pp.).

Downloaded from https://pubs.geoscienceworld.org/books/chapter-pdf/3755373/9780903056434_ch27.pdf
by guest

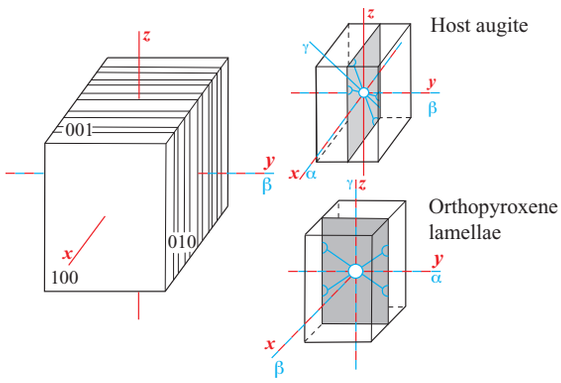


Fig. 91. Lamellae of orthopyroxene parallel to (100) in magnesium-rich augite host (after Poldervaart, A. & Hess, H.H., 1951, *J. Geol.*, **59**, 472–89).

pairs and the position of augite–orthopyroxene–pigeonite three-phase triangles at 800, 900 and 1000ºC at 0.1–0.2 GPa, 0.1 GPa and <0.1 MPa pressure respectively are illustrated in Fig. 93. At 1000ºC the relationships are affected by the presence of ferrobustamite at compositions close to $CaFeSi_2O_6$ (see p. 113).

There are many studies of the distribution of Mg and Fe and other elements between coexisting clinopyroxenes and orthopyroxenes. In general the Ca-rich phase has higher contents of Fe^{3+}, Ti, both $[Al]^4$ and $[Al]^6$, as well as higher Mg/(Mg + Fe) values. The Mg–Fe distribution between clinopyroxene and coexisting minerals, such as orthopyroxene, olivine and garnet, offers potential as a geothermometer or geobarometer; interpretations are, however, by no means straightforward.

Augite is commonly altered to a greenish-blue (uralitic) amphibole, either as a single crystal or as an aggregate of small prismatic crystals. The alteration usually begins at the periphery and along the cleavages, and in the early stages the alteration may be accompanied by an irregular bleaching of the crystal resulting in the formation of patchy areas of colourless pyroxene flecked with small plates of amphibole. In augites in which the amount of alteration is small the amphibole occurs as narrow, sometimes submicroscopic, lamellae along {010} interfaces with the pyroxene host, that appear as an exsolution feature. In more highly altered regions the amphibole can contain regions of triple and higher multiple chains, as well as the normal double chains. Chlorite is also a common alteration product of augite; less common products include epidote and carbonates.

Optical and physical properties

There is a systematic relationship between the optical properties and chemical composition of the diopside–hedenbergite–enstatite–ferrosilite pyroxenes. The variation of the β refractive index for pyroxenes in which the optic axial plane is parallel to (010), and the variation of the α index for those in which the optic axial plane is perpendicular to (010) are plotted, together with the variation in 2V, in Fig. 94. As the β vibration is parallel to *y* for pyroxenes in which the optic plane is perpendicular to (010), and as β and α are coincident at 2V = 0, the two indices can be used to construct a continuous set of curves. These curves are constructed for pyroxenes containing normal amounts of the minor constituents, Al, Fe^{3+}, Ti, Cr, Mn and Na; expressed as per cent oxides, these are: Al_2O_3, 3; Fe_2O_3, 1.5; Na_2O, 0.4; TiO_2, 0.4; MnO, 0.3 but higher in the more iron-rich pyroxenes; Cr_2O_3, 1.1 in the magnesium-rich augites but neglible in minerals more iron-rich than $(CaMg)_{87}Fe_{13}$. The effect of the minor constituents on the refractive indices depends not only on their absolute amount but also on their position in the pyroxene

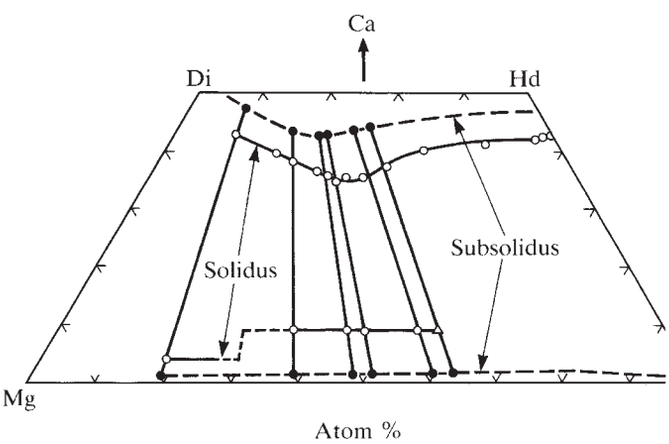


Fig. 92. Crystallization trends of the Ca-rich and Ca-poor pyroxenes of the Skaergaard intrusion showing the solidus and subsolidus trends (solidus: Brown, G.M. & Vincent, E.A., 1963, *J. Petrol.*, **4**, 175–95; sub-solidus: Nwe, Y.Y., 1976, *Contrib. Mineral. Petrol.*, **55**, 105–26).

Downloaded from https://pubs.geoscienceworld.org/books/chapter-pdf/3755373/9780903056434_ch27.pdf
by guest

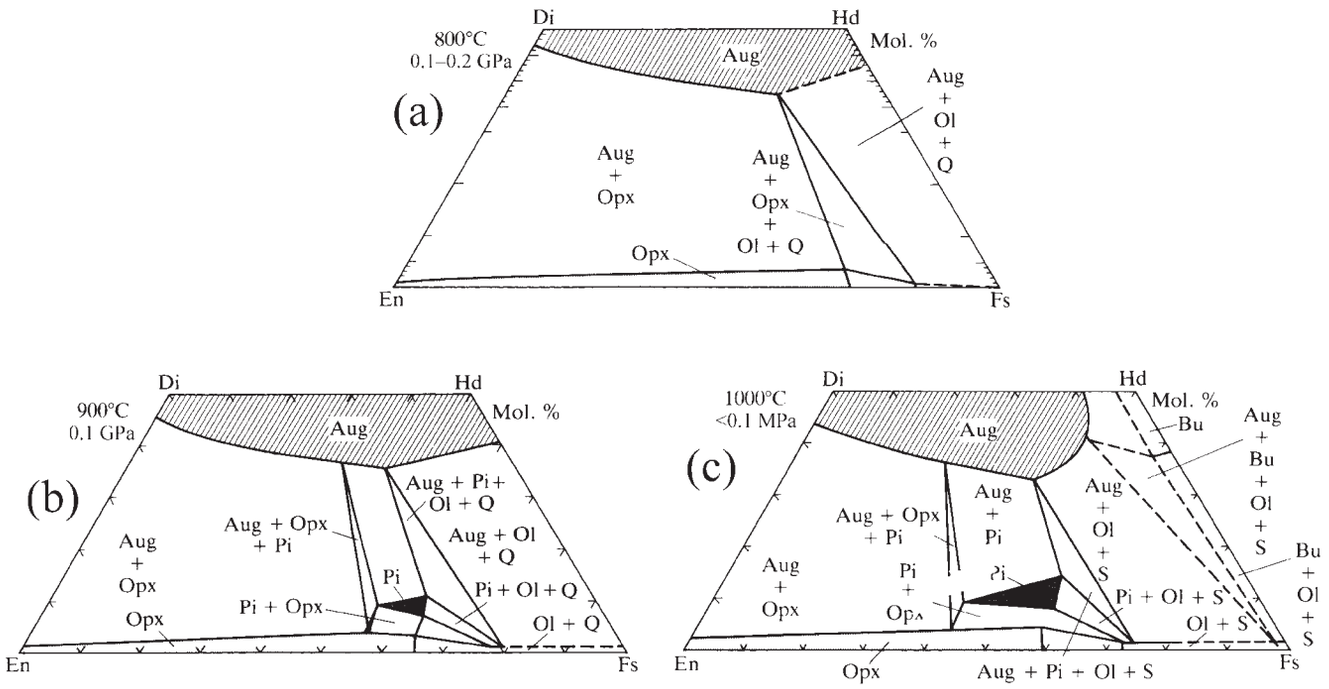


Fig. 93. Ca–Mg–Fe–pyroxenes phase relations: (a) 800ºC, P_{H_2O} 0.1–0.2 GPa, FMQ buffer; (b) 900ºC, P_{H_2O} 0.1 GPa, FMQ buffer; (c) 1000ºC, P < 0.1 MPa, Fe^0 buffer. Assemblages with olivine and either quartz or silica polymorphs constitute the 'forbidden zone' within which pyroxenes are not stable at low pressures (after Lindsley, D.H., 1983, *Amer. Min.*, **68**, 477–93). Ol: olivine; Bu: bustamite; Q: quartz; S: silica polymorph.

structure; thus Al, Ti and Fe^{3+} in tetrahedral coordination increase the optic axial angle and lower the refractive index, whereas in octahedral coordination the same ions have the opposite effect. As a result of these factors, compositions estimated from the optical properties may differ by as much as 5% of the Ca, Mg or Fe^{2+} content from their true value.

Crushed fragments of the monoclinic pyroxenes include tablets lying parallel to the prismatic cleavage {110} and a smaller number of tablets parallel to the {100} parting. The latter are easy to recognize by their low birefringence and their orientation can be checked by observing the interference figure, which will show an off-centre optic axis figure. If, on rotating the stage until the isogyre is east–west, the brush divides the field exactly, then the optic axial plane is normal to the section and the β vibration direction is north–south.

Zoning is a relatively common feature of augites (Fig. 95) and particularly in titanian varieties. The latter often display sector (hourglass) as well as concentric or oscillatory zoning (Fig. 96). Sector zoning has been reproduced experimentally and the element partitioning in different growth sectors and between core and rim has been related to variable growth rates and degree of supercooling.

Ferrian aluminian augites are strongly pleochroic, and display anomalous interference colours and very strong dispersion.

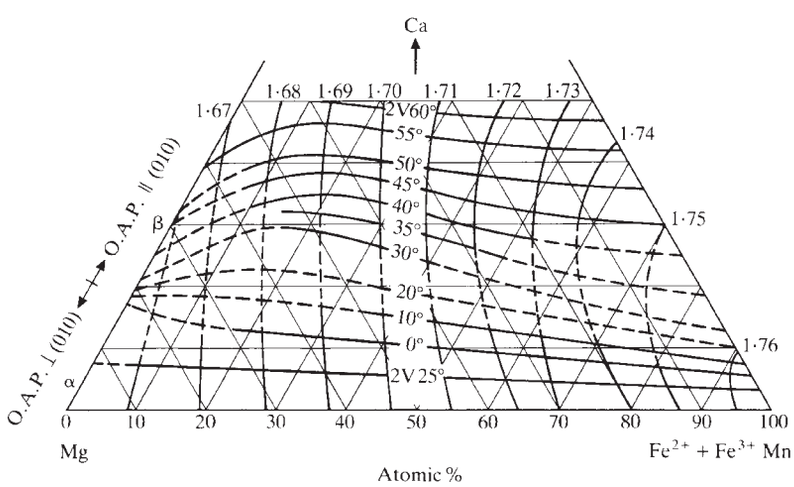


Fig. 94. Variation of the optical properties with chemical composition of clinopyroxenes included in the system $CaMgSi_2O_6$–$CaFeSi_2O_6$–$Mg_2Si_2O_6$–$Fe_2Si_2O_6$ (after Hess, H.H., 1949, *Amer. Min.*, **34**, 621–66).

Downloaded from https://pubs.geoscienceworld.org/books/chapter-pdf/3755373/9780903056434_ch27.pdf
by guest

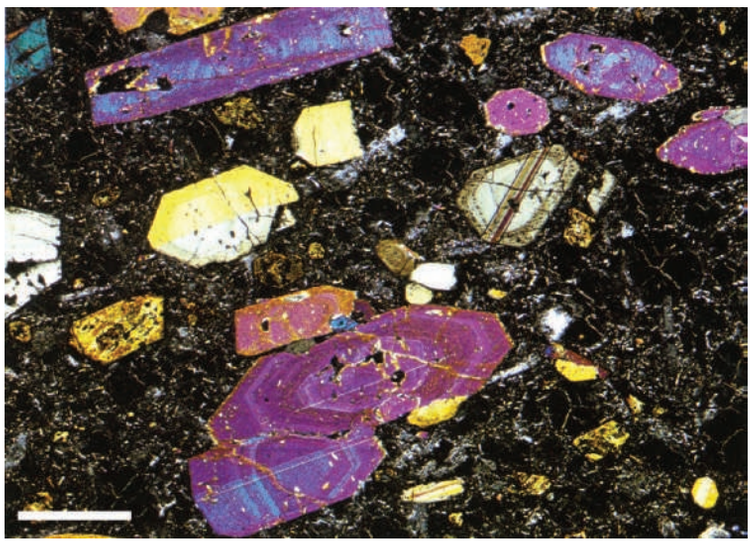


Fig. 95. Augite in phonolite, Highwood Mts., Montana, USA (crossed polars, scale bar 1 mm), with interference colours up to middle second order blue and showing zoning, and both simple and lamellar twinning (W.S. MacKenzie collection, courtesy of Pearson Education).

Distinguishing features

The continuous chemical variation between diopside, hedenbergite, augite and ferroaugite means it is not always possible to identify these minerals precisely on the basis of their optical properties. In general augite is distinguished from diopside by smaller birefringence, higher refractive indices and stronger dispersion, and the more (Mg,Fe)-rich augites have smaller optic axial angles than members of the diopside–hedenbergite series; ferroan augites have smaller optic axial angles and smaller extinction angles than hedenbergite. Titanian augites are typically distinguished by their stronger colour and characteristic pleochroism with a violet colour in the γ vibration direction; sodium-rich augites have a stronger green absorption colour, and higher optic axial angles and extinction angles than augite with more normal contents of sodium.

Augite is distinguished from aegirine-augite and aegirine by the strong colour, higher birefringence and higher γ:z extinction angles and higher optic axial angles of the latter minerals. Magnesium-rich augites are difficult to distinguish from both omphacite and ferrian aluminian augites but these pyroxenes may sometimes be distinguished from augite by their lower birefringence combined with their pale green colour. Augite is distinguished from spodumene and jadeite by its larger extinction angle and refractive indices, and from johannsenite by its smaller optic axial angle. The orthopyroxenes typically have higher birefringence, smaller optic axial angles, are optically negative and the extinction angle is straight in all sections of the [001] zone. Augite is distinguished from wollastonite by the presence of only two cleavages, higher refractive indices and birefringence; wollastonite has inclined extinction in all [001] zone sections. Rhodonite is similarly distinguished from augite except that there is an overlap with the refractive indices of the more iron-rich augites.

Paragenesis

Augites are common constituents of basic igneous rocks; they also occur in ultramafic rocks, lherzolite and websterite and in the ultrabasic nodules and megacrysts in basic rocks.

A wide and continuous range in composition occurs in the augites of layered basic intrusions. In the lowest part of the basal series of the Bushveld complex the pyroxene has a diopsidic composition, $Ca_{45}Mg_{50}Fe_5$. Above this the composition changes to augite,

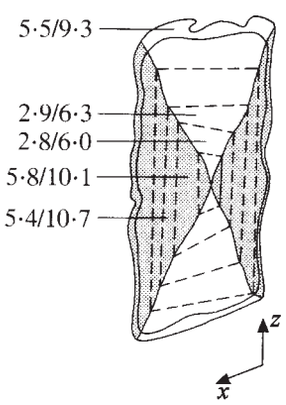


Fig. 96. Zoning in titanian augite. Shaded areas represent more deeply coloured zones. Continuous lines represent hourglass sector boundaries. The TiO_2 and Al_2O_3 contents of the zones are shown, e.g. zone 1 TiO_2 5.40, Al_2O_3 10.7 wt.% (after Wass, S.K., 1973, *Mineral. Mag.*, **39**, 133–44).

Downloaded from https://pubs.geoscienceworld.org/books/chapter-pdf/3755373/9780903056434_ch27.pdf
by guest

$Ca_{33}Mg_{31}Fe_{36}$, prior to an abrupt change in trend to $Ca_{40.5}Mg_{18.7}Fe_{40.8}$; crystallization terminating close to the hedenbergite–ferrosilite join at the composition $Ca_{42.7}Mg_{0.5}Fe_{56.8}$ (see Fig. 90, p. 117). In the Skaergaard intrusion the pyroxene ranges from $Ca_{42.4}Mg_{47.9}Fe_{9.7}$ to hedenbergite, $Ca_{42.5}Mg_{0.4}Fe_{57.1}$, the latter derived by inversion of a ferrobustamite. In contrast, Bushveld hedenbergite shows no evidence of such an inversion. Initially augite is associated with an enstatite but at Mg:Fe ratios varying between 75:25 and 60:40 in different intrusions the orthopyroxene is replaced by pigeonite. Further fractional crystallization proceeds with the cotectic formation of augite and pigeonite to the two-pyroxene boundary.

Augites are common constituents of many hypabyssal rocks from picrites to ferrodolerites. In the Palisade Sill, New Jersey, the compositional variation of the augites, $Ca_{38}Mg_{51}Fe_{11}$ to $Ca_{38}Mg_{10}Fe_{52}$, is comparable with the range in many layered intrusions.

Augite is the common pyroxene of basic lavas and occurs in tholeiitic and alkali olivine-basalt suites. In tholeiitic lavas, augites are commonly subcalcic in composition due to rapid cooling at high temperatures. Although optically homogeneous these phases may be unmixed on a submicroscopic scale. Subcalcic phases are particularly common as groundmass constituents and the formation of low-calcium augites during the later stages of crystallization is illustrated by their occurrence as rims around the early phenocrysts. Augites in the basalts and andesitic basalts of the Thingmuli volcano, eastern Iceland, are rimmed by pigeonite. The compositions of the two phases are distinct and there is a well defined miscibility gap between the augite and pigeonite.

Augites, except aluminium-rich varieties, are not common products of contact metamorphism. However, the latter, associated with spinel, occur in metamorphosed limestones; they also occur at igneous–carbonate contacts where associated phases include garnet, vesuvianite, scapolite, epidote and pargasitic amphiboles, as well as in eclogite inclusions in nephelinite and kimberlitic pipes. Titanian augite is a relatively common constituent of alkaline dyke rocks, such as monchiquites, essexites and camptonites.

Further reading

Bulakh, A.G. and Zolotarev, A.A. (2004) End-member compositions of augite and its varieties. *Neues Jahrbuch für Mineralogie, Monatshefte*, 361–372.

Davidson, J.M. and Lindsley, D.H. (1989) Thermodynamic analysis of pyroxene-olivine-quartz equilibria in the system CaO-MgO-FeO-SiO_2. *American Mineralogist*, **74**, 18–30.

Gasparik, T. (1986) Experimental study of subsolidus phase relations and mixing properties of clinopyroxenes in the silica-saturated system CaO-MgO-Al_2O_3-SiO_2. *American Mineralogist*, **71**, 686–693.

Hess, H.H. (1949) Chemical composition and optical properties of common clinopyroxenes, Part I. *American Mineralogist*, **34**, 621–666.

Huebner, J.G. and Turnock, A.C. (1980) The melting relations at 1 bar of pyroxenes composed largely of Ca-, Mg-, and Fe-bearing components. *American Mineralogist*, **65**, 225–271.

Lindsley, D.H. (1983) Pyroxene thermometry. *American Mineralogist*, **68**, 477–493.

Molin, G. and Zanazzi, P.F. (1991) Intracrystalline Fe^{2+}-Mg ordering in augite: experimental study and geothermometric applications. *European Journal of Mineralogy*, **3**, 863–875.

Nakajima, Y. and Ribbe, P.H. (1981) Textural and structural interpretations of the alteration of pyroxene to other biopyriboles. *Contributions to Mineralogy and Petrology*, **78**, 230–239.

Poldervaart, A. and Hess, H. (1951) Pyroxenes in the crystallization of basaltic magma. *Journal of Geology*, **59**, 472–489.

Reid, H. and Fuess, H. (1986) Lamellar exsolution systems in clinopyroxenes. *Physics and Chemistry of Minerals*, **13**, 113–118.

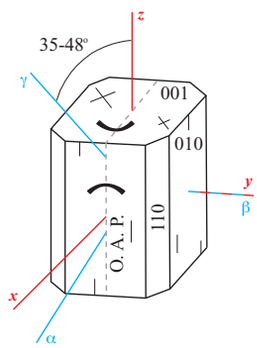
Wass, S.Y. (1973) The origin and petrogenetic significance of hourglass zoning in titaniferous clinopyroxenes. *Mineralogical Magazine*, **39**, 133–144.

Downloaded from https://pubs.geoscienceworld.org/books/chapter-pdf/3755373/9780903056434_ch27.pdf
by guest

Omphacite $(Ca,Na)(Mg,Fe^{2+},Fe^{3+},Al)[Si_2O_6]$

Monoclinic (+)

α	1.662–1.701
β	1.670–1.712
γ	1.685–1.723
δ	0.012–0.028
$2V_\gamma$	56–84°
Orientation	γ:*z*, 34–48°; O.A.P. (010)
D (g/cm^3)	3.16–3.43
H	5–6
Cleavage	{110} good, {100} parting; (110):(1$\bar{1}$0) ~ 87°
Twinning	{100} simple, lamellar, common
Colour	Green, dark green; colourless to pale green in thin section
Pleochroism	Feeble α colourless β very pale green γ very pale green, blue–green (darker in ferroan variety)
Unit cell	*a* 9.45–9.68 Å, *b* 8.57–8.90 Å, *c* 5.23–5.28 Å, β 105°–108° Z = 4; space group *C*2/*c* or *P*2/*n*
Special features	Insoluble in HCl



Although it would not fall within the modern definition, omphacite has been retained as a mineral species for practical reasons and is used extensively by petrologists. It can be defined as a solid solution of jadeite (20%–80%) and augite (80%–20%) with significant aegirine and calcium and aluminium-rich clinopyroxene components. Omphacite is a high-pressure phase, which is found as a pale green mineral, commonly associated with garnet, typically in eclogites and related rock types

Structure

The structures of omphacites are, in general, similar to those of other clinopyroxenes but whereas the more diopside-rich and jadeite-rich members of the $CaMgSi_2O_6$–$NaAlSi_2O_6$ series have the normal *C*2/*c* space group symmetry those with a range of intermediate compositions have space group *P*2/*n*. In these omphacites the Mg and Al atoms are ordered between two kinds of *M*1 site and alternate in successive octahedra parallel to the *z* direction, and the Ca and Na atoms are ordered between the two kinds of *M*2 site. Figure 97 illustrates an omphacite with maximum cation ordering. The greatest degree of ordering found by X-ray diffraction has complete Mg/Al ordering in the *M*1 site, but the *M*2 sites alternate between ¾Ca, ¼Na and ¼Ca, ¾Na. An ideal formula for a pure Jd–Di ordered omphacite could thus be expressed as $Na_{0.5}Ca_{0.5}Mg_{0.5}Al_{0.5}Si_2O_6$ ($Jd_{50}Di_{50}$); actual compositions range at least between $Jd_{40}Di_{60}$ and $Jd_{55}Di_{45}$.

Many omphacites display exsolution lamellae and antiphase domains. These microstructures in jadeitic–augitic solid solutions can be interpreted in terms of a combined system in which a field of cation ordering (*P*2/*n*) at intermediate compositions (omphacites) is superimposed on to a broad immiscibility gap between disordered (*C*2/*c*) end-members (Fig. 98a). Although not confirmed experimentally, such relationships are consistent with the petrographic evidence of broad two-phase fields between impure jadeite and omphacite and between omphacitic and sodium-rich augite. The phase diagram for the ternary system jadeite–augite–aegirine is shown in Fig. 98b). At sufficiently high temperatures all compositions between $CaMgSi_2O_6$ and $CaAlSi_2O_6$ have *C*2/*c* symmetry, and some omphacites retain a disordered structure from their high-temperature origin.

Downloaded from https://pubs.geoscienceworld.org/books/chapter-pdf/3755496/9780903056434_ch28.pdf
by guest

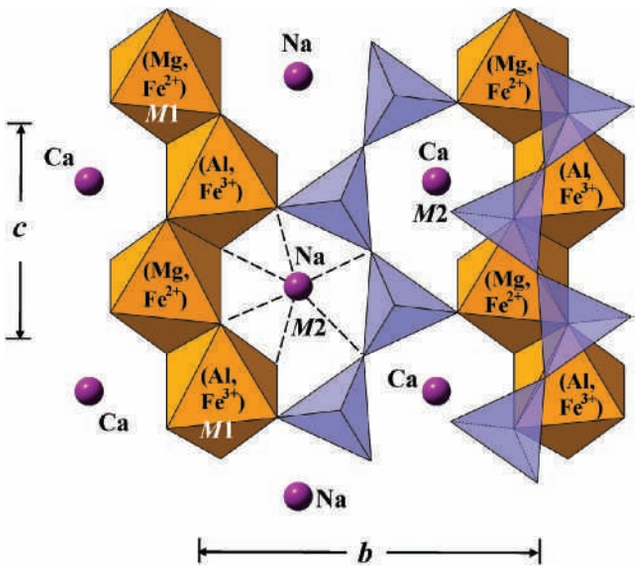


Fig. 97. Part of the structure of omphacite showing pyroxene chains (blue), and maximum* cation ordering among the sites as labelled (after Clark, J.R. & Papike, J.J., 1968, *Amer. Min.*, **53**, 840–68. Fig. produced by M.D. Welch).
* See text, p. 122

Chemistry

Omphacite is essentially a solid solution of jadeite and diopside with significant aegirine (commonly up to 10 wt.%) and $CaAl_2SiO_6$. The omphacite compositional range in the system $(Ca,Mg,Fe)_2Si_2O_6$–$NaAlSi_2O_6$–$NaFe^{3+}Si_2O_6$ lies between the boundary planes $0.2 \leqslant Na/(Na + Ca) \leqslant 0.8$ and is limited to the ratio $^{[6]}Al/(^{[6]}Al + Fe^{3+}) \geqslant 0.5$ (see Fig. 69, p. 95).

Alteration, during retrograde metamorphism, in some omphacites leads to the formation of a border zone of hornblende and the development of homoaxial fibres of amphibole within the pyroxene. In other omphacites the alteration involves the transformation to a symplectitic intergrowth of diopside and plagioclase. Some mantle-derived eclogite omphacites break down to an aluminium-rich augite intergrown with the host omphacite and quartz. The probable reaction:

$$2\,Ca_{0.5}\square_{0.5}AlSi_2O_6 \rightarrow CaAlAlSiO_6 + 3\,SiO_2$$

indicates that the original omphacite had some *M*-site vacancies and was stabilized by pressures of the order of 3 GPa but highly unstable at lower pressures.

Optical and physical properties

There is a relatively wide variation in the refractive indices and optic axial angle of omphacites but little correlation of the optical properties and chemical composition is apparent. Patchy and undulose extinction,

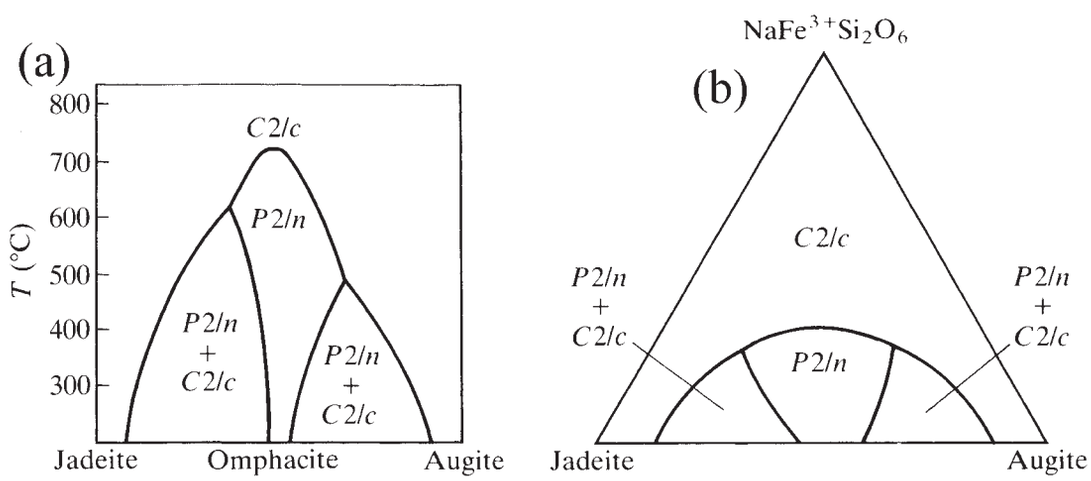


Fig. 98. Equilibrium phase diagrams proposed for jadeite–augite and jadeite–augite–aegirine. (a) A single field of ordered omphacite with *P*2/*n* symmetry is bounded by wide two-phase fields at low temperatures. The *C*2/*c* → *P*2/*n* ordering transformation is thought to be second order in character so there is no two-phase region between the ordered and disordered fields at high temperatures. (b) In the ternary system the presence of $NaFe^{3+}Si_2O_6$ is analogous to increasing temperature and the isothermal stability fields are topographically similar to those in the binary system (after Carpenter, M.A., 1980, *Contrib. Mineral. Petrol.*, **71**, 289–300).

Downloaded from https://pubs.geoscienceworld.org/books/chapter-pdf/3755496/9780903056434_ch28.pdf
by guest

due to high concentrations of stacking faults, is not uncommon in omphacites in rocks of the blueschist facies. The density of omphacites is high in relation to their chemical composition, in accord with their crystallization in high-pressure environments.

Distinguishing features

Omphacite is distinguished from diopside and diopsidic augite by larger optic axial angle and from jadeite by its stronger colour, higher refractive indices, birefringence and extinction angle. Aegirine-augites are distinguished from omphacite by their higher refractive indices, small extinction angles and stronger pleochroism. In rocks in which omphacite is associated with hornblende it is distinguished from the amphibole by its paler colour and weaker pleochroism as well as by the pyroxene cleavage.

Paragenesis

Omphacite is a diagnostic mineral of rocks generally considered to have formed in a high-pressure environment. It is particularly characteristic of eclogites and closely related rocks. The chemical composition of many eclogites is comparable with those of basic igneous rocks; the formation of omphacite and garnet, due to crystallization or recrystallization of pre-existing igneous rocks under conditions of high $P-T$, may be expressed by the equation:

$$\underset{\text{labradorite}}{3\,CaAl_2Si_2O_8} + 2\,NaAlSi_3O_8 + \underset{\text{olivine}}{3\,Mg_2SiO_4} + n\,\underset{\text{diopside}}{CaMgSi_2O_6} \rightarrow$$

$$\underset{\text{omphacite}}{2\,NaAlSi_2O_6} + n\,CaMgSi_2O_6 + \underset{\text{garnet}}{3\,CaMg_2Al_2Si_3O_{12}} + \underset{\text{quartz}}{2\,SiO_2}$$

In eclogites (type A) of very deep-seated origin, e.g. kimberlite pipes, omphacite and garnet are associated with kyanite or corundum. In eclogites (type B), see Fig. 17, p. 23, of migmatitic gneisses the pyroxene occurs in assemblages that include hornblende and scapolite. In eclogites (type C) of Alpine-type orogenic zones, associated phases include lawsonite, pumpellyite, glaucophane, epidote and hornblende, assemblages formed at relatively low temperature and high water pressures; these omphacites have a high content of the $NaFe^{3+}Si_2O_6$ component. Omphacites in kimberlite inclusions, that cooled rapidly from high temperature, are almost invariably completely disordered. Slowly cooled omphacites of gneisses and alpine eclogites have a high degree of cation ordering. Partition coefficients of $Mg-Fe^{2+}$ distribution between omphacite and garnet are related to the $P-T$ environment of formation; the lowest values occur in omphacite–garnet pairs of type A and the highest in type C eclogites.

Further reading

Ballaran, T.B., Carpenter, M.A., Domeneghetti, C. and Tazzoli, V. (1998) Structural mechanisms of solid solution and cation ordering in augite-jadeite pyroxenes. 1. A macroscopic perspective. *American Mineralogist*, **83**, 419–433.

Carpenter, M.A. (1980) Mechanisms of exsolution in sodic pyroxenes. *Contributions to Mineralogy and Petrology*, **71**, 289–300.

Carpenter, M.A. (1981) Time-temperature-transformation (TTT) analysis of cation disordering in omphacite. *Contributions to Mineralogy and Petrology*, **78**, 433–440.

Clark, J.R. and Papike, J.J. (1968) Crystal chemical chaacterization of omphacites. *American Mineralogist*, **53**, 840–868.

Davidson, P.M. and Burton, P.B. (1987) Order-disorder in omphacitic pyroxenes: a model for coupled substitution in the point approximation. *American Mineralogist*, **72**, 337–344.

Fitzherbert, J.A., Clarke, C.L and Powell, R. (2003) Lawsonite–omphacite-bearing metabasites of the Pam Peninsula, NE New Caledonia: evidence for disrupted blueschist- to eclogite-facies conditions. *Journal of Petrology*, **44**, 1805–1831.

Meyre, C., De Capitani, C. and Partzsch, J.H. (1997) Solid solution model for omphacite and its application to geothermobarometry of eclogites from the Middle Adula nappe (Central Alps, Switzerland). *Journal of Metamorphic Geology*, **15**, 687–700.

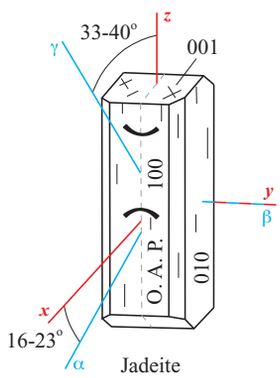
Ross, C.R. (1988) Statistical mechanical modelling of the kinetics of order–disorder in omphacite pyroxenes. *Physics and Chemistry of Minerals*, **15**, 274–282.

Smyth, J.R. (1980) Cation vacancies and the crystal chemistry of breakdown reactions in kimberlitic omphacites. *American Mineralogist*, **65**, 1185–1191.

Downloaded from https://pubs.geoscienceworld.org/books/chapter-pdf/3755496/9780903056434_ch28.pdf
by guest

Jadeite — $NaAl[Si_2O_6]$
Kosmochlor — $NaCr[Si_2O_6]$

	Jadeite Monoclinic (+)	**Kosmochlor** Monoclinic (−)
α	1.640−1.681	1.740−1.766
β	1.645−1.684	1.756−1.778
γ	1.652−1.692	1.742−1.781
δ	0.006−0.021	0.015−0.022
$2V_\gamma$	60−96°	53° ($2V_\alpha$)
Orientation	γ:*z* 32−55°	α:*z* 8−22°
	β = *y*; O.A.P. (010)	β = *y*; O.A.P. (010)
D (g/cm^3)	3.24−3.43	3.6
H	6	6
Cleavage	{110} good; (110):(1$\bar{1}$0) ~ 87°	{110} good; (110):(1$\bar{1}$0) ~ 87°
Twinning	{100}, {001} simple, lamellar	{100}, {001} simple, lamellar
Colour	Colourless, white, green, greenish blue, more rarely blue and violet; colourless in thin section	Dark emerald green; green or yellow in thin section
Pleochroism		α yellowish green β grass green γ emerald green
Unit Cell	*a* ~ 9.4 Å, *b* ~ 8.6 Å,	*a* ~ 9.5 Å, *b* ~ 8.7 Å
	c ~ 5.2 Å, β ~ 107.6°	*c* ~ 5.3 Å, β ~ 107.4°
	Z = 4; space group *C*2/*c*	
Special features	Insoluble in HCl	Insoluble in HF



Jadeite, generally associated with albite and less commonly with lawsonite, occurs in Alpine-type metamorphic rocks involving metagreywackes or blueschists. Kosmochlor is a rarer dark green mineral which may be found in Cr-rich rocks

Chemistry

The composition of jadeite does not usually depart greatly from the ideal $NaAlSi_2O_6$, and in most natural jadeites more than 80% of the *M*1 and *M*2 sites are occupied by Al and Na, respectively. The amount of Cr in jadeite is generally negligible but a few very rare chromium-rich pyroxenes are known; kosmochlor may contain as much as 83 mol% $NaCrSi_2O_6$. Pyroxenes with compositions intermediate between jadeite and diopside are discussed under omphacite (p. 122).

The composition of jadeite is intermediate between nepheline and albite but the mineral does not crystallize in the binary system $NaAlSiO_4$–$NaAlSi_3O_8$ (see Fig. 235, p. 330) or the ternary system Na_2O–Al_2O_3–SiO_2 at low pressures. Natural jadeite heated to 800°C first forms a glass which subsequently crystallizes to a mixture of nepheline and albite. Nepheline and albite have a framework structure and densities of ~2.6, the density of jadeite is ~3.3 g/cm^3. The formation of jadeite by the reactions:

$$\text{nepheline} + \text{albite} \rightarrow 2\ \text{jadeite}$$

and

$$\text{albite} \rightarrow \text{jadeite} + \text{quartz}$$

involve volume reductions, $\Delta V = -34.9$ and -17.8 cm^3/mol, respectively. The stability fields of jadeite and albite + nepheline between 1.0 and 2.5 GPa and 600 and 1200°C are shown in Fig. 99(a). At pressures above 2.9 GPa, jadeite melts congruently,

Downloaded from https://pubs.geoscienceworld.org/books/chapter-pdf/3755658/9780903056434_ch29.pdf
by guest

between 2.5 and 2.9 GPa it melts incongruently, and below 2.5 GPa it is replaced by albite and nepheline; the temperature–pressure relations for the composition $NaAlSi_3O_8$ are shown in Fig. 99b. There is complete solid solution in the experimental system $NaAlSi_2O_6$–$NaCrSi_2O_6$ at 800ºC and >1.8 GPa.

Optical and physical properties

The range of optical properties of jadeite is relatively small. The variation in refractive indices does not show any precise correlation with the replacement of Al by Fe^{3+} but some jadeites in which this substitution is relatively large are distinguished by anomalous interference colours and by very strong dispersion of the optic axes ($2V_r > 2V_v$). Kosmochlor has much higher refractive indices and is also distinguished from jadeite by its strong pleochroism (α yellowish green, β grass green, γ emerald green).

Distinguishing features

The refractive indices of jadeite are lower than those of all other pyroxenes except spodumene. Jadeite is distinguished from spodumene by its lower birefringence and higher extinction angle. Jadeite is distinguished from omphacite and Al-rich augite by its lower refractive indices and birefringence, and from aegirine by the absence of colour in thin section, higher extinction angle and lower refractive indices and birefringence. It is distinguished from actinolite by its pyroxene cleavage, higher extinction angle and lack of colour. In some jadeites the erratic variation of optic axial and extinction angles, strong dispersion, anomalous interference colours and low birefringence may lead to its confusion with zoisite, but the latter shows straight extinction and higher refractive indices.

Kosmochlor is distinguished from other monoclinic members of the pyroxene group except aegirine by the negative optic axial angle. It is distinguished from aegirine by the more intense pleochroism and lower birefringence of the latter.

Paragenesis

Jadeite, originally considered to be an uncommon pyroxene, is now recognized as a relatively common and important mineral in Alpine-type metamorphic terranes. In almost all of its known occurrences, jadeite is associated with albite. Jadeite and jadeitic pyroxenes are relatively common constituents in the metagreywackes and related rocks of regional metamorphic belts. In rocks of the blueschist facies of the Franciscan formation, California, jadeitic pyroxenes (Jd 70–90%) coexist with quartz in the metagreywackes and with omphacite or acmitic pyroxenes in the metabasites. The original bedding planes are preserved in the quartz–jadeite rocks, the other phases of which include glaucophane, lawsonite, sericite, chlorite and albite; the latter being largely replaced by jadeite. In the more highly reconstructed sediments, aragonite may be present in the jadeite-bearing rocks and sheaves and stellate prismatic groups of the jadeite pyroxene retain the original clastic outlines of the feldspar; relict grains of lawsonite may persist in the jadeite:

$$NaCaAl_3Si_5O_{16} + 2\,H_2O \rightarrow$$
plagioclase
$$NaAlSi_2O_6 + CaAl_2Si_2O_7(OH)_2.H_2O + SiO_2$$
jadeite lawsonite quartz

With increasing metamorphic grade, the jadeitic component of the pyroxene decreases and the mineral becomes more omphacitic in composition. Gabbros under similar conditions of regional metamorphism give rise to jadeite-pumpellyite-rich assemblages.

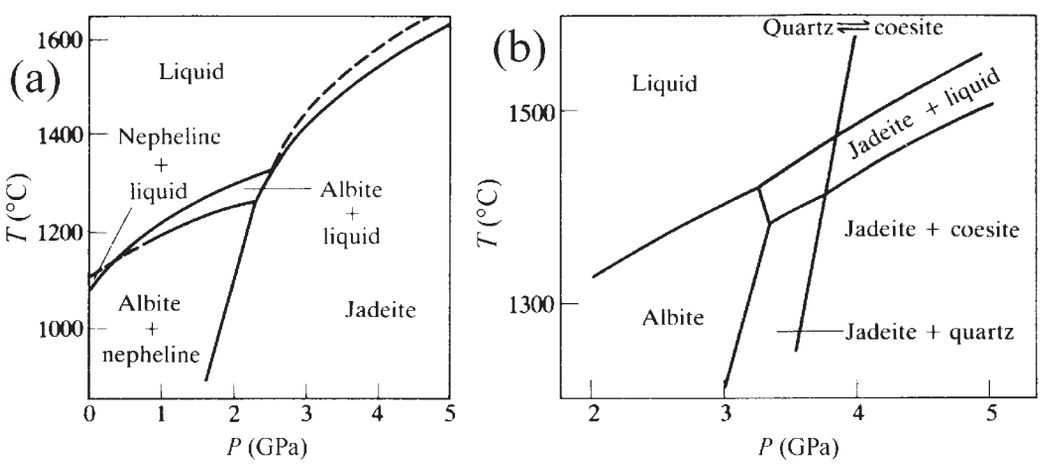


Fig. 99. Temperature–pressure relations (a) for jadeite composition, (b) for $NaAlSi_3O_8$ (albite) composition (after Bell, P.M. & Roseboom, E.H., 1969, *Min. Soc. Amer., Spec. Paper* **2**, 151–61).

Downloaded from https://pubs.geoscienceworld.org/books/chapter-pdf/3755658/9780903056434_ch29.pdf
by guest

Jadeite, in association with analcime, occurs also in veins and pods in blueschist-facies rocks, and in jadeite-bearing amygdales in regionally metamorphosed mafic lavas which may have developed from analcime amygdales during the metamorphism.

Terrestrial occurrences of kosmochlor and chromium-rich jadeitic pyroxenes include those of the jadeitites of the jade mines of Burma (Myanmar) where they are associated with chromite and sodic amphiboles (particularly eckermannite), and the chromite-bearing rocks of Williams Creek, California. Kosmochlor occurs in hexahedrite and octahedrite meteorites.

Further reading

Ballaran, T.B., Carpenter, M.A., Domeneghetti, C. and Tazzoli, V. (1998) Structural mechanisms of solid solution and cation ordering in augite-jadeite pyroxenes: I. A macroscopic perspective. *American Mineralogist*, **83**, 419–433.

Bell, P.M. and Roseboom, E.H. (1969) Melting relationships of jadeite and albite to 45 kilobars with comments on melting diagrams of binary systems at high pressures. *Mineralogical Society of America, Special Paper* **2**, 151–161.

Coleman, R.G. and Clark, J.R. (1968) Pyroxenes in the blueschist facies of California. *American Journal of Science*, **266**, 43–59.

Okay, A.I. (2002) Jadeite–chloritoid–glaucophane–lawsonite blueschists in northwest Turkey: unusually high *P/T* ratios in continental crust. *Journal of Metamorphic Geology*, **20**, 757–768.

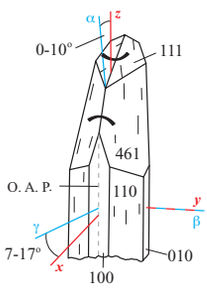
Popp, R.K. and Gilbert, M.C. (1972) Stability of acmite–jadeite pyroxenes at low pressure. *American Mineralogist*, **57**, 1210–1231.

Williams, D.W. and Kennedy, G.C. (1970) The melting of jadeite to 60 kilobars. *American Journal of Science*, **269**, 481–488.

Downloaded from https://pubs.geoscienceworld.org/books/chapter-pdf/3755658/9780903056434_ch29.pdf
by guest

Aegirine — $NaFe^{3+}[Si_2O_6]$
Aegirine-augite — $(Na,Ca)(Fe^{3+},Fe^{2+},Mg)[Si_2O_6]$

Aegirine
Monoclinic (−)



Aegirine-augite
Monoclinic (−)(+)

α	1.750−1.776	1.700−1.760
β	1.780−1.820	1.710−1.780
γ	1.795−1.836	1.730−1.813
δ	0.040−0.060	0.030−0.050
$2V_\alpha$	60−70º	70−110º
Orientation	α:*z* 0−10º (in β obtuse); O.A.P. (010)	α:*z* 0−20º (in β acute); O.A.P. (010)
D (g/cm^3)	3.55−3.60	3.40−3.60
H	6	6
Cleavage	{110} good; {100} parting; (110):(1$\bar{1}$0) ~ 87º	{110} good; {100} parting; (110):(1$\bar{1}$0) ~ 87º
Twinning	{100} simple and lamellar, common	{100} simple and lamellar, common
Colour	Dark green to greenish black, occasionally reddish brown; pale to dark green and yellowish green in thin section	Dark green to black, green, yellow-green or brown; pale green, green and yellowish green in thin section
Pleochroism	α emerald-green, deep green β grass-green, deep green γ brownish green, yellowish brown	α bright green, deep green, brownish green β yellowish green γ yellow, greenish brown, brownish green
Unit Cell	*a* ~ 9.7 Å, *b* ~ 8.8 Å, *c* ~ 5.3 Å β ~ 107.5º Z = 4; space group *C*2/*c*	*a* ~ 9.7−9.75 Å, *b* ~ 8.8−8.9 Å, *c* ~ 5.25−5.3 Å β ~ 105−107º Z = 4; space group *C*2/*c*
Special features	Insoluble in HCl	

The names aegirine and acmite have both been used to describe clinopyroxenes close to $NaFe^{3+}Si_2O_6$ in composition. The name aegirine, originally restricted to the green-to-black crystals bluntly terminated by faces of the form {111}, is now used to describe all pyroxenes with this composition irrespective of their colour or crystal form. The name aegirine-augite is used to describe green, highly pleochroic pyroxenes with higher α:*z* extinction angles and compositions intermediate between aegirine and augite. The $NaFe^{3+}Si_2O_6$ content of a pyroxene is described traditionally using the symbol Ac.

Downloaded from https://pubs.geoscienceworld.org/books/chapter-pdf/3755731/9780903056434_ch30.pdf
by guest

Chemistry

Aegirines and aegirine-augites show a wide range of chemical composition but in the majority the main replacement is $NaFe^{3+} \leftrightarrow Ca(Mg,Fe^{2+})$. The content of Al in members of the series is small and in aegirine the replacement of Si by Al is often negligible. Some aegirine-augites have an unusually high content of vanadium (as high as 14.5 wt.% V_2O_5) and of manganese (up to 7.2 wt.% MnO) which are equivalent to 0.43 V^{3+} and 0.25 Mn atoms pfu, respectively. Small amounts of Zr and Cl may also be present. An aegirine with up to ~7.0 wt.% ZrO_2 has been reported and it is possible that in this mineral there is a coupled substitution in the octahedral sites of the form $(Fe,Mg)^{2+} + Zr^{4+} \leftrightarrow 2Fe^{3+}$.

Aegirine is readily synthesized from the appropriate molecular proportions of SiO_2, Fe_2O_3 and $Na_2CO_3.H_2O$ fused with NaCl; it melts incongruently at 990ºC with the formation of hematite (and magnetite) and liquid. The incongruent melting in the presence of water is relatively insensitive to total pressure. The melting curves have low dT/dP values, −50ºC/GPa and ~0ºC/GPa under HM and QFM conditions, respectively (Fig. 100a). Reducing the partial pressure of oxygen leads to a marked lowering of the high-temperature stability of aegirine. At conditions controlled by the iron–wüstite and wüstite–magnetite buffers, aegirine ceases to be stable and is replaced by an arfvedsonite–riebeckite solid solution.

The $NaFe^{3+}Si_2O_6$–$CaMgSi_2O_6$ solid solutions melt incongruently at atmospheric pressure. The incongruent melting range shows a gradual decrease as the diopside content increases, and the range is considerably smaller at higher pressures (Fig. 100b).

Optical and physical properties

The refractive indices of the aegirine–augite series vary linearly with composition (Fig. 101), correlation is best for members rich in Fe^{3+}; for others it is less precise due to Mg-for-Fe^{2+} replacement. The extinction angle α:z (in obtuse angle β) is 10º for the pure $NaFe^{3+}Si_2O_6$ end-member, the angle decreases to zero at a composition of approximately $Fe^{3+}_{0.7}$, and with further replacement of Fe^{3+} by (Mg,Fe^{2+}) the extinction angle (in acute angle β) increases and at a composition of about $Fe^{3+}_{0.2}$ is 20º (Fig. 101).

Aegirines and aegirine-augite commonly show colour zoning, and varying pleochroism and extinction angles; the zoning, which may have an hourglass pattern, is usually from a more augite-rich core to a more aegirine-rich margin. Aegirine may occur in stout prismatic crystals, slender needles elongated parallel to the z axis, or more rarely in bundle-like or felted aggregates of minute fibres (Fig. 102).

Distinguishing features

Aegirine is distinguished from other pyroxenes by its small α:z extinction angle, high refractive indices, high birefringence, negative optic axial angle and strong pleochroism, and aegirine-augites by their higher α:z extinction angles, large optic axial angles and characteristic strong pleochroism. Aegirine and aegirine-augite may resemble some alkali amphiboles; in basal and near-basal sections the pyroxene cleavage angle is diagnostic and in prismatic sections the pleochroism is sufficiently characteristic to distinguish them from arfvedsonite and

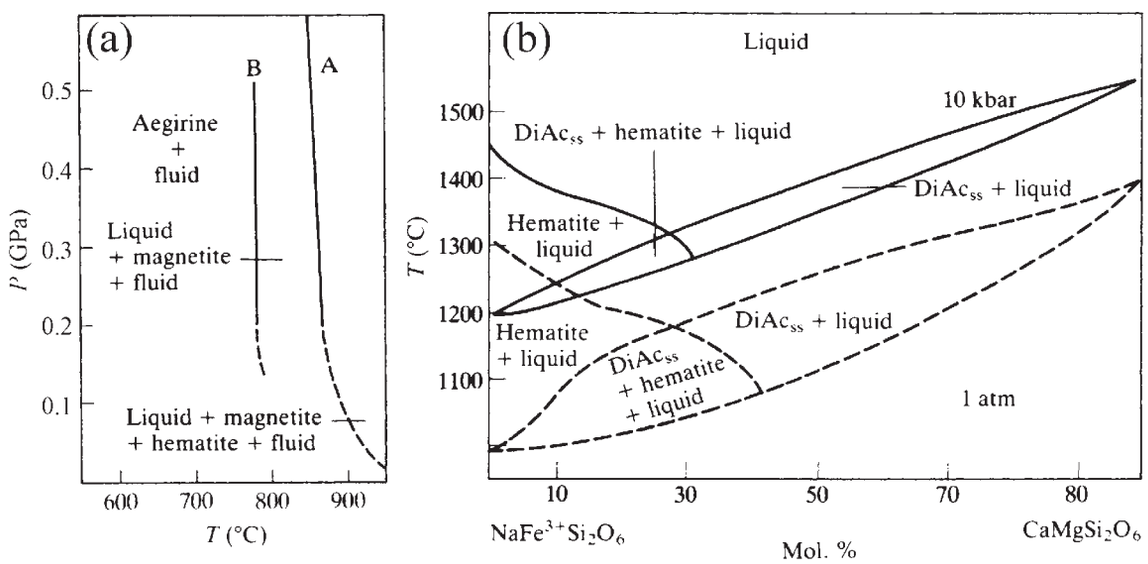


Fig. 100. (a) A P_{total}–T diagram for aegirine + excess water: (A) magnetite–hematite buffer; (B) quartz–fayalite–magnetite buffer (after Bailey, 1969). (b) Melting curves for $NaFe^{3+}Si_2O_6$–$CaMgSi_2O_6$, at 1 atm (broken lines) and 10 kbar (full lines) (after Cassie, 1971, *Carnegie Inst. Washington, Ann. Rept. Dir. Geophys. Lab.*, 1969–70, 170–5).

Downloaded from https://pubs.geoscienceworld.org/books/chapter-pdf/3755731/9780903056434_ch30.pdf
by guest

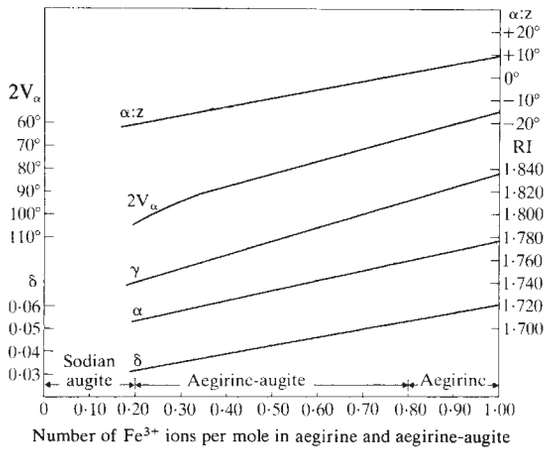


Fig. 101. The relation between the optical properties and the number of Fe^{3+} ions per mole in aegirine and aegirine-augite (after Deer, W.A. *et al.*, 1978, *Single-Chain Silicates*. Rock-Forming Minerals, 2nd Edn. **2A**, Geological Society, London. 668 pp.)

riebeckite. The length-fast optical character of aegirine and aegirine-augite distinguishes them from other amphiboles. Aegirine and aegirine-augite have refractive indices, birefringence, α:*z* extinction angles, optical axial angles, colour and pleochroism comparable with those of iron-rich epidotes. They have stronger absorption colours, however; this reduces the apparent birefringence, and they can generally be distinguished from epidote by the higher interference colours of the latter mineral. In sections showing one cleavage and small extinction angles the optic axial plane is parallel to the cleavage in aegirine and aegirine-augite and normal to the cleavage in epidote. Aegirine and aegirine-augites are distinguished from tourmaline by their biaxial character, higher refringence and birefringence, and better cleavage.

Paragenesis

Aegirine and aegirine-augite are pre-eminently the products of the crystallization of alkaline magmas, and many peralkaline rocks ($Na_2O + K_2O > Al_2O_3$) consist essentially of aegirinic pyroxene (+ sodium-rich amphiboles) and alkali feldspar with either nepheline or quartz. The sodium-rich pyroxenes are thus common constituents of alkali granites, quartz syenites, syenites and nepheline syenites and their associated pegmatites and veins. They are present in many ultra-alkaline basic rocks, malignite, ijolite and melteigite, and tinguaites and phonolites. In these alkaline rocks the sodium-rich pyroxenes are associated with arfvedsonitic amphiboles, magnesioriebeckite, melanite, sodalite, astrophyllite, aenigmatite, catapleiite and låvenite. In most of these rocks, aegirine forms late in the crystallization sequence and commonly mantles earlier augitic or sodium-rich pyroxenes; it is not a product of reaction between these earlier phases and residual liquids. Aegirine-augites are found in regionally metamorphosed rocks, occurring in glaucophane- and riebeckite-bearing schists. Aegirine occurs in some quartzose rocks and in granulites.

Further reading

Bailey, D.K. (1969) The stability of acmite in the presence of H_2O. *American Journal of Science*, **267A** (Schairer vol.), 1–16.

Larsen, L.M. (1976) Clinopyroxenes and coexisting mafic minerals from the alkaline Ilímaussaq intrusion, South Greenland. *Journal of Petrology*, **17**, 258–290.

Pilonen, P.C., McDonald, A.M. and Lalonde, A.E. (1998) The crystal chemistry of aegirine from Mont Saint-Hilaire, Quebec. *The Canadian Mineralogist*, **36**, 77–91.

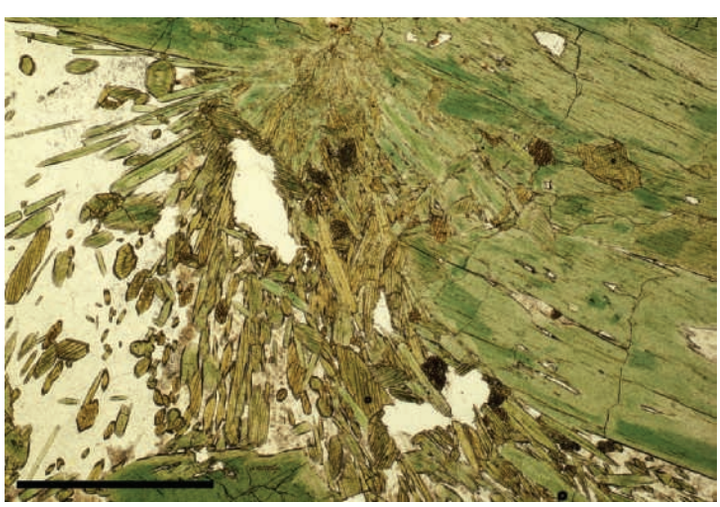


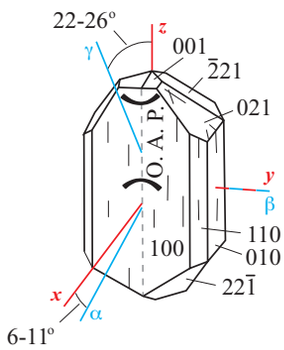
Fig. 102. Aegirine in sodalite syenite, Ilímaussaq intrusion, West Greenland (ppl, scale bar 1 mm) showing the typical brownish yellow colour and pleochroism diagnostic of sodium-bearing pyroxenes (W.S. MacKenzie collection, courtesy of Pearson Education).

Downloaded from https://pubs.geoscienceworld.org/books/chapter-pdf/3755731/9780903056434_ch30.pdf
by guest

Spodumene $LiAl[Si_2O_6]$

Monoclinic (+)

α	1.648–1.662
β	1.655–1.669
γ	1.662–1.679
δ	0.014–0.027
$2V_\gamma$	58–68º
Orientation	γ:*z*, 20–26º; β = *y*; O.A.P. (010)
D (g/cm^3)	3.03–3.23
H	6½–7
Cleavage	{110} good; {100}, {010} partings; (110):(1$\bar{1}$0) ~ 87º
Twinning	{100} common
Colour	Colourless, greyish white, pale amethyst, pale green, yellowish emerald-green (hiddenite), lilac (kunzite); usually colourless in thin section
Pleochroism	*Kunzite*: α purple, γ colourless *Hiddenite*: α green, γ colourless
Unit cell	*a* 9.45 Å, *b* 8.39 Å, *c* 5.215 Å, β 110º, Z = 4; space group *C*2/*c*
Special features	Insoluble in acids



Spodumene occurs typically in Li-rich granite pegmatites, where it is commonly associated with lepidolite. The naturally occurring lithium-bearing clinopyroxene is α-spodumene. The other polymorphs are β- and γ-spodumene; transitions between these three forms are reconstructive. α-Spodumene is the low-temperature phase with *C*2/*c* space group symmetry. β-Spodumene is a high-temperature tetragonal form which is isostructural with the silica polymorph, keatite. The third phase has hexagonal symmetry and may be isostructural with β-quartz. The α- → β-spodumene transition at atmospheric pressure occurs between 530 and 550ºC. For the spodumenes $LiScSi_2O_6$ and $ZnSiO_3$ a displacive transformation takes place at high pressure to a form with space group $P2_1/c$.

Spodumene, with the exception of minor Li ↔ (Na,K), shows little variation from the ideal formula, $LiAlSi_2O_6$. In some spodumenes there is a small amount of Si in excess of 2 atoms pfu that may represent SiO_2 originally present in solid solution in β-spodumene. The common inclusions of albite and mica may also account for the excess Si. Spodumene alters readily, particularly as the result of late alkaline hydrothermal activity, the common product consisting of a mixture of eucryptite (hexagonal $LiAlSiO_4$) and albite.

There is little variation in the optical properties of spodumene except for the higher birefringence of the more sodium-rich compositions. The green colour of the hiddenite variety of spodumene is due to small amounts of Cr, and the pink colour of the kunzite variety to the presence of small amounts of Mn in association with a low Fe:Mn ratio.

Spodumene is distinguished from other clinopyroxenes, by the small γ:*z* extinction angle. It is distinguished from aegirine-augite by the strong pleochroism and higher refractive indices of the latter.

Spodumene is a characteristic mineral of the lithium-rich granitic pegmatites. Common associates include quartz, petalite, albite, lepidolite and beryl. Crystals up to 80 cm in length occur in the North Carolina spodumene pegmatite belt.

Further reading

Arit, T. and Angel, R.J. (2000) Displacive transformations in *C*-centred clinopyroxenes; spodumene $LiScSi_2O_6$ and $ZnSiO_3$. *Physics and Chemistry of Minerals*, **27**, 719–731.

Černý, P. and Ferguson, R.B. (1972) The Tanco pegmatite at Bernic Lake, Manitoba. *In* Petalite and spodumene relations. *The Canadian Mineralogist*, **11**, 660–678.

Charoy, B., Lhote, F. and Dusausoy, Y. (1992) The crystal chemistry of spodumene in some granitic aplite-pegmatites of northern Portugal. *The Canadian Mineralogist*, **30**, 639–651.

Drysdale, D.J. (1975) Hydrothermal synthesis of various spodumenes. *American Mineralogist*, **60**, 105–110.

Downloaded from https://pubs.geoscienceworld.org/books/chapter-pdf/3755939/9780903056434_ch31.pdf
by guest

Triclinic (−)

α	1.616−1.640
β	1.628−1.650
γ	1.631−1.653
δ	0.013−0.014
$2V_\alpha$	36−60°
Orientation	α:*z* = 30−44°, β:γ ~ 0−5°; O.A.P. approx. (010)
D (g/cm^3)	2.86−3.09
H	4½–5
Cleavage	{100} perfect; {001} and {102} good; on (010) sections (100):(001) = 84½°, (100):(102) = 70°
Twinning	Common; twin axis [010], composition plane (100)
Colour	Usually white, sometimes colourless, grey or very pale green; colourless in thin section
Unit cell	*a* 7.94 Å, *b* 7.32 Å, *c* 7.07 Å, α 90.03°, β 95.37°, γ 103.43°
	Z = 6; space group $P\bar{1}$
Special features	Decomposed by concentrated HCl

Although it is a single-chain silicate, wollastonite is not a pyroxene. It has a three-tetrahedra repeat structure rather than the two tetrahedra repeat of the pyroxenes, and has been classified as a pyroxenoid. Wollastonite occurs typically in metamorphosed impure limestones.

Structure

There are two principal $CaSiO_3$ structures. Pseudowollastonite (β-$CaSiO_3$), the high-temperature form, is triclinic (pseudo-orthorhombic) and contains isolated trisilicate rings. Wollastonite (α-$CaSiO_3$), the low-temperature form, is a chain silicate for which a number of closely related polytypic structures (monoclinic and triclinic) have been reported (Fig. 103). The most common of these are wollastonite-2*M* and wollastonite-*Tc* (Table 19). The wollastonites are not related structurally to the pyroxene group: they have a different type of infinite-chain structure, with three tetrahedra per unit cell arranged parallel to *y*, this repeat unit consisting of a pair of tetrahedra joined apex-to-apex as in the $[Si_2O_7]$ group, alternating with a single tetrahedron with one edge parallel to the chain direction. Other chain silicates with similar structures include bustamite, ferrobustamite and pectolite. Longer repeats along the chain produce related structures

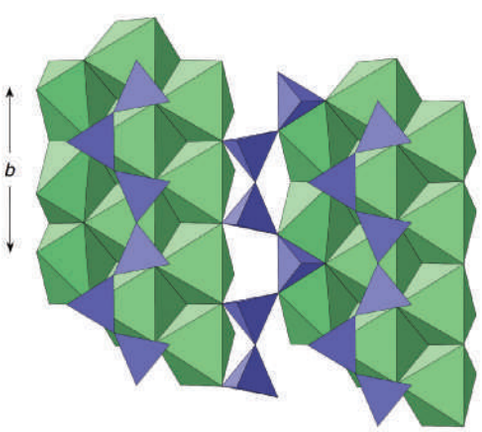


Fig. 103. Part of the structure of wollastonite-*Tc* showing chains of Si−O tetrahedra (blue) parallel to *y*, linked laterally by distorted Ca−O octahedra (green) (after Ohashi, Y. & Finger, L.W., 1978, *Amer. Min*., **63**, 274−88, but with cell axes chosen here to conform with those given above and in Table 19).

Downloaded from https://pubs.geoscienceworld.org/books/chapter-pdf/3755941/9780903056434_ch32.pdf
by guest

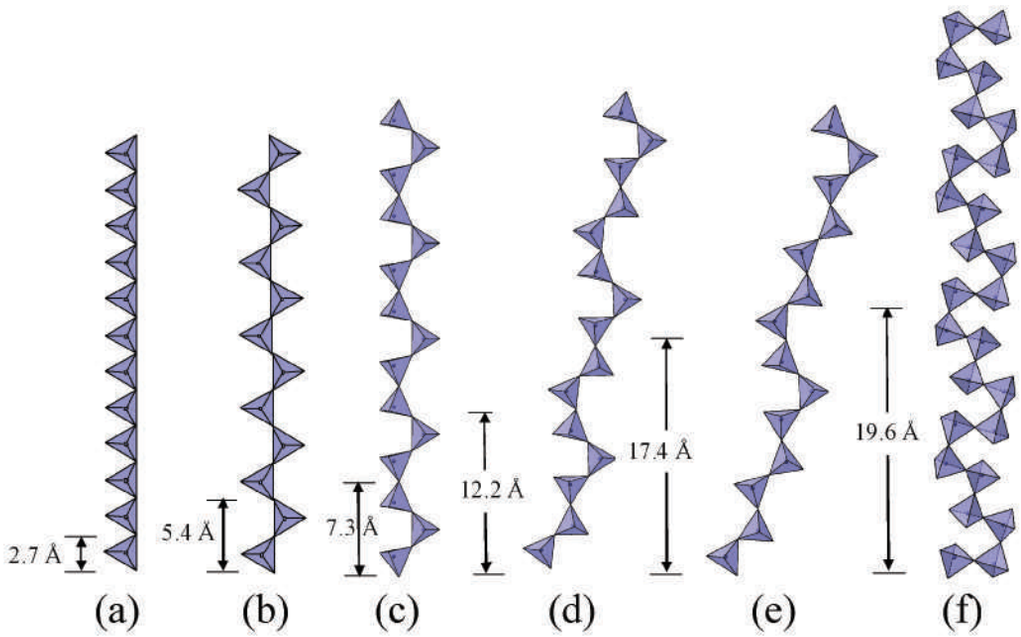


Fig. 104. Schematic diagram of possible arrangements of chains of linked SiO_4 tetrahedra of composition $(SiO_3)_n$ with repeats of: (a) one tetrahedron, (b) two tetrahedra (fully extended chain; high temperature pyroxene), (c) three tetrahedra (wollastonite), (d) five tetrahedra (rhodonite), and (e) seven tetrahedra (pyroxmangite). Also (f) alamosite ($PbSiO_3$). (a–e after Liebau, F., 1959, *Acta Cryst*., **12**, 177–81. Fig. produced by M.D. Welch).

including rhodonite, aenigmatite and sapphirine (see Fig. 104). Wollastonite-2*M* is related to wollastonite-*Tc* by a simple stacking modification. The cell parameters for the three polymorphs are listed in Table 19.

Chemistry

Although it is normally fairly pure $CaSiO_3$, wollastonite can accept considerable amounts of Fe and Mn replacing Ca. Natural manganoan and ferroan wollastonites have been reported from the contact metamorphism and metasomatism of impure limestones (Table 20, analysis 3). Wollastonite can be synthesized readily from its component oxides, or from hydrous gels via xonotlite, $Ca_6(Si_6O_{17})(OH)_2$, which breaks down on heating to yield wollastonite. It forms a solid solution in the series $CaSiO_3$–$FeSiO_3$, but there is a break in this series at around $Ca_{0.90}Fe_{0.10}SiO_3$, the limit of the wollastonite structure. More iron-rich compositions have a bustamite-type structure. For compositions on the join $CaMgSi_2O_6$ (diopside)–$CaFeSi_2O_6$ (hedenbergite), wollastonite crystallizes at high temperatures but is converted to wollastonite + hedenbergite at low temperatures. This may have occurred in the fayalite ferrodiorite of the Skaergaard intrusion, giving rise to small interlocking grains of pyroxene.

Wollastonite is commonly formed as a result of the reaction of quartz and calcite in metamorphosed limestones; the univariant P_{CO_2}–T curve for the reaction:

$$CaCO_3 + SiO_2 \rightleftharpoons CaSiO_3 + CO_2$$

is given in Fig. 304, p. 459. The reaction

$$\text{wollastonite} + \text{calcite} \rightleftharpoons \text{spurrite} + \text{carbon dioxide}$$

has also been investigated experimentally; at 33 MPa CO_2 pressure the reaction takes place at about 1000ºC. The P–T curve for the reaction:

$$\text{wollastonite} + \text{monticellite} \rightleftharpoons \text{åkermanite}$$

lies between 700 and 750ºC in the pressure range 0.2–0.4 GPa, i.e. the P–T curve for this reaction is nearly parallel to the pressure axis. The inversion wollastonite–pseudowollastonite takes place at about

Table 19. Cell parameters of $CaSiO_3$.

	a (Å)	*b* (Å)	*c* (Å)	α	β	γ	Space group	Z
Wollastonite-*Tc*	7.94	7.32	7.07	90.03º	95.37º	103.43º	$P\bar{1}$	6
Wollastonite-2*M*	15.43	7.32	7.07	90º	95.40º	90º	$P2_1/a$	12
Pseudowollastonite	6.90	11.78	19.65	90º	90.30º	90º	$P1$ or $P\bar{1}$	24

Downloaded from https://pubs.geoscienceworld.org/books/chapter-pdf/3755941/9780903056434_ch32.pdf
by guest

Table 20. Wollastonite analyses.

	1	2	3	Numbers of ions on the basis of 18 O								
					1			2			3	
SiO_2	51.56	50.78	49.37	Si	5.976	}		5.928	}		5.948	}
Al_2O_3	0.15	0.54	0.20	Al	0.021	}	6.01	0.074	}	6.01	0.028	} 6.01
Fe_2O_3	0.21	0.13	0.42	Fe^{3+}	0.018	}		0.011	}		0.038	}
FeO	0.08	0.72	5.32	Mg	0.045	}		0.019	}		0.153	}
MnO	0.06	0.53	9.18	Fe^{2+}	0.007	}		0.070	}		0.536	}
MgO	0.26	0.11	0.85	Mn	0.006	}		0.053	}		0.937	}
CaO	47.73	46.62	33.93	Na	0.004	}	5.99	0.040	}	6.03[a]	–	} 6.01
Na_2O	0.02	0.18	–	Na	5.928	}		5.831	}		4.380	}
K_2O	0.00	0.04	–	K	–	}		0.006	}		–	}
H_2O^+	0.03	0.05	0.37									
H_2O^-	0.02	0.02	0.13									
Total	100.12	99.89	99.77									

1 White wollastonite-2*M* (parawollastonite) associated with vesuvianite, blue calcite and diopside, Crestmore, California, USA (Deer, W.A., Howie, R.A. & Zussman, J., 1978, *Rock Forming Minerals*, vol. 2A, Longman).
2 Wollastonite, wollastonite ijolite, Oldoinyo Lengai, Tanzania (Dawson, J.B. & Sahama, Th.G., 1963, *Schweiz. Min. Petr. Mitt.*, **43**, 131–33. Includes SrO 0.10, TiO_2 0.07%).
3 Manganoan wollastonite, calcareous zone of hornfels in Mn ore deposit, Hijikuzu mine, Japan (Nambu, M., *et al.*, 1971, *Min. J. Japan*, **7**, 180–201).

[a] Includes Ti 0.006, Sr 0.007.

1120ºC but this temperature is raised to 1368ºC by the solid solution of 21% diopside in wollastonite.

Optical and physical properties

Typical values of the optical properties of pure $CaSiO_3$ in the various structural modifications are listed in Table 21.

The introduction of iron increases the refractive indices and the optic axial angle of wollastonite. After the change in the $CaSiO_3$–$FeSiO_3$ series at around $Ca_{0.90}Fe_{0.10}SiO_3$, to the bustamite-type structure $2V_\alpha$ increases more rapidly. The effect of the entry of manganese is in general similar to that of iron, up to a structural discontinuity at $Ca_{0.75}Mn_{0.25}SiO_3$.

Distinguishing features

Wollastonite commonly occurs as bladed or fibrous crystal masses or, rarely, as tabular, frequently twinned or acicular single crystals. In thin section, wollastonite differs from tremolite and pectolite in its weaker birefringence and its variable sign of elongation ($\beta \parallel y$); diopside, with which it is often associated, has higher relief, higher 2V and is optically positive. The three cleavages of wollastonite may also be noticeable. The distinction between wollastonite-*Tc* and wollastonite-2*M* is based on the extinction angle β:*y*, which is ~4º in wollastonite-*Tc* and 0º in wollastonite-2*M*. These two forms may also be distinguished by X-ray diffraction methods.

Paragenesis

Wollastonite is a common mineral of metamorphosed limestones and normally occurs as the triclinic polytype, wollastonite-*Tc*. Wollastonite-2*M*, although it may occur in the same paragenesis, is rarer. Wollastonite may occur in contact-altered calcareous sediments where the Si is metasomatically introduced, and also in the invading igneous rocks as the result of contamination. In most of these occurrences it is the result of the reaction $CaCO_3 + SiO_2 \rightarrow CaSiO_3 + CO_2$ (Fig. 303, p. 458); in some

Table 21. Optical properties of $CaSiO_3$.

	α	β	γ	δ	α:*z*	β:*y*	Sign
Wollastonite-*Tc*	1.618	1.630	1.632	0.014	39º	4º	(–)
Wollastonite-2*M*	1.618	1.630	1.632	0.014	38º	0º	(–)
Pseudowollastonite	1.610	1.611	1.654	0.044	9º	–	(+)

Downloaded from https://pubs.geoscienceworld.org/books/chapter-pdf/3755941/9780903056434_ch32.pdf
by guest

circumstances the CO_2 pressure may be effectively reduced, either by dilution by another volatile component or by the escape of CO_2 through fissures, and under these conditions wollastonite may form at somewhat lower temperatures than those indicated. In the progressive metamorphism of siliceous dolomites, the early stages of the sequence are talc-tremolite-diopside-forsterite-wollastonite-periclase-monticellite, the formation of wollastonite normally approximating to the highest grade of contact metamorphism against a granite. Wollastonite may occur in regionally metamorphosed rocks of appropriate composition.

Wollastonite occurs also in some alkaline igneous rocks, as in the Alnö alkaline complex, Sweden, the ijolite alkaline rocks of East Africa and in wollastonite phonolites. In regionally metamorphosed rocks, wollastonite may occur in the amphibolite and granulite facies; wollastonite-*Tc* has also been recorded as acicular crystals in the Allende chondritic meteorite. Pseudowollastonite is rare but has been reported as a natural occurrence in pyrometamorphosed rocks in southwest Iran, where sediments were baked by the burning of hydrocarbon seepages in prehistoric times; it is common in slags and glasses. Wollastonite is an important industrial mineral with uses in the ceramics industry, for metal, plastic and paint production and friction products such as brake linings.

Further reading

Bowen, N.L., Schairer, J.F. and Posnjak, E. (1933) The system CaO-FeO-SiO_2. *American Journal of Science*, Series 5, **26**, 193–283.

Duzs-Moore, A., Leavens, P.B., Jenkins, R.E. and Altounian, N.M. (2003) Wollastonite fom the Sterling Hill Fe-Zn-Mn ore body, Ogdensburg, New Jersey. *Mineralogy and Petrology*, **79**, 225–241.

Harker, R.I. and Tuttle, O.F. (1956) Experimental data on the P_{CO_2}-T curve for the reaction: calcite + quartz $\rightleftharpoons$ wollastonite + carbon dioxide. *American Journal of Science*, **254**, 239–256.

Sabine, P.A. (1975) Refringence of iron-rich wollastonite. *Bulletin of the Geological Survey of Great Britain*, No. 52, 65–67.

Downloaded from https://pubs.geoscienceworld.org/books/chapter-pdf/3755941/9780903056434_ch32.pdf
by guest

Amphibole Group

Introduction

Members of the amphibole group of minerals occur in a wide range of $P-T$ environments and are common constituents of both igneous and metamorphic rocks. Among igneous rocks they are found in all the major groups ranging from ultrabasic to acid and alkaline types, but are particularly common constituents of the intermediate members of the calc-alkali series. Amphiboles occur characteristically in plutonic rocks and in general are relatively unimportant minerals of volcanic rocks. Amphiboles crystallize in a large variety of regionally metamorphosed rocks formed under conditions ranging from the greenschist to lower granulite facies. They occur less commonly in the environment of contact metamorphism but nevertheless are not uncommon in contact-metamorphosed limestones, dolomites and other calcium-rich sediments.

Structure

The essential feature of the structures of all amphiboles is the presence of (Si,Al)−O tetrahedra linked to form chains which have double the width of those in pyroxenes and have the composition $(Si,Al)_4O_{11}$ (Fig. 105a and c). These chains repeat along their length at intervals of approximately 5.3 Å and this defines the c parameter of the unit cell. The apical oxygens of the tetrahedra of chains (a) and (c) are below and above a ribbon of M−O octahedra as illustrated in Fig. 105b. The composite 'sandwiches' so formed are shown end-on outlined (top left) in Fig. 106 and are sometimes referred to as 'I-beams'. These are linked laterally by other cations ($M4$) and in some amphiboles by additional cations at a site labelled A and shown in Fig. 106. Unshared oxygens of the octahedral sheet form (OH) groups. A perspective view of the structure is shown in Fig. 107.

The sizes of the cations at $M1$, $M2$, $M3$ and $M4$ determine the way in which they are surrounded by oxygens of the $(Si,Al)O_4$ chains, and this in turn determines the positions of a pair of chains relative to one another. In most cases the stacking of chains is such as to produce a monoclinic cell, as for example in tremolite, $Ca_2Mg_5Si_8O_{22}(OH)_2$ with $M1 = M2 = M3 =$ Mg, and $M4$ = Ca, which has a 9.84 Å, b 18.05 Å, c 5.275 Å, β 104.7º; Z = 2.

For amphiboles in which the $M4$ site contains predominantly (Mg,Fe) rather than the larger (Ca,Na)

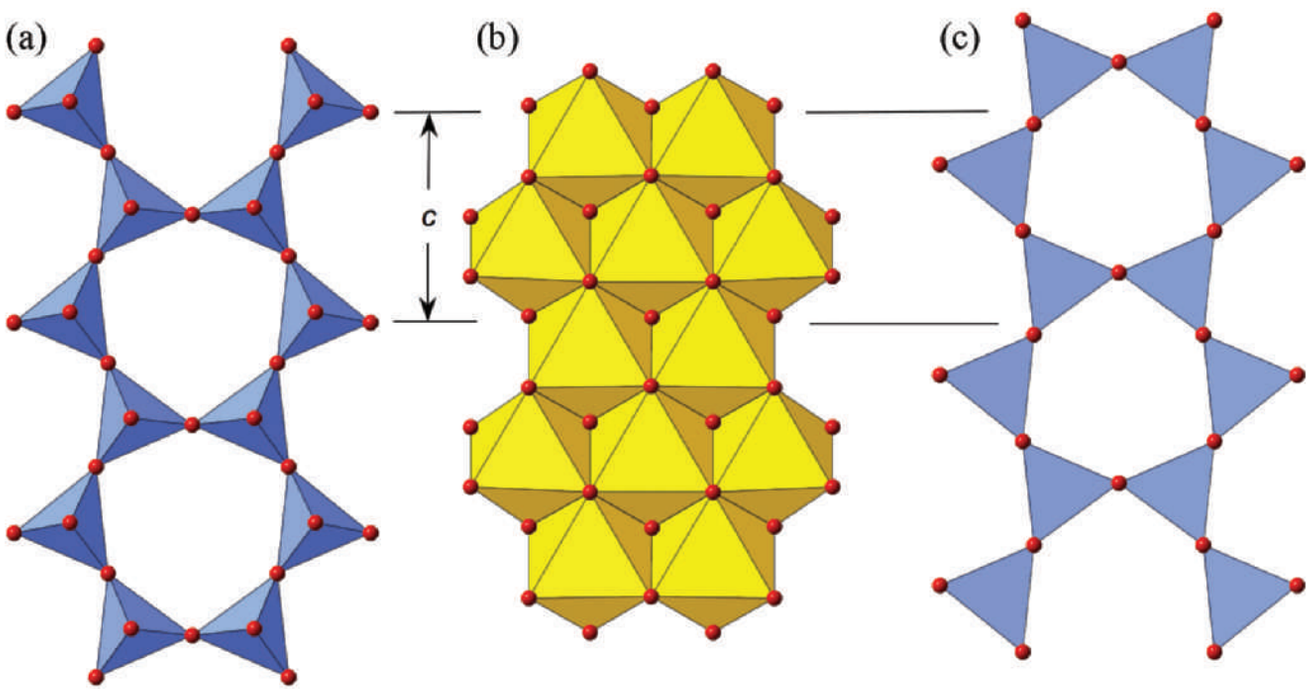


Fig. 105. (a and c) Idealized double chains of tetrahedra which form an essential parts of the amphibole structure. (b) Ribbon of linked octahedra, under and above which are attached chains (a) and (c).

Downloaded from https://pubs.geoscienceworld.org/books/chapter-pdf/3756010/9780903056434_ch33.pdf
by guest

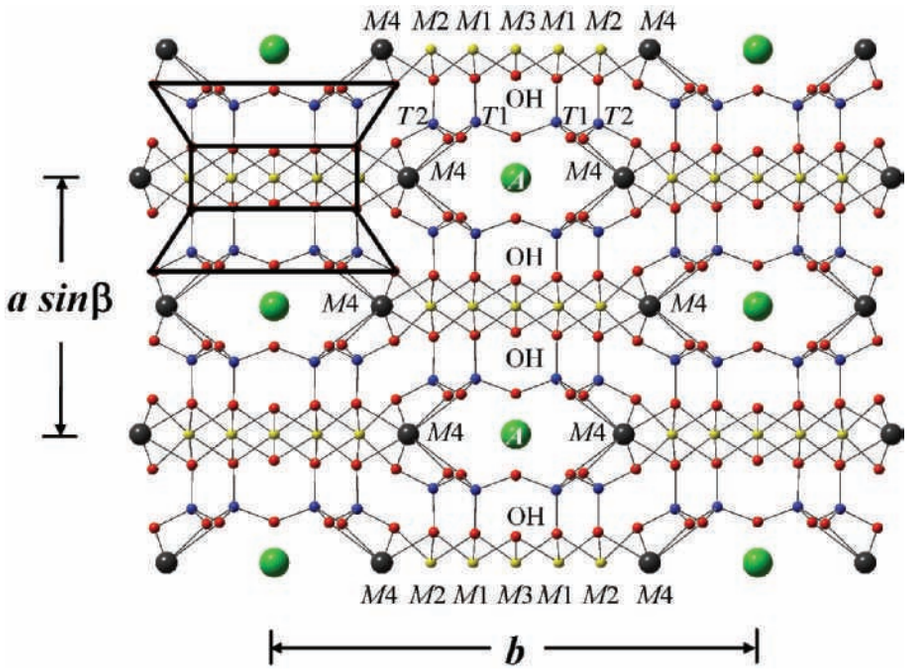


Fig. 106. Projection along *z* of an idealized amphibole structure, showing the amphibole chains and four distinct cation sites *M*1, *M*2, *M*3 and *M*4. The latter are in oxygen polyhedra, which also form bands parallel to *z*. The *A* site, which is vacant in many amphiboles is also shown (green). Areas such as that outlined are often referred to as I-beams and are used to simplify diagrams of pyroxene and amphibole structures (Cameron, M. and Papike, J.J. (1979). *Fortschritte Min.*, **57**, 28–67. Fig produced by M.D. Welch).

cations, the mode of stacking of pairs of chains can result in either a monoclinic cell as in cummingtonite, $(Mg,Fe^{2+})_7Si_8O_{22}(OH)_2$, or an orthorhombic cell as in anthophyllite, $(Mg,Fe^{2+})_7Si_8O_{22}(OH)_2$, which has Z = 4 and cell parameters $a \sim 18.6$ Å, $b \sim 18.0$ Å, $c \sim 5.3$ Å.

The relationships between the monoclinic and orthorhombic cells are similar to those found in pyroxenes, i.e. the *b* and *c* cell edges are unchanged but *a* (orthorhombic) ~ *2a* sin β (monoclinic).

In tremolite and cummingtonite the *A* sites are vacant, but in some amphiboles these sites are either partially or completely occupied and such amphiboles contain more than two (Ca,Na,K) ions per formula unit. In structural formulae the vacant *A* site is denoted by the symbol □.

The presence of similar but not identical sites in the amphibole structure (i.e. *M*1, *M*2, *M*3 octahedra; *T*1, *T*2 tetrahedra: Fig. 106) gives scope for the ordering of cations among them. In the tetrahedra, Al strongly

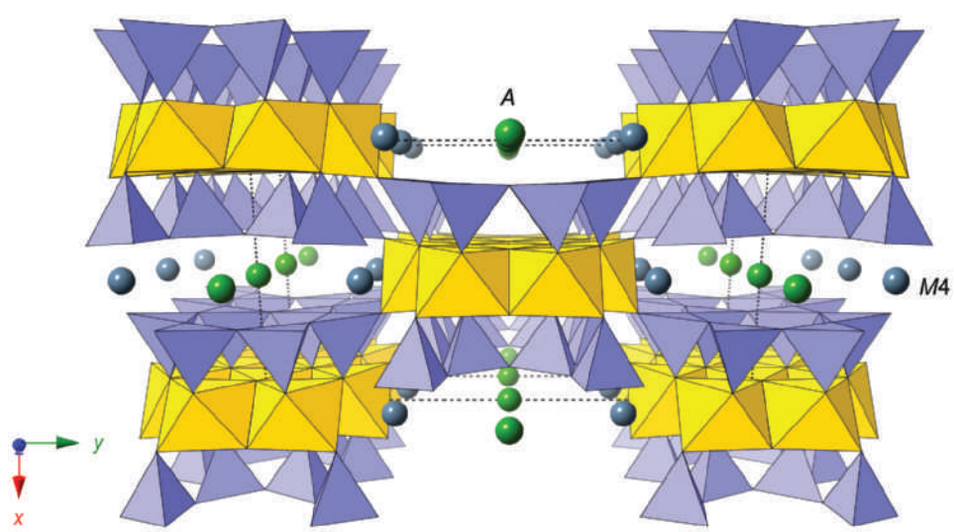


Fig. 107. The structure (perspective from a direction close to the *z* axis) of the amphibole tremolite, $Ca_2Mg_5Si_8O_{22}(OH)_2$. (CrystalMaker image). Yellow: Mg–(O,OH) octahedra; blue: Si–O tetrahedra; blue spheres: Ca in the *M*4 sites; green spheres: the *A* sites; vacant in tremolite.

Downloaded from https://pubs.geoscienceworld.org/books/chapter-pdf/3756010/9780903056434_ch33.pdf
by guest

prefers *T*1 and in octahedra Al and Fe^{3+} prefer *M*2. Preferences of Fe^{2+} as between the *M*1, *M*2, *M*3, *M*4 sites vary from one amphibole subgroup to another.

The structures of amphiboles (double-chain), pyroxenes (single-chain) and micas (layers) are closely related and it is therefore not surprising that faults in their formation can and do occur. Thus in many amphiboles electron microscopy has revealed small regions of single-chain and multiple-chain (triple, quadruple, etc.) structure. The frequency of such defects is generally not sufficient to produce a significant departure from the amphibole chemical formula.

Chemistry

A general amphibole formula may be written as $A_{0-1}B_2C_5T_8O_{22}(OH,F)_2$, where A, B, C and T cations are, respectively, in the (*A*), (*M*4), (*M*1, *M*2 and *M*3) octahedral and (*T*) tetrahedral sites. The most common cations which may enter each structural site are: *A* = Na, K; *B* = Na, Ca, Mg, Fe^{2+}, Mn, Li; *C* = Mg, Fe^{2+}, Al, Fe^{3+}, Mn, Li but also Ti, Cr, Zn: *T* = (Si, Al). Hydroxyl ions can be replaced by Cl as well as F, and by oxygen.

Five main groups of amphibole are recognized, based on the relative numbers of the different *B* cations.

Group 1: The (Mg, Fe, Mn, Li) group, in which $\Sigma^B(Mg,Fe^{2+},Mn^{2+},Li) \geqslant 1.50$ pfu. In holmquistite the dominant *B* cation is lithium.

Group 2. The calcium group, in which $\Sigma^B(Mg,Fe^{2+},Mn^{2+},Li) \leqslant 0.50$ pfu, $^B(Ca,Na) \geqslant 1.00$ and $^BNa < 0.50$ pfu.

Group 3. The sodium-calcium group, in which $\Sigma^B(Mg,Fe^{2+},Mn^{2+},Li) \leqslant 0.50$, $^B(Ca,Na) \geqslant 1.00$ and $0.50 \leqslant {}^BNa \leqslant 1.50$ pfu.

Group 4. The sodium group, in which $\Sigma^B(Mg,Fe^{2+},Mn^{2+},Li) \leqslant 0.50$ and $^BNa \geqslant 1.50$ pfu.

Group 5. The Na-Ca-Mg-Fe-Mn-Li group, in which $0.50 < \Sigma^B(Mg,Fe^{2+},Mn^{2+},Li) < 1.50$ and $0.50 \leqslant {}^B(Na,Ca) < 1.50$.

The above compositional boundaries are those recommended by the International Mineralogical Association Commission on New Minerals and Mineral Names and reported by Leake *et al.* (1997); see also Leake *et al.* (2004). At the time of writing, a further revision of the classification and nomenclature of the amphibole group has been approved by the IMA Commission on New Minerals, Nomenclature and Classification (CNMNC), but is yet to be published* (see however Oberti *et al*., 2012). In this scheme the lithium amphiboles are treated separately in three additional sub-groups in which the principal elements are Li, Li,Na and Li,Mg,Fe,Mn. There is also a broad division of the amphiboles according to whether the dominant anion in the (O,OH,F) site is divalent O^{2-} or a monovalent anion. If O^{2-} is dominant at this site (a relatively uncommon situation) the prefix oxo- is added to the name.

* subsequently published by Hawthorne *et al*. (2012).

Table 22. Cation distribution in magnesium end-members of the more common amphibole minerals.

	A	*B*	*C*	*T*	
Cummingtonite (Anthophyllite)	□	Mg_2	Mg_5	Si_8	Magnesium amphiboles
Gedrite	□	Mg_2	Mg_3Al_2	Si_6Al_2	
Tremolite	□	Ca_2	Mg_5	Si_8	Calcium amphiboles
Magnesiohornblende	□	Ca_2	Mg_4Al	Si_7Al	
Tschermakite	□	Ca_2	Mg_3Al_2	Si_6Al_2	
Edenite	Na	Ca_2	Mg_5	Si_7Al	
Pargasite	Na	Ca_2	Mg_4Al	Si_6Al_2	
Winchite	□	NaCa	Mg_4Al	Si_8	Sodium-calcium amphiboles
Barroisite	□	NaCa	Mg_3Al_2	Si_7Al	
Richterite	Na	NaCa	Mg_5	Si_8	
Katophorite	Na	NaCa	Mg_4Al	Si_7Al	
Taramite	Na	NaCa	Mg_3Al_2	Si_6Al_2	
Glaucophane	□	Na_2	Mg_3Al_2	Si_8	Sodium amphiboles
Eckermannite	Na	Na_2	Mg_4Al	Si_8	

Downloaded from https://pubs.geoscienceworld.org/books/chapter-pdf/3756010/9780903056434_ch33.pdf
by guest

Nomenclature

Although the substitution Mg ↔ Fe is of prime importance in consideration of the optical and physical properties of amphiboles and their parageneses, this is a comparatively simple substitution which involves no charge imbalance. It can usually be described by using the prefixes magnesio- or ferro-, but specific names are sometimes used (see later sections).

Four other important substitutions may, however, occur in the amphiboles: Al ↔ Si, (Mg,Fe) ↔ Al, Na ↔ Ca and the introduction of either Na or K, or both, into the *A* site. More than one substitution of this type must occur in a given amphibole in order to maintain charge balance. The range of amphibole compositions can be expressed in terms of various end-members as indicated in Table 22. This table has been simplified by ignoring possible substitutions of Fe^{2+} and other divalent ions for Mg, and of Fe^{3+} and other trivalent ions for Al in *B* and *C*. The prefixes ferri- and alumino- can generally be used for the latter substitutions. Although tremolite, which is colourless in hand specimen, is used for the end-member $Ca_2Mg_5Si_8O_{22}(OH)_2$, with $Mg/(Mg + Fe^{2+}) \geqslant 0.90$,

Table 23. Amphibole analyses.

	1	2	3	4	5	6	7
SiO_2	55.00	40.75	55.57	49.01	58.54	54.73	51.40
TiO_2	0.35	0.25	0.18	0.05	–	0.21	0.74
Al_2O_3	2.11	19.81	0.89	0.00	0.79	1.46	3.88
Fe_2O_3	1.59	1.22	0.06	0.00	0.22	0.00	3.90
FeO	13.45	19.29	17.48	44.99	0.37	9.60	14.91
MnO	0.25	0.25	0.45	0.37	tr.	0.16	0.33
MgO	23.97	13.81	21.85	3.17	24.45	17.94	11.22
CaO	0.97	0.27	1.29	0.31	13.59	12.76	10.17
Na_2O	0.33	1.92	0.13	0.04	0.27	1.44	1.67
K_2O	0.05	0.04	0.01	0.00	0.12	tr.	0.09
H_2O+	1.51	2.68	2.01	1.28	2.12	2.27	1.90
H_2O-	0.04	–	0.06	0.31	0.00	0.00	0.04
F	–	0.01	–	1.00	–	–	–
	99.62	100.38	99.98	100.63	100.47	100.57	100.25
$-O \equiv F,Cl$	–	0.00	–	0.42	–	–	
Total	99.62	100.38	99.98	100.21	100.47	100.57	100.25
	Numbers of ions on the basis of 23 O, ignoring H_2O: anals 1 and 3, 24 (O,OH,F): anals 2, 4, 5, 6, 7						
Si	7.685 } 8.00	5.874 } 8.00[a]	7.884 } 8.00	7.917 } 7.92	7.918 } 8.00	7.731 } 7.97	7.543 } 8.00
Al	0.315	2.121	0.116	–	0.082	0.243	0.457
Al	0.032	1.245	0.032	–	0.044	–	0.215
Ti	0.037	0.027	0.020	–	–	0.022	0.082
Fe^{3+}	0.168	0.132	0.007	–	0.022	–	0.430
Mg	4.989	2.967	4.620	0.763	4.928	3.777	2.453
Fe^{2+}	1.571 } 7.07	2.326 } 6.79[b]	2.074 } 7.04	6.078 } 6.96	0.042 } 5.04	1.134 } 4.95	1.830 } 5.05
Mn	0.029	0.030	0.054	0.051	–	0.019	0.040
Ca	0.145	0.042	0.196	0.054	1.970	1.932	1.599
Na	0.089	0.537 } 0.54	0.036	0.013	0.071 } 2.06	0.394 } 2.33	0.474 } 2.09
K	0.008	0.007	0.002	–	0.021	–	0.018
OH	2.00	2.578 } 2.58	2.00	1.379 } 1.89	1.913	2.139	1.861
F	–	0.005	–	0.511	–	–	–

1 Anthophyllite, anthophyllite amphibolite, Nakagawa area, Japan, α 1.629, β 1.636, γ 1.647, $2V_\alpha = 90°$ (Tiba, T., Hashimoto, M. & Kato A., 1970, *Lithos*, **3**, 335–40).

2 Gedrite, quartz-anthophyllite-biotite-garnet-staurolite-sillimanite schist, Ammonnosuc volcanics, Orange area, Massachusetts, USA (Robinson, P. & Jaffe, H., 1969, *Min. Soc. Amer. Spec. Paper* **2**, 251–74. Includes Cr_2O_3 0.01, NiO 0.001, SrO 0.001, BaO 0.001, Li_2O 0.03, P_2O_5 0.04, Cl 0.01).

3 Cummingtonite, hornblende-cummingtonite amphibolite (metamorphosed pyroxenite), Nero Hill, Central Tanzania (Haslam, H.W. & Walker, D.G., 1971, *Mineral. Mag.*, **38**, 58–63).

4 Grunerite, grunerite-quartz schist, Wabush Iron Formation, Labrador, Newfoundland (Klein, C. Jr., 1964, *Amer. Min.*, **49**, 963–982. Includes P_2O_5 0.1).

5 Tremolite, marble, Gouverneur, New York State, USA (Shido, F., 1959, *Geol. Soc. Japan. J.*, **65**, 563–9).

6 Actinolite, hornblende-clinozoisite schist, Salcombe Estuary, south Devon, UK (Tilley, C.E., 1938, *Geol. Mag.*, **75**, 497–511).

7 Actinolite, albite-stilpnomelane-actinolite schist, New Zealand (Hutton, C.O., 1940, *Dept. Sci.* and *Ind. Res.*, *New Zealand*, *Geol. Mem.*, **5**, 90 pp).

[a] Includes P 0.005.

[b] Includes Cr 0.002, Li 0.017.

Downloaded from https://pubs.geoscienceworld.org/books/chapter-pdf/3756010/9780903056434_ch33.pdf
by guest

actinolite which is a yellow-green, is used for the range 0.50 to 0.89.

The progression tremolite–magnesiohornblende–tschermakite involves increasing substitutions in the $M(1,2,3)$ and T sites of the type Mg,Si ↔ Al,Al. The edenite and pargasite formulae can be regarded as derived from tremolite and magnesiohornblende, respectively, by the addition of Na in the A site and the substitution of Al for Si. The name hornblende has been widely used to describe calcic amphiboles with appreciable Al, but strictly it refers to a specific calcium amphibole $\square Ca_2(Mg,Fe^{2+})_4(Al,Fe^{3+})[Si_7AlO_{22}](OH)_2$, which can contain some Na and K but for which the majority of A sites are vacant (Leake *et al*., 1997). The continuous chemical variation towards the neighbouring composition fields of edenite, pargasite and tschermakite (see Fig. 114, p. 155) may result in green, brown or green-brown amphibole being described petrographically as hornblende when the more appropriate names if chemical data were available, would be for the Mg end-members, magnesiohornblende, edenite, pargasite or tschermakite. Kaersutite has a formula similar to pargasite but with Ti replacing Al in the $M(1,2,3)$ sites (which may require some replacement of OH by O).

Table 23. Amphibole analyses (continued).

	8	9	10	11	12	13	14
SiO_2	47.95	50.70	42.70	36.34	40.27	58.04	51.50
TiO_2	0.88	0.32	0.45	0.94	7.23	0.66	0.20
Al_2O_3	6.46	5.45	18.26	14.06	10.70	10.31	4.41
Fe_2O_3	4.45	1.81	3.14	4.38	1.82	2.89	15.51
FeO	10.49	6.59	12.07	22.99	12.45	6.12	7.65
MnO	0.63	0.17	0.07	0.75	0.24	0.07	0.05
MgO	13.33	15.89	8.42	3.14	10.73	11.71	10.19
CaO	12.08	12.22	10.65	11.82	11.85	1.37	2.13
Na_2O	1.06	2.80	1.42	1.14	2.40	6.97	6.18
K_2O	0.53	1.23	0.49	2.66	0.69	0.02	0.20
H_2O+	1.89	2.08	2.13	1.81	1.46	1.98	1.88
H_2O-	0.05	0.00	–	0.01	0.03	0.00	–
F	0.17	–	–	0.02	–	0.02	–
	100.00	99.80	99.80	100.06	99.87	100.17	100.00
$-O \equiv F,Cl$	0.08	–	–	0.01	–	0.01	–
Total	99.92	99.80	99.80	100.05	99.87	100.16	100.00
	Numbers of ions on the basis of 24 (O,OH,F) (anals 8–13), 23 O (anal. 14)						
Si	7.015 } 8.00	7.284 } 8.00	6.218 } 8.00	5.813 } 8.00	6.066 } 7.97	7.913 } 8.00	7.469 } 8.00
Al	0.985	0.716	1.782	2.187	1.900	0.087	0.531
Al	0.129	0.207	1.353	0.464	0.000	1.570	0.219
Ti	0.097	0.035	0.049	0.113	0.819	0.068	0.026
Fe^{3+}	0.490	0.196	0.344	0.527	0.206	0.297	1.691
Fe^{2+}	1.284	0.792	1.470	3.075	1.568	0.693	0.924
Mn	0.078	0.021	0.009	0.102	0.031	0.008	0.009
Mg	2.906	3.402	1.827	0.749	2.409	2.379	2.205
	4.98	4.72[d]	5.05	5.03	5.03	5.02	5.07
Na	0.301	0.780	0.401	0.354	0.701	1.842	1.734
Ca	1.894 } 2.29	1.881 } 2.89	1.662 } 2.15	2.026 } 2.92	1.913 } 2.75	0.200 } 2.05	0.331 } 2.10
K	0.099	0.225	0.091	0.543	0.133	0.003	0.035
OH	1.845 } 1.93[c]	1.993	2.069	1.934 } 1.94	1.467	1.801 } 1.81	2.00
F	0.079	–	–	0.010	–	0.009	–

8 Magnesiohornblende, granodiorite, Central Sierra Nevada Batholith, California, USA (Dodge, F.C.W., Papike, J.J. & Mays, R.E., 1968, *J. Petr*., **9**, 378–410. Includes Cl 0.03. □ site 0.29).

9 Edenite, amphibolite, Kushalnagar, Coorg District, Mysore, India (Leake, B.E., 1971, *Mineral. Mag*., **38**, 389–407. Includes Cr_2O_3 0.48, NiO 0.06%. □ site 0.89).

10 Aluminotschermakite; kyanite-plagioclase-quartz-chlorite schist, Frodalera, Lukmanier, Switzerland (Leake, B.E., 1971, *Mineral. Mag*., **38**, 389–407. □ site 0.15).

11 Potassic hastingsite, amphibolite, Tilbuster, Armidale, New England, New South Wales, Australia (Binns, R.A., 1965, *Mineral. Mag*., **34**, 52–65. □ site 0.92).

12 Kaersutite, titanaugite–kaersutite teschenite, Sakamoto-zawa, Yaizu, Japan (Aoki, K., 1963, *J. Petr*., **4**, 198–210. □ site 0.75).

13 Glaucophane, glaucophane schist, Tiburon Peninsula, Marin Co., California, USA (Papike, J.J. & Clark, J.R., 1968, *Amer. Min*., **53**, 1156–73. Includes Cl 0.01).

14 Magnesioriebeckite, amphibole limestone, Pralognan, Western Alps (Bocquet, J., 1974, *Schweiz Min. Pet. Mitt*., **54**, 425–48. Includes P_2O_s 0.10).

[c] Includes Cl 0.007.
[d] Includes Ni 0.007 and Cr 0.055.

Downloaded from https://pubs.geoscienceworld.org/books/chapter-pdf/3756010/9780903056434_ch33.pdf
by guest

Pargasite in which $^{M(1,2,3)}Fe^{3+} > Al$ is called hastingsite. If Na is introduced into the *M*4 site replacing Ca, charge compensation can occur by the substitution of Al for Mg in *C* as in winchite, and over-compensation by additional Al in *C* and be offset by Al for Si as in barroisite. Alternatively, the substitution of Na for Ca in *B* can be coupled with Na entering *A* as in richterite, katophorite and taramite. These five end-members form the subgroup of sodium-calcium amphiboles (Group 3).

Glaucophane and eckermannite are related to tremolite and pargasite, respectively, by the complete replacement of Ca_2 by Na_2, which is compensated by the replacement of Mg_3Al_2 for Mg_5 and Si_8 for Si_6Al_2, respectively. These two minerals and their Fe^{2+} and Fe^{3+}-substituted variants (riebeckite and arfvedsonite) constitute the sodium group (Group 4).

In comparing calcium and iron-magnesium amphiboles, there is a large difference in the size of the cation in the *M*4 site; this may lead to a lack of solid solution between the two groups and to the possibility of exsolution lamellae of one in the other, e.g. cummingtonite in actinolite or hornblende. A similar gap in solid solution

Table 23. Amphibole analyses (continued).

	15	16	17	18	19	20	21
SiO_2	58.01	54.85	50.21	53.80	48.51	57.10	60.16
TiO_2	0.37	0.40	0.12	0.10	1.32	0.35	1.64
Al_2O_3	9.41	11.65	1.66	1.37	6.60	6.19	1.10
Fe_2O_3	2.09	1.00	16.51	1.89	4.09	8.01	9.12
FeO	5.49	16.75	21.23	0.00	9.48	2.69	20.60
MnO	0.21	0.25	0.09	8.69	0.19	0.34	2.27
MgO	12.86	5.40	1.07	18.45	14.79	9.13	0.92
CaO	2.77	1.05	0.55	5.43	5.60	0.31	1.32
Na_2O	6.24	6.45	6.46	5.63	6.01	9.77	6.85
K_2O	0.05	0.30	0.52	1.72	2.20	2.38	3.61
H_2O+	2.28	1.45	1.65	1.91	1.47	0.50	1.64
H_2O-	0.12	0.05	–	0.14	–	0.08	0.04
F	–	–	0.10	0.36	–	2.69	0.39
	99.91	99.85	100.17	100.02	100.26	101.28	99.98
$-O \equiv F,Cl$	–	–	0.04	0.16	–	1.13	0.16
Total	99.91	99.85	100.13	99.86	100.26	100.15	99.82
	Numbers of ions on the basis of 23 O (anal. 16), 24 (O,OH,F) (anals 15, 17–21)						
Si	7.903 } 8.00	7.792 } 8.00	7.802 } 8.00	7.748 } 7.98	7.119 } 8.00	8.021 } 8.02	7.887 } 8.00[h]
Al	0.097	0.208	0.198	0.232	0.881	–	0.050
Al	1.413	1.746	0.106	–	0.259	1.025	0.153
Ti	0.038	0.042	0.014	0.011	0.145	0.037	0.194
Fe^{3+}	0.214	0.111	1.931	0.206	0.452	0.847	1.079
Mg	2.612 } 4.93	1.143 } 5.06	0.248 } 5.07	3.961 } 5.24	3.235 } 5.28	1.911 } 4.89[g]	0.213 } 4.66[i]
Fe^{2+}	0.625	1.988	2.759	–	1.164	0.316	2.709
Mn	0.024	0.026	0.012	1.061	0.024	0.040	0.302
Na	1.648	1.775	1.946	1.572	1.708	2.660	2.087
Ca	0.404 } 2.06	0.162 } 1.99	0.092 } 2.14	0.838 } 2.74[e]	0.880 } 3.00	0.046 } 3.03	0.221 } 3.03
K	0.008	0.051	0.103	0.315	0.412	0.425	0.725
OH	2.072 } 2.08	2.00	1.711 } 1.76	1.834 } 2.01[f]	1.440 } 1.44	0.469 } 1.66	1.722 } 1.92
F	–	–	0.049	0.163	–	1.193	0.194

15 Glaucophane, glauophane-lawsonite-chlorite-albite-epidote metagabbro, vallon du Lonquet, Molines-en-Queyras (Piedmont zone), French Alps. (Bocquet, J., 1974, *ibid*. Includes P_2O_5 0.01): *a* 9.521, *b* 17.804, *c* 5.292 Å, β 103.72º, *V* 871.47 Å^3.

16 Ferroglaucophane, amphibole-mica schist, Pralognan, Western Alps (Bocquet, J., 1974, *ibid*. Includes P_2O_5 0.25).

17 Riebeckite, pegmatite, Masokani Hill, Machokos District, Kenya (Cambell Smith, W., Hey, M.H. & Kempe, D.R.C., 1968, *Mineral. Mag*., **36**, 1164–7).

18 Manganorichterite, metamorphosed limestone, Sweden (Sundius, N., 1945, *Geol. För. Förh. Stockholm*, **67**, 266–70. Includes BaO 0.30, Cl 0.04, SO_3 0.19. □ site 0.74).

19 Magnesiokataphorite, theralite, Montana, USA (Wolff, J.E., 1939, *Bull. Geol. Soc. America*, **49**, 1569–626. □ site 1.00).

20 Eckermannite, nepheline syenite, Norra Kärr, Sweden (Sundius, N., 1945, *Årsbok, Sveriges Geol. Undersok*., **39**, No. 8. Includes Li_2O 1.15, ZnO 0.59. □ site 1.00).

21 Arfvedsonite, Be-bearing paragneiss, Seal Lake, Labrador, Newfoundland (Nickel, E.H. & Mark, E. 1965, *Can. Min*., **8**, 185–97. Includes BeO 0.18, Nb_2O_5 0.14. □ site 1.00).

[e] Includes Ba 0.017.
[f] Includes Cl 0.010.
[g] Includes Li 0.650, Zn 0.061.
[h] Includes Be 0.063.
[i] Includes Nb 0.010.

Downloaded from https://pubs.geoscienceworld.org/books/chapter-pdf/3756010/9780903056434_ch33.pdf
by guest

would be expected between sodic and Mg-Fe amphiboles. Another well established gap is that between anthophyllites (poorer in Al and Na) and gedrites (Al- and Na-richer).

Chemical analyses of a range of natural amphiboles are presented in Table 23. The name amphibole is from the Greek *amphibolos* (ambiguous), in prescient allusion to the great variety of compositions and appearances shown by this mineral group.

Further reading

Esawi, E.K. (2011) Calculations of amphibole chemical parameters and implementation of the 2004 recommendations of the IMA classification and nomenclature of amphiboles. *Journal of Mineralogical and Petrological Sciences*, **106**, 123–129.

Hawthorne, F.C. and Oberti, R. (2006) On the classification of amphiboles. *The Canadian Mineralogist*, **44**, 1–21.

Hawthorne, F.C., Oberti, R., Harlow, G.E., Maresch, W.V., Martin, R.F., Schumacher, J.C. and Welch, M.D. (2012) Nomenclature of the amphibole supergroup. *American Mineralogist*, **97**, 2031–2048.

Leake, B.E., Woolley, A.R., Arps, C.E.S., Birch, W.D, Gilbert, M.C., Grice, J.D., Hawthorne, F.C., Kato, A., Kisch, H.J., Krivovichev, V.G., Linthout, K., Laird, J., Mandarino, J., Maresch, W.V., Nickel, E.H., Rock, N.M.S., Schumacher, J.C., Smith, D.C., Stephenson, N.C.N., Ungaretti, L., Whittaker, E.J.W. and Youzhi, G. (1997) Nomenclature of amphiboles. Report of the Subcommittee on Amphiboles of the International Mineralogical Association, Commission on New Minerals and Mineral Names. *Mineralogical Magazine*, **61**, 295–321.

Leake, B.E., Woolley, A.R., Birch, W.D., Burke, E.A.J., Ferraris, G., Grice, J.D., Hawthorne, F.C., Kisch, H.J., Krivovichev, V.G., Schumacher, J.C., Stephenson, N.C.N. and Whittaker, E.J.W. (2004) Nomenclature of amphiboles: additions and revisions to the International Mineralogical Association's amphibole nomenclature. *European Journal of Mineralogy*, **16**, 191–196.

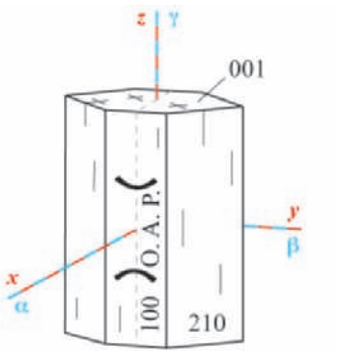
Oberti, R., Cannillo, E. and Toscani, G. (2012) How to name amphiboles after the IMA2012 report: rules of thumb and a new PC program for monoclinic amphiboles. *Periodico di Mineralogia*, **81**, 257–267.

Downloaded from https://pubs.geoscienceworld.org/books/chapter-pdf/3756010/9780903056434_ch33.pdf
by guest

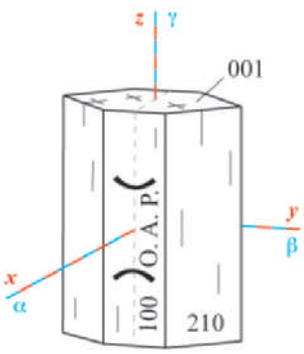
Anthophyllite — $(Mg,Fe^{2+})_7[Si_8O_{22}](OH)_2$
Gedrite — $(Mg,Fe^{2+})_5Al_2[Si_6Al_2O_{22}](OH)_2$

Orthorhombic (−)(+)

Anthophyllite



Gedrite



	α 1.587–1.694	
	β 1.602–1.710	
	γ 1.613–1.722	
	δ 0.013–0.029	
$2V_\gamma$	111–59°	71–98°
Orientation	$\alpha = x$, $\beta = y$; $\gamma = z$; O.A.P. (010)	
D (g/cm^3)	2.85–3.57	
H	5½–6	
Cleavage	{210} perfect; {010}, {100} imperfect; (210):(2$\bar{1}$0) ~ 54½°	
Twinning	None	
Colour	White, grey, green, clove-brown, yellow-brown, dark brown; colourless to pale green or yellow in thin section	
Pleochroism	Feeble to moderate, absorption $\gamma = \beta > \alpha$; or $\gamma > \beta = \alpha$; commonly $\alpha = \beta$ pale yellow or grey-brown, γ brown-grey to clove-brown	
Unit cell	a ~ 18.6 Å, b ~ 17.9 Å, c ~ 5.2–5.3 Å	
	Z = 4; space group *Pnma*	

Orthoamphiboles such as anthophyllite and gedrite occur only rarely in igneous rocks, but are relatively common in the greenschist and lower amphibolite facies of metamorphic rocks, and in metasomatic rocks. They are commonly associated with staurolite and cordierite

Chemistry

The major variations in the composition of the anthophyllite–gedrite series involve the substitutions $Mg \leftrightarrow Fe^{2+}$, $(Mg,Fe^{2+}) + Si \leftrightarrow Al + Al$ and $Na + Al \leftrightarrow \square + Si$. The latter substitutions can couple together and compositions follow a trend of enrichment in both Na and Al. The boundary between anthophyllite and gedrite is at Si_7, half way between the end member compositions. There is a low-temperature solvus between anthophyllite and gedrite; compositions in the middle of the series occur only in high-temperature rocks, and exsolution is common, usually as fine (010) lamellae that can impart iridescence to composite grains. The prefix 'ferro' attached to the mineral name indicates $Fe^{2+} > Mg$.

The anthophyllite–gedrite amphiboles show the complete range of (Mg,Fe^{2+}) substitution, but Mg-rich compositions are much more common and the

Downloaded from https://pubs.geoscienceworld.org/books/chapter-pdf/3756055/9780903056434_ch34.pdf
by guest

monoclinic cummingtonite–grunerite amphiboles tend to be more iron-rich.

The presence of relatively small amounts of Ca (+Na) replacing (Fe^{2+},Mg) in anthophyllite-gedrite (up to about 0.3 atoms pfu) reflects the limited solid solution between the magnesium–iron–manganese amphiboles and the calcium amphiboles.

Holmquistite is a lithium-rich orthorhombic amphibole of composition $Li_2(Mg_3Al_2)Si_8O_{22}(OH)_2$ which shows significant Mg ↔ Fe^{2+} solid solution; ferroholmquistite occurs but is not common.

Experimental

Laboratory experiments have been carried out involving the formation of anthophyllite at higher temperatures by such reactions as:

$$\text{talc} + \text{forsterite} \rightarrow \text{anthophyllite} + H_2O$$
$$\text{talc} \rightarrow \text{anthophyllite} + \text{quartz} + H_2O$$

and also involving its decomposition by the reactions:

$$\text{anthophyllite} + \text{forsterite} \rightarrow \text{enstatite} + H_2O$$
$$\text{anthophyllite} \rightarrow \text{enstatite} + H_2O$$

The results of these studies have shown some inconsistencies but the range of temperature for anthophyllite stability appears to be from about 650 to 800ºC at about 0.5 GPa.

Experiments using rock compositions have yielded useful results such as the $P-T$ diagram of Fig. 108, defining gedrite stability. For gedrites, the presence of small amounts of Na increases stability and those compositions with a higher Mg/Fe ratio are stable to higher temperatures.

Optical and physical properties

The substitution of Mg by Fe^{2+} within either the anthophyllite or gedrite solid-solution series raises the refractive indices, and as the substitution of Mg,Si by Al,Al has a similar effect, the refractive indices of a gedrite are higher than those of an anthophyllite with similar X = Fe/(Fe + Mg) values. For anthophyllite, γ ranges from about 1.61 (X = 0) to 1.67 (X = 0.4), and for gedrite from about 1.66 (X = 0.2) to 1.72 (X = 1.0). Synthetic Mg-anthophyllite has α 1.587, β 1.602, γ 1.613.

Magnesium-rich anthophyllites are optically negative; $2V_\alpha$ increases with the replacement of Mg by Fe^{2+} and the more iron-rich anthophyllites are optically positive. Gedrites, except for compositions close to $Fe_5Al_4Si_6O_{22}(OH)_2$, have large optic axial angles and are optically positive. Holmquistite differs from the other orthorhombic amphiboles by its light blue to violet colour, and by its yellowish to bluish-violet pleochroism. The anthophyllite minerals vary in habit from fibrous and asbestiform to bladed and prismatic, all with elongation parallel to z. The fibres of anthophyllite, unlike those of some cummingtonite–grunerites (p. 149), and riebeckites (p. 164), do not have great tensile strength.

Some specimens of anthophyllite and gedrite exhibit iridescence due to the presence of fine-scale exsolution lamellae of one mineral in the other. Exsolution lamellae of ilmenite or rutile may also occur.

Distinguishing Features

Magnesium-rich anthophyllites may be distinguished from the magnesium-rich gedrites by the optically negative character of the anthophyllites, and from ferrogedrites by the higher refractive indices of the latter minerals. The orthorhombic amphiboles are distinguished from the monoclinic amphiboles by their parallel extinction in all [001] zone sections. In addition, anthophyllite and gedrite may be distinguished from the members of the cummingtonite–grunerite series by the stronger birefringence and the common multiple twinning of the latter minerals and from common

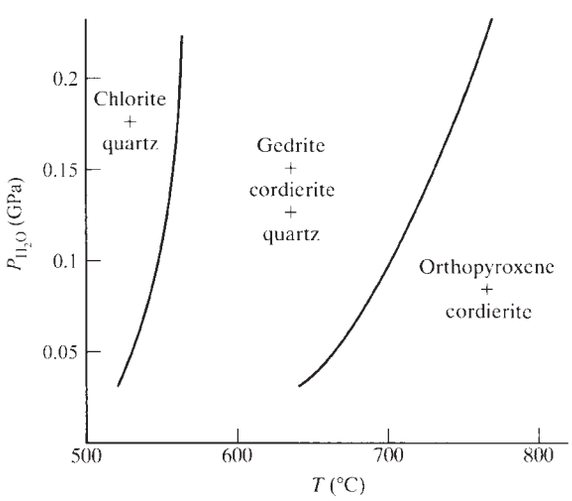


Fig. 108. A $P-T$ diagram showing the approximate stability field for gedrite + cordierite + quartz (from Akella, J. & Winkler, H.G.F., 1966, *Contrib. Mineral. Petrol.*, **12**, 1–12

Downloaded from https://pubs.geoscienceworld.org/books/chapter-pdf/3756055/9780903056434_ch34.pdf
by guest

hornblende by its twinning and stronger absorption colours. In zoisite the cleavage is parallel to (100), the optic axial angle is small to moderate and the birefringence is weaker. The orthopyroxenes have pyroxene cleavages, generally higher refractive indices, weaker birefringence and for a considerable range of composition their optic axial angles are smaller. Sillimanite has a small optic axial angle, (010) cleavage, and the prism angle is close to 90º.

Paragenesis

The orthorhombic amphiboles occur only rarely in igneous rocks, where they are more sodic in composition than in rocks of metamorphic and metasomatic origin. Anthophyllite and gedrite, however, occur in a wide range of rocks of metamorphic and metasomatic origin. Anthophyllite and gedrite are common products in the reaction zone between ultramafic bodies (e.g. serpentinized peridotites) and country rocks.

In regional metamorphism orthoamphiboles generally appear in the lower amphibolite facies, possibly by reactions involving chlorite and quartz with or without plagioclase, which introduces the sodium commonly found in gedrites and also leads to the formation of calcium as well as Mg–Fe amphibole. Minerals commonly associated with orthoamphiboles are staurolite + cordierite (relatively low P and T); garnet + cordierite (low P, high T); and aluminosilicate (high P). Other coexisting minerals include talc, chlorite, spinel, olivine, ortho-pyroxene, hornblende, plagioclase and quartz. In anthophyllite-talc schists, the anthophyllite may exhibit an asbestiform habit.

Anthophyllite-cordierite gneisses, e.g. of the Orijärvi region, Finland, are of a composition very different from the normal range of igneous, metamorphic or sedimentary rocks, so there has been much discussion about their origin. It could be that the rocks from which they are derived had been altered by weathering, hydrothermal or volcanic processes, or by metasomatic chemical changes (addition of Fe, Mg or Al; removal of Ca) during metamorphism. Another possibility is that the parent rocks were themselves residues of a partial melting process.

Higher grades of metamorphism result in the dehydration and breakdown of orthoamphibole to orthopyroxene.

Other parageneses of anthophyllite-gedrite include its occurrence as rims surrounding orthopyroxene formed during the retrograde metamorphism of earlier thermally metamorphosed rocks, and as a hornfels constituent within the metamorphic aureoles of intermediate intrusives.

Holmquistite typically occurs at the contact of lithium-rich pegmatites with country rocks, and its origin, commonly from hornblende, is always associated with lithium metasomatism.

Further reading

Abati, J. and Arenas, R. (2005) Metamorphic evolution of anthophyllite/cummingtonite-cordierite rocks from the upper unit of the Ordenes Complex (Galicia, NW Spain). *European Journal of Mineralogy*, **17**, 57–68.

Driouch, Y., Dahmani, A., Debat, P., Lelubre, M. and Roux, L. (1997) L'association à cordiérite-gédrite de Gèdre (Pyrénées, France. *Compte Rendus Académie de Sciences, Série II*, **325**, 493–498.

Elliot-Meadows, S.R., Froese, E. and Appleyard, E.C. (1999) Cordierite-anthophyllite-cummingtonite rocks from the Lar deposit, Laurie Lake, Manitoba. *The Canadian Mineralogist*, **37**, 375–380.

Schindler, M., Sokolova, E., Abdu, Y., Hawthorne, F.C., Evans, B.W. and Ishida, K. (2008) The crystal chemistry of the gedrite-group amphiboles. I. Crystal structure and site populations. *Mineralogical Magazine*, **72**, 703–730.

Smelik, E.A. and Veblen, D.R. (1993) A transmission and analytical electron microscope study of exsolution microstructures and mechanisms in the orthoamphiboles anthophyllite and gedrite. *American Mineralogist*, **78**, 511–532.

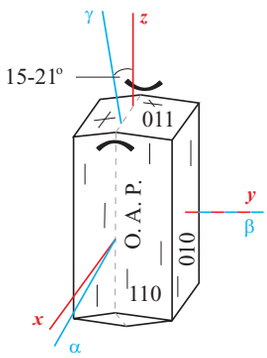
Spear, F.S. (1980) The gedrite–anthophyllite solvus and the composition limits of orthoamphibole from the Post Pond Volcanics. *American Mineralogist*, **65**, 1103–1118.

Su, S.-C. (2003) A rapid and accurate procedure for the determination of refractive indices of regulated asbestos minerals. *American Mineralogist*, **88**, 1979–1982.

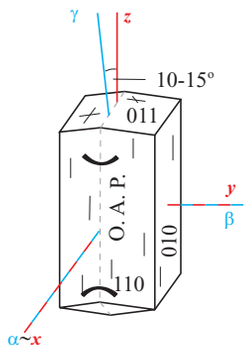
Downloaded from https://pubs.geoscienceworld.org/books/chapter-pdf/3756055/9780903056434_ch34.pdf
by guest

Monoclinic (+)(−)

Cummingtonite
Monoclinic (+)



Grunerite
Monoclinic (−)



α	1.630–1.696
β	1.644–1.709
γ	1.652–1.730
δ	0.020–0.045
$2V_\gamma$	65–96°
Orientation	γ:*z* 21–10°, β = y; O.A.P. (010)
D (g/cm^3)	3.10–3.60
H	5–6
Cleavage	{110} good; (110):(1$\bar{1}$0) ~ 55°
Twinning	{110} simple, lamellar, very common
Colour	Dark green, brown; colourless to pale green in thin section
Pleochroism	*Magnesium-rich cummingtonite*: non-pleochroic
	Iron rich cummingtonite: α = β colourless, γ pale green
	Grunerite: α = β very pale yellow or brown, γ pale brown
Unit cell	*a* 9.5–9.6 Å, *b* 18.1–18.4 Å, *c* 5.30–5.35 Å, β ~ 102°
	Z = 2; space group *C*2/*m*[a]

Cummingtonite is typically found in Ca-poor amphibolites, whereas grunerite occurs commonly in metamorphosed banded ironstones. Both are rare in igneous rocks. Lamellar twinning is characteristic.

Chemistry

Members of the cummingtonite–grunerite series with more than 70% $Mg_7Si_8O_{22}(OH)_2$ have in some cases been called magnesiocummingtonites but in this range of composition the orthorhombic amphibole anthophyllite is more common. The name cummingtonite is used to describe minerals containing $Mg > Fe^{2+}$ and grunerite for those with $Fe^{2+} > Mg$ (Table 23, anals 3, 4). The replacement of (Mg,Fe) by Mn is generally small but manganese-rich species occur, in which up to two of the seven *M*(1,2,3,4) sites are occupied by Mn, e.g. in high-

[a] Some Mg-rich cummingtonites have been reported with space group $P2_1/m$; they transform to *C*2/*m* above a relatively low temperature which is a function of the Fe/(Fe + Mg) ratio.

Downloaded from https://pubs.geoscienceworld.org/books/chapter-pdf/3756139/9780903056434_ch35.pdf
by guest

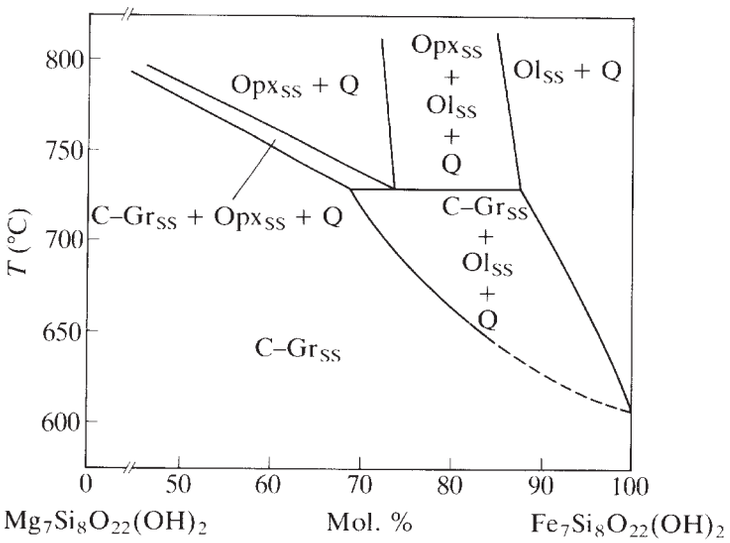


Fig. 109. Upper stability limits of grunerites at pressure of ~0.3 GPa and with f_{O_2} defined by fayalite–magnetite–quartz buffer (after Fonarev, V.I. & Korolkov, G.Ya., 1980, *Contrib. Mineral. Petrol.*, **73**, 413–20). C–Gr$_{ss}$: cummingtonite–grunerite solid solution; Opx$_{ss}$: orthopyroxene solid solution; Ol$_{ss}$: olivine solid solution.

grade metamorphic iron formations; the end-members $Mn_2Mg_5Si_8O_{22}(OH)_2$ and $Mn_2Fe_5Si_8O_{22}(OH)_2$ are called manganocummingtonite and manganogrunerite (previously named tirodite and dannemorite), respectively.

The calcium content, although greater than in anthophyllite, tends to be small (about 0.2 atoms pfu) and contents of Na (and K) are also low, these chemical features reflecting the limited solid solution between iron-magnesium amphiboles on the one hand and calcic or alkali amphiboles on the other. Cummingtonites tend to have lower contents of Al, Fe^{3+} and Na than anthophyllites.

Grunerite has been synthesized hydrothermally at about 550–600ºC from hematite + quartz and also from quartz + fayalite + magnetite. Monoclinic fluor- (Mg-Fe)-amphiboles have been synthesized by heating (Mg,Fe) pyroxenes with NaF. The upper stability limits for Mg-Fe hydroxyamphiboles have been determined experimentally (Fig. 109). The breakdown of ferrogrunerite occurs at about 600ºC yielding fayalite + quartz; with increasing magnesium content the temperature of decomposition to olivine + orthopyroxene + quartz or orthopyroxene + quartz is raised and the effect of increased total pressure is to expand the amphibole field to higher temperatures.

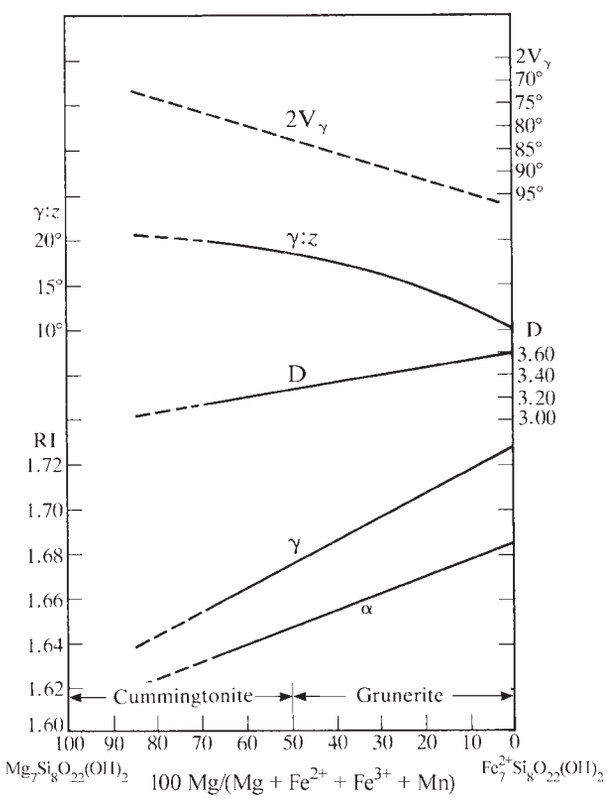


Fig. 110. The variation of the optical properties and density with composition in the cummingtonite–grunerite series.

Downloaded from https://pubs.geoscienceworld.org/books/chapter-pdf/3756139/9780903056434_ch35.pdf
by guest

The phase relationships are dependent on oxygen fugacity as well as temperature, $P_{(total)}$ and P_{H_2O}, and the maximum stability of grunerite is found at the intermediate f_{O_2} of the fayalite–quartz–magnetite buffer.

Optical and physical properties

The variation of optical properties and density with composition are illustrated in Fig. 110, and can be used to estimate the compositions of members within the series. Manganese lowers the refractive indices and the manganese-rich cummingtonites are commonly light green and non-pleochroic.

Exsolution lamellae of one mineral in the other have been observed (by light- or electron-microscopy) for cummingtonite–grunerite in association with actinolite, or hornblende, or arfvedsonite; the lamellae are usually close to the planes (100) and ($\bar{1}$01). The characteristic habit of the cummingtonite–grunerite series of minerals is acicular or fibrous. Asbestiform varieties are common. Amosite and montasite were names given to the harder, more iron-rich, and softer, more magnesium-rich, fibres which were once of economic importance but which constitute a serious health hazard. Their industrial use is banned in many countries.

Distinguishing features

Cummingtonite is distinguished from tremolite and actinolite by its higher refractive indices and by its optically positive character, and from anthophyllite by the straight extinction in all [001] zone sections of the latter mineral. Grunerite is distinguished from ferro-actinolite by higher refractive indices and birefringence. The most valuable diagnostic feature of the cummingtonite–grunerite series of minerals is the very characteristic multiple twinning on (100), the twin lamellae of which are typically very narrow. The division of the series between cummingtonite and grunerite occurs near the change in optic sign; extinction angles lower than $\gamma:z = 15^{\circ}$ also serve to distinguish grunerite from cummingtonite.

Paragenesis

Cummingtonite is most commonly found in low-Ca amphibolites produced by regional metamorphism from basic igneous rocks. In such rocks it is associated with common hornblendes either as individual crystals or in crystals sharply zoned by the calcic amphibole, thereby expressing the lack of complete miscibility between the Ca-rich and Ca-poor amphiboles at the $P-T$ conditions of normal metamorphism. Mg-rich cummingtonite also occurs together with anthophyllite in isochemically metamorphosed ultrabasic rocks. Cummingtonite is not uncommon in hybrid rocks of intermediate composition and in such rocks is the middle member of the reaction series orthopyroxene → cummingtonite → hornblende.

The more iron-rich (and sometimes Mn-rich) members of the cummingtonite–grunerite series are common minerals of moderately metamorphosed iron formations, being stable from the biotite isograd up through the garnet and staurolite isograds. Possible derivations are by the breakdown of minnesotaite or by such reactions as:

ferrodolomite + quartz + H_2O → grunerite + calcite + CO_2

Where the metamorphism has been predominantly of a regional nature, the characteristic assemblage is magnetite-grunerite-quartz; in rocks which have undergone both contact and regional metamorphism grunerite is commonly associated with fayalite, hedenbergite and almandine.

Minerals of the cummingtonite–grunerite series are relatively rare in the igneous environment but they occur in some silicic volcanic rocks and also, along with hornblende, in some diorites.

Further reading

Boffa Ballaran, J.B., Angel, R.J. and Carpenter, M.A. (2000) High-pressure transformation behaviour of the cummingtonite–grunerite solid solution. *European Journal of Mineralogy*, **12**, 1195–1213.

Evans, B.W. and Medenbach, O. (1997) The optical properties of cummingtonite and their dependence on Fe-Mg order-disorder. *European Journal of Mineralogy*, **9**, 993–1003.

Forbes, W.C. (1977) Stability relations of grunerite $Fe_7Si_8O_{22}(OH)_2$. *American Journal of Science*, **277**, 735–749.

Miyano, T. and Klein, C. (1983) Phase relations of orthopyroxene, olivine, and grunerite in high-grade metamorphic iron-formation. *American Mineralogist*, **68**, 699–716.

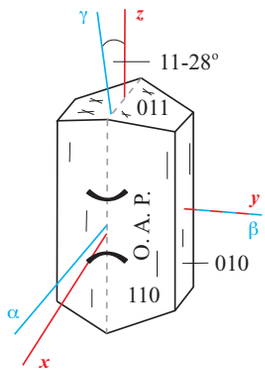
Yang, H., Hazen, R.M., Prewitt, C.T., Finger, L.W., Lu, R. and Hemley, R.J. (1998) High-pressure single-crystal X-ray diffraction and infrared spectroscopic studies of the $C2/m$-$P2_1/m$ phase transition in cummingtonite. *American Mineralogist*, **83**, 288–299.

Downloaded from https://pubs.geoscienceworld.org/books/chapter-pdf/3756139/9780903056434_ch35.pdf
by guest

Tremolite–Ferro-actinolite $\square Ca_2(Mg,Fe^{2+})_5[Si_8O_{22}](OH,F)_2$

Monoclinic (−)

α	1.599−1.688
β	1.610−1.697
γ	1.620−1.705
δ	0.027−0.017
$2V_\alpha$	86−62°
Orientation	γ:*z* 28−10°, β = *y*; O.A.P. (010)
D (g/cm^3)	2.99−3.48
H	5−6
Cleavage	{110} good; {100} parting; (110):(1$\bar{1}$0) ~ 56°
Twinning	{100} simple, lamellar, common; {001} lamellar, rare
Colour	*Tremolite*: colourless or grey
	Actinolite: pale to dark green
	Ferro-actinolite: dark green to black
	Colourless, pale green, deep green in thin section
Pleochroism	*Tremolite*: non-pleochroic
	Actinolite and *ferro-actinolite*: strength of pleochroism related to iron content, with α pale yellow, yellowish green; β pale yellow-green, γ pale green, deep greenish blue
Unit cell	*a* ~ 9.85 Å, *b* ~ 18.1 Å, *c* ~ 5.3 Å, β ~ 105°
	Z = 2; space group *C*2/*m*



The name actinolite is applied to iron-rich intermediates in the tremolite–ferro-actinolite series and is extensively used in petrology; its compositional field does not reflect the modern chemically based definitions of most other amphibole-group minerals. Both tremolite and actinolite are found typically in low-grade rocks of both contact and regional metamorphism. Actinolites are distinguished by their green colour and pleochroism. Tremolite is common in metamorphosed impure dolomitic limestones. Actinolite occurs as a retrograde metamorphic product of basic rocks. Ferro-actinolite has a restricted occurrence.

Chemistry

Calcic amphiboles commonly show considerable departure from the tremolite–ferro-actinolite end-member compositions by the substitution of Al for Si which is compensated by either Al for (Mg,Fe) (towards tschermakite) or by Na in the *A* site (towards edenite) or by both of these (towards pargasite) (see Table 23, p. 140 and Fig. 114). The extent of solid solution of the more aluminous end-members (hornblendes) in tremolite–ferro-actinolite is considerable, particularly at higher temperatures, but it is convenient to consider the Al-poor calcium amphiboles separately, defining these as containing not less than 7.5Si atoms pfu.

Within the Mg−Fe series the names tremolite, actinolite and ferro-actinolite are used for the ranges of X = Mg/(Mg + Fe) = 1.0−0.9, 0.9−0.5 and 0.5−0.0, respectively. Members of this series with X less than 0.5 are uncommon, higher contents of Fe generally occurring in the more aluminous amphiboles. Rare Mn- and/or Zn-rich varieties occur but usually the content of these elements is low.

Replacement of Ca by Na accompanied by Al for Mg and/or Na in the *A* site tends to be relatively minor (up to about 0.4 atoms pfu) in natural tremolite–ferro-actinolites, probably reflecting the limited solid solution between calcic and alkali amphiboles at moderate temperatures. There appears to be more solid

Downloaded from https://pubs.geoscienceworld.org/books/chapter-pdf/3756212/9780903056434_ch36.pdf
by guest

solution towards the richterite than towards the glaucophane composition. There is similarly little substitution of Mg or Fe for Ca (0.1 or 0.2 atom pfu), more of this occurring in higher-grade metamorphic amphiboles which have a higher Al content. The maximum solid solution of cummingtonite–grunerite in actinolite is about 15% at about 600ºC.

There has been much controversy as to immiscibility between tremolite–ferro-actinolite and hornblende. Coexisting pairs may represent a replacement or an earlier and later stage of progressive metamorphism rather than an equilibrium relationship and therefore do not necessarily indicate immiscibility. More certain evidence has, however, been provided in some cases by the observation of exsolution lamellae by light- or electron-microscopy. Furthermore, the existence of a homogeneous amphibole with an intermediate composition does not rule out immiscibility since it may represent hypersolvus crystallization.

Experimental

The $P-T$ curve for the stability of tremolite is shown in Fig. 111 (curve 1). However, in most metamorphic rocks tremolite disappears at a much lower grade than indicated by curve 1, through such reactions as:

$$\text{tremolite} + \text{calcite} + \text{quartz} \rightarrow \text{diopside} + CO_2 + H_2O$$

which takes place at 500–550ºC. Also, the formation of tremolite, for example, by the reaction:

$$\text{dolomite} + \text{quartz} + \text{fluid} \rightarrow \text{tremolite} + \text{calcite} + \text{fluid}$$

would occur at lower temperatures. The fugacities of CO_2 and H_2O are important in each of these reactions.

Curve 2 (Fig. 111) shows that the stability of tremolite is lowered markedly by the substitution of Fe for Mg. At f_{O_2} higher than the magnetite–quartz–fayalite buffer, ferro-actinolite is not stable at any temperature. The substitution of F for (OH) increases the stability of tremolite. At intermediate Fe/Mg compositions, in the presence of CO_2, actinolites decompose on heating to give cummingtonite + pyroxene + quartz + H_2O, and ferro-actinolites give olivine + pyroxene + quartz + H_2O.

At very high hydrostatic pressures the stability field of tremolite is terminated by the reaction

$$\text{tremolite} \rightarrow \text{diopside} + \text{talc}$$

the highest temperature for stability being 915ºC at 1.5 GPa.

Experiments to determine the limits of solid solution in calcic amphiboles have proved difficult, but for tschermakite (Ts) in tremolite (Tr) it is about 55%. At compositions with more of the Ts molecule, the solid solution $Tr_{45}Ts_{55}$ is formed together with anorthite and other phases. Tschermakite is thus a purely theoretical end-member.

Optical and physical properties

The refractive indices and densities of members of the tremolite–ferro-actinolite series increase approximately linearly whereas 2V, γ:z and δ decrease with increasing Fe content (Fig. 112). Although this is the major source of variation, other factors include the Mn, Al and F contents. Crystal habits (Fig. 113) may vary from prismatic through acicular to asbestiform and there is also a very hard compact microcrystalline variety nephrite, one of the two forms of precious jade (the other, jadeite, is a pyroxene).

Distinguishing Features

The more magnesium-rich members of the series are distinguished from cummingtonite by their negative optical character and lower refractive indices, while the more iron-rich minerals have smaller optic axial angles and a lower birefringence than the more iron-rich members of the cummingtonite–grunerite series.

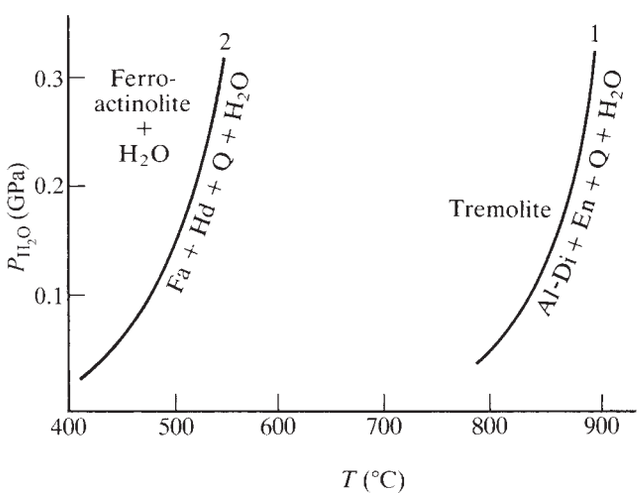


Fig. 111. The $P-T$ stability relations for (1) tremolite (after Boyd, 1959) and (2) ferro-actinolite (after Ernst, 1966), the latter at f_{O_2} defined by the magnetite–quartz–fayalite buffer. Fa: fayalite; Hd: hedenbergitic pyroxene; Q: quartz; Al-Di: aluminium diopside; En: enstatite (Boyd, F.R., 1959, Hydrothermal investigations of the amphiboles. In *Research in Geochemistry*, P.H. Abelson (Ed.), John Wiley & Sons; Ernst, W.G., 1966, *Amer. J. Sci.*, **264**, 37–65).

Downloaded from https://pubs.geoscienceworld.org/books/chapter-pdf/3756212/9780903056434_ch36.pdf
by guest

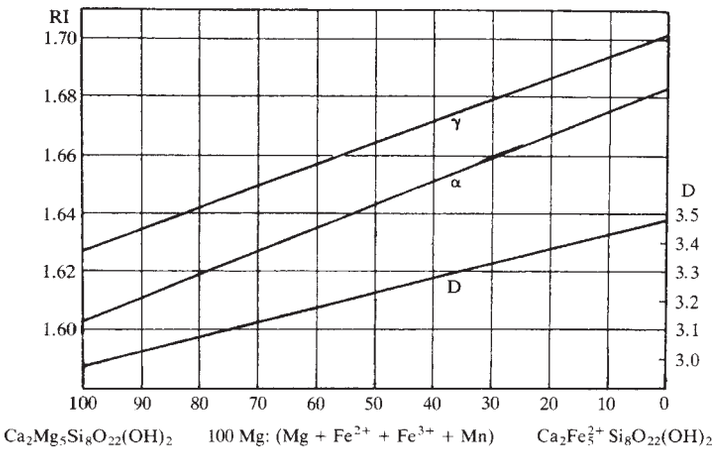


Fig. 112. The relation between chemical composition and refractive indices and density for the tremolite–ferro-actinolite series.

Multiple twinning is less common and is generally not on the fine scale so characteristic of cummingtonite and grunerite. Distinction of the actinolite–ferro-actinolite series from the orthorhombic amphiboles may be made by the straight extinction of the latter in all [001] zone sections. Tremolite and the more magnesium-rich actinolites, because of the lack of colour or very pale green colour, are not difficult to distinguish from hornblendes. The optical properties of the more iron-rich actinolites are commonly transitional to those of the common hornblendes: extinction angles (γ:z) between 10º and 15º are, however, indicative of ferro-actinolite. Tremolite is distinguished from wollastonite by its higher birefringence and optic axial angle and by the presence of the amphibole cleavage. Pyroxenes have their characteristic cleavages at about 90º.

Paragenesis

Tremolite and actinolite are essentially metamorphic minerals and occur in both contact and regionally metamorphosed rocks. In thermally metamorphosed impure dolomites, tremolite forms early by reaction between dolomite and quartz:

$$5\,CaMg(CO_3)_2 + 8\,SiO_2 + H_2O \rightarrow Ca_2Mg_5Si_8O_{22}(OH)_2 + 3\,CaCO_3 + 7\,CO_2$$

dolomite, quartz → tremolite, calcite

At higher grades of metamorphism tremolite is unstable and if SiO_2 is still available after the above reaction the tremolite reacts with calcite to form diopside:

$$Ca_2Mg_5Si_8O_{22}(OH)_2 + 3\,CaCO_3 + 2\,SiO_2 \rightarrow 5\,CaMgSi_2O_6 + 3\,CO_2 + H_2O$$

tremolite, calcite, quartz → diopside

In contrast, if there is an excess of dolomite relative to quartz, the early-formed tremolite reacts with the dolomite to give forsterite and calcite:

$$Ca_2Mg_5Si_8O_{22}(OH)_2 + 11\,CaMg(CO_3)_2 \rightarrow 8\,Mg_2SiO_4 + 13\,CaCO_3 + 9\,CO_2 + H_2O$$

tremolite, dolomite → forsterite, calcite

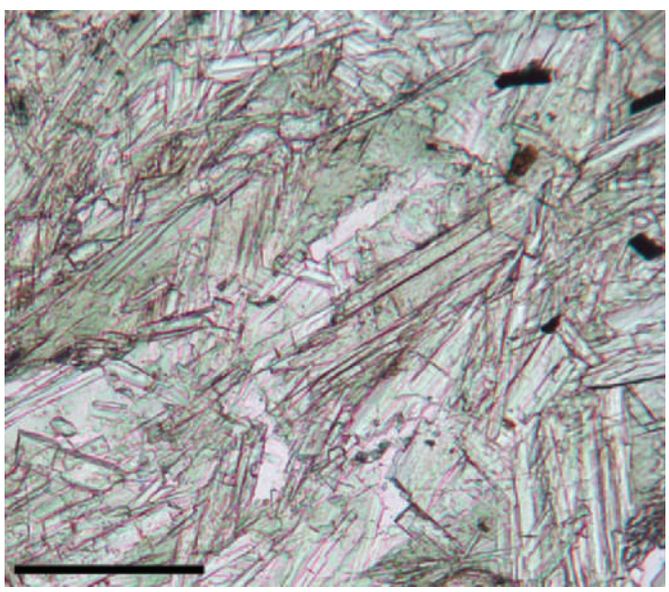


Fig. 113. Actinolite, actinolite-chlorite rock, Unst, Shetland (ppl, scale bar 0.3 mm), showing decussate aggregates of actinolite needles with typical high relief (courtesy of G.T.R. Droop).

Downloaded from https://pubs.geoscienceworld.org/books/chapter-pdf/3756212/9780903056434_ch36.pdf
by guest

The temperatures for the above reactions are dependent upon H_2O and CO_2 concentrations. In carbonate-free skarns, tremolite can persist into the sillimanite zone.

Tremolite and actinolite are characteristic minerals in low-grade regionally metamorphosed ultrabasic rocks such as tremolite-talc and tremolite-carbonate-antigorite schists. Actinolite (mainly Mg-rich), associated with epidote and chlorite is commonly produced by low-temperature metamorphism of rocks of basaltic composition by reactions involving pumpellyite, or chlorite + calcite + quartz, or prehnite. Actinolite can thus range from the higher part of the prehnite-pumpellyite to the main part of the greenschist facies.

Actinolite-hornblende associations are found in the low- and medium-pressure metamorphic terranes of the greenschist, amphibolite and epidote-amphibolite facies. Their coexistence may relate to progressive metamorphism, with hornblende being formed at higher grade by a reaction such as:

actinolite + epidote + chlorite + quartz → hornblende + H_2O

If, however, equilibrium can be assumed, the actinolite–hornblende pair can be taken to indicate immiscibility

Actinolite is also a constituent of some glaucophane schists, and here is associated particularly with albite, chlorite, epidote, pumpellyite, lawsonite and stilpnomelane (e.g. Table 23, anal. 7). Actinolite is a common product of the retrograde metamorphism of basic rocks; with increasing grade of metamorphism its content of aluminium increases and in the biotite and garnet zones the amphibole becomes hornblendic in composition.

The natural occurrence of ferro-actinolite is very restricted because of its narrow temperature range of stability, its restriction to highly reducing environments, and its chemical requirement of high Fe yet virtual absence of Na and Al. The main occurrences of iron-rich members of the series are in metamorphosed iron formations together with calcite, dolomite and cummingtonite.

In many basic rocks pyroxene is altered marginally to a pale green amphibole to which the name uralite is often given. This amphibole is commonly considered to be actinolitic in composition and to be derived by the pneumatolytic action of the residual water-enriched magmatic fluids on the earlier crystallized pyroxenes (see also p. 159).

Further reading

Day, H.W. and Springer, R.K. (2005) The first appearance of actinolite in the prehnite-pumpellyite facies, Sierra Nevada, California. *The Canadian Mineralogist*, **43**, 89–104.

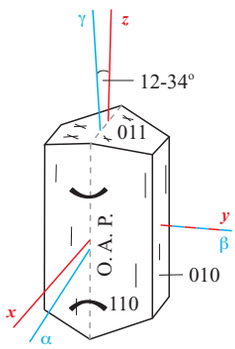
Verkouteren, J.R. and Wylie, A.G. (2000) The tremolite–actinolite–ferro-actinolite series: systematic relationships among cell parameters, composition, optical properties, and habit, and evidence of discontinuities. *American Mineralogist*, **85**, 1239–1254.

Downloaded from https://pubs.geoscienceworld.org/books/chapter-pdf/3756212/9780903056434_ch36.pdf
by guest

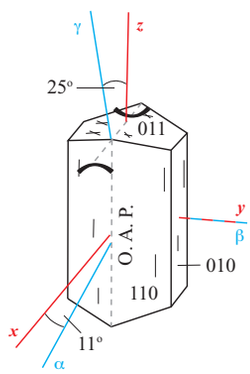
Hornblendes

Magnesiohornblende–Ferrohornblende	$\square Ca_2(Mg,Fe^{2+})_4Al[Si_7AlO_{22}](OH)_2$
Tschermakite–Ferrotschermakite	$\square Ca_2(Mg,Fe^{2+})_3Al_2[Si_6Al_2O_{22}](OH)_2$
Edenite-Ferro-edenite	$(Na,K)Ca_2(Mg,Fe^{2+})_5[Si_7AlO_{22}](OH)_2$
Pargasite–Ferropargasite	$(Na,K)Ca_2(Mg,Fe^{2+})_4Al[Si_6Al_2O_{22}](OH)_2$
Magnesiohastingsite–Hastingsite	$(Na,K)Ca_2(Mg,Fe^{2+})_4Fe^{3+}[Si_6Al_2O_{22}](OH)_2$

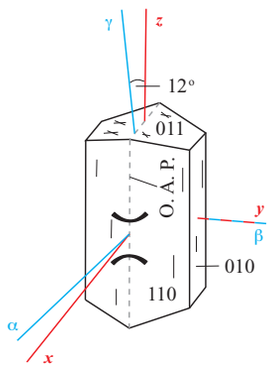
Monoclinic (−)(+)



Magnesio- and Ferrohornblende



Pargasite



Hastingsite

Hornblendes (General)

α	1.610–1.728
β	1.612–1.731
γ	1.62–1.76
δ	~ 0.02

$2V_\alpha$	90–44°; mostly optically negative, although Mg-rich pargasites are positive with $2V_\gamma$ 56–90°; hastingsites have lower $2V_\alpha$ down to zero
Orientation	$\beta = y$; $\gamma:z$ 12–34°; for pargasite and ferropargasite $\gamma:z$ ~ 25°; O.A.P. (010)
D (g/cm^3)	3.02–3.59 (highest values are for hastingsites)
H	5–6
Cleavage	{110} good; {100}, {001} partings; (010):(1$\bar{1}$0) ~ 56°
Twinning	{100} simple, lamellar, common
Colour	*Hornblende*: green, dark green, black; pale green, green, light yellow-brown to brown in thin section *Pargasite*: light brown, brown; colourless, very light brown, bluish green in thin section *Hastingsite*: dark green, black; yellow, brown–green, dark green in thin section
Pleochroism	*Hornblende*: variable in greens, yellow-green, bluish green and brown; absorption $\gamma \geqslant \beta > \alpha$ or $\beta > \gamma > \alpha$ *Pargasite*: α yellow, greenish yellow; β = γ light brown, bluish green *Hastingsite*: α yellow, greenish brown, yellowish green; β deep greenish blue, brownish green, dark olive-green; γ deep olive green, smoky blue–green, very dark green
Unit cell	a ~ 9.9 Å, b ~ 18.0 Å, c ~ 5.3 Å, β ~ 105.5° Z = 2; space group $C2/m$

Downloaded from https://pubs.geoscienceworld.org/books/chapter-pdf/3756593/9780903056434_ch37.pdf
by guest

With the exception of tschermakite, the above-listed amphiboles are very common constituents of plutonic igneous rocks, ranging from ultramafic to mafic, intermediate and acid lithologies. They are less common in hypabyssal rocks and lavas. In metamorphic rocks they are found from the greenschist to the lower granulite facies. Their typical green colour, cleavage angle of 56° and extinction angle of ⩽34° are characteristic. For classification purposes (Leake *et al.*, 1997) the term hornblende is used only within the names magnesiohornblende and ferrohornblende for the end members $Ca_2Mg_4Al[Si_7AlO_{22}](OH)_2$ and $Ca_2Fe_4Al[Si_7AlO_{22}](OH)_2$, respectively and not as a mineral name itself. It is very useful, however, if a mineral in hand specimen or thin section belongs to the above group but has not been analysed, or in discussions of the group as a whole, to use the term hornblende or hornblendes, and this use has been adopted in the following text.

Chemistry

The terms magnesiohornblende (with Mg > Fe^{2+}) and ferrohornblende (Fe > Mg) are used for the end-members $Ca_2Mg_4Al[Si_7AlO_{22}](OH)_2$ and $Ca_2Fe_4Al[Si_7AlO_{22}](OH)_2$, respectively. Hornblende has been used – as a general term – for all calcic amphiboles with appreciable aluminium content. In the latter sense, hornblendes can be conveniently regarded as following three trends away from the Al-free composition of end-member tremolite–actinolite. The first is towards magnesio- and ferrohornblende with one Al replacing Si balanced by Al for (Mg,Fe), i.e. with the replacements AlAl ↔ Si(Mg,Fe), which if continued go to tschermakite–ferrotschermakite, $Ca_2(Mg,Fe)_3Al_2Si_6Al_2O_{22}(OH)_2$. The second trend is towards edenite–ferro-edenite, $NaCa_2(Mg,Fe)_5Si_7AlO_{22}(OH)_2$, in which the replacement of Si by Al is balanced by the entry of Na in the otherwise vacant *A* site (AlNa ↔ Si□). The third trend is a combination of the above two towards pargasite–ferropargasite, $NaCa_2(Mg,Fe)_4AlSi_2Al_2O_{22}(OH)_2$, in which the substitution of two Al for two Si is compensated partly by Al for (Mg,Fe) and partly by Na in the *A* site, $Al_2AlNa \leftrightarrow Si_2(Mg,Fe)\square$. In the majority of the above species the replacement of Si by Al does not exceed two atoms per formula unit.

Whereas many natural amphiboles are close in composition to tremolite–actinolite, magnesio- and ferrohornblende and pargasite–ferropargasite, fewer correspond with tschermakite–ferrotschermakite and edenite–ferro-edenite, and most specimens are intermediates between two or more end-members. The ranges of composition which are associated with each end-member name are illustrated in Fig. 114, which plots the number of (Na + K) atoms in *A* sites and number of Si atoms per formula unit. In each case Fe^{2+} can replace Mg, and the iron-rich version, usually with $Fe^{2+}/(Fe^{2+} + Mg) > 0.5$, can be indicated by the prefix 'ferro' [tremolite–actinolites with Fe/(Fe + Mg) between 0.1 and 0.5 are called actinolite, and those with Fe/(Fe + Mg) > 0.5 ferro-actinolite]. Within the calcic amphiboles as a whole the range of Fe/(Fe + Mg) ratios is complete but those with high Si content tend to be

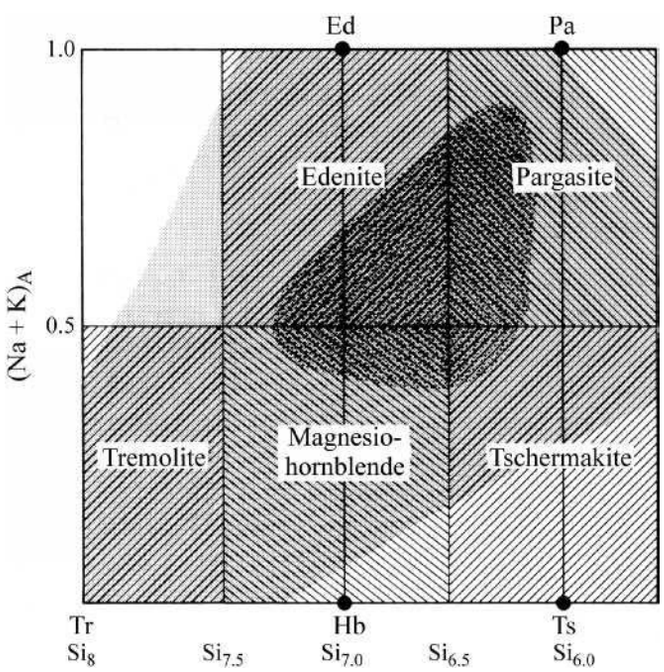


Fig. 114. The chemical variation of calcic amphiboles expressed as numbers of (Na + K) in *A* sites and Si atoms per formula unit. End-members are: Tr, tremolite; Hb, magnesiohornblende; Ed, edenite; Pa, pargasite; Ts, tschermakite. The more densely stippled areas show the more commonly occurring compositions. Only Mg end-members are shown.

Downloaded from https://pubs.geoscienceworld.org/books/chapter-pdf/3756593/9780903056434_ch37.pdf
by guest

more magnesium-rich whereas in pargasite and tschermakite iron-rich members are more common.

In the more iron-rich hornblendes significant substitution of Fe^{3+} for Al in *M*(1,2,3) sites, see p. 139, i.e. $^{[6]}Al$, can occur but the ratio Fe^{3+}/Fe^{2+} is rarely greater than unity. The Fe^{3+}-rich equivalents ($Fe^{3+} > {}^{[6]}Al$) of pargasite and ferropargasite are magnesiohastingsite, $NaCa_2Mg_4Fe^{3+}Si_6Al_2O_{22}(OH)_2$ and hastingsite, $NaCa_2Fe^{2+}_4Fe^{3+}Si_6Al_2O_{22}(OH)_2$, respectively. The entry of Fe^{3+} can also be balanced by the substitution of O for (OH) [see oxo-hornblende]. The titanium content is generally low except for the Ti-rich (Ti > 0.5 atom) version of pargasite known as kaersutite. High Ti (and K) contents occur particularly in the hornblendes of charnockites and granulites, and the highest Ti tends to occur in igneous amphiboles.

Some substitution of (Mg,Fe) for (Ca,Na) in the *M*4 site can occur but because of the marked differences in ionic sizes this substitution is very limited. There is little solid solution toward cummingtonite–grunerite and each can show exsolution lamellae in the other. In coexisting hornblende and cummingtonite (also anthophyllite), the latter usually have the higher Fe/(Fe+Mg) ratio. The amount of manganese, normally replacing (Mg,Fe) or Ca, is usually less than 0.05, but up to 0.5 atom per formula unit can occur. The range of zinc contents is generally similar.

Although Ca and Na are both suitably sized cations to enter the *M*4 site, and they do so in approximately equal proportions in the sodium–calcium amphiboles (e.g. richterite and barroisite), it appears that calcium and sodium amphiboles are not completely miscible at all temperatures and that the latter relatively uncommon minerals may represent hypersolvus crystallization. The solvus limb is steeper on the Na side, so whereas hornblende may become more barroisitic at higher temperatures, there is less scope for the substitution of Ca in the alkali amphiboles. The border between sodic-calcic and calcic amphiboles is defined somewhat arbitrarily according to whether $(Na)_B$ is greater or less than 0.5. In calcic amphiboles there is generally only about 0.1 $(Na)_B$ atom pfu.

Potassium, usually 0–0.2, but up to about 0.5 atom pfu in natural specimens, is restricted to the *A* site. Experiments have demonstrated complete solid solution between Na and K in edenite and up to 0.5 K in pargasite.

Whereas a miscibility gap between calcium and other amphiboles (Fe,Mg or alkali) is not unexpected, a gap between hornblendes and the tremolite–actinolites seems less likely. There is, however, some evidence of such a gap from both natural occurrences and laboratory experiments. Some coexisting actinolite–hornblende pairs may alternatively be indications of progressive (gradual or sudden) metamorphism rather than immiscibility.

Some chemical analyses show more H_2O+ than is required to give two (OH,F,Cl) ions per formula unit; this may represent extra hydrogen ions which are associated with oxygens as (OH) replacing O, but is commonly due to water absorbed on fine-grained material. In other hornblendes the number of monovalent anions is apparently less than two per formula unit; in some the low value may be due to the omission of the determination of fluorine and chlorine in the analysis. Both these anions are important constituents in many amphiboles and in some pargasite–ferrohastingsites the replacement of OH by F is as much as one atom per formula unit. Chlorine is highest in Fe-rich hornblendes.

Oxo-hornblende

If a low content of H_2O+ is accompanied by a high Fe^{3+}:Fe^{2+} ratio, the substitution of O^{2-} for $(OH)^-$ is implied, which could be a primary feature of the amphibole, or more likely the result of the oxidation–dehydroxylation reaction:

$$Fe^{2+} + (OH)^- \rightarrow Fe^{3+} + O^{2-} + \tfrac{1}{2}H_2$$

The transformation of a hornblende to oxo-hornblende can be effected in the laboratory by heating in air to about 800ºC and can be reversed by heating in hydrogen.

Examples of chemical analyses of amphiboles of different kinds and their formulae are given in Table 23. If a full and reliable chemical analysis of an amphibole is available, the formula is usually calculated on the basis of 24 (O,OH,F) anions, but if the amount of H_2O+, corresponding with structural (OH) ions, is unknown or suspected of error, the formula can be calculated on the basis of 23 oxygen equivalents, ignoring any estimate of H_2O. This in effect assumes that there are two (OH,F) ions per formula unit and is the usual means of estimating cations pfu with electron probe microanalysis data in which direct analysis for water is not possible.

Experimental

A wide range of both hydroxy- and fluor-hornblende compositions have been synthesized by dry and hydrothermal methods.

Hydrothermal experiments have determined the upper stability limits of pargasite, ferropargasite, magnesiohastingsite and hastingsite, Fig. 115a. By comparing the four curves it can be seen that whereas the replacement by Fe^{2+} of Mg lowers the stability, the substitution of Fe^{3+} for Al raises it. Among the breakdown products from hornblende, clinopyroxene, spinel and plagioclase feldspar and/or nepheline are commonly present; in addition, magnesium-rich hornblendes yield olivine, and iron-rich hornblendes give garnet. Except for pargasite, the oxidation state of Fe is important so that experiments with different oxygen activities produce different results. Ferropargasite and hastingsite have maximum stability at f_{O_2} of the wüstite–magnetite

Downloaded from https://pubs.geoscienceworld.org/books/chapter-pdf/3756593/9780903056434_ch37.pdf
by guest

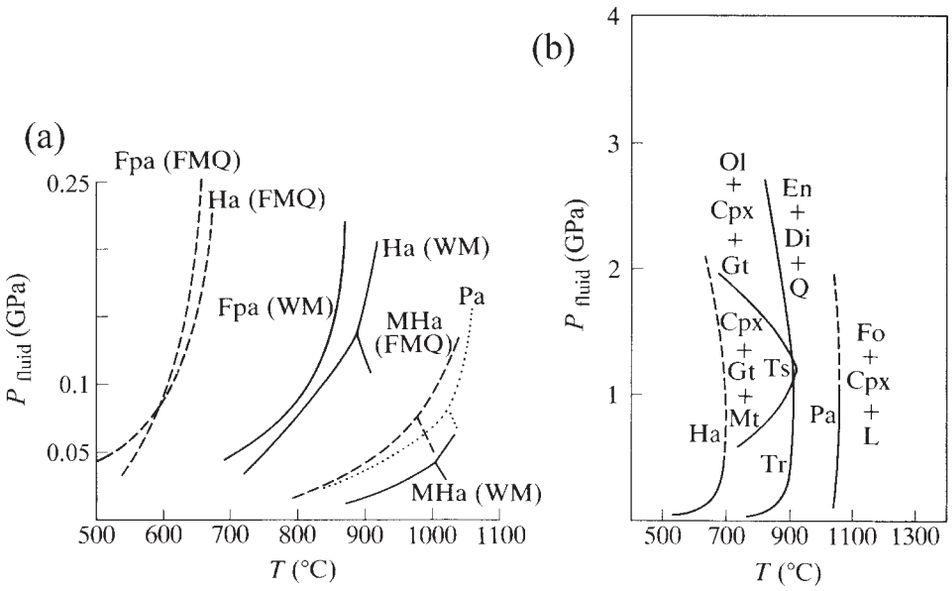


Fig. 115. (a) Experimentally determined $P-T$ stability curves for end-member pargasite (Pa), ferropargasite (Fpa) magnesiohastingsite (MHa) and hastingsite (Ha) with different oxygen buffers (FMQ: fayalite–magnetite–quartz; WM: wüstite–magnetite; HM: hematite–magnetite). (b) $P-T$ curves determined experimentally at high pressures for pargasite (Pa), hastingsite (Ha), tschermakite (Ts) and tremolite (Tr). All are (OH)-amphiboles and are in conditions of excess H_2O. Fo: forsterite; Cpx: clinopyroxene; En: enstatite; Di: diopside; Q: quartz; Ol: olivine; Gt: garnet; Mt: magnetite; L: liquid (after Gilbert, M.C. *et. al*., 1981, in *Reviews in Mineralogy*, Min. Soc. Amer., **9B**, 250 and 254).

buffer, whereas the more Fe^{3+}-rich magnesiohastingsite has maximum stability with the hematite–magnetite buffer. All of the amphibole reactions are sensitive to fluid compositions (e.g. H_2O/CO_2); those of Fig. 115a relate to conditions of excess water. Experiments have shown that the substitution of F for (OH) significantly increases the stabilities of ferropargasite, hastingsite and magnesiohastingsite. At higher total pressures than those shown in Fig. 115a, the stability curves rise steeply and slope back towards the P axis (Fig. 115b).

Experiments on the tremolite–pargasite join at 0.1 GPa have shown the existence of a wide miscibility gap between the end-members which is narrower, however, for Fe-rich compositions. No gap was observed at 0.5 GPa. Pargasite and richterite form a solid solution series at 850–900ºC (0.1 GPa) but there is a solvus gap at lower temperatures. For intermediate compositions breakdown occurs at a much lower temperature than for either end-member.

Edenite has been synthesized and its stability curve lies, as expected, at a somewhat higher temperature than that of tremolite but not as high as for pargasite. The stability of tschermakite appears to be restricted to moderately high pressures (Fig. 115b).

Optical and physical properties

The major effect of chemical variation on the optical properties of the hornblendes is that exerted by the substitution of Fe for Mg which increases α and γ, and decreases 2V. Other chemical variations (e.g. substitutions of Al for Si, Na for Ca) also have significant effects, however, so correlation of optical properties with composition cannot be precise. For magnesiohornblende and ferrohornblende, α and γ range approximately linearly from ~1.61 and 1.64 to ~1.68 and 1.71 respectively as Mg is replaced by Fe. A similar range is shown by the progressive substitution of Fe for Mg in the more aluminous hornblendes, extending to significantly higher values only for the most iron-rich hastingsites. Hornblendes are optically negative with moderate to large 2V, except for hastingsites which have lower 2V and the Mg-rich pargasites which are optically positive.

The extinction angle, $\gamma:z$, even of minerals of comparable composition, may show considerable variation and this property is of little diagnostic value. The absorption scheme is variable but the strongest absorption is coincident with either the γ or β vibration direction. The colours of hornblendes are influenced mainly by the concentrations of Fe^{2+}, Fe^{3+} and Ti.

Immiscibility between hornblende and cummingtonite–grunerite is sometimes evident through exsolution lamellae which are oriented close to (100) and $(\bar{1}01)$ (C-centred cell).

The conversion of magnesiohornblende to oxo-magnesiohornblende on heating at about 800ºC is accompanied by an increase in refractive indices and birefringence, and a decrease in the extinction angle which may range to as low as 0º.

Oxo-hornblendes are coloured brown or black and are brown to dark brownish red in thin section. They typically show pleochroism with α pale yellow to yellow, β dark chestnut-brown and γ dark brown, sometimes with a reddish tinge. Many oxo-hornblendes show peripheral resorption effects, and the crystal

Downloaded from https://pubs.geoscienceworld.org/books/chapter-pdf/3756593/9780903056434_ch37.pdf
by guest

margins are dusty with fine grains of black iron minerals, or with reddish brown grains of hematite; in some cases the hornblende may be completely replaced by iron oxide or by pyroxene.

Distinguishing features

Magnesiohornblende cannot in all cases be distinguished from the other Ca-rich amphiboles. It is, however, distinguished from Mg-rich tremolites by higher refractive indices and moderate to strong pleochroism, and from actinolite and ferro-actinolite by larger optic axial angle and birefringence. It is distinguished from pargasite by its optically negative character and from hastingsite by its larger optic axial angle and extinction angle; in general, it cannot with certainty be distinguished optically from the edenitic and tschermakitic varieties. Both cummingtonite and grunerite can generally be distinguished by their characteristic multiple twinning on (100); cummingtonite is further distinguished from the Ca-rich amphiboles, except pargasite, by its optically positive character, whereas grunerite has higher refractive indices and stronger birefringence. Oxo-hornblende and kaersutite are distinguished by their intense absorption and pleochroism. Oxo-hornblende is distinguished from aenigmatite by the smaller optic axial angle, higher refractive indices and more intense γ absorption colour of the latter mineral. Hastingsite is distinguished from arfvedsonite by the weaker pleochroism and orientation of the optic axial plane parallel to the symmetry plane of the former mineral.

Paragenesis

The extremely wide range of chemical substitutions possible in hornblende, including (Mg,Fe), (Na,Ca), (Si,Al), (Fe^{3+},Fe^{2+}), (O,OH,F) leads to their existence in a wide variety of igneous and metamorphic petrogenetic conditions. Thus although they are particularly characteristic minerals of intermediate plutonic rocks, they also occur by primary crystallization in basic and ultrabasic rocks as well as in rocks of acid and alkali composition. Primary magnesiohastingsite occurs in rocks of the alkali basalt and calc-alkali series but does not commonly occur in oceanic tholeiites because in these f_{H_2O} and f_{O_2} are too low. In andesitic rocks hornblende is commonly accompanied by olivine and it has been suggested that the amphibole is formed at a high temperature by reaction between olivine and andesitic liquid. With regard to the Mg/(Mg + Fe) ratio, there is a continuous series from the more magnesium-rich hornblende [X = Mg/(Mg + Fe) ~ 0.75] of the gabbros to the iron-rich ferrohastingsites [X ~ 0.05] of nepheline syenites and granites. The typical hornblendes of diorites and other intermediate rocks of the calc-alkaline series have X ~ 0.5 and a moderate content of aluminium (~1.5 Al per formula unit). The hornblendes of basaltic and andesitic rocks tend to be richer in alkalis and Fe^{3+} and to contain less fluorine.

Although in general the crystallization of amphibole follows the sequence of Bowen's discontinuous reaction series, i.e. amphiboles before biotite, this order can be reversed in crystallization from K-rich magmas with low f_{H_2O}.

In some basic igneous rocks, and particularly in troctolites and olivine gabbros, edenite occurs as a component of the symplectic coronas between olivine and plagioclase. In the typical corona sequence, the amphibole, usually in vermicular intergrowth with spinel, forms the outer zone in contact with the plagioclase. The reaction which gives rise to the formation of the corona may be expressed by:

$$\underset{\text{olivine}}{14\,(Mg,Fe^{2+})_2SiO_4} + 2\,\underset{\text{labradorite}}{NaAlSi_3O_8.4CaAl_2Si_2O_8} + 2\,H_2O \rightarrow$$
$$\underset{\text{orthopyroxene}}{14\,(Mg,Fe^{2+})SiO_3} + 2\,\underset{\text{edenite}}{NaCa_2(Mg,Fe^{2+})_5AlSi_7O_{22}(OH)_2} + \underset{\text{spinel}}{4\,(Mg,Fe)Al_2O_4}$$

Hornblende is one of the most common constituents of regionally metamorphosed basic or ultrabasic rocks and is stable in a wide range of $P-T$ conditions from upper greenschist through epidote-amphibolite and amphibolite into the lower part of the granulite facies. Hornblende and plagioclase feldspar are the main, and sometimes the sole, constituents of hornblende schists, hornblende gneisses and amphibolites, rocks which constitute the main bulk of the amphibolite facies.

Increasing metamorphic grade tends to produce changes in amphibole composition, i.e. increases in $^{[4]}Al$, $^{[6]}Al$, Ti, Fe^{3+}, Na and K, and decreases in Si, Fe^{2+}, Mg and Ca, but rock composition and f_{O_2} are influential as well as temperature. The mineralogical sequence corresponding with the above progression would be actinolite–hornblende–pargasite, and this is commonly accompanied by a change from fibrous to acicular to prismatic or even equant crystal habits. For rocks with excess silica, however, the tendency of amphibole composition is away from pargasite, in accordance with the reaction:

$$\underset{\text{pargasite}}{2\,NaCa_2Mg_4Al_3Si_6O_{22}(OH)_2} + 8\,\underset{\text{quartz}}{SiO_2} \rightarrow$$
$$\underset{\text{tremolite}}{Ca_2Mg_5Si_8O_{22}(OH)_2} + \underset{\text{tschermakite}}{Ca_2Mg_3Al_4Si_6O_{22}(OH)_2} + 2\,\underset{\text{albite}}{NaAlSi_3O_8}$$

The transition from greenschist to amphibolite facies can be represented by the reaction:

$$\text{albite} + \text{chlorite} + \text{epidote} + \text{actinolite} \rightarrow \text{hornblende} + \text{plagioclase}$$

Downloaded from https://pubs.geoscienceworld.org/books/chapter-pdf/3756593/9780903056434_ch37.pdf
by guest

which has been found to occur experimentally at about 550ºC (0.2 GPa). The amphibole becomes more sodic and the plagioclase more calcic so that there is in effect an exchange of Ca, Na and Al between these two minerals. In quartz-bearing rocks the reaction:

albite + actinolite → edenite + quartz

may occur.

At a higher grade of metamorphism (upper granulite facies), hornblende is transformed to pyroxene by a dehydration reaction of the type:

hornblende + quartz →
orthopyroxene + augite + plagioclase + H_2O

As indicated above, tschermakitic amphiboles occur in rocks of high metamorphic grade, e.g. kyanite amphibolites. They are also common in altered eclogites, and in this paragenesis are derived from omphacite in the early stages of retrograde metamorphism. At a later stage the garnet is replaced by hornblende-plagioclase symplectites, the hornblende of which is often in optical continuity with that derived from the omphacite.

The occurrence of magnesiohornblende and pargasites very rich in magnesium is restricted to metamorphosed impure dolomitic limestones; more iron-rich pargasites occur in regionally metamorphosed skarns and are commonly associated with hydroxyl-, fluorine- or boron-metasomatism.

The hornblende in many igneous rocks is secondary in origin and derived from primary pyroxene. The secondary character of the hornblende is not obvious in all cases but is apparent where its development is related to joints and other smaller, less regular fractures which facilitated the movement of solutions. Some secondary amphiboles are tremolites or cummingtonites but the difficulty of identifying the composition of the more fibrous amphibole varieties has led to the common use of the name *uralite*, a term first applied to minerals with the habit of pyroxene and the structure of an amphibole, but now commonly used to describe a secondary fibrous light blue-green amphibole of undetermined composition. The alteration of pyroxenes to fibrous amphiboles is described as uralitization and the formation of these secondary hornblendes is generally ascribed to the action of hydrothermal solutions which may be associated with the late-stage crystallization of igneous rocks, or may be a post-consolidation process unrelated to the igneous activity from which the rocks were derived; in the latter case the uralitization may be associated with either regional, contact or metasomatic metamorphism.

Oxo-hornblendes occur in a large variety of volcanic rocks varying in composition from basalts to trachytes, and are particularly characteristic constituents of andesites, latites, basanites and tephrites, and their corresponding tuffs. Most oxo-hornblendes probably crystallized initially as magnesio- or ferrohornblende and were oxidized after eruption during the later stages of the consolidation of lava.

Further reading

Anderson, A.T. (1980) Significance of hornblende in calc-alkaline andesites and basalts. *American Mineralogist*, **65**, 837–851.

Bojar, H.-P. and Walter, F. (2006) Fluoro-magnesiohastingsite from Dealul Uroi (Hunedoura county, Romania): mineral data and crystal stucture of a new amphibole end-member. *European Journal of Mineralogy*, **18**, 503–508.

Cho, M. and Ernst, W.G. (1991) An experimental determination of calcic amphibole solid solution along the join tremolite–tschermakite. *American Mineralogist*, **76**, 985–1001.

Gilbert, M.C. (1966) Synthesis and stability relations of the hornblende ferropargasite. *American Journal of Science*, **264**, 698–742.

Harker, R.I. and Leahy, T. (2001) The significance of a hastingsite granite in the Carn Chuinneag-Inchbae complex. *Journal of Geology*, **37**, 53–57.

Kostyuk, E.A. and Sobolev, V.S. (1969) Paragenetic types of calciferous amphiboles and metamorphic rocks. *Lithos*, **2**, 67–81.

Na, K.C., McCauley, M.L., Crisp, J.A. and Ernst, W.G. (1986) Phase relations to 3 kbar in the systems edenite + H_2O and edenite + excess quartz + H_2O. *Lithos*, **49**, 153–163.

Oba, T. and Yagi, K. (1987) Phase relations in the actinolite–pargasite join. *Journal of Petrology*, **28**, 23–36.

Ravna, E.K. (2000) Distribution of Fe^{2+} and Mg between coexisting garnet and hornblende in synthetic and natural systems: an empirical calibration of the garnet–hornblende Fe-Mg geothermometer. *Lithos*, **53**, 265–277.

Rutherford, M.J. and Devine, J.D. (2003) Magmatic conditions and magma ascent as indicated by hornblende phase equilibria and reactions in the 1995-2002 Soufrière Hills magma. *Journal of Petrology*, **44**, 1433–1454.

Sharma, A. and Jenkins, D.M. (1999) Hydrothermal synthesis of amphiboles along the tremolite–pargasite join and in the ternary system tremolite–pargasite–cummingtonite. *American Mineralogist*, **84**, 1304–1308.

Thomas, W.M. (1982) Stability relations of the amphibole hastingsite. *American Journal of Science*, **282**, 136–164.

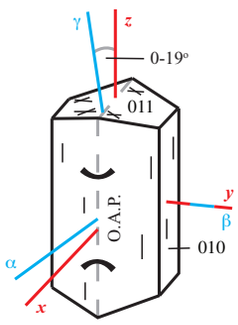
Tiepolo, M., Zanetti, A. and Oberti, R. (1999) Detection, crystal-chemical, mechanical and petrological implications of $^{[6]}Ti^{4+}$ partitioning in pargasite and kaersutite. *European Journal of Mineralogy*, **11**, 345–354.

Downloaded from https://pubs.geoscienceworld.org/books/chapter-pdf/3756593/9780903056434_ch37.pdf
by guest

Kaersutite–Ferrokaersutite $(Na,K)Ca_2(Mg,Fe^{2+},Fe^{3+},Al)_4(Ti,Fe^{3+})[Si_6Al_2O_{22}](O,OH,F)_2$

Monoclinic (−)

α	1.669−1.696
β	1.683−1.725
γ	1.695−1.743
δ	0.028−0.047
$2V_\alpha$	74−82°
Orientation	γ:*z* 0−19°, β = *y*; O.A.P. (010)
D (g/cm^3)	~ 3.3
H	5−6
Cleavage	{110} perfect; {100}, {001} partings; (110):(1$\bar{1}$0) ~ 56°
Twinning	{100} simple, lamellar, common
Colour	Dark brown to black; yellow−brown, brown, reddish brown and occasionally greenish brown in thin section
Pleochroism	α brownish yellow, light yellow−brown, pale yellow β reddish, reddish brown γ dark reddish brown, greenish brown
Unit cell	*a* ~ 9.85 Å, *b* ~ 18.0 Å, *c* ~ 5.3 Å, β ~ 105° Z = 2; space group *C*2/*m*



Kaersutite is found mainly in hypabyssal and volcanic alkaline igneous rocks. It is relatively rich in TiO_2, giving it a characteristic reddish brown colour in thin section.

Kaersutite (Table 23, anal. 12 and Fig. 116) is characterized chemically by its very high titanium content (5−10 wt.% TiO_2; equivalent to 0.5 to 1.0 atom pfu). Kaersutites, like oxo-hornblendes, are mostly magnesium-rich with the substitution of Mg by (Fe^{2+} + Fe^{3+}) limited approximately to 1.5 atoms pfu, but ferrokaersutite has also been reported. The Fe^{3+}/Fe^{2+} ratios cover a wide range, the highest values occurring in oxidized kaersutites, and it is the latter that exhibit the higher refractive indices in the ranges given above. A wide range is also shown by the (OH + F) content since kaersutites in lavas can be oxidized during eruption,

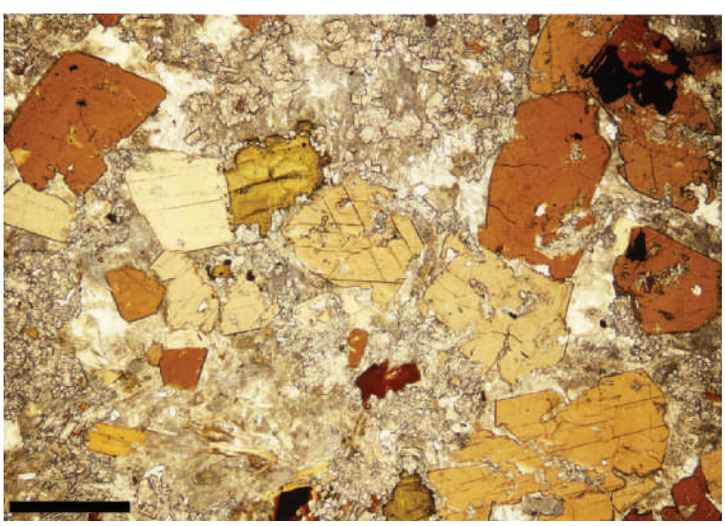


Fig. 116. Kaersutite (ppl, scale bar 1 mm), showing the characteristic reddish brown colour and strong pleochroism. The crystal in the centre of the field displays amphibole habit and cleavage (Lugar Sill, Ayrshire, Scotland) (W.S. MacKenzie collection, courtesy of Pearson Education).

Downloaded from https://pubs.geoscienceworld.org/books/chapter-pdf/3756849/9780903056434_ch38.pdf
by guest

converting Fe^{2+} to Fe^{3+} and OH to O. A correlation between Fe^{3+} and (OH,F) is not always discernible, however.

Kaersutites, except those with relatively high Fe^{3+}:Fe^{2+} ratios, are distinguished from oxo-hornblende by the nearly equal absorption in the β and γ directions; hastingsitic hornblendes and katophorite have a small optic axial angle, and aenigmatite has a smaller optic axial angle, higher refractive indices and more intense γ absorption. Titanian augite has a higher extinction angle and a paler and more violet absorption colour as well as the pyroxene cleavage.

Kaersutite is a typical constituent of alkaline volcanic rocks, and occurs as phenocrysts in trachybasalts, trachyandesites, trachytes and alkali rhyolites; in the more silica-rich rocks it occurs also as a groundmass constituent. Reaction rims of kaersutite around olivine phenocrysts, and the partial or complete replacement of titanian augite by kaersutite, are commonly found in trachybasalts; the kaersutite of these rocks is invariably surrounded by opaque margins of magnetite. Kaersutite occurs in camptonite dykes, and it is an abundant constituent of some monzonites. It also occurs in eclogites.

Further reading

Colville, A.A. and Novak, G.A. (1991) Kaersutite megacrysts and associated crystal inclusions from the Cima volcanic field, San Bernardino County, California. *Lithos*, **27**, 107–114.

Kesson, S. and Price, R.C. (1972) The major and trace element chemistry of kaersutite and its bearing on the petrogenesis of alkaline rocks. *Contributions to Mineralogy and Petrology*, **35**, 119–124.

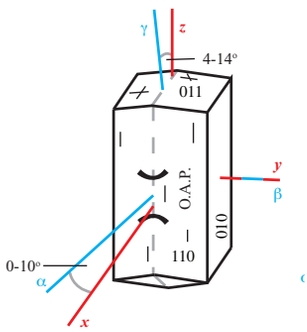
Yamaguchi, Y. and Makino, K. (2004) Ti-substitution mechanism in plutonic oxy-kaersutite from the Larvik alkaline complex, Oslo rift, Norway. *Mineralogical Magazine*, **68**, 675–685.

Downloaded from https://pubs.geoscienceworld.org/books/chapter-pdf/3756849/9780903056434_ch38.pdf
by guest

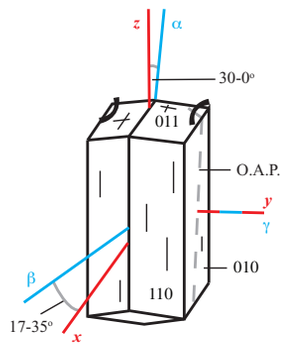
Glaucophane — $\square Na_2(Mg,Fe^{2+})_3Al_2[Si_8O_{22}](OH)_2$
Magnesioriebeckite–Riebeckite — $\square Na_2(Mg,Fe^{2+})_3Fe^{3+}_2[Si_8O_{22}](OH)_2$

Monoclinic

Glaucophane (−)



Riebeckite (+)(−)



α	1.594−1.630	1.650[a]−1.701
β	1.612−1.650	1.655[a]−1.711
γ	1.618−1.652	1.670[a]−1.717
δ	0.023−0.020	0.006−0.016
$2V_\alpha$	50−0°	40−100°
Orientation	γ:*z* 4−14°, β = *y*; O.A.P. (010)	α:*z* 30−0°, γ = *y*; O.A.P. ⊥(010)
D (g/cm^3)	3.05−3.15	3.15−3.50
H	6	5
Cleavage	{110} good; (110):(1$\bar{1}$0) ~56°	{110} good; (110):(1$\bar{1}$0) ~ 56°
Twinning	{100} simple, lamellar	{100} simple, lamellar
Colour	Grey, lavender-blue; lavender-blue to colourless in thin section	Dark blue, black, dark yellow green in thin section
Pleochroism	α colourless, yellow β lavender-blue γ blue	α blue, indigo β yellow–brown, yellow–green γ dark blue
Unit cell	*a* ~ 9.55 Å, *b* ~ 17.7 Å, *c* ~ 5.30 Å, β ~ 103.6° Z = 2; space group *C*2/*m*	*a* ~ 9.76 Å, *b* ~ 18.05 Å, *c* ~ 5.33 Å, β ~ 103.6° Z = 2; space group *C*2/*m*

Glaucophane occurs typically in low-temperature high-pressure metamorphic rocks derived from basalts. Its characteristic pleochroism ranges from virtually colourless to lavender-blue. Riebeckite is found in acid plutonic rocks and occasionally in low-grade schists.

Chemistry

Sodium amphiboles are those for which $Na_B \geqslant 1.50$ atoms per formula unit, but they are split into two groups depending upon the occupancy of the *A* site. Those with <0.5(Na + K) in *A* are members of a solid-

[a] Lower values refer to magnesioriebeckite.

Downloaded from https://pubs.geoscienceworld.org/books/chapter-pdf/3756925/9780903056434_ch39.pdf
by guest

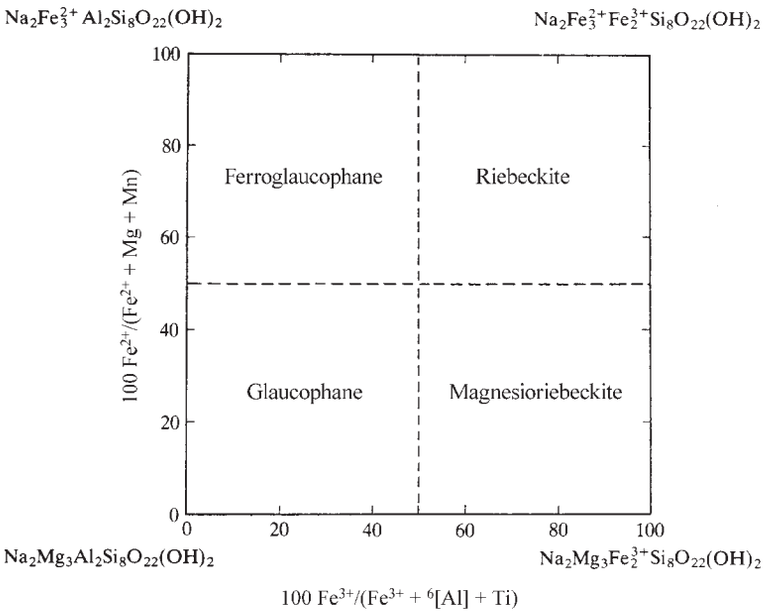


Fig. 117. The variation in chemical composition and nomenclature of the glaucophane–riebeckite sodic amphiboles.

solution series defined by four end-members, glaucophane, magnesioriebeckite, ferroglaucophane and riebeckite (Fig. 117), which embrace two kinds of substitution, Fe^{3+} for Al and Fe^{2+} for Mg.

Although in general iron atoms (Fe^{2+} and Fe^{3+}) may be assigned to *M*1, *M*2 or *M*3 sites, in riebeckite and magnesioriebeckite as in other amphiboles which have appreciable Na in *M*4 this is accompanied by a preference of Fe^{3+} for the *M*2 site.

There appears to be only limited miscibility between alkali and calcic amphiboles at the temperatures of the greenschist, epidote-amphibolite and glaucophane schist facies, but the gap is narrower at higher temperatures, leading to the existence of sodium-calcium amphiboles (p. 167).

Sodic amphiboles with compositions near the pure Mg and pure Fe^{2+} end-members are relatively less common than intermediates, but the substitution $Fe^{3+} \leftrightarrow Al$ covers a wide range. Although sodium is the dominant large cation, small amounts of Ca and K may be present.

The *P*–*T* stability field for glaucophane is illustrated in Fig. 118. In the high-pressure region glaucophane is replaced by jadeite + talc and in the low-pressure region by albite + talc + mica. The *P*–*T* curves for the breakdown of magnesioriebeckite, riebeckite and ferroglaucophane are shown in Fig. 119, from which the very marked lowering of stability by the substitution of Fe^{2+} for Mg and Fe^{3+} for Al is evident. The stabilities of alkali amphiboles which contain Fe^{3+} are considerably

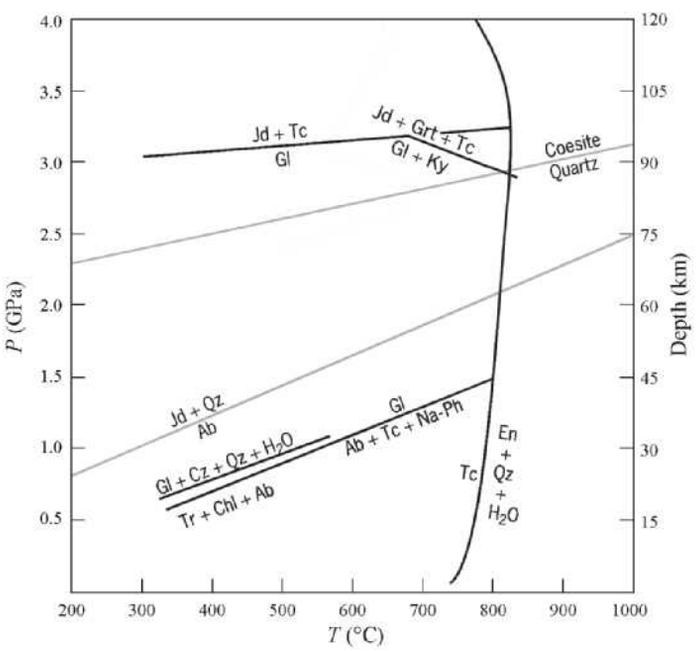


Fig. 118. Pressure–temperature diagram showing the upper and lower pressure limits for the stability of glaucophane. Also shown are the high pressure *P*/*T* curve for the reaction albite → jadeite + quartz, and the ultra-high-pressure curve for the quartz–coesite transformation. Tc: talc; Jd: jadeite; Gl: glaucophane; Cz: clinozoisite; Qz: quartz; H_2O: water; Tr: tremolite; Chl: chlorite; E: enstatite; Grt: garnet; Ky: kyanite; Na-Ph: sodium phlogopite; Ab: albite (after Carman, J.H. & Gilbert, M.C., 1983, *Amer. J. Sci.*, **283-A**, 414–437 and Liou, J.G., Corona, J.C. & Tayimon, T. 2008, *Encyclopedia of Science & Technology, 11th ed.* McGraw-Hill, New York, 142–144).

Downloaded from https://pubs.geoscienceworld.org/books/chapter-pdf/3756925/9780903056434_ch39.pdf
by guest

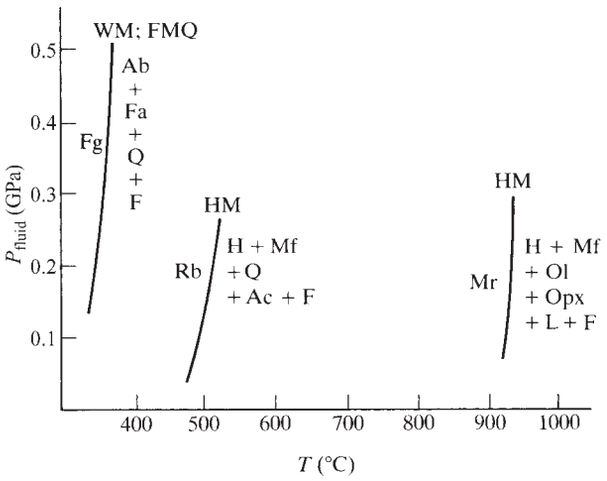


Fig. 119. Upper stability curves for magnesio-riebeckite (Mr), riebeckite (Rb) and ferroglaucophane (Fg). HM: hematite–magnetite; WM: wüstite–magnetite; FMQ: fayalite–magnetite–quartz buffer; Ab: albite; Fa: fayalite; Q: quartz; H: hematite; Mf: magnesioferrite; Ac: actinolite; Ol: olivine; Opx: orthopyroxene; L: liquid; F: fluid. (Fg curve: Hoffmann, C., 1972, *Contrib. Mineral. Petrol.*, **34**, 135. Rb curve; Ernst, W.G., 1962, *J. Geol.*, **70**, 689. Mr curve: Ernst, W.G., 1960, *Geochim. Cosmochim. Acta*, **19**, 10).

influenced by oxygen fugacity. Ferroglaucophane has the lowest upper stability temperature of any amphibole, and since it also needs very low f_{O_2} it is fairly rare in nature. It should be noted also that because of the effect of Fe on $P-T$ fields, sodium amphiboles other than glaucophane are not indicators of high pressure.

Optical and physical properties

Members of the glaucophane–riebeckite series display a very considerable range of optical properties; both main replacements, Mg ↔ Fe^{2+} and Al ↔ Fe^{3+}, have a marked effect on the refractive indices, and the latter substitution is accompanied in addition by large changes in optic axial angles, and by a change in orientation of the optic axial plane. In the magnesioriebeckite–riebeckite series the substitution is Fe^{2+} for Mg. In the glaucophane–riebeckite series Fe^{2+},Fe^{3+} replaces Mg,Al and, as the effect of $^{[6]}$Al does not differ appreciably from that of Mg, the increase in the refractive indices is more rapid than it is in the magnesioriebeckite–riebeckite minerals (Fig. 120).

In glaucophane the optic axial plane is (010) and the obtuse bisectrix γ makes a small angle with the z axis. Increasing replacement of Al by Fe^{3+} is first accompanied by a reduction in 2V which becomes zero and then opens out in the plane perpendicular to (010) in minerals in which the Fe^{3+}:$^{[6]}$Al ratio is greater than unity. The replacement in riebeckite of Fe^{2+} by Mg is accompanied by a reduction in the optic axial angle and an increase in the extinction angle (magnesioriebeckite 2V 40 to 50º and α:z 15 to 30º).

The pleochroism of riebeckite is variable but in most specimens the absorption colour parallel to β is indigo-blue; the absorption is most commonly $\alpha < \beta \leqslant \gamma$. Zoned crystals are common and often consist of a glaucophane-rich core rimmed by magnesioriebeckite.

Glaucophane and riebeckite both occur in prismatic crystals and columnar aggregates; in riebeckite the crystals commonly have a needle-like appearance. Riebeckite occurs also in mossy aggregates as well as in fibrous and asbestiform habits. Fibres of the blue asbestos, commonly known as crocidolite, have greater tensile strength and lower heat resistance than chrysotile. In many countries, however, the industrial use of

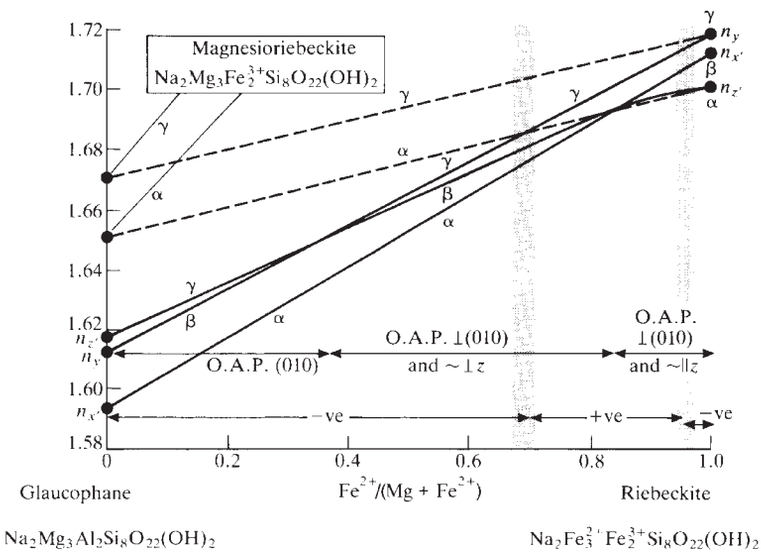


Fig. 120. Refractive indices, optic sign and optical orientation of minerals in the series glaucophane–riebeckite. The symbols $n_{x'}$ and $n_{z'}$ denote refractive indices for vibration directions nearest to x and z, respectively. Also shown are the approximate trends for α and γ in the series magnesioriebeckite–riebeckite (after Borg, I.Y., 1967, *Contrib. Mineral. Petrol.*, **15**, 67–92).

Downloaded from https://pubs.geoscienceworld.org/books/chapter-pdf/3756925/9780903056434_ch39.pdf
by guest

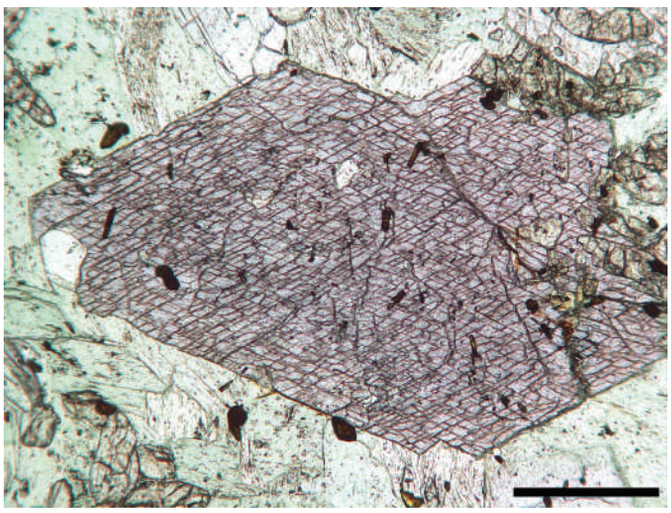


Fig. 121. Glaucophane in garnet-chlorite-glaucophane granofels, Adler Pass, Switzerland (ppl, scale bar 0.5 mm) with a cross-section of a euhedral prism of pale lilac glaucophane with typical amphibole habit and cleavage (courtesy of G.T.R. Droop).

crocidolite and other varieties of asbestos have been banned because inhalation of their finely fibrous particles causes asbestosis and pleural mesothelioma.

Distinguishing features

The pale blue colour and less intense pleochroism of glaucophane (Fig. 121) is usually sufficiently characteristic to distinguish it from both magnesioriebeckite and riebeckite. Glaucophane is also distinguished from riebeckite by its lower refractive indices, smaller optic axial angle and positive elongation. It is distinguished from arfvedsonite, eckermannite and riebeckite in having the optic plane parallel to (010). Glaucophane may be confused with tourmaline but the latter is uniaxial and shows stronger absorption parallel to the elongation. Riebeckite is distinguished from arfvedsonite by smaller extinction angles and pleochroism, the arfvedsonite pleochroic scheme usually including a brownish colour not shown by riebeckite; moreover arfvedsonite rarely shows complete extinction in white light.

Paragenesis

Glaucophane schists, resulting from the metamorphism of basaltic rocks, are usually located in orogenic belts and are commonly associated with greenschists and epidote-amphibolites. They are sometimes referred to as blueschists, but the former name may be preferable since some such rocks are not very blue, and others, with riebeckite and arfvedsonite and no glaucophane, can be blue.

Glaucophane schists are characteristic of low-temperature (100–250ºC) high-pressure (0.4–0.9 GPa) metamorphism. The minerals present, i.e. glaucophane, lawsonite, pumpellyite, epidote, aragonite, jadeite or omphacite, are different from those of the greenschists, but titanite can be present in both. Glaucophane may be formed by reactions such as:

plagioclase + chlorite + tremolite → glaucophane + lawsonite

and

plagioclase + chlorite + epidote + quartz + H_2O → glaucophane + lawsonite

Glaucophane can also form by the alteration of jadeite and by the retrograde metamorphism of eclogite. In the latter paragenesis it may be accompanied by pumpellyite as well as lawsonite.

Riebeckite has been found in a few low-grade regionally metamorphosed schists, and it may also form authigenically in sediments.

The best known occurrences of crocidolite are in the Iron Formations of South Africa and Western Australia where it occurs in seams conformable with the bedding of the ironstone. The composition of the crocidolite is closely comparable with that of the ironstone, and the crystallization of the amphibole, initially in the form of massive riebeckite, occurred with little or no addition of material and under conditions of moderate temperature and pressure produced by burial of the ironstones to moderate depths. The transformation of the riebeckite to the fibrous crocidolite may result from the instability of the massive riebeckite during a period when the ironstones were subjected to shearing stress.

Riebeckite is found in granites and syenites, in microgranites and in acid volcanic rocks. It is now recognized that, at least in some 'riebeckite granite', the riebeckite is formed at the subsolidus stage probably through the action of oxidizing fluids, not at the magmatic stage of crystallization, which is more appropriate to the formation of arfvedsonite rather than riebeckite.

Further reading

Carman, J.H. and Gilbert, M.C. (1983) Experimental studies on glaucophane stability. *American Journal of Science*, **283-A**, 414–437.

Jenkins, D.M. and Corona, J.-C. (2006) The role of water in the

Downloaded from https://pubs.geoscienceworld.org/books/chapter-pdf/3756925/9780903056434_ch39.pdf
by guest

synthesis of glaucophane. *American Mineralogist*, **91**, 1055–1068.

Maruyama, S. and Liou, J.G. (1988) Petrology of Franciscan metabasites along the jadeite-glaucophane type facies series. *Journal of Petrology*, **29**, 1–37.

Welch, M.D. and Graham, C.M. (1992) An experimental study of glaucophanic amphiboles in the system Na_2O–MgO–Al_2O_3–SiO_2–SiF_4–(NMASF): some implications for glaucophane stability in natural and synthetic systems at high temperatures and pressures. *Contributions to Mineralogy and Petrology*, **111**, 249–259.

Werner, A.J., Hochella, M.F., Guthrie, G.D., Hardy, J.A., Aust, A.E. and Rimstidt, J.D. (1995) Asbestiform riebeckite (crocidolite) dissolution in the presence of Fe chelators: implications for mineral-induced disease. *American Mineralogist*, **80**, 1093–1103.

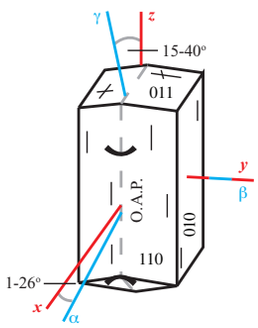
Zhang, Y.R. and Liou, J.G.(1994) Coesite-bearing eclogite in Henan Province, central China: detailed petrography, glaucophane stability and P–T path. *European Journal of Mineralogy*, **6**, 217–233.

Downloaded from https://pubs.geoscienceworld.org/books/chapter-pdf/3756925/9780903056434_ch39.pdf
by guest

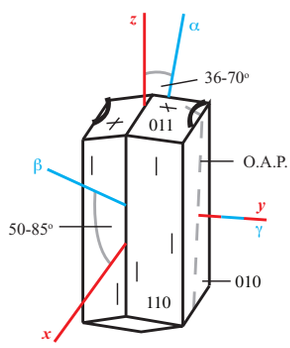
Richterite–Ferrorichterite — $(Na,K)CaNa(Mg,Al,Fe^{2+},Mn)_5[Si_8O_{22}](OH)_2$
Magnesiokatophorite–Katophorite — $(Na,K)CaNa(Mg,Fe^{2+})_4Al[Si_7AlO_{22}](OH)_2$

Monoclinic (−)

Richterite−Ferrorichterite



Magnesiokatophorite−Katophorite



α	1.604−1.690[a]	1.639−1.681
β	1.616−1.700	1.658−1.688
γ	1.622−1.712	1.600−1.690
δ	0.015−0.029[a]	0.007−0.021
$2V_\alpha$	55−87[a]	0−70°
Orientation	γ:*z* 5−55[a], β = *y*; O.A.P. (010)	*a*:*z* 36−70°, β = *y*; O.A.P. (010) for magnesiokatophorite; γ = *y*, O.A.P. ⊥(010) for katophorite
D (g/cm^3)	2.97−3.45	3.20−3.50
H	5−6	5−6
Cleavage	{110} perfect; {100}, {001} partings; (110):(1$\bar{1}$0) ~ 56°	
Twinning	{100} simple, lamellar	{100}
Colour	Brown, yellow, brownish red, pale to dark green; colourless, pale yellow, violet in thin section	Rose-red, dark red-brown; bluish black in iron-rich varieties; yellow, reddish brown, bluish green in thin section
Pleochroism	Very variable, usually in pale yellow, orange and reddish tints, sometimes violet and blue	α yellow, yellow–red, pale brown; β greenish brown, brownish red, deep brown; γ reddish yellow, deep purple–red–brown, greenish brown
	Anomalous interference colours shown by some varieties; absorption variable but generally β > γ > α	α pale yellow, β bluish green, γ dark green to black for some iron-rich varieties; absorption γ > β ≈ α for magnesiokatophorite, γ > β > α for katophorite
Unit cell	*a* 9.90−10.17 Å, *b* 17.98−18.22 Å, *c* 5.269−5.298 Å, β 104.2−103.7° Z = 2; space group *C*2/*m*	

Intermediate in composition between the calcic and sodic amphiboles are the sodium-calcium amphiboles; in these $(Ca + Na)_B > 1.00$ and $0.50 < Na_B < 1.50$ pfu. The sodium−calcium amphiboles can be divided further according to the occupancy of the *A* site:

richterite−katophorite−taramite, with $(Na + K)_A > 0.5$
and winchite−barroisite with $(Na + K)_A < 0.5$

[a] Maximum values refer to ferririchterite. The refractive indices of Mg-rich richterites are normally in the range α 1.605−1.624, γ 1.627−1.641.

Downloaded from https://pubs.geoscienceworld.org/books/chapter-pdf/3756955/9780903056434_ch40.pdf
by guest

The formula for end-member richterite is $NaCaNaMg_5Si_8O_{22}(OH)_2$ and the principal variations are the isovalent substitution of Fe^{2+} for Mg and the coupled substitution of Al for Mg and Si. In the richterite subgroup of sodium-calcium amphiboles we have therefore:

richterite–ferrorichterite
$$NaCaNa(Mg,Fe^{2+})_5[Si_8O_{22}](OH)_2$$
magnesiokatophorite–katophorite
$$Na(CaNa)((Mg,Fe^{2+})_4Al)[Si_7AlO_{22}](OH)_2$$
magnesiotaramite–taramite
$$NaCaNa((Mg,Fe^{2+})_3,Al_2)[Si_6Al_2O_{22}](OH)_2$$

Some richterite–ferrorichterites contain more calcium and less sodium than the ideal composition and the group as a whole shows more extensive solid solution with the calcic amphiboles than do members of the sodium amphibole group. Most richterites are Mg-rich and if appreciable iron is present it is mostly Fe^{3+}; Fe^{2+}-rich richterites do, however, occur and the complete range has been synthesized. The substitution of Fe for Mg lowers the stability limit from about 1000 to 500ºC. Manganese can also substitute for (Mg,Fe). There is commonly some substitution of K for Na in the *A* site and it can be complete, but Ca does not appear to enter the *A* site. The substitution of F for (OH) is not uncommon.

Katophorites (and still more so the rare mineral taramite) are unusual for alkali amphiboles in showing appreciable replacement of Si by Al. The Fe^{3+}:$^{[6]}$Al ratio is high and in this respect katophorite resembles arfvedsonite; the latter, however, contains only about half as much calcium.

The common replacement of Mg by (Al,Fe^{3+}) is associated with higher refractive indices and extinction angles, deeper colours and stronger dispersion.

For the katophorites, as for the glaucophane–riebeckite and the eckermannite–arfvedsonite series, the optic axial plane is parallel to (010) in the magnesium-rich and perpendicular to (010) in the iron-rich members; the composition at which the change in optical orientation occurs is not known with certainty. The extinction angle, γ:*z*, is high in all members of the series, but the higher values occur in the iron-rich minerals.

Richterites are usually distinguishable from other amphiboles by their distinctive pleochroism and lower refractive indices, birefringence and optic axial angle.

Katophorite is distinguished from other amphiboles (except kaersutite and oxo-hornblende) by its characteristic yellow, reddish yellow and brownish absorption colours. It is distinguished from aenigmatite by its less intense absorption colours and lower refractive indices.

Most richterites occur in metamorphic rocks, e.g. contact metamorphosed limestones, and in skarns. K-rich magnesiorichterite, which has an extensive stability field, is also known to occur in alkaline to peralkaline basalts, lamprophyres and mica-peridotites; Fe-rich richterites occur in pantellerite and in late-stage facies of granitic rocks. Richterite also occurs as a hydrothermal alteration product.

Magnesiokatophorite and katophorite are comparatively rare amphiboles which occur, often associated with arfvedsonite and aegirine, in the more alkaline rocks such as phonolite and trachyte.

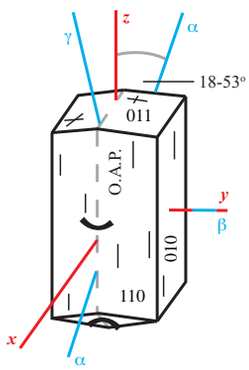
Further reading

Meizer, S., Gottschalk, M., Andrut, M. and Heinrich, W. (2000) Crystal chemistry of K-richterite–richterite–tremolite solid solutions: a SEM, EMP, XRD, HRTEM and IR study. *European Journal of Mineralogy*, **12**, 273–291.

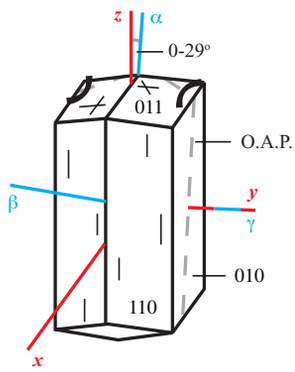
Downloaded from https://pubs.geoscienceworld.org/books/chapter-pdf/3756955/9780903056434_ch40.pdf
by guest

Monoclinic (−)

Eckermannite



Arfvedsonite



α	1.612−1.640	1.623−1.700
β	1.625−1.646	1.631−1.706
γ	1.630−1.655	1.635−1.710
δ	0.013−0.020	0.010−0.012
$2V_\alpha$	80−72°	8−87°[a]
Orientation	α:*z*, 18−53°	0−29°
	β = *y*; O.A.P. (010)	γ:*y*,[b] O.A.P.⊥(010)
D (g/cm^3)	3.00−3.20	3.30−3.50
H	5−6	5− 6
Cleavage	{110} perfect; {010} parting; (110):(1$\bar{1}$0) ~ 56°	
Twinning	{100} simple, lamellar	{100} simple, lamellar
Colour	Dark bluish green; pale bluish green in thin section	Greenish black, black; yellowish green, brownish green, grey–green or grey–violet in thin section
Pleochroism	α bluish green	α deep blue, blue−green, green or indigo
	β light bluish green	β lavender-blue, green−blue, dark olive-green, yellow-brown
	γ pale yellowish green	γ light yellowish green, greenish yellow
	Absorption α > β > γ	Absorption variable
Unit cell[c]	*a* 9.7−10.0 Å, *b* 17.7−18.1 Å, *c* ~ 5.3 Å, β ~ 104°	
	Z = 2; space group *C*2/*m*	

Eckermannite occurs in alkaline igneous rocks such as nepheline syenites, accompanied by aegirine. It is typically bluish green in colour in contrast to arfvedsonite which is commonly deep blue to yellow brown. Arfvedsonite occurs in peralkaline granites and syenites.

Chemistry

Sodium amphiboles are those for which $Na_B \geqslant 1.50$ atoms pfu, but they are split into two groups depending upon the occupancy of the *A* sites. Those with more than 0.5 (Na + K) in *A* are classified with reference to four end-members; eckermannite, $Na(Na_2)(Mg_4Al)[Si_8O_{22}](OH)_2$; ferro-eckermannite, $Na(Na_2)(Fe^{2+}_4Al)[Si_8O_{22}](OH)_2$;

[a] Optically positive afrvedsonite with high 2V has been reported.
[b] Arfvedsonites with low Fe content have β = *y*, O.A.P. (010).
[c] *a*, *b* and β increase with Ca and Fe^{2+}; *a* and *b* decrease with increasing Li.

Downloaded from https://pubs.geoscienceworld.org/books/chapter-pdf/3756959/9780903056434_ch41.pdf
by guest

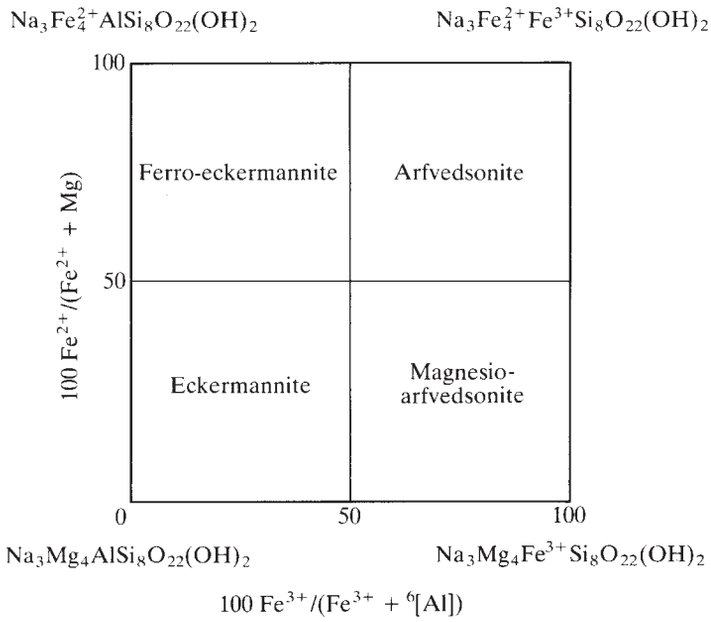


Fig. 122. The variation in chemical composition and nomenclature of the eckermannite-arfvedsonite sodium amphiboles.

magnesio-arfvedsonite, $Na(Na_2)(Mg_4Fe^{3+})[Si_8O_{22}](OH)_2$; and arfvedsonite, $Na(Na_2)(Fe_4^{2+}Fe^{3+})[Si_8O_{22}](OH)_2$ (Fig. 122). Members of the group, however, only rarely correspond closely with these ideal compositions. Potassium is commonly present in *A* sites (up to 0.7 atoms pfu). The *A* site is not always full and most specimens contain appreciable calcium replacing sodium, compensated by the substitution of Al for Si. Higher temperatures of origin appear to favour more complete filling of the *A* site.

There is a solid solution between arfvedsonite and riebeckite involving the substitution Na + R^{2+} ↔ □ + R^{3+} and also with richterite involving the substitution Na + R^{3+} ↔ Ca + R^{2+}. There is also solid solution between arfvedsonites and Si-rich calcium amphiboles. There appears to be little or no solid solution towards the Fe,Mg amphiboles or with Al-rich amphiboles such as hastingsite.

Eckermannite can contain appreciable lithium and this element is present in varied quantities, substituting for Fe^{2+} in other members of the group. The manganese end-member $Na(Na_2)((Mn_4^{2+}(Fe^{3+},Al^{3+}))[Si_8O_{22}](OH)_2$ is kôzulite. Fluorine replaces (OH) in some species.

The relative contents of Mg, Fe^{2+}, Fe^{3+} and Al are very variable, but iron-rich members are the most common. The content of Fe^{3+} sometimes exceeds the one per formula unit allowed for in the ideal formulae. If Fe^{3+} is present it shows, as with other Na-rich amphiboles, a preference for the *M*2 site.

Experiments have shown that arfvedsonite breaks down at a considerably higher temperature than riebeckite, and is therefore more compatible with a purely igneous origin.

Optical and physical properties

The determination of the optical properties, particularly of arfvedsonite (Fig. 123), is difficult due to strong absorption, strong dispersion, and anomalous extinction.

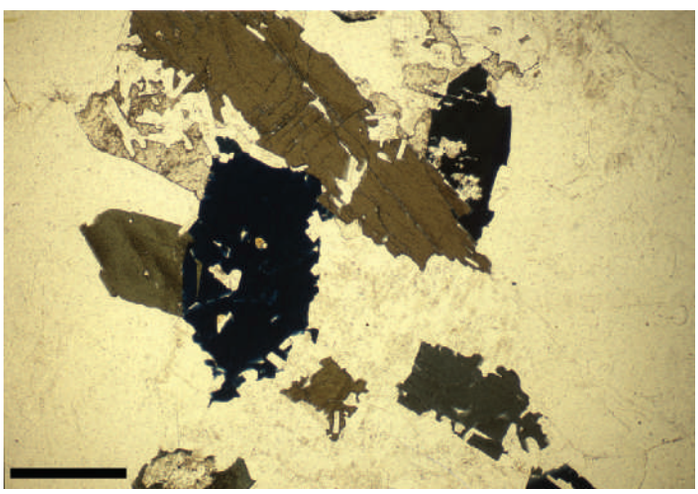


Fig. 123. Arfvedsonite, syenite, Ilímaussaq intrusion, West Greenland (ppl, scale bar 1 mm), recognizable by its absorption colours which range from a deep Prussian blue to a brownish green. The blue may be so dark that the crystals appear opaque (W.S. MacKenzie collection, courtesy of Pearson Education).

Downloaded from https://pubs.geoscienceworld.org/books/chapter-pdf/3756959/9780903056434_ch41.pdf
by guest

In general, refractive indices (and density) increase with increasing Fe/Mg ratio, but birefringence is greater for the more Mg-rich members of the series. The optic axial plane is parallel to (010) in the Mg-rich (>70%) and perpendicular to (010) in other members; the division between eckermannite and arfvedsonite was once defined in this way rather than by the current chemical criteria (Fig. 122). In eckermannite 2V and the extinction angle α:*z* are large, whereas in arfvedsonites they range down to almost zero. Arfvedsonites are often anomalous in that (010) sections do not exhibit complete extinction even in monochromatic light. After heating at temperatures above 700ºC such minerals show normal extinction and it is possible that the anomalous extinction is due to the presence of a fine intergrowth of two amphiboles.

Distinguishing features

Eckermannite is distinguished from cummingtonite by its lower refractive indices and smaller birefringence and extinction angles, from tremolite by its smaller birefringence, larger extinction angle and pleochroism, and from magnesiohornblende by its characteristic $\alpha > \beta > \gamma$ absorption. Arfvedsonite is distinguished from all other amphiboles except riebeckite and some katophorites by the orientation of the optic axial plane perpendicular to the symmetry plane. It is also distinguished from these amphiboles by its lower birefringence and characteristic pleochroism. The pleochroism of ferrohastingsite is less intense and its birefringence greater. Glaucophane has lower refractive indices and less intense absorption. Arfvedsonite is distinguished from tourmaline by the stronger absorption parallel to the elongation, by its amphibole cleavages and its biaxiality.

Paragenesis

Members of this group occur commonly associated with aegirine in silica-saturated peralkaline rocks (e.g. lamprophyres, lamproites, syenites, alkali granites and their pegmatites) and in carbonatites. Aenigmatite is commonly reported as an associated mineral. Arfvedsonites are formed by essentially magmatic/subsolidus processes in reducing environments, by contrast with the hydrothermal and oxidizing conditions which favour riebeckite. Many so-called 'riebeckite granites' (e.g. that of Ailsa Craig, Scotland) are in fact riebeckitic arfvedsonite granites which have been subjected to post-crystallization oxidation of Fe^{2+} to Fe^{3+}. At the type locality (Norra Kärr, southern Sweden) eckermannite is associated with pectolite and aegirine in a nepheline syenite.

Further reading

Farrow, C.M., Herriot, C.M. and Leake, B.E. (1982) A Carboniferous arfvedsonite-aegirine trachyte from West Kilbride, Scotland. *Mineralogical Magazine*, **46**, 399–401.

Giret, A., Bonin, B. and Leger, J. (1980) Amphibole compositional trends in oversaturated and undersaturated alkaline plutonic ring-complexes. *The Canadian Mineralogist*, **18**, 481–495.

Strong, D.F. and Taylor, R.P. (1984) Magmatic-subsolidus and oxidation trends in composition of amphiboles from silica-saturated peralkaline igneous rocks. *Tschermaks Mineralogische und Petrographische Mitteilungen*, **32**, 211–222.

Downloaded from https://pubs.geoscienceworld.org/books/chapter-pdf/3756959/9780903056434_ch41.pdf
by guest

Mica Group

Introduction

The micas as a whole show considerable variation in chemical and physical properties, but all are characterized by a platy morphology and perfect basal cleavage which is a consequence of their layered atomic structure. Of the micas, muscovite, phlogopite-biotite and lepidolite are of economic importance. The following sections deal with the most common micas; muscovite, paragonite, glauconite, phlogopite, biotite, lepidolite and zinnwaldite. For the most part each is a distinct mineral which does not form a complete solid-solution series with any of the others, but phlogopite and biotite are separated merely for convenience in dealing with otherwise so large a group.

Nomenclature

A new system of classification, nomenclature and notation for micas has been developed and approved by the International Mineralogical Association (Rieder *et al*., 1998). The general formula can be written as $I_2M_{4-6}\square_{2-0}T_8O_{20}A_4$, where:

I is commonly K or Na, but Cs, NH_4, Rb, Ca, Ba and other cations may occur;
M is commonly Mg, Fe^{2+}, Fe^{3+}, Al, Li, but also Ti, Mn, Zn, Cr, V and other cations;
$\square$ is a vacant site;
T is commonly Si, Al, and more rarely Fe^{3+}
A is commonly (OH), F but can also be Cl, O and S.

The number of approved names for micas has been considerably reduced in the new scheme.

Structure

The basic structural feature of mica is a composite layer in which a sheet of octahedrally coordinated M cations (mainly Al, Mg, Fe) is sandwiched between two identical and opposing sheets of linked $(Si,Al)O_4$ tetrahedra. Two of these tetrahedral sheets, of composition $(Si,Al)_4O_{10}$, are illustrated in Fig. 124. On the left is a sheet in which all tetrahedra are pointing upwards, as may be seen from the 'elevation' view below it, and on the right is a sheet of tetrahedra which point downwards. The two sheets are superimposed and are linked by a plane of *M* cations as shown in Figs 125 and 126. Hydroxyl ions (marked A in Fig. 125), together with the apical oxygens of the inward-pointing tetrahedra, complete the octahedral coordination of the central sheet of cations. The structure may also be regarded as having a central brucite-like sheet $M_3^{2+}(OH)_6$ (trioctahedral) or a gibbsite-like sheet $M_2^{3+}(OH)_6$ (dioctahedral), in which four out of six (OH) ions are replaced by apical oxygens of the tetrahedral sheets (two on each side). The (OH) ions that are not replaced by oxygens are situated at the centres of 6-membered rings

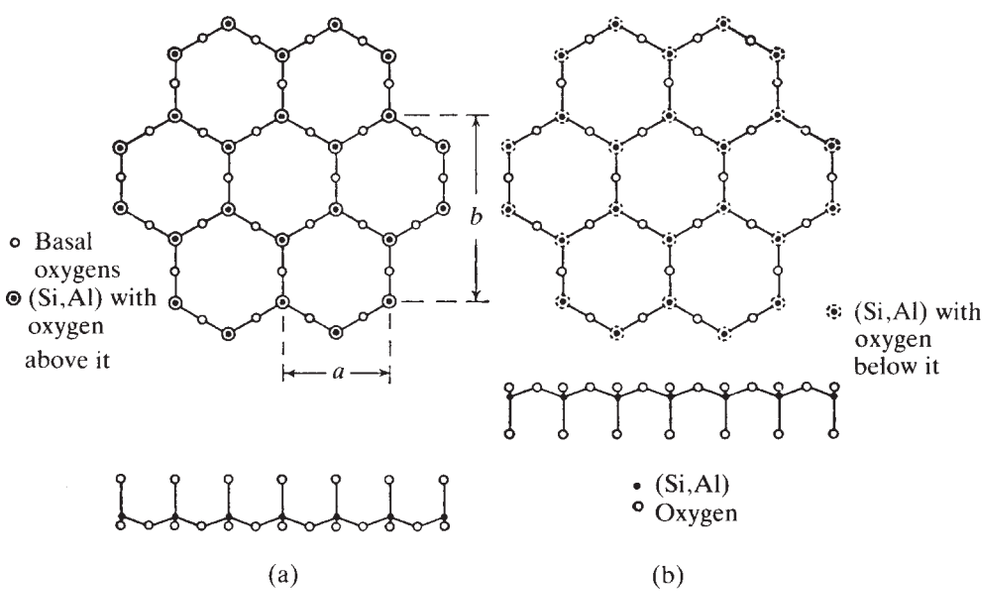


Fig. 124. Mica structure. (a) Plan of tetrahedral sheet $(Si,Al)_4O_{10}$ with tetrahedra pointing upwards, and end view of layer looking along *y* axis. (b) Plan and elevation of tetrahedral sheet with tetrahedra pointing downwards (Deer *et al*., 1992, *An Introduction to the Rock-Forming Minerals*, Longman, UK).

Downloaded from https://pubs.geoscienceworld.org/books/chapter-pdf/3757038/9780903056434_ch42.pdf
by guest

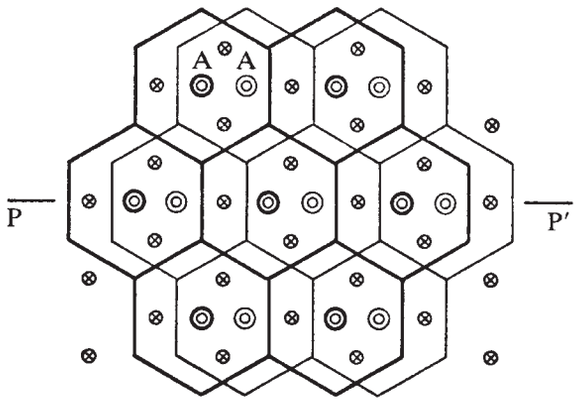


Fig 125. Mica structure (trioctahedral). Plan of (a) and (b) of Fig. 124 superimposed and linked by a plane of cations. In dioctahedral micas the *M* site on the mirror plane (P−P′) is vacant and the other two *M* sites are occupied mainly by Al (Deer *et al*., 1992, *An Introduction to the Rock-Forming Minerals*, Longman, UK).

⊗ Octahedrally coordinated (*M*) cations; mainly Mg, Al or Fe
○ Hydroxyl ions
◯ *M* ions below bottom layer (K,Na,Ca)
○ *M* ions above upper layer (K,Na,Ca)
Thick lines: bottom $(Si,Al)_2O_5$ layer
Thin lines: upper $(Si,Al)_2O_5$ layer

formed by the tetrahedral vertices (Fig. 124). The (OH) positions can also be seen in the side view (*y*-axis projection) of the structure of phlogopite in Fig. 126 in which the sequence and numbers of cations in successive planes of the structure are also indicated.

The central M cations determine the positions of the two tetrahedral sheets so that they are displaced relative to one another by *a*/3 in the *x* direction. The layers have a symmetry plane PP′ and are repeated on a rectangular network with dimensions approximately 5.3×9.2 Å. In the micas these layers (sometimes referred to as T−O−T or 2:1 layers) have a net negative charge which is balanced by planes of I cations (commonly K, Na) lying between them. The repeat distance perpendicular to the layers is approximately 10 Å or a multiple thereof. A perspective illustration (mainly polyhedral) of a mica structure is shown in Fig. 127.

The interlayer cations are in approximately 12-fold (6+6) coordination by oxygens because they lie centrally on the line joining the centres of hexagons formed by the basal oxygens of tetrahedral sheets, and no lateral displacement is introduced in going from the basal oxygens of one layer to those of its neighbour. The hexagons may be superimposed, however, in six different ways. Thus one hexagon may be related to the next by rotation through 0º or by a multiple of 60º, and this, combined with the stagger of *a*/3 introduced by the *M* layer, determines the location of corresponding atoms in successive cells. Various sequences of layer rotations are possible, and if they are repeated regularly these build up unit cells with one, two, three or more layers (Fig. 128).

The most common stacking sequences lead to either one- or two-layered monoclinic polytypes (symbols 1M,

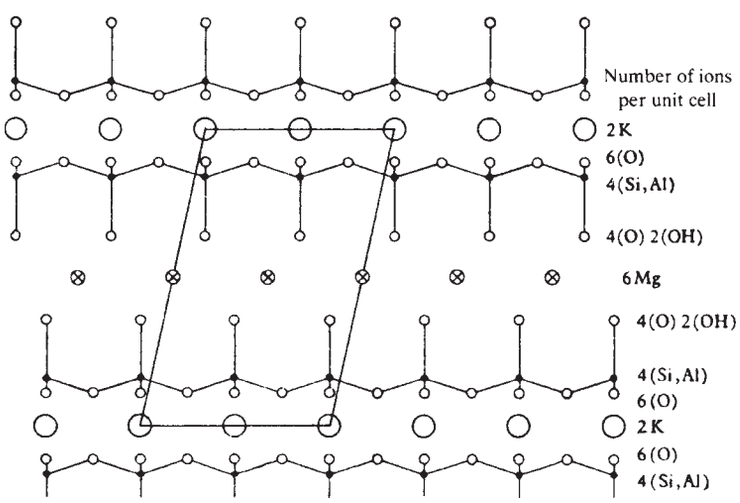


Fig. 126. Mica structure (trioctahedral; 1M polytype). Elevation of Fig. 124a and b, superimposed and linked by a plane of octahedrally coordinated cations. Layers are shown linked by potassium ions, and the simplest unit cell is outlined. View is along *y* axis (Deer *et al*., 1992, *An Introduction to the Rock-Forming Minerals*, Longman, UK).

Downloaded from https://pubs.geoscienceworld.org/books/chapter-pdf/3757038/9780903056434_ch42.pdf
by guest

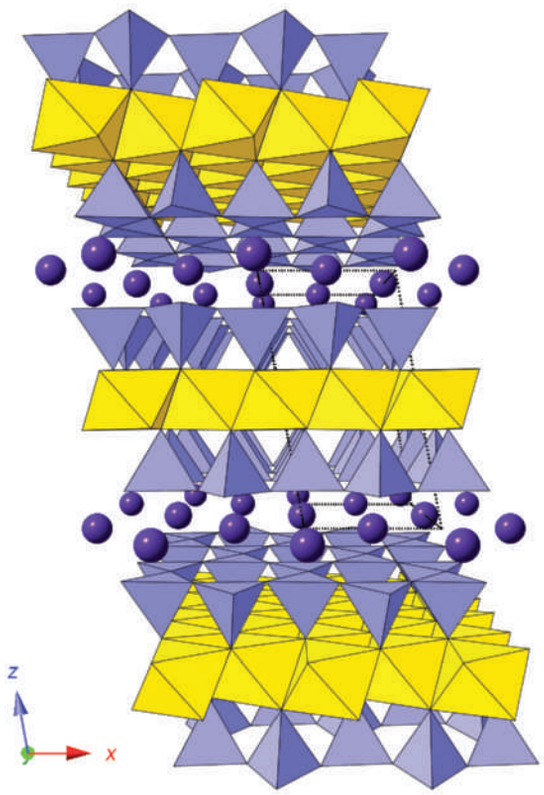


Fig. 127. The structure of phlogopite mica. Perspective view from direction close to the *y* axis, showing sheets of Mg−O octahedra (yellow) between sheets of (Si_3Al)−O tetrahedra (blue) separated by sheets of interlayer K cations (purple) (CrystalMaker image).

$2M_1$), a different two-layered monoclinic ($2M_2$) or a three-layered trigonal (3T) polytype. From Fig. 128 it can be seen that polytypes 1M and 2O involve layer shifts parallel to one *x* axis, $2M_1$ and $2M_2$ along two, and 3T and 6H along all three *x* axes. Disordered crystals are not uncommon.

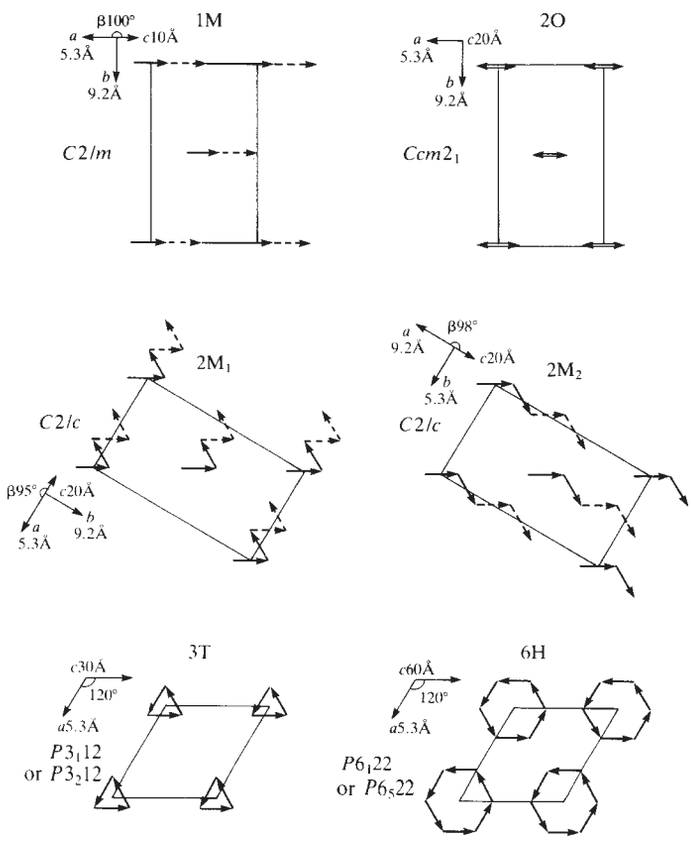


Fig. 128. The six simple ways of stacking mica layers in an ordered manner. The arrows are the interlayer stacking vectors. Full line vectors show the layer stacking in one unit cell, whereas broken line vectors show the positions of layers in the next unit cell. The base of the unit cell is shown by thin lines, and the space group and lattice parameters are listed by the side of the diagram in each case (after Smith, J.V. & Yoder, H.S., 1956, *Mineral. Mag.*, **31**, 209−34).

Downloaded from https://pubs.geoscienceworld.org/books/chapter-pdf/3757038/9780903056434_ch42.pdf
by guest

The above description of the fundamental mica layer is idealized; in the true mica structure the tetrahedra are rotated (Fig. 130, p. 182) so that $(Si,Al)_2O_5$ sheets have di-trigonal instead of hexagonal symmetry. These distortions help to achieve a dimensional match between the octahedral and the somewhat larger ideal tetrahedral components, and are greater in dioctahedral than in trioctahedral micas (see below).

In the common micas, muscovite, phlogopite and biotite, there appears to be no ordering of the different cation species, (Fe,Mg), etc., in octahedral and (Si,Al) in tetrahedral sites, but in some other micas distinct site preferences do occur.

The cell parameters of micas are influenced by the various ionic substitutions; thus dioctahedral and trioctahedral micas can in general be distinguished by the position of the (060) reflection in an X-ray powder pattern. For the former d_{060} ~1.50 Å and for the latter d_{060} ~1.53–1.55 Å.

Chemistry

The general formula which describes the chemical composition of micas is $I_2M_{4-6}T_8O_{20}(OH,F)_4$ where

I is mainly K, Na or Ca but also Ba, Rb, Cs, etc.
M is mainly Al, Mg or Fe but also Mn, Cr, Ti, Li, etc.
T is mainly Si or Al and possibly also Fe^{3+} and Ti.

Two broad subdivisions of the mica minerals are those between dioctahedral and trioctahedral species, for which ΣM is 4 and 6 respectively, and between the true micas (e.g. muscovite and phlogopite), in which the interlayer cations are mainly (K,Na) and the brittle micas (e.g. margarite and clintonite) in which they are mainly Ca or more rarely Ba. Further subdivisions of the true micas are made according to the principal M and T cation substitutions. For muscovite and paragonite, a ratio of Si/Al greater than 6:2 can be balanced by equivalent substitution of divalent cations for Al in *M* sites, as in phengite/celadonite. These divisions are listed in Table 24. Yet another subdivision allows for 'interlayer-deficient micas' (e.g. glauconite) in which the total charge of the I cations is between 1.6 and 1.2 pfu instead of 2.0 (see also illites, under Clay Minerals).

The principal variations in mica compositions can also be depicted graphically as in Fig. 129.

The minerals talc and pyrophyllite are closely related structurally to the micas but differ in having no I ions and no Al in *T* sites.

A chemical feature which most micas have in common is their water content; analyses, except for those with high fluorine content, show approximately 4–5% H_2O+. Both dioctahedral and trioctahedral micas are found in fine-grained 'clay mica' form, commonly with higher water content and other characteristic features discussed elsewhere (p. 231).

Examples of chemical analyses of the principal micas are given in Table 25.

Optical and physical properties

The optical properties of micas cover a wide range but all have negative sign and have α approximately perpendicular to their perfect (001) cleavage. Sections showing the cleavage therefore have positive elongation. Most are biaxial, with 2V moderate for dioctahedral and generally small for trioctahedral micas; relatively few specimens appear to be strictly uniaxial. Birefringence is generally very low in the plane of cleavage flakes but strong in transverse sections; pleochroism is high in coloured micas and the absorption is, with rare exceptions, greatest for vibration directions parallel to the cleavage. In thin sections, relief relative to the mounting medium is low for lepidolite and phlogopite but moderate to high for other micas. The dioctahedral micas generally have their optic axial planes perpendicular to (010) whereas others (with the exception of certain biotites which have the $2M_1$ structure) have the optic axial plane parallel to (010). All micas may show twinning on the 'mica twin law' with composition plane

Table 24. Approximate chemical formulae (cations) of principal micas.

		I	M	T
		——— Dioctahedral micas ———		
True micas	Muscovite	K_2	Al_4	Si_6Al_2
	Paragonite	Na_2	Al_4	Si_6Al_2
	Celadonite	K_2	$(Fe^{3+},Al)_2(Mg,Fe)_2$	Si_8
Brittle micas	Margarite	Ca_2	Al_4	Si_4Al_4
		——— Trioctahedral micas ———		
True micas	Phlogopite	K_2	Mg_6	Si_6Al_2
	Biotite	K_2	$(Mg,Fe,Al)_6$	$Si_{6-5}Al_{2-3}$
	Lepidolite	K_2	$(Li,Al)_{6-5}$	$Si_{6-7}Al_{2-1}$
	Zinnwaldite	K_2	$(Fe,Li,Al)_6$	$Si_{5-7}Al_{3-1}$
Brittle micas	Clintonite	Ca_2	Mg_4Al_2	Al_6

Downloaded from https://pubs.geoscienceworld.org/books/chapter-pdf/3757038/9780903056434_ch42.pdf
by guest

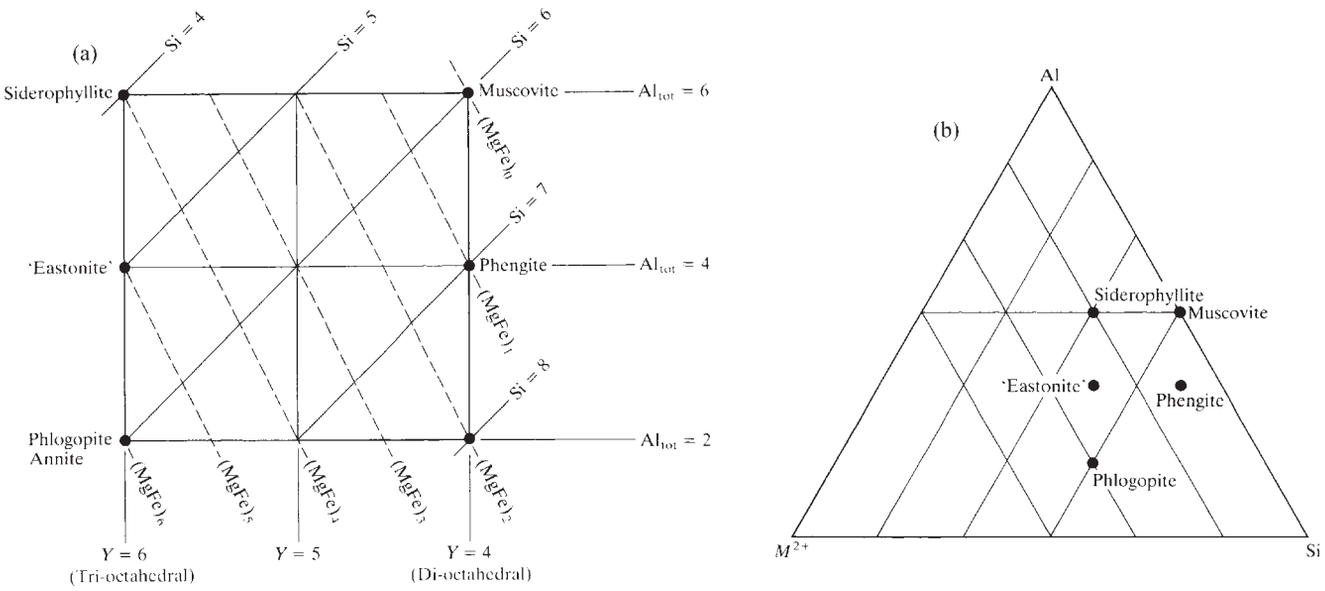


Fig. 129. (a) Principal variations in mica compositions showing for each the number of octahedral sites filled (dioctahedral, 4; trioctahedral, 6) and Si, Al and M^{2+} atoms per formula unit. (b) A similar plot in which the triangular coordinates Si, Al and M^{2+} are emphasized (Deer *et al*., 1992, *An Introduction to the Rock-Forming Minerals*, Longman, UK).

{001} and twin axis [310], and well formed crystals often show {110} faces as well as {010} and therefore pseudohexagonal outline.

On suitable specimens, the crystallographic orientation of a mica flake can be determined by the percussion figure test. A blow with a dull point on a cleavage plate produces a six-rayed percussion figure, the most prominent line of which is parallel to (010), the others being at 60º intervals. For 1M micas, the optic axial plane is parallel to one of the percussion rays, whereas for the $2M_1$ micas the optic axial plane bisects the angle between two rays.

Paragenesis

The paragenesis of each species of mica is discussed in the appropriate section; the following list, however, outlines the principal occurrences in igneous, metamorphic and sedimentary rocks.

Igneous

Muscovite: granites, granitic pegmatites and aplites;
Phlogopite: peridotites and kimberlites;
Biotite: gabbros, norites, diorites, quartz- and nepheline syenites, quartz monzonites, granites, pegmatites;
Lepidolite and zinnwaldite: pegmatites and high-temperature veins.

Metamorphic

Muscovite, paragonite and biotite: phyllites, schists and gneisses;
Phlogopite: metamorphosed limestones and dolomites.

Sedimentary

Muscovite and paragonite: detrital and authigenic sediments;
Glauconite: greensands.

Further reading

Bailey, S.W. (Editor) (1984) *Micas*. Reviews in Mineralogy, **13**, Mineralogical Society of America, Washington, D.C., 584 pp.

Fleet, M.E. (2003) *Micas*. Rock-Forming Minerals, 2nd Edn. **3A**, (W.A. Deer, R.A. Howie and J. Zussman, editors), Geological Society, London. 758 pp.

Mottana, A., Sassi, F.P., Thompson, J.B. and Guggenheim, S. (Editors) (2002) *Micas: Crystal Chemistry and Metamorphic Petrology*. Reviews in Mineralogy & Geochemistry, **46**, Mineralogical Society of America and Geochemical Society, Washington, D.C., 499 pp.

Rieder, M., Cavazzini, G., D'Yakonov, Y.S., Frank-Kamenetski, V.A., Gottardi, G., Guggenheim, S., Koval, P.V., Muller, G., Neiva, A.M.R., Radoslovich, E.W., Robert, J.L., Sassi, F.P., Takeda, H., Weiss, Z. and Wones, D.R. (1998) Nomenclature of the micas. *The Canadian Mineralogist*, **36**, 905–912; also *Clays and Clay Minerals*, **46**, 586–595 and (1999). *Mineralogical Magazine*, **63**, 267–279.

Smith, J.V. and Yoder, H.S. (1956) Experimental and theoretical studies of the mica polymorphs. *Mineralogical Magazine*, **31**, 209–235.

Downloaded from https://pubs.geoscienceworld.org/books/chapter-pdf/3757038/9780903056434_ch42.pdf
by guest

Table 25. Mica analyses.

	1	2	3	4	5	6	7	8
SiO_2	45.24	45.45	50.72	39.3	33.82	38.32	33.63	49.76
TiO_2	0.01	0.48	0.49	2.11	1.25	2.89	4.94	0.22
Al_2O_3	36.85	35.99	27.65	13.6	9.95	15.21	17.17	25.31
Fe_2O_3	0.09	0.21	–	2.52	7.59	1.49	3.35	0.80
FeO	0.02	1.00	3.70	4.64	32.18	15.58	22.20	3.20
MnO	0.12	0.00	0.03	0.06	2.47	0.22	0.46	0.42
MgO	0.08	0.69	2.37	22.7	0.59	13.17	5.88	0.09
CaO	0.00	0.00	–	0.05	–	0.74	0.19	0.05
Li_2O	0.49	–	–	0.01	–	–	–	4.35
Na_2O	0.64	0.65	0.17	0.31	0.46	0.20	0.02	0.61
K_2O	10.08	10.79	11.53	9.81	8.78	8.01	8.19	9.20
F	0.91	0.44	–	1.40	0.56	–	0.46	3.96
H_2O+	4.12	4.30	–	3.10	3.28	4.04	3.65	2.81
H_2O-	0.46	–	–	–	–	–	–	0.33
	100.24	100.00	96.66	100.92	100.96	100.00	100.32	101.95
$-O \equiv F$	0.38	0.19	–	0.60	0.25	–	0.23	1.67
Total	99.86	99.81	96.66	100.32	100.72	100.00	100.09	100.28
	Numbers of ions on the basis of 24 (O,OH,F) or 22 oxygen equivalents (anal.3)							
Si	6.050 } 8.00	6.064 } 8.00	6.754 } 8.00	5.656 } 8.00[b]	5.658 } 8.00[e]	5.678 } 8.00	5.206 } 8.00	6.642 } 8.00
Al	1.950	1.936	1.246	2.306	1.954	2.324	2.794	1.358
Al	3.860	3.722	3.092	0.000	0.008	0.336	0.338	2.623
Ti	–	0.048	0.050	0.228	0.158	0.322	0.576	0.023
Fe^{3+}	0.092	0.022	0.000	0.034	0.568	0.166	0.390	0.080
Fe^{2+}	0.002 } 4.25	0.112 } 4.04	0.412 } 4.03	0.558 } 5.98[c]	2.502 } 5.73	1.930 } 5.69	2.874 } 5.594	0.357 } 5.48
Mn	0.014	0.000	0.004	0.008	0.350	0.028	0.060	0.047
Mg	0.022	0.138	0.470	4.870	0.148	2.908	1.356	0.018
Li	0.264	0.000	0.000	0.006	0.000	–	0.000	2.336
Ca	–	0.000	0.000	0.008	0.000	0.118	0.032	0.007
Na	0.176 } 1.99[a]	0.168 } 2.00	0.044 } 2.02	0.086 } 1.92[d]	0.150 } 2.02	0.058 } 1.69	0.006 } 1.66	0.157 } 1.80[f]
K	1.720	1.836	1.958	1.802	1.874	1.514	1.618	1.567
F	0.386	0.186	–	0.638	0.296	–	0.226	1.672
Cl	– } 4.06	– } 4.02	–	0.012 } 3.63	0.008 } 3.96	– } 4.00	0.048 } 4.04	– } 4.18
OH	3.676	3.826	–	2.976	3.660	4.00	3.768	2.503

1. Rose muscovite, pegmatite, New Mexico, USA (Heinrich, E.W. & Levinson, A.A., 1953, *Amer. Min*., **38**, 25–49. Includes Rb_2O 0.93, Cs_2O 0.20).
2. Muscovite $2M_1$, peraluminous granite, Sardinia, Italy (Brigatti M.F., Frigieri, P. & Poppi, L., 1998, *Amer. Min*., **83**, 775–85).
3. Phengite 3T, metamorphic glaucophane-, phengite- and quartz-rich layered dyke rock. UHP Seisa zone (quartz eclogite facies), Cima Pal, Val Savenca, western Alps, Italy (Ivaldi, G., Ferraris, G., Curetti, N. & Compagnoni, R., 2001, *Eur. J. Min*., **13**, 1025–34).
4. Phlogopite, median composition (Tischendorf, G., Förster, H-J. & Gottesmann, B., 2001, *Mineral. Mag*., **65**, 249–76).
5. Annite, nepheline syenite, Poudrette quarry, Mont St.-Hilaire, Quebec; α 1.613, β 1.679, γ 1.679, $2V_\alpha$ 11º, α orange-brown, β olive green, γ olive green (Lalonde , A.E., Rancourt, D.G. & Chao, G.Y., 1996, *Mineral. Mag*., **60**, 447–60).
6. Biotite, granulite facies gneiss, Warriup Hill, southern Western Australia (Stephenson, N.C.N., 1977, *Lithos*, **10**, 9–27. Includes P_2O_5 0.13).
7. Biotite, porphyritic biotite granite, Viseu region, central Portugal (Neves, J.P.F., 1997, *Eur. J. Min*., **9**, 849–57).
8. Lepidolite in aplite dyke, Meldon, Devon, UK (Chaudhry, M.N. & Howie, R.A., 1973, *Mineral. Mag*., **39**, 289–96. Includes Rb_2O 0.67, Cs_2O 0.17).

[a] incl. 0.080 Rb,0.012 Cs
[b] incl. 0.019 Fe^{3+}
[c] incl 0.074 Cr, 0.002 V, 0.002 Zn, 0.020 Ni
[d] incl. 0.020 Ba, 0.002 Rb
[e] incl. 0.388 Fe^{3+}
[f] incl 0.058 Rb, 0.010 Cs.

Downloaded from https://pubs.geoscienceworld.org/books/chapter-pdf/3757038/9780903056434_ch42.pdf
by guest

MICAS

All micas

Micas are common in many kinds of igneous and metamorphic rocks. They are all silicates with a layered crystal structure in which sheets of M−(O,OH) octahedra are sandwiched between two inward pointing sheets of linked T−O tetrahedra (M mostly Mg, Al and Fe, and T, Si and Al) forming '2:1 layers' which themselves are separated by planes of larger I cations (mainly K,Na). These features give the micas highly anisotropic optical and physical properties including their platy habit and perfect cleavage parallel to (001). Nearly all are biaxial (−) with straight or nearly straight extinction, and α approximately perpendicular to (001). Twinning is common. Birefringence is very low in the plane of cleavage and high perpendicular to it, and pleochroism is strong in coloured micas with the greatest absorption for vibration directions within, and the least for those perpendicular to, the cleavage plane. Chemically their characteristic T:O ratio is 2:5, and a general formula is $IM_{2-3}T_4O_{10}(OH,F)_2$.

Variations in micas

Two micas are very well known, the lighter coloured **muscovite**, in which two out of three octahedral sites are occupied (mainly by Al), and the more ferromagnesian and mostly darker **biotite**, in which all octahedral sites are occupied, mainly by (Fe,Mg). These are referred to structurally as dioctahedral and trioctahedral micas, respectively. Micas exhibit many modes of layer stacking (polytypes), but the most common for muscovite is a two-layered ($2M_1$) and for biotite, a one-layer (1M) cell.

The biotites have low 2V, optic axial plane parallel to (010) and high birefringence (up to ~0.07), whereas muscovite has a moderate 2V, O.A.P perpendicular to (010) and less high birefringence. Biotites cover a range of compositions from Mg-rich (**phlogopite**) to Fe-rich (**annite**, **siderophyllite**). Among the less common chemical substitutions in micas are Na for K (**paragonite**), and Li for Mg plus Si for $^{[4]}$Al (**lithium micas**).

Phlogopite occurs mainly in ultramafic rocks and dolomitic marbles, muscovite in granitic, and biotite in ferromagnesian igneous rocks, lithium micas in pegmatites and both biotite and muscovite in phyllites, gneisses and schists. Muscovite and K-depleted fine-grained variants occur in authigenic sediments.

Differences from other layered silicates

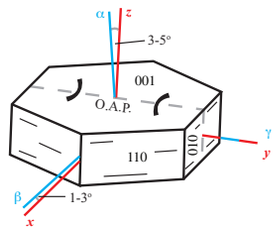
Micas are characterized by their high layer-charge, which is compensated by interlayer K cations, their ~10 Å basal spacing compared with chlorite (~14 Å), serpentine and kaolinites (~7 Å), and by a lack of the interlayer swelling properties of smectite and vermiculite clay minerals. Talc and pyrophyllite have no interlayer cations and are very soft; their interlayer spacings are ~9.5 Å and ~9.3 Å, respectively.

Downloaded from https://pubs.geoscienceworld.org/books/chapter-pdf/3757038/9780903056434_ch42.pdf
by guest

Muscovite $K_2Al_4[Si_6Al_2O_{20}](OH,F)_4$

Monoclinic (−)

α	1.552−1.574
β	1.582−1.610
γ	1.587−1.616
δ	0.035−0.042
$2V_\alpha$	28−47°
Orientation	α: *z*, 0−5°, β:*x* 1−3°, γ = *y*; O.A.P. ⊥ (010)
D (g/cm^3)	2.77−2.88
H	2½−3½
Cleavage	{001} perfect
Twinning	Composition plane {001}, twin axis [310]
Colour	Colourless, or light shades of green, red or brown; colourless in thin section
Pleochroism	Weak: absorption greater for vibration directions in the plane of cleavage
Unit cell	*a* ~ 5.20 Å, *b* ~ 9.00 Å $2M_1$ polytype ; *c* ~ 20 Å, β ~ 95° Z = 2; space group *C*2/*c* 1M polytype ; *c* ~ 10 Å, β ~ 101° Z = 1; space group *C*2/*m*. 3T and $2M_2$ polytypes also occur



Muscovite is one of the most common of the micas and occurs in a wide variety of geological environments. Its well known properties of electrical and thermal insulation made it a mineral of industrial importance, and in technical applications these are enhanced by its perfect lamellar cleavage and the mechanical strength of its cleavage sheets. Muscovite and phlogopite are the most transparent of the micas and, having a comparatively low content of iron, they have the best electrical insulating properties.

Structure

The general features of the structures of all micas have already been described (p. 174). In muscovite a quarter of the tetrahedral sites are randomly occupied by Al and three-quarters by Si. The 6-membered ring of tetrahedra has ditrigonal rather than hexagonal symmetry, through rotation of its tetrahedra in alternate senses (Fig. 130) by about 13° as compared with 3 to 7° for phlogopite/biotite and a range of 1 to 22° over micas generally.

In the octahedral sheet the large *M*1 site is generally unoccupied and the two smaller *M*2 sites are symmetry related and so are randomly occupied by the predominant Al and its replacements (including Fe^{3+}). The *M*1 and *M*2 sites are also referred to as *trans* and *cis*, respectively, in reference to the different disposition of the two (OH) anions near to them. The hydroxyl bonds in muscovite $2M_1$ lie approximately in the (001) plane (Fig. 131). Small amounts of Fe^{2+} may occur in *M*1.

The approximately 12-fold (6+6) coordinated positions between composite layers are fully occupied by potassium ions, and the stacking of successive layers gives rise in this case to the $2M_1$ polytype (see p. 176). A perspective view of the structure of muscovite is given in Fig. 132. Some fine-grained muscovite specimens from sedimentary and low-grade metamorphic rocks have the 1M or 1M*d* (disordered) structure; 3T structures also occur in muscovites and phengites but less commonly than $2M_1$.

In muscovite X-ray diffraction powder patterns, d_{002} decreases with the substitution of Na for K, and d_{060} increases with the substitution of (Mg,Fe) for Al.

Downloaded from https://pubs.geoscienceworld.org/books/chapter-pdf/3757132/9780903056434_ch43.pdf
by guest

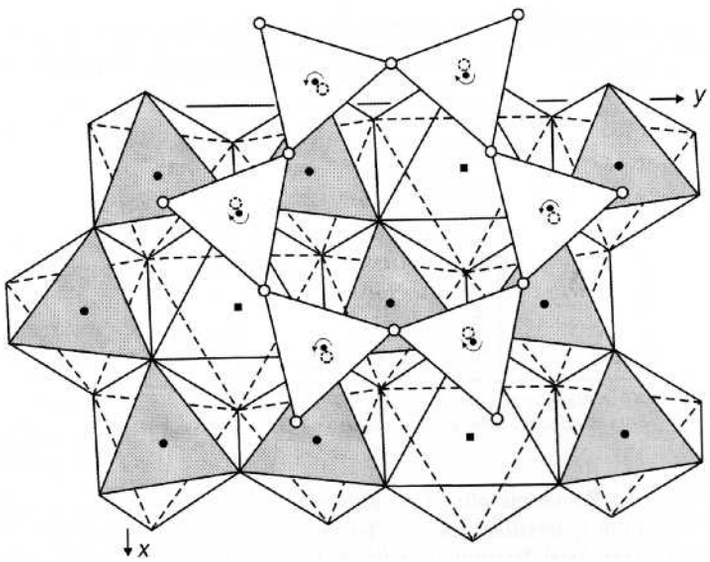


Fig. 130. Part of the structure of muscovite showing departures from the ideal structure. The tetrahedral sheet is di-trigonal rather than hexagonal, and the vacant *M*1 octahedra (unshaded and marked by small black squares) are larger than the other octahedra (below shaded tetrahedra), which are occupied by Al (after Bailey, 1984 and Fleet, 2003, *Rock-Forming Minerals*, **3A**, *Micas*, Geol. Soc., London).

Chemistry

The principal isomorphous replacements that have been reported in muscovite are as follows:

For K: Na, Rb, Cs, Ca, Ba;
For octahedral Al: Mg, Fe^{2+}, Fe^{3+}, Mn, Li, Cr, Ti, V;
For (OH): F;
(Si_6Al_2) can vary to (Si_7Al).

The rose-coloured muscovites (rose muscovites) have near-ideal composition, with low manganese and lithium contents, and total iron contents that are typically less than manganese (Table 25, analysis 1). The varieties of muscovite which result from various substitutions are discussed below, but certain replacements and combinations of replacements result in compositions and structures which can no longer be regarded as appropriate to muscovite; these are dealt with more fully in sections on other micas.

Muscovites with appreciable Fe_2O_3 content have been reported commonly, and some with equally high FeO content (usually associated with high SiO_2) are also known. Most muscovites contain less than 1% MnO but purple and blue varieties containing about 2% MnO have been described. Chromium is normally present in muscovites only in trace amounts, but chromian muscovites ('fuchsites') with as much as 6% Cr_2O_3 are known. Micas with high lithium contents are

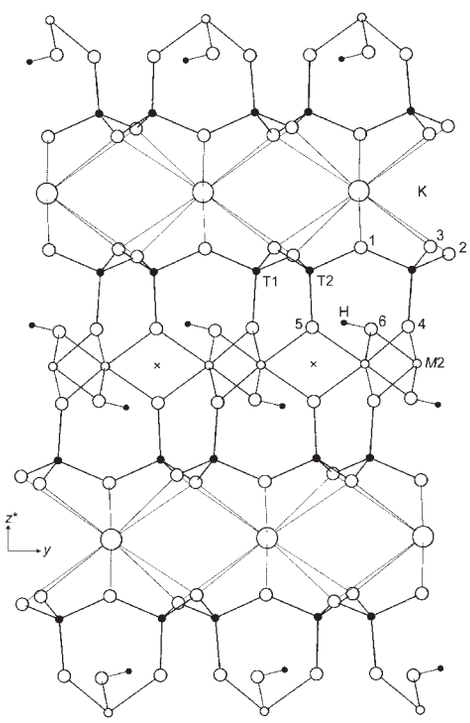


Fig. 131. Elevation (*x*-axis projection) view of the structure of muscovite-2M_1. Crosses indicate vacant *M*1 (*trans*) sites. Hydroxyl ions are shown here approximately in the plane of apical oxygens of tetrahedra (after Fleet, 2003, *Rock-Forming Minerals*, **3A**, *Micas*, Geol. Soc., London).

Downloaded from https://pubs.geoscienceworld.org/books/chapter-pdf/3757132/9780903056434_ch43.pdf
by guest

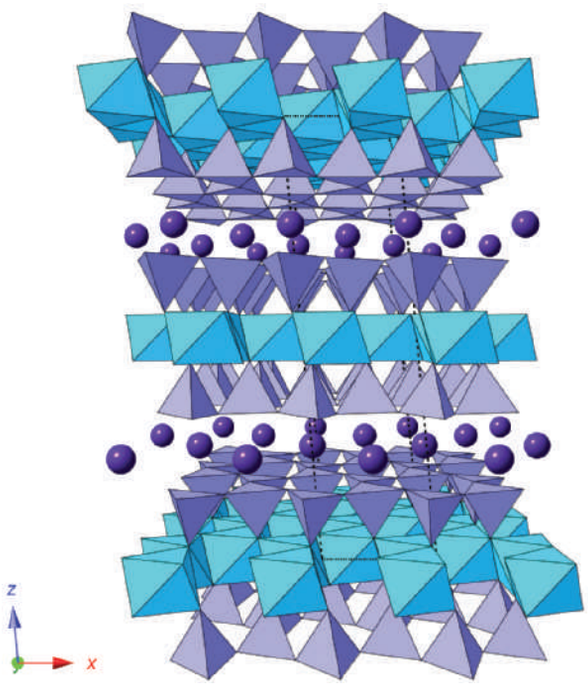


Fig. 132. Perspective view along *y* of the structure of muscovite showing sheets of Al–O octahedra (blue) shared either side with sheets of (Si,Al)–O tetrahedra (purple), and interlayer K ions (purple spheres). Vacant sites can be seen best in the top and bottom octahedral sheets [cf. structure of phlogopite, with all three octahedral sites filled (Fig. 127)] (CrystalMaker image).

commonly either polylithionite or trilithionite, a series which is collectively described as lepidolite, and described on p. 195. Nevertheless, many $2M_1$ muscovites contain significant Li_2O, sometimes exceeding ~4% Li_2O (i.e. one atom of Li pfu). Lithium may replace $^{[6]}$Al and/or enter the *M*1 vacant site, with charge compensation by substitution of Si for $^{[4]}$Al. The average fluorine content of natural muscovites is about 0.6% (~0.1 pfu) and the fluorine dominant analogue in which (OH) is completely replaced by F has been synthesized. In igneous muscovites fluorine generally increases with lithium content.

The term 'sericite' has been used historically for fine-grained aggegates of white micas (muscovite or paragonite), which are commonly found as alteration products of feldspars; this, however, is usually chemically indistinguishable from muscovite, although it can show high SiO_2, MgO and H_2O, and low K_2O.

The term phengite is used to describe muscovites in which the Si:Al ratio is greater than 3:1 and in which increase of Si is accompanied by substitution of Mg or Fe^{2+} for Al in octahedral sites.

The name hydromuscovite has been used for muscovites with high H_2O and low K_2O content, but it has been suggested that these are more likely to be mixed-layer minerals such as biotite-vermiculite or illite-smectite. Chemically illites (see under Clay Minerals, p. 224) can be classified as 'dioctahedral interlayer deficient' micas, the replacement of Al by Si being offset by low (K,Na) content. Muscovites with relatively small deficiencies in the total interlayer cation content are not uncommon, particularly in lower grade mica schists.

The results of experimental studies in the system $K_2O–Al_2O_3–SiO_2–H_2O$ are illustrated in Fig. 133 which presents curves for the reactions:

muscovite → sanidine + corundum + water (1)

muscovite + quartz → sanidine + Al_2SiO_5 + water (2)

Reaction (2) occurs only 30ºC below (1). Although it has some bearing on the breakdown of muscovite in nature, other reactions involving muscovite and the formation of feldspar may occur and, furthermore, the presence of chemical substitutions in natural muscovites may give rise to considerably different breakdown pathways. The substitution of Na for K, for example, lowers the temperature of reaction (1).

In the various syntheses of muscovite the 1M*d* polytype was obtained in low temperature experiments, 1M at intermediate temperatures and 2M generally at the highest.

The Mg and $^{[6]}$Al contents of coexisting mineral pairs, e.g. muscovite-chlorite, and muscovite-biotite, have been used as a geothermometer, as has the Na/K ratio for muscovite-plagioclase, (F,OH) for muscovite-topaz, and (Fe,Mg) for phengite-garnet; the phengitic substitution MgSi for $^{[6]}$Al$^{[4]}$Al in muscovite, which correlates with low-*T*–high-*P* conditions, has found use as a geobarometer. Muscovites and phengites have been used extensively for K/Ar and ^{40}Ar/^{39}Ar geochronology.

The weathering of muscovite may proceed through illite to montmorillonite and eventually kaolinite, by loss of potassium and increase of water and silica.

Optical and physical properties

The refractive indices of rose muscovites are lower than the averages for all muscovites, and their 2V is higher. This is in accordance with a trend throughout the muscovites for refractive indices (and birefringence) to

Downloaded from https://pubs.geoscienceworld.org/books/chapter-pdf/3757132/9780903056434_ch43.pdf
by guest

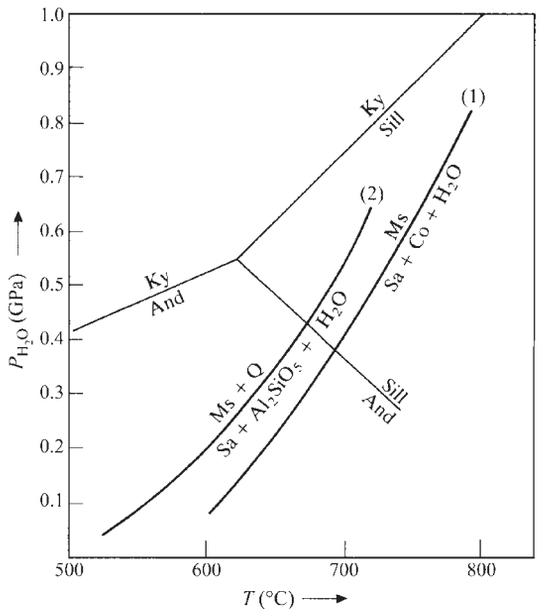


Fig. 133. $P-T$ curves for the breakdown of (1) muscovite and (2) muscovite-quartz. Also shown are the stability fields of the Al_2SiO_5 polymorphs (after Chatterjee, N.D. & Johannes, W., 1974, *Contrib. Mineral. Petrol.*, **48**, 89–114). Ms: Muscovite; Sa: sanidine; Co: corundum; Ky: kyanite; Sill: sillimanite; And: andalusite; Q: quartz.

increase with increase in iron (particularly Fe^{3+}) and Mn content, and for those with least Mg and Fe to have the largest 2V. Refractive indices increase also with decreasing Al content.

Although the colour of rose muscovite is similar to that of lepidolite there is no correlation between colour and Li content. The pink colour in both is related to the small amount of Mn present, perhaps as Mn^{3+}, its preponderance over Fe^{2+}, and the absence of Fe^{3+}. Pale green, red or brown muscovites owe their colours to varying amounts of Fe^{2+} and Fe^{3+}. The presence of Cr leads to pleochroism with α colourless to light green, β green, and γ dark green, and refractive indices increase with chromium content. Lithian muscovites have lower refractive indices, but their optical properties are influenced more by the content of iron and manganese than by the percentage of Li_2O. The refractive indices of phengites and illites are higher than those of normal muscovites because of the replacement of $^{[4]}$Al by Si and of $^{[6]}$Al by Fe^{2+} or Mg.

Parallel intergrowths of muscovite with biotite are not uncommon and in most cases their respective optic axial planes are mutually inclined at 60º. The hardness of muscovite on the Mohs' scale is usually given as 2½–3, but as would be expected from the sheet-like structure, hardness varies with direction, from 2½ parallel to (001) to ~4 perpendicular to (001).

Distinguishing features

Muscovite differs from phlogopite and biotite in having its optic axial plane perpendicular to (010). It is often possible to determine the [010] direction by a percussion figure (see p. 178). Biotite specimens are generally much darker. Muscovite usually has a higher 2V than phlogopite, biotite and talc, and this serves to distinguish it from the latter mineral for which the optic axial plane is also perpendicular to (010). The high birefringence of muscovites distinguishes them from kaolinites, chlorites and other platy silicates with the exception of pyrophyllite which, however, has a larger 2V. X-ray powder patterns may be used to distinguish dioctahedral from trioctahedral micas, and they can also be used to distinguish between the different polytypes of muscovite.

Paragenesis

Muscovite occurs over a wide range of metamorphic grades from lower greenschist to upper amphibolite facies. Its principal metamorphic occurrences are in metapelites and metamarls and it is also found in metagreywackes, and crystallizes during the metamorphism of impure limestones and of intermediate to acid igneous rocks. In low-grade metamorphic environments muscovite is formed by the recrystallization of illites and other clay minerals, yielding for example albite-chlorite-muscovite schists or muscovite phyllites. Figure 134 shows muscovite in a psammitic schist. If the original sediments were rich in aluminium, muscovite is commonly associated with chlorite and chloritoid. Above upper-amphibolite grade, muscovite is commonly replaced by potassium feldspar and aluminium silicate. The metamorphism of intermediate igneous rocks gives rise to calcite-albite-chlorite-muscovite schists and those of acid composition yield muscovite-quartz schists.

Muscovite occurs also in rocks of the blueschist facies, together with glaucophane, lawsonite and sodic pyroxene. Here the higher pressures prevailing, and reactions with other phases, are accompanied by enrichment of the celadonite component of the

Downloaded from https://pubs.geoscienceworld.org/books/chapter-pdf/3757132/9780903056434_ch43.pdf
by guest



Fig. 134. Subhedral 'books' of muscovite in psammitic schist, Landale river, Argyll, Scotland (ppl, scale bar 0.5 mm), showing moderate relief, excellent cleavage and absence of colour (courtesy of G.T.R. Droop).

muscovite, i.e. substitution of (Mg,Fe) for Al in *M* and Si for Al in *T* sites (both of which are reflected in a larger *b* cell parameter). An increase in substitution of Na for K and in Ti content correlates with higher-temperature conditions, but at the highest temperatures albite is formed and the muscovite becomes enriched in potassium. The effects of moderate temperatures on the muscovite-paragonite solvus and the relation of the celadonite component to pressure give rise to a potential geothermometer and geobarometer, respectively.

Muscovite is less common than biotite in acid igneous rocks but occurs in the peraluminous muscovite and muscovite-biotite granites, and more rarely in rhyolites. In the latter the muscovites are generally more fluorine-rich and hence have greater thermal stability. Most muscovite-bearing granites contain both potassium feldspar and plagioclase and also are usually rich in quartz. In such granites, muscovite occurs in interstitial crystals as well as in small dispersed flakes within feldspar.

The $P-T$ stability curve of muscovite intersects the $P-T$ minimum melting curve of granite at approximately 0.35 GPa pressure and 700ºC. Thus muscovite can crystallize from a liquid of granitic composition at pressures above 0.35 GPa, but below this pressure muscovite can form only in the solid state. The larger interstitial muscovite crystals in granites could thus have formed in equilibrium with the liquid, or have crystallized in the solid state at any pressure or temperature, below the stability curve of muscovite. The smaller flakes of muscovite commonly dispersed within the feldspar probably crystallized by the leaching of K and Si from the feldspar at temperatures below the granite liquidus.

Some muscovite-bearing granites contain cordierite, e.g. the Dartmoor granite, and in such granites the muscovite may, in part or whole, have been derived from the alteration of cordierite.

Micas formed directly from the melt as distinct from secondary, lower temperature processes are, in general, characterized not only by texture but also by being richer in Ti, Al and Na and poorer in Mg and Si, and by the associated minerals. If the mineral assemblage is Al-poor, muscovite is likely to be secondary.

Muscovite, with quartz as interstitial crystals and scattered flakes within feldspar, is a characteristic product of fluorine metasomatism (greisenization) at granite-slate contacts, and the production of the white mica at the expense of such minerals as feldspar, andalusite and cordierite is a reversal of the processes by which these minerals are formed in contact metamorphism. Greisenization is especially typical of the inner aureoles of muscovite-bearing granites, e.g. Dartmoor, Skiddaw and Leinster granites.

Muscovite, accompanied by biotite, is a common constituent of pegmatites associated with granites and granodiorites. In these it may occur as large 'books' crystallizing from the melt or as fine-grained sericite which replaces Al-rich primary pegmatitic minerals (e.g. tourmaline, spodumene, eucryptite, beryl, topaz or kyanite) which have reacted with late, low-temperature fluids. Such sericite is usually located in the wall rock at the pegmatite margins; dendritic intergrowths with quartz are not uncommon. Pegmatitic muscovite is likely to have an appreciable lithium content, and some 'phengitic' substitution.

Muscovite is less common in sedimentary rocks than previously supposed; much of the fine-grained 'micaceous' material in these rocks consists of muscovite-smectite mixed layers, and mixtures of pyrophyllite, kaolinite and illite, the latter being either authigenic or the product of alteration of detrital muscovite. The muscovite which is found in sedimentary rocks is usually of the 1M or 1M*d* polytype.

Further reading

Bailey, S.W. (1984) Classification and structures of the micas. Pp. 1–12 in: *Micas* (S.W. Bailey, editor). Reviews in Mineralogy, **13**, Mineralogical Society of America, Washington, D.C.

Bailey, S.W. (1984) Crystal chemistry of the true micas. Pp. 13–60

Downloaded from https://pubs.geoscienceworld.org/books/chapter-pdf/3757132/9780903056434_ch43.pdf
by guest

in: *Micas* (S.W. Bailey, editor). Reviews in Mineralogy, **13**, Mineralogical Society of America, Washington, D.C.

Černý, P. and Burt, D.M. (1984) Paragenesis, crystallochemical characteristics, and geochemical evolution of micas in granitic pegmatites. Pp. 257–297 in: *Micas* (S.W. Bailey, editor). Reviews in Mineralogy, **13**, Mineralogical Society of America, Washington, D.C.

Guidotti, C.V. (1984) Micas in metamorphic rocks. Pp. 357–367 in: *Micas* (S.W. Bailey, editor). Reviews in Mineralogy, **13**, Mineralogical Society of America, Washington, D.C.

Guidotti, C.V. and Sassi, F.P. (1988) Petrogenetic significance of Na–K white mica mineralogy: recent advances for metamorphic rocks. *European Journal of Mineralogy*, **10**, 815–854.

Miller, C.F., Stoddard, E.F., Bradfish, L.J. and Dollase, W.A. (1981) Composition of plutonic muscovite: genetic implications. *The Canadian Mineralogist*, **19**, 25–34.

Mottana, A., Sassi, F.P., Thompson, J.B. and Guggenheim, S. (Editors) (2002) *Micas: Crystal Chemistry and Metamorphic Petrology*. Reviews in Mineralogy & Geochemistry, **46**, Mineralogical Society of America and Geochemical Society, Washington, D.C., 499 pp.

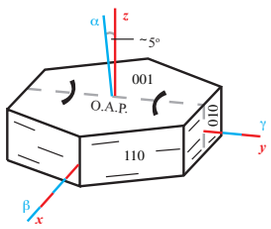
Speer, J.A. (1984) Micas in igneous rocks. Pp. 299–356 in: *Micas* (S.W. Bailey, editor). Reviews in Mineralogy, **13**, Mineralogical Society of America, Washington, D.C.

Downloaded from https://pubs.geoscienceworld.org/books/chapter-pdf/3757132/9780903056434_ch43.pdf
by guest

Paragonite $Na_2Al_4[Si_6Al_2O_{20}](OH)_4$

Monoclinic (−)

α	1.564−1.580
β	1.594−1.609
γ	1.600−1.609
δ	0.028−0.038
$2V_\alpha$	0−45°
Orientation	β nearly parallel to *x*, γ = *y*; O.A.P. ⊥(010)
D (g/cm^3)	2.85
H	2½
Cleavage	{001} perfect
Colour	Colourless, pale yellow; colourless in thin section
Unit cell	*a* ~ 5.15 Å, *b* ~ 8.9 Å, *c* ~ 19.3Å, β ~ 94°
	Z = 1 ($2M_1$ polytype); space group *C*2/*c*



The chemical composition of paragonite differs from that of muscovite in that sodium replaces potassium. This results in a smaller unit cell, particularly in the *z* direction, but in other respects the two structures are similar. The principal polytype for paragonite is $2M_1$ (3T is of rare occurrence and 1M has been synthesized). Brammallite is a clay mineral which bears a relation to paragonite similar to that of illite to muscovite.

At room temperature there is very limited solid solution of paragonite in muscovite and of muscovite in paragonite but the amount increases with temperature up to about 10 and 20% respectively.

The equilibrium curve for the hydrothermal breakdown:

paragonite → albite + corundum + water

runs from about 520ºC at 0.1 GPa to 630ºC at 0.7 GPa; this curve lies at about 100ºC lower than the curve for muscovite → sanidine + corundum + water. In the presence of quartz the reaction (at ~500ºC, 0.1 GPa) is:

paragonite + quartz → albite + Al_2SiO_5 + water

At higher pressures (about 2.5 GPa) paragonite breaks down to jadeite, kyanite and water. Paragonite may be formed by the reaction:

kaolinite + albite → paragonite + quartz + water

Paragonite may also be formed in sedimentary low-temperature environments from illite or montmorillonite.

The high birefringence of paragonite distinguishes it from margarite, kaolinite and chlorite and many other platy silicates. The optical properties of paragonite and muscovite are, however, very similar, but the two minerals can be distinguished by chemical or microprobe analysis, or by X-ray diffraction. Powder X-ray diffraction data have been used to determine the Na/(Na + K) ratios in paragonites.

Paragonite is most commonly found as fine-grained aggregates with other Al-rich minerals. It is widespread in metamorphic rocks (schists, phyllites, gneisses) mainly ranging from greenschist facies to the sillimanite zone of the amphibolite facies, but it also occurs in blueschist-facies rocks. It has also been recorded in fine-grained sedimentary rocks.

Further reading

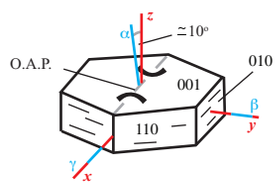
Guidotti, C.V. and Sassi, F.P. (1998) Petrogenetic significance of Na-K white mica mineralogy. Recent advances for metamorphic rocks. *European Journal of Mineralogy*, **10**, 815−854.

Downloaded from https://pubs.geoscienceworld.org/books/chapter-pdf/3757580/9780903056434_ch44.pdf
by guest

Glauconite $(K,Ca,Na)_{1.2-1.7}(Fe^{3+},Al,Mg,Fe^{2+})_4[Si_{7.8-7.6}Al_{1-0.6}O_{20}](OH)_4.nH_2O$

Monoclinic (−)

α	1.59−1.61
β ~ γ	1.61−1.64
δ	0.02−0.03
$2V_\alpha$	0−20°
Orientation	α approx. ⊥(001), β = γ; O.A.P. (010)
D (g/cm^3)	2.4−2.95
H	2
Cleavage	{001} perfect
Colour	Colourless, yellowish green, green, blue-green; usually green in thin section
Pleochroism	α yellowish green or green β = γ deeper yellow or bluish green
Unit cell	*a* ~ 5.25 Å, *b* ~ 9.09 Å, *c* ~ 10.03 Å, β ~ 100° Z = 1; space group *C*2/*m* (polytype 1M)



Although it is extensively used in petrology, particularly by sedimentologists, glauconite is not a well defined mica-group mineral, and is probably best considered to be a mineral series, the end-members of which remain to be defined. It occurs most commonly in marine sediments, particularly in greensands. It is generally found in rounded fine-grained aggregates of poorly formed platelets, or thin coatings.

Although glauconites are structurally similar to dioctahedral micas, and have a total octahedral (*M* site) content of close to two cations pfu, they differ from muscovite in having a significant deficiency of interlayer cations (I) and from both muscovite and illite in having a higher content of Fe^{3+} and (Mg,Fe^{2+}) substituting for Al in the *M* sites.

The common layer stacking in the structure of glauconite is similar to that of biotite (1M polytype); the layers may be stacked with some disorder and may contain some interstratified smectite layers (which may explain the deficiency of K below 2 pfu in some glauconites, and the fact that some glauconites are expandable). The number of I cations, though always less than 2 pfu, is greater than the number of Al ions in tetrahedral positions (*T* sites). The excess I ions are compensated in glauconite by the presence of divalent instead of trivalent ions in the *M* site.

The mineral celadonite is similar to glauconite but it is a true (Fe-rich) mica which has a more ordered structure, less $^{[4]}Al$, $^{[6]}Al$ and $^{[6]}Fe^{3+}$ and more Mg and K.

In its optical properties, glauconite resembles biotite rather than muscovite, its refractive indices and depth of colour increase with Fe^{3+} content. Other green minerals which might be mistaken for glauconite include the chlorites, which generally have a lower birefringence.

Glauconites are formed from a variety of starting materials (e.g. biotite) by diagenesis, usually in fairly shallow waters. They are found in impure limestones, sandstones and siltstones; greensands are so called because of their high content of glauconite. There is much evidence for the authigenic formation of glauconites in moderately reducing conditions, which are typically produced by the decomposition of organic material.

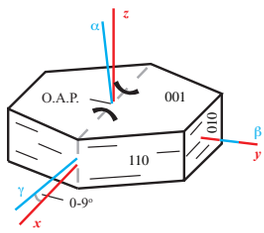
Celadonites occur mostly in basalts in vesicles or as replacements of ferromagnesian minerals.

Downloaded from https://pubs.geoscienceworld.org/books/chapter-pdf/3757830/9780903056434_ch45.pdf
by guest

Phlogopite	$K_2Mg_6[Al_2Si_6O_{20}](OH)_4$
Annite	$K_2Fe^{2+}_6[Al_2Si_6O_{20}](OH)_4$
Eastonite	$K_2Mg_4Al_2[Al_4Si_4O_{20}](OH)_4$
Siderophyllite	$K_2Fe^{2+}_4Al_2[Al_4Si_4O_{20}](OH)_4$

Monoclinic (−)

α	1.53−1.63
β	1.56−1.69
γ	1.56−1.70
δ	0.03−0.07
$2V_\alpha$	0−25°
Orientation	β = *y*, γ:*x* = 0−9°; O.A.P. (010)
D (g/cm^3)	2.7−3.3
H	2−3
Cleavage	{001} perfect
Twinning	Composition plane (001), twin axis [310]
Colour	Colourless, yellowish brown, green, reddish brown, dark brown, black; pale yellow or pale green to yellow, green or brown in thin section
Pleochroism	α yellow, greyish yellow, brownish green, brown β = γ brownish red, yellow, green, dark green, dark reddish brown, dark brown
Unit cell	*a* ~ 5.3 Å, *b* ~ 9.2 Å, *c* ~ 10.3 Å, β ~ 100° (1M polytype) Z = 1; space group *C*2/*m*



The term biotite is commonly employed by field geologists to describe any dark coloured mica. In its more precise mineralogical usage it corresponds to a group of dark micas including the well known species phlogopite, siderophyllite, annite and eastonite and a number of rarer end-members. Biotites are the most important trioctahedral micas. Neither phlogopite nor annite has Al in *M* sites but, in most natural biotites, there is appreciable substitution of Al for (Mg,Fe) balanced by Al for Si in tetrahedral sites (the so-called Tschermak's substitution), leading towards the end-members $K_2Fe_4Al_2Si_4Al_4O_{20}(OH)_4$ (siderophyllite) and $K_2Mg_4Al_2Si_4Al_4O_{20}(OH)_4$ (eastonite). Several other substitutions do also occur.

Structure

In the biotites the octahedral sites of the mica structure (p. 174) are ideally completely filled, but many analyses show that some vacancies occur and that M ions can range from 6 down to about 5.6 pfu. The most common polytype is 1M, but 2M and 3T also occur and disordered stacking of layers (1M*d*) is not uncommon. Stacking sequences, faults and twinning have all been investigated by TEM high resolution imaging and by X-ray diffraction.

The occupation of octahedral sites by Fe^{2+} and Mg appears to be random, as also is that of tetrahedral sites by Si and Al, but Mössbauer spectroscopy indicates that Fe^{3+} enters the smaller of the two octahedral sites preferentially. Cations of lower charge or vacancies occur usually at the larger *M*1 site rather than *M*2. In F-rich phlogopites short-range ordering occurs producing domains in which Fe^{2+} associates with OH and Mg with F.

As the (Fe,Mg) octahedra in biotites are larger than the Al octahedra in muscovite there is a better match between the octahedral and tetrahedral sheets in biotite, and this means that in biotite the rotations of tetrahedra away from hexagonal towards a trigonal configuration (see Fig. 130, p. 182) are less marked. They do, however, increase with increasing substitution of Al for Si until the consequent decrease in interlayer spacing reaches its limit.

Downloaded from https://pubs.geoscienceworld.org/books/chapter-pdf/3757971/9780903056434_ch45a.pdf
by guest

The substitution of Mg by Fe in biotites results in an increase in the *b* cell parameter, but this does not provide a reliable method of estimating the Mg/Fe ratio because other substitutions, such as Fe^{3+}, Al and F, also affect the cell parameters. The Fe/Mg ratio may, however, be determined approximately by measuring the ratios of intensities of appropriate X-ray powder reflections.

In trioctahedral micas the (OH) bond is nearly perpendicular to (100) and this increases layer separation. The substitution of F for (OH) counters this effect and increases stability.

A perspective view of the structure of phlogopite is presented in Fig. 127, p. 176.

Chemistry

A basic feature of the compositions of biotites (Table 25, p. 179) is the substitution of Fe for Mg in the range from phlogopite $K_2Mg_6Si_8O_{20}(OH)_4$ to annite $K_2Fe_6Si_8O_{20}(OH)_4$, but these end-members and their intermediates also exhibit substitution of Al for (Mg,Fe), balanced by Al for Si, towards the range between end members eastonite, ideally, $K_2Mg_4Al_2Si_4Al_4O_{20}(OH)_4$ and siderophyllite, ideally, $K_2Fe_4Al_2Si_4Al_4O_{20}(OH)_4$. The extremes of iron enrichment are uncommon except in synthetic micas, and the substitutions of Al for (Mg,Fe) balanced by Al for Si rarely go beyond $(Mg,Fe)_5Al$ and Si_5Al_3, respectively. Such substitutions are less common in the more magnesium-rich (phlogopitic) micas. The substitution of Al for (Mg,Fe) can alternatively be balanced by vacancies in the *M* sites (see below).

Other common substitutions are:

(a) Replacements of K in interlayer sites by Na, Ca, Ba, Rb and Cs. Of these, sodium is generally present in the greatest concentration but rarely exceeds 0.5 atoms pfu.

(b) Replacements in octahedral (*M*) sites of Mg or Fe^{2+} by Mn, Ti, Fe^{3+}, Li. Manganese rarely exceeds 0.2 atom pfu but a manganese-dominated phlogopite, shirozulite, has been described. The monovalent lithium ion can occur in *M* sites substituting for (Fe,Mg) and compensated by some $^{[6]}$Al, and Si for $^{[4]}$Al as in some lepidolites and zinnwaldites (see p. 195). Titanium occurs in an octahedral site (usually *M*2), balanced primarily by the loss of two hydrogens in the OH site (Ti-oxy exchange) and also by Al for Si or by *M*-site vacancies. These substitutions are favoured by higher temperatures. Fe^{3+} also substitutes for $^{[6]}$Al, but this is governed mainly by oxidation conditions. Biotites rich in Fe^{3+} are known as tetraferriannite or tetraferriphlogopite. For structural reasons and on evidence from Mössbauer spectroscopy a significant amount of the iron in the end-member annite must be Fe^{3+}.

The total number of M ions in biotites is rarely as high as the ideal 6 pfu, ranging typically between 5.6 and 5.9. Intermediate compositions are not uncommon in the case of Li-bearing micas, bridging compositions between lithian muscovite and lepidolites (p. 195). An unusual mica, montdorite, has one out of six *M* sites vacant, the others being occupied by Fe^{2+}, Mn and Mg, and the charge balance restored by having all tetrahedra occupied by Si.

With regard to anions, fluorine and to a lesser extent chlorine occur in biotites substituting for (OH), the amount generally increasing with increase in the Mg/Fe ratio. The fluorine content of a biotite decreases with temperature and H_2O/HF ratio of any fluid in equilibrium with it.

Hydrothermal synthesis of phlogopite has been achieved using a variety of starting materials and its hydrothermal breakdown reaction, at about 1300ºC is:

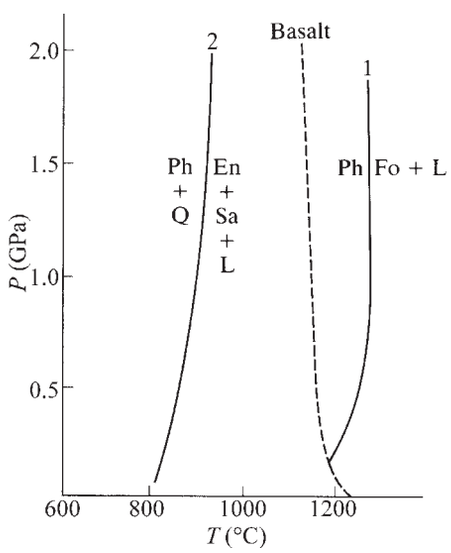


Fig.135. Univariant equilibrium curve for the 'fluid absent' breakdown of (1) phlogopite (after Yoder, H.S. & Kushiro, I., 1969, *Amer. J. Sci*., **267A**, 558–82) and (2) phlogopite + quartz (after Bohlen *et al*., 1983, *Contrib. Mineral. Petrol*., **83**, 270–7). Ph: phlogopite; Q: quartz; En: enstatite; Sa: sanidine; Fo: forsterite; L: liquid. The melting curve for basalt is also shown.

Downloaded from https://pubs.geoscienceworld.org/books/chapter-pdf/3757971/9780903056434_ch45a.pdf
by guest

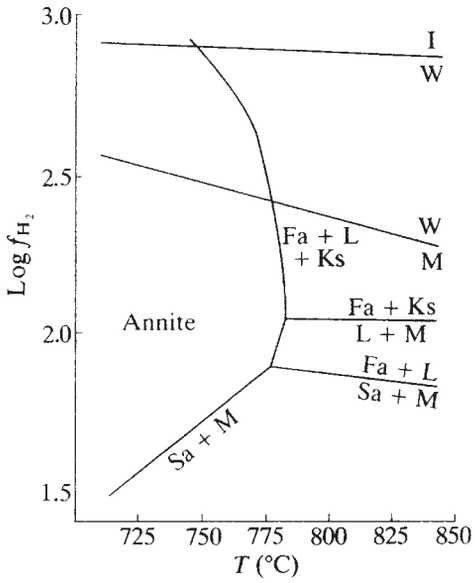


Fig. 136. Phase relations at 0.1 GPa for breakdown of annite at varying f_{H_2}. Buffers: IW: iron–wüstite; WM: wüstite–magnetite; Fa: fayalite; Sa: sanidine; M: magnetite; Ks: kalsilite; L: leucite (after D.A. Hewitt & Wones, D.R., 1984, Experimental phase relations of the micas. In *Reviews in Mineralogy*, Min. Soc. Amer. **13**, 215).

2 phlogopite →
leucite + kalsilite + 3 forsterite + 2 H_2O (1)

and is only slightly pressure dependant. The equilibrium curve for the 'fluid absent' breakdown of phlogopite is shown in Fig. 135, and the curve for

phlogopite + quartz → enstatite + sanidine + melt

is similar but at about 400ºC lower (Vielzeuf & Clemens, 1992). Compared with phlogopite, breakdown temperatures for annite are considerably lower.

Experiments with controlled f_{O_2} and f_{H_2} showing the breakdown reactions of the Fe^{2+} end-member annite are as depicted in Fig. 136. At high f_{O_2}, sanidine is accompanied by hematite or magnetite and at highest f_{H_2} by iron. Intermediate oxidation conditions yield the iron equivalent of reaction (1), i.e. leucite + kalsilite + fayalite + water. The reactions of annite + quartz at varying oxygen fugacity are shown in Fig. 137. Using these results, observations of the assemblage of minerals accompanying biotite can in, principle, give an indication of prevailing, f_{H_2O} and f_{O_2} conditions, but there are many complicating factors.

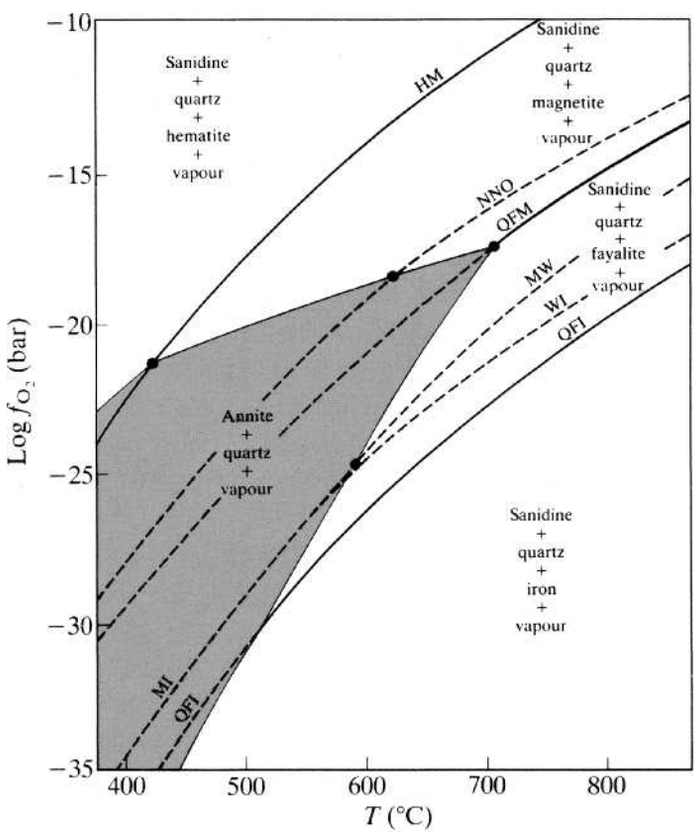


Fig. 137. Stability of annite + quartz in relation to oxygen fugacity at 0.2 GPa. Oxidation buffer curves: HM: hematite–magnetite; NNO: nickel–nickel oxide; QFM: quartz–fayalite–magnetite; MW: magnetite–wüstite; WI: wüstite–iron; QFI: quartz–fayalite–iron (after Eugster, H.P. & Wones, D.R., 1962, *J. Petrol.*, **3**, 82–125). Note: log f_{O_2} (MPa) = log f_{O_2} (bar) + 1.

Downloaded from https://pubs.geoscienceworld.org/books/chapter-pdf/3757971/9780903056434_ch45a.pdf
by guest

Experiments indicate that the Fe^{3+} content of biotites increases with f_{O_2}, and that this leads to higher refractive indices and smaller unit-cell dimensions. Experiments also show that the stabilities of intermediate compositions between phlogopite and annite are consistent with ideal mixing of end-member components. The substitution of Al for Fe and Si in annite–siderophyllite leads to increased stability. The replacement of K by Na in micas decreases stability.

The stability curves discussed above are particularly pertinent to the reactions of biotites in ultramafic and siliceous rocks. Many other reactions involving biotites have been studied experimentally, but among them the following two have particular relevance to the occurrence of biotites in calcareous and pelitic rocks, respectively:

phlogopite + calcite + quartz → tremolite + K-feldspar

biotite + sillimanite + quartz →
garnet/cordierite + K-feldspar + H_2O

In Al-rich rocks, biotite is accompanied by such minerals as garnet, cordierite and the Al_2SiO_5 polymorphs. Many studies have been made of the distribution of Mg and Fe between biotite and coexisting garnet. The distribution coefficient:

$$K_{D\,\mathrm{Mg/Fe}}^{\mathrm{Gt/Bi}} = (\mathrm{Mg/Fe})_{\mathrm{Gt}}/(\mathrm{Mg/Fe})_{\mathrm{Bi}}$$

corresponding with the exchange reaction

$KMg_3AlSi_3O_{10}(OH)_2 + Fe_3Al_2Si_3O_{12} \rightleftharpoons$
phlogopite almandine garnet
$Mg_3Al_2Si_3O_{12} + KFe_3AlSi_3O_{10}(OH)_2$
pyrope garnet annite

can provide a useful geothermometer (see garnet geothermometry, p. 24). The Mg/Fe ratio in biotite is usually lower than in coexisting cordierite. This and other element partitioning relations (e.g. biotite/pyroxene, biotite/epidote) have been used as geothermometers. The distributions of F and (OH) between biotites and coexisting apatites, of Rb and K between biotite and feldspar, and Ti between biotite and magnetite are also potential indicators of temperature, but there are greater uncertainties with these methods.

No method has been found to produce a substitute for natural mica in the form of large blocks from which undistorted sheets may be split, but synthetic fluorphlogopite is well suited for the manufacture of glass-bonded ceramics and reconstituted synthetic mica sheet.

Biotite alteration products include chlorite, muscovite and sericite; illite, kaolinite and other clay minerals; calcite, epidote-zoisite, leucoxene and rutile; and pyrite and other sulphides. Mineralizing solutions commonly leach iron and magnesium, and substitute potassium, yielding secondary muscovite and sericite pseudomorphous after biotite. The alteration of biotite by weathering produces either montmorillonite or vermiculite.

Optical and physical properties

Refractive indices generally increase with increasing iron content but are also affected appreciably by other substitutions (they increase with Mn and Ti content and decrease with F), thus an optical method of determining the Fe/Mg ratio is not reliable. Most biotites (those with the 1M structure) have the optic axial plane parallel to (010), but for those with the $2M_1$ structure it is perpendicular to (010). The acute bisectrix is approximately normal to (001), so that cross-sections perpendicular to the (001) cleavage show positive elongation.

Optical and Mössbauer spectroscopy give information about proportions of trivalent and divalent iron, and whether Fe^{3+} is in 6- or 4-fold coordination. Infrared absorption bands can be associated with different aspects of the structure, e.g. O–H stretching and Si–O stretching and bending modes, and X-ray absorption spectra give information about atomic coordination geometry.

The colours of biotites are related to their composition and particularly to the relative proportions of Fe^{3+}, Fe^{2+} and Ti. Biotites with low Ti range from blue-green to yellow or green-brown and brown with increasing Fe, whereas those with high Ti are reddish brown regardless of Fe content.

Acicular inclusions of rutile, and more rarely tourmaline, aligned in specific directions (perpendicular to (010) and at 60º intervals) occur in some phlogopites. These are responsible for the phenomenon of 'asterism', which is observed when a small light source is viewed through a thin sheet of mica. The inclusions are commonly arranged in zones, with inclusion-free zones showing no asterism. Colour zoning may be either alternating (e.g. light and dark green) or of the core-margin type (e.g. medium brown core, pale yellow margin).

Pleochroism is marked in biotites with high absorption for light vibrations parallel to (001); it increases with Fe content, particularly if Fe^{3+} is present because of the exchange of electrons between Fe^{2+} and Fe^{3+} in adjacent octahedra. Biotite commonly exhibits pleochroic haloes (Fig. 138) which are attributed to the presence of inclusions of zircon or other minerals containing radioactive elements.

Biotite commonly occurs in large well formed crystals with tabular {001} habits and pseudohexagonal outlines. The percussion figure test may be applied to determine crystallographic orientation, but as with other micas it is not always easy to perform or interpret (see p. 178).

Distinguishing features

Phlogopite can be distinguished from muscovite which has a greater 2V, and from the more iron-rich biotites which have higher refractive indices. The biotites are generally darker in colour and more highly

Downloaded from https://pubs.geoscienceworld.org/books/chapter-pdf/3757971/9780903056434_ch45a.pdf
by guest

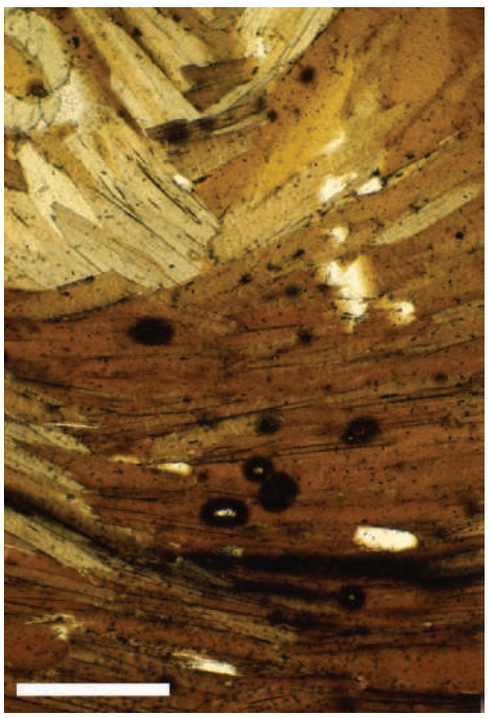


Fig. 138. Biotite in biotite-kyanite gneiss, Ross of Mull, Scotland (ppl, scale bar 0.5 mm), showing numerous dark brown to black pleochroic haloes. Many of the crystals show the perfect cleavage; the most intense absorption colour is seen when the polarizer is parallel to the cleavage (W.S. MacKenzie collection, courtesy of Pearson Education).

pleochroic than the other micas, and have higher refractive indices. Biotites can be distinguished from muscovite by their low 2V. Vermiculite has lower refractive indices and birefringence, and chlorites have a much lower birefringence.

Lepidolites can be distinguished from biotites by their paler colour, but they can be similar to phlogopite in appearance and optical properties. The lithium flame test and X-ray powder diffraction may be of assistance in making a positive distinction.

Paragenesis

Biotites occur in a greater variety of geological environments than any of the other micas. In metamorphic rocks they crystallize in a wide range of temperature and pressure conditions, and occur abundantly in many contact and regionally metamorphosed sediments. In intrusive igneous rocks biotites occur commonly in granites and granite pegmatites, granodiorites, tonalites, diorites, norites, quartz and nepheline syenites and quartz monzonites. Biotites are particularly characteristic of the intermediate rocks of calc-alkaline affinities and occur in a wide range of rocks of hybrid origin. They are less common in extrusive igneous rocks, but occur in rhyolites, trachytes, dacites, latites, andesites and some basalts.

Metamorphic rocks

The most common modes of formation of biotites are by the metamorphism of pelites, basic and ultrabasic rocks and siliceous limestones and dolomites. Biotites also occur in metagreywackes and metagranites.

For pelitic schists, there are a large number of reactions which can relate to the entry or exit of biotite from the mineral assemblages and only a few examples can be given here. The entry of biotite ('biotite grade') generally results from continuous reactions involving some or all of muscovite, chlorite, quartz and K-feldspar:

$$\text{celadonitic muscovite} \rightarrow \text{biotite} + \text{K-feldspar} + \text{quartz} + H_2O$$

or:

$$\text{muscovite} + \text{chlorite} \rightarrow \text{biotite}$$

or, in greywacke type rocks:

$$\text{chlorite} + \text{K-feldspar} \rightarrow \text{biotite} + \text{quartz} + H_2O$$

The amount of muscovite decreases and it becomes less celadonitic [the biotite has more (Mg,Fe) and Si]; the amount of chlorite decreases and it becomes more Al-rich (the biotite has less Al). With increasing grade, biotite and chlorite are joined by garnet and then by staurolite. Above the Al_2SiO_5 isograd biotite is accompanied by cordierite, but above this metamorphic grade, in granulites, biotite is absent.

In metabasic rocks, biotite is generally accompanied by muscovite in greenschist and epidote-amphibolite facies, but at higher-grade (amphibolite facies) muscovite can react with amphibole thus:

$$\text{muscovite} + \text{Ca amphibole} \rightarrow \text{biotite} + \text{quartz} + H_2O$$

and biotite continues up to granulite facies where its breakdown to pyroxene + K-feldspar occurs.

In the context of metamorphosed impure limestones and dolomites, again many reactions have been suggested (on the basis of experiments and observations) involving phlogopite or biotite among the reactants or products including:

$$\text{phlogopite} + \text{calcite} + \text{quartz} \rightarrow \text{tremolite} + \text{K-feldspar} + CO_2 + H_2O$$

$$\text{dolomite} + \text{muscovite} \rightarrow \text{biotite} + \text{chlorite} + \text{calcite} + CO_2$$

Igneous rocks

Biotites occur in a wide range of igneous rocks from granitic rocks to peralkaline types. There have been many attempts to correlate the chemical compositions of biotites with the kinds of igneous rocks in which they occur. There is, as expected, some correlation with overall rock chemistry but this is limited because other factors such as physical crystallization conditions and the nature of accompanying minerals are also important. In

Downloaded from https://pubs.geoscienceworld.org/books/chapter-pdf/3757971/9780903056434_ch45a.pdf
by guest

general, with increasing acidity of the host rock, the biotites show an increase in Fe^{2+} and a decrease in Mg content. Within a particular intrusion this trend is followed in passing from early to later formed biotites, and in addition there may be enrichment in Al and Fe^{3+}, depletion of Si and Ti, and variations in trace-element concentrations (e.g. increase of Ge:Al, Li:Mg, Mn:Fe^{2+} and Rb:K, and decrease in Ni:Mg, Co:Fe^{2+} and Ba:K ratios). Phlogopite occurs mainly in ultrabasic rocks; it is a particularly characteristic constituent of kimberlite in which it is commonly present in amounts of 6 to 8%. In some kimberlites phlogopite displays reaction rims of iron oxides, chlorite and calcite, and occurs also as rims attached to corroded grains of chromium-rich diopside. Inclusions of phlogopite rock and other less phlogopite-rich inclusions are known from some kimberlite pipes.

Phlogopite is a primary mineral in some leucite-rich rocks. In the West Kimberley area of Western Australia, for example, it occurs in massive, vesicular and fragmental rocks consisting of varying proportions of leucite, katophoritic amphibole and diopside. Other phlogopite- and leucite-bearing rocks are wyomingite (leucite, phlogopite, pyroxene) and jumillite (leucite, phlogopite, pyroxene, olivine, sanidine).

Although biotite is most common in intermediate and acid plutonic rocks it is also an important constituent of some basic rocks. Thus biotite is an abundant constituent in the quartz-biotite norites and cordierite norites of the Haddo House district, NE Scotland.

Biotite occurs much less abundantly in volcanic than in plutonic rocks, and if present it is commonly partially altered to other minerals. The different behaviour of biotite in plutonic and volcanic rocks can be explained in terms of the experimentally determined stability curve of phlogopite and its relation to the minimum melting curve of basalt. The phlogopite stability curve crosses the basalt melting curve at low pressure, and in a basic rock phlogopite is stable at depth but becomes unstable on extrusion. Micas having a biotitic composition do, however, occur in extrusive rocks, although they are commonly partially or completely resorbed, a feature which is most marked in the biotites of the least siliceous extrusives (e.g. in the volcanic rocks of the San Juan region, Colorado).

Biotites of volcanic rocks are in general poorer in Fe^{2+} and richer in Fe^{3+} and Ti than those in their intrusive equivalents.

Further reading

Bailey, S.W. (1984) Classification and structures of the micas. Pp. 1–12 in: *Micas* (S.W. Bailey, editor). Reviews in Mineralogy, **13**, Mineralogical Society of America, Washington, D.C.

Bailey, S.W. (1984) Crystal chemistry of the true micas. Pp. 13–60 in: *Micas* (S.W. Bailey, editor). Reviews in Mineralogy, **13**, Mineralogical Society of America, Washington, D.C.

Brigatti, M.F., Frigieri, P., Ghezzo, C. and Poppi, L. (2000) Crystal chemistry of Al-rich biotites coexisting with muscovites in peraluminous granites. *American Mineralogist*, **85**, 436–448.

Cesare, B., Satish-Kumar, M., Cruciani, S., Pocker, S. and Nodari, L. (2008) Mineral chemistry of Ti-rich biotite from pegmatite and metapelitic granulites of the Kerala Khondalite Belt (southeast India): Petrology and further insight into titanium substitutions. *American Mineralogist*, **93**, 327–338.

Clemens, J.D. (1995) Phlogopite stability in the silica-saturated portion of the system $KAlO_2$–MgO–SiO_2–H_2O: new data and a reappraisal of phase relations to 1.5 GPa. *American Mineralogist*., **80**, 982–997.

Ferrow, E.A., Kalinowski, B.E., Veblen, D.R. and Schweda, P. (1999) Alteration products of experimentally weathered biotite studied by high-resolution TEM and Mössbauer spectroscopy. *European Journal of Mineralogy*, **11**, 999–1010.

Guidotti, C.V. (1984) Micas in metamorphic rocks. Pp. 357–367 in: *Micas* (S.W. Bailey, editor). Reviews in Mineralogy, **13**, Mineralogical Society of America, Washington, D.C.

Guidotti, C.V. and Dyar, M.D. (1991) Ferric iron in metamorphic biotite and its petrological and crystallochemical implications. *American Mineralogist*, **76**, 161–175.

Laurora, A., Brigatti, M.F., Mottana, A., Malferrari, D. and Caprilli, E. (2007) Crystal chemistry of trioctahedral micas in alkaline and subalkaline volcanic rocks: A case study from Mt. Sassetto (Tolfa district, Latium, central Italy). *American Mineralogist*, **92**, 468–480.

Luth, R.W. (1997) Experimental studiy of the system phlogopite–diopside from 3.5 to 17 GPa. *American Mineralogist*, **82**, 1198–1209.

Redhammer, G.J., Beran, A. Schneider, J., Amthauer, G. and Lottermoser, W. (2000) Spectroscopic and structural properties of synthetic micas on the annite-siderophyllite binary: synthesis, crystal structure refinement, Mössbauer, and infrared spectroscopy. *American Mineralogist*, **85**, 449–465.

Takeda, H. and Ross, M. (1995) Mica polytypism: Identification and origin. *American Mineralogist*, **80**, 715–24.

Tischendorf, G., Rieder, M., Förster, H.-J., Gottesmann, B. and Guidotti, C.V. (2004) A new graphical presentation and subdivision of potassium micas. *Mineralogical Magazine*, **68**, 649–667.

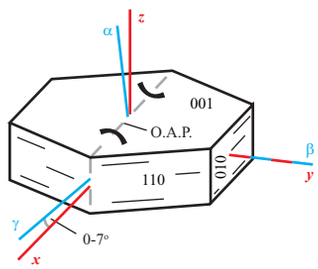
Veblen, D.E. and Ferry, J.M. (1983) A TEM study of the biotite-chlorite reaction and comparison with petrologic observations. *American Mineralogist*, **68**, 1160–1168.

Vielzeuf, D. and Clemens, J.D. (1992) The fluid-absent melting of phlogopite + quartz: experiments and models. *American Mineralogist*, **77**, 1206–1222.

Downloaded from https://pubs.geoscienceworld.org/books/chapter-pdf/3757971/9780903056434_ch45a.pdf
by guest

Monoclinic (or Trigonal) (−)

α	1.525−1.548
β	1.551−1.585
γ	1.554−1.587
δ	0.018−0.035
$2V_\alpha$	0−58° usually 30−50°
Orientation	γ:*x* 0−7°, β = *y*; O.A.P. (010)
D (g/cm^3)	2.80−2.90
H	2½−4
Cleavage	{001} perfect
Twinning	Composition plane {001}, twin axis [310]
Colour	Colourless and shades of pink and purple; colourless in thin section
Pleochroism	Absorption greater for vibration directions in the plane of cleavage
Unit cell	1M polytype: *a* ~ 5.3 Å, *b* ~ 9.2 Å, *c* ~ 10.2 Å, β ~ 100°
	Z = 1; space group *C2/m* or *C2*
	$2M_2$ polytype: *a* ~ 9.2 Å, *b* ~ 5.3 Å, *c* ~ 20 Å, β ~ 90°
	Z = 2; space group *C2/c*
	3T polytype: *a* 5.20 Å, *c* 29.8 Å
	Z = 3[a]; space group $P3_112$



Lepidolite is no longer regarded as a mineral species, but the name is in common use to describe lithium-rich micas with compositions close to polylithionite and trilithionite. The principal lithium-rich micas, lepidolite and zinnwaldite, are late-stage crystallization products of extreme fractionation of granitic magma and pegmatitic melts and fluids associated with granites, related pegmatites and aplites. They have also been reported from Sn-bearing hydrothermal veins.

Structure

The essential features of the structure of the lithium micas have already been described. The most common polytypes are 1M and $2M_2$. Less commonly $2M_1$, 3T, and mixtures of polytypes also occur. The 3T structure has *a* ~ 5.3 Å, *c* ~ 30.0 Å, space group $P3_112$ and Z = 3.[a] In both lepidolite and zinnwaldite, the smaller octahedral site (*M*2) is preferentially occupied by Al and Fe^{3+} and the larger *M*1 and *M*3 sites by Fe^{2+} and other divalent ions. Whereas there is little or no solid solution between the common dioctahedral and trioctahedral micas (e.g. muscovite and phlogopite/biotite), this structural gap is progressively reduced by the introduction of lithium and closes beyond 1.2 Li pfu to give a single mica of intermediate composition and structure with a high proportion of vacant octahedral sites. Most lepidolites have between 5 and 6 octahedral sites occupied.

[a] 3 $K(Li,Al)_{2.5-3}[Si_{3-3.5}\ Al_{1.0-1.5}]O_{10}(OH,F)_2$

Chemistry

Within the general formula of lepidolite presented above, the ranges of Li, $^{[6]}$[Al], $^{[4]}$[Al] and Si can be expressed in terms of three end-members: muscovite $K_2Al_4[Si_6Al_2O_{20}](OH,F)_4$ (Li-free); trilithionite, $K_2(Li_3Al_3)[Si_6Al_2O_{20}](OH,F)_4$; and polylithionite, $K_2(Li_4Al_2)[Si_8O_{20}](OH,F)_4$. Figure 139 shows on a plot of $^{[6]}$Al against Li atoms pfu, the distribution of a number of analysed lepidolites and lithian muscovites in relation to these end-members.

Most lepidolites have more than 3 out of 6 octahedral sites occupied, but there may be a continuous range between the dioctahedral muscovite and the mostly trioctahedral lepidolites. Interlayered mixtures

Downloaded from https://pubs.geoscienceworld.org/books/chapter-pdf/3758795/9780903056434_ch46.pdf
by guest

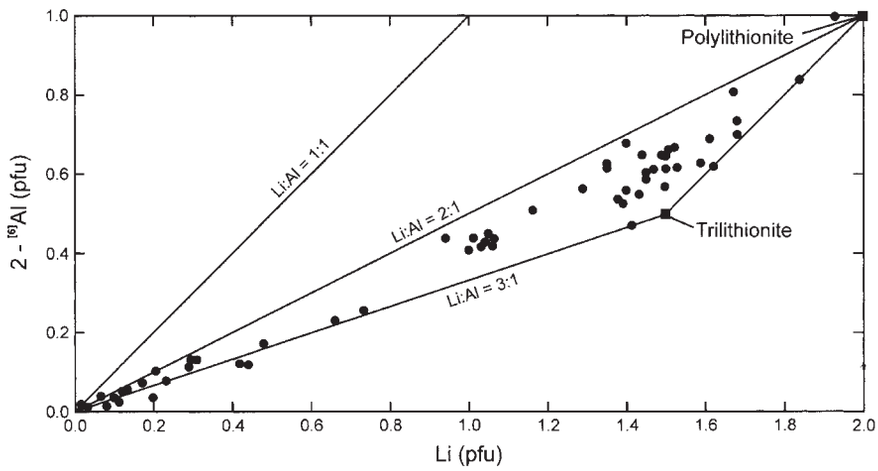


Fig.139. Plot of lithian muscovite and lepidolite compositions (all with low R^{2+} content) (after M.E. Fleet, *Rock-forming Minerals*, **3A**, p. 658, Fig 325, 2003, Geol. Soc. London).

of dioctahedral and trioctahedral micas could also, however, be responsible for intermediate chemical compositions.

In addition to the substitutions discussed above, considerable amounts of sodium, rubidium and caesium may substitute for potassium; and iron, manganese and magnesium may enter the octahedral sites. Other ions which are commonly present in small quantities include Ca, Ba, Sr, Ca, Nb and Ti. Lepidolite is one of the few minerals with an appreciable Rb content and it has found considerable use in the radioactive method of age determination in which the ^{87}Rb:^{87}Sr ratio is determined.

Lepidolites commonly show considerable replacement of (OH) by F and its extent appears to correlate with increasing Li content. The substitution of Fe^{2+} in the *M* sites yields ferroan lepidolites ranging towards zinnwaldite, which itself could be regarded as a high-iron lepidolite or as a lithium-rich biotite. An example of a lepidolite analysis is given in Table 25, analysis 8, p. 179.

Experiments on the hydrothermal stability of synthetic lepidolites are difficult because of the need to control f_{HF} as well as f_{H_2O}. With high f_{HF} and at 0.2 GPa pressure, polylithionite melts congruently at 770ºC whereas trilithionite melts incongruently forming eucryptite ($LiAlSiO_4$) + liquid at 678ºC. The stabilities of both are lower at lower f_{HF} and markedly lower in the presence of quartz, these two conditions being more relevant to the occurrence of lepidolites in pegmatites.

Optical and physical properties

The optical properties of lepidolites show a wide range of variation depending on the content of manganese and iron (particularly Fe^{3+}) rather than on the amount of lithium present. The upper and lower limits of observed optical parameters are listed above, but most lepidolites lie within the narrower ranges: α 1.529–1.537, β 1.552–1.565, γ 1.555–1.568, $2V_\alpha$ 30–50º. Generally the effect of increasing iron or manganese is to increase the refractive indices and to decrease 2V, so that the higher values for iron- and manganese-rich lepidolites approach the lower limits for muscovites. Lithian muscovites have lower refractive indices than true muscovites and fall in the lepidolite range. The polytypes of lepidolite are not distinguishable by their optical properties although there is a tendency for 1M specimens to have a higher 2V.

As with rose muscovites, the colour of lepidolites is related not to their lithium content but to the dominance of Mn over Fe^{3+} ions in the absence of Fe^{2+}. Thus, with higher Mn/Fe ratios, colours deepen from colourless or grey through shades of pink and lilac to purple. If Fe is high enough to mask the effect of Mn the resulting colour is brown.

Distinguishing features

Lepidolite can usually be distinguished from muscovite by its lower refractive indices, its colour, and by the lithium flame test. It is easily confused, however, with rose muscovite and although it usually has a more purplish tinge, X-ray powder diffraction or an Li_2O determination may be necessary to distinguish these micas. These methods are also necessary for distinguishing between lepidolite and lithian muscovite.

Paragenesis

Lepidolite is the most common lithium-bearing mineral, and occurs almost exclusively in granite pegmatites associated with other lithium minerals [amblygonite $LiAl(F,OH)PO_4$, spodumene, zinnwaldite], tourmaline, topaz, cassiterite, beryl and quartz. It has also been reported in granites and aplites and from high-temperature hydrothermal veins.

Downloaded from https://pubs.geoscienceworld.org/books/chapter-pdf/3758795/9780903056434_ch46.pdf
by guest

Most lepidolites are thought to have a metasomatic origin, either by replacement of muscovite or biotite, or by the reaction between K-feldspar and Li,Al silicates in the presence of F-rich fluids. Lepidolites can also form by direct crystallization of residual magma.

In general, if the fluorine activity is low, spodumene rather than lepidolite is the principal Li-bearing mineral to form, and in environments with high phosphorus and fluorine activities amblygonite predominates.

Further reading

Černý, P. and Burt, D.M. (1984) Paragenesis, crystallochemical characteristics and geochemical evolution of micas in granite pegmatites. Pp. 257–298 in: *Micas* (S.W. Bailey, editor). Reviews in Mineralogy, **13**, Mineralogical Society of America, Washington, D.C.

Guggenheim, S. (1981) Cation ordering in lepidolite. *American Mineralogist*, **66**, 1221–1232.

Henderson, C.M.B., Martin, J.S. and Mason, R.A. (1989) Compositional relations in Li-micas from S.W. England and France: an ion- and electron-microprobe study. *Mineralogical Magazine*, **53**, 427–449.

Munoz, J.L. (1971) Hydrothermal stability relations of synthetic lepidolite. *American Mineralogist*, **56**, 2069–2087.

Stone, M., Klomínský, J. and Rajpoot, G.S.W. (1997) Composition of trioctahedral micas in the Karlovy Vary pluton, Czech Republic and a comparison with those in the Cornubian Batholith, SW England. *Mineralogical Magazine*, **61**, 791–807.

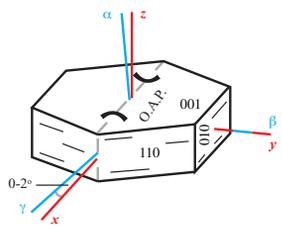
Tischendorf, G., Gottesmann, B., Forster, H.-J. and Trurnbull, R.B. (1997) On lithium-bearing micas: estimating Li from electron microprobe analyses and an improved diagram for graphical representation. *Mineralogical Magazine*, **61**, 809–834.

Downloaded from https://pubs.geoscienceworld.org/books/chapter-pdf/3758795/9780903056434_ch46.pdf
by guest

Zinnwaldite $K_2(Li,Fe^{2+},Al,Fe^{3+},\square)_6[(Si,Al)_8O_{20}](OH,F)_4$

Monoclinic (−)

α	1.535−1.558
β	1.570−1.589
γ	1.572−1.590
δ	~0.035
$2V_\alpha$	0−40º
Orientation	β = *y*, γ:*x* = 0−2º, O.A.P. (010)
D (g/cm^3)	2.90−3.02
H	2½−4
Cleavage	{001} perfect
Twinning	Composition plane {001}, twin axis [310]
Colour	Grey-brown, yellowish brown, pale violet; colourless or light brown in thin section
Pleochroism	α < β < γ α colourless to yellow-brown β colourless to grey-brown γ colourless to grey-brown
Unit cell	1M polytype. *a* 5.30, *b* 9.14, *c* 10.10 Å, β 100.8º *Z* = 1, *C*2 $2M_1$ polytype *a* 5.29, *b* 9.19, *c* 19.94 Å, β 95.4º *Z* = 2, *Cc*



Zinnwaldite is no longer regarded as a mineral species, but the term remains in common use by petrologists to describe dark lithium-bearing micas on the siderophyllite–polylithionite join. Zinnwaldite is one of the less common trioctahedral micas; its properties are similar to those of the biotites and, like them, it can occur in any of three polytypic forms (1M, $2M_1$, 3T) of which 1M is the most common

X-ray structure determination has indicated that there can be ordering of the octahedral cations differentiating the two *M*2 sites and consequent lowering the symmetry of space group to *C*2 instead of *C*2/*m*.

The major-element contents of zinnwaldites mostly lie on the join trilithionite, $K_2Li_3Al_3[Si_6Al_2]O_{20}(F,OH)_4$–siderophyllite $K_2Fe_4Al_2[Si_4Al_4O_{20}](OH)_4$, but a large number of further substitutions can occur (e.g. Ti, Mg and Mn for octahedral Al and partial replacement of K by Na, Ba, Rb, Sr and small amounts of Ca). Masutomilite is an Mn-rich analogue of zinnwaldite. Zinnwaldites resemble lepidolites in their high Si:Al ratio, Li content and replacement of OH by F, and also in their number of ions in *M* sites often being appreciably less than the ideal six. The higher iron content of zinnwaldite leads to higher refractive indices and density, greenish as well as yellow-brown colouration and slightly stronger pleochroism.

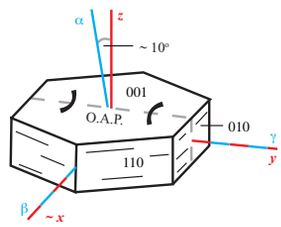
Zinnwaldite occurs mainly in granite pegmatites and in cassiterite-bearing veins. It is usually associated with other lithium-bearing minerals (lepidolite, spodumene), and with topaz, cleavelandite, beryl, tourmaline, monazite and fluorite.

Downloaded from https://pubs.geoscienceworld.org/books/chapter-pdf/3758897/9780903056434_ch47.pdf
by guest

Pyrophyllite $Al_4[Si_8O_{20}](OH)_4$

Monoclinic or Triclinic (−)

α	1.552−1.556
β	1.586−1.589
γ	1.596−1.601
δ	~0.050
$2V_\alpha$	53−62º
Orientation	γ = *y*, β approx. ∥ *x*; O.A.P. ⊥(010)
D (g/cm^3)	2.65−2.90
H	1−2
Cleavage	{001} perfect
Colour	White, yellow, pale blue, greyish or brownish green; pearly lustre; colourless in thin section
Pleochroism	Absorption greater for vibration directions in (001) plane
Unit cell	*a* ~ 5.17 Å, *b* ~ 8.96 Å, *c* ~ 18.68 Å, β ~ 100º; Z = 2; space group *C*2/*c* or *Cc* — or — *a* ~ 5.16 Å, *b* ~ 8.96 Å, *c* ~ 9.35 Å, α ~ 91º, β ~ 100º, γ ~ 90º; Z = 1; space group $C\bar{1}$



Pyrophyllite is a relatively uncommon mineral which occurs principally in Al-rich metamorphic rocks; it is also formed by hydrothermal alteration of minerals in highly to moderately siliceous rocks. It has been used industrially for its insulating properties, in cements, and also as a pressure medium and gasket material in high-pressure experiments.

Pyrophyllite, like muscovite, has a dioctahedral layered structure in which a sheet of octahedrally coordinated Al ions is sandwiched between two sheets of linked SiO_4 tetrahedra (Fig. 141). Two-thirds of the available octahedral sites are occupied by Al and the remainder are empty. The layers thus formed are electrically neutral so that no additional cations are accommodated between them. The stacking of successive layers in pyrophyllite is different from that in micas in that the six-membered rings of tetrahedra are laterally displaced across the interlayer gap. Weak van der Waals bonding between layers leads to pyrophyllite having very low hardness and an indistinct crystal habit, and exhibiting stacking disorder. The commonest polytype is two-layered and monoclinic but a one-layered triclinic structure also occurs.

Pyrophyllites show little deviation from the ideal chemical formula; small replacements of Si by Al, and of $^{[6]}$Al by Mg, Fe^{2+}, Fe^{3+} and Ti may occur, and minor amounts of Ca, Na and K may be present. A ferric iron analogue of pyrophyllite, ferripyrophyllite, has been reported. Some replacement of OH by F may occur, and of some O by OH, the latter providing some weak interlayer hydrogen bonding.

Differential thermal analysis experiments show that pyrophyllite loses water over the range 450−850ºC producing a metastable 'pyrophyllite dehydroxylate' by the reaction $2(OH) \rightarrow H_2O + O$.

Phase equilibrium studies in the system Al_2O_3–SiO_2–H_2O show the formation curve for kaolinite + quartz → pyrophyllite + H_2O at about 300ºC (0.1 to 1 GPa), and the breakdown curve for pyrophyllite → quartz and andalusite/kyanite + H_2O at about 350−420ºC increasing with pressure; above 1 GPa diaspore is formed. In the presence of CO_2, pyrophyllite has a wider field of stability. In natural rock systems pyrophyllite stability is more usually terminated by such reactions as:

pyrophyllite + chlorite → chloritoid + quartz + H_2O
or
pyrophyllite + calcite → margarite + quartz + H_2O + CO_2

Pyrophyllite is found in three main forms, fine-grained foliated lamellae with platy cleavage; radiating granular larger crystals and needles; and massive compact spherulitic aggregates of smaller crystals. It can be distinguished from talc and muscovite by its higher 2V, and from kaolinite, which has lower

Downloaded from https://pubs.geoscienceworld.org/books/chapter-pdf/3758928/9780903056434_ch48.pdf
by guest

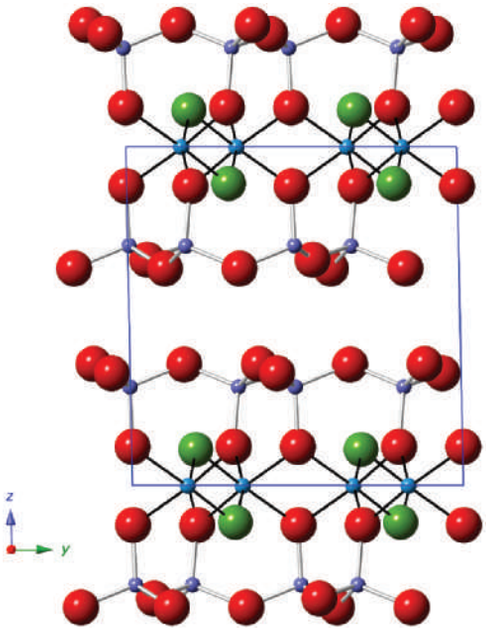


Fig. 141. The structure of pyrophyllite as viewed along the *x* axis. Blue: Si; red: oxygen; green: OH (CrystalMaker image).

birefringence. Although the data are similar, the distinction from talc is best achieved using X-ray powder diffraction.

Pyrophyllite occurs principally in Al-rich metamorphic rocks (metapelites, metabauxites, metaquartzites) up to greenschist facies but also in blueschist high-pressure low-temperature metamorphic conditions, and by hydrothermal alteration of minerals (e.g. feldspars, muscovite) in highly to moderately siliceous rocks, leaving them enriched in aluminium.

Further reading

Deer, W.A., Howie, R.A. and Zussman, J. (2009) *Rock-Forming Minerals*, Vol. **3B**, *Layered Silicates Excluding Micas and Clay Minerals*, 46–80. Geological Society, London.

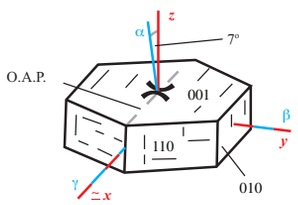
Wang, L., Zhang, M., Redfern, S.A.T. and Zhang, Z. (2002) Dehydroxylation and transformation of the 2:1 phyllosilicate pyrophyllite at elevated temperatures: an infrared spectroscopic study. *Clays and Clay Minerals*, **50**, 272–283.

Downloaded from https://pubs.geoscienceworld.org/books/chapter-pdf/3758928/9780903056434_ch48.pdf
by guest

Stilpnomelane $(K,Na,Ca)_{0.6}(Mg,Fe^{2+},Fe^{3+})_6Si_8Al(O,OH)_{27}.2–4H_2O$

Triclinic (−)

α	1.54−1.63
β ~ γ	1.58−1.75
δ	0.03−0.11
$2V_\alpha$	~0°
Orientation	β = *y*, γ ~ *x*; O.A.P. (010)
D (g/cm^3)	2.6−2.9
H	3−4
Cleavage	{001} perfect, {010} imperfect
Colour	*Ferrostilpnomelane*: pale yellow, green, brown *Ferristilpnomelane*: golden brown, reddish brown, black; green or dark brown in thin section
Pleochroism	*Ferrostilpnomelane*: α pale yellow, β = γ deep green *Ferristilpnomelane*: α golden yellow, β = γ deep reddish brown to nearly black
Unit cell	*a* ~ *b* 21.7−22.1 Å, *c* ~ 17.6 Å, d_{001} 12.1−12.6 Å, α ~ 125°, β ~ 96°, γ = 120° Z = 8; space group $P\bar{1}$
Special features	Soluble in warm 1:1 H_2SO_4 and HF



Stilpnomelane has a more complex layer structure than the micas and occurs in two varieties: ferrostilpnomelane contains abundant Fe^{2+} whereas ferristilpnomelane contains abundant Fe^{3+}. These substitutions influence both colour and pleochroism. Stilpnomelane has a perfect cleavage on {001} and an approximately perpendicular imperfect cleavage on {010}. It occurs in rocks of low metamorphic grade, especially greenschists, in silicate-iron formations and is also found in blueschists.

Structure

Stilpnomelane is one of a number of minerals with what are termed 'modulated layer structures'. Common to several of them is a continuous octahedral layer, but the tetrahedral layer which shares (O,OH) with it is not continuous as it is in micas. In stilpnomelane, 'islands' of seven rings of six tetrahedra occur in a regular pattern and are joined to the octahedral layer, but they occur on alternate sides of it (Fig. 140). Where they join, the layers are curved with octahedra on the outside of the curve. This effect is reminiscent of the curved layers of serpentine which serve to match the smaller repeat of a tetrahedral to the larger repeat of an octahedral layer. In stilpnomelane the match is only achieved over an 'island' of tetrahedra and beyond this another configuration is adopted. Joining 'islands' laterally are single six-membered rings of tetrahedra (with di-trigonal not hexagonal symmetry) and these share apices with similar rings attached to the next octahedral layer. Where 'islands' come back-to-back alkali atoms are located, analogous to the interlayer K atoms in muscovite, but in stilpnomelane they are fewer in number, and successive sheets are quite strongly bonded by the shared tetrahedral rings. The interlayer space is larger; d_{001} ~12.2 Å, as compared with ~10 Å in micas. Ferrostilpnomelanes have smaller d_{001} and larger *a* than ferristilpnomelanes.

Evidence for a two-layer polytype of stilpnomelane has been provided by high-resolution electron microscopy and other multilayer polytypes are known.

Chemistry

Stilpnomelanes exhibit a large range of compositions, the principal variations being in Fe^{2+}, Fe^{3+} and to a lesser extent Mg. Where Fe^{2+} is replaced by Fe^{3+}, $(OH)^-$ is replaced by $(O)^{2-}$ and additional water

Downloaded from https://pubs.geoscienceworld.org/books/chapter-pdf/3758918/9780903056434_ch48a.pdf
by guest

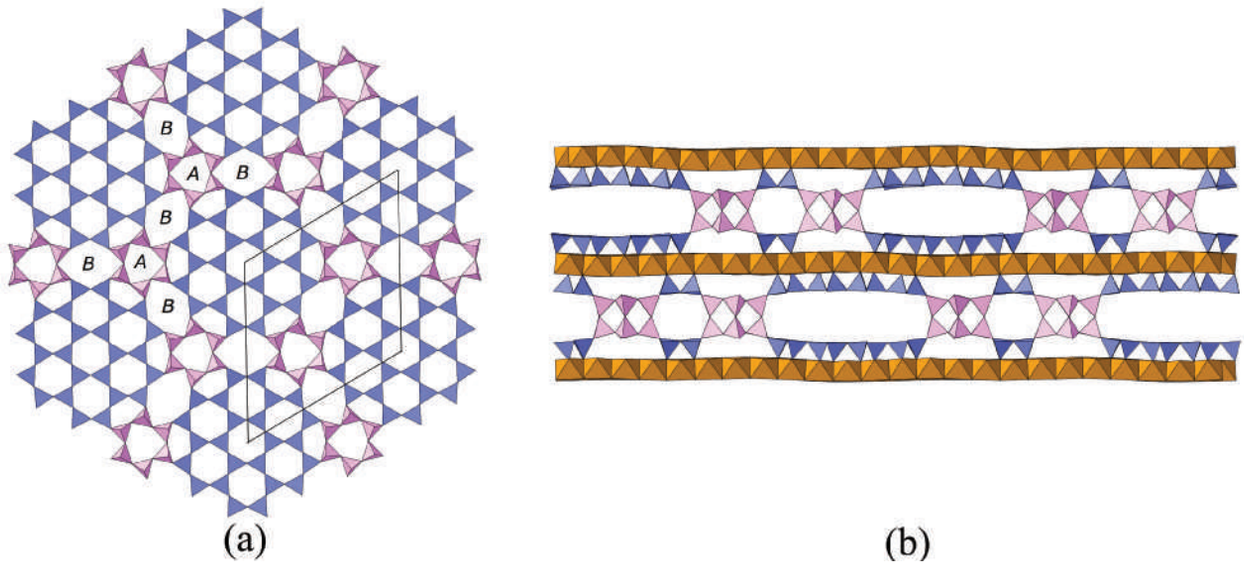


Fig. 140. Idealized structure of stilpnomelane. (a) Plan view of tetrahedral linkages. A and B are two kinds of interlayer site for the five alkali atoms per unit cell. (b) Side view showing a layer of (Mg,Fe)–(O,OH) octahedra (yellow) and interlayer (Si,Al)–O tetrahedra (blue and pink) (CrystalMaker image).

molecules are accommodated. The names ferrostilpnomelane and ferristilpnomelane are used respectively for Fe^{2+}- and Fe^{3+}-rich varieties. End-member ideal formulae for the unit-cell content are $K_5Fe^{2+}_{48}(Si_{63}Al_9)O_{166}(OH)_{48}.12H_2O$ for ferro- and $K_5Fe^{3+}_{48}(Si_{63}Al_9)O_{212}.36H_2O$ for ferri-stilpnomelane. These formulae can be simplified by dividing by eight. Departures from the ideal formulae include some Al and Mn as well as Mg substituting for Fe^{2+} in octahedra and some Na and Ca for the interlayer K ions (Table 26). An Mn-rich mineral with similar chemistry, parsettensite, has, however, a structure distinct from that of stilpnomelane.

On heating, stilpnomelane first loses interlayer water molecules and above about 450ºC Fe^{2+} is progressively oxidized and equivalent structural (OH) is lost. Although

Table 26. Stilpnomelane analyses.

	1	2		Numbers of ions per unit-cell[a] 1		2	
SiO_2	48.21	44.88	Si	65.2	72.0	61.9	72.0
TiO_2	0.04	0.52	Al	6.8		10.1	
Al_2O_3	4.35	6.69	Al	0.01	47.6	0.8	45.6
Fe_2O_3	13.03	25.46	Fe^{3+}	13.2		26.4	
FeO	14.00	2.73	Fe^{2+}	15.8		3.1	
MnO	0.27	0.53	Mn	0.3		0.6	
MgO	9.11	7.16	Mg	18.3		14.7	
CaO	0.28	0.79	Ca	0.4	4.0	1.2	4.2
Na_2O	0.06	0.12	Na	0.2		0.3	
K_2O	1.99	1.54	K	3.4		2.7	
P_2O_5	0.00	0.03	OH	37.7		30.3	
CO_2	N.D.	1.21	H_2O	17.6		23.3	
H_2O	8.46	8.80					
Total	99.80	'99.46'					

1 Pale green stilpnomelane, Iron Formation, Auburn Mine, Minnesota, USA (Eggleton, R.A. & Chappell, B.W., 1978, *Mineral. Mag.*, **42**, 361–8).
2 Ferristilpnomelane, greenschist, Matukituki, Otago, New Zealand (Eggleton, R.A. & Chappell, B.W., 1978, *ibid*).

[a] These formulae are calculated using the measured cell volumes and densities. TiO_2, P_2O_5 and CO_2 have been ignored.

Downloaded from https://pubs.geoscienceworld.org/books/chapter-pdf/3758918/9780903056434_ch48a.pdf
by guest

some Fe^{3+} in stilpnomelane may be the result of secondary oxidation it is thought that a wide range of Fe^{2+}/Fe^{3+} ratios can occur also as a primary feature depending upon oxidation conditions at the time of formation. Stilpnomelane decomposes to biotite and almandine garnet at higher temperatures and to zussmanite and chlorite at higher pressures. Stilpnomelane has been synthesized from gels and from synthetic magnesian chlorite + albite at 630ºC and 0.2 GPa.

Optical and physical properties

The wide range in proportions of Mg, Fe^{2+} and Fe^{3+} in stilpnomelanes is accompanied by a correspondingly large variation in their optical and physical properties. Refractive indices, birefringence and density increase with increasing iron content, Fe^{3+} having a greater effect than Fe^{2+}. The micaceous cleavage and deep colour of stilpnomelane make it difficult to determine refractive indices accurately. The great majority of stilpnomelanes show a negative uniaxial figure but minerals having a small optic axial angle have occasionally been noted. Stilpnomelane is commonly zoned; the core, consisting of ferrostilpnomelane, is surrounded by a peripheral zone richer in ferric iron. It typically forms spherulitic aggregates and fan-shaped bundles.

Distinguishing features

Stilpnomelane may be mistaken for biotite; both minerals occur in green and brown pleochroic varieties, and have a very small optic axial angle (most stilpnomelanes appear uniaxial) and similar pleochroism. The basal cleavage of stilpnomelane, however, is less perfect than that of biotite, and the former has a second cleavage perpendicular to {001}. In the extinction position stilpnomelane does not show the characteristic mottling effect of biotite. Ferrostilpnomelanes are distinguished by their greater birefringence from chlorite, chloritoid and clintonite. In hand specimen stilpnomelane can be distinguished by its brittle character from both biotite and chlorite.

Paragenesis

Stilpnomelane occurs as a mineral of low-grade metamorphism along with chlorite, muscovite and albite in greenschists (e.g. western Otago, New Zealand), but also together with magnetite as a major constituent of silicate-iron formations (e.g. Mesabi Range, Minnesota, and Hamersley, Western Australia). In the iron formations it is accompanied by other iron-rich silicates such as minnesotaite, greenalite, chamosite and grunerite. Another type of occurrence is with glaucophane and garnet in blueschists (e.g. in the Kanto Mountains, central Japan, and with deerite, howieite and zussmanite at Laytonville, California). Stilpnomelane occurs in reconstituted acid gneiss xenoliths in the gabbros and also in granophyres of the Skaergaard complex, east Greenland. It is also found associated with some sulphide deposits in which it is a product of surface weathering.

Further reading

Crawford, E.S., Jefferson, D.A. and Thomas, J.M. (1977) Electron microscope and diffraction studies of polytypism in stilpnomelane. *Acta Crystallographica*, **A33**, 548–553.

Currie, K.L. and Van Stahl, C.R. (1999) The assemblage stilpnomelane-chlorite-phengitic mica: a geobarometer for blueschist and associated greenschist terranes. *Journal of Metamorphic Geology*, **17**, 613–620.

Eggleton, R.A. (1972) The crystal structure of stilpnomelane II. The full cell. *Mineralogical Magazine*, **38**, 693–711.

Guggenheim, S. and Eggleton, R.A. (1987) Modulated 2:1 layer silicates. Reviews, systematics and predictions. *American Mineralogist*, **72**, 724–738.

Klein, C. (1974) Greenalite, stilpnomelane, minnesotaite, crocidolite and carbonates in a very low-grade metamorphic Precambrian iron-formation. *Canadian Mineralogist*, **12**, 475–498.

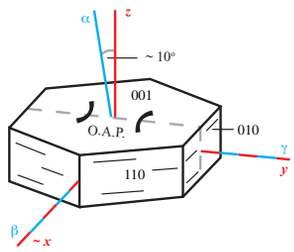
Li, G., Essene, E.J., Peacor, D.R. and Coombs, D.S. (2000) Reactions leading to the formation and breakdown of stilpnomelane in the Otago Schist, New Zealand. *Journal of Metamorphic Geology*, **18**, 393–407.

Miyano, T. and Klein, C. (1989) Phase equilibria in the system K_2O–FeO–MgO–Al_2O_3–SiO_2–H_2O–CO_2 and the stability limit of stilpnomelane in metamorphosed Precambrian iron formations. *Contributions to Mineralogy and Petrology*, **102**, 478–491.

Downloaded from https://pubs.geoscienceworld.org/books/chapter-pdf/3758918/9780903056434_ch48a.pdf
by guest

Triclinic or Monoclinic (−)

α	1.54−1.55
β	1.58−1.59
γ	1.58−1.60
δ	~0.05
$2V_\alpha$	0−30º
Orientation	$\gamma = y$, $\beta \sim \parallel x$; O.A.P. $\perp(010)$
D (g/cm^3)	~2.6
H	1
Cleavage	{001} perfect
Colour	Colourless, white, pale green, dark green, brown; colourless in thin section
Unit cell	$a \sim 5.29$ Å, $b \sim 9.15$ Å or $a \sim 5.29$ Å, $b \sim 9.15$ Å,
	$c \sim 9.45$ Å, $\alpha \sim 90.5$º, $c \sim 18.9$ Å, $\beta \sim 100$º
	$\beta \sim 99$º, $\gamma \sim 99$º
	Z = 1; space group $C\bar{1}$ Z = 2; space group $C2/c$ or Cc



Talc occurs mainly in metamorphosed ultrabasic rocks. It is also formed by replacement of tremolite and olivine in siliceous dolomites and high-grade kyanite-talc rocks (whiteschists). It is the major constituent of economic deposits of 'soapstones' or 'steatites', blocks of which can be used for thermal and electrical insulating purposes. It also finds use in ceramics, talcum powder, as a lubricant and as a filler in paints, paper and rubber.

Structure

The structure of talc (Fig. 142) is similar to that of pyrophyllite except that octahedral sites in the composite layers are occupied by magnesium instead of aluminium, and none is vacant; talc is thus a trioctahedral layered mineral. As in pyrophyllite, the ideal constituent layers are uncharged so that there are no interlayer cations and only very weak interlayer bonding; this leads to very low hardness and the prevalence of stacking disorder. It should be noted also that successive six-membered rings of tetrahedra are displaced relative to one another across the interlayer gap rather than being directly superimposed as in the micas. Small rotations of the tetrahedra cause the six-membered rings to be ditrigonal rather than hexagonal. One-layered triclinic (1Tc), two-layered monoclinic (2M) and two-layered orthorhombic (2O) polytypes have been reported.

The two kinds of octahedral site in talc differ only slightly; Mössbauer data indicate that if Fe substitutes for Mg it prefers the *M*2 site. The X-ray powder patterns of talc and pyrophyllite are similar but the *d* values of talc are larger and in particular d_{060} is 1.52 Å as compared with 1.49 Å for pyrophyllite. Basal spacings are not affected by organic liquids nor by heating to 700ºC since there are no interchangeable cations and no water molecules between the structural layers.

Chemistry

There appears to be little variation generally in the chemical composition of talc (Table 27); small amounts of Al or Ti substitute for Si, and small amounts of manganese or aluminium and moderate amounts of iron (Fe^{2+} and Fe^{3+}) may substitute for magnesium. Some samples have been reported, however, with as much as 2 Fe per formula unit. Larger amounts of iron are accommodated in the modulated layer structure of minnesotaite which, although chemically similar [approximate formula is $(Fe,Mg)_6Si_8O_{19}(OH)_6$], is not structurally an Fe analogue of talc. Willemseite has nickel as the major octahedral cation. The relatively minor contents of Ca and alkalis in talc may represent direct substitutions for Mg. However, it is more probable that they are interlayer ions or impurities. Some analyses show minor F substituting for (OH) and some show an unusually high water content which could

Downloaded from https://pubs.geoscienceworld.org/books/chapter-pdf/3759327/9780903056434_ch49.pdf
by guest

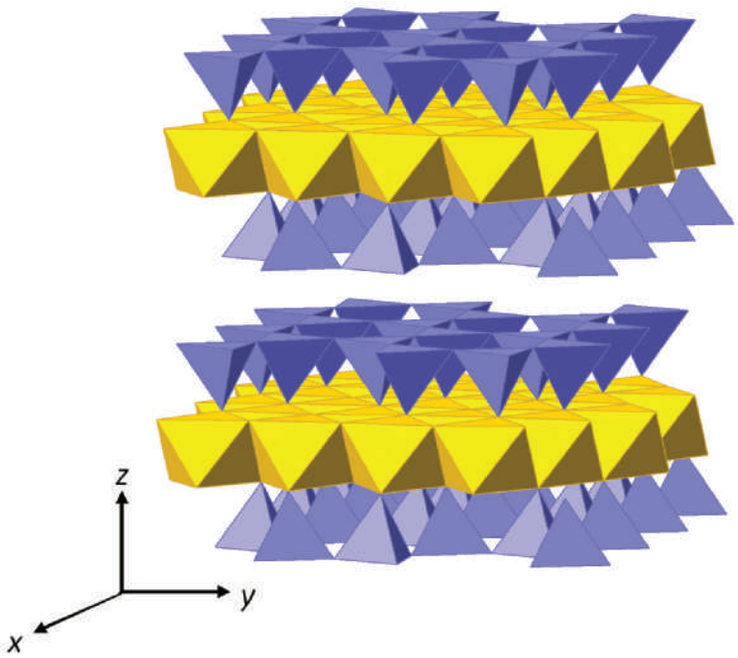


Fig. 142. Low angle perspective view of the structure of talc showing that all octahedral sites are occupied. Yellow: Mg–(O,OH) octahedra; blue: Si–O tetrahedra (CrystalMaker image).

be present as interlayer molecules or as tightly held adsorbed water. At pressures above 5 GPa a '10 Å phase' which has a higher H_2O content is stable with respect to talc + H_2O.

Talc undergoes thermal decomposition at about 800ºC to yield enstatite and cristobalite or amorphous silica.

$$Mg_3Si_4O_{10}(OH)_2 \rightarrow 3MgSiO_3 + SiO_2 + H_2O$$

Talc can be prepared at temperatures below 800ºC from mixtures of MgO and SiO_2 at water vapour pressures between 0.05 and 0.2 GPa. Calculated equilibrium curves for reactions in the system MgO–SiO_2–H_2O involving talc are shown in Fig. 143. The common association of talc with forsterite is evident, but talc is replaced at high temperatures by enstatite (together with serpentine at high pressure). The assemblage talc + enstatite is the high-pressure, low-temperature equivalent of anthophyllite. The addition of FeO has a marked effect on these reactions, generally lowering the temperature of stability of talc.

Table 27. Talc analyses.

				Numbers of ions on the basis of O (OH) equivalents		
				24 (O,OH)	24 (O,OH)	22 O
	1	2	3	1	2	3
SiO_2	62.92	60.92	61.21	Si 8.013 } 8.01	7.714 } 8.00	8.020 } 8.02
TiO_2	–	0.20	0.01	Al 0.000 }	0.277 }	0.001 }
Al_2O_3	0.09	2.82	0.40	Al 0.013	0.143	–
Fe_2O_3	0.59	–	–	Ti –	0.019	0.062
FeO	–	0.37	6.22	Fe^{3+} 0.057	–	–
MnO	0.02	–	0.00	Mg 5.896	5.825	5.184
NiO	–	–	–	Fe^{2+} – } 5.98	0.039 } 6.08	0.681 } 5.93
MgO	31.11	30.86	26.50	Ni –	–	–
CaO	0.02	–	–	Mn 0.001	–	–
Na_2O	0.01	0.31	–	Ca 0.006	–	–
K_2O	0.02	–	–	Na 0.002	0.076	–
H_2O+	4.60	4.66	–	K 0.003	–	–
Total	99.61	100.30	94.34	OH 3.992[a]	4.002	–

[a] Includes F 0.092.

1 Talc, Trimouns talc-chlorite deposit, Luzenac, Ariège, France (Martin, F. *et al*., 1999, *Can. Min*., **37**, 997–1006. Includes F 0.23).
2 Talc in talc-kyanite-quartz-rutile-hematite whiteschist, Chilapila Hill, Zambia (Grew, E.S. *et al*., 1998, *Dokl. Akad. Nauk. SSSR*, **299**, 1222–6. Includes F 0.19, Cl 0.04, less O = F,Cl 0.07).
3 Ferroan talc, glaucophane-chloritoid-garnet high-grade blueschist, Gran Paradiso basement, Lécharenne, Bonneval, Western Alps (Chopin, C., 1981, *J. Petrol*., **22**, 628–50. Probe analysis; all Fe as FeO).

Downloaded from https://pubs.geoscienceworld.org/books/chapter-pdf/3759327/9780903056434_ch49.pdf
by guest

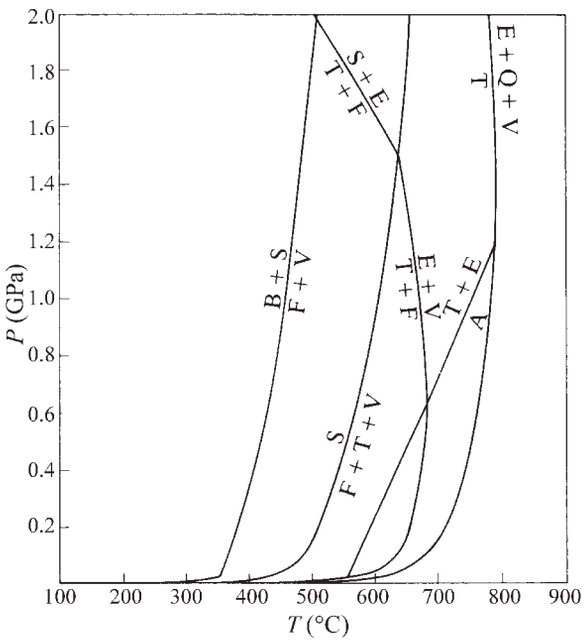


Fig. 143. $P-T$ curves for equilibria involving talc, calculated from thermodynamic data (after Evans, B.W. & Guggenheim, S., 1988, *Reviews in Mineralogy*, Min. Soc. Amer., **19**, 225–94). B: brucite; S: serpentine; F: forsterite; T: talc; E: enstatite; Q: quartz; A: anthophyllite; V: vapour.

Important equilibrium studies are those involving Ca and CO_2 as well as H_2O. These show that the assemblage talc + calcite has only a narrow field of stability so that talc is less common than tremolite in low-grade metamorphosed siliceous dolomites. Experiments and calculations have also been undertaken on more complex systems including Al, Na and K in relation to associations talc-kyanite (whiteschists), talc-phengite, talc-chloritoid and talc-kornerupine.

Optical and physical properties

Talc occurs most commonly in massive foliated or fibrous aggregates or in globular stellate groups (Fig. 144), but the rarer tabular crystals exhibit perfect {001} cleavage, yielding flexible, slightly elastic, lamellae. Talc in nearly all its forms has a greasy feel and pearly lustre, and it is taken as one of the standards of hardness, having the value 1 on the Mohs' scale. The variations in optical properties shown by talc specimens may result from small amounts of substituent ions (e.g. Ti, Mn, etc.) or from adsorbed water.

Distinguishing features

Pyrophyllite and muscovite have a larger 2V than talc, and the 'high silica' mica, phengite, has higher refractive indices and lower birefringence. Brucite has refractive indices similar to β and γ for talc, but it is uniaxial positive. Ferrous talc and minnesotaite are best distinguished by X-ray diffraction.

Paragenesis

The occurrence of talc depends largely upon the availability of sufficient magnesium; the main parageneses are therefore by low-grade metamorphism (and

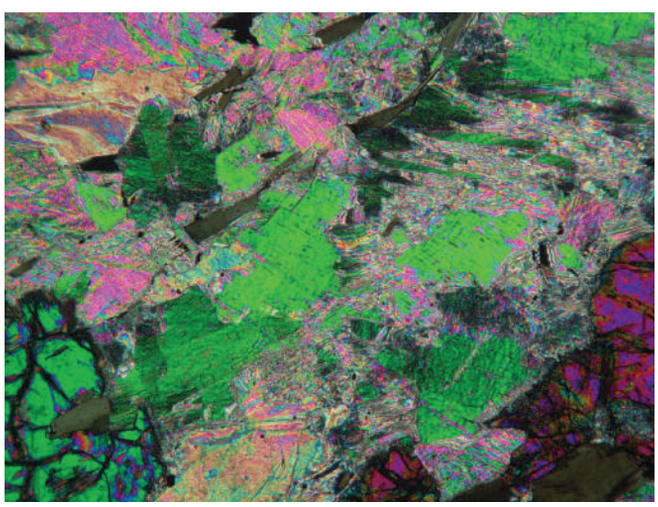


Fig. 144. Aggregate of talc crystals showing typical high interference colours, good cleavage and intracrystalline strain. Also present: olivine (high relief) and chlorite (grey-brown interference colours). Field of view 2 mm across. Crossed polars. Olivine-talc-schist, Swiss Alps (courtesy of G.T.R. Droop).

Downloaded from https://pubs.geoscienceworld.org/books/chapter-pdf/3759327/9780903056434_ch49.pdf
by guest

hydrothermal alteration) of ultrabasic rocks, by contact and regional metamorphism of siliceous dolomitic rocks, and the high grade metamorphism of basic rocks and their subsequent exhumation.

If, however, there is also abundant Al, Ca or K, the formation of chlorite, tremolite or phlogopite, respectively, would be favoured except at high pressure. In ultrabasic rocks talc is commonly accompanied by serpentine and olivine in lenticular veins. Metasomatism with high Si activity favours the formation of talc. The conversion of serpentine to talc may occur by the addition of silica and removal of magnesia, or by the addition of CO_2:

$$\underset{\text{serpentine}}{2\,Mg_3Si_2O_5(OH)_4} + 3\,CO_2 \rightarrow \underset{\text{talc}}{Mg_3Si_4O_{10}(OH)_2} + \underset{\text{magnesite}}{3\,MgCO_3} + 3\,H_2O$$

In siliceous dolomites, economic deposits may be formed by retrograde replacement of amphibole and olivine and the assemblage may include tremolite, anthophyllite, chlorite, magnesite, dolomite and quartz.

In the Broadford–Kilchrist area, Skye, talc occurs at the contact of chert nodules with the dolomite, and its formation can be ascribed to a reaction between dolomite and silica:

$$\underset{\text{dolomite}}{3\,CaMg(CO_3)_2} + \underset{\text{quartz}}{4\,SiO_2} + H_2O \rightarrow \underset{\text{talc}}{Mg_3Si_4O_{10}(OH)_2} + \underset{\text{calcite}}{3\,CaCO_3} + 3\,CO_2$$

The major talc deposit at Trimouns in the Pyrenees, was formed by metasomatic replacement of dolomite. Talc is also formed (e.g. Western Alps) at high pressure (eclogite-facies metamorphism) from the progressive breakdown of chlorite + quartz in pelitic or mafic rocks, producing successively talc + garnet, talc + chloritoid (Mg-rich) and talc + kyanite; examples of reactions include:

$$\text{chlorite} + \text{quartz} \rightarrow \text{kyanite} + \text{talc} + H_2O$$

The talc in the so-called 'whiteschists' may also be accompanied by phengite, implying pressures in excess of 1 GPa. Deposits of massive ferroan talc have been described associated with pyrrhotite and smectite on the ocean floor along a segment of spreading ridge in the Guyamas Basin (Gulf of California).

Further reading

Chopin, C. (1981) Talc–phengite: a widespread assemblage in high grade pelitic blueschists of the Western Alps. *Journal of Pertrology*, **22**, 628–650.

Corona, J.C. and Jenkins, D.M. (2007) An experimental investigation of the reaction glaucophane + 2 quartz = 2 albite + talc. *European Journal of Mineralogy*, **19**, 147–158.

Hemley, J.J., Montoya, J.W., Christ, C.L. and Hostetler, P.B. (1977) Mineral equilibria in the MgO–SiO_2–H_2O system: talc–chrysotile–forsterite–brucite stability relations. *American Journal of Science*, **277**, 322–351.

Hemley, J.J., Montoya, J.W., Shaw, D.R. and Luce, R.W. (1977) Mineral equilibria in the MgO–SiO_2–H_2O system. II. Talc–aragonite–forsterite–enstatite stability relations and some geological implications in the system. *American Journal of Science*, **277**, 353–383.

Nesbitt, H.W. and Bricker, O.F. (1978) Low temperature alteration processes affecting ultramafic bodies. *Geochimica et Cosmochimica Acta*, **42**, 403–409.

Schosseler, P.M., Weidlert, P.G. and Gehring, A.U. (1998) Octahedral sites in talc revisited: an EPR study. *Clay Minerals*, **33**, 661–664.

Schreyer, W. (1977) Whiteschists: their composition and pressure – temperature regime based on experimental, field and petrographic evidence. *Tectonophysics*, **43**,127–144.

Schreyer, W. (1988) Experimental studies on metamorphism of crustal rocks under mantle pressures. *Mineralogical Magazine*, **52**, 1–26.

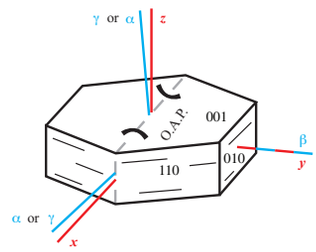
Downloaded from https://pubs.geoscienceworld.org/books/chapter-pdf/3759327/9780903056434_ch49.pdf
by guest

Chlorite Group

Clinochlore $(Mg)_{10}Al_2[Al_2Si_6O_{20}](OH)_{16}$
Chamosite $(Fe^{2+})_{10}Al_2[Al_2Si_6O_{20}](OH)_{16}$

Monoclinic (+)(−)

α	1.57−1.67
β	1.57−1.69
γ	1.57−1.69
δ	0.00−0.02
2V	20(−)−60°(+)
Orientation	Bx_a approx. ⊥ (001); O.A.P. (010) or ~ (010)
Cleavage	{001} perfect
D (g/cm^3)	2.6−3.3
H	2−3
Twinning	(a) twin plane {001}; (b) twin axis [310], composition plane {001}
Colour	Green, white, yellow pink, red, brown; mostly colourless or green in thin section
Pleochroism	Weak to moderate with either α < β = γ or α = β < γ: stronger absorption colours in iron-rich chlorites are usually dark or olive green, pale yellow−green
Unit cell	*a* ~ 5.3 Å, *b* ~ 9.2 Å, *c* ~ 14.3 Å, β ~ 97° (α ~ 90.5°, β ~ 97°, γ ~ 90° in triclinic polytype) Z = 1; space group *C*2/*m* (*C*$\bar{1}$ or *C*1 less common)
Special features	Readily attacked by strong acids. Anomalous brown or violet or blue interference colours common



In petrology the term chlorite is commonly used to describe intermediate compositions in the common and widespread clinochlore–chamosite solid-solution series. Other widespread but less well known chlorite-group minerals include the low temperature sedimentary phases donbassite and sudoite, and the manganese-bearing chlorite pennantite. The chlorites are a group of minerals with layered structure, which in many respects resemble the micas. Their principal occurrences are in low-grade regionally metamorphosed rocks, as hydrothermal alteration products of ferromagnesian minerals in igneous rocks and, together with clay minerals, in argillaceous sedimentary rocks. The chlorites have perfect cleavage yielding flexible but inelastic laminae. They occur commonly as fine-grained scaly or massive aggregates.

The occurrence of very substantial, varied and often continuous cation substitution in the chlorite minerals has led to a proliferation of varietal names based chiefly on differences in chemical composition; commonly these cannot be specifically characterized optically.

Structure

The structure of the common chlorites consists of regularly alternating negatively charged tetrahedral–octahedral–tetrahedral, 2:1, layers [i.e. talc-like layers with composition $M_6T_8O_{20}(OH)_4$] and positively charged interlayer brucite-like sheets, $M_6(OH)_{12}$, where *M* and T represent octahedral and tetrahedral sites, respectively (Fig. 145). The pseudohexagonal networks of these components all have an *a* parameter of approximately

Downloaded from https://pubs.geoscienceworld.org/books/chapter-pdf/3759628/9780903056434_ch50.pdf
by guest

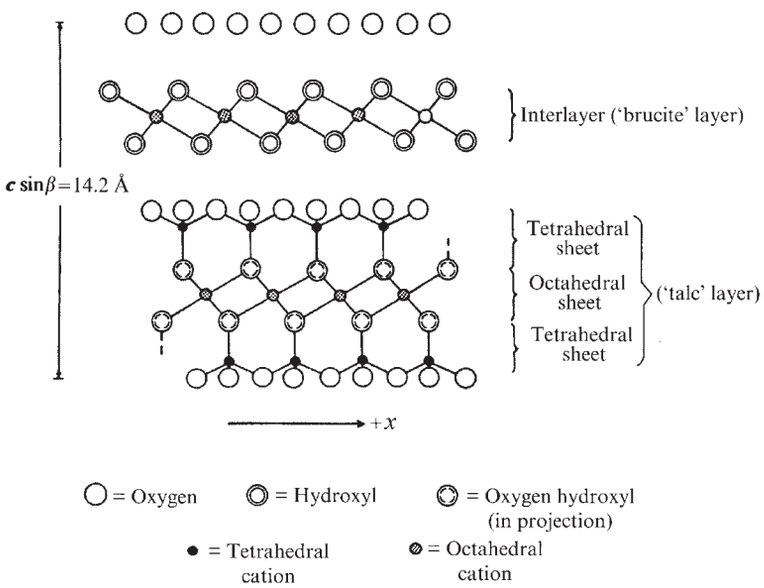


Fig. 145. Idealized chlorite structure; projection on (010) (after Bailey, S.W., 1988, Chlorites: structure and crystal chemistry. In *Hydrous Silicates (Exclusive of Micas)*. Ed. S.W. Bailey. *Reviews in Mineralogy*, Min. Soc. Amer., **19**, 347–403).

5.3 Å. A perspective view of the basic chlorite structure is given in Fig. 146.

The presence of aluminium in both the octahedral and tetrahedral sheets is essential to produce the similar *a*- and *b*-axis parameters that are necessary for the formation of a stable structure; an aluminium content of between 20 and 35 cation per cent is required for the best fit. The cell that results from this superposition of the octahedral and tetrahedral sheets has $a \sim 5.3$ Å, $b \sim 9.2$ Å, $c \sim 14.3$ Å, $\beta \sim 97°$. The height of the cell ($c \sin \beta$) is the thickness of one chlorite layer (2:1 layer plus interlayer sheet), and the β angle results from a layer displacement of $a/3$ in successive cells; the symmetry is $C2/m$.

A variety of regular stacking arrangements occurs in chlorites and can give rise to one- and two-layer polymorphs (polytypes) with lower symmetry than $C2/m$. Disordered stacking arrangements also occur very commonly, involving layer shifts which are directly observable using high-resolution electron microscopy.

In most common chlorites there are 12.0 octahedral cations per $O_{20}(OH)_{16}$, and approximately equivalent amounts of aluminium in tetrahedral and octahedral sites [e.g. clinochlore, $Mg_{10}Al_2(Si_6Al_2O_{20})(OH)_{16}$]; such minerals are referred to as trioctahedral chlorites. In a small number of chlorites the number of octahedral cations per $O_{20}(OH)_{16}$ is $\leqslant 10$. These varieties are described as dioctahedral and are made up of dioctahedral 2:1 layers (pyrophyllite-like) and trioctahedral interlayers (brucite-like), or of two dioctahedral layers (pyrophyllite and gibbsite-like layers); the two

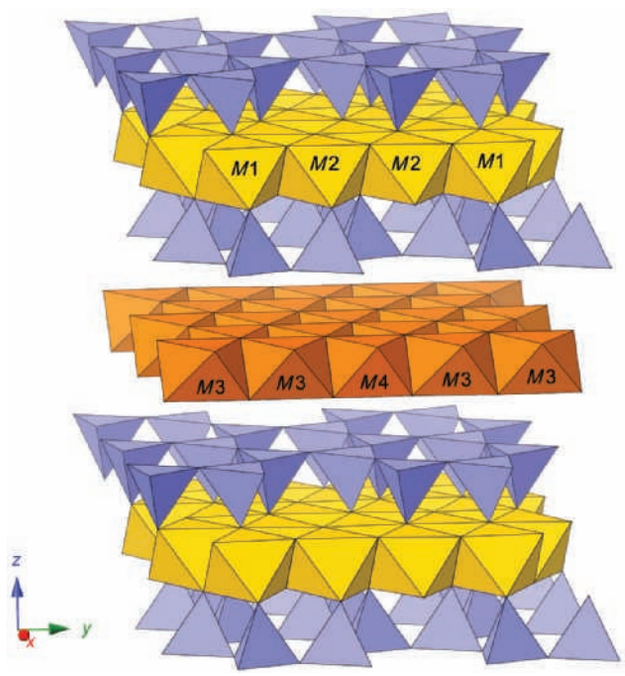


Fig. 146. A perspective view, approximately along *x* of the basic structure of a one-layer $C2/m$ tri-octahedral chlorite showing two talc-like components [a sheet of (Mg,Al)–(O,OH) octahedra (yellow) between two sheets of (Si,Al)–O tetrahedra (blue)] interleaved with a layer of (Mg,Al)–(OH) octahedra (orange), the 'brucite-like' layer. Structurally distinct octahedral sites are labelled *M*1, *M*2, *M*3, *M*4 (CrystalMaker image).

Downloaded from https://pubs.geoscienceworld.org/books/chapter-pdf/3759628/9780903056434_ch50.pdf
by guest

types of dioctahedral chlorites are designated di-trioctahedral and di-dioctahedral, respectively (see chemistry section).

In chlorites in which the amount of aluminium is insufficient to balance the negative charge of the tetrahedral sheet the charge deficiency is made up by Fe^{3+}, the presence of which need not indicate oxidation of the ferrous iron content. The Cr^{3+} that is present in some chlorites, is located in the octahedral interlayer and does not replace Al in tetrahedral sites.

If different cations (Mg,Fe,Al) occur in octahedral sites they may show varying degrees of ordering within a talc-like or brucite-like component, and in some cases showing preferences for one or other of these two layer components. In the tetrahedral component, however, Si/Al substitution appears to be random.

The cell parameters of chlorites vary with chemical composition. Thus the substitution of Al for Si together with Al for (Mg,Fe) reduces the basal spacing d_{001}: the value of b is relatively unaffected by Al substitution, but both a and b increase with the substitution of Mg by (Fe,Mn). The d_{001} spacing, cell parameters, and relative intensities of basal X-ray reflections may be used as a guide to composition.

Ordered or random interstratifications of chlorite with many other layered silicates (including serpentine, kaolinite, talc, vermiculite, smectite and mica) have been reported. Such mixed-layer sequences can be revealed indirectly by X-ray diffraction and in some cases directly by high-resolution transmission electron microscopy. Some ordered species have been assigned specific names, e.g. corrensite, which is a 1:1 trioctahedral chlorite/vermiculite.

Some layered minerals (e.g. amesite, berthierine, cronstedtite) which are chemically similar to chlorites are structurally similar to serpentine. Their X-ray powder patterns have a strong basal reflection at about 7 Å, none at 14 Å, and they are decomposed on heating to 500–600ºC.

Both vermiculites and montmorillonites have basal reflections at ~14 Å but can be distinguished from chlorites by heating to about 600ºC, which enhances the {001} reflection.

Chemistry

Most chlorite compositions can be represented by the formula:

$$^{[6]}(M^{2+},M^{3+})_{12}Si_{8-x}{}^{[4]}M^{3+}_{x}O_{20}(OH)_{16}$$

where M^{2+} = Mg, Fe, Mn, Ni, Zn; M^{3+} = Al, Fe, Cr; and x (generally) ~ 1–3.

In a small number of chlorites the number of octahedral ions is less than 12 and aluminium is the dominant octahedral ion.

The Mg ↔ Fe substitution occurs over a very wide range and natural trioctahedral chlorites can as a first approximation be expressed as a binary combination of the $(Mg_{10}Al_2)(Si_6Al_2O_{20})(OH)_{16}$ clinochlore and $(Fe^{2+}_{10}Al_2)(Si_6Al_2O_{20})(OH)_{16}$ (chamosite) end-members.

Although most chlorites contain only small amounts of manganese and chromium, a few have significant quantities; in the manganoan chlorite, pennantite (Table 28, analysis 4) associated with the manganese ore of the Benallt mine, Caernarvonshire, manganese makes up approximately two-thirds of the octahedral cations. A nickel-rich chlorite, nimite, in which ~40% of the octahedral sites are occupied by Ni is present in the Barberton nickel ore-body, South Africa; a zinc-rich chlorite with up to 30.5 wt.% of ZnO and 43% of the octahedral sites occupied by Zn occurs in skarn at Chillagoe, Queensland, Australia (analysis 6). Trioctahedral chlorites with Zn as the dominant octahedral cation with an ideal formula $(Zn_{10}Al_2)(Si_6Al_2)O_{20}(OH)_{16}$ are described as bailey-chlore. Cookeite is a di-trioctahedral lithian chlorite, $LiAl_4Si_3AlO_{10}(OH)_8$. Some ferric iron is present in most chlorite; its role is not always certain. In chlorite in which octahedral Al is low there is little doubt that Fe^{3+} proxies for Al in providing sufficient octahedral positive charge to balance the negative charge of the tetrahedral layer. Chlorites with above-average amounts of Fe^{3+} have in some cases a low H_2O content and less than the ideal 12 octahedral cations. It is possible that such specimens have been oxidized so that the reaction $Fe^{2+} \rightarrow Fe^{3+}$ was accompanied by loss of hydrogen. Other chlorites containing considerable Fe_2O_3, however, have a normal H_2O content and some or all of the Fe^{3+} is a necessary constituent for structural balance related to low octahedral Al, and should be regarded a primary constituent in the absence of other evidence of secondary oxidation.

A wide range of chlorite compositions have been synthesized, e.g. in the system $MgO–Al_2O_3–SiO_2–H_2O$, compositions between $(Mg_{11}Al)(Si_7AlO_{20})(OH)_{16}$ and $(Mg_8Al_4)(Si_4Al_4O_{20})(OH)_{16}$. For clinochlore the dissociation curve for the reaction:

$$5\,Mg_5Al_2Si_3O_{10}(OH)_8 \rightarrow \underset{\text{forsterite}}{10\,Mg_2SiO_4} + \underset{\text{cordierite}}{Mg_2Al_4Si_5O_{18}.nH_2O} + \underset{\text{spinel}}{3\,MgAl_2O_4} + (20-n)\,H_2O$$

at temperatures between 600 and 750ºC and P_{H_2O} to 0.3 GPa is shown in Fig. 147(a) At pressures greater than 0.3 GPa the upper thermal stability is controlled by the reaction (Fig. 147b):

$$\text{chlorite} \rightarrow \text{enstatite} + \text{spinel} + \text{forsterite} + H_2O$$

At higher pressures the breakdown temperature rises to about 875ºC and the products include enstatite or garnet instead of cordierite.

In the Mg–Fe chlorite series, increased Fe leads to lower breakdown temperatures. The maximum stability temperature of pure Mg chlorite is reduced by about 175ºC by the presence of quartz.

Downloaded from https://pubs.geoscienceworld.org/books/chapter-pdf/3759628/9780903056434_ch50.pdf
by guest

Table 28. Chlorite analyses

	1	2	3	4	5	6
SiO_2	27.12	25.62	25.07	22.64	32.73	32.0
TiO_2	–	0.88	0.12	–	0.00	–
Al_2O_3	27.68	21.19	19.78	18.60	7.96	12.9
Cr_2O_3	–	–	–	–	8.31	–
Fe_2O_3	0.20	3.88	3.50	4.43	–	–
FeO	1.24	21.55	35.80	–	2.29	12.5
MnO	0.54	0.35	0.50	38.93	0.02	0.13
NiO	–	–	–	–	0.00	–
ZnO	–	–	–	–	–	30.4
MgO	30.96	15.28	1.11	1.48	34.88	4.40
CaO	–	0.16	1.04	–	–	1.0
Na_2O	–	0.00	0.18	–	–	–
K_2O	–	0.00	0.93	–	–	–
H_2O+	12.82	10.87	10.82	9.40	13.82[d]	–
H_2O-	0.01	0.19	1.13	–	–	–
Total	100.57	99.97	99.98	96.81	100.01	93.3
Numbers of ions[a]						
Si	5.037 } 8.00	5.364 } 8.00	5.667 } 8.00	5.335 } 8.00	6.38 } 8.00	7.034 } 8.00
Al	2.963	2.636	2.333	2.667	1.62	0.966
Al	3.098	2.595	2.939	2.497	0.22	2.386
Ti	–	0.138	0.020	–	–	–
Cr	–	–	–	–	1.28	–
Fe^{3+}	0.029	0.611	0.594	0.784	–	–
Mg	8.570	4.767	0.373	0.520	10.16	1.428
Fe^{2+}	0.193 } 11.98	3.775 } 11.98	6.770 } 11.39[b]	– } 11.70[c]	0.38 } 12.04	2.290 } 11.29
Ni	–	–	–	–	–	–
Zn	–	–	–	–	–	4.936
Mn	0.085	0.062	0.095	7.770	0.00	0.024
Ca	–	0.035	0.251	–	–	0.224
OH	15.89	15.180	16.320	16.000	16.00	–

1 Mg–Al chlorite (clinochlore) talc-serpentine schist, Camberousse, Savoy, France (Orcel, J., 1927, *Bull. Soc Franç. Min.*, **50**, 75–454).
2 Mg–Fe chlorite, chlorite-epidote-albite schist, Limebury Point, Salcombe Estuary, South Devon, UK (Tilley, C.E., 1938, *Geol. Mag.*, **75**, 497–554).
3 Fe-chlorite (chamosite), vein in granite, Silent Valley quarry, east Mourne mountains, Northern Ireland (Nockolds, S.R. & Richey, J.E., 1939, *Amer. J. Sci.*, **237**, 27–47).
4 Manganese chlorite (pennantite), manganese ore, Benallt mine, Rhiw, Caernarvonshire, Wales, UK (Smith *et al.*, 1946, *Mineral. Mag.*, **27**, 217–20. Includes BaO 1.33).
5 Chromian chlorite (kammererite), Gumushane, Turkey (Phillips *et al.*, 1980, *Amer. Min.*, **65**, 112–22. Probe analysis. Total Fe as FeO).
6 Zinc chlorite (baileychlore), calcite vein in breccia containing altered andesite and garnet-vesuvianite skarn, Chillagoe, Queensland, Australia (Rule, A.C. & Radke, F., 1988, *Amer. Min.*, **73**, 135–9. Probe analysis. Total Fe as FeO).

[a] Where (OH) is given as 16.00 the formula has been calculated on the basis of 28 oxygen equivalents, ignoring H_2O; in other cases 36(O,OH) has been assumed.
[b] Includes Na 0.27, K 0.08.
[c] Includes Ba 0.132.
[d] H_2O computed by difference.

The oxidation reaction:

$$Fe_5Al_2Si_3O_{10}(OH)_8 \text{ (in Fe–Mg chlorite)} + \tfrac{5}{6}O_2 \rightarrow Al_2SiO_5 + \tfrac{2}{3}Fe_3O_4 + 2\,SiO_2 + 4\,H_2O$$

buffered with magnetite and hematite has been determined under $P_{total} = P_{H_2O}$ conditions over the P–T range 0.2–0.6 GPa, 575–625ºC. The experimental data show that the equilibrium Fe/(Fe + Mg) ratios in chlorite are a function of oxygen fugacity and independent of the bulk change in composition (the latter, however, determines the mineral assemblages).

The aluminium-rich chlorite (sudoite), $(Mg_4Al_6)(Al_2Si_6O_{20})(OH)_{16}$, is a stable phase in the system $MgO–Al_2O_3–SiO_2–H_2O$ at temperatures below 370–390ºC at pressures up to 0.7 GPa. At higher temperature it decomposes to magnesian chlorite, an Al_2SiO_5 phase and quartz:

$$5\,(Mg_2Al_3)(AlSi_3O_{10})(OH)_8 \rightarrow 2\,Mg_5Al_2Si_3O_{10}(OH)_8 + 8\,Al_2SiO_5 + SiO_2 + 12\,H_2O.$$

Differential thermal analysis curves of chlorites generally have endothermic peaks at about 600ºC and

Downloaded from https://pubs.geoscienceworld.org/books/chapter-pdf/3759628/9780903056434_ch50.pdf
by guest

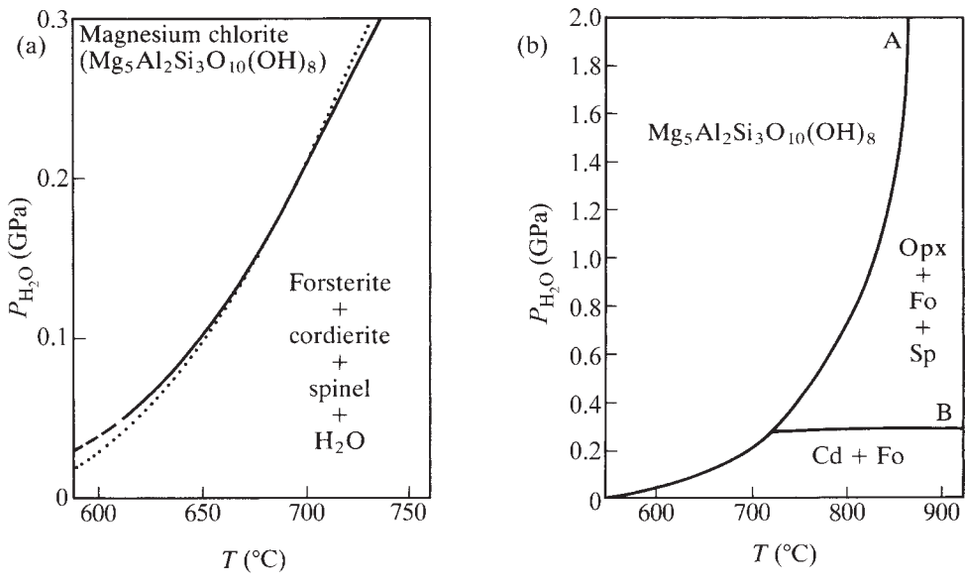


Fig. 147. (a) Dissociation curve for the reaction magnesian chlorite (chlinochlore) → forsterite + cordierite + spinel + vapour. Solid line, reaction involving anhydrous cordierite; broken line, reaction involving 1.8 wt.% H_2O in cordierite (after Cho, M. & Fawcett, J.J., 1986, *Amer. Min.*, **71**, 68–77). (b) P–T curves for the reactions: Mg–chlorite ⇌ orthopyroxene + spinel + forsterite + H_2O (A) and cordierite + forsterite ⇌ orthopyroxene + spinel (B) in the system H_2O–MgO–Al_2O_3–SiO_2 with excess H_2O (after Jenkins, D.M. & Chernosky, J.V., 1986, *Amer. Min.*, **71**, 924–36).

850ºC that probably correspond with dehydration of first the brucite-like and then the talc-like layers of the structure, but the positions of these as well as the exothermic peak at about 900ºC vary considerably according to chemical composition.

Comparison of Fe/Mg ratios for chlorites and coexisting minerals such as garnet, chloritoid or biotite have been used as geothermometers and, in some cases, geobarometers.

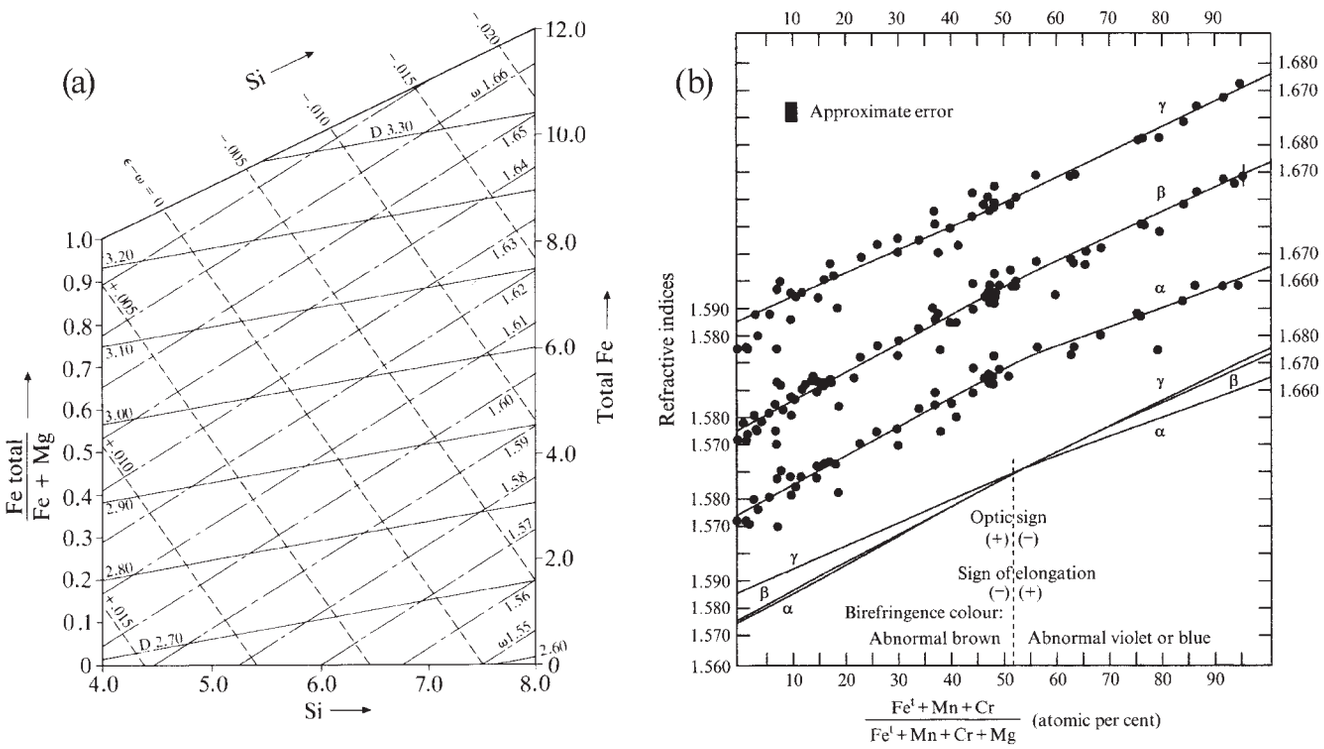


Fig. 148. (a) Refractive index (ω), birefringence (ε–ω) and density in g/cm^3 (D) of chlorites in relation to composition. For oxidized chlorites ω and D are higher and (ε–ω) is lower in proportion to percentage of Fe_2O_3 (after Hey, M.H., 1954, *Mineral. Mag.*, **30**, 277–92). (b) Correlation between optical properties and (Fe + Mn + Cr)/(Fe + Mn + Cr + Mg) in chlorites (after Albee, 1962, *Amer. Min.*, **47**, 851–70).

Downloaded from https://pubs.geoscienceworld.org/books/chapter-pdf/3759628/9780903056434_ch50.pdf
by guest

Optical and physical properties

The principal factors influencing the optical properties are the iron/magnesium ratio and the replacement of Si by Al (Fig. 148). Refractive indices increase with increasing iron and aluminium contents. The more iron-rich chlorites have a negative optic sign, and the more magnesium-rich are optically positive. In chlorites with intermediate Fe/Mg ratios the difference in the refractive indices of the two vibrations in the (001) plane is small and the minerals appear isotropic (Fig. 148b). The sign of the elongation is opposite to the optic sign and is more easily obtained than the optic sign in fine-grained specimens.

Pleochroism is generally exhibited more strongly by chlorites with higher iron content. The manganese chlorite (pennantite) is orange-brown in colour and pleochroic with α orange-yellow, γ orange: the nickel-rich chlorite (nimite) is yellowish green and faintly pleochroic with α yellow–green, γ apple-green; chromian chlorites are pink to red to violet in colour and are strongly pleochroic.

Anomalous interference colours are common, the more Mg-rich varieties in browns, the more Fe-rich in violet or blue.

Pleochroic haloes similar to those found in micas sometimes occur in chlorites and are related to inclusions of zircon at their centres. Fission tracks are present in some chlorites; their retention up to temperatures of 600ºC render them suitable for fission track geochronology.

Distinguishing features

Chlorites are usually green and pleochroic (Fig. 149), and some show anomalous interference colours. Birefringence is much lower than that of the micas, illites, montmorillonites and vermiculite, and refractive indices are higher than those of kaolinite. Some serpentines have a similar platy morphology but have lower refractive indices than chlorites and show little or no pleochroism. The serpentine-group mineral berthierine can have similar optical properties, and distinction is best made using the X-ray powder patterns of heated and unheated samples (see p. 210).

Paragenesis

Chlorite is a very common mineral, particularly in low- to medium-grade metamorphic rocks formed at temperatures up to about 400ºC and pressures of about 0.3 GPa. Chlorites are a common constituent of igneous rocks in which they have usually been derived by the hydrothermal alteration of primary ferromagnesian minerals. They are a common product of weathering and occur in many argillaceous rocks and in some iron-rich sediments.

Metamorphic Rocks

Chlorites form in the early stages of metamorphic alteration during the development of slaty cleavage in argillaceous sediments. The Al-rich chlorites, sudoite and donbassite, in particular, occur in fine-grained intimately intergrown mixtures of clay minerals in diagenetic environments.

These chlorites develop from mixed-layer clay materials resulting from the expulsion of interlayer alkali ions, the fixation of (Fe,Mg) and increased tetrahedral substitution that occur concurrently with increasing grain size. In the earliest stages the grains contain a high density of dislocations and incoherent boundaries between layers. In the slates most grains are defect-free but irregular interlayers of chlorite, illite, paragonite and phengite are common. The packets of 14 Å chlorite layers and 10 Å dioctahedral mica layers are usually several hundred nanometres in thickness; variable contents of Fe and Mg in different microstructural domains occur in some chlorites.

Chlorite is a common constituent in rocks of the zeolite facies. In the lower part of the facies, chlorite is associated with laumontite, stilbite and heulandite, and may appear to contain appreciable amounts of Ca, K and Na due to the presence of interlayered dioctahedral

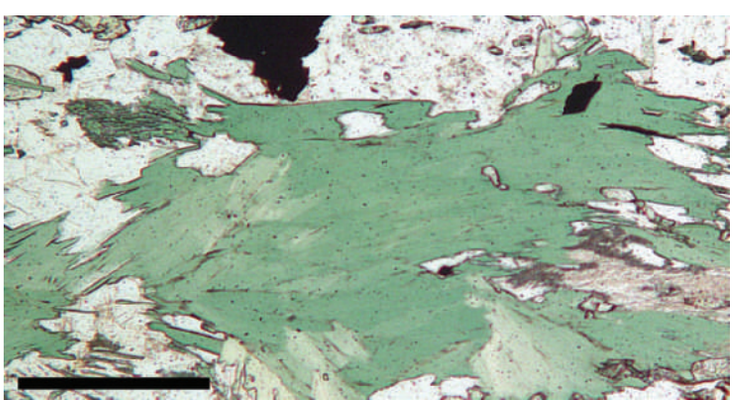


Fig. 149. Chlorite in epidote-albite-chlorite schist (ppl, scale bar 0.5 mm) from Döllach, Austria, showing moderate relief and platy habit, with pleochroism in shades of green (courtesy of G.T.R. Droop).

Downloaded from https://pubs.geoscienceworld.org/books/chapter-pdf/3759628/9780903056434_ch50.pdf
by guest

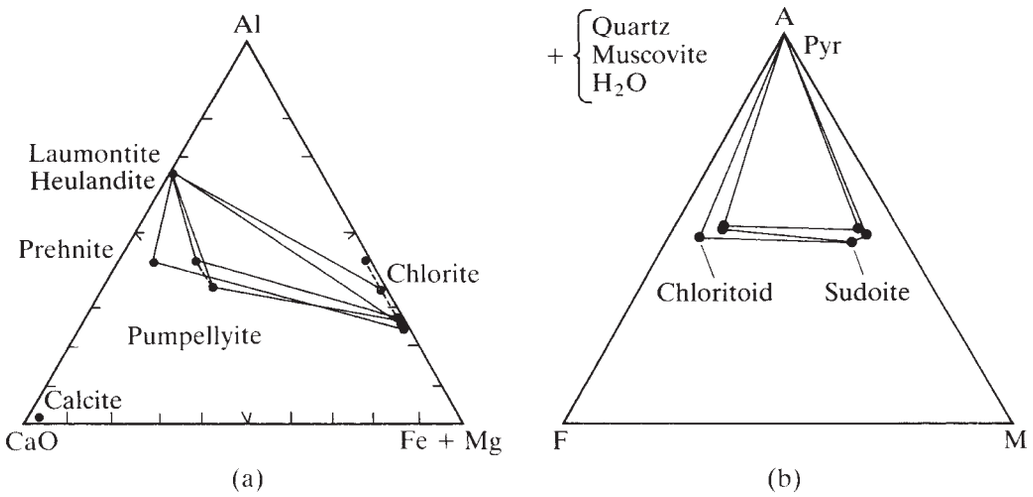


Fig. 150. (a) Compositions of chlorites and associated phases in zeolite facies mesozoic sediments in the Southland syncline, New Zealand. Typical tie lines between coexisting phases (after Boles, J.R. & Coombs, D.S., 1977, *Amer. J. Sci.*, **277**, 992–1012). (b) AFM (Al_2O_3–FeO–MgO) plot of sudoite–pyrophyllite–Fe-chloritoid assemblage in clastic metasediment, northern Appenines, Italy. Quartz and muscovite occur as excess phases (after Franceschelli, M. *et al.*, 1989, *Contrib. Mineral. Petrol.*, **101**, 274–9).

clays, such as illite and smectite. In the upper part of the zeolite facies, chlorite occurs in assemblages with prehnite and pumpellyite (Fig. 150a) and is involved in the reactions:

$$\text{chlorite} + \text{laumontite} + \text{prehnite} \rightarrow \text{pumpellyite} + H_2O \quad (1)$$

$$\text{laumontite} + \text{chlorite} + \text{calcite} \rightarrow \text{pumpellyite} + H_2O + CO_2 \quad (2)$$

Sudoite occurs in the Triassic clastic sediments of the northern Apennines where it is associated with muscovite, pyrophyllite and chloritoid (Fig. 150b).

In chlorite-zone pelitic rocks the typical chlorite is an intermediate magnesian variety; associated phases include muscovite, plagioclase, quartz, calcite and ilmenite. Chlorite remains as an important phase until the onset of the $P-T$ conditions of the biotite zone in which chlorite progressively diminishes in amount as a result of the reaction:

$$\text{chlorite} + \text{muscovite} + \text{quartz} \rightarrow \text{andalusite} + \text{biotite} + \text{cordierite} + H_2O$$

Chlorite-actinolite-epidote-albite assemblages are common in greenschists (Fig. 149). With increasing grade, chlorite decreases in amount and is involved with epidote and/or actinolite in the formation of Al-rich amphiboles. In rocks of the garnet and higher zones, chlorite is present in only minor amounts and is usually the result of retrogressive formation from ferromagnesian phases such as garnet, staurolite and biotite. The assemblage chlorite-andalusite-quartz is common in rocks of argillaceous composition in the outer part of thermal aureoles. The upper pressure limit of the stability field of the assemblage is given by the andalusite → kyanite transition, and the upper temperature stability limit is marked by the incoming of cordierite. Pinite, the most common breakdown product of cordierite, consists of chlorite and sericite; this reaction requires the availability of a potassium-bearing solution:

$$\text{cordierite} + K^+ + OH + H_2O \rightarrow \text{chlorite} + \text{muscovite}$$

Igneous rocks

Chlorite is a common product of the hydrothermal alteration of pyroxenes, amphiboles and biotite in igneous rocks. The composition of the chlorite is often related to that of the original igneous mineral, so that more iron-rich chlorites are commonly found as replacements of the iron-rich ferromagnesian minerals. Partial and complete chloritization of biotite is particularly common in granites and in most cases the transformation is markedly pseudomorphous.

Chlorite is commonly found filling amygdales in lavas, and together with epidote, alkali feldspar, quartz, sericite, zeolites, carbonates and pyrite, is an important product of the intense hydrothermal alteration (propylitization) of andesites and, to a smaller extent, of basalts. Chlorite also occurs as dense slickensided lamellar coatings along joint planes and fissures, particularly in basalts. Chlorite is an abundant constituent of spilites, in which it occurs in angular interstitial areas, in small rounded pools, in fine veinlets and in amygdales.

The association of chlorite with albite and quartz is an essential characteristic of adinoles, and chlorite-quartz pseudomorphs after andalusite in the adinoles are developed in Devonian slates metasomatized by albite dolerite at Dinas Head, Cornwall, UK.

Chlorite also occurs in fissure veins in some massive igneous rocks, and many low-temperature hydrothermal veins of alpine type in low-grade metamorphosed sediments carry chlorite in addition to adularia and

Downloaded from https://pubs.geoscienceworld.org/books/chapter-pdf/3759628/9780903056434_ch50.pdf
by guest

quartz. Aluminium chlorite (donbassite) occurs in hydrothermal ore veins; an aluminium chlorite, $(Al_{4.3}Fe_{0.1})(Si_{2.8}Al_{1.2})O_{10}(OH)_8$, also occurs as a hydration reaction product of andalusite. Manganese-rich chlorites are generally associated with manganese ore deposits.

Sedimentary rocks

Chlorite-group minerals are common constituents of argillaceous sedimentary rocks, in which they occur both as detrital and as authigenic crystals. Due to their usual fine-grained nature their characterization is often difficult, and in many sediments the chlorite is present in mixed-layer structures, e.g. in regular interstratification with vermiculite. The chlorites are derived by the aggradation of less organized sheet minerals, by the degradation of pre-existing ferromagnesian minerals, and by crystallization from dilute solutions of their compounds.

Further reading

Bailey, S.W. (1988) Chlorites: structures and crystal chemistry. Pp. 347–398 in: *Hydrous Phyllosilicates (Exclusive of Micas)* (S.W. Bailey, editor). Reviews in Mineralogy, **19**, Mineralogical Society of America, Washington, D.C.

Bryndzia, L.T. and Scott, S.D. (1987) The composition of chlorite as a function of sulfur and oxygen fugacity: an experimental study. *American Journal of Science*, **287**, 50–76.

Cho, M. and Fawcett, J.J. (1986) A kinetic study of clinochlore and its high temperature equivalent forsterite-cordierite-spinel at 2 kbar water pressure. *American Mineralogist*, **71**, 68–77.

Deer, W.A., Howie, R.A. and Zussman, J. (2009) *Layered Silicates Excluding Micas and Clay Minerals*. 81–156. Geological. Society of London.

Jenkins, D.M. and Chernosky, J.V. (1986) Phase equilibria and crystallochemical properties of Mg-chlorite. *American Mineralogist*, **71**, 924–936.

Laird, J. (1988) Chlorites: metamorphic petrology. Pp. 405–447 in: *Hydrous Phyllosilicates (Exclusive of Micas)* (S.W. Bailey, editor). Reviews in Mineralogy, **19**, Mineralogical Society of America, Washington, D.C.

Lee, I.H., Peacor, D.R., Lewis, D.D. and Wintsch, R.P. (1984) Chlorite–illite/muscovite interlayered and interstratified crystals: a TEM/STEM study. *Contributions to Mineralogy and Petrology*, **88**, 372–385.

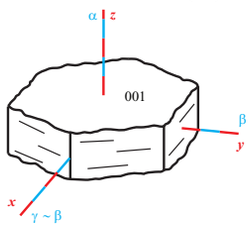
Piqué, A. and Wybrecht, E. (1987) Origine des chlorites de l'épizone, Héritage et cristallisation synschisteuse. Exemple des grauwackes cambriennes du Maroc occidental. *Bulletin de Minéralogie*, **110**, 665–682.

Vidal, O., Parra, T. and Veillard, P. (2005) Thermodynamic properties of the Tschermak solid solution in Fe-chlorite: application to natural examples and possible role of oxidation. *American Mineralogist*, **90**, 347–358.

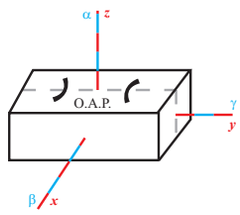
Welch, M.D. and Chrichton, W.A. (2005) A high-pressure polytypic transformation in type-1 chlorite. *American Mineralogist*, **90**, 1135–1145.

Downloaded from https://pubs.geoscienceworld.org/books/chapter-pdf/3759628/9780903056434_ch50.pdf
by guest

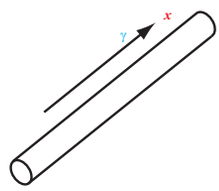
Trigonal, Monoclinic or Orthorhombic (−)



Lizardite



Antigorite



Chrysotile

	ε 1.538−1.554	α 1.558−1.567	α 1.532−1.549
	−	β ~1.566	−
	ω 1.546−1.560	γ 1.562−1.574	γ 1.545−1.556
δ	0.006−0.008	0.004−0.007	0.013−0.017
$2V_\alpha$	−	37−61°	−
		O.A.P. ⊥ (010)	
Orientation	−	α ~ ‖ *z*, γ = *y*	−
D (g/cm^3)	~2.55	2.6	⩽2.55
H	2½	2½−3½	2½
Cleavage	{001} perfect	{001} perfect	fibrous (‖*x*)
Twinning	−	Occasional	−
Colour	Green, white; colourless to pale green in thin section	Green, green-blue, white; colourless to pale green in thin section	Yellow, white, grey, green; colourless to pale green in thin section
Unit cell	*a* ~ 5.3 Å	*a* ~ 33−51 Å	*a* ~ 5.3 Å
		b ~ 9.25 Å	*b* ~ 9.25 Å
	c ~ 7.25 Å[a]	*c* ~ 7.25 Å	*c* ~ 14.6 Å
		β ~ 91.4°	β ~ 93.3 or 90°[b]
	Z = 2; space group *P*31*m*	Z = 2	Z = 4

There are three principal forms of serpentine: lizardite, antigorite and chrysotile, all with the approximate composition $Mg_3Si_2O_5(OH)_4$. The most abundant is lizardite and the least is chrysotile, but the latter is perhaps the best known as it commonly occurs in veins of silky fibres and has been the most important source of commercial asbestos. Its mechanical strength combined with thermal stability and low thermal conductivity made asbestos and asbestos composites useful in a wide range of important products. However, it is now known that inhalation of asbestos dust is a serious health hazard (it may cause asbestosis or pleural mesothelioma), so its use is now prohibited in many countries and dismantling of old installations and buildings containing asbestos, and disposal of asbestos waste, are undertaken with great care.

Chrysotile fibres are usually aligned approximately across the veins although 'slip' (or parallel) fibres also occur and their length, though generally less than 1 cm, can reach as much as 15 cm.

Although serpentine itself shows only minor substitutions for Mg and Si, the minerals berthierine, amesite and cronstedtite are structurally similar and have, respectively, major substitutions of Fe^{2+} for Mg, Al for Mg and Si, and Fe^{3+} for Si together with Fe^{2+} and Fe^{3+} for Mg.

[a] Multilayer polytypes of lizardite occur also, e.g. with two-, six- and nine-layer cells.
[b] For two-layer clinochrysotile and orthochrysotile, respectively. One-layer clinochrysotiles have slightly different β.

Downloaded from https://pubs.geoscienceworld.org/books/chapter-pdf/3760332/9780903056434_ch51.pdf
by guest

SERPENTINES

All serpentines

The term serpentine is commonly used to describe the minerals lizardite, antigorite and chrysotile and may also be used more widely to refer to other minerals in the serpentine group. The term serpentinite describes a rock that contains abundant serpentine. Serpentine minerals are generally products of hydrothermal alteration of ultrabasic rocks or pre-existing serpentinites, and less commonly occur in metamorphosed dolomitic rocks. Chemically they are approximately $Mg_3Si_2O_5(OH)_4$. They are all basically trioctahedral 1:1 layered silicates comprising a sheet of Mg–(O,OH) octahedra, sharing oxygens on one side with the apices of a sheet of Si–O tetrahedra with a characteristic Si:O ratio of 2:5; the interlayer repeat is ~7.2 Å. Hand specimens are mostly light to dark green, yellow or colourless, and thin sections between crossed polars show very low first-order birefringence colours and commonly mesh and hour-glass textures.

Variations in serpentines

There is a dimensional mismatch between the octahedral and tetrahedral sheets of the serpentine structure, which is overcome in various ways leading to three significantly different serpentine minerals, **lizardite**, **chrysotile** and **antigorite**. Lizardite has platy or lath-like morphology but poor crystallinity; variations within lizardites include multilayer unit cells, 'polygonal' and 'polyhedral' structures. In chrysotile the 1:1 layers are curled around the *x* axis to form submicroscopic scrolls or tubes; on the macro scale, aggregates of fibrils take the form of chrysotile asbestos, a serious health hazard if particles are inhaled. Antigorite forms good crystals but the layers curve about *y* with periodic reversal and result in superstructures with large *a* parameters (e.g. ~43 Å). The above features are evident from X-ray and electron diffraction and electron microscopy. Of the three varieties, antigorite has slightly higher refractive indices, and in its chemical composition a lower ratio of Mg to Si. Differences in parageneses are not clear-cut but lizardite appears to result in low-, chrysotile in medium- and antigorite in high-temperature hydrothermal conditions.

Differences from other layered silicates.

The ~7.2 Å interlayer spacing contrasts with ~10 Å and ~14 Å for micas and chlorites, respectively. Kaolinite has an ~7 Å interlayer spacing but is dioctahedral. Micas and most chlorites have higher refractive indices.

Downloaded from https://pubs.geoscienceworld.org/books/chapter-pdf/3760332/9780903056434_ch51.pdf
by guest

Structure

Although some of the serpentine minerals are fibrous, the structures of all of them are of a layered type similar to that found in the kaolinite group. Serpentines differ from the latter minerals, however, in being trioctahedral, and in the mode of stacking of their fundamental layers. One part of the serpentine layer is a pseudo-hexagonal network of linked SiO_4 tetrahedra, with approximate parameters a 5.3 Å, b 9.2 Å. All tetrahedra in the sheet point one way; joined to the sheet is a brucite-like layer in which, on one side only, two out of every three hydroxyls are replaced by apical oxygens of the SiO_4 tetrahedra (Fig. 151). The perpendicular repeat distance between composite sheets of this type is approximately 7.3 Å. A perspective view of the structure of serpentine (lizardite) is illustrated in Fig. 152.

The lateral dimensions of the ideal octahedral and tetrahedral components of a serpentine layer do not match well, the former being similar to brucite, 5.4×9.3 Å, and the latter comparable to tridymite, 5.0×8.7 Å, and the various structures and textures of the serpentines correspond with different ways of overcoming this mismatch. Moreover, as with other layered minerals, various regular and disordered stacking arrangements may occur, giving rise to additional polymorphs.

There are four ways in which better matching of the layer components can be achieved.

(a) By substitution of larger ions for Si and/or smaller ions for Mg, the most common substituent being Al in both cases.

(b) By distortion of the ideal octahedral and/or tetrahedral networks leading to a strained configuration which could perhaps be stabilized by strong interlayer hydrogen bonding.

(c) Relief of the strains suggested above by periodic discontinuity, e.g. omission of tetrahedra, or change of layer orientation (a non-serpentine mineral may result).

(d) By curvature of the composite sheet with its tetrahedral component on the inside of the curve.

Combinations of the above methods may occur.

Much of the matrix material containing veins of chrysotile is lizardite. This is usually extremely fine-grained but electron microscopy shows it to have platy morphology. The unit cell is usually effectively single-layered, and though trigonal it can be described by an orthohexagonal cell ($b \sim\sqrt{3}a$); some specimens have a mixture of layers in different orientations. The stable existence of this simple ideal flat-layer serpentine is favoured by the presence in many lizardites of some Al and Fe^{3+} substituting for Si and Mg.

The fibrous nature of chrysotile is explained by its consisting of layers curved cylindrically or spirally usually about the x axis (in the rare polytype parachrysotile, the axis of curvature is y). The fundamental fibrils have various diameters but the average outer and inner diameters are about 250 Å and 75 Å, respectively (see Fig. 153a).

Electron-microscopic studies have revealed another apparently fibrous morphology, that of polygonal serpentine. Here again the fibre elongation is along x

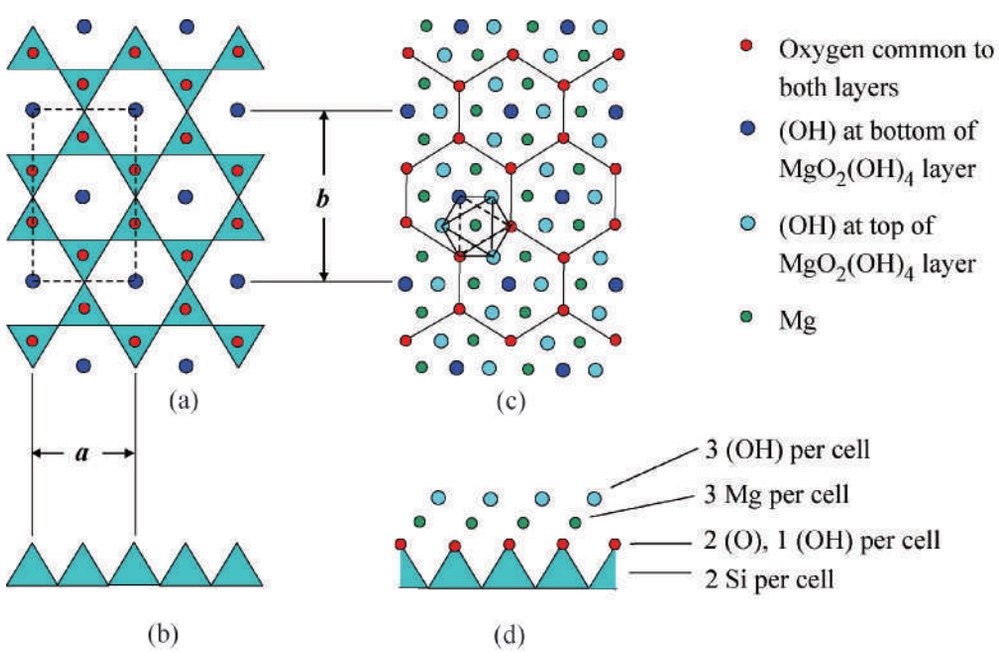


Fig. 151. Structure of serpentine layer. (a) Tetrahedral Si_2O_5 network in plan. (b) Tetrahedral network as viewed along y axis. (c) Tri-octahedral component of serpentine layer (plan). (d) Serpentine layer as viewed along y axis. In (a), (b) and (d), Si atoms within tetrahedra are not shown (after Zussman, J., 1954, *Mineral. Mag.*, **30**, 498–512. Fig. produced by M.D. Welch).

Downloaded from https://pubs.geoscienceworld.org/books/chapter-pdf/3760332/9780903056434_ch51.pdf
by guest

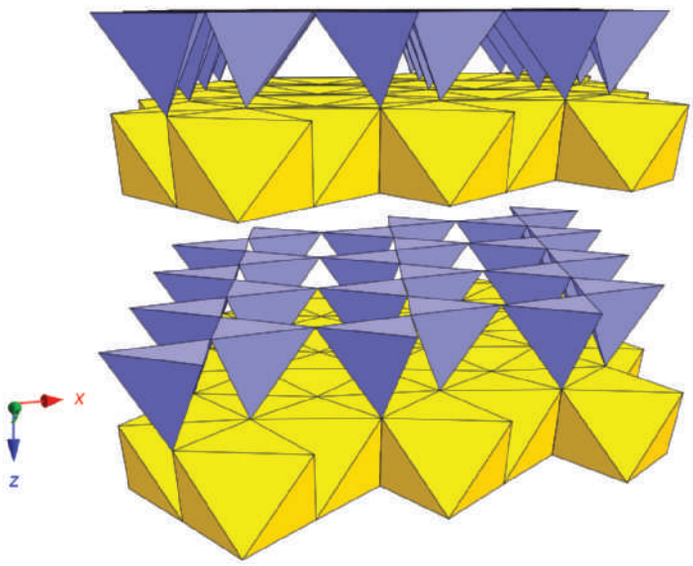


Fig. 152. A perspective view of the structure of lizardite. Yellow: Mg–(O,OH) octahedra; blue: Si–O tetrahedra. Hydrogen bonding between layers (not shown in this figure) can play an important part in the various configurations (cylindrical, polygonal, spherical, corrugated) adopted by serpentine minerals (CrystalMaker image).

but transverse sections show that flat lath-like layers are stacked to form polygonal sectors. Most commonly there are either 15 or 30 sectors (Fig. 153b) and they may or may not surround a core of cylindrical chrysotile. The angular discontinuity between neighbouring sectors is structurally controlled and it is another way of overcoming the problem of mismatching components. Yet another configuration of lizardite layers, in polyhedral spheroids up to 1 μm in diameter, has recently been reported.

Antigorite is another serpentine mineral which is structurally distinct. The structure has *b* and (001) spacings similar to those of lizardite and chrysotile but the *a* cell parameter ranges mostly between 33 and 51 Å. The large *a* repeat is explained by the curvature of serpentine layers about *y* and their inversion to form a corrugated sheet structure with periodicity *a* (Fig. 154). Alternative models have been proposed for the precise nature of the structure at the lines of inversion. Different values of *a* for different antigorites result when different discrete numbers of tetrahedra and/or octahedra occur in the 'wavelength' of the structure. Higher equilibration temperatures have been shown to produce slightly shorter values of *a*.

Chemistry

The chemistry of the serpentine group as a whole is relatively simple in that most natural specimens deviate little from the ideal composition $H_4Mg_3Si_2O_9$. The principal replacements are of silicon by aluminium,

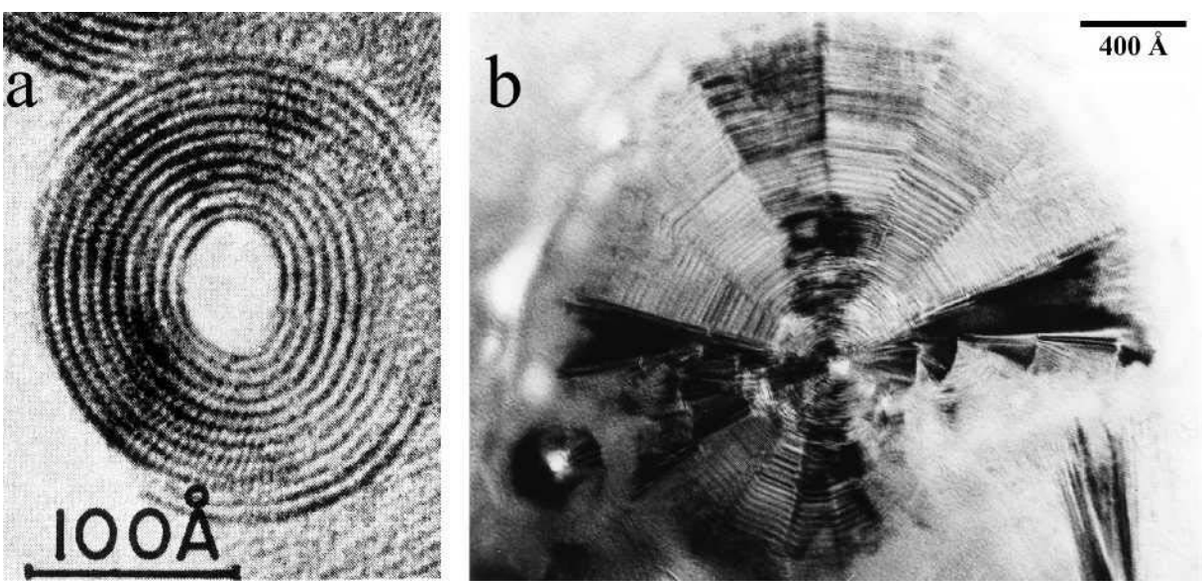


Fig. 153. (a) Transmission electron micrograph (TEM) of cross-section of a fibril of chrysotile. The structural layers are seen to be arranged in concentric cylindrical fashion. (Yada, K., 1971, *Acta Cryst.*, **A27**, 659–64). (b) TEM of cross-section of a fibril of polygonal serpentine with lizardite layers in 15 (24°) sectors. (Cressey, B.A. *et al*., 1994, *Can. Min.*, **32**, 257–70).

Downloaded from https://pubs.geoscienceworld.org/books/chapter-pdf/3760332/9780903056434_ch51.pdf
by guest

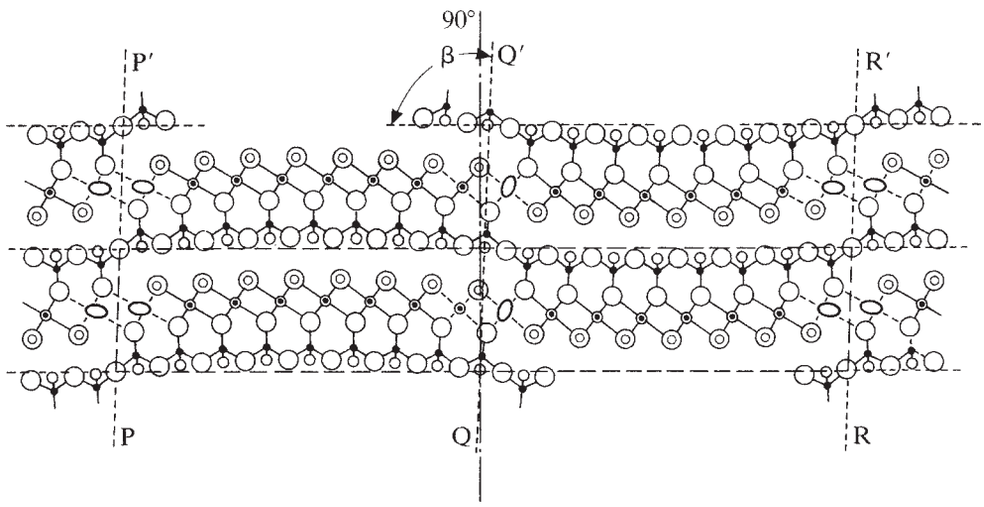


Fig. 154. Structure of antigorite as viewed along *y* axis. The curved layers (radius of curvature 75 Å) reverse polarity at PP′, RR′ and near QQ′ (after Kunze, G., 1956, *Z. Krist.*, **108**, 82–107). The number of tetrahedra within the large *a* cell repeat distance is usually denoted by *m*; in this instance a = 40.6 Å and m = 17.

and of magnesium by aluminium, ferrous iron and ferric iron (Table 29). With regard to Al substitution there appears to be a complete solid solution between serpentine and amesite, $Mg_2Al[AlSiO_5](OH)_4$. The point at which the misfit between octahedral and tetrahedral components is zero is calculated to be near $Al_{1.2}$. Beyond this the tetrahedral layer becomes larger than the octahedral layer and this mismatch can be resolved by tetrahedral rotations as in kaolinite.

The substitution of the larger Fe^{2+} for Mg worsens the structural mismatch so that this substitution is very limited in serpentine. When serpentines are formed in peridotitic rocks, most of the iron present in the original olivine or pyroxene is incorporated in magnetite (very rarely hematite), although in many cases some is taken up by lizardite

That nickel can adopt the role of magnesium is shown by the synthesis of a pure nickel serpentine and by the existence of pecoraite, a naturally occurring nickel serpentine, but most magnesium serpentines contain little nickel (average ~0.25% NiO).

Of the serpentine minerals, chrysotile shows least deviation from the ideal composition, containing very little Al or Fe. Antigorites have a slightly but significantly lower Mg/Si ratio as some octahedra are omitted at layer inversions; there is also a small deficiency in (OH).

On heating serpentine in air, olivine (forsterite) is formed at about 600ºC:

$$2\,Mg_3Si_2O_5(OH)_4 \rightarrow 3\,Mg_2SiO_4 + SiO_2 + 4\,H_2O$$

The DTA curves for serpentines show an endothermic peak at about 700–800ºC corresponding with the expulsion of 'structural' water, and this is followed usually at about 800–820ºC by an exothermic peak related to the formation of olivine. A weak, broad, low-temperature endothermic peak is shown by some serpentines, corresponding with the expulsion of water which is held on the surface of fine-grained material. In chemical analyses of chrysotile some water of this kind may be registered erroneously as H_2O+ since prolonged heating at 110ºC is required to remove it completely.

Clinochrysotile is readily synthesized hydrothermally from a mixture of MgO, SiO_2 and water at temperatures below its decomposition to talc + forsterite + water.

The reaction curve:

$$\underset{\text{brucite}}{Mg(OH)_2} + \underset{\text{serpentine}}{Mg_3Si_2O_5(OH)_4} \rightarrow 2\,\underset{\text{forsterite}}{Mg_2SiO_4} + 3\,H_2O$$

plots at ~350ºC and 560ºC at 0.1 and 3 GPa, respectively.

In reactions in which P_{H_2O} is reduced (e.g. by adding CO_2, or $P_{H_2O} < P_{Total}$) the dehydration equilibria move to lower temperatures. It should also be noted that the different kinds of serpentine can be formed and can persist metastably.

Laboratory studies in the system $MgO–SiO_2–H_2O$ have defined the *P–T* fields for the reactions:

antigorite → talc + forsterite + water (1)
antigorite → forsterite + clinoenstatite + water (2)

For reaction 1 the relationship is approximately linear with a positive slope from ~0.2 GPa, 500ºC to ~1.4 GPa, 640ºC, and for reaction 2 the relationship is a curve with a negative slope from ~2 GPa, 640ºC, to ~4 GPa, 590ºC and ~5 GPa, 520ºC. The addition of Al into antigorite raises its stability limit to significantly higher pressures and temperatures. It has been suggested that antigorite serpentinite may play an important role in taking appreciable water deep into the Earth's mantle and releasing it into a subducting wedge to induce partial melting.

Aluminium-free lizardites probably have hydrothermal stability relationships similar to those of chrysotile, but increasing Al increases the breakdown temperature. With appreciable Al, chlorite rather than lizardite is the more stable phase.

Downloaded from https://pubs.geoscienceworld.org/books/chapter-pdf/3760332/9780903056434_ch51.pdf
by guest

Table 29. Serpentine analyses.

	1	2	3	4
SiO_2	41.83	41.25	40.76	43.60
TiO_2	0.02	0.02	–	0.01
$A1_2O_3$	0.30	0.54	2.22	1.03
Fe_2O_3	1.29	1.32	–	0.90
Cr_2O_3	–	–	0.29	0.02
FeO	0.08	0.09	2.18	0.81
NiO	–	–	0.18	0.16
MnO	0.04	0.07	0.05	0.04
MgO	41.39	41.84	40.88	41.00
CaO	tr.	0.02	–	0.05
Na_2O	–	–	–	0.01
K_2O	–	–	–	0.03
H_2O+	13.66	13.68	11.69	12.18
H_2O-	1.57	0.97	–	0.08
Total	100.18	99.80	98.45	99.92
Numbers of ions: 1, 2, 3 on the basis of 9(O,OH). 4 on basis $\Sigma Z = 2$[a]				
Si	1.950	1.924	1.957	1.946
Al	–	0.030	0.043	0.054
ΣZ	1.95	1.95	2.00	2.000
Al	0.016	–	0.082	–
Fe^{3+}	0.045	0.046	–	0.030
Cr	0.003	–	0.011	–
Fe^{2+}	0.001	0.004	0.087	0.030
Ni	–	–	0.005	0.005
Mn	0.001	0.002	–	0.001
Mg	2.877	2.904	2.922	2.728
Ca	–	0.001	–	0.002
Na	–	–	–	0.001
K	–	–	–	0.001
ΣY	2.94	2.96	3.11	2.80
OH	4.25	4.25	3.74	3.63

1 Chrysotile, cross-fibre vein (metamorphosed limestone occurrence), Transvaal (Brindley, G.W. & Zussman, J., 1957, *Amer. Min.*, **42**, 461–74).

2 Lizardite, matrix containing chrysotile vein of analysis no. 1, Transvaal (Deer, W.A., Howie, R.A. & Zussman, J., 1962, *Rock-Forming Minerals*, *vol.* 3, Longman).

3 Lizardite-1*T*, completely serpentinized harzburgite, Cassiar, north-central, British Columbia (O'Hanley & Dyar, 1993, *Amer. Min.*, **78**, 391–404).

4 Antigorite, vicinity of Caracas, Venezuela (Hess, H.H., Smith, R.J. & Dengo, G., 1952, *Amer. Min.*, **37**, 68–75).

[a] The (O,OH) content pfu of antigorite is lower than in the idealized serpentine structure and varies with the 'wavelength' of its corrugated layers. Formulae are therefore more conveniently expressed and compared when based on 2 Si, or 2 (Si,$^{[4]}$Al) as in the present case, rather than 9 (O,OH).

Optical and physical properties

The fine-grained nature of most serpentine minerals makes a complete optical description impossible except for certain specimens. Antigorites are, however, commonly found as reasonably large euhedral crystals which allow determination of all three refractive indices, optic axial angle and optic orientation. Lizardites have a mean refractive index between 1.54 and 1.55, whereas the plate-like grains of antigorite in general have higher refractive indices. The ranges of refractive indices for antigorites and lizardites are barely separated, however, so that distinction cannot be made by this method. Refractive indices increase with Ni content.

Chrysotile fibres yield different values of refractive index for the directions parallel and perpendicular to their length, and most have positive elongation. A true interpretation of the optical properties of chrysotile may be complicated by the rolling of the fundamental serpentine layers, by the random orientation of fibrils about the fibre axis, and also by the phenomenon of form birefringence consequent upon the extremely small particle size.

The serpentine minerals occur with a wide variety of textures and optical appearances. Although these are recognizable, they can be correctly interpreted only by use of microbeam X-ray diffraction, electron optical methods and micro-Raman spectroscopy. Many textures (e.g. 'mesh' and 'hour-glass', Fig. 155) are pseudomorphous after olivine and 'bastite' after pyroxene, amphibole and layered silicates. Some of the components of those textures are chrysotile, which is optically 'length-slow', but other material, which is apparently fibrous and 'length-fast', consists of lizardite platelets stacked perpendicular to the apparent fibre axis. Non-pseudomorphous textures are composed mainly of interpenetrating blades of antigorite.

Chrysotile asbestos was widely mined and used industrially for its thermal insulation properties, but this has been banned in most countries after recognition that inhalation of its particles constitutes an extremely serious health hazard (see p. 216).

Distinguishing features

Antigorites may be distinguished from micas as the latter have higher birefringence. Most chlorites have higher refractive indices, and some are noticeably pleochroic. Serpentine asbestos fibres have γ less than 1.58, whereas fibres of amphibole asbestos have γ greater than 1.58. When ground in a mortar, amphibole fibres generally rub to a powder, but chrysotile fibres form a matted aggregate which can only be powdered with great difficulty. Serpentine fibres become stained with a solution of iodine in glycerol, whereas amphibole fibres do not.

Paragenesis

The serpentine minerals form principally by retrograde hydrothermal alteration of ultrabasic rocks, e.g. dunites, peridotites or pyroxenites. Serpentinization may involve reactions such as:

$$\underset{\text{forsterite}}{2\,Mg_2SiO_4} + 3\,H_2O \rightarrow \underset{\text{serpentine}}{Mg_3Si_2O_5(OH)_4}$$

Downloaded from https://pubs.geoscienceworld.org/books/chapter-pdf/3760332/9780903056434_ch51.pdf
by guest

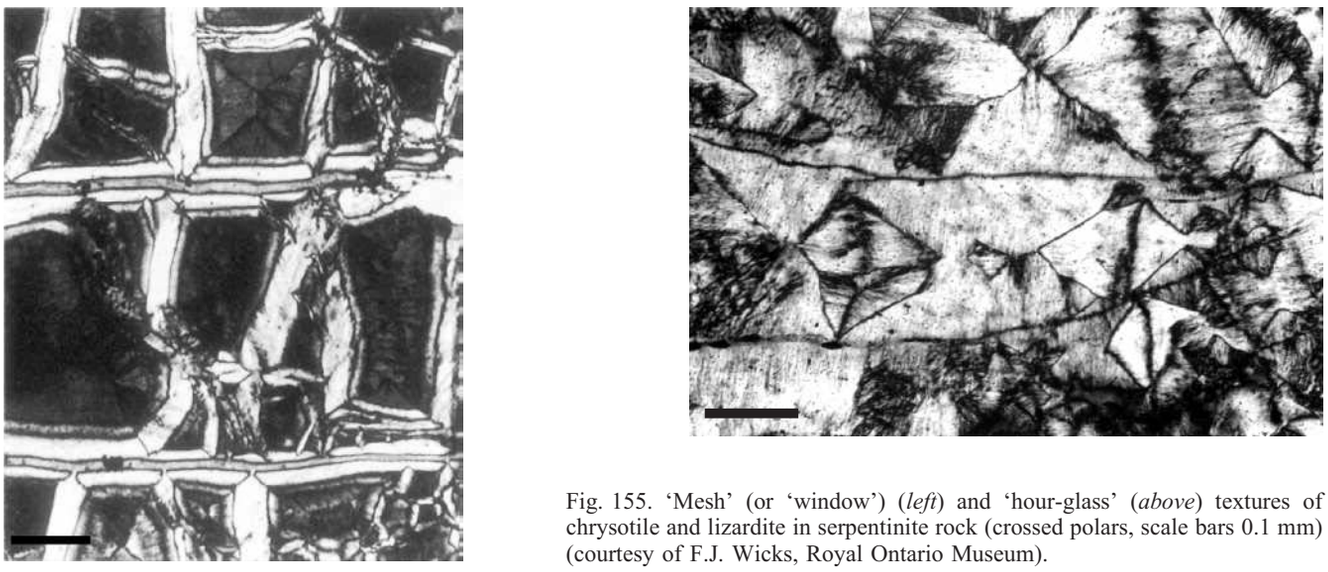


Fig. 155. 'Mesh' (or 'window') (*left*) and 'hour-glass' (*above*) textures of chrysotile and lizardite in serpentinite rock (crossed polars, scale bars 0.1 mm) (courtesy of F.J. Wicks, Royal Ontario Museum).

or

$$3\,Mg_2SiO_4 + 4\,H_2O + SiO_2 \rightarrow 2\,Mg_3Si_2O_5(OH)_4$$

The most common retrograde product is lizardite in pseudomorphic textures, with or without brucite and magnetite, but antigorite can also occur in this manner. The most common prograde reaction results in antigorite in massive serpentinite, with or without magnetite, but at a lower temperature a mixture of chrysotile and lizardite may result. The latter conditions are commonly associated with the formation of asbestos. In a typical asbestos deposit (e.g. at Cassiar, British Columbia) the varieties of serpentine occurring with increasing grade follow the sequence: pseudomorphous retrograde lizardite → lizardite + chrysotile → chrysotile + antigorite → antigorite. The serpentinization reaction is typically accompanied by volume expansion, which is manifested on the outcrop scale by "kernels" of unaltered peridotite, surrounded by serpentinite with expansion cracks filled by chrysotile; and in some thin sections by cracks radiating from relict olivines.

The reaction is also accompanied in many cases by the precipitation of Ni, Co, Fe alloy minerals. Chrysotile slip fibres are sometimes converted to polygonal serpentine, lizardite and a splintery form of antigorite referred to as picrolite.

The sequence of events which leads to the formation of chrysotile asbestos fibre veins is not known with certainty although various possibilities have been discussed. The fibre may form at the same time as the matrix serpentine rock from the same parent material, or it may form later. In the latter case the fibres may replace existing matrix material, perhaps starting at a fissure and growing inwards, or they may grow in pre-existing fissures from solutions which permeate the rock. Studies of oxygen isotopes in vein and wall-rock serpentine can help elucidate the process and the provenance of the water involved. Large deposits of chrysotile asbestos derived from peridotite occur in the Thetford area of Quebec and in South Africa, Russia and elsewhere. Certain serpentines of the Transvaal are examples, however, of a different paragenesis and are found in metamorphosed limestones or dolomites (e.g. Table 29, analysis 1). In the Transvaal, serpentinized dolomitic rocks are associated with diabase sills and, in these circumstances, veins of chrysotile, parallel to the contact, are free from magnetite and other impurities except for small amounts of talc. The siliceous dolomite is transformed to forsterite which is subsequently serpentinized.

The natural occurrence of a carbonated serpentinite (known as 'listwanite') formed by the reactions:

$$\text{serpentine} + \text{olivine} + \text{brucite} + CO_2 \rightarrow \text{serpentine} + \text{magnesite} \rightarrow \text{magnesite} + \text{talc} \rightarrow \text{magnesite} + \text{quartz}$$

has led to the suggestion, in the context of countering global warming, that CO_2 could be sequestrated by *in situ* reaction with serpentinite.

Amesite, $(Mg_2Al)(SiAl)O_5(OH)_4$, occurs as a metamorphic mineral in environments rich in Al, e.g. the emery deposits of Chester, Massachusetts, USA. Cronstedtite occurs in low-temperature hydrothermal sulphide veins and has been reported in carbonaceous chondrites. Berthierine has long been reported in sedimentary iron formations and in oolitic ironstones, but it was previously termed chamosite, a name now restricted to the true chlorite species. Berthierine is increasingly recognized as a recent clay mineral at shallow depth in certain marine sediments.

Further reading

Andreani, M., Grauby, U., Barronet, A. and Muñoz, M. (2008) Occurrence, composition and growth of polyhedral serpentine. *European Journal of Mineralogy*, **20**, 159–171.

Bromiley, G.D. and Pawley, A.R. (2003) The stability of antigorite in the systems $MgO–SiO_2–H_2O$ (MSH) and $MgO–Al_2O_3–$

Downloaded from https://pubs.geoscienceworld.org/books/chapter-pdf/3760332/9780903056434_ch51.pdf
by guest

SiO_2–H_2O (MASH): the effects of Al^{3+} substitution on high-pressure stability. *American Mineralogist*, **88**, 99–108.

Cressey, G. Cressey, B.A. and Wicks, F.J. (2008) Polyhedral serpentine: a spherical analogue of polygonal serpentine? *Mineralogical Magazine*, **72**, 1229–1242.

Cressey, G., Cressey, B., Wicks, F.J. and Yada, K. (2010) A disc with fivefold symmetry: the proposed fundamental seed structure for the formation of chrysotile asbestos fibres, polygonal serpentine fibres and polyhedral lizardite spheres. *Mineralogical Magazine*, **74**, 29–37.

Evans, B.W. (2004) The serpentinite multisystem revisited: Chrysotile is metastable. *International Geology Review*, **46**, 479–506.

Hansen, L.D., Dipple, G.M., Gordon, T.M. and Kellett, D.A. (2005) Carbonated serpentinite (listwanite) at Atlin, British Columbia: A geological analogue to carbon dioxide sequestration. *The Canadian Mineralogist*, **43**, 225–239.

Mellini, M., Trommsdorff, V. and Compagnoni, R. (1987) Antigorite polysomatism: Behavior during progressive metamorphism. *Contributions to Mineralogy and Petrology*, **97**, 147–155.

O'Hanley, D.S. (1996) *Serpentinites: Records of Tectonic and Petrologic History*. Oxford University Press, Oxford, UK, 277 pp.

O'Hanley, D.S., Chernovsky, J.V. and Wicks, F.J. (1989) The stability of lizardite and chrysotile. *The Canadian Mineralogist*, **27**, 483–493.

Rumori, C., Mellini, M. and Viti, C. (2004) Oriented, non-topotactic olivine serpentine replacement in mesh-textured serpentinized peridotites. *European Journal of Mineralogy*, **16**, 731–741.

Wicks, F.J. and O'Hanley, D.S. (1988) Serpentine minerals: structure and petrology. Pp. 91–167 in: *Hydrous Phyllosilicates (Exclusive of Micas)* (S.W. Bailey, editor). Reviews in Mineralogy, **19**, Mineralogical Society of America, Washington, D.C.

Yada, K. (1979) Microstructures of chrysotile and antigorite by high resolution electron microscopy. *The Canadian Mineralogist*, **17**, 679–691.

Downloaded from https://pubs.geoscienceworld.org/books/chapter-pdf/3760332/9780903056434_ch51.pdf
by guest

Clay Minerals

Introduction

For some purposes the word 'clay', commonly in the term 'clay fraction', is used purely to denote that part of a particulate assemblage with average grain sizes less than about 2 (some say 4) μm, regardless of chemical or other features. In mineralogical usage, the constituents of clays may be assigned to two groups, those called clay minerals, mostly layered silicates, which by their nature give the clay body its plasticity when wet and propensity to harden when dried and fired, and others which are accessory 'non-clay minerals'. The clay minerals have a number of characteristics in common. Their structures are, with a few minor exceptions, based on composite layers built from components with tetrahedrally and octahedrally coordinated cations. Most of them occur as platy particles in fine-grained aggregates which when mixed with water yield materials which have varying degrees of plasticity. Chemically, all are hydrous silicates (principally of aluminium or magnesium) which, on heating, lose adsorbed and constitutional water, and at high temperatures yield refractory materials. Important differences among the clay minerals, however, lead to their subdivision into several main groups. The four important layered clay mineral groups are kaolinites, illites, smectites and vermiculites. These have characteristic basal spacings of approximately 7 Å, 10 Å, 15 Å and 14.5 Å, respectively, but for some categories the layer separation is variable since swelling may occur through the intercalation of water or organic liquids, and shrinkage may result from dehydration. The clay minerals attapulgite and sepiolite have columnar structural features and are less common than the layered clay minerals. Clay mineral particles can have variable degrees of long-range order (crystallinity); they can be platy or fibrous and, although sub-millimetric in size, vary from nanoparticles to grains observable under a petrological microscope.

The composition varies according to the extent of replacement of Si, Al and Mg by other cations, the nature and quantity of interlayer cations, and the water content (see Table 30). The clay minerals vary in their dehydration and breakdown characteristics and in their decomposition products, and they also differ in their cation exchange properties according to the nature of their interlayer cations and residual surface charges. Their uses are many, some, for example, being particularly suitable as components of drilling muds, some for catalysts in petroleum processing, some in paper manufacture, and some for ceramic and refractory ware. The clay minerals are the main constituents of one class of sediments (consequently called argillaceous) which on accumulation and compaction yield shales or mudstones. Whether in sedimentary deposits or not, the clays are usually products of either weathering or hydrothermal alteration, different clays resulting according to physicochemical conditions and the nature of parent materials, e.g. feldspars, micas, volcanic glasses, or ferromagnesian minerals.

Clay minerals play an important role in the textures and properties of soils.

The principal clay minerals are:

(1) Kaolinite group, including kaolinite, dickite, nacrite and halloysite.
(2) Illite group, including illite and brammallite.
(3) Smectite group, including montmorillonite, beidellite, nontronite, hectorite, saponite and sauconite.
(4) Vermiculite.

Table 31 lists very briefly some of the important characteristics of the principal clay mineral groups.

Whereas the text deals with each clay mineral separately, clay specimens containing layers of more than one clay mineral group ('mixed layers') e.g. illite/smectite, are not uncommon. The component layers can occur in a regularly repeating sequence or can show varying degrees of disorder. Non-clay and clay mineral components may also be interstratified as, for example, in mica/vermiculite.

A fifth group, which includes palygorskite and sepiolite, will not be discussed at length here. Palygorskite and sepiolite are finely fibrous minerals which nevertheless have much in common with the layered clay minerals. Their structures have continuous $(Si,Al)_2O_5$ sheets, but ribbons rather than sheets of (Al,Mg,Fe) octahedra leaving channels which can accommodate water and organic molecules. They have similar uses to those of other clays (absorbent, catalytic, thixotropic). They occur in a wide range of environments (marine and lacustrine sediments, soils, palaeosols and calcretes) but only rarely in large deposits (e.g. Georgia and Florida, USA; Valecas, Spain). Fine-grained chlorites and glauconites also occur as clay minerals in sedimentary rocks but these are dealt with elsewhere in the present text (p. 208 and p. 188), and berthierine is referred to under serpentine and chlorite.

Downloaded from https://pubs.geoscienceworld.org/books/chapter-pdf/3760814/9780903056434_ch52.pdf
by guest

Table 30. Analyses of clay minerals.

	1	2	3	4	5	6	7	8
SiO_2	46.20	44.46	51.25	56.59	55.80	51.46	50.25	34.04
TiO_2	0.09	0.15	0.17	0.06	0.26	0.05	0.03	–
Al_2O_3	39.20	36.58	23.53	20.06	28.60	2.20	4.44	15.37
Fe_2O_3	0.23	0.36	2.02	3.19	0.41	24.70	0.50	8.01
FeO	–	0.07	0.33	–	–	–	–	–
MnO	–	–	–	0.03	–	0.03	0.02	–
MgO	0.07	0.18	3.32	3.10	2.03	3.27	23.81	22.58
CaO	0.06	0.19	0.59	0.68	2.23	1.45	1.70	0.00
Na_2O	0.09	0.01	0.05	2.17	0.09	1.06	0.76	0.00
K_2O	0.21	0.51	7.61	0.45	0.48	0.24	0.10	0.00
H_2O+	13.80	13.38	5.87	13.67	9.70	15.34	7.25	19.93
H_2O-	–	4.05	5.26	–	–	–	10.76	–
Total	99.95	100.12	100.02	100.00	99.60	99.80	99.69	99.93
Numbers of ions on the basis of 18 (O, OH) (anals 1 and 2); 22 O equivalents, ignoring H_2O+ (anals 3–8)								
Si	3.981	4.01	7.163	7.776	7.271	7.950	7.513	Si 5.44
Al	0.019 } 4.00	– } 4.01	0.837 } 8.00	0.224 } 8.00	0.729 } 8.00	0.050 } 8.00	0.487 } 8.00	Al 2.56 } 8.00
Al	3.962	3.89	3.040	3.026	3.664	0.351	0.296	Al 0.32
Ti	0.006	0.01	0.018	0.006	0.025	0.006	0.003	Ti –
Fe^{3+}	0.015 } 3.99	0.02 } 3.95	0.212 } 4.00	0.330 } 4.00	0.040 } 3.99	2.872 } 3.99	0.056 } 5.67[a]	Fe^{3+} 0.96 } 6.00
Fe^{2+}	–	0.01	0.039	–	–	–	–	Fe^{2+} –
Mn	–	–	–	0.003	–	0.004	0.003	Mn –
Mg	0.009	0.02	0.692	0.635	0.394	0.753	5.306	Mg 4.72
Ca	0.006	0.02	0.088	0.100	0.311	0.240	0.272	Mg 0.64
Na	0.015	0.00	0.014 } 1.46	0.578 } 0.76	0.023 } 0.41	0.318 } 0.60	0.220 } 0.51	Ca – } 0.64
K	0.023	0.06	1.357	0.079	0.080	0.047	0.019	K –
OH	7.980	8.04	4.000	4.000	4.000	4.000	4.000	Na –
								H_2O 8.64
								OH 4.00

1 Kaolinite, St Austell, Cornwall, UK; Contains 1–2% mica (Jepson, W.B. & Rowse, J.B., 1975, *Clays Clay Min*., **23**, 310–17).
2 White halloysite, Bedford, Indiana, USA (Kerr, P.F., Hamilton, P.K. & Pill, R.J., 1950, Reference clay minerals. *Amer. Petroleum Inst. Res. Proj*., **49**, Columbia Univ., New York. Includes P_2O_5 0.18).
3 Illite, Aymestry Limestone, Showers End, Worcs., UK (Środoń, J. & Karlinger, M.R., 1986, *Clays Clay Min*., **34**, 368–78. Includes P_2O_5 0.02. Contains 7% smectite layers).
4 Montmorillonite, Creme, Recoaro Terme, Vicenza, Italy (Brigatti, M.F., 1983, *Clay Min*., **18**, 177–86).
5 Beidellite, Castle Mountains, California, USA (Heystek, H., 1963, *Clays Clay Min*., **11**, 158–68).
6 Nontronite, Andreasberg, Germany (Brigatti, M.F., 1983, *Clay Min*., **18**, 177–86).
7 Saponite, Ballarat, Inyo Co., California, USA (Post, J.G., 1984, *Clays Clay Min*., **32**, 147–53. Includes NiO 0.07).
8 Vermiculite, Kenya (Mathieson, A.McL. & Walker, G.F., 1954, *Amer. Min*., **39**, 231–55).

[a] Includes 0.01 Ni

Further reading

Bailey, S.W. (Editor) (1988) *Hydrous Phyllosilicates (Exclusive of Micas)*. Reviews in Mineralogy, **19**, Mineralogical Society of America, Washington, D.C., 725 pp.

Brindley, G.W. and Brown, G. (Editors) (1980) *Crystal Structures of Clay Minerals and their X-ray Identification.* Monograph **5**, Mineralogical Society, London, 495 pp.

Guggenheim, S. and Martin, R.T. (1995) Definition of clay and clay minerals: joint report of the AIPEA nomenclature and CMS nomenclature committees. *Clays and Clay Minerals*, **43**, 255–256.

Moore, D.M. and Reynolds, R.C. (1990) *X-ray Diffraction and the Identification and Analysis of Clay Minerals.* Oxford University Press, 332 pp.

Newman, A.C.D. (Editor) (1987) *Chemistry of Clays and Clay Minerals*, Monograph **6**, Mineralogical Society, London, 480 pp.

Wilson, M.J. (2013) *Clay Minerals*. Rock-Forming Minerals, 2nd Ed. **3C**, (W.A. Deer, R.A. Howie and J. Zussman, editors), Geological Society, London. ~700 pp.

Downloaded from https://pubs.geoscienceworld.org/books/chapter-pdf/3760814/9780903056434_ch52.pdf
by guest

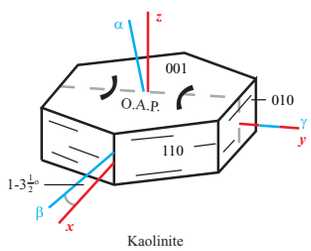
Downloaded from https://pubs.geoscienceworld.org/books/chapter-pdf/3760814/9780903056434_ch52.pdf
by guest

Table 31. Summary of the principal characteristics of the clay mineral groups.

	Kaolinites	Illites	Smectites	Vermiculites
Structure type:	1:1 tetrahedral and octahedral components	2:1	2:1	2:1
Octahedral component:	Dioctahedral	Mostly di-octahedral	Dioctahedral or trioctahedral	Mostly trioctahedral
Principal interlayer cations:	Nil	K	Ca, Na	Mg
Interlayer water:	Only in halloysite (one layer water mols)	Variable	Ca, two layers; Na, one layer water mols	One or two layers
Basal spacing:	7.1 Å (10 Å in halloysite)	10 Å	Variable, most ~ 15 Å (for Ca)	Variable; 14.4 Å when fully hydrated
Glycol:	Taken up by halloysite only	No effect	Takes two layers glycol, 17 Å	Takes one layer glycol, 14 Å
Chemical formula:	$Al_4Si_4O_{10}(OH)_8$, little variation	$K_{1.0-1.5}Al_4(Si,Al)_8O_{20}(OH)_4$	$M^+_{0.7}(Y^{3+},Y^{2+})_{4-6}(Si,Al)_8O_{20}(OH)_4nH_2O$	$(Y^{2+},Y^{3+})_6(Si,Al)_8O_{20}(OH)_48H_2O$
Acids:	Kaolinite scarcely soluble in dil. acids	Not readily attacked	Attacked	Readily attacked
Heating 200ºC	Halloysite collapses to ~7.4 Å; others unchanged	No marked change	Collapse to approx. 10 Å	Exfoliation; shrinkage of layer spacing
650ºC:	Kaolinite → metakaolinite (7 Å) Dickite → metadickite strong (14 Å)	10 Å	9.6–10 Å	Collapse to 9 Å
Optics				
α	1.55–1.56	1.54–1.57	1.48–1.61	1.52–1.57
γ	1.56–1.57	1.57–1.61	1.50–1.64	1.53–1.58
δ	~0.006	~0.03	0.01–0.04	0.02–0.03
$2V_\alpha$	24–50º	<10º	Variable	<18º
Paragenesis:	Alteration of acid rocks, feldspars. Acidic conditions.	Alteration of micas, feldspars, etc. Alkaline conditions. High Al and K concentrations.	Alteration of basic rocks, or volcanic material. Alkaline conditions. Availability of Mg and Ca; deficiency of K	Alteration of biotite flakes or of volcanic material, chlorites, hornblende, etc.

Triclinic or Monoclinic (−)

α	1.553−1.565
β	1.559−1.569
γ	1.560−1.570
δ	~0.006
$2V_\alpha$	24−50º
Orientation	β:*x*=1−3½º, γ = *y*; O.A.P. ⊥ (010)
D (g/cm^3)	2.61−2.68
H	2−2½
Cleavage	{001} perfect
Twinning	Rare
Colour	White, sometimes with reddish, brownish or bluish tints; colourless in thin section
Pleochroism	Very slight; least absorption for vibration direction perpendicular to cleavage
Unit cell	*a* ~ 5.15 Å, *b* ~ 8.95 Å, *c* ~ 7.4 Å, α ~ 91.8º, β ~ 104.8º, γ ~ 90º Z = 1; space group *C*1 *Halloysite-10Å*: *c* ~ 10.25 Å, β 99.7º *Halloysite-7Å*: *c* ~ 14.9 Å, β 102º



Kaolinite

Kaolinite is the most important member of the kaolinite group; dickite and nacrite are rarer polymorphs. The minerals halloysite-10Å and halloysite-7Å are chemically similar to the kaolinites and have compositions with and without interlayer water, respectively. Kaolinite is widely used in the manufacture of bricks and ceramics and also as a coating or filler for papers, paints and plastics.

Structure

The fundamental unit of the kaolinite structure is an extended layer which can be regarded as having two constituents. A layer of composition $(Si_4O_{10})^{4-}$ is formed by the linkage of SiO_4 tetrahedra in a hexagonal array, the bases of tetrahedra being approximately coplanar and their vertices all pointing in one direction. The apical oxygens, together with some additional $(OH)^-$ ions located under the centres of hexagons, form the upper plane of a gibbsite-type layer of Al−(O,OH) octahedra with composition $(OH)_2O_4$−Al_4−$(OH)_6$. This combination of a sheet of tetrahedra with one of octahedra is sometimes referred to as a T−O or 1:1 layer. A low angle perspective view of this composite $Al_4Si_4O_{10}(OH)_8$ layer is shown in Fig. 156. Only two out of each set of three available octahedral sites are occupied by Al ions, and the third is vacant.

Successive layers of kaolinite are superimposed so that in general oxygens at the bases of tetrahedra in one layer are hydrogen-bonded to outer (OH) ions of its neighbour, resulting in a single-layered triclinic unit cell. Stacking defects are common, involving translations of layers by ±*nb*/3 or rotations of ±120º; the latter may also be regarded as variations according to which of the three octahedral sites is vacant. The degree of order in the structure of kaolinites affects the relative intensities of certain powder X-ray reflections and various ratios have been used as a 'crystallinity index'. The minerals dickite and nacrite are chemically identical to kaolinite but have their layers stacked in different regular sequences (i.e. they are polytypes); both have a two-layer monoclinic unit cell.

Halloysite has a single layer of water molecules in each interlayer space, which increases d_{001} from the characteristic 7.4 Å of kaolinite to about 10 Å. Dehydrated halloysite has d_{002} ~7 Å and the two minerals are referred to as halloysite-10Å and halloysite-7Å. The layer stacking in halloysite produces a two-layered cell and although there is probably an optimum arrangement of water molecules for hydrogen

Downloaded from https://pubs.geoscienceworld.org/books/chapter-pdf/3760832/9780903056434_ch53.pdf
by guest

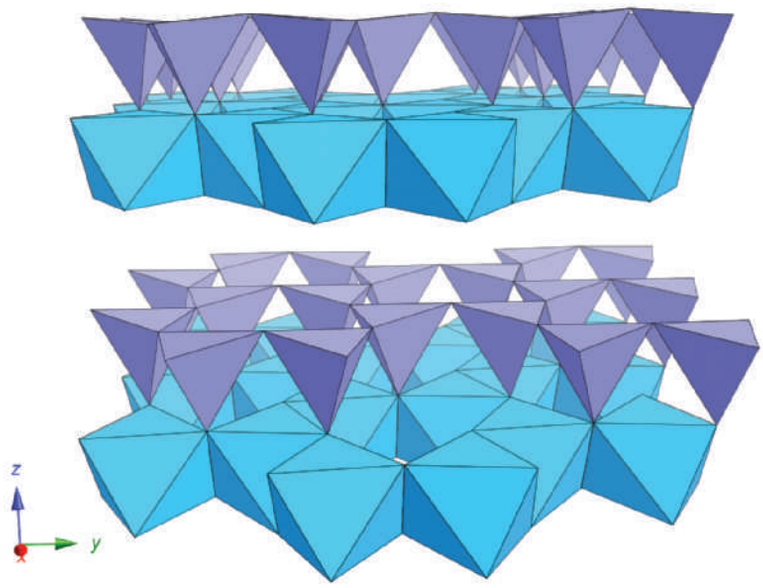


Fig. 156. Perspective view, approximately along *x*, of the structure of kaolinite showing Si–O tetrahedra (lavender) and Al–(O, OH) octahedra (blue) (CrystalMaker image).

bonding there is usually a high degree of disorder. There is a marked tendency for the layers of halloysite to roll up into cylinders or scrolls, or to adopt spheroidal shapes. This, and disorder, lead to broad and asymmetric rather than sharp X-ray reflections.

The interlayer water of halloysite may be replaced by glycol, which increases d_{001} from 10 to about 11 Å. Other kaolinite minerals show no swelling with water but can show swelling with a few specific organic compounds.

Chemistry

The chemical composition of kaolinite is subject to little variation. Analyses show small amounts of various ions, e.g. Fe, Cr, Ti, Mg and K, but because of the fine-grained nature of clays these may not be present in the structure but may be in impurities such as anatase and rutile or in interlayered mica. Although minerals which structurally are trioctahedral analogues of kaolinite (e.g. serpentine, amesite, berthierine, cronstedtite) are well known, substitution in kaolinite of (Mg,Fe) for Al, with or without Al for Si, leading towards trioctahedral composition, is negligible. Halloysites show more variable compositions, and tend to have a higher Al/Si ratio. While the formula of kaolinite can be written in terms of oxides as $Al_2O_3.2SiO_2.2H_2O$, that of halloysite is ideally $Al_2O_3.2SiO_2.4H_2O$. In this fully hydrated form of halloysite, $2H_2O$ corresponds with structural (OH) ions and the remainder occurs as interlayer water which is extremely loosely held so that even at room temperature, in an unsaturated environment, most of this water is lost. Thus most, if not all, of the interlayer water is not recorded in the H_2O+ values in chemical analysis but appears as H_2O-.

Kaolinite has a low cation exchange capacity (about 10, but up to 100 μeq./g through impurities) compared with other clays, e.g. illite 200 and smectite 1000 μeq./g. For halloysite the value is about 400 μeq./g. By contrast the anion exchange capacity of kaolinite is greater than that for most clay minerals, through the presence of replaceable $(OH)^-$ ions on the outside of its structural layers.

Differential thermal analysis and dehydration experiments are widely used for the characterization and identification of clay minerals. The dehydration of halloysite proceeds in a number of stages. Some of its adsorbed water (surface and interlayer) is lost on heating to 110ºC as with any other mineral, but the remainder is lost gradually and is not completely expelled until about 400ºC. For kaolinite, little or no surface adsorbed water is present and most of the dehydration (loss of constitutional OH) takes place between 400 and 525ºC, and this is responsible for an endothermic peak in its DTA pattern at 550–600ºC. The dehydroxylated product is sometimes referred to as metakaolin. The corresponding temperatures for dickite and nacrite are higher, probably through larger particle size.

If kaolinite minerals are heated beyond about 800ºC their structures are further disrupted and cannot be reconstructed by rehydration. An exothermic peak occurs at 900–1000ºC and decomposition produces mullite and/or γ-alumina, and α-cristobalite.

The hydrothermal synthesis of kaolinite, and in some cases dickite and nacrite, has been achieved commencing with gels of suitable $Al_2O_3–SiO_2$ or $Al(OH)_3–SiO_2$ composition at temperatures between 120 and 450ºC.

Optical and physical properties

The kaolinite minerals may occur in compact massive blocks, in vermiform or granular aggregates, as radiating platelets, or as piles of platelets (or 'books'), the latter

Downloaded from https://pubs.geoscienceworld.org/books/chapter-pdf/3760832/9780903056434_ch53.pdf
by guest

form being particularly common for dickite. The perfect {001} cleavage yields flexible but inelastic plates which are sometimes large enough for determination of optical properties. Such measurements must, however, be interpreted with care since they may be considerably affected by the presence of impurities and/or adsorbed water. Penetration of the crystals by organic liquid immersion media changes the refractive indices of some clay minerals but does not affect kaolinite. Birefringence measurements, moreover, may vary according to the immersion liquid used, indicating that the particles are small enough for form birefringence to be superimposed upon true birefringence. For the fine-grained specimens only an average refractive index can be measured, which for halloysite (approximately 1.530) is lower than for kaolinite. In all of the crystalline varieties γ is parallel to *y* and the optic plane perpendicular to (010). Electron micrographs of kaolinite show a high proportion of particles with well defined straight edges and sometimes thin elongated plates with prominent 60º angles.

Halloysite generally has a fibrous, spheroidal or irregular morphology and its fibres appear in electron micrographs to be tubular or scroll-like with elongation parallel to *y*. There are, however, examples of platy halloysites and 'fibrous' kaolinites.

Scanning electron microscopy can be very useful within a study of a specific clay mineral occurrence but, because of wide morphological variability, is less useful in the context of mineral identification in a broad sense.

The density of a clay mineral varies considerably with its state of hydration. For kaolinite, values of about 2.63 g/cm^3 are usually obtained and are reproducible, but halloysites may vary from 2.55 g/cm^3 for dehydrated material to 2.0 g/cm^3, depending on water content. The density of dickite and of nacrite is approximately 2.60 g/cm^3 which is close to the theoretical value. The plastic properties of kaolinite and other clay minerals when mixed with water are well known, but are not fully understood. There is an optimum amount of water required to produce maximum plasticity and there is evidence that the water molecules are arranged in a definite pattern rather than in a disordered liquid state, and that they are probably linked by hydrogen bonds to each other and to the oxygen and hydroxyl ions on the outsides of kaolinite layers.

Distinguishing features

Optical properties, if available, can be used to distinguish kaolinite from dickite and nacrite. Dickite is optically positive, and has a lower refractive index and β:*x* = 14–20º; nacrite is negative but also has a greater extinction angle β:*x*. Sericite and montmorillonite have greater birefringence and the latter has a lower refractive index. X-ray powder patterns of untreated and of heated and glycolated specimens may, however, be necessary, in conjunction with DTA, infrared spectroscopy, staining and other tests, in order to distinguish fine-grained kaolinite minerals from each other and from other clay and non-clay layered minerals. Serpentine and chlorite are readily decomposed by dilute HCl whereas kaolinite is not.

Paragenesis

The principal occurrences of kaolinite are as residual deposits formed by the weathering or low-temperature hydrothermal alteration of feldspars, muscovite and other Al-rich silicates usually in acid rocks (e.g. granites, rhyolites, quartz diorites). The derivation from feldspar can be expressed as:

$$2\,KAlSi_3O_8 + 3\,H_2O \rightarrow Al_2Si_2O_5(OH)_4 + 4\,SiO_2 + 2\,K(OH)$$

the silica and KOH being leached away. If potassium is not lost, illite rather than kaolinite is likely to form.

Kaolinite also occurs in deposits where it or its parent minerals have been transported under suitable non-alkaline conditions and deposited in deltaic, lagoonal or other non-marine environments. Prime examples of these types of deposits are those of Georgia and South Carolina, USA, which are believed to be derived from the granites and gneisses of the Piedmont plateau.

A well known example of residual/hydrothermal origin is the so-called China Clay deposit formed *in situ* from the St Austell granite in Cornwall, UK.

Most sedimentary kaolinite is detrital with its origin in soils, but it is also found as an authigenic mineral formed at shallow depths and low temperatures in mudrocks, clastic sediments and coals.

Further reading

Brindley, G.W. and Brown, G. (1980) *Crystal Structures of Clay Minerals and their X-ray Identification*. Monograph **5**, Mineralogical Society, London, 495 pp.

Giese, R.F. (1988) Kaolin minerals: structures and stabilities. Pp. 29–66 in: *Hydrous Phyllosilicates (Exclusive of Micas)*. Reviews in Mineralogy, **19**, Mineralogical Society of America, Washington, D.C.

Ma, C. and Eggleton, R.A. (1999) Surface layer types of kaolinite: a high resolution transmission electron microscope study. *Clays and Clay Minerals*, **47**, 181–191.

Newman, A.C.D. and Brown, G. (1987) *Chemistry of Clays and Clay Minerals.* Monograph **6**, Mineralogical Society, London, 480 pp.

Wilson, M.J. (Editor) (1987) *A Handbook of Determinative Methods in Clay Mineralogy.* Blackie, 308 pp.

Wilson, M.J. (2004) Weathering of the primary rock-forming minerals: processes, products and rates. *Clay Minerals*, **39**, 233–266.

Young, R.A. and Hewat, A.W. (1988) Verification of the triclinic structure of kaolinite. *Clays and Clay Minerals*, **36**, 225–239.

Downloaded from https://pubs.geoscienceworld.org/books/chapter-pdf/3760832/9780903056434_ch53.pdf
by guest

Monoclinic (−)

α	1.54−1.57
β	1.57−1.61
γ	1.57−1.61
δ	~0.03
$2V_\alpha$	Generally less than 10°
Orientation	α approx. ⊥ (001)
D (g/cm^3)	2.6−2.9
H	1−2
Cleavage	{001} perfect
Colour	White and various pale colours; colourless in thin section
Unit cell	1M polytype: a ~ 5.2 Å, b ~ 9.0 Å, d_{001} ~ 10 Å Z = 1

The term illite, although widely used by sedimentary petrologists, is not particularly well defined, many illites have potassium-deficient muscovite compositions. Illites, smectites and vermiculites are all clay minerals which are structurally related to the micas, but the closest similarity is shown by the illite group of minerals as their principal interlayer cation is potassium. Most illites are dioctahedral, like muscovite, but some are trioctahedral, like biotite. A general formula for illite can be expressed as $K_yAl_4(Si_{8-y},Al_y)O_{20}(OH)_4$ where y is less than 2 and most commonly around 1.5. Thus illite differs from muscovite chemically in having more silica and less potassium, and physically in having clay-size (<2 μm) particles.

Structure

The fundamental unit of the structure of illite is similar to that of a mica in that it has a plane of octahedrally coordinated cations sandwiched between two inward-pointing sheets of linked $(Si,Al)O_4$ tetrahedra (the so-called 2:1 layered structure). The mica structure, which contains layers of this type alternating with layers of potassium atoms, has been more fully described on pp. 174−6.

Most of the illite minerals have fewer interlayer cations than muscovite so that bonding between layers is weaker and there is consequently less regularity of stacking. The most common polymorph for illites has a disordered one-layered monoclinic cell (1M*d*; see p. 175); other polytypes which are known for muscovite (3T, $2M_1$ or disordered versions of them) are known also for illite.

Basal X-ray reflections are unaffected by stacking irregularities, so that illites may be recognized by their strong 10 Å reflection and successive higher orders of varying intensity. Illites (*sensu stricto*) contain little or no interlayer water and are not penetrated by organic liquids, so that the basal reflections are unaffected by heating to 500°C, and an illite which is uncontaminated by a smectite, vermiculite or halloysite should show no swelling characteristics when treated with glycol.

Most natural samples of illite contain smectite layers (montmorillonite/beidellite, see p. 234) which may be regularly or randomly interstratified. An illite/smectite (I/S) mixed-layer aggregate is in fact the most abundant clay mineral constituent of sedimentary rocks. If smectite units are interlayered with illite the basal spacing (d_{001}) is increased and the specimen shows to some degree the characteristics of a smectite, i.e. swelling on treatment with glycol, collapse of layers on heating, and cation exchange properties (K exchangeable, e.g. for Na on treating with NaCl). The proportions of smectite in an I/S specimen can be determined quantitatively. It has been suggested that two more-or-less regular structural sequences are preferred: ISISIS... (50% expandable) and ISII... (25% expandable) and that specimens displaying other proportions are in fact mixtures of these two.

Electron-micrographic study of some very fine-grained material shows particles of very few fundamental illite layers (thickness ~ 20 Å) even though the X-ray diffraction patterns seem to indicate substantial numbers of mixed layers of illite and smectite. It has been suggested that the X-ray pattern is produced by a

Downloaded from https://pubs.geoscienceworld.org/books/chapter-pdf/3760845/9780903056434_ch54.pdf
by guest

succession of thin illite units without intervening smectite. The interfaces between particles can adsorb water or organic liquids and thus give rise to the expandability otherwise attributed to interlayered smectite. This alternative view of I/S is not universally accepted.

The width of X-ray powder reflections increases with diminishing particle size and has been used as a 'crystallinity index', increasing particle size being associated also with higher temperature of formation and therefore with a more advanced stage of diagenesis/metamorphism. The presence of I/S intergrowths, however, also broadens X-ray diffraction peaks and care is needed in separating these two effects.

Chemistry

In illite the octahedral layer contains 4Al pfu as in muscovite, and the excess charge on the tetrahedral components through their higher Si/Al ratio is compensated by there being a deficiency of interlayer K ions (Table 30, analysis 3, p. 225). The mineral phengite also has a high Si/Al ratio and it can occur in a fine-grained state, but the charge compensation is effected by the substitution of (Mg,Fe^{2+}) for $^{[6]}Al$. It has been suggested that some illite is a mixture of two types, one with ~2.0 K pfu and another with ~1.1 K pfu giving a bulk composition of about 1.55 K pfu. Analyses of illites show a higher content of structural water $(H_2O)^+$, probably representing additional protons bonded to oxygens at surfaces and edges of the extremely thin illite particles.

The term 'sericite' is generally used to describe a fine-grained white mica which may be muscovite or paragonite, but it is sometimes applied to less well characterized specimens which may deviate from the muscovite composition in any of the ways described above. Illites commonly contain some Ca,Na replacing K as well as Mg,Fe replacing $^{[6]}Al$, but these could be located in interlayer spaces and/or within the illite layers.

Glauconite can be regarded as a clay mineral related to illite, though more iron-rich, since it is dioctahedral and has a similar deficiency of interlayer cations below 2 pfu compensated mainly by Si for $^{[4]}Al$; in the present text it is discussed along with the micas (p. 188). Brammallite is a less common illite in which sodium is the major interlayer cation, and the ammonium ion, made available by organic material, can also proxy for potassium.

Illites exhibit a cation exchange capacity of between 10 and 40 meq./g which, though greater than that for kaolinite, is considerably less than those for halloysite, smectite and vermiculite. The illites in soils, however, are often weathered forms deficient in potassium and perhaps altered towards smectite or vermiculite, and these have a high capacity to take up and fix potassium from fertilizing salts. The exchange property of illite is associated with cations in interlayered smectite, or at the edges or other surfaces of fine crystallites. Certain organic complexes and organic polymers have been found to replace potassium at external surface or edge sites and can play a role in the formation of soil aggregates, which are of interest in agriculture; they also have been involved in the formulation of drilling fluids in the petroleum industry.

The dehydration of illites, whether dioctahedral or trioctahedral, proceeds in a number of stages. Most of the water adsorbed on the surface of particles and the small amount which may be interlayered with illite sheets is lost rapidly below 110ºC, and the remainder more slowly between 110 and 350ºC. Water formed by expulsion of $(OH)^-$ ions is lost rapidly at first between 350 and 600ºC, but a small amount remains and is given off on further heating. By contrast, micas lose little or no water at the lower temperatures and their constitutional water from $(OH)^-$ ions is driven off at somewhat higher temperatures than that of illite, probably because of the larger particle sizes.

The DTA curves of illite show three endothermic peaks, one between 100 and 200ºC representing loss of loosely held water, one at 550–650ºC corresponding with loss of $(OH)^-$, and one at 850–950ºC corresponding with disruption of the remaining structure. This is followed by an exothermic peak at 900–1000ºC when spinel is formed.

Illites have been synthesized in the laboratory using a variety of starting materials, e.g. smectites or gels of smectite composition. The kinetics of their formation have been studied, but so far only a limited number of the many variables in the complex natural process of burial diagenesis have been incorporated in experiments. Random or ordered illite/smectites are usually formed as intermediates, but starting with muscovite or illite compositions can lead to the formation of illite directly. The effect of pressure is to inhibit the formation of illite from smectite. Illites have also been synthesized by dissolution of kaolinite in highly alkaline conditions (pH >11) in a high-potassium environment.

A theoretical diagram illustrating the relative stabilities of illite as compared with other clay minerals and related non-clay minerals is shown in Fig. 157, and experimental results in general confirm these relationships.

Optical and physical properties

Illite specimens show a rather wide variation of refractive indices owing to the various substitutions possible (refractive indices increase with iron content), the degree of hydration, and interlayering with other minerals. The refractive indices are a little below those of the corresponding micas muscovite and biotite. Measurement of optical properties generally cannot be

Downloaded from https://pubs.geoscienceworld.org/books/chapter-pdf/3760845/9780903056434_ch54.pdf
by guest

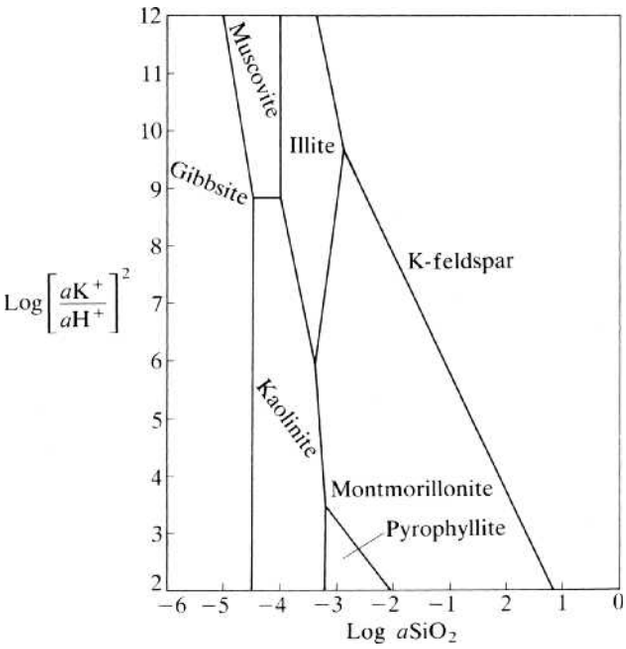


Fig. 157. Theoretical plot of ion activities showing stabilities of phases using idealized compositions and assuming that illite/smectite is a mixture rather than a solid solution (from Garrels, R.M, 1984, *Clays Clay Min.*, **32**, 161–6. Reproduced with kind permission of The Clay Minerals Society, publisher of *Clays and Clay Minerals*).

made with great precision because of the extremely small size of illite particles.

Electron microscopy shows that illites occur with a variety of morphologies including irregular platy particles, well formed hexagonal platelets, very thin (20–100 Å) platelets, laths with elongation parallel to *x*, and narrow filaments referred to as 'fibrous' or 'hairy' illite. The latter commonly occur within the cavities in porous sandstones and may adversely affect the recovery of petroleum from such sources.

Pure illites are colourless, but impurities such as fine-grained iron oxides or hydroxides may colour them yellow, green or brown, and they may show slight pleochroism. Densities, like refractive indices, are variable as they are affected by the degree of hydration, and by the presence of fine-grained impurities, but generally they are a little lower than those of corresponding micas.

Distinguishing features

The extremely fine-grained nature of most illite specimens makes identification by optical methods difficult. Average refractive indices are similar to those for corresponding micas, but the 2V is generally smaller than that of muscovite. Reliable identification can only be achieved by a combination of chemical analysis, DTA and X-ray diffraction applied to samples before and after treatment by heat and with organic liquids.

A number of features of the X-ray powder pattern can help to distinguish illite from other layered silicates. Thus a d_{001} spacing of 10 Å indicates a 2:1 layered structure, d_{060} ~1.50Å indicates dioctahedral character, intensities $I_{002} > I_{001}$ follow from Al rather than Fe being the major octahedral cation, and Ir = $(I_{001}/I_{003})_{\text{air-dried}}/(I_{001}/I_{003})_{\text{glycolated}}$ = 1 indicates no expandability. The index Ir is commonly greater than unity because of interlayered smectite components.

Paragenesis

Illites and illite/smectites are the most abundant clay minerals in sedimentary rocks and can be formed from a variety of precursors including muscovite, kaolinite and feldspar, but their principal occurrences are as a result of diagenetic/low-grade metamorphic processes (burial metamorphism) acting upon smectites. In such circumstances it appears that potassium ions without hydration shells are more stable in interlayer sites than the hydrated sodium ions of smectites. With increasing temperature, the grain size of the <2 μm fraction increases, the proportion of interlayered expandable material decreases (smectite → ordered I/S → ISII → illite), and the ratio of $2M_1$ to 1M polytype increases.

The fibrous material which forms in sandstone pores can be illite or illite/smectite, but that which replaces kaolinite, often as pseudomorphs, is usually low in (Mg,Fe), and has little or no I/S component. In both circumstances the 1M polytype predominates.

Illites may be formed by similar processes in hydrothermal environments, e.g. in geothermal fields and associated with ore deposits, either diagenetically or by direct crystallisation from hot fluids of appropriate composition.

The process of 'sericitization' produces illites or illite/smectites derived from feldspars at the lower parts of weathering zones, and they are produced also by repeated cycles of wetting and drying acting upon smectites. For this process of potassium fixation the potassium is supplied either by the smectite itself or by feldspar associated with it.

Downloaded from https://pubs.geoscienceworld.org/books/chapter-pdf/3760845/9780903056434_ch54.pdf
by guest

Further reading

Kohler, S.J., Bosbach, D. and Oelkers, E.H. (2005) Do clay mineral dissolution rates reach a steady state? *Geochimica et Cosmochimica Acta*, **69**, 1997–2006.

Meunier, A. (2004) *Illite; Origins, Evolution and Metamorphism*. Springer, Berlin. 286 pp.

Perry, E.A. (1970) Burial diagenesis of Gulf Coast pelitic sediments. *Clays and Clay Minerals*, **18**, 165–177.

Sass, B.M., Rosenberg, P.E. and Kittrick, J.A. (1987) The stability of illite/smectite during diagenesis. An experimental study. *Geochimica et Cosmochimica Acta*, **51**, 2103–2115.

Środoń, J. and Eberl, D.D. (1984) Illite. Pp. 495–544 in: *Micas* (S.W. Bailey, editor). *Reviews in Mineralogy*, **13**, Mineralogical Society of America, Washington, D.C.

Downloaded from https://pubs.geoscienceworld.org/books/chapter-pdf/3760845/9780903056434_ch54.pdf
by guest

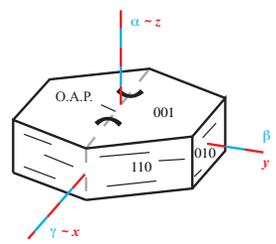
Smectite Group

Dioctahedral $(½Ca,Na)_{0.7}(Al,Mg,Fe)_4[(Si,Al)_8O_{20}](OH)_4.nH_2O$

Trioctahedral $(½Ca,Na)_{0.7}(Mg,Fe,Al)_6[(Si,Al)_8O_{20}](OH)_4.nH_2O$

Monoclinic (−)

α	1.48−1.61
β	1.50−1.64
γ	1.50−1.64
δ	0.01−0.04
$2V_\alpha$	Mostly small
Orientation	α approx. ⊥(010), β = *y*; O.A.P. (010)
D (g/cm^3)	2−3, variable
H	1−2
Cleavage	{001} perfect
Colour	Commonly white, yellow or green; colourless, yellow, green in thin section
Unit cell	*a* ~ 5.2 Å, *b* 9.1−9.2 Å; d_{001} commonly 10−15 Å, depending on water content



Montmorillonite, Beidellite, Nontronite

The smectites are a group of clay minerals which show expandability, taking up water or organic molecules between their structural layers, and also marked cation exchange properties. The principal smectites are montmorillonite, beidellite and nontronite, all of which are dioctahedral 2:1 layered silicates, and saponite, hectorite and sauconite, which are trioctahedral. Structurally and chemically the two groups can be related to pyrophyllite and talc respectively. Smectites are common constituents of sedimentary rocks and they also play an important role in soils with regard to structure and uptake of nutrients. The smectites are useful, as are most other clay minerals, in the manufacture of bricks, ceramics, drilling muds, paper, rubber, paints and moulding sands. They are also used as decolorizing, clarifying and filtration agents and as catalysts for hydrogenation and other chemical reactions. Their ion exchange properties lead to potential uses in the treatment of radioactive waste.

Structure

The dioctahedral smectites have structures based upon that of pyrophyllite (Fig. 141, p. 203). The latter mineral consists of superimposed layers each of which contains a plane of Al ions sandwiched between two inward-pointing sheets of linked SiO_4 tetrahedra. The central section may be regarded as a layer of gibbsite, $Al_2(OH)_6$, in which two out of every three (OH) ions are replaced by apical oxygens of an Si_4O_{10} pseudohexagonal network. Trioctahedral smectites have structures similar to that of talc, where the central section is like brucite, $Mg_3(OH)_6$. In both pyrophyllite and talc there are no significant substitutions for Al, Si or Mg, so the composite sheets are electrically neutral and there are no cations between them. In smectites the charge balance is upset by substitutions in either octahedral (Al or Mg) sites, or tetrahedral (Si) sites and is redressed by the presence of a small number of interlayer cations, usually Ca or Na.

For pyrophyllite the interlayer spacing d_{001} is approximately 8.9 Å and for the micas and illites it is about 10 Å. In smectites the basal spacing can vary over a wide range with a minimum, corresponding with the fully collapsed state, at about 9.6 Å. The interlayer cations are sufficient only to balance the layers' negative charge and therefore do not fill all available sites, as do, for example, K ions in muscovite. They are probably arranged in alternating sequences of occupied and vacant sites. Water molecules are readily adsorbed, forming hydration shells around the interlayer cations rather than continuous sheets. Hydrogen bonding plays some role in determining the positions of cations and water molecules.

Downloaded from https://pubs.geoscienceworld.org/books/chapter-pdf/3760848/9780903056434_ch55.pdf
by guest

The number of layers of water molecules is influenced to some extent by the nature of the interlayer cation, calcium montmorillonites (the most common in nature) usually having two or three layers per cell and d_{001} ~15.5 Å or 19 Å, and the sodium varieties having one (d_{001} ~12.5 Å), two (15.5 Å), three (19 Å) or more layers per cell. Since specimens may contain randomly mixed cells with various water contents, the range of effective basal spacings that may be recorded is continuous between 10 and about 21 Å, and can vary with humidity and the nature of the cation. The X-ray powder patterns of dehydrated montmorillonite and saponite are similar to those of pyrophyllite and talc, respectively.

The layers of smectites usually exhibit turbostratic disorder leading to diffuse *hk* bands rather than sharp *hkl* reflections in the X-ray powder pattern. Some dioctahedral smectites exhibit partial order, yielding some sharp and some diffuse X-ray reflections. Successive cycles of drying and wetting with K-bearing solutions can give a well ordered structure (*C*2/*m*, β ~100º) with K fixed as the interlayer cation.

Fully or partially ordered or random interlayering of smectites with other layered silicates occurs, most commonly as illite/smectite (see p. 230) and chlorite/smectite. If there is a regularly alternating sequence of layers specific mineral names have been assigned, e.g. rectorite (illite/smectite), tosudite (chlorite/smectite), aliettite (saponite/talc). If fully ordered, d_{001} is the sum of the basal spacings for each of the two components; if partially ordered, the first basal peak lies between those that would be given by separate components. Mixed layers of two smectites (montmorillonite and beidellite) can also occur.

The interlayer spaces in smectites can be penetrated not only by water and exchange cations but also by certain organic cations, e.g. alkyl-ammonium ions, and by various polar organic liquids such as glycol and glycerol. These are adsorbed in integral numbers of layers and yield regular layer sequences with characteristic basal spacings. The only other common swelling clay minerals are halloysite, which expands d_{001} with glycerol to about 11 Å, and vermiculite to 14 Å, as compared with 17 Å for smectites.

On heating at between 100 and 200ºC smectites lose their interlayer water reversibly, and the basal spacing shifts from between 12 and 15 Å to about 10 Å. With heating at 500ºC, d_{001} is reduced further to between 9.6 and 10 Å depending upon the nature of the interlayer cation.

Chemistry

The chemical formulae of all smectites are similar to those of either pyrophyllite or talc in which substitutions in octahedral (*M*) or tetrahedral (*T*) sites by ions of lower valency are accompanied by the addition of an equivalent number of interlayer cations; octahedral vacancies may be similarly compensated. The required extent of such substitution ranges up to about 1.4 additional monovalent cations or their equivalent per formula unit (based on 20 oxygens) and an average of about 1.0, and these ions are, in general, exchangeable.

The smectites are subdivided according to the substitutions involved and these are illustrated in an idealized manner in Table 32. Thus in montmorillonite and hectorite substitution is almost entirely in the *M* sites, whereas in beidellite and saponite it takes place principally in the *T* sites.

Substitutions other than those shown in Table 32 commonly occur (Table 30, anals 4, 5, 6, p. 225). In dioctahedral smectites the *M* sites may contain minor amounts of Fe^{2+}, Mn and Ni. Furthermore intermediates may exist possessing features of two or more of the smectites listed in Table 32. Thus montmorillonite commonly has some replacement of Si by Al, and there is usually some Mg in beidellite and nontronite so that montmorillonite–beidellite–nontronite may form a continuous range (Table 30, anals 4, 5, 6). The series montmorillonite–beidellite can be expressed by the formula $Al_{4-y}Mg_ySi_{8-x}Al_xO_{20}(OH)_4(½Ca,Na)_{x+y}$, and

Table 32. Smectites, pyrophyllite and talc.

	T	M	I (exchange cations)
Dioctahedral			
Pyrophyllite	Si_8	Al_4	–
Montmorillonite	Si_8	$Al_{3.3}Mg_{0.7}$	$(½Ca,Na)_{0.7}$
Beidellite	$Si_{7.3}Al_{0.7}$	Al_4	$(½Ca,Na)_{0.7}$
Nontronite	$Si_{7.3}Al_{0.7}$	Fe^{3+}_4	$(½Ca,Na)_{0.7}$
Trioctahedral			
Talc	Si_8	Mg_6	–
Saponite	$Si_{7.2}Al_{0.8}$	Mg_6	$(½Ca,Na)_{0.8}$
Hectorite	Si_8	$Mg_{5.3}Li_{0.7}$	$(½Ca,Na)_{0.7}$
Sauconite	$Si_{6.7}Al_{1.3}$	$Zn_{4-6}(Mg,Al,Fe^{3+})_{2-0}$	$(½Ca,Na)_{0.7}$

Downloaded from https://pubs.geoscienceworld.org/books/chapter-pdf/3760848/9780903056434_ch55.pdf
by guest

divided such that for montmorillonite $y > x$ and for beidellite $y < x$. In these aluminous smectites mean values for octahedral Al, Mg, Fe^{3+} and Fe^{2+} are, respectively, 3.0, 0.7, 0.4 and 0.4, and for tetrahedral Al about 0.4 atom pfu. With regard to Fe^{2+}, nontronites generally have more than three and montmorillonite/beidellite less than three atoms per formula unit.

In the trioctahedral smectites Mg is the principal M cation but considerable and perhaps complete replacement by Fe^{2+} can occur, producing the iron-dominant mineral ferrosaponite. Saponite (Table 30, analysis 7) typically contains some trivalent ions in *M* sites and has correspondingly more Al replacing Si; some Fe^{3+} in saponite may, however, result from oxidation of original Fe^{2+}. Hectorite typically has appreciable replacement of (OH) by F.

The total of M ions in smectites generally lies within the ranges 4–4.5 and 5.7–6.0 and although there may not be intermediate compositions in a single layer, mixtures of dioctahedral and trioctahedral layers may occur, yielding intermediate bulk chemistry.

Cation exchange

The most commonly occurring exchangeable cations are sodium and calcium, but smectites can be prepared containing potassium, caesium, strontium, magnesium, hydrogen and other interlayer (I) cations which are to varying degrees exchangeable. In some analyses of dioctahedral smectites the total of M ions exceeds four and it is likely that some of the Mg ions occupy interlayer sites and contribute to the cation exchange capacity. The interlayer cations of smectites may be already in the specimen when it is formed, or may be the result of subsequent exchange, as some cations are more readily substituted than others. The cation exchange capacity is usually in the range 0.8–1.5 but for hectorite it is around 0.5 meq./g. Exchange capacity varies with particle size and nature of the cation, the sequence of increasing replacing power being Li < Na < K < Rb < Cs for monovalent and Mg < Ca < Sr < Ba for divalent ions. Generally the replacing power of ions with higher valency is greater and their replaceability is less, so that calcium is more firmly held than sodium.

Interlayer molecules

The amount of interlayer water adsorbed varies according to the type of smectite, the nature of the interlayer cations and the physical conditions. Calcium smectites usually take up two or three layers of water molecules in each space, whereas the amount taken by sodium compounds appears to be continuously variable, and in general they show a greater swelling capacity. Some of the interlayer water may be regarded as molecules of water of hydration surrounding the replaceable cations. Various organic molecules can also be accommodated in interlayer spaces, and because of this smectites (the principal constituent of Fuller's earth) are extensively used as decolorizing agents, for purifying fats and oils, and in the refinement of petroleum.

Some organic compounds (e.g. alcohols, ketones, amines, urea and amides) coordinate directly with exchangeable metal ions, in general being more attracted to Na, Ca and Mg than to K, and in some cases hydrogen bonding involving (OH) or (NH) groups takes place. Methods have been devised for introducing stable organic or organometallic cations which, by keeping smectite layers well apart, form clays with enhanced porosity and catalytic properties, the so-called 'pillared clays'.

The adsorption of long chain organic molecules and cationic polymers on the surfaces of clay particles also has important industrial applications (e.g. as flocculants and coagulants).

Thermal effects

On heating, the interlayer water of smectites is lost mostly between 100 and 250ºC but some remains to about 300ºC, at which temperature slow loss of constitutional (OH) water begins. Rapid loss of (OH) water takes place at about 500ºC and is complete at about 750ºC. The dehydration of montmorillonite is at least partly reversible as long as it is not taken to completion, and even after heating to 600ºC some interlayer water can be regained slowly. Saponites and smectites with higher Fe content usually break down at somewhat lower temperatures. When the dehydroxylate is heated further, breakdown occurs to high-temperature phases such as cristobalite, mullite, cordierite or a spinel-type compound.

Differential thermal analysis curves of smectites show considerable variations, but in general they display at least one endothermic peak at low temperatures (100–250ºC) corresponding with the loss of interlayer water, and another one (or two) corresponding with loss of (OH) water at about 700ºC.

Experimental

Smectites have been synthesized in many different ways from gels, oxides, solutions and glasses of appropriate compositions and have been formed by chemical alteration of rocks and minerals in the laboratory. Reactions carried out at low temperatures (up to 150ºC) most closely mimic natural conditions but are very slow and higher temperatures have been used to give faster results. Among the reagents used for syntheses are sodium metasilicate, sodium aluminate, NaOH, $Ca(OH)_2$, hydrated silica, and sulphates and chlorides of magnesium and iron. The relatively rare Li- and F-rich smectite, hectorite, is valuable through its high viscosity and has been synthesized by hydrothermal treatment of SiO_2 and $Mg(OH)_2$ gels with NaOH and Li(OH) or LiF.

Downloaded from https://pubs.geoscienceworld.org/books/chapter-pdf/3760848/9780903056434_ch55.pdf
by guest

Optical and physical properties

Smectites occur most commonly in fine-grained aggregates which may be vermiform, lamellar or spherulitic. Rarely the constituents of such aggregates are well oriented and give the appearance of well formed crystals, but examination under the electron microscope reveals that the fundamental particles are extremely thin platelets. Most platelets are irregular in outline but some are hexagonal or rhombic, and elongated laths or fibres are not uncommon.

The most common colours of montmorillonites are pink, buff, grey or light brown, and many are white, whereas nontronites are usually bright green. Those which are coloured show distinct pleochroism, the colours for nontronite being green parallel to (001), and yellow perpendicular to (001). Because of their fine-grained nature, and because their optical properties are affected by hydration and sometimes by the immersion liquid as well as by compositional changes, only approximate ranges of optical constants are given for smectites in Table 33.

Refractive indices are only slightly influenced by the substitutions Si ↔ Al and Al ↔ Mg, but are considerably dependent upon iron content. All smectites are optically negative, but $2V_\alpha$ is variable over a wide range. Refractive indices increase with loss of interlayer water, and densities are also affected considerably by degree of hydration.

Distinguishing features

The average refractive indices for smectites are similar to those for illites and kaolinites, but minerals of the kaolinite group have lower birefringence than most smectites, and illites generally have higher birefringence. Dehydrated montmorillonites and saponites which have low iron content have refractive indices similar to those of pyrophyllite and talc, respectively, but the birefringences are lower. Optical methods alone are not reliable for the identification of smectites and it is usually necessary to observe several other properties, such as DTA curves, dehydration curves and X-ray powder patterns before and after treatment by heating and by organic liquids. Electron optical and spectroscopic methods may also be required.

For smectites the d_{001} spacing expands to 12 Å on saturation with K^+ or NH_4^+ ions, to 15 Å with Ca or Mg ions and to 17 Å with glycol. The d_{001} spacing decreases to 10 Å on heating to about 150ºC (250ºC for saponite). For montmorillonite and beidellite d_{060} is about 1.50 Å and for saponite it is about 1.53 Å.

Nontronite and saponite are readily decomposed by acid treatment whereas montmorillonite and beidellite are more resistant.

Paragenesis

Smectites form in sedimentary deposits by diagenetic/hydrothermal processes which can either involve transformation of precursor clay or non-clay material or neoformation from solutions or colloids. In general, smectites are found in petroleum reservoir rocks only at relatively shallow depths. In the burial diagenesis of mudrocks, increasing depth and temperature facilitate the conversion of dioctahedral smectites to illite/smectite and illite, and trioctahedral smectites to chlorite. These changes are accompanied by the release of water and the resulting increase of pore-fluid pressure may influence oil and gas migration. It has been suggested that the conversion of smectite to illite involving incorporation of K and substitution of Al for Si may be by a process of dissolution followed by precipitation. In more acidic conditions, smectite reacts to convert via smectite/kaolinite to kaolinite.

Montmorillonite and beidellite are the principal constituents of bentonite clay deposits. These are formed by the alteration of eruptive igneous rocks, usually tuffs and volcanic ash, and contain in addition varying amounts of cristobalite, zeolites, biotite, quartz, feldspar and zircon. Alteration has usually occurred *in situ*, in an aqueous (mostly marine) environment. Except for the Wyoming bentonites, calcium rather than sodium is the naturally occurring exchange cation. 'Fuller's earth' is a name given to a clay which has a high absorptive capacity (see p. 236); its principal clay mineral constituent is usually montmorillonite. Most of the Fuller's earth in Europe has been produced by weathering of basic igneous rocks, or occurs in a sedimentary product derived from them. The name is also used in England to denote a particular stratigraphical formation. Smectites also occur as hydrothermal

Table 33. Optical properties of smectites.

	α	β = γ	δ	$2V_\alpha$
Montmorillonite–beidellite series	1.48–1.57	1.50–1.60	0.02–0.03	0–30º
Nontronite	1.56–1.61	1.57–1.64	0.03–0.045	25–70º
Saponite	1.48–1.53	1.50–1.59	0.01–0.036	Moderate
Hectorite	~1.49	~1.52	~0.03	Small
Sauconite	1.55–1.58	1.59–1.62	0.03–0.04	Small

Downloaded from https://pubs.geoscienceworld.org/books/chapter-pdf/3760848/9780903056434_ch55.pdf
by guest

alteration products around metalliferous veins or deposits, and near hot springs and geysers.

Nontronite occurs as an authigenic clay mineral in recent submarine sediments and as a hydrothermal precipitate from hot brines at 'spreading centres'. It is also found as a weathering product of basalts, ultrabasic rocks and volcanic glasses, in mineral veins (commonly with opal and quartz) and in association with sedimentary iron ores. The zinc smectite sauconite, and those rich in Ni, Co, Cu, Mn or Fe, occur around orebodies, in laterites and in saprolites of ultramafic rocks. Saponites occur mainly associated with mineral veins but are also commonly formed from basic volcanic material, sometimes filling amygdales in basalt. Hectorite is relatively rare; at the Hector deposit in California it is believed to have formed as a result of the alteration of pyroclastic material by Mg-, Li- and F-rich solutions.

Smectites, particularly beidellite and nontronite, are widely found (often mixed with illites) in soils derived from the weathering of basic rocks.

Further reading

Brindley, G.W. and Brown, G. (Editors) (1980) *Crystal Structures of Clay Minerals*. Mineralogical Society Monograph **5**, Mineralogical Society, London, 495 pp.

Christidis, G.E., Blum, A.E. and Eberl, D.D. (2006) Influence of layer charge and charge distribution on the flow behaviour and swelling of bentonites. *Applied Clay Science*, **34**, 125–138.

Güven, N. (1988) Smectites. Pp. 497–552 in: *Hydrous Phyllosilicates (Exclusive of Micas)* (S.W. Bailey, editor). *Reviews in Mineralogy*, **19**, Mineralogical Society of America, Washington, D.C.

Kloprogge, J.T., Komareni, S. and Amonette, J.E. (1999) Synthesis of smectite clay minerals: a critical review. *Clays and Clay Minerals*, **47**, 529–554.

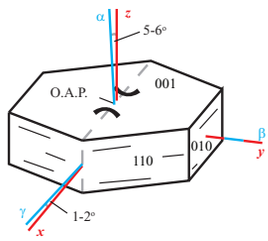
Newman, A.C.D. (Editor) (1987) *Chemistry of Clays and Clay Minerals*, Mineralogical Society Monograph **6**, Mineralogical Society, London, 480 pp.

Odom, I.E. (1984) Smectite clay minerals; properties and uses. *Philosophical Transactions of the Royal Society of London*, **A311**, 391–409.

Downloaded from https://pubs.geoscienceworld.org/books/chapter-pdf/3760848/9780903056434_ch55.pdf
by guest

Vermiculite $(Mg,Ca)_{0.6–0.9}(Mg,Fe^{3+},Al)_{6.0}[(Si,Al)_8O_{20}](OH)_4.nH_2O$

Monoclinic (−)



α	1.520−1.564
β	1.530−1.583
γ	1.530−1.583
δ	0.02−0.03
$2V_\alpha$	0−18°
Orientation	α approx. ⊥(010); O.A.P. (010)
D (g/cm^3)	~2.3
H	~1½
Cleavage	{001} perfect
Colour	Colourless, yellow, green, brown; colourless in thin section
Pleochroism	α paler shades than β and γ
Unit cell	a ~ 5.3 Å, b ~ 9.25 Å, c ~ 14.4 Å, β ~ 97°
	Z = 1; space group $C2/m$

Vermiculite bears close similarities to the trioctahedral micas and smectites but its special characteristics warrant its description as a separate mineral. The name, which is derived from the Latin *vermiculare*, to breed worms, alludes to the peculiar exfoliation phenomenon exhibited when specimens are rapidly heated. Exfoliated vermiculite provides a low-density material with excellent thermal and acoustic insulation properties. Vermiculite can also be used to remove metallic ions from contaminated effluents and wastewater.

Structure

The structure of vermiculite (Fig. 158) is similar to that of phlogopite since it contains a central octahedrally coordinated sheet of (Mg,Fe) ions which lie between two inward-pointing sheets of linked $(Si,Al)O_4$ tetrahedra. As in phlogopite, the central part of this composite layer may be regarded as one of brucite in which two out of three (OH) ions on each side are replaced by the apical oxygen of an SiO_4 tetrahedron. Replacement of Si by Al causes a negative charge which is only partially compensated by (Al,Fe^{3+}) for Mg in the central layer, the net negative charge being balanced by interlayer cations, which in vermiculite are mainly magnesium rather than potassium.

A further difference from phlogopite is the occurrence of water molecules between the structural layers. The interlayer water molecules and cations occupy definite positions with respect to the oxygens of neighbouring tetrahedral layers. The water molecule sites form a distorted hexagonal pattern such that each molecule is linked by a hydrogen bond to an oxygen on the silicate layer surface and in a naturally occurring Mg-vermiculite two of these hexagonal networks occur in each interlayer space. Weak hydrogen bonding links together water molecules in the same plane, and the pairs of water planes are held together by the exchangeable cations which lie midway between them: the cations thus have a hydration shell of water molecules around them. Not all available sites are in fact occupied by water molecules in normal atmospheric conditions and many of the water molecules do not enclose a cation. Those which do not surround a cation may be referred to as unbound water, and this water is readily expelled below 110ºC. An Mg-vermiculite at ordinary temperatures and humidity has a basal spacing of d_{001} ~14.3 Å. At low humidity or at higher temperatures an Mg-vermiculite has only one rather than two layers of water molecules and d_{001} reduces to 11.7 Å. In an intermediate state d_{001} ~13.8 Å and β ~90º. For Ca- and Na-vermiculites with two layers of H_2O, d_{001} increases to 14.9 and 14.8 Å, respectively. A higher value of d_{001} (~18.9 Å) can occur for a more swollen Mg-vermiculite and a minimum value of about 9 Å for a fully collapsed structure.

Glycol or glycerol may also be intercalated in vermiculite giving d_{001} spacings which vary according to the nature and amount of the interlayer cations. For

Downloaded from https://pubs.geoscienceworld.org/books/chapter-pdf/3760854/9780903056434_ch56.pdf
by guest

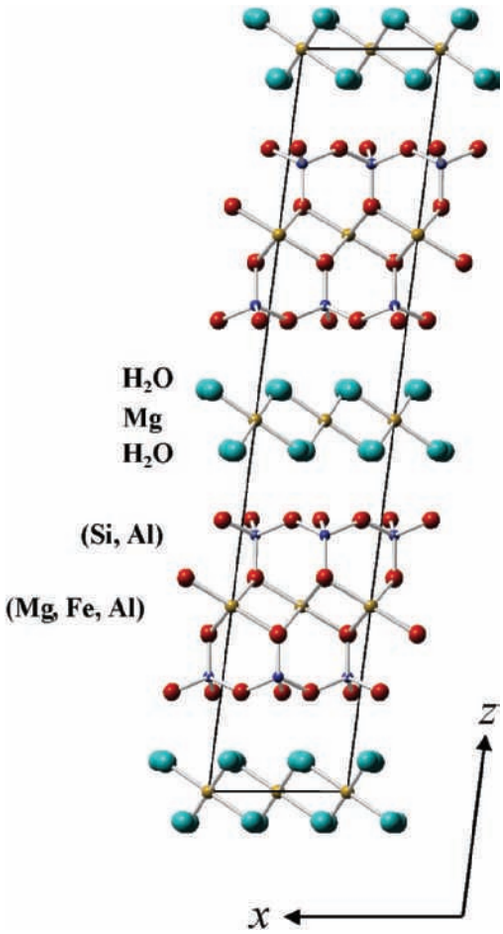


Fig. 158. The crystal structure of Mg-vermiculite projected on (010), showing T–O–T phlogopite-like layers and inter-layer sheets of Mg cations each side of which lie sheets of water molecules (after Mathieson, A.McL. & Walker, G.F., 1954, *Amer. Min.*, **39**, 231–55. Fig. produced by M.D. Welch).

an Mg-saturated vermiculite treatment with glycerol results in a d_{001} of 14.3 Å.

The stacking of successive layers of vermiculite can follow an ordered pattern but more commonly is semi-ordered, i.e. with regular offsets of $a/3$ or $a/6$ in the x direction but random $\pm b/2$, $\pm b/3$ or $\pm b/6$ shifts along y. An anhydrous K-saturated vermiculite is, however, well ordered with a structure similar to that of phlogopite. The structures of most vermiculites, though disordered, may be related to the 1M mica polytype, but some have features of the $2M_1$ stacking.

In general a more ordered structure results if the interlayer space has a higher charge and also if the humidity is high enough to give well bonded water layers. The stacking sequences adopted may be influenced by hydrogen bonding between interlayer water molecules and oxygens of the silicate layers. For Na-vermiculites intercalation with alkylammonium ions increases the regularity of stacking.

The structure of Mg-vermiculite resembles that of a chlorite in many respects but differs mainly in the reduced occupation of the interlamellar atomic sites, and because the 'brucite' sheet of chlorite is replaced by a partially filled $H_2O-Mg^{2+}-H_2O$ double sheet in vermiculite. Many occurrences of mixed-layer vermiculite/chlorite, vermiculite/kaolinite and vermiculite/mica clay minerals have been described.

Chemistry

Vermiculites are chemically similar to trioctahedral micas and smectites, in particular phlogopite and saponite. In phlogopite, appreciable substitution of Al for Si is balanced by a full complement of interlayer potassium ions. In vermiculite, a similar substitution is balanced partly by (Al,Fe^{3+}) for Mg in the central octahedral layer and partly by interlayer cations, which are mainly the divalent Mg rather than monovalent K. Saponite has far less Al for Si and little (Al,Fe^{3+}) for Mg and consequently requires less interlayer balancing charge, which is usually provided by Ca,Na rather than Mg or K.

Although in natural vermiculites (e.g. Table 30, analysis 8, p. 225) magnesium is the most common interlayer cation, calcium and more rarely sodium also occur. The interlayer charge is the equivalent of about 0.7 divalent cations compared with 0.7 monovalent cations in smectites. Accordingly, the cation exchange capacity of vermiculites (between 1.2 or 2.4 meq./g) is about twice that of smectites and indeed is the highest of all clay minerals. Vermiculites with Mg, Ca, Na, K, Rb, Cs, Ba, Li, H^+ and N as interlayer cations can be prepared. Although the octahedral sites in vermiculites are occupied mainly by Mg, some Fe^{2+} and appreciable Al and Fe^{3+}, other ions such as Ti, Li, Cr and Na are commonly also present in minor amounts. Vermiculites with dioctahedral character are uncommon but are known to occur in soils.

Vermiculites and smectites both contain interlayer water molecules but the amount of water taken up by natural vermiculites is less variable, and the maximum for them corresponds with two layers of water molecules in each available space. The ranges of substitution which occur in most natural vermiculites are indicated by the formula

$$(Mg,Ca)_{0.6-0.9}\underbrace{Mg_{4.5-5.0}(Fe^{3+},Al)_{1.5-1.0}}_{6.0}\underbrace{Al_{2.2-2.6}Si_{5.8-5.4}}_{8.0}O_{20}(OH)_4\cdot(H_2O)_{7.0-9.0}$$

Vermiculites also show the property of absorbing organic liquids between their layers.

The unusual phenomenon of exfoliation occurs when vermiculite is heated suddenly to about 300ºC or higher, and is due to the rapid generation of steam which cannot escape without buckling and separating the structural layers. Exfoliation, which may cause as much as a 30-fold expansion in the direction

Downloaded from https://pubs.geoscienceworld.org/books/chapter-pdf/3760854/9780903056434_ch56.pdf
by guest

perpendicular to the cleavage planes, can also be brought about by treatment with hydrogen peroxide (H_2O_2) and it is thought that in this case oxygen is liberated by chemical action with interlayer magnesium ions. Vermiculite does not exfoliate if the water is driven off slowly, even at 250ºC.

The DTA curves of Mg-vermiculite show endothermic peaks at about 140ºC and 240ºC, corresponding with the transition from two layers of water to one, and one to zero. These water losses are reversible up to about 550ºC but at higher temperatures the structure breaks down by the endothermic loss of (OH) ions and by exothermic reactions at temperatures depending upon the chemistry of the initial material, but generally beginning at about 800ºC.

Optical and physical properties

Although vermiculite occurs with minute particle sizes, e.g. as a constituent of soil clays, it is also found in large crystalline plates, principally when it is an alteration product of biotite. Optical properties may therefore be measured more easily than for other clay minerals, but again variable hydration and cation content lead to a range of values. The optical properties are close to those of phlogopite but some vermiculites contain considerable amounts of iron and these have higher refractive indices. Also, values of 2V tend to be higher than those for phlogopite.

Distinguishing features

Vermiculites generally have lower refractive indices than biotite or hydrobiotite and higher refringence than chlorites. Their birefringence is lower than that of either biotite or talc. The X-ray powder patterns of vermiculites which have been treated with an ammonium salt and glycerol serve to distinguish them from montmorillonite and chlorite. The principal differences between vermiculites and smectites may be summarized as follows.

(1) Vermiculites generally have a larger grain size.
(2) Vermiculites have higher cation exchange capacity and greater substitution of $^{[4]}$A] for Si.
(3) In vermiculite the deficiency of positive charge in the 'talc' layers lies mainly in the tetrahedral component.
(4) Vermiculites take up at most one layer of glycerol molecules, giving a basal spacing of about 14 Å, whereas smectites take double layers, the basal spacing swelling to 17 Å.
(5) Smectites dehydrate more readily, and vermiculites rehydrate more readily.
(6) Vermiculites are formed mainly by the weathering of large flakes of biotite.

The distinction between the two groups, however, is not precise, and some smectites (particularly saponites) possess several of the above characteristics.

Paragenesis

The major commercial deposits of vermiculite are in ultrabasic and basic rocks where the mineral occurs as an alteration product of phlogopite/biotite, chlorite and pyroxene, by weathering, or hydrothermally, or by percolating groundwater. When derived in this way from mica it is found as large crystal pseudomorphs. Vermiculite may be derived in a similar fashion from biotites in other types of rock (e.g. gneisses and schists). It is also widespread as a clay-size constituent of certain soils. Vermiculite is also found at the contacts between acid intrusives and basic or ultrabasic rocks, in which circumstances it may be associated with corundum, apatite, serpentine, chlorite or talc.

Vermiculites derived from mica-type materials are comparatively rare in marine sediments; those which do occur are derived from non-micaceous sources such as volcanic material, chlorite and hornblende. Vermiculites (generally containing little iron) are also found associated with carbonatites, and in metamorphosed limestones.

Further reading

Calle, C. de la and Suquet, H. (1988) Vermiculite. Pp. 455–496 in: *Hydrous Phyllosilicates (Exclusive of Micas)* (S.W. Bailey, editor). Reviews in Mineralogy, **19**, Mineralogical Society of America, Washington, D.C.

Newman, A.C.D. (Editor) (1987) *Chemistry of Clays and Clay Minerals*, Monograph **6**, Mineralogical Society, London.

Shirozu, H. and Bailey, S.W. (1960) Crystal structure of a two-layer Mg-vermiculite. *American Mineralogist*, **51**, 1124–1143.

Downloaded from https://pubs.geoscienceworld.org/books/chapter-pdf/3760854/9780903056434_ch56.pdf
by guest

CLAY MINERALS

1. The majority of clay minerals are aluminosilicates which have layered crystal structures and occur as very fine-grained ($\leqslant 4$ μm) platy particles, mostly as a result of weathering or low-temperature hydrothermal alteration of parent rocks. They therefore cannot be identified in thin section as their crystals are too small to be seen optically; other methods (usually X-ray diffraction) are used to identify them.

2. The structural layers are made up of (Si,Al)−O tetrahedra (T) and (Al,Mg,Fe)−O octahedra (O).

3. The T and O components can be linked in T−O pairs, with a T:O ratio of 1:1, as in the kaolinite group, or in T−O−T 'sandwiches' with a T:O ratio of 2:1, as in illites, smectites and vermiculites (Fig. 159).

4 In illites and smectites the composite layer has a net negative charge which is balanced by an interlayer of large cations (K, Na, Ca), and in vermiculite* mainly by Mg. In the kaolinite* group minerals there are no interlayer cations.

5. The interlayer cations are fixed in illites but exchangeable in smectites and vermiculites.

6. In smectites, vermiculites and halloysite (a kaolinite-type mineral) the interlayer space contains water molecules.

7. The repeat distances perpendicular to the structural layers are: ~7, ~10, ~15 and ~14.5 Å in kaolinite, illite, smectite and vermiculite, respectively.

8. Smectites can absorb or lose interlayer water (also organic liquids), so that their basal repeat distances vary depending on whether they are wet or dry, a useful diagnostic feature measurable by XRD.

9. Clay specimens not uncommonly contain mixed layers of more than one of the above-mentioned four groups, or contain mixed layers of clay and non-clay layered minerals.

* For chemical formulae see main text.

Downloaded from https://pubs.geoscienceworld.org/books/chapter-pdf/3760854/9780903056434_ch56.pdf
by guest

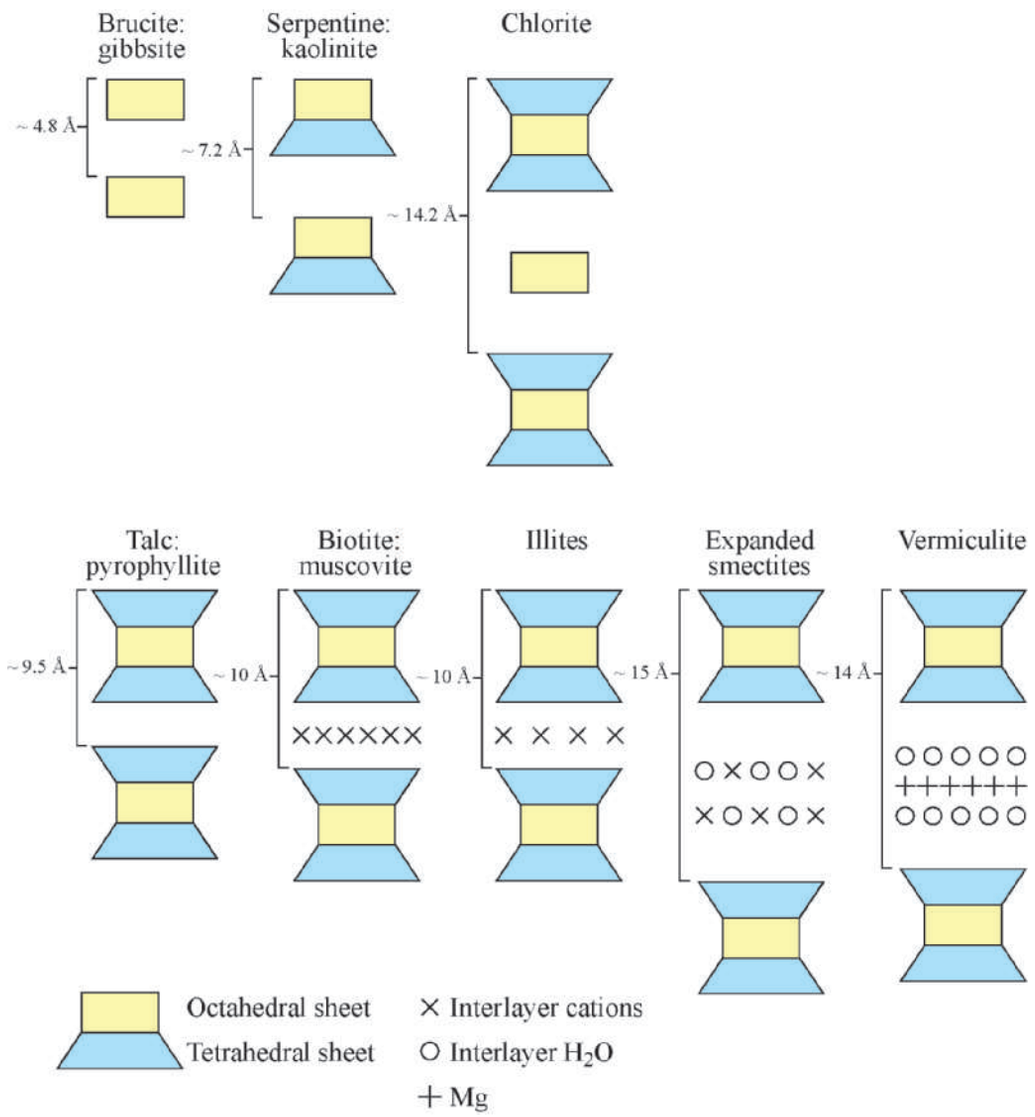


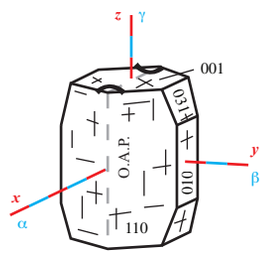
Fig. 159. Schematic illustration of the structures of common dioctahedral and trioctahedral layered silicates.

Downloaded from https://pubs.geoscienceworld.org/books/chapter-pdf/3760854/9780903056434_ch56.pdf
by guest

Prehnite $Ca_2(Al,Fe^{3+})[AlSi_3O_{10}](OH)_2$

Orthorhombic (+)

α	1.611–1.621
β	1.615–1.637
γ	1.632–1.673
δ	0.022–0.051
$2V_\gamma$	62–69º
Orientation	α = *x*, γ = *z*; O.A.P. (010)
D (g/cm^3)	2.90–2.97
H	6–6.5
Cleavage	{001} good, {110} weak
Twinning	Fine lamellar twinning may occur
Colour	Pale green, yellow, grey or white; colourless in thin section
Unit cell	*a* 4.61–4.65 Å, *b* 5.47–5.49 Å, *c* 18.51 Å, *V* 470–472 Å^3 *Z* = 2; space group *P*2*cm*, *P*2/*n* (with α ~ 90.6º) or *Pncm*



Prehnite is green, yellow or white in hand specimen and generally colourless in thin section. The variation in colour in hand specimen is due to the substitution of Fe^{3+} for Al. The relief is relatively high with high birefringence. Prehnite occurs as a secondary or hydrothermal mineral in veins and amygdales in basic volcanic rocks and in contact metamorphism of calcareous rocks. It is an important phase in the prehnite-pumpellyite facies of low-grade regional metamorphism and burial metamorphism.

Structure

In prehnite the aluminium ions occur in two different sites: four-coordinated Al forms tetrahedra with four oxygens and is linked with Si–O tetrahedra to form a sheet of type $[Si_3AlO_{10}]$. This sheet lies parallel to (001) and gives the good (001) cleavage. These silicate sheets are linked with Al–OH–Ca chains parallel to (010), the Al here being six-coordinated (4 O and 2 OH) and the Ca seven-coordinated (5 O and 2 OH).

Chemistry

The only appreciable substitution in prehnite is of Fe^{3+} for Al, the Fe/(Fe + Al) ratio ranging up to ~0.32; the alkalis, manganese and magnesium are usually low (Table 34). Most of the structural water is lost only on heating to between 600 and 750ºC; prehnite cannot therefore be classed with the zeolites with which it is commonly associated. Prehnite can be synthesized fairly rapidly at relatively low temperatures (e.g. 350ºC at 0.3 GPa), from a glass of appropriate composition. At higher temperatures it breaks down to anorthite + wollastonite + H_2O. The reaction of chlorite + prehnite to give pumpellyite + quartz, which is characteristic of the transition from the prehnite to the pumpellyite zone in the prehnite-pumpellyite facies, occurs at 260ºC at 0.7 GPa. The low-temperature alteration of prehnite may produce a zeolite or a chloritic material.

Optical and physical properties

The refractive indices and birefringence increase with increasing iron content; the density also increases. Some specimens show optical anomalies including wavy or incomplete extinction and abnormal interference colours, due possibly to the intimate intergrowth of two structural types. Distinct individual crystals of prehnite are relatively rare; tabular groups, barrel-shaped aggregates and reniform globular masses are common often giving a characteristic imperfect columnar 'bow-tie' or 'hour-glass' appearance.

Distinguishing features

Prehnite differs from many hydrothermal minerals in its relatively high relief and its strong birefringence.

Downloaded from https://pubs.geoscienceworld.org/books/chapter-pdf/3760861/9780903056434_ch57.pdf
by guest

Table 34. Prehnite analyses.

	1	2	3	4
SiO_2	43.7	42.41	42.89	43.54
Al_2O_3	24.05	22.45	19.33	16.38
Fe_2O_3	0.93	3.19	6.05	10.56
MnO	0.00	0.07	–	0.01
MgO	0.11	–	–	–
CaO	26.85	26.78	25.84	24.95
Na_2O	0.04	–	–	0.27
K_2O	0.00	–	–	0.05
H_2O	4.54	4.50	–	4.50
Total	100.33	99.40	94.54	100.44
α	1.615	–	–	1.621
β	1.624	–	–	1.657
γ	1.643	–	–	1.673
$2V_\gamma$ (°)	69	–	–	68
D	2.93	–	–	2.97

Numbers of ions on the basis of 24 (O,OH) or 22 O

	1		2		3		4	
Si	5.990	8.00	5.922	8.00	6.083	8.00[a]	6.142	8.00
Al	2.010		2.078		1.871		1.858	
Al	1.874	1.97	1.616	1.95	1.360	2.01	0.865	1.99
Fe^{3+}	0.096		0.335		0.646		1.121	
Mn	–	3.96	0.008	4.01	–	3.93	0.001	3.88[b]
Mg	0.019		–		–		–	
Ca	3.943		4.006		3.926		3.770	
K	–		–		–		0.009	
OH	4.050		4.181		–		4.234	

1 Translucent, very pale green, botryoidal prehnite, in cavities in dolerite, Prospect Quarry, New South Wales, Australia (Coombs *et al.*, 1959, *Geochim. Cosmochim Acta*, **17**, 227–50; includes FeO 0.03, P_2O_5 0.02, Ag 0.01, Pb 0.04, SnO 0.01, H_2O^- 0.03).
2 Secondary prehnite in chlorite, Galway granite, Connemara, Ireland (Leake, B.E., 1998, *Mineral. Mag.*, **62**, 381–6).
3 Prehnite, prehnite-pumpellyite-epidote metabasite, Elk River, Karmutsen area, Vancouver Island, British Columbia (Terabayashi, M., 1998, *Contrib. Mineral. Petrol.*, **100**, 53–107; includes TiO_2 0.43).
4 Prehnite, altered gabbro-dolerite, Noril'sk pluton, Russia (Zolotukin, V.V. *et al.*, 1965, *Dokl. Acad. Nauk SSSR (Earth Sci. Sect.)*, **164**, 138–41; includes FeO 0.18).

[a] Includes Ti 0.046.
[b] Includes Fe^{2+} 0.021, Na^+ 0.074.

Lawsonite has lower birefringence and slightly higher refractive indices; datolite, which may be found associated with prehnite, has only a very poor cleavage and has a higher birefringence, while andalusite, topaz and wollastonite all have lower birefringence.

Paragenesis

Prehnite occurs fairly commonly in basic volcanic rocks as a secondary or hydrothermal mineral in veins, cavities and amygdales, in this assemblage it is associated with calcite and zeolites. It is also found in veins in plutonic rocks and as pseudomorphs after such minerals as laumontite and clinozoisite. It is a well known constituent of the Deccan Traps of western India, and is found in well developed crystals in the basalt. In Prospect Quarry, New South Wales, Australia, it occurs as translucent, very pale green crystals (Table 34, analysis 1) in dolerite, and in association with zeolites in the Paterson basalt quarries, New Jersey, USA.

In metamorphic rocks it occurs in contact-altered impure limestones and marls, and in rocks which have undergone calcium metasomatism such as rodingites or garnetized gabbros, often associated with diopside and hydrogrossular. Fine crystals of prehnite are associated with grossular, diopside and vesuvianite in rodingite dykes intruding peridotite at the Jeffrey mine, Asbestos, Quebec. It is also of fairly common occurrence as interleaving lenticular inclusions along the cleavage planes of biotite or chlorite (analysis 2).

In low-grade metamorphic rocks, the prehnite-pumpellyite facies bridges the gap between low-grade metamorphism and diagenetic processes involving thick sedimentary sequences in mineralogical and textural reconstitution. A prehnite-actinolite facies between the zeolite and greenschist facies was suggested by Liou *et al*. (1985) at temperatures in the range 200–350ºC at a maximum fluid pressure of 0.2–0.3 GPa for the Fe-free system. The definitive reaction separating it from the prehnite-pumpellyite facies is prehnite + chlorite + quartz → pumpellyite + H_2O. With increasing temperatures, prehnite-actinolite assemblages give way directly to the greenschist facies by the reaction prehnite + chlorite + quartz → clinozoisite + tremolite + H_2O. A rather different petrogenetic grid based purely on thermodynamic calculations is given in Fig. 160.

The prehnite-bearing rocks of the Upper Triassic Karmutsen area of Vancouver Island, British Columbia, are an example of the contact metamorphism of basaltic flows, pillow lavas and pillow breccias in the aureole of the Jurassic Coast Range plutons, where the thermal effects have been superimposed on prehnite-pumpellyite facies regional metamorphic rocks. In an area of 6 km-

Downloaded from https://pubs.geoscienceworld.org/books/chapter-pdf/3760861/9780903056434_ch57.pdf
by guest

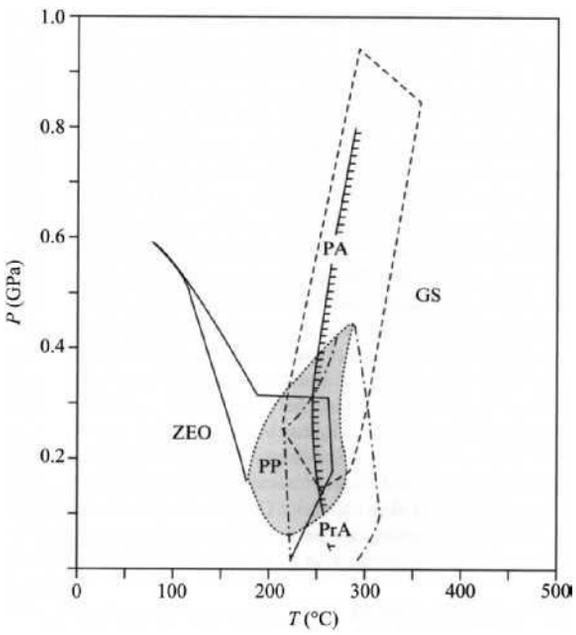


Fig. 160. $P-T$ fields for various low-grade metamorphic facies. The boundaries for the prehnite-actinolite facies (PrA) and the prehnite-pumpellyite facies (PP) are shown as dash-dotted and dashed lines, respectively. The minimum low-T limit of the greenschist facies (GS) is shown by solid lines with ticks. ZEO: zeolite facies; PA: prehnite-pumpellyite (after Frey *et al*., 1991, *J. Metam. Geol*., **9**, 497–509).

thick Karmutsen metabasic rocks, Terabayashi (1988) found that the $Fe^{3+}/(Fe^{3+} + Al)$ ratio in prehnite (e.g. Table 34, analysis 3) systematically decreases with metamorphic grade. The appearance of prehnite depends greatly on the bulk FeO/MgO ratio which may explain the relative scarcity of prehnite in common metabasic rocks.

In North Wales, a thick concordant dolerite sill intruded into Ordovician volcanic and pyroclastic rocks underwent regional metamorphism which produced prehnite-pumpellyite-epidote assemblages. A metamorphic temperature of 310ºC at 0.185 GPa was estimated using the $P-T-X$ grid of Liou *et al*. (1985), implying a field gradient of ~44ºC/km. Assuming that the regional metamorphism was due to depth of burial, an overburden thickness of ~7 km is indicated.

The widespread development of prehnite by very low-grade (burial) metamorphism of greywackes, argillites and cherty rocks is known, the rocks appearing little altered in hand specimen although in thin section the alteration of plagioclase, glass, radiolaria and matrix to prehnite is observed.

The reaction:

$$5\,\text{prehnite} \rightleftharpoons 2\,\text{grossular} + 2\,\text{zoisite} + 3\,\text{quartz} + 4\,H_2O$$

probably defines the upper limit of prehnite stability and occurs at about 400ºC at 0.2–0.4 GPa where $P_{H_2O} = P_{total}$. In natural environments the temperature range of the prehnite-pumpellyite facies at 0.3 GPa has been estimated as ~250–380ºC. The disappearance of prehnite in metagreywacke assemblages separates the prehnite-pumpellyite from the pumpellyite-actinolite facies.

Further reading

Bevins, R. and Merriman, R.J. (1988) Compositional controls on coexisting prehnite-actinolite and prehnite-pumpellyite facies assemblages in the Tal y Fan metabasite intrusion, North Wales: implications for Caledonian metamorphic field gradients. *Journal of Metamorphic Geology*, **6**, 17–39.

Cho, M. and Liou, J.G. (1987) Prehnite-pumpellyite to greenschist facies transition in the Karmutsen metabasites, Vancouver Island, B.C. *Journal of Petrology*, **27**, 467–494.

Coombs, D.S. (1960) Lower grade mineral facies in New Zealand. *Reports of the 21st International Geological Congress, Section*, **13**, 339–351.

Frey, M., de Capitani, C. and Liou, J.G. (1991) A new petrogenetic grid for low grade metabasites. *Journal of Metamorphic Geology*, **9**, 497–509.

Liou, J.G. (1971) Synthesis and stability relations of prehnite, $Ca_2Al_2Si_3O_{10}(OH)_2$. *American Mineralogist*, **56**, 507–511.

Liou, J.G., Maruyama, S. and Cho, M. (1985) Phase equilibria and mixed paragenesis of metabasites in low-grade metamorphism. *Mineralogical Magazine*, **49**, 321–333.

Terabayashi, M. (1988) Actinolite-forming reaction at low pressure and the role of Fe^{2+}–Mg substitution. *Contributions to Mineralogy and Petrology*, **100**, 268–280.

Zolotukhin V.V., Vasil'yev, Yu.R. and Zyuzin, N.I. (1965) [Iron-rich modification of prehnite and a new diagram for prehnites.] *Doklady Akademi Nauk SSSR (Earth Sciences Section)*, **164**, 138–141.

Downloaded from https://pubs.geoscienceworld.org/books/chapter-pdf/3760861/9780903056434_ch57.pdf
by guest

Feldspar Group

Alkali Feldspars	**$(K,Na)[AlSi_3O_8]$ with minor $CaAl_2Si_2O_8$**
Barium Feldspars	**$(K,Na,Ba)[(Al,Si)_4O_8]$ to $Ba[Al_2Si_2O_8]$**
Plagioclase Feldspars	**$Na[AlSi_3O_8]-Ca[Al_2Si_2O_8]$ with minor $KAlSi_3O_8$**

Introduction

The members of the feldspar group of minerals are the most abundant constituents of igneous rocks. The ubiquity of the feldspars together with their wide range in composition has led, inevitably, to their use as a primary tool in the classification of the igneous rocks. In the great majority of these rocks, whether acid, alkaline, intermediate or basic, the feldspars are the major constituents, and they are absent only from some ultrabasic and rare alkaline rocks. Feldspars are the most important constituents of the simple pegmatites and are common in mineral veins. They are major constituents of most gneisses and schists, and occur also in many thermally as well as regionally metamorphosed rocks. Although the feldspars are susceptible to alteration and weathering they are second in abundance to quartz in the arenaceous sediments, in which they occur as detrital grains and as authigenic crystals. It is only in the argillaceous, and to a greater degree in the carbonate, rocks that the feldspars are of relatively minor importance.

Common feldspars are ternary solid solutions of three *components*: $NaAlSi_3O_8$, albite (Ab), $KAlSi_3O_8$, orthoclase (Or), and $CaAl_2Si_2O_8$, anorthite (An) (Fig. 161a). Solid solutions with a predominance of An + Ab are called plagioclase feldspars, those predominantly composed of Ab + Or are called alkali feldspars. At stable equilibrium a rock can contain only two feldspar phases, a plagioclase phase (called below PL) and an alkali feldspar phase (AF), but in practice more than two phases are often present metastably. At high temperatures feldspars exhibit extensive solid solution and can occur anywhere within the coloured area on Fig. 161a. The boundary between plagioclase and alkali feldspar can most usefully be placed on the line where An = Or. At low temperatures (Fig. 161b) solid solution is limited to the small black areas. Unless they have been cooled very rapidly to surface temperature, feldspar crystals in the coloured areas are intimate intergrowths on a wide range of scales. In the alkali feldspar field the intergrowths are commonly visible in an optical microscope, and are known generically as perthite. In the plagioclase field intergrowths are almost always sub-optical.

To achieve a proper understanding of feldspar relationships it is necessary to characterize them not only according to chemical composition, but also according to structural state, the latter depending on the temperature of crystallization and on subsequent thermal history. Feldspars which retain a structure appropriate to their high-temperature formation are called high-temperature feldspars; most feldspars of volcanic rocks are of this type. Low-temperature feldspars are those with structure appropriate either to crystallization at lower temperatures, or to slow cooling from elevated temperatures as, for example, in plutonic rocks. Feldspars may also occur in intermediate-temperature structural states. Although the terms high, low and intermediate are very useful, they do not have sharply defined boundaries within what is a range of structural states.

The difference between high- and low-structural state in a feldspar depends on the degree of ordering of Al and Si atoms between tetrahedral sites. It can involve lattice geometry with or without a change of symmetry or space group. The stable structure is disordered at high temperatures and ordered at low temperatures. Information about ordering can be obtained using optics, provided the chemical composition is known, from cell parameters obtained by X-ray and electron diffraction, or most directly from interatomic distances determined by structural refinement. Methods such as nuclear magnetic resonance, infrared and Raman spectroscopy can also be used.

In feldspars, Si–Al ordering usually takes place, to varying extents, during cooling of all except the most rapidly cooled alkali feldspars. In Or-rich feldspars it leads to a symmetry change, from monoclinic, disordered sanidine to triclinic, ordered microcline (Fig. 161b), with accompanying change in optical properties. Microcline is structurally triclinic but individual crystals usually appear macroscopically monoclinic because of fine-scale 'tartan' twinning (Fig. 181, p. 268). With increasing order, microcline shows a continuous gradation in deviation of the α and γ cell angles from 90°, up to 90.6° and 87.7°, repectively; this is variously called the 'triclinicity' or

Downloaded from https://pubs.geoscienceworld.org/books/chapter-pdf/3761008/9780903056434_ch58.pdf
by guest

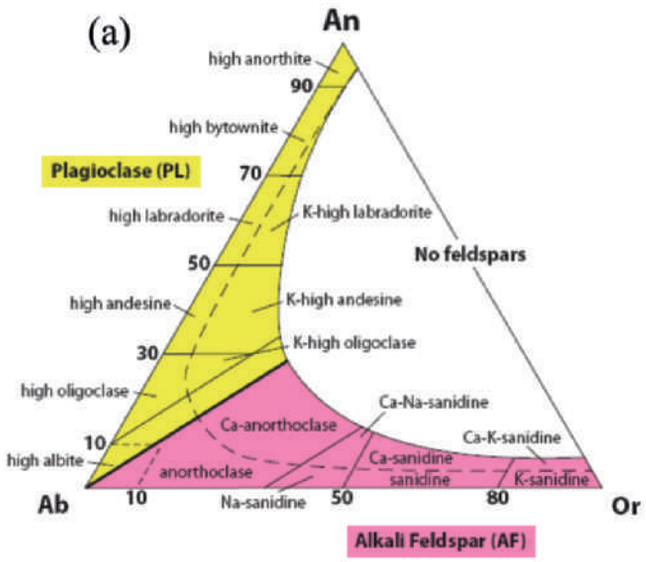
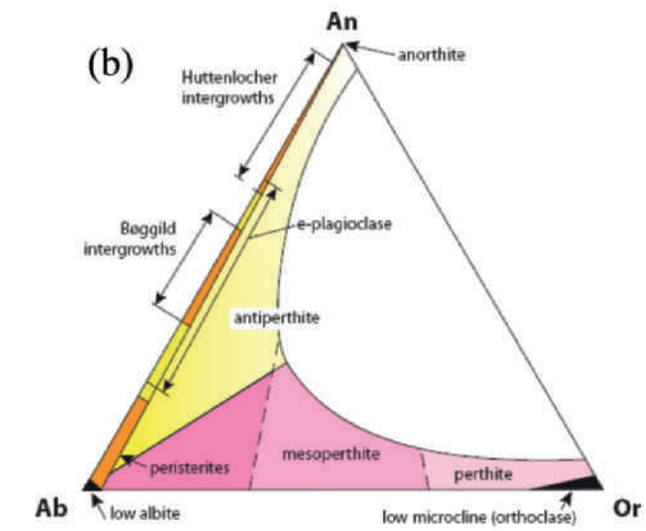


Fig. 161. (a) The maximum extent of solid solution in feldspars at >1000ºC. No feldspars crystallize in the unshaded field. The boundary between plagioclase (PL) and alkali feldspar (AF) is placed, for convenience only, on the line where An = Or. The named subdivisions of PL at 10, 30, 50, 70 and 90 mol% An are based solely on composition. Anorthoclase and high albite are triclinic at room temperature but are monoclinic when *observed* at elevated temperature because of the shearing transformation. Sanidine is monoclinic at all temperatures (after Smith, J.V. & Brown, W.L., 1988, *Feldspar Minerals, vol. 1.*, Springer-Verlag).



(b) Feldspars stable below ~300ºC. Solid solution is limited to the black shaded areas. In all coloured areas the feldspars form intergrowths. In AF these are often visible in the optical microscope but in PL they are almost always sub-optical except in some Or-rich plagioclase (antiperthite). The stable phases are triclinic low microcline, low albite and anorthite, all with Si−Al order. Orthoclase is a metastable monoclinic Or-rich feldspar with a 'tweed' microtexture composed of alternating triclinic ordered domains at the scale of a few nanometres. In PL, ordering (giving low plagioclase) leads to changes in lattice type and optical properties but not crystal class. PL in the range ~An_{25}−An_{75} has a structure known as e-plagioclase in which thin slabs with albite-like and anorthite-like ordering patterns alternate with a periodicity that is out of step ('incommensurate') with the overall lattice. (modified slightly after Smith, J.V. & Brown, W.L., 1988, *Feldspar Minerals, vol. 1.*, Springer-Verlag).

(better) the 'obliquity' of the feldspar. Microcline with maximum obliquity is called low microcline, that with less obliquity is intermediate microcline. Although intermediate microcline occurs naturally it may be a transitional metastable phase. Ordering and disordering are relatively slow processes, and microcline remains triclinic for many hours even near its melting point.

At high temperatures disordered alkali and plagioclase feldspars form continuous solid solutions which may be preserved to room temperature by very rapid cooling. Under most cooling conditions alkali feldspars undergo exsolution, initially by solid-state diffusion of Na and K, giving regular two-phase perthitic intergrowths usually on scales up to a few μm. Subsequently these intergrowths are often partially or completely modified and coarsened by dissolution−reprecipitation reactions in aqueous fluids. Intergrowths visible with the unaided eye are called macroperthite, at the optical scale microperthite, and those requiring electron microscopy, cryptoperthite. Exsolution is driven by the large difference in ionic radius between $^{[8]}Na^{+}$ (1.18 Å) and $^{[8]}K^{+}$ (1.51 Å). Because Al and Si diffusion is much slower than that of the alkali ions it is possible to have cryptoperthitic intergrowths with Si−Al disorder. Perthite *sensu stricto* refers to intergrowths with a predominance of an Or-rich phase (Fig. 161b), antiperthite has a predominance of an albite or Ca-bearing plagioclase phase, and mesoperthites have roughly equal proportions of Or- and Ab-rich phases. Compositional and scale terms may be combined, as in 'cryptomesoperthite'. Some alkali feldspars display iridescence, caused by diffraction of light by lamellar cryptoperthitic intergrowths. The architectural variety of syenite, known as larvikite, is a familiar example.

The nomenclature of high temperature (i.e. highly to moderately disordered) alkali feldspars is based on crystal symmetry (Fig. 161a). Feldspars in the sanidine field are monoclinic from room temperature up to their

Downloaded from https://pubs.geoscienceworld.org/books/chapter-pdf/3761008/9780903056434_ch58.pdf
by guest

melting point. Those with substantial Na are called sodian sanidine. Feldspars in the anorthoclase field are triclinic at room temperature but become monoclinic instantaneously when heated to a temperature which depends on (Ab + An):Or. The symmetry change is reversed instantaneously on cooling, and the monoclinic form can be observed only at elevated temperatures. This is called a 'shearing' or 'displacive' transformation because it requires only changes in the relative tilt of (Si,Al)–O tetrahedra, without breaking of bonds. Fully disordered high albite is monoclinic above 980ºC, forming monalbite, and the anorthoclase field extends slightly into the plagioclase field as defined on Fig. 161b. All other plagioclase is triclinic at all temperatures.

The word 'orthoclase' is used both for the $KAlSi_3O_8$ (Or) component in feldspars and also for a highly ordered monoclinic potassium feldspar with a microstructure of alternating ordering domains on the scale of a few unit cells. This 'tweed' microtexture (Fig. 198, p. 288) forms during continuous ordering of low sanidine. The transition to twinned microcline is difficult to accomplish by a continuous process and has not been achieved experimentally. In Nature it often involves fluid–feldspar reaction or deformation. Many alkali feldspars in plutonic rocks are mixtures of orthoclase and microcline (Fig. 198). Ordering in albite probably occurs at a similar rate to that in sanidine, but there is no symmetry change and the high–low albite transformation has been accomplished in the laboratory.

Adularia is a low-temperature potassium feldspar with a characteristic {110} habit. This habit is characteristic of feldspars growing in low temperature veins and during diagenesis. The habit also commonly defines subgrains in feldspars that have undergone replacement reactions. The state of ordering varies from place to place within individual crystals leading to gradational optical properties and diffuse spots in single crystal X-ray or electron diffraction.

Plagioclase feldspars also form a 'high' disordered series which is a continuous solid solution. It is divided for practical purposes into six compositional ranges on a molecular (Ab:An) basis: albite, oligoclase, andesine, labradorite, bytownite, anorthite (Fig. 161a). The ranges are unrelated to underlying changes in structure or space group. Extra refinement is sometimes added by terms such as 'sodic-oligoclase' or 'calcic-labradorite'. In nature end-member anorthite is always fully ordered.

Investigations by X-ray diffraction and electron microscopy show that ordered ('low') plagioclases are intergrowths of two or more phases. The ionic radius of $^{[8]}Ca^{2+}$ (1.12 Å) is very similar to that of Na, and the intergrowths arise because of variation in patterns of ordering in solid solutions in which the Si:Al ratio is variable. The Si:Al ratio is coupled to that of Na:Ca to obtain charge-balance so that the distribution of Na and Ca is conditional on Si–Al ordering. As Si and Al diffusion is slow, intergrowths in plagioclase feldspars are usually sub-optical, often on scales of only a few nanometres. It seems likely that the only ordered plagioclase feldspars stable at room temperature are nearly pure low albite and anorthite.

The compositional ranges of the peristerite, Bøggild and Huttenlocher intergrowths are shown in Fig. 161b. There is also a very fine-scale periodic structure called e-plagioclase that can coexist with them. As optical methods of obtaining plagioclase composition, and electron microprobe analysis, average all these fine microstructures, the same nomenclature for the compositional ranges is employed for both high- and low-temperature plagioclase. The only easily obtained evidence of the fine microtextures is iridescence, the best known example being 'labradorescence' caused by Bøggild intergrowths.

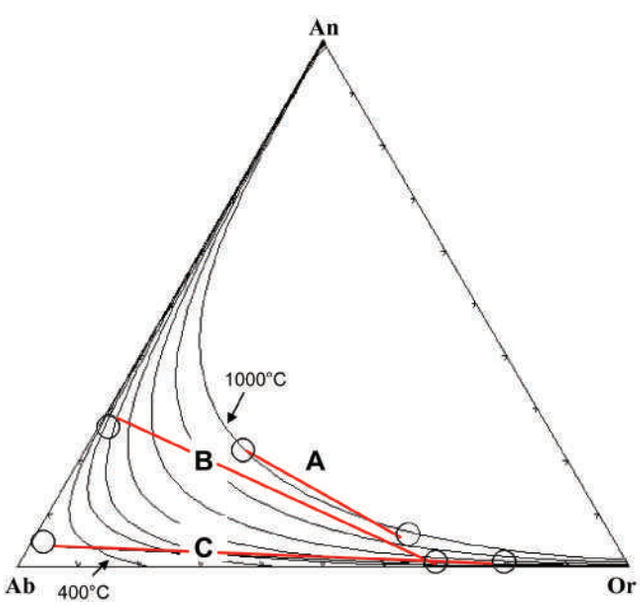


Fig. 162. Isotherms on the ternary feldspar solvus with examples of tielines for some natural feldspar pairs obtained using two-feldspar geothermometry. The isotherms are at 100ºC intervals and apply to disordered feldspars; pressure is 100 MPa. Pair **A** are the bulk compositions of a cryptomesoperthitic feldspar (left) and a cryptoperthitic feldspar (right) in interstices between plagioclase crystals in an alkali gabbro from the Klokken intrusion, South Greenland. The calculated temperature is 950ºC. Pair **B** is an oligoclase coexisting with a bulk film cryptoperthite (Fig. 172, p. 262) in the Shap granite, Cumbria, UK. The calculated temperature is 610ºC. Pair **C** are the Ab-rich phase and the Or-rich phase in a coarse patch perthite (Fig. 192, p. 279, right-hand side) from the Klokken intrusion. The calculated temperature is 390ºC. The temperatures calculated for **B** and **C** are low by ~80ºC because the feldspars are likely to have been fully or partially ordered when in compositional equilibrium. Calculated using the using the computer package SOLVCALC.

Downloaded from https://pubs.geoscienceworld.org/books/chapter-pdf/3761008/9780903056434_ch58.pdf
by guest

The equilibrium distribution of the three components, Ab, Or and An, between two feldspar phases (PL and AF) depends on temperature and pressure and forms the basis of a two-feldspar geothermometer. It is necessary to make an estimate of pressure and to know the ternary composition of both alkali feldspar and plagioclase phases, which at any temperature will lie on a unique tie-line on the ternary feldspar solvus (e.g. Fig. 162). The thermometer is extremely sensitive to low concentrations of Or in PL, and low concentrations of An in AF. However, because only feldspar components are involved in the exchange reaction the thermometer is independent of all other components in the rock or system of interest. Figure 162 is based on the thermodynamic properties of disordered feldspars and is therefore most reliable for high-temperature feldspar pairs.

The barium ion is present in small quantities in the majority of feldspars as the $BaAl_2Si_2O_8$ component, celsian (Cn). In general, feldspars are considered to be barium varieties when their BaO content is >2 wt.%. There is a continuous solid solution between $KAlSi_3O_8$ and $BaAl_2Si_2O_8$. Those with more than 75 mol% of Cn are called celsian, and those with 15–75 mol% Cn are called hyalophane.

The name feldspar (in American work felspar) as originally given was feldtspat and it is believed that this had reference to the presence of the spar (spath) in tilled fields (Swedish: *feldt* or *fält*) overlying granite, rather than to the German *Fels*, meaning rock.

Further reading

Brown, W.L. (Editor) (1984) *Feldspars and Feldspathoids. Structures, Properties and Occurrences*. NATO ASI Series C 137. D. Reidel Publishing Company, Dordrecht, 541 pp.

Deer, W.A., Howie, R.A. and Zussman, J. (2001) *Framework Silicates: Feldspars*. *Rock Forming Minerals, Volume 4A, Second Edition*. The Geological Society, London, 972 pp.

Parsons, I. (Editor) (1994) *Feldspars and their Reactions*. NATO ASI Series C 421. Kluwer Academic Publishers, Dordrecht, pp. 650.

Ribbe, P.H. (Editor) (1983) *Feldspar Mineralogy (2nd Edition)*. Reviews in Mineralogy, **2**. Mineralogical Society of America, Washington, D.C., 362 pp.

Smith, J.V. (1974a) *Feldspar Minerals vol. 1, Crystal Structure and Physical Properties*. Springer-Verlag, Berlin, xix + 627 pp.

Smith, J.V. (1974b) *Feldspar Minerals vol. 2, Chemical and Textural Properties*. Springer-Verlag, Berlin, xii + 690 pp.

Smith, J.V. and Brown, W.L. (1988) *Feldspar Minerals vol. 1, Crystal Structure, Physical, Chemical and Microtextural Properties (Second Revised and Extended Edition)*. Springer-Verlag, Berlin, xvii + 828 pp.

Downloaded from https://pubs.geoscienceworld.org/books/chapter-pdf/3761008/9780903056434_ch58.pdf
by guest

Monoclinic (−), Triclinic (+) or (−)

	High albite	Low albite	High sanidine	Low microcline
α	1.527	1.529	1.519	1.518
β	1.534	1.533	1.523	1.522
γ	1.536	1.539	1.524	1.525
δ	0.009	0.010	0.005	0.007
$2V_\alpha$	47°	103°	54°[a]	83°[b]
Extinction angles[c]	8°	20°	5°	5°
D (g/cm^3)	2.60	2.61	2.56	2.56
H	6−6½			
Cleavage	(001), (010) common, perfect; (100), {110} less perfect; partings in $(\bar{2}01)$ and non-integral planes between $(\bar{6}01)$ and $(\bar{8}01)$ (the Murchison plane)			
Twinning	Simple twins can be developed in both monoclinic and triclinic feldspars, on the Carlsbad, Baveno and Manebach laws. Repeated twins are exhibited only by triclinic feldspars, on the Albite and Pericline laws. Combined Albite and Pericline twins are often called 'tartan' twins (for details see pp. 264−269).			
Colour	Colourless in small grains when clear and non-turbid. Large masses of non-turbid feldspar are dark green or bluish-black. Turbid crystals are white, cream, pink and red: green and yellow feldspars result from high Pb and Fe^{3+}, respectively.			

Unit cell	High albite	Low albite	High sanidine	Low microcline
a (Å)	8.16	8.14	8.60	8.59
b (Å)	12.87	12.79	13.03	12.97
c (Å)	7.11	7.16	7.18	7.22
α	93.5°	94.3°	90°	90.6°
β	116.4°	116.6°	116.0°	115.9°
γ	90.3°	87.7°	90°	87.7°
Z	4	4	4	4
Space Group	$C\bar{1}$	$C\bar{1}$	$C2/m$	$C\bar{1}$

The alkali feldspars are major constituents of acid and alkaline plutonic igneous and volcanic rocks, acid gneisses, granulite-facies rocks and, usually as potassium rich orthoclase, in thermally metamorphosed argillaceous rocks. They persist as detrital grains in some siliciclastic sedimentary rocks. Both sodium- and potassium-rich feldspars grow as discrete crystals or overgrowths during diagenesis. Almost all alkali feldspars are ternary solid solutions of *three components*: $NaAlSi_3O_8$, albite (Ab), $KAlSi_3O_8$, orthoclase (Or), and $CaAl_2Si_2O_8$, anorthite (An). At high temperatures, Or and Ab form a continuous solid solution between high albite and high sanidine, with a disordered (Si,Al) distribution. They may contain significant An. Except when cooled very rapidly in volcanic rocks, alkali feldspar solid solutions unmix to an intergrowth of Or- and Ab-rich phases known generically as perthite. In cryptoperthite the intergrowth is sub-optical, microperthite is visible in an optical microscope, and macroperthite is visible to the unaided eye. The temperature at which exsolution begins depends on Na:K ratio, pressure and markedly on An content.

[a] O.A.P. || (010); [b] O.A.P. ⊥ (010)
[c] Angles measured on (010) from the trace of the (001) cleavage.

Downloaded from https://pubs.geoscienceworld.org/books/chapter-pdf/3761011/9780903056434_ch59.pdf
by guest

Structure

The following discussion of the structures of alkali feldspars is divided into four parts: (1) potassium feldspars with little or no sodium; (2) sodium feldspars with little or no potassium; (3) alkali feldspars in general; and (4) perthites.

(1) Potassium feldspars

Sanidine. The essential features of the crystal structure of the feldspar minerals were first determined in 1933 in the study of a sanidine. The structure of sanidine is typical of a 'framework' silicate in which tetrahedra of $(Si,Al)O_4$ are linked to one another (by shared oxygens) in all directions rather than in chains or in sheets. Although discrete chains of tetrahedra do not exist in the structure, its nature may be more easily understood by considering the atomic arrangement as the linking of chains in two directions perpendicular to their length. The chains themselves are formed by the linking of horizontal rings of four tetrahedra as shown in Fig. 163a. The repeat distance in the chain direction (x) is approximately four times the height of a tetrahedron. When viewed in the direction of the chain axis a horizontal ring appears approximately as in Fig. 163b, and this can be further simplified in its representation as in Fig. 163c. The configuration shown in Fig. 163 is often described as a 'double crankshaft', and the upward- and downward-pointing tetrahedra in a horizontal ring are labelled U and D respectively.

In the actual structure the rings are considerably distorted (Fig. 164). They are tilted out of the horizontal plane, and are twisted about the chain axis direction. Successive horizontal rings of a chain are, however, related by vertical glide planes [reflection in (010) and translation of $a/2$] passing through their centres, and the view down the chain axis may be idealized as in Fig. 163d: the first, third, fifth and succeeding odd numbered rings are represented by thick and the even numbered rings by thin lines. The double crankshaft is also illustrated in Fig. 164. The linkage of rings in directions at right angles to their length is as follows. At the level of the first ring a network of oxygen linkages is formed as shown in Fig. 165, producing a plane of four-membered and eight-membered rings of tetrahedra. The eight-membered rings are of two kinds, UUUUDDDD and DUUDUDDU, which are characteristic of feldspars as distinct from other framework silicates (e.g. zeolites). The plane of these rings is $(20\bar{1})$, defined by the [010] and [102] zone axes.

Vertical symmetry planes and glide planes are marked m and g in Fig. 165. A similar network is formed by the rings of tetrahedra below the first network and the two arrays are linked by the oxygen atoms (such as P, Q, Fig. 163a) forming vertical four-membered rings. The

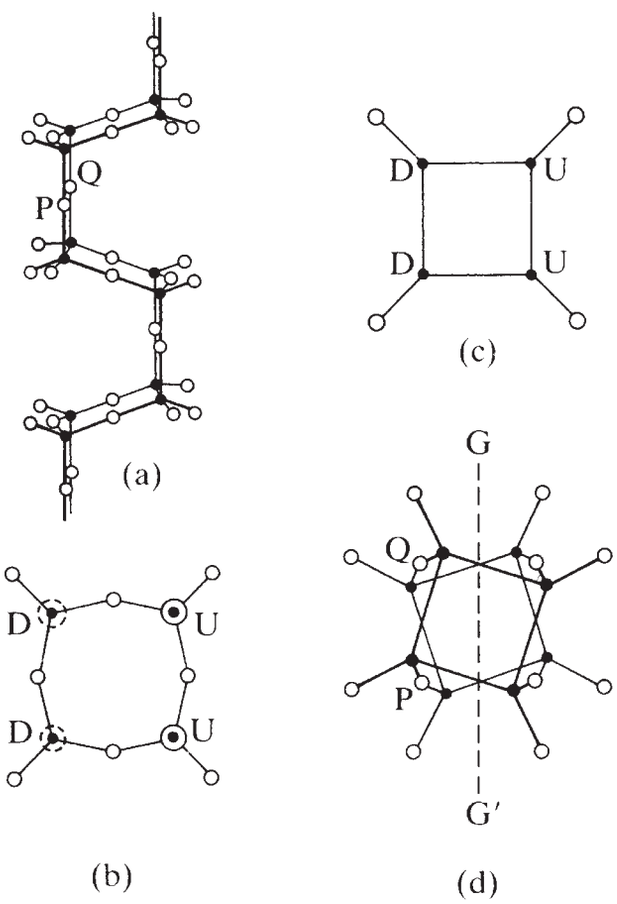


Fig. 163. Idealized illustrations of the feldspar 'chain' (see text) (after Taylor, W.H., 1933, *Z. Krist*., **85**, 425–42).

Downloaded from https://pubs.geoscienceworld.org/books/chapter-pdf/3761011/9780903056434_ch59.pdf
by guest

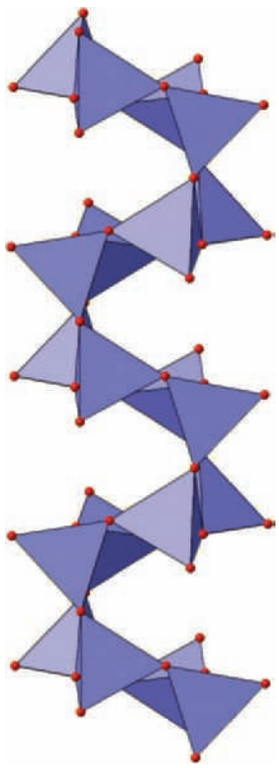


Fig. 164. The 'double crankshaft' chain of (Si,Al)−O tetrahedra which runs parallel to *x* in the feldspar structure showing distortions from the idealized structure. (Crystalmaker image). Blue: (Si,Al)−O tetrahedra; red: oxygen.

resultant framework of tetrahedra has large interstices which are occupied by potassium ions, and these too are shown in Fig. 165. Atoms K and O_{A_2} are in special positions on symmetry planes, O_{A_1} is in a special position on a diad axis, and the remaining atoms are in general positions in the unit cell. Potassium atoms are rather irregularly coordinated by nine oxygens, the K−O distances being ~3 Å. Figure 166 is a projection which emphasizes the (Si,Al) tetrahedra. Another view of part of the structure of sanidine is presented in Fig. 168.

Accurate structure determinations of high sanidine show that average (Si,Al)−O distances are equal for all tetrahedra (1.64 Å) indicating that Al atoms are distributed randomly (disordered) between T_1 and T_2 sites (Figs 165−168).

Microcline. The low temperature form of potassium feldspar, microcline, is triclinic. Although the basic structure is the same as sanidine, the (Si,Al)−O tetrahedra are twisted slightly with respect to each other, so that the mirror plane and two-fold axis of monoclinic sanidine are lost. The structure is therefore like that of albite (Fig. 167b). In microcline average (Si,Al)−O distances are not equal for all tetrahedra because the Al atoms are concentrated in a site called $T_1(0)$ (Fig. 168) and the structure is said to be ordered. The departure of the α and γ lattice angles from 90° (the value in sanidine) is a measure of the degree of order between the $T_1(0)$ and $T_1(m)$ sites, and is called the 'obliquity' or, in older work, the 'triclinicity' of the

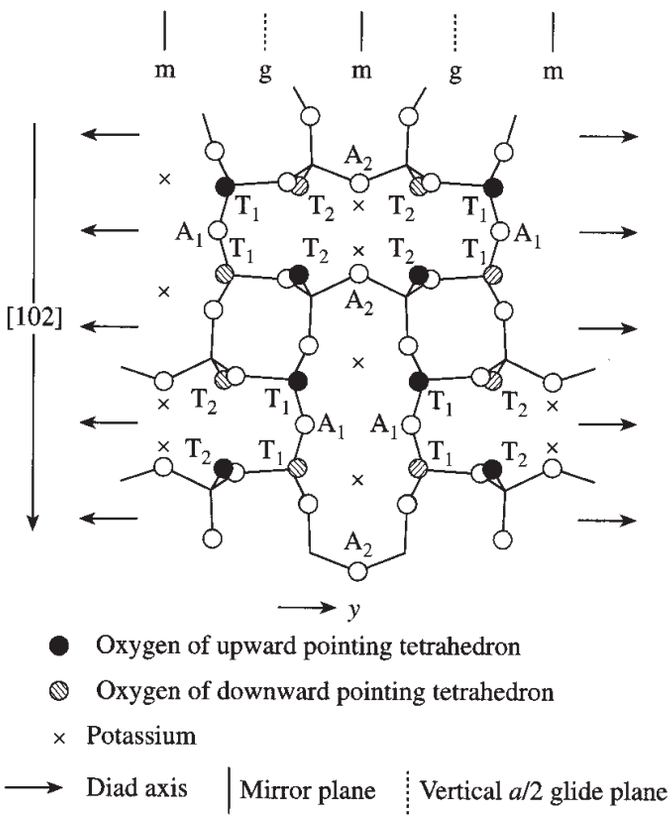


Fig. 165. Part of the structure of sanidine in projection down *x* (crankshaft chain direction) showing how chains are linked laterally to form a layer of 4- and 8-membered rings of (Si,Al)−O tetrahedra (after Taylor, W.H., 1933, *Z. Krist.*, **85**, 425−42).

Downloaded from https://pubs.geoscienceworld.org/books/chapter-pdf/3761011/9780903056434_ch59.pdf
by guest

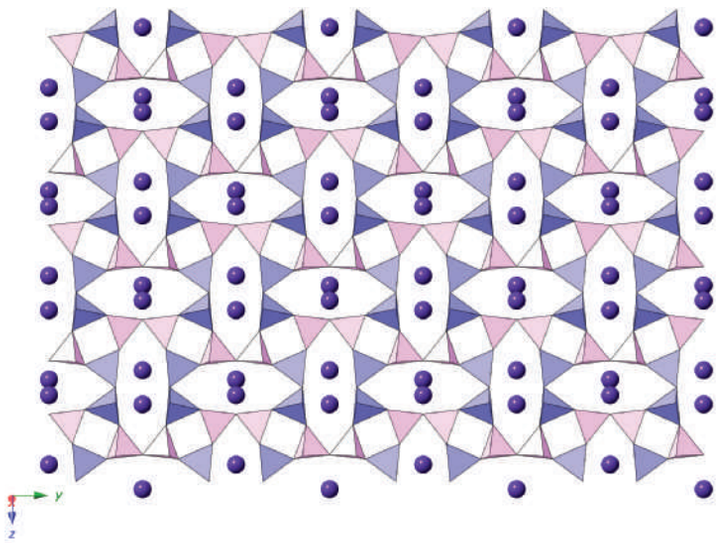


Fig. 166. Similar projection to Fig. 165 showing (Si,Al)−O tetrahedra. Purple spheres: potassium; blue tetrahedra: T_1; pink: T_2. In the monoclinic structure shown, Al occupies tetrahedra at random when fully disordered. With complete non-convergent order all the Al would be in T_1 tetrahedra, but distributed randomly between them (CrystalMaker image).

feldspar. An estimate can be made using X-ray powder patterns. The largest departures from 90º (α = 90.6º, γ = 87.7º) correspond with fully ordered low microcline (sometimes called 'maximum' microcline); microcline with lower departures is called 'intermediate' microcline. Although intermediate microcline occurs naturally, it is not certain that it is a stable phase. When microcline is heated at elevated temperatures it transforms slowly into sanidine.

Silicon−aluminium ordering and the microstructure of orthoclase. The process of ordering and its relationship to crystal symmetry can best be understood by reference to Fig. 168. Oxygen is not shown in the diagram, and only two 'chains' of Si^{4+} and Al^{3+} ions are indicated. Si or Al occupy all positions where lines in the framework join (T-sites), all surrounded by tetrahedra of O^{2-}. Some short linkages from tetrahedral nodes are with unit cells above or below the unit cell outlined by the rectangle in the centre of the drawing, emphasizing that although feldspar structures can be usefully simplified into chains and sheets, the structure is a three-dimensional framework. Because (001) is not at right angles to *c* (the lattice angle β is close to 116º) the *c* axis in the drawing is inclined, indicated by a tapered arrow. In this projection Si and Al tetrahedra form ten-membered rings around the M-site, which has a complex shape to which it is difficult to apply simple ideas of coordination number.

In most feldspars at high temperatures all possible positions for Al and Si (called 'equivalent sites') are

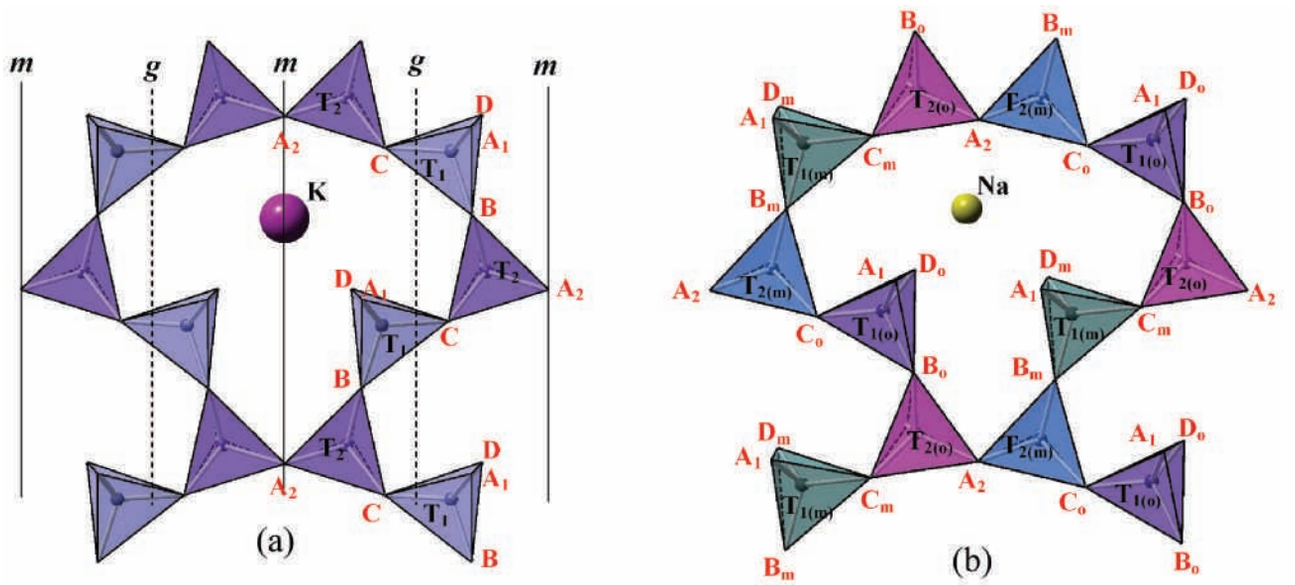
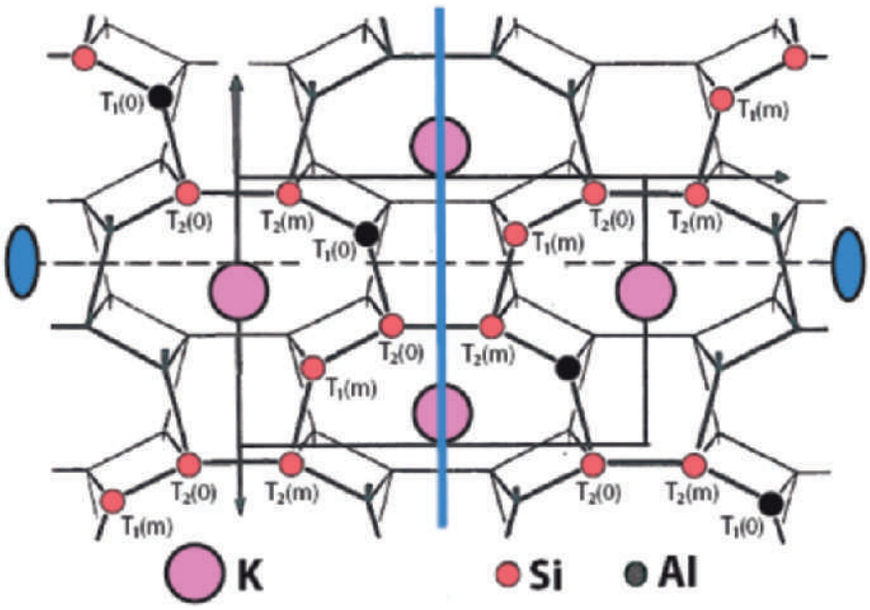


Fig. 167. (a) Part of the sanidine structure viewed normal to (001); m and g indicate mirror and glide planes of symmetry, respectively (structural data from Phillips, M.W. & Ribbe, P.H., 1973, *Amer. Min.*, **58**, 263−70). (b) Part of the albite structure viewed normal to (001), clearly lacking planes of symmetry (structure data from Prewitt, C.T., Sueno, S. & Papike, J.J., 1976, *Amer. Min.* **61**, 1213−25. Fig. produced by M.D. Welch).

Downloaded from https://pubs.geoscienceworld.org/books/chapter-pdf/3761011/9780903056434_ch59.pdf
by guest



Fig, 168. Structure of sanidine viewed on (001). The framework of T sites (occupied randomly by Si and Al, in the ratio 3:1 in high sanidine) is shown but not the oxygen tetrahedra surrounding them. During nonconvergent ordering Al becomes concentrated in T_1 sites, but as long as it remains randomly distributed in the T_1 sites 2/*m* symmetry is preserved. During convergent ordering Al becomes concentrated in $T_1(0)$ sites of which one set is shown in black. Symmetry is broken if Al becomes locally concentrated in $T_1(0)$, and the structure becomes slightly distorted from that shown. This can happen in both a 'left'- and 'right'-handed sense, leading to the fine-scale 'tweed' microtexture of orthoclase, and ultimately to the 'tartan' twinning of microcline. (modified from Ribbe, P.H. (editor) 1983. Pp. 1–19 in *Feldspar Mineralogy*. Reviews in Mineralogy, Min. Soc. Amer., **2**).

occupied at random by Si and Al ions, and the feldspar is then said to be *disordered*. Ignoring for a moment the colouring of T ions in Fig. 168, there is a 1-in-4 chance of encountering an Al on any T site. This is the situation in high sanidine. However, the equivalent sites are of two types, labelled T_1 and T_2. The sites occur in pairs which in monoclinic feldspars are related by mirror symmetry (Figs 166, 167, 168). T_2 sites are closer together than T_1 and have a different relationship to the M cation. As temperature decreases, T_1 sites become energetically favourable for Al, which diffuses from T_2 sites into T_1. In principle, all Al can occupy T_1 sites, with none remaining in T_2. There is then a 1-in-2 chance of finding an Al on any T_1 site. If T_1 sites are occupied at random this *partially ordered* structure retains overall monoclinic symmetry. This type of ordering is said to be *nonconvergent*. The most highly ordered low sanidine crystals may approximate to this structure.

However, in any set of four equivalent sites there is only one Al, so that even in the hypothetical case in which all Al is in T_1 there is a local loss of mirror symmetry, as in the $T_1(0)$, $T_1(m)$, $T_2(0)$, $T_2(m)$ ring in the centre of Fig. 168. A second type of ordering (*convergent ordering*) occurs in which Al becomes concentrated in the $T_1(0)$ site over large regions of the structure. There are two ways in which this can happen. In albite, framework ordering takes place in a structure which is triclinic because of the shearing transformation (ST in Fig. 169). The T site in which all Al will be sited in low albite [$T_1(0)$, Fig. 168] is defined as soon as an Ab-rich feldspar becomes triclinic. In this case Fig. 168 is distorted slightly (in a 'right-' or 'left-handed' sense) from monoclinc symmetry, and the ordering phase transition can occur by a continuous process.

The process is different in the case of monoclinic sanidine, in which the Al has two 'choices' of T_1 site, related by symmetry [labelled $T_1(0)$ and $T_1(m)$ in Fig. 168, although in a monoclinic framework they are indistinguishable]. Al thus concentrates in T_1 sites, by diffusion from T_2, while the crystal maintains monoclinic symmetry. However, because in any set of four equivalent T sites there is only one Al, mirror symmetry must be lost locally, and the position of the Al *defines* which of the two T_1 sites can be labelled $T_1(0)$. As there are two choices, small 'left' and 'right' triclinic ordering domains develop, within which Al is in the same equivalent site in a small number of adjacent unit cells. Each corresponds with a slightly distorted version of Fig. 168 and its mirror-image. These embryos give rise to a very fine-scale 'tweed' microstructure which is composed of alternating domains, orientated like Albite and Pericline twins in microcline, each domain being only a few unit-cells thick (Fig. 198, p. 288). This is the microstructure of orthoclase. Orthoclase is optically monoclinic, with large 2V (>50º), and is monoclinic in powder XRD patterns, but in single crystal XRD and electron diffraction patterns individual Bragg diffraction spots are sometimes streaked normal to the tweed modulations.

Downloaded from https://pubs.geoscienceworld.org/books/chapter-pdf/3761011/9780903056434_ch59.pdf
by guest

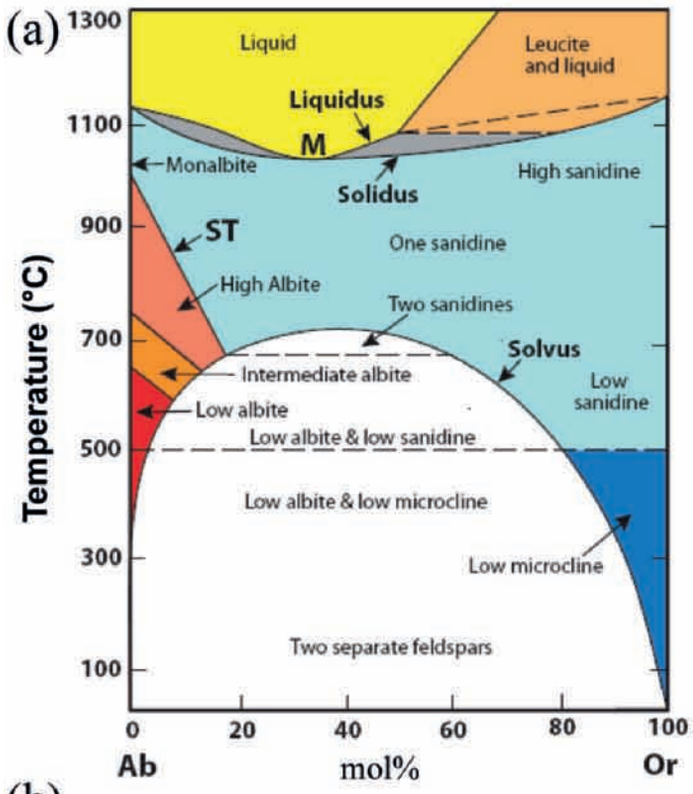


Fig. 169. (a) Stable equilibrium 'strain-free' phase diagram for An-free alkali feldspars with equilibrium (Si,Al) ordering, at atmospheric pressure. (Liquidus and solidus curves are from Schairer, J.F., 1950, *J. Geol*., **58**, 512–7. Subsolidus boundaries are slightly modified from fig. 8a in Brown, W.L. & Parsons, I., 1989, *Mineral. Mag*., **53**, 25–42.).

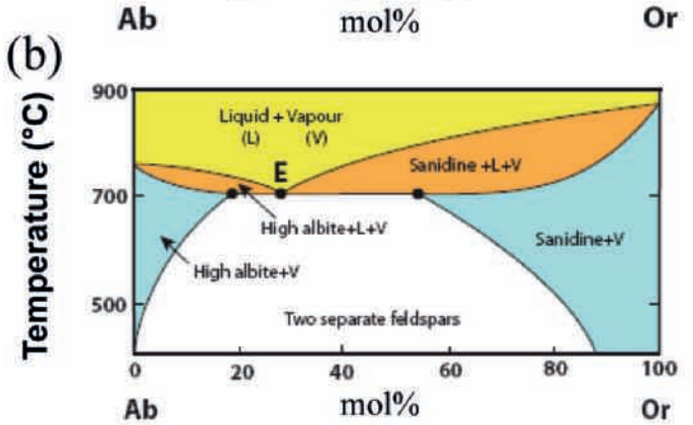


Fig. 169 (b) Metastable phase diagram for An-free alkali feldspars at P_{H_2O} 500 MPa. Two feldspars are in equilibrium with liquid at the eutectic, E. (Liquidus and solidus curves are from Morse (1970), *J. Petrol*., **11**, 221–51. The solvus is from Smith P. & Parsons, I., 1974, *Mineral. Mag.*, **39**, 747–67, at 100 MPa, adjusted upwards in temperature by 22ºC/100 MPa, the pressure dependence recommended by Hovis *et al*., 1991, *Amer. Min*. **76**, 913–27).

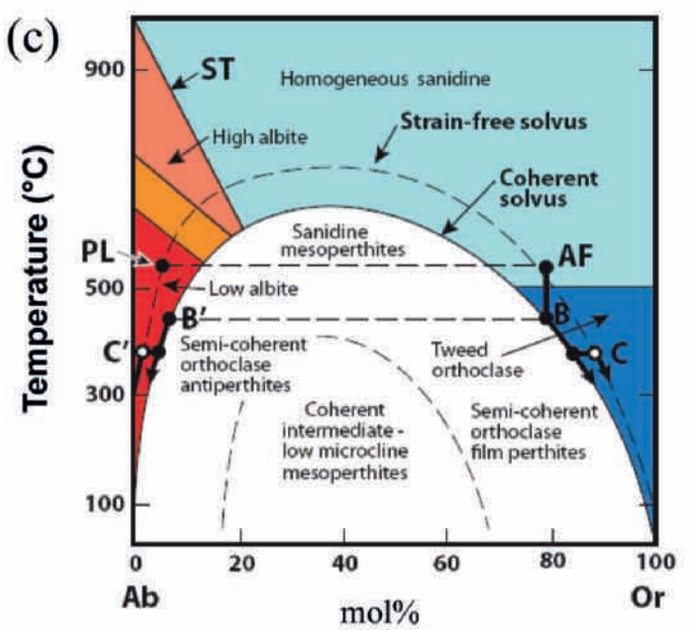


Fig. 169 (c) Behaviour diagram for coherent and semicoherent An-free alkali feldspars. (Based on fig. 8b in Brown W.L. & Parsons, I., 1989, *Mineral. Mag*., **53**, 25–42.)

Downloaded from https://pubs.geoscienceworld.org/books/chapter-pdf/3761011/9780903056434_ch59.pdf
by guest

The orthoclase microstructure persists over very long timescales because the free energy released by further Si–Al ordering is balanced by strain energy acquired in the walls of the triclinic domains, which are constrained to maintain an average monoclinic shape. Further ordering, leading to stable triclinic microcline, is blocked. The orthoclase is therefore in a metastable equilibrium that will persist indefinitely unless some 'unzipping' event such as reaction with fluids or deformation can occur. Orthoclase should therefore not appear on conventional phase diagrams (Figs 169a) but is appropriate on behaviour diagrams (Fig. 169c). The upper stability limit of microcline has been placed in the range 500–480ºC, based on petrological and geological evidence.

Microcline rarely occurs untwinned, and the intersecting Albite and Pericline twins, often called 'tartan' twinning, are a valuable aid to recognition under the microscope. It should be noted, however, that this style of twinning commonly occurs on a sub-optical scale. Twins on the two laws are at right angles, and this has long been held to indicate that triclinic microcline forms from a monoclinic precursor, presumed to be orthoclase. However, the transformation has never been achieved in the laboratory and the mechanism of tartan microcline formation is obscure. There are many examples of microcline forming by a replacement process involving local dissolution and reprecipitation, but the means by which the monoclinic parent communicates with the growing, twinned microcline is unknown. Microcline can also form in deformed orthoclase, and it is possible that some highly organized twin textures form by a solid-state coarsening process.

Adularia. The potassium feldspar adularia is characterized by a well developed {110} habit and develops in low temperature environments such as veins and during diagenesis. The habit is very common in subgrains formed during replacement of pre-existing feldspars. Adularia shows variation in optical properties and complex diffraction contrast in transmission electron microscope images within single grains which are the result of variable ordering. Some adularia crystals have microtextures resembling poorly developed 'tartan' twinning. The existence of adularia suggests that ordered K-feldspars can grow directly at low temperatures, without a monoclinic precursor.

(2) Sodium feldspars

Albite. The structure of albite, $NaAlSi_3O_8$, is essentially the same as that of sanidine (Figs 167b, 168) except that the tilts between adjoining (Si,Al)–O tetrahedra are more irregular because of the triclinic symmetry imposed by the shearing transformation. The mirror symmetry and the two-fold axis (Fig. 168) are lost. The cell dimensions are smaller (see p. 253), reflecting the smaller ionic radius of Na^+ compared with K^+. The main contraction is in *a*, parallel to the 'chain' axis (Fig. 164, p. 255). In alkali feldspars the coordination number of the Na and K ions, which defines the effective ionic radius, is difficult to establish because of the irregular shape of the cavity in which they reside (Figs 167, 168). Coordination numbers for K in the range 9–7, and for the smaller Na ion, 7–5, have been suggested.

As is the case with sanidine and microcline, a continuum exists between disordered high albite and ordered low albite. Fully disordered albite is monoclinic at the melting point (monalbite, Fig. 169) but the α and γ lattice angles begin to depart from 90º at the shearing transformation (980ºC in pure albite), and their departure from 90º (obliquity) increases continuously as temperature decreases. Angular changes caused by shearing occur irrespective of cooling rate and monalbite (and monoclinic anorthoclase) can be observed only at high temperatures. Samples cooled rapidly remain disordered (high albite), but during relatively slow cooling, or during laboratory annealing at fixed temperature, an equilibrium state of Si,Al ordering is reached relatively quickly leading to intermediate albites and low albite. Because ordering in albite is relatively rapid, the high–low albite transition has been studied experimentally (Fig. 186, p. 274). Most ordering [diffusion of Al into $T_1(0)$ sites] occurs over a relatively narrow range of temperatures around 700ºC (orange band on Fig. 169) but the transformation is continuous. At high pressure the range of major ordering moves to higher temperatures and takes place over a larger range of temperatures. Intermediate albite is stable in the ordering band, but because ordering in albite is rapid, intermediate albite is rare in nature and in most geological circumstances low albite forms. As noted in the preceding section, in albite there is no kinetic barrier to ordering analogous to that encountered when sanidine transforms to microcline because albite is triclinic throughout the ordering process, and does not become stranded with a balanced 'tweed' microtexture. Ordered or partially ordered albite that when heated does not transform into monalbite before melting is strictly called high albite; disordered albite which transforms to monalbite is known as analbite.

Pericline. The Na equivalent of adularia, with the same {110} habit, is called pericline (not to be confused with the Pericline twin law). It also shows variable optical properties and complex diffraction contrast in transmission electron microscope images because of variable ordering. It is found in similar environments to adularia. Large-scale replacement by albite (albitization) is common in ocean-floor basaltic rocks and in diagenesis, during which replacive subgrains with the {110} habit often form.

(3) The alkali feldspar system

Phase relationships for An-free alkali feldspars and their nomenclature are shown in Fig. 169a. Below the solidus three processes affect alkali feldspar solid

Downloaded from https://pubs.geoscienceworld.org/books/chapter-pdf/3761011/9780903056434_ch59.pdf
by guest

solutions. (1) Exsolution, which predominantly involves Na and K diffusion over relatively large distances through the Si,Al−O framework and leads to the intergrowths known as perthite. (2) The rapid shearing phase transition (ST on Fig. 169) described above in albite, caused by changes in the relative tilt of framework tetrahedra, but not involving diffusion, affects alkali feldspars up to $Ab_{60}Or_{40}$. (3) The slow ordering transition, discussed above for albite and for the sanidine−microcline transition, in which Si and Al exchange position locally by diffusion, affects all but very rapidly cooled monoclinic alkali feldspars, but the formation of tweed texture means that the low-sanidine–microcline symmetry change is difficult to achieve, so that partially disordered orthoclase often persists over long timescales. The three processes act cooperatively but can be considered separately for convenience.

Exsolution at the feldspar solvus. The white area in the phase diagram is defined by a *solvus* curve. Igneous rocks in which only one feldspar phase has crystallized from the magma are said to be 'hypersolvus', those in which two feldspars, an alkali feldspar and a plagioclase feldspar have crystallized are 'subsolvus' (see Paragenesis section p. 283). At stable equilibrium a single homogeneous feldspar cannot exist below the solvus, although under conditions of very rapid cooling, for example in volcanic ash, homogeneous alkali feldspars may be preserved metastably to surface temperature. At most natural cooling rates a feldspar which crystallizes in the coloured areas will undergo a process of exsolution when it cools through the solvus. The crystal breaks down, in the solid state, into two feldspar phases, with compositions lying on the solvus curve. The two-feldspar intergrowth is called, generically, *perthite*. The bulk composition dictates the relative proportions of the two phases, which for convenience can be described by the terms perthite (*sensu stricto*), mesoperthite and antiperthite (Fig. 161b). The majority of feldspars that have grown in the coloured areas of Fig. 169 become perthitic as they cool, although in volcanic rocks the intergrowths are often sub-optical in scale (cryptoperthite). Even in rocks that have cooled slowly more Or-rich feldspars are often cryptoperthitic, because exsolution begins at low temperatures where diffusion is slow.

There are two broad types of perthite. Those in which the two phases share a continuous, or partly continuous, Si,Al−O framework are said to be coherent or semicoherent. The relationships of the two phases in such intergrowths require the use of a 'behaviour diagram' (Fig. 169c), discussed further below. Perthites in which the boundaries between the phases are discontinuous are said to be incoherent. Coherent intergrowths are usually crypto- or micro-perthitic and regular in shape and orientation (Figs 172b, 173, 174, left-hand side of Fig. 192, p. 279). Incoherent intergrowths are coarser and more irregular, and crystals are usually turbid, indicating that they have experienced reactions with aqueous fluids (Figs 172a, right-hand side of Fig. 192).

The composition (Or-content) of homogeneous feldspars can be obtained using X-ray diffraction, from cell parameters or most simply from the $\bar{2}01$ *d* spacing (Fig. 170; this diagram is for feldspars with Si−Al disorder). The method can be used to determine whether an alkali feldspar is homogeneous or perthitic, when two $\bar{2}01$ reflections are obtained. The compositions of the intergrown phases can then be obtained from $d_{\bar{2}01}$, although corrections must be applied if the intergrowths are coherent or ordered. The X-ray method may also be used to obtain the bulk composition of originally perthitic crystals that have been 'homogenized' by heating above the solvus, usually near the melting point.

In a magma crystallizing at low temperatures, for example at high water vapour pressure (Fig. 169b), two feldspars crystallize simultaneously on the solvus. This is the situation in so-called 'subsolvus' igneous rocks. However, the ternary solvus is very sensitive to low concentrations of anorthite in both plagioclase and alkali feldspar phases, forming a very steep dome in the ternary system Or−Ab−An (Fig. 187). Figure 169b cannot be used to obtain crystallization temperatures and a ternary geothermometer, such as Fig. 162, must be used. Subsequent to subsolvus crystallization, both feldspar phases may individually unmix, giving a coexisting perthitic alkali feldspar and an antiperthitic

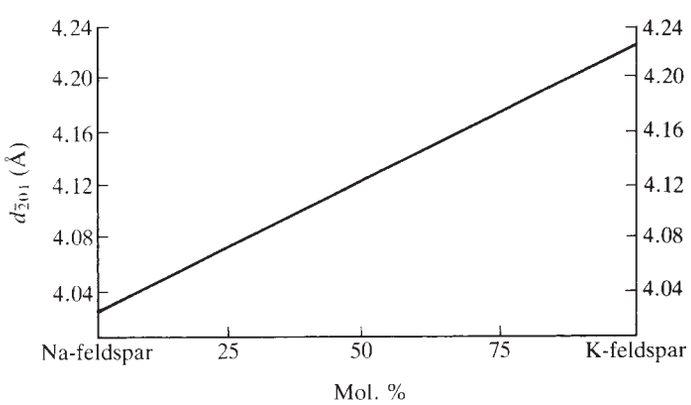


Fig. 170. Variation of $\bar{2}01$ spacing with compositon for synthesized or homogenized natural alkali feldspar (after Orville, P.M., 1967, *Amer. Min.*, **52**, 55−86)

Downloaded from https://pubs.geoscienceworld.org/books/chapter-pdf/3761011/9780903056434_ch59.pdf
by guest

plagioclase feldspar. However, because the solvus is asymmetrical (Fig. 169), particularly when An is present (Fig. 187, p. 275), albite in the perthitic intergrowth will be conspicuous whereas the Or-rich feldspar in the antiperthite will be minor in volume. This is the situation in many granites.

The exact position of the solvus curve depends on the degree of Si–Al order. Exsolution in alkali feldspars with equilibrium order begins at about 80ºC higher temperatures than in disordered feldspars, for compositions near the top of the solvus. The solvus in Fig. 169a is constructed from experimental data using natural starting materials with varying states of order and is an approximation to the limit of solid solution for feldspars with an equilibrium degree of order for the temperature of interest. The solvus in Fig. 169b is for disordered feldspars produced in direct synthesis experiments, and therefore the feldspars in the blue fields are high albite and sanidine, respectively. The solvus is also sensitive to pressure, moving to higher temperatures by ~220ºC GPa^{-1}. However, this effect is much less than that of P_{H_2O} in depressing the solidus (compare Figs 169a and b). It should be noted that pressure alone *increases* the melting point of feldspars, like most silicates.

The shearing or displacive phase transition. Homogeneous high sanidine–high albite solid solutions more albitic than $Ab_{60}Or_{40}$ undergo a monoclinic ↔ triclinic symmetry change if they are cooled or heated through the line ST (Fig. 169a,c). During cooling the α and γ cell angles begin to depart from 90º at ST, and the departure (obliquity) increases smoothly and continuously as temperature decreases. Cell angles must be measured at the required temperatures, and the structure reverts immediately and reversibly to monoclinic symmetry when heated above ST. Samples cooled so quickly that they have not exsolved undergo this phase transition at the metastable extension of ST below the solvus, which intersects the *x* axis at ~$Ab_{60}Or_{40}$ at room temperature if the feldspar is disordered. If the feldspar is ordered the hypothetical extension of the shearing transformation moves towards Or (Fig. 171). In most perthitic alkali feldspars, which have bulk compositions to the right of the intersection of ST with the solvus (Fig. 169a) the Ab-rich phase will undergo the shearing phase transition when it moves down the solvus and encounters its intersection with ST. Albite twinning develops in the Ab-rich phase when this occurs.

The ordering transition. The ordering process in end member Ab and Or feldspars is described above. In the system Ab–Or ordering takes place throughout the region between solidus and solvus (Fig. 169a), initially without change of symmetry. In all except very rapidly cooled rocks, an equilibrium Si–Al distribution will be maintained as sanidine crystals cool. Ordering in sanidine is non-convergent and monoclinic symmetry is maintained. Sodian sanidines cooling from above the shearing transformation will undergo convergent ordering once they pass the shearing transformation, when they have the high albite structure and are called anorthoclase. The ordering process in Ab-rich sanidine is therefore relatively rapid and continuous.

Ordering affects the temperature of the monoclinic–triclinic shearing transformation and it is probable that if exsolution did not occur it would be connected to the low-sanidine–microcline symmetry change in Or-rich feldspars as shown in Fig. 171. This shows a band for intermediate albite, in which most convergent ordering occurs, connected to a similar band for intermediate microcline. However, although intermediate microcline occurs occasionally in Nature, there is some experimental evidence that the sanidine–microcline transition is first-order (discontinuous) and that intermediate microcline does not therefore have a field of stability. The low sanidine–microcline ordering transition is

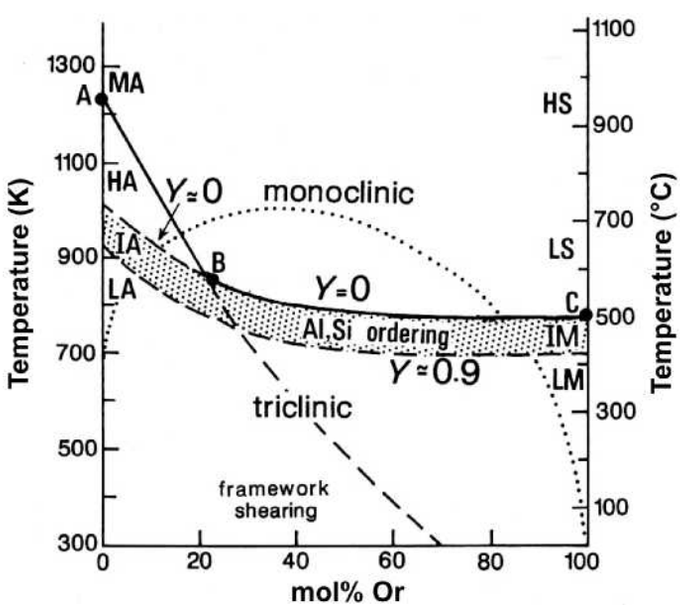


Fig. 171. Supposed equilibrium variation of the monoclinic–triclinic symmetry change (ABC) as function of temperature and composition in the hypothetical case where exsolution does not occur. The stippled band indicates where most convergent ordering occurs. *Y* is given by $t_1(0) - t_1(m)$, which are respectively the fractions of the $T_1(0)$ and $T_1(m)$ sites (Fig. 168) occupied by Al. $t_1(0) = 1$ in fully ordered An-free feldspars, 0.25 when fully disordered. MA: monalbite; HA, IA, LA: high, intermediate and low albite; HS, LS: high and low sanidine; IM, LM: intermediate and low microcline. IM may not be a stable phase (from Brown W.L. & Parsons, I., 1989, *Mineral. Mag*., **53**, 25–42).

Downloaded from https://pubs.geoscienceworld.org/books/chapter-pdf/3761011/9780903056434_ch59.pdf
by guest

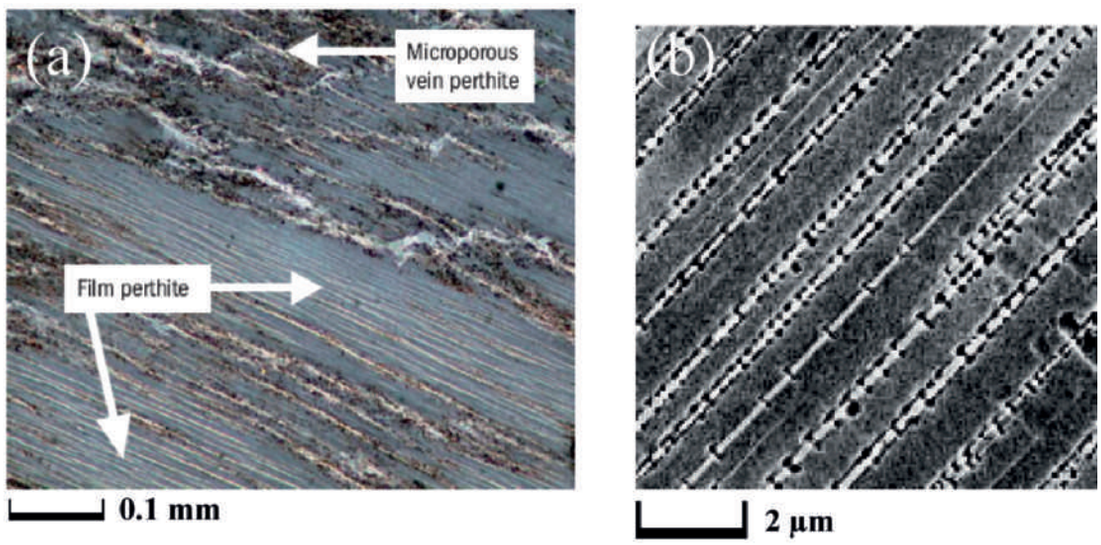


Fig. 172. (a) Strain-controlled film microperthite, modified and cross-cut by areas of turbid, replacement vein perthite. Phenocryst from the Shap granite, Cumbria. The bulk composition of the film perthite is ~$Ab_{29}Or_{70}An_1$. Optical micrograph, crossed polarizers, viewed approximately normal to (001). (b) Scanning electron microscope image of a (001) cleavage surface of a region of film microperthite (Fig. 172a) that has been etched in HF acid vapour. Film albite lamellae stand out in relief above the orthoclase matrix. Black dots, which occur in pairs, are etch-pits formed where misfit dislocation loops, which encircle the flat lenticular albite lamellae, crop out on the cleavage surface. The lamellae are therefore *semicoherent* and correspond with area 2 on Fig. 173 (courtesy of I. Parsons).

usually discontinuous because of the development of tweed microtexture, leading to the metastable monoclinic form orthoclase.

(4) Perthite: coherent phase behaviour in alkali feldspars

The morphology of perthitic intergrowths is very varied and is strongly dependent on the proportions of the Ab- and Or-rich phases and the history of the crystal including cooling rate, interactions with aqueous fluids, and deformation. The relationships between *coherent* intergrowths cannot be shown on conventional phase equilibrium diagrams, such as Figs 169a and b, but require the use of a *phase behaviour diagram*, such as Fig. 169c. This shows coherent phase behaviour, in which the phases, which share a continuous Si,Al−O framework, are coupled by coherency strain at their interfaces. This affects not only the composition of the phases but also the polymorphs that occur. The stable equilibrium strain-free solvus has been inserted from Fig. 169a. The different ionic radii of Na^+ and K^+ (1.12 and 1.51 Å, respectively) mean that the framework in K-rich regions (for example in the lamellar intergrowth in Fig. 172b) is slightly expanded relative to that in Na-rich regions, leading to coherency strain energy

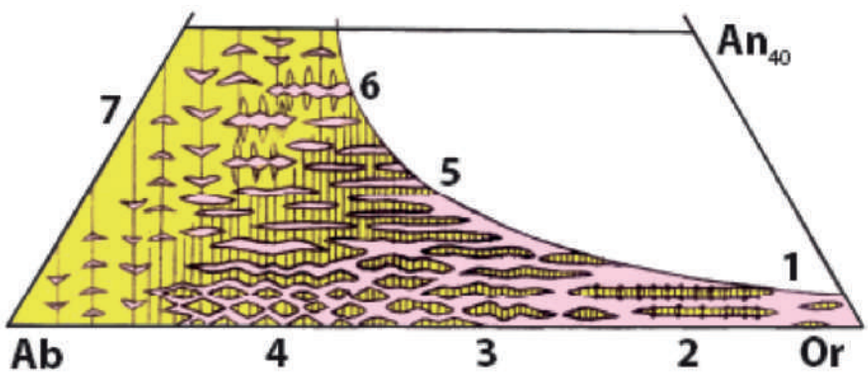


Fig. 173. Cartoon (not to scale) showing variation in strain-controlled micro- and crypto-perthites with respect to bulk composition in slowly cooled rocks. The Ab-rich phase is green, the Or-rich phase lilac. Vertical lines are Albite twins in the perthitic albite and plagioclase. 1: Fully coherent lenticular film lamellae; 2: semicoherent film lamellae with misfit dislocations in orthoclase; 3: zigzag intermediate microcline mesoperthite; 4: braid mesoperthite (Fig. 174a); 5: sinuous film mesoperthite (Fig. 174b); 6: corrugated sanidine lenses in cryptoantiperthite, with tapering Albite twins propagating into plagioclase matrix; 7: sanidine platelets nucleated on Albite twin composition planes in PL (slightly modernized after Brown, W.L. & Parsons, I., 1988, *Contrib. Mineral. Petrol.*, **98**, 444−54).

Downloaded from https://pubs.geoscienceworld.org/books/chapter-pdf/3761011/9780903056434_ch59.pdf
by guest

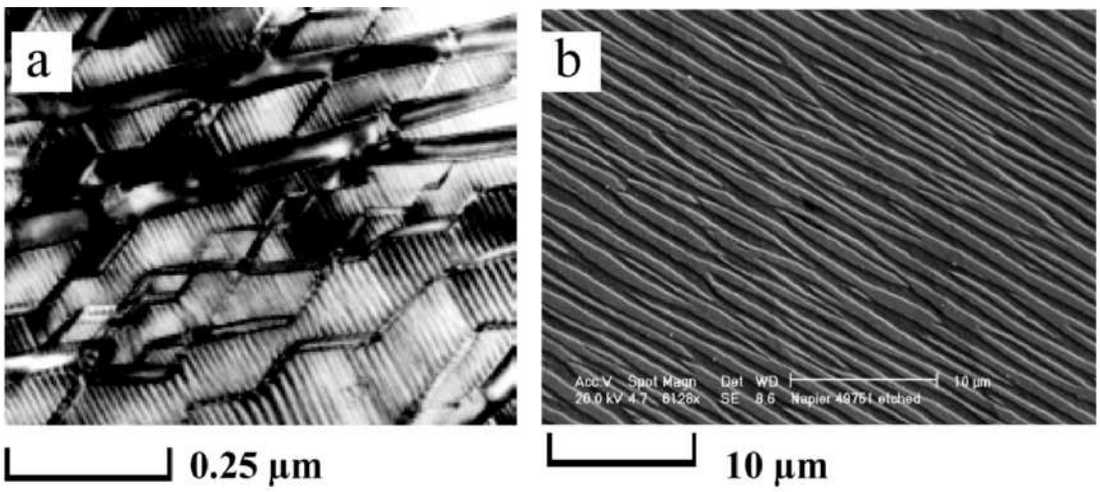


Fig. 174. (a) TEM image of braid cryptoperthite (area 4, Fig. 173) viewed parallel to *c*. Diamond shaped areas are Albite twinned albite, zigzag bands are low microcline. Each zig and each zag is a twin in a relationship called the diagonal association. The bulk composition is $Ab_{58}Or_{41}An_1$. Syenite, Klokken intrusion, South Greenland (from Brown, W.L. *et al*. 1983, *Contrib. Mineral. Petrol*. **82**, 13–25). (b) Scanning electron microscope image of (001) cleavage surface of a sinuous bifurcating mesoperthite (area 5, Fig.173) that has been etched in HF vapour. Albite lenses stand out in relief above orthoclase. They are fully coherent. The bulk composition is $Ab_{36}Or_{61}An_3$. Granulite-facies gneiss, Napier Complex, Antarctica (micrograph courtesy of N. Cayzer).

which must be added to the free-energy of the solid solution. This leads to a coherent solvus below the strain-free solvus. Strictly speaking the total strain energy varies with bulk composition (because this defines the surface area of the coherent interfaces) so each bulk composition will have its own coherent solvus. The compositions of the phases on the coherent solvus are not independent of the amounts of the phases, as they would be in a conventional phase diagram. For bulk compositions inside the solvus, although the two main processes of exsolution and framework ordering are still driving microtextural change, the phase assemblage that is adopted is to a large extent governed by the minimization of coherency strain energy.

It is important to note that Fig. 169 is for hypothetical, An-free feldspars. In an An-free liquid at high P_{H_2O} (Fig. 169c) two feldspars would crystallize in equilibrium at the intersection of the solidus and solvus, as shown on Fig. 169b. In a real granitic liquid an alkali feldspar would crystallize with a small amount of An in solid solution, together with a plagioclase with more An, characteristically an oligoclase. The two feldspars would lie on a tie-line on the ternary feldspar solvus (similar to B on Fig. 162, p. 250) and the intersection of the solidus with the solvus would occur at a considerably higher temperature.

Fig. 169c illustrates the basic principles that control the microtextures in a typical subsolvus granitic alkali feldspar (AF) which will crystallize together with a plagioclase (PL, usually an oligoclase, not in the plane of the diagram). In plutonic rocks AF will crystallize as a homogeneous sanidine, developing the tweed microtexture (Fig. 198, p. 288) of orthoclase as it cools and orders. At or just below the coherent solvus (point B) it will begin to exsolve an Ab-rich second phase, B′. As temperature continues to fall the B–B′ pair changes composition down the solvus and the perthitic exsolution textures become coarser. The solidus plagioclase, PL, does not participate in these reactions. The original AF and PL phases behave as closed systems, and the phase rule is violated. To obey the phase rule PL and AF would each have to change composition and remain on the strain-free solvus, and this rarely, if ever, happens. Coherent exsolution of feldspar AF, beginning below B, will lead to the film microperthite characteristic of granites, illustrated in Fig. 172a,b.

In most alkali feldspars in plutonic rocks there is evidence that the crystals have reacted with fluids at least once in their history. This leads to the development of turbidity, which is almost universally developed to variable extents in plutonic alkali feldspars. Turbidity is caused by myriads of tiny pores at scales of a μm or less which form at the junctions between incoherent subgrains that replace the film microtexture during dissolution–reprecipitation reactions. In Fig. 169c partial or complete reactions with fluids on the isotherm passing through C leads to the much coarser vein perthite illustrated in Fig. 172a. During this process of ‘deuteric coarsening’ the regular intergrowths lose coherency, and phase compositions move onto the strain-free solvus, indicated by C–C′ (Fig. 169c). Analyses of the vein perthite, and of coarsened, turbid regions along film lamellae in Fig. 172a, have shown that these crystals have been affected by at least two stages of replacement. Tweed orthoclase is commonly replaced by microcline at the deuteric stage, by what has been described as an ‘unzipping’ reaction. This has possibly happened in Fig. 198.

The orientation and morphology of coherent micro- and crypto-perthite in slowly cooled feldspars depends on bulk composition, shown in cartoon form in Fig. 173. The interfaces between Ab- and Or-rich phases are planes of minimum coherency strain energy, which

Downloaded from https://pubs.geoscienceworld.org/books/chapter-pdf/3761011/9780903056434_ch59.pdf
by guest

readjust themselves as exsolution proceeds. Coherent exsolution in Or-rich feldspars (crypto- and microperthite *sensu stricto*, Fig. 161b, p. 249, areas 1 and 2 in Fig. 173) leads to straight or slightly sinuous film perthite (Fig. 172) in an 'irrational' plane between $(\bar{8}01)$ and $(\bar{6}01)$ (the 'Murchison plane, Fig. 179). Optical diffraction by fine-scale lamellae of this type causes the silvery iridescence characteristic of moonstone. The lamellae are actually, in three dimensions, very flat lenses. The periodicity of simple planar intergrowths can be used to calculate the cooling rate of the host rock, using experimentally determined diffusion coefficients for Na and K. Initially the Si, Al−O framework will remain fully coherent, but during cooling, as the film lamellae coarsen and the feldspar framework becomes elastically stiffer, coherency strains increase and misfit dislocations nucleate (revealed by the etch-pits in Fig. 172b) to lower strain energy. The intergrowth is then said to be semicoherent. Structure around these dislocations is highly soluble in deuteric fluids, and many plutonic alkali feldspars contain orthogonal networks of 'nanotunnels' on the surfaces of film lamellae. These are very important in dissolution of feldspars during weathering (Fig. 194, p. 281), and in replacement reactions during diagenesis.

In coherent mesoperthitic alkali feldspars (Fig. 173, areas 3 and 4) straight exsolution lamellae form initially, but the cooperative effects of the shearing transformation, Si−Al ordering and twinning cause lamellar interfaces to become zigzag and then rotate into planes of the form $\{\bar{6}\bar{6}1\}$, giving rise to a complex intergrowth known as 'braid perthite' in which lozenge-section rods of low albite are surrounded by zigzag bands of microcline (Fig. 174a). The Or-rich phase does not become stranded with the monoclinic tweed orthoclase structure but can transform continuously into triclinic microcline because of coherency with a triclinic Ab-rich phase. Thus the structure of the Or-rich phase is a function of the feldspar bulk composition. Its variation with respect to temperature and composition have to be described using a behaviour diagram, as indicated by the fields inside the solvus on Fig. 169c.

Braid perthite (Fig. 174a) commonly occurs in alkali feldspars in syenites, and forms crypto- or fine microperthite. Diffraction of light by cryptomesoperthitic intergrowths is the cause of the blue iridescence of the feldspars in the common architectural syenite called larvikite. Coherent mesoperthitic feldspars with relatively high concentrations of An (Fig. 173, area 5) are commonly found in granulite-facies rocks which have experienced long periods at elevated temperatures below the solvus. Lamellae tend to be slightly sinuous and may be several tens of μm in thickness (Fig. 174b). They are not iridescent because of the large periodicity and irregularity of the lamellae.

Coherent and semicoherent cryptoantiperthites (Fig. 173, areas 6 and 7) have been described using transmission electron microscopy in alkali gabbros and syenodiorites, but have been reported rarely. The shape of the ternary solvus (Fig. 187, p. 275) and the abundance of ternary plagioclase in the andesine−oligoclase range (Fig. 161a) suggest that they should be common. Coherent micro- and cryptoantiperthites also occur in some granulite-facies rocks.

Morphology and twinning

As triclinic feldspars do not deviate greatly from monoclinic symmetry, several characteristic habits are common to both monoclinic and triclinic members of the feldspar group. Some of the habits that occur most frequently have the forms {001} and {010} well-developed and the presence of {110} in addition often gives a prominent prism zone parallel to *z* (Fig. 175a). Some crystals (e.g. in feldspar microlites) are elongated parallel to *x* and the prism zone formed by {010} and {001} predominates (Fig. 175b). Orthoclase and microcline crystals can have either of these habits, but sanidine is commonly flattened in (010) (Fig. 175c). In the low-temperature K-feldspar adularia {110} predominates, and crystals have an orthorhombic appearance because (001) and $(10\bar{1})$ make nearly equal angles with *z* (Fig. 175e). Albite is also often tabular parallel to (010) but the low temperature variety pericline can have a similar habit to adularia or be elongated parallel to *y* (Fig. 175d). The high-temperature sodium-rich feldspar anorthoclase is often found in rhomb-shaped crystals (Fig. 175f).

Feldspars have perfect {001} and {010} cleavages which in the monoclinic varieties intersect at right angles, and very nearly so in triclinic feldspars. However, because repeated fine-scale twinning is very common, many structurally triclinic feldspars appear macroscopically monoclinic, with these cleavages at right angles.

Twin laws

Twinning in feldspars can occur by three different mechanisms: (a) as a primary phenomenon during crystal growth; (b) as glide twinning induced by deformation; (c) as a result of phase transitions leading to lower symmetry. Many different kinds of pseudosymmetry are exhibited by the feldspar structures, and accordingly, twinning is very common and may follow a number of different laws. In Table 35 the more common twin laws which are found in feldspars are divided into three groups; normal, parallel and complex. Normal twins have their twin axis normal to a possible crystal face and this face is parallel to the composition plane. For a centrosymmetric crystal this twinning process is equivalent to reflection in the composition plane. Parallel twins have as their twin axis a possible crystal edge (i.e. a zone axis); the composition plane is parallel to the twin axis and need not define a

Downloaded from https://pubs.geoscienceworld.org/books/chapter-pdf/3761011/9780903056434_ch59.pdf
by guest

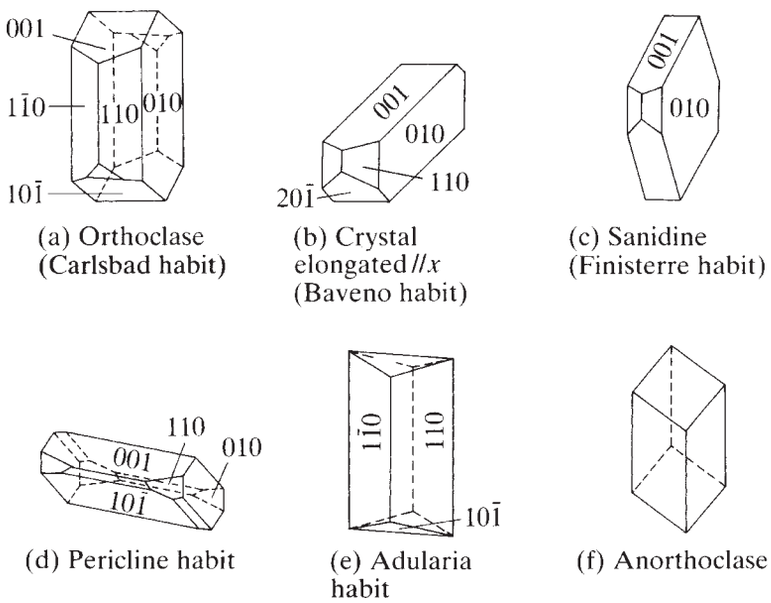


Fig. 175. Some common feldspar habits (Deer *et al*., 1992, *An Introduction to the Rock-Forming Minerals*, Longman, UK).

possible crystal face. In some cases an individual B is related to another, A, by a normal twin law, and an individual C is related to B by a parallel twin law with the same composition plane as the normal twin. In this case C and A are related by a 'complex' (or 'edge-normal') twin law. The twin axis of the resultant complex twin lies in the composition plane and is normal to a possible crystal edge (i.e. at 90º to the twin axis of the parallel twin). The intermediate individual B, which is related to A and C by simple twin laws, may or may not be present. The relationships in a complex twin are illustrated in the stereogram of Fig. 176.

Illustrations of some common feldspar twins are presented in Fig. 177.

Carlsbad, Baveno and Manebach twins are found in both monoclinic and triclinic feldspars, mainly with only two individuals but in some cases with three, four or even six.

Albite and Pericline twinning

Repeated (or 'polysynthetic') twins on the Albite and Pericline laws (Table 35) are restricted to triclinic crystals but are extremely common both in alkali and plagioclase feldspars. Plagioclase without repeated twins is very uncommon, although albitic plagioclases in some low-grade albite schists, and authigenic albite, often lack optically visible twins. The twins provide a very useful

Table 35. Feldspar twin laws.

Name	Twin axis	Composition plane	Remarks
Normal twins			
Albite	⊥ (010)	(010)	Repeated; triclinic only
Manebach	⊥ (001)	(001)	Simple
Baveno (right)	⊥ (021)	(021)	Simple, rare in plagioclases
Baveno (left)	⊥ (0$\bar{2}$1)	(0$\bar{2}$1)	
Prism (right)	⊥ (110)	(110)	
Prism (left)	⊥ (1$\bar{1}$ 0)	(1$\bar{1}$0)	
Parallel twins			
Carlsbad	[001] (*z* axis)	(*hk*0), usually (010)	Simple
Pericline	[010] (*y* axis)	(*h*0*l*), 'rhombic section' parallel to *y*	Repeated; triclinic only
Ala	[100] (*x* axis)	(0*kl*), 'rhombic section' parallel to *x*	Repeated
Complex twins			
Albite–Carlsbad (Roc Tourné)	⊥*z*	(010)	Repeated
Albite–Ala	⊥*x*	(010)	
Manebach–Pericline	⊥*y*	(001)	
Manebach–Ala	⊥*x*	(001)	
X–Carlsbad	⊥*z*	(100)	
X–Pericline	⊥*y*	(100)	

Downloaded from https://pubs.geoscienceworld.org/books/chapter-pdf/3761011/9780903056434_ch59.pdf
by guest

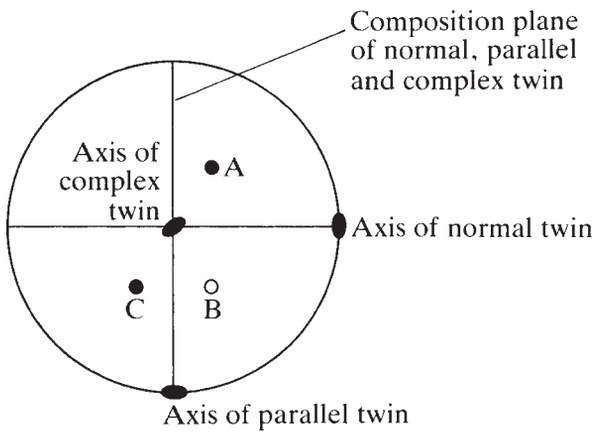


Fig. 176. Stereographic illustration of relationships in a complex twin (Deer *et al*., 1992, *An Introduction to the Rock-Forming Minerals*, Longman, UK).

and simple method of distinguishing feldspars in thin section, and in plagioclase provide a means of obtaining crystal compositions using extinction angles (see p. 304). The two twin laws frequently occur together leading, for example, to the 'tartan' twinning of microcline (Fig. 181) and the more regular intersecting twins in anorthoclase (Fig. 182) and plagioclase (Fig. 211, p. 304). Repeated twinning can form during crystal growth, particularly in plagioclase, as a product of deformation, again most obviously in plagioclase, or in response to both of the monoclinic–triclinic phase transitions in alkali feldspars. In the latter the detailed character of the twins (see below) reflects the shearing or ordering character of the phase transition, and the orientation of the twins is diagnostic for microcline and anorthoclase (Fig. 182). Both Albite and Pericline twins are normally fully coherent, although deformation may cause periodic dislocations to form on composition planes.

In Albite twinning, (010) is both the twin plane (across which reflection occurs) and the composition plane. The twin axis (about which two-fold rotation occurs), is the normal to (010) (y*). The angle between y* and y is called the obliquity, φ, which varies between 0º and 4º in feldspars. Albite twinning produces gentle corrugations in the average (001) cleavage of a plagioclase, which can sometimes be seen with a hand lens, or even the unaided eye, on a freshly cleaved surface. In the field this provides a useful way of distinguishing plagioclase from alkali feldspar.

In Pericline twinning y is the twin axis and the composition plane is a non-integral plane containing y, called the 'rhombic section' (Fig. 178). The name arose because the rhombic section is a special plane which makes a perfect rhombus, with diagonals at right angles, where it intersects faces of the form {110} in a triclinic feldspar (a feldspar in which one would not expect to encounter a 90º angle). In terms of the lattice, the composition plane of Pericline twins is the unique section of a triclinic cell which has a rectangular shape. The position of the rhombic section is specified by the angle σ which its trace makes with the trace of (001) measured on (010). Two examples are illustrated in Fig. 178, (a) with a small positive value of σ, and (b) with a slightly larger, negative value. The angle σ is extremely sensitive to the inter-axial angles of the unit cell. The composition plane of pericline twins therefore rotates about b depending on the composition and structural state of the feldspar (Fig. 179) and provides a useful diagnostic property; σ is said to be +ve if the rhombic section is between $+x$ and $+z$, and negative if it is between $+x$ and $-z$. Thus in Fig. 179, σ is +100º in low microcline, +32º in low albite, and −3º in high albite.

Twinning in sanidine and orthoclase

In this and the following sections the twin laws exhibited by the different forms of alkali feldspar are described. Monoclinic feldspars cannot exhibit Albite and Pericline twinning; Carlsbad twins, of either the

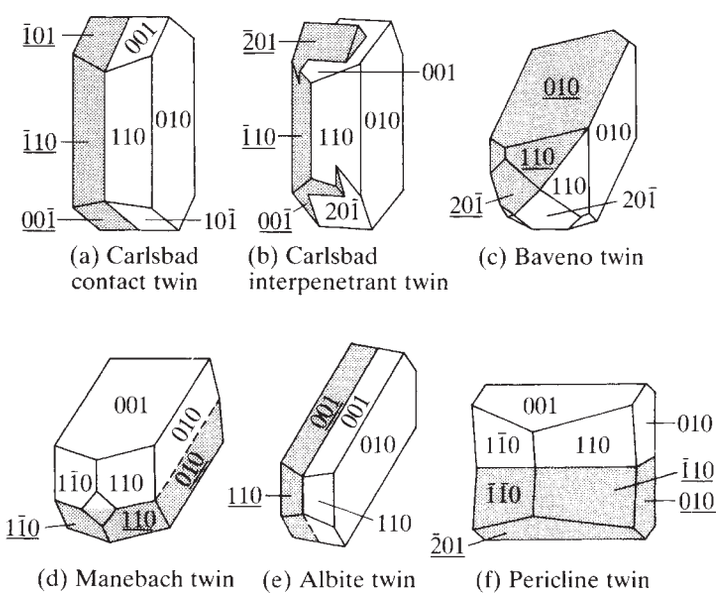


Fig. 177. Some common feldspar twins. Indices for the second individual are underlined. Albite and Pericline twins occur only in triclinic feldspars, often in combination with twins on the other laws (Deer *et al*., 1992, *An Introduction to the Rock-Forming Minerals*, Longman, UK).

Downloaded from https://pubs.geoscienceworld.org/books/chapter-pdf/3761011/9780903056434_ch59.pdf
by guest

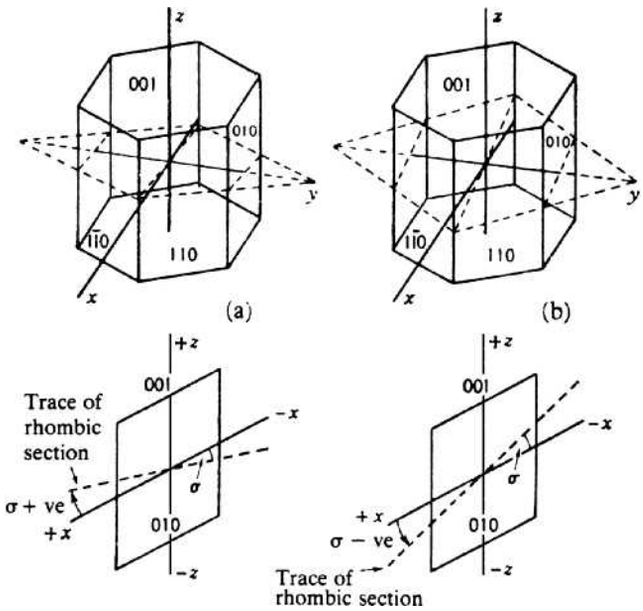


Fig. 178. Rhombic section (broken lines) in two different orientations (after Chudoba, K., 1933, *The Determination of the Feldspars in Thin Section* (translated by W.Q. Kennedy), Murby, London).

interpenetrant or contact type, are the most common (Fig. 180). In the latter the re-entrant angle between the (001) and ($\bar{1}$01) normals is very small. Under the microscope the twins are best seen in sections cut parallel to the *y* crystallographic axis (i.e. normal to the composition plane). As orthoclase is monoclinic both individuals show straight extinction, but except in sections parallel or normal to the *z* axis they show different birefringence. If the crystal is rotated about *y* both halves remain in extinction.

Baveno twins form nearly square prisms since the angle (001):(021) is approximately 45º. Multiple twins with three or four individuals are not uncommon. Under the microscope Baveno twinning is easily recognized, particularly on a (100) section, by the orientation of the composition plane with respect to the {001} or {010} cleavage. In a (100) section there is straight extinction in each individual, and because the twin plane is approximately at 45º to (010) the two parts extinguish simultaneously. Their optical orientations, however, are opposed.

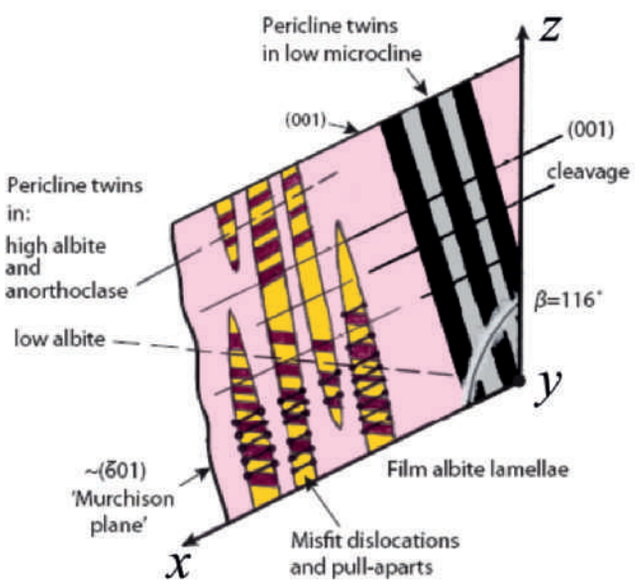


Fig. 179. Orientation of common features of alkali feldspars seen in a fragment lying on a (010) cleavage surface. Perthitic film albite lamellae are orange, Pericline twins in these lamellae are lilac, and Pericline twins in low microcline black and grey. Twins on the Albite law are parallel to (010) and therefore not visible. The fragment is defined by its (001) cleavage and by the non-integral 'Murchison plane', which is a plane of weakness defined by dislocation loops on the surfaces of film albite lamellae. 'Pull-aparts' are tiny cleavage cracks that connect opposite sides of dislocation loops. These defects are important in the response of feldspars to weathering (Fig. 194, p. 281) (Parsons, 2010).

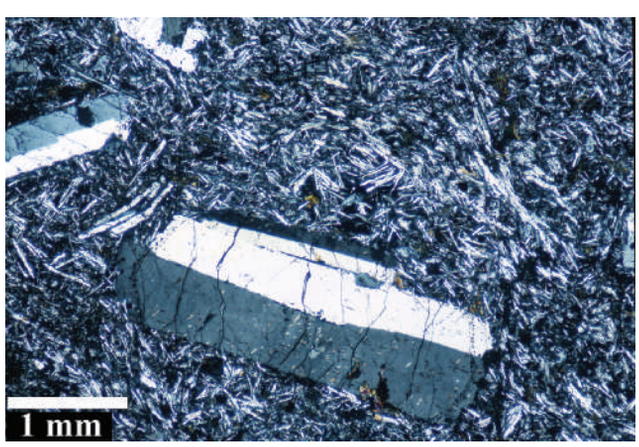


Fig. 180. Sanidine in phonolite, Ischia, Italy, showing simple Carlsbad twinning. All feldspars may develop Carlsbad twins during growth, but the absence of Albite and Pericline twinning would suggest that this crystal is sanidine. Crossed polars (W.S. MacKenzie collection, courtesy of Pearson Education).

Downloaded from https://pubs.geoscienceworld.org/books/chapter-pdf/3761011/9780903056434_ch59.pdf
by guest



Fig. 181. Perthitic microcline viewed approximately on (001). The microcline has combined Albite and Pericline 'tartan' twinning. Note how the twinning is in places very diffuse. The sinuous grey bands are perthitic 'vein' albite, with Albite twinning visible in the bottom centre and left. Crossed polars, scale bar 0.8 mm (Deer *et al*., 1992, *An Introduction to the Rock-Forming Minerals*, Longman, UK).

Manebach twinning is in general more difficult to identify as the re-entrant angles are extremely small and the composition plane is parallel to the principal cleavage. Sections cut parallel to *y* show straight extinction in each individual and, except for those accurately parallel or normal to (001), the birefringences differ. In (010) sections extinction directions make an angle of about 10º on either side of the composition plane (001).

Microcline

Microcline is almost always twinned on the Albite and Pericline laws, forming an intimate cross-hatched or 'tartan' microtexture (Fig. 181) in which the composition planes of the two twin laws are at right-angles when viewed on (001). Although individual twins are triclinic, the average monoclinic symmetry of the original crystal is maintained. This has long been held to indicate that microcline forms from a monoclinic precursor. The twin lamellae are spindle shaped in section and at high magnification have curved intersections. In places the twins become diffuse and may vanish completely. Sub-optical twinning is common in microcline, and crystals that appear optically to be microcline commonly contain regions with the sub-optical 'tweed' texture characteristic of orthoclase (Fig. 198, p. 288). The tweed microtexture of precursor orthoclase, in which the ordering domains are orientated in the same way as Albite and Pericline twins, perhaps provides a template for growth of twins, but the detailed mechanism is not understood. There is considerable variation in the appearance of twinned microcline at the transmission electron microscope scale, from very diffuse, irregular twinning, to sharply defined, periodic twins. There is reason to think that irregular twins form during relatively low temperature fluid–feldspar reactions, and it is possible, but uncertain, that the more regular tartan intergrowths form by a slow diffusive coarsening process.

The orientation of the rhombic section in microcline (Fig. 179) is such that Pericline twins are visible (and most sharply defined) viewed on (001). A single prominent cleavage, (010), is then visible, parallel to the Albite twins. Viewed on (100) both (010) and (001) cleavages are visible, at right-angles, together with Albite twins, and on (010) Pericline twins are visible, but not, in general, at right angles to the (001) cleavage (Fig. 179). Fine-scale perthitic albite lamellae parallel to *y* are hard to see between crossed polarizers in microcline because they are parallel to Pericline twins. In this case (and in alkali feldspars in general) it is best to search for exsolution lamellae in plane polarized light, as they may stand out because of differences in relief.

Albite

Sodium feldspars may show simple twinning on the Carlsbad, Baveno, Manebach or Ala laws, which may be combined with repeated twinning on the Albite and Pericline laws. The orientation of the Pericline twins (Fig. 179) changes as the feldspars order, from high- to low-albite. Because albite orders relatively rapidly, high albite rarely occurs naturally. However, if Albite twins form in high albite it is very difficult for the composition plane to rotate into the low albite orientation as the feldspar orders. Thus Pericline twins in low albite can be in the high albite orientation.

Anorthoclase

A combination of Albite and Pericline twinning, superficially similar to that found in microcline, occurs in anorthoclase (Fig. 182). The twins form when a sodian sanidine, crystallized at high temperatures, passes through the monoclinic–triclinic shearing transformation (ST on Fig. 169a,c, p. 258). In contrast to microcline the twins are generally straight-sided, and have angular, 90º intersections. An important difference to the cross-hatched twinning in microcline (Fig. 181) is that if the twinned anorthoclase is observed as it is heated on a heated microscope stage the contrast in birefringence of

Downloaded from https://pubs.geoscienceworld.org/books/chapter-pdf/3761011/9780903056434_ch59.pdf
by guest

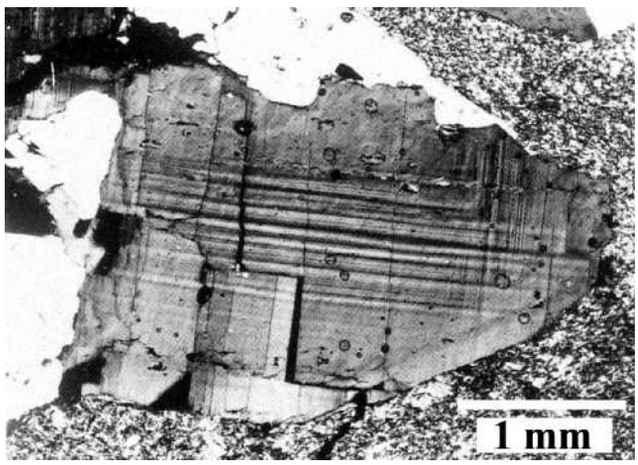


Fig. 182. Anorthoclase with combined Albite and Pericline twinning, viewed on (100). Both (010) and (001) cleavages are visible, approximately E–W and N–S respectively. Crossed polars (Deer *et al*., 1992, *An Introduction to the Rock-Forming Minerals*, Longman, UK).

the twins decreases until the twins vanish at the shearing transformation. On cooling, twins reappear immediately. The behaviour of twins in microcline is quite different, because they reflect the pattern of ordering of Si and Al in the feldspar framework, and can be destroyed only by diffusion. Twins in microcline persist for many hours even close to the melting point, and once destroyed, do not reappear on cooling.

Anorthoclase can be distinguished from microcline by considering the relationship between repeated twin planes (Fig. 183) and cleavages. Because the composition plane of Pericline twins in anorthoclase is almost parallel to (001) (Fig. 179) cross-hatched twinning in anorthoclase is visible viewed on (100), in which case intersecting (001) and (010) are also visible (Fig. 182). Only Albite twins are visible on (001), and viewed on (010) Pericline twins are visible almost parallel to the (001) cleavage.

Chemistry

The general formula of rock-forming feldspars is MT_4O_8, where T is an Si or Al atom at the centre of a tetrahedron of oxygen atoms. These tetrahedra are linked together to form a three-dimensional framework, and each oxygen is shared between two tetrahedra (see Figs 163–168); M is an alkali or alkaline-earth atom which occurs in relatively large and irregular cavities in this framework. Each Si^{4+} ion is balanced electrostatically by 4 O^{2-} half-ions, each of which is shared with another tetrahedron, but each Al^{3+} tetrahedron is unbalanced by a single charge on oxygen, O^-. Overall charge balance is maintained by monovalent M ions, mainly Na^+ and K^+, or by a divalent Ca^{2+}. To maintain neutrality, if a divalent M ion is present, an additional Al^{3+} is required, so that in solid solutions the substitution of Ca^{2+} and Al^{3+} is coupled. This coupling, together with the large difference in ionic radii of K and Na (1.51 and 1.18 Å for eightfold coordination, respectively), whereas the ionic radii of Na and Ca (1.12 Å) are essentially identical, accounts for the very great difference in the structural properties of alkali feldspar and plagioclase solid solutions. Alkali feldspars with bulk compositions close to pure end-members occur in low temperature veins and grow during diagenesis. Minor and trace-element concentrations in such feldspars are often low.

There is a huge literature on minor and trace-element concentrations in alkali feldspars. It should be noted that obtaining meaningful bulk chemical analyses from perthitic crystals using microbeam analytical techniques (electron microprobe, laser ablation mass-spectrometry) is not trivial and requires careful attention to beam size relative to the scale of the microtextures, or use of traversing methods. Analyses obtained using 'wet' methods (Table 36) are probably more reliable than many produced using microbeam techniques.

The most important substitutions in *M* sites (ionic radii are given in brackets in Å for eight-fold coordination) are Cs^+ (1.74), Rb^+ (1.61), Ba^{2+} (1.42), Pb^{2+} (1.29) and Sr^{2+} (1.26). The Ba feldspars are described below (p. 291) as a distinct species. In general terms the very large Cs and Rb ions have their highest concentrations in Or-rich feldspars, and where two feldspars are present, as in some granites and granitic pegmatites, and in perthitic crystals, they partition strongly into the Or-rich phase. In alkali feldspar from most rocks Cs is $\leqslant$100 ppm, but 1.5 wt.% Cs_2O has

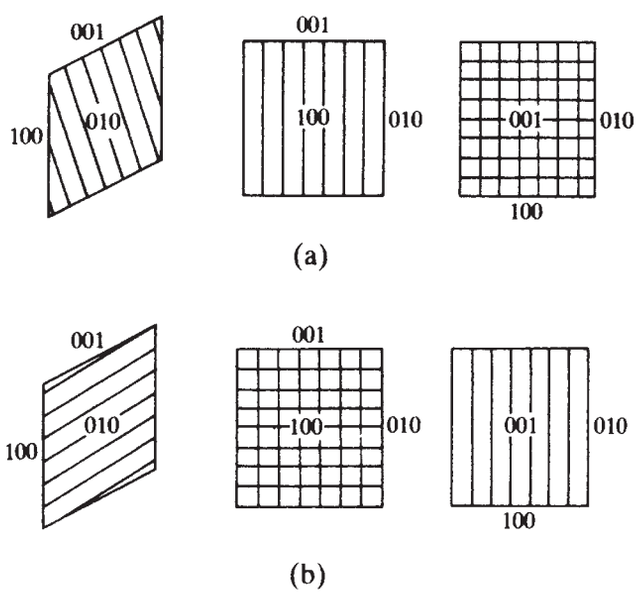


Fig. 183. Orientation of Albite and Pericline twinning in (a) microcline (b) anorthoclase. Albite twinning is always parallel to the (010) cleavage, but the composition plane of Pericline twinning (the rhombic section) changes orientation by rotation about *y* (Deer *et al*., 1992, *An Introduction to the Rock-Forming Minerals*, Longman, UK).

Downloaded from https://pubs.geoscienceworld.org/books/chapter-pdf/3761011/9780903056434_ch59.pdf
by guest

been reported from a granitic pegmatite. The Rb content is usually $\leqslant$1000 ppm, but 26 wt.% Rb_2O has been reported in alkali feldspar from the same pegmatite, corresponding with 91 mol% of the Rb-feldspar equivalent of microcline, rubicline. The Pb content is <1000 ppm, and typically between 100 and 10 ppm. Strontium is rather more abundant and 1 wt.% has been reported; it is particularly high in some anorthoclase phenocrysts. Rare-earth elements have ionic radii close to those of Na and Ca and are likely to reside in *M* sites. An unusual *M* site substitution is ammonium, giving the rare feldspar buddingtonite, $NH_4AlSi_3O_8.½H_2O$, which occurs only in sedimentary rocks, the ammonia being derived from the decomposition of organic matter.

Table 36. Alkali feldspar analyses.

	1	2	3	4	5	6	7	8	9	10	11	12
SiO_2	65.76	64.76	64.66	63.66	64.20	63.68	64.46	67.27	63.62	66.97	64.28	64.94
TiO_2	0.08	–	–	–	–	0.01	–	–	0.08	0.04	–	0.00
Al_2O_3	20.23	19.96	19.72	19.54	19.10	19.57	18.55	18.35	19.12	18.75	19.19	16.74
Fe_2O_3	0.18	0.08	0.08	0.10	0.40	0.29	0.14	} 0.92	} 0.47	} 0.88	0.09	2.56
FeO	–	tr.	–	–	–	0.24	–				–	0.00
MgO	0.10	tr.	tr.	–	–	0.05	0.00	0.00	0.05	0.00	0.10	0.04
BaO	0.63	–	–	–	–	0.34	–	–	1.56	–	0.11	–
CaO	1.19	0.84	0.34	0.50	0.34	0.40	0.17	0.15	0.05	0.36	0.11	0.03
Na_2O	8.44	5.54	3.42	0.80	2.60	1.56	0.49	6.45	2.66	7.88	0.92	0.79
K_2O	3.29	8.12	11.72	15.60	12.76	14.21	16.07	7.05	12.09	5.39	15.30	15.33
H_2O+	0.37	0.54	0.18	–	0.72	0.04	–	0.08	0.11	0.01	0.36	–
H_2O-	0.08	–	–	–	–	0.07	0.06	0.08	0.00	0.03	–	0.00
Total	100.35	99.84	100.12	100.20	100.12	100.46	99.94	100.35	99.81	100.31	100.46	100.43
α	1.528	1.5256	1.5217	1.5188	1.5204	–	–	1.5232	–	1.5239	1.5192	1.5265
β	1.533	1.5296	1.5259	1.5230	1.5240	–	–	1.5289	–	1.5299	1.5228	1.531
γ	1.537	1.5236	1.5279	1.5236	1.5265	–	–	1.5296	–	1.5308	1.5245	1.5315
$2V_\alpha$	78°	82.8°	69.1°	43.6°	79.9°	83–86°	–	33°	–	46°	68.4°	32–33½°
Ext. on (010)	14°	11.7°	9.5°	5.3°	7.5°	–	–	–	–	–	5.25°	5°
D (g/cm^3)	–	2.5950	2.5778	2.5632	2.5771	–	–	–	–	–	2.5661	–
	Numbers of ions on the basis of 32 O											
Si	11.719	11.750	11.794	11.759	11.831	11.730	11.938	12.030	11.770	11.932	11.852	12.011
Al	4.249	4.269	4.240	4.254	4.148	4.249	4.050	3.868	4.169	3.938	4.170	3.650
Fe^{3+}	0.024	0.011	0.011	0.014	0.055	0.040	0.019	0.124	0.096	0.118	0.012	0.356
Ti	0.011	–	–	–	–	0.001	–	–	0.011	0.005	–	–
Mg	0.027	–	–	–	–	0.014	–	–	0.013	–	0.028	0.011
Na	2.916	1.949	1.209	0.286	0.929	0.557	0.176	2.236	0.954	2.722	0.329	0.283
Ca	0.227	0.163	0.066	0.099	0.067	0.078	0.003	0.029	0.010	0.069	0.022	0.006
K	0.748	1.880	2.727	3.676	3.000	3.340	3.797	0.609	2.855	1.226	3.599	3.618
Ba	0.044	–	–	–	–	0.024	–	–	0.113	–	0.008	–
ΣT	16.00	16.03	16.04	16.03	16.03	16.02	16.01	16.02	16.05	15.99	16.03	16.02
Σ(Mg,Na,Ca,Ba)	3.96	3.99	4.00	4.06	4.00	4.05[a]	4.01	3.87	3.95	4.02	3.99	3.92
Mol.% Or	20.0	47.1	68.1	90.5	75.1	83.1	94.8	41.5	75.5	30.5	90.5	92.4[b]
Mol.% Ab	73.6	48.8	30.2	7.1	23.2	13.7	4.4	57.7	23.9	67.8	8.3	7.2
Mol.% An	6.4	4.1	1.7	2.4	1.7	3.2	0.8	0.8	0.6	1.7	1.2	0.4

1 Sodium-rich orthoclase cryptoperthite, ijolite-nepheline syenite, Mogok, Burma (Tilley, C.E., 1954, *Amer. J. Sci.*, **252**, 65–79).
2 Orthoclase microperthite with white schiller, Burma (Spencer, E., 1930, *Mineral. Mag.*, **22**, 291–365).
3 Orthoclase microperthite (moonstone), Ceylon (Spencer, E., 1937, *Mineral. Mag.*, **24**, 453–94).
4 Orthoclase, Mogok, Burma (Spencer, E., 1930, *Mineral. Mag.*, **22**, 291–365).
5 Microcline microperthite, quartz-feldspar-tourmaline pegmatite, Orissa, India (Spencer, E., 1937, *Mineral. Mag.*, **24**, 453–94).
6 Microcline microperthite, charnockite, St Thomas' Mt, Madras, India (Howie, R.A., 1955, *Trans. Roy. Soc. Edinburgh*, **62**, 725–63).
7 Low microcline, pegmatite in grennaite, Norra Kärr, Sweden (MacKenzie, W.S., 1954, *Mineral. Mag.*, **30**, 354–66).
8 Sanidine, rhyolite, Mitchell Mesa, Texas, USA (Tuttle, O.F., 1952, *Amer. J. Sci.*, Bowen vol., 553–67).
9 Sanidine, leucite-nepheline dolerite, Vogelsberg, Germany (Tilley, C.E., 1958, *Amer. Min.*, **43**, 758–61).
10 Anorthoclase, Grande Caldeira, Azores (Tuttle, O.F., 1952, *Amer. J. Sci.*, Bowen vol., 553–67).
11 Adularia, St Gotthard, Switzerland (Spencer, E., 1937, *Mineral. Mag.*, **24**, 453–94).
12 Amber-yellow ferriferous orthoclase, Itrongay, Madagascar (Coombs, D.S., 1954, *Mineral. Mag.*, **30**, 409–27).

[a] Includes Fe^{2+} 0.037.
[b] Includes 9.0 mol%, Fe-orthoclase.

Downloaded from https://pubs.geoscienceworld.org/books/chapter-pdf/3761011/9780903056434_ch59.pdf
by guest

Important substitutions in T sites in alkali feldspars include Fe^{3+} (ionic radius 0.49 Å for four-fold coordination), Ga^{3+} (0.47 Å), Ti^{4+} (0.42 Å) and B^{3+} (0.11 Å). End-member gallium feldspars, $NaGaSi_3O_8$ and $KGaSi_3O_8$, can be synthesized, but the concentration in natural alkali feldspars is low and generally <50 ppm. Pure $KFeSi_3O_8$ can also be synthesized, in both monoclinic 'iron sanidine' and triclinic 'iron microcline' forms, the latter replete with 'tartan' twinning. However care must be taken in interpreting Fe and Ti contents of natural feldspars because in turbid feldspars both elements occur in sub-micrometre particles in micropores, as particulate hematite and titanomagnetite. Turbidity is a clear marker that the feldspar has been pervasively affected by fluids during its history. It is not, in general, known whether the Fe and Ti were in the feldspar structure prior to the fluid–feldspar reaction, or were introduced by the fluid. Some natural feldspars certainly contain considerable amounts of Fe^{3+} replacing Al in the T site. The best known are the 'gem quality' yellow orthoclase and sanidine crystals from Itrongay, Madagascar (Table 36, analysis 12), which contain up to 10 mol% of the $KFeSi_3O_8$ molecule. An unusual naturally occurring feldspar is reedmergnerite, $NaBSi_3O_8$, which crystallizes in sediments in which B has been concentrated in solutions.

More than 40 compounds with the feldspar structure that do not occur in Nature have been synthesized and 30 binary systems containing such compounds have been studied. Some of these systems are of interest because they exhibit much faster reaction kinetics than Si–Al feldspars and can be used as analogues. For example $KFeSi_3O_8$ and $KGaSi_3O_8$ both undergo the monoclinic–triclinic ordering transformation on laboratory timescales, and solid solutions in the system $NaAlGe_3O_8$–$KAlGe_3O_8$ undergo very rapid coherent exsolution.

Experimental

Phase diagrams for the system Ab–Or were given earlier, as Figs 169a–c, p. 258, because of their importance in feldspar nomenclature and physical properties. The present section gives experimental detail, considers phase relationships involving silicate liquid and aqueous fluids, and presents some data for systems involving components other than Ab, Or and An. Many systems that include feldspar have been studied experimentally and only a few particularly important examples are described herein.

Systems with silicate liquid. It is extremely difficult to obtain equilibrium between silicate liquids of feldspar composition and feldspars in the absence of water, and the solidus and liquidus curves in Fig. 169a are approximate. Fractional crystallization drives liquids towards the minimum M, either by crystallization and fractionation of very Or-rich feldspars or by fractionation of Ab-rich feldspars. The latter is the case also for crystallization in the ternary system Ab–Or–An, the most important factor in igneous evolution being fractionation of plagioclase. Thus mildly alkaline basalts fractionate towards trachytes with feldspar bulk compositions near M. Note that the very flat form of the solidus means that a large range of feldspar compositions can be in equilibrium with a narrow range of liquids over a small temperature interval. Fractionation drives liquids very efficiently to M.

In the presence of water (Fig. 169b), crystal–liquid equilibrium, and exchange equilibria between feldspar pairs on the solvus, are accomplished more rapidly than in the 'dry' system. In the absence of H_2O the incongruent melting point of sanidine is ~1150ºC (Fig. 169). In the system $KAlSi_3O_8$–H_2O the melting point is lowered considerably as P_{H_2O} increases, and sanidine melts congruently at ~950ºC at P_{H_2O} ~0.25 GPa. Similarly, the dry melting point of albite is 1118ºC, but it melts at 905ºC and 825ºC at P_{H_2O} 0.1 and 0.2 GPa, respectively. In the system Ab–Or–H_2O (Fig. 169b) the liquidus and solidus curves move to lower temperatures and intersect the solvus at the point at which P_{H_2O} is slightly above 0.4 GPa. The minimum M at low P_{H_2O} becomes a eutectic E. Three phases, the eutectic liquid, an Ab-rich feldspar and an Or-rich feldspar are then in equilibrium. The composition of E moves towards Ab with increasing pressure, an effect seen in the normative composition of granitic rocks.

The lowering of the melting point of feldspars when water is present is of profound importance for magmatism and high grade metamorphism in the Earth's crust. Another important implication is that crystallization of feldspathic liquids can be accomplished by reduction in P_{H_2O} alone, without cooling (adiabatic crystallization).

At low P_{H_2O}, Or-rich feldspars melt incongruently to the feldspathoid leucite, $KAlSi_2O_6$, and an SiO_2-rich liquid (Fig. 169a). As P_{H_2O} increases the field of leucite decreases in size and slightly above 0.2 GPa sanidine melts congruently. Low-pressure phase relationships on the join leucite–silica are shown in Fig. 184. The solid phases are leucite, sanidine, and a high-temperature silica polymorph, either cristobalite or tridymite. Sanidine melts incongruently at ~1150ºC on the isotherm that passes through the reaction point R (also called a peritectic). A silica-undersaturated liquid such as A, with a bulk composition at Y, between leucite and sanidine, must, when completely crystallized, be composed of those phases in the proportions YZ:XY. Liquid A begins to crystallize only leucite at B and large amounts are precipitated as the liquid composition moves down the liquidus to R. At the reaction point some of the the leucite reacts with the remaining liquid until it is used up, when the solids are in the proportion YZ:XY. A more siliceous liquid, C, with a composition between sanidine and a silica polymorph, precipitates leucite at first, but when it reaches R all the leucite reacts with liquid to give sanidine. With further cooling the liquid continues to precipitate sanidine until it

Downloaded from https://pubs.geoscienceworld.org/books/chapter-pdf/3761011/9780903056434_ch59.pdf
by guest

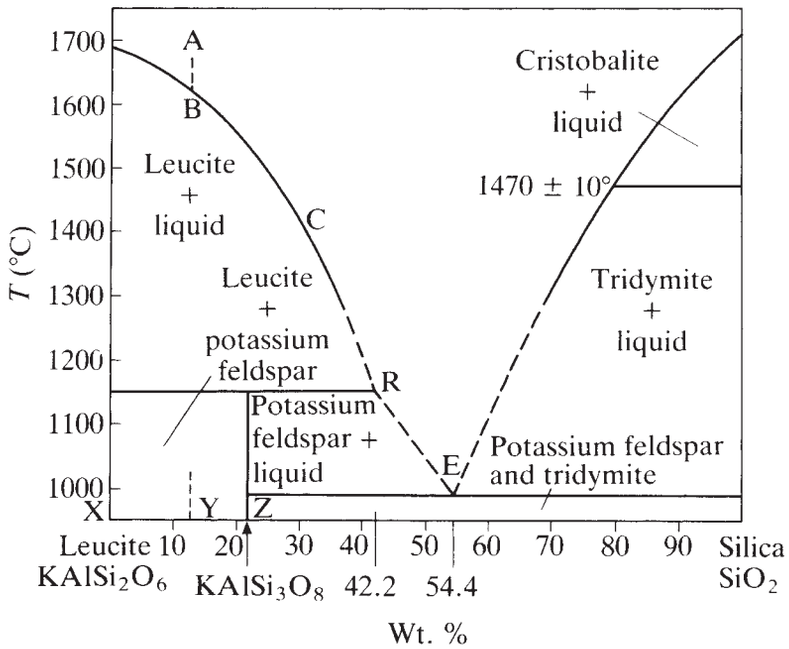


Fig. 184. Phase diagram for the system $KAlSi_2O_6$ (leucite)–SiO_2 (silica, either cristobalite or tridymite) which includes $KAlSi_3O_8$ (sanidine) as an intermediate phase. Water is not present. (After Schairer, J.F. & Bowen, N.L., 1955, *Amer. J. Sci.*, **253**, 681–746).

reaches the eutectic E, when tridymite appears and the final liquid is used up.

Perhaps the most important system involving alkali feldspar is Ab–Or–Q–H_2O, the simplified granite system (Fig. 185). Relationships in real granites are more complex because their magmas contain An as well as non-feldspar components, but because low-An feldspars and quartz make >80% of many granites it is a useful approximation to the natural situation. The exact form of the ternary system Ab–Or–An has not been fully determined experimentally because of difficulties in reaching equilibrium and in analysing the individual feldspar phases in fine-grained experimental products. Its general form has been deduced partly from natural assemblages and thermodynamic models and is described in the Paragenesis section (Fig. 196, p. 285).

The work illustrated in Fig. 185 is a classic study and the first to apply on a large scale the then new 'hydrothermal' method using welded platinum capsules containing glass or crystalline silicate starting materials plus water so that P_{H_2O} could be controlled. Feldspar compositions were determined using the $\bar{2}01$ *d* spacing (Fig. 170, p. 260). Crystallization behaviour in the system is described in the caption. Although the relationships are shown as involving only feldspar components, the system is not strictly ternary because H_2O is present, some of which dissolves in the silicate melt. Sufficient water was placed in each capsule to ensure that the silicate liquid was saturated with water. The vapour contains small amounts of silicate in solution. The diagrams represent a section through an Ab–Or–An–H_2O tetrahedron at approximately constant H_2O content.

Order–disorder. Albite grown in the laboratory initially has a disordered Si–Al framework that orders with time to an equilibrium state of order that varies with temperature. The degree of order can be obtained from cell parameters or using the separation of X-ray reflections that are particularly sensitive to the α and γ cell angles, such as 131 and $1\bar{3}1$ ($\Delta 2\theta_{131}$, Fig. 186). Equilibrium is reached more rapidly at high pressure so $\Delta 2\theta_{131}$ has been reversed, using both ordering and disordering experiments at 1.8 GPa, to give the solid curve on Fig. 186. Estimates of the temperature–order curve at low pressure (the dashed line) can be made, less reliably, from a combination of experiments from various sources. The steep part of the latter curve corresponds with the intermediate albite band in Fig. 169a. The axes at the right are *order parameters*: $t_1(0)$ and $t_1(m)$ are the fractions of the $T_1(0)$ and $T_1(m)$ sites occupied by Al. The value of $t_1(0) + t_1(m)$ is a measure of the fraction of Al that has diffused from T_2 to T_1 sites (*non-convergent ordering*, see Structure section, p. 257). The value of $t_1(0) - t_1(m)$ is a measure of the fraction Al in $T_1(0)$ sites (*convergent ordering*).

The relationship between temperature and equilibrium order for Or-rich feldspars is much less well understood. Because high- and low-sanidine are monoclinic an order parameter based on lattice angles cannot be used. The most practical order parameter is the optic axial angle, $2V_\alpha$, (see Fig. 190), although it is necessary to know the composition of the feldspar. The variation of $2V_\alpha$ with respect to temperature has been determined experimentally in both sanidine and anorthoclase at 850–650ºC. However the low-sanidine–microcline monoclinic–triclinic transition has never been achieved experimentally, because the fine-scale 'tweed' microtexture (see Structure section, p. 257 and Fig. 198, p. 288) develops and the structure becomes stranded in a partially ordered state and is unable to order further. In Nature, dissolution–reprecipitation reactions and/or deformation

Downloaded from https://pubs.geoscienceworld.org/books/chapter-pdf/3761011/9780903056434_ch59.pdf
by guest

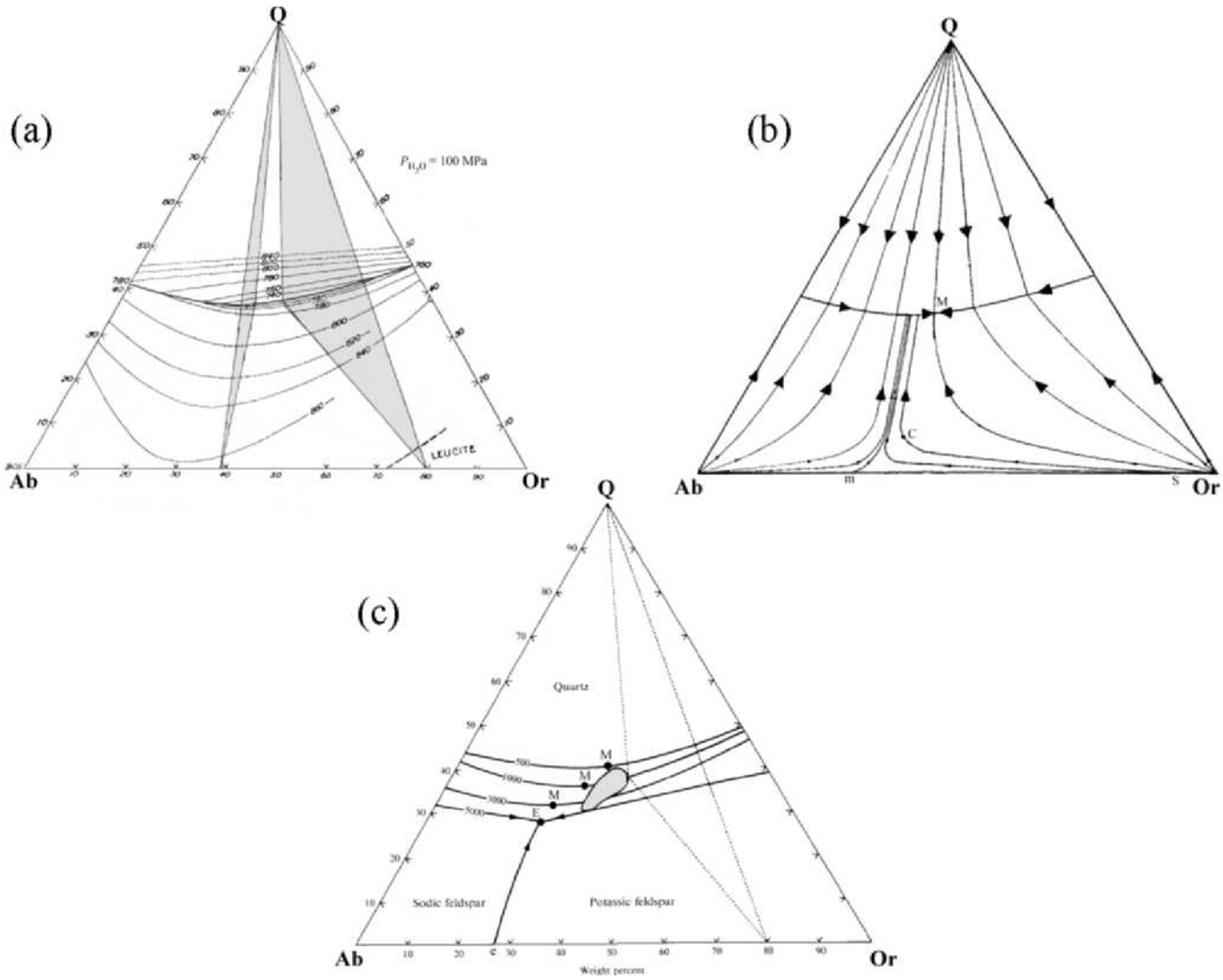


Fig. 185. Phase diagrams for the system Ab–Or–Q–H_2O. Silicate liquids are saturated with water throughout crystallization, and crystallization is at constant P_{H_2O} (isobaric crystallization). (a) The liquidus at P_{H_2O} 0.1 GPa, with isotherms at 20ºC intervals. The Q–AF field boundary joins two binary eutectics, that on the Q–Or join corresponding with E in Fig. 184. The two grey triangles are three-phase triangles involving a liquid on the field boundary, Q and AF in equilibrium. During crystallization, the liquid apex of the three-phase triangles moves along the field boundary. In the right-hand triangle the coexisting AF becomes more albitic, on the left richer in Or. During equilibrium crystallization the last liquid is used up when the trailing edge of the triangle, between Q and AF, passes though the starting composition. An isobaric *T* minimum on the field boundary [M in (b)] lies between the apices of the triangles, and this may be reached during fractional crystallization. This is often called the 'granite minimum'. Note that the Ab:Or ratio at M is not the same as that at the minimum m on the Ab–Or join. (b) Fractionation curves on the liquidus at P_{H_2O} 0.1 GPa. These can be constructed if liquid and feldspar compositions are known, because a liquid-crystal tie-line is always tangential to a fractionation curve. There is an infinite number of fractionation curves and all originate at either Ab or Or except for one, which joins the minimum m, on the feldspar join, to the Q–feldspar field boundary. This is sometimes called the 'unique fractionation curve' (UFC). Fractionation of AF with a very large range of compositions leads to a concentration of fractionation curves in the vicinity of the UFC, which has been likened to a 'thermal valley'. When a liquid on any fractionation curve encounters the Q–AF field boundary, Q starts to grow and the liquid moves along the boundary towards the ternary minimum M. At this stage the majority of liquids become richer in Or as does the coexisting AF. In principle, a zoned feldspar crystallizing from liquids on a curve such as S–C–M would initially become more albitic, and then more Or-rich when the liquid reaches the field boundary. (c) Field boundaries in the system at various P_{H_2O}, including 0.5 GPa, when the minimum on the Ab–Or join has become a eutectic, e (Fig. 169b). The quartz and feldspar fields then meet at a ternary eutectic, E. When this is the case a liquid in one of the feldspar fields initially crystallizes a single, Ab- or Or-rich feldspar which is joined by a second feldspar when the liquid encounters the boundary between the two feldspar fields. The shaded area shows the concentration of analysed granitic rocks with >80% normative *ab*, *or* and *Q*. (Data from Tuttle, O.F. & Bowen, N.L., 1958, *Geol. Soc. Amer. Mem.*, **74**, pp. 153 and Luth *et al*., 1958, *J. Geophys. Res*., **69**, 759–73.)

often appear to have been involved in the development of microcline. The upper stability limit of microcline is conventionally placed in the range 500–480ºC (Figs 169a,c) on the basis of estimates of temperature gradients in a contact aureole and some unreversed experiments. It is not clear whether, in the absence of tweed formation, the order parameter would vary continuously between sanidine and microcline (as it

Downloaded from https://pubs.geoscienceworld.org/books/chapter-pdf/3761011/9780903056434_ch59.pdf
by guest

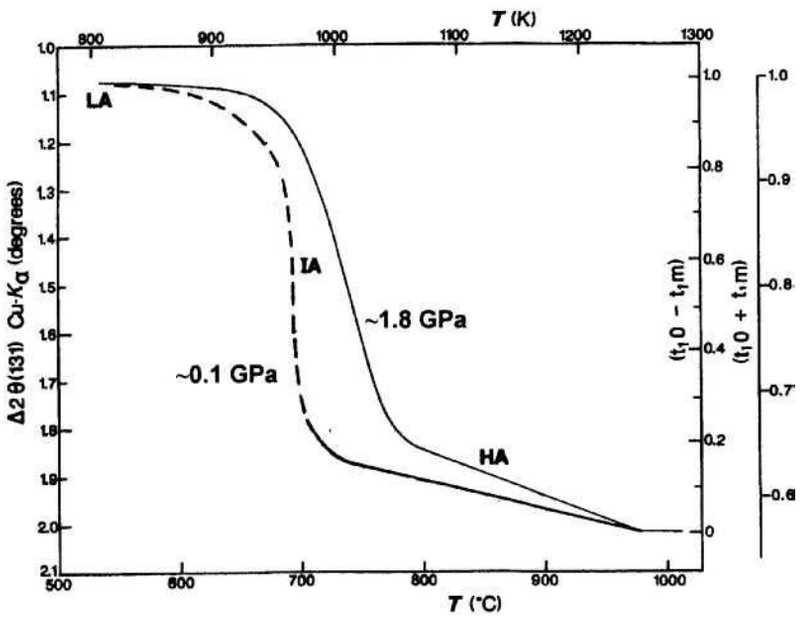


Fig. 186. Experimentally determined variation in equilibrium Si−Al order with respect to temperature in albite. Order was estimated from the separation of the 131 and $1\bar{3}1$ diffraction peaks ($\Delta 2\theta_{131}$). The axes at the right are order parameters, discussed in the text. HA: high albite; IA: intermediate albite; LA: low albite. The curve at 1.8 GPa was obtained in reversed experiments by Goldsmith J.R. & Jenkins, D.M, 1985, *Amer. Mineral*., **70**, 911−23, and that at 0.1 GPa is considerably less reliable and was assembled from various literature sources by Brown W.L. & Parsons, I., 1989, *Mineral. Mag*., **53**, 25−42.

does between high- and low-albite, with a range of stability for intermediate microcline, Fig. 186) or discontinuously, in which case the steep section on the K-feldspar equivalent of Fig. 186 would be vertical.

The probable configuration of the monoclinic–triclinic symmetry change in intermediate alkali feldspars, in the absence of exsolution, is shown in Fig. 171, (p. 261) although the existence of an intermediate microcline field is uncertain. The symmetry-breaking process at the albite side of the diagram is the instantaneous shearing transformation, whereas at the K-feldspar side it is the slow ordering transformation. Most Or-rich feldspars grow with monoclinic symmetry as sanidine whereas many Ab-rich feldspars (and all those with even low An-contents) grow with triclinic symmetry below the shearing transformation. The hypothetical An-free Ab-rich feldspar growing at the solidus−solvus intersection in Fig. 169b would grow just inside the monoclinic sanidine field and become triclinic anorthoclase very soon after when it intersects the shearing transformation. There is no reason to think that ordering rates in albite and K-feldspar are greatly different; it is the intervention of the tweed microtexture that makes the sanidine−microcline transition so difficult to achieve in the laboratory. There is evidence that low albite and microcline can grow directly from aqueous solutions in geothermal systems and during sedimentary diagenesis.

Solvus curves. The solvus curves in Figs 169a and b are defined by feldspar pairs that do not share a common Si,Al−O framework. Such discontinuous feldspar pairs are said to be 'strain-free'. In Fig. 169b pairs of feldspars grow at the solidus−solvus intersection, the situation in a 'sub-solvus' granite (although note that the An component is omitted and has a very large effect on exsolution temperatures, as illustrated in Fig. 187). Experimental crystallization of amorphous starting materials such as glass or gel to determine solvus curves (Fig. 169b) gives a mosaic of tiny Ab- and Or-rich crystals whose composition is usually determined using X-ray diffraction (Fig. 170). Strain-free feldspar assemblages also form relatively irregular, coarsely perthitic intergrowths in crystals that have interacted with fluids and undergone dissolution – reprecipitation reactions (Fig. 192 right). In this case relatively large alkali feldspar crystals are made of mosaics of incoherent and semicoherent subgrains.

The alkali feldspar solvus is sensitive to pressure and moves to higher temperature by ~220ºC/GPa. This is much less than the depression of the solidus by P_{H_2O} (Figs 169a,b). Figure 169a shows the solvus at atmospheric pressure but for hypothetical feldspars with equilibrium Si−Al order, a combination unlikely to be found in Nature. The solvus is also sensitive to Si−Al order. It is not possible to obtain a curve that takes account of ordering by direct synthesis because ordering is too slow. The curve in Fig. 169a was constructed from a series of solvi obtained using natural feldspars with differing degrees of order. Ordering increases exsolution temperature; for disordered feldspars the critical temperature (the top) of the solvus is at 635ºC at 0.1 MPa. Figure 169a is the best estimate we can make of the stable equilibrium phase diagram for alkali feldspars at atmospheric pressure, but in the absence of water in the system, equilibrium is unlikely to be reached in Nature. Figure 169b is a metastable equilibrium diagram, in which all feldspars are disordered. This is a diagram appropriate for experimental synthesis of feldspars if the duration of experiments is short and little or no Si−Al ordering can occur. The process which defines the solvus, Na−K exchange, is very much faster, so a solvus is defined which is metastable with respect to ordering.

However, natural assemblages of individual Or-rich alkali feldspar and Ab-rich plagioclase crystals do not

Downloaded from https://pubs.geoscienceworld.org/books/chapter-pdf/3761011/9780903056434_ch59.pdf
by guest

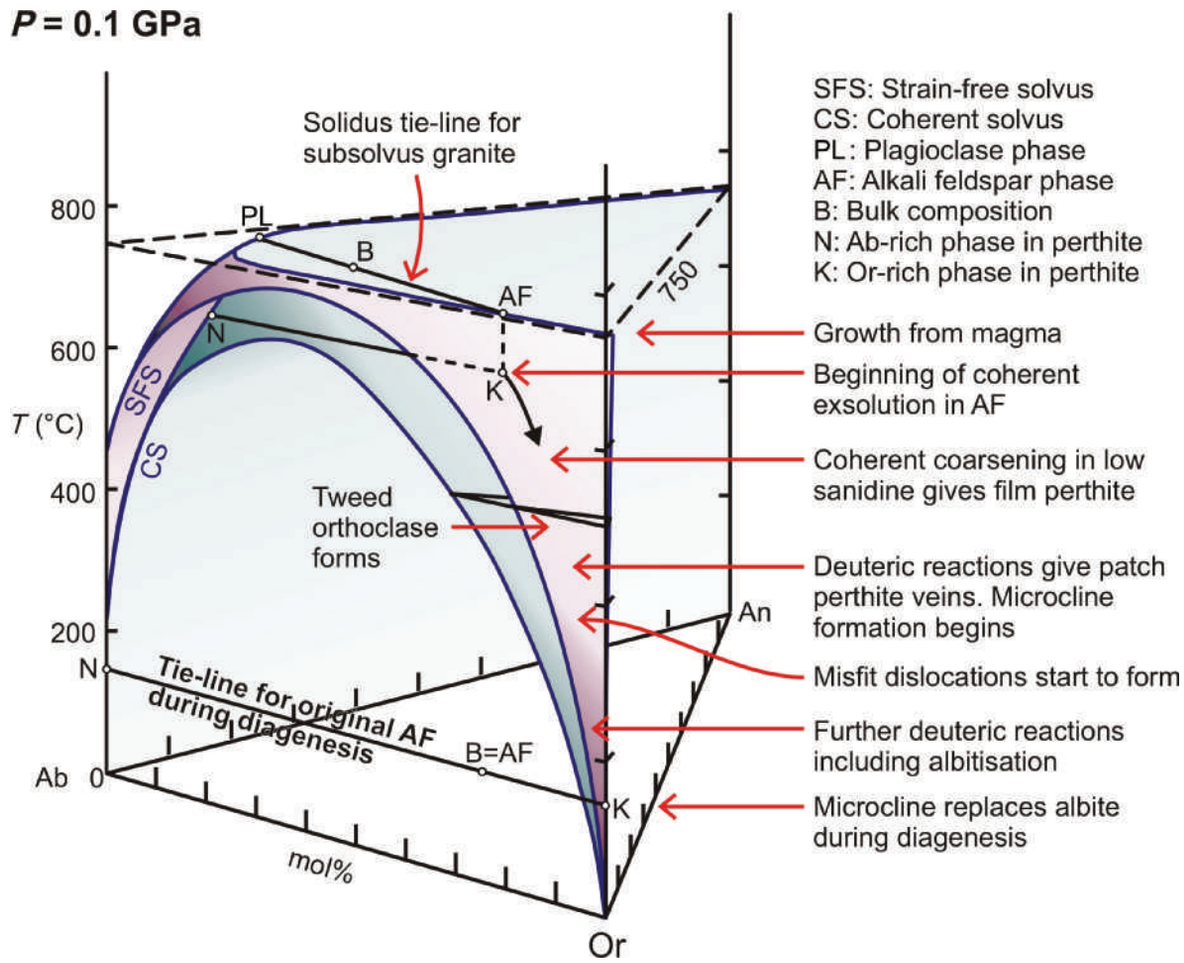


Fig. 187. The ternary solvus dome in the Ab−Or−An system. *SFS*, in purple, is the strain-free solvus, used for geothermometry in rocks in which two feldspar phases, PL and AF, crystallize in equilibrium on a tie-line (see Fig. 162, p. 250). PL and AF lie on the solidus, the temperature of which is strongly sensitive to magma composition and especially to P_{H_2O}. The solvus tie-line is not affected by magma composition or P_{H_2O}, but is sensitive to pressure, moving to higher temperature by 220ºC/GPa. Note the extreme sensitivity of the thermometer to An in AF and Or in PL.

Events marked with arrows on the right apply to the alkali feldspar in a typical two-feldspar granite as it cools and experiences fluid–feldspar reactions, including replacement when, after exhumation, the feldspar is incorporated in a siliciclastic sedimentary rock. *CS*, in blue, is the coherent solvus. Alkali feldspar AF will begin coherent exsolution when it cools slightly below this surface, giving a pair of coherent feldspars N−K, whose composition changes down the solvus surface as the intergrowth coarsens. Interactions with deuteric fluids begin when tweed orthoclase (Fig. 198) has formed, giving vein perthite (Fig. 172a). Misfit dislocations (Fig. 172b) form as the crystal structure stiffens. Replacement by very Ab- and Or-rich feldspars can continue to diagenetic temperatures. (From Parsons, I. *et al*., 2005, *J. Sed. Res*., **75**, 921−42).

usually remain in equilibrium on the strain-free solvus as the rock cools. Each crystal behaves as a closed system and undergoes coherent exsolution as an individual (see sub-section 4 in Structure section). Coherent relationships require the use of a behaviour diagram (Fig. 169c). Coherent exsolution is a relatively slow process and solvus curves must be obtained by annealing homogeneous or exsolved alkali feldspars of known bulk composition and observing the appearance and disappearance of exsolution lamellae using transmission electron microscopy. Coherent solvus curves have been obtained for feldspars with both disordered and ordered frameworks. The curve on Fig. 169c is an attempt to define a curve for equilibrium order by using the coherent solvus for disordered feldspars near the critical point and that for ordered feldspars at lower temperature. Note, again, that this curve is for hypothetical An-free feldspars and would be at considerably higher temperatures in most natural feldspars. Because the solvus curves are asymmetrical, an alkali feldspar growing at high temperature simultaneously with an albitic plagioclase, for example from a granite magma, contains more Ab in solid solution than there is Or in the plagioclase. Following exsolution the alkali feldspar will be conspicuously perthitic, and although the plagioclase may be antiperthitic, the intergrowths may be difficult to see.

Mechanisms of exsolution. As discussed in the Structure section, the orientation of coherent inter-

Downloaded from https://pubs.geoscienceworld.org/books/chapter-pdf/3761011/9780903056434_ch59.pdf
by guest

growths varies with bulk composition (Fig. 173, p. 262) to minimize coherency strain energy. The mechanism of coherent exsolution also varies with bulk composition. Crystals with bulk compositions in the middle region of the solvus probably unmix by a process called spinodal decomposition, in which a low-amplitude compositional wave develops which increases in amplitude at a specific 'initial wavelength' which subsequently coarsens with time. Spinodal decomposition is a rapid process which occurs at a spinodal curve inside the solvus, which touches the solvus at its critical point. Intergrowths formed by spinodal decomposition show great regularity through large volumes of the crystal, are often sinuous and sometimes bifurcate (Fig. 174b). Exsolution and coarsening with time of lamellar sanidine cryptoperthites can be studied experimentally in isothermal annealing experiments, using transmission electron microscopy to study the products. Initial wavelengths of ~8 nm coarsen to ~50 nm after ~2 y at 560ºC. The diffusion coefficients obtained have been used to calculate cooling rates of volcanic rocks, dykes and sills, and appear to extrapolate reasonably well to slowly cooled plutons. Complex intergrowths such as braid perthite (Fig. 174a) cannot be created experimentally because the slow process of framework ordering is essential to their development, but studies of variation of lamellar periodicity in syenite plutons have shown a simple relationship to contacts and hence cooling rate.

For bulk compositions near the limbs of the solvus, most importantly those in the range $Ab_{30}Or_{70}$–Ab_5Or_{95}, which occur in subsolvus granites (Figs 172a, b, Fig. 173 areas 1 and 2), the exsolution mechanism is probably coherent nucleation. Compositions near the limbs of the solvus intersect the spinodal curve only at low temperature, and a nucleation process is likely to occur just below the coherent solvus before the spinodal is encountered. In a nucleation process one component forms an embryo (for example of albite in sanidine) which depletes surrounding sanidine in the Ab component. The embryo forms a stable nucleus only if the loss of free energy due to clustering of Na ions exceeds the gain in energy at the surface of the embryo, which may be coherent or incoherent. Nuclei may form spontaneously in a perfect structure (homogeneous nucleation) or on pre-existing imperfections (heterogeneous nucleation). Or-rich lamellae often form on twin composition planes in antiperthites (Fig. 174, area 7). Nucleation produces intergrowths that are less regularly distributed than those produced by spinodal decomposition but the periodicities of coherent and semicoherent lamellar microperthites (Fig. 172) are in order-of-magnitude agreement with the experimental diffusion data.

The ternary solvus. The shape of the ternary Ab–Or–An solvus (Fig. 187) is less well known than the binary solvus on the Ab–Or join, mainly because it is difficult to reach equilibrium if the coupled $Ca^{2+} \leftrightarrow Al^{3+}$ substitution is involved in the reaction, as it involves redistribution of ions that are part of the strong feldspar framework. The binary system Ab–Or involves only $Na^+ \leftrightarrow K^+$ exchange and framework bonds do not have to break. It is also difficult to measure ternary feldspar compositions accurately in experimental products. Relationships between silicate liquids and ternary feldspars have been deduced mainly from work on natural rocks and are discussed in the Paragenesis section (Figs 195–197).

The ternary solvus tunnel has a dome shape (Fig. 187) and a plagioclase feldspar and an alkali feldspar pair in equilibrium will lie on a unique tie-line at any particular pressure and temperature. This is the basis of the two-feldspar geothermometer (Fig. 162, p. 250). Although experimental synthesis contributed greatly to the development of earlier two-feldspar geothermometers, the most recent version (Fig. 162) uses a thermodynamic approach and is based on calorimetric and cell volume data. An important advantage of the two-feldspar thermometer is that it depends only on equalizing the chemical potentials of the three components in the two feldspar phases (see Introduction) and is thus independent of the composition of the rock, or the medium through which equilibrium is reached, such as silicate liquid or aqueous solution. The positive pressure dependence of the solvus is 220ºC/GPa, considerably less than the effect of P_{H_2O} in lowering the solidus temperature of silicate melts. Thus magmas intersect the dome at different temperatures depending on their composition and particularly because of their water content, which depends on P_{H_2O}. A variety of tie-lines, for different geological settings, are shown on Fig. 162. Ternary solid solution is greatest in hot, dry rocks, lower in intermediate-temperature rocks, such as two-feldspar granites, when water is present, and negligible for feldspar pairs which form in geothermal systems or during diagenesis. Note that in rocks in which the alkali feldspar is perthitic its *bulk composition* must be used to obtain crystallization temperatures. Because alkali feldspars in igneous rocks are often subject to late replacement reactions the most reliable way to estimate composition at the time of crystal growth is to obtain the bulk composition of a region of *regular* microperthite, such as that shown in Fig. 172.

Complications in the application of the two-feldspar geothermometer are introduced in lower-temperature environments by Si–Al ordering, which raises solvus temperatures. Existing geothermometers are all based on disordered feldspars. It is also likely that a ternary coherent solvus exists below the strain-free ternary solvus (Fig. 187) and in principle this should be applied if one wishes to determine the temperature at which coherent exsolution begins. The steep surface of the solvus dome at low concentrations of An and the uncertain effect of ordering, make applications of the geothermometer to temperatures below ~500ºC uncertain.

Reactions with aqueous fluids. As alkali feldspars are so abundant in the crust they have a strong role in defining fluid compositions. In rocks containing two

Downloaded from https://pubs.geoscienceworld.org/books/chapter-pdf/3761011/9780903056434_ch59.pdf
by guest

feldspars, such as two-feldspar granites, the Na:K ratio in crustal brines is buffered to a fixed value at any temperatures for a very large range of Ab:Or in the rock (the horizontal lines on Fig. 188). As temperature decreases the solution becomes richer in Na and is close to a pure NaCl solution at surface temperature, even if the feldspars have a bulk composition rich in Or. A brine cooling in equilibrium with two feldspars will exchange K for Na in the feldspars, thus increasing Na in the fluid. If the temperature of a brine increases it will exchange Na with the feldspars to increase its K content. This corresponds with the 'albitization' which commonly occurs in the deeper parts of sedimentary basins. The exchange reaction is likely to take place by dissolution followed by reprecipitation.

Because of their importance in weathering and soil formation the rates and mechanisms of feldspar dissolution have been studied extensively. Dissolution rates depend on the composition of the solution and particularly on pH. At pH 6 the log dissolution rate (mol feldspar cm^{-2} sec^{-1}) of both albite and K-feldspar is about −16.5, but at pH 1 and 12 it is two orders-of-magnitude faster at −14.5. In detail, however, dissolution rates and mechanical degradation rates are strongly dependent on micotexture features such as exsolution lamellae and associated dislocations (see Fig. 194).

Optical and physical properties

The optical properties of the alkali feldspars depend on their composition and on the degree of Si−Al ordering (structural state). Twinning is a valuable diagnostic tool, and exsolution textures can be informative concerning the thermal history of the feldspar. The presence of coherent strain-controlled exsolution textures (Figs 172−174) can provide direct information on cooling rates, and perhaps more importantly can be used to demonstrate that the feldspar has not experienced deuteric reactions since the strain controlled intergrowths formed. Deuteric coarsening of perthite, with associated development of turbidity, is a secure indication that the feldspar (and the rock in which it is contained) has experienced dissolution–reprecipitation reactions involving a fluid. In the example given as Fig. 172a two phases of replacement have been identified on the basis of microtextures and chemical analysis using an electron microprobe.

The optical orientation of alkali feldspars is given in Fig. 189. The anorthoclase is similar to high albite, but $2V_\alpha$ is considerably larger (100º) in low albite. The variation in $2V_\alpha$ with composition and degree of order is summarized in Fig. 190. The diagram is contoured in Σt_1, the sum of the fraction of Al in the $T_1(0)$ and $T_1(m)$ sites. In a completely disordered feldspar Σt_1 is 0.5; in a fully ordered feldspar it is 1. In the absence of a full structure determination, $2V_\alpha$ is the only convenient way of estimating the state of order in monoclinic alkali feldspars.

An important feature illustrated in Fig. 189 is the change in position of the optic axial plane (O.A.P) between high- and low-sanidine. In high sanidine it is parallel to (010), in low sanidine and orthoclase it is normal to (010), and in triclinic feldspars (high and low albite, microcline, it is nearly normal to (010). If ordering occurs as high sanidine is cooled, $2V_\alpha$ decreases to zero while the O.A.P. is parallel to (010), and then increases again as low sanidine with its O.A.P. normal to (010).

Intergrowths on a crypto- or micro-perthitic scale have optical properties that are the average of the two phases, although the meaning of Σt_1 (Fig. 190) is

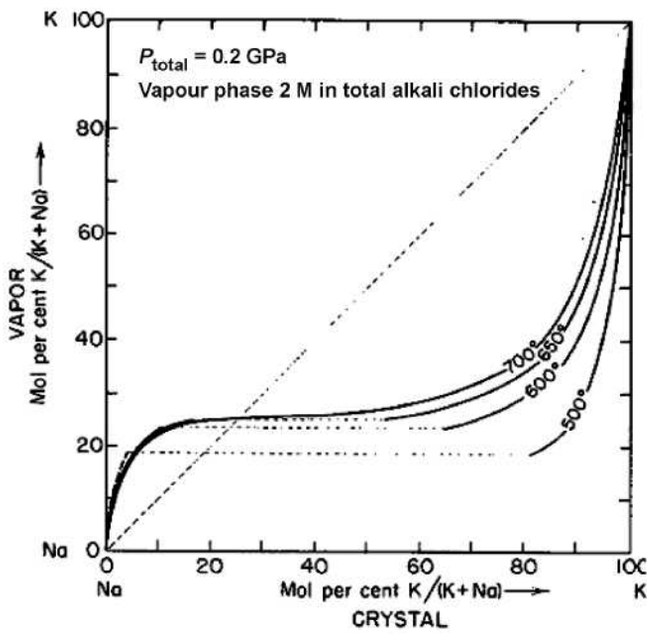


Fig. 188. Mol % K/(K + Na) in 2M alkali chloride brines in equilibrium with alkali feldspars at various temperatures and 200 MPa. The dashed horizontal lines are isotherms across the alkali feldspar solvus. Two-feldspar assemblages with bulk compositions anywhere on these lines coexist with a fluid of fixed or 'buffered' composition which becomes richer in Na with decreasing temperature. (From Orville, P.M., 1963, *Amer. J. Sci.*, **261**, 201−37.)

Downloaded from https://pubs.geoscienceworld.org/books/chapter-pdf/3761011/9780903056434_ch59.pdf
by guest

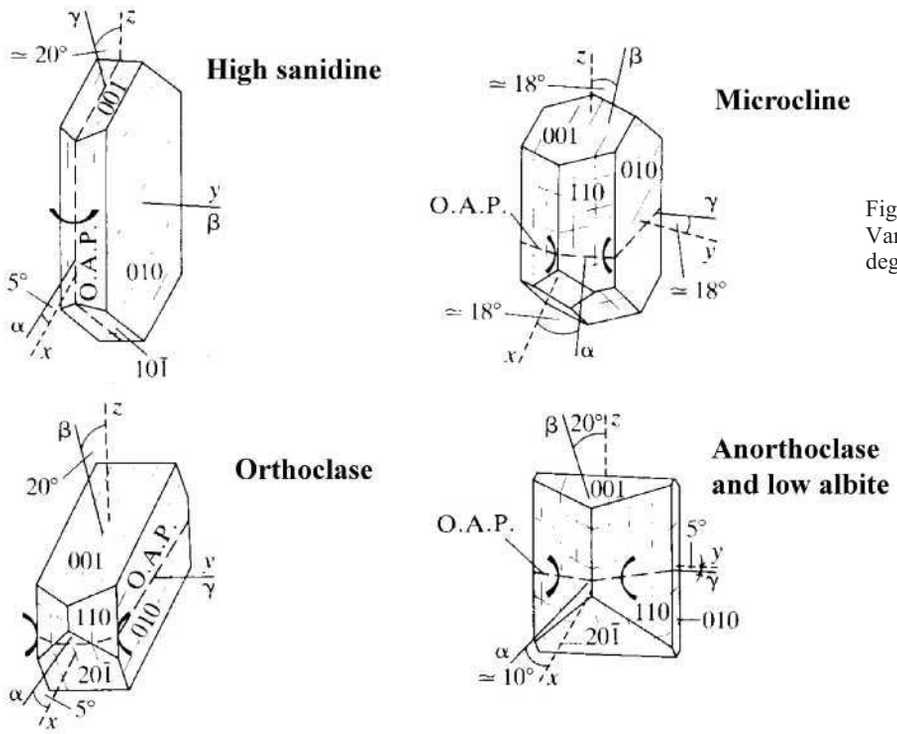
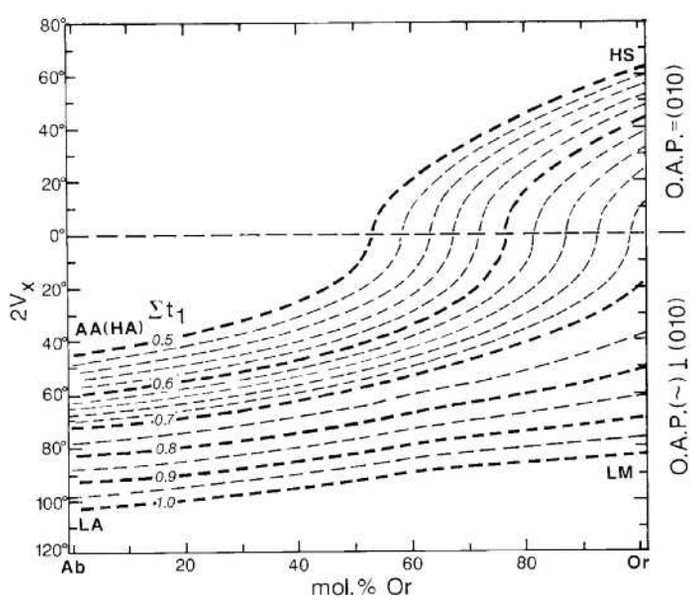


Fig. 189. Optical orientation of alkali feldspars. Variation in 2V with respect to composition and degree of order is given in Fig. 190.

uncertain if the two phases have different states of order. For most ordered feldspars $2V_\alpha$ varies little with composition so this is unimportant. Ordered feldspars in the central region of Fig. 190 are relatively uncommon, because of the alkali feldspar solvus. However in hypersolvus igneous rocks such as syenites, fully ordered crypto- and micro-perthitic textures can occur, with average optical properties on the low albite–low microcline line. The braid perthite in Figs 174a and 192 is of this type. In coarse perthites such as the patch perthite in Fig. 192, $2V_\alpha$ can be measured in the individual phases.

Extinction angles, α', to the trace of the (001) cleavage on (010), can be used to obtain the composition of alkali feldspars of low-temperature origin, but are relatively insensitive to composition in high-temperature examples. Refractive indices increase from Or-rich to Ab-rich feldspars but the differences are small and also sensitive to structural state (Fig. 191). There is considerable scatter in the measured values.

Ordered feldspars of intermediate composition will be exsolved, to perthite, mesoperthite or antiperthite, depending on bulk composition. When describing perthitic intergrowths it is most important to take



Fig, 190. Plot of $2V_\alpha$ against Or (mol%) contoured in Σt_1, the sum of the fraction of Al in the $T_1$0 and T_1m tetrahedral sites. AA is analbite (high albite) that will adopt monoclinic symmetry if heated above the shearing transformation. HS: high sanidine; LA: low albite; LM: low microcline (after Su, S.-C. *et al*., 1986, *Amer. Mineral*., **71**, 1285–96).

Downloaded from https://pubs.geoscienceworld.org/books/chapter-pdf/3761011/9780903056434_ch59.pdf
by guest

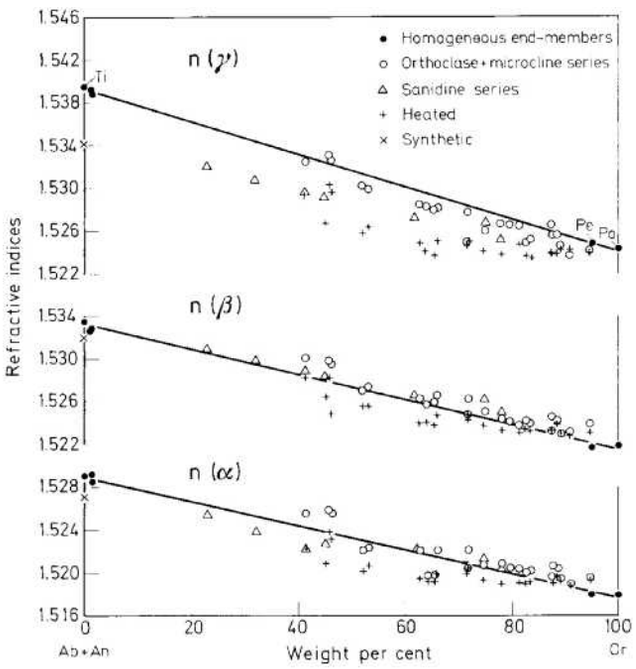


Fig. 191. Refractive indices of ordered and disordered alkali feldspars. Most natural intermediate members will be perthitic intergrowths. (Fig. 8.3a from Smith & Brown, 1988, *Feldspar Minerals vol. 1*, Springer-Verlag).

account of orientation. The film albite lamellae in Figs 172a and b are viewed approximately normal to (001), and appear as thin, actually lenticular, sheets. In contrast the *x*-axis is nearly normal to the exsolution lamellae (Fig. 179) and if viewed from near *x* the same microtexture would appear as irregular patches of albite in orthoclase. Many alkali feldspars in granites contain patch and vein perthite produced during deuteric reactions, replacing the regular film lamellae (Fig. 172a). In a thin section in which alkali feldspars are randomly orientated one can obtain a false impression of great variability, produced by viewing a limited range of microtextures from random directions.

In thin section the best approach is to look for *sharply defined* twinning on the Albite law in the albite-rich feldspar, if necessary using high magnification. Albite twinning is always parallel to the conspicuous (010) cleavage. Pericline twins are not, except in certain special cases, parallel to a cleavage (Fig. 179). If a second, sharply defined cleavage, (001), is visible at right angles to the Albite twin composition plane the crystal is being viewed from near the *x* axis, the least informative direction for observing exsolution features, because regular planar lamellar intergrowths will be normal to the viewing direction. Irregular coarse vein lamellae (Fig. 181) are commonly orientated overall in the same plane, and appear to have a patch texture. Patch perthite (Fig. 192) appears as stumpy rods viewed from near *x* and *y*. Viewed from roughly parallel to *y* film lamellae are not at right angles to the (001) cleavage.

Zoning in alkali feldspars is less common than in plagioclase, because Na and K are not coupled to Si and Al in the framework. If it occurs in alkali feldspars it may be related to relatively small variations in An, and perhaps also to celsian distribution. Oscillatory zoning in

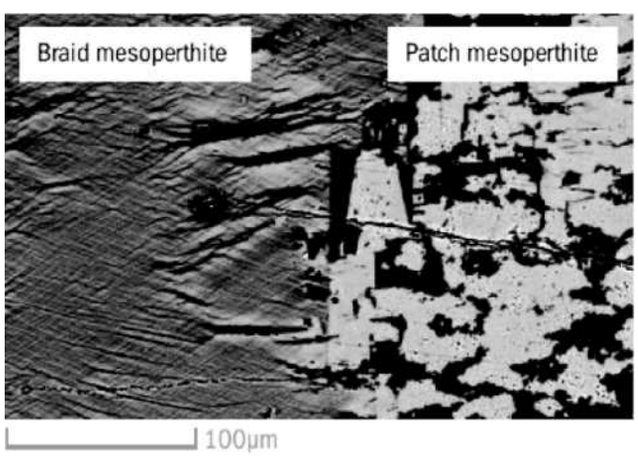


Fig. 192. Back-scattered electron image showing contrasting microtextures in an alkali feldspar single crystal from the Klokken syenite intrusion, with a bulk composition ~$Ab_{60}Or_{40}$. Light grey is microcline, dark grey low albite. The plane of the section is ~(001). The braid perthite (left) is a fully coherent, strain-controlled cryptoperthite, similar to Fig. 174a, p. 263. The much coarser patch intergrowth (right) is a strain-free mosaic of microcline and low albite subgrains formed by dissolution–reprecipitation in an aqueous fluid. The black dots are micropores, abundant in patch perthite but absent from the braid perthite (from Parsons, I. & Lee, M.R., 2009, *Contrib. Mineral. Petrol.*, **157**, 641–61).

Downloaded from https://pubs.geoscienceworld.org/books/chapter-pdf/3761011/9780903056434_ch59.pdf
by guest

plutonic microperthitic crystals can be displayed as zones in which lamellar perthite varies in coarseness because of variation in these minor components, which require diffusion of Al to be coupled to Ca during coarsening. This zoning is commonly visible in slightly weathered specimens because weathering affects zones with coarse lamellae, which have developed reactive misfit dislocations, more than zones with finer, fully coherent lamellae (Fig. 194).

Feldspars vary considerable in transparency, from glass-clear in large fragments to essentially opaque even in small cleavage fragments. Petrographically this turbidity is one of the most important variables when describing a feldspar, and it is considered in the next section. Sanidine in volcanic rocks is often glass-clear and colourless and glass-clear 'gem-quality' feldspar is occasionally found in pegmatites. Structural Fe^{3+} causes a yellow colour, as in the gem-quality orthoclase crystals from Madagascar. A strong green colour often correlates with a high Pb content. A commonplace plutonic rock in which the feldspar is clear in small fragments or thin section is the variety of syenite known as larvikite, which is used as an architectural stone because of the striking blue iridescence of its alkali feldspars. The feldspar is a cryptomesoperthite (Fig. 174a) and the iridescence is caused by coherent scattering (Bragg diffraction) of light by exsolution lamellae. In massive lumps, feldspar in larvikitic syenites ranges from light blue-grey to dark bottle green, almost black. Comparable non-turbid feldspars in granulite facies gneisses and charnockites are often green but do not show iridescence because of the coarser spacing and irregularity of their exsolution textures. In Or-rich alkali feldspars, silvery or blue iridescence (seen in the gem variety moonstone) is caused by lamellar intergrowths similar to those in Fig. 172, p. 262, but on a finer scale. Some microcline, called aventurine, exhibits a golden schiller which is caused by orientated platelets of hematite. Schiller can also be caused by flakes of biotite. The term schiller should be reserved for light scattered by visible inclusions of other minerals, whereas iridescence should be used for scattering by periodic microstructures in the mineral itself.

Electron microscopy

Many exsolution microtextures in feldspars are beyond the resolution limit of a conventional optical microscope, and for a full characterization it is necessary to use electron microscopy. Statements in optical petrographic descriptions that alkali feldspars are 'non-exsolved' are likely to be wrong unless the bulk composition of the feldspar is very close to the Or or Ab end-member, or the rock is volcanic and has cooled extremely quickly. Although in a general way coherent and semicoherent perthitic intergrowths are coarsest in slowly cooled rocks, cryptoperthite commonly occurs between microperthitic lamellae, even in high-grade metamorphic rocks.

The presence of two or more phases can be demonstrated by X-ray diffraction but this does not provide any spatial information about the character of the intergrowths. Transmission electron microscopy (TEM), which provides lattice-scale resolution, is the ultimate method of study but it is time-consuming and provides images of extremely small areas, usually <10 μm across (Fig. 174a, p. 263). Scanning electron microscopy (SEM) is a practical compromise, with a resolution of the order of a few tens of nanometres on polished sections. If an SEM or electron probe with a back-scattered electron detector is available perthitic intergrowths are most easily characterized using cleavage fragments, which most commonly lie on (001) or (010) (Fig. 179). Back-scattered electron (BSE) images are best obtained on polished surfaces although freshly created cleavage surfaces can be used. The intensity of electron scattering is a function of mean atomic number so that the Or-rich phase normally appears brighter than the Ab-rich phase (Fig. 192). Cleavages are usually visible on cleavage fragments, which is helpful for establishing orientation, and micropores can be imaged at low (Fig. 192) and high (Fig. 193) magnification. The braid microtexture imaged with TEM in Fig. 174a, with a periodicity of ~100 nm, corresponds with the braid texture made visible using BSE in an SEM on the left side of Fig. 192.

The HF etching technique used to produce Figs 172b and 174b is best applied to cleavage fragments cemented to SEM stubs. The method is particularly

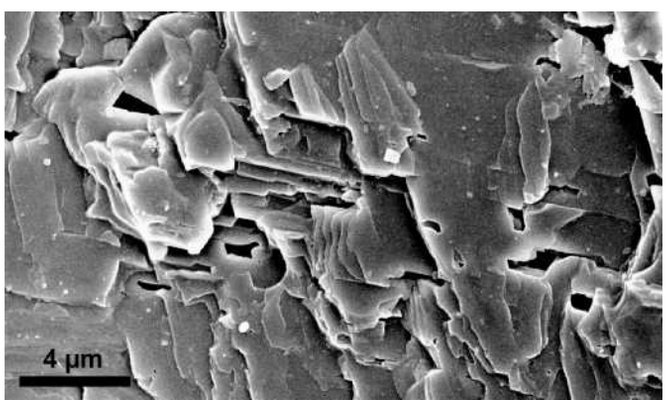


Fig. 193. Large, subhedral micropores in a turbid alkali feldspar from the Klokken intrusion, viewed on the (010) cleavage. Secondary electron SEM image. (From Walker *et al*., 1995, *Mineral. Mag*., **59**, 505–34.)

Downloaded from https://pubs.geoscienceworld.org/books/chapter-pdf/3761011/9780903056434_ch59.pdf
by guest

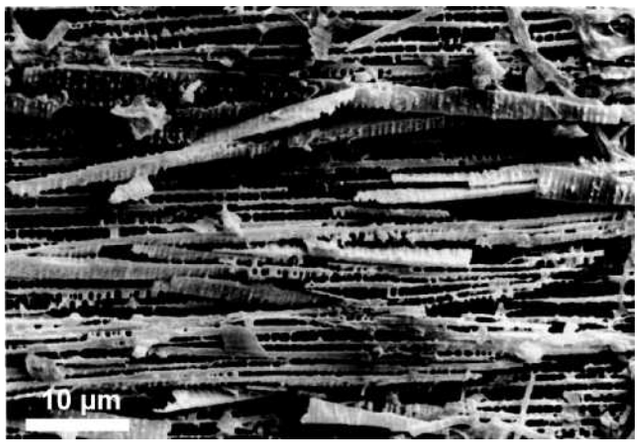


Fig. 194. Secondary electron image of the (001) surface of a fragment of an alkali feldspar phenocryst, bulk composition ~$Ab_{30}Or_{70}$, taken from a peat soil on top of the Shap granite. The crystal surface has not been cleaned. The black trenches mark the sites of film albite exsolution lamellae, in ($\bar{6}01$) (Fig. 172), that have almost completely dissolved in acidic peaty water. Dissolution has occurred initially at the outcrops of misfit dislocation loops which have enlarged into oval tunnels with, in places, thin walls of residual albite between them. Most of the feldspar remaining is orthoclase, which has remained as fragile sheets between albite lamellae, and has in places broken off as thin flakes lying on the crystal surface. (From Lee M.R. *et al*., 1998, *Geochim. Cosmochim. Acta*, **62**, 2771–88.)

useful for revealing dislocations (Fig. 172b), which are, in turn important in controlling degradation during weathering (Fig. 194), which is essentially a natural etching process. In this method the etched surface is imaged using secondary electrons (SE) in the SEM.

The brownish or greyish turbidity of many plutonic alkali feldspars in thin section has often been ascribed to alteration products but in many specimens the turbidity is caused by micropores on scales from a few micrometres to nanometres (Fig. 193). A proportion may contain sub-micrometre mineral particles which impart colour to the feldspar, hematite in pink examples, titanomagnetite in grey or white ones. The pores may be, or may have been, fluid-filled. It has been calculated that fluid inclusions in feldspars contain in total more water than all the hydrous minerals in the upper crust combined. Turbidity is a marker of replacement reactions by dissolution–reprecipitation in crystals in general, and in plutonic feldspars is evidence for pervasive fluid–rock interactions affecting large volumes of the crust. The micropores usually form at the junctions between subgrains within what are morphologically single crystals, and are often associated with deuteric coarsening of perthites (Fig. 192). Rare, primary micropores in strain-controlled microperthites may contain fluids present at the time of crystal growth, because they have escaped low-temperature replacement.

The change in microtexture illustrated in Fig. 192 is very profound. In that instance the bulk composition of the parent braid perthite and product patch perthite are the same for major elements and most trace elements and the process is called ‘mutual replacement’. The alkali feldspar crystals retain their original external morphology. The reaction is driven by reduction in coherency strain energy in the braid perthite. As a result of coherency strain the braid perthite has higher free energy than the product, ‘strain-free’, patch perthite, even though the latter is made up of large numbers of subgrains with associated surface energy. The replacement process is said to be ‘interface-coupled’ and it is believed that fluid films advance through the braid perthite. These films are supersaturated with respect to strain-free feldspar which nucleates behind the advancing dissolution front forming a microporous subgrain mosaic. An important consequence is that the diffusion distance for atoms like ^{40}Ar and ^{18}O in the braid perthite, in which the phases share a continuous Si–Al–O framework, is considerably larger than that of the patch perthite, which is a permeable subgrain mosaic, even though the exsolution texture of the patch perthite is a factor of 10^3 coarser than the braid perthite. It has recently been shown that, following patch perthite formation, Or-rich patches, which still contain some Ab, can undergo a second phase of coherent exsolution, leading to film perthite.

Replacement reactions in feldspars are commonly non-isochemical. This might be termed ‘true’ replacement, where components have been introduced from outside the alkali feldspar, and the driving force is the chemical potential of the feldspar components in the rock–fluid system as a whole. The microporous vein perthite in Fig. 172a has oligoclase ($Ab_{90}An_9Or_1$) as the Ab-rich phase, requiring considerably more Ca than is available in the matrix film perthite. Replacement by albite (‘albitization’) is commonly reported, in a variety of regimes from deuteric and hydrothermal fluids to diagenesis (Fig. 187). The K-equivalent, replacement by orthoclase or microcline, occurs frequently but is less commonly reported as it is best detected using electron microscopy. Replacement of perthitic albite lamellae in orthoclase, by microcline, giving a lamellar intergrowth that is not strictly a perthite, has been found in both relatively high-temperature deuteric alteration and during diagenesis. Large-scale replacement by Or-rich feldspar has been called ‘microclinization’ but the term is ambiguous because it has also been used for the transition between orthoclase and microcline.

It is not easy to distinguish ‘mutual’ from ‘true’ replacement in alkali feldspars, and both styles may coexist within single crystals. Constancy in bulk composition of individual crystals throughout a rock sample is the best evidence for mutual replacement but it can be demonstrated only by careful electron microprobe analysis, using a large beam diameter or a traversing method. True replacement is likely to be localized near crystal edges, or to follow fractures and cleavages. It is unlikely that the bulk composition of individual crystals would be constant throughout a rock sample. Careful

Downloaded from https://pubs.geoscienceworld.org/books/chapter-pdf/3761011/9780903056434_ch59.pdf
by guest

SEM work, combined if possible with simultaneous chemical analysis, is probably the most practical routine approach.

Semicoherent and incoherent perthitic microtextures have a marked effect on the weathering behaviour of feldspars, particularly in solutions that are close to equilibrium with minerals, such as soil waters. Defects such as misfit dislocations (Figs 172b, 194), and also subgrain boundaries in vein or patch perthites, provide reactive sites that define the early stages of dissolution, and lead ultimately to mechanical degradation. As the dissolution rate is a function of reactive surface area, defects considerably enhance dissolution rates particularly when dissolution is sufficiently advanced to lead to surface fragility, as shown in Fig. 194.

Distinguishing features at the optical scale

The monoclinic alkali feldspars (sanidine and orthoclase) cannot have repeated lamellar (polysynthetic) twinning on the Albite and Pericline laws whereas members of the plagioclase series, and the triclinic alkali feldspars microcline and anorthoclase usually, although not invariably, have lamellar twins at the optical scale. Optical scale intergrowths of two feldspars are uncommon in plagioclase, but perthitic intergrowths are almost universal, at a variety of scales, in alkali feldspars from plutonic rocks. Alkali feldspars have lower refractive indices and density than plagioclase. They can be distinguished from quartz because of their cleavages, particularly (010) and (001), at right angles, their biaxial character, and in most rocks by their turbidity. Sanidine in volcanic rocks often has a poorly developed cleavage and may be glass-clear making it hard to distinguish from quartz. The interference figure will usually allow identification. Glass-clear diagenetic overgrowths sometimes occur in siliciclastic sedimentary rocks, and clear K-feldspars sometimes occur as a late phase in pegmatites. In both cases the development of cleavage distinguishes the feldspar from quartz. Nepheline is often turbid but can be distinguished from feldspar by its low birefringence, poor cleavage, uniaxial character, absence of twinning and occasional hexagonal crystal habit.

The naming of alkali feldspars with respect to degree of Si–Al ordering using optical methods is complicated by TEM observations that show that some 'orthoclase' crystals are sub-optically twinned microcline, and also that many plutonic K-feldspars are mixtures of orthoclase and microcline (Fig. 198, p. 288). Such crystals commonly exhibit undulatory extinction. Figure 190 shows that $2V_\alpha$, the best indicator of degree of order, is also a function of composition, and that both variables form a continuum. There are, however, some practical generalizations. In high sanidine the optic axial plane (OAP) is (010) and therefore parallel to a pronounced cleavage. In low sanidine, orthoclase and microcline the OAP is at right angles to (010) and not, in general, parallel to any cleavage. In Or-rich high and low sanidines $2V_\alpha$ is small and strongly sensitive to both ordering and composition, but in all ordered alkali feldspars $2V_\alpha$ is mainly a function of ordering. High and intermediate albite are relatively rare. Compositions intermediate between low albite and ordered K-feldspar are invariably exsolved. If the intergrowth is sub-optical in scale, it is reasonable to assume that $2V_\alpha$ is an average for the two intergrown phases, and if it is coarsely exsolved it is possible to measure $2V_\alpha$ in the individual phases. A practical definition of orthoclase is that it is an optically monoclinic feldspar with $2V_\alpha >$ ~50º, although it is possible that such a feldspar would be triclinic to X-rays (and therefore properly called microcline) because of sub-optical Albite–Pericline ('tartan') twinning. It is unlikely to be confused with high sanidine, which occurs only in volcanic rocks; the distinction can be made from the orientation of its OAP (Fig. 189).

Microcline almost invariably has tartan twinning (Fig. 181, p. 268), although it is sharply defined only in sections close to (001) (Fig. 183). Viewed parallel to *x*, only Albite twins can be seen, at right angles to the (001) cleavage; viewed parallel to *y*, only Pericline twins, making an angle of ~80º with (001) can be seen. Anorthoclase also shows twinning on both laws (Fig. 182), but the twins are parallel-sided rather than spindle-shaped as in microcline (Fig. 181), and the intersections of the twins are angular, rather than curving. Anorthoclase forms only in volcanic rocks, orthoclase in plutonic rocks. Much plagioclase has straight-sided, relatively broad twins, mainly on the Albite law (Fig. 212, p. 305), but Pericline twins may also be present (Fig. 211), also straight-sided and having angular junctions with Albite twins. In general, the higher refractive index of plagioclase is diagnostic. As the An content of low plagioclase increases, the composition plane of Pericline twins rotates about *y* from the low albite position (Fig. 179) towards *x*, becoming sub-parallel to the (001) cleavage in An-rich compositions.

The low-temperature K-feldspar adularia is characterized by its distinctive {110} habit and often very variable extinction. The OAP can vary from parallel to normal to (010), reflecting variable degrees of order probably related to growth rate.

There are a number of techniques for staining potassium feldspar in thin sections so that it may easily be distinguished from quartz or untwinned plagioclase feldspar. A rapid method which can be used at room temperature involves uncovering the thin section and etching it with HF by placing it face downwards over an HF bath for 15–30 seconds to prepare the minerals for staining. The stain is applied by immersing the section in a solution of sodium cobaltinitrite (60 g per 100 ml water) for 15–20 seconds, after which the section is rinsed immediately in water. Potassium feldspar takes a

Downloaded from https://pubs.geoscienceworld.org/books/chapter-pdf/3761011/9780903056434_ch59.pdf
by guest

pale yellow stain and although white mica and clay minerals may sometimes absorb the stain they can be distinguished, where potassium feldspar is also present for comparison, by their different relief and intensity of stain. Quartz and plagioclase feldspar are unaffected, though in antiperthite the alkali feldspar blebs may take the stain.

Paragenesis

The alkali feldspars are essential constituents of the alkaline and acid igneous rocks and are abundant in syenites, granites, granodiorites and their volcanic equivalents; they are also major constituents of granitic pegmatites and many acid and intermediate gneisses. Small amounts of alkali feldspar, often together with quartz, can occur in the interstices between plagioclase crystals in some gabbroic rocks, representing the final products of fractionational crystallization. Potassium feldspars grow during medium-grade thermal and regional metamorphism, and commonly occur as large porphyroblasts in acid gneisses. Strongly ternary alkali feldspars with a large range of compositions crystallize in high-grade granulite-facies rocks. Feldspars rich in orthoclase crystallize in geothermal systems and as separate authigenic crystals and overgrowths during diagenesis. Detrital alkali feldspars occur in arkosic sedimentary rocks, sometimes preserving perthitic intergrowths that may provide information on provenance.

Relationships in magmas

Magmatic rocks with alkali feldspar are divided into two main types depending on whether one or two feldspar phases crystallized simultaneously from the magma. If the three feldspar components are contained in a single feldspar phase the rock is said to be 'hypersolvus'. If two feldspar phases, a plagioclase (PL) and an alkali feldspar (AF), each composed of the three feldspar components, grew simultaneously, the rock is said to be 'subsolvus'. The terms are most commonly applied to granitic rocks although they apply equally to volcanic series.

Phase relationships in the simplified An-free system Ab–Or–H_2O are shown in Fig. 169, p. 258. The solvus in figures (a) and (b) is a 'strain-free' curve for separate AF and PL phases. Figure 169a shows hypersolvus relationships, for a hypothetical 'dry' liquid. A single feldspar crystallizes, either more Ab- or more Or-rich than the minimum on the solidus, depending on liquid composition. Under subsolvus conditions (Fig. 169b) two feldspars grow in equilibrium with liquid at the eutectic. The compositional variable leading to the difference between these diagrams is the water content of the liquid, which in Fig. 169b is saturated with water at 0.5 GPa. As P_{H_2O} increases, the solidus moves to lower temperature, and the solvus moves to slightly higher temperature. The two curves intersect at ~0.4 GPa.

The system Ab–Or–An–H_2O. As feldspars make up more than 50% of most igneous rocks, liquid–crystal relationships in the ternary feldspar system (Fig. 195) are essential for understanding igneous fractionation and crustal melting processes. The ternary solvus is a steep dome (Figs 187, 195) that is independent of the magma composition. One mol% An increases the solvus temperature for a feldspar from a typical 'two-feldspar' granite by between ~150 and 300ºC, depending on the Ab:Or ratio. The liquidus and solidus, in contrast, depend strongly on magma composition, especially on its water content, which in turn depends on P_{H_2O}, as illustrated in Fig. 169. Other components in the magma also affect the liquidus and solidus curves, to extents that are poorly understood but which ultimately determine the changing composition of natural feldspars and evolving magmatic liquids.

Although the three *binary* systems, Ab–Or, Ab–An and Or–An (Fig. 195) have been determined experimentally, the exact shapes of the *ternary* liquidus and solidus are known imperfectly. Figure 195 is largely based on thermodynamic models which may require revision. Nevertheless the general topology of the system is known and its salient features with respect to alkali feldspars are given here. Relationships of plagioclase are discussed in the appropriate section.

An AF is the first phase to crystallize only in very Or-rich liquids, in the wedge-shaped region between the cotectic curve E–C (and its continuation as a minimum to M) and the Ab–Or join. Throughout the remainder of the system PL crystallizes first and AF begins to crystallize only when a liquid reaches the field boundary at L. Initial crystallization in both AF and PL fields is hypersolvus, but when the liquid reaches the cotectic line it becomes subsolvus. At high P_{H_2O} (> 0.4 GPa), when the cotectic line reaches the Ab–Or join and the minimum M is a eutectic, subsequent crystallization is relatively simple. The liquid moves from L down temperature towards M (under these conditions a eutectic) and both AF (S on the diagram) and PL become more albitic; L, PL and S form a three-phase triangle. Under equilibrium crystallization conditions the last liquid will be used up when the trailing edge of the triangle S–PL passes through L, at which point the two solid phases and the liquid are on the same tie-line. During fractional crystallization the liquid may evolve along the cotectic curve towards the minimum M on the Ab–Or join. In principle liquids can fractionate to the An-free eutectic on the Ab–Or join, when AF and PL crystallize on the binary solvus (Fig. 169b), although they rarely, if ever, do so. The AF and PL may in principle be strongly zoned, although zoning in AF is usually destroyed rapidly by Na–K diffusion or obscured by subsequent exsolution. Because of Ca–Al and Na–Si coupling, zoning in plagioclases is preserved and is commonplace.

Downloaded from https://pubs.geoscienceworld.org/books/chapter-pdf/3761011/9780903056434_ch59.pdf
by guest

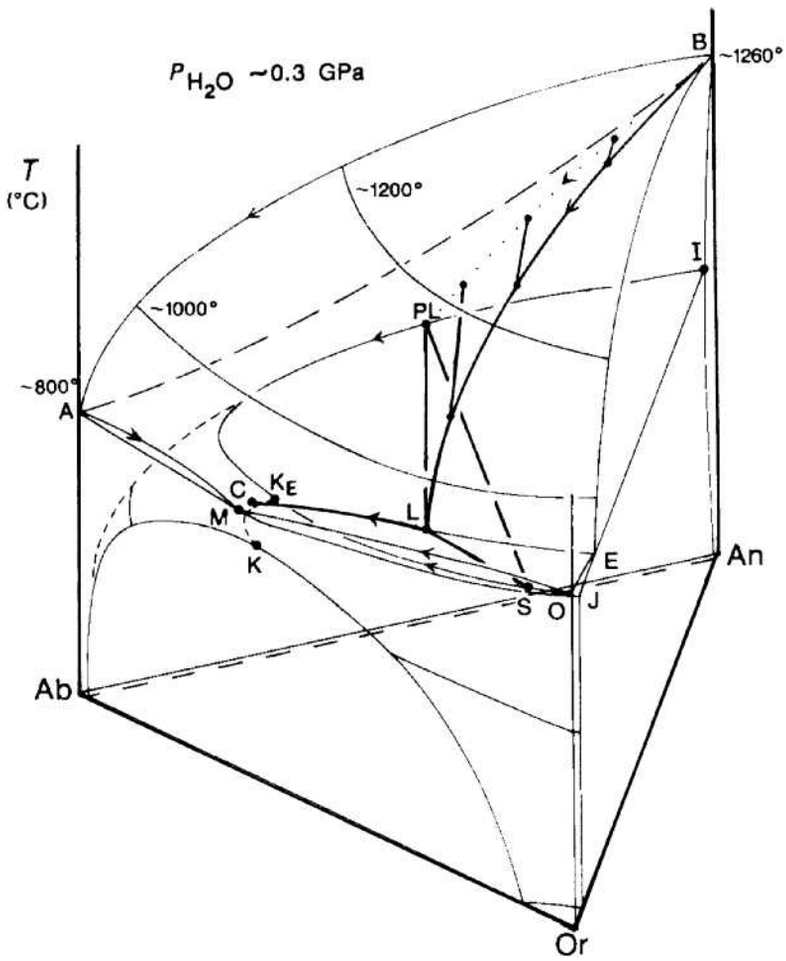


Fig. 195. Ternary feldspar phase relationships at ~P_{H_2O} ~0.3 GPa. The liquidus surface is B–A–M–O–E–B and the solidus is B–A–M–O–J–E–I–B. The solvus–solidus intersection is J–K_E–PL–I. The field boundary E–L–C defines the fields in which an alkali feldspar (AF, here called S) or plagioclase feldspar (PL) phase crystallizes first. The point E is a eutectic and the boundary is a cotectic curve, along which two feldspars are in equilibrium with liquid, forming a three-phase triangle such as S–L–PL. At C the cotectic curve dies out, and the liquidus and solidus are in contact at a minimum, analogous to the binary minimum M (see also Fig. 169a, p. 258) and only a single feldspar can coexist with liquid. The single feldspar at C has the composition K_E, and it is joined to the critical temperature of the binary solvus K, by the *critical solution* or *consolute* curve. This is the line along which two-feldspar pairs on solvus isotherms come to have the same composition. At P_{H_2O} slightly above 0.4 GPa, the boundary curve reaches the Ab–Or join and M becomes a eutectic (Fig. 169b). (From Brown, W.L., 1993, *Contrib. Mineral. Petrol.* **113**, 115–25.)

At lower P_{H_2O}, or under conditions of low water activity (a_{H_2O}) at high pressure, the field boundary terminates at C. Liquids move down a special line, along which solidus and liquidus touch, to the minimum M (Fig. 169a). A single feldspar crystallizes (crystallization becomes hypersolvus). At C (Fig. 195) the three phase triangle becomes a line and a single feldspar crystallizes at K_E. The line K_E–K, along which feldspar pairs on solvus isotherms come to have the same composition, is called the *critical solution* or *consolute* curve. Its exact location is poorly known but for application of the two-feldspar geothermometer the PL and AF phases must lie on either side of the critical solution line, including its extension further into the ternary prism. Detailed crystallization relationships in the vicinity of the termination of the field boundary at C are very complex. One- and two-feldspar paths on the solidus and solvus, recorded as crystal zoning, may bend back on themselves.

The system Ab–Or–An–Q. This system (Fig. 196) approximates to a rhyolitic or granitic liquid and its configuration has been largely deduced from phenocryst–groundmass relationships in natural rhyolites. The course of crystallization depends on liquid composition and the evolution of a somewhat calcic rhyolitic liquid, with composition at L1, is given as an example. The diagram shows a tetrahedron with Ab, Or, An and Q (SiO_2) as its apices. All feldspars plot on the front face of the tetrahedron, plagioclases (PL) P1 to P4, and alkali feldspars (AF) A2 to A4. Liquids are all inside the tetrahedron, L1 closest to the front face, L4 furthest away. There are three primary phase volumes defined by two internal surfaces. Quartz is the first phase to crystallize in the volume *W–S–G–X*–Q, AF first in the wedge-shaped area below the plane *F–E–G–H*. This plane is called the two-feldspar surface. In the remainder of the tetrahedron, a very large volume, PL is the first phase to crystallize. Most magmas have compositions in the PL volume, and it is fractionation of plagioclase that leads eventually to crystallization of AF- and finally Q-rich rocks.

When liquid L1 cools the first crystalline phase to appear is plagioclase P1, in equilibrium with L1. As temperature falls the liquid becomes richer in SiO_2, and moves on a curved path towards the two-feldspar surface, the plagioclase reacting with liquid to become more sodic, eventually reaching P2. If the rock were erupted in this interval it would be porphyritic, with phenocrysts of andesine. When the liquid reaches the two-feldspar surface the plagioclase, P2, is joined by an alkali feldspar, A2. The liquid path changes sharply in direction and moves along the two-feldspar surface,

Downloaded from https://pubs.geoscienceworld.org/books/chapter-pdf/3761011/9780903056434_ch59.pdf
by guest

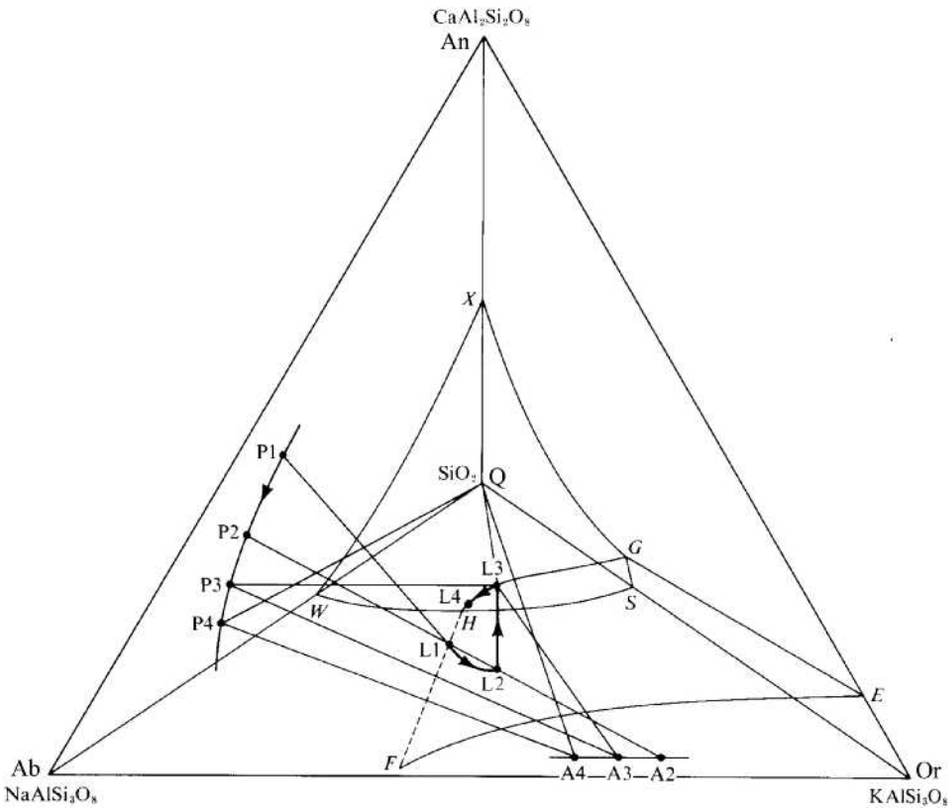


Fig. 196. Diagram illustrating the course of crystallization of a somewhat calcic rhyolitic liquid L1 in the Ab−Or−An−Q tetrahedron at low P_{H_2O}. The base triangle corresponds with the simplified granite system depicted in Fig. 185, and the front face is a plan view of the cotectic curve and solidus−solvus intersection in Fig. 195. The composition L1 is inside the tetrahedron, in the plagioclase volume, above the two-feldspar surface *F*−*E*−*G*−*H*. Feldspars P (plagioclase) and A (sanidine) are on the front face of the tetrahedron and joined to the evolving liquids L1−L4 by a series of tie-lines and three-phase triangles that slope away from the reader. The line *E*−*F* corresponds with the field boundary E−C in Fig. 195, and lines P1−P4 and A2−A3 correspond with points on the solvus−solidus intersection in Fig. 195. The line *E*−*F*, and hence the two-feldspar surface, terminates before reaching the Ab−Or−Q plane (see Fig. 195), so that *F*−*H* is shown as a broken line. Liquids L1−L4 evolve along the heavy line away from the reader until they collide with the surface of the Q volume at L3, when quartz appears, the liquid changes direction and moves down the intersection of the two-feldspar surface with the quartz volume towards the 'granite minimum' (Fig. 185). In many rhyolites the SiO_2 polymorphs tridymite or cristobalite would crystallize rather than quartz. (From Carmichael, I.S.E. *et al*., *Igneous Petrology*, 1974, McGraw Hill Book Company, pp. 739).

crystallizing both PL and AF (sanidine) both of which become more sodic. At this stage the rock, if erupted, would contain both PL and AF phenocrysts. Eventually, when the liquid has reached L3, Q begins to precipitate together with feldspars P3 and A3. The liquid now moves down the line which marks the intersection of the two-feldspar surface with the surface of the Q volume. When it reaches L4 crystallization is (under equilibrium conditions) complete, because P4, A4 and Q lie in a triangular plane that includes the starting liquid composition, L1.

Crystallization histories of this type can be deduced for other compositions in the tetrahedron. Liquids which are An-poor will miss the two-feldspar surface, so that a single feldspar precipitates throughout crystallization, and the plagioclase changes composition into the anorthoclase range. Liquids below the two-feldspar surface, in the AF volume, crystallize sanidine first, joined by plagioclase only if the amount of An in the liquid exceeds that which can be accommodated in solid solution in sanidine.

Phenocrysts of sandine (both high and low) or plagioclase or anorthoclase can occur separately, in 'one-feldspar' (hypersolvus) rhyolites, trachytes and phonolites, or coprecipitate in their 'two-feldspar' (subsolvus) equivalents. Both phenocrysts and groundmass phases (Fig. 197) may be strongly zoned (in the direction of the arrows) from calcic plagioclase towards anorthoclase and from sanidine to anorthoclase. In assemblages of two feldspars plus liquid both feldspars become more sodic as crystallization proceeds. In groundmass assemblages both alkali and plagioclase feldspars crystallize simultaneously. The analyses in Fig. 197 are fractionation paths on the solvus−solidus intersection (Fig. 195). This is general behaviour in evolving salic liquids (both volcanic and plutonic), although the exact compositional path depends on the changing composition of the magma (particularly its water content) which controls the intersection of the solidus with the compositionally fixed solvus.

As a result of crystal−liquid relationships, during fractionation and during partial melting of crustal

Downloaded from https://pubs.geoscienceworld.org/books/chapter-pdf/3761011/9780903056434_ch59.pdf
by guest

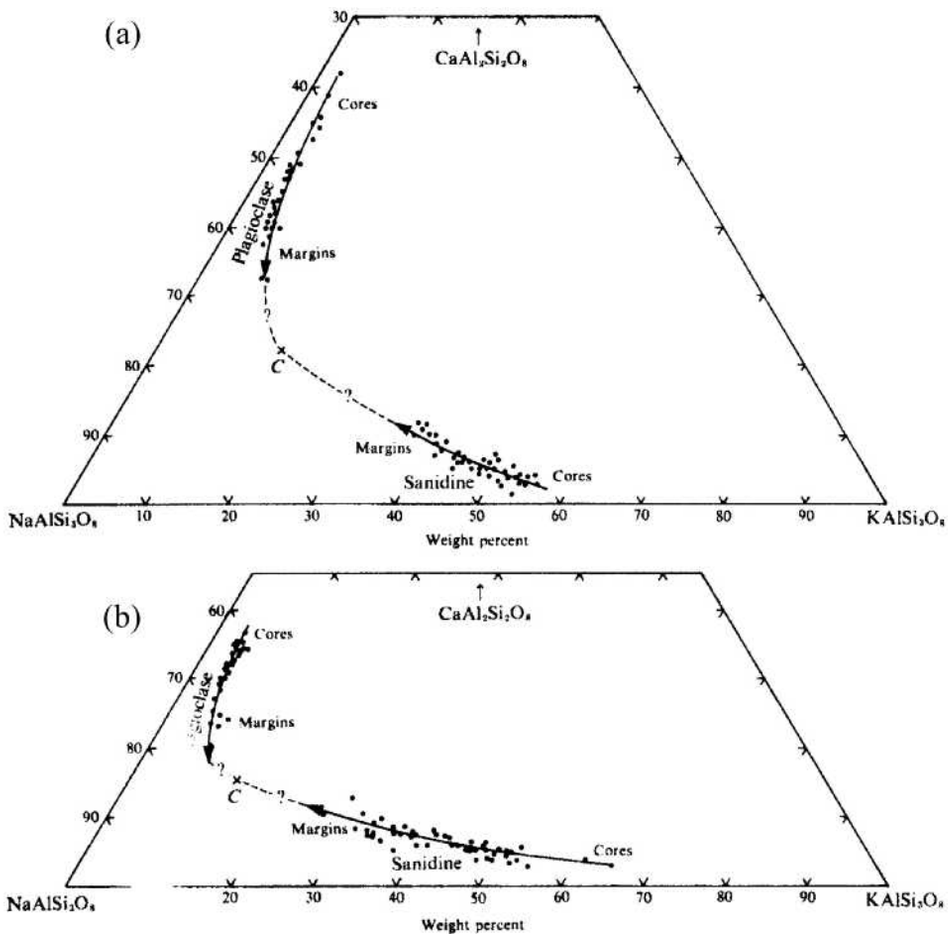


Fig. 197. Electron microprobe analyses of zoned plagioclase and sanidine in the groundmass of alkaline lavas. The arrows show the direction of zoning in individual crystals and represent fractionation paths along the solvus–solidus intersection (Figs. 195, 196). (a) Feldspars in two shoshonites, a relatively K-rich type of basalt in which plagioclase is mantled by sanidine. (b) A nepheline trachyte. As expected, the paths in the latter approximate to lower temperature solvus isotherms. The point *C* is an estimate of the critical solution point (K_E on Fig. 195). It is probably at a more Or-rich composition than shown. (From Carmichael, I.S.E. *et al*., *Igneous Petrology*, 1974, McGraw Hill Book Company, pp. 739).

protoliths, the bulk compositions of perthitic alkali feldspars in hypersolvus acid and alkaline igneous rocks are strongly concentrated in relatively small areas of the system Ab–Or–SiO_2–H_2O, corresponding with temperature minima on the liquidus (Fig. 185, p. 273). In subsolvus plutonic igneous rocks the bulk feldspar composition (AF + PL) is defined by similar minima, but the bulk composition of AF (and therefore the proportion of albite in perthitic intergrowth) depends on the ternary solvus–solidus intersection (Figs 187, 195) and thus primarily on An in the total feldspar and P_{H_2O}. As pressure increases the Ab-content of granitic liquids increases relative to Or and quartz (Fig. 185c).

Hypersolvus granites and syenites have compositions that correspond with minimum melting compositions in the system Ab–Or–Q (Fig. 185). In syenites, many of which contain >80 vol.% alkali feldspar with minor quartz or nepheline, feldspars usually cluster around $Ab_{65}Or_{35}$, the composition of the liquidus minimum on the Ab–Or join at low P_{H_2O} (M in Fig. 169a, p. 258 and m in Fig. 185b). In hypersolvus granites, feldspars in equilibrium with liquids crystallizing quartz are slightly more Or-rich ($Ab_{50}Or_{50}$) at low pressure, becoming more Ab-rich at higher pressure (M in Fig. 185b). Quartz syenites commonly lie in the 'thermal valley' in Fig. 185b. In nepheline syenites alkali feldspars cluster around ~$Ab_{70}Or_{30}$, a composition defined by the nepheline syenite minimum in the system silica–nepheline–kalsilite. However, it should be noted that the very flat solidus in the Ab–Or join (Fig. 169a) means that the first crystals to form in all alkali feldspar-rich rocks may be either extremely Or-rich or Ab-rich depending on the liquid composition. Crystal–liquid tie-lines in magmas are particularly long for liquids on the Ab + An side of the minimum in Ab–Or–An (Fig. 195), and unreacted cores of An-rich plagioclase can be found in alkali feldspars in some syenites. In hypersolvus rocks the minimum crystallization temperature for an alkali feldspar can be obtained from solvus isotherms (Fig. 162) provided the bulk ternary composition is known and some estimate of pressure can be made. Similar estimates

Downloaded from https://pubs.geoscienceworld.org/books/chapter-pdf/3761011/9780903056434_ch59.pdf
by guest

can be made for the mesoperthitic alkali feldspars in granulite-facies metamorphic rocks, which may have high An contents. Many granulites are two-feldspar rocks for which temperatures may be estimated as for igneous rocks. In such cases pressure is usually estimated from pressure-sensitive reactions (geobarometers) involving other minerals.

As noted in the Experimental section, the strong dependence of the feldspar solidus on P_{H_2O} has the important implication that crystallization of feldspathic liquids can be accomplished by reduction in P_{H_2O} alone, without cooling (adiabatic crystallization). It is likely that the rise of water-bearing granite magmas in the crust is arrested as much by reduction in pressure as by heat-loss. In high-grade metamorphism, the beginning of melting is strongly dependent on the presence of water, which may be contributed by the breakdown of hydrous mafic minerals, and progressive melting is halted by dissolution of water in the melt fraction.

Perthites

Alkali feldspars in volcanic rocks are often glass-clear and optically featureless. Although they are often described as 'unexsolved', electron microscopy suggests that many, and probably most, are cryptoperthitic. The periodicity of the coherent lamellar intergrowths may be on the scale of a few tens of nanometres. Lamellae with similar periodicities have been produced experimentally, and their coarsening rate studied in long annealing experiments. The diffusion parameters so obtained have been successfully applied to calculate the cooling rates of tuffs, lavas, dykes and sills, and are in order-of-magnitude agreement with the coarseness of intergrowths in plutonic rocks (Figs 172b, p. 262, 174b, p. 263).

In plutonic rocks, alkali feldspars are almost always perthitic, at a very large range of scales from macro- to crypto-perthite, often both together within single crystals (see sections on Perthite, p. 262, and on Electron microscopy, p. 280). The intergrowths provide a considerable amount of information about thermal history, and especially fluid–feldspar reaction. The variation in strain-controlled microtextures (i.e. those unaffected by deuteric unmixing) is summarized in Fig. 173, and examples of deuteric unmixing are given in Figs 172a and 192. Regular, coherent or semicoherent intergrowths orientated to minimize coherency strain ('strain-controlled' intergrowths, see Figs 172–174, 179, 192) are generally at scales at or below a few micrometres, except in some granulite-facies metamorphic rocks in which elevated temperature has been sustained for long periods (Fig. 174b). Alkali feldspars from granulites may contain complex mixtures of coarse microperthite and coherent cryptoperthite, indicating multiple phases of exsolution. Alkali feldspar porphyroblasts in acid gneisses have microtextures that are generally indistinguishable from those in phenocrysts in granites. In both igneous and metamorphic rocks coherent intergrowths usually occur in non-turbid crystals or parts of crystals. They cannot survive fluid–feldspar replacement reactions and their bulk composition is likely to provide the best guide to the feldspar composition at the time of crystal growth. The periodicity of coherent intergrowths has been shown to be related to cooling rate in a few hypersolvus intrusions, but coherent exsolution begins at low temperature in alkali feldspars in many subsolvus granitic plutons and periodicities vary little with respect to intrusive contacts, probably because thermal gradients are low.

Irregular 'vein' (Figs 172a, 181) and 'patch' (Fig. 192, right) perthite corresponds with turbid, microporous feldspar (Fig. 193), which is commonly white or pink and has recrystallized by interface-coupled replacement. Alkali feldspars with these properties are the norm in plutonic rocks, showing that reactions between alkali feldspars and aqueous fluids, usually at temperatures below 500ºC, have affected large volumes of the upper crust. As described earlier, replacement may be isochemical 'mutual replacement' or non-isochemical replacement, or both. After replacement it is thus no longer certain that the feldspar bulk composition is that with which it first grew. During these 'deuteric coarsening' reactions the intergrown feldspars in perthitic crystals move from the coherent solvus to the strain-free solvus. Examples are known in which a further phase of coherent exsolution in Or-rich patches follows deuteric coarsening.

Polymorphism

Sanidine and/or anorthoclase occur in volcanic rocks, both as phenocrysts and in the groundmass. The twinning of anorthoclase (Figs 182, 183) is distinctive. Sanidine can grow metastably during sedimentary diagenesis. Some studies have suggested that quantitative estimates of cooling rate can be obtained by measurement of degree of Si–Al order in sanidine.

The Or-rich phase in plutonic alkali feldspars is orthoclase or microcline. Many crystals are mixtures of orthoclase and microcline at a sub-optical scale (Fig. 198). The factors that control the polymorph present in any plutonic igneous or metamorphic rock are not always clear, but the main control is not cooling rate, although this is often stated to be the case. As described in the Structure section (p. 254), the key step is the transformation of the 'tweed' microstructure (p. 257) of orthoclase, which is composed of alternating ordered domains at the scale of a few nm and which is monoclinic both optically and using X-ray and electron diffraction, into tartan-twinned microcline which is triclinic using all methods. Fluid–feldspar reactions appear to be involved in some cases and deformation in others, but in the absence of such factors tweed orthoclase may be preserved even in Archaean rocks. Note the diffuse tweed–tartan boundaries in Fig. 198.

Downloaded from https://pubs.geoscienceworld.org/books/chapter-pdf/3761011/9780903056434_ch59.pdf
by guest

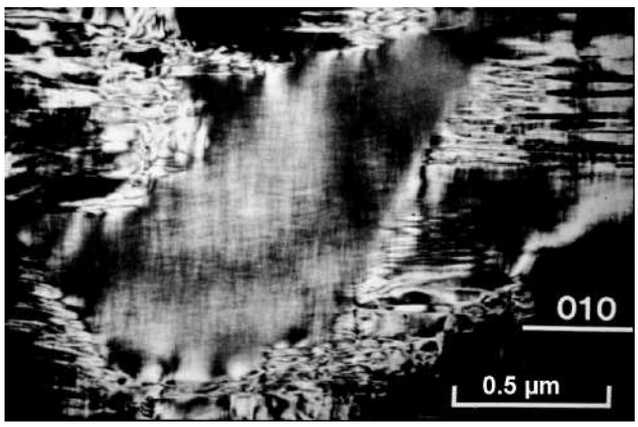


Fig. 198. Transmission electron microscope image of an Or-rich feldspar from a granitic rock that is a mixture of 'tweed' orthoclase and irregular microcline showing combined Albite and Pericline 'tartan' twinning. The tweed microtexture gives single electron diffraction spots indicating monoclinic symmetry, whereas the microcline gives paired spots indicating twinning and triclinic symmetry. All features are sub-optical. In an optical microscope the sample shows undulatory extinction, with variable extinction angles, and areas with very fine-scale tartan twinning. Elsewhere the sample is microperthitic. (From Fitz Gerald, J.D. & McLaren, A.C., 1982, *Contrib. Mineral. Petrol.*, **80**, 219–229).

In 'braid' perthite (Figs 173, 174a), which has a high proportion of albite (Fig. 173), low microcline develops because of coherency with the low albite which is triclinic because of the shearing transformation (Fig. 169). However in crystals with more Or-rich bulk compositions it is not clear whether microcline can form by a continuous diffusional process from orthoclase. It is possible for microcline to crystallize directly in exceptionally low-temperature magmatic rocks, such as some in the alkaline Ilimaussaq intrusion, where it has a distinctive style of twinning, and in geothermal systems and low-temperature veins, where it commonly has the {110} adularia habit. The Ab-rich phase in all plutonic alkali feldspars is always low albite, although the orientation of Pericline twins may be that of high albite, indicating a disordered precursor.

Metamorphic rocks

Potassium feldspar is a stable product of both high-grade thermal and regional metamorphism. It is a typical mineral of the sillimanite zone of metamorphism and in rocks of argillaceous composition does not appear at lower grades.

The formation of potassium feldspar in high-grade metamorphic rocks is due largely to the instability of the micas in this $P-T$ environment, and the following reactions may operate:

$$\underset{\text{biotite}}{K(Mg,Fe)_3AlSi_3O_{10}(OH)_2} + 3\,SiO_2 \rightarrow \underset{\text{orthoclase}}{KAlSi_3O_8} + 3\,\underset{\text{orthopyroxene}}{(Mg,Fe)SiO_3} + H_2O$$

$$\underset{\text{siderophyllite}}{2\,K(Mg,Fe)_{1.5}Al_2Si_3O_{10}(OH)_2} + 3\,SiO_2 \rightarrow 2\,\underset{\text{orthoclase}}{KAlSi_3O_8} + \underset{\text{pyrope-almandine}}{(Mg,Fe)_3Al_2Si_3O_{12}} + 2\,H_2O$$

$$\underset{\text{muscovite}}{KAl_3Si_3O_{10}(OH)_2} + SiO_2 \rightarrow \underset{\text{orthoclase}}{KAlSi_3O_8} + \underset{\text{sillimanite}}{Al_2SiO_5} + H_2O$$

K-feldspar porphyroblasts, often several centimetres in size, form by replacement in the country rocks adjacent to granites, or in xenoliths in granites. They are common in schists and gneisses in the vicinity of acid igneous rocks, and in pelitic xenoliths, where replacement clearly requires the introduction of feldspar components from an external source. Experimental work (Fig. 188) shows that in a temperature gradient in which alkali ions may exchange through an intercrystal fluid, albite will replace K-feldspar in the hotter region, with the reverse in the cooler region.

Alkali feldspars in granulite facies rocks are usually non-turbid and green, brown or black in hand specimen. Retrogression leads to turbidity and in some cases to the development of microcline from orthoclase. They range in composition from perthite to antiperthite and commonly have complex perthitic textures on a range of scales from crypto- to micro-perthitic within single crystals. The cryptoperthitic textures probably arise from extremely long periods of heating at relatively low-temperature. Sinuous micromesoperthites (Fig. 174b) are particularly characteristic of the granulite facies.

Low-T feldspars

At low temperatures, alkali feldspars approach pure end-member compositions, defined by the solvus for ordered feldspars. Thus authigenic feldspars often have <2 mol% of the second component. Some authigenic K-feldspars contain significant celsian. Low-temperature feldspars commonly have the {110} adularia habit, and can have variable degrees of order, from sanidine to low microcline, probably reflecting growth rate. Single, euhedral crystals may grow, as in the Green River Formation, Wyoming, and the Cambrian Fucoid Bed in the North-west Highlands of Scotland, or {110} overgrowths may form on detrital feldspar cores. Albite and K-feldspar overgrowths with this habit are common in siliciclastic sedimentary rocks. Replacive feldspar, within the outline of an original feldspar crystal, often has the {110} habit, which is easily imaged using back-scattered electrons or the HF etching technique. The habit develops during deuteric replacement at ~500ºC down to low diagenetic temperatures.

As in low-temperature metamorphism the precipitation of Na- or K-rich feldspar in a sedimentary basin containing interstitial brine in a temperature gradient is likely to be governed by the relationships depicted in Fig. 188. Albitization, at the expense of K-feldspar,

Downloaded from https://pubs.geoscienceworld.org/books/chapter-pdf/3761011/9780903056434_ch59.pdf
by guest

occurs in the hotter, deeper part of the basin, and the corresponding brines become more K-rich. It should be noted that large-scale transfer of Si and Al is not required, just local exchange of Na and K in what potentially may be a dilute solution.

Feldspars extracted from active geothermal systems, such as the Salton Sea system, California, are fully ordered and have compositions on the alkali feldspar solvus for ordered feldspars (Fig. 169a) in good agreement with temperature (~350–250ºC) measured in boreholes. The Salton Sea geothermal system has been running for only ~16000 years, showing that extremely long times are not required to produce microcline.

Intergrowths with non-feldspar phases

Alkali feldspars form intergrowths with a number of other mineral species. There are several types of intergrowth between alkali feldspars and quartz.

Myrmekite is an intergrowth of vermicular (i.e. worm-like) quartz and albitic plagioclase at the boundary between a more calcic plagioclase and perthitic K-feldspar. The overall shape of the region showing the intergrowth is often wart-like (the name, myrmekite, comes from the Ancient Greek for wart), projecting into the K-feldspar, or as a rim between K-feldspar and calcium-bearing plagioclase. Within the myrmekite the quartz worms thin-out and disappear towards the K-feldspar. The intergrowth can be seen in an optical microscope and is common in two-feldspar granites and gneisses. Deformation has often been suggested to be part of the reaction process, but myrmekite also occurs in undeformed granites.

The exact mechanism of myrmekite formation is not fully understood but the essential parts of the process are replacement of K-feldspar by albite:

$$2\,KAlSi_3O_8 + Na_2O \rightarrow 2\,NaAlSi_3O_8 + K_2O$$

coupled with albitization of Ca-bearing plagioclase:

$$2\,CaAl_2Si_2O_8 + Na_2O + 2\,SiO_2 \rightarrow 2\,NaAlSi_3O_8 + 2\,CaO + Al_2O_3$$

Granophyric texture is an intimate intergrowth of alkali feldspar and quartz which does not involve plagioclase. It is sometimes similar in appearance to myrmekite, with vermicular quartz, although the quartz sometimes has an angular outline. It is common in high-level acid intrusive rocks, particularly the variety of microgranite known as granophyre, and is generally thought to form by rapid simultaneous growth of quartz and sanidine in a silicate liquid close in composition to the 'granite minimum' (Fig. 185). The granophyric texture commonly nucleates on alkali feldspar phenocrysts, and coarsens away from the phenocrysts. Feldspar in granophyres is almost always intensely turbid and reddened by hematite inclusions (for example, in the granitic rocks of the Red Cuillin, Isle of Skye), indicating extreme interaction with post-magmatic aqueous fluids. Granophyres often contain drusy cavities, indicating that the silicate liquid became water-saturated during crystallization, and it is possible that rapid simultaneous crystallization of quartz and feldspar, in what are often quite large bodies of granite, occurred because of sudden reduction in P_{H_2O} (a 'pressure-quench'), rather than cooling.

Graphic intergrowth is also composed of quartz and alkali feldspar but is coarser than the granophyric intergrowth and is characteristically found in pegmatites, often in giant feldspar crystals. The included quartz rods have angular cross-sections that are reminiscent of ancient forms of writing and in three dimensions clusters of rods sometimes form a coral-shaped single crystal. The intergrowth is described as 'graphic granite' although the amount of quartz is in many cases too low to correspond with cotectic crystallization in the system Ab–Or–Q–H_2O (Fig. 185). It is generally accepted that graphic granite forms by simultaneous crystallization of K-feldspar and quartz in conditions in which large amounts of aqueous vapour are present, but it has also been produced experimentally by replacement.

K-feldspar also forms intimate vermicular intergrowths with nepheline. These sometimes form pseudomorphs that have the characteristic icositetrahedral shape of leucite, the bulk composition of Na-bearing leucite, $(K,Na)AlSi_2O_6$, and are known as *pseudoleucite*. Although leucite can crystallize from K-rich silicate liquids at low P_{H_2O} (Fig. 169a, 184), Na-rich leucite does not occur in rocks, and it seems likely that Na-exchange is involved in pseudoleucite formation.

Further reading

Brown, W.L. (1993) Fractional crystallization and zoning in igneous feldspars: ideal water-buffered liquid fractionation lines and feldspar zoning paths. *Contributions to Mineralogy and Petrology*, **113**, 115–125.

Brown, W.L. (Editor) (1984) *Feldspars and feldspathoids. Structures, properties and occurrences*. NATO ASI Series C 137. D. Reidel Publishing Company, Dordrecht, 541 pp.

Brown, W.L. and Parsons, I. (1981) Towards a more practical two feldspar geothermometer. *Contributions to Mineralogy and Petrology*,**76**, 369–377.

Brown, W.L. and Parsons, I. (1989) Alkali feldspars: ordering rates, phase transformations and behaviour diagrams for igneous rocks. *Mineralogical Magazine*, **53**, 25–42.

Brown, W.L., Becker, S.M. and Parsons, I. (1983) Cryptoperthites and cooling rate in a layered syenite pluton. *Contributions to Mineralogy and Petrology*, **82**, 13–25.

Carmichael, I.S.E., Turner, F.J. and Verhoogen, J. (1974) *Igneous Petrology*. McGraw-Hill Book Company, New York, xiii + 739 pp.

Deer, W.A., Howie R.A. and Zussman, J. (2001) *Rock Forming Minerals, Volume 4A, Framework Silicates: Feldspars*. The Geological Society, London, viii + 972 pp..

Eggleton, R.A. and Buseck, P.R. (1980) The orthoclase-microcline inversion: a high resolution transmission electron microscope study and strain analysis. *Contributions to Mineralogy and Petrology*, **74**, 123–133.

Fitz Gerald, J.D. and McLaren, A.C. (1982) The microstructures of microcline from some granitic rocks and pegmatites.

Downloaded from https://pubs.geoscienceworld.org/books/chapter-pdf/3761011/9780903056434_ch59.pdf
by guest

Contributions to Mineralogy and Petrology, **80**, 219–229.
Fuhrman, M.L. and Lindsley, D.L. (1988) Ternary feldspar modelling and thermometry. *American Mineralogist*, **73**, 201–215.
Goldsmith, J.R. and Jenkins, D.M. (1985) The high–low albite relations revealed by reversal of degree of order at high pressure. *American Mineralogist*, **70**, 911–923.
Laves, F. (1950) The lattice and twinning of microcline and other potash feldspars. *Journal of Geology*, **58**, 548–547.
Lee, M.R. and Parsons, I. (1995) Microtextural controls of weathering of perthitic alkali feldspars. *Geochimica et Cosmochimica Acta*, **59**, 4465–4488.
Lee, M.R., Waldron, K.A. and Parsons, I. (1995) Exsolution and alteration microtextures in alkali feldspar phenocrysts from the Shap granite. *Mineralogical Magazine*, **59**, 63–78.
MacKenzie, W.S. and Zussman, J. (Editors) (1974) *The Feldspars.* Manchester University Press. xi + 717 pp.
McDowell, S.D. (1986) Composition and structural state of coexisting feldspars, Salton Sea geothermal field. *Mineralogical Magazine*, **50**, 75–84.
Parsons, I. (Editor) (1994) *Feldspars and their Reactions*. NATO ASI Series C 421. Kluwer Academic Publishers, Dordrect, xxx + 650 pp.
Parsons, I. (2010) Feldspars defined and described: a pair of posters published by The Mineralogical Society. Sources, and supporting information. *Mineralogical Magazine*, **74**, 529–551.
Parsons, I., Thompson, P., Lee, M.R. and Cayzer, N. (2005) Alkali feldspar microtextures as provenance indicators in siliciclastic rocks and their role in feldspar dissolution during transport and diagenesis. *Journal of Sedimentary Research*, **75**, 921–942.
Ribbe P.H. (Editor) (1983) *Feldspar Mineralogy.* Reviews in Mineralogy 2, Mineralogical Society of America, xii + 362 pp.
Smith, J.V. (1974a) *Feldspar Minerals vol. 1, Crystal Structure and Physical Properties*. Springer-Verlag, Berlin, xix + 627 pp.
Smith, J.V. (1974b) *Feldspar Minerals vol. 2, Chemical and Textural Properties*. Springer-Verlag, Berlin, xii + 690 pp.
Smith, J.V. and Brown, W.L. (1988) *Feldspar Minerals vol. 1, Crystal Structure, Physical, Chemical and Microtextural Properties (Second Revised and Extended Edition)*. Springer-Verlag, Berlin, xvii + 828 pp.
Su, S.-C., Ribbe P.H. and Bloss, F.D. (1986) Alkali feldspars: structural state determined from composition and optic axial angle 2*V*. *American Mineralogist*, **71**, 1285–1296.
Taylor, W.H. (1933) The structure of sanidine and other feldspars. *Zeitschrift für Kristallographie*, **85**, 425–442.
Tuttle, O.F. and Bowen, N.L. (1958) Origin of granite in the light of experimental studies in the system $NaAlSi_3O_8$–$KAlSi_3O_8$–SiO_2–H_2O. *Geological Society of America, Memoir* **74**, xi + 153 pp.
Wen, S.X. and Nekvasil, H. (1994) Solvcalc – an interactive graphics program package for calculating the ternary feldspar solvus and for 2-feldspar geothermometry. *Computers and Geosciences*, **20**, 1025–1040.
Willaime, C. and Brown, W.L. (1974) A coherent elastic model for the determination of the orientation of exsolution boundaries: application to the feldspars. *Acta Crystallographica* A, **30**, 313–331.
Worden, R.H., Walker, F.D.L., Parsons, I. and Brown, W.L. (1990) Development of microporosity, diffusion channels and deuteric coarsening in perthitic alkali feldspars. *Contributions to Mineralogy and Petrology*, **104**, 507–515.

Downloaded from https://pubs.geoscienceworld.org/books/chapter-pdf/3761011/9780903056434_ch59.pdf
by guest

Barium Feldspars

Celsian — $Ba[Al_2Si_2O_8]$

Hyalophane — $(K,Na,Ba)[(AlSi)_4O_8]$

Monoclinic (+) or (−)

	Celsian	Hyalophane
α	1.579−1.589	1.520−1.542
β	1.583−1.593	1.524−1.545
γ	1.588−1.600	1.526−1.547
δ	0.009−0.013	0.005−0.010
$2V_\gamma$	83−92º	101−132º
Orientation	α:*z*, 3−5º, β = *y*; O.A.P. (010)	α:*x*, 0−20º, γ = *y*; O.A.P. ⊥ (010)
D (g/cm^3)	3.10−3.39	2.58−2.82
H	6−6½	6−6½
Cleavage	{001} perfect, {010} good, {110} poor	{001} perfect, {010} good
Twinning	Carlsbad, Manebach, Baveno laws	
Colour	Colourless, white or yellow; colourless in thin section	
Unit cell	*a* 8.64 Å, *b* 13.05 Å, *c* 14.40 Å, β 115.1º Z = 4;. Space group *I*2/*c*	

The barium feldspar celsian (Cn) is isostructural with sanidine with which it forms a continuous solid-solution series at high *T*. At high *T* there is extensive solid solution in the quaternary system $BaAl_2Si_2O_8$ (Cn)–$CaAl_2Si_2O_8$ (An)–$NaAlSi_3O_8$ (Ab)–$KAlSi_3O_8$ (Or) but natural assemblages suggest several miscibility gaps at low *T*. Forms with different degrees of Si–Al order occur naturally. Feldspars with dominant K or Ba in the range $Cn_{15–75}$ are conveniently described using the term hyalophane.

The barium ion is present in small quantities in the great majority of feldspars, but only rarely occurs as a major constituent: in general, feldspars are considered as barium-rich varieties when their barium content is in excess of approximately 2% BaO. In addition to replacing potassium, barium also may replace calcium and sodium. Celsian has an ideal end-member formula $BaAl_2Si_2O_8$: calciocelsian is a variety with 25% of the anorthite molecule. Barium-bearing plagioclase feldspars are rather rare, but barium-oligoclase and barium-bytownite are known. The high-temperature synthetic celsian is hexagonal.

The increasing contents of barium are associated with higher refractive indices and higher densities.

The barium feldspars have a very restricted occurrence, mostly in association with manganese deposits. They are known from the Kaso mine, Japan; from Broken Hill, New South Wales, Australia; from the Benallt manganese mine, North Wales; from Aberfeldy, Scotland; from Franklin, New Jersey; and from Otjosundu, Namibia.

Further reading

Essene, F.J., Claflin, C.L., Georgetti, G., Mata, P.M., Peacor, D.R., Árkai, P. and Rathmell, M.A. (2005) Two-, three- and four-feldspar assemblages with hyalophane and celsian: equilibria in $BaAl_2Si_2O_8$–$CaAl_2Si_2O_8$–$NaAlSi_3O_8$–$KAlSi_3O_8$. *European Journal of Mineralogy*, **17**, 515−535.

Gay, P. and Roy, N.N. (1968) The mineralogy of the potassium-barium feldspar series. III. Subsolidus relationships. *Mineralogical Magazine*, **36**, 914−932.

Lagache, M. and Catel, N. (1992) Solid solution and unmixing in the (Ba,K,Na) feldspars. Part 1: The albite–celsian solvus determined by ion-exchange experiments. *European Journal of Mineralogy*, **4**, 209−212.

Roy, N.N. (1965) The mineralogy of the potassium-barium feldspar series; I. The determination of the optical properties of natural members. *Mineralogical Magazine*, **35**, 508−518.

Downloaded from https://pubs.geoscienceworld.org/books/chapter-pdf/3761667/9780903056434_ch60.pdf
by guest

Triclinic (+) or (−)

	High Albite $NaAlSi_3O_8$	Low Albite $NaAlSi_3O_8$	Anorthite $CaAl_2Si_2O_8$
α	1.528	1.528	1.575
β	1.532	1.533	1.583
γ	1.534	1.539	1.588
δ	0.007	0.010	0.013
2V	50º(−)	77º(+)	78º(−)
Orientation	For optic orientations see Fig. 210, p. 304		
D (g/cm^3)	2.62	2.62	2.76
H	−	6−6½	6−6½
Cleavage	{001} perfect, {010} good, {110} poor		
Twinning	(a) Multiple lamellar albite twins [Composition plane (010), twin axis ⊥ (010)]		
	(b) Simple Carlsbad twins [Composition plane (010), twin axis *z*]		
	(c) Many other normal, parallel and complex twins (see Table 35, p. 265)		
Colour	Normally colourless or white, but may be yellow, pink, green or black; colourless in thin section		
Unit cell			
a (Å)	8.16	8.14	8.18
b (Å)	12.87	12.79	12.88
c (Å)	7.11	7.16	14.17
α	93.5º	94.3º	93.2º
β	116.4º	116.6º	115.8º
γ	90.3º	87.7º	91.2º
Z	4	4	8
Space group	$C\bar{1}$	$C\bar{1}$	$P\bar{1}$

The cell parameters above are for room temperature. Above approximately 950ºC albite becomes monoclinic, *C*2/*m*. Above ~240ºC anorthite inverts to $I\bar{1}$ symmetry. Both of these symmetry changes are displacive in character.

Plagioclase feldspars are ubiquitous and are the most common rock-forming mineral species. High temperature plagioclases occur in many volcanic igneous rocks and form a simple ideal solid solution series. Low temperature plagioclase is common in plutonic igneous rocks and in metamorphic rocks. It forms a non-ideal solid solution which leads to a variety of complex intergrowths. Detrital plagioclase occurs in some clastic sedimentary rocks, although it is less resistant to weathering than alkali feldspar. Low albite commonly grows during diagenesis and low-temperature replacement processes.

Like the alkali feldspars most plagioclases are ternary solid solutions of *three components*: $NaAlSi_3O_8$, albite (Ab), $CaAl_2Si_2O_8$, anorthite (An), and $KAlSi_3O_8$, orthoclase (Or). In plagioclase the last is usually at low concentrations except in Ab-rich plagioclase in high-temperature rocks (Fig. 161a, p. 249). Although the plagioclase structure is essentially the same as that of alkali feldspars, the two solid solutions differ profoundly because although Na^+ and Ca^{2+} have similar ionic radii, the substitution of Na^+ by Ca^{2+} requires coupled substitution of Si^{4+} by Al^{3+} to maintain charge neutrality. High-temperature plagioclases near the solidus have Si−Al disorder, except for An-rich compositions, which may have long-range order, and form a simple solid-solution series. Low plagioclases, however, have Si−Al order, but the possible ways of distributing Al in an ordered arrangement in a solid-solution series in which the Si:Al ratio is variable are limited, and lead to the presence of several miscibility gaps. Almost all plutonic plagioclases are complex

Downloaded from https://pubs.geoscienceworld.org/books/chapter-pdf/3761680/9780903056434_ch61.pdf
by guest

intergrowths at a sub-optical scale. Natural anorthite is always fully ordered, although metastable partially disordered forms can be synthesized.

For descriptive purposes plagioclase solid solutions are subdivided purely on the basis of composition, $(Ab + Or)_xAn_{100-x}$ (Fig. 161a): An 0–10: albite, 10–30: oligoclase, 30–50: andesine, 50–70: labradorite, 70–90: bytownite, 90–100: anorthite. As intergrowths in low plagioclase are generally on sub-micrometre scales, their optical and many physical properties appear to vary continuously with Ab:An and may be used to determine composition. Plagioclase composition is the most important variable in the classification of igneous rocks.

Structure

Anorthite

The structures of high and low albite, which differ because of Si,Al order-disorder, are described under the alkali feldspars (p. 259). In contrast, natural end-member anorthite has a fully ordered structure in which the equal numbers of Si and Al atoms alternate with strict regularity. This ordering leads to a doubling of the *c* dimension as compared with albite (Fig. 199), and with regard to Si and Al locations the unit cell could be monoclinic and body-centred. The distortion of the framework about the relatively small Ca ions, however, leads to triclinic symmetry. There are nearly equivalent alternative sites for the Ca atoms and if these atoms are mobile between the two sites the average structure has body-centred symmetry, $I\bar{1}$. When one or other of the two sites is adopted, either throughout a crystal or in domains within it, the symmetry is reduced further to primitive, $P\bar{1}$. The $P\bar{1} \leftrightarrow I\bar{1}$ transformation occurs at ~240°C in pure anorthite but moves to lower temperatures with increasing Ab (Fig. 200). Investigations of *P*-anorthite by transmission electron microscopy have shown that irregularly shaped domain walls outline adjacent regions in which Ca atoms are in

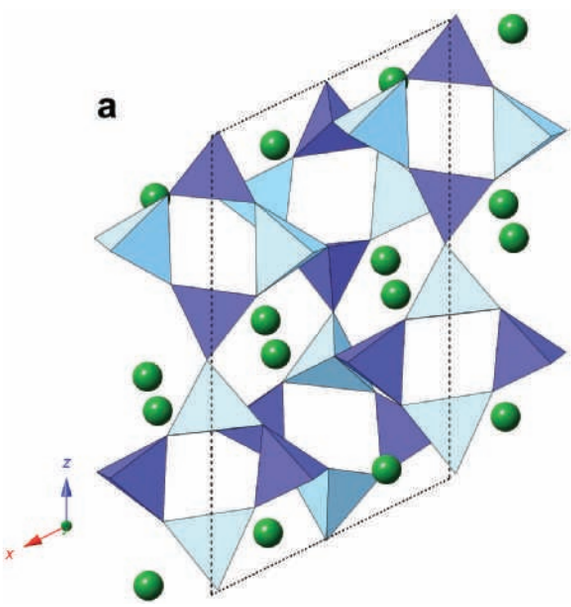
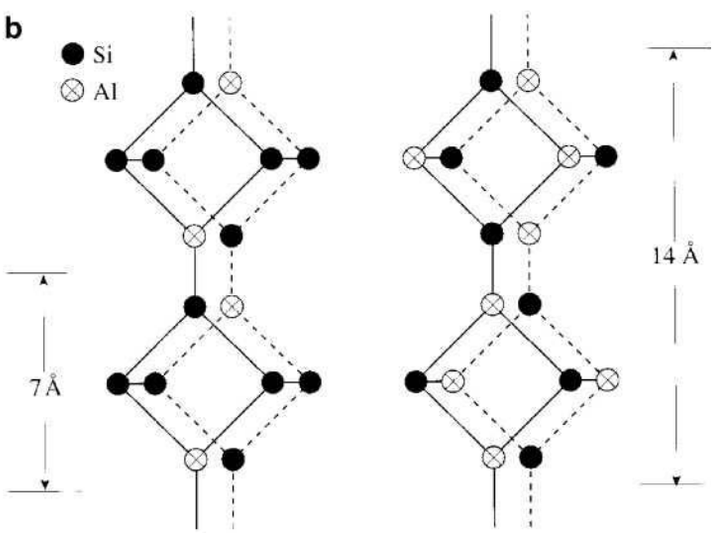


Fig. 199. (a) The structure of primitive anorthite viewed along *y*, showing the regular alternation of Si–O (blue) and Al–O (light blue) tetrahedra, thus doubling the *c* parameter (CrystalMaker image). Ca cations green. Unit cell outlined.



(b) Simplified structures of (left) low albite (or microcline) and (right) anorthite to illustrate the role of Al/Al avoidance in intermediate plagioclase. Oxygen tetrahedra are omitted. The Al/Al-avoidance principle requires that two Al atoms cannot share any of the lines on these diagrams. In the low-albite structure, with Si:Al of 3:1, it is impossible to add an Al without violating this rule, and a continuous transition to an ordered oligoclase is not allowed. It is possible to disorder the Si, and Al distribution, and heating leads continuously to high albite. In anorthite the distribution shown is the only way in which T atoms can be distributed without violating Al avoidance. Natural anorthite is therefore always fully ordered. The *c* axis is doubled. It is possible to add Si to this structure, so that Na-bearing plagioclase can be derived from the anorthite structure (reprinted from Megaw, H.D., 1962, *Norsk. Geol. Tidsskr.*, **42**, 104–37).

Downloaded from https://pubs.geoscienceworld.org/books/chapter-pdf/3761680/9780903056434_ch61.pdf
by guest

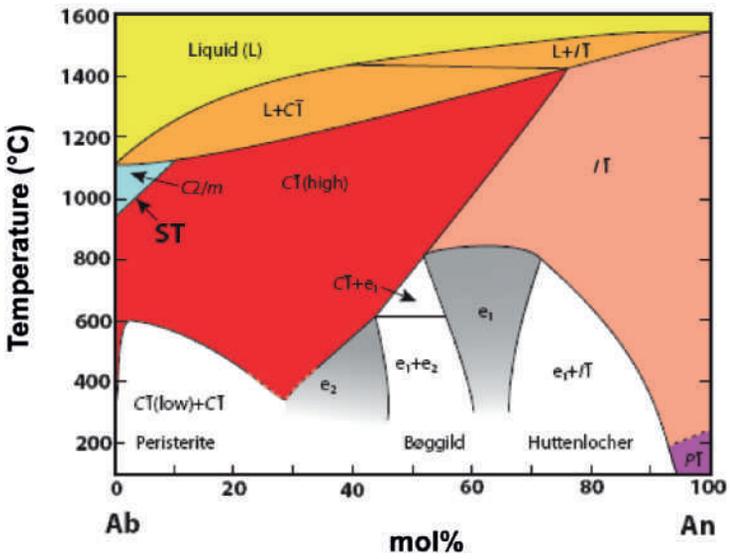


Fig. 200. Phase diagram for Or-free plagioclase feldspars at atmospheric pressure. Liquidus and solidus curves from Bowen, N.L., 1913, *Amer. J. Sci.*, **35**, 577–99. Subsolidus phase transitions and miscibility gaps from Carpenter, M.A., 1994, pp. 221–69 in: *Feldspars and their Reactions* (I. Parsons, editor). NATO ASI Series C 421. Kluwer Academic Publishers, Dordrecht, The Netherlands.

'left' and 'right' positions. If a sample is heated the domains become smaller, and the walls disappear at the phase transition, when Ca is moving dynamically between 'left' and 'right' positions. This process is accompanied by a displacive change in framework geometry. Upon cooling the domain walls reappear, enlarging and returning to the shape they had before heating, suggesting that some fault-like feature involving T atoms defines their boundaries.

Compositions rich in An have long-range order even at high temperature, because as noted above, natural anorthite is always fully ordered. However crystals grown from glass at 1100–1400ºC have metastable disorder and essentially $C\bar{1}$ symmetry. Subsequent annealing leads to anorthite with a lamellar microstructure resembling that in (e) plagioclase (see below) and then to an ordered $I\bar{1}$ structure.

The plagioclase series

The complexities of plagioclase solid solutions are best understood with reference to a phase diagram (Fig. 200). At high temperatures, just below the solidus, high plagioclase appears to form a continuous, largely disordered solid-solution series, with stable long-range order developing in An-rich compositions. Unlike alkali feldspars, disordered plagioclase does not unmix at any cooling rate. The changes in space group, $C2/m$–$C\bar{1}$–$I\bar{1}$, do not lead to immiscibility. The $C2/m$–$C\bar{1}$ transition (ST) is caused by framework shearing, and corresponds with the shearing transformation in alkali feldspars (ST in Fig. 169, p. 258). There is thus a small *T-X* field in which Ab-rich plagioclase is monoclinic. The $C\bar{1}$–$I\bar{1}$ transition marks a change from a disordered high albite structure to an ordered anorthite structure (see below).

The structure and phase relationships of low plagioclase are extremely complex and poorly understood. The way the transition lines meet and their relationship to the miscibility gaps on Fig. 200 are uncertain. Strictly speaking Fig. 200 is probably a behaviour diagram (see Fig. 169c for its equivalent in alkali feldspars). The apparent breakdown of single crystals of plagioclase to albite + anorthite mixtures in metamorphic amphibolites and other instances of breaks in metamorphic plagioclase compositions (Fig. 216, p. 308), are consistent with complete immiscibility at low temperature, near end-member anorthite and albite being the only stable plagioclase feldspars. Such instances are rare, however, and most plutonic plagioclase occurs as intergrowths (Fig. 200), of largely unexplored petrogenetic significance.

The *peristerite*, *Bøggild* and *Huttenlocher* intergrowths (Fig. 200) are coherent lamellar intergrowths (i.e. they all have a continuous Si–Al–O framework) believed to form on solvus curves that are 'conditional' on Si–Al ordering. With very rare exceptions they are on sub-micrometre scales and not visible in an optical microscope. Depending on their periodicity they can cause iridescence, the best known being the 'labradorescence' caused by Bøggild intergrowths. Intergrowths must otherwise be detected using transmission electron microscopy (TEM) or single crystal X-ray diffraction. As in many alkali feldspars, the microtextures seen using TEM are commonly consistent with development by spinodal decomposition, but the fundamental driving forces for exsolution in the alkali feldspar and plagioclase solid solutions are very different. In the former the driving force is primarily the different ionic radii of Na^+ and K^+ which impose large local strains on the Si–Al framework. Perthitic exsolution occurs in alkali feldspars with disordered frameworks.

In contrast, in plagioclase the ionic radii of Na^+ and Ca^{2+} are effectively identical, but there is coupling between M and T ions because each Ca^{2+} ion must be accompanied by an Al^{3+}, replacing Si^{4+} to maintain charge balance. The Si:Al ratio changes from 3:1 in Ab to 1:1 in An. The extreme complexity of chemically intermediate, ordered plagioclase feldspar structures, in

Downloaded from https://pubs.geoscienceworld.org/books/chapter-pdf/3761680/9780903056434_ch61.pdf
by guest

which Al and Si are arranged regularly (ordered) on four equivalent structural sites, is a consequence of what is known as Lowenstein's rule, often called Al/Al avoidance. This rule, which applies to many, but not all, framework aluminosilicates, states that whenever two tetrahedra are linked by a common oxygen, only one of them can be occupied by Al. The underlying principle is the extra energy involved in forming an Al−O−Al linkage compared with an Al−O−Si linkage. Figure 199b can be used to explore the implications of the avoidance rule.

In disordered high plagioclase there are no symmetry-related structural constraints on the position of Si and Al and many ways of distributing Al and Si that do not violate Al/Al avoidance. The solid solution is continuous and close to ideal. However the end-members of the ordered low-plagioclase series have very different properties because of their different Al:Si ratios. In low albite (Fig. 199b, left) there are no positions in which additional Al can be placed (to create a hypothetical oligoclase, for example) that do not violate Al/Al avoidance. On the other hand, it is possible to disorder low albite, by heating, without such violation, and low albite transforms continuously into high albite. In anorthite, with its 2:2 Al:Si ratio, there is only one arrangement (Fig. 199b, right), in which Al alternates between T_1 and T_2 sites, that does not violate Al/Al avoidance. This arrangement is fully ordered and to maintain Al/Al avoidance it cannot be disordered. Pure anorthite is thus always fully ordered except very close to the melting point or during crystallization from glass. However, it is possible to place additional Si in the anorthite structure (to create a hypothetical bytownite). The two end-members of the ordered plagioclase series thus have different ordering schemes.

Together with the coupled exchange Na + Si ↔ Ca + Al this simple difference in behaviour underlies much of the complexity of low plagioclase, including the three established miscibility gaps and the (e)-plagioclase structure. Single-crystal X-ray reflections from feldspars are of four main types, a−d. All four are exhibited by *P*-anorthite:

a $(h + k)$ even, l even
b $(h + k)$ odd, l odd
c $(h + k)$ even, l odd
d $(h + k)$ odd, l even

In addition if there are satellites to the main reflections they may have the following properties:

e reflections lie in pairs symmetrically about b reflections
f reflections lie in pairs symmetrically about a reflections

Type a reflections are common to all feldspars, but type b reflections occur only in plagioclase with less than ~40 mol% Ab. They are indicative of structures with Al_2Si_2 ordering of the anorthite type (Fig. 199b). Type c reflections arise when Ca ions move to one side of the cavity in which the M ions reside, causing deformation of the Si–Al–O framework, and type d reflections have the same cause but are weaker.

In e_1 plagioclase (see fields on Fig. 200) there are sharp e and f satellite reflections whereas in e_2 the e reflections are diffuse and f absent. The presence of satellite reflections shows the existence of a slab-like 'superstructure', in which the slabs are arranged in a sequence that is out-of-step, or 'incommensurate', with the overall lattice, with a repeat distance on the scale of a few nanometres. Although earlier workers imagined that the slabs necessarily varied compositionally the modern view is that the slabs arise because of different ordering patterns. An e-like lamellar microtexture has been developed by experimental annealing of metastable disordered pure anorthite. It was also assumed that the incommensurate e-structure was a kinetically controlled precursor to stable phase separation, whereas on Fig. 200 incommensurate e_1 and e_2 structures are both seen as having fields of stability. The strongest evidence that the e structure is stable is that no correlation between its periodicity and geological thermal history has been found.

Peristerite intergrowths, lamellar compositions from ~An_1 to ~An_{25}, correspond with the limits of a coherent solvus, and affect crystals in the range from ~Ab_2 to An_{16}, probably the limits of a coherent spinodal. The Ab-rich phase is ordered low albite, while the An-rich phase is less-ordered oligoclase, with short-range order in some cases leading to an incommensurate structure, as shown by diffuse e reflections. The spinodal is conditional on Si–Al ordering, and the top of the asymmetric solvus (Fig. 200) is placed at ~600ºC, below the temperature band in which most ordering occurs in albite (Fig. 169, p. 258). Very rarely peristerite intergrowths are visible in an optical microscope but they usually have lamellar periodicities of a few tens of nanometres. Most peristerites that have been described come from regional metamorphic rocks and pegmatites but they have recently been discovered in a relatively rapidly cooled, high-level igneous intrusion and may be common in albitic plagioclase in granites. There is good evidence from low-temperature metamorphic rocks that metastable homogeneous disordered oligoclase may grow at sub-solvus temperatures in the peristerite range, subsequently ordering and unmixing.

Bøggild intergrowths develop in the range ~An_{46} to ~An_{60} (Fig. 200). The intergrowths are coherent and also consistent with spinodal decomposition. Varieties showing labradorescence are commonly found in deep-seated anorthosites, and may have >2 mol% Or in solid solution. Some Bøggild intergrowths from granulite-facies rocks with 200 nm periodicities have zero Or however, and the role of Or in all three plagioclase solvi is not well understood. It seems likely that the Bøggild gap is related to changes in ordering behaviour with respect to composition. The experimentally determined $C\bar{1} \leftrightarrow I\bar{1}$ phase transition and the sub-horizontal $I\bar{1} \leftrightarrow e_1$

Downloaded from https://pubs.geoscienceworld.org/books/chapter-pdf/3761680/9780903056434_ch61.pdf
by guest

boundary meet in the centre of the Bøggild gap (Fig. 200), and the volume proportions of the Ab- and An-rich phases are symmetrical about this composition. Natural occurrences of Bøggild intergrowths suggest that extended periods at elevated temperature are required. They are not found, for example, in plagioclase of appropriate composition from the high-level Skaergaard intrusion.

Huttenlocher intergrowths form in the range ~An_{67} to ~An_{90} and the microtextures are usually consistent with spinodal decomposition. The Ab-rich phase has an e_1 microstructure, the An-rich phase an $I\bar{1}$ structure with diffuse c and d reflections caused by $P\bar{1}$ distortions (Fig. 200). The experimentally determined limit of e_1 ordering in An-rich plagioclase occurs close to the crest of the Huttenlocher solvus. The coarsest exsolution, just visible in an optical microscope, occurs in the range ~$An_{69}-An_{76}$, suggesting that the solvus is slightly asymmetric.

The e-plagioclase microstructure is usually depicted as slabs, a few unit cells thick, of alternating albite-like and anorthite-like structure. There are several detailed models in the literature, based on interpretations of single-crystal diffraction and on high-resolution, lattice-scale TEM images, of which Fig. 201 is a pioneering example. The white bead-like objects are effectively lattice nodes, not individual atoms. Diffuse bands with an albite-like structure run NE–SW across the micrograph, separated by anorthite-like bands composed of alternating columns of white and black subcells in an antiphase relationship. A simple example of an antiphase relationship would be a translation of $c/2$ in adjacent chains in the anorthite structure depicted in Fig. 199b. The incommensurate structure is thus composed of sequences of layers *-ab-an-ab-an*-ab-an-ab-an** in which the anorthite-like layers *an* and *an** are in an antiphase relationship.

Depending on the bulk composition of the plagioclase, and its relationship with the three solvus regions, the e-plagioclase microstructure may occur in one or both of the coexisting phases in the coarse intergrowths. Thus crystals on the Ab-rich side of the Huttenlocher region may develop an e microstructure and subsequently exsolve An-rich regions without e lamellae. In Bøggild intergrowths both phases may have an e-superstructure, with periodicities that may or may not differ between the two sets of exsolution lamellae.

In geochemical work using a thermodynamic approach plagioclase is often treated as an ideal solid solution. The disordered plagioclase (high-plagioclase) range behaves as a near-ideal solid solution and its composition–activity relationships can be expressed in terms of simple $\Delta G/X$ curves that merge smoothly at the $C\bar{1}-I\bar{1}$ and $C\bar{1}-C2/m$ phase transitions (Fig. 200). This cannot be the case for low-plagioclase which must be strongly non-ideal, probably depending on the cooling and annealing history. The fine scale of the intergrowths in low-plagioclase is a result of the coupling of M and T ions, the energetics of ordering within the constraints imposed by Al/Al avoidance, and complex coherency strains. These lead to slow exsolution kinetics but tell us nothing about the magnitude of the non-ideality of the solid solution. The relationship between microstructures in low-plagioclase, geological history and plagioclase thermodynamics is a largely unexplored field.

The lattice parameters of plagioclase feldspars vary with An content so that it is possible to estimate their compositions by measuring the separations of suitable pairs of X-ray powder reflections. The separation $131-1\bar{3}1$ is useful for low-temperature plagioclases,

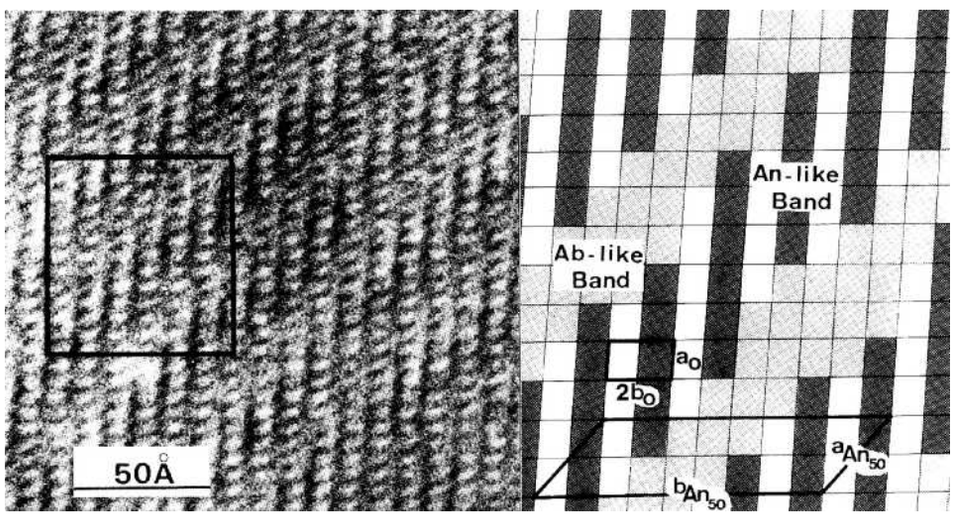


Fig. 201. Lattice-scale TEM image (left) and interpretation of the boxed area (right), of an An-rich lamella in a Bøggild intergrowth, bulk An_{52}, with an incommensurate e-plagioclase microstructure, viewed down the [312] albite axis. The structure is most easily seen if the micrograph is viewed at a low angle from the bottom of the page (from Nakajima, Y., Morimoto, N. and Kitahara M., 1977, *Phys. Chem. Min.*, **1**, 213–25).

Downloaded from https://pubs.geoscienceworld.org/books/chapter-pdf/3761680/9780903056434_ch61.pdf
by guest

but changes are only slight across the high-temperature series. As the thermal state influences peak positions, it is in general necessary to know either thermal state or composition in order to determine the other. Electron microprobe analysis is in most cases the preferred method for determining composition.

Antiperthite

Antiperthite (plagioclase with exsolved K-feldspar, Fig. 161b, p. 249) is less commonly reported than perthite or mesoperthite. This is a reflection of the asymmetry of the ternary feldspar solvus and its steepness parallel to the Ab–An join (Figs 187, p. 275 and 195, p. 284). The solubility of Or in calcic plagioclase is low even at high temperature. Intergrowths visible at the optical scale (strictly microantiperthites) are commonly found in granulite-facies metamorphic rocks (Fig. 202a) and charnockites, which crystallize at high temperature and experience long, and sometimes complex, cooling histories. Granulites also contain cryptoantiperthites, in which sub-microscopic incoherent blebs of sanidine have nucleated on albite twin composition planes. Coarse antiperthites (Fig. 202a) might arise by continuous coarsening of such textures over very long timescales, but fluid-related coarsening and replacement have been demonstrated in several occurrences. Antiperthites in sub-solvus granites are commonly patchy in shape and irregularly developed, suggesting that they originate by deuteric coarsening and/or replacement.

Fully coherent cryptoantiperthites have been found in some syenites and alkali gabbros. In Fig. 202b Albite twin thicknesses change with the thickness of albite lamellae, showing that the twins have adjusted their thickness during coarsening to minimize coherent elastic energy. The variation with composition of coherent antiperthites is summarized in Fig. 173, p. 262, fields 6 and 7. The intergrowth in Fig. 202b formed in field 6, probably by spinodal decomposition. It comes from a relatively rapidly cooled intrusion and is therefore a cryptoantiperthite. Antiperthitic crystals nearer the Ab–An join (field 7), which are common in granulites, form by coherent nucleation on the limb of the coherent solvus (Fig. 187), at relatively low temperatures, but then experience long periods of annealing producing microantiperthites.

Morphology and twinning

The principal forms exhibited by plagioclase crystals are similar to those of the alkali feldspars, and because the obliquity of the triclinic cell is slight, plagioclase habits differ little from those of some monoclinic feldspars. As a result of repeated twinning, plagioclase crystals are usually macroscopically monoclinic. They are often tabular with {010} prominent but are sometimes elongated parallel to the x axis, and more rarely parallel to z. The unusual pericline habit of albite, elongated parallel to y is illustrated in Fig. 175, p. 265. Low-temperature albite, particularly when developed by

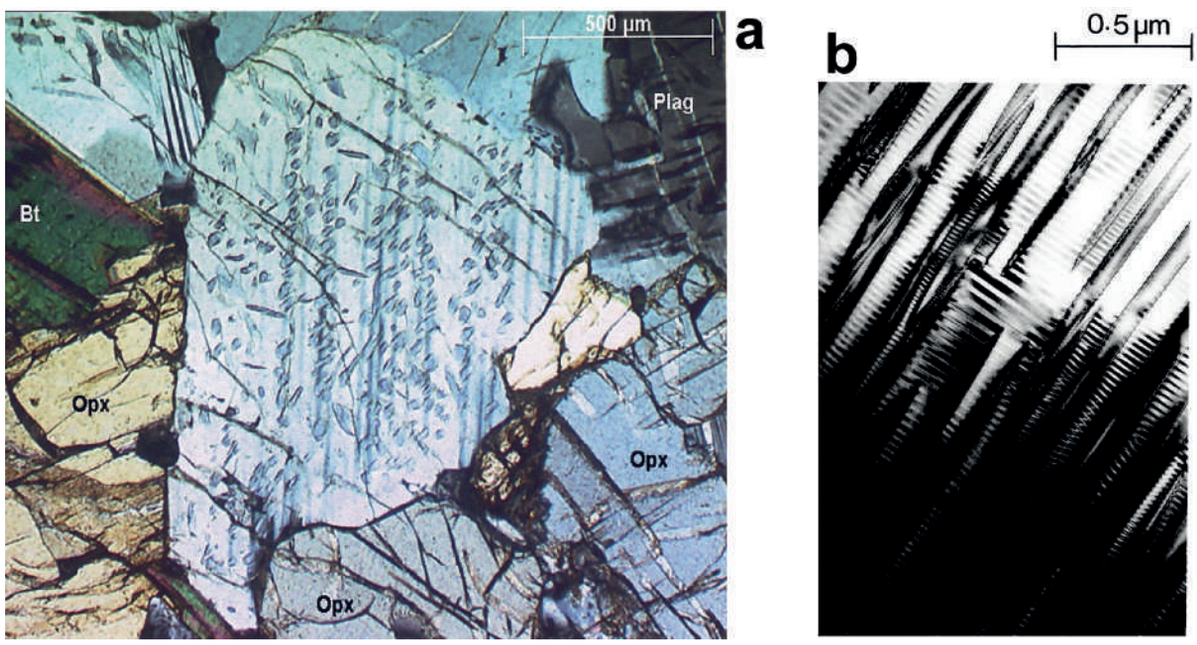


Fig. 202. (a) Optical micrograph (crossed polars) of an antiperthite from a high-grade granulite-facies gneiss, Mather Peninsula, Antarctica. Stumpy rods of orthoclase appear to have nucleated on Albite twins in plagioclase. The feldspar would have been homogeneous above ~1040ºC at a pressure of 1.0–1.2 GPa (from Cayzer, N., 2002, Ph.D. thesis, University of Edinburgh). (b) TEM micrograph of cryptoantiperthite from the Klokken intrusion, South Greenland. Featureless lenses parallel to $(\bar{6}01)$ are low sanidine, in an Albite twinned oligoclase matrix (from Brown, W.L. & Parsons, I., 1988, *Contrib. Mineral. Petrol.*, **98**, 444–54).

Downloaded from https://pubs.geoscienceworld.org/books/chapter-pdf/3761680/9780903056434_ch61.pdf
by guest

replacement, often adopts a {110} habit similar to adularia and can also be called pericline. The cleavelandite habit of albite is platy parallel to (010). Perfect cleavage on {001} and good {010} cleavage intersect at an angle of about 94º, and poor {110} and {1$\bar{1}$0} cleavages are observable in some cases.

Plagioclase feldspars usually show repeated twinning on a microscopic scale, but occasionally simple Manebach, and very rarely, simple Baveno twins occur. Carlsbad twinning is quite common and may be either repeated or simple. Repeated twins on the Albite and/or Pericline laws are the most common of all, Albite twinning rarely being absent, and twins on other laws (e.g. Ala, Albite-Carlsbad, Albite-Ala) are not uncommon; see Table 35, p. 265. Pericline and Albite twinning commonly occur in one crystal, and other combinations of two or more laws have been observed.

The position of the rhombic section (see p. 266 and Fig. 178, p. 267) depends upon the angles of the crystal lattice and these are influenced in the plagioclase series both by chemical composition and by structural state. In low-temperature specimens the angle of the rhombic section σ (Fig. 178) ranges from about +32º for An_0 to about −20º for An_{100}, but for high-temperature plagioclases σ changes little with composition from the value (−3º) for high albite.

Chemistry

Although they are predominantly aluminosilicates of Na and Ca varying from pure $NaAlSi_3O_8$ (Ab) to pure $CaAl_2Si_2O_8$ (An), the plagioclase series normally contains some of the orthoclase molecule, $KAlSi_3O_8$ (Or), varying from a maximum of 5 mol% Or in anorthite to ~30% in oligoclase (Fig. 161, p. 249). Other ions which may be present in very limited amounts include Ti, Fe^{3+}, Fe^{2+}, Mn, Mg, Ba and Sr. Analyses of plagioclases are shown in Table 37, in which each analysis has been recalculated on the basis of the 32(O) contained in the unit cell. Most of the iron reported in feldspar analyses is Fe^{3+}, and for the purposes of recalculation this has been assumed to be replacing Al^{3+} in *T* sites. Any Fe^{2+} has been assumed to be replacing Ca^{2+} in *M* sites. In reality Fe in many feldspars is contained in Fe oxide and sulphide inclusions. Note that in the plagioclase series the molecular weights of $NaAlSi_3O_8$ and $CaAl_2Si_2O_8$ are closely similar, so that the molecular percentages given at the bottom of Table 37 are essentially the same as weight percentages. This is useful when considering older phase diagrams, which often use wt.%.

The rare earth elements often occur in minor amounts in plagioclase, and may yield information of petrological importance. Europium, in particular, can occur in both divalent and trivalent oxidation states, in contrast to the trivalent nature of all the other *REE*. Eu^{2+} enters the non-framework *M* site of plagioclase, whereas Eu^{3+} and its neighbouring *REE* enter the coexisting liquid phase. It is possible to derive an estimate of the oxygen fugacity (f_{O_2}) from the relative partition coefficients of Eu and the other *REE*. Plagioclase usually shows a 'europium anomaly' in which the amount of Eu (normalized to the *REE* content of an average chondritic meteorite) is greater than that for the neighbouring rare earths. An early example is given as Fig. 203.

Experimental

The liquidus and solidus curves for the binary plagioclase system Ab−An at atmospheric pressure (Figs 200, 204) were determined by N.L. Bowen in 1913 working at the Geophysical Laboratory in

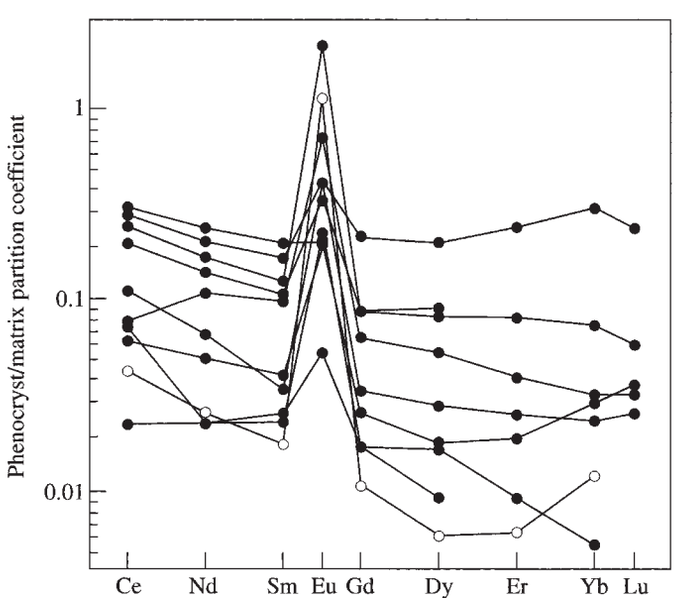


Fig. 203. Partition coefficients for rare earth elements between feldspar and matrix in some volcanic rocks (after Schnetzler, C.C. & Philpotts, I.A., 1970, *Geochim. Cosmochim. Acta*, **34**, 331−40).

Downloaded from https://pubs.geoscienceworld.org/books/chapter-pdf/3761680/9780903056434_ch61.pdf
by guest

Washington, D.C. It is a foundation work in experimental mineralogy, introducing the quenching method, locating the liquidus and solidus curves of a silicate solid solution for the first time and clarifying the concepts of 'isomorphous series' and 'solid solution'. Figure 204 can be used to demonstrate the processes of equilibrium and fractional crystallization in this system, which underlie the evolution of the majority of igneous rocks.

A liquid of composition $An_{50}Ab_{50}$ (A) begins to crystallize at about 1450ºC, the first crystals having the composition of approximately $An_{82}Ab_{18}$ (B). With further cooling under equilibrium conditions both liquid and crystals change their composition along the liquidus and solidus respectively until at 1285ºC the crystals reach a composition of $An_{50}Ab_{50}$ (D) as the last of the liquid, of composition (C), is used up. This continuous change in composition of the plagioclase crystals with falling temperature occurs only if there is sufficient time for the earlier crystals to react with the liquid: if there is insufficient time for this interchange of material the crystals will be zoned.

The resultant product will then have an average composition of $An_{50}Ab_{50}$ but the inner core will be more calcic and the outer zones more sodic. Thus as a result of fractionation by zoning a continuous offsetting

Table 37. Plagioclase feldspar analyses.

	1	2	3	4	5	6	7	8
SiO_2	67.84	67.3	64.10	58.10	52.42	49.06	44.17	43.88
TiO_2	0.00	–	0.00	tr.	0.09	–	tr.	–
Al_2O_3	19.65	20.6	22.66	26.44	29.70	32.14	34.95	36.18
Fe_2O_3	0.03	–	0.14	0.04	0.36	0.27	0.56	0.08
FeO	0.02	–	0.17	0.15	0.13	–	0.08	0.00
MgO	0.04	–	0.25	0.03	0.08	0.20	0.00	–
CaO	0.00	1.26	3.26	7.84	12.65	15.38	18.63	19.37
Na_2O	11.07	10.5	9.89	6.48	4.01	2.57	0.79	0.22
K_2O	0.29	0.89	0.05	1.10	0.21	0.17	0.05	0.00
H_2O+	0.56	–	0.17	0.03	–	0.13	0.84	0.28
H_2O-	0.30	–	0.06	0.06	–	0.03	0.17	0.08
Total	99.80	100.55	100.75	100.27	99.65	99.95	100.24	100.10
α	1.529	–	1.5351	–	–	1.5657	1.5351	1.5754
β	1.533	–	1.5393	–	–	1.5701	1.5393	1.5833
γ	1.539	–	1.5437	–	–	1.5754	1.5437	1.5885
2V	79º(+)	–	89º(+)	88º(+)	–	89º(−)	78º(−)	76.8−77.7º(−)
α′:(010)	–	–	11½º	–	–	–	–	–
D (g/cm^3)	–	–	2.646	–	–	–	–	2.749
	Numbers of ions on the basis of 32 O							
Si	11.964	11.761	11.267	10.413	9.540	8.990	8.237	8.126
Al	4.085	4.243	4.695	5.586	6.373	6.942	7.683	7.898
Fe^{3+}	0.004	–	0.018	0.005	0.049	0.037	0.078	0.011
Mg	0.011	–	0.065	0.008	0.022	0.055	–	–
Fe^{2+}	0.003	–	0.025	0.023	0.020		0.012	–
Na	3.785	3.557	3.370	2.252	1.436	0.913	0.285	0.079
Ca	–	0.236	0.614	1.505	2.467	3.020	3.723	3.844
K	0.066	0.198	0.011	0.252	0.049	0.040	0.012	–
Z	16.05	16.00	15.98	16.00	15.97	15.97	16.00	16.03
X	3.87	3.99	4.08	4.04	4.01	4.03	4.03	43.92
Mol.% Ab	98.0	89.1	82.5	56.0	35.7	22.7	7.1	2.0
Mol.% An	0.3	5.9	17.2	37.7	63.1	76.3	92.6	98.0
Mol.% Or	1.7	5.0	0.3	6.3	1.2	1.0	0.3	–

1 Albite, pegmatite, near Court House, Amelia Co., Virginia, USA (Kracek, F.C. & Neuvonen, K.J., 1952, *Amer. J. Sci*., Bowen vol., 293−318).
2 Albite phenocryst with quartz and sanidine, Honeycomb Hills rhyolite, Utah (Congdon, R.D. & Nash, W.P., 1991, *Amer. Min.*, **76**, 1261−8).
3 Glassy oligoclase, pegmatite, Kioo Hill, Kenya (Game, P.M., 1949, *Mineral. Mag*., **28**, 682−7).
4 Andesine antiperthite, two-pyroxene granulite, charnockite series, Madras, India (Howie, R.A., 1955, *Trans. Roy. Soc. Edinburgh*, **62**, 725−68).
5 Gem-quality labradorite megacryst in cinders in basaltic pyroclastic deposits, Crater Elegante, Sonora, Mexico (Gutman, J.T. & Martin, R.F., 1976, *Schweiz. Min. Petr. Mitt.*, **56**, 55−64. Includes SrO 0.105).
6 Bytownite, norite, Rustenburg platinum mines, Transvaal (Kracek, F.C. & Neuvonen, K.J., 1952, *Amer. J. Sci*., Bowen vol., 293−318).
7 Anorthite, olivine norite, Grass Valley, California, USA (Kracek, F.C. & Neuvonen, K.J., 1952, *loc. cit*.).
8 Anorthite, calc-silicate rock, Sittampundi complex, India (Subramaniam, A.P., 1956, *Bull. Geol. Soc. Amer.*, **67**, 217. Includes SrO 0.01).

Downloaded from https://pubs.geoscienceworld.org/books/chapter-pdf/3761680/9780903056434_ch61.pdf
by guest

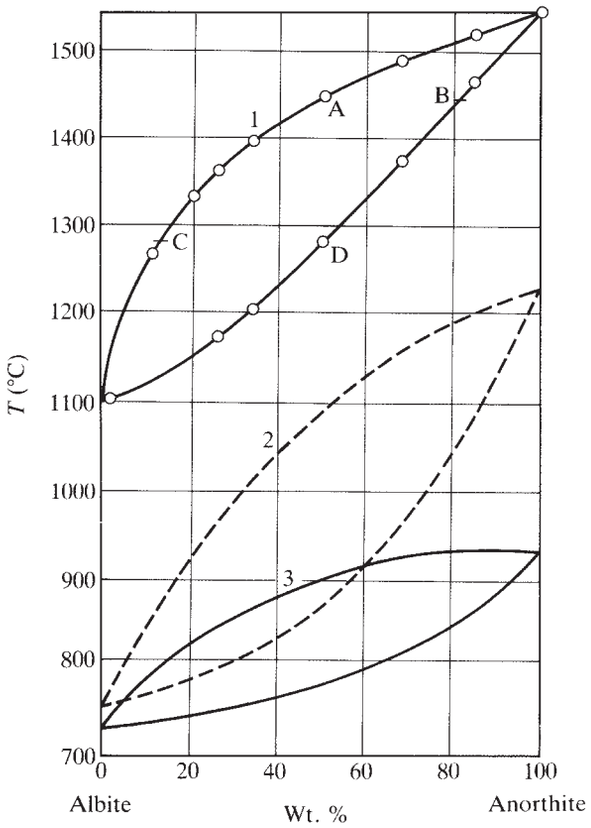


Fig. 204. Equilibrium liquidus and solidus curves for the plagioclase feldspars under (1) anhydrous conditions (after Bowen, N.L., 1913, *Amer. J. Sci.*, 4 th ser., **35**, 577–99); and (2) at 0.5 GPa water pressure (after Yoder, H.S. *et al*., 1957, *Ann. Rept. Dir. Geophys. Lab*., 1956–57, 207). (3) shows cotectic liquidus and solidus in the albite–anorthite–quartz–H_2O system at 0.2 GPa (after Johannes, W., 1989, *Contrib. Mineral. Petrol*., **103**, 270–6).

of the composition of the liquid towards albite is brought about together with a great increase in the range of consolidation temperatures. Such 'normal zoning', from more calcic cores to sodic rims, is common in plagioclases, but 'oscillatory zoning' in which the composition is alternately less and more calcic and simple 'reverse zoning', where the crystals become more calcic outwards are fairly common.

Unlike alkali feldspars, in which zoning is rarely preserved, complex zoning is common in plagioclase (e.g. Fig. 215, p. 307). It owes its preservation to the coupling of Ca and Na to Al and Si in the feldspar framework, in which diffusion is slow. Zoning is preserved in phenocrysts in basalts (Fig. 215) although it is often destroyed by diffusion in slowly cooled gabbros of equivalent composition. Zoning in plagioclase in plutonic environments is most commonly preserved in relatively evolved rocks such as granodiorites in which crystallization temperatures are relatively low. Crystal settling of early formed plagioclase in magma chambers or large sills leads to progressive fractionation towards more albitic liquids and is a major factor in the evolution of the igneous rocks.

As with the alkali feldspars the presence of water lowers the temperature of the liquidus-solidus loop of plagioclase considerably and under water-saturated conditions at P_{H_2O} 0.5 GPa the curves are at ~300ºC lower temperature (Fig. 204, curve 2). When excess SiO_2 is present in the liquid, and quartz and plagioclase are in equilibrium on the quartz–plagioclase cotectic (Fig. 205 and Fig. 196, line XW, p. 285) liquids are at even lower temperatures (Fig. 204, curve 3, is at P_{H_2O} 0.2 GPa) and the contrast between Ab:An in liquid and solid phases is larger. Note that in Fig. 204, the liquidus (curve 3) is not in the plane of the diagram but is on the cotectic curve in Fig. 205. Note also that the natural plagioclase starting material used contained ~2 mol% Or, and that the liquid contained up to 8 mol% Or. The large compositional differences are relevant to the formation of Na-rich residual liquids during magmatic fractionation as well as to the development of partial melts from rocks containing intermediate or basic plagioclase.

In the ternary system Ab–An–Or the effect of the orthoclase component on the liquidus and solidus is very large (Fig. 195, p. 284). This is particularly the case for An-rich compositions in which the solidus is lowered by over 400ºC by a few % Or (the line BI on Fig. 195). The effect is less pronounced in more albitic compositions. Tie-lines between evolving liquids (Fig. 195, line BL) and plagioclase are very long, and quite calcic plagioclase can initially crystallize from extremely Ab and Or rich liquids. Early plagioclase initially follows a one-feldspar solidus path (line BP) which corresponds with natural sequences such as the basalts shown on Fig. 214. Depending on the initial Or content of the liquid it may evolve along an entirely one-feldspar (hypersolvus) path, or, like the liquid on BL in Fig. 195, encounter the field boundary between plagioclase and alkali feldspar at L and begin precipitating a second feldspar, sanidine S. Further crystallization is discussed in the text near Fig. 195, p. 284.

Downloaded from https://pubs.geoscienceworld.org/books/chapter-pdf/3761680/9780903056434_ch61.pdf
by guest

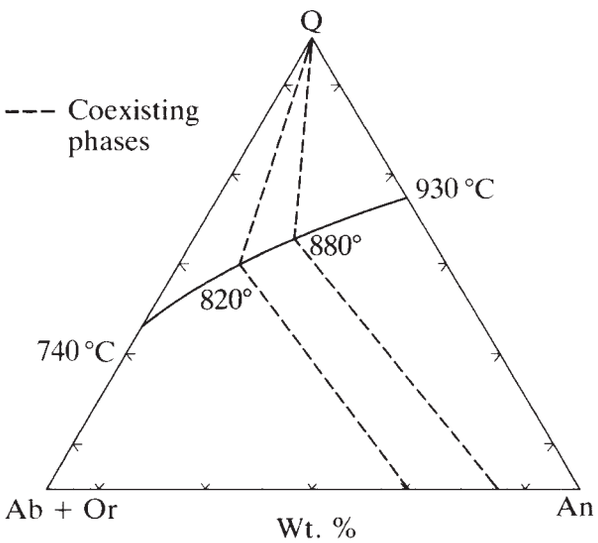


Fig. 205. Compositions of melt and coexisting crystalline phases in the quasi-ternary system (Ab + Or)−An−quartz at P_{H_2O} = 0.2 GPa (after Johannes, W., 1989, *Contrib. Mineral. Petrol.*, **103**, 270−6).

Under anhydrous conditions anorthite melts congruently to 0.9 GPa at which a maximum temperature of 1570ºC is reached, and anorthite begins to melt incongruently to corundum plus liquid. With increasing pressure the melting curve adopts a negative slope, falling to 1450ºC at 2.9 GPa (Fig. 206). Above 0.9 GPa, corundum appears in anorthite below the temperature at which melting begins. Thus at about 0.9 GPa corundum is formed by two distinct processes, incongruent melting and exsolution in the solid state accompanied by the formation of non-stoichiometric anorthite.

As corundum occurs both below and above the $CaAl_2Si_2O_8$ melting curve, some of the reaction anorthite (Al-deficient) + corundum takes place at temperatures below the principal breakdown reaction:

$$\underset{\text{anorthite}}{3\,CaAl_2Si_2O_8} \rightarrow \underset{\text{grossular}}{Ca_3Al_2Si_3O_{12}} + \underset{\text{kyanite}}{2\,Al_2SiO_5} + SiO_2$$

for which equation the reaction curve is:

$$P(\text{GPa}) = -0.21 + 0.00232T(^{\circ}\text{C})$$

and its slope 2.32 MPa/ºC.

In the system anorthite + water, anorthite breaks down in the $P-T$ range 0.7−1.0 GPa, 550−725ºC according to the reaction:

$$\underset{\text{anorthite}}{4\,CaAl_2Si_2O_8} + H_2O \rightarrow \underset{\text{zoisite}}{2\,Ca_2Al_3Si_3O_{12}(OH)} + \underset{\text{kyanite}}{Al_2SiO_5} + \underset{\text{quartz}}{SiO_2}$$

The reaction [described by P(GPa) = −0.4590 + 0.00204T(ºC)] is terminated at an invariant point at 725ºC, 1.02 GPa, which marks the beginning of partial melting of anorthite and the development of a zoisite + kyanite + liquid + vapour field (Fig. 207).

A single boundary curve separates the plagioclase and diopside fields in the ternary system $CaMgSi_2O_6$–$CaAl_2Si_2O_8$–$NaAlSi_3O_8$ (the join An−Di is not strictly binary, due to the presence of small amounts of aluminium in the pyroxene phase). Compared with the An−Ab system, crystallization of plagioclase of a given composition occurs at an appreciably lower temperature (~250ºC) from a diopside-containing melt.

The reaction:

$$\underset{\text{jadeite}}{NaAlSi_2O_6} + \underset{\text{quartz}}{SiO_2} \rightarrow \underset{\text{high-albite}}{NaAlSi_3O_8}$$

has been studied in the range 600−1200°C, 1.6−3.3 GPa. The $P-T$ line, dP/dT= 2.65 MPa/ºC, can be described by the equation:

$$P(\text{GPa}) = 0.035 + 0.00265T(^{\circ}\text{C}) \pm 0.05\ \text{GPa}$$

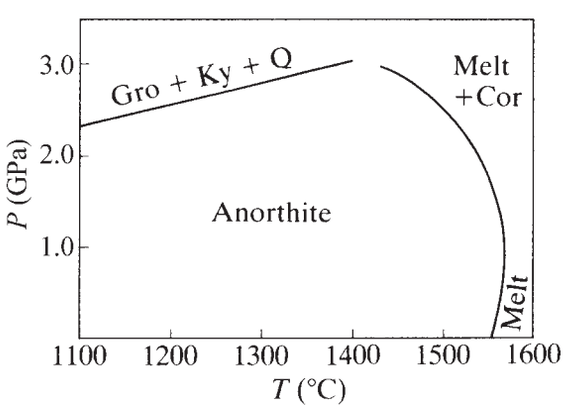


Fig. 206. The melting curve of anorthite and the $P-T$ curve for the anorthite breakdown reaction: $3\,CaAl_2Si_2O_8 \rightarrow Ca_3Al_2Si_3O_{12} + 2\,Al_2SiO_5 + SiO_2$ (after Goldsmith, J.R., 1980, *Amer. Min.*, **65**, 272−84). Gro: grossular; Ky: kyanite; Q: quartz; Cor: corundum.

Downloaded from https://pubs.geoscienceworld.org/books/chapter-pdf/3761680/9780903056434_ch61.pdf
by guest

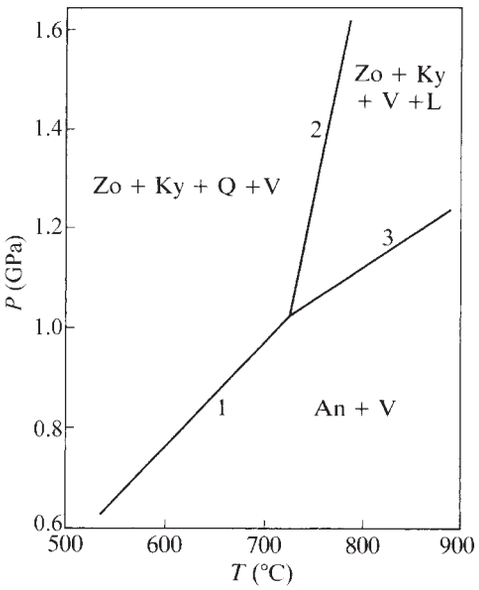


Fig. 207. $P-T$ relations in the system anorthite ($CaAl_2Si_2O_8$)–H_2O. Curve 1, reaction 4 An + V ⇌ 2 Zo + Ky + Q + V; curve 2, reaction Zo + Ky + Q + V ⇌ L; curve 3, reaction An + V ⇌ L. Compositions of the liquid and vapour in the field bounded by curves 2 and 3 vary with P and T, as do the relative ratios of L and V to Ky and to Zo (assuming water-saturated conditions) (after Goldsmith, J.R., 1981, *Amer. Min.*, **66**, 1183–8).

Alteration

The plagioclase feldspars are susceptible to the action of hydrothermal solutions, the more sodic varieties being more stable than those richer in the anorthite component. The alteration products include montmorillonite, scapolite, prehnite and various zeolites.

The alteration of plagioclase has been investigated experimentally. Crystals of albite suspended in an autoclave with pure water at 200–350ºC, 30 MPa, break down to particles having colloidal dimensions which constitute an alumina-silica gel, and which subsequently form crystals of a zeolite (probably analcime). Hydrolysis equilibria involving albite and its decomposition products in an aqueous chloride environment at elevated temperatures and pressures show that at high temperatures (>400ºC, 0.1 GPa total pressure) albite is altered to paragonite plus quartz, which may later be converted to pyrophyllite; at lower temperatures the corresponding reactions are the decomposition of albite to montmorillonite and the alteration of montmorillonite to kaolinite.

Synthetic anorthite and natural Ca-rich plagioclases are albitized on heating under pressure with Na_2CO_3 and $NaHCO_3$. The formation of albite mirrors the natural reaction that occurs during spilitization (p. 306).

Like the alkali feldspars, plagioclase feldspars are commonly turbid because of micrometre-scale pores, which may be filled with fluid or contain other minerals. Some plagioclases appear cloudy due to the presence of numerous minute dark particles distributed throughout the crystals. This clouding is distinct from the turbidity related to alteration caused by the development of kaolinite or sericite and is due to the presence of iron-bearing minerals, typically magnetite, ilmenite or hematite, but also spinel, garnet, biotite, rutile or hornblende. Such clouding is attributed to the exsolution of iron oxides, due to thermal metamorphism. It has also been suggested that the iron-bearing material has been introduced into the crystal after its formation.

Optical and physical properties

The refractive indices increase steadily with An content (Fig. 208), and this relationship has been used to determine composition. Measurement of α gives a reliable estimate of the composition of a plagioclase regardless of its structural state.

Approximate refractive indices of the more sodic plagioclases may be estimated in thin section by observing the Becke line on boundaries with quartz (ω 1.544, ε 1.553), or with the mounting medium if its refractive index is reliably known. In this way it may be possible to place a plagioclase more sodic than about An_{48} into one of five compositional subdivisions.

Another optical method for plagioclase determination involves measuring the single refractive index of a quenched glass made from the specimen. The result is very little affected by the presence of appreciable K-feldspar component, and is clearly independent of the specimen's original structural state.

Optical methods have largely given way to direct analysis by electron microprobe or analytical SEM when available, but the perfect {001} and good {010} cleavages allow the extinction angles and, to a lesser extent, the optic axial plane and angle 2V to be used to determine composition (see below).

The optic axial angle of plagioclase of the plutonic low-temperature series is always large (>75º); the optic sign is (+) for albite, changes to (–) in the more calcic oligoclase range, becomes (+) again for most andesines and reverts to (–) in bytownite and anorthite. High-temperature plagioclases have different optical properties; thus volcanic albites have $2V_\alpha$ ~ 50º. The

Downloaded from https://pubs.geoscienceworld.org/books/chapter-pdf/3761680/9780903056434_ch61.pdf
by guest

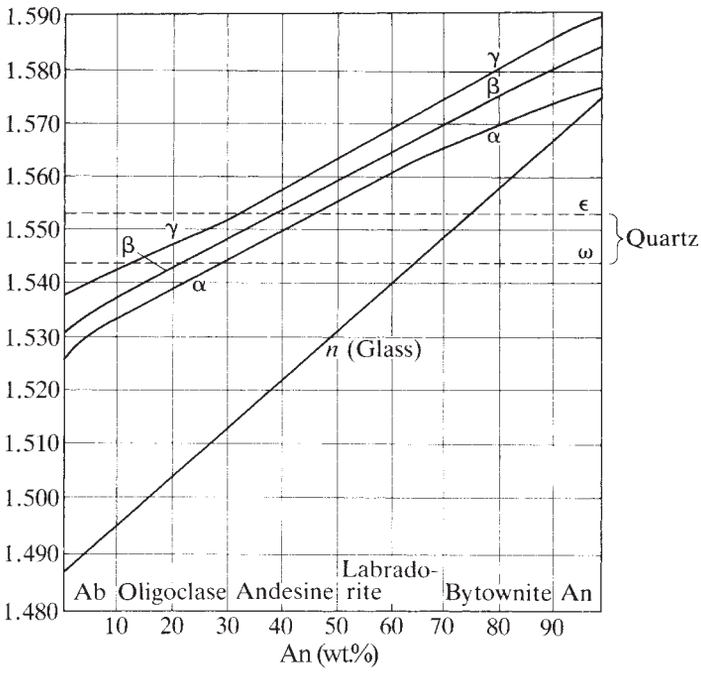


Fig. 208. Refractive indices of the albite-anorthite feldspars. The variation refers to highly ordered plagioclases. Curves for highly disordered plagioclases show small differences at the albite- and anorthite-rich ends of the series. The refractive indices of glasses of plagioclase compositions are also shown (Deer *et al*., 1992, *An Introduction to the Rock-Forming Minerals*, Longman, UK).

variation of the optic axial angles for both series together with values for specimens heated at near-solidus temperatures is shown in Fig. 209.

The optic axial plane varies considerably with composition. In low albite it is approximately perpendicular to *z* but in the more calcic plagioclases it tilts over until in anorthite it is nearly parallel to *z* (Fig. 210). The effect of the changing orientation results in systematic variations in extinction angles.

Universal stages and spindle stages have been used to facilitate the determination of optical properties of crystals in desired precise orientations, and on selected zones of faces.

In the majority of twinned plagioclase crystals the composition plane is parallel to the crystal length. In plutonic and hypabyssal rocks the plagioclases are elongated parallel to [001] and flattened on (010) with multiple twinning predominantly on the Albite law (Fig. 211) often in combination with Carlsbad twins. Pericline twins, if present, are usually subordinate to Albite twins. Intersections between Albite and Pericline twins are sharp and angular, in contrast with the spindle shaped tartan-twinning of microcline. The composition plane of Pericline twins in low albite is shown on Fig. 178, p. 267. In low plagioclase it rotates about the *y* axis to a position 18º below the *x* axis in anorthite. In high albite the Pericline composition plane is almost parallel to *x*. In many volcanic rocks plagioclase occurs as microlites, is not twinned and is elongated parallel to [100]. In metamorphic rocks twinning is usually simple and commonly is not present at all; combined Albite-Carlsbad twinning does not occur.

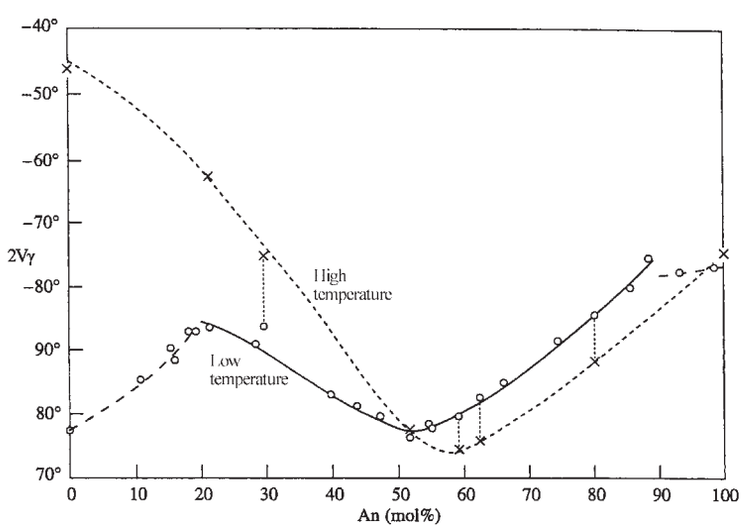


Fig. 209. Optic axial angle as a function of plagioclase composition (after Smith, J.R., 1958, *Amer. Min*., **43**, 1179−94).

Downloaded from https://pubs.geoscienceworld.org/books/chapter-pdf/3761680/9780903056434_ch61.pdf
by guest

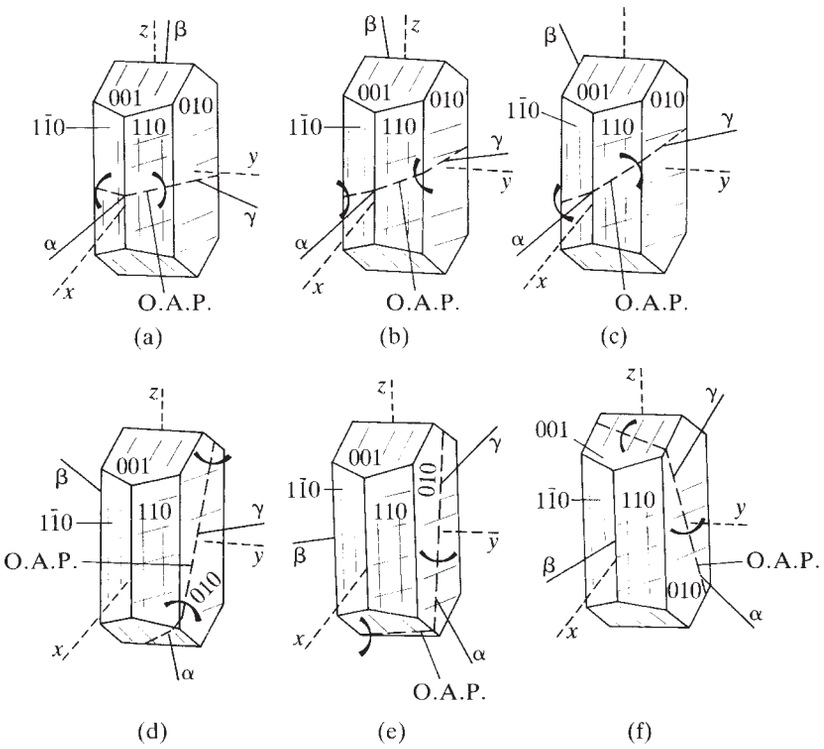


Fig. 210. Optical orientation of the low plagioclases: (a) albite; (b) oligoclase; (c) andesine; (d) labradorite; (e) bytownite; (f) anorthite (Deer *et al*., 1992, *An Introduction to the Rock-Forming Minerals*, Longman, UK).

Extinction angles

Measurements of the extinction angle of Albite twins can be used to obtain the composition of plagioclase feldspars in thin section. These methods are used routinely by petrologists because of the abundance of plagioclase and because its composition is a valuable guide to the identity of igneous and metamorphic rocks. With care the methods can also be used on crystals with complex zoning. There are two main methods:

Maximum symmetrical extinction angle, sometimes called the Michel-Lévy method. The method is based on measurements of the maximum extinction angle measured from the fast-ray direction to the composition plane, (010), of Albite twins. The following steps must be followed rigorously:

(1) Between crossed polarizers find a plagioclase in which the Albite twins are sharply defined, with no blurring along the composition plane. The twin boundaries should remain sharp as the focus of the microscope is changed slightly. This is a section normal to (010).
(2) Rotate the crystal so that the twin lamellae are N–S. They must all be the same shade of grey; ideally the twins will be visible only as thin lines marking the composition planes.
(3) Rotate microscope stage clockwise, measuring the angle to extinction in one twin (Fig. 212, right).
(4) Repeat from N–S, turning stage anti-clockwise. The two angles should be equal or nearly so, measuring the angle to extinction for the other set of twins (Fig. 212, left).

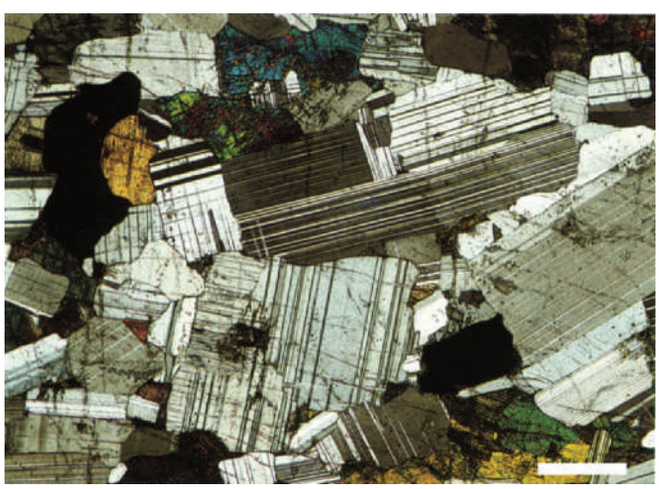


Fig. 211. Gabbro from the Skaergaard intrusion, East Greenland (crossed polars, scale bar 0.7 mm), showing stout, prismatic, subhedral plagioclase crystals with multiple Albite twinning, less obvious Pericline twins, and examples of combined Carlsbad-Albite twinning (W.S. MacKenzie collection, courtesy of Pearson Education).

Downloaded from https://pubs.geoscienceworld.org/books/chapter-pdf/3761680/9780903056434_ch61.pdf
by guest

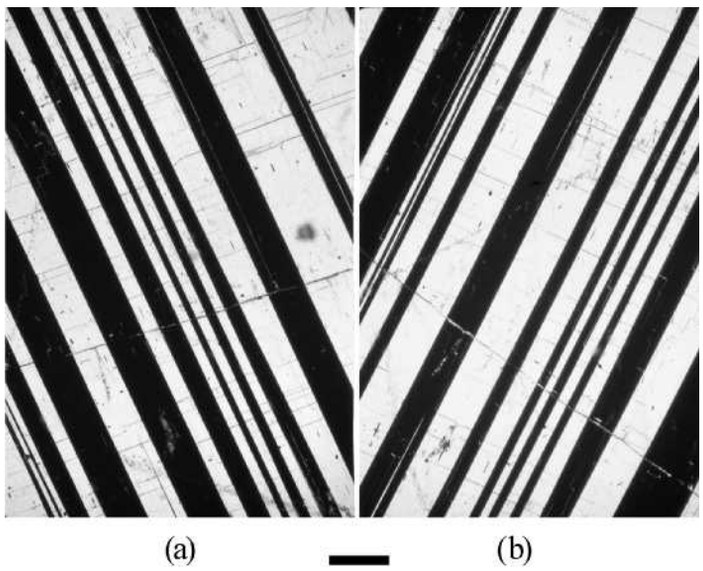


Fig. 212. Repeated lamellar Albite twinning in a section of plagioclase cut perpendicular to *x* showing the extinction positions for alternate lamellae when the microscope stage is rotated in opposite directions. The twin lamellae are on (010) and the cleavage visible is (001) (xpl, scale bar 1 mm). The extinction angle is about 25º. If this is the maximum extinction angle found, it corresponds with ~An_{45} (see Fig. 213a) (W.S. MacKenzie collection, courtesy of Pearson Education).

(5) If the two extinction angles differ by <5º, average them and record the result.

(6) Remembering that when an anisotropic crystal is at extinction the fast and slow vibration directions are parallel to the microscope cross-wires, it is now necessary to establish that the fast ray is closest to the twin composition plane. Return one set of twins to the extinction position, and then turn the same set of twins to the 45º position. Use a sensitive tint plate to establish whether the twins are length-fast or length-slow. If they are length-fast the extinction angle is <45º. If they are length-slow stages 3 to 5 must be repeated, but record the angle when the second set of twins goes to extinction. It is usually necessary to carry out stage 6 only once during a determination unless extinction angles are near 45º. An extinction angle of >45 applies only to plagioclases >An_{80}, and is relatively uncommon.

(7) Repeat the process using as many crystals as possible in the thin section. The *largest mean extinction angle* recorded at stage 5 is then used to obtain the composition from Fig. 213a. For Ab-rich compositions up to ~An_{40} there are two solutions, but these may usually be resolved by comparing the refractive index to quartz, which is commonly present in rocks with plagioclase of this composition.

Note that the method assumes that all plagioclase crystals in the rock are of the same composition, but note also that once a crystal with maximum extinction has been located it can be used to estimate the extent of any zoning present.

Combined Albite-Carlsbad method. This method has the advantage that a determination of composition can be made on a single crystal, but the disadvantage that in coarsely crystalline rocks it is often not possible to find

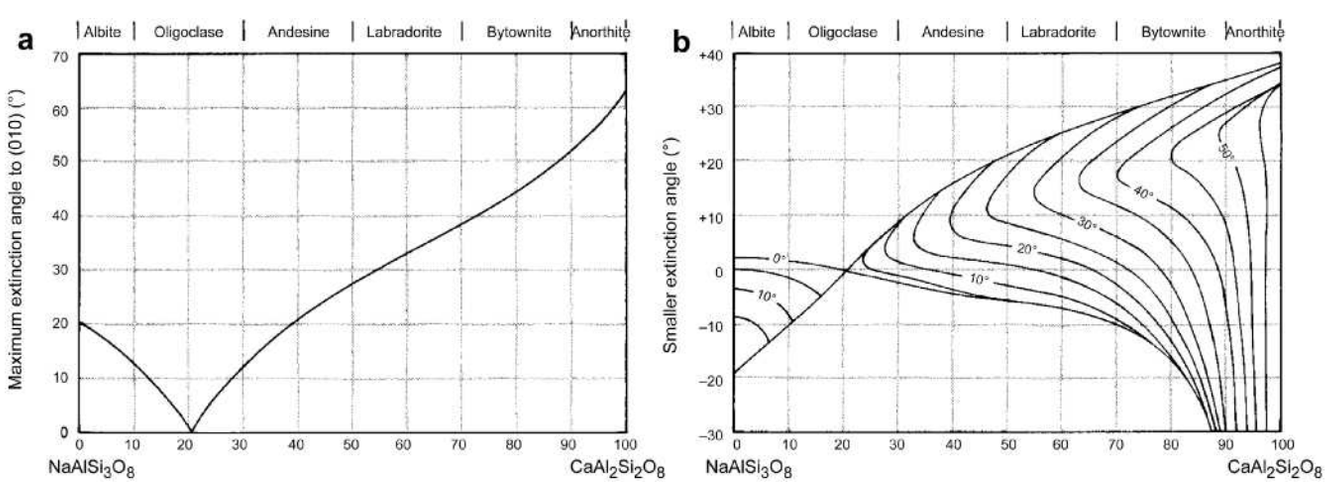


Fig. 213. (a) Variation with composition of the maximum extinction angles of Albite twins in sections cut at right angles to (010), the composition plane of Albite twins. (b) Extinction angles of Albite twins in the two individuals of a Carlsbad twin (after Heinrich, E.W., 1965, *Microscopic Identification of Minerals*. McGraw-Hill, New York).

Downloaded from https://pubs.geoscienceworld.org/books/chapter-pdf/3761680/9780903056434_ch61.pdf
by guest

a suitably orientated grain in a thin section. The steps in a determination are:

(1) Find a plagioclase section normal to (010) as described in stage 1, above. It should be twinned on both the Carlsbad and Albite laws. Examples can be seen slightly above the centre, and far right in Fig. 211.
(2) Rotate the crystal so that the twin composition planes are N–S. Within each Carlsbad twin the Albite twin lamellae should show the same interference colour, but the interference colour of the Carlsbad twins can be different.
(3) Repeat stages 3–6, above, for each of the Carlsbad twins. This will give two mean extinction angles.
(4) Find the smaller extinction angle on the ordinate of Fig. 213b and locate its intersection with the curved contour line appropriate for the larger extinction angle. The composition equivalent to this point can be read from the abscissa. As in the first method ambiguities can be resolved using refractive index.

Iridescence and colour

The peristerite, Bøggild and Huttenlocher intergrowths all exhibit iridescence caused by coherent scattering (Bragg diffraction) of light by exsolution lamellae. The name 'peristerite' is an allusion to the play of colours on a pigeon's neck (greek, *peristera*, a pigeon). Best known is the intense iridescence of some Bøggild intergrowths, which is commonly described as 'labradorescence'. This is caused by lamellae with periodicities in the range 80–250 nm. The periodicity increases systematically with An content, and the colour of the iridescence obeys Bragg's law and changes from blue to red. Plagioclase can also exhibit the golden schiller called 'aventurine', which is usually caused by orientated platelets of hematite but also possibly by flakes of biotite. Pink schiller caused by plates of metallic copper has also been described. As noted in the section on alkali feldspars, the term schiller should be reserved for light scattered by visible inclusions of other minerals, whereas iridescence should be used for scattering by periodic microstructures in the mineral itself.

Plagioclase is usually colourless if it is entirely fresh but typically has a white translucency caused by micrometre-scale micropores. These tend to be less abundant but larger than those that cause the translucency of alkali feldspars (e.g. Fig. 193, p. 280). Like alkali feldspar, plagioclase is often a pink colour, caused by finely divided hematite.

Other colours are also generally due to inclusions: for example, anorthite crystals in xenoliths may be pink or blue from enclosed sillimanite or corundum (sapphire), while the bytownite of a contaminated eucrite from Carlingford, Ireland, is so full of iron ore that it is almost black in hand specimen.

Distinguishing features

In thin section the plagioclase feldspars may be distinguished by their low relief, lack of colour, low birefringence, and the biaxial character of their interference figures. Albite twinning on (010) giving rise to lamellae showing different interference colours is characteristic: in its absence, or in a section approaching parallelism to (010), the presence of a good cleavage may distinguish plagioclase from quartz and the refractive indices may distinguish the more calcic varieties from the potassium feldspars. In thin section, if the presence of untwinned plagioclase is suspected, it may be advantageous to stain the potassium feldspars, using sodium colbaltinitrite solution (p. 282). Although cordierite sometimes shows twinning and occurs in transparent grains with similar optical characters, its tendency to form yellowish alteration products may distinguish it. Untwinned plagioclase can also be distinguished from quartz by the latter's uniaxial character and lack of turbidity.

Optical methods for determining the composition of plagioclase are given in the preceding section, and X-ray diffraction methods are mentioned in the section on structure. In XRD studies of rocks and soils the presence of even small amounts of feldspar can be established by their strong reflections in the range 27–28º2θ (Cu-$K\alpha$ radiation).

Paragenesis

Igneous rocks

Plagioclase is the most abundant mineral in the great majority of basic and intermediate lavas, in which it occurs both as phenocrysts and as a groundmass constituent (Fig. 214). In almost all of these rocks the plagioclase shows some degree of zoning. In many lavas and particularly those of intermediate composition the zoning of the plagioclase extends over a wide range and may be oscillatory in character (Fig. 215). In basalts the plagioclase phenocrysts commonly have a wide homogeneous core of labradorite–bytownite composition, which is surrounded by narrower zones of more sodium-rich plagioclase. The broad cores of uniform composition indicate slow crystallization and the growth of these crystals occurred before extrusion and final consolidation of the magma.

Albite is the most characteristic mineral of spilites. In some of these submarine lavas relict labradorite or andesine is enclosed within the albite, a relationship considered to indicate that the composition of the plagioclase is the result of a replacement process by which normal basalts are albitized to spilites.

Under plutonic conditions the first plagioclase to crystallize from most basic magmas, like that of basalts, is bytownite. In layered basic intrusions plagioclase can occur in feldspar-rich bands formed by the accumulation

Downloaded from https://pubs.geoscienceworld.org/books/chapter-pdf/3761680/9780903056434_ch61.pdf
by guest

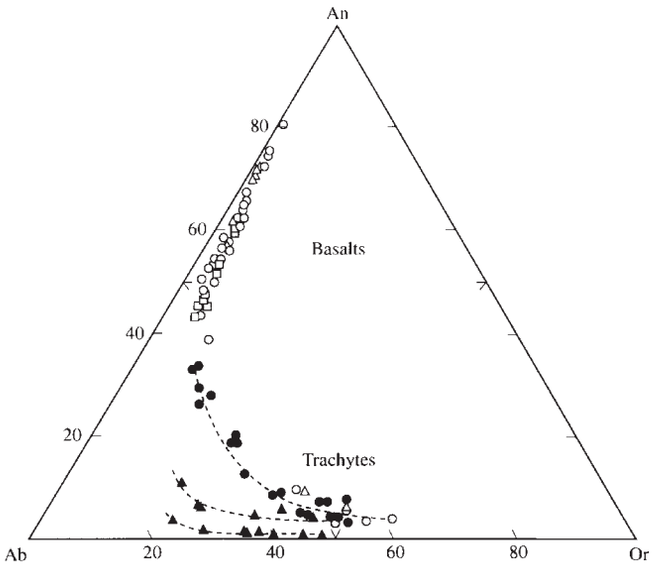


Fig. 214. Feldspar compositional data for lavas from Gough Island: ○: aphyric and finely porphyritic basalts; ●: trachytes; △: pyroxene-olivine phyric basalts; ▲: aegirine-augite trachytes (after Le Roex, A.P., 1985, *J. Petrol.*, **26**, 149–86). Other plagioclase zoning paths are shown in Fig. 197, p. 286.

of the primary precipitate plagioclase; the crystals of these bands are usually idiomorphic and free from conspicuous zoning. In contrast, primary precipitate plagioclase may be entirely absent from the ferromagnesian-rich bands in which the feldspar occurs as a product of the crystallization of intercumulus liquids; such plagioclase is poikilitic in texture and may be zoned. In the differentiated basic rocks of layered intrusions the compositional range of the plagioclase is normally restricted to between An_{85} and An_{30}.

Plagioclase is the only essential constituent of anorthosite. The plagioclase may be bytownite, labradorite or andesine, e.g. the anorthosites of the Adirondacks consist essentially of plagioclase in the range An_{38} to An_{50}. In the Nain, Labrador, anorthosite, the plagioclase is also andesine–labradorite; it shows no significant zoning and makes up more than 90 vol.% of the rock. Leuconorites in the same region consist of plagioclase and orthopyroxene approximating closely to the 75:25 cotectic composition in the system plagioclase–olivine–SiO_2.

Plagioclase feldspars are the main constituents of dolerites and many other hypabyssal rocks. In the basic alkaline rocks such as olivine-theralite, crinanite and essexite, in which plagioclase is associated with olivine, pyroxene and nepheline, the feldspars are usually strongly zoned (Fig. 215).

Metamorphic rocks

The composition of plagioclase in metamorphic rocks is generally related to the grade of the host rock. Thus albite is the stable plagioclase in the chlorite and biotite zones of regional metamorphism, occurring in such rocks as chlorite-biotite-epidote-albite amphibolites and chlorite-albite schists, and the An component is not present in significant quantities until the garnet zone. Plagioclase between An_7 and An_{15} in composition is

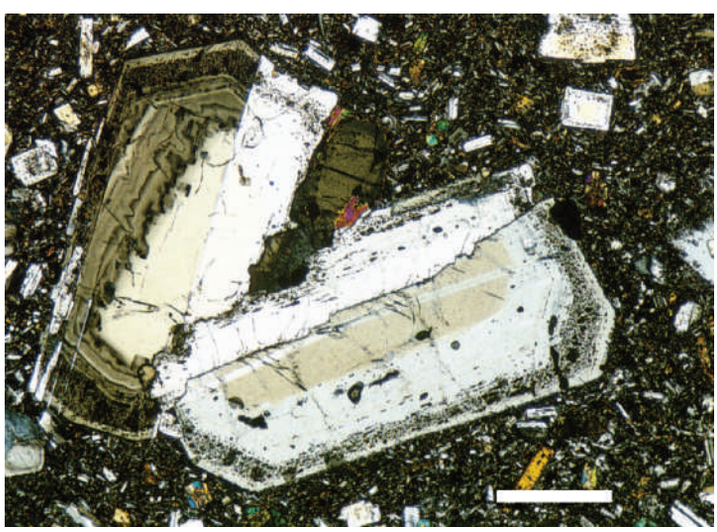


Fig. 215. Porphyritic andesite from Hakone volcano, Japan (crossed polars, scale bar 1 mm), with plagioclase showing discontinuous and oscillatory zoning. The zoning is emphasized by a band of melt inclusions near the margins of both crystals (W.S. MacKenzie collection, courtesy of Pearson Education).

Downloaded from https://pubs.geoscienceworld.org/books/chapter-pdf/3761680/9780903056434_ch61.pdf
by guest

absent in low- to medium-grade schists; this compositional break corresponds with the change in grade between the greenschist and almandine-amphibolite facies. The sharp break can be correlated with the peristerite solvus (Fig. 200, p. 294). The width of the gap depends on metamorphic temperature and pressure, and plagioclases on both sides of the gap exhibit peristeritic exsolution textures. A similar distribution has been found in detrital plagioclase grains in North Sea petroleum reservoir rocks, suggesting that their source was low-grade metamorphic rocks.

Plagioclase composition is also related both to the composition of the metamorphic host rock and to the three miscibility gaps (Fig. 200). For example, in calc-silicate rocks from amphibolite-facies gneisses in the Central Alps, which contain plagioclases with a very large range of compositions, electron-probe analyses of 1883 plagioclase grains from 147 rocks show distinct minima (Fig. 216) in frequency, corresponding with the peristerite, Bøggild and Huttenlocher gaps. In low-grade amphibolite schists of ophiolitic origin near the Bergell granite in the Central Alps, a combination of electron probe and TEM work has shown that intermediate plagioclase (mostly $An_{30}-An_{40}$) has decomposed to mixtures of albite (An <5 mol%) and anorthite (An >95 mol%). These and similar studies clearly show the importance of the non-ideality of low plagioclase solid solutions in low-grade metamorphism, and are consistent with the suggestion that the only plagioclases stable at low temperatures are close to end-member albite and anorthite.

Where rocks of the amphibolite facies are subjected to a further increase in confining pressure and to a moderate increase in temperature, conditions of the granulite facies are reached; a characteristic reaction of the boundary conditions may be represented by the reaction:

$$\underset{\text{amphibole}}{Ca_2Mg_3Al_4Si_6O_{22}(OH)_2} + SiO_2 \rightarrow 2\,\underset{\text{anorthite}}{CaAl_2Si_2O_8} + 3\,\underset{\text{orthopyroxene}}{MgSiO_3} + H_2O$$

The plagioclase feldspars of the intermediate and acid rocks of the granulite facies commonly are sodic andesine; thus in the rocks of the charnockite series the majority of the plagioclase is between An_{30} and An_{35} in composition, although labradorite is present in some of the more basic charnockitic rocks. Rocks of the amphibolite facies affected by increasing temperature and decreasing pressure are converted to the characteristic biotite-pyroxene-plagioclase assemblage of the pyroxene hornfels facies in which part of the plagioclase is derived from the breakdown of hornblende as expressed by the equation:

$$\underset{\text{amphibole}}{NaCa_2Mg_3Fe^{2+}Al_3Si_6O_{22}(OH)_2} + 4\ SiO_2 \rightarrow \underset{\text{plagioclase}}{NaAlSi_3O_8 + CaAl_2Si_2O_8} + \underset{\text{diopside}}{CaMgSi_2O_6} + \underset{\text{orthopyroxene}}{Mg_2Fe^{2+}Si_3O_9} + H_2O$$

Plagioclase feldspar is not stable in the $P-T$ environment of the eclogite facies; under these conditions the albite and anorthite components of the plagioclase enter respectively into the composition of omphacitic pyroxene and garnet as shown below:

$$\underset{\text{albite}}{NaAlSi_3O_8} + \underset{\text{olivine}}{(Mg,Fe)_2SiO_4} \rightarrow \underset{\text{omphacite}}{NaAlSi_2O_6} + 2\,\underset{\text{omphacite}}{(Mg,Fe)SiO_3}$$

$$\underset{\text{anorthite}}{CaAl_2Si_2O_8} + \underset{\text{olivine}}{(Mg,Fe)_2SiO_4} \rightarrow \underset{\text{garnet}}{Ca(Mg,Fe)_2Al_2Si_3O_{12}}$$

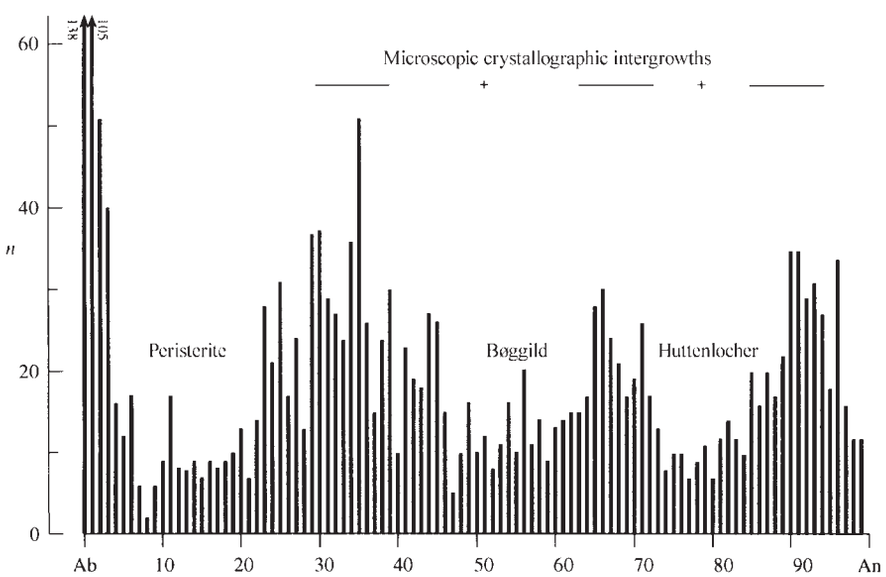


Fig. 216. Frequency distribution of plagioclase compositions from1883 microprobe results for 147 metamorphic calc-silicate rocks in the Central Alps (after Wenk *et al*., 1991).

Downloaded from https://pubs.geoscienceworld.org/books/chapter-pdf/3761680/9780903056434_ch61.pdf
by guest

Plagioclase of intermediate composition can occur in symplectic vermicular intergrowths with hornblende in kelyphitic rims around eclogitic garnet.

Sedimentary rocks

Albite is a common authigenic mineral and forms contemporaneously with sedimentation as well as by replacement of detrital material. In accordance with the solvus relationships of the alkali feldspars at low temperature, authigenic albite rarely contains more than 3 mol% potassium feldspar (Fig. 187, p. 275). The calcium content is generally even lower and the usual upper limit is about 0.3%, equivalent to 1 mol% $CaAl_2Si_2O_8$. In some sediments the replacement origin of authigenic albite is demonstrated by the development of idiomorphic crystals in cavities, and by the replacement of fossils. In other sediments the interlocking fabric indicates that the sodium feldspar may be of indigenous origin, formed by the partial solution of detrital grains under pressure at points of contact and precipitated at places of lower pressure. Much authigenic albite shows simple growth twins, and multiple twin lamellae are absent.

Authigenic albite has low concentrations of minor and trace elements and is commonly identified by absence of cathodoluminescence.

Meteorites and lunar rocks

Plagioclase is abundant in many stony meteorites. Compositionally, these plagioclases occur in two main clusters: around $An_{90\pm5}$ and $An_{15\pm10}$. Maskylenite, the name given to high-density glass of plagioclase composition with a high refractive index, is found frequently in meteorites.

The great majority of lunar feldspars are plagioclases of composition An_{90-97}, which form anorthosites which probably make up more than 80% of the Moon's exposed surface (the remainder being mare basalts).

Further reading

Bruni, P. (1976) Plagioclase determination through measurement of the extinction angle in sections normal to (010) and (001). *Schweizerische Mineralogische und Petrographische Mitteilungen*, **56**, 39–54.

Carpenter, M.A. (1994) Subsolidus phase relations of the plagioclase feldspar solid solution. Pp. 221–269 in *Feldspars and their Reactions* (I. Parsons, editor). Dordrecht/Boston/London (Kluwer Academic Publishers).

Deer, W.A., Howie, R.A. and Zussman, J. (2001) *Rock-Forming Minerals,* **4A**, *Framework Silicates: Feldspars.* London (The Geological Society).

Ribbe, P.H. (Editor) (1983) *Feldspar Mineralogy*. Reviews in Mineralogy, **2**, Mineralogical Society of America, Washington, D.C., 362 pp.

Smith, J.V. and Brown, W.L. (1988) *Feldspar Minerals, I, Crystal Structures, Physical, Chemical and Microtextural Properties.* Springer-Verlag, 828 pp.

Su, S.-C., Ribbe, P.H. and Goldsmith, J.R. (1986) Optical properties of single crystals in the order-disorder series low albite-high albite. *American Mineralogist*, **71**, 1384–1392.

Wayte, G.J., Worden, R.H., Rubie, D.C. and Droop, G.T.R. (1989) A TEM study of disequilibrium plagioclase breakdown at high pressure: the role of infiltrating fluid. *Contributions to Mineralogy and Petrology*, **101**, 426–437.

Wenk, E., Schwander, H. and Wenk, H.-R. (1991) Microprobe analyses of plagioclase from metamorphic carbonate rocks of the Central Alps. *European Journal of Mineralogy*, **3**, 181–191.

Wenk, H.-R. (1979) An albite–anorthite assemblage in low-grade amphibolite facies rocks. *American Mineralogist*, **64**, 1294–1299.

Downloaded from https://pubs.geoscienceworld.org/books/chapter-pdf/3761680/9780903056434_ch61.pdf
by guest

Silica Minerals

Quartz
Tridymite, Cristobalite

SiO_2

	α-Quartz Trigonal (+)	α-Tridymite Orthorhombic (+)	α-Cristobalite Tetragonal (–)
	ω 1.544 ε 1.553	α 1.469–1.479 β 1.470–1.480 γ 1.473–1.483	ε 1.484 ω 1.487
	δ 0.009	δ 0.002–0.004	δ 0.003
$2V_\gamma$		66–90°	
Orientation		α = *y*; O.A.P. (100)	
D (g/cm^3)	2.65	2.27	2.33
H	7	7	6–7
Cleavage	None	Poor prismatic cleavage	None
Twinning	(1) Twin axis *z* (2) Twin plane {11$\bar{2}$2} (3) Twin plane {11$\bar{2}$0}	Common on {110}	Spinel-type twins on {111}
Colour	Colourless, white, yellow, pink, black, purple, smoky; colourless in thin section	Colourless or white; colourless in thin section	Colourless, white or yellowish; colourless in thin section
Special features	Insoluble in acids except HF; soluble in molten Na_2CO_3 Twinning in quartz rarely seen in thin section.		

	Quartz		Tridymite		Cristobalite	
Unit cell	α-Trigonal	β-Hexagonal	α-Orthorhombic	β-Hexagonal	α-Tetragonal	β-Cubic
a (Å)	4.912	5.00	8.60	5.05	4.97	7.13
b (Å)	–	–	~5.03	–	–	–
c (Å)	5.404	5.46	~8.22	8.26	6.93	–
Z	3	3	8	4	4	8
Space group	$P3_121$ or $P3_221$	$P6_222$ or $P6_422$	*Cc*	$P6_3/mmc$	$P4_12_12$ or $P4_32_12$	$Fd3m$

Quartz is one of the most abundant minerals and occurs as an essential constituent of many igneous, sedimentary and metamorphic rocks. It is also found as an accessory mineral, and as a secondary mineral in veins and metasomatic deposits. 'Quartz' appears to have replaced the name 'crystal' or 'rock crystal' for this mineral towards the end of the 18th Century.

Quartz is the most common natural polymorph of SiO_2. The more important SiO_2 polymorphs and their ranges of stability are:

α-Quartz: stable at ambient temperatures and up to 573ºC.

β-Quartz: stable from 573 to 870ºC. Metastable above 870ºC.

α-Tridymite: metastable from ambient temperatures up to 117ºC.

β-Tridymite: metastable above 117ºC and is the most stable polymorph from 870 to 1470ºC. Metastable above 1470ºC. Melts at 1670ºC.

α-Cristobalite: metastable from ambient temperatures up to 200–275ºC.

β-Cristobalite: metastable above 200–275ºC and is the most stable polymorph from 1470ºC to its melting point 1713ºC.

Downloaded from https://pubs.geoscienceworld.org/books/chapter-pdf/3761882/9780903056434_ch62.pdf
by guest

Coesite: a high-pressure phase, produced at 450–800ºC and 3.8 GPa pressure. Found in rocks subjected to the impact of large meteorites and in xenoliths in kimberlites.

Stishovite: a high-density polymorph of silica, with a density of 4.3 g/cm^3, synthesized at 13 GPa and >1200ºC. Occurs in Meteor Crater, Arizona.

Seifertite: a hard and dense polymorph of silica which is stable only at extremely high pressure.

Cryptocrystalline silica (chalcedony): compact varieties containing minute crystals of quartz with submicroscopic pores.

Mogánite is the microcrystalline length-slow fibrous polymorph of silica, it is commonly found intergrown with chalcedonic quartz.

Opal, $SiO_2 \cdot nH_2O$, consists of amorphous silica and crystalline cristobalite and/or tridymite.

In precious opal the colour is an interference phenomenon due to the regular stacking of spherical aggregates (lepispheres).

Silica glass (vitreous silica; lechatelierite) is metastable up to 1000ºC, above which its rate of crystallization increases rapidly. It is an unstable glass at all temperatures below 1713ºC.

It should be noted that the nomenclature used here is of α for a lower temperature phase and β for a higher temperature phase. Four different notations for temperature dependent polymorphic modifications exist and to avoid confusion the lengthier though more precise method of using the prefixes high- and low- is generally preferable.

Structure

The three principal crystalline forms of SiO_2 (quartz, tridymite and cristobalite) have quite distinct crystal structures, each with a well defined field of stability under equilibrium conditions. The transformations from one to another are, however, somewhat sluggish, so that the higher temperature forms, cristobalite and tridymite, are metastable below their inversion temperatures. Each of the three polymorphs also has a low- and high-temperature modification designated α and β, respectively. The six structures are described below, the form with highest symmetry for each pair being dealt with first: cell parameters are listed on p. 311. In each case the structure is built from SiO_4 tetrahedra which are linked by sharing each of their corners with another tetrahedron. In the three-dimensional framework thus formed every silicon has four oxygens and every oxygen has two silicons as nearest neighbours.

Quartz

β-Quartz has hexagonal symmetry and belongs to the enantiomorphous crystal class 622. A projection of the ideal structure on the basal plane (001) is shown in Fig. 217a. The SiO_4 tetrahedra may be regarded as based on a cube of side p with silicon at its centre and oxygens at four of its eight corners (Fig. 217b). When viewed along diad axes these cubes appear as squares (shaded in Fig. 217a); lower edges of tetrahedra are shown by a broken line whereas upper edges are solid. Tetrahedra are grouped to form regular hexagonal and trigonal helices, and their heights (referred to their Si atoms) are expressed as fractions of the c repeat distance. In the ideal structure built from regular tetrahedra the height of the cell = $3p$ and the side $a = p\ (1 + \sqrt{3})$ so that c/a is 1.098. The helices of ...Si–O–Si–O... atoms (Fig. 218) are either all right-handed or all left-handed in each of the enantiomorphous forms of quartz. This can show itself in the crystal morphology of quartz (see Fig. 223, p. 317), and

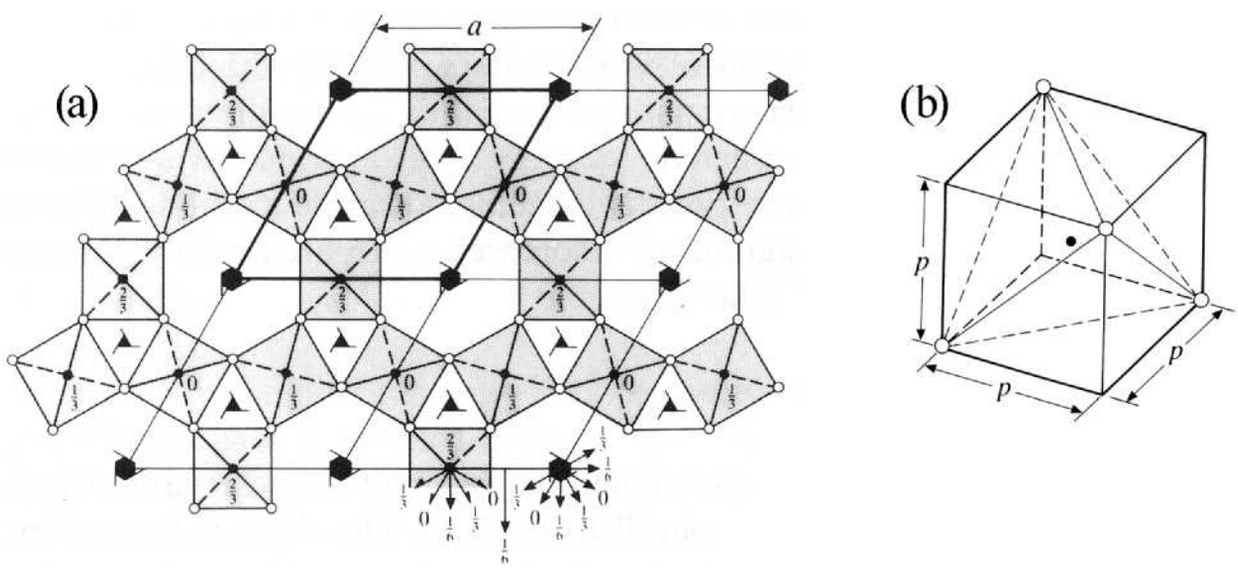


Fig. 217. (a) Structure of β-quartz projected on (0001). (b) Regular tetrahedron inscribed in cube (Deer *et al*., 1992, *An Introduction to the Rock-Forming Minerals*, Longman, UK).

Downloaded from https://pubs.geoscienceworld.org/books/chapter-pdf/3761882/9780903056434_ch62.pdf
by guest

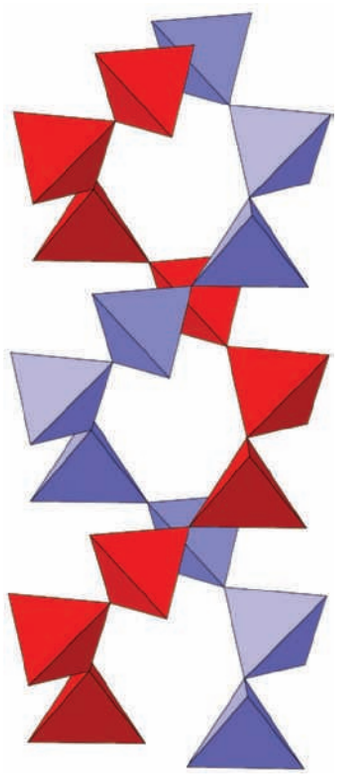


Fig. 218. A double helix of SiO_4 tetrahedra running parallel to the z axis in β-quartz.

also leads to the rotation in one sense or other of the plane of polarization of polarized light travelling parallel to the z axis.

α-Quartz has trigonal symmetry and belongs to the enantiomorphous crystal class 32. Its structure is similar to that of β-quartz but the SiO_4 tetrahedra are less regular and are rotated from their ideal positions; thus the α−β transformation is one of relatively minor atomic movements involving no breakage of Si−O bonds or interchange of atoms. In comparison to tridymite and cristobalite, quartz has a very densely packed arrangement of tetrahedra, and the disposition of its oxygen ions is not related to either hexagonal or cubic close packing.

The cell parameters of α-quartz have been measured for many specimens and by many workers, and for some time the constancy of values obtained for quartz from different localities led to its use as a standard for the calibration of X-ray powder diffraction methods. Accurate methods of measurement, however, have revealed significant differences which are probably associated with solid solution of other ions.

Tridymite

β-Tridymite is hexagonal, and its structure is best regarded as formed by the linkage of sheets parallel to (0001). The sheet is formed by an open network of SiO_4 tetrahedra, sharing oxygens to form six-membered rings. The triangular bases of all tetrahedra lie in the (0001) plane but their apices point alternately in opposite directions. Successive parallel sheets of tetrahedra share apical oxygens and are related by mirror planes passing through them so that the silicons and basal oxygens of a downward-pointing tetrahedron in one sheet lie directly above those of an upward-pointing tetrahedron in the sheet below. A perspective view of the structure is shown in Fig. 219. In the ideal structure the c axis is four times the height of a tetrahedron standing on its base, and the a axis twice the tetrahedral edge, so that c/a is $2\sqrt{(\frac{2}{3})}$ (= 1.633).

α-Tridymite is orthorhombic but its structure involves only slight changes from the high-temperature form. The simplest cell is orthorhombic (pseudo-hexagonal); a and c are similar to those for β-tridymite and $b \sim \sqrt{3}a$. More complex orthorhombic and monoclinic cells have been reported with multiple c parameters. Unlike quartz, tridymite has a very open structure containing channels in which large impurity ions may be trapped, possibly influencing which of these structural modifications is adopted.

Cristobalite

β-Cristobalite is cubic and its structure may be described by analogy with that of β-tridymite as it is based upon similar sheets of six-membered rings of SiO_4 tetrahedra. Tetrahedra in successive sheets are again linked by Si−O−Si bonds which are normal to (0001) but the basal oxygens of a tetrahedron, instead of being directly superimposed, are rotated by 60° with respect to those of the tetrahedron below it. The comparison is illustrated in Fig. 220 showing projections on to the plane of the rings of tetrahedra for cristobalite and slightly offset from a similar direction for tridymite.

Thus as far as the oxygen layers are concerned, although these are not densely packed, their relationship in tridymite and cristobalite is similar to hexagonal (sequence ...ABABAB...) and cubic close packing (...ABCABCABC...), respectively. The two structures are also similar to those of wurtzite and sphalerite, respectively. The repeat distance perpendicular to (0001) in cristobalite is the height of six tetrahedra instead of four as in tridymite. The idealized structure of β-cristobalite has cubic symmetry and can alternatively be described with a cubic cell containing 8 SiO_2. From this point of view the structure may be likened to that of diamond, with silicon atoms occupying the positions of carbons, and an oxygen at the mid-point of each Si−Si join (Fig. 221). Variations in the size of the unit cell of cristobalite may be attributed to impurities in natural specimens, as cristobalite, like tridymite, has a very open structure which can easily accommodate foreign ions. α-Cristobalite is tetragonal but its structure is very closely related to that of β-cristobalite.

The open structures of tridymite and cristobalite may be kept open by thermal agitation at high temperatures,

Downloaded from https://pubs.geoscienceworld.org/books/chapter-pdf/3761882/9780903056434_ch62.pdf
by guest

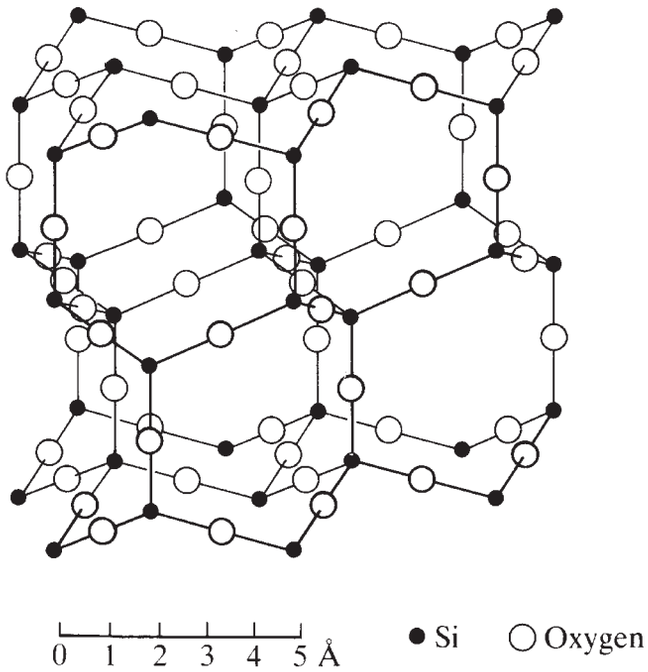


Fig. 219. The structure of β-tridymite (after Bragg, W.L., 1937, *Atomic Structure of Minerals*, Cornell University Press).

and their persistence at lower temperatures probably owes much to the supporting influence of foreign ions. The introduction of foreign cations into structural cavities is probably accompanied by the charge-balancing substitution of Al for Si. The extreme case of regular substitution of half of the Si atoms by Al, and introduction of an equal number of Na atoms, results in the structure of nepheline, $NaAlSiO_4$, which closely resembles that of tridymite with half of its voids filled by Na ions. Similarly, the regular filling of half the voids of cristobalite gives the higher temperature form of $NaAlSiO_4$, carnegieite. There can be no 'quartz' structure for $NaAlSiO_4$ as quartz has no voids for the accommodation of Na ions.

Although transformations from α- to β-forms for each of the three SiO_2 minerals involve only minor atomic movements (displacive transformations), the changes between quartz, tridymite and cristobalite are more disruptive (reconstructive transformations). The change from quartz to a higher temperature polymorph must involve the breaking of Si–O bonds and the movement of both Si and O atoms in several directions. The change from tridymite to cristobalite similarly involves the breaking of bonds and changing the disposition of nearest neighbours, but as both have similar layer units [parallel to (0001) in tridymite and (111) in cristobalite], this can be achieved with more restricted atomic movements.

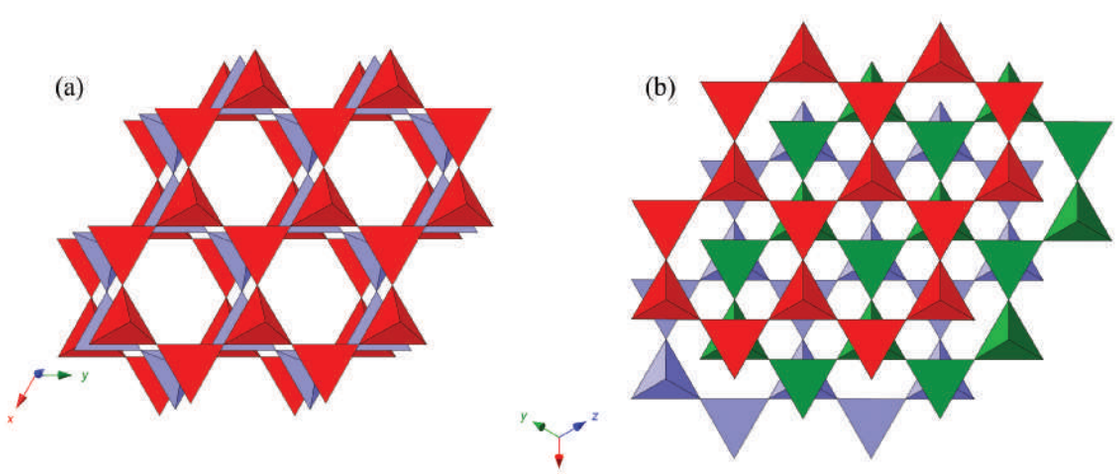


Fig. 220 (a) Idealized perspective view of the structure of high-temperature tridymite. The six-membered rings of Si–O tetrahedra in successive layers (red and blue) are related by (0001) mirror planes and would be superimposed if viewed exactly down *z*, so a slightly oblique view is shown here. (b) Corresponding view of the structure of cristobalite, but from exactly normal to the layers of tetrahedra (body diagonal of the cubic unit cell) and showing the sequence red–green–blue–red (CrystalMaker images).

Downloaded from https://pubs.geoscienceworld.org/books/chapter-pdf/3761882/9780903056434_ch62.pdf
by guest

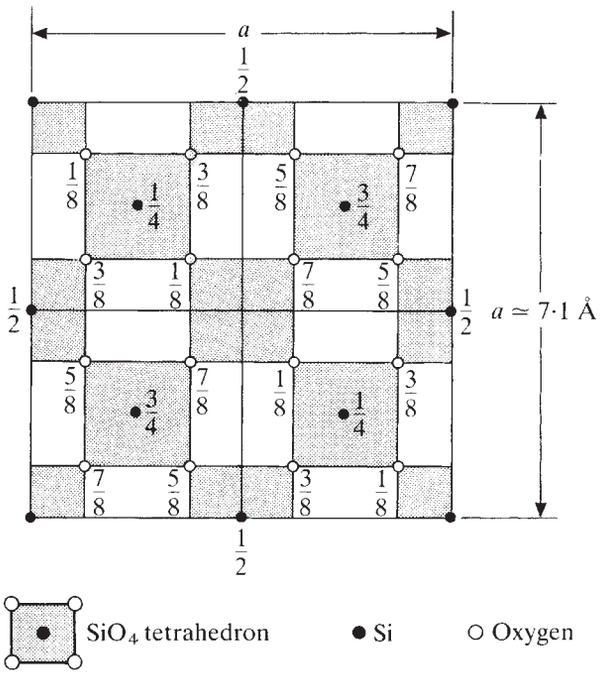


Fig. 221. Idealized structure of β-cristobalite projected on (001) (Deer *et al*., 1992, *An Introduction to the Rock-Forming Minerals*, Longman, UK).

Coesite and stishovite

Coesite is monoclinic and has a feldspar-like structure consisting of two kinds of four-membered tetrahedral rings mutually linked to form a double crankshaft chain similar to that of feldspars. In contrast to other silica minerals, stishovite contains silicon in six-fold coordination. It is tetragonal and has the same structure as rutile (TiO_2), p. 393.

Chemistry

Quartz

The composition of quartz is normally very close to 100% SiO_2. If chemical analyses reveal small amounts of other oxides, these are generally due either to small inclusions of other minerals or to the liquid infillings in cavities within the quartz. For high-grade crystals of visibly pure quartz, however, these may be assumed to be at a minimum: analytical results for such samples are given in Table 38. The substitution of Al^{3+} for Si^{4+} appears to be accompanied by the introduction of the alkali ions Li^+ or Na^+ (see also Müller and Koch-Müller, 2009).

It has been shown that substitution of Ti^{4+} for Si^{4+} in quartz increases systematically with increasing temperature, resulting in the development of the TitaniQ geothermometer (Wark and Watson, 2006). Modern electron microprobe techniques have detection limits for Ti in quartz down to 20 ppm or better, allowing this geothermometer to be routinely applied over the temperature range 600 to 1000ºC with a precision of ±5ºC, corresponding to Ti contents of between ~20 and 530 ppm. The use of secondary ion mass spectrometry may allow this to be extended to temperatures as low as 400ºC, or even lower temperatures in TiO_2 under-saturated systems. However, the effect of pressure on Ti solubility in quartz and consequent implications for the applicability of the TitaniQ geothermometer have yet to be fully explored.

Relatively large crystals of synthetic quartz were first produced in 1900 using a technique based on the greater solubility of quartz in a solution of sodium metasilicate at temperatures above 300ºC than below it. Modern requirements of high-grade quartz for piezoelectric uses has led to an intensive study of its synthetic production, and crystals of up to 300 g can be grown in one month. Experimental work on the effect of pressure and temperature on the rate of formation of quartz from silicic acid shows that quartz does not appear in significant quantities until two other phases, cristobalite and keatite (see p. 317), have formed.

Table 38. Analyses for trace elements (ppm) in silica polymorphs.

	1	2	3	4	5
Al	3200	13	110	7300	300
Ti	1.5	0	20	1200	0
Fe	–	–	–	–	100
Na	980	60	–	3600	200
K	200	<16	230	3500	0
Li	0–200	<0.4	–	0.9	–

1 Mean values for quartz from Benfjord, Iceland (electron probe).
2 Quartz, Herkimer, New York (ion probe).
3 β-quartz phenocryst, Logtung W-Mo deposit, Yukon, Canada.
4 Tridymite, Mexico.
5 Coesite, Roberts Victor mine, South Africa.

Downloaded from https://pubs.geoscienceworld.org/books/chapter-pdf/3761882/9780903056434_ch62.pdf
by guest

The α–β quartz inversion takes place at about 573ºC but the exact temperature varies inversely with the temperature of formation: over 95% of quartz specimens invert within a 2.5ºC range. In most cases the temperature of this inversion can be used only as a 'fingerprint' method of comparing quartz from various sources and for the study of zoning within rock masses. The inversion point is raised approximately 1ºC by each 4 MPa increase in pressure. The β-quartz–tridymite inversion takes place at 867 ± 3ºC: at a pressure of 0.1 GPa the temperature of this inversion is raised by approximately 180ºC (Fig. 222).

The solubility of quartz, measured in a continuous-flow apparatus, is 1 g/10^6 g of water at 400ºC and 3.3 MPa, and about 2600 g/10^6 g of water at 500ºC and 10 MPa. Both solution and crystallization are accelerated several orders of magnitude by NaOH or NaCl solutions.

Quartz is one of the most stable minerals and, in addition to being resistant chemically to most attacking solutions, its hardness and lack of cleavage help it to resist many of the other agencies of weathering. The replacement of quartz by orthoclase has been recorded in which the crystal structure of the quartz has governed the orientation of the feldspar replacement. The micro-etching or 'frosting' of quartz grains by carbonate replacement has also been described.

Quartz is an extremely important mineral in many industrial processes. At the simplest level it represents raw material for the production of glasses, ceramics and foundry moulds. Most quartz sands are a golden yellow due to the quartz particles being encased by a thin coating of iron oxides and/or hydroxides; this iron content is sufficient to cause any glass manufactured from the quartz to be dark green. In certain geological situations, however, the beach sands may be rolled to and fro by the tides for several million years, leading to the erosion of the iron coating and formation of 'silver sands', which are much sought after for glass manufacture. For more technical applications requiring an even higher degree of purity, colourless vein quartz is used, or nowadays reliance is placed on the manufacture of synthetic crystals of quartz in an autoclave. One of the main technical aspects of quartz lies in its piezoelectric properties, whereby the crystal develops an electrical polarization when mechanically stressed in an appropriate direction. In the manufacture of quartz oscillators, thin plates of quartz are cut in a particular direction specified to generate the desired resonant vibrational frequency. Quartz, reduced by carothermic reaction, is also the main source for silicon and silicon compounds used in a wide range of industries, the most notable being silicon wafers used in microelectronics.

Tridymite

Natural tridymites commonly depart from pure SiO_2 and contain appreciable aluminium and alkalis. This can be related to the more open structure of tridymite which can accommodate the relatively large ions of the alkali group, balanced by the replacement of the Si^{4+} ion by Al^{3+} in tetrahedral coordination.

Tridymite has been synthesized from silica gel in the presence of fluorides and carbonates of sodium and potassium, but attempts to produce it from pure amorphous silica at various temperatures and pressures have rarely been successful. At water vapour pressures above approximately 40 MPa, tridymite melts to a hydrous liquid: at pressures above about 140 MPa it is not formed as a stable phase. The tridymite–cristobalite inversion takes place at 1470ºC at atmospheric pressure. Because cristobalite is more dense than tridymite, this inversion temperature is lowered by an increase in pressure, i.e. the cristobalite–tridymite boundary has a negative slope.

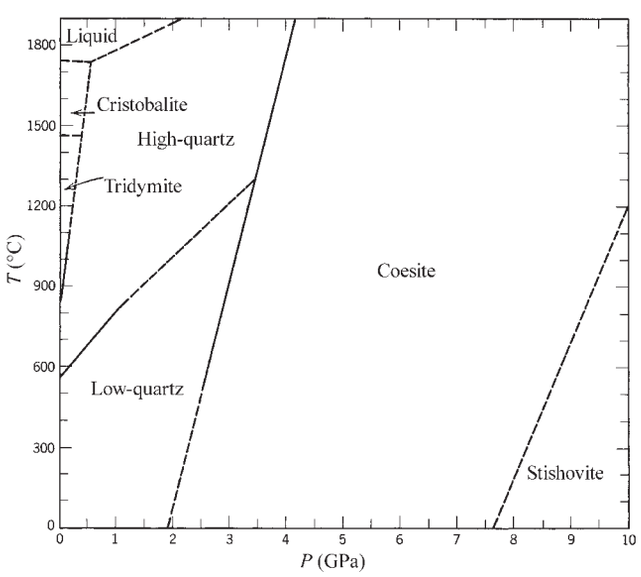


Fig. 222. Phase diagram for the silica system (after Klein, C. & Hurlbut, C.S., 1973, *Manual of Mineralogy*, p. 527 (John Wiley & Son).

Downloaded from https://pubs.geoscienceworld.org/books/chapter-pdf/3761882/9780903056434_ch62.pdf
by guest

Cristobalite

Cristobalite, like tridymite, has a very open structure compared with that of quartz, permitting replacement of Si^{4+} by Al^{3+} together with the introduction of alkali or alkali earth ions to balance the charge deficiency.

Using powdered silicic acid with water at pressures of 0.1–0.4 GPa and temperatures of 330–440ºC, cristobalite is always the first phase to form, later being converted to quartz. The melting point of cristobalite is 1713 ± 5ºC.

Coesite and stishovite

The dense high-pressure phase coesite was first synthesized at 3.5 GPa. It is almost insoluble in HF, but is dissolved and volatilized in fused $(NH_4)HF_2$. A less dense high-pressure phase, silica K or keatite, has been produced from silica gel, with water and a very small amount of alkali in an autoclave at 33–110 MPa and 380–585ºC; it is soluble in cold HF, but unlike coesite it has not been reported in nature.

The high-density polymorph of SiO_2, stishovite, has been synthesized at 1200–1400ºC and at pressures of around 13 GPa. It is less soluble than coesite in HF. Experimental studies indicate that stishovite, in contrast to other silica polymorphs, can contain appreciable aluminium, up to 5% by weight at 25 GPa. Aluminium may either directly substitute for octahedrally coordinated silicon or be incorporated into large interstitial sites, charge-balanced by interstitial hydrogen or oxygen vacancies.

Optical and physical properties

Quartz

The refractive indices of quartz show little variation from ω 1.544 and ε 1.553. Accurate measurements using optical quartz of known purity, for λ 589.29 nm, give values of ω 1.544258 and ε 1.553380, at 18ºC. The enantiomorphism of quartz causes it to be 'optically active'; the plane of polarization of light passing along the optic axis is rotated either clockwise or anti-clockwise depending on the 'hand' of the crystal. A right-handed quartz rotates the plane of polarization clockwise when viewed towards the light source. This rotation of the plane of polarization may affect the interference figure seen in convergent light, so that for sections appreciably thicker than normal the central part of the black cross is faint or absent and the space within the inner ring may appear brightly coloured.

The enantiomorphism of quartz gives rise to right- or left-handed crystals. The convention used is that in a right-handed crystal the face $(11\bar{2}1)$ (*s* in Fig. 223) of the trigonal bipyramid, if present, lies to the right of the $(10\bar{1}0)$ face (*m* in Fig. 223) lying below the predominant positive rhombohedron $(10\bar{1}1)$ (*r* in Fig. 223); the trigonal trapezohedron $\{51\bar{6}1\}$ (*x* in Fig. 223) may also be present. In a left-handed crystal the equivalent forms are $\{2\bar{1}\bar{1}1\}$ and $\{6\bar{1}\bar{5}1\}$ (Fig. 223). There appears to be an equal numerical distribution of right- and left-handed crystals in nature.

In some metamorphic and igneous rocks quartz develops undulatory extinction due to strain, and in such quartz fine lamellae may occur which have been attributed to translation gliding. Undulatory extinction has been produced experimentally at pressures of about 13.8 GPa, the optic axis being displaced by 2–7º. In some instances quartz may develop a distinctly biaxial character, with 2V as high as 8º or 10º. These strain phenomena are generally eliminated if later recrystallization occurs. Metamorphic quartz grains are commonly composite and show sutured subgrain boundaries (Fig. 224).

Twinning, although rarely seen in thin sections, is fairly common and may be observed in some hand specimens of well developed crystals of quartz. The most common twin laws are:

(a) twin axis *z*, twin plane $\{10\bar{1}0\}$, Dauphiné law;
(b) twin plane $\{11\bar{2}0\}$, Brazil law;
(c) twin plane $\{11\bar{2}2\}$, Japan law;
(d) combined Dauphiné–Brazil law.

None of these types of twinning can be detected optically in thin sections of normal thickness.

The piezoelectric property of quartz (see above) is shown in the development of electric charge on the surface of a quartz crystal if it is subjected to mechanical stress, or the converse effect of mechanical deformation produced if a crystal is subjected to an electrical field: this latter property has been applied to controlling and stabilizing the frequency of electronic oscillator circuits, e.g. for radio transmission or reception, or for time-keeping.

The colour of quartz ranges through colourless, yellow and grey-brown to black, pink and purple, the coloured varieties being called citrine, smoky quartz, rose quartz and amethyst, respectively. Citrine appears to owe its colour to a submicroscopic distribution of colloidal ferric hydroxide, whereas the colour of rose quartz has been ascribed to Tyndall scattering by tiny oriented rutile needles and/or the presence of Ti^{3+}. The

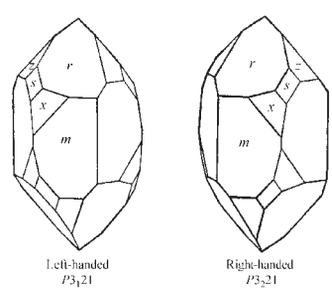


Fig. 223. The morphology of left-handed and right-handed quartz. The faces *s, x* and *z* follow a right- and left-handed helix in right- and left-handed quartz, respectively (Heaney, P.J. *et al*., 1994).

Downloaded from https://pubs.geoscienceworld.org/books/chapter-pdf/3761882/9780903056434_ch62.pdf
by guest

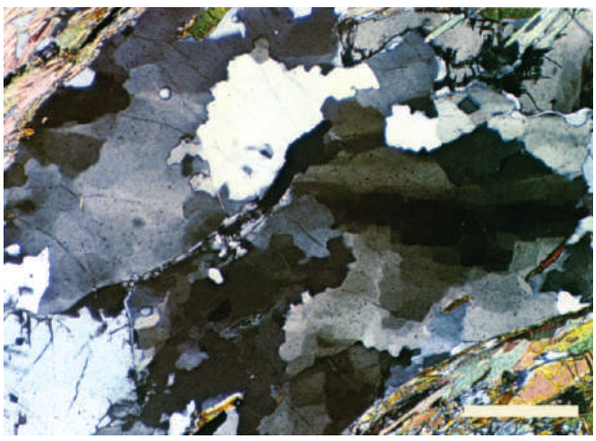


Fig. 224. Cordierite-sillimanite gneiss, Madagascar (crossed polars, scale bar 0.5 mm), with individual quartz crystals showing typical low birefringence with undulose extinction (W.S. MacKenzie collection, courtesy of Pearson Education).

colour in amethyst is related to the presence of iron, possibly in conjunction with exposure to natural radioactivity. The colour of smoky quartz may be linked with the presence of Al in the structure. Asterism in rose quartz is due to rutile needles: the latter may also be responsible for the greyish blue and blue quartz typical of granulite-facies rocks, though in some such blue quartz the TiO_2 is in a colloidal state. Pegmatitic quartz owing its colour to tiny needles of tourmaline is also known.

Fluid inclusions are common in quartz. They range from <1 μm to several millimetres in maximum dimension but typically are 1–10 μm in size and may be abundant. The composition of the aqueous fluid in the inclusions can range from 0 to 70 wt.% NaCl when trapped, and many inclusions contain halite and sylvite 'daughter' minerals (Fig. 225). Information relevant to temperature and conditions of crystallization of the parent quartz can be obtained by heating until any bubbles in a three-phase inclusion disappear, giving the original trapping temperature (subject to a correction for pressure), whereas the freezing temperature will give an indication of the composition of the aqueous phase.

A feeble cleavage may occur in quartz on $\{10\bar{1}1\}$ or $\{01\bar{1}1\}$. Experimental deformation of quartz at 450ºC and 0.4 GPa gives rise to cleavage fragments with rhombohedral or prismatic bounding planes.

Chalcedony is a group name for the compact varieties of silica composed of minute crystals of quartz with submicroscopic pores. The colour and texture vary considerably according to the impurities present but in general such materials may be subdivided into chalcedony, in which the colour is fairly uniform, and agate, in which the colour is arranged in bands or concentric zones. The terms 'chert' and 'flint' are used for opaque dull-coloured or black chalcedony, and in common usage chert is taken as the name for this material when it occurs in stratified or massive form in rocks, whereas the term flint is restricted to dark chalcedony occurring in nodular form in a rock matrix, particularly in the Chalk. Flint commonly has about 1% water and a lower density (2.57–2.64 g/cm^3) than quartz (2.65 g/cm^3). The red opaque massive form of chalcedony is called jasper.

Tridymite

The refractive indices of tridymite vary slightly due to the presence of varying amounts of Al and Na; synthetic material has α 1.469, γ 1.473 and a density of

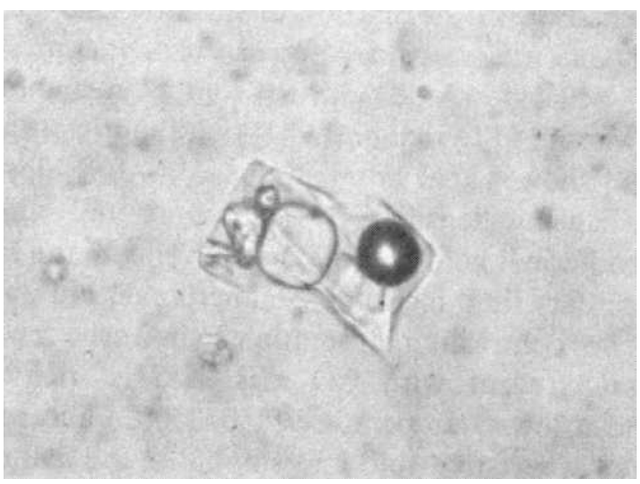


Fig. 225. Fluid inclusion in quartz, St Austell granite, Cornwall, UK, showing a spherical vapour bubble, in aqueous solution with several daughter phases: halite (the largest crystal) and smaller crystals of Fe- and K-bearing chlorides. Inclusion is ~20 μm in length (courtesy of D.H.M. Alderton).

Downloaded from https://pubs.geoscienceworld.org/books/chapter-pdf/3761882/9780903056434_ch62.pdf
by guest

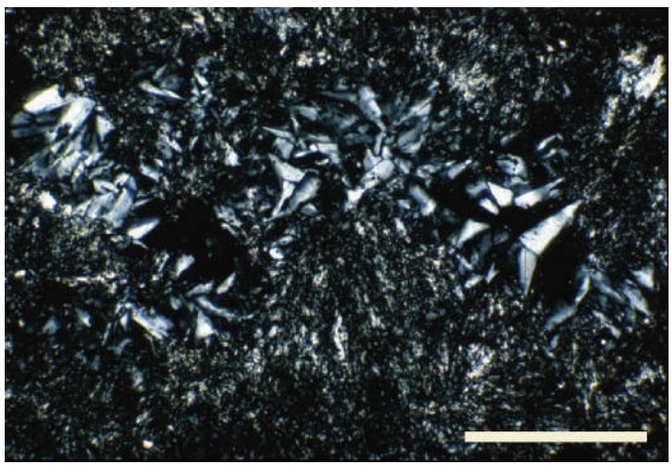


Fig. 226. Vein of tridymite in dacite (crossed polars, scale bar 0.5 mm), Hakone volcano, Japan, showing characteristic wedge-shaped crystals with very low birefringence (W.S. MacKenzie collection, courtesy of Pearson Education).

2.26 g/cm^3. Twinning is fairly common and gives rise to wedge-shaped crystals of two or more individuals, including the trillings from which tridymite derives its name (Fig. 226).

Cristobalite

Synthetic material has refractive indices close to ε 1.484 and ω 1.487, but for natural material slightly higher values have been reported. The birefringence is generally low but some fine-grained cristobalite is apparently almost isotropic, possibly due to overlapping crystallites. Interpenetrant spinel-type twins on {111} are fairly common.

Opal

Natural hydrous silica may be divided into three well defined structural groups: opal-C (well ordered γ-cristobalite), opal-CT (disordered α-cristobalite, α-tridymite) and opal-A (highly disordered, nearly amorphous). The terms 'opal' and 'opaline silica' may conveniently be applied to natural hydrous silica for which there is insufficient information (X-ray, spectroscopic or thermal) to place the material in one of these categories. Opal, therefore, is not a mineral in the modern sense as it is made variously of cristobalite, tridymite and amorphous silica. Opal may be colourless, milky white, yellow, red, green, blue or black. In precious opal, a play of delicate colours is seen, due not to chemical impurities or spectral effects but to optical diffraction from a randomly faulted close-packed structure of minute (around 0.25 μm) transparent silica spheres (Fig. 227). The play of colours depends on the size and uniformity of the particles and extent of faulting. The more common varieties of opal show a rather pearly reflection or "opalescence". The composition of opal is $SiO_2.nH_2O$ with the water content 6–10% in precious opal. The density is 2.01–2.16 g/cm^3 and the refractive index varies from 1.441 to 1.459.

Coesite

Synthetic coesite has α 1.590–1.594 and γ 1.597–1.604, with $2V_\gamma$ 54–64° and a density of 2.92 g/cm^3.

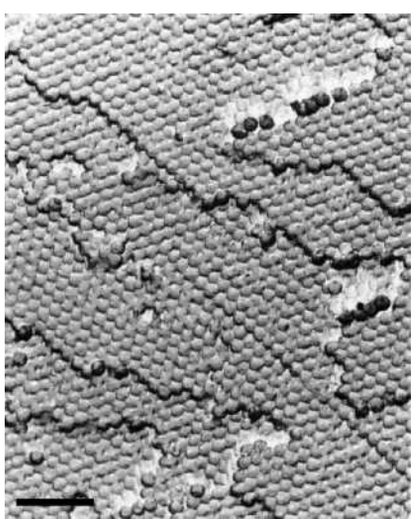


Fig. 227. Scanning electron micrograph of a fractured surface of precious opal showing a regular array of spheroidal particles (lepispheres) of uniform size (scale bar 1.75 μm) (Sanders, J.V. & Darragh, P.J., 1971, *Min. Record*, **2**, 261–68).

Downloaded from https://pubs.geoscienceworld.org/books/chapter-pdf/3761882/9780903056434_ch62.pdf
by guest

Stishovite

Synthetic stishovite has ω 1.800 and ε 1.845, whereas fine-grained natural stishovite appears to have refractive indices in the 1.77–1.78 range and a density of 4.28 g/cm^3.

Seifertite

Seifertite crystallizes at ultrahigh pressures; it is a hard SiO_2 polymorph found in Martian meteorites, and has a calculated refractive index of ~1.89 and a density of 4.29 g/cm^3.

Distinguishing features

Quartz is most readily distinguished under the microscope by its lack of colour, cleavage and visible twinning, and by its low relief and weak birefringence. Typically it is fresh and unaltered and is unattacked by acids other than HF; in hand specimen it commonly has a distinctive crystal habit and vitreous lustre. Its hardness and lack of cleavage easily distinguish it from calcite. In thin section its uniaxial figure distinguishes it from cordierite and the feldspars, and in addition the alkali feldspars normally have lower refractive indices and in most cases a lower birefringence. Beryl and scapolite differ in being length-fast and optically negative: nepheline is also negative, gelatinizes with acids and is rarely completely clear. Criteria for distinguishing natural α-quartz from that formed originally above 573ºC include the presence of three-fold symmetry either in the distribution of Dauphiné or Brazil twinning as revealed by etching, or in colour and inclusions.

Tridymite and cristobalite may be identified by their moderate relief, their refractive indices of 1.47–1.49 being considerably less than that of the normal mounting medium (1.54). The twinning of tridymite and the wedge-shaped crystals are characteristic. The refractive indices of tridymite are lower than those of cristobalite and these two minerals differ in optic sign.

Paragenesis

Quartz

Next to the feldspars, quartz is the most abundant mineral in the Earth's crust. It is a common constituent in many igneous, sedimentary and metamorphic rocks, and also occurs as secondary material, as forming a cementing medium in sediments. Quartz is also a common constituent of hydrothermal veins.

In granites, microgranites and tonalites, quartz typically forms anhedral grains but it may show euhedral outlines in the fine-grained rapidly cooled rhyolites, pitchstones and quartz porphyries, although in some of these rocks the quartz phenocrysts may later suffer magmatic corrosion.

In the igneous rocks of intermediate acidity the amount of quartz is less than in those of granitic composition, and in basic rocks it usually amounts to less than 5% though it is more abundant in some quartz dolerites and similar rock types. Quartz is chemically incompatible with nepheline and the other feldspathoids and is thus absent from the undersaturated igneous rocks.

Because of its chemical and physical resistance to corrosion, quartz is an abundant mineral and becomes concentrated during sedimentary processes to give rise to sands and sandstones of various types. Secondary quartz is commonly deposited around pre-existing grains (of quartz or other minerals) and is a cementing material in sedimentary rocks. In some relatively porous sandstones the secondary quartz may be deposited in crystallographic continuity with the detrital quartz, the boundary between the two generations of silica being visible only by the occasional presence of a rim of iron-staining on the detrital grain. Authigenic quartz occurs rarely in limestones, where it may form well developed crystals, and small doubly terminated crystals of quartz have been found embedded in limonite in a ferruginous sandstone replacing dolomite. In some oolites, quartz fragments occur as nuclei, and examples are known where the quartz grains have become enlarged by secondary silica and transgress across the calcareous boundaries.

In fibrous quartz and chalcedony the common direction of elongation is along one of the polar $<11\bar{2}0>$ directions; length-slow chalcedony fibres with their z axes parallel to the fibres are much less common but this variety is almost always associated with evaporite and/or sulphate minerals and an alkaline environment of deposition.

Quartz is a common mineral in many metamorphic rocks, occurring in the metamorphosed equivalents of quartz-bearing sedimentary and igneous rocks. Although in the low grades of metamorphism quartz may survive unchanged, in the higher grades it undergoes recrystallization with concomitant increase in grain size. In addition much quartz is developed by the release of SiO_2 in reactions taking place during metamorphism.

Intergrowths of quartz and other minerals are fairly common, particularly those of quartz and potassium feldspar as in graphic or micrographic granite, and quartz and plagioclase (myrmekite, see p. 289, and Fig. 228) in association with potassium feldspar. Such intergrowths are common in many types of acid igneous and metamorphic rocks: particular mention may be made also of the intimately intergrown quartz and feldspar typical of many granophyres.

Tridymite

The typical occurrence of tridymite is in acid volcanic rocks such as rhyolite, obsidian, trachyte, andesite and dacite. In such rocks it is often found in

Downloaded from https://pubs.geoscienceworld.org/books/chapter-pdf/3761882/9780903056434_ch62.pdf
by guest

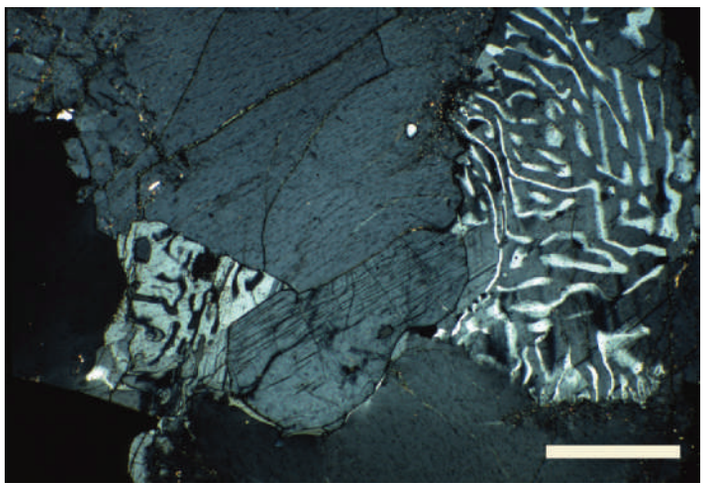


Fig. 228. Myrmekite (an intergrowth of plagioclase and quartz with vermicular texture), charnockite, NW of Fort Dauphin, Madagascar (crossed polars, scale bar 0.4 mm) (W.S. MacKenzie collection, courtesy of Pearson Education).

cavities and may be associated with sanidine and, more rarely, augite or fayalite. It occurs with cristobalite in the mesostasis of lunar basalts. In some igneous rocks there is doubt whether it ever occurs magmatically rather than as a 'metamorphic' mineral involving pneumatolytic metamorphism. Rocks collected from Mt Pelée soon after the eruptions contained no tridymite but the mineral began to appear in the volcanic rocks of this centre about six months later.

Tridymite has been recorded as an abundant mineral in some of the rhyolitic tuffs of the Tertiary volcanic rocks of the San Juan region, Colorado, where in part it acts as the binder for the tuffs, crystallizing after the tuff was deposited. In the rhyolites and quartz latites of this region it is the chief silica mineral and many of the rocks contain as much as 25% tridymite. It is a fairly common constituent of highly metamorphosed impure limestones and arkoses adjacent to basic igneous intrusions. The geological interpretation of the occurrence of tridymite in terms of the temperature and pressure of its crystallization is fraught with difficulty: the presence of cristobalite or tridymite in a rock does not necessarily imply that at the time of formation of these minerals the temperature was above the respective inversion points (1470ºC and 870ºC).

Cristobalite

Cristobalite, like tridymite, is typically a mineral of volcanic rocks, where it may occur in cavities, commonly in association (metastable) with tridymite. It has been found in hollow spherulites (lithophysae) in obsidian and in rhyolite, trachyte, andesite, dacite and olivine basalt. It is often a late product of crystallization, and may replace tridymite, and may also be associated with anorthoclase, chlorite and even calcite. It occurs along with tridymite in the groundmass of lunar basalts (Fig. 229). Cristobalite is also known from thermally metamorphosed sandstones and from sandstone xenoliths in basaltic or other basic rocks, where the sandstone has been converted into buchite. As noted above for tridymite, the ability of cristobalite to occur as a metastable polymorph, outside its equilibrium field, means that no definite conclusions can be drawn as to conditions at the time of its crystallization.

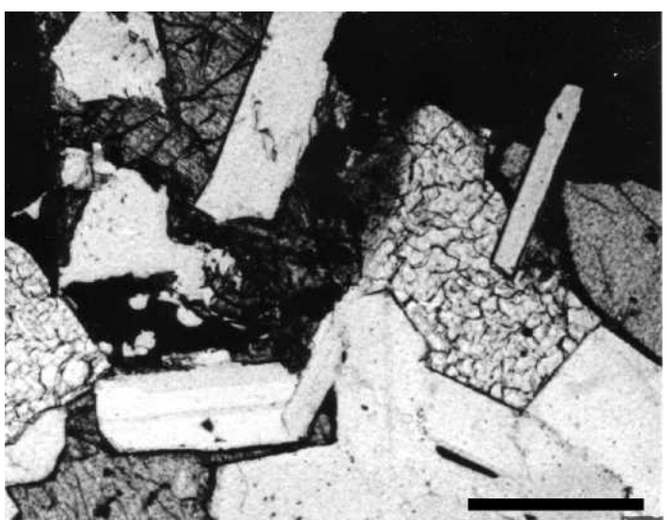


Fig. 229. Coarse-grained lunar basalt (ppl, scale bar 0.3 mm) sampled on Apollo 17 mission, with cristobalite showing characteristic 'tile' structure, with plagioclase, pyroxene and ilmenite (courtesy of NASA, USA).

Downloaded from https://pubs.geoscienceworld.org/books/chapter-pdf/3761882/9780903056434_ch62.pdf
by guest

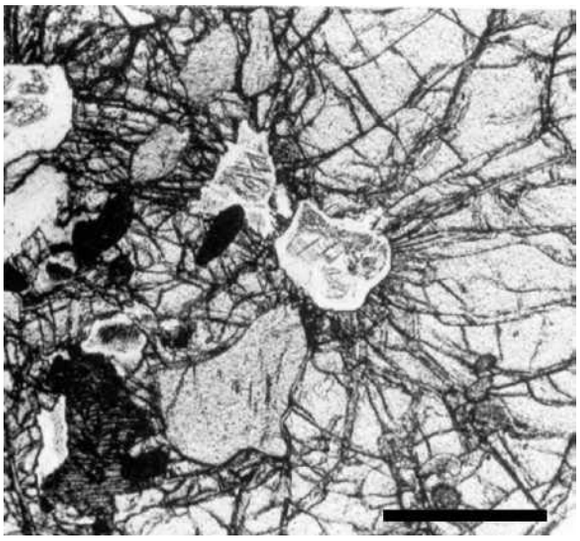


Fig. 230. Crystals of coesite with rims of quartz in garnet in a high-grade pyrope quartzite (ppl, scale bar 0.5 mm) in the Western Alps. The expansion caused by the transition of the coesite to quartz shattered the garmet (W.S. MacKenzie collection, courtesy of Pearson Education).

Opal

The geological conditions for the occurrence of opal require a source of silica, and space in which the opal may accumulate by evaporation from solution. These requirements may be met in both sedimentary and volcanic environments; the silica concentrations necessary may be no greater than 100–200 ppm. In volcanic rocks the silica may be produced by the hydrothermal alteration of silicates or from hot springs. Opal may also occur as an important constituent in marine siliceous ooze, originating from biogenic amorphous silica such as diatom frustules and radiolarian tests; the diagenetic alteration process generally involves opal-A (siliceous ooze) → opal-CT (porcellanite) → chalcedony or cryptocrystalline quartz (chert). Under conditions of unobstructed diagenetic growth, opal-CT usually forms spherical aggregates (Fig. 227), so-called 'lepispheres', consisting of opal-CT blades intergrown according to the twinning laws of tridymite.

Coesite and stishovite

The SiO_2 polymorph coesite occurs with quartz and fused silica glass in sheared porous sandstones at Meteor Crater, Arizona, and in granite and pumiceous tuff near the rim of the Ries crater, Bavaria, developed by the shock wave generated by the meteoritic impact. Fine-grained stishovite also occurs in the Meteor Crater impact-metamorphosed sandstone. In pyrope quartzite in the western Alps, large pyrope garnets in an undeformed matrix of polygonal quartz contain coesite inclusions, which have partly inverted to quartz, resulting in radial cracking of the host garnet around the inclusions (Fig. 230). Similar occurrences are known from China and Norway. The coesite is considered to have crystallized in nearly static pressure conditions of $\geqslant$2.8 GPa. Coesite typically occurs also in xenoliths in diamond-bearing kimberlites. Seifertite, an exceedingly rare high-pressure form of silica isostructural with α-PbO_2 and stable at pressures exceeding those for stishovite has been described from its occurrence in the Shergotty meteorite.

Further reading

Breiter, K. and Müller, A. (2009) Evolution of rare-metal granitic magmas documented by quartz chemistry. *European Journal of Mineralogy*, **21**, 334–346.

Buerger, M.J. (1935) The silica framework crystals and their stability fields. *Zeitschrift für Kristallographie*, **90**, 186–192.

Chopin, C. (1984) Coesite and pure pyrope in high-grade blueschist of the Western Alps: a first record and some consequences. *Contributions to Mineralogy and Petrology*, **86**, 107–118.

Folk, R.I. and Pittman, J.S. (1971) Length-slow chalcedony: a new testament for vanished evaporates. *Journal of Sedimentary Petrology*, **41**, 1045–1058.

Heaney, P.J., Prewitt, C.T. and Gibbs, G.V. (Editors) (1994) Pp. 1–40 in: *Silica: Physical Behavior, Geochemistry and Materials Applications*. Reviews in Mineralogy, **29**, Mineralogical Society of America, Washington, D.C.

Jones, J.B. and Segnit, E.R. (1971) The nature of opal. I. Nomenclature and constituent phases. *Journal of the Geological Society of Australia*, **18**, 57–68.

Kastner, M., Keene, J.B. and Gieskes, J.M. (1977) Diagenesis of siliceous oozes. I. Chemical controls on the rate of opal-A to opal-CT transformation – an experimental study. *Geochimica et Cosmochimica Acta*, **41**, 1041–1059.

Müller, A. and Koch-Müller, M. (2009) Hydrogen speciation and trace element contents of igneous, hydrothermal and metamorphic quartz from Norway. *Mineralogical Magazine*, **73**, 569–583. (See also many other papers in this issue devoted to Frontiers in Quartz Research)

Roedder, E. (Editor) (1984) *Fluid Inclusions*. Reviews in Mineralogy, **12**, Mineralogical Society of America, Washington, D.C., 644 pp.

Wark, D.A. and Watson, E.B. (2006) TitaniQ: a titanium-in-quartz geothermometer. *Contributions to Mineralogy and Petrology*, **152**, 743–754.

Downloaded from https://pubs.geoscienceworld.org/books/chapter-pdf/3761882/9780903056434_ch62.pdf
by guest

SILICA MINERALS

The three principal forms of silica (SiO_2) are quartz (trigonal; by far the most common), tridymite (tetragonal) and cristobalite (cubic), the latter two being less dense minerals which are stable at higher temperatures. As these three polymorphs have very different structures their transformations on cooling are very sluggish and they occur metastably at ambient temperature. Each of the three has itself a high- and low-temperature form and the transitions between these involve only small displacements of atoms and are therefore spontaneously reversible; the high temperature forms cannot therefore persist metastably.

The structure of quartz lacks a centre of symmetry and its crystals can exist with right- or left-handed morphology (enantiomorphism) and they are piezoelectric, a property exploited in their important use as oscillators for frequency control for time-keeping or radio transmission.

Whereas the chemical composition of quartz deviates very little from ideal SiO_2, tridymite and cristobalite commonly contain small amounts of other cations such as sodium and aluminium which can be accommodated in their more open structures. The wide range of colours exhibited by quartzes such as amethyst, citrine and smoky quartz are variously attributed to micro-inclusions, trace-element content and 'colour centres'.

Coesite (monoclinic), stishovite (tetragonal) and seifertite (orthorhombic) are high-density forms of silica produced by high pressure, and occur mostly in meteorites and impactites.

The cryptocrystalline forms of silica chalcedony, agate, chert and flint commonly contain small amounts of the metastable monoclinic polymorph mogánite, which gradually alters over geological time into quartz. Opal is a low density water-rich variety of silica, which is not strictly a mineral in the modern sense of the word, being made up of various combinations of cristobalite, tridymite and amorphous silica.

Quartz is the second most abundant mineral (after feldspar) in the Earth's crust, occurring in many types of igneous and metamorphic rocks, and, because of its resistance to both physical and chemical corrosion, it is also a common mineral in many sedimentary rocks.

Downloaded from https://pubs.geoscienceworld.org/books/chapter-pdf/3761882/9780903056434_ch62.pdf
by guest

Feldspathoids

Nepheline — $Na_3(Na,K)[Al_4Si_4O_{16}]$
Kalsilite — $K[AlSiO_4]$

Hexagonal (−)

	Nepheline	Kalsilite
ε	1.526−1.547	1.532−1.537
ω	1.529−1.551	1.535−1.543
δ	0.003−0.006	0.005−0.006
D (g/cm^3)	2.56−2.665	2.59−2.625
H	5½−6	6
Cleavage	{10$\bar{1}$0}, {0001}, poor	{10$\bar{1}$0}, {0001}, poor
Twinning	{10$\bar{1}$0}, {33$\bar{6}$5}, {11$\bar{2}$2}	
Colour	Colourless, white, grey; colourless in thin section	
Unit Cell	*a* 10.0 Å, *c* 8.4 Å	*a* ~ 5.2 Å, *c* ~ 8.7 Å
	Z = 2; space group $P6_3$	Z = 2; space group $P6_3$
Special features	Gelatinizes in strong HCl	

Nepheline and kalsilite are not isostructural, but both structures have a tridymite-type framework in which approximately half of the silicon atoms are replaced by aluminium; the charge balance is maintained by the presence of alkali atoms in the structural cavities. In addition to structural differences for different compositions, polymorphism is present over the greater part of the chemical range of the Na−K series. Nepheline is the most most common of the feldspathoid minerals and is the most characteristic mineral of alkaline rocks.

Structure

The structure of nepheline is based on a tridymite framework (β-tridymite cell, hexagonal, $P6_3/mmc$, *a* 5.04, *c* 8.24 Å; nepheline, hexagonal $P6_3$, $a \sim 2 \times 5.0$, *c* ~ 8.4 Å). In tridymite (see p. 313) layers of SiO_4 tetrahedra are formed by their linkage in six-membered rings, with neighbouring tetrahedra pointing in opposite directions. The apices of tetrahedra which are not shared within rings are shared by apices in layers above and below. In nepheline approximately half of the Si atoms are replaced by Al, and when fully ordered these Si and Al atoms alternate regularly, and the negative charge resulting from Al for Si substitution is balanced by alkali ions occupying cavities, which form channels in the framework parallel to *z*. The nepheline–kalsilite minerals are therefore commonly described as 'stuffed derivatives' of tridymite. The idealized structure of a nepheline with composition $Na_{0.75}K_{0.25}SiAlO_4$ is shown in Fig. 231. In reality the tridymite structure-type framework is distorted by rotations of the tetrahedra around the *z* axis direction and the alkali sites are of two different sizes, one quarter (*A* sites) suitable for the larger K atom, and three quarters (*B* sites) appropriate for Na (Fig. 232a). Potassium atoms lie in 9-fold coordination between 6-membered ditrigonal rings and Na in 8-fold coordination between distorted oval-shaped rings. Tetrahedra in successive layers are in the 'eclipsed' as compared with 'staggered' configuration (Fig. 232b) and this is accompanied by variations in the linkage of adjacent layers. The resulting minor energy differences between structures with slightly different Si−O−(Al,Si) bond angles, and the topological variety of networks of corner-shared tetrahedra give rise to several $NaAlSiO_4$−$KAlSiO_4$ polymorphs that are related either by reconstructive or displacive phase transformations.

Carnegieite. Carnegieite, the main high-temperature polymorph of nepheline, is cubic (*a* 7.326 Å at 750ºC) and has a cristobalite-like framework structure. Carnegieite itself has high- and low-temperature forms.

Downloaded from https://pubs.geoscienceworld.org/books/chapter-pdf/3762048/9780903056434_ch63.pdf
by guest

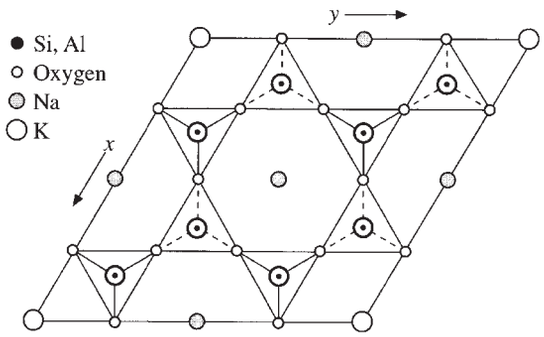


Fig. 231. Idealized structure of nepheline, $Na_3KAl_4Si_4O_{16}$, projected on (0001), based on the arrangement of tetrahedra in high tridymite.

At low temperatures its symmetry is low, possibly triclinic, and it shows intimate twinning. There is little or no disordering of Si,Al even in the high-temperature forms of $NaAlSiO_4$.

Kalsilite. Although kalsilite ($KAlSiO_4$) has the same $P6_3$ symmetry as nepheline, the six-membered rings show different deformations and different linking of adjacent (Si–O) sheets. In nepheline a quarter of the rings have the hexagonal arrangement, and the remainder are oval in shape; in kalsilite all the six-membered rings have a di-trigonal configuration (see Table 39). The many complexities in the structure of kalsilite have been investigated widely, but as it occurs relatively rarely compared with nepheline in nature, only a brief account is given here. In the structure of the low-temperature form of kalsilite, pairs of tetrahedra linking successive layers are in the 'staggered' rather than the basic 'eclipsed' relationship found in high-kalsilite, nepheline and the many other structures of $(Na,K)AlSiO_4$ phases (Fig. 232a,b). Kalsilite may contain relatively large amounts of sodium. In minerals containing ~20 to 30% of the $NaAlSiO_4$ component two distinct structures occur. These two phases, trikalsilite and tetrakalsilite (now known as panunzite, but described as tetrakalsilite herein to emphasize its relationship to kalsilite), have *a* cell parameters of 15.4 Å and 20.5 Å, respectively: both phases have been synthesized. The structures can be regarded as stuffed tridymite derivatives intermediate between nepheline and kalsilite (Table 40).

In the structures of nepheline and kalsilite the oxygens shared between neighbouring sheets, as a result of the rotations referred to above, are displaced slightly towards one of the three neighbouring alkali atoms, and this is accompanied by variations in the linking of adjacent layers. Variations in the types of 6-membered rings that occur in the $NaAlSiO_4$–$KAlSiO_4$ polymorphs are indicated in Table 39 and variations in symmetry and cell parameters in Table 40.

The composition of most nephelines is close to $Na_3K(SiA1O_4)_4$, which is regarded as a distinct ordered intermediate compound in the binary $NaAlSiO_4$–$KAlSiO_4$ system.

In nephelines containing less potassium than the ideal composition, some of the larger cavities are occupied by sodium. In such sub-potassic nephelines the distortion at lower temperatures of the framework around the sodium atoms in the layer cavities gives rise to structural differences that are dependent on composition and thermal history. These include a reversible phase transition to an orthorhombic form in very Na-rich [Na/(Na + K) > 0.975] nepheline.

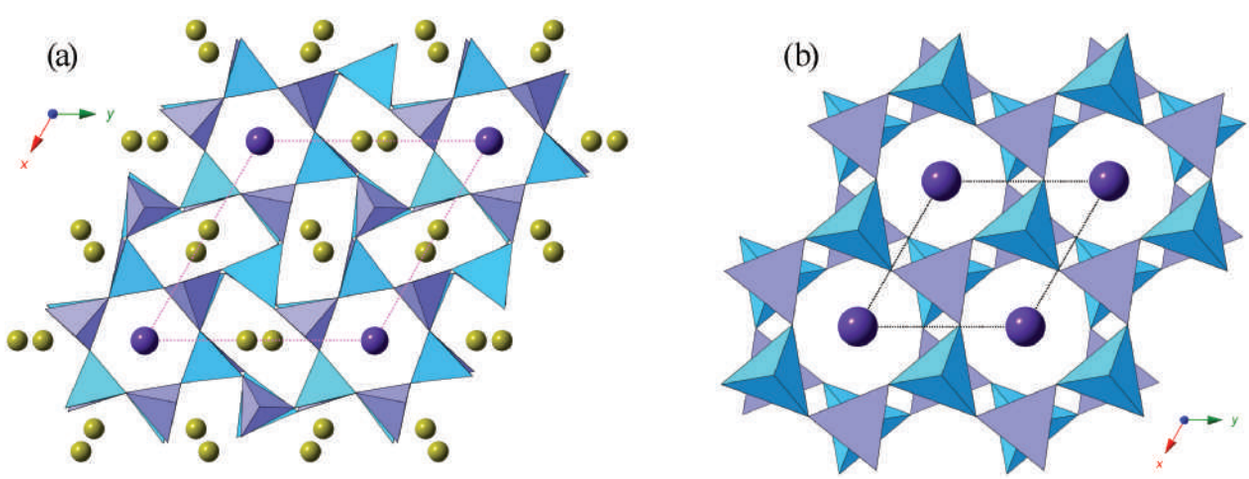


Fig. 232. (a) Crystal structure of nepheline viewed along *z* showing the 'hexagonal' site for potassium and the 'oval' site for sodium. Pairs of Na^+ in projection are in fact separated by *c*/2. (b) Crystal structure of a kalsilite viewed along *z* showing the staggered relationship between successive (Si–O) sheets. Lavender: SiO_4 tetrahedra; blue: AlO_4 tetrahedra; yellow: Na^+; purple: K^+.

Downloaded from https://pubs.geoscienceworld.org/books/chapter-pdf/3762048/9780903056434_ch63.pdf
by guest

Table 39. Types of six-membered rings in $NaAlSiO_4$–$KAlSiO_4$ phases.

Phase Ideal composition	Nepheline $Na_{0.75}K_{0.25}$	Trikalsilite $Na_{0.33}K_{0.67}$	Tetrakalsilite* $Na_{0.18}K_{0.82}$	Kalsilite $KAlSiO_4$
Hexagonal	2	2	2	0
Ditrigonal	0	4	12	2
Oval	6	12	18	0

* Also known as panunzite.

Members of the nepheline-kalsilite group, including carnegieite and O_1-kalsilite, the highest-temperature phases in the system, show nearly complete Al,Si ordering. Excess Si over the 1:1 stoichiometric Si/Al ratio appears, however, to substitute randomly for Al.

There are a number of phases, generally designated as kaliophilite, close to $KAlSiO_4$ in composition that are characterized by layers of six-membered tetrahedral rings but with different layer topologies. Naturally occurring kaliophilite is an hexagonal phase with a large unit cell (*a* 26.9 Å, *c* 8.5 Å), that is possibly related to the presence of very fine-scale modulated domains.

The substitution of Na by K in nepheline is accompanied by an increase in both *a* and *c* parameters. For compositions with *x* (in the formula $Na_{8-x}K_xAl_8Si_8O_{32}$) between 0.25 and 2.0 there is a 5.82 $Å^3$ linear increase in cell volume and between *x* 2.0 and 4.7, an increase of 11.8 $Å^3$ per K ion. A change in lattice parameters also occurs in nephelines, the composition of which can be described precisely only with reference to the ternary system $NaAlSiO_4$–$KAlSiO_4$–SiO_2, i.e. in nephelines in which there is an excess of Si compared with the idealized composition $Na_3KAl_4Si_4O_{16}$. The charge balance is maintained by vacancies at the potassium sites; further vacancies at these sites may result also from the substitution of Na^+ by Ca^{2+}. In natural nephelines the number of vacancies necessary to maintain charge balance is normally of the order of one-third of the available K sites. The experimentally determined composition at which the change occurs can be expressed by the formula:

$$Na_{5.97}K_{1.64}\square_{0.39}Al_{7.61}Si_{8.39}O_{32}$$

Thus it appears that the change in approximate lattice parameters occurs in omission solid solution nephelines, $Na_6K_2Al_8Si_8O_{32}$–$Na_6\square_2Al_6Si_{10}O_{32}$, if the six smaller voids are occupied by sodium atoms and there are no sodium atoms in the larger voids suitable for potassium, i.e. omission substitution occurs only in relation to the large potassium sites (Fig. 233).

Chemistry

Almost all nephelines contain more silicon and less aluminium than is represented by the basic formula $NaAlSiO_4$; the sum of the Si and Al atoms, however, is usually close to the ideal cell content of 16. The excess SiO_2 compared with the compositions of solid solutions between $NaAlSiO_4$ and $KAlSiO_4$ is shown in the normative percentages of the sodium molecule (Ne), the potassium molecule (Ks) and SiO_2 (Q) in Table 41. Although in the synthetic system $Na_2Al_2Si_2O_8$–$CaAl_2Si_2O_8$, nepheline can take 35 mol% anorthite into solid solution, most natural nephelines contain only relatively small amounts of calcium.

The common excess of Si over Al in nephelines is balanced by vacancies in *A* sites indicated by □ in the general formula:

$$Na_xK_yCa_z\square_{8-(x+y+z)}Al_{(x+y+2z)}Si_{16-(x+y+2z)}O_{32}$$

Table 40. Symmetry and lattice parameters of $(Na,K)AlSiO_4$ phases.

	$NaAlSiO_4$ (wt.%)	Symmetry	Lattice parameters (Å) *a*	*b*	*c*
Nepheline	100–30	Hexagonal	10.0–10.2	–	8.4–8.5
High-temperature carnegieite	100–90	Cubic	7.3	–	–
Kalsilite	0–20	Hexagonal	5.2	–	8.7
Orthorhombic kalsilite	0–10	Orthorhombic	9.1	15.7	8.6
Trikalsilite	~30	Hexagonal	15.4	–	8.5
Tetrakalsilite*	~25	Hexagonal	20.5	–	8.6
Kaliophilite	0–10	Hexagonal	26.9	–	8.5

* Also known as panunzite.

Downloaded from https://pubs.geoscienceworld.org/books/chapter-pdf/3762048/9780903056434_ch63.pdf
by guest

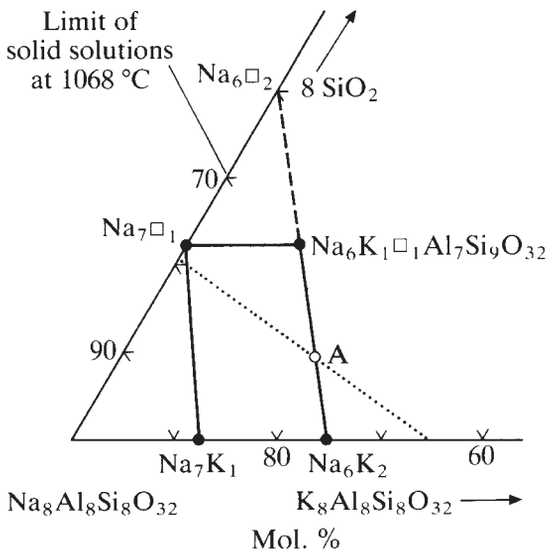


Fig. 233. Diagram showing part of the system $NaAlSiO_4$–$KAlSiO_4$–SiO_2. Dotted line represents approximately the limit of nepheline solid solution at 700ºC. The position of the break in lattice parameters, marked by point A, lies very close to the line representing six of the eight alkali sites filled by Na atoms (after Hamilton, D.L. & MacKenzie, W.S., 1960, *J. Petrol.*, **1**, 56–72).

Experimental

The phase relations in the system nepheline–kalsilite are shown in Fig. 234. Compositions between Ne_{100} and $Ne_{37.5}$ at temperatures above the solvus consist of a single-phase solid solution. At the pure sodium end of the series, low-temperature nepheline is the stable phase at atmospheric pressure up to ~872ºC, at which temperature it transforms to high-temperature nepheline. The phase relationships in sub-potassic nepheline (<2.75 mol.% $KAlSiO_4$) are complex and involve orthorhombic–hexagonal transitions (not shown in Fig. 234).

At 1245ºC sodium nepheline ($NaAlSiO_4$) undergoes a slow quenchable reconstructive transition to the high-temperature polymorph carnegieite. This has the cristobalite structure, is cubic at high temperature but transforms rapidly to a lower symmetry, probably triclinic, on cooling to room temperature. Neither form of carnegieite has been found in nature. The temperatures of both the low- to high-temperature nepheline and carnegieite transitions are raised by the substitution of sodium by potassium; that of low- to high-temperature nepheline rises rapidly and reaches a maximum of 1248ºC at a composition Ne_{95}, whereas in more potassium-rich nephelines the low-temperature phase inverts directly to carnegieite. Sodium nepheline transforms at 1000ºC and pressures above 18 GPa to a phase with the calcium ferrite structure (*a* 8.740 Å, *b* 2.746 Å, *c* 10.206 Å, space group *Pnma*, Z = 4) involving a −31.9% volume change.

At the potassium end of the series, kalsilite inverts at approximately 850ºC to orthorhombic $KAlSiO_4$ (O_1). Two potassium-rich phases, trikalsilite and tetrakalsilite, crystallize at temperatures above the solvus (Fig. 234) from compositions between Ks_{90} and Ks_{70}. The

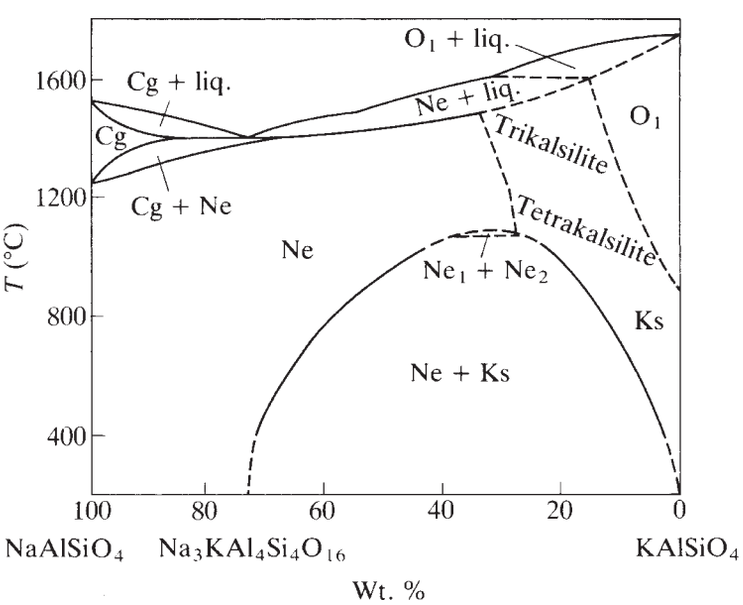


Fig. 234. Simplified phase diagram (0.1 MPa) of the system $NaAlSiO_4$–$KAlSiO_4$. Inferred boundaries are shown by broken lines; boundaries for potassium-rich compositions beteen solidus and solvus are omitted. Trikalsilite and tetrakalsilite fields not located precisely (after Tuttle, O.F. & Smith, J.V., 1958, *Amer. J. Sci.*, **256**, 571–89). Cg: carnegeiete; Ne: nepheline; Ks: kalsilite; O_1: orthorhombic kalsilite.

Downloaded from https://pubs.geoscienceworld.org/books/chapter-pdf/3762048/9780903056434_ch63.pdf
by guest

Table 41. Nepheline and kalsilite analyses.

	1	2	3	4	5	6
SiO_2	46.50	41.88	40.20	38.47	38.48	37.87
TiO_2	–	0.03	0.05	0.00	0.05	–
Al_2O_3	32.60	32.99	32.51	30.81	31.01	32.07
Fe_2O_3	0.00	0.74	1.82	1.63	1.12	0.08
MgO	–	0.00	0.10	0.63	0.00	–
CaO	–	0.78	1.44	0.20	0.03	–
Na_2O	16.54	16.11	10.86	2.09	0.30	0.04
K_2O	4.40	6.82	12.22	25.65	28.33	30.21
H_2O+	–	0.71	0.00	0.20	0.67	–
H_2O-	–	0.03	0.00	0.00	–	–
Total	100.04	100.16	99.77	99.94	100.00	100.27
ε	–	–	1.539	1.537	1.533	–
ω	–	–	1.543	1.543	1.539	–
	Numbers of ions on the basis of 32 O					
Si	8.78	8.179	8.014	8.044	8.125	7.981
Al	7.255	7.595	7.641	7.596	7.720	7.966
Ti	–	0.005	0.007	–	0.008	–
Fe^{3+}	0	0.109	0.369[b]	0.301[c]	0.180[d]	0.013
Mg	–	0.102[a]	0.030	0.196	–	–
Na	6.055	6.098	4.198	0.847	0.1237	0.016
Ca	–	0.163	0.308	0.045	0.006	–
K	1.06	1.699	3.108	6.846	7.635	8.123
ΣR[e]	7.12	8.12	7.92	7.78	7.77	8.139
Ne (mol.%)	76.0	76.1	54.7	9.9	1.4	0.2
Ks (mol.%)	13.3	23.6	45.3	88.9	96.8	101
Q (mol.%)	10.7	0.3	–	1.2	1.8	−1.2

1 Nepheline, nepheline syenite, Deer Mountain, Otero County, New Mexico (Dollase, W.A. & Thomas, W.M., 1978, *Contrib. Mineral. Petrol.*, **66**, 311–18).
2 Nepheline, foyaite, Transvaal (Tilley, C.E., 1956, *Kon. Ned. Geol. Mijnb., Geol. Ser.*, Brouwer vol., 403–13. Includes MnO 0.07).
3 Nepheline, potash ankaratrite, Congo (Sahama, Th.G., 1952, *Amer. J. Sci.*, Bowen vol., 457–70. Includes FeO 0.57).
4 Kalsilite, venanzite, Italy (Bannister, F.A., Sahama, Th.G. & Wiik, H.B., 1952, *Mineral. Mag.*, **30**, 46–78. Includes FeO 0.26).
5 Kalsilite, complex phenocryst of kalsilite and nepheline, Congo (Sahama, Th., Neuvonen, K.J. & Hytonen, K., 1956, *Mineral. Mag.*, **31**, 200–8. Analysis recalculated after correcting for 10% nepheline, 31.1 atomic% K/(K + Na + Ca) in sample; total iron as Fe_2O_3; includes MnO 0.01).
6 Kalsilite in kalsilite-leucite-hibonite association, gneiss, Punalur, southern India (Sandiford, M. & Santosh, M., 1991, *Mineral. Petrol.*, **43**, 225–36.

[a] Includes Mn 0.012..
[b] Includes Fe^{2+} 0.096.
[c] Includes Fe^{2+} 0.045.
[d] Includes Mn 0.002.
[e] $\Sigma R = (Na + K + 2\,Ca)$.

relationships between these phases, as well as with kalsilite and orthorhombic kalsilite have not been fully determined.

Kaliophilite has been synthesized at ambient pressure and 135ºC by various processes including the reaction of a boiling solution of K_2CO_3 with a mixture of opal and bayerite, $Al(OH)_3$.

For compositions between about Ne_{40} and Ne_{20} the phase relations above the solvus are more complex. In the synthetic system two phases are present at solidus temperatures, high-temperature orthorhombic kalsilite (O_1-kalsilite) and tetrakalsilite. Orthorhombic kalsilite inverts to the hexagonal kalsilite at temperatures dependent on the composition of the solid solution. The precise status of tetrakalsilite is less certain, particularly in relation to trikalsilite that occurs as a subsolidus phase in a similar compositional range as tetrakalsilite. The almost complete absence of natural occurrences of these two phases (see Paragenesis, p. 332) suggests that they may be metastable at low temperatures and it is possible that tetrakalsilite forms by inversion from a potassium-rich nepheline (~Ne_{70}), either directly or through an intermediate phase. The distribution of Na^+ and K^+ in trikalsilite and tetrakalsilite shows progressive ordering that precedes the exsolution to nepheline and kalsilite at the solvus.

The maximum temperature of the solvus is ~1070ºC at 0.1 MPa at a composition of approximately Ne_{30}; the

Downloaded from https://pubs.geoscienceworld.org/books/chapter-pdf/3762048/9780903056434_ch63.pdf
by guest

solvus is stable to at least 1000ºC up to 0.5 GPa. It is truncated by the reaction:

$$\text{Na-rich nepheline} + \text{kalsilite} \rightleftharpoons \text{K-rich nepheline}$$

that gives rise to two high-temperature phase assemblages, an Na-rich nepheline + K-rich nepheline and K-rich nepheline + kalsilite. The solvus is slightly asymmetric towards $Na_3K(AlSiO_4)_4$ and intersects the join nepheline–kalsilite close to the compositions Ne_{73} and Ne_0. Thus solid solution of potassium in the nepheline structure is limited to about 25 mol% at ordinary temperatures, but increases with temperature to about 60 mol%. The amount of sodium that can enter kalsilite increases with temperature to about 25 mol%.

Below the solvus, compositions between ~Ne_{73} and Ne_0 under equilibrium conditions exsolve at the appropriate temperature to nepheline and kalsilite. The unmixing of nepheline–kalsilite solid solution is thus comparable with the formation of alkali feldspar intergrowths, and in the same way that the feldspar intergrowths can be homogenized by heating, so can those of nepheline and kalsilite. The exsolution is rapid due to the high diffusivity of the alkali ions; in intrusive rocks exsolution tends to be complete and exsolution textures are absent. In volcanic rocks exsolution textures occur and vary from cryptoperthitic to coarse-grained intergrowths. The common approximation of nephelines of plutonic rocks to the composition $Na_3K(AlSiO_4)_4$, and the observation that the sodium-rich limb of the solvus approaches but does not cross this composition, are consistent with the conclusion that this composition is unique in the $NaAlSiO_4$–$KAlSiO_4$ solid solution series (see p. 326).

In the synthetic system nepheline–albite (Fig. 235) about 33 wt.% albite can be accommodated in solid solution in nepheline. In the system $NaAlSiO_4$–$NaAlSi_3O_8$–H_2O the limit of nepheline–albite solid solution at 750ºC and P_{H_2O} 0.1 GPa is $Ne_{75}Ab_{25}$.

The equilibrium pressure–temperature curve for the reaction nepheline + albite → 2 jadeite is given by the equation:

$$P\ (\text{GPa}) = 0.0025T\ (\text{ºC}) - 0.4$$

(see jadeite, p. 125). In the system nepheline–diopside–sanidine, nepheline coexists with diopside, olivine and liquid at the piercing point at 1158ºC and composition $Ne_{51}Di_{21}Or_{28}$ (A in Fig. 236). At a second piercing point (B) at 1120ºC nepheline coexists with leucite, diopside and liquid at the composition $Ne_{44.5}Di_{12}Or_{43.5}$. The system is thus non-ternary and on crystallization the liquids move into the undersaturated portion of the join in the quaternary system nepheline–kalsilite–diopside–silica.

Nepheline commonly alters to analcime, cancrinite, sodalite, muscovite and the zeolites natrolite and thomsonite.

Optical and physical properties

The effect of the substitution of Na by K on the refractive indices of nephelines is small. The relatively minor increase in refractive indices with increasing substitution of potassium is commonly masked by the effects of omission solid solution and by the presence of Ca in alkali cation sites. In consequence, refractive indices cannot be used to estimate chemical composition. The replacement of sodium by potassium increases the density of nepheline solid solutions. The refractive indices of kalsilite overlap with those of the more potassium-rich nepheline solid solutions, and kalsilite cannot be distinguished from them by optical measurements.

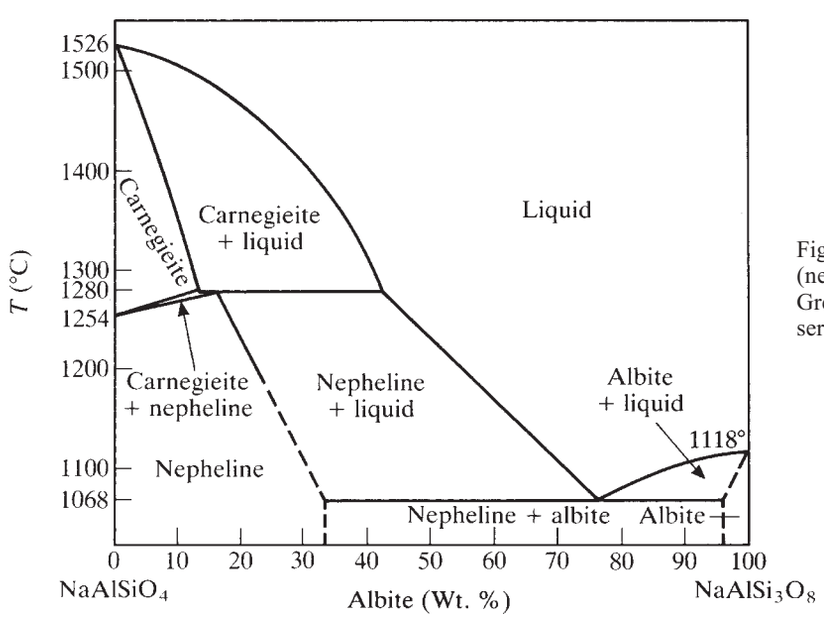


Fig. 235. Phase diagram of the system $NaAlSiO_4$ (nepheline, carnegeiete)–$NaAlSi_3O_8$ (albite) (after Greig, J.W. & Barth, T.F.W., 1938, *Amer. J. Sci.*, 5th series, **35A**, 93–112).

Downloaded from https://pubs.geoscienceworld.org/books/chapter-pdf/3762048/9780903056434_ch63.pdf
by guest

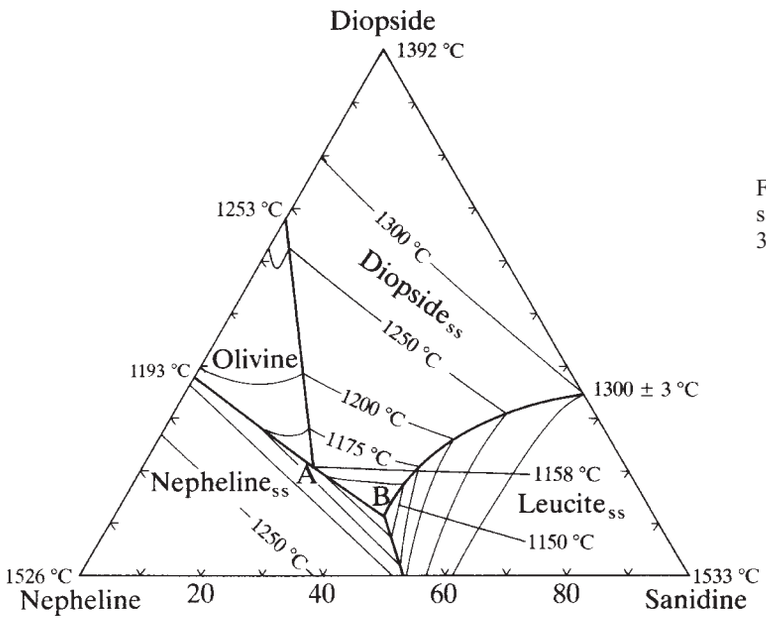


Fig. 236. Phase relations in the system diopside–nepheline–sanidine (after Sood, M.K. *et al*, 1970, *Can. Min.*, **10**, 380–94). A and B are at 1158ºC and 1120ºC, respectively.

Zoned nephelines are not uncommon and, although they are usually found in volcanic rocks, examples also occur in plutonic rocks. The zoning is marked by variations in both ω and ε refractive indices; birefringence changes are usually negligible. The zoning may be related to change in Al ↔ Fe^{3+} replacement or to Si or Ca content. Nephelines may exhibit a patchy extinction due to incipient unmixing of an originally homogeneous phase to a less silica-rich nepheline and alkali feldspar.

Distinguishing features

The main diagnostic features of nepheline are its low birefringence and poor cleavage (Fig. 237) which, together with its uniaxial character, distinguish it from the alkali feldspars; nepheline is readily soluble in HCl. Apatite and melilite have a similar range of birefringence, but both have higher refringence. Scapolites have higher refractive indices and those which have a high meionitic content have higher birefringence. Analcime and sodalite are isotropic, and leucite characteristically displays complex twinning. The difference in refringence and birefringence between nepheline and kalsilite is too small to distinguish in thin section between individual grains of the two minerals. Nepheline commonly contains minute inclusions whereas kalsilite is usually clear. The two can be distinguished by X-ray powder diffraction.

Paragenesis

Nepheline is the most characteristic mineral of the SiO_2-undersaturated igneous rocks and occurs as a primary phase in many plutonic, hypabyssal and volcanic rocks of extremely varied mineralogical and

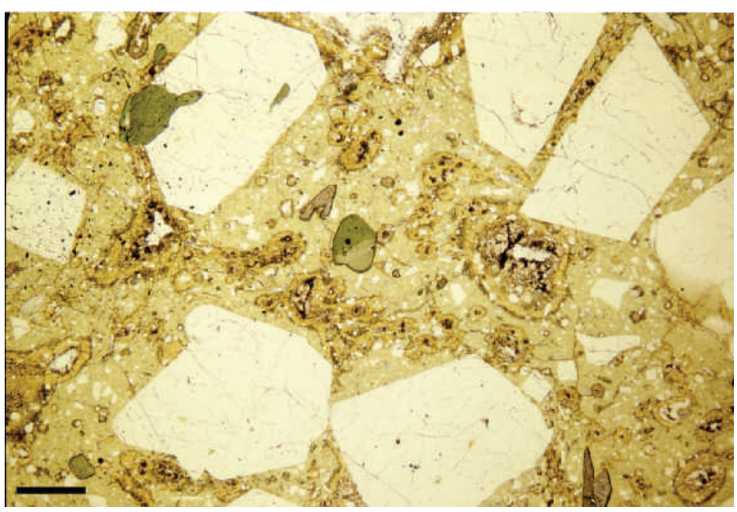


Fig. 237. Nepheline in phonolite, ejected block, Oldoinyo Lengai, Tanzania (crossed polars, scale bar 10 mm), showing nepheline phenocrysts with typical low birefringence and an approximation to hexagonal morphology (W.S. MacKenzie collection, courtesy of Pearson Education).

Downloaded from https://pubs.geoscienceworld.org/books/chapter-pdf/3762048/9780903056434_ch63.pdf
by guest

chemical composition. There are three common parageneses, as a primary phase of magmatic crystallization, as a product of metasomatism and as a result of reaction (contamination) of both basic and acid magmas with calcium-rich sediments.

Nepheline occurs in a wide variety of plutonic rocks ranging from nepheline syenites, pulaskite and foyaite in which it is associated with aegirine-augite and alkali amphiboles, through basic alkaline rocks, ijolite, jacupirangite and melteigite to ultrabasic alkaline rocks such as damkjernite in which associated phases include forsterite, spinel and perovskite. Where nepheline is an early-crystallizing constituent the mineral occurs in well formed crystals. In other rocks (e.g. malignite of the Poohbah Lake complex, Ontario) nepheline occurs as large poikilitic phenocrysts that crystallized from the intercumulus liquid and encloses earlier cumulus phases. Nepheline commonly occurs in textural intergrowths with K-feldspar, and less commonly with plagioclase. Nepheline of the latter intergrowths usually have a relatively high content of calcium and such intergrowths may originate by the partial replacement of the feldspar by nepheline. In most plutonic rocks, nepheline compositions are restricted to $Ne_{80}Ks_{20}$–$Ne_{75}Ks_{25}$.

In the alkaline basic rocks of small high-level intrusions, the earlier nephelines have a higher content of the Ne and Ks components and the later minerals a greater amount of Q (~$Ne_{80}K_{15}Q_5$ to $Ne_{65}Ks_5Q_{30}$). The more silica-rich nephelines lie in the nepheline + feldspar stability field and probably formed metastably from the melt under conditions of high fractionation during the final stages of crystallization.

Analcime occupying wedge-shaped interstices between plagioclase laths is a characteristic feature of many alkaline basic sills, but nepheline is considered to have been the first to crystallize, subsequently being altered to analcime during subsolidus interaction with deuteric and/or hydrothermal fluids. Nepheline phenocrysts rimmed by cancrinite and analcime occur in some tinguaites.

In volcanic rocks the composition of nephelines varies more widely than those of plutonic paragenesis; they are also more closely related to the host rock composition. Thus, compared with nephelines of plutonic paragenesis, they include more sodium- and more potassium-rich varieties. Furthermore many volcanic nephelines contain more than 4 Si per formula unit and the excess, calculated as SiO_2, may be as much as 6 wt.%. These differences reflect the fact that at higher temperatures the tolerance of both alkali sites of the structure is increased and permits greater departure from the $Na_3KAl_4Si_4O_{16}$ composition.

In addition to changes in the composition of nepheline by adjustment of the Na:K ratio, and by the replacement of Si by Al at lower crystallization temperatures, ion-exchange between nepheline and feldspar occurs at subsolidus temperatures.

Some nepheline-bearing rocks are metasomatic in origin and have arisen by the process of so-called nephelinization. In most examples of such rocks (e.g. in the Haliburton–Bancroft area, Ontario; Alnö, Sweden; and Fen, Norway) the nephelinization is due to the action of fluids derived from nepheline-bearing magmas on country rocks of varying compositions, i.e. limestones, amphibolites and granitic gneisses. Textural evidence of the nephelinization includes the presence of nepheline enclosing rounded and embayed grains of feldspar, and of vermicular nepheline–albite intergrowths.

Localized occurrences of nepheline-bearing basic rocks formed by the reaction of basic magmas with carbonate-rich sediments are found at the olivine gabbro–limestone contact, Camas Mor, Muck, and the dolerite–Chalk junction, Scawt Hill, Northern Ireland. At these localities the syntectic assemblages include nepheline dolerite, melilite-nepheline dolerite and theralite, rocks comparable mineralogically with nephelinite, melilite nephelinite and nepheline tephrite lavas.

Kalsilite occurs almost exclusively in extrusive rocks; it is an important constituent of the groundmass of potassium-rich lavas, e.g. the mafurites of south-west Uganda, in which the kalsilite, Ks_{98} in composition, may have formed by the reaction of phlogopite to kalsilite, forsterite, leucite and vapour. Kalsilite occurs as phenocrysts as well as being a groundmass constituent in lavas of Mt Nyiragongo, Congo. The phenocrysts display a 'perthitic' relationship of kalsilite and nepheline and have developed from an originally homogeneous K-rich high-temperature phase. Kalsilite in assemblages with K-feldspar, leucite and nosean/haüyne ± nepheline, is present in volcanic ejecta in tuffs of the Sabatini volcanic system, north-east Rome.

Kalsilite is rare in plutonic rocks but kalsilite, $Ks_{89}Ne_{11}$, occurs, with K-feldspar and biotite, as a primary magmatic mineral in syenites of the Yakshinsk pluton, USSR, and has been reported in a syenite from the Seward Peninsula, Alaska. Kalsilite–K-feldspar intergrowths formed by decomposition of leucite occur in the alkalic ultramafic Batbjerg intrusion, East Greenland.

Natural tetrakalsilite (panunzite) occurs in microperthitic association with nepheline in metamorphic ejecta, Monte Vesuvius. Trikalsilite is known only from a porphyritic lava of the Virunga volcanic field, Congo. It occurs in parallel intergrowths with kalsilite and/or nepheline.

Further reading

Bonaccorsi, E., Merlino, S. and Pasero, M. (1988) Trikalsilite: its structural relationships with nepheline and tetrakalsilite. *Neues Jahrbuch für Mineralogie, Monatshefte*, 559–567.

Brown, W.L. (Editor) (1984) *Feldspars and Feldspathoids. Structures, Properties and Occurrences*. NATO ASI Series C 137. D. Reidel Publishing Company, Dordrecht, 541 pp.

Capobianco, C. and Carpenter, M. (1989) Thermally induced changes in kalsilite ($KAlSiO_4$). *American Mineralogist*, **74**, 797–811.

Dollase, W.A. and Thomas, W.M. (1978) The crystal chemistry of silica-rich, alkali-deficient nephelines. *Contributions to Mineralogy and Petrology*, **66**, 311–318.

Downloaded from https://pubs.geoscienceworld.org/books/chapter-pdf/3762048/9780903056434_ch63.pdf
by guest

Ferry, J.M. and Blencoe, J.G. (1978) Subsolidus phase relations in the nepheline–kalsilite system at 0.5, 2.0 and 5.0 kbar. *American Mineralogist*, **63**, 1225–1240.

Henderson, C.M.B. and Gibb, F.G.F. (1983) Felsic mineral crystallization trends in differentiating alkaline basic magmas. *Contributions to Mineralogy and Petrology*, **84**, 355–364.

Henderson, C.M.B. and Roux, J. (1977) Inversions in sub-potassic nephelines. *Contributions to Mineralogy and Petrology*, **67**, 279–298.

Hovis, G.L. and Crelling, J.A. (2000) The effects of excess silica on immisciblity in the nepheline–kalsilite system. *American Journal of Science*, **300**, 238–249.

Palmer, D.C. (1994) Stuffed derivatives of the silica polymorphs. Pp. 83–122 in: *Silica: Physical Behavior, Geochemistry and Materials Applications*. Reviews in Mineralogy, **29**, Mineralogical Society of America, Washington, D.C.

Stebbins, J.F., Murdoch, J.B., Carmichael, I.S.E. and Pines, A. (1986) Defects and short-range order in nepheline group minerals: a silicon-29 nuclear magnetic resonance study. *Physics and Chemistry*, **13**, 371–381.

Tait, K.T., Sokolova, E., Hawthorne, F.C. and Khomyokov, A.P. (2003) The crystal chemistry of nepheline. *The Canadian Mineralogist*, **41**, 61–70.

Downloaded from https://pubs.geoscienceworld.org/books/chapter-pdf/3762048/9780903056434_ch63.pdf
by guest

Leucite $K[AlSi_2O_6]$

Tetragonal (Pseudocubic) (+)

n	1.508–1.511
δ	0.001
D (g/cm^3)	2.47–2.50
H	5½–6
Cleavage	{110} very poor
Twinning	{110} repeated
Colour	White or grey; colourless in thin section
Unit cell	α ~ 13.0 Å, *c* ~ 13.8 Å
	Z = 16; space group $I4_1/a$
Special features	Decomposed by HCl

Leucite occurs typically in potassium-rich basic lavas such as leucite nephelinite, leucite phonolite and leucite lamproite. If it occurs as phenocrysts it may show very weak birefringence and complex twinning. It is a major groundmass phase in leucitites and occurs also as microphenocrysts in many minettes. It is rarely found in rocks older than the Tertiary, probably due to its ready alteration to analcime. *Pseudoleucite* is a name applied to cloudy, granular or fibrous, radiating trapezohedral intergrowths of K-feldspar, nepheline and zeolites, possibly originally leucite.

Structure

At ordinary temperatures leucite is tetragonal (pseudo-cubic) with *a* ~13.0 and *c* ~13.8 Å; with increasing temperature the *a* axis expands and the *c* axis contracts, the processes culminating at about 630ºC at which point leucite is cubic with *a* ~13.4 Å. Both cubic and tetragonal leucite have 16($KAlSi_2O_6$) in the unit cell but whereas in the cubic cell oxygens occupy a set of 96-fold equivalent positions, in the tetragonal cell they are distributed among six sets of 16-fold positions. The structure is based on an (Si,Al)–O framework similar to that of analcime, $NaAlSi_2O_6.H_2O$, and pollucite, $Cs_3Na(Al_4Si_8O_{24}).nH_2O$. In all three minerals $(Si,Al)O_4$ tetrahedra are linked by sharing corners to form rings of six tetrahedra and rings of four tetrahedra. In cubic leucite the six- and four-membered rings are normal to triad and tetrad axes, respectively. The cubic cell is illustrated in Fig. 238, in which purple circles show the positions of K ions in leucite but also represent the positions of (Cs,Na) in pollucite and of water molecules in analcime. These 16 positions are in line with the centres of channels (formed by six-membered rings of tetrahedra) which run along four non-intersecting triad directions (Fig. 239). At ordinary temperatures the potassium ions in leucite are probably too small to fill the large cavities in the cubic structure, and the resultant collapse of the (Si,Al)–O framework about them can be correlated with the change to lower symmetry. The distortion of the structure involves the movement of potassium ions away from their normal positions, but the deviation decreases with increasing temperature and disappears at about 625ºC. Studies of the low-to-high-temperature leucite inversion show that the transformation is not a simple process but involves either the formation of a transient intermediate phase, or an Al,Si order–disorder relationship.

The variation in cell parameters with temperature has been measured to determine thermal contraction and phase changes with decreasing temperature (Fig. 240).

Chemistry

The compositions of natural leucites do not depart significantly from the ideal formula, $KAlSi_2O_6$; the Si/Al ratio approximates closely to 2:1 (Table 42) and the replacement of K by Na rarely exceeds 10%. Small amounts of ferric iron are present in most leucites but there is usually <1.0 wt.% Fe_2O_3. Leucite in lamproites can contain up to 3.0 wt.% Fe_2O_3 (~10 mol.% iron leucite, $KFe^{3+}Si_2O_6$).

Downloaded from https://pubs.geoscienceworld.org/books/chapter-pdf/3762474/9780903056434_ch64.pdf
by guest

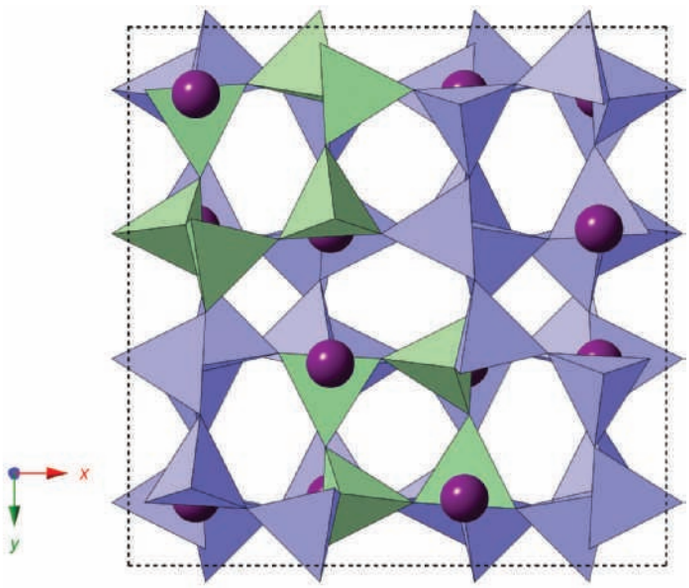


Fig. 238. Part of the structure of cubic leucite viewed along one of the cell axes. Most of the (Si,Al)−O tetrahedra are shown as lavender blue, but one ring of six and one of four tetrahedra are emphasized by being coloured green. The (Si,Al) is distributed randomly among the tetrahedral sites (CrystalMaker image).

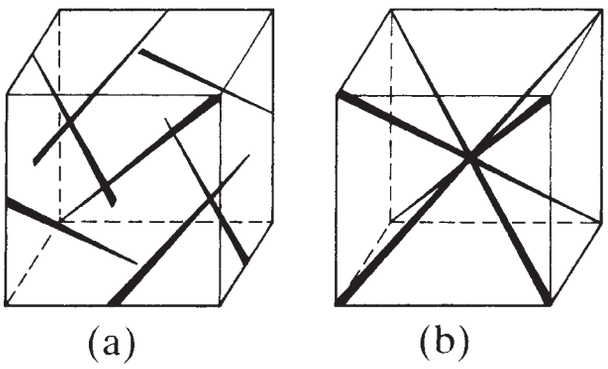


Fig. 239. Arrangement of channels parallel to triad axes, (a) non-intersecting as in leucite and analcime, (b) intersecting as in sodalite (after Barrer, R.M. & Falconer, J.D., 1956, *Proc. Roy. Soc.*, **A**, **236**, 227−49).

Pure leucite melts congruently at 1686ºC at 0.1 MPa. Potassium feldspar melts incongruently at 1150ºC to leucite and liquid, the composition of which is leucite 57.8%, silica 42.2%. In the system $KAlSi_3O_8$−H_2O, leucite is not stable above approximately 0.25 GPa P_{H_2O} when the temperature is 950ºC; above 0.25 GPa potassium feldspar melts to a liquid of hydrated feldspar composition (Fig. 241). In the system $NaAlSi_3O_8$–$KAlSi_3O_8$−H_2O the leucite field diminishes in size with increasing water pressure. Thus in the dry system at 0.1 MPa the leucite field extends to 51% $NaAlSi_3O_8$, at a P_{H_2O} of 0.1 GPa to 29%, and at 0.2 GPa to 5% $NaAlSi_3O_8$ (see Fig. 184, p. 272). The range of crystallization temperatures at 0.1 GPa and 0.2 GPa P_{H_2O} is 1135−1000ºC and 1000−960ºC, respectively. In the system $NaAlSiO_4$–$KAlSiO_4$–SiO_2, leucite is the first phase to crystallize from a wide range of potassium-rich liquids, and continues to a temperature of 1020ºC either as a single phase or with nepheline or

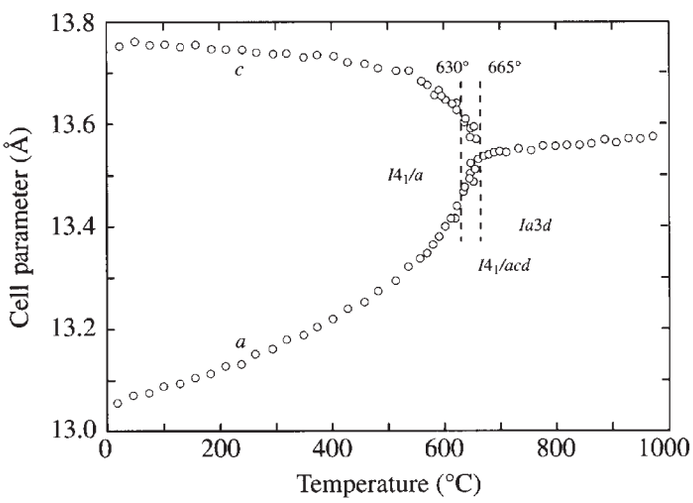


Fig. 240. The effect of temperature on the unit cell parameters of leucite, reflecting rotation of the framework around channel K cations and the decrease in *T*−O bond lengths (after Palmer *et al.*, 1989, *Phys. Chem. Min.*, **16**, 714−719).

Downloaded from https://pubs.geoscienceworld.org/books/chapter-pdf/3762474/9780903056434_ch64.pdf
by guest

Table 42. Leucite and pseudoleucite analyses.

	1	2	3		– Numbers of cations on the basis of 6 O – 1		2		3	
SiO_2	55.48	54.66	57.42	Si	2.016		1.992		2.034	
TiO_2	–	0.17	0.24	Al	0.959		0.995		0.912	
Al_2O_3	22.39	23.15	21.85	Ti	–		0.005		0.006	
Fe_2O_3	0.77	0.36	1.70	Fe^{3+}	0.021	0.99	0.010	1.02	0.045	0.98[b]
FeO	–	0.11	0.00	Mg	–		0.002		0.004	
MnO	–	0.01	0.03	Fe^{2+}	–		0.003		–	
MgO	–	0.04	0.07	Ca	0.001		0.004		0.007	
CaO	0.02	0.11	0.19	Na	0.005	0.99[a]	0.045	0.98	0.328	0.93
Na_2O	0.07	0.63	4.78	K	0.984		0.932		0.606	
K_2O	21.22	20.04	13.40							
H_2O+	–	0.36	0.27							
H_2O-	–	0.05	0.03							
Total	99.98	99.77	100.26							
n	1.509	–	–							

1 Leucite, lamproite dyke, Napoleon Bay, Baffin Island, Canada. (Hogarth, D.D., 1997. *Can. Min*., **35**, 53–78). Includes BaO 0.03.
2 Leucite, giant leucite aggregate, Congo (Sahama, Th.G., 1960, *J. Petrol*., **1**, 146–70). Includes P_2O_5 0.08.
3 Pseudoleucite, tinguaite, Montana, USA (Zies, E.G. & Chayes, F., 1960, *J. Petrol*., **1**, 86–98). Includes BaO 0.28.

[a] Includes Ba 0.007.
[b] Includes Mn 0.001, Ba 0.004.

potassium feldspar. At 1020ºC, leucite reacts with the liquid to give nepheline and K-feldspar.

The relationships in the system $NaAlSiO_4$–$KAlSiO_4$–SiO_2–H_2O at a P_{H_2O} of 0.1 GPa are shown in Fig. 242. Compared with the anhydrous system the liquidus temperatures are substantially lower and the stability field of leucite is considerably reduced, and disappears at 0.84 GPa. There is a well marked minimum (M) on the nepheline–feldspar boundary curve at about 750ºC, and the reaction point or peritectic (R) at a temperature of approximately 800ºC is more clearly defined than the corresponding reaction point (~1020ºC) in the anhydrous system. Early studies suggested an extensive solid solution between $KAlSi_2O_6$ and $NaAlSi_2O_6$ amounting to 28 wt.% $NaAlSi_2O_6$ at P_{H_2O} 0.1 GPa. It was also suggested that the solid solution of $AlSi_3O_8$ in leucite is extensive and amounts to up to 30 wt.% in the temperature range 800–1000ºC at P_{H_2O} 0.1 GPa, but later work suggested these compositions were metastable with a maximum of 4% $NaAlSi_2O_6$ in solid solution (Roux and Mackenzie, 1978).

Leucite has been prepared by heating analcime in a concentrated solution of KC1 at 200ºC, and the two phases are readily interconvertible by ion exchange:

$$NaAlSi_2O_6.H_2O + K^+_{(aq)} \rightleftharpoons KAlSi_2O_6 + Na^+_{(aq)} + H_2O$$

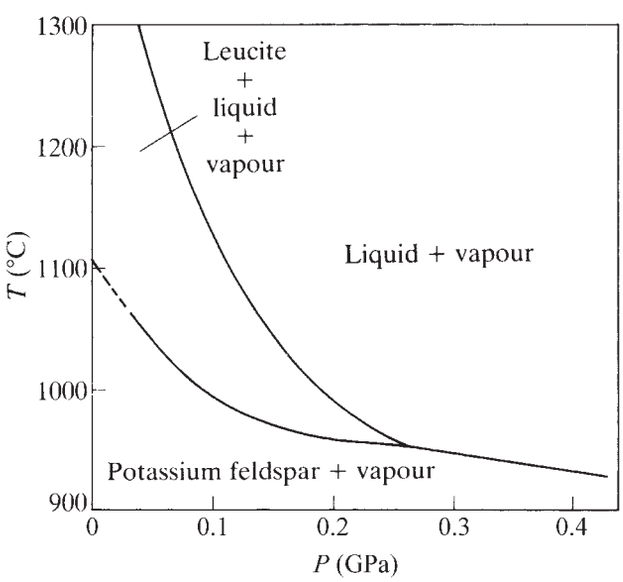


Fig. 241. Projection on the P–T plane of the system $KAlSi_3O_8$–H_2O (after Goranson, R.W., 1938, *Amer. J. Sci.*, 5th Ser., **35A**, 71–91).

Downloaded from https://pubs.geoscienceworld.org/books/chapter-pdf/3762474/9780903056434_ch64.pdf
by guest

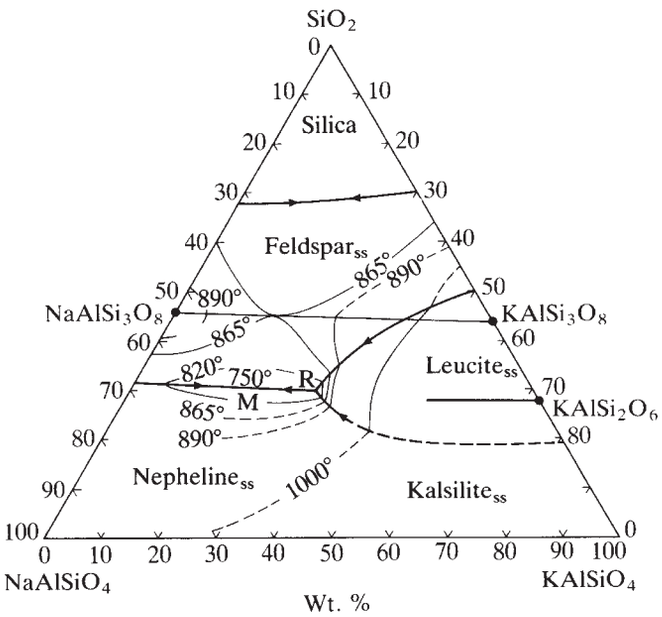


Fig. 242. Liquidus relationships in part of the system $NaAlSiO_4$–$KalSiO_4$–SiO_2–H_2O at P_{H_2O} 0.1 GPa projected on the anhydrous base of the tetrahedron. The curve labelled M is the minimum curve on the liquidus surface along the nepheline–feldspar boundary curve; R reaction point (after Fudali, R.F., 1963, *Bull. Geol. Soc. Amer.*, **74**, 1101–26).

It is a fast exchange reaction and in the $NaAlSiO_4$–$KAlSiO_4$–SiO_2–H_2O system, leucite–analcime solid solutions can develop from leucite crystals and hydrous glass; it is possible that primary leucites may be modified by subsolidus reaction with Na-rich hydrous glass of the matrix in natural rocks.

Some leucites crystallized from hydrous melts display a lamellar structure. The lamellae are not the result of inversion twinning but may represent an exsolved 'analcimic' or 'sodic leucite' phase.

The water-saturated phase relations of three Leucite Hill lavas (diopside phlogopite lamproites) show that leucite is stable to the highest pressures (0.1–0.3 GPa) in the least siliceous rocks, whereas leucite does not occur in the most siliceous at pressure greater than 50 MPa (Fig. 243). Leucite disappears from the phase assemblage of the wyomingite composition at temperatures below 900ºC. Leucite decreases in amount at pressures between 50 and 100 MPa when the crystallization of sanidine begins, and indicates a possible reaction relationship:

$$\text{leucite}_{ss} + \text{liquid} \rightleftharpoons \text{sanidine}_{ss}$$

At atmospheric pressure leucite and a silica-rich liquid are formed by the incongruent melting of sanidine.

At pressures between 6 and 10 GPa at 1000ºC, leucite breaks down to the assemblage kalsilite + kyanite + $K_2Si_4O_9$ and at pressure in excess of 10 GPa to kalsilite + $KAlSi_3O_8$ (hollandite type).

Optical and physical properties

The small range of ionic replacements shown by leucite is accompanied by correspondingly minor variations in its optical and physical properties; the refractive index is generally 1.510 ± 0.001 and the density 2.485 ± 0.015 g/cm^3. Though normally uniaxial, leucite may show a very small optic axial angle and weak anisotropy; except in very small crystals, it shows complex repeated twinning on {110} (Fig. 244) which in

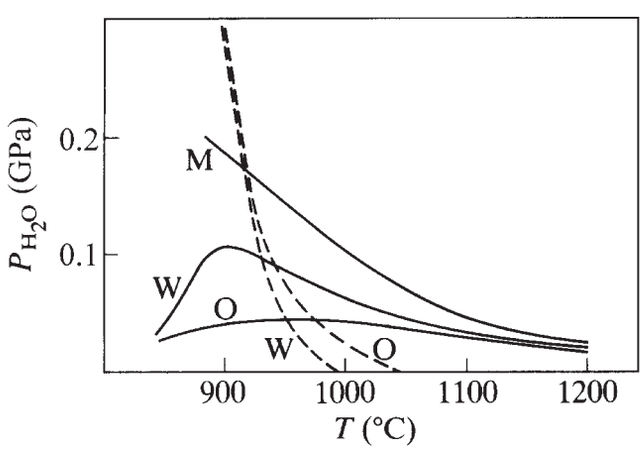


Fig. 243. A comparison of the stability curves for leucite (——) in the three Leucite Hill lavas (leucite stable below curve in each case) and sanidine (— — —) in wyomingite and orendite. M: madupite; W: Wyomingite; O: orendite (after Barton, M. & Hamilton, D.L., 1978, *Contrib. Mineral. Petrol.*, **66**, 41–9).

Downloaded from https://pubs.geoscienceworld.org/books/chapter-pdf/3762474/9780903056434_ch64.pdf
by guest

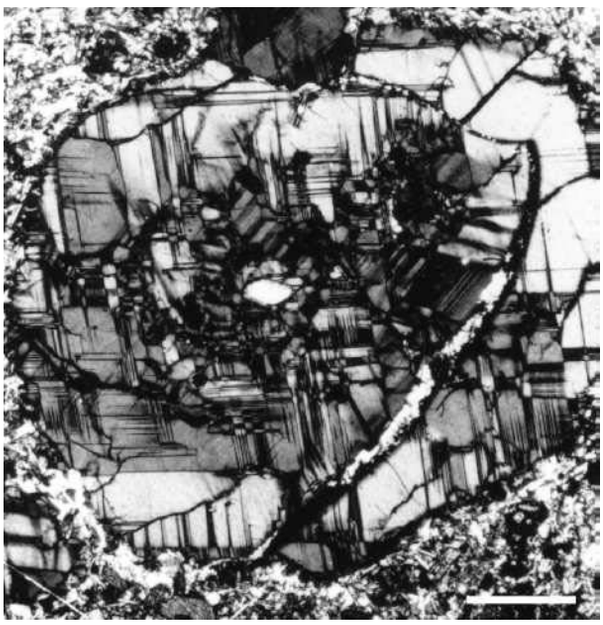


Fig. 244. Leucite (crossed polars, scale bar 0.4 mm) showing complex twinning (W.S. MacKenzie collection, courtesy of Pearson Education).

hand specimen may show as striations on the crystal faces. The striated faces are not coplanar but form re-entrant angles; these disappear on heating the crystal to the low-to-high-temperature inversion temperature. Leucite is usually developed as equant and often euhedral crystals with icositetrahedral {211}, or more rarely the dodecahedral {110}, habit, and exhibits octagonal outlines in thin section. Skeletal growths and inclusions, the latter arranged in regular, either radial or concentric patterns, are not uncommon.

Distinguishing features

Leucite is distinguished from analcime by the common presence of complex twinning, and by having a higher refractive index. These characteristics also serve to distinguish leucite from the sodalite group of minerals which may be pale blue. Even in the groundmass, leucite is slightly anisotropic compared with isotropic sodalite. Microcline has a higher birefringence and higher refringence.

Paragenesis

Leucite is a characteristic mineral of potassium-rich basic lavas such as leucite basanite, leucite tephrite, leucite–melilite basalt, leucite ankaramite, leucite nephelinite and phonolite, in which it is commonly the dominant phenocrystal or microphenocrystal constituent. Leucite is also an essential component of the potassium-rich ultrabasic rocks, ugandite (olivine + augite + leucite) and katungite (melilite + leucite glass with or without leucite). In diopside lamproite and sanidine lamproite, leucite occurs mainly as a matrix constituent. Leucite is also a major groundmass phase in leucitites and occurs as microphenocrysts in some minettes; associated phases include phlogopite, augite, apatite, olivine and sanidine. If leucite occurs as phenocrysts it shows weak birefringence and repeated twinning and may enclose small inclusions of pyroxene or glass arranged concentrically close to the crystal margins. Leucite occurs in volcanic ejecta in which it may be variously associated with kalsilite, K-feldspar, nepheline and häuyne/nosean.

In some volcanic rocks, leucite is replaced by an intergrowth of potassium-rich alkali feldspar and nepheline that shows a euhedral outline characteristic of sections through the icositetrahedral crystal form. In other examples leucites with well defined crystal boundaries are surrounded by a rim consisting mainly of alkali feldspar and nepheline. Such crystals are described as *pseudoleucite*. Less well defined intergrowths are present in some plutonic rocks, e.g. the borolanite of Assynt, Scotland. These intergrowths have rounded margins and merge with the other constituents of the syenite. Similarly the pseudoleucites of the plutonic alkali rocks of the Tangua complex, Brazil, have poorly developed morphologies in contrast to the 2–15 cm diameter pseudoleucites in the subvolcanic microsyenites of the same complex. The latter consist principally of microperthitic orthoclase and nepheline with minor amounts of analcime and other zeolites. Leucites in lamproites do not alter to "true pseudoleucite" but typically alter to pure potassium feldspar. Based on the phase diagram of the system nepheline–kalsilite–SiO_2, Bowen and Ellestad (1937) suggested that if a leucite of composition P (Fig. 245) reacts with the liquid of composition S, it should give solid products F (K-feldspar) and N (nepheline) with a bulk composition near point T to give pseudoleucite.

Downloaded from https://pubs.geoscienceworld.org/books/chapter-pdf/3762474/9780903056434_ch64.pdf
by guest

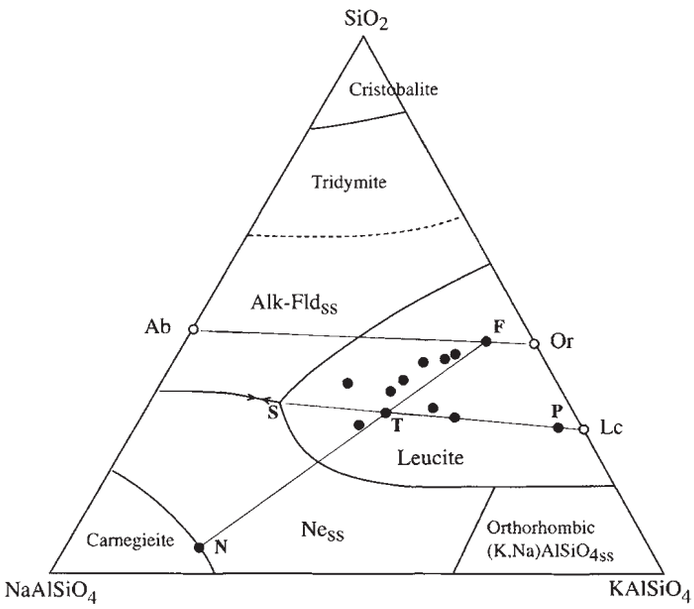


Fig. 245. Plot of pseudoleucite compositions in the system nepheline–kalsilite–SiO_2 (after Bowen, N.L. & Ellestadt, R.B., 1937, *Amer. Min.*, **29**, 409–15).

An alternative suggested origin for pseudoleucite is that it occurs by the breakdown of a sodium-rich leucite.

The general absence of leucite in plutonic rocks can be attributed to the role of P_{H_2O} in suppressing the leucite stability field. Furthermore, leucites crystallized under plutonic conditions and cooled in the presence of water would be affected by the breakdown reaction:

$$\text{leucite} \rightleftharpoons \text{kalsilite} + \text{potassium feldspar}$$

Leucite occurs in rocks of Tertiary or younger age and its absence in older rocks may result from its alteration to analcime. The exchange reaction (see above) has been demonstrated experimentally to have a very small activation energy and to take place very rapidly.

The solid solution of $NaAlSi_2O_6$ in leucite has been shown experimentally to be extensive at the temperatures at which it crystallizes, and moreover the amount of solid solution varies with the water vapour pressure. Most leucites contain only small amounts of sodium but sub-solidus alkali ion exchange could account for the development of more sodic leucites, a process that is not at variance with the experimental evidence that the $K \leftrightarrow Na$ substitution occurs very easily in the leucite structure. Analcimes containing 20% of the leucite component occurring as phenocrysts in basalt are known, and the possibility that some pseudoleucites may have arisen from the subsolidus breakdown of metastable potassium-rich analcime cannot be entirely discounted.

Further reading

Bowen, N.L and Ellestad, R.B. (1937) Leucite and pseudoleucite. *American Mineralogist*, **22**, 409–415.

Gittins, J., Fawcett, J.J., Brooks, C.K. and Rucklidge, J.C. (1980) Intergrowths of nepheline-potassium feldspar and kalsilite-potassium feldspar: a re-examination of the pseudoleucite problem. *Contributions to Mineralogy and Petrology*, **73**, 119–126.

Liu, L.-G. (1987) High pressure phase transitions of potassium aluminosilicates with emphasis on leucite. *Contributions to Mineralogy and Petrology*, **95**, 1–3.

Mitchell, R.H. and Bergman, S.C. (1991) *Petrology of Lamproites*. Plenum Press, New York. 447 pp.

Palmer, D.C., Salje, E.K.W. and Schmahl, W.W. (1989) Phase transitions in leucite: X-ray diffraction studies. *Physics and Chemistry of Minerals*, **16**, 714–719.

Roux, J. and MacKenzie, W.S. (1978) Sodium in leucite and its petrogenetic significance: an experimental study. *Bulletin de Minéralogie*, **101**, 478–484.

Taylor, D. and MacKenzie, W.S. (1975) A contribution to the pseudoleucite problem. *Contributions to Mineralogy and Petrology*, **49**, 321–333.

Downloaded from https://pubs.geoscienceworld.org/books/chapter-pdf/3762474/9780903056434_ch64.pdf
by guest

Sodalite Group

Sodalite	$Na_8[Al_6Si_6O_{24}]Cl_2$
Nosean	$Na_8[Al_6Si_6O_{24}]SO_4.H_2O$
Haüyne	$Na_6Ca_2Al_6Si_6O_{24}(SO_4)_2$
Lazurite	$Na_6Ca_2Al_6Si_6O_{24}S_2$

Cubic

	Sodalite	Nosean	Haüyne
n	1.48–1.49	1.48–1.49	1.49–1.51
D (g/cm^3)	2.27–2.33	2.30–2.40	2.44–2.50
H	5½–6	5½	5½–6
Cleavage	{110} poor	{110} poor	{110}
Twinning	{111}	{111}	{111}
Colour	Pale pink, grey, yellow, blue, green; colourless or very pale pink or blue in thin section	Grey, brown or blue; colourless or blue in thin section	White, grey, green or blue; colourless or pale blue in thin section
Unit cell	*a* 8.87–8.92 Å Z = 1; space group $P\bar{4}3n$	*a* 9.07–9.11 Å Z = 1; space group $P\bar{4}3m$	*a* 9.07–9.13 Å Z = 1; space group $P\bar{4}3n$
Special features	Readily gelatinized by acids		

Sodalite-group minerals occur in alkaline igneous rocks, typically associated with nepheline and other undersaturated silicates. Nosean and haüyne are both minerals found in phonolites and related rock types. Lazurite occurs in lapis lazuli in metamorphosed limestones at contacts with alkaline igneous rocks. All are cubic; they have low refractive indices and range in colour from white to blue in hand specimen.

Structure

The aluminosilicate framework of sodalite-group minerals is formed by the linkage of SiO_4 and $A1O_4$ tetrahedra in approximately equal numbers, each corner oxygen being shared by two tetrahedra; Al and Si are completely ordered. In sodalite, cage-like cubo-octahedral units are formed (Fig. 246) bounded by six rings of four tetrahedra parallel to {100} and eight rings of six tetrahedra parallel to {111}; the six-membered rings define a set of channels which intersect to form large cavities or cages. In sodalite the cavities are occupied by chloride ions and these are tetrahedrally coordinated by sodium ions.

In nosean single SO_4^{2-} groups replace the two Cl^- per cell of sodalite. Haüyne contains a greater proportion of SO_4^{2-} groups and also has some Ca replacing Na. In the lazurite variety, although Al and Si are completely ordered, there is positional disorder of the framework O atoms over two sets of sites, because the S^{2-} ions occupy different-size cages than SO_4^{2-}; the non-framework cations (Na,Ca) are disordered over three sets of sites. In the synthetic basic sodalite (hydrosodalite), $Na_8Al_6Si_6O_{24}(OH)_2.2H_2O$, although $(OH)^-$ can be regarded chemically as in the role of Cl^-, its oxygens, and those of the water molecules, do not lie on the body diagonals of the unit cell but are displaced randomly over 24 nearby sites. Requirements of space and hydrogen bonding limit the number of such oxygens to four per unit cell.

Chemistry

Sodalite differs from the other minerals of the group in containing chlorine as an essential constituent. There is little variation in the Na content beyond a slight substitution of Na by both K and Ca.

Downloaded from https://pubs.geoscienceworld.org/books/chapter-pdf/3762599/9780903056434_ch65.pdf
by guest

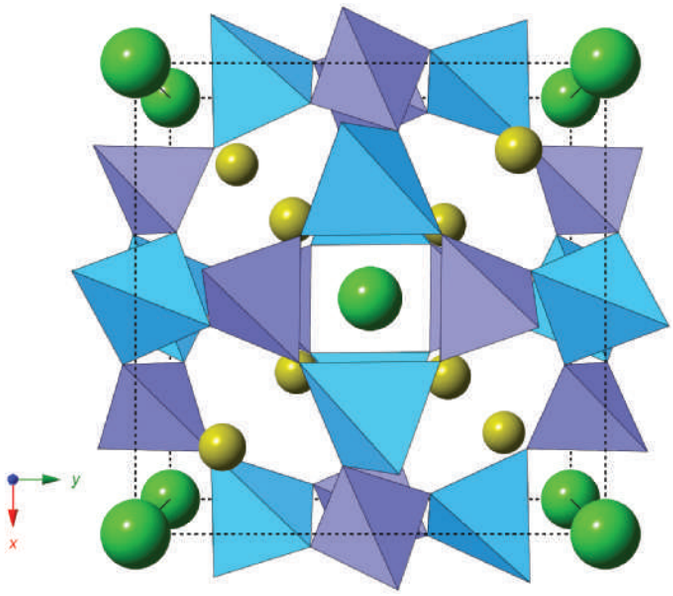


Fig. 246. Perspective view along one axis of the unit cell (dashed line) of the structure of sodalite (CrystalMaker image). Lavender: SiO_4 tetrahedra; pale blue: AlO_4 tetrahedra; green: Cl ions; gold: Na ions.

Sodalite may be synthesized easily by hydrothermal treatment of the component oxides together with NaCl, or by heating muscovite or kaolinite with NaCl at about 500ºC. Sodalite is stable at 400–800ºC at 0.1 GPa P_{H_2O} in the SiO_2-undersaturated portion of the $NaAlSiO_4$–SiO_2–NaCl–H_2O system. So-called 'basic' sodalite, in which the Cl is replaced by OH, can be produced from Na,Al silicate gels or from analcime. It is believed that for the synthesis of the hackmanite variety trace amounts of sulphur are necessary. Sodalite may alter to thomsonite, natrolite, gismondine, kaolinite or cancrinite.

Nosean has an ideal formula $Na_8Al_6Si_6O_{24}.SO_4.H_2O$ with a limited amount of substitution of Ca for Na permitting an increase in the sulphate anion groups over the ideal value of one per unit cell (Table 43): the upper limit is two sulphate ions, for compositions grading towards haüyne. The substitution of some K for Na may also occur. Small amounts of Fe^{3+} are present in some specimens, presumably substituting for Al though in some samples it may represent iron oxide impurities. The Ca content varies, and may amount to over 4% CaO. Sulphate is the dominant anion but it may be partially replaced by chloride. Nosean has been synthesized by hydrothermal treatment of a gel of composition $Na_2O.Al_2O_3.2SiO_2$ + Na_2SO_4, nosean being produced in the presence of an excess of alkali. The experimentally determined limits of solid solution on the sodalite–nosean join are shown in Fig. 247. Sodalite–nosean solid solutions are stable to a higher temperature than sodalite but their immiscibility increases with pressure (at 1100ºC and 0.5 GPa, coexisting phases contain ~5 and ~30% of the nosean component). Nosean may be altered to cancrinite and calcite.

Haüyne differs chemically from nosean in having a much higher proportion of Ca and in being richer in the sulphate radical. Some haüynes have minor replacement of Al by Fe^{3+}, and the substitution of K for Na is more

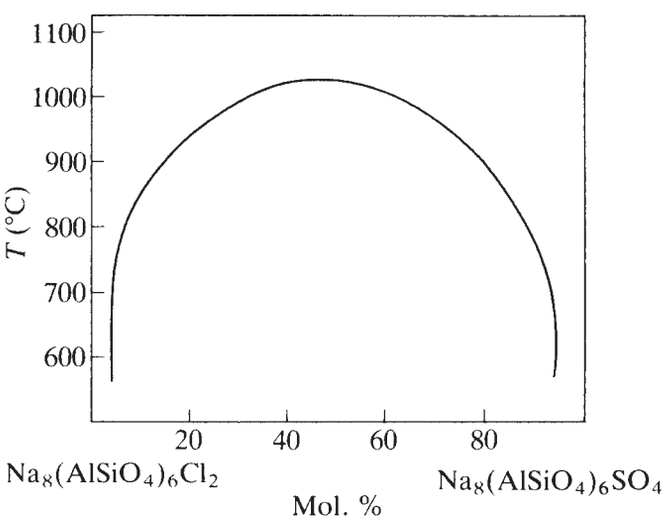


Fig. 247. The experimentally determined sodalite–nosean solvus (after Tomisaka, T. & Eugster, H.P., 1968, *Mineral. J.*, **5**, 249–75).

Downloaded from https://pubs.geoscienceworld.org/books/chapter-pdf/3762599/9780903056434_ch65.pdf
by guest

Table 43. Sodalite, nosean and haüyne analyses.

	1		2		3		4		5		6	
SiO_2	37.61		37.95		35.94		34.42		33.00		36.37	
TiO_2	n.d.		–		0.03		tr.		–		0.05	
Al_2O_3	29.60		31.42		23.94		26.16		27.68		24.22	
Fe_2O_3	0.22		0.39		2.79		0.36		–		<0.05	
MnO	tr.		0.08		0.01		tr.		0.0		n.d.	
MgO	0.04		–		0.39		0.15		0.0		0.39	
CaO	0.57		–		3.43		8.00		8.25		5.06	
Na_2O	23.64		24.16		16.56		16.07		16.99		18.81	
K_2O	0.05		0.05		2.59		0.56		0.28		0.97	
H_2O+	0.69		–		4.24		0.51		–		1.90	
CO_2	1.43		–		–		0.90		–		1.70	
SO_3	1.07		0.09		8.79		12.19		14.06[d]		7.31	
S	–		–		–		–		–		1.18	
Cl	6.69		7.33		1.34		0.64		0.42		1.19	
$-O \equiv Cl,S$	1.42		1.65		0.30		0.14		0.09		0.86	
Total	100.19		99.82		100.16		99.82		100.64		98.54	
n	1.486				–		1.500		–		1.504	
D	2.31				–		2.43		–		–	
a (Å)	8.877		8.877		–		9.071		–		9.088	
	Numbers of ions on the basis of 21 O in the $3\,Al_2O_3.6\,SiO_2$ framework											
Si	6.179	11.94	6.062	11.98	6.428	11.86[b]	6.258	11.91	6.029	11.99	6.604	11.80[f]
Al	5.733		5.917		5.048		5.607		5.962		5.185	
Fe^{3+}	0.027		–		0.376		0.049		–		–	
Mg	0.010	7.65	–	7.56[a]	0.104	7.10[c]	0.040	7.39	–	7.71[e]	0.106	7.994
Na	7.531		7.483		5.743		5.665		6.018		6.623	
Ca	0.100		–		0.657		1.558		1.615		0.984	
K	0.010		0.010		0.591		0.130		0.066		0.225	
Cl	1.863	2.00	1.984	1.59	0.406	1.59	0.197	1.86	0.129	2.06	0.367	1.776
S	–		–		–		–		–		0.402	
SO_3	0.132		0.010		1.180		1.663		1.928		0.996	

1 Blue sodalite, sodalite-bearing nepheline syenite pegmatite, Laven, Langesundsfjord, Norway (Taylor, D., 1967, *Contrib. Mineral. Petrol*., **16**, 172–88).
2 Hackmanite, nepheline syenite, Mont St-Hilaire, Quebec, Canada (Peterson, R.C., 1983, *Can. Min*., **21**, 549–52). Includes FeO 0.39%.
3 Nosean, miaskitic phonolite, Aldis, Cantal, France (Brousse, R., Varet, J. & Bizouard, H., 1969, *Contrib. Mineral. Petrol*., **22**, 169–84). Includes FeO 0.04, P_2O_5 0.03, H_2O 0.34%.
4 Pale blue haüyne, haüyne-feldspar ejectamenta, Thelenberg (Laacher See volcanics), Germany (Taylor, D., 1967, *Contrib. Mineral. Petrol*., **16**, 172–88).
5 Pale blue lazurite, calcite-saponite-lazurite lapis lazuli, Italian Mountain, Colorado, USA (Hogarth, D.D. & Griffin, W.L., 1980, *Can. Min*., **18**, 59–70). Includes FeO 0.05%.
6 Sky-blue lazurite, diopsidic marble, Baffin Island (Hogarth, D.D. & Griffin, W.L., 1976, *Lithos*, **9**, 39–54).

[a] Includes Fe^{2+} 0.052.
[b] Includes Ti 0.004.
[c] Includes Fe^{2+} 0.006.
[d] All S reported as SO_3.
[e] Includes Fe^{2+} 0.008.
[f] Includes Ti 0.006.

important in haüyne and nosean than in sodalite, probably due to their relatively open structure. Chloride ions may partially replace the sulphate ion, and as with nosean, haüyne can contain clathrated CO_2 molecules in addition to H_2O and minor CO_3^{2-}.

Lazurite is the dominant sodalite-group mineral in lapis lazuli, ultramarine being a synonym which is generally applied specifically to synthetic materials. Natural lazurite contains both sulphide and sulphate ions in addition to calcium and sodium. For synthetic ultramarines the general formula is $M_8Al_6Si_6O_{24}S_x$, where M represents alkalis or alkaline earths and $x = 1–2$.

If analyses of sodalite-group minerals are plotted on a triangular grid $CaO–Na_2O–K_2O$, each mineral species plots in a specific region limited by the dashed boundaries in Fig. 248. The maximum CaO content in nosean is 4.5 mol%. Lazurite may be defined as sulphur-bearing haüyne (Fig. 249).

Downloaded from https://pubs.geoscienceworld.org/books/chapter-pdf/3762599/9780903056434_ch65.pdf
by guest

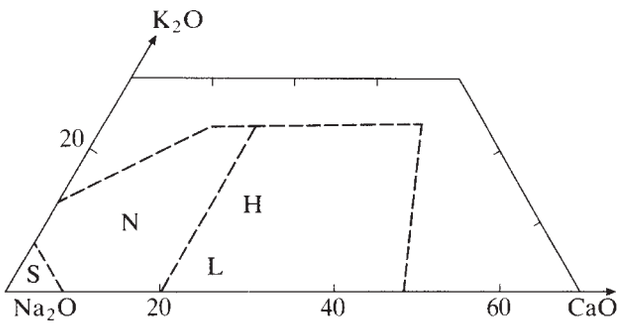


Fig. 248. Compositions of the sodalite group recalculated to cation percentage (after Lessing, P. & Grout, C.H., 1971, *Amer. Min.*, **56**, 1096–100). S: sodalite; N: nosean; H: haüyne; L: lazurite.

Optical and physical properties

The minerals of the sodalite group are isotropic or, rarely, weakly anisotropic: nosean and haüyne may show weak birefringence in samples containing inclusions. The refractive index is lowest for sodalite, increases with the introduction of sulphate in nosean and rises slightly higher for haüyne, but for all the minerals of the group the refractive index is comparatively low and considerably less than that of the standard mounting medium. The densities of minerals of the group rise from sodalite (2.27 to 2.33 g/cm^3) to haüyne (2.44 to 2.50 g/cm^3); for nosean the lighter varieties (2.30 g/cm^3) are those poor in Ca while those with around 4% CaO have a higher density.

The colour of the minerals of the sodalite group is extremely variable, ranging from colourless or white, to grey, yellow, green, brown, pink or most typically blue. Blue, green, red and violet ultramarines have been synthesized, and for these the depth of colour is considered to be related mainly to the sulphur content: this has been confirmed for natural lazurites. In sodalite itself, however, the blue colour does not appear to be directly related to the chemistry of its major constituents. Hackmanite is a variety of sodalite which has a distinct pink tinge when freshly fractured, but whose colour fades on exposure to light and returns when the mineral is kept in the dark for a few weeks, or is bombarded with X-rays. This phenomenon of fluorescence is probably related to trace amounts of sodium sulphide and sodium polysulphide.

Distinguishing features

The X-ray diffraction patterns are distinctive but other methods can in some circumstances be useful. The minerals of the sodalite group may be distinguished by their isotropic character and by their refractive index being considerably less than that of the standard mounting medium. Fluorite has an even lower refractive index and a much better cleavage and leucite generally has weakly birefringent twins. Within the sodalite group, chemical tests may differentiate the minerals: if the mineral on a glass slide is treated with nitric acid and the solution is allowed to evaporate slowly, the formation of cubic crystals of NaCl indicates sodalite, whereas monoclinic needles of gypsum indicate haüyne. If neither product is formed before the addition of $CaCl_2$, and both appear after it is added, nosean is indicated. Ultra-violet light or cathodoluminescence may be helpful by causing the sodalite to fluoresce a distinctive orange-red colour, thus distinguishing it from nepheline and feldspar.

Paragenesis

Sodalite commonly occurs in nepheline syenites and associated rock types (Table 43, analysis 1). It is typically associated with nepheline, cancrinite, melanite garnet and fluorite. Sodalite may also occur in metasomatized calcareous rocks at alkaline igneous contacts. The hackmanite variety is also found in

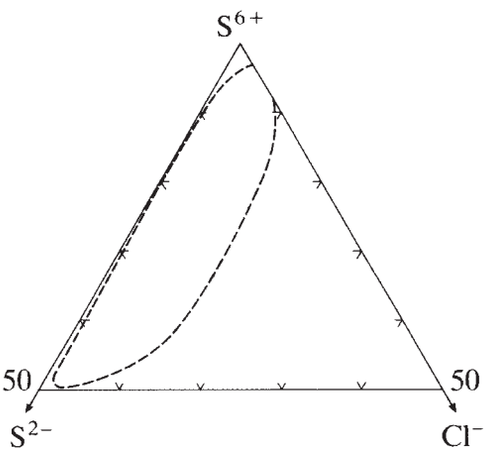


Fig. 249. Lazurite compositions plotted on an atomic basis with respect to S^{6+}, S^{2-} and Cl^- (after Hogarth, D.D. & Griffin, W.L., 1976, *Lithos*, **9**, 39–54).

Downloaded from https://pubs.geoscienceworld.org/books/chapter-pdf/3762599/9780903056434_ch65.pdf
by guest

nepheline syenites and related rocks: at Magnet Cove, Arkansas, it occurs surrounded by a mottled zone of blue sodalite in irregular lenses in a tinguaite dyke. It is well known also from the Kola peninsula and from the nepheline-syenites of the Bancroft area, Ontario.

Nosean occurs chiefly in phonolites and related undersaturated volcanic rocks and in volcanic bombs and ejected blocks. The nosean phonolite of the Wolf Rock, Cornwall, UK, is well known for its abundant zoned phenocrysts of nosean, which have a clear rim and a centre turbid with iron minerals. It is not common in other than volcanic rocks, though a series of nosean-bearing aegirine-augite syenites and porphyries have been reported.

Haüyne is found in phonolites and related rock types: the ejected blocks in the 'peperino' of the Alban Hills provide fine examples of white haüyne, with leucite and melilite. Haüyne also occurs in some monticellite alnöites and nepheline alnöites, and it is common in the volcanic rocks of the Eifel district of Germany (Table 43, analysis 4).

Lazurite occurs in lapis lazuli in metamorphosed limestone and at the contacts of pegmatites with limestone.

Further reading

Antao, M. and Hassan, I. (2002) Thermal analysis of sodalite, tugtupite, danalite and helvite. *The Canadian Mineralogist*, **40**, 163–172.

Bellatreccia, F., Della Ventura, G., Piccinini, M., Cavallo, A. and Brilli, M. (2009) H_2O and CO_2 in minerals of the haüyne-sodalite group: an FTIR spectroscopy study. *Mineralogical Magazine*, **73**, 399–413.

Burragato, F., Maras, A. and Rossi, A. (1982) The sodalite group minerals in the volcanic areas of Latium. *Neues Jahrbuch für Mineralogie, Monatshefte*, 433–445.

Fleet, M.E., Liu, X., Harmer, S.L. and Nesbitt, H.W. (2005) Chemical state of sulfur in natural and synthetic lazurite by S *K*-edge XANES and X-ray photoelectron spectroscopy. *The Canadian Mineralogist*, **43**, 1589–1603.

Henderson, C.M.B., Pendlebury, D. and Foland, K.A. (1989) Mineralogy and petrology of the Red Hill alkaline igneous complex, New Hampshire, U.S.A. *Journal of Petrology*, **30**, 627–666.

Hogarth, D.D and Griffin, W.L. (1976) New data on lazurite. *Lithos*, **9**, 39–54.

Kondo, D. and Beaton, D. (2009) Hackmanite/sodalite from Myanmar and Afghanistan. *Gems & Gemology*, **45**, 38–43.

Taylor, D. (1967) The sodalite group of minerals. *Contributions to Mineralogy and Petrology*, **16**, 172–188.

Zaitsev, A.N., Zaitseva, O.A., Buyko, A.K., Keller, J., Klaudius, J. and Zolotarev, A.A. (2009) Gem-quality yellow-green haüyne from Oldoinyo Lengai volcano, northern Tanzania. *Gems & Gemology*, **45**, 200–203.

Downloaded from https://pubs.geoscienceworld.org/books/chapter-pdf/3762599/9780903056434_ch65.pdf
by guest

Hexagonal (−)

ε	1.486−1.543
ω	1.491−1.528
δ	0.005−0.020
D (g/cm^3)	2.32−2.65
H	5−6
Cleavage	{10$\bar{1}$0} perfect, {0001} poor
Twinning	Lamellar, rare
Colour	Colourless, white, light blue to light greyish blue, honey-yellow, reddish; colourless in thin section
Unit cell	a ~ 12.6−12.9 Å, c ~ 5.1−5.3 Å Z = 1. Space group $P6_3$
Special features	Gelatinizes in acids; carbonate-rich varieties effervesce in HCl

The cancrinite group contains several mineral species the structures of which are based upon the stacking of six-membered rings of $(Si,Al)O_4$ tetrahedra to form 'cancrinite cages'. The more commonly occurring minerals are members of the cancrinite–vishnevite solid solution series, and in these there are also twelve-membered rings forming parallel channels. The cages contain mainly (Na,Ca) and water molecules and the wide channels house (Na,Ca) and, CO_3 in cancrinite, and SO_4 in vishnevite. Minerals of the cancrinite–vishnevite series occur typically in nepheline syenites and related alkaline plutonic rocks. They have low refractive indices and are colourless in thin section.

Structure

The structures of the cancrinite−vishnevite minerals are characterized by six-membered rings of alternating $A1O_4$ and SiO_4 tetrahedra, linked laterally and above one another to form a three-dimensional framework with composition $SiAlO_4$. The stacking sequence of the rings in the z direction varies in different members of the group. In cancrinite and vishnevite the structure has a stacking sequence ABAB resulting in a c ~ 5.1 Å repeat; the sequence ABCABC is characteristic of the sodalite group. The ABAB sequence generates wide channels parallel to z formed by twelve-membered rings (Fig. 250a,b), and columns of base-sharing 'cancrinite cages' (Fig. 250c). The wide channels contain carbonate groups in cancrinite and sulphate groups in vishnevite, and the 'cancrinite cages' contain alternating (Na,Ca) cations and water molecules. The pores in the framework may also host other anions and molecules such as Cl^- and CO_2.

There is a complete solid solution series between cancrinite and vishnevite, with intermediate compositions being termed sulphatic cancrinite and carbonatic vishnevite. The substitution of SO_4^{2-} for CO_3^{2-} groups along the series is correlated with the entry of K in the channels: if (Na,Ca) and K are nearly equal there is the possibility of doubled a parameters and complex stacking sequencies.

Chemistry

The ideal formula of cancrinite, the Ca and CO_3 member of the series, is $Ca_2Na_6Al_6Si_6O_{24}(CO_3)_2.2H_2O$; that of the sodium-rich vishnevite is $Na_8Al_6Si_6O_{24}SO_4.2H_2O$. The replacement of CO_3^{2-} by SO_4^{2-} on a 1:1 basis has not been established in natural minerals and in general the sulphatic minerals contain a smaller number of CO_3 + SO_4 anions per formula unit than the carbonate members of the series (Table 44, anals 1, 2). A complete solid-solution series between cancrinite and vishnevite can be visualized as consisting of a mixture of CO_3^{2-} and SO_4^{2-} cells; the broken line in Fig. 251 represents the ideal variation for the series. Compositions that lie to the left of the line indicate anion deficiencies in excess of those for ideal solutions. As noted in the structural section, stacking sequences within the cancrinite group are not restricted to the simple ABAB repetition of the cancrinite−vishnevite series. In the majority of cancrinites, chloride is present in minor amounts. In some members of the group,

Downloaded from https://pubs.geoscienceworld.org/books/chapter-pdf/3762670/9780903056434_ch66.pdf
by guest

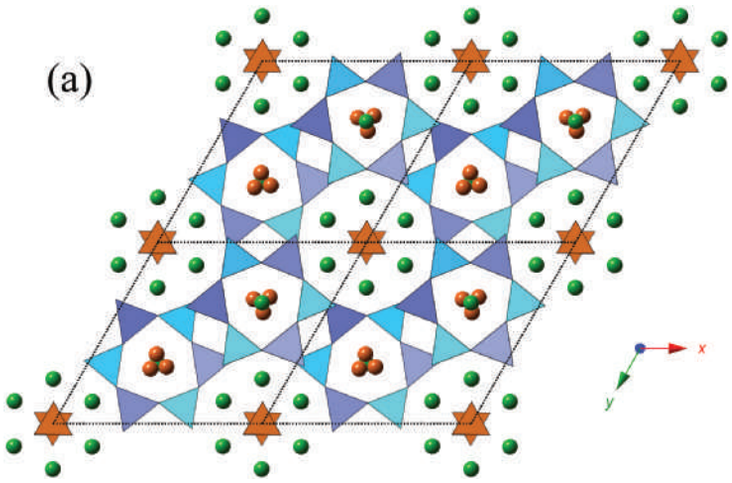
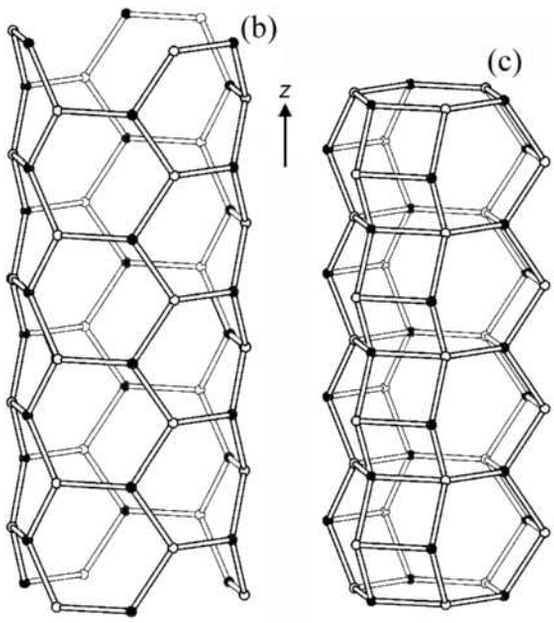


Fig. 250. (a) A section of the structure of cancrinite projection on (0001) showing the twelve-membered rings of (Si,Al) tetrahedra that form channels parallel to *z*, and six-membered rings that form columns (also parallel to *z*) of 'cancrinite cages'. The tetrahedra in the 'layer' of structure shown all point downwards. (CrystalMaker image). Dark blue: Si−O tetrahedra; light blue: Al−O tetrahedra; green circles: (Na,Ca); orange circle: H_2O or (OH); overlapping orange triangles: (CO_3 groups).



(b) Schematic model of a wide channel in the structure of cancrinite that houses carbonate groups and (Na,Ca). In this style of model, tetrahedral sites for Si and Al are shown by filled and unfilled circles. Linkages between tetrahedra are also indicated, but for simplicity the bridging oxygens are omitted.

(c) Schematic model of a column of 'cancrinite cages' which houses (Na,Ca) cations and water molecules (Deer *et al*., 2004, *Rock Forming Minerals, Volume 4B: Silica Minerals*. Geological Society, London).

however, chloride is the principal channel anion, e.g. davyne (Table 44, analysis 3).

Cancrinites of various compositions have been synthesized in the P_{H_2O}−T range between 60 and 200 MPa and 500 and 750ºC, respectively. A compound with the formula $Na_8[Al_6Si_6O_{24}]CO_3$, synthesized at 600ºC, is hexagonal with a ~12.7 Å, c ~5.2 Å, comparable with natural cancrinites; at higher temperatures the synthetic product is cubic (a 9.02 Å) and is similar in structure to nosean (a 9.05 Å) (p. 340).

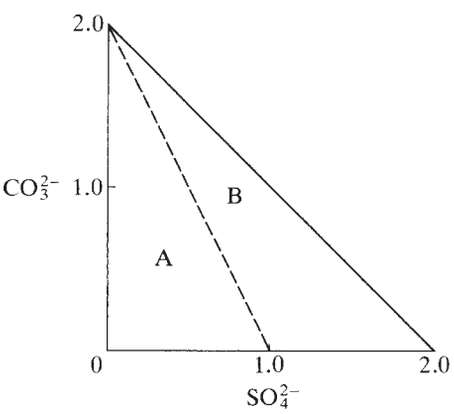


Fig. 251. The relationship between the number of CO_3^{2-} and SO_4^{2-} groups per unit cell (relative to cancrinite) for cancrinite minerals. Broken line shows the ideal range in composition for members of the cancrinite–vishnevite solid solution series. Specimens to the left (area A) have greater non-stoichiometry than is ideal; those to the right (area B) are cancrinite-type minerals with complex stacking sequences (after Hassan, I. & Grundy, H.D., 1984, *Can. Min*., **22**, 333−40).

Downloaded from https://pubs.geoscienceworld.org/books/chapter-pdf/3762670/9780903056434_ch66.pdf
by guest

Table 44. Cancrinite–vishnevite analyses.

	1	2	3		Numbers of ions on the basis of 12 (Si,Al) 1		2		3	
SiO_2	34.16	34.53	32.50	Si	6.025		5.980		5.81	
Al_2O_3	28.75	29.06	29.40	Al	5.975		5.931[a]		6.14	
CaO	10.10	1.48	10.40	Na	5.477	}	5.543	}	5.16	}
Na_2O	16.02	16.51	14.90	Ca	1.908	7.42	0.275	6.97[b]	1.99	7.19
K_2O	0.14	5.11	0.17	K	0.031	}	1.129	}	0.04	}
H_2O+	3.43	5.35	1.50	H_2O	2.088		3.876		1.79	
H_2O-	0.12	1.36	–	C	1.613	}	0.061	}	–	}
CO_2	6.70	0.26	–	S	–	1.64	0.652	0.99	0.89	2.62
SO_3	–	5.02	6.60	Cl	0.036	}	0.026	}	1.73	}
Cl	0.12	0.09	5.70							
	99.56	99.54	101.17							
$-O \equiv Cl,F$	0.04	0.02	1.36	100C/(C+S)	100		8.5		–	
Total	99.52	99.52	99.81							

1 Cancrinite, in calcite-garnet-diopside-nepheline skarn assemblage, York River, Bancroft, Ontario, Canada (Foit, F.F. Jr *et al*., 1973, *Can. Min*., **11**, 940–51). Includes F 0.02.
2 Vishnevite, Vishnevy-Ilmen Mountains, Southern Urals, Russia (Belyankin, D.S., 1944, *Dokl. Nauk SSSR*, **42**, 304–6, 201–7). Includes Fe_2O_3 0.19, MgO 0.10.
3 Cancrinite (davyne), metabasalt, St John's Island, Red Sea, Egypt (Takla, M.A. & Griffin, W.L., 1980, *Neues Jahrb. Min., Monat*., 345–52). Probe analysis; H_2O calculated.

[a] Includes Fe^{3+} 0.088.
[b] Includes Mg 0.023.

Optical and physical properties

The optical properties of the cancrinite–vishnevite series show a fair correlation with the varying contents of CO_3 and SO_4, both the ε and ω indices being lower in the more sulphatic varieties. The rate of decrease of the ω index with increasing content of the vishnevite component is greater than that of the ε index, and the birefringence varies from about 0.025 for cancrinite to between 0.002 to 0.004 for vishnevite. Anomalous biaxial optical characters are shown by some cancrinites; the chlorine-rich cancrinite, davyne, is optically positive.

Distinguishing features

The carbonate-rich varieties of the cancrinite–vishnevite series are distinguished from nepheline by their stronger birefringence, from scapolite by their different cleavage and lower refractive indices, and from calcite by their much weaker birefringence. Cancrinite may be confused with basal and near-basal sections of muscovite, but is normally distinguished by its uniaxial optical character, as it is also from biaxial zeolites. Vishnevite has lower refractive indices and better cleavage than nepheline.

Paragenesis

Members of the cancrinite–vishnevite series are common constituents of many nepheline syenites and nepheline syenite pegmatites. The cancrinite may occur as individual grains formed during the late stages of crystallization, or as reaction rims between nepheline and calcite. The sequence nepheline → cancrinite → calcite is usually interpreted as a normal magmatic reaction series in which cancrinite has formed by reaction between the early nepheline and CO_2-rich residual liquids. This interpretation is consistent with the phase relations in the synthetic system nepheline–calcite in which cancrinite occurs as a binary compound and melts incongruently, under a P_{CO_2} of 10 MPa, to nepheline and liquid. Cancrinite-group minerals may be found also in some contact metasomatic replacement deposits between alkaline rocks and limestone or marble. Such skarn assemblages consist typically of calcite, garnet, diopside, nepheline and cancrinite, the cancrinite being a product of the reaction between calcite and nepheline. Thus davyne (previously reported as cancrinite or microsommite) occurs in replacement veins cutting metabasalts on Zabargad (St John's Island), in the Red Sea (Table 44, analysis 3). Several of the rarer species of the cancrinite group occur in lithic blocks within fall-out deposits from phreatomagmatic eruptions, as in the Latium district of Italy.

Further reading

Ballirano, P., Bonaccorsi, E., Merlino, S. and Maras, A. (1998) Carbonate groups in davyne: structural and crystal-chemical considerations. *The Canadian Mineralogist*, **36**, 1285–1292.

Bonaccorsi, E and Merlino, S. (2005) Modular microporous minerals: cancrinite-davyne group and C-S-H phases. Pp. 241–290 in: *Micro- and Mesoporous Mineral Phases* (G. Ferraris and S.

Downloaded from https://pubs.geoscienceworld.org/books/chapter-pdf/3762670/9780903056434_ch66.pdf
by guest

Merlino, editors). Reviews in Mineralogy and Geochemistry, **57**, Mineralogical Society of America & Geochemical Society, Washington, D.C.

Cámara, F., Bellatreccia, F., Della Ventura, G., Mottana, A., Bindi, L., Gunther, M.E. and Sebastiani, M. (2010) Fantappièite, a new mineral of the cancrinite-sodalite group with a 33-layer stacking sequence; occurrence and crystal structure. *American Mineralogist*, **95**, 472−480.

DellaVentura, G., Bellatreccia, F., Parodi, G.C., Cámara, F. and Piccinini, M. (2007) Single crystal FTIR and X-ray study of vishnevite, ideally $[Na_6(SO_4)][Na_2(H_2O)_2](Si_6Al_6O_{24})$. *American Mineralogist*, **92**, 713−721.

Edgar, A.D. and Burley, B.J. (1963) Studies on cancrinites. I. Polymorphism in sodium carbonate rich cancrinite-natrodavyne. *The Canadian Mineralogist*, **7**, 631−642.

Hassan, I. and Grundy, H.D. (1984) The character of the cancrinite–vishnevite solid solution series. *The Canadian Mineralogist*, **22**, 333−340.

Downloaded from https://pubs.geoscienceworld.org/books/chapter-pdf/3762670/9780903056434_ch66.pdf
by guest

Tetragonal (−)

	Marialite $Na_4[Al_3Si_9O_{24}]Cl$	Meionite $Ca_4[Al_6Si_6O_{24}]CO_3$
ε	1.540−1.541	1.556−1.564
ω	1.546−1.550	1.590−1.600
δ	0.004−0.005	0.024−0.034
D (g/cm^3)	2.50−2.62	2.74−2.78
H	5−6	5−6
Cleavage	{100}, {110} good	{100}, {110} good
Colour	Colourless, white, bluish grey, pale greenish yellow, yellow, pink, violet, brown or orange−brown, colourless in thin section Yellow and violet coloured scapolites are dichroic.	
Unit cell	*a* 12.05 Å *c* ~ 7.56 Å Z = 2. Space group $P4_2/n$ or $I4/m$	*a* 12.20 Å *c* ~ 7.58 Å
Special features	Sodium-rich scapolites are almost insoluble; calcium-rich scapolite decomposes in HCl	

Scapolites occur in a wide range of regionally metamorphosed rocks and in metasomatic rocks and skarns at the contact of impure calcareous rocks with igneous rocks. They are generally colourless in thin section, with low refractive indices, but with appreciable birefringence in the calcium-rich (meionitic) varieties.

Structure

The end-member scapolite minerals have a structure with space-group symmetry $I4/m$ built from two kinds of four-membered rings of $(Si,Al)O_4$ tetrahedra, one with all four tetrahedra ($T1$) pointing in the same direction along the z axis and another ring in which the tetrahedra ($T2$) point alternately in opposite z directions (Fig. 252). The $T2$ rings are linked above and below to form chains, and laterally to $T(1)$ tetrahedra to form a 3-dimensional framework of composition $(Si,Al)O_2$. The framework contains oval-shaped channels parallel to z that contain the M site, occupied mainly by Na^+ in marialite (8-coordinated) and Ca^{2+} in meionite (9-coordinated), and larger cages that contain the A site occupied by Cl^- in marialite and disordered CO_3^{2-} anions centred on A in meionite.

With increasing Ca and Al replacing Na and Si in the scapolite series, a change in structure occurs at approximately Me_{15} where the four $T(2)$ tetrahedral sites become two pairs, $T(2)$ and $T(3)$, and the symmetry becomes $P4_2/n$. Similarly in decreasing Me% from the meionite end-member, symmetry becomes $P4_2/n$ at approximately Me_{60}. The variation of cell parameters between marialite and meionite is not uniform across the series; there are discontinuities due to structural displacements and variations in (Si,Al) disorder associated with the above changes of symmetry (Fig. 253). In $Na_4[Al_3Si_9O_{24}]Cl$, the $T(1)$ site is occupied entirely by Si and $T(2)$ by Si and Al in the ratio of 5:3. As the composition changes towards meionite, Al enters $T(2)$ preferentially, and after the symmetry change to $P4_2/n$ and split of $T2$ into $T2$ and $T3$, Al slightly prefers $T(2)$.

Several possible reasons for the $I4/m$ to $P4_2/n$ phase transformations have been offered including thermal history, or variations in ordering of (Si,Al) at T sites, or (Na,Ca,Cl,CO_3) at or near A sites. Sokolova and Hawthorne (2008), derive an explanation in terms of a dimensional misfit between the $(Na,Ca)_4[Cl,(CO_3)]$ and the $(Al,Si)_{12}O_{24}$ frameworks. They show that the consequent structural strain is minimized at intermediate compositions, which have short range clusters of Na_2Ca_2, by adoption of the lower symmetry $P4_2/n$, whereas nearer to end-member compositions, where Na_3Ca and $NaCa_3$ clusters dominate, the structure reverts to the higher symmetry of $I4/m$ (Fig. 253).

Downloaded from https://pubs.geoscienceworld.org/books/chapter-pdf/3762690/9780903056434_ch67.pdf
by guest

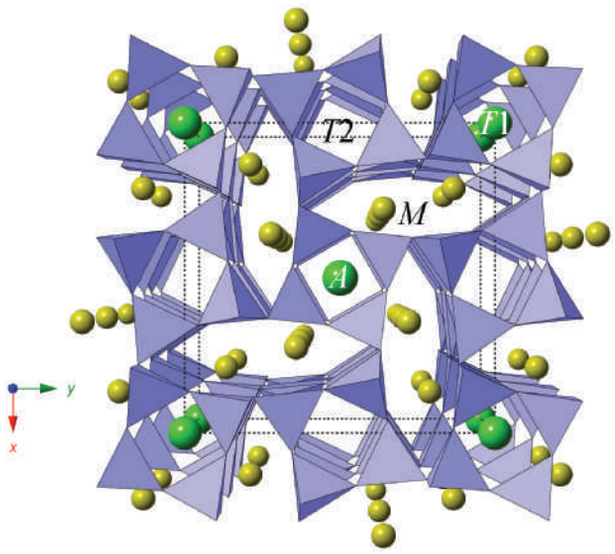


Fig. 252. Perspective view from the *z*-axis direction of the structure of scapolite (marialite). In this image, Type 1 and Type 2 rings of tetrahedra (see text) surround the corners and mid-points of edges, respectively, of the marked unit cell. Blue: $(Si,Al)O_4$ tetrahedra; green spheres: Cl^-; gold spheres: Na^+.

Chemistry

The chemical composition of scapolite may be expressed by the general formula $M_4T_{12}O_{24}A$, where M = Ca,Na,K,Sr; T = Si,Al; A = Cl,CO_3,SO_4.

The scapolite minerals form a non-binary solid solution series between the simplified end-member formulae marialite, $Na_4[Al_3Si_9O_{24}]Cl$ (Ma), and meionite, $Ca_4[Si_6Al_6O_{24}]CO_3$ (Me), and the position in this series (Me%) can be expressed by Ca/(Ca + Na), or, taking account of other cation substitutions, by $\Sigma M^{2+}/\Sigma(M^{2+}+M^{+})$. The end-member chemical formulae are sometimes also expressed as $3\,NaAlSi_3O_8 + 1\,NaCl$, and $3\,CaAl_2Si_2O_8 + 1\,CaCO_3$, involving plagioclase feldspar formulae, and can be plotted in a tetrahedral diagram with corners Ab, An, NaCl and $CaCO_3$ (Fig 254).

The charge on the (Si,Al)−O framework for the ideal marialite and meionite compositions varies between 3 and 6 and the valency balance is maintained as shown below:

$$(Na,Ca)_4[Al_3(Al,Si)_3Si_6O_{24}](Cl,CO_3,OH,SO_4)$$
$$4 \rightarrow 8 \qquad 3 \rightarrow 6 \qquad 1 \rightarrow 2$$
$$(+) \qquad (-) \qquad (-)$$
$$4 \rightarrow 8$$
$$(-)$$

Three coupled substitutions between, Na^+ and Ca^{2+}, Al^{3+} and Si^{4+}, Cl^- and CO_3^{2-}, occur in members of the series. Compilations of analyses of natural scapolites show that Ca and Al increase and Na and Si decrease steadily throughout the range from $Me_{\sim 5}$ to $Me_{\sim 95}$. Little CO_3, however, appears to enter the *A* site in place of chlorine between $Me_{\sim 5}$ and $Me_{\sim 25}$, and little Cl in place of CO_3 between $Me_{\sim 75}$ and $Me_{\sim 95}$. Replacement of Cl by CO_3 thus occurs mainly between Me_{25} and Me_{75}.

Meionite scapolites in which the SO_4^{2-} is the dominant A anion are not uncommon and have been named sylvialite (Table 45, analysis 5). In addition to Cl^-, CO_3^{2-} and SO_4^{2-} anions, minor amounts of H_2O+ have been recorded in analyses of scapolite which may be present in the structure as (OH), H^+ or water molecules. Natural pure end-members are unknown and the majority of scapolite compositions range from Me_{20} to Me_{80}. The content of minor elements is generally low, with TiO_2, MnO and MgO <0.1, and FeO <0.4 wt.%.

Pure end-member marialite has been synthesized dry from mixtures of Al_2O_3, Na_2O, $6\,SiO_2$ and NaCl at atmospheric pressure between 700 and 850ºC. It has also been synthesized from glass of albite composition and NaCl at 1000ºC and 1.5 GPa. Experimental data for the reactions

$$3\,CaAl_2Si_2O_8 + CaCO_3 \rightarrow 3\,CaAl_2Si_2O_8.CaCO_3$$

and

$$3\,CaAl_2Si_2O_8 + CaSO_4 \rightarrow 3\,CaAl_2Si_2O_8.CaSO_4$$

(sulphate meionite) are shown in Fig. 255.

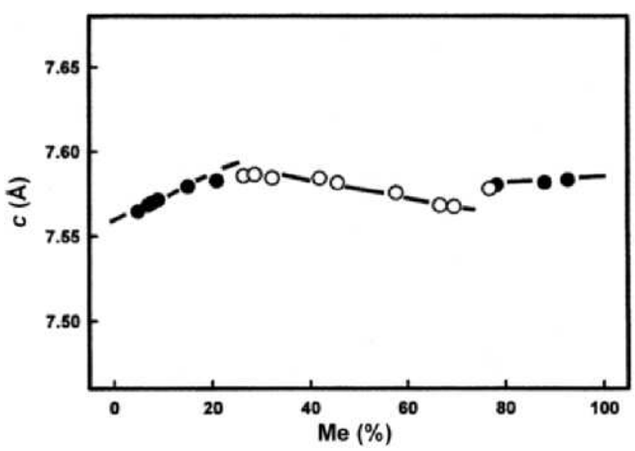


Fig. 253. Variation of *c* cell parameter with Me% in the marialite–meionite series. Black and open circles indicate $I4/m$ and $P4_2/n$ structures respectively (after Sokolova & Hawthorne, 2008).

Downloaded from https://pubs.geoscienceworld.org/books/chapter-pdf/3762690/9780903056434_ch67.pdf
by guest

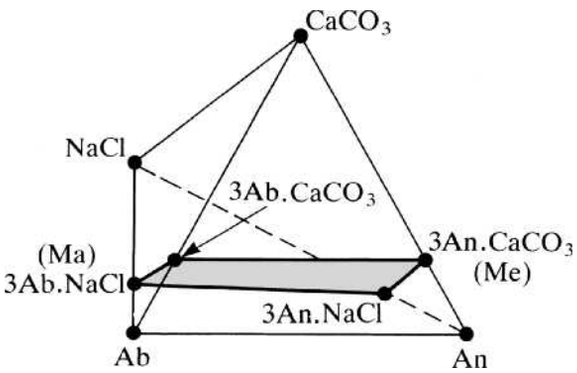


Fig. 254. Composition space for marialite–meionite scapolites. The shaded area denotes the theoretically possible plane for scapolite compositions (after Chamberlain, C.P. *et al*., 1985, *Amer. Min*., **70**, 134–40).

Meionite is stable only at temperatures above ~800ºC and has a high thermal stability at pressures up to ~1.8 GPa. At higher temperatures and pressures meionite breaks down to grossular, kyanite, quartz and calcite by the reaction:

$$3\,CaAl_2Si_2O_8.CaCO_3 \rightarrow Ca_3Al_2Si_3O_{12} + 2\,Al_2SiO_5 + SiO_2 + CaCO_3$$

The curve for the reaction anorthite + anhydrite $\rightleftharpoons$ sulphate meionite has a negative dP/dT of 2 MPa/ºC; the minimum temperature–pressure stability is 775ºC at 1.2 GPa (Fig. 255b).

The effect of compositional variation of binary H_2O–CO_2 fluids on the stability of calcic meionite, Me_{83}, is illustrated in Fig. 256, showing the T–X_{CO_2} phase relations at a fluid pressure of 0.5 GPa for the composition $3\,An_{77} + 2\,CaCO_3$. The scapolite + calcite field expands towards the region of H_2O-rich fluid compositions but is unstable in the presence of fluids where X_{CO_2} <0.12.

The experimentally determined stabilities of carbonate and sulphate meionite at high temperature and pressure provides support for the possibility that scapolite may act as a reservoir for CO_2 and SO_2 in the lower crust and constitute a liquidus phase in appropriate magma compositions.

Thermogravimetic analysis of members of the marialite–meionite series show that in the temperature range up to 800ºC the loss of H_2O, SO_2, CO_2, NaCl and KCl occurs continuously with five discernible steps.

Scapolite alteration products include analcime and prehnite.

Optical and physical properties

The mean refractive index $(\varepsilon + \omega)/2$ and the birefringence show an approximately linear variation with composition; both values increase with increasing Me content according to the relationship:

$$(\varepsilon + \omega)/2 = 1.5346 + 0.0000507\ (Me,\%)$$

For most scapolites the uncertainty is ±6.5% but it may be greater for specimens containing relatively large amounts of K, S or Cl. Compositions estimated from birefringence values do not involve an appreciably greater uncertainty. Yellow- and violet-coloured scapolites are dichroic with absorption $\varepsilon > \omega$. A gem-quality

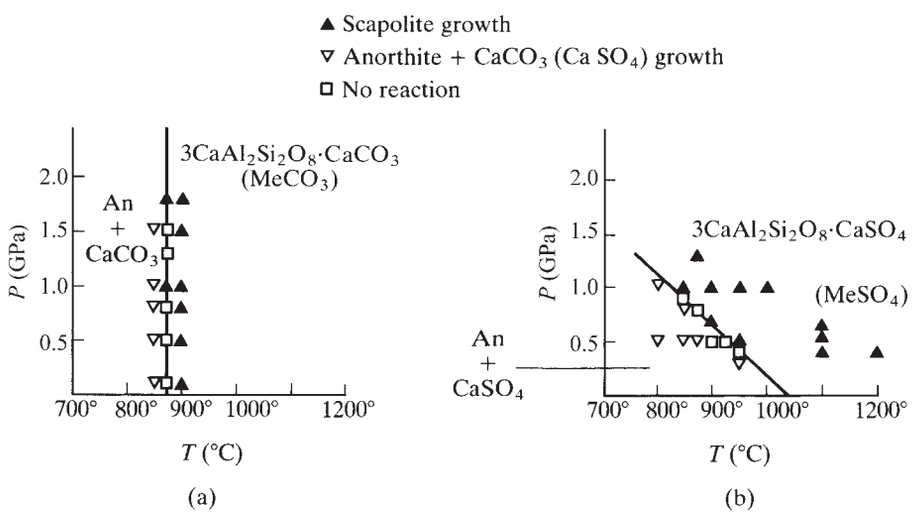


Fig. 255. The P–T curves for the reactions (a) 3 anorthite + $CaCO_3$ → 3 $CaAl_2Si_2O_8.CaCO_3$, (b) 3 anorthite + $CaSO_4$ → 3 $CaAl_2Si_2O_8.CaSO_4$ (after Goldsmith, J.R. & Newton, R.C., 1977, *Amer. Min*., **62**, 1063–81).

Downloaded from https://pubs.geoscienceworld.org/books/chapter-pdf/3762690/9780903056434_ch67.pdf
by guest

violet scapolite (Me_{10} containing 3.9 Cl pfu.) has ε deep violet, ω colourless. A set of gem scapolites from Burma was described as ranging with increasing Me content, from violet/deep blue to mauve, pink, pale blue, beige, pale yellow and greenish yellow to grey and colourless. Many yellow scapolites display strong fluorescence and more rarely aventurescence (spangled appearance).

An infrared absorption band at 610 cm^{-1} can be used to estimate the Me content of a scapolite.

Paragenesis

The formation of scapolite is largely restricted to metamorphic and metasomatic environments. Scapolites occur in a wide variety of regionally metamorphosed rocks ranging from the greenschist to the granulite facies. The mineral composition is broadly related to metamorphic grade, the meionite content increasing in scapolites of the higher grade rocks. Calcium-rich scapolites, Me_{65-72}, associated with wollastonite, calcite,

Table 45. Scapolite analyses.

	1	2	3	4	5
SiO_2	57.89	53.19	47.52	40.84	45.26
TiO_2	0.01	-	–	–	–
Al_2O_3	21.62	23.44	25.21	30.49	26.25
Fe_2O_3	0.07	–	–	–	0.22
FeO	–	0.13	0.30	0.17	–
MnO	0.01	–	0.02	–	–
MgO	0.03	–	0.14	–	–
CaO	4.81	10.40	15.48	22.17	16.95
Na_2O	10.50	7.44	4.52	0.64	3.49
K_2O	1.16	0.92	0.10	0.48	0.06
H_2O+	0.44	–	0.22	–	–
H_2O-	0.06	–	0.08	–	–
CO_2	1.11	1.89	2.16	4.41	1.92[a]
SO_3	0.03	1.22	4.17	0.23	4.82
Cl	2.96	1.91	0.06	0.13	0.02
$-O \equiv Cl$	−0.67	−0.43	0.01	0.03	–
Total	100.03	100.22	100.00	99.67	99.08
Numbers of ions on the basis of 12 (Si,Al)					
Si	8.331	7.896	7.382	6.385	7.13
Al	3.668	4.102	4.618	5.617	4.87
ΣT	12.00	12.00	12.00	12.00	12.00
Fe^{3+}	0.007	–	–	–	0.024
Mg	0.006	–	0.033	–	–
Fe^{2+}	–	0.016	0.039	0.022	–
Mn	0.001	–	0.003	–	–
Na	2.930	2.142	1.360	0.194	1.06
Ca	0.742	1.655	2.577	3.713	2.86
K	0.212	0.174	0.020	0.096	0.011
ΣM	3.90	3.996	4.03	4.039	3.96[b]
C	0.218	0.383	0.458	0.941	0.414
S	0.003	0.136	0.486	0.027	0.57
Cl	0.722	0.481	0.016	0.032	0.002
ΣA	0.94	1.00	0.96	1.00	0.99
Me	19.3	42.0	65.7	92.8	72.2
H	0.422	–	0.228	–	–

1. Marialite, syenite pegmatite, Ontario, Canada (Shaw, D.M., 1960, *J. Petrol.*, **1**, 218–60).
2. Calcium marialite; yellowish transparent crystals from vugs in marble blocks. Monte Somma, Italy (Sokolova & Hawthorne, 2008). Electron probe analysis.
3. Meionite, garnet-hornblende-pyroxene-scapolite gneiss. Ghana (Knorring, O. von & Kennedy, W.Q., 1958, *Mineral. Mag.*, **31**, 846–50). Includes P_2O_5 0.03.
4. Gemstone; yellowish white meionite, Monte Somma, Italy (Sokolova & Hawthorne, 2008). Electron probe analysis.
5. Sylvialite, garnet granulite xenolith in olivine nephelinite, McBride Province, North Queensland, Australia. *a* 12.160, *c* 7.560, ω 1.583, ε 1.558, density 2.75 g/cm^3 (Teerstra *et al.*, 1999, *Mineral. Mag.*, **63**, 321–9). Electron probe analysis. Includes SrO 0.08, Sr 0.001.

[a] CO_2(calc.) = [Na+K+2(Ca+Fe+Sr)−Al−Cl−2S]/2.
[b] ΣM includes SrO 0.001.

Downloaded from https://pubs.geoscienceworld.org/books/chapter-pdf/3762690/9780903056434_ch67.pdf
by guest

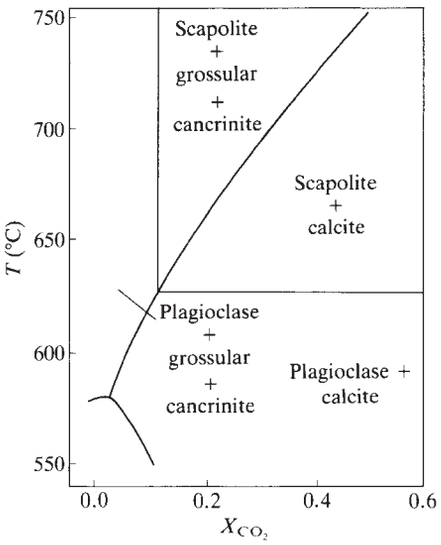


Fig. 256. The $T-X_{CO_2}$ phase relations for the bulk composition 3 plagioclase (An_{77}) + 2 $CaCO_3$ at P_{fluid} = 0.5 GPa (after Aitken, B.G, 1983, *Geochim. Cosmochim. Acta*., **47**, 351–62).

diopside and plagioclase, are particularly characteristic of the calc gneisses and granulite-facies rocks of the Scourie complex, northwest Scotland. Meionite scapolites occur in granulitic xenoliths in basaltic and kimberlitic diatremes. The presence of meionite (3 An.$CaCO_3$) rather than zoisite (3 An.$Ca(OH)_2$) indicates their formation under high CO_2/H_2O pressure; more generally scapolites are important indicators of the volatile constituents of the lower crust. Paragneisses and mafic granulitic rocks of the southwest Kola Peninsula contain up to 20 wt.% scapolite, the SO_4^{2-}, Cl^- and OH^- content of which is considered to represent the anionic fraction of bound water in stratified rocks and thus to be a specific indication of the evaporitic nature of the original sediments.

In many metamorphic rocks, scapolite is metasomatic in origin. It is a common consituent in skarns at calcareous sediments–igneous contacts. Metasomatic scapolite also occurs on a regional scale (e.g. a Cl-rich marialitic scapolite is widely developed in the metasediments of the Cloncurry district, Queensland; here its formation is associated with extensive albitization of the original argillaceous sediments).

Scapolite also occurs in pneumatolytically and hydrothermally altered basic igneous rocks, e.g. in the scapolite–hornblende rocks of the Kragerø region, southern Norway, where the original basic rocks have been extensively modified by CO_2- and Cl-rich solutions. The product of such regional scapolitization is invariably marialitic in composition. In the Humboldt lopolith, Nevada, marialite occurs as a pervasive replacement of plagioclase, as a poikiloblastic constituent of the scapolite dykes, as a fracture filling with analcime, albite and sphene, and in scapolite (up to 80 vol.%) veins.

Scapolite is uncommon in igneous parageneses but it occurs as megacrysts in tephra in the Puy de Dôme region, France, as phenocrysts in latite and in some pegmatites. The high-sulphur scapolite, sylvialite occurs typically in granulite-facies metamorphic rocks and from mafic and ultramafic xenoliths from the lower crust or upper mantle. The sylvialite from McBride Province, north Queensland, (Table 45, analysis 5) is interpreted as a primary cumulate phase precipitated from a basaltic magma under conditions of elevated f_{O_2} and f_{SO_2}.

A sodium-rich scapolite, Me_{17}, has been reported from a granular textured clast in the Bishunpur (LL3) chondritic meteorite.

Further reading

Aitken, B.C. (1983) $T-X_{CO_2}$ stability relations and phase equilibria of a calcic carbonate scapolite. *Geochimica et Cosmochimica Acta*, **47**, 351–362.

Antao, S.M. and Hassan, I. (2011) Complete Al-Si order in scapolite $Me_{37.5}$, ideally $Ca_3Na_5[Al_8Si_{16}O_{48}](CO_3)$, and implications for antiphase domain boundaries (APBS). *The Canadian Mineralogist*, **49**, 581–586.

Chamberlain, C.P., Docka, J.A., Post, J.E. and Burnham, C.W. (1985) Scapolite alkali atom configurations, antiphase domains and compositional variations. *American Mineralogist*, **70**, 134–140.

Graziani, G. and Lucchesi, S. (1982) The thermal behavior of scapolite. *American Mineralogist*, **67**, 1229–1241.

Hassan, I. and Buseck, R.R. (1988) HRTEM characterization of scapolite solid solutions. *American Mineralogist*, **73**, 119–134.

Hawthorne, F.C. and Sokolova, E. (2008) The crystal chemistry of the scapolite-group minerals. II The origin of the $I4/m \rightleftharpoons P4_2/n$ phase transformation and the non-linear variations in chemical composition. *The Canadian Mineralogist*, **46**, 1555–1575.

Sokolova, E. and Hawthorne, F.C. (2008) The crystal chemistry of the scapolite-group minerals. 1. Crustal structure and long range order. *The Canadian Mineralogist*, **46**, 1527–1554.

Stolz, A.J. (1987) Fluid activity in the lower crust and upper mantle: mineralogical evidence bearing on the origin of amphibole and scapolite in ultramafic and mafic granulite xenoliths. *Mineralogical Magazine*, **51**, 719–732.

Teerstra, D.K. and Sheriff, B.L. (1997) Substitutional mechanisms, compositional trends and the end-member formulae of scapolite. *Chemical Geology*, **136**, 233–260.

Teerstra, D.K., Schindler, M., Sherriff, B.L. and Hawthorne, F.C. (1999) Silvialite, a new sulfate-dominant member of the scapolite group with an Al-Si composition near the $I4/m-P4_2/n$ phase transition. *Mineralogical Magazine*, **63**, 321–329.

Downloaded from https://pubs.geoscienceworld.org/books/chapter-pdf/3762690/9780903056434_ch67.pdf
by guest

FELDSPATHOID OVERVIEW

Feldspathoids are aluminosilicates of Na, K and Ca which are silicon deficient compared with feldspars and thus occur mainly in rocks which are undersaturated with regard to silica. The crystal structures are based upon (Si,Al)–O tetrahedra sharing all four corners and thus have the O–(Si,Al) ratio of 2:1, which is characteristic of the other major framework silicates, the feldspars and zeolites. Feldspathoids have a more open framework (and lower density) than feldspars, and a less open framework (and higher density) than zeolites.

Feldspathoid structures contain rings of tetrahedra which form cages and in some cases channels, containing non-framework cations (mainly Na, Ca and K), which unlike those in zeolites, are not readily removed or replaced. In scapolite, sodalite, cancrinites and related minerals the cavities and channels variously accommodate also polyatomic anions such as, SO_4^{2-}, CO_3^{2-}, Cl^-, OH^- and S^{2-}. Water molecules may also occur in structural cavities and channels as in analcime and cancrinite.

Simplified formulae are:

Nepheline–Kalsilite	$(Na,K)_4[Al_4Si_4O_{16}]$	Analcime	$Na_4[Al_4Si_8O_{24}]\cdot H_2O$
Leucite	$K_4[Al_4Si_8O_{24}]$	Sodalite	$Na_8[Al_6Si_6O_{24}]Cl_2$
Cancrinite	$Ca_2Na_6[Al_6Si_6O_{24}](CO_3)_2\cdot 2H_2O$		

Scapolite:

Marialite $Na_4[Al_3Si_9O_{24}]Cl$, Meionite $Ca_4[Al_6Si_6O_{24}]CO_3$

In nepheline, sodalite, cancrinite and meionitic scapolite, Al and Si are present in nearly equal numbers in the frameworks, but in analcime, leucite and marialitic scapolite there is appreciably more Si. In nepheline, analcime and leucite the non-framework cations are approximately equal in number to the framework Al, but in sodalite and cancrinite there are more (Na,Ca,K) than Al and overall charge balance is maintained by the other non-framework constituents as anions.

The feldspathoid minerals occur mainly in alkaline rocks but some associations are more specific (though not exclusive), (e.g. sodalite, cancrinite and scapolite in volatile-rich environments; nephelines, sodalites and cancrinites in nepheline syenites; scapolites in skarns at igneous contacts; and leucites in potassic undersaturated volcanic and hypabyssal rocks). Nepheline is the most common feldspathoid, forming as a primary magmatic mineral, by metasomatic ‘nephelinization’, and by the reaction of magma with Ca-rich sediments.

Downloaded from https://pubs.geoscienceworld.org/books/chapter-pdf/3762690/9780903056434_ch67.pdf
by guest

Zeolite Group

General formula $(Na_2,K_2,Ca,Ba)[(Al,Si)O_2]_x{\cdot}nH_2O$

Introduction

Ever since the name was introduced in 1756, in allusion to the bubbling of water vapour when zeolites are heated in a blowpipe flame, through to the present day, the mineralogical concepts of this group have been evolving constantly. Once thought to occur only in fractures and cavities in igneous rocks, some zeolite minerals are now known to be significant constituents in sedimentary rocks. Many of these are of economic importance (e.g. as pore-filling cements that limit the extent of some petroleum reservoirs, or others that are mined for their gas absorption properties). From the seven zeolite species that were recognized at the beginning of the 19th century, their numbers grew to around 22 in 1900, to 45 in the second edition (1992) of this text, to, at the time of writing (2012), about 100 recognized species and 40 distinct structure types. Improved analytical instrumentation has revealed wide compositional variation and has helped to characterize many new species. A system of nomenclature was recommended by a sub-committee of the International Mineralogical Association (Coombs *et al*., 1997), which also gave the following definition: "A zeolite mineral is a crystalline substance with a structure characterized by a framework of linked tetrahedra each consisting of four O atoms surrounding a cation. This framework contains open cavities in the form of channels and cages These are usually occupied by H_2O molecules and extra-framework cations that are commonly exchangeable. The channels are large enough to allow the passage of guest species."

In the hydrated phases, dehydration occurs at temperatures mostly beneath about 400ºC and is largely reversible. The framework may be interrupted by (OH,F) groups; these occupy a tetrahedron apex, which is not shared with adjacent tetrahedra.

Some zeolites can host a wide range of cations, and in order to avoid a plethora of new names, the rules adopted require the use of suffixes to denote the dominant cation (e.g. chabazite-Ca).

Chemically, the zeolites are aluminosilicates with a framework structure enclosing cavities occupied by large ions and water molecules, both of which have

Name	Formula	System	n_{min}	n_{max}	2V	D (g/cm^3)	Space group
Analcime	$Na[AlSi_2O_6]{\cdot}H_2O$	Cubic	1.485			2.26–2.29	*Ia*3*d*
Natrolite	$Na_{16}[Al_{16}Si_{24}O_{80}]{\cdot}16H_2O$	Orthorhombic	1.479	1.491	61º (+)	2.20–2.26	*Fdd*2
Thomsonite	$Na_4Ca_8[Al_{20}Si_{20}O_{80}]{\cdot}24H_2O$	Orthorhombic	1.510	1.542	52º (+)	2.3	*Pncn*
Mesolite	$Na_2Ca_2[Al_6Si_9O_{30}]{\cdot}8H_2O$	Orthorhombic	1.504	1.512	80º (+)	2.26	*Fdd*2
Phillipsite	$K_2(Ca_{0.5},Na)_4[Al_6Si_{10}O_{32}]{\cdot}12H_2O$	Monoclinic	1.476	1.503	60–90º (+)	2.15	$P2_1/m$
Harmotome	$Ba_2[Al_4Si_{12}O_{32}]{\cdot}12H_2O$	Monoclinic	1.503	1.514	80º (+)	2.4	$P2_1/m$
Gismondine	$Ca[Al_2Si_2O_8]{\cdot}4H_2O$	Monoclinic	1.515	1.546	15–90º (–)	2.2	$P2_1/c$
Laumontite	$Ca_4[Al_8Si_{16}O_{48}]{\cdot}16H_2O$	Monoclinic	1.510	1.524	23–47º (–)	2.27	*C*2/*m*
Heulandite	$(Ca_{0.5},Na,K)_9[Al_9Si_{27}O_{72}]{\cdot}24H_2O$	Monoclinic	1.496	1.515	Var. (+)	2.2	*C*2/*m*, *C*2 or *Cm*
Clinoptilolite	$(Na,K)_6[Al_6Si_{30}O_{72}]{\cdot}24H_2O$	Monoclinic	1.476	1.481	36º (+)	2.16	*C*2/*m*, *C*2 or *Cm*
Stilbite	$(Ca_{0.5},Na,K,)_9[Al_9Si_{27}O_{72}]{\cdot}30H_2O$	Monoclinic	1.484	1.513	30–49º (–)	2.1–2.2	*C*2/*m*
Chabazite	$Ca_2[Al_4Si_8O_{24}]{\cdot}12H_2O$	Trigonal	1.460	1.517	(–)	2.1	$R\bar{3}m$
Erionite	$K_2(Na,K,Ca_{0.5})_8[Al_{10}Si_{26}O_{72}]{\cdot}28H_2O$	Hexagonal	1.468	1.476	(–)	2.0	$P6_3/mmc$
Gmelinite	$(Na,Ca_{0.5})_2[Al_2Si_4O_{12}]{\cdot}6H_2O$	Hexagonal	1.474	1.494	(–)	2.1	$P6_3/mmc$
Mordenite	$Na_3KCa_2[Al_8Si_{40}O_{96}]{\cdot}28H_2O$	Orthorhombic	1.471	1.478	76–90º (+)	2.13	$Cmc2_1$

Downloaded from https://pubs.geoscienceworld.org/books/chapter-pdf/3762850/9780903056434_ch68.pdf
by guest

considerable freedom of movement, permitting ion exchange and reversible dehydration; they may be transformed to feldspars when subjected to thermal metamorphism.

Zeolites have long been known from amygdales and fissures in basic volcanic rocks where they commonly occur as well developed crystals. More recently they have been recognized as important and abundant authigenic constituents in sedimentary rocks. They have been found as major constituents of volcanic tuffs in ancient saline-lake deposits and in thick marine tuffs. In low-grade metamorphic rocks they occur as a result of hydrothermal activity and by burial metamorphism. Although zeolitic tuffs have been used as building materials for at least 4000 years, it is only within the last 40 years that the zeolite contents of these materials has been recognized, and in the same period their industrial application as cation-exchangers, adsorbents, molecular sieves and desiccants, has been increasingly realized.

The synthetic production of zeolites is largely aimed at tailoring their properties to specific industrial needs. Laumontite, heulandite–clinoptilolite and analcime are the most abundant naturally occurring zeolites.

Although analcime is commonly included as a member of the zeolite group, it has close affinities with the feldspathoids and can have a somewhat higher-temperature paragenesis than the other zeolites.

Structure

The basic structural feature of all zeolite minerals is an aluminosilicate framework composed of $(Si,Al)O_4$ tetrahedra, each oxygen of which is shared between two tetrahedra. The net negative charge on the framework is balanced by the extra-framework cations, in most cases Ca, Na or K, which are situated in cavities within it. This type of structure is also present in the feldspar and feldspathoid minerals. The feldspars have compact structures in which the (Na,Ca,K) ions are in relatively small cavities and are completely surrounded by oxygens of the framework: the cations and framework are strongly interdependent so that cations cannot easily move unless framework bonds are broken, and replacement of Na or K by Ca necessarily involves a change in the Si/Al ratio. The feldspathoids have somewhat more open aluminosilicate frameworks and their (Na,Ca,K) ions (and in some cases certain anions) occupy, but do not always fill, larger cavities which are intercommunicating. Thus in the feldspathoids there are channels through which ions can be introduced, and some through which small molecules may pass, without disruption of the framework. The zeolite aluminosilicate frameworks are similar but many are still more open, containing larger cavities and larger channels (density of zeolites 2–2.3 g/cm^3, feldspathoids 2.3–2.5 g/cm^3, feldspars 2.6–2.7 g/cm^3); zeolites may therefore exhibit to a greater extent the properties of ion exchange and molecular absorption. An additional feature which differentiates the zeolites still further from minerals of the other two groups is the presence of water molecules within the structural channels. These are relatively loosely bound to the framework and cations, and like the cations can be removed and replaced without disrupting framework bonds. As the zeolite framework is structurally almost independent of the (Na,Ca,K) cations, and as the latter do not fill all the cavities, replacements of the type Ca $\leftrightarrow$ 2(Na,K) can occur as well as the more usual CaAl $\leftrightarrow$ (Na,K)Si.

The channel systems in the various zeolites are made up of different combinations of linked rings of tetrahedra; the wider the channels at their narrowest parts, the larger the cation that can be introduced into the structure. Those with eight- and twelve-membered rings have channels large enough for the admission of organic molecules as well as cations; thus zeolites can act as ion or molecular sieves, each having its characteristic upper limit for the size of ion or molecule to which it is permeable. A grading of some zeolites according to the openness of structure is shown in Table 46. Channel width, however, is not the only criterion for permeability, as the presence of many cations may block the channels, and ionic or molecular diffusion is also affected by water content. Cation exchange capacity in general diminishes with loss of water; cations are most mobile in zeolites with low cation content. Sodium is more mobile than Ca since it is monovalent and is thus held by a weaker electrostatic bond.

In most zeolites the water molecules are probably distributed among a number of possible sites and can jump from one to another. In general the Ca zeolites absorb more water, and in chabazite, heulandite and stilbite, water retentivity is greater with Ca than with K in the framework.

The zeolites can be subdivided, on the basis of their structures, into a number of subgroups, as described in the following text.

Table 46. Numbers of tetrahedra in rings and approximate dimensions of widest channels in various zeolites.

Mineral	No. of tetrahedra in rings	Approx. dimensions of widest channel (Å)
Natrolite	4, 5 and 8	2.6
Phillipsite	4 and 8	3.6
Harmotome	4 and 8	3.6
Erionite	4, 6 and 8	3.6×5.1
Chabazite	4, 6 and 8	3.8
Heulandite	4, 5, 8 and 10	3.0×7.6
Laumontite	4, 6, and 10	4.0×5.3
Gmelinite	4, 6, 8 and 12	7.0
Mordenite	4, 5, 8 and 12	7.0
Faujasite	4, 6 and 12	7.4

Downloaded from https://pubs.geoscienceworld.org/books/chapter-pdf/3762850/9780903056434_ch68.pdf
by guest

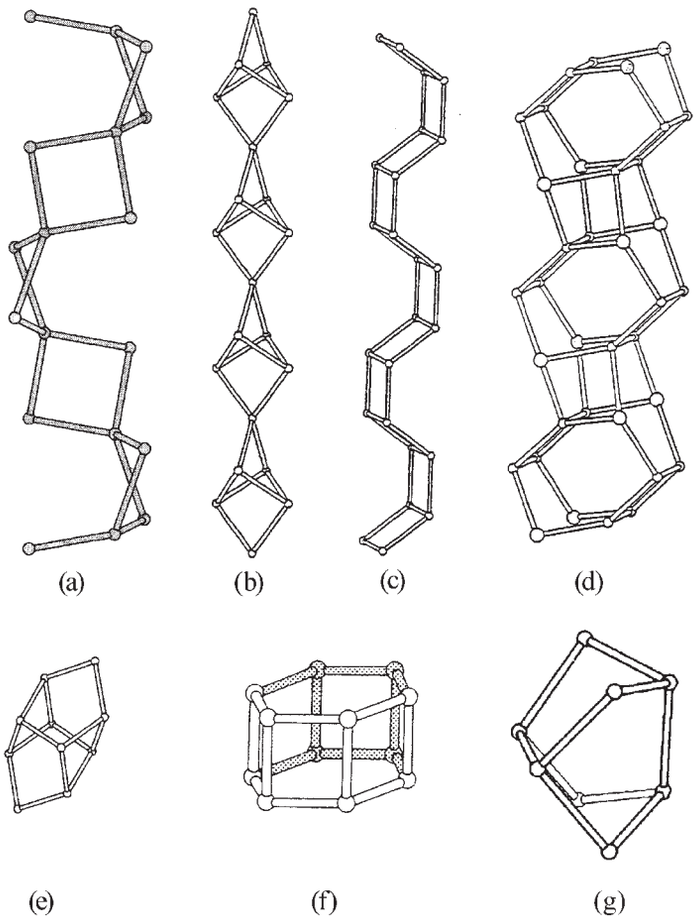


Fig. 257. Schematic illustrations of the building units of zeolite structures in which only tetrahedral sites (T), indicated as circles, and T−T linkages are shown, omitting oxygens of the T−O−T bonds. (a) A chain of singly-connected four-rings of T−O tetrahedra which is a building unit in the structure of analcime. Similar chains connect by corner-sharing to form a 3D cage-like framework with four-, six- and eight-rings of tetrahedra similar to that in leucite (see Fig. 238, p. 335). (b) The T_5O_{10} chain that occurs in natrolite and related fibrous zeolites. (c) The crankshaft chain of doubly connected four-rings that occurs in phillipsite/harmotome and other zeolites as well as in feldspars. (d) Complex chains of tetrahedra that are linked laterally to tetrahedra of other chains to form the framework structure of laumontite. (e) The building unit of the structure of heulandite, a polyhedron containing four- and five-membered rings of tetrahedra. (f) The double six-ring of tetrahedra building unit of the structure of chabazite. (g) A polyhedral cage unit of the structure of zeolites of the mordenite group (after Wise, 2004).

(1) The analcime subgroup, including wairakite and pollucite: chain-like building units (Fig. 257a) which run parallel to each cube tetrad axis and link to other tetrahedra to form four-, six- and eight-membered T−O rings and a cage-like framework structure (see leucite, Fig. 238, p. 335; also schematic Fig. 257a).

(2) The natrolite subgroup; including natrolite, mesolite, scolecite, thomsonite, gonnardite and edingtonite. A fundamental chain-like unit (Fig. 257b) figures prominently in the structures of this group and its members commonly have a fibrous morphology. Other zeolites, however, also may be fibrous (e.g. erionite).

(3) The harmotome/phillipsite subgroup, including gismondine, contains doubly connected four-membered rings which form crankshaft-like chains (Fig. 257c) similar to those in feldspars. The chains are linked in a different manner, but as in the feldspars the resulting framework has eight- and four-membered rings.

(4) This subgroup (including laumontite and others) contains rings of four tetrahedra which share with others to form chains schematically illustrated in Fig. 257d. The lateral linkage of chains produces six- and nine- or ten-membered as well as the four-membered rings.

(5) The structural unit common to zeolites of the heulandite group, including stilbite and brewsterite, contains four- and five-membered rings (Fig. 257e). These units share vertices to form chains which are linked to form sheets which themselves are connected through mirror planes. The tabular morphology of members of this group is a reflection of this layered structure.

(6) The chabazite subgroup contains single (lévyne, erionite, offretite) or double (chabazite, gmelinite, faujasite) six-membered rings of tetrahedra (Fig. 257f) which lie perpendicular to a triad or hexad axis. The three-dimensional linkages form four- and eight- and in some cases twelve- as well as six-membered rings. These minerals have very open structures with cages that can be described as truncated octahedra or truncated cubo-octahedra.

(7) The structures of the mordenite subgroup, including dachiardite, epistilbite and ferrierite, are based upon a polyhedral building unit (Fig. 257g) which contains five-membered rings of tetrahedra. These are linked to form chains which are linked by four-membered rings to form sheets parallel to (010). In addition there are eight- and twelve-membered rings in mordenite and ten-membered rings in dachiardite and epistilbite.

Further details on the structures of specific zeolites are given in the following text.

Downloaded from https://pubs.geoscienceworld.org/books/chapter-pdf/3762850/9780903056434_ch68.pdf
by guest

Chemistry

The zeolites form a well defined group of hydrous aluminosilicates which contain elements of groups one and two of the periodic table, and are characterized also by having a $(Ca,Sr,Ba,Na_2,K_2)O/Al_2O_3$ ratio equal to unity and (Al + Si)/O in the framework in a ratio that is always 1:2. A general formula can be written $M_xD_y[Al_{x+2y},Si_zO_{2x+4y+2z}].nH_2O$, where M = Na, K or other monovalent cations and D = Mg, Ca, Sr, Ba or other divalent cations. Thus the simplified formula of the zeolite heulandite can be written as $CaO.Al_2O_3.7SiO_2.6H_2O$ or $Ca_4[Al_8Si_{28}O_{72}].24H_2O$ on a unit-cell basis, the cations outside the square brackets being exchangeable and those inside the brackets combining with oxygen to make up the framework. The ratio SiO_2/Al_2O_3 is always $\geqslant$2:1. The chemistry of many zeolites is rather variable and can deviate considerably from the schematic formulae of p. 355, which are at best only an approximation of what the composition of a particular zeolite may be. Analyses of 10 zeolites are given in Table 47.

There are several ways to illustrate these compositional variations, and more than one may be required to convey and demonstrate the important variables. A triangular diagram which is commonly used shows the T_{Si} [= Si/(Si + Al)] or (Si/Al) content (Fig. 258). This diagram usefully illustrates the relative silica content of zeolites.

The synthesis of molecular sieves not known in nature was first accomplished in 1948 and their widespread industrial use as adsorbents began in 1954. The production of synthetic zeolites tailored according to specific industrial needs became possible and this has led also to the production of a new set of compounds with a very high silica content (Si/Al ratio in the range 10−100) with silicalite as the pure silica end-member. In the absence of tetrahedral Al, silicalite does not have ion-exchange properties and has a strong hydrophobic character; it cannot be considered strictly to be a synthetic zeolite but certainly qualifies as a molecular sieve.

A combination of ion-exchange, catalytic and molecular-sieve properties has led to the extensive use of zeolites, both natural and synthetic, in a great range of applications. Such industrial uses include: fillers in high-brightness paper, upgrading of natural gas with low heat values, removal of radioactive isotopes from nuclear wastes, dietary supplements for pigs and poultry, purification of petroleum products, carriers of pesticides, traps for heavy metals in the food chain, reduction of various offensive odours from decaying organic material and as a polishing agent in fluoride-containing toothpaste. Erionite, a fibrous zeolite which occurs in altered volcanic glass in the Cappadocia area of Turkey, has been implicated in the endemic occurrence of malignant mesotheliomas among residents of the area.

Optical and physical properties

Pure zeolites are typically colourless or white, but many specimens are coloured because of the presence of finely divided oxides of iron or other impurities. Their densities range between 2.0 and 2.3 g/cm^3, except for the barium-rich zeolites, for which D is between 2.4 and 2.8 g/cm^3. Refractive indices range between 1.46 and 1.54 and birefringence between zero and 0.015.

Distinguishing features

The identification of individual zeolite species is commonly difficult because of the similarity of their

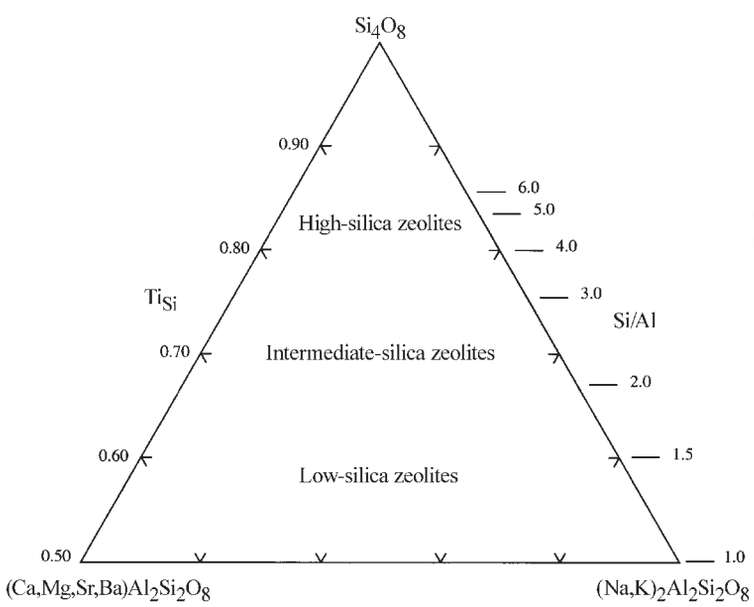


Fig. 258. Compositional diagram illustrating major variations in zeolite compositions. The components are Si_4O_8: mol. proportion [Si – 2(Ca + Mg + Sr + Ba) − 2(Na + K)]/4; $(Ca,Mg,Sr,Ba)Al_2Si_2O_8$: mol. proportion (Ca + Mg + Sr + Ba); and $(Na,K)_2Al_2Si_2O_8$: mol. proportion (Na + K)/2 (after Wise, 2004)

Downloaded from https://pubs.geoscienceworld.org/books/chapter-pdf/3762850/9780903056434_ch68.pdf
by guest

optical and other properties. Recourse may be had to their X-ray powder diffraction patterns, DTA behaviour, and infrared spectra. With the electron probe, zeolites at least partially dehydrate unless a defocused beam is used combined with counting for short intervals at any single point.

Paragenesis

The occurrence and paragenesis of natural zeolites have been extensively studied in the last two decades. Being hydrous aluminosilicates they are relatively sensitive to changes in temperature and pressure. The

Table 47. Zeolite analyses.

	1	2	3	4	5	6	7	8	9	10
SiO_2	47.33	54.40	46.67	54.88	59.45	63.94	68.38	53.77	52.06	64.65
Al_2O_3	27.67	16.27	16.35	16.99	16.63	15.79	14.42	16.77	21.50	13.10
Fe_2O_3	0.00	0.35	–	0.02	0.00	0.19	0.05	0.08	0.04	0.06
MgO	0.00	0.04	–	–	0.34	0.63	0.2	0.03	–	0.02
BaO	–	0.08	20.35	–	0.00	0.01	0.37	–	–	0.03
SrO	–	0.04	–	–	0.00	–	–	–	–	0.05
CaO	0.22	1.20	1.78	0.02	4.91	1.59	0.02	7.75	11.64	2.36
Na_2O	14.74	2.95	–	9.52	0.57	8.19	7.94	1.81	0.06	4.37
K_2O	0.50	8.32	0.23	1.17	4.74	1.19	1.04	0.07	0.43	0.83
H_2O+	9.64	16.70	14.66	17.40	–	–	–	19.75	–	14.59
H_2O-	–	–	–		–	–	–	–	–	–
Total	100.10	100.35	100.04	100.00	86.64	91.53	92.42	100.03	85.73	100.06
α	1.479	–	–	–	–	1.480	1.474	–	–	–
β	1.482	–	–	–	–	1.484	1.477	–	–	–
γ	1.491	–	–	–	–	1.488	1.478	–	–	–
2V (º)	+63	–	–	–	+ve	−85	−85	–	–	–
	Numbers of cations and H_2O on basis of framework of:									
	80 O	32 O	32 O	24 O	72 O	72 O	72 O	72 O	48 O	96 O
Si	23.902	11.799	11.291	8.792	27.153	27.685	28.769	26.26	16.124	38.816
Al	16.468	4.159	4.662	3.208	8.951	8.057	7.150	9.66	7.848	9.269
Fe^{3+}	–	0.057	–	0.002	–	0.062	0.016	0.03	0.009	0.027
ΣT	40.370	16.015	15.953	12.002	36.104	35.804	35.935	35.95	23.981	48.112
Mg	–	0.013	–	–	0.231	0.407	0.125	0.02	0.000	0.018
Ca	0.119	0.279	0.461	0.003	2.403	0.005	0.009	4.06	3.862	1.518
Sr	–	0.005	–	–	–	–	–	–	–	0.017
Ba	–	0.007	1.929	–	–	0.270	0.061	–	–	0.007
Na	14.431	1.240	–	2.957	0.505	6.875	6.476	1.71	0.036	5.087
K	0.332	2.302	0.071	0.239	2.762	0.657	0.558	0.04	0.170	0.636
Σn-f*	14.872	3.846	2.461	3.199	5.901	8.214	7.230	5.83	4.068	7.283
H_2O	16.204	12.056	11.805	9.278	–	–	–	32.17	–	29.157

1 Natrolite, large translucent crystals, Benallt manganese mine, Rhiw, Carnarvonshire, North Wales (Hey, M.H., 1932, *Mineral. Mag.*, **23**, 243−89).
2 Phillipsite, Neapolitan yellow tuff, Phlegraean fields, Naples, Italy (Passaglia, E. *et al.*, 1990, *Eur. J. Min.*, **2**, 827−39).
3 Harmotome, hydrothermal vein associated with Brocken granite, Andreasberg, Harz, Germany (Rinaldi, R. *et al.*, 1974, *Acta Cryst.*, **B30**, 2426−33).
4 Chabazite-Na, small hexagonal plates epitaxially grown on gmelinite, basalt underlying borax beds, Boron, California (Wise, W.S. & Kleck, W.D., 1988, *Clays Clay Min.*, **36**, 131−6).
5 Erionite-K, vesicular basalt north of Thumb Butte, Graham County, Arizona (Wise, W.S. & Tschernich, R.W., 1976, *Amer. Min.*, **61**, 853−63).
6 Heulandite-Na, colourless overgrowths on clinoptilolite, cavities in basalt, underlying borax beds, Boron, California (Wise, W.S. & Kleck, W.D., 1988, *Clays Clay Min.*, **36**, 131−6).
7 Clinoptilolite-Na, clay-coated crystals in cavities in basalt underlying borax beds, Boron, California (Wise, W.S. & Kleck, W.D., 1988, *Clays Clay Min.*, **36**, 131−6).
8 Stilbite, amygdaloidal Tertiary basalt, Flodigarry, N. Skye, UK (Passaglia, E. *et al.*, 1978, *Bull. Min.*, **101**, 368−75).
9 Laumontite, in assemblage with prehnite, Karmutsen metabasite, Vancouver Island, British Columbia, Canada (Cho, M. *et al.*, 1986, *J. Petrol.*, **27**, 467−94).
10 Mordenite, white to yellow fibrous masses in Triassic basalt, type locality near Morden, Bay of Fundy, Kings County, Nova Scotia (Passaglia, E., 1975, *Contrib. Mineral. Petrol.*, **50**, 65−77).

* n-f: non-framework

Downloaded from https://pubs.geoscienceworld.org/books/chapter-pdf/3762850/9780903056434_ch68.pdf
by guest

lowest temperatures at which zeolites form (4ºC) are in deep-sea sediments, where phillipsite crystallizes at the sediment–water interface and continues to grow in the sediment. Phillipsite is most common in Miocene and younger sediments whereas clinoptilolite is abundant in Cretaceous and early Tertiary sediments, though it has been reported that phillipsite is derived from basaltic glass and clinoptilolite from acidic glass. Deep-sea zeolites, however, may be found in the fabric of radiolarian tests, suggesting a non-volcanic origin, the silica perhaps being supplied from biogenic opal.

The importance of zeolites as products of diagenesis and in the early stages of the metamorphism of volcanic sedimentary rocks was demonstrated in Southland, New Zealand, where 10 km of Triassic sedimentary rocks with a large amount of volcanic detritus, but with a lack of intrusive rocks, showed progressive changes in the alteration assemblage with depth in apparent response to the increase in temperature and pressure with depth of burial. It was the detailed study of this section that led to the concept of burial metamorphism and the establishment of the zeolite facies (Coombs *et al.*, 1959).

The most widespread and economically important zeolite occurrences are in diagenetically altered sediments and sedimentary rocks which contain volcanic clasts, and pyroclastic rocks. Diagenetic alteration may occur in various environments, including the deep sea floor, shallow alkaline lakes and sandstone beds in shallow to deep basins. These alteration reactions merge with those of burial metamorphism. Diagenetic processes producing zeolites can be classified by the environments in which they occur. These include hydrologically open systems, hydrologically closed systems, soils and surface deposits, and marine sediments from arc-source terranes.

Hydrologically open systems. Most terrestrial accumulations of volcanic material, lavas and pyroclastic deposits are subject to alteration by meteoric water and groundwater, the meteoric water percolating through permeable pyroclastic deposits and reacting with glass shards to form smectitic clay and alkaline solutions. The upper surface of the zeolitic alteration is generally almost planar, suggesting that it is related to the water table. Two or three zones may occur, a second zone with clinoptilolite as an abundant replacement of glass shards, and a third zone containing analcime. At deeper levels authigenic albite and K-feldspar replace the zeolites.

Hydrologically closed systems. Tephra beds in lacustrine deposits are commonly replaced by zeolites, especially if the lake is saline and alkaline. The development of a playa lake depends largely on a lack of effluent streams. The particular zeolite alteration products formed are controlled to a large extent by the composition of the lake water. Unaltered glass persists if pore solutions have a pH less than about 8.5. This is succeeded by a clinoptilolite zone, followed by a zone bearing analcime and finally a zone of K-feldspar. In closed basins, the development of high salinity and alkalinity along the margins of lakes or in mudflats provides the chemical environment for zeolite formation without volcanic material being involved.

Marine sediments. Zeolites occur as a component of many deep marine sediments that include calcareous ooze, chalk, radiolarian ooze, hyaloclastite, ash layers and volcaniclastic debris. Clinoptilolite is common in the deeper, older sediments and phillipsite at shallower depths. Where volcaniclastic materials are deposited into fore-arc or back-arc basins, zeolite-bearing sedimentary rocks are commonly abundant. They are also a common diagenetic product in feldspathic sand in fore-arc basins along convergent continental margins. In many such sections, zoning is common, typically grading from unaltered glass to clinoptilolite or mordenite, to analcime and heulandite, followed by laumontite and then albite. The zonal boundaries are in general parallel with the stratification and may be temperature-dependent.

Very low-grade metamorphism and the zeolite facies. The lowest grade of metamorphism with the diagenetic assemblages containing a zeolite, commonly laumontite or analcime, may develop via burial metamorphism, contact metamorphism or ocean-floor metamorphism. The burial of sediments derived from arc-terranes, containing abundant volcanic detritus and plagioclase sand grains, produces zeolites during diagenesis. At higher temperatures and pressures, the zeolites give way to prehnite, pumpellyite and feldspar. The lowest temperature zones of thermal metamorphic aureoles in volcanic terranes may contain zeolites, typically laumontite. The time required for the alteration of volcanic tuffs or ash to zeolites has been demonstrated to be a few thousand years.

Zeolites in lava flows. Almost every known silicate zeolite may occur in cavities in basaltic rocks. Notable localities include the Tertiary lavas of Iceland, the Antrim lavas in Northern Ireland, the Deccan traps in India, the Triassic basalts in and around Paterson, New Jersey, and in Nova Scotia. The zeolites in these occurrences may have originated in several different ways, including burial metamorphism, burial diagenesis, reaction with groundwater in areas of high heat and fluid flow (high geothermal gradient) and reactions with surface water during the initial cooling of a lava. The effect of depth on zeolite crystallization in subaerial flood basalt flows was demonstrated by Walker (1960) in his study on the distribution of amygdale minerals in the basalt flows of Iceland. The zeolites define almost flat-lying zones that cut across the lava stratigraphy. The lowest zone, which is rich in mesolite and scolecite among others, extends from below sea-level to an altitude of almost 800 m Fig. 259. The diagnostic

Downloaded from https://pubs.geoscienceworld.org/books/chapter-pdf/3762850/9780903056434_ch68.pdf
by guest

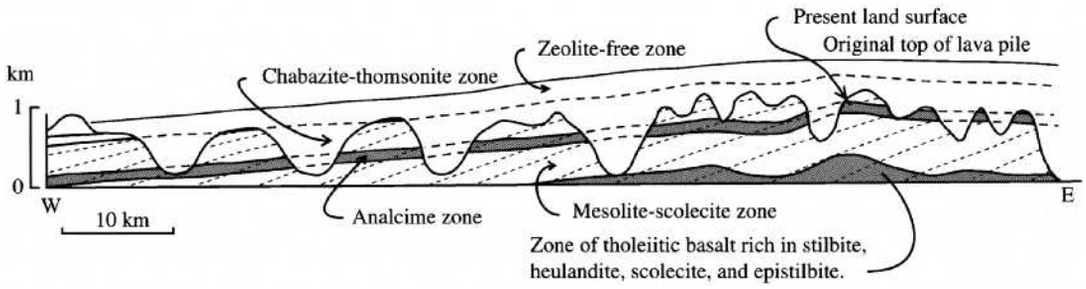


Fig. 259. Diagrammatic section through the Tertiary lava pile of eastern Iceland, showing the inferred relationships between the lava stratigraphy (sloping dashed lines) and the distribution of amygdale minerals (sub-horizontal grey and white bands) (after Walker, G.P.L., 1960, *J. Geol.*, **68**, 515–28).

zeolite in the next zone, which is about 150 m thick is analcime. Above this is the thomsonite-chabazite zone, which is about 300 m thick, about 400 m above the analcime zone the vesicles are empty. This vertical sequence is related to temperature. Similar occurrences of regionally zoned zeolites have been described from several areas, including the Deccan Traps in India, the Paraná lavas in Brazil and the Tertiary basalt flows in Northern Ireland.

Many of the regions that produce relatively large crystals of zeolites in basaltic cavities are those with thick accumulations of lavas in areas of ongoing volcanic activity and possibly associated with high heat flow. In eastern Iceland the interval between the chabazite zone and the mesolite-scolecite zone in geothermal areas is about 70ºC and occurs at a depth of about 0.5 km below the inferred surface. This would indicate a geothermal gradient of about 100ºC/km. Drill cores from currently active geothermal systems, e.g. Wairakei geothermal field, New Zealand, and Yellowstone National Park, Wyoming, provide evidence of warm to hot (70–150ºC) waters circulating through large volumes of rock. These active systems may contain acidic or alkaline hydrothermal fluids; zeolites occur only in those with alkaline solutions.

Other occurrences. At the land surface, zeolites are formed readily from suitable materials (e.g. volcanic glass, tuff, nepheline, feldspar) in conditions of high pH resulting from the concentration of sodium carbonate–bicarbonate by evaporation in an arid or semi-arid environment. In saline alkaline lakes zeolites are common and widespread: in the western USA clinoptilolite, phillipsite and erionite are found replacing rhyolitic tuffs in Plio-Pleistocene lake deposits. Reactions are relatively rapid, with vitric tuff altering to zeolites in about 1000 years. In water of moderately high salinity these zeolites can alter to analcime; in highly saline water, all zeolites can alter to K-feldspar. In open hydrological systems, tephra may show a vertical zonation of zeolites as meteoric water moves through the system: thus clay minerals (commonly smectites) are formed by hydrolysis of vitric ash, altering to zeolites such as clinoptilolite at depth and then analcime at still greater depth.

In areas of hydrothermal alteration, zeolitization may also demonstrate a zonal pattern, with clinoptilolite or mordenite in the shallowest and coolest zones; progressively deeper zones may contain analcime, heulandite, laumontite and wairakite. Various zeolites were recorded in the masonry of Roman hot-water baths and laumontite is found, for example, in radiators fed by natural hot spring water in Kamchatka, Russia.

The regional occurrence of zeolites in low-grade metamorphic rocks was first recognized in southern New Zealand. A zeolite facies was later defined as 'that set of mineral assemblages that is characterized by the association calcium zeolite–chlorite–quartz in rocks of favourable bulk composition'. Such an alteration sequence, typically involving the breakdown of calcic plagioclase to laumontite or heulandite is due chiefly to the increasing temperature associated with progressive burial. Such zeolite occurrences are relatively common in the circum-Pacific area, as in Japan and the western coast of North America. Zeolites in any type of occurrence change ultimately to more thermodynamically stable minerals such as alkali feldspar or other non-zeolite minerals, through intermediate zeolites such as analcime and laumontite, due to the increase in pressure and temperature or to the increase in concentration of porewater. The time taken for the analcime–albite transformation during burial diagenesis has been estimated to be 400 000 years. In areas where intercalated lavas and intrusive rocks are present, zeolitization may have been influenced by emplacement of the igneous intrusives at some distance from the contact, e.g. in Mull, Scotland.

The best known occurrences of zeolites are probably those in which the minerals form well developed crystals in the vesicles and amygdales of basalts. These zeolites are generally considered to be the result of late-stage fluids that permeated the basalts after their extrusion. Typically such amygdales contain more than one species of zeolite, e.g. chabazite and analcime, which may be associated also with calcite. Certain zeolite assemblages are typical of individual basalt

Downloaded from https://pubs.geoscienceworld.org/books/chapter-pdf/3762850/9780903056434_ch68.pdf
by guest

flows, though in the Tertiary lavas of Northern Ireland and of eastern Iceland the zeolite zones cut discordantly across the lava stratigraphy.

Uses of natural zeolites

In those areas where beds of vitric tuff or other volcanic-rich sedimentary rock have been altered to nearly pure zeolite, the deposits may be suitable for economic exploitation. Applications have been developed in agriculture, using the cation-exchange capacity, cation selectivity and molecular sieve properties. Zeolites are used also in the remediation of soils. The zeolite which most commonly occurs in large quantities is clinoptilolite; which has a selectivity for certain heavy metals and is thus the basis for many applications in water and wastewater treatment. Where zeolite tuff is abundant, it has been used in the construction of buildings and as a lightweight aggregate as in the production of pozzolanic cement. Of the many zeolites with industrial applications, erionite should be avoided as it has known carcinogenic properties.

Further reading

Armbruster, T. and Gunter, E. (2001) Crystal structures of natural zeolites. Pp. 1–67 in: *Natural Zeolites: Occurrence, Properties, Applications* (D.L. Bish and D.W. Ming, editors). Reviews in Mineralogy and Geochemistry, **45**, Mineralogical Society of America & Geochemical Society, Washington, D.C.

Bish, D.L. and Carey, J.W. (2001) Thermal behaviour of natural zeolites. Pp. 403–452 in: *Natural Zeolites: Occurrence, Properties, Applications* (D.L. Bish and D.W. Ming, editors). Reviews in Mineralogy and Geochemistry, **45**, Mineralogical Society of America & Geochemical Society, Washington, D.C.

Coombs, D.S. (1954) The nature and alteration of some Triassic sediments from Southland, New Zealand. *Transactions of the Royal Society of New Zealand*, **82**, 65–109.

Coombs, D.S., Alberti, A., Armbruster, T., Artioli, G., Collela, C., Galli, E., Grice, J.D., Liebau, F., Mandarino, J.A., Minato, H., Nickel, E.H., Passaglia, E., Peacor, D.R., Quartieri, S., Rinaldi, R., Rosa, M., Sheppard, R.A., Tillemans, E. and Vezzalini, G. (1997) Recommended nomenclature for zeolite minerals. *The Canadian Mineralogist*, **35**, 1571–1606.

Dyer, A. (1988) *An Introduction to Zeolite Molecular Sieves.* Wiley, Chichester, UK.

Flanigen, E.M., Bennett, J.M., Grose, R.W., Cohen, J.P., Patton, J.R., Kirchner, R.M. and Smith, J.V. (1978) Silicalite, a new hydrophobic crystalline silica molecular sieve. *Nature*, **271**, 512–516.

Gottardi, G. and Galli, E. (1985) *Natural Zeolites.* Springer-Verlag, Heidelberg, Germany, 409 pp.

Meier, W.M., Olsen, D.H. and Baerlocher, C. (1996) Atlas of zeolite structure types. *Zeolites*, **17**, 1–230.

Passaglia, E. and Sheppard, R.A. (2001) The crystal chemistry of zeolites. Pp. 69–116 in: *Natural Zeolites: Occurrence, Properties, Applications* (D.L. Bish and D.W. Ming, editors). Reviews in Mineralogy and Geochemistry, **45**, Mineralogical Society of America & Geochemical Society, Washington, D.C.

Walker, G.P.L. (1951) The amygdale minerals in the Tertiary lavas of Ireland. I. The distribution of chabazite habits and zeolites in the Garron Plateau area, County Antrim. *Mineralogical Magazine*, **29**, 773–791.

Wise, W.S. (2004) The zeolite group *in* Deer, W.A., Howie, R.A. and Zussman, J. *Rock-Forming Minerals*, **4B**, pp 493–959.

Downloaded from https://pubs.geoscienceworld.org/books/chapter-pdf/3762850/9780903056434_ch68.pdf
by guest

Analcime $Na[AlSi_2O_6]\cdot H_2O$

Cubic

n	1.479–1.493
D (g/cm^3)	2.24–2.29
H	5
Cleavage	{001} very poor
Twinning	{001}, {110} lamellar
Colour	White, pink or grey; colourless in thin section
Unit cell	*a* ~ 13.72 Å
	Z = 16 space group *Ia3d*
Special features	Gelatinizes in HCl

Analcime is a common zeolite which occurs in cavities in mafic volcanic rocks which have been subjected to burial metamorphism, possibly as a primary phase in some undersaturated volcanic rocks and in sediments as a diagenetic mineral. Wairakite, the calcium analogue, is a rare zeolite found in geothermal areas and in some low-grade rocks in metamorphic aureoles.

Structure

The analcime aluminosilicate framework is built of $(SiAl)O_4$ tetrahedra linked in such a way that each corner oxygen is shared by two tetrahedra (Fig. 257a, p. 357). The framework contains rings of six tetrahedra and four tetrahedra normal to triad and tetrad axes, respectively. A set of 16 large cavities forming non-intersecting channels are occupied by water molecules, whereas an adjacent set of 24 smaller cavities are two-thirds occupied by sodium and the remainder are vacant. Partial ordering of Si and Al in tetrahedral sites occurs due to aluminium avoidance. The analcime framework is isostructural with that of leucite (see Fig. 238, p. 335). Small deviations from cubic symmetry are common. Wairakite, the Ca analogue, is monoclinic with *a* 13.69, *b* 13.68, *c* 13.56 Å, β 90.5º.

Chemistry

The only appreciable chemical variation in natural analcime is the partial replacement of sodium by potassium, caesium or calcium, and the substitution of Al for Si which necessitates an increase in the (Na + K + Ca) ions to maintain charge balance. Analcime may contain up to ~2% K_2O and complete solid solution between analcime and pollucite, its caesium analogue, is possible. In a series of analcimes from an igneous differentiation series it has been shown that with decreasing temperature the main substitution is $NaAl \leftrightarrow Si$; the SiO_2/H_2O molecular ratio remains at 2:1. In sedimentary analcime the Si/Al ratio varies between 2 and 3 (e.g. analysis 3, Table 48) with Si/Al 2.57. For these analcimes, as the Si content increases the number of exchangeable cations decreases. Wairakite is the calcium analogue of analcime, in which the sodium is replaced by calcium on a valency basis, i.e. Ca for 2 Na, giving $CaAl_2Si_4O_{12}.2H_2O$.

Analcime can be synthesized at 100ºC from aluminosilicate gels or from glasses of appropriate composition. Analcimes have been produced hydrothermally varying from $Na_4Al_4Si_6O_{20}.3H_2O$ (partially dehydrated natrolite composition) to $Na_2Al_2Si_6O_{16}.3H_2O$ (hydrous albite composition): the water contents of these synthetic analcimes vary linearly with Si, but the range of (NaAl)/Si ratios is much greater than that found in natural material.

In the system $NaAlSi_3O_8$(Ab)–$KAlSi_3O_8$(Or)–$NaAlSiO_4$(Ne)–$KAlSiO_4$(Ks)–H_2O the assemblage analcime + melt (± nepheline, albite and orthoclase) can only exist in the pressure range 0.5–1.3 GPa at temperatures between 640 and 600ºC. The dehydration of analcime to albite, nepheline and H_2O occurs at 492 ± 5ºC at 0.3 GPa. In the presence of quartz, analcime dehydrates to albite and water (Fig. 260).

Optical and physical properties

Analcime occurs as transparent to opaque, colourless to white euhedral crystals, or in irregular granular masses. The structure of analcime ideally is cubic and, although some specimens are isotropic, many show

Downloaded from https://pubs.geoscienceworld.org/books/chapter-pdf/3762859/9780903056434_ch69.pdf
by guest

Table 48. Analcime analyses.

	1	2	3		Numbers of ions on the basis of 96 O in the framework 1	2[a]	3[b]
SiO_2	52.67	54.16	58.62	Si	31.13	31.99	34.30
Al_2O_3	23.79	22.83	19.37	Al	16.58	15.90	13.36
Fe_2O_3	1.26	0.58	0.95	Fe^{3+}	0.56	0.26	0.42
FeO	0.15	0.26	–	Fe^{2+}	0.07	0.13	–
MgO	tr.	–	0.23	Mg	–	–	0.20
CaO	0.71	tr.	0.15	Ca	0.45		0.09
Na_2O	12.94	13.12	11.00	Na	14.83	15.02	12.48
K_2O	0.25	0.29	0.38	K	1.88	0.22	0.28
H_2O+	8.00	8.41	8.22	H_2O	15.77	16.57	16.04
H_2O-	0.32	0.22	–				
Total	100.09	99.96	99.02				

1 Analcime, analcime tinguaite, Portobello, Otago Harbour, New Zealand (Wilkinson, J.F.G., 1968, *Contrib. Mineral. Petrol*., **18**, 252–69). Analyst, G.I.Z. Kalocsai.
2 Analcime, blairmorite, Crowsnest Volcanics, Carbondale River, Alberta, Canada (Crook, K.A.W., *In* Coombs, D.S. & Whetton, J.T., 1967, *Bull. Geol. Soc. Amer.*, **78**, 269–82). Analyst, A. Stelmach. Includes TiO_2 0.05, Cs_2O 0.04%.
3 Sedimentary silica-rich analcime, Big Sandy formation, Arizona, USA (Sheppard, R.A. & Gude, A.J., 3rd., 1973, *U.S. Geol. Survey*, *Prof. Paper*, **830**). Includes TiO_2 0.06, SrO 0.02, BaO 0.02%.

[a] Also Ti 0.02, Cs 0.01.
[b] Also Ti 0.03, Sr 0.01.

slight birefringence (usually $\leqslant 0.001$): some of these analcimes are anomalously biaxial and show repeated lamellar twinning on {001} or {110}.

Wairakite is colourless to white and has a density of 2.26 g/cm^3, and a hardness of 5½–6. It is biaxial with α 1.498, γ 1.502, $2V_\gamma$ 70–105º, and is commonly twinned on {110}; the orientation is $\alpha \sim y$, $\beta \sim x$, $\gamma \sim z$.

Distinguishing features

Analcime is very similar to leucite, but the latter mineral has a slightly higher refractive index and a different paragenesis; it is anhydrous and usually shows complex twinning. In vugs in volcanic rocks, crystals of analcime have a more vitreous lustre than leucite, which typically has a more chalky appearance. Sodalite resembles analcime but can be distinguished by a chemical test for chloride. When analcime is treated with concentrated HC1 it gelatinizes and takes a stain from a solution of Malachite Green.

Paragenesis

Analcime is a widespread zeolite, occurring in many different environments, including amygdaloidal cavities in basaltic rocks, as a replacement of rhyolitic vitric tuff and as a precipitate from strongly alkaline lakes. Although it has been widely reported as a primary mineral in some igneous rocks, in many such occurrences it may be interpreted as replacing primary

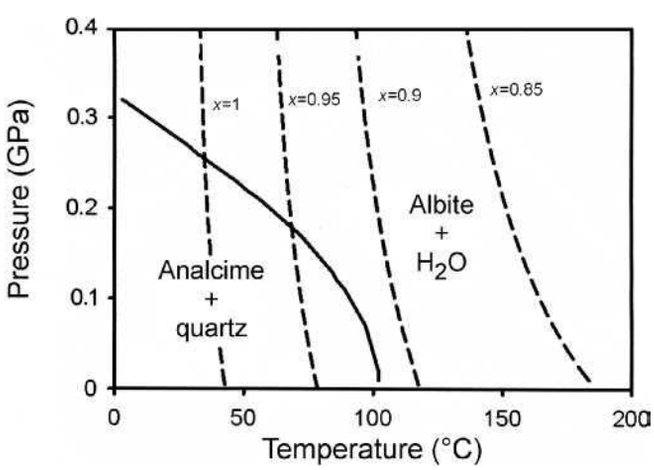


Fig. 260. A P_{fluid}–T diagram for the reaction analcime + quartz ⇌ albite + H_2O (solid curve) along with isopleths of analcime composition in equilibrium with quartz and water (dashed curves, labelled for number of Al pfu) calculated from data and models presented by Neuhoff, P.S. *et al*., 2004, *Amer. J. Sci*., **304**, 21–66).

Downloaded from https://pubs.geoscienceworld.org/books/chapter-pdf/3762859/9780903056434_ch69.pdf
by guest

leucite or nepheline. It is an important constituent of volcaniclastic sediments affected by burial metamorphism or hydrothermal alteration.

In plutonic igneous rocks such as teschenites, the analcime may amount to around 20%, but in many such rocks it is secondary after nepheline. In glenmuirites (analcime essexites) the analcime may amount to 17%. The large idiomorphic crystals of analcime found in blairmoreite (analcime phonolite) of the Crowsnest volcanic suite in Alberta must have been generated in an environment of ~600ºC and a partial pressure of water of 0.8–1.5 GPa (28–50 km depth). They have been shown by isotopic analyses to have been involved either in subsolidus exchange or replacement of pre-existing leucite.

In hypabyssal igneous rocks analcime is found in some olivine dolerites. In the doleritic sills of western Scotland analcime is often abundant, particularly in analcime dolerite (or crinanite), but this analcime could have formed only by alteration of pre-existing Na-rich phases at subsolidus temperatures.

In volcanic rocks analcime is known as a constituent in some basalts, where typically it is restricted to the groundmass; it is known also from trachybasalts, where it may be associated with pseudoleucite. The hydrothermal crystallization of analcime in igneous rocks typically occurs in vesicles, where analcime may be found in association with prehnite, chabazite, thomsonite, stilbite and other zeolites. In burial-metamorphosed igneous rocks, the presence of analcime is an important indicator of metamorphic grade. Water-clear analcime has been found in association with chabazite in cavities and fissures in the amygdaloidal basalts of Antrim. Boreholes drilled in alkaline parts of a geyser basin in Yellowstone Park showed that the Na and Ca of the feldspars in rhyolitic and dacitic lavas are replaced by K, while at higher levels the Na gives rise to the formation of abundant analcime.

In sedimentary rocks analcime may occur as an authigenic mineral in sandstones; analcime-rich rocks interbedded with phosphatic siltstones and sandstones, and consisting of 35% analcime set in a cryptocrystalline groundmass of laumontite, fluorite, calcite and quartz, are known. A thick series of greywackes with beds of volcanic tuff in New Zealand Triassic sediments show an alteration of glassy fragments to analcime and heulandite: with increasing depth the analcime is replaced by a laumontite-bearing assemblage. In the Eocene lacustrine beds of the Green River Formation of Wyoming, Utah and Colorado, analcime is by far the most widespread and abundant of the silicate minerals. A formation in the central Sahara some 20 m thick and extending over 10000 to 15000 km^2, consists essentially of analcime: this analcime is considered to be either a primary precipitate or to have been derived from the alteration of pyroclastics or clays, though no traces of these are seen.

Analcime commonly coexists with clinoptilolite (± phillipsite) in deep-sea volcaniclastic sediments and calcareous oozes; its abundance appears to increase with sediment age and it may have been derived by the alteration of clinoptilolite. It is also a typical component of tuff-bearing alkaline saline lakes, where its crystallization is related more to the brine composition than to the chemistry of the volcanic glass and sedimentary components.

In the zeolite facies the analcime–heulandite stage appears to mark the boundary between diagenesis and low-grade metamorphism. Where an analcime–wairakite solid solution exists with both epidote and prehnite its Na/(Na + Ca) ratio may indicate the water pressure conditions during metamorphism.

Analcime pseudomorphs after leucite are also known, and it has been suggested that the analcime of some igneous rocks is an ion-exchanged alteration product of leucite.

Wairakite, the calcium analogue of analcime, was originally recorded in tuffaceous sandstones and breccias, vitric tuffs and ignimbrite which had been altered by alkaline hydrothermal fluids associated with geothermal steam in New Zealand. It is known from many other geothermal fields and also from low-grade metamorphic rocks in Japan and elsewhere.

Further reading

Bish, D.L. and Ming, D.W. (Editors) (2001) *Natural Zeolites: Occurrence, Properties, Applications*. Reviews in Mineralogy and Geochemistry, **45**, Mineralogical Society of America and Geochemical Society, Washington, D.C. 654 pp.

Coombs, D.S. and Whetten, J.T. (1967) Composition of analcime from sedimentary and burial metamorphic rocks. *Bulletin of the Geological Society of America*, **78**, 269–282.

Gatta, G.D., Sartbaeva, A. and Wells, S.A. (2009) Compression behaviour and flexibility window of the analcime-like feldspathoids: experimental and theoretical findings. *European Journal of Mineralogy*, **21**, 571–580.

Gottardi, G. and Galli, E. (1985) *Natural Zeolites.* Springer Verlag, 409 pp.

Henderson, C.M.B. and Gibb, F.G.F. (1983) Felsic mineral crystallization trends in differentiating alkaline basic magmas. *Contributions to Mineralogy and Petrology*, **84**, 355–364.

Iijima, A. and Hay, R.L. (1968) Analcime compositions in tuffs of the Green River Formation of Wyoming. *American Mineralogist*, **53**, 184–200.

Mumpton, F.A. (Editor) (1977) *Mineralogy and Geology of Natural Zeolites.* Mineralogical Society of America, Short Course Notes, **4,** 233 pp.

Neuhoff, P.S., Hovis, G.L., Balassone, G. and Stebbins, J.F. (2004) Thermodynamic properties of analcime solid solutions. *American Journal of Science*, **304**, 21–66.

Roux, J. and Hamilton, D.L. (1976) Primary igneous analcite: an experimental study. *Journal of Petrology*,**17**, 244–257.

Wilkinson, J.F.G. and Hensel, H.D. (1994) Nephelines and analcimes in some alkaline igneous rocks. *Contributions to Mineralogy and Petrology*, **118**, 79–91.

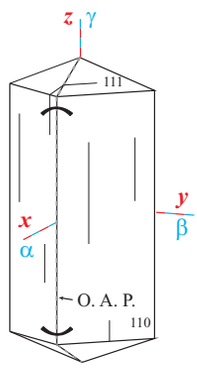
Wise, W.S. (2004) Analcime *in* Deer, W.A., Howie, R.A. and Zussman, J. *Rock-Forming Minerals*, **4B**, pp. 528–566.

Downloaded from https://pubs.geoscienceworld.org/books/chapter-pdf/3762859/9780903056434_ch69.pdf
by guest

Natrolite $Na_2[Al_2Si_3O_{10}]\cdot 2H_2O$

Orthorhombic (+)

α	1.473–1.483
β	1.476–1.486
γ	1.485–1.496
δ	0.012
$2V_\gamma$	58–73°
Orientation	α = *x*, β = *y*, γ = *z*
D (g/cm^3)	2.20–2.26
H	5–5.5
Twinning	{110}, {011}and {031} rare
Cleavage	{110} perfect.
Colour	Colourless, white, grey, bluish, yellowish; colourless in thin section
Unit cell	*a* 18.272 Å, *b* 18.613 Å, *c* 6.593 Å Z = 8. Space group *Fdd*2
Special features	Gelatinized by dilute HCl



Natrolite is relatively common as vesicle fillings in altered basalt. It is also common as a deuteric alteration product in syenitic plutonic rocks.

Structure

The natrolite group includes natrolite, mesolite, scolecite, thomsonite, gonnardite and edingtonite. The fundamental chain-like unit (Fig. 257b, p. 357 and Fig. 261) is prominent in all of their structures and the first three commonly have a fibrous morphology. Each unit of the chain has four tetrahedra which link laterally to the other chains (Fig. 262). Each chain is translated by *c*/4, avoiding Al–O–Al linkages. The spaces between four linked chains form channels parallel to the chain lengths (the *z* axis), which accommodate the Na cations around the tetrad, and water molecules, but unlike in many other zeolites these are held tightly in fixed positions, which affects cation exchange and dehydration properties. The Na cations are symmetrically located along a screw-diad in the centre of each channel, each cation being coordinated by four framework oxygen anions on one end of the oval-shaped channel (Fig. 262) and by the oxygen atoms of two water molecules. The hydrogen atoms of the water molecules are bonded to framework oxygen atoms, and each water oxygen is bonded to two sodium atoms.

Although the topological symmetry of the framework is tetragonal, the bonding of non-framework cations

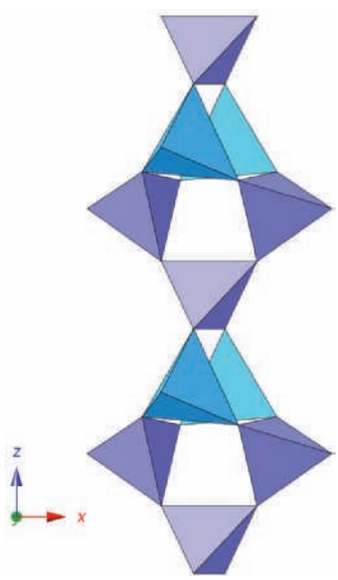


Fig. 261. Side view of the basic $Si_2Al_3O_{10}$ chain of (Si,Al)–O tetrahedra that occurs in the structure of natrolite. Dark blue tetrahedra contain Si, and light blue contain Al cations at their centres (CrystalMaker image).

Downloaded from https://pubs.geoscienceworld.org/books/chapter-pdf/3762915/9780903056434_ch70.pdf
by guest

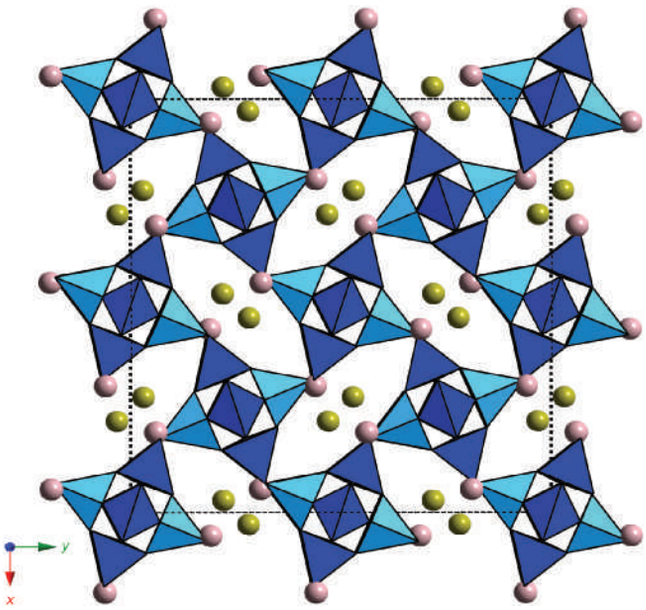


Fig. 262. Projection (down *z*) of the structure of natrolite showing the lateral linkage of neighbouring chains, and Na cations in roughly oval-shaped channels defined by successive rings of eight tetrahedra. Neighbouring chains are arranged in a helix relative to each other and translated by *c*/4 so that Al–O–Al bonds are avoided (CrystalMaker image). Dark blue: Si–O tetrahedra; light blue: Al–O tetrahedra; green: Na; pink: water molecules.

produces a partial collapse of the channel through the rotation of about 24º for each chain, reducing the crystal symmetry to orthorhombic.

The individual members of the natrolite group differ through alternative lateral 'chain' linkages and the positions of non-framework cations and water molecules; there are also differences in the nature and degree of Si,Al ordering.

Chemistry

The range shown by the chemical composition of natrolite is very small, all analyses being near the pure sodium end-member (Table 47, analysis 1, p. 359).

Experimentally, natrolite has proved difficult to synthesize, but its successful production from gels in the composition range (1–2) $Na_2O{\cdot}Al_2O_3{\cdot}SiO_2 + H_2O$ in the presence of natural seed crystals, in the temperature range 100–200ºC has been reported. Natrolite dehydrates in a single step, starting at about 250ºC and completing by 350ºC; this is accompanied by a contraction of the *a* and *b* cell dimensions.

Optical and physical properties

In general terms, as there is little variation in the chemical composition, the optical properties of natrolite reflect this. It is optically positive and length slow with a moderate birefringence.

Distinguishing features

Natrolite is generally well crystallized, typically as elongate to acicular, pseudo-tetragonal prisms. Its fairly unique optical properties allow it to be recognized even within intergrowths.

Paragenesis

Natrolite is a common zeolite worldwide; it is found in cavities and veins in altered basaltic rocks. Some notable occurrences are in breccia zones and cavities in Lower Jurassic basaltic pillow lavas in New Jersey and also in Oregon, USA. It is widespread in the highly altered Tertiary basalts of Co. Antrim, Northern Ireland, and in the Puy de Dôme, Auvergne, France. At the type locality at Hohentwiel, Hegau, Gemany, natrolite occurs in veins cutting phonolite. There are rare ocurrences as diagenetic alteration products in sedimentary rocks and it is found as a late-stage product of autometasomatism or deuteric alteration of alkaline intrusions such as nepheline syenites. At Mont Saint-Hilaire, Quebec, natrolite is abundant, and it is common in late hydrothermal veins in the nepheline syenites of the Khibiny and Lovozero alkaline complexes in the Kola Peninsula.

Further reading

Alberti, A., Pongiluppi, D. and Vezzalini, G. (1982) The crystal chemistry of natrolite, mesolite and scolecite. *Neues Jahrbuch für Mineralogie, Monatshefte*, 31–248.

Gatta, G.D. (2005) A comparative study of fibrous zeolites under pressure. *European Journal of Mineralogy*, **17**, 411–421.

Gunter, E.M. and Ribbe, P.H. (1993) Natrolite group zeolites: correlations of optical properties and crystal chemistry. *Zeolites*, **13**, 435–440.

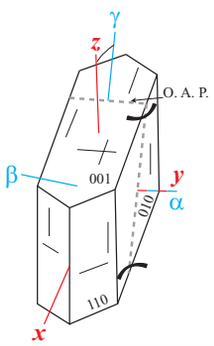
Hey, M.H. (1932) Studies on the zeolites. Part III. Natrolite and metanatrolite. *Mineralogical Magazine*, **23**, 243–289.

Ross, M., Flohr, M.J.K. and Ross, D.R. (1992) Crystalline solution series and order-disorder within the natrolite mineral group. *American Mineralogist*, **77**, 685–703.

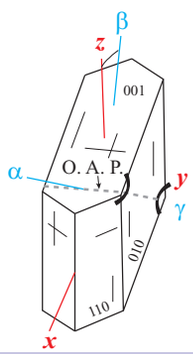
Downloaded from https://pubs.geoscienceworld.org/books/chapter-pdf/3762915/9780903056434_ch70.pdf
by guest

Monoclinic (+) or (–)

Phillipsite



Harmotome



α	1.483–1.508	
β	1.484–1.509	
γ	1.486–1.514	
δ	0.003–0.010	
$2V_\gamma$	60–80º	
Orientation	β:*x* = 46–65º, α = *y*; O.A.P. ⊥ (010)	α:*x* = 63–67º, γ = *y*; O.A.P. ⊥ (010)
D (g/cm^3)	2.20	2.41–2.47
H	4–4.5	
Cleavage	{010}, {110} distinct.	
Twinning	Ubiquitous on {001} and {20$\bar{1}$}, and on {011}	
Colour	Colourless, pink, grey, yellowish; colourless in thin section	
Unit cell	*a* 9.87 Å, *b* 14.30 Å, *c* 8.67 Å, β ~142º	*a* 9.87 Å, *b* 14.13 Å, *c* 8.71 Å, β ~125º
	Z = 1. Space group $P2_1/m$.	
Special features	Gelatinized by dilute HCl	

Minerals of the phillipsite series typically occur as low-temperature alteration products of volcanic rocks and in sediments with a volcaniclastic component.

Structure

The basic building block of the phillipsite framework is a chain of doubly connected four-membered rings, linking in a UUDD arrangement resembling a double crankshaft (see Fig. 257c, p. 357). Each tetrahedral node of the double crankshaft chain bonds through an oxygen bridge to another chain parallel to *x*, giving rise to (010) mirror planes (Fig. 263). Cross-linking of the chains creates channels of eight-membered rings with effective diameters of ~3.5 Å in both the *x* and *y* directions. The non-framework cations and water molecules are located in these channels, the bonding being sufficiently strong to distort the framework, reducing the symmetry from orthorhombic to monoclinic.

Chemistry

The lowest Si (about 9.2 atoms per unit cell) and highest divalent cation contents occur in those phillipsite crystals from undersaturated basalt. The highest Si (up to 12.3 atoms per unit cell) and most alkali-rich come from replacement of rhyolitic pyroclastic sediments in saline environments. The member of the series with Ba as the dominant cation is harmotome, $(Ba_{0.5},Ca_{0.5},K,Na)_x[Al_xSi_{16-x}O_{32}].12H_2O$ (Table 47, analysis 3, p. 359), but phillipsite-K, the most common species, often contains appreciable Ba.

Phillipsite has been synthesized by reacting K-, Na- and Ca-bearing aluminosilicate glass with NaOH + KOH solutions at about 250ºC, by reacting rhyolitic glass with

Downloaded from https://pubs.geoscienceworld.org/books/chapter-pdf/3762920/9780903056434_ch71.pdf
by guest

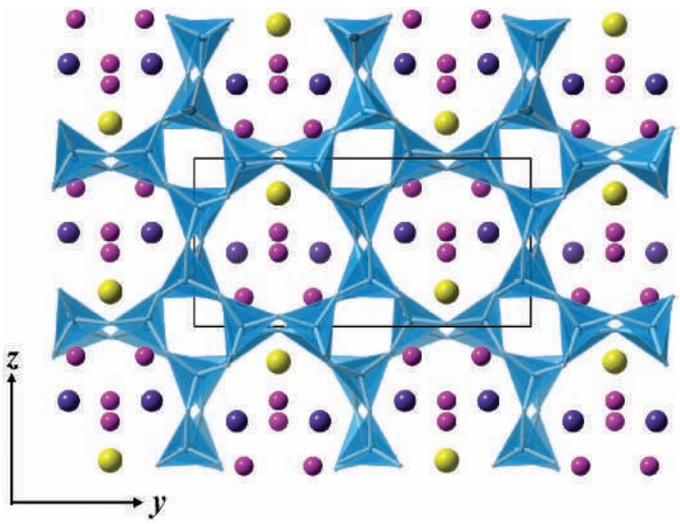


Fig. 263. The structure of phillipsite looking down the 'crankshaft' chains, which are parallel to *x* (based on data from Rinaldi *et al*., 1974. Fig. produced by M.D. Welch). Blue: (Si,Al) tetrahedra (disordered); yellow: K sites (Ba in harmotome) coordinated by four framework oxygens and water molecules; purple: sites partially occupied by Na and Ca, and bonded to one side of the channel and to water molecules; mauve: water molecules.

alkaline solutions (pH > 9) at 80ºC, and by reacting sea-water with trachytic glass at 200ºC in as little as four days. On heating, phillipsite loses most of its water at ~200ºC, and the remainder at 300–400ºC.

Optical and physical properties

High-silica phillipsites have the lowest refractive indices, but the nature of the non-framework cations has relatively little effect.

Distinguishing features

The habit and ubiquitous twinning of phillipsite are generally sufficient to allow the identification of macroscopic crystals. X-ray powder difffraction may be used to identify fine-grained occurrences; the diagnostic *d* values are 6.4 Å, 4.13 Å and 3.15 Å.

Paragenesis

Minerals of the phillipsite series occur in many different environments, including in amygdales in basaltic rocks. They are also found replacing rhyolitic vitric tuff and welded tuff in terrestrial settings and as abundant authigenic constituents in deep-sea sediments (Table 47, analysis 2, p. 359). Generally phillipsite replaces glass shards in reactions with alkaline and saline waters. In deep-sea sediments phillipsite occurs near the sediment–water interface to depths of several hundred metres. Rare occurrences have also been recorded as a late-stage alteration product in some alkaline igneous intrusions and pegmatite dykes.

Further reading

Galli, E. and Loschi Ghittoni, A.G. (1972) The crystal chemistry of phillipsites. *American Mineralogist*, **57**, 1125–1145.

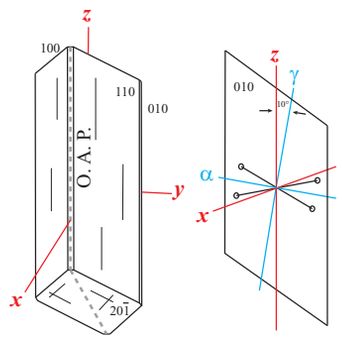
Kawano, M. and Katsutoshi, T. (1997) Experimental study of the formation of zeolites from obsidian by interaction with NaOH and KOH solutions at 150 and 200ºC. *Clays and Clay Minerals*, **45**, 365–377.

Rinaldi, R., Pluth, J.J. and Smith, J.V. (1974) Zeolites of the phillipsite family. Refinement of the crystal structure of phillipsite and harmotome. *Acta Crystallographica*, **B30**, 2426–2433.

Sheppard, R.A., Gude, A.J. and Griffin, J.J. (1970) Chemical composition and physical properties of phillipsite from the Pacific and Indian Oceans. *American Mineralogist*, **55**, 2053–2062.

Downloaded from https://pubs.geoscienceworld.org/books/chapter-pdf/3762920/9780903056434_ch71.pdf
by guest

Monoclinic (−)



α	1.510–1.514
β	1.518−1.522
γ	1.522−1.525
δ	0.010−0.012
$2V_\alpha$	23–47°
Orientation	β = *y*, O.A.P. (010); γ:*z* = 8–10° (in acute β angle)
D (g/cm^3)	2.27
Cleavage	{110} perfect, {010} and {001} poor
Twinning	On {110} fairly common
Colour	White to grey, pink, yellowish, brownish; colourless in thin section
Unit cell	*a* 14.724 Å, *b* 13.075 Å, *c* 7.559 Å, β 112.01°
	Z = 1. Space group *C*2/*m*
Special features	Gelatinized by dilute HCl.

Laumontite is a diagnostic mineral of the zeolite facies in mafic to intermediate volcaniclastic rocks which have been subjected to very low grade metamorphism; in sedimentary rocks it is a widespread diagenetic alteration product of calcic plagioclase.

Structure

The laumontite framework consists of chains of (Si,Al)−O tetrahedra (Fig. 257d, p. 357) linked laterally by four-membered rings of tetrahedra to form ten-membered rings and channels parallel to *z* which contain all the Ca ions and water molecules; the Si,Al distribution is highly ordered (Fig. 264). The common crystal form is the {110} prism, parallel to the channels, and the prominent cleavage {110} breaks the bonds connecting the chains. Fully hydrated laumontite has 18 water molecules per formula unit located in the wide channels, but occupancy is generally appreciably less.

Chemistry

The composition of laumontite (Table 47, analysis 9, p. 359) varies little from the average formula $Ca_4[Al_8Si_{16}O_{48}]\cdot 18H_2O$. Most analyses show minor Na and K, and there is little replacement of Ca by Mg. In some crystals, Fe^{3+} replaces tetrahedral Al, giving an orange colour, but the red colour shown by some vein laumontite is more likely to be due to hematite inclusions. Laumontite tends to partially dehydrate in low humidity air, but immersion in water allows full rehydration although the crystals do not recover their mechanical strength and crumble readily to powder. Leonhardite is a now discredited name for a partially dehydrated laumontite with approximately 14 H_2O per unit cell.

Experimentally, the synthesis of laumontite has proved difficult, but crystals of laumontite have been grown from glass of composition $CaO\cdot Al_2O_3\cdot 4SiO_2$ at 0.1 GPa water pressure over a temperature range of 30−450ºC. The stability relations of laumontite were examined in detail by Liou (1971).

Optical and physical properties

As there is relatively little compositional variation between laumontite samples, their optical and physical properties show only a limited range. Any partial dehydration lowers the refractive indices and increases the extinction angle. The DTA and TG curves indicate that the first peak equated with water loss of 3 H_2O occurs at around 100ºC, the second at 240ºC, 5 H_2O, and the third at 400ºC, 5 H_2O.

Distinguishing features

Freshly exposed laumontite crystals in amygdales or veins are translucent or transparent prisms, but exposure

Downloaded from https://pubs.geoscienceworld.org/books/chapter-pdf/3762924/9780903056434_ch72.pdf
by guest

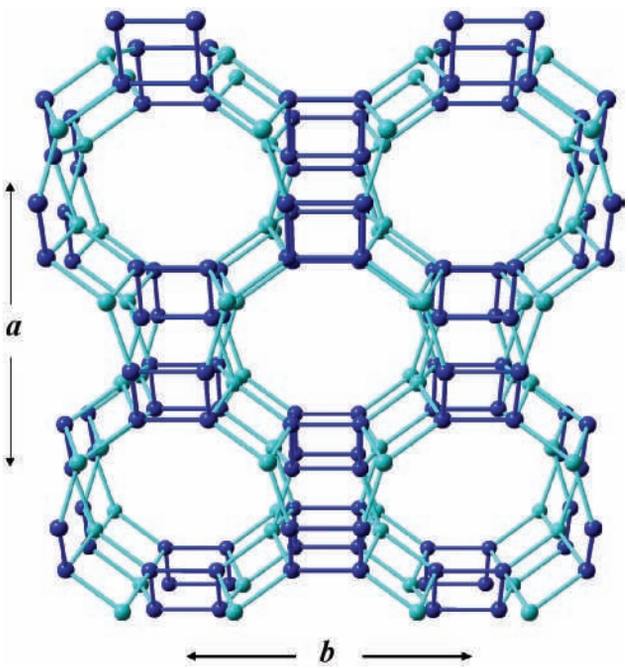


Fig. 264. Perspective view from near the *z* axis direction of the framework of laumontite, in which only the tetrahedral sites (small spheres) and T−T linkages are shown. The Si,Al distribution is highly ordered. The linkages coloured dark blue are part of the basic building unit of the laumontite structure (see Fig. 257d, p. 357), and these are linked laterally by 4-membered rings of (Si,Al) tetrahedra, forming a framework containing wide channels bounded by 10-membered rings (structure based on data from Stahl, K. *et al*., 1996, *Phys. Chem. Min*., **23**, 328−36). Dark blue, Si; light blue, Al.

to the atmosphere causes them to partially dehydrate and after a week or two they turn milky and may begin to decompose into powder. The birefringence is somewhat higher than for many zeolites, and at around 0.010−0.012 is the same as for quartz and feldspars.

Paragenesis

Most laumontite occurs as an alteration product of rocks rich in calcic plagioclase and/or basaltic glass and which have been exposed to slightly elevated temperatures (50–250ºC) in the presence of water. In the diagenesis of basalt flows it may occur associated with chabazite, heulandite, prehnite, quartz and calcite. In thick accumulations of volcaniclastic sediments, laumontite is a common alteration product at depth.

Laumontite is an important constituent in the diagenesis and burial of marine sediments. In the Southland syncline of New Zealand which exposes about 10 km of Triassic sediment with a large component of volcanic detritus, there is a lack of intrusive rocks but a progressive change in alteration minerals with depth, apparently in response to the increase in temperature and pressure due to burial. This led to the concept of burial metamorphism and the establishment of the zeolite facies. Laumontite occurs in the lower half of the section associated with albite or albitized plagioclase. This assemblage is now recognized in many areas of volcanigenic sediment accumulation all over the world.

The Upper Triasssic Karmutsen Group, Vancouver Island, British Columbia, consists of about 6000 m of basaltic pillow lava, breccia, tuff and massive amygdaloidal basalt flows. These rocks were first subjected to burial metamorphism and later to thermal metamorphism by the intrusion of a batholith. This led to the development firstly of zeolite facies with laumontite and later to the progressive breakdown of this assemblage to give the pumpellyite facies:

laumontite + prehnite + chlorite →
pumpellyite + quartz + H_2O

Further reading

Armbruster, T. and Kohler, T. (1992) Re- and dehydration of laumontite: a single crystal X-ray study at 100 K. *Neues Jahrbuch für Mineralogie, Monatshefte*, 385−397.

Artioli, G. and Ståhl, K. (1993) Fully hydrated laumontite: a structure study by flat-plate and capillary powder diffraction techniques. *Zeolites*, **13**, 249−255.

Cho, M., Maruyama, S. and Liou, J.G. (1987) An experimental investigation of heulandite–laumontite equilibrium at 1000 to 2000 bar P_{fluid}. *Contributions to Mineralogy and Petrology*, **97**, 43−50.

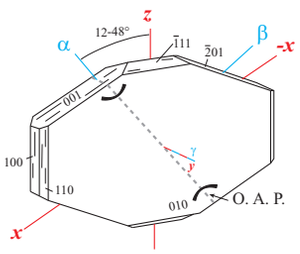
Coombs, D.S., Ellis, A.J., Fyfe, W.S. and Taylor, A.M. (1959) The zeolite facies, with comments on the interpretation of hydrothermal syntheses. *Geochimica et Cosmochimica Acta*, **17**, 53−107.

Liou, J.G. (1971) P-T stabilities of laumontite, wairakite, lawsonite and related minerals in the system $CaAl_2Si_2O_8$−SiO_2−H_2O. *Journal of Petrology*, **12**, 379−411.

Downloaded from https://pubs.geoscienceworld.org/books/chapter-pdf/3762924/9780903056434_ch72.pdf
by guest

Heulandite Series — $(Ca_{0.5},Sr_{0.5},Ba_{0.5},Mg_{0.5},Na,K)_9[Al_9Si_{27}O_{72}]\cdot 24H_2O$
Clinoptilolite Series — $(K,Na,Ca_{.0.5},Sr_{0.5},Ba_{0.5},Mg_{0.5})_6[Al_6Si_{30}O_{72}]\cdot 30H_2O$

Monoclinic (+)



	Heulandite-Ca	Clinoptilolite-K
α	1.492–1.505	1.476–1.478
β	1.494–1.506	1.477–1.479
γ	1.501–1.512	1.479–1.481
δ	0.006–0.009	0.003
$2V_\gamma$	35–75°	58–73°
Orientation	$\gamma = y$, $\alpha : z = 20°$, O.A.P. ⊥ (010)	α or $\beta = y$, $\gamma:z = 58–38°$, O.A.P. (010)
D (g/cm^3)	2.14–2.21	2.14–2.17
H	3.5–4	3.5–4
Cleavage	{010} perfect	{010} perfect
Colour	Colourless or white, pinkish, orange to red; colourless in thin section	
Unit cell	*a* 17.72 Å, *b* 17.90 Å, *c* 7.43 Å, β 116.4°	*a* 17.69 Å, *b* 17.90 Å, *c* 7.41 Å, β 116.5°
	Z = 1. Space group *C*2/*m*, *C*2 or *Cm*	
Special features	Not readily attacked by dilute HCl	

Minerals of the heulandite structure group (which includes the clinoptilolite series) are among the commonest zeolites, occurring in a wide variety of parageneses ranging from diagenetic alteration products in deep-sea sediment to volcaniclastic sedimentary rocks, cavities in volcanic rocks, pegmatitic dykes and in active hydrothermal systems.

Structure

In the structure of heulandite (Fig. 265), chains of the basic building units (Fig. 257e, p. 357) parallel to *z* are cross-linked by T–O–T linkages to form (010) sheets, which give rise to the (010) cleavage. The structure contains four different channels which give the mineral its microporous character. Two prominent channels are parallel to *z*; the larger is a channel of ten-membered rings with effective widths of 7.6 and 7.0 Å and the smaller is a channel of eight-membered rings with widths of 4.6 and 3.3 Å. A channel made up of eight-membered rings is parallel to *x* and another is parallel to [201]. All extra-framework cations in heulandite and clinoptilolite lie on the (010) mirror planes bisecting the channels, and water molecules are in sites near the channel walls.

Chemistry

The five heulandite species (-Ca, -Na-, -K, -Sr and -Ba) have compositions with Si/Al less than 4, whereas the clinoptilolites are defined as members of the heulandite structural group with Si/Al greater than 4. Chemical analyses given in Table 47, p. 359, show the relatively Ca-poor, alkali rich nature of clinoptilolite.

Experimentally, heulandite is readily synthesized from gels and oxide mixes of the appropriate composition at relatively high temperatures (200–360°C) and pressures of 100–250 MPa. Clinoptilolite has been synthesized from a gel and also from rhyolite glass at 150°C in an alkali carbonate solution.

Downloaded from https://pubs.geoscienceworld.org/books/chapter-pdf/3762929/9780903056434_ch73.pdf
by guest

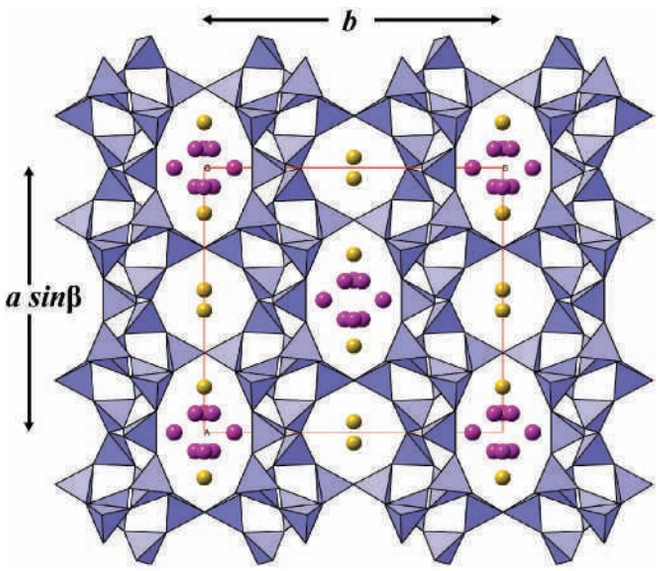


Fig. 265. Crystal structure of heulandite projected down *z*. showing two sets of wide channels parallel to *z*. (Si,Al) distribution in tetrahedral sites is disordered. Blue: (Si,Al)−O tetrahedra; yellow: (Na, Ca, K); mauve: water molecules (based on data from Gunter, M.E. *et al*., 1994, *Amer. Min*., **79**, 675−82).

Optical and physical properties

Although the values for the refractive indices quoted above refer only to the most common species, i.e. heulandite-Ca and clinoptilolite-K, the values for the other species in the series do not deviate appreciably from these (with the possible exception of heulandite-K). Most crystals of the heulandite and clinoptilolite series are optically positive with γ and the optic axial plane perpendicular to (010). The DTA curves show that more than half of the water in the channels is lost from both heulandite and clinoptilolite by heating to around 200ºC; further heating of heulandite results in partial framework collapse near 300ºC associated with the release of many of the remaining water molecules.

Distinguishing features

As all the mineral species in these two series are isostructural and differ in composition by simple solid solution exchanges, such as NaSi ↔ CaAl or 2 Na ↔ Ca, their distinction within the series is difficult and requires chemical data. In thin section these species have strong negative relief and very low birefringence. The commonly coffin-shaped crystals of heulandite and clinoptilolite have an excellent cleavage and are fairly easy to recognize.

Paragenesis

The minerals of the heulandite structural group occur in various low-temperature environments, most commonly as a result of the alteration of volcanic rocks and interstitial debris. This alteration occurs as a reaction between volcanic glass and interstitial solutions during diagenesis. Heulandite-series zeolites commonly replace glass with moderate amounts of silica available, such as that in basaltic or andesitic volcaniclastic sediments, whereas the clinoptilolite-series replace more siliceous rocks, e.g. those ranging from andesitic to rhyolitic in composition.

In many hydrologically closed basins the glass particles of tuff beds react with the interstitial water incorporated at the time of deposition. For a zeolite to be produced, this water must have a high salinity and pH (generally higher than those of sea-water). This sort of situation may occur where rhyolitic ash falls into saline, alkaline lakes that form in an arid environment. The replacement of vitric tuff in hydrologically closed systems tends to produce beds of virtually pure zeolite, typically clinoptilolite, which in many areas have a substantial economic value.

Further reading

Alberti, A. (1972) On the crystal structure of the mineral heulandite. *Tschermaks Mineralogische und Petrographische Mitteilungen*, **18**, 29−146.

Alberti, A. (1975) The crystal structure of two clinoptilolites. *Tschermaks Mineralogische und Petrographische Mitteilungen*, **22,** 25−37.

Broxton, D.E., Bish, D.I. and Warren, R.G. (1987) Distribution and chemistry of diagenetic minerals at Yucca Mountain, Nye County, Nevada. *Clays and Clay Minerals*, **35**, 89−110.

Coombs, D.S. (1954) The nature and alteration of some Triassic sediments from Southland, New Zealand. *Transactions of the Royal Society of New Zealand*, **82**, 65−109.

Kawano, M. and Katsutoshi, T. (1997) Experimental study of the formation of zeolites from obsidian by interaction with NaOH and KOH solutions at 150 and 200ºC. *Clays and Clay Minerals*, **45**, 365−367.

Sheppard, R.A., Gude, A.J. and Munson, E.I. (1965) Chemical composition of diagenetic zeolites from tuffaceous rocks in the Mojave Desert and vicinity, California. *American Mineralogist*, **50**, 244−249.

Downloaded from https://pubs.geoscienceworld.org/books/chapter-pdf/3762929/9780903056434_ch73.pdf
by guest

Triclinic (pseudotetragonal) (−) or (+)

α	1.460−1.515
β	1.460−1.516
γ	1.461−1.517
δ	0.001−0.005
2V	0–40º
D (g/cm^3)	2.05−2.20
H	4−5
Cleavage	{100}, {010} and {001}; in the pseudotrigonal forms {10$\bar{1}$1}, distinct
Twinning	About {111}, pseudotrigonal {0001}, interpenetrant, simple and lamellar
Colour	White, yellow, pink, red, colourless; colourless in thin section
Unit cell	*a* 9.40−9.44 Å, *b* 9.39−9.44 Å, *c* 9.40−9.44 Å, α 94.2−94.3º, β 94.1−94.3º, γ 94.1−94.5º Z = 1. Space group $P\bar{1}$ (or $R\bar{3}m$ for pseudotrigonal cell)

Chabazite series minerals are commonly recognized by their almost cubic rhombohedral morphology. The distinction of individual species requires chemical analysis and X-ray diffraction.

Structure

The framework structure consists of double six-membered rings of Si,Al tetrahedra (Fig. 257f, p. 357) at each apex of a rhombic unit cell with a stacking sequence in the order ...AABBCCAA.... (Fig. 266). The double six-membered rings linked as shown and involving also four-membered rings and eight-membered rings, make up the chabazite 'cage' which contains all the extra-framework cations and water molecules. If Si and Al are randomly distributed, the framework has the space group symmetry $R\bar{3}m$. The extra-framework cations partially fill four different sites (Fig. 267). The zeolites erionite and lévyne have cage-like structures broadly similar to that of chabazite, but the sequences of stacking double six-membered rings are ...AABAACAAB... and ...AABCCABBCAAB..., respectively.

Chemistry

Minerals with the chabazite structure have a wide compositional range, both in the Si/Al content of the framework and in extra-framework cations, which are most commonly Ca, K and Na and more rarely Mg and Sr. There are two major types of chabazite occurrence: crystals in cavities in basaltic rocks (typically Ca-dominant) and the authigenic components of volcaniclastic sediments and sedimentary rocks which range from Ca- to Na-dominant (e.g. Table 47, p. 359, analysis 4).

Experimentally, chabazite has been grown using natural minerals and glasses as starting materials, in reactions with Na- and K-solutions of high pH. Chabazite crystallizes readily at temperatures from 50 to 100ºC; at temperatures between 100 and 200ºC, chabazite crystallizes initially but is replaced by analcime. With rhyolite glass, fluids with 0.05 to 0.1 M KOH concentrations are required to crystallize chabazite. Chabazite may also be grown from gels at temperatures between 60 and 100ºC.

Optical and physical properties

Although most chabazites are morphologically rhombohedral, the crystals generally have a biaxial character and low birefringence. Basal sections are divided into sectors with varying extinction positions due to the optic planes being in different orientations. Chabazite-Ca and chabazite-Na are optically negative; some crystals appear uniaxial in some parts and biaxial in others.

Downloaded from https://pubs.geoscienceworld.org/books/chapter-pdf/3762981/9780903056434_ch74.pdf
by guest

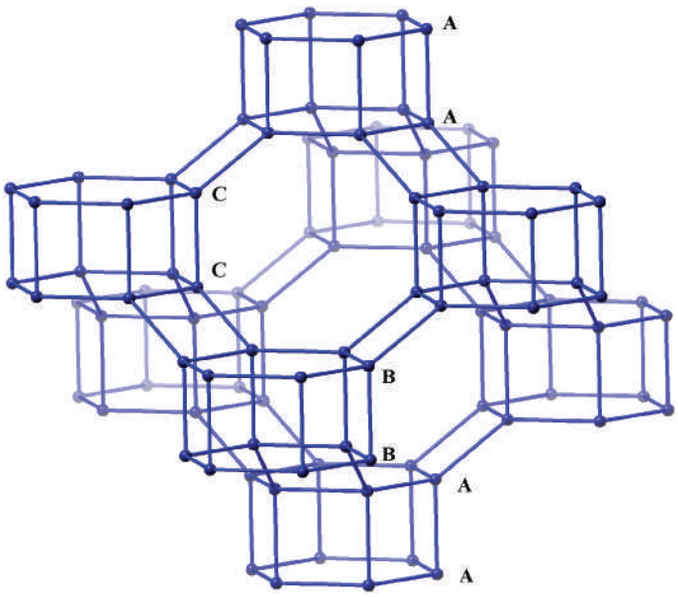


Fig. 266. Clinographic view of the framework of chabazite, in which only tetrahedral sites and T–T linkages are shown and T−O−T bridging oxygens are omitted. Four pairs of six-membered rings are darkened and labelled AA, BB, CC, AA to indicate their stacking sequence in chabazite (after Wise W.S. *in* Deer *et al*., 2004, *Rock-Forming Minerals*, **4B**. pp. 588−606).

Distinguishing features

Minerals of the chabazite series may be recognized generally, both in hand specimen and in SEM, by their almost cubic rhombohedral habit. The individual species in the series require a chemical analysis for their distinction. In thin sections of massively replaced vitric tuff, the chabazite is generally anhedral and commonly intergrown with other zeolites, making an XRD identification necessary.

Paragenesis

Chabazite is fairly common in cavities in basaltic rocks and occurs also as an authigenic mineral in some altered pyroclastic rocks. It may be found replacing rhyolitic vitric tuff in lacustrine beds in saline lakes, and is relatively common in trachytic tuff as in central Italy.

It occurs as an alteration product in several types of sedimentary rocks, e.g. in rhyolitic tuff and in trachytic ignimbrite and tuff. In the rocks of the zeolite facies developed by burial metamorphism chabazite does occur but is less common than analcime and laumontite. Both chabazite-Ca and chabazite-Na are relatively common, along with suites of other zeolites, in amygdaloidal cavities in basaltic rocks. In eastern Iceland, Walker (1960) found regional occurrences of chabazite in the upper zeolite zone in olivine basalt flows, above the boundary with the analcime zone, cutting across the flow boundaries of the basalts, showing that the zeolite

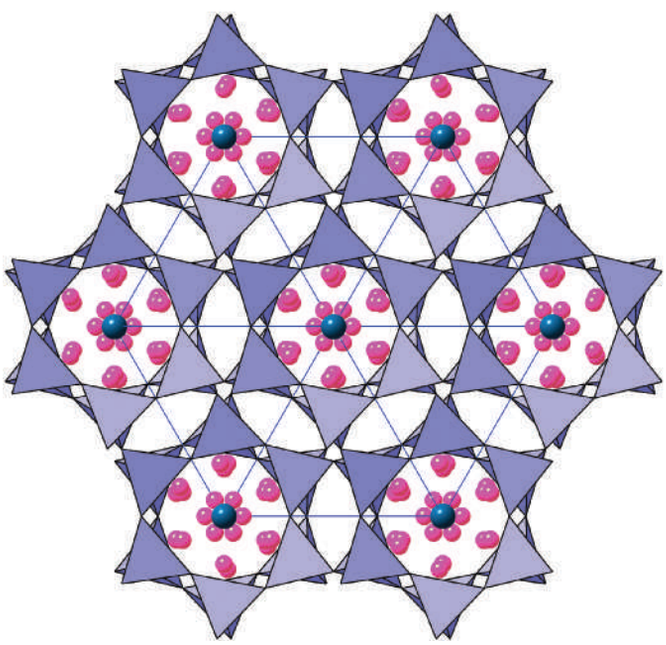


Fig. 267. Projection of the crystal structure of chabazite on to (111) showing six-membered rings and four-membered rings with random (Si,Al) occupation (based on data from Mazzi, F. & Galli, E., 1983, *Neues Jahrb. Mineral., Monats*., 461−80. Fig. produced by M.D. Welch). Pale blue: (Si,Al)−O tetrahedra; dark blue: (Ca,Na,K,Sr); pink: water molecules.

Downloaded from https://pubs.geoscienceworld.org/books/chapter-pdf/3762981/9780903056434_ch74.pdf
by guest

zones were formed diagenetically long after the eruption and cooling of the lavas (see Fig. 259, p. 361).

Further reading

Dent, I.S. and Smith, J.V. (1958) Crystal structure of chabazite: a molecular sieve. *Nature*, **181**, 1794–1796.

Passaglia, E. (1970) The crystal chemistry of chabazites. *American Mineralogist*, **55**, 1278–1301.

Vitali, F., Blanc, G. and Larqué, P. (1995) Zeolite distribution in volcaniclastic deep-sea sediments from The Tonga Trench margin (SW Pacific). *Clays and Clay Minerals*, **43**, 92–104.

Walker, G.P.L. (1951) The amygdale minerals in the Tertiary lavas of Ireland. I. The distribution of chabazite habits and zeolites in the Garron plateau area, County Antrim. *Mineralogical Magazine*, **29**, 773–791.

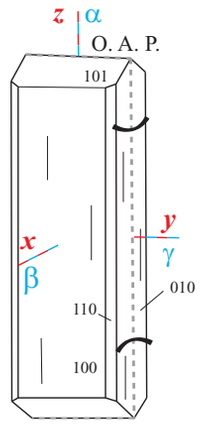
Walker, G.P.L. (1960) Zeolite cones and dike distribution in relation to the structure of the basalts of eastern Iceland. *Journal of Geology*, **68**, 515–528.

Downloaded from https://pubs.geoscienceworld.org/books/chapter-pdf/3762981/9780903056434_ch74.pdf
by guest

Mordenite $(Na,Ca_{0.5},K)_8[Al_8Si_{40}O_{96}]\cdot 28H_2O$

Orthorhombic (+)

α	1.472–1.483
β	1.475–1.485
γ	1.477–1.487
δ	0.004–0.005
$2V_\gamma$	76–104°
Orientation	$\alpha = z$, $\beta = x$, $\gamma = y$, O.A.P. (100), length fast
D (g/cm^3)	2.12–2.15
H	3–4
Cleavage	{100} perfect, {010} distinct
Twinning	Parallel to *z*
Colour	White, yellowish or pinkish; colourless in thin section
Unit cell	*a* 18.05–18.17 Å, *b* 20.40–20.53 Å, *c* 7.50–7.54 Å
	Z = 1. Space group *Cmcm* or $Cmc2_1$
Special features	Insoluble in dilute HCl



Mordenite occurs in cavities in volcanic rocks, as a diagenetic replacement product in rhyolitic pyroclastic rocks and as a hydrothermal mineral. It commonly has a fibrous habit.

Structure

The topology of the structural framework is characterized by five-membered rings of (Si,Al)–O tetrahedra forming part of a polyhedron of the type shown in Fig. 257g (p. 357). These polyhedra are linked by edge-sharing to form chains parallel to *z*, which are in turn linked laterally by four-membered rings to form a sheet parallel to (010) perforated with eight-membered ring holes. Successive sheets are linked across (010) planes in such a way that these holes do not align to form channels in the *y* direction. This, however, produces a very open structure which has channels parallel to *z* bounded by other eight-membered rings and also twelve-membered rings, as can be seen in Fig. 268, a perspective view down the *z* direction. These channels are partially occupied by extra-framework cations (Ca,K,Na) and water molecules. The Si,Al distribution in framework sites is largely disordered.

Chemistry

Mordenite invariably occurs as very fine fibres, which are commonly intergrown with other minerals, making high-quality analyses difficult to obtain. Most mordenites are relatively Na-dominant (e.g. Table 47, analysis 10, p. 359).

Experimental work on mordenite has mostly been to develop methods to synthesize phases with specific Si/Al compositions for industrial applications. It can be produced from gels of appropriate compositions, or from a series of oxide mixes and a range of glass starting materials. It has also been made from rhyolitic glasses in NaOH solutions maintained at 250ºC for three days.

Optical and physical properties

Because of the small range of compositional variation in mordenite, there is little variation in optical properties. The DTA and TG curves show a fairly steady release of water with heating, the endothermic maximum occurring near 180ºC; nearly 90% of the water is lost by 400ºC.

Distinguishing features

Because of the fibrous and commonly matted habit of mordenite, it is best identified by X-ray diffraction. In

Downloaded from https://pubs.geoscienceworld.org/books/chapter-pdf/3763019/9780903056434_ch75.pdf
by guest

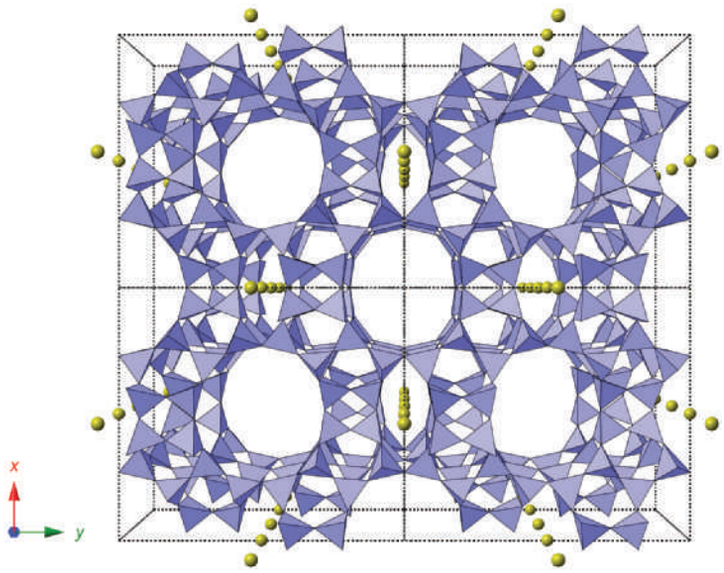


Fig. 268. Perspective view along *z* of the (Si,Al)−O framework of the structure of mordenite showing 4- and 5-membered rings of Si,Al tetrahedra and channels bounded by 8- and 12-membered rings. (Na,Ca,K)-sites are shown in the narrower channels. Water molecules and some further (Na,Ca,K) cations occupy sites in the wider channels, but are not shown here (CrystalMaker image). Blue: (Si,Al)−O tetrahedra; pale green: (Na,Ca,K).

thin section it has a low birefringence (0.003−0.005) and parallel extinction; it may be distinguished from other fibous zeolites (such as erionite) by being length-fast.

Paragenesis

Mordenite may be found replacing volcanic glass or pre-existing zeolites. It is one of several diagenetic zeolites replacing rhyolitic tuff in lacustrine sediments. It is a relatively common mineral in basaltic amygdales and cavities (e.g. Table 47, analysis 10, p. 359), and has been found in drill cores in geothermal fields.

Further reading

Alberti, A., Davoli, P. and Vezzalini, G. (1986) The crystal structure refinement of a natural mordenite. *Zeitschrift für Kristallographie*, **175**, 249−256.

Ueda, S., Murata, H., Koizumi, M. and Nishimura, H. (1980) Crystallization of mordenite from aqueous solutions. *American Mineralogist*, **65**, 1012−1019.

Walker, G.P.L. (1960) Zeolite zones and dike distribution in relation to the structure of the basalts of eastern Iceland. *Journal of Geology*, **68**, 515−528.

Downloaded from https://pubs.geoscienceworld.org/books/chapter-pdf/3763019/9780903056434_ch75.pdf
by guest

ZEOLITE OVERVIEW

All zeolites. The structures are based on frameworks of (Si,Al) tetrahedra all sharing corner oxygens and hence with O:(Si + Al) = 2. Cavities in the framework (cages and channels) enclose alkali and alkaline earth cations (commonly Na, Ca and K but also Ba and Sr) and water molecules. Cavities are usually only partially filled, so replacements with unequal numbers of cations like 2 Na for Ca are possible as well as equal numbers like Na for Ca with charge-compensating Si for Al substitutions. Extra-framework cations are readily exchangeable, and water molecules are expelled reversibly at relatively low temperatures. The more open frameworks lead to the lower densities of zeolites compared with feldspars and feldspathoids, and all occur in low temperature/low pressure water-saturated environments. Nearly all can be found in cavities in mafic volcanic rocks, and less commonly in veins cutting granite. Most zeolites are also widespread in diagenetically altered volcanic sedimentary rocks.

Variations. Some zeolites (e.g. natrolite) have fibrous and some (e.g. heulandite) platy crystal habits, whereas stilbite is commonly found in sheaf-like aggregates. Twinning is very common in stilbite and phillipsite.

The cages and channels in zeolite structures, to varying extents depending on shapes and sizes, can selectively absorb organic molecules, a property with significant industrial importance for natural and manufactured zeolites. There is wide variation in the Si:Al ratio, from 5:1 in clinoptilolite, to 1:1 in gismondine, and in the nature of the extra-framework cations. The water content also varies considerably. There is some correlation between the zeolites found and formation conditions, which typically vary from diagenetic alteration to zeolite-facies metamorphism.

Downloaded from https://pubs.geoscienceworld.org/books/chapter-pdf/3763019/9780903056434_ch75.pdf
by guest

Oxides

Periclase — MgO

Cubic

n	1.735
D (g/cm^3)	3.56–3.68
H	5½–6
Cleavage	{001} perfect
Twinning	Spinel-type twins on {111} in synthetic crystals
Colour	Greyish white to yellow or brown; colourless in thin section
Unit cell	*a* 4.212 Å
	Z = 4, space group *Fm*3*m*
Special features	Soluble in dilute HCl

Periclase is a mineral of metamorphosed limestones and dolomites.

The structure of periclase is similar to that of halite (see p. 483), with magnesium and oxygen occupying the sites of sodium and chlorine, respectively. It consists of planes of oxygen atoms stacked in the sequence of cubic close packing ...ABCABC... with a 60º rotation between successive planes. The oxygens form an array of edge-sharing octahedra; the four octahedral sites per unit cell contain Mg and the eight tetrahedral sites are vacant. Above 450 GPa periclase adopts the body-centred cubic caesium chloride structure.

Iron, manganese, zinc and nickel may substitute partly for magnesium in the natural mineral. The iron-bearing variety 'ferropericlase' commonly contains 5–13% FeO, but considerably higher Fe content has been reported in rocks associated with mantle origin. Periclase can be synthesized readily from $MgCl_2$ or $Mg(OH)_2$ or by heating natural magnesite. A complete series of synthetic crystals from MgO to FeO (wüstite) can be obtained; the name magnesiowüstite has been used for intermediate members. A common alteration product is brucite, $Mg(OH)_2$, which may in turn alter to hydromagnesite. Ferropericlase alters to brucite with separation of iron oxide.

In the synthetic series MgO–FeO the refractive index rises from 1.732 to 2.32. The colour varies from white to yellow or brown with increase of iron content. The Vickers hardness number VHN_{100} for natural iron-bearing periclase is approximately 980.

The cubic cleavage, isotropic character and high relief are distinctive, and the alteration to fibrous brucite is characteristic. With $AgNO_3$ solution periclase gives a brown stain of Ag_2O.

Periclase is a relatively high-temperature mineral resulting from the metamorphism of dolomites and magnesian limestones. It is found typically in contact aureoles, having been formed by the dissociation of dolomite, $CaMg(CO_3)_2 \rightarrow CaCO_3 + MgO + CO_2$. It is commonly surrounded by a rim of brucite developed by the hydration of the periclase. In the sequence of minerals in the progressive metamorphism of siliceous dolomites it forms after wollastonite but at a lower temperature than monticellite.

Periclase may be an important constituent of the lower mantle, but examples are limited to its occurrence in chondrite meteorites and as inclusions in diamond from kimberlites.

Further reading

Duffy, T.H., Hemley, R.J. and Mao, H.K. (1995) Equation of state and shear strength at multimegabar pressures: magnesium oxide to 227 GPa. *Physical Review Letters*, **74**, 1371–1374.

Ferry, J.M. and Rumble, D. (1997) Formation and destruction of periclase by fluid flow in two contact aureoles. *Contributions to Mineralogy and Petrology*, **128**, 313–334.

Downloaded from https://pubs.geoscienceworld.org/books/chapter-pdf/3763074/9780903056434_ch76.pdf
by guest

Cassiterite SnO_2

Tetragonal (+)

ω	1.990–2.010
ε	2.093–2.100
δ	0.096–0.098
D (g/cm^3)	6.98–7.02
H	6–7
Cleavage	{100} and {110} poor, {111} parting
Twinning	Commonly on {011}, may be repeated
Colour	Commonly reddish brown to almost black; in thin section almost colourless, yellow, brown or red
Pleochroism	Variable: very weak to strong; yellow, brown, or red; absorption ε > ω
Unit cell	*a* 4.73 Å, *c* 3.18 Å Z = 2, space group $P4_2/mnm$
Special features	Adamantine lustre; attacked slowly by acids; fusible in alkalis

Cassiterite is the most important ore of tin and is found typically in veins closely associated with granite, in granite pegmatites and in greisens.

The structure of cassiterite resembles that of rutile (see p. 393), each tin ion being surrounded by six oxygen ions approximately at the corners of a regular octahedron, and each oxygen having three tin ions around it forming a nearly equilateral triangle.

Cassiterite typically contains tantalum and niobium and generally appreciable amounts of ferrous or ferric iron, and smaller amounts of Mn, Ti and Sc. Cassiterite commonly contains solid and fluid inclusions and bulk analyses should be treated with caution. Cassiterite can be synthesized by the action of steam on $SnCl_4$ at red heat or by passing HC1 gas over amorphous tin oxide.

It has extremely high refractive indices and birefringence, and although normally uniaxial positive, some material shows anomalous optics with a $2V_\gamma$ of 0 to 38º. The strongly coloured varieties may show zoning and moderate-to-intense pleochroism, a typical example having ω pale greenish yellow, ε deep reddish brown. Twinning is common on {011} giving the familiar 'knee' twin: this may be repeated cyclically. In reflected light it is light grey and strongly anisotropic. Cassiterite is normally lighter in colour in thin section than rutile and has less extreme birefringence and refractive indices: allanite has a very much lower birefringence and melanite garnet is only weakly birefringent.

Cassiterite is usually found in acid igneous rocks such as granites and microgranites, and occurs frequently in granite pegmatites, greisen, high-temperature hydrothermal veins and skarns. It is often found associated with wolframite, tourmaline, topaz, lepidolite and fluorite. It has been found as pseudomorphs after hematite and orthoclase. Wood-tin is a colloform variety formed by secondary processes in the zone of oxidation. Cassiterite is a common detrital mineral in sediments derived from tin-bearing acid rocks: the important Malaysian tin deposits are alluvial in origin.

Further reading

Farmer, C.B., Searl, A. and Halls, C. (1991) Cathodoluminescence and growth of cassiterite in the composite lodes at South Crofty mine, Cornwall, England. *Mineralogical Magazine*, **55**, 447–458.

Kontak, D.J. and Clark, A.H. (2002) Genesis of the giant, bonanza San Rafael lode tin deposit, Peru: origin and significance of pervasive alteration. *Economic Geology*, **97**, 1741–1777.

Neiva, A.M.R. (1996) Geochemistry of cassiterite and its inclusions and exsolution products from tin and tungsten deposits in Portugal. *The Canadian Mineralogist*, **34**, 745–768.

Downloaded from https://pubs.geoscienceworld.org/books/chapter-pdf/3763076/9780903056434_ch77.pdf
by guest

Corundum α-Al_2O_3

Trigonal (–)

ε	1.759–1.765
ω	1.767–1.774
δ	0.008–0.009
D (g/cm^3)	3.98–4.02
H	9; VHN_{100} 2490
Cleavage[a]	none; parting on {0001} and on $\{11\bar{2}1\}$
Twinning[a]	Simple twinning on {0001) or $\{10\bar{1}1\}$ uncommon; apparent lamellar twinning on $\{10\bar{1}1\}$ and $\{11\bar{2}1\}$
Colour	White, grey, blue, red, yellow, orange, green; only weakly coloured in thin section
Pleochroism	Absorption $\omega > \varepsilon$, e.g. in thick sections ω dark blue, ε light blue, or ω blue, ε yellow green
Unit cell	a_{hex} 4.76 Å, c_{hex} 12.99 Å; a_{rh} 5.130 Å, α 55°17′
	$Z_{hex} = 6$; $Z_{rh} = 2$. Space group $R\bar{3}c$
Special features	Insoluble in acids. Can be decomposed after fusion with potassium bisulphate

Corundum is typically found in aluminous metamorphic rocks. It also occurs in igneous rocks undersaturated with respect to silica, such as nepheline syenites, and in aluminous xenoliths in igneous rocks. It is the main component of emery deposits and may be found as a detrital mineral in well sorted beach sands. Red (ruby) and blue (sapphire) varieties may be used as gemstones.

Structure

The structure of corundum is based upon the stacking of sheets of oxygen atoms in approximately hexagonal close packing. Between these sheets are sites for Al cations octahedrally coordinated by six oxygens, but in corundum only two-thirds of the available positions are filled (Fig. 269). Each Al–O octahedron shares one face (three oxygens) with another in the layer above or below. As can be seen in Fig. 269, aluminium ions do not lie midway between oxygen planes because repulsion between pairs of Al ions causes displacement away from the shared face. The cell dimensions of ruby show a linear increase with increasing Cr content.

Although only α-Al_2O_3 is found in nature, other modifications are known from synthetic and experimental work, including β-Al_2O_3 which is hexagonal and may contain alkalis and Ca, and γ-Al_2O_3 which is cubic: on heating, both these forms are converted to corundum.

[a] Indices for cleavage and twin planes are based upon the morphological cell with c 6.49 Å. Apparent lamellar twinning may be exsolution along the cleavage.

Chemistry

Although corundum consists essentially of pure Al_2O_3, minor amounts of other ions may be found, notably Fe^{3+} (see Table 49). Ruby contains a moderate amount of chromium (e.g. analyses 4, 5) whereas the colour of the blue sapphire variety is related to the presence of iron and titanium. Yellow and green corundum containing ferric and ferrous iron (e.g. the yellow corundum of analysis 3 contains 9.17% Fe_2O_3 and no FeO, and traces of Ti, V, Fe, Ga and Cr) are considered to be characteristic of natural rubies and sapphires and their relative proportions may indicate the paragenesis. The melting point of pure corundum is in the range 2000–2050°C.

Corundum can be produced artificially by heating Al_2O_3 gel, or by heating gibbsite, boehmite or diaspore, corundum being the stable phase above about 450°C; large amounts are manufactured for abrasives by heating bauxite.

Synthetic corundum in a high state of purity suitable for use in lasers or X-ray monochromators may be produced by heating $AlCl_3 \cdot 6H_2O$. In synthetic gem production the Verneuil process is used; small amounts of chromium or ferric iron being added to give the

Downloaded from https://pubs.geoscienceworld.org/books/chapter-pdf/3763079/9780903056434_ch78.pdf
by guest

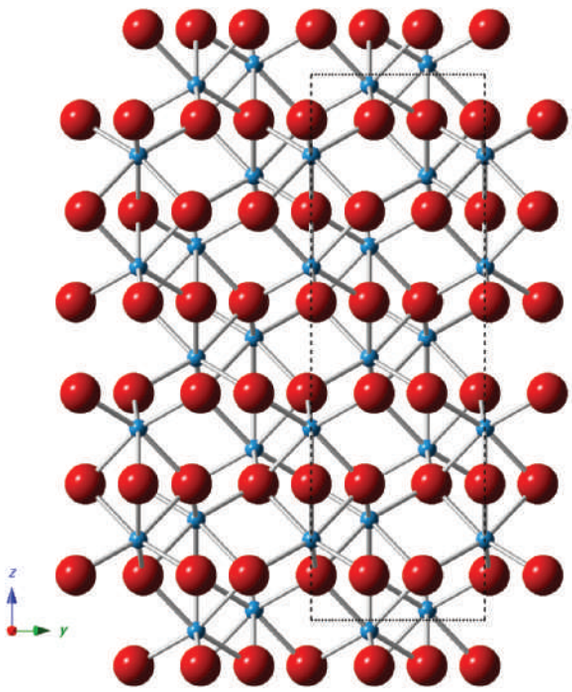


Fig. 269. The structure of corundum, showing layers of oxygens (red) and Al cations (blue) occupying two-thirds of the octahedral interlayer sites. Unit cell is outlined. (CrystalMaker image).

appropriate colour. For synthetic star-sapphires a small amount of TiO_2 is also added; this crystallizes as rutile needles oriented in three directions at 120º and perpendicular to the *z* axis. The addition of vanadium to synthetic corundum gives it the appearance of alexandrite: in daylight the crystal appears green whereas in artificial light it has a reddish colour. Synthetic ruby can also be produced hydrothermally, generally on a seed of natural ruby.

Table 49. Corundum analyses (wt.%).

	1	2	3	4	5
SiO_2	0.20	0.01	0.94	0.58	–
TiO_2	0.32	0.03	0.37	0.10	–
Al_2O_3	98.84	99.8	89.40	90.37	86.43
Cr_2O_3	tr.	0.06	–	8.58	12.89
Fe_2O_3	0.14	0.16	9.17		0.24
FeO	0.06	–	–	0.28	–
V_2O_5	0.00	–	–		–
NiO	tr.	–	–		–
MnO	tr.	0.01	–	0.04	–
MgO	0.04	0.01	–	0.40	–
CaO	0.34	0.00	–	0.01	–
Total	99.94	100.1	99.88	100.37	99.56

1 Dark blue corundum, contact altered marble, Urals (Gavrusevich, B.A., 1941, *Dokl. Acad. Sci. USSR*, **31**, 686–8).
2 Corundum, kyanite-eclogite nodule, Bellsbank kimberlite, South Africa. Carswell, D.A. *et al*., 1981, *Mineral. Mag.*, **44**, 79–89).
3 Yellow iron corundum, metamorphosed lithomarge (porcellanite) in dolerite plug, Tievebulliagh, Northern Ireland (Agrell, S.O. & Langley, J.M., 1958, *Proc. Roy. Irish Acad.*, **59**, **B**, 93–127), ε 1.785, ω 1.794.
4 Ruby inclusion in diamond, São Luiz alluvial mine, Brazil (Watt, G.R. *et al*., 1994, *Mineral. Mag*., **58**, 490–493). Includes Na_2O 0.01.
5 Dark red lamellae of ruby, Cr-rich boulder derived from ultramafic rocks, Westland, New Zealand (Grapes R. & Palmer, K., 1996, *J. Petrol*., **37**, 293–315).

Optical and physical properties

In thin section corundum has a high relief, and although its birefringence is low it may show rather high interference colours in some sections as, because of its extreme hardness, the thin section may be thicker than normal. Although normally uniaxial negative, some specimens may show an anomalous biaxial character with a 2V of 30º or more; this feature may be related to twinning. Twinning on $\{10\bar{1}1\}$ is known, often in lamellar bands or as glide-twins; exsolved boehmite, however, may also occur along $\{10\bar{1}1\}$, helping to produce the $\{10\bar{1}1\}$ parting. As described above, the colours of the varieties of corundum are related to the amount of other ions replacing aluminium. In general, Cr^{3+} + V^{3+} causes the red of ruby, Fe^{3+} causes green or yellow; Ti^{3+} gives a pink hue whereas Fe^{2+} + Ti^{4+} produce the blue of sapphire (Schmetzer and Bank, 1981). Combinations of these impurities together with the pleochroism of corundum leads to many intermediate hues. The substitution of Cr or Fe raises the refractive indices slightly.

Distinguishing features

The combination of very high relief, low to moderate birefringence and the occurrence of twin lamellae is diagnostic. Zoning patterns, the nature of inclusions, trace-element chemistry and absorption spectra are used

Downloaded from https://pubs.geoscienceworld.org/books/chapter-pdf/3763079/9780903056434_ch78.pdf
by guest

to distinguish natural from synthetic gem corundum. Some sapphires may appear very pale blue in thin section. Sapphirine, although rarer than corundum, may occur in similar environments but is always biaxial and does not have twin lamellae. The hardness, form, high density, insolubility and high melting point of corundum are also characteristic.

Paragenesis

Corundum occurs in a wide variety of igneous, metamorphic, sedimentary and extraterrestrial rocks. Metamorphism can be significant in producing corundum and sedimentary processes in producing local concentrations. Corundum is often formed at high pressure and appears in xenoliths in rocks formed deep in the crust and as a result of high-pressure metamorphism. A large proportion of granitic and andesitic rocks are corundum normative without containing modal corundum, perhaps due to amphibole fractionation. Experimental evidence indicates that a 2% increase of $A1_2O_3$ from the eutectic composition in the system $K_2O-Al_2O_3-SiO_2$ raises the liquidus temperature by 180ºC: thus it is likely that a small increase in normative corundum in a magma produces a large rise in the liquidus temperature. This means that even the hottest magmas of granitic composition are not likely to contain much alumina in excess of that required for the feldspars and hence the potential for corundum is restricted. Corundum may occur on a fairly large scale in pegmatites and other rocks associated with nepheline syenites. In the Haliburton and Bancroft areas in Ontario corundum is distributed erratically through a banded complex of rocks rich in scapolite, nepheline and andesine feldspar, and is abundantly developed in contact zones between this complex and a younger hybrid alkaline syenite.

Corundum occurs as veins in amphibolite associated with dunite; in some amphibolites the corundum is altered to margarite, $Ca_2Al_4[Si_4Al_4]O_{20}(OH)_4$. Dyke rocks containing corundum, such as the plumasites and corundum plagioclasites, may be derived by the desilication of an acid igneous rock in contact with more basic material, or may be of hydrothermal origin. The ruby variety has been recorded in glimmerites and is known as inclusions in diamond.

In metamorphic rocks, corundum is found in silica-poor hornfelses; it also occurs in thermally or regionally metamorphosed bauxite deposits, as in the emery deposits of Samos and Naxos in the Aegean. Corundum may also be found in recrystallized limestones and marbles; the Kashmir sapphire and rubies and the rubies from Mogok, Myanmar, are found in coarse-grained calcitic marbles. Most gem-quality corundum, however, is obtained from placer deposits. Corundum is also found as a normal detrital mineral in sediments of all ages, having been derived from pre-existing igneous or metamorphic rocks; the colourless or yellowish varieties are of most common occurrence.

Further reading

Bowles, J.F.W., Howie, R.A., Vaughan, D.J. and Zussman, J. (2011) *Rock-forming Minerals. Non-silicates: Oxides, Hydroxides and Sulphides*, **5A**. 920 pp. Geological Society, London.

Carr, R.M. (1968) The problem of quartz–corundum stability. *American Mineralogist*, **53**, 2092–2095.

Cawthorn, R.G. and Brown, P.A. (1976) A model for the formation and crystallization of corundum normative calc-alkaline magmas through amphibole fractionation. *Journal of Geology*, **84**, 467–476.

Guo, J., O'Reilly, S.Y. and Griffin, W.L. (1996) Corundum from basaltic terrains: a mineral inclusion approach to the enigma. *Contributions to Mineralogy and Petrology*, **122**, 368–386.

Moyd, L. (1949) Petrology of the nepheline and corundum rocks of south eastern Ontario. *American Mineralogist*, **34**, 736–751.

Schmetzer, K. and Bank, H. (1981) The colour of natural corundum. *Neues Jahrbuch für Mineralogy, Monatshefte*, 59–68.

Sutherland, F.L., Hoskin, P.W.O., Fanning, C.M. and Coenraads, R.R. (1988) Models of corundum origin from alkali basalt terrains: a reappraisal. *Contributions to Mineralogy and Petrology*, **133**, 356–372.

Sutherland, F.L., Coenrads, R.R., Schwarz, D., Rayner, L.R., Barrow, B.J. and Webb, G.B. (2003) Al-rich diopside in alluvial ruby and corundum-bearing xenoliths. Australian and SE Asian basalt fields. *Mineralogical Magazine*, **67**, 717–732.

Downloaded from https://pubs.geoscienceworld.org/books/chapter-pdf/3763079/9780903056434_ch78.pdf
by guest

Hematite α-Fe_2O_3

Trigonal (−)

ε	2.87−2.94
ω	3.15−3.22
δ	0.28
D (g/cm^3)	5.254 (often less)
H	5−6; VHN_{100} 1000−1100
R % (air)	23−29 (589 nm)
Cleavage	None, but may show parting on {0001} and {10$\bar{1}$1}
Twinning	On {0001}, and {10$\bar{1}$1} usually lamellar
Colour	Black, steel-grey, and bright to dull red (some crystals may be iridescent); opaque in thin section; blood-red in very thin splinters; grey-white with a slight blue tint in polished section
Unit cell	a_{rh} 5.42 Å, α 55°17′ (rhombohedral unit cell) a_{hex} 5.03 Å, c_{hex} 13.75 Å (hexagonal unit cell) Z_{rh} = 2, Z_{hex} = 6; space group $R\bar{3}c$
Special features	Soluble in HCl. Distinctive cherry-red streak. Becomes magnetic in a reducing flame

Hematite is a very important ore of iron, occurring chiefly in sedimentary rocks and their metamorphosed equivalents. It is also found in soils and as a weathering product of iron-bearing minerals.

There are several varieties of hematite characterized by the habit and texture of the mineral. The common massive ore is red hematite; this may be botryoidal with a radiating fibrous structure giving kidney ore or, when broken up into compact splinters, pencil ore. The crystalline material with metallic lustre is known as specular hematite, specularite or iron-glance, or as micaceous hematite if the structure is platy. Thin black plates occur rarely as rosettiform aggregates known as iron roses. Ground hematite is red and was first used as a pigment for Prehistoric rock art. Martite is a name given to hematite occurring in dodecahedral or octahedral pseudomorphs after magnetite or pyrite: γ-Fe_2O_3 is the mineral maghemite, which has a spinel-type structure.

Structure

The structure of hematite is similar to that of corundum (p. 384) except that it has Fe^{3+} in place of Al. In hematite planes of oxygen atoms in a slightly distorted arrangement of hexagonal close packing, alternate with planes of Fe^{3+} cations which occupy two-thirds of the available octahedral sites between the oxygen planes. As for Al in corundum, Fe^{3+} cations do not lie midway between oxygen planes, but repel each other away from the shared octahedral faces. All Fe^{3+} cations are in six-fold coordination, thus differing from the spinel structure in which some four-fold interplanar sites are also occupied.

Hematite is antiferromagnetic and weakly ferromagnetic. With rising temperature the Néel (antiferromagnetic–paramagnetic) transition occurs at 675ºC, and the Curie (ferromagnetic–paramagnetic) transition at ~690ºC. The antiferromagnetism is parallel to the *x* axis; below about −24ºC (the Morin transition) the antiferromagnetism is re-oriented to parallel to the *z* axis. All of these temperatures are lowered by ilmenite in solid solution. Any small amounts of the more strongly ferrimagnetic maghemite (γ-Fe_2O_3) associated with hematite can appear to increase the magnetism.

Hematite provides a significant component of the natural remanent magnetism (NRM) of iron-bearing sedimentary rocks and oxidized volcanic rocks. Fine-grained hematite-bearing sediments are used widely in the study of palaeomagnetism as their NRM is extremely stable.

Downloaded from https://pubs.geoscienceworld.org/books/chapter-pdf/3763086/9780903056434_ch79.pdf
by guest

Chemistry

The ideal composition of hematite is Fe_2O_3, but a small amount of MnO and FeO may be found in solid solution. Titanohematite is an optically homogeneous Fe-Ti rhombohedral phase with an oxide stoichiometry ~ R_2O_3 and with >50 mol% hematite. Although larger contents of Ti have been reported in hematites, most analyses show no more than a few percent TiO_2. The isotopic compositions of oxygen and iron in hematite are important indicators of palaeo-environmental conditions.

Experimentally it has been shown that at 800ºC only a limited amount of TiO_2 can enter α-Fe_2O_3: at temperatures of more than 1050ºC, however, there is complete solid solution between hematite and ilmenite. Only very small (<1%) amounts of Fe_3O_4 (magnetite) can be taken into solid solution. In the system Fe_2O_3–Al_2O_3, hematite can take into solid solution ~2 wt.% Al_2O_3 at 400ºC, rising to ~10 wt.% at 1000ºC and to ~20% at 1300ºC. On heating in air, hematite alters to Fe_3O_4 at about 1390ºC: its true melting point under sufficient pressure of oxygen to prevent dissociation is probably between 1700 and 1800ºC. As little as 10 wt.% TiO_2 raises the temperature of the hematite → magnetite transformation in air from 1390 to 1524ºC. The transformation of hematite to goethite can occur in soils, aided by warm and wet tropical conditions, whereas drier climates lead to hematite accumulations in nodules or hard caps. Hematite in tropical soils can contain as much as 15 mol% of substituted Al^{3+}. At 90% humidity and 20ºC, laboratory samples show surface alteration within a week, developing a framework of goethite as spherules of acicular crystals. The reduction of hematite is economically important in the production of iron from hematite ores. Hematite can be reduced to magnetite and then to iron by heating to 535ºC in hydrogen.

Optical and physical properties

In thin section hematite is opaque but at very thin edges it appears dark blood-red in transmitted light, and it may show dichroism from brownish red (ω) to yellowish red (ε), this becoming more marked in oil. Hematite has a moderate reflectance of 23–29% in air, and may show deep red internal reflections, especially in oil. In reflected light, hematite can be distinguished by its white colour which is lighter than for most Fe-Ti oxides, although Ti-rich hematite is darker than pure hematite.

Hematite is paramagnetic above, but is dominantly antiferromagnetic below, the Néel transition temperature at ~690ºC. A weak ferromagnetism is, however, observed down to the Morin transition temperature (~–24ºC) at which there is a change of the antiferromagnetic axis from perpendicular to parallel to the z axis.. Small amounts of the much more strongly magnetic γ-Fe_2O_3 (maghemite) may remain and add to the apparent magnetism of hematite.

Distinguishing features

If it is present as a powder or in thin scales, hematite is easily distinguished from magnetite or ilmenite by its blood-red colour. In massive material the red streak is a useful distinction (cinnabar, also with a red streak, is much heavier and may show a perfect prismatic cleavage). The opaque metallic material is lighter in colour in reflected light than magnetite or ilmenite. The hydrated iron oxides are usually softer and may have a brown streak. Hematite is only weakly magnetic, but on heating under reducing conditions a magnetic product is obtained.

Paragenesis

Hematite is uncommon in large amounts in igneous rocks. It is a very important ore of iron occurring chiefly in sedimentary rocks and their metamorphosed equivalents. A large proportion of hematite is secondary; it is found in soils and as a weathering product of iron-bearing minerals.

In igneous rocks it occurs if the magma is poor in ferrous iron (i.e. in granites, syenites, rhyolites and trachytes) and as a late-stage product of volcanic activity, especially with ilmenite, as thin crystals sublimed on to earlier material. It is also found as an intergrowth representing exsolved material in other iron ore minerals and in such material as aventurine. Intimately mixed and oriented aggregates of hematite and chlorite may result from the pseudo-morphous replacement of olivine in basalt.

In metamorphic rocks, quartz (jasper)–hematite ore may be found interbedded with gneisses and metacherts derived from volcanic activity followed by granulite-facies metamorphism. In amygdaloidal lava flows of the Karmutsen Group, Vancouver Island, hematite occurs as an alteration product of Fe-Ti oxides, where it formed during devolatilization shortly after extrusion. It has also been found in compact ores following tectonic compression and recrystallization of ferruginous quartzites, and as metamorphosed iron-rich palaeoplacers. In hydrothermal deposition, the platy habit of hematite is often common.

Most of the economically important hematite ores are associated with sedimentary rocks, especially the banded iron formations (BIF) such as those of the Hamersley Province, Western Australia; Minas Gerais, Brazil; Lake Superior, USA; and the Labrador Trough, Canada. Most BIF have an age of 3800–1800 Ma, contain 20–40% Fe and were formed in deep water by chemical precipitation under anoxic conditions. Supergene weathering (0–80 Ma) has increased the grade of many of these deposits. Reworking of the Hamersley iron ores has led to the formation of detrital and channel iron ores. The latter consist of early Tertiary palaeochannels up to 150 km long containing up to 59% Fe. In the

Downloaded from https://pubs.geoscienceworld.org/books/chapter-pdf/3763086/9780903056434_ch79.pdf
by guest

metamorphic BIF of the Quadrilátero Ferrifero, Brazil, hematite ore (> 65% Fe) was formed by the oxidation of magnetite followed by regional metamorphism and later recrystallization. Chemical precipitation of colloidal Fe_2O_3 and diagenetic alteration of iron-rich sediments also contribute to the formation of hematite; it is also a common constituent of acid mine wastes, where it is commonly associated with goethite. Spherules of hematite occur in some meteorites and in sedimentary rocks on the planet Mars.

Further reading

Dalstra, H. and Guedes, S. (2004) Giant hydrothermal hematite deposits with Mn-Fe metasomatism: a comparison of the Carajás, Hamersley, and other iron ores. *Economic Geology*, **99**, 1793–1800.

Dunlop, D.J. (1970) Hematite: intrinsic and defect ferromagnetism. *Science*, **169**, 858–860.

Klein, C. (2005) Precambrian banded iron formations (BIFs) from around the world: their age, geologic setting, mineralogy, metamorphism, geochemistry, and origin. *American Mineralogist*, **90**, 1473–1499.

Rosière, C.A. and Rios, F.J. (2004) The origin of hematite in high-grade iron ores based on infrared microscopy and fluid inclusion studies: the example of the Conceição, Quadrilátero Ferrfero, Brazil. *Economic Geology*, **99**, 611–624.

Downloaded from https://pubs.geoscienceworld.org/books/chapter-pdf/3763086/9780903056434_ch79.pdf
by guest

Ilmenite $Fe^{2+}TiO_3$

Trigonal (−)

Refractive indices	~ 2.7 (opaque)
D (g/cm^3)	4.70−4.79
H	5−6; VHN_{100} 566−700
Cleavage	None; parting on {0001} and {10$\bar{1}$1}
Twinning	{0001} simple, {10$\bar{1}$1} lamellar
Colour	Black (opaque in transmitted light; pink-brown in reflected light) and strong anisotropy (grey)
R (air)	19–20% in the range 470−650 nm
R (oil)	5−7% in the range 470−650 nm
Unit cell	a_{hex} 5.09 Å, c_{hex} 14.08 Å a_{rh} 5.537 Å, α 54°51′ Z_{hex} = 6, Z_{rh} = 2; space group $R\bar{3}$
Special features	Very slowly soluble in HCl; variable solubility in HF

Ilmenite is a common accessory mineral in many igneous and metamorphic rocks, occasionally occurring as massive veins or layers. It is also found as a detrital mineral in sedimentary deposits, where it accumulates in the heavier fraction due to its density. It is an important ore of Ti.

Structure

Ilmenite has a hexagonal structure comparable to that of corundum (see p. 384) but has two elements (Fe and Ti) having similar roles in the structure. The unit cell is rhombohedrally centred, corresponding with the $R\bar{3}$ space group of hematite. Along the triad axis, pairs of Ti ions alternate with pairs of Fe^{2+} ions. Each pair is grouped about a vacant site in the structure, and the cations are displaced from their ideal positions toward the vacant site. The paired distribution of cations along the triad axis produces an uneven distribution of Fe and Ti in successive layers perpendicular to the triad axis. In pure ilmenite the cations are highly ordered into these layers. Layers consisting predominantly of Fe (96−98% in natural ilmenite) alternate with layers in which the majority of the cations (84−94%) are Ti.

The unit-cell dimensions of ilmenite are reduced by the entry of Fe^{3+} into the structure and also by the entry of Al and Mg, but are increased by the substitution of Mn. At elevated temperature ilmenite has the less ordered $R\bar{3}c$ structure of hematite, and in the series $FeTiO_3$−Fe_2O_3 (hematite–ilmenite) the temperature at which the transition to lower symmetry occurs rises steeply with increasing Ti.

Chemistry

The formula of ilmenite may be more fully expressed as $(Fe,Mg,Mn)TiO_3$, there being extensive solid solution between ilmenite and geikielite (to 70 mol% $MgTiO_3$) and between ilmenite and pyrophanite (up to 64 mol% $MnTiO_3$). Although there appear to be continuous variations from pure ilmenite to at least these limits in naturally occurring ilmenites, the majority of terrestrial, lunar and chondritic ilmenites contain Fe_2O_3 up to 5 mol% and only minor amounts of MgO and MnO. An exception occurs in ilmenite in kimberlites and ultrabasic xenoliths which commonly contain major amounts of the geikielite molecule (Table 50, analysis 4) and the pyrophanite molecule may become important in ilmenites in differentiated acid rocks (analysis 5) and in carbonatites. It is noteworthy that, for coexisting ilmenite and magnetite in igneous and metamorphic rocks, the Mn is always preferentially found in the ilmenite. Minor elements that occur in ilmenite include Cr and V substituting for Fe^{3+} and Zr^{4+} substituting for Ti.

Experimentally it has been found that at high temperatures there is complete solid solution between ilmenite and hematite (see Fig. 275, p. 406), but at lower temperatures a miscibility gap develops and the solubility

Downloaded from https://pubs.geoscienceworld.org/books/chapter-pdf/3763090/9780903056434_ch80.pdf
by guest

Table 50. Ilmenite analyses.

Wt.%	1	2	3	4	5
TiO_2	48.90	49.89	55.83	51.99	52.0
SiO_2	0.11	0.14	0.18	–	–
Fe_2O_3	5.70	6.26	–	9.36	0.41
Cr_2O_3	–	–	0.12	0.92	–
Al_2O_3	0.54	0.02	0.09	0.38	0.3
V_2O_3	–	0.18	–	–	0.06
FeO	43.32	40.39	37.66	24.49	32.5
MnO	0.35	0.41	0.34	0.20	14.1
MgO	0.56	2.27	6.10	12.38	–
CaO	0.65	0.34	0.17	–	–
Total	100.13	99.96	100.49	99.72	99.37
Numbers of cations on the basis of 6 O					
Ti	1.851	1.868	2.005	1.810	1.981
Si	0.005	0.007	0.006	–	–
Fe^{3+}	0.216	0.234	–	0.326	0.017
Cr	–	–	0.007	0.034	–
Al	0.032	0.001	0.005	0.020	0.018
V	–	0.007	–	–	0.002
Fe^{2+}	1.824	1.682	1.504	0.946	1.377
Mg	0.042	0.168	0.434	0.854	–
Mn	0.015	0.017	0.014	0.008	0.605
Ca	0.035	0.018	0.009	–	–

1 Ilmenite, two-pyroxene granulite of the charnockite series, Madras, India (Howie, R.A., 1955, *Trans. Roy. Soc. Edinburgh*, **62**, 725–68).
2 Ilmenite, gabbro, Skaergaard intrusion, east Greenland (Vincent, E.A. & Phillips, R., 1954, *Geochim. Cosmochim. Acta*, **6**, 1–26). Includes H_2O 0.06.
3 Ilmenite, Luna 20 soil sample (Haggerty, S.E., 1973, *Geochim. Cosmochim. Acta*, **37**, 857–67). Microprobe analysis.
4 Magnesian ilmenite megacryst, Amalia kimberlite, Namibia (Mitchell, R.H., 1987, *Neues Jahrb. Min., Abhdl.*, **157**, 267–83). Microprobe analysis.
5 Manganoan ilmenite, adamellite, Sierra Nevada, California, USA (Snetsinger, K.G., 1969, *Amer. Min.*, **54**, 431–36). Microprobe analysis.

of hematite in ilmenite decreases with decreasing temperature. In natural ilmenite, the amount of hematite in solid solution depends on the crystallization temperature, the rate of cooling and the degree of subsolidus re-equilibration which has taken place. The relationship is complicated by the antiferromagnetic/paramagnetic (Néel) transition at the hematite-rich end of the series.

Ilmenite has been synthesized by the floating-zone method at 1390ºC and an oxygen fugacity of 0.01 Pa. It has also been crystallized within the anhydrous melting range of a tholeiitic andesite (1075–1225ºC) at pressures of 0.5–2.6 GPa. Reduction by CO in the range 900–1200ºC is used to separate Ti from ilmenite, the reduction proceeding by different sequences above and below 1150ºC to produce metallic iron.

The compositions of coexisting ilmenite and magnetite have been widely used as a geothermometer/geobarometer. Partitioning of Mg and Fe^{2+} between ilmenite and olivine or ilmenite and pyroxene also provides a geothermometer.

The alteration of ilmenite may take place in stages leading to the development of exsolution lamellae, patchy ilmenite, amorphous Fe–Ti oxides, and leucoxene. The latter is normally finely crystallized rutile ± pseudorutile ($Fe_2^{3+}Ti_3O_9$); hematite, anatase, brookite and limonite may also be present. Exsolution of hematite from ilmenite is common. In coexisting magnetite, exsolved ulvöspinel ($Fe_2^{2+}TiO_4$) is subsequently oxidized to form ilmenite with the development of further textures at the border between the initial ilmenite and magnetite.

Optical and physical properties

Ilmenite is opaque but appears brown, sometimes with a pinkish tinge in reflected light. In comparison with coexisting magnetite or hematite it appears darker. The reflectance in air is in the range 19–20%, but this falls to 14–15% towards geikielite; in oil the reflectance of ilmenite is much less (5–7%).

The density of around 4.70–4.79 g/cm^3 is less than that of coexisting magnetite; it is reduced by the entry of an appreciable amount of the geikielite (4.05) or pyrophanite (4.54) molecules in solid solution. The microindentation hardness (VHN_{100}) lies in the range 566-700 (magnesian ilmenite is appreciably harder). Ilmenite has no good cleavage, only partings possibly related to twinning; geikielite has good $\{10\bar{1}1\}$ cleavage and pyrophanite has perfect $\{02\bar{2}1\}$ and good $\{10\bar{1}2\}$ cleavages. Pure ilmenite is paramagnetic except at temperatures well below 0ºC, but its magnetic properties are changed significantly by any hematite content. Ilmenite is an important commercial source of titanium, used principally in alloys and paints.

Distinguishing features

Ilmenite may give rise to a greyish white alteration product, leucoxene, which may serve to distinguish it from magnetite in hand specimen. It also has a tendency to form skeletal crystals. In reflected light the pink-brown colour is distinctive, contrasting with the grey colour of magnetite and the blue-white of hematite. The reflection pleochroism (stronger in oil) is diagnostic and marked in comparison with coexisting magnetite. A test for titanium may be made by dissolving a small amount in HCl and adding a drop of the solution to a solution of phenol in H_2SO_4 which gives a brick-red colour. Ilmenite is only weakly magnetic; its response to a hand magnet is noticeable but feeble.

Paragenesis

Ilmenite is common as an accessory mineral in many igneous and metamorphic rocks. It may also occur in

Downloaded from https://pubs.geoscienceworld.org/books/chapter-pdf/3763090/9780903056434_ch80.pdf
by guest

veins, in stratiform layers or as extensive disseminated deposits, in association with gabbros, norites, anorthosites, etc. It can be one of the earlier constituents of a magma to crystallize although the important magmatic ore deposits are usually in rocks rich in pyroxene (commonly orthopyroxene) rather than olivine. A significant proportion of the ilmenite in these rocks is also derived from alteration of titaniferous magnetite during cooling. In metamorphic rocks it is found in many orthogneisses, and particularly in rocks of the granulite facies. The titaniferous iron ores of the west coast of Norway have been subjected to regional metamorphism sufficiently strong to extinguish primary features.

Magnesian ilmenite is a prominent constituent of kimberlites and of the xenoliths contained within them, and is also common in lunar basalts and soils. Its occurrence has been used as an exploration tool in the search for kimberlites. Ilmenite contributes to the MARID (mica-amphibole-rutile-ilmenite-diopside) assemblage of xenoliths of glimmerite nodules in kimberlite pipes. Manganoan ilmenite is found in granitic igneous rocks and also in some carbonatites (where it may also contain appreciable Mg ± Nb).

Supergene weathering of ilmenite in soils, placer deposits, or during diagenesis, leads to the formation of pseudorutile ($Fe_2^{3+}Ti_3O_9$). The first stage of alteration to pseudorutile is due to oxidation and leaching in the saturated part of the weathering profile, with an increase in the H_2O content and oxidation of Fe^{2+} to Fe^{3+}. The subsequent alteration to form rutile ± hematite involves leaching in a more oxidising environment with a loss of H_2O, Fe and O.

Ilmenite is a ubiquitous mineral in detrital sediments and placer deposits and may become concentrated in beach sands as in Florida and India; the west coast of the South Island of New Zealand has large deposits estimated to contain an average of 5.5% ilmenite.

Ilmenite is a significant constituent of lunar rocks, particularly in the Ti-rich basalts, and normally its composition contains appreciable amounts of MgO associated with the reducing conditions of its crystallization. Ilmenite is also found as a component of achondrite and mesosiderite meteorites.

Further reading

Andersen, D.H. (1979) The olivine-ilmenite thermometer. *Proceedings of the 10th Lunar Planetary Science Conference. Geochimica et Cosmochimica Acta, Supplement* **1**, 493–507.

Bishop, F.C. (1980) The distribution of Fe^{2+} and Mg between coexisting ilmenite and pyroxene with application to geothermometry. *American Journal of Science*, **280**, 46–77.

Buddington, A.F. and Lindsley, D.H. (1964) Iron–titanium oxide minerals and synthetic equivalents. *Journal of Petrology*, **5**, 310–357.

Burton, B.P. (1985) Theoretical analysis of chemical and magnetic ordering in the system Fe_2O_3–$FeTiO_3$. *American Mineralogist*, **70**, 1027–1035.

Burton, B.P., Robinson, P., McEnroe, S.A., Fabian, K. and Boffa Ballaran, T. (2008) A low-temperature phase diagram for ilmenite compositions in the system Fe_2O_3–$FeTiO_3$. *American Mineralogist*, **93**, 1260–1272.

Dawson, J.B. and Smith, J.V. (1977) The MARID (mica-amphibole-rutile-ilmenite-diopside) suite of xenoliths in kimberlite. *Geochimica et Cosmochimica Acta*, **41**, 309–323.

Lindsley, D.H. (1973) Delimitation of the hematite–ilmenite miscibility gap. *Bulletin of the Geological Society of America*, **84**, 657–662.

O'Neill, H.St.C. (1988) Partitioning of Fe and Mn between ilmenite and olivine at 1100ºC: constraints on the thermodynamic mixing properties of $(Fe,Mn)TiO_3$–ilmenite solid solutions. *Contributions to Mineralogy and Petrology*, **133**, 284–296.

Taylor, R.W. (1964) Phase equilibria in the system FeO–Fe_2O_3–TiO_2 at 1300ºC. *American Mineralogist*, **49**, 1016–1030.

Windley, B.F., Herd, R.K. and Ackermand, D. (1989) Geikielite and ilmenite in Archaean meta-ultramafic rocks, Fiskenaesset, West Greenland. *European Journal of Mineralogy*, **1**, 427–437.

Downloaded from https://pubs.geoscienceworld.org/books/chapter-pdf/3763090/9780903056434_ch80.pdf
by guest

Rutile TiO_2

Tetragonal (+)

ω	2.605–2.613
ε	2.899–2.901
δ	0.286–0.296
D (g/cm^3)	4.23–5.5
H	6–6½; VHN_{100} 894–974
Cleavage	{110} good, {100} moderate; parting on {092} and {011}
Twinning	Common on {011}, often geniculate or cyclic; also glide-twins on {011} and {092} and rare contact twins on {031}
Colour	Characteristically reddish brown, may be black, violet, yellow or green (synthetic: white); typically yellowish to reddish brown in thin section
Pleochroism	Weak to distinct, ε > ω in brownish red, yellow and green
Unit cell	*a* 4.593 Å, *c* 2.959 Å Z = 2; space group $P4_2/mnm$
Special features	Insoluble in acids; decomposed by alkali carbonate fusion

Rutile is a widespread accessory mineral in metamorphic rocks and in granite pegmatites. It is a common detrital mineral in sediments, and occurs as acicular crystals in quartz. Anatase and brookite are the tetragonal and orthorhombic low-temperature polymorphs of rutile, respectively. All three minerals occur as accessory constituents of igneous and metamorphic rocks and as detrital minerals in beach sands.

Structure

The structure of rutile is based on layers of oxygen in quasi-hexagonal close packed arrangement with Ti atoms filling half of the 6-coordinated octahedral interstices. It may also be viewed as chains of Ti–O octahedra formed by each sharing one pair of opposite edges (Fig. 270). The chains run parallel to *z* and are linked laterally to each other by sharing the remaining corner oxygens. Neighbouring chains are rotated 90º and displaced by *c*/2 along *z*. The octahedra are almost regular and the longest edge (parallel to *z*) defines the *c* cell parameter.

Chemistry

Although essentially TiO_2 (Table 51, analysis 1), some rutiles contain considerable amounts of both ferrous and ferric iron and major amounts of Nb and Ta. The close similarity in ionic radius between Ti^{4+} and both Nb^{5+} and Ta^{5+} enables the latter ions to enter titanium minerals, the structure being electrostatically balanced either by vacancies in some lattice positions or by the complementary substitution of divalent ions such as Fe^{2+} (e.g. Table 51, analysis 4); the variety 'niobian rutile' was previously known as ilmenorutile. Lunar rutile from the Apollo 12 site contains both Nb and Cr together with La and Ce. In the varieties rich in Ta, Sn is often found in moderate amounts, and Cr and V may also be present. Rutile from eclogites contains appreciable Al and Cr; there is a positive correlation between the Cr in the rutile and the pyrope content of the host rock. Up to ~4% H_2O has been found in natural rutile. The hydrogen may bond to oxygens forming OH, compensating for the substitution of Ti by trivalent ions.

Rutile can be produced artificially by heating a solution of $TiCl_4$ to 950ºC. Single crystals of pure rutile are produced by flame-fusion methods. The melting point of pure TiO_2 is 1825ºC. Rutile is also produced by heating anatase to above 730ºC. Although it is commonly an alteration product of other titanium-bearing minerals, rutile is very stable; it may, however, alter to titanite or possibly ilmenite or, more rarely, to anatase.

Optical and physical properties

In thin section rutile is characteristically reddish brown in transmitted light, the depth of colour being

Downloaded from https://pubs.geoscienceworld.org/books/chapter-pdf/3763094/9780903056434_ch81.pdf
by guest

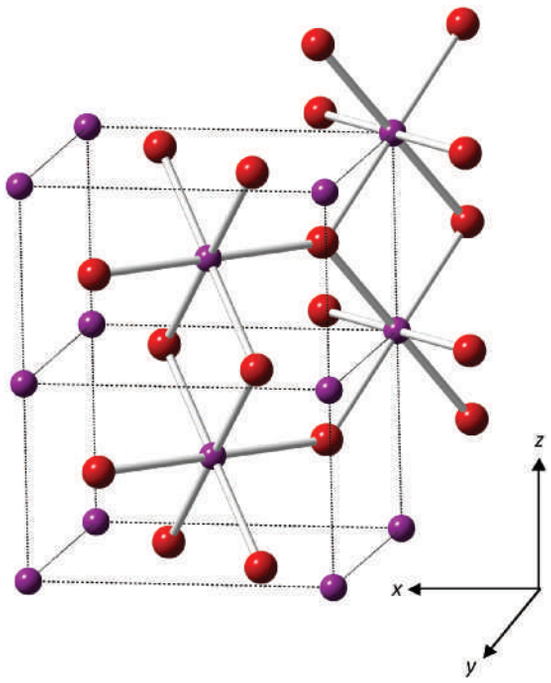


Fig. 270. The structure of rutile showing bands of octahedra parallel to *z* linked to each other laterally by sharing corner oxygens. Purple: Ti; red: oxygen; broken lines: unit cell (after Evans, R.C., 1964, *An Introduction to Crystal Chemistry*. Cambridge University Press. Fig. produced by M.D. Welch).

related to the content of ferric iron, niobium and tantalum, some varieties being almost opaque. In reflected light rutile appears light grey with a reflectance similar to that of magnetite. Synthetic rutile is black and opaque; heating in oxygen changes the colour through dark blue, light blue and green to a pale milky yellow or colourless final stage: it has a dispersion much higher than diamond (B−G ~0.3) and is used as a gemstone.

Distinguishing features

In thin section rutile usually has a characteristic deep red-brown colour which, together with the very high relief and extreme birefringence, is diagnostic: baddeleyite (ZrO_2) is normally less strongly coloured and has much lower birefringence. In polished section, the hardness, reflectance and very bright internal reflections are indicative of rutile. Compared with cassiterite, rutile

Table 51. Rutile analyses.

Wt.%	1	2	3	4		– Numbers of ions on the basis of 2 O – 1	2	3	4
TiO_2	98.51	(99)	95.3	66.28					
Cr_2O_3	0.87	0.04	3.16	–	Ti	0.990	0.989	0.965	0.772
Al_2O_3	0.05	0.07	–	–	Si	–	0.001	–	0.005
Fe_2O_3	–	1.1	1.2	–	Cr	0.009	–	0.034	–
Nb_2O_5	–	–	–	8.64	A1	0.001	0.001	–	–
Ta_2O_5	–	–	–	15.44	Nb	–	–	–	0.061
FeO	0.41	–	–	8.00	Ta	–	–	–	0.070
MnO	–	0.03	0.02	tr.	Fe^{3+}	–	0.011	0.012	0.104
MgO	0.06	0.03	0.08	–	Fe^{2+}	0.005	–	–	–
CaO	–	0.04	0.01	–	Mg	0.001	0.001	0.002	–
Total	99.90	100.39	99.8	100.10	Σ	1.01	1.00[a]	1.01	1.02[b]

1 Rutile, chromitic pyroxenite, Jagdlust, east Bushveld (Cameron, E.N., 1979, *Amer. Min.*, **64**, 140−50). Microprobe analysis.
2 Rutile, rutile eclogite, Vissuri, Tanzania (Smith, J.V. & Dawson, J.B., 1975, *Phys. & Chem. Earth*, **9**, 309−22). Microprobe analysis. Includes SiO_2 0.08, TiO_2 by difference.
3 Chromian rutile, MARID xenolith in kimberlite, Blumfontein, South Africa (Dawson, J.B. & Smith, J.V., 1977, *Geochim. Cosmochim. Acta*, **41**, 309−23). Microprobe analysis. Includes K_2O 0.02, SiO_2 0.01.
4 Tantalum-rich rutile (strüverite), Globe Hill, Western Australia (Edwards, A.B., 1940, *Proc. Austral. Inst. Mining & Metall.*, no. 120, 731−44). Includes SnO_2 1.24, SiO_2 0.32, H_2O 0.18.

[a] includes Ca 0.001.
[b] Includes Sn 0.008.

Downloaded from https://pubs.geoscienceworld.org/books/chapter-pdf/3763094/9780903056434_ch81.pdf
by guest

has a good prismatic cleavage, a much higher birefringence and a considerably lower density.

Paragenesis

Rutile is the most common form of TiO_2 in nature. It is the high-temperature polymorph and as it has the smallest molecular volume of the TiO_2 polymorphs it tends to occur in high-$P-T$ assemblages. It is very widely distributed as minute grains in many igneous, chiefly plutonic, rocks and is also an accessory mineral in metamorphic rocks, being particularly common in some amphibolites and eclogites, and in metamorphosed limestones. It may reach 3% in the mica–amphibole–rutile–ilmenite–diopside (MARID) suite of xenoliths found in nodules in kimberlites.

Its occurrence in larger crystals is limited to some granite pegmatites and apatite and quartz veins. It is of fairly common occurrence as inclusions in other minerals, notably quartz, where it may take the form of long hair-like needles: intergrowths of rutile with ilmenite and less commonly with biotites are also found. In sediments it may be formed as fine needle-like crystals during the reconstitution processes in clays and shales, and is also found in their contact metamorphosed equivalents.

Rutile may be formed by hydrothermal processes and by diagenesis. It is also a common detrital mineral and in some beach sands it may constitute a commercial source of titanium.

Rutile occurs both in meteorites and in lunar rocks.

Further reading

Černý, P., Chapman, R., Simmons, W.B. and Chackowsky, L.E. (1999) Niobian rutile from the McGuire granitic pegmatite, Park County, Colorado: solid solution, exsolution and oxidation. *American Mineralogist*, **84**, 754–763.

Foley, S.F., Barth, M.G. and Jenner, G.A. (2000) Rutile/melt partition coefficients for trace elements and an assessment of the influence of rutile on the trace element characteristics of subduction zone magmas. *Geochimica et Cosmochimica Acta*, **64**, 933–938.

Jamieson, J.C. and Olinger, S. (1969) Pressure–temperature studies of anatase, brookite, rutile and TiO_2-II: a discussion. *American Mineralogist*, **54**, 1477–1481.

Meagher, E.P. and Lager, G.A. (1979) Polyhedral thermal expansion in the TiO_2 polymorphs: refinement of the crystal structures of rutile and brookite at high temperatures. *The Canadian Mineralogist*, **17**, 77–85.

Tossell, J.A., Vaughan, D.J. and Johnson, K. (1974) The electronic structure of rutile, wüstite and hematite from molecular orbital calculations. *American Mineralogist*, **59**, 319–334.

Downloaded from https://pubs.geoscienceworld.org/books/chapter-pdf/3763094/9780903056434_ch81.pdf
by guest

Anatase TiO_2

Tetragonal (−)

ε	2.488
ω	2.561
δ	0.073
D (g/cm^3)	3.82−3.97
H	5½−6; VHN_{100} 616−698
Cleavage	{110} and {100} perfect
Twinning	Rare, on {112}
Colour	Brown, yellow greenish blue, blue-black; showing lighter shades of the same colours in grains or thin sections
Pleochroism	Usually weak, ω < ε or ω > ε
Unit cell	*a* 3.78 Å, *c* 9.51 Å
	Z = 4; space group $I4_1/amd$
Special features	Insoluble in acids

Anatase is polymorphous with rutile. It may be found as a minor accessory in metamorphic and igneous rocks and veins, and is fairly common as a detrital mineral in sedimentary rocks.

The structure of anatase (Fig. 271), rutile and brookite illustrate alternative forms of 6:3 coordination, i.e. Ti coordinated by six oxygens and O coordinated by three Ti atoms. In anatase double chains of Ti−O octahedra run parallel to *z*, and each octahedron has four shared edges compared with three in brookite and two in rutile; in anatase the octahedra are considerably distorted. Neighbouring chains are displaced by *c*/2 with respect to each other.

Although essentially TiO_2, minor amounts of Fe and Sn may occur; niobian and tantalian varieties are known. Anatase can be synthesized by hydrolysing sulphuric acid solutions of $TiCl_4$ at about 200ºC. The production of single crystals is assisted by the addition of 0.2−0.5 mol% of Al^{3+}, Cr^{3+} or Mg^{2+}. The rate of transformation of anatase to rutile on heating depends on the fineness of the material, and also on temperature, pressure and time: it is slow below about 600ºC.

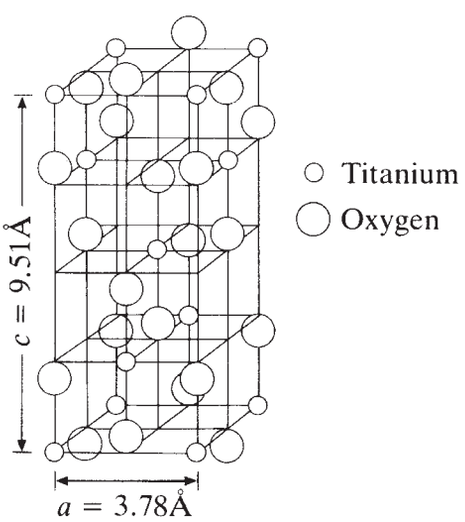


Fig. 271. The structure of anatase (after Bragg, W.L. & Claringbull, G.F., 1965, *Crystal Structures of Minerals*, G. Bell & Sons, London).

Downloaded from https://pubs.geoscienceworld.org/books/chapter-pdf/3763100/9780903056434_ch82.pdf
by guest

Anatase is typically found in shades of yellow or blue, ranging to orange, reddish brown and bluish green. Although normally uniaxial, biaxial crystals with a small 2V are also known: some crystals show zoning. In reflected light anatase is grey, similar to rutile, with strong white to blue-grey internal reflections. The density is rather variable from 3.82 to 3.97 g/cm^3; lower values down to 3.1 are due to high porosity.

Anatase is distinguished from rutile and brookite by its uniaxial optically negative character: compared with other minerals it has a very high relief, and its colour and tetragonal form are often diagnostic.

Anatase is the low-temperature polymorph of TiO_2 and is found as a minor constituent of igneous and metamorphic rocks and in veins and druses in granite pegmatites: it also occurs as an alteration product of other Ti-bearing minerals such as titanite and ilmenite. It is a fairly common detrital mineral in sediments, where it may be authigenic. Anatase can be formed at moderate to low temperatures by hydrothermal crystallization in alkaline, neutral and mildly acid solutions, whereas acidic conditions produce rutile. A shock-induced polymorph (TiO_2-II) of anatase (and rutile) has been identified in breccias from the Chesapeake Bay impact structure, USA.

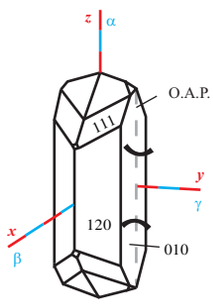
Further reading

Jackson, J.C., Horton, J.W., Chou, L.-M. and Belkin, H.E. (2006) A shock-induced polymorph of anatase and rutile from the Chesapeake Bay impact structure, Virginia, U.S.A. *American Mineralogist*, **91**, 604–608.

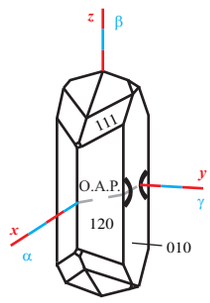
Yau, Y.-C., Peacor, D.R. and Essene, E.J. (1987) Authigenic anatase and titanite in shales from the Salton Sea geothermal field. *Neues Jahrbuch für Mineralogie, Monatshefte*, 441–452.

Downloaded from https://pubs.geoscienceworld.org/books/chapter-pdf/3763100/9780903056434_ch82.pdf
by guest

Orthorhombic (+)



Blue light



Red light

α	2.58
β	2.58–2.59
γ	2.70–2.74
δ	0.12–0.16
$2V_\gamma$	0–30°
Orientation	O.A.P. (001) for red light, (100) for blue light; Bx_a always ⊥(010)
Reflectivity	~19–23% in air, ~6–9% in oil
Dispersion	Strong, variable
D (g/cm^3)	4.08–4.18
H	5½–6; VHN_{100} 989–1018
Cleavage	{120} poor {001} very poor
Colour	Yellowish to brown, red-brown or black; yellow or brown in thin section
Pleochroism	Very weak, in yellow and brown
Unit cell	*a* 5.45 Å, *b* 9.18 Å, *c* 5.14 Å Z = 8; space group *Pcab*
Special features	Insoluble in acids. Soluble after fusion in alkali carbonate

Brookite occurs as an accessory mineral in some igneous and metamorphic rocks, and is usually of secondary origin; it is common as a detrital mineral.

As with the other TiO_2 polymorphs, the structure of brookite has Ti in six-fold coordination by oxygen and each O has three Ti nearest neighbours. There are chains of Ti–O octahedra parallel to *z* but these are kinked rather than straight and each octahedron shares three edges, two with its neighbours in the chain and one with an octahedron in the neighbouring chain. The octahedra are somewhat distorted.

The composition is essentially TiO_2, but brookite usually contains a small amount of Fe^{3+}: a niobian-bearing variety is known. The substitution of Ti by Nb and Fe may follow the coupled substitution mechanisms: $2\,Ti^{4+} \leftrightarrow Nb^{5+} + Fe^{3+}$ and $3\,Ti^{4+} \leftrightarrow 2\,Nb^{5+} + Fe^{2+}$. Attempts to synthesize brookite yield anatase at low temperatures, which inverts to rutile on heating. It can be prepared under hydrothermal conditions at 220–560ºC and 0.1 GPa P_{H_2O} by neutralization of $TiCl_4$ and $CaCl_2$ solutions via anatase and a titanate in Ca-bearing solutions. The chief natural alteration product of brookite is rutile, and pseudomorphs of magnetite after brookite are known.

Brookite is yellowish brown to dark brown in transmitted light. The dispersion is very strong, with the optic axial plane (001) for red and yellow light with

Downloaded from https://pubs.geoscienceworld.org/books/chapter-pdf/3763120/9780903056434_ch83.pdf
by guest

2V decreasing and reaching 0º for yellowish green light (at about 555 nm at 25ºC) when it is uniaxial. In green and blue light 2V increases with decreasing wavelength, with the optic axial plane (100): γ is parallel to *y* in all cases. This phenomenon of crossed axial plane dispersion is best observed under monochromatic light of various wavelengths: in white light the interference figure is symmetrical but anomalous and without true isogyres.

The high refractive indices and birefringence and the abnormally strong dispersion are fairly characteristic. Rutile has a better cleavage and pseudobrookite (an entirely different mineral, $Fe_2^{3+}TiO_5$, though resembling brookite) has a larger 2V and no marked dispersion. The tabular crystal habit is distinctive, especially as between the TiO_2 polymorphs.

Brookite occurs as an accessory mineral in some igneous and metamorphic rocks and in hydrothermal veins. The formation of brookite, anatase or rutile under hydrothermal conditions is sensitive to the concentration of Na in solution as well as temperature. Brookite is often of secondary origin and associated with titanite, chlorite, adularia and albite. As a detrital mineral brookite is fairly common in grits and sandstones and in gold and diamond placer deposits. It occurs as an authigenic phase in sediments and it may be produced near hot springs.

Further reading

Mitsuhashi, T. and Watanabe, M. (1978) Brookite formation from precipitates containing calcium ions. *Mineralogical Journal (Japan)*, **9**, 236–240.

Starkey, R.E. and Robinson, G.W. (1972) Famous mineral localities: Prenteg, Tremadog, Gwynedd, Wales. *Mineralogical Record*, **23**, 391–399.

Werner, M. and Cook, N. J. (2001) Nb-rich brookite from Gross Brukkaros, Namibia: substitution mechanisms and Fe^{2+}/Fe^{3+} ratios. *Mineralogical Magazine*, **65**, 437–440.

Downloaded from https://pubs.geoscienceworld.org/books/chapter-pdf/3763120/9780903056434_ch83.pdf
by guest

Perovskite $(Ca,Na,Fe^{2+},Ce,Sr)(Ti,Nb)O_3$

Orthorhombic (+)

n	2.30–2.38
$2V_\gamma$	~90º
Orientation	$\beta = y$, $\gamma:z = 45º$
D (g/cm^3)	3.95–4.84
H	5½; VHN_{100} 967–1142
Cleavage	{001} poor
Twinning	Abundant, interpenetrant lamellar twinning on {110) and {112}
Colour	Black, brown, reddish brown or yellow; dark brown to colourless in thin section
Pleochroism	Weak, with absorption $\gamma > \alpha$
Unit cell	*a* 5.383 Å, *b* 5.446 Å, *c* 7.645 Å
	Z = 4. Space group *Pbnm*
Special features	Decomposed by concentrated H_2SO_4 and HF

Perovskite occurs as an accessory mineral in igneous rocks and in metamorphosed calcareous rocks in contact with basic or alkaline igneous rocks. This mineral also lends its name to the 'perovskite structure', a structure adopted by the dominant mineral in the Earth's lower mantle and by a range of industrially important materials.

The idealized perovskite structure (Fig. 272a) is cubic, with Ti atoms in 6-fold coordination; these share corners and form 12-coordinated sites which are occupied by Ca. However, natural perovskite shows a displacement of both O and Ca relative to Ti, which reduces the symmetry to orthorhombic (Fig. 272b). Perovskite also lends its name to an extensive class of compounds with the same type of structure, either in idealized cubic form or distorted versions of this, with tetragonal or orthorhombic variants being the most common.

The perovskite structure has the general stoichiometry ABX_3, where A and B are cations of varying charge and X is an anion. Relative ion size in the perovskite structure determines the degree of structural distortion. The perovskite structure is extremely densely packed and is therefore of interest in studies of high pressure phases in the mantle. The Earth's lower mantle is believed to consist predominantly of a phase of composition $(Mg,Fe)SiO_3$ with an orthorhombic perovskite structure.

Although the composition of perovskite is essentially $CaTiO_3$, most analyses report considerable substitutions of the rare earths or alkalis for Ca and often of Nb or Ta for Ti. Loparite-(Ce) is the alkali-bearing cerian variety with end-member composition $(Na,Ce)TiO_3$ with Na and Ce in equal atomic proportions. The name Ce-perovskite is used to refer to compositions with Ca > (Na + Ce). The term Nb-perovskite is restricted to those perovskites with (Nb + Fe) < Ti and latrappite is used for varieties with (Nb + Fe) > Ti. Lueshite is the Na,Nb end-member $NaNbO_3$ and tausonite is the $SrTiO_3$ end-member. Perovskite usually shows considerable enrichment in the *LREE*.

Perovskite has been synthesized by pelletizing equimolar mixtures of powdered CaO and TiO_2 at 34.5 MPa followed by heating at 1000–1200ºC for 4 hours in an oxidizing atmosphere. Many materials with the perovskite structure have been synthesized, including $NaTiO_3$, $KNbO_3$, $BaTiO_3$, $CdTiO_3$ and $CaThO_3$, some with oxygen deficiency and some with oxygen excess. The compounds $MgSiO_3$ and $CaSiO_3$ adopt the perovskite structure at 25–30 GPa and $(Mg,Fe)SiO_3$ is considered to be the dominant mineral of the Earth's deep mantle. The stability relations of perovskite show that it cannot coexist with quartz, enstatite, albite or sanidine as it reacts with these minerals at temperatures between 600 and 800ºC at 100 MPa to form titanite and other silicates. The principal occurrences of perovskite are thus restricted to very silica-undersaturated rocks.

Perovskite is colourless to dark brown in thin section and has a very high relief: small crystals may appear completely isotropic but larger grains generally appear to have weak birefringence, usually in conjunction with

Downloaded from https://pubs.geoscienceworld.org/books/chapter-pdf/3763249/9780903056434_ch84.pdf
by guest

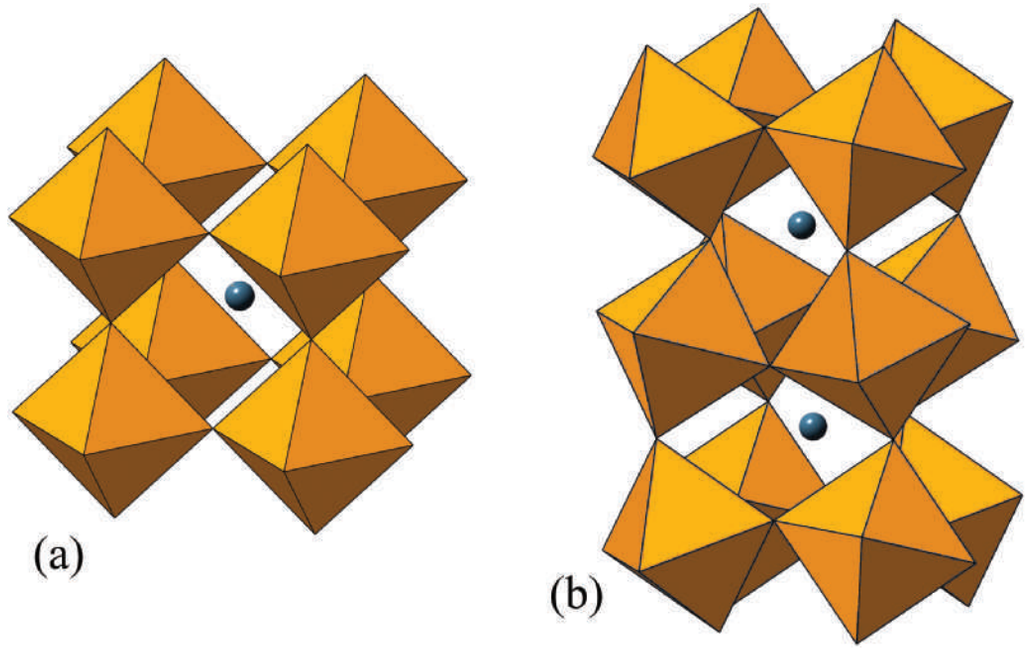


Fig. 272. The structure of perovskite showing Ca cations (blue), and corner-sharing TiO_6 octahedra (yellow); (a) idealized, (b) showing tilted octahedra (Yagi *et al*., 1978. Fig. produced by M.D. Welch).

complex lamellar twinning. The refractive index is very high and increases in *REE*-bearing varieties. The colour in reflected light is grey with a bluish tint and there are strong internal reflections. Close packing in synthetic, perovskite-structured materials and the ability of the structure to distort *via* displacement of atoms means that they exhibit an enormous range of interesting and industrially useful properties. They are dielectric and ferroelectric materials which can exhibit piezo- and pyro-electrical effects, electro-optical effects, and 'colossal magnetoresistance' and may also be relatively high-temperature superconductors. The extremely high relief, brownish colour and weak birefringence are characteristic; the latter distinguishes perovskite from rutile. The complex twinning is also distinctive.

In igneous rocks perovskite occurs as an accessory mineral in basic and alkaline rock types, commonly in association with melilite, leucite or nepheline. It is found in kimberlites both as reaction rims around magnesian ilmenite and as discrete crystals in the groundmass. The rare-earth-bearing varieties are found in alkaline plutonic rocks such as those in the alkaline massifs of the Kola Peninsula. In metamorphic rocks it may be found in contact metamorphosed impure limestones, where it often occurs as the Ce- or Nb-bearing varieties. Perovskite is relatively common in chondrites and is among the minerals that are thought to be early condensates of the primitive solar nebula.

Further reading

Buttner, R.H. and Maslen, E.N. (1992) Electron difference density and structural parameters in $CaTiO_3$. *Acta Crystallographica*, **B48**, 644–649.

Campbell, L.S., Henderson, P., Wall, F. and Nielsen, T.F.D. (1997) Rare earth chemistry of perovskite group minerals from the Gardiner Complex, East Greenland. *Mineralogical Magazine*, **61**, 197–212.

Chakhmouradian, A.R. and Mitchell, R.H. (1997) Compositional variation of perovskite-group minerals from the carbonatite complexes of the Kola Alkaline Province. *The Canadian Mineralogist*, **35**, 1293–1310.

Mitchell, R.H. and Reed, S.J.B. (1988) Ion microprobe determination of rare earth elements in perovskites from kimberlites and alnöites. *Mineralogical Magazine*, **52**, 331–339.

Ono, S., Ohishi, Y. and Mibe, K. (2004) Phase transition of Ca-perovskite and stability of Al-bearing Mg-perovskite in the lower mantle. *American Mineralogist*, **89,** 1480–1485.

Schuiling, R.D. and Vink, B.W. (1967) Stability relations of some titanium-minerals (sphene, perovskite, rutile, anatase). *Geochimica et Cosmochimica Acta*, **31**, 2399–2411.

Yagi, T., Mao, H.-K. and Bell, P.M. (1978) Structure and crystal chemistry of perovskite-type $MgSiO_3$. *Physics and Chemistry of Minerals*, **3**, 97–110.

Downloaded from https://pubs.geoscienceworld.org/books/chapter-pdf/3763249/9780903056434_ch84.pdf
by guest

Spinel Group

Cubic

	n	D (g/cm^3)	*a* (Å)	Formula
Spinel	1.72	3.55	8.103	$MgAl_2O_4$
Hercynite	1.84	4.40	8.135	$Fe^{2+}Al_2O_4$
Gahnite	1.82	4.62	8.08	$ZnAl_2O_4$
Galaxite	1.92	4.04	8.28	$MnAl_2O_4$
Magnesioferrite	2.38	4.52	8.383	$MgFe^{3+}_2O_4$
Magnetite	2.42	5.20	8.396	$Fe^{2+}Fe^{3+}_2O_4$
Maghemite	2.52–2.7	4.88	8.34	γ-$Fe^{3+}_2O_3$
Ulvöspinel	2.2	4.78	8.536	$Fe^{2+}_2TiO_4$
Franklinite	2.36	5.34	8.43	$ZnFe^{3+}_2O_4$
Jacobsite	2.3	4.87	8.505	$MnFe^{3+}_2O_4$
Trevorite	2.3	5.33	8.34	$NiFe^{3+}_2O_4$
Magnesiochromite	2.00	4.43	8.334	$MgCr_2O_4$
Chromite	2.16	5.09	8.378	$Fe^{2+}Cr_2O_4$

H	7½–8
Cleavage	None; octahedral {111} parting may be developed
Twinning	Common on {111}, the spinel law
Colour	Variable; red, brown, blue, black, green, yellow, grey or almost colourless; the darker varieties are opaque in thin section
Unit cell	Z = 8; space group *Fd*3*m*
Special features	Insoluble or soluble with difficulty in acids. Decomposed by fusion with $KHSO_4$

The spinel group has the general formula $A^{2+}B^{3+}_2O_4$. Many elements may enter the spinel cubic close-packed structure. Among naturally occurring spinels, A may be Mg, Fe^{2+}, Zn, Mn, Ni, Co, Cu and Ge, whereas B may include Al, Fe^{3+}, Cr, V and Ti. Materials with the spinel structure are of considerable importance to the electronics industry

The spinel group is subdivided into three series, according to whether the dominant trivalent ion is Al, Fe or Cr:

	Spinel series (Al)	Magnetite series (Fe^{3+})	Chromite series (Cr)
Mg	Spinel	Magnesioferrite	Magnesiochromite
Fe^{2+}	Hercynite	Magnetite	Chromite
Zn	Gahnite	Franklinite	
Mn	Galaxite	Jacobsite	
Ni		Trevorite	

In addition, the minerals maghemite (γ-Fe_2O_3) and ulvöspinel ($Fe^{2+}_2TiO_4$) have the spinel structure. Maghemite has a composition that differs from the general spinel-group stoichiometry; it can be regarded as having a cation deficiency. In ulvöspinel the formula is also different in detail as a result of the substitution $2\,Fe^{3+} \leftrightarrow Fe^{2+} + Ti^{4+}$.

The members of the spinel group are common accessory minerals of both igneous and metamorphic rocks and occur also as detrital grains in many

Downloaded from https://pubs.geoscienceworld.org/books/chapter-pdf/3763251/9780903056434_ch85.pdf
by guest

sedimentary rocks. Magnetite is found in most igneous rocks and chromite is common in ultrabasic igneous rocks. Magnetite and chromite may be locally abundant and may occur as monomineralic masses, pods or layers to form magnetitite and chromitite, which are of economic importance. Magnetite also occurs in metamorphic rocks and the coloured spinels may also be found in metamorphic assemblages, where they may be of gemmological interest.

Structure

In the minerals of the spinel group there are 32 oxygen ions and 24 cations in the cubic unit cell (a 8.08–8.54 Å, Z = 8); eight of the cations are in four-fold coordination (the A sites), and 16 in six-fold coordination (the B sites); see Fig. 273. Perpendicular to a triad axis, sheets of oxygen ions alternate with sheets of cations: the cation sheets in which all the cations are in six-fold coordination alternate with others in which the cations are distributed among A and B sites in the proportions of two A to one B. Two structural types occur, differing in their distribution of cations among the A and B sites, and known as normal and inverse spinels. With the general formula $R^{2+}_8R^{3+}_{16}O_{32}$ the two distributions are:

Normal $8R^{2+}$ in A, $16R^{3+}$ in B
Inverse $8R^{3+}$ in A, $8R^{2+} + 8R^{3+}$ in B

The minerals $FeAl_2O_4$ (hercynite), $ZnAl_2O_4$ (gahnite) and $MnAl_2O_4$ (galaxite) are normal spinels whereas $MgFe^{3+}_2O_4$ (magnesioferrite) and $FeFe^{3+}_2O_4$ (magnetite) have the inverse structure: thus the magnetite formula may be written $Fe^{3+}(Fe^{2+}Fe^{3+})O_4$. Spinels generally are not entirely either N or I, but have intermediate structures and properties.

A further structural variety within the spinel group is demonstrated by the ability of the spinels to take up in solid solution the oxides Al_2O_3 and Fe_2O_3, the end-members being represented by γ-Al_2O_3 and γ-Fe_2O_3 (maghemite): the latter has the inverse spinel structure with a cation deficiency.

A general formula giving the cell edge a of members of the spinel group as a function of the ionic radii of the divalent ions R^{2+} and of the trivalent ions R^{3+} is:

$$a\ (\text{Å}) = 5.790 + 0.95R^{2+} + 2.79R^{3+}$$

Twinning is common on {111}; this is so typical that the term *spinel law twinning* is used commonly to describe twinning in other cubic phases. This twinning is usually simple, but multiple and lamellar twins are known.

Chemistry

In the spinel group the pure end-members are rare as natural minerals, but the species may be subdivided on the basis of the dominant R^{2+} and R^{3+} ions, the varieties being designated by the next most dominant constituent. Compositions in the multicomponent spinel system may be plotted in a spinel prism (e.g. Fig. 274).

Spinel series

Spinel, $MgAl_2O_4$. Spinel *sensu stricto*, followed by hercynite, is the commonest mineral in the spinel series. There is a continuous replacement series from spinel to hercynite, $Fe^{2+}Al_2O_4$: spinels with a considerable amount of Fe^{2+} replacing Mg, with the Mg:Fe^{2+} ratio from 3 to 1, are termed ‘pleonaste’. Zinc may substitute for magnesium, giving an isomorphous series from spinel to gahnite, $ZnAl_2O_4$; these Zn-bearing spinels are termed ‘gahno-spinel’ or ‘zincian spinel’. The Al ion may be replaced by Cr, grading into magnesiochromite in the chromite series: the varietal name ‘picotite’ is restricted to hercynite with appreciable Cr replacing Al, much of the so-called picotite being either pleonaste or ferroan chromian spinel.

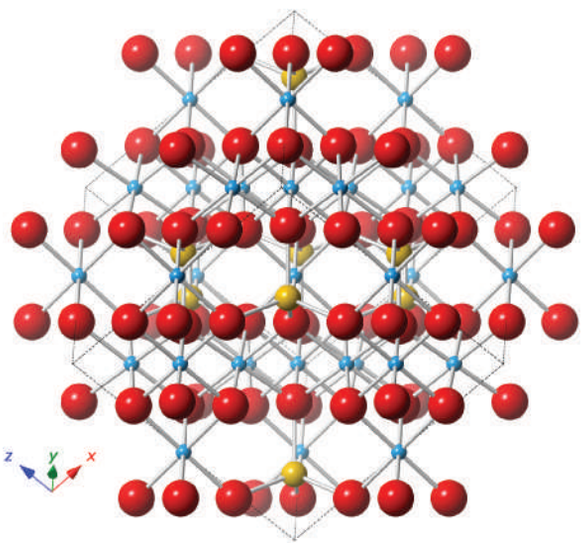


Fig. 273. The structure of spinel showing an extended cubic unit cell, oriented to emphasize the (111) planes of oxygens and the tetrahedral and octahedral sites lying between them. Planes of oxygen are stacked above one another in the sequence of cubic closest packing. (CrystalMaker image). Red: oxygen; blue: octahedral (B) sites; yellow: tetrahedral (A) sites.

Downloaded from https://pubs.geoscienceworld.org/books/chapter-pdf/3763251/9780903056434_ch85.pdf
by guest

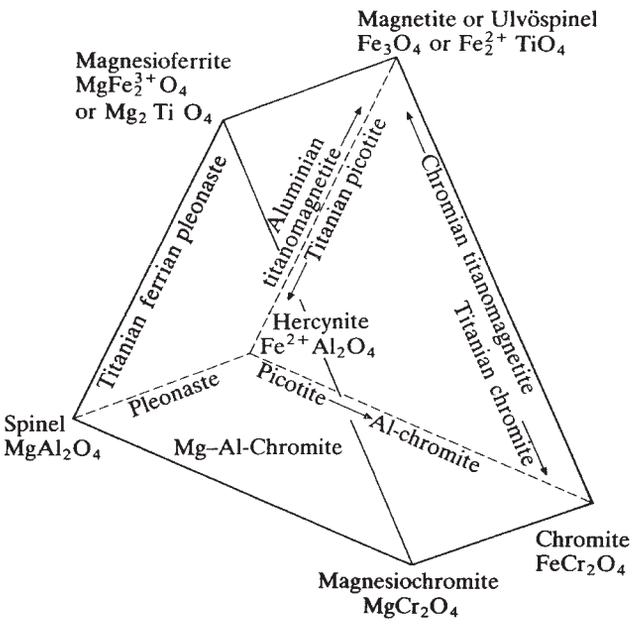


Fig. 274. Nomenclature for compositions in the multi-component spinel prism. The bases of the triangles are defined by normal spinels and the vertices by inverse spinels (Haggerty, 1991).

Spinel may be readily synthesized by sintering or fusing MgO and $A1_2O_3$ with or without a mineralizer such as boric oxide or water vapour. It is produced commercially by the Verneuil process, and is coloured red by the addition of Cr_2O_3. The melting point of normal spinel, $MgAl_2O_4$, is 2135 ± 20ºC.

The colour of spinel varies from almost colourless through a great range of colours including red (Cr), blue (Fe^{2+}), brown (Fe^{3+}), yellow and pink. Most of the gem spinels are spinel *sensu stricto*, including the so-called ruby spinel, one of the best examples of which is the 'Black Prince's Ruby' in the Imperial State Crown: the name 'balas ruby' is used for paler varieties.

Hercynite, $Fe^{2+}Al_2O_4$. In addition to the substitution $Fe^{2+} \leftrightarrow$ Mg, considerable Al $\leftrightarrow Fe^{3+}$ substitution may occur though there does not appear to be a complete natural series to magnetite. The substitution Al ↔ Cr is continuous, there being complete solid solution between hercynite and chromite: the term 'picotite' is used for a variety of hercynite with appreciable chromium, with Al > Cr and with Fe/Mg between 3 and 1. The system $FeAl_2O_4$ (hercynite)–Fe_3O_4 (magnetite) has been investigated experimentally: above 858ºC there is complete solid solution, but below this temperature the two-phase region of exsolution widens with decreasing temperature. Hercynite is dark green to black in colour.

Gahnite, $ZnAl_2O_4$. There is normally considerable substitution of Fe and Mg for Zn (Table 52, analysis 3), and there is probably complete solid solution between $ZnAl_2O_4$ and $MgAl_2O_4$. Gahnite is usually a dark bluish green.

Galaxite, $MnAl_2O_4$. Galaxite is an uncommon member of the spinel series and is mahogany-red to black in colour: replacements include Mn $\leftrightarrow Fe^{2+}$ and Al $\leftrightarrow Fe^{3+}$.

Magnetite series

Magnesioferrite, $MgFe_2^{3+}O_4$. In natural minerals considerable replacement of Mg by Fe^{2+} takes place. Analyses are few, as the mineral is usually intergrown or intimately associated with hematite: it is magnetic and brownish black to black in colour.

Magnetite, $Fe^{2+}Fe_2^{3+}O_4$. Analysis 4 (Table 52) is of material close to the theoretical magnetite end-member composition. Small amounts of Al substitute for Fe^{3+} and generally similar small proportions of Ca, Mn and Mg replace Fe^{2+}, though continuous replacement between Mg and Fe^{2+} to magnesioferrite can occur. A considerable amount of Ti can enter the magnetite structure and there is a continuous relationship between magnetite and the ulvöspinel molecule, Fe_2TiO_4. The term titanomagnetite is best restricted to those specimens where the presence of an ulvöspinel component can be demonstrated by X-ray or similar techniques. Other replacements occurring in magnetite include the partial substitution of Cr and V for Fe^{3+}, whereas Fe^{2+} may be partially replaced by Ni, Co and Zn in addition to Mg, Mn and some Ca.

Magnetite may be synthesized by the oxidation of iron at high temperatures in air or steam, by heating Fe_2O_3 in a reducing atmosphere, or by heating $FeCO_3$ in steam or nitrogen at dull red heat. It is the stable form in air above 1388ºC, hematite (α-Fe_2O_3) being the stable form beneath that temperature. The melting point of pure magnetite is 1594ºC. At 1452ºC magnetite can contain 30% Fe_2O_3 which on cooling separates out as hematite along the {111} planes of the magnetite. Phase equilibrium studies in the ternary system FeO–Fe_2O_3–TiO_2 show that magnetite (solid solution) is the primary crystalline phase in the composition range 0–12 wt.% TiO_2, with liquidus temperatures decreasing from 1594ºC to a minimum at 1524ºC. Three solid-solution

Downloaded from https://pubs.geoscienceworld.org/books/chapter-pdf/3763251/9780903056434_ch85.pdf
by guest

Table 52. Spinel group analyses.

	1		2		3		4		5		6	
SiO_2	0.28		–		–		0.27		–		0.09	
TiO_2	0.02		–		–		tr.		19.0		0.32	
Al_2O_3	64.85		60.7		58.18		0.21		4.3		21.6	
Cr_2O_3	0.03		–		–		–		–		43.8	
Fe_2O_3	2.21		–		–		68.85		33.2		6.86	
FeO	13.70		34.7		10.50		30.78		43.2		9.26	
MnO	0.01		0.2		0.08		–		–		0.30	
MgO	18.74		4.3		3.30		tr.		0.2		17.2	
ZnO	–		–		27.71		–		–		–	
CaO	–		0.1		–		tr.		–		–	
Total	99.84		100.0		99.77		100.11		99.9		99.6	
Numbers of ions on the basis of 32 O												
Si	0.057		–		–		0.083		–		0.022	
Al	15.564		16.01		16.01		0.077		1.473		6.159	
Cr	0.005	15.97	–		–		–	16.05	–		8.373	15.86
Fe^{3+}	0.337		–		–		15.886		7.263		1.248	
Ti	0.003		–		–		–		4.154	23.48	0.058	
Mg	5.678		1.434		1.148		–		0.087		6.199	
Fe^{2+}	2.332		6.492		2.049		7.896		10.502		1.873	
Zn	–	8.01	–	7.99	4.775	7.99	–		–		–	8.17[a]
Mn	0.002		0.038		0.015		–		–		0.061	
Ca	–		0.024		–		–		–		–	

1 Ferroan spinel, sapphirine-phlogopite-taaffeite-apatite metasomatic rock in pyroxenite, Musgrave Ranges, Central Australia (Wilson, A.F. & Hudson, D.R., 1967, *Chem. Geol*., **2**, 209–15).
2 Hercynite, corundum-spinel-ilmenite rock, Plössberg, northern Bavaria (Propach, G., 1971, *Neues Jahrb. Min*., *Abhdl*., **115**, 120–2).
3 Gahnite, Archaean iron-formation, Malene supracrustal belt, Godthåb area, western Greenland (Appel, P.W.V., 1986, *Mineral. Mag*., **50**, 175–77). Microprobe analysis.
4 Magnetite, Lover's Pit, Mineville, New York State (Newhouse, W.H. & Glass, J.J., 1936, *Econ. Geol*., **31**, 699–711).
5 Equant ulvöspinel in skeletal pseudobrookite in rapidly quenched dyke, White Mountain batholith, New Hampshire (Rice, J.M. *et al*., 1971, *Amer. Min*., **56**, 158–62). Microprobe analysis.
6 Magnesiochromite, komatiite, Gorgona Island, Colombia (Echeverria, L.M., 1980, *Contrib. Mineral. Petrol*., **73**, 253–66). Microprobe analysis. Includes NiO 0.19.

[a] Includes Ni 0.037.

series exist in the system: the pseudobrookite series (orthorhombic), the hematite–ilmenite series (trigonal) and the magnetite–ulvöspinel series (Fig. 275); in the latter series a continuous solid solution exists at high temperatures, with exsolution taking place below 600ºC. Magnetite is black with a black streak and is opaque in thin section. Many varieties are soluble in HCl but some magnetites require fusion with a flux before decomposition.

Maghemite, γ-Fe_2O_3. Some natural magnetites contain an excess of Fe_2O_3 grading towards the end-member maghemite. For such a series of mixed crystals in the range Fe_3O_4–Fe_2O_3, the number of metal ions per 32 oxygens falls below the theoretical 24 for pure Fe_3O_4, and for end-member maghemite is 21.33. Maghemite is metastable and inverts to hematite (α-Fe_2O_3) on heating: the inversion temperature varies from 200 to 700ºC depending on the previous history of the sample.

Ulvöspinel, $Fe_2^{2+}TiO_4$. Naturally occurring specimens at or near end-member ulvöspinel composition are rare, but the occurrence of ulvöspinel as an exsolution within magnetite or pseudobrookite has been increasingly recognized (Table 52, analysis 5). Near end-member ulvöspinel occurs in lunar basalts. The type mineral in the dolerite of Södra Ulvön, Sweden, has 51.8% Fe_2TiO_4. The melting point of synthetic Fe_2TiO_4 is 1470ºC.

Franklinite, $ZnFe_2^{3+}O_4$. Although essentially an oxide of zinc and ferric iron, franklinite normally contains a considerable proportion of Mn^{2+} substituting for Zn.

Jacobsite, $MnFe_2^{3+}O_4$. This is a relatively rare mineral: appreciable Mn^{3+} may replace Fe^{3+} and some replacement of Mn^{2+} by Mg may occur.

Trevorite, $NiFe_2^{3+}O_4$. Minor amounts of Mg and Fe^{2+} may replace Ni.

Downloaded from https://pubs.geoscienceworld.org/books/chapter-pdf/3763251/9780903056434_ch85.pdf
by guest

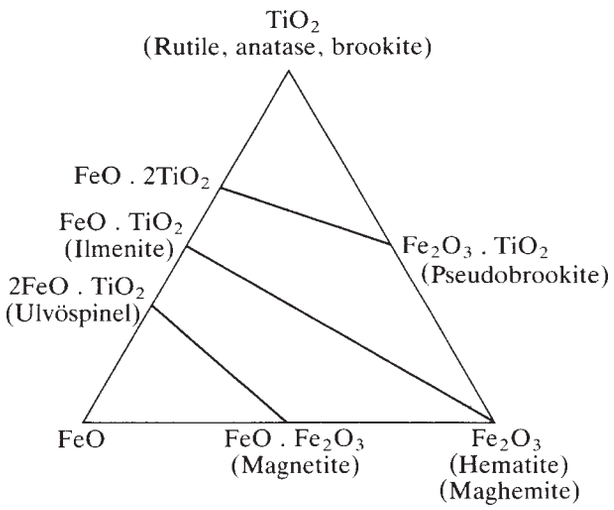


Fig. 275. The system $FeO-Fe_2O_3-TiO_2$ showing the major high-temperature solid solution series magnetite–ulvöspinel, hematite–ilmenite, pseudobrookite–$FeTi_2O_5$ plotted on a mol% basis (Deer *et al*., 1992, *An Introduction to the Rock-Forming Minerals*, Longman, UK).

Chromite series

Magnesiochromite, $MgCr_2O_4$. All natural magnesiochromites contain a considerable amount of Fe^{2+} replacing Mg, and there is a continuous variation through to chromite itself which has Fe^{2+} > Mg. There is also appreciable replacement of Cr by Al and by Fe^{3+} (Table 52, analysis 6).

Chromite, $FeCr_2O_4$. The majority of natural chromites show a considerable amount of Mg replacing Fe^{2+} and generally have appreciable aluminium and lesser ferric iron. Zinc-bearing chromites are also known.

Optical and physical properties

In the spinel group the lowest refractive indices and densities occur in the members of the aluminous spinel series. The chromite series have intermediate values for these properties, and the highest refractive indices and densities occur in the magnetite series though there is a considerable overlap in the densities of the magnesian magnetites and chromites. The minerals of the magnetite series are normally opaque except in the very thinnest flakes, and their refractive indices (>2.3) are not usually determined. The spinel series are the most transparent, even hercynite generally appearing transparent dark green in thin section, and they are also the most refractory members of the group (Fig. 276).

Assuming that the physical properties of spinels are additive functions of the molecular proportions of the end-members and that components other than those plotted are not present in significant amounts, it is possible to construct diagrams relating *n, a* and D with composition in various portions of the spinel group (Fig. 277).

Twinning is common on {111}, the spinel law. The twinning is usually simple, but multiple or lamellar twins are known. There is no well developed cleavage but in spinel and magnetite an octahedral parting may occur.

Magnetite is a typical ferrimagnetic material and has a Néel point (i.e. the temperature at which, on heating, the ferrimagnetism is lost and the substance becomes paramagnetic) of 578ºC. It is black with a black streak and is opaque in thin section: in reflected light it appears grey and has moderate reflectance (~20.7%). Chromite is black in hand specimen but gives a chocolate brown streak; in thin section it may appear yellowish brown to brown or black; reflectance is lower (~14%) than for magnetite.

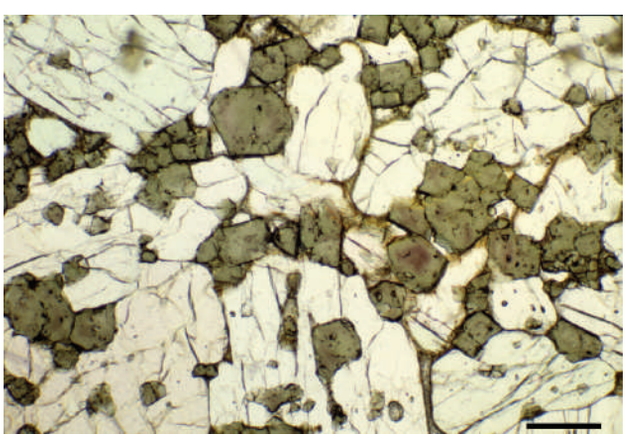


Fig. 276. Spinel-forsterite xenolith, Vesuvius (ppl, scale bar 0.4 mm), showing dark green spinel with olivine. The spinel crystals are subhedral, and in some the colour is zoned with some crystals showing a brownish core (W.S. MacKenzie collection, courtesy of Pearson Education).

Downloaded from https://pubs.geoscienceworld.org/books/chapter-pdf/3763251/9780903056434_ch85.pdf
by guest

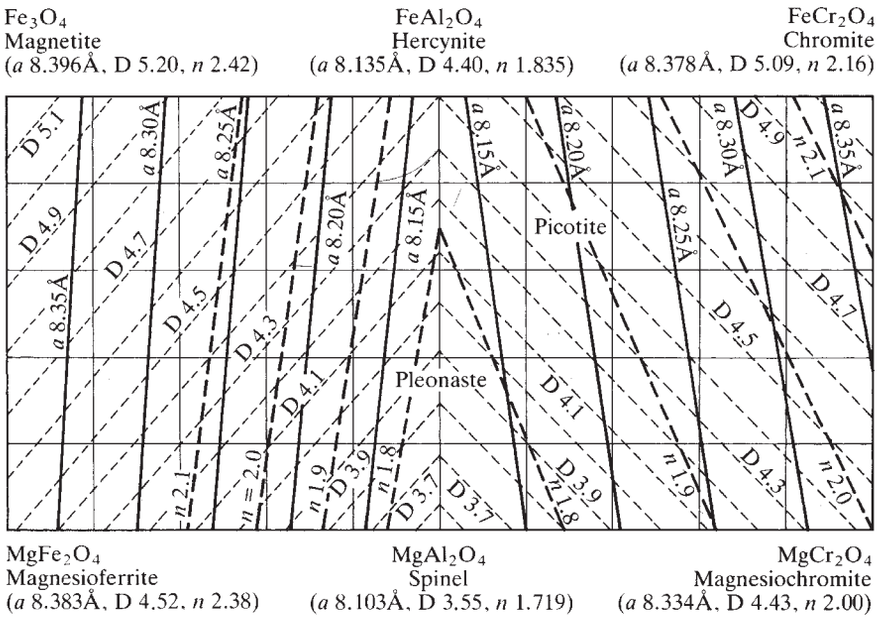


Fig. 277. Refractive indices, specific gravities and cell edges for some members of the spinel group.

Distinguishing features

The isotropic nature, high relief and lack of cleavage are characteristic. Spinel differs from garnet in having a well developed octahedral form, and {111} twins. In the absence of these features the pink, red or brown spinels may be distinguished from members of the garnet series by their slightly lower refractive indices and densities. Periclase differs from spinel in having perfect {001} cleavage.

Paragenesis

Spinel series

Spinel (sensu stricto) is a common high-temperature mineral in metamorphic rocks and in alumina-rich xenoliths. It occurs with forsterite and diopside, in contact-metamorphosed limestones and is found in a similar association in regionally metamorphosed limestones, where it may occur also with chondrodite, phlogopite and calcite. In thermally metamorphosed argillaceous rocks poor in SiO_2, spinel or pleonaste may form, commonly with cordierite or orthopyroxene.

Hercynite, the ferroan aluminium spinel (Table 52, analysis 2), is found commonly in highly metamorphosed argillaceous sediments somewhat richer in iron than those yielding pleonaste. It occurs also in some basic and ultrabasic igneous rocks and in metamorphic pyroxenites, and is also found in some acid granulitic assemblages, the iron spinel, unlike spinel itself, being stable in the presence of free silica.

Gahnite, the zinc spinel, occurs chiefly in granitic pegmatites but it is also found in metasomatic replacement veins. The rare manganese aluminium spinel, *galaxite*, is known mainly from manganese-rich vein deposits.

Magnetite series

Pure magnesioferrite is a rare mineral which is found in volcanic regions: the more common ferroan magnesioferrite may occur in similar associations to those of magnetite. The range of compositions of spinel group minerals (mainly the magnetite and chromite series) in igneous rocks is shown in Fig. 278.

Magnetite is one of the most abundant and ubiquitous oxide minerals in igneous and metamorphic rocks and is the principal magnetic ore (e.g. Table 52, analysis 4). It occurs typically as an accessory mineral in many igneous rocks, but is occasionally concentrated in magmatic segregations or by crystal settling, sometimes forming magnetite bands, e.g. in the Bushveld Complex. In many igneous rocks the magnetite is appreciably titaniferous, particularly in the more basic rock types. Magnetite also occurs in important amounts in many skarn deposits, where it has been metasomatically introduced into calcareous rocks: here it may be associated with an andradite–hedenbergite assemblage and often with sulphides and oxides of Zn, Pb and Cu. It is also found in varying amounts in thermally metamorphosed sediments, any hydrated ferric oxide cement or limonitic staining being reduced first to hematite and then at higher grades of metamorphism to magnetite. In sedimentary rocks magnetite commonly occurs as a heavy detrital mineral, and under suitable conditions it may become concentrated by stream or tidal action to produce magnetite sands of economic importance.

Downloaded from https://pubs.geoscienceworld.org/books/chapter-pdf/3763251/9780903056434_ch85.pdf
by guest

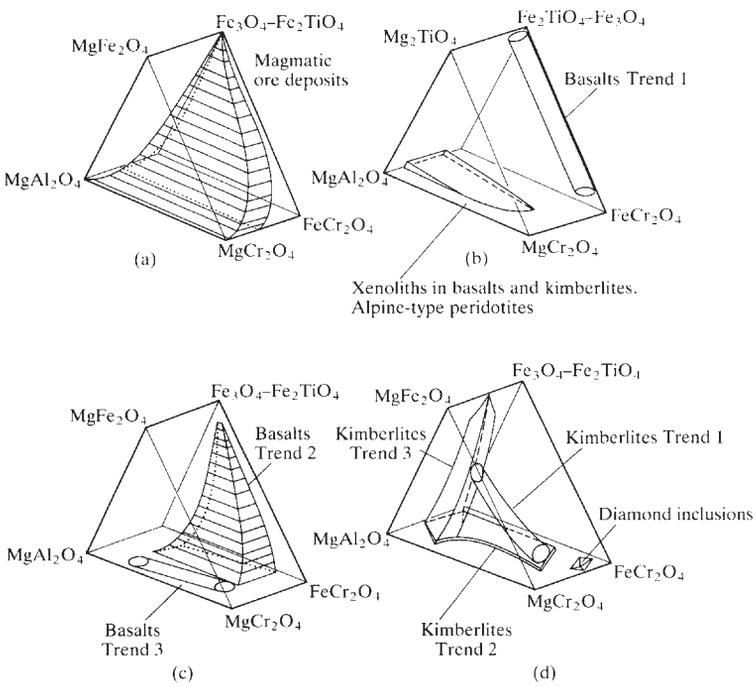


Fig. 278. Spinel distributions for a variety of rock types and geological settings. Basalt trends 1–3 are respectively for subaerially extruded olivine basalts, island-arc volcanism, and deep-sea basalts (after Haggerty, 1991).

Maghemite is commonly formed as a result of the supergene alteration of magnetite deposits. The few examples known of spinel deposits with *ulvöspinel* as a significant molecule occur in basic igneous rocks or their metamorphosed equivalents.

Franklinite occurs in the zinc ore deposits in Precambrian limestone at Franklin and Sterling Hill, New Jersey, as the result of complex metamorphic and metasomatic processes. The manganese and ferric iron spinel, *jacobsite*, occurs in metasomatic manganese deposits, whereas the rare nickel iron spinel, *trevorite*, is known from a green talcose phyllite in the Transvaal, and at Scotia talc mine, Bon Accord, Barberton, South Africa.

Chromite series

In general terms the magnesiochromites and the chromites (*sensu stricto*) have the same paragenesis, the most common member of the series probably being ferroan magnesiochromite (e.g. Table 52, analysis 6). Chromite can form nearly monomineralic bands and segregations in igneous rocks and these are the major economic source of chromium. Such deposits have a complicated genesis, and concentration from a large body of magma may require magma mixing, magma contamination, crystal fractionation and accumulation. In ultrabasic igneous rocks these deposits can be associated with valuable platinum group minerals. Chrome ore is produced from these deposits in the Bushveld, South Africa, at Kemi, Finland and at Masinloc, Luzon, Phillipines. Chromium-bearing spinels occur in the olivine-rich inclusions found in basaltic rocks, but in general these inclusions are members of the spinel series rather than the chromite series. Titanian chromite and chromian ulvöspinel occur in lunar rocks. As a heavy mineral, chromite is found in detrital stream and beach sands; it is also known from meteorites.

Further reading

Barnes, S.J. and Roeder, P.L. (2001) The range of spinel compositions in terrestrial mafic and ultramafic rocks. *Journal of Petrology*, **42**, 2279–2302.

Bowles, J.F.W., Howie, R.A., Vaughan, D.J. and Zussman, J. (2011) *Rock-forming Minerals. Non-silicates: Oxides, Hydroxides and Sulphides*, **5A**. 920 pp. Geological Society, London.

Daneu, N., Rečnik, A., Yamazaki, T. and Dolenec, T. (2007) Structure and chemistry of (111) twin boundaries in $MgAl_2O_4$ spinel crystals from Mogok. *Physics and Chemistry of Minerals*, **34**, 233–247.

Girnis, A.V. and Brey, G.P. (1999) Garnet-spinel-olivine-orthopyroxene equilibria in the FeO–MgO–Al_2O_3–SiO_2–Cr_2O_3 system: II. Thermodynamic analysis. *European Journal of Mineralogy*, **11**, 619–636.

Haggerty, S.E. (1991) Oxide mineralogy of the upper mantle. Pp. 355–416 in *Oxide Minerals: Petrologic and Magnetic Significance* (D.H. Lindsley, editor). Reviews in Mineralogy, **25**, Mineralogical Society of America, Washington, D.C.

Harrison, R.J. and Putnis, A. (1996) Magnetic properties of the magnetite–spinel solid solution: Curie temperatures, magnetic susceptibilities, and cation ordering. *American Mineralogist*, **81**, 375–384.

Ivanyuk, G.Yu., Pakhomovsky, Yu.A., Konopleva, N.G., Yakovenchuk, Yu.P., Menshikov, Yu.P. and Mikhailova, Yu.A. (2006) [Spinel-group minerals in rocks of Khibiny alkaline massif, Kola Peninsula.] *Proceedings of the Russian Mineralogical Society*, **135(5)**, 64–75 (Russian with English abstract).

Downloaded from https://pubs.geoscienceworld.org/books/chapter-pdf/3763251/9780903056434_ch85.pdf
by guest

Mg and Al hydroxides and oxyhydroxides

Brucite $Mg(OH)_2$

Trigonal (+)

ω	1.560–1.590
ε	1.580–1.600
δ	0.014–0.020
D (g/cm^3)	2.39
H	2½
Cleavage	Basal {0001} perfect; may be fibrous
Colour	White, greenish or brownish; colourless in thin section
Unit cell	*a* 3.14 Å, *c* 4.76 Å
	Z = 1; space group $P\bar{3}m1$
Special features	Soluble in HCl

The layered structure of brucite has a sheet of Mg atoms sandwiched between two sheets of (OH) parallel to (0001). Each Mg is coordinated by six (OH), forming a layer of Mg–OH octahedra (Fig. 279), and each (OH) has three Mg on one side, and three (OH) from the next layer, on the other. The layers are themselves charge-balanced so that interlayer forces are weak [leading to perfect (0001) cleavage] and are thought to be mainly the result of oxygen-to-(OH) dipole attraction.

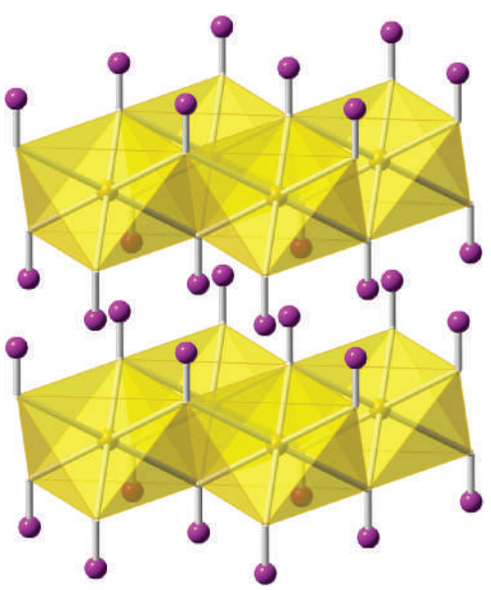


Fig. 279. The structure of brucite showing layers of Mg–OH octahedra (yellow) and the positions of hydrogen ions (mauve) (based on data from Catti, M. *et al*., 1995, *Phys. Chem. Min.*, **22**, 200–6. Fig. produced by M.D. Welch).

In the brucite structure, Fe^{2+} and Mn may replace Mg to a limited extent and trace amounts of Ni and Zn may occur. A fibrous variety, nemalite, is commonly rich in iron, but this is generally attributable to the presence of magnetite among the fibres. Ferrobrucite, the iron-bearing variety, may turn brown on exposure. Although brucite commonly forms by the alteration of periclase, it is readily altered to hydromagnesite, $Mg_5(CO_3)_4(OH)_2{\cdot}4H_2O$, or less commonly to chrysotile and other serpentine minerals.

Brucite may exhibit optical anomalies due to deformation or to fibre aggregates; in nemalite, the fibrous variety, the *z* axes are perpendicular to the length of the fibre. The birefringence varies with wavelength from 0.020 to 0.015, giving anomalous interference colours. The softness and perfect cleavage are notable: muscovite, talc and gypsum differ in being optically negative, and colourless chlorite has a lower birefringence.

The most common occurrence of brucite is as an alteration product of periclase in contact metamorphosed dolomites. It is also found as a low-temperature hydrothermal vein mineral in serpentinites and chlorite schists.

Further reading

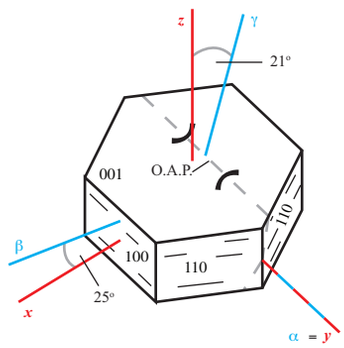
D'Antonio, M. and Kristensen, M.B. (2004) Serpentine and brucite of ultramafic clasts from the South Chamorro Seamount (Ocean Drilling Program Leg 195, Site 1200): inferences for the serpentinization of the Mariana forearc mantle. *Mineralogical Magazine*, **68**, 887–904.

Duffy, T.S., Meade, C., Fei, Y., Mao, H.K. and Hemley, R.J. (1995) High-pressure phase transition in brucite, $Mg(OH)_2$. *American Mineralogist*, **80**, 222–230.

Downloaded from https://pubs.geoscienceworld.org/books/chapter-pdf/3763381/9780903056434_ch86.pdf
by guest

Monoclinic (+)

α	1.56–1.58
β	1.56–1.58
γ	1.58–1.60
δ	~0.02
$2V_\gamma$	0–40°
Orientation	α = *y*, γ:*z* ~–21°; O.A.P. ⊥(010)
D (g/cm^3)	~2.4
H	2½–3½
Cleavage	{001} perfect
Twinning	Common on {001}; parallel twins [130], {001}; less commonly on {100} and {110}
Colour	White, pale pink, pale green, grey, light brown; colourless to pale brown in thin section
Unit cell	*a* 8.64 Å, *b* 5.07 Å, *c* 9.72 Å, β 94°34′ Z = 8, space group $P2_1/n$



The fundamental unit of the gibbsite structure is a layer of Al ions sandwiched between two sheets of hexagonally packed hydroxyl ions. In the brucite, $Mg(OH)_2$, structure all of the octahedrally coordinated sites between the oxygen layers are occupied by cations; in gibbsite only two out of three are occupied. In both gibbsite and brucite the layers may be regarded as built of octahedra linked laterally by sharing edges; the network so formed may be described by an orthogonal (pseudohexagonal) cell with parameters (for gibbsite) *a* ~ 8.6 Å, *b* ~ 5 Å (~$a/\sqrt{3}$). In brucite the oxygen layers are in the sequence of hexagonal close packing ...ABABAB..., whereas in gibbsite the sequence is ...ABBAABBA.... Thus in the ideal structure of gibbsite, oxygens at the bottom of the layer lie directly above oxygens at the top of the layer below (Fig. 280). The structure of gibbsite is in fact somewhat distorted from the ideal, resulting in a monoclinic cell: there are two layers in each cell. Bayerite is a dimorph with similar layers of octahedra but these are stacked differently to yield a single-layer cell.

Analyses of gibbsite usually show the presence of Fe_2O_3 and minor amounts of other oxides. It seems likely that some Fe^{3+} and perhaps small amounts of other ions could substitute for Al in the structure, but some oxides are no doubt present as impurities. Heating gibbsite produces γ-alumina, usually with boehmite formation as an intermediate stage. In the system Al_2O_3–H_2O, gibbsite is the stable form at lower temperatures; at higher temperatures diaspore is the

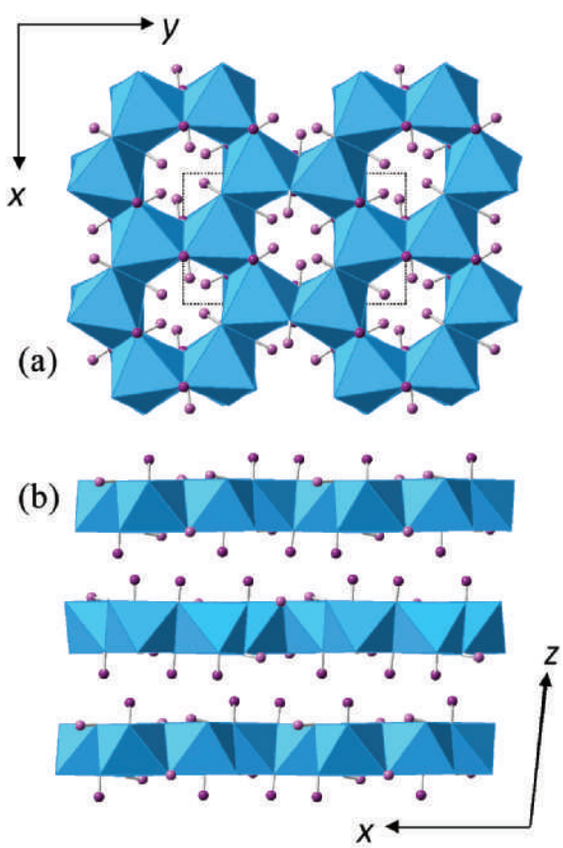


Fig. 280. The structure of gibbsite (a) viewed normal to (001); (b) projection on (010). Structure based on data from Saalfeld, H. & Wedde, M., 1974, *Z. Krist.*, **139**, 129–35 (fig. produced by M.D. Welch). Blue: Al–O octahedra; mauve: hydrogen ions.

Downloaded from https://pubs.geoscienceworld.org/books/chapter-pdf/3763388/9780903056434_ch87.pdf
by guest

stable phase, but boehmite can exist metastably, and above about 450ºC corundum is the stable phase.

Gibbsite often occurs as small tabular {001} crystals with a pseudo-hexagonal outline conferred by the forms {100} and {110}: it may also occur in prismatic crystals and in lamellar or stalactitic aggregates. Gibbsite may be distinguished from muscovite by its positive optical sign, and from kaolinite which has lower birefringence. It has lower refractive indices and lower 2V than boehmite and diaspore.

Gibbsite, diaspore and boehmite are the three hydrates of alumina which are the main constituents of bauxites and laterites, and gibbsite is the predominant mineral in many cases. Bauxites (mainly aluminium hydrates) result from the weathering, under tropical conditions, of aluminium silicate rocks yielding clays which are subsequently desilicated. Among the minerals associated with the alumina hydrates in bauxites and in laterites (ferruginous bauxites) are the analogous iron compounds (goethite and lepidocrocite), and also hematite and the clay minerals kaolinite and halloysite. Some gibbsite may be found in emery deposits which are formed by the metamorphism of bauxites; gibbsite can occur as an alteration crust on corundum.

Gibbsite also occurs as a low-temperature hydrothermal mineral in veins or cavities in aluminium-rich igneous rocks. It has been reported as the end-product of granitic weathering, the sequence being plagioclase → amorphous or allophanic material → halloysite → gibbsite.

Further reading

Dietzel, M. and Böhme, G. (2005) The dissolution rates of gibbsite in the presence of chloride, nitrate, silica, sulphate and citrate in open and closed systems at 20ºC. *Geochimica et Cosmochimica Acta*, **69**, 1199–1211.

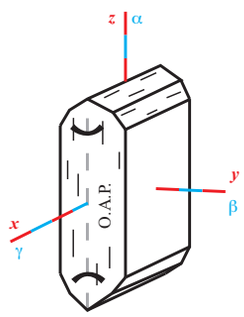
Trolard, F. and Tardy, Y. (1987) The stabilities of gibbsite, boehmite, aluminous goethites and aluminous hematites in bauxites, ferricretes and laterites as a function of water activity, temperature and particle size. *Geochimica et Cosmochimica Acta*, **51**, 945–957.

Verdes, G., Gout, R. and Castet, S. (1992) Thermodynamic properties of the aluminate ion and of bayerite, boehmite and diaspore. *European Journal of Mineralogy*, **4**, 767–792.

Downloaded from https://pubs.geoscienceworld.org/books/chapter-pdf/3763388/9780903056434_ch87.pdf
by guest

Orthorhombic (+)

α	1.68–1.71
β	1.70–1.73
γ	1.73–1.75
δ	0.04–0.05
$2V_\gamma$	84–86°
Orientation	α = *z*, β = *y*, γ = *x*; O.A.P. (010)
D (g/cm^3)	3.3–3.5
H	6½–7
Cleavage	{010} perfect; {110}, {210}, {100} less common
Colour	White, grey-white or colourless; colourless in thin section Iron or manganese varieties green, grey, brown, yellow, pink in hand specimen
Pleochroism	Strongly coloured specimens may have absorption α < β < γ
Unit cell	*a* 4.40 Å, *b* 9.42 Å, *c* 2.85 Å Z = 4, space group *Pbnm*



The structure of diaspore is based upon layers of oxygen atoms, the sequence of which is that of hexagonal close packing. Aluminium ions occupy octahedrally coordinated sites between layers in such a way as to form strips of octahedra, the direction of which defines the *c* parameter of the unit cell. The strips have the width of two octahedra and yield an orthorhombic cell in which *a* is twice the distance between oxygen layers, and $b/2 \sim c\sqrt{3}$ (Fig. 281).

When diaspore is heated corundum is produced but the outward form of the diaspore crystal is retained; there is a close orientational relationship between diaspore and its decomposition products. The structural relationships between aluminium and analogous iron compounds are illustrated in Table 53.

The principal substitutions in diaspore are of relatively small amounts of iron and, to a lesser extent, of manganese. On heating, diaspore decrepitates strongly, separating into white scales and, on stronger heating, water is given off. Diaspore is sometimes described as α-alumina hydrate and its formula written as $\alpha\text{-}Al_2O_3.H_2O$ although there are no water molecules in its structure. The compounds within the system $Al_2O_3–H_2O$ are gibbsite, bayerite, boehmite, diaspore, corundum, and γ-alumina, the first five of which are known definitely to occur as minerals. With increasing temperature, first gibbsite, then diaspore, then corundum, is the stable phase, and boehmite exists probably metastably at intermediate temperatures.

Diaspore crystals commonly occur in the form of thin plates on {010} elongated parallel to *z*; they are sometimes acicular, and rarely tabular parallel to {100}. Diaspore also occurs in thin scales and as massive aggregates and may be stalactitic. Although it is most commonly colourless, diaspore may be coloured by the presence of iron and manganese; the coloured varieties are quite strongly pleochroic in thin section.

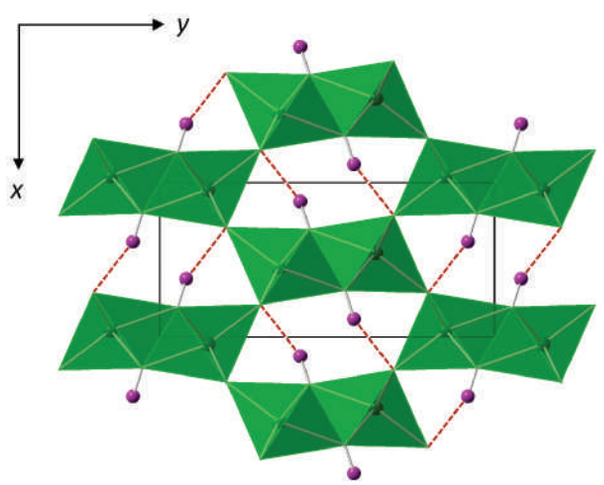


Fig. 281. The structure of diaspore viewed along the *z* axis. Structure based on data from Hill, R.J., 1979, *Phys. Chem. Min.*, **5**, 179–200 (fig. produced by M.D. Welch). Green: Al–(O,OH) octahedra; mauve: hydrogen ions; broken red lines: hydrogen bonds.

Downloaded from https://pubs.geoscienceworld.org/books/chapter-pdf/3763392/9780903056434_ch88.pdf
by guest

Table 53. Structural relationships between analogous oxides of aluminium and iron.

Oxygens in h.c.p. arrangement	Oxygens in c.c.p. arrangement
α-AlO(OH) diaspore	γ-AlO(OH) boehmite
α-Al_2O_3 corundum	γ-Al_2O_3 γ-alumina
α-FeO(OH) goethite	γ-FeO(OH) lepidocrocite
α-Fe_2O_3 hematite	γ-Fe_2O_3 maghemite

Diaspore may be distinguished from corundum in grains or thin section by the higher refractive indices and lower birefringence of the latter, and from sillimanite which has lower refringence and birefringence.

The principal occurrences of diaspore are in bauxite and in emery deposits, but diaspore and boehmite occur also in fireclays. Hydrolysis of silicates in a tropical climate produces an alumina silica gel; after subsidence and burial, diaspore crystallizes from the gel and is followed by kaolinite. In emery deposits (e.g. at Chester, Massachusetts, USA) diaspore occurs as an intermediate stage in the formation of corundum by the metamorphism of bauxite deposits. Diaspore is frequently found as one of the products of hydrothermal alteration of aluminous minerals, e.g. sillimanite, kyanite, andalusite, pyrophyllite or corundum.

Further reading

Fockenberg, T., Wunder, B., Grevel, K.-D. and Burchard, M. (1996) The equilibrium diaspore–corundum at high pressures. *European Journal of Mineralogy*, **8**, 1293–1299.

Löffler, L. and Mader, W. (2001) Electron microscopic study of the dehydration of diaspore. *American Mineralogist*, **86**, 293–303.

Papezik, V.S. and Keats, H.F. (1976) Diaspore in pyrophyllite deposit on the Avalon Peninsula, Newfoundland. *The Canadian Mineralogist*, **14**, 442–449.

Perkins, V.S., Essene, E.J., Westrum, E.F and Wall, V.J. (1979) New thermodynamic data for diaspore and their application to the system Al_2O_3–SiO_2–H_2O. *American Mineralogist*, **64**, 1080–1090.

Downloaded from https://pubs.geoscienceworld.org/books/chapter-pdf/3763392/9780903056434_ch88.pdf
by guest

Orthorhombic (+)

α	1.64−1.65
β	1.65−1.66
γ	1.66−1.67
δ	0.015−0.020
$2V_\gamma$	74−88°
Orientation	α = *y* or *z*, β = *z* or *y*, γ = *x*; O.A.P. (001) or (010)
D (g/cm^3)	~3.05
H	3½−4
Cleavage	{010} very good, {100} good
Colour	White if pure; colourless in thin section
Unit cell	*a* 3.69 Å, *b* 12.23 Å, *c* 2.86 Å
	Z = 4, space group *Amam*

In the structure of boehmite (Fig. 282) double sheets of Al−(O,OH) octahedra form layers parallel to (010). The sheets consist of chains of octahedra, the repeat distance of which defines the *a* parameter of the unit cell. Hydroxyl anions occur at those corners of octahedra that are not shared with other octahedra. The double sheets of octahedra, between which there is hydrogen bonding, are stacked such that the unit cell contains two layers and has orthorhombic symmetry with four Al(OH)O in the unit cell.

In diaspore the oxygens are in a hexagonal close-packed layer; those within the double octahedral layers in boehmite are in a cubic packing relationship (Fig. 282). These differences in oxygen packing are consistent with the behaviour of the two polymorphs of AlO(OH) on dehydration in that diaspore yields α-alumina (trigonal) and boehmite yields γ-alumina which has the cubic structure of a spinel (see Table 53). Boehmite has a good cleavage on {010}, the plane defining structural layers of AlO(OH) octahedra.

Most specimens of boehmite, whether naturally occurring or synthetic, are made up of submicroscopic crystals, so that there is some uncertainty as to its optical properties: X-ray methods are usually necessary for a positive identification. Boehmite is a principal constituent of some bauxite deposits, in which it is sometimes found together with its dimorph, diaspore; it is also known as an alteration product in syenites. Bauxite clay deposits are the main source of aluminium metal; alumina is produced by calcination and the metal is recovered by an electrolytic process.

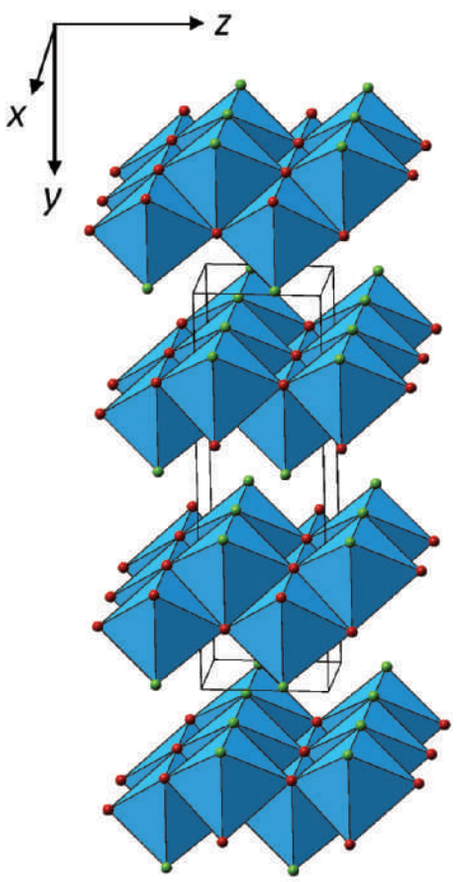


Fig. 282. Perspective view of the structure of boehmite showing (010) layers of Al−(O,OH) octahedra (blue) and outline of the unit cell. Structure based on data from Bokhimi, X. *et al.*, 2001, *J. Sol. State Chem.*, **159**, 32−40. Red: oxygen; green: (OH).

Downloaded from https://pubs.geoscienceworld.org/books/chapter-pdf/3763401/9780903056434_ch89.pdf
by guest

Further reading

Peryea, F.J. and Kittrick, J.A. (1988) Relative solubility of corundum, gibbsite, boehmite and diaspore at standard state conditions. *Clays and Clay Minerals*, **36**, 391–396.

Shelley, D., Smale, D. and Tulloch, A.J. (1977) Boehmite in syenite from New Zealand. *Mineralogical Magazine*, **41**, 398–400.

Tettenhorst, R. and Hofmann, D.A. (1980) Crystal chemistry of boehmite. *Clays and Clay Minerals*, **28**, 373–380.

Downloaded from https://pubs.geoscienceworld.org/books/chapter-pdf/3763401/9780903056434_ch89.pdf
by guest

The Fe oxyhydroxides

There are several Fe^{3+} oxyhydroxides which may occur in weathering conditions, including:

Goethite	**α-$Fe^{3+}OOH$**
Akaganéite	**β-$Fe^{3+}OOH$**
Lepidocrocite	**γ-$Fe^{3+}OOH$**
Feroxyhyte	**δ-$Fe^{3+}OOH$**
Ferrihydrite	**$Fe_2O_3 \cdot 2FeOOH \cdot 2.6H_2O$**

Only goethite, lepidocrocite and ferrihydrite are considered here, akaganéite and feroxyhyte being of less common occurrence. All five minerals are, however, being recognized as of importance in environmental studies. They are found particularly in mine wastes, where they occur typically as microscopic grains necessitating identification by skilled interpretation of X-ray diffraction, electron microscope and thermal or other spectral data. In rivers and estuaries draining such mine wastes, they may give a characteristic orange-red stain to the water, or stain the associated sediments (Fig. 283). Although considered originally to be a separate species, 'limonite' has been shown to consist mainly of cryptocrystalline goethite or lepidocrocite along with some adsorbed water; some hematite may also be present. The name limonite is now retained as a field term or to describe hydrated oxides of iron with poorly crystalline character whose real identity has not been determined.

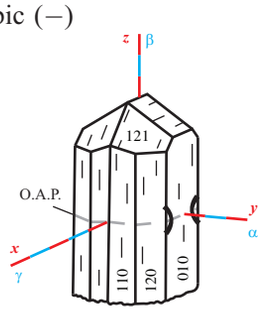
The iron oxyhydroxides are good examples of what are termed 'nano-minerals', i.e. minerals that mostly or exclusively occur as particles in the nanometre size range. Reviews of the nature and characteristics of nano-minerals are provided by Hochella (2008, *Elements*, **4**, 73–79).



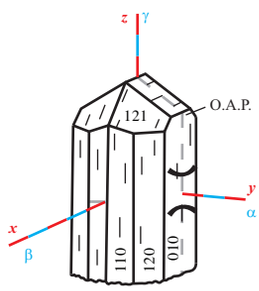
Fig. 283. Reddish orange discoloration of seawater due to acid mine drainage from a now abandoned tin mine, southwest Cornwall (photograph, 1968, courtesy of R.M.F. Preston).

Downloaded from https://pubs.geoscienceworld.org/books/chapter-pdf/3763427/9780903056434_ch90.pdf
by guest

Orthorhombic (−)



For yellow, green or blue light



For red light

α	2.260−2.275
β	2.393−2.409
γ	2.398−2.515
δ	0.138−0.140
$2V_\alpha$	0−27°

Orientation	O.A.P. (100) for red light, (001) for green light; Bx_a always ⊥ (010)
D (g/cm^3)	~4.3
H	5−5½
Cleavage	{010} perfect {100} moderate
Colour	Yellowish brown to red; yellow to orange-red in thin section; in reflected light, grey with moderate anisotropy; yellow streak
Pleochroism	Variable, in yellow and orange, absorption α > γ > β
Unit cell	*a* 4.59 Å, *b* 9.94 Å, *c* 3.02 Å Z = 4; space group *Pbnm*
Special features	Soluble in HCl. Dehydrates to α-Fe_2O_3. Well crystallized material may show extreme dispersion.

Goethite is a very common weathering product of iron-bearing minerals such as siderite, magnetite and pyrite. It is formed typically in oxidizing conditions, and as a direct precipitate in bogs. It may form prismatic or tabular crystals but occurs more usually as acicular sprays, or as botryoidal or stalactitic masses. It includes much material that is commonly described as limonite.

The structure of goethite is similar to that of diaspore (α-AlO.OH), the unit cell containing 4(FeO.OH). It consists essentially of layers of oxygen ions in the sequence of hexagonal close packing, with the iron ions in the octahedral interstices.

The commonest substituent ion is aluminium, with Al^{3+} replacing up to a third of the Fe^{3+} ions in some samples; Mn^{3+} may also be present, groutite (α-$Mn^{3+}O.OH$) being isostructural with goethite. The SiO_2 reported in some analyses is probably present as an impurity. The goethite–water $^{18}O/^{16}O$ fractionation factor varies with temperature. Goethite can be prepared artificially by oxidizing solutions of ferrous compounds and by slow hydrolysis of ferric salts such as $Fe(NO_3)_3$.

The optic axial angle varies both with the wavelength and with the temperature, goethite being uniaxially negative at normal temperatures for wavelengths between 610 and 620 nm. It often occurs in fibrous varieties which may show anomalous optical effects. A determination by XRD is recommended for identification.

Goethite differs from hematite in having a yellow streak. In general it is a strong yellowish brown in

Downloaded from https://pubs.geoscienceworld.org/books/chapter-pdf/3763460/9780903056434_ch91.pdf
by guest

colour whereas lepidocrocite is a moderate shade of orange. On dehydration it alters to hematite (α-Fe_2O_3), whereas lepidocrocite alters to maghemite (γ-Fe_2O_3).

Goethite commonly occurs as a weathering product of iron-bearing minerals such as siderite, magnetite and pyrite. It is normally formed under oxidizing conditions, and includes much material hitherto classed as limonite. Laterite contains goethite in addition to hematite and the mineral is also found as the pigment in yellow ochre. It accumulates as a direct precipitate from both marine and meteoric waters and occurs in bogs and springs. In some sedimentary iron ores of economic importance it may be the principal constituent, as in the Lorraine basin of France and in the Clinton ores of the eastern USA. Goethite is a very common mineral in soils, and poorly crystalline goethite occurs in acid mine drainage, commonly as an alteration product of ferrihydrite. The solid solution of α-AlO.OH in goethite increases the thermodynamic stability of goethite with respect to hematite and thus even very fine-grained but Al-bearing goethite particles in a soil may be thermodynamically stable.

Further reading

Alvarez, M., Ruedo, E.H. and Sileo, E.E. (2007) Simultaneous incorporation of Mn and Al in the goethite structure. *Geochimica et Cosmochimica Acta*, **71**, 1009–1020.

Cornell, R.M. and Schwertmann, U. (2003) *The Iron Oxides: Structure, Properties, Reactions, Occurrences and Uses*. 2nd Edition, Wiley–VCH Verlag, Weinheim, 703 pp.

Davidson, L.E., Shaw, S. and Benning, L.G. (2008) The kinetics and mechanism of schwertmannite transformation to goethite and hematite under alkaline conditions. *American Mineralogist*, **93**, 1326–1337.

Goss, C.J. (1987) The kinetics and reaction mechanism of the goethite to hematite transformation. *Mineralogical Magazine*, **51**, 437–451.

Kampf, N. and Schwertmann, U. (1982) Quantitative determination of goethite and hematite in kaolinitic soils by X-ray diffraction. *Clay Minerals*, **17**, 359–363.

Scheinost, A.C. and Schwertmann, U. (1999) Color identification of iron oxides and hydroxysulfates: use and limitations. *Soil Science Society of America Journal*, **63**, 1463–1471.

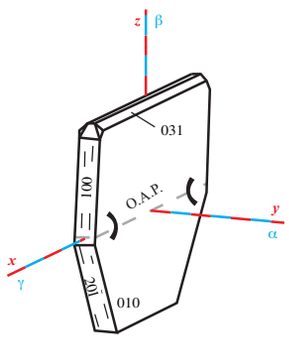
Singh, B., Wilson, M.J., McHardy, W.J., Fraser, A.R. and Merrington, G. (1999) Mineralogy and chemistry of ochre sediments from an acid mine drainage near a disused mine in Cornwall, UK. *Clay Minerals*, **34**, 301–317.

Yapp, C.J. (1987) Oxygen and hydrogen isotope variations among goethite (α-FeOOH) and the determination of paleotemperatures. *Geochimica et Cosmochimica Acta*, **51**, 355–364.

Downloaded from https://pubs.geoscienceworld.org/books/chapter-pdf/3763460/9780903056434_ch91.pdf
by guest

Orthorhombic (−)

γ-FeO.OH



α	1.94
β	2.20
γ	2.51
δ	0.57
$2V_\alpha$	83°
Orientation	α = *y*, β = *z*, γ = *x*; O.A.P. (001)
D (g/cm^3)	4.09
H	5
Cleavage	{010} perfect {100} and {001} moderate
Colour	Brownish to red; yellow to orange and red in thin section; in reflected light, greyish white with strong anisotropy; orange streak
Pleochroism	Strong, absorption α < β < γ, light yellow to orange-red
Unit cell	*a* 3.87 Å, *b* 12.53 Å, *c* 3.06 Å Z = 4; space group *Amam.*
Special features	Soluble in HCl. Dehydrates to γ-Fe_2O_3

Lepidocrocite is much less common than goethite, but the paragenesis is similar, both occurring in oxidized weathering products of iron-bearing minerals.

The structure of lepidocrocite consists of iron-centred oxygen octahedra linked in double chains by sharing diagonally opposite edges, the chains running parallel to the *z* axis. The sheets are held together by hydrogen bonds, their weakness being responsible for the perfect {010} cleavage. Lepidocrocite is isostructural with boehmite, γ-AlO(OH).

Lepidocrocite is dimorphous with goethite and, as for the latter, the traces of SiO_2 reported in analyses are due to impurities: some Mn^{3+} may replace Fe^{3+}. It can be prepared artificially by the slow oxidation of dilute solutions of $FeCl_2$ with NaOH at pH 7.

It is strongly pleochroic from yellow to orange-red and differs from goethite in having a larger 2V, smaller dispersion, and maximum absorption parallel to the length of the fibres. Dehydration gives γ-Fe_2O_3, maghemite, which is ferrimagnetic, whereas goethite yields antiferromagnetic α-Fe_2O_3, hematite.

Like goethite, lepidocrocite crystallizes in oxidizing conditions as a weathering product of iron-bearing minerals in soils and mineral deposits; it is also commonly found as a precipitate from groundwater and may occur intermingled with goethite. Lepidocrocite is red in thin platelets, hence the colloquial German name "Rubinglimmer" (ruby mica), and bright orange in fine particles. Goethite, which is much more common and brown, is the pigment in brown ochre.

Further reading

Carlson, L. and Schwertmann, U. (1990) The effect of CO_2 and oxidation rate on the formation of goethite versus lepidocrocite from an Fe(II) system at pH 6 and 7. *Clay Minerals*, **25**, 65−71.

Pedresen, H.D., Postma, D., Jakobsen, R. and Larsen, O. (2005) Fast transformation of iron oxyhydroxides by the catalytic reaction of aqueous Fe(II). *Geochimica et Cosmochimica Acta*, **69**, 3967−3977.

Schwertmann, U. and Fechter, H. (1994) The formation of green rust and its transformation to lepidocrocite. *Clay Minerals*, **29**, 87−92.

Schwertmann, U. and Taylor, R.M. (1972) The transformation of lepidocrocite to goethite. *Clays and Clay Minerals*, **20**, 151−158.

Smeck, N.E., Bigham, J.M., Guertal, W.F. and Hall, G.F. (2002) Spatial distribution of lepidocrocite in a soil hydrosequence. *Clay Minerals*, **37**, 687−697.

Downloaded from https://pubs.geoscienceworld.org/books/chapter-pdf/3763474/9780903056434_ch92.pdf
by guest

Ferrihydrite $Fe_2O_3 \cdot 2FeOOH \cdot 2.6H_2O$

Hexagonal

D (g/cm^3)	3.96 (synthetic)
H	Soft
Colour	Yellow, brown, ochre to dark brown.
Unit cell	*a* 5.12 Å or 2.96 Å, *c* 9.4 Å
	Space group *P*31*c*
Special features	Highly soluble in ammonium oxalate solution

Ferrihydrite is of widespread occurrence in the relatively soluble fraction of soils and weathered rocks. It is also found in lake and river waters, in acid mine drainage waters, and around both hot and cold springs.

Most investigations of the crystal structure of ferrihydrite have been on synthetic material. The details of the X-ray powder diffraction patterns depend on the size of the crystallites; this has led to an empirical nomenclature using the terms two-line or six-line ferrihydrite, where these numbers refer to the number of peaks in the pattern between 2.56 and 1.58 Å. Drits *et al.* (1993) concluded that the main structural differences between 2- and 6-line ferrihydrite lies in the size of their coherent scattering domains which is extremely small for the 2-line structure. Natural poorly crystalline ferrihydrite commonly contains appreciable Si or C.

Experimentally, ferrihydrite is readily produced by the hydrolysis of ferric salts. It transforms to hematite or goethite with ageing.

The nanocrystalline nature of ferrihydrite (e.g. as poorly crystalline spheres ~10 nm in diameter) has precluded any detailed optical investigations; it is fairly soft and yellowish brown in colour; DTA curves show an endothermic peak near 180ºC and an exothermic reaction at around 350–400ºC. The high solubility in acid ammonium oxalate solution in the dark allows it to be differentiated from most other iron oxides.

Ferrihydrite is of widespread occurrence in the soluble fraction of soils and weathered rocks. For example, the fresh ochreous sediments from near the disused West Chiverton Pb-Cu-Zn mine, Cornwall, consist of ferrihydrite and goethite. In soils formed on fluvial deposits ferrihydrite may be initially abundant, but the proportion decreases progressively in older soils due to its transformation to hematite, accompanied by a change in colour from yellow or brown to red.

Further reading

Childs, C.W. (1992) Ferrihydrite: A review of structure, properties and occurrence in relation to soils. *Journal of Plant Nutrition and Soil Science*, **155**, 441–448.

Drits, V.A., Sakharov, B.A., Salyn, A.I. and Manceau, A. (1993) Structural models for ferrihydrite. *Clay Minerals*, **28**, 185–207.

Karim, Z. (1984) Characteristics of ferrihydrites formed by oxidation of $FeCl_2$ solutions containing different amounts of silica. *Clays and Clay Minerals*, **32**, 181–184.

Michel, F.M., Ehm, L., Antao, S.M., Lee, P.L., Chupas, P.J., Liu, G., Strongin, D.R., Schoonen, M.A.A., Phillips, B.L. and Parise, J.B. (2007) The structure of ferrihydrite, a nanocrystalline material. *Science*, **316**, 1726–1729.

Rancourt, D.J. and Meunier, J.-F. (2008) Constraints on structural models of ferrihydrite as a nanocrystalline material. *American Mineralogist*, **93**, 1412–1417.

Singh, H.B., Wilson, M.J., McHardy, W.J., Fraser, A.R. and Merrington, G. (1999) Mineralogy and chemistry of ochre sediments from an acid mine drainage near a disused mine in Cornwall, UK. *Clay Minerals*, **34**, 301–317.

Downloaded from https://pubs.geoscienceworld.org/books/chapter-pdf/3763499/9780903056434_ch93.pdf
by guest

Sulphides

Economics, the Environment (and the Origin of Life?)

Metal sulphides are a highly important group of minerals as they are the major source of most of the world's non-ferrous metals, occurring in large concentrated orebodies, and also as minor, but significant, accessory minerals in a wide variety of rocks, some of which are also important sulphide ore deposits.

Metal sulphide minerals are also much studied because of the processes of 'Acid Rock Drainage' (ARD) and 'Acid Mine Drainage' (AMD), by which their acidifying reaction with natural waters can damage or destroy vegetation, fish and other aquatic forms of life. Such acid waters may also increase the dissolution of minerals containing potentially toxic elements (e.g. arsenic, lead, cadmium and mercury) which may also cause environmental damage and, if affecting the water supply, can constitute a serious hazard to human health. Much research is therefore aimed at elucidating the mechanisms of sulphide mineral–fluid interaction.

Research on sulphide minerals has also been stimulated by the discovery of active hydrothermal systems in the deep oceans. Forms of life have been found there which have chemical rather than photosynthetic metabolisms and occur in association with newly forming sulphides, and it has been suggested that the sulphide surfaces catalyse reactions leading to the formation of complex molecules which are the precursors of life on Earth.

Downloaded from https://pubs.geoscienceworld.org/books/chapter-pdf/3763505/9780903056434_ch94.pdf
by guest

Pyrite FeS_2

Cubic

D (g/cm^3)	4.95–5.02
H	6–6½; VHN_{100} 1505–1620
R % (589 nm)	53.5 (in air), 40.5 (in oil)
Cleavage	{001} poor
Twinning	Interpenetrant on {011} with twin axis [001]
Colour	Pale brassy yellow; black when fine grained; metallic lustre and greenish or brownish black streak; iridescent tarnish; opaque even in thinnest sections; yellowish white in polished section
Unit cell	*a* 5.418 Å Z = 4; space group $Pa\bar{3}$
Special features	Insoluble in HCl; powder soluble in strong HNO_3

Pyrite is the most abundant of all sulphide minerals. It is a common accessory mineral in igneous, metamorphic and sedimentary rocks and occurs as a major phase in many sulphide orebodies. It is mined from some deposits mainly for the production of sulphuric acid. Marcasite is the orthorhombic dimorph of pyrite. Pyrite may contain Ni,Co or, more rarely, Cu replacing Fe. Pyrite, marcasite, arsenopyrite (FeAsS) and löllingite ($FeAs_2$) belong to a family of structurally related minerals characterized by the presence of the di-anion groups. The term 'iron pyrites' has been used in reference to both pyrite and marcasite.

Structure

Pyrite is cubic with unit-cell edge *a* ~ 5.42 Å; Fe atoms are at the corners and face centres of the cube, and S atoms are arranged in 'dumb-bell' pairs centred at the mid-points of the cube edges and at the cube's body centre (Fig. 284a). The four S–S joins are respectively parallel to four non-intersecting body diagonal directions. Each iron atom is surrounded by six sulphur atoms at the corners of an octahedron (Fig. 284b), and each sulphur atom is equidistant from three iron atoms which form a triangular planar group to one side of it. If the mid-points of sulphur pairs are considered, these are in the arrangement of cubic close packing, and an Fe atom lies in each of the octahedral interstitial sites. Compared with many other sulphides the structure of pyrite is very densely packed. Both NiS_2 (vaesite, *a* 5.679 Å) and CoS_2 (cattierite, *a* 5.535 Å) possess the pyrite structure, and the substitution of Fe by Ni or Co in pyrite increases the length of the cell edge.

The mineral marcasite is dimorphous with pyrite. It is orthorhombic with *a* ~ 4.44 Å, *b* ~ 5.41 Å, *c* ~ 3.38 Å, Z = 2, space group *Pmnn*. As in pyrite, iron is octahedrally coordinated by sulphur, but the sulphur pairs are in layers with hexagonal rather than cubic stacking and the octahedra share edges rather than corners. The structure of marcasite projected on (101) is similar to that of pyrite on (100): $a_{pyrite} \sim b_{marcasite}$ and a_{pyrite} is approximately equal to the $a-c$ diagonal of the marcasite cell; intergrowths are formed with these faces in common.

Chemistry

Pyrite with small amounts of Ni and Co substituting for Fe are not uncommon; specimens with larger contents of these two elements are comparatively rare and have been described as bravoite. Minor amounts of other substituents for Fe can be present in solid solution in pyrite, including Ag, Au, Bi, Cu, Pb, Ti, V and Zn. Hauerite, MnS_2, is isostructural with pyrite, but there is only very little replacement of Fe by Mn in pyrite.

There does not appear to be extensive anion substitution in the structure of pyrite, but the highly poisonous element arsenic is found in appreciable quantities, and this can lead to a serious environmental hazard when run-off waters from metalliferous mine wastes may contaminate drinking water supplies. There is also interest in arsenian pyrite because it can also

Downloaded from https://pubs.geoscienceworld.org/books/chapter-pdf/3763526/9780903056434_ch95.pdf
by guest

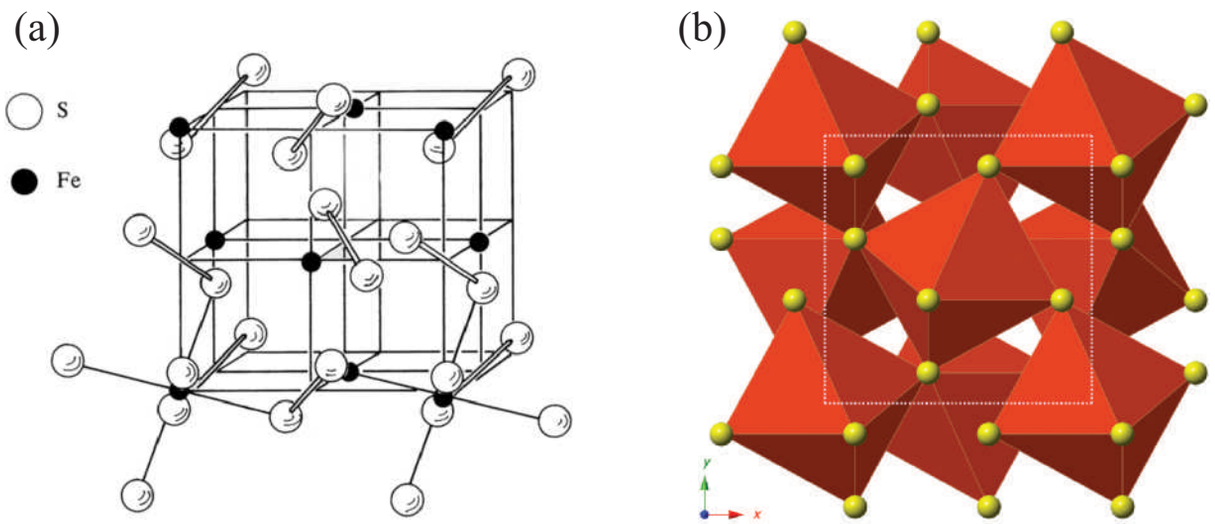


Fig. 284. (a) The structure of pyrite (after Vaughan, D.J. & Craig, J.R., 1978, *Mineral Chemistry of Metal Sulfides*, Cambridge University Press). (b) Polyhedral representation of the structure of pyrite showing the stacking of Fe–S octahedra. Brown: Fe–S octahedra; yellow: sulphur atoms (CrystalMaker image).

contain gold either as a coupled substitution with arsenic, or as separate nano-particles.

Pyrite can be synthesized in various ways, e.g. by heating powdered iron and sulphur in the correct proportions *in vacuo*. In most of the wet chemical methods of preparation (e.g. from sulphur and ferrous sulphide, H_2S on ferric sulphate or ferric chloride), weakly acid, neutral or alkaline conditions favour the formation of pyrite, whereas in strongly acid conditions (and generally at lower temperatures) marcasite is formed.

It may be that marcasite formation is favoured by the greater availability in acid conditions of elemental sulphur as opposed to polysulphide ions. Another explanation is in terms of the interaction of S_2^{2-} and H^+ ions in solution and the difference in chemical bonding between pyrite and marcasite.

In the Fe–S system the pyrrhotite in equilibrium with pyrite above 400ºC shows increasing iron deficiency with increasing temperature, whereas the pyrite composition remains constant. This relationship is illustrated in Fig. 285, and has been used as a geological thermometer for natural pyrite–pyrrhotite equilibrium assemblages. This geothermometer is however only valid for conditions of rapid quenching since re-equilibration of the pyrrhotite composition continues down to much lower temperatures (see p. 430). The Fe/S ratio of a pyrrhotite may be estimated by an X-ray powder method.

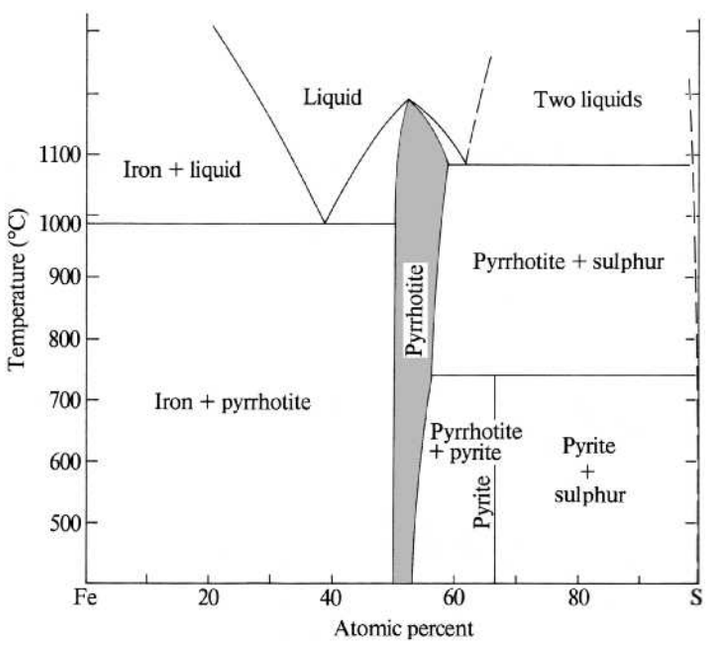


Fig. 285. Phase relations among condensed phases in the Fe–S system above 400ºC (after Kullereud, G. & Yoder, H.S., 1959, *Econ. Geol.*, **54**, 533–72; Arnold, R.G., 1971, *Econ. Geol.*, **66**, 1121–30).

Downloaded from https://pubs.geoscienceworld.org/books/chapter-pdf/3763526/9780903056434_ch95.pdf
by guest

Pyrite melts incongruently to pyrrhotite and liquid sulphur at 742ºC.

Other systems involving pyrite which have been investigated include Cu–Fe–S, Fe–Zn–S, Fe–As–S, Fe–Ni–S and Fe–S–O. The As content of arsenopyrite, in conjunction with Fe in sphalerite, can be used as a geothermometer.

Laboratory experiments show that there is complete solid solution between FeS_2 and CoS_2 above 600ºC but a large miscibility gap between FeS_2 and NiS_2 at this temperature. Naturally occurring phases do, however, cover the whole range of compositions and some are presumably therefore metastable. In coexisting pyrite–pyrrhotite there is a preference for Co over Ni in the pyrite and Ni over Co in the pyrrhotite.

The stability of pyrite in aqueous solutions is of interest since much pyrite is found in sedimentary or hydrothermal environments. For the system Fe–S–O–H several variables including Eh, pH, P_{S_2}, P_{O_2}, affect the stability fields of pyrite, pyrrhotite and iron oxides. At a sulphur activity of 10^{-1} the field for pyrite is large and for pyrrhotite very small. Under more oxidizing conditions hematite is the principal iron mineral. With lower sulphur activity the pyrite field is reduced and magnetite increased. Because of the limited variation of pH, particularly in marine environments, the P_{S_2}, and Eh are of greater importance. The relationships are shown in Fig. 286. Again pyrite predominates over pyrrhotite and iron oxide forms only if the sulphur activity is very low. The more common occurrence of pyrite rather than pyrrhotite in sedimentary rocks is in accord with these experimental results but in addition to the above physical parameters metastable phases such as marcasite, mackinawite ($Fe_{1+x}S$) and greigite (Fe_3S_4) may play an important role as precursors for the formation of pyrite.

The solubility of pyrite in pure water even at moderately high temperatures is negligible, so the formation of complexes, e.g. chlorides, is involved in the processes of solution and transport for hydrothermal ore formation.

Alteration of pyrite usually proceeds by oxidation to sulphates and eventually to iron hydroxides and oxyhydroxides. Among the common minerals which form as pseudomorphs after pyrite are hematite, goethite and graphite.

Optical and physical properties

The reflectance of pyrite is 53.5% (589 nm). Although pyrite is cubic it almost invariably exhibits some anisotropy; among the possible reasons for this are arsenic or nickel impurity, a surface film of marcasite, variation in Fe/S ratio, internal strain, an oxidation layer, or surface strain due to the specimen polishing process. It has also been suggested that the anisotropy of pyrite is related to the low symmetry (class 23) of its crystal structure.

One crystal habit adopted by pyrite is the pentagonal dodecahedron (pyritohedron), but cubes and octahedra also commonly occur. Crystal faces are sometimes striated due to the alternate development of two forms in one crystal, e.g. {100} and {210}, with one predominating. The directions of striations on different faces betray the hemihedral symmetry of the crystal class even in the cube. Interpenetration twins sometimes occur with the shape of a cross, the 'iron cross' twin. Although well formed crystals are not uncommon, much pyrite occurs in massive aggregates, in radiating clusters and in reniform, globular, granular and stalactitic formations. Pyrite commonly occurs in spheroidal aggregates (framboidal texture); early studies, and some recent, associated their formation with microorganisms, but they have been produced experimentally by inorganic processes. The electrical properties of pyrite have aroused interest because of its possible use in solar cells A fine-grained black amorphous, or cryptocrystalline, material of colloidal origin and with the composition of pyrite has been called melnikovite (melnikovite pyrite).

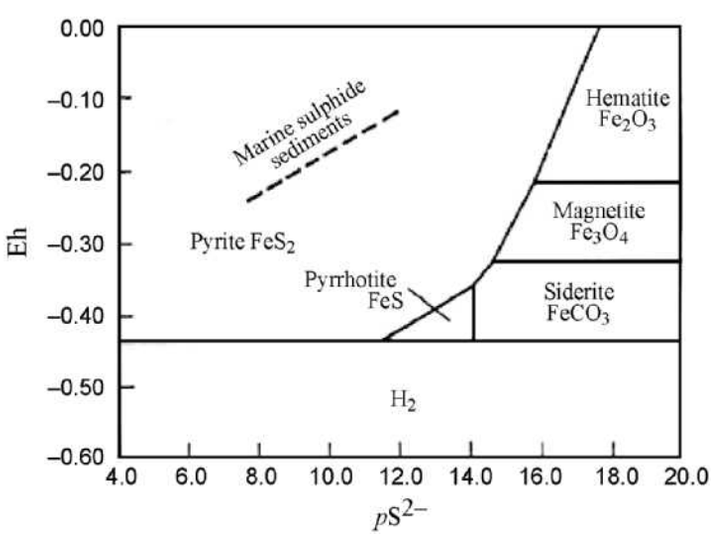


Fig. 286. Plot of Eh against pS^{2-} for pyrite, pyrrhotite, hematite, magnetite and siderite at 25ºC and at atmospheric pressure (0.1 MPa) and with pH = 7.37, log pCO_2 = 2.4 (after Berner, R.A., 1971, *Principles of Chemical Sedimentology*. McGraw Hill, New York).

Downloaded from https://pubs.geoscienceworld.org/books/chapter-pdf/3763526/9780903056434_ch95.pdf
by guest

Marcasite, in appearance, can be very much like pyrite; it may have a tabular or pyramidal habit but it is more usually found in radiating fibrous masses. Its density is 4.89 g/cm^3, hardness 6–6½, and it is optically strongly anisotropic.

Distinguishing features

Pyrite can be recognized in hand specimen by its metallic lustre and pale brassy yellow colour. Chalcopyrite has a deeper yellow colour and pyrrhotite is bronze-coloured in comparison. Pyrite is much harder than either of these and is harder than most other opaque minerals, although the related phases marcasite and arsenopyrite are also very hard; arsenopyrite has a more silvery appearance than pyrite. Pyrite often occurs as well developed cubes, octahedra or pyritohedra; marcasite may occur as tabular or prismatic crystals, cockscomb aggregates and arrowhead twins of stalactitic, concentric and radiating forms. Both pyrite and marcasite may occur as massive or granular material, and in these cases the distinction between them can be made only in polished section or by X-ray diffraction.

In polished section, pyrite is recognized by its reflectance, yellowish white colour and isotropy. It is also very hard and generally polishes well. Marcasite and arsenopyrite, although similar in reflectance, are both distinctly anisotropic.

Paragenesis

Pyrite is the most abundant of the sulphide minerals and is very widespread. It occurs in large masses or veins of hydrothermal origin both as a primary and secondary mineral, in igneous rocks and in sedimentary (principally argillaceous and carbonaceous) rocks.

In ultramafic and mafic intrusive rocks, such as those of Skaergaard (Greenland), Stillwater (Montana), and Sudbury (Ontario), pyrite is generally common though less abundant than pyrrhotite. This and other sulphides occur as a result of the immiscibility of sulphur-rich and silica-rich melts.

Pyrite is the main iron sulphide in porphyry copper deposits, occurring as disseminated grains and veinlets in intrusions varying from quartz-diorite to quartz-monzonite (e.g. Bingham, Utah; Butte, Montana). It occurs as an accessory in a wide range of felsic igneous rocks, and as a skarn mineral. Pyrite is a major phase in most hydrothermal vein deposits, many of which are associated with (commonly felsic) intrusive rocks. It is the major ore mineral of volcanogenic and volcano-sedimentary deposits, of the Kuroko, Besshi and Troodos types, and is predominant among the massive stratiform sulphide ores (e.g. the Kupferschiefer, northern Europe, and the Copper Belt, Zambia and Congo), in which pyrite occurs disseminated in black shales or in carbonate rocks. The range of sedimentary occurrences is wide, pyrite accompanying for example the lead-zinc-baryte-fluorite associations in limestones, U-V-Cu minerals in sandstones and Au-U minerals in iron ores.

In sediments, pyrite and glauconite are commonly found together. They form diagenetically in muds on the sea floor, usually in shallow water and under reducing conditions. Poorly crystallized forms of pyrite are more generally found in sedimentary and in low-temperature hydrothermal deposits. Raspberry-like aggregates of tiny spherical particles of pyrite are referred to as 'framboidal'. Pyrite is the major opaque mineral to be found in coals. The formation of iron sulphides in sediments is an example of biologically induced mineralization; its rate of formation depends primarily on the rate of microbial sulphate reduction. The role of microbes is equally important in sulphide dissolution, which is catalysed by Fe- and S-oxidizing bacteria such as *Acidithioibacillus ferrooxidans*.

As the dominant sulphide mineral in metalliferous ores and in coals, pyrite is also the most abundant sulphide in many mine wastes. It is highly reactive when exposed to air and water, and is the main cause of the type of pollution termed 'acid mine drainage', where it leads to the development of distinct generations of fine-grained iron oxyhydroxides (akaganéite, feroxyhyte, ferrihydrite) as well as goethite and lepidocrocite (see p. 420). A particular hazard is the presence of arsenian pyrite in some mine wastes and its effect on run-off waters.

Ideas have been developed recently giving a key role to sulphides, including pyrite, in some theories on the origin of life. It has been suggested that sulphide minerals could have catalysed the production of the first biomolecules. The formation of pyrite could have provided the energy source for the first organism, reducing CO_2 in the process, and resulting in organic molecules:

$$CO_2(aq) + FeS + H_2S \rightarrow HCOOH + FeS_2 + H_2O.$$

In an alternative scenario, it has been suggested that life started at a redox and pH front at hot vents on the deep seafloor, where acidic, warm (~90ºC) water of the early ocean merged with reduced, alkaline, disulphide-bearing, hot (~150ºC) water from diffuse submarine vents, to give colloidal FeS.

Among the minerals after which pseudomorphs of pyrite have been found are pyrrhotite, hematite, chalcopyrite, arsenopyrite, marcasite, fluorite, calcite and baryte. Marcasite does not occur as a magmatic mineral: it is formed only in sediments or in metalliferous veins, usually in conditions of low temperature. It has been suggested that whereas marcasite forms in aqueous solution by slow reaction between elemental sulphur and a pre-existing sulphide, pyrite forms from Fe^{2+} or highly reactive FeS clusters and polysulphide ions or H_2S. It may be that Fe-chloride

Downloaded from https://pubs.geoscienceworld.org/books/chapter-pdf/3763526/9780903056434_ch95.pdf
by guest

also plays a part in forming some pyrite-rich ore deposits.

The ratio of sulphur isotopes $^{32}S/^{34}S$ in pyrite has been used alone or along with ratios in other coexisting sulphides to deduce temperatures of formation. Bacterial reduction of sulphates enriches the ^{32}S isotope; high ratios are therefore taken as indicating that the sulphur has passed through sedimentary conditions. The isotope ratio can, however, also be influenced by pH and f_{O_2}.

Further reading

Abraitis, P.K., Pattrick, R.A.D. and Vaughan, D.J. (2004) Variations in the compositional, textural and electrical properties of natural pyrite: a review. *International Journal of Mineral Processing*, **74**, 41–59.

Al, T.A.., Blowes, D.W., Martin, C.J., Cabri, L.J. and Jambor, J.L. (1997) Aqueous geochemistry and analysis of pyrite surfaces in sulfide-rich mine tailings. *Geochimica et Cosmochimica Acta*, **61**, 2353–2366.

Bowles, J.F.W., Howie, R.A., Vaughan, D.J. and Zussman, J. (2011) *Rock-forming Minerals. Non-silicates: Oxides, Hydroxides and Sulphides*, **5A**. 920 pp. Geological Society, London.

Cody, D.G. (2005) Geochemical connections to primitive metabolism. *Elements*, **1**, 139–143.

Hazen, R.M. (2005) Genesis, rocks, minerals, and the geochemical origin of Life. *Elements*, **1**, 135–137.

Paktunc, A.D. and Davé, N.K. (2002) Formation of secondary pyrite and carbonate minerals in the lower Williams Lake tailings basin, Elliot Lake, Ontario, Canada. *American Mineralogist*, **87**, 593–602.

Posfai, M. and Dunin-Borkowski, R. (2006) Sulfides in biosystems. Pp. 679–714 in: *Sulfide Mineralogy and Geochemistry* (D.J. Vaughan, editor), Reviews in Mineralogy and Geochemistry, **61**, Mineralogical Society of America & Geochemical Society, Washington, D.C.

Vaughan, D.J. (Editor) (2006) *Sulfide Mineralogy and Geochemistry*. Reviews in Mineralogy and Geochemistry, Mineralogical Society of America & Geochemical Society, **61**, Mineralogical Society of America & Geochemical Society, Washington, D.C., 714 pp.

Downloaded from https://pubs.geoscienceworld.org/books/chapter-pdf/3763526/9780903056434_ch95.pdf
by guest

Pyrrhotite ~Fe_7S_8–FeS (troilite)

Monoclinic (Pseudohexagonal)–Hexagonal

D (g/cm^3)	4.6–4.9
H	3½–4½; VHN_{100} monoclinic 258–378, hexagonal 230–318, troilite 250
R % (589 nm)	monoclinic (in air) 38.6–43.4, (in oil) 25.7–30.1 hexagonal (in air) 38.6–42.0, troilite (in air) 36.2–40.5
Cleavage	none; distinct {0001} parting
Twinning	on $\{10\bar{1}2\}$
Colour	bronze-yellow to brownish or reddish with a metallic lustre; opaque even in thinnest sections; creamy brown, reddish brown in polished sections
Unit cell	monoclinic pyrrhotite *a* 11.90 Å, *b* 6.86 Å, *c* 22.79 Å, β 90.4º Z = 8 (Fe_7S_8); space group *F*2/*d* troilite *a* 5.97 Å, *c* 11.76 Å Z = 12 (FeS); space group $P\bar{6}2c$
Special features	Soluble in HCl. Monoclinic forms are slightly magnetic

The name pyrrhotite is applied to iron sulphides which are closely related compositionally and structurally. The compositions lie within the range $Fe_{1-x}S$ where $0 < x < 0.125$ and the structures are all based on that of NiAs (niccolite). Stoichiometric FeS, which has a hexagonal structure that is a distortion of the NiAs-type, is a distinct species, *troilite*. The composition Fe_7S_8 has a monoclinic structure and some distinctive properties that enable it to be distinguished as *monoclinic pyrrhotite*. As well as the vacancy ordering pattern which produces the monoclinic superstructure with composition Fe_7S_8, other ordered vacancies occur at less metal-deficient compositions; the overall symmetry of these phases is commonly hexagonal, and they are sometimes described using the general term *hexagonal pyrrhotite*.

Structure

The pyrrhotites have crystal structures based on the NiAs-type structure in which metals occur in octahedral coordination and anions in trigonal prismatic coordination as shown in Fig. 287a. The metals and anions occur in layers parallel to the basal plane and the metal–anion octahedra share faces along the *z* axis (Fig. 287b). This structure is rarely retained at low temperatures, where superstructures and distorted structures are found.

Stoichiometric FeS (troilite) has a NiAs-type derivative structure which is stable at room temperature. This structure is a distorted form such that the unit cell is related to the simple NiAs structure by $a \sim A\sqrt{3}$ and $c \sim 2C$ where *A* and *C* represent the *a* and *c* parameters of the simple NiAs-type cell.

An important feature of the NiAs structure is its ability to omit metal atoms, leaving holes or vacancies. In the pyrrhotites, up to approximately one-eighth of the iron atoms can be omitted, giving rise to an omission solid solution series (Fig. 288). At > ~350ºC, the vacancies are randomly distributed and solid solution is complete; at lower temperatures ordering of vacancies occurs, resulting in various superstructures, such as that of monoclinic pyrrhotite (Fe_7S_8), in which the vacancies are found in alternate layers of iron atoms parallel to the basal plane, and in alternate rows within these layers.

Chemistry

Small amounts of Ni, Co, Mn and Cu can substitute for Fe in pyrrhotite, but in many specimens these elements are probably present in impurities, e.g. as Ni and Co in pentlandite $(Fe,Ni)_9S_8$, and Cu in chalcopyrite.

Most analyses of natural pyrrhotites show a deficiency of iron below that required for the stoichiometric formula FeS. If the formula is written

Downloaded from https://pubs.geoscienceworld.org/books/chapter-pdf/3763567/9780903056434_ch96.pdf
by guest

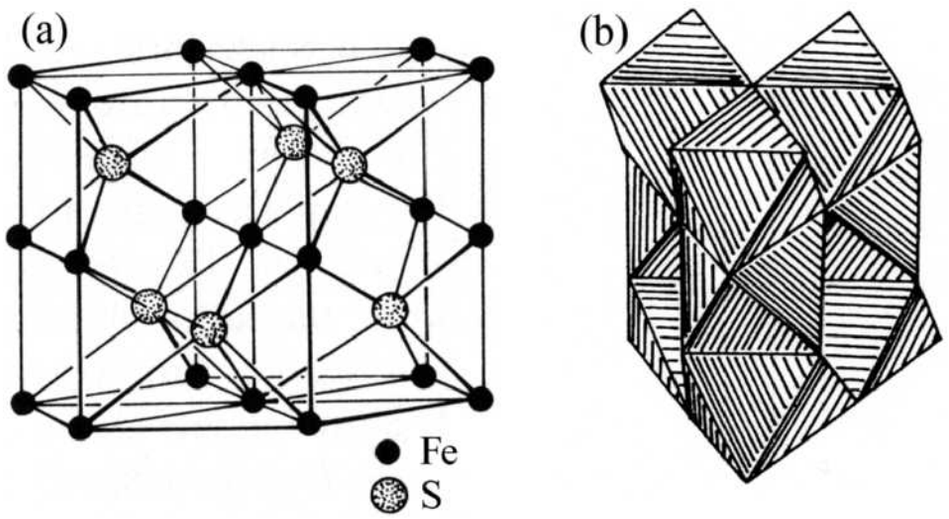


Fig. 287. Idealized structure of pyrrhotite (NiAs type) (a) showing linkages between Fe and S atoms in a unit cell and (b) stacking of octahedral units (after Vaughan, D.J. & Craig, J.R., 1978, *Mineral Chemistry of Metal Sulfides*, Cambridge University Press).

$Fe_{1-x}S$, the range of pyrrhotite compositions is such that x varies from zero to about 0.125. Pyrrhotite has been synthesized by the direct combination of iron and sulphur, and by heating pyrite in an atmosphere of H_2S at 550ºC.

In the Fe–S system the pyrrhotite in equilibrium with pyrite above 400ºC shows increasing iron deficit with increasing temperature. This relationship is illustrated in Fig. 285, p. 425, and can be used as a geothermometer but only in conditions of very rapid cooling, otherwise the pyrrhotite composition continues to change at lower temperatures. At lower temperatures, phase relations are extremely complex because of the many hexagonal and monoclinic structural variants of pyrrhotite. In the system Fe–Zn–S there can be considerable replacement of Fe for Zn in sphalerite but little or no solid solution of Zn in pyrrhotite. Other systems studied in the laboratory include Fe–S–O, Fe–S–Se, Cu–Fe–S, Fe–Ni–S and Fe–As–S.

Natural alteration products of pyrrhotite include pyrite, marcasite and other sulphides, but alteration may also take place by oxidation to iron sulphates, carbonates and oxides. Among the minerals which have been found pseudomorphous after pyrrhotite are pyrite, marcasite, chalcopyrite, arsenopyrite, magnetite and quartz.

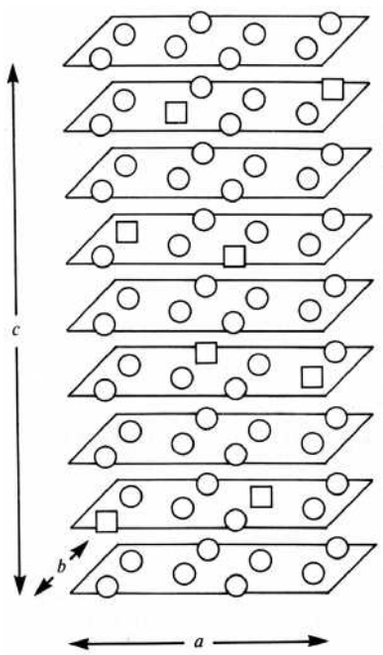


Fig. 288. Schematic illustration of the arrangement of iron atoms in the structure of Fe_7S_8 monoclinic pyrrhotite. Circles, iron atoms; squares, vacancies (after Vaughan, D.J. & Craig, J.R., 1978, *Mineral Chemistry of Metal Sulfides*, Cambridge University Press).

Downloaded from https://pubs.geoscienceworld.org/books/chapter-pdf/3763567/9780903056434_ch96.pdf
by guest

Optical and physical properties

Pyrrhotite usually occurs in massive or granular aggregates, but tabular {0001} and pyramidal habits, and sometimes rosette formations, are not uncommon. The bronze-coloured surface of pyrrhotite tarnishes very easily and commonly develops iridescent colours, but polished sections may be examined by reflected light, and the mineral can then be seen to be strongly anisotropic with ε brownish cream and ω reddish brown. Density varies with Fe/S ratio, and values between 4.55 and 4.87 g/cm^3 have been recorded. Many specimens of pyrrhotite are ferrimagnetic (i.e. capable of acting as a magnet; those which are closest to the composition Fe_7S_8 show the effect most strongly, and troilite, with composition FeS, is ideally antiferromagnetic).

Distinguishing features

Pyrrhotite is decomposed by HC1 with the evolution of H_2S whereas pyrite is not. Other distinguishing features are its bronze rather than brass colour and its lower hardness. Troilite is attacked more readily by dilute nitric acid than is pyrrhotite.

Pentlandite $(Fe,Ni)_9S_8$ resembles pyrrhotite but is slightly paler, has an octahedral parting and is isotropic. In polished section, the creamy pinkish brown colour and moderately high reflectance of pyrrhotite, combined with distinct bireflectance and pleochroism (creamy brown–reddish brown) and very strong anisotropy, are all highly characteristic.

Paragenesis

Pyrrhotite occurs mainly in basic igneous rocks (e.g. in the Skaergaard and Bushveld layered intrusions) and it is also found in pegmatites, in contact-metamorphic deposits, in high-temperature hydrothermal veins and in stratiform sedimentary environments. It can occur alone but it is usually associated with other sulphides, e.g. pyrite, marcasite, chalcopyrite, pentlandite and sphalerite. Troilite is common in meteorites and also in lunar rocks both as a primary phase and in the meteoritic component; the primary troilite usually has less Ni and Pb and more Co than that of meteoritic origin. In igneous rocks generally pyrrhotite and troilite are likely to have formed as a result of the immiscibility of sulphide and silicate melts. Pyrrhotite is an important phase in the development of acid mine drainage; its relative resistance to breakdown via oxidation varies according to local conditions.

Further reading

Jambor, J.L. (1994) Mineralogy of sulfide-rich tailings and their oxidation products. Pp. 59–102 in: *Environmental Geochemistry of Sulfide Minewastes* (J.L. Jambor and D.W. Blowes, editors). *Mineralogical Association of Canada Short Course Series*, **22**, 59–102.

Kissin, S.A. and Scott, S.D. (1982) Phase relations involving pyrrhotite below 350ºC. *Economic Geology*, **77**, 1739–1754.

Power, L.F. and Fine, H.A. (1976) The iron–sulphur system. *Mineral Science and Engineering*, **8**, 106–128.

Vaughan, D.J. and Lennie, A.R. (1991) The iron sulphide minerals: their chemistry and role in nature. *Science Progress*, **75**, 371–388.

Wager, L.R., Vincent, E.A. and Smales, A.A. (1957) Sulphides in the Skaergaard intrusion, East Greenland. *Economic Geology*, **52**, 855–903.

Wang, H. and Salveson, I. (2005) A review on the mineral chemistry of the non-stoichiometric iron sulphide $Fe_{1-x}S$ ($0 < x < 0.125$): polymorphs, phase relations and transitions, electronic and magnetic structures. *Phase Transitions*, **78**, 547–567.

Downloaded from https://pubs.geoscienceworld.org/books/chapter-pdf/3763567/9780903056434_ch96.pdf
by guest

Chalcopyrite $CuFeS_2$

Tetragonal

D (g/cm^3)	4.1–4.3
H	3½–4½; VHN_{100} 181–203
R % (589 nm)	47.6 (in air), 35.0 (in oil)
Cleavage	{011}, {111}, generally poor
Twinning	Lamellar on {112}, {102}, {110}; deformation twins on {110} and {012}; interpenetrant twins
Colour	Brass-yellow; often tarnished and iridescent in hand specimen; metallic lustre; greenish black streak; opaque even in thinnest sections; yellow to brassy yellow in polished section
Unit cell	a 5.281 Å, c 10.401 Å Z = 4; space group $I\bar{4}2d$
Special features	Soluble in HNO_3 with precipitation of sulphur

Chalcopyrite is the most widely occurring copper-bearing mineral, and is the major ore mineral of copper.

Structure

The structure (Fig. 289) of chalcopyrite is similar to that of sphalerite (p. 435) with c (chalcopyrite) ~ $2a$ (sphalerite). In each half of the chalcopyrite cell, the four zinc atoms of sphalerite are replaced by two copper atoms and two iron atoms, such that copper and iron occupy alternate positions along the z axis, resulting in a cell with twice the volume (c_{chalc} ~ $2a_{sphal}$). As in sphalerite, the sulphur atoms are arranged in layers stacked in cubic close packing; these layers are parallel to {112} planes of the chalcopyrite unit cell. In chalcopyrite each metal atom is coordinated by a tetrahedron of sulphur and each sulphur by a tetrahedron of metal atoms (2 Fe and 2 Cu). The Fe tetrahedron in chalcopyrite is very regular (Fe–S = 2.256 Å; tetrahedral angles 109.4–109.6º), whereas the Cu tetrahedron is somewhat distorted (Cu–S = 2.299 Å; tetrahedral angles 108.68–111.06º

The rather open array of S ions in chalcopyrite can accommodate additional metal ions giving rise to ordered

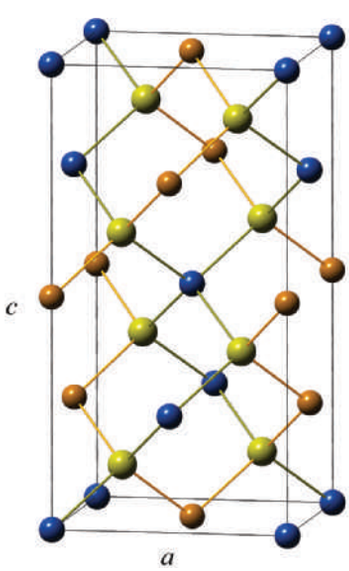


Fig. 289. The crystal structure of chalcopyrite (after Pauling, L. & Brockway, L.O., 1932, *Z. Krist.*, **82**, 188–94). Brown: Fe; blue: copper; yellow: S.

Downloaded from https://pubs.geoscienceworld.org/books/chapter-pdf/3763570/9780903056434_ch97.pdf
by guest

superstructures with stoichiometric compositions such as $Cu_9Fe_8S_{16}$, $Cu_9Fe_9S_{16}$ and $Cu_8Fe_{10}S_{16}$, with cubic, tetragonal and orthorhombic super-cells, respectively. Heating produces disorder and the simple sphalerite-like cubic unit cell. Cooling from high temperature can produce different phases, some of which are metastable, depending on cooling rates. The existence of such phases may be overlooked because of their similarities with chalcopyrite.

Chemistry

Natural chalcopyrite deviates very little from the ideal composition $CuFeS_2$. Minor and trace amounts of many elements have been reported as present in chalcopyrite. The metallic elements Co, Ni, Mn, Zn and Sn probably replace Cu or Fe and As and Se replace S; Ag, Au, Pt, Pb, V, Cr, In, Al, Sb and Bi have also been reported. In many cases these elements may be present in finely intergrown minerals (e.g. As in arsenopyrite, Sn in stannite, Zn in sphalerite and Pt in sperrylite). Despite the similarities in the structures of chalcopyrite and sphalerite there is only very limited solid solution of ZnS in $CuFeS_2$, and of $CuFeS_2$ in ZnS.

Chalcopyrite can be prepared artificially in a variety of ways (e.g. fusion of pyrite with chalcocite (Cu_2S), heating mixed powders of pyrite and copper, and by the action of ammoniacal cuprous chloride on $KFeS_2$). Phase relations in the system Cu–Fe–S are complex, and involve a wide range of Cu-Fe solid solutions embracing such sulphides as digenite (Cu_9S_5) as well as pyrite and pyrrhotite. The temperature at which chalcopyrite breaks down is between 547 and 557ºC depending upon precise composition. The breakdown is incongruent giving a cubic phase with slightly higher metal content plus a small amount of pyrite. At temperatures not far below 550ºC there is a range of intermediate solid solutions near the $CuFeS_2$ composition which are metal-rich. The solid solutions break down on cooling to give metal-rich phases with various intergrowth textures. The conditions for the crystallization and stability of such phases (e.g. $Cu_9Fe_8S_{16}$) are not well understood.

In order to relate to hydrothermal conditions of sulphide formation the system Cu–Fe–S–H_2O needs to be considered. Whereas chalcopyrite appears to be stable under reducing conditions over a wide range of pH, oxidizing conditions at low pH produce much Cu^{2+} and Fe^{3+} in solution; at high pH cuprite and tenorite precipitate. The aqueous oxidation of chalcopyrite is the basis for a method for the extraction of copper from sulphide ore.

Chalcopyrite is oxidized on exposure to air and water, or with slight heating, to sulphates and oxides of iron and copper. In nature these are usually altered further to carbonates, hydroxides and oxides. Among the common pseudomorphs after chalcopyrite are copper, chalcocite, covellite, bornite, pyrite, tetrahedrite, calcite and iron oxides.

Optical and physical properties

Chalcopyrite usually occurs in massive aggregates which are sometimes botryoidal or reniform. Oriented intergrowths occur with tetrahedrite, cubanite, galena and sphalerite. Chalcopyrite is weakly anisotropic in polished section. The reflectance varies strongly with wavelength in the visible region giving rise to its pronounced yellow colour. The Vickers hardness is greater on a basal than on a prism cross-section.

The antiferromagnetic nature of chalcopyrite results from high-spin Fe^{3+} ions in tetrahedral sites being ordered with opposite polarity on alternate (001) planes. The Cu atoms have virtually zero magnetic moment. Mössbauer spectroscopy confirms the formula $Cu^{+}Fe^{3+}S_2$. Chalcopyrite behaves at normal pressures as an n-type semiconductor. Increased pressure causes chalcopyrite to lose its antiferromagnetism and at higher pressure it behaves as a metal.

Distinguishing features

Chalcopyrite is distinguished from pyrite by its lower hardness and from pyrrhotite by its lack of ferromagnetism and from both (and also bornite) by its more distinctly yellow colour. In small grains it can resemble gold but chalcopyrite is harder and more brittle, and gold forms an amalgam with mercury. In polished section the yellow colour is more pronounced than that of pyrite; gold has a higher reflectance and lower polishing hardness.

Paragenesis

Chalcopyrite is the most widely occurring copper-bearing mineral and is an important ore of the metal. It occurs as polycrystalline aggregates and in veins in mafic and ultramafic igneous rocks (e.g. in the 'sulphide nickel' deposits of Sudbury, Canada, and Norilsk, Russia) having exsolved from a Cu–Fe–Ni–S solid solution which itself occurred probably through sulphide/silicate liquid immiscibility. In felsic igneous rocks such as quartz diorites or quartz monzonites (as in porphyry copper deposits, e.g. Bisbee, Arizona; Butte, Montana; and Bingham, Utah) chalcopyrite (the major copper mineral) formed by precipitation from late-stage saline fluids. It is an important constituent of Cu–Pb–Zn–Ag- or Cu–Zn–As-bearing assemblages in hydrothermal vein deposits, its common intergrowth in sphalerite being known as 'chalcopyrite disease'. Another mode of occurrence of chalcopyrite is in ores of

Downloaded from https://pubs.geoscienceworld.org/books/chapter-pdf/3763570/9780903056434_ch97.pdf
by guest

submarine volcanic origin including those of the Cyprus, Kuroko and Besshi types.

Chalcopyrite occurs also in sediments where there is no evident link with volcanism, e.g. in the important copper ores of the copper shales (Kupferschiefer) of central Europe, and those of the Zambian copper belt.

Metamorphosed massive sulphide deposits (e.g. Mt Isa and Broken Hill, Australia) also commonly contain appreciable amounts of chalcopyrite.

The alteration products malachite, azurite and chrysocolla are often found near the surface of copper ore deposits.

Further reading

Fleet, M.E. (2006) Phase equilbria at high temperatures. Pp. 365–419 in: *Sulfide Mineralogy and Geochemistry* (D.J. Vaughan, editor). Reviews in Mineralogy and Geochemistry, **61**, Mineralogical Society of America & Geochemical Society, Washington, D.C.

Putnis, A. and McConnell, J.D.C. (1976) The transformation behaviour of metal-enriched chalcopyrite. *Contributions to Mineralogy and Petrology*, **58**, 127–136.

Vaughan, D.J., England, K.E.R., Kelsall, G.H. and Yin, Q. (1995) Electrochemical oxidaton of chalcopyrite ($CuFeS_2$) and the related metal-enriched derivatives $Cu_4Fe_5S_8$, $Cu_9Fe_9S_{16}$ and $Cu_9Fe_8S_{16}$. *American Mineralogist*, **80**, 725–731.

Downloaded from https://pubs.geoscienceworld.org/books/chapter-pdf/3763570/9780903056434_ch97.pdf
by guest

Sphalerite ZnS

Cubic

n (589 nm)	2.37
D (g/cm^3)	4.1
H	3½–4; VHN_{100} 208–224
R % (589 nm)	~16.3 (in air), 4.70 (in oil)
Cleavage	{011} perfect
Twinning	{111} and {211}; multiple contact twins and lamellar intergrowths
Colour	Pale yellow, brown or black (more rarely red, green, white or colourless); yellow to brown or colourless in thin section; grey with brown tint in polished section
	Resinous or adamantine lustre
Unit cell	*a* 5.41 Å
	Z = 4; space group $F\bar{4}3m$
Special features	Soluble in HCl with evolution of H_2S

Sphalerite is the most common zinc-bearing mineral and the major ore of zinc. Pure ZnS is colourless, but almost all natural samples are coloured by the presence of impurities, most commonly iron, which can produce yellow, brown or virtually opaque black varieties; other common impurities are Mn, Cd and Cu. The synonyms *zinc blende* or *blende* are used for sphalerite in some older texts. The resinous to adamantine lustre is unusual amongst the metal sulphides.

Structure

The unit cell of the sphalerite structure is a cube with zinc at the corners and face-centres (Fig. 290a). Each of the four sulphur atoms within each unit cell is coordinated by a regular tetrahedron of zinc, and each zinc by a regular tetrahedron of sulphur atoms. The non-holosymmetric space group $F\bar{4}3m$ reflects the fact that the tetrahedra of zinc atoms (Fig. 290b) are all similarly oriented, giving the structure the symmetry of a tetrahedron rather than a cube, and opposite senses of the direction [111] are not equivalent. The substitution of Fe for Zn causes an increase in the length of the unit-cell edge.

The high-temperature polymorph of ZnS is wurtzite, a much rarer mineral in which the arrangement of tetrahedra is such that the structure has hexagonal rather than cubic symmetry (Fig. 291a,b). The relationship

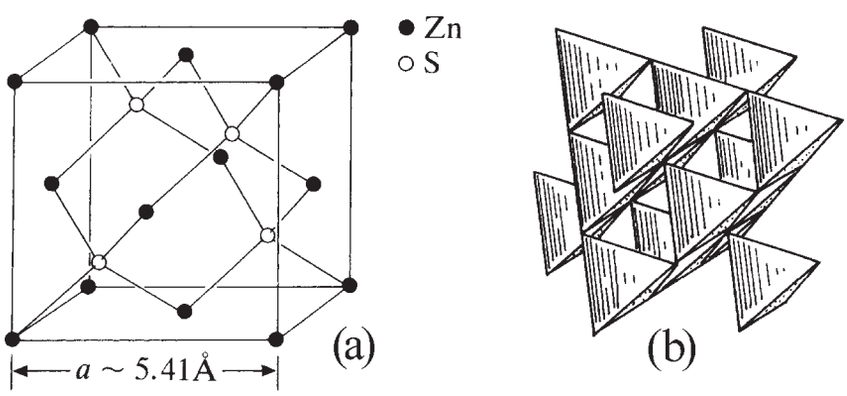


Fig. 290. The crystal structure of sphalerite showing (a) the cubic unit cell and linkage of Zn and S atoms, and (b) the linkage between ZnS_4 tetrahedra (after Vaughan, D.J. & Craig, J.R., 1978, *Chemistry of Metal Sulfides.* Cambridge University Press).

Downloaded from https://pubs.geoscienceworld.org/books/chapter-pdf/3763573/9780903056434_ch98.pdf
by guest

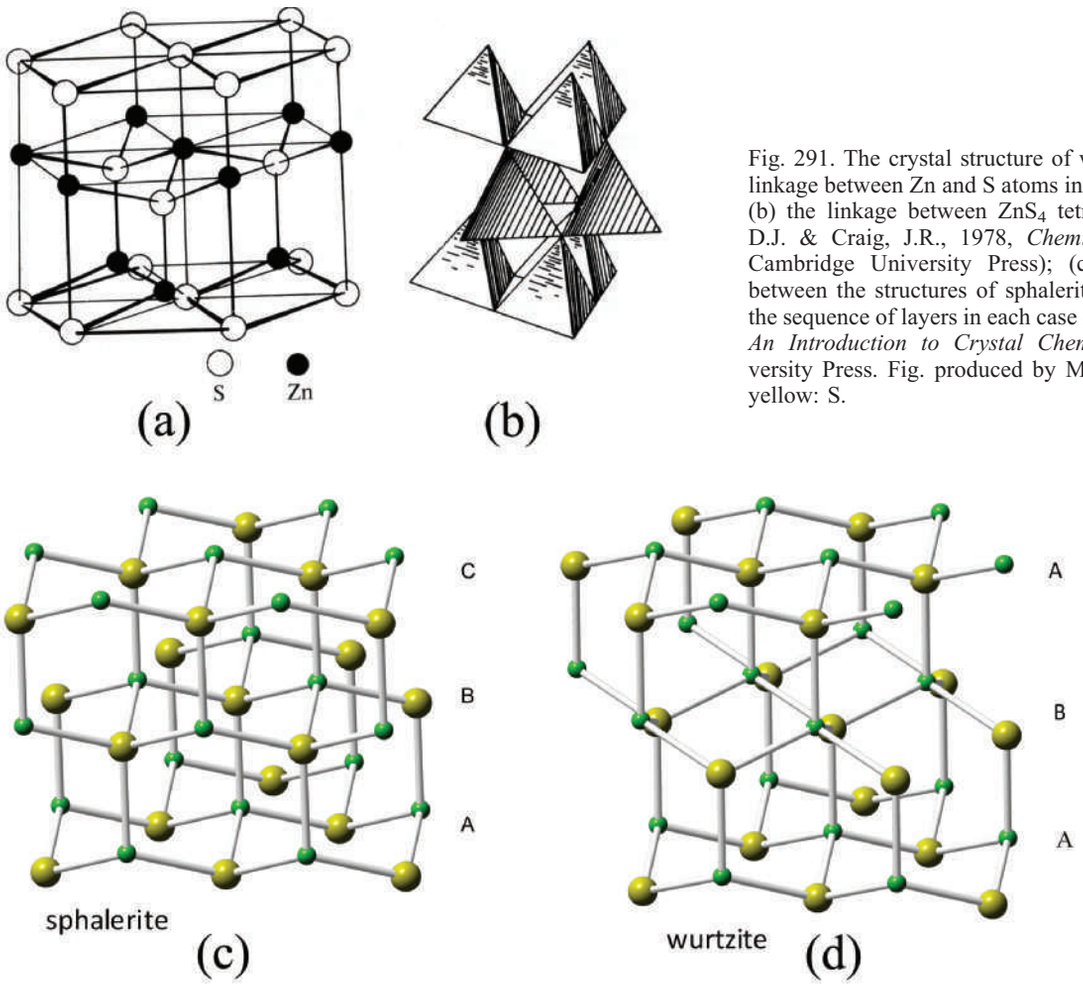


Fig. 291. The crystal structure of wurtzite showing (a) the linkage between Zn and S atoms in the hexagonal structure; (b) the linkage between ZnS_4 tetrahedra (after Vaughan, D.J. & Craig, J.R., 1978, *Chemistry of Metal Sulfides.* Cambridge University Press); (c) and (d) comparison between the structures of sphalerite and wurtzite showing the sequence of layers in each case (after Evans, R.C., 1964, *An Introduction to Crystal Chemistry*. Cambridge University Press. Fig. produced by M.D. Welch). Green: Zn; yellow: S.

between the structures of wurtzite and sphalerite is that between hexagonal and cubic close packing of anions, as may be seen by viewing them along [0001] and [111] respectively, in which case layers of Zn (or sulphur) atoms occupy positions ...ABABAB.... in wurtzite and ....ABCABC.... in sphalerite. Perspective views illustrating this distinction are shown in Fig. 291c,d.

The alternative layer stacking arrangements result in a large number of possible ZnS polytypes with different stacking sequences. In one system of notation, sphalerite is defined as having a stacking sequence *ccc* and the simplest wurtzite polytype as *hh*, where *c* signifies three layers with cubic, and *h* two layers with hexagonal stacking. An alternative system of notation gives the number of layers in the ideal stacking sequence followed by a letter designating the overall symmetry (C, cubic; H, hexagonal; R, rhombohedral). Thus sphalerite is the 3C polytype and, in the simplest case, wurtzite is 2H. A very large number of hexagonal and cubic polytypes have, however, been reported, e.g. 8H, 12R, and even 44H and 114R.

The electronic structure (chemical bonding) in ZnS, and particularly in surface structures has been the subject of considerable study because of the interest of solid state physicists and material scientists as well as mineralogists. The modern approach to these materials involves combining information on properties and spectroscopic data with quantum mechanical calculations.

The substitution of iron for zinc in sphalerite may reach up to around 56 mol%, and although there appears to be no stable iron end-member, a metastable FeS with the sphalerite structure has been reported. Iron substitution causes an increase in the cell dimension of sphalerite (Barton and Toulmin, 1966):

$$a\ (\text{Å}) = 5.4903 + 0.0005637\,(\text{mol\% FeS}) - 0.000004107\,(\text{mol\% FeS})^2.$$

Some caution is necessary, however, when applying this determinative curve to give the Fe content in a natural sphalerite, as MnS, CdS, HgS, ZnSe and ZnO are also soluble in ZnS and may affect the cell dimensions. Barton and Skinner (1967) suggest a modified equation to represent and correct for these impurities.

Chemistry

The principal substituent for zinc in sphalerite is iron, the highest iron content reported in natural occurrences being 26 wt.% Fe, which corresponds with 45 mol%

Downloaded from https://pubs.geoscienceworld.org/books/chapter-pdf/3763573/9780903056434_ch98.pdf
by guest

FeS. As noted above, experimental studies suggest an upper limit of about 56 mol% FeS. The minor and trace element content of natural sphalerites have been studied extensively. Virtually complete solid solutions have been reported between sphalerite and ZnSe, CdS and HgS, and despite the relatively low concentrations of Cd, In, Ge and Ga, sphalerite is the major source of these important metals. Copper, silver and tin are also commonly reported in sphalerite analyses, but some of these elements may be present in small inclusions of other minerals.

Pure sphalerite transforms to wurtzite at 1020ºC if oxidation is prevented, but the inversion temperature is lowered by the presence of iron or manganese. Wurtzite is metastable below the inversion temperature, grinding can be sufficient to convert it to sphalerite. The amount of iron that can be accommodated in the sphalerite structure increases with increasing temperature but it is also strongly influenced by a_{S_2} (sulphur activity). Experiments show that for a given temperature lower iron contents are found in sphalerites formed at higher a_{S_2}. The combined determination of As in arsenopyrite and Fe in sphalerite coexisting with pyrite or pyrrhotite can provide a useful estimate of temperature. Both determinations can be made by measuring suitable interplanar spacings by powder X-ray diffraction methods. The Fe content is also sensitive to pressure and has led to its use as a geobarometer. Pure sphalerite sublimes at 1185ºC, and melts congruently at 1830ºC and 0.37 MPa.

Sphalerite can be non-stoichiometric by small Zn deficiency and wurtzite by S deficiency (each <1%), and it has been suggested that this may influence the stacking sequences and the inversion temperature.

The solubility of ZnS in pure water is very low (~10^{-7} mg/litre) so the processes of transport and ore formation involve complexes such as $[Zn(HS)_3]^{-1}$, or $[Zn(HS)]^{+}$.

On heating in air, sphalerite is oxidized to zinc sulphate, but if much iron is present ferric and ferrous sulphates are also formed and at higher temperatures (above 1000ºC) zinc ferrites result. Sphalerite may also be converted to ZnO by heating and in some cases the oxide is pseudomorphous after the sulphide. Smithsonite and hemimorphite are the most common oxidation products of sphalerite, other replacement minerals include iron oxides and hydroxides.

Optical and physical properties

Sphalerite crystals commonly adopt tetrahedral habits with curved faces. Multiple contact twins, penetration twins, and lamellar intergrowths are common, twinning principally on {111} and {211}; the twinning on {111} is caused by pressure in some cases. Wurtzite generally has a hemimorphic pyramidal habit; it may be tabular or fibrous and is usually untwinned. Although sphalerite has a perfect {011} cleavage its brittleness leads to conchoidal fracture.

Pure Zn sphalerites can be colourless and transparent but translucency decreases and the yellow-brown-black colour deepens as iron content increases; colour banding is common. Spectroscopic analyses of sphalerite suggest that the colours of different specimens may also be associated with the presence of certain other elements, green with Co and Fe, red with Sn, In, Ag and Mo, and yellow with Ge, Ga, Cu, Hg and Cd. The minor-element content also contributes to the range of luminescence exhibited by sphalerites.

Although crystallographically cubic, sphalerite is not often optically isotropic. The positive uniaxial anisotropy exhibited may be due to intergrowth of sphalerite with wurtzite polytypes: some specimens of sphalerite show strain birefringence. Sphalerite has high dispersion; the refractive index is 2.47 for violet, about 2.37 for yellow light and about 2.30 for infrared. Wurtzite is uniaxial positive, with ω 2.356 and ε 2.378, and its density is similar to that of sphalerite, i.e. approximately 4.1 g/cm^3.

Pure ZnS is a diamagnetic semiconductor (p-type in sphalerite and n-type in wurtzite). Because of their polar structures both sphalerite and wurtzite exhibit piezo-electricity. Many industrially important synthesized semi-conductors have the sphalerite structure.

Distinguishing features

Although extremely variable in colour, sphalerite can be recognized by its resinous lustre, low hardness, high refractive index, weak or zero birefringence, cleavage and lamellar twinning. In polished section its grey colour, low reflectance, isotropy and common internal reflections are characteristic. Magnetite is harder and has no internal reflections.

Paragenesis

Sphalerite, the major ore of zinc, occurs with galena in many types of ore deposit but is most common in those of a hydrothermal nature. Thus deposits bearing lead, zinc, copper and silver occur in open fractures, or by replacement, usually in carbonate but also in other sedimentary rocks. Sphalerite-galena-baryte-fluorite associations occur in environments typified by the Triassic sediments of the Eastern Alps, Mississippi Valley Palaeozoic sediments, and the English Pennines. Sphalerite and galena, together with iron and copper sulphides, occur also disseminated in stratiform and strata-bound deposits, e.g. the Kupferschiefer in Europe, Sullivan, British Columbia and Skellefte District, Sweden. At Mt Isa and Broken Hill (Australia), lead and zinc sulphides occur in rocks in which metamorphism has obscured the original textures. Sphalerite is a major ore phase in the Cu-Fe-Zn Cyprus, Kuroko

Downloaded from https://pubs.geoscienceworld.org/books/chapter-pdf/3763573/9780903056434_ch98.pdf
by guest

and Besshi-type deposits associated with volcanism. Sphalerite (and wurtzite) have been reported from modern hydrothermal systems in 'black smokers'. Sphalerite and galena also occur in some pegmatite veins and in some skarn deposits formed by metasomatic replacement of carbonate rocks by intrusions. Sphalerite has also been reported from chondritic meteorites.

Sphalerite weathers readily and is not generally preserved as a detrital phase in sediments or placer deposits. It is, however, found as a minor phase in some bituminous shales and coals, probably resulting from the activity of sulphate-reducing bacteria during diagenesis. Both sphalerite and wurtzite have been found as crystalline chemically pure ZnS nanoparticles in biofilms in close association with metabolically active *Desulphobacteriaceae* in a flooded Pb-Zn mine and in the tubes of a deep-sea hydrothermal vent worm.

Pseudomorphs of sphalerite after galena, tetrahedrite and calcite have been reported.

Wurtzite, though less common, is often found together with sphalerite.

Studies of $^{34}S/^{32}S$ isotope ratios in sphalerite have helped determine whether the sulphur has igneous, hydrothermal or sedimentary affinities, and zinc isotopes ($\delta^{66}Zn$ values) in sphalerite have also been used as a tracer for studying hydrothermal processes.

Further reading

Barton, P.B. and Skinner, B.J. (1967) Sulfide mineral stabilities. In: *Geochemistry of Hydrothermal Ore Deposits* (H.L. Barnes, editor). Holt, Reinhart and Winston, New York.

Barton, P.B. and Toulmin, P. (1966) Phase relations involving sphalerite in the Fe–Zn–S system. *Economic Geology*, **61**, 815–849.

Fleet, M.E. (2006) Phase equilibria at high temperatures. Pp. 365–419 in: *Sulfide Mineralogy and Geochemistry* (D.J. Vaughan, editor). Reviews in Mineralogy and Geochemistry, **61**, Mineralogical Society of America & Geochemical Society, Washington, D.C.

John, S.G., Rouxel, O.J., Craddock, P.R., Engwall, A.M. and Boyle, E.A. (2008) Zinc stable isotopes in seafloor hydrothermal vent fluids and chimneys. *Earth and Planetary Science Letters*, **269**, 17–28.

Moreau, J.W., Webb, R.I. and Banfield, J.F. (2004) Ultrastructure, aggregation-state, and crystal growth of biogenic nanocrystalline sphalerite and wurtzite. *American Mineralogist*, **89**, 950–960.

Ohmoto, H. (1986) Stable isotope geochemistry of ore deposits. Pp. 185–225 in: *Stable Isotopes in High Temperature Geological Processes* (J.W. Valley, H.P. Taylor, Jr. and J.R. O'Neil, editors). Reviews in Mineralogy and Geochemistry, **16**, Mineralogical Society of America, Washington, D.C.

Scott, S.D. (1983) Chemical behaviour of sphalerite and arsenopyrite in hydrothermal and metamorphic environments. *Mineralogical Magazine*, **47**, 427–435.

Downloaded from https://pubs.geoscienceworld.org/books/chapter-pdf/3763573/9780903056434_ch98.pdf
by guest

Galena PbS

Cubic

D (g/cm^3)	7.5–7.6
H	2½; VHN_{100} 61–104
R % (589 nm)	42.7 (in air), 27.3 (in oil)
Cleavage	{001} perfect, {111} parting
Twinning	Penetration and contact twinning on {111}; lamellar and deformation twins on other planes
Colour	Lead grey; metallic lustre and lead grey streak; opaque in thin section; white in polished section
Unit cell	*a* 5.94 Å
	Z = 4; space group *Fm*3*m*
Special features	Decomposed by H_2SO_4 and by dilute HNO_3

Galena is the most important ore of lead.

Structure

The cubic structure of galena is similar to that of halite. The cubic unit cell shown in Fig. 292 contains sulphur atoms at its corners and face centres, and lead atoms at the mid points of cell edges. A description with an alternative choice of origin for the unit cell would reverse these assignments. The structure is based on planes of sulphur atoms parallel to {111} in the ...ABCABC... arrangement of cubic close packing; both lead and sulphur atoms are in octahedral coordination. The PbS_6 octahedra share all twelve edges with adjacent octahedra and the Pb–S distance is 2.965 Å.

Chemistry

Substitution of other atoms for lead in galena is not very extensive. Among the elements which do occur in small amounts are Sb, As, Bi, Ag, Tl, Zn, Cd, Fe, Mn and Cu. In many cases these are probably present in impurity minerals rather than in the galena structure. There is however a complete solid solution from galena to clausthalite (PbSe) and to altaite (PbTe).

Galena is decomposed by dilute nitric acid with the separation of sulphur and formation of $PbSO_4$; some specimens effervesce, giving off H_2S. Galena melts at 1115ºC. It can be prepared by heating pyrite with a

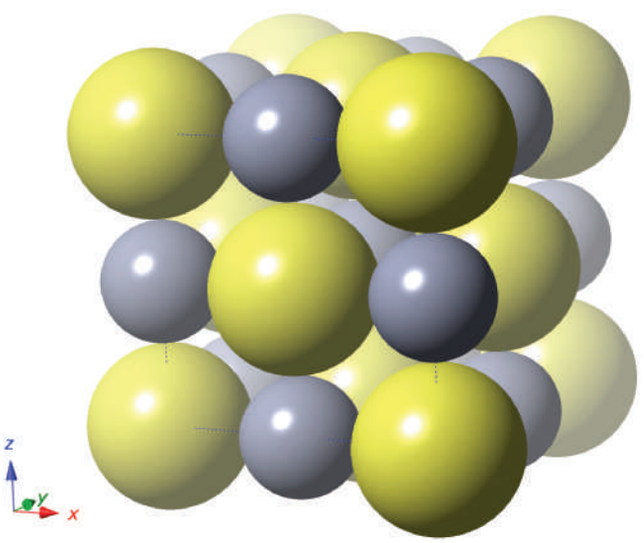


Fig. 292. The crystal structure of galena (CrystalMaker image). Grey: lead; green: sulphur.

Downloaded from https://pubs.geoscienceworld.org/books/chapter-pdf/3763629/9780903056434_ch99.pdf
by guest

solution of $PbCl_2$. Galena and pyrrhotite form a eutectic intergrowth at about 750ºC with composition 71% PbS, 29% FeS. The solubility of galena in pure water is very low; the formation of ore deposits by transport in hydrothermal solutions involves lead chloride complexes.

Among the alteration products of galena are cerussite, $PbCO_3$, and anglesite, $PbSO_4$ (under alkaline and acid conditions, respectively) and pyromorphite, $Pb_5(PO_4)_3Cl$. Pseudomorphs after galena include chalcocite and covellite.

Optical and physical properties

Galena is optically isotropic, and has a reflectance of 43% at 589 nm. The most common forms are the cube and octahedron, although the latter is rarely present alone, and the habit is often tabular on (001). Massive specimens can be coarse- or fine-grained, and fibrous aggregates are known: crystals commonly exhibit a lineage structure. Galena has a perfect cubic cleavage and specimens often have abundant triangular pits. There appears to be a close relationship between the nature of crystal parting and the presence and location of impurities and trace elements. Galena deforms readily along cube planes and slip occurs in the [110] direction. Oriented overgrowths of galena on other minerals and of these on galena often occur, e.g. galena on pyrite, chalcopyrite or pyrrhotite, and anglesite on galena.

Distinguishing features

Galena is easily recognizable, except perhaps when fine grained, by its colour, metallic lustre, lead-grey streak, perfect {100} cleavage, low hardness and high density. It can be distinguished from stibnite by its cubic cleavage, higher density and crystal habit. In polished section galena is characterized by its white colour, moderately high reflectance, isotropy, low hardness and the presence of triangular polishing pits. Crystals of galena commonly exhibit cube and/or octahedral faces.

Paragenesis

Galena is the principal ore of lead; it occurs most commonly with sphalerite, and the lead-zinc ores often contain recoverable amounts of copper, silver, antimony and bismuth. Occurrences of lead and zinc sulphides may be of low-, intermediate- or high-temperature origin. Thus galena of high-temperature origin is found in veins and replacements in pegmatites, calc-silicate rocks, limestones and other sediments, and in lavas; in limestones and sandstones the galena is of lower temperature hydrothermal origin (e.g. Mississippi Valley types). In the well known Australian lead and zinc deposits of Mt Isa (Queensland), Broken Hill (New South Wales) and many others elsewhere original sedimentary textures have been appreciably changed by metamorphism.

In addition to various sulphides, commonly associated minerals include baryte, fluorite, quartz and calcite; pseudomorphs after galena include cerussite, anglesite, pyromorphite, chalcocite and covellite.

The relative abundances of the various isotopes of lead (^{204}Pb, ^{206}Pb, ^{207}Pb, ^{208}Pb) in galena specimens have been used to estimate their ages, and the fractionation of the sulphur isotope ratios $^{34}S/^{32}S$ between coexisting pyrite and galena, for example, have been used as a geothermometer, and also to determine the source of the sulphur.

Further reading

Doe, B.R. (1970) Lead isotopes. *Minerals, Rocks and Inorganic Materials.* Springer-Verlag, 137 pp.

Vaughan, D.J. and Ixer, R.A. (1980) Studies of the sulphide mineralogy of North Pennine ore and its contribution to genetic models. *Transactions of the Institution of Mining and Metallurgy (Section B: Applied Earth Science)*, **89**, 99–108.

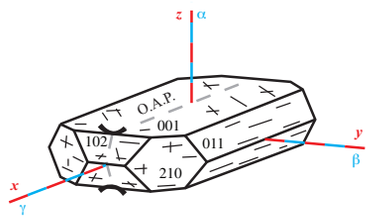
Downloaded from https://pubs.geoscienceworld.org/books/chapter-pdf/3763629/9780903056434_ch99.pdf
by guest

Sulphates

Baryte $BaSO_4$

Orthorhombic (+)

α	1.635–1.637
β	1.636–1.639
γ	1.646–1.649
δ	~0.012
2Vγ	37–39°
Orientation	α = *z*, β = *y* , γ = *x*; O.A.P. (010)
D (g/cm^3)	~4.5
H	2½–3½
Cleavage	{001} perfect, {210} very good, {010} good
Twinning	Glide twinning on {110} common in massive material
Colour	White, yellowish, grey, pale green, pale blue, red, brown; colourless in thin section
Pleochroism	Slight in coloured varieties; absorption γ > β > α
Unit cell	*a* 8.88 Å, *b* 5.45 Å, *c* 7.15 Å Z = 4; space group *Pnma*



Baryte is the least soluble sulphate and the most abundant barium mineral in the Earth's crust. It is the principal source of barium compounds and is widely used in drilling muds for the petroleum industry, or in other dense fluid media, and is used as a filler or extender in the manufacture of papers, cards, plasters, rubber and plastics. Baryte also finds uses in glasses and ceramics after conversion to the carbonate, chloride or hydroxide, and in the manufacture of sulphuric acid.

Structure

The structure of baryte is illustrated in Fig. 293. The SO_4 ions are approximately regular tetrahedra lying with S and two oxygens on mirror planes; the other two oxygens of each tetrahedron are equidistant from, and on opposite sides of, these planes. The Ba ions also lie on the mirror planes and link the sulphate ions in such a way that each Ba is coordinated by 12 oxygens. Six of the 12 oxygens form a distorted octahedron, and edge-sharing chains of such octahedra are linked laterally by SO_4 tetrahedra. Minerals with structures similar to that of baryte are anglesite ($PbSO_4$) and celestine ($SrSO_4$): cell parameters of all three are given below:

	a (Å)	*b* (Å)	*c* (Å)
Baryte	8.88	5.45	7.15
Anglesite	8.48	5.40	6.96
Celestine	8.36	5.35	6.87

Chemistry

Although specimens of baryte are generally nearly pure $BaSO_4$, barium can be replaced by strontium in a continuous solid-solution series from baryte to celestine. Appreciable replacement of Ba by Ca is uncommon; at room temperature only about 6% $CaSO_4$ can enter into solid solution in the baryte structure. The solubility of baryte in water is very slight but it is increased by heating and by the presence of chlorides. If they are gently heated, some crystals of baryte decrepitate, giving off H_2S; the variety hepatite does this to a marked extent.

The $\delta^{34}S$ and $^{87}Sr/^{86}Sr$ isotope ratios and Th values appear to be diagnostic in distinguishing between baryte of marine and continental origin; in particular, baryte from deep-sea sediments has been reported to have ~34 ppm, whereas the continental samples have ~0.1 ppm, of Th. Hydrothermal baryte tends to be enriched in ^{34}S with $\delta^{34}S$ values +12 to +36‰.

Downloaded from https://pubs.geoscienceworld.org/books/chapter-pdf/3763660/9780903056434_ch100.pdf
by guest

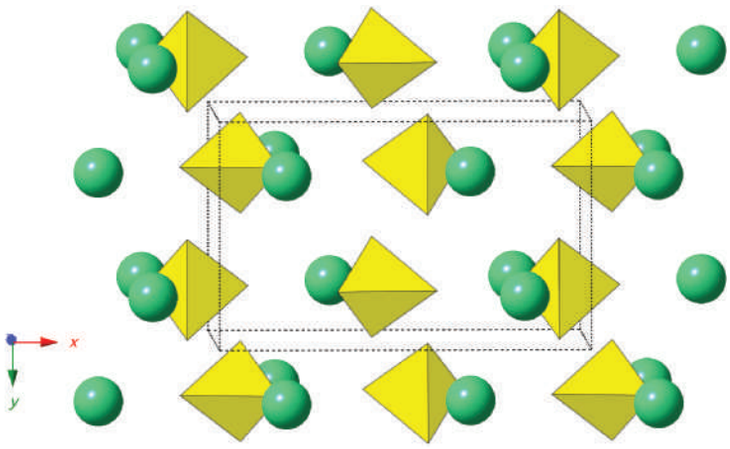


Fig. 293. Perspective view of the structure of baryte from direction near *z*. Dashed lines: unit cell; green: Ba^{2+} cations; yellow: $[SO_4]^{2-}$ anion tetrahedral groups (CrystalMaker image).

$BaSO_4$ crystals have been prepared by double decomposition using $BaCl_2$ and sulphate solutions.

Optical and physical properties

Baryte commonly occurs in well formed crystals but it is also found as globular concretions and as fibrous, lamellar, granular and earthy aggregates. Clusters of platy crystals are found, usually containing sand grains and coloured pink, which assume rosette shapes and are called 'desert roses'. Gypsum also commonly forms desert roses. Crystals of baryte have a vitreous to resinous (and sometimes pearly) lustre, and are colourless or white when pure. Yellow, red and brown varieties result from the presence of impurities, principally iron oxides and hydroxides, sulphides and organic matter. Many specimens are blue, probably as a result of exposure to radiation from radium; it is known that exposure of baryte to such radiation turns it blue, and the presence of Ra in natural specimens is quite likely in view of the similarities between the Ba and Ra atoms. Some specimens of baryte are fluorescent (white, yellow or orange) in ultraviolet light and are subsequently phosphorescent; thermoluminescence also occurs. Baryte is brittle, shows perfect {001} cleavage, and less perfect cleavage on {210} and {010}: the {210} cleavages intersect at an angle of approximately 78º. The average hardness of baryte is about 3 on the Mohs' scale but it varies somewhat because of chemical substitutions; Sr decreases and Pb increases the density. Refractive indices and birefringence are lowered slightly by the substitution of Sr for Ba and increased by substitution of Pb, whereas the optic axial angle is increased by either of these replacements, but for Sr reaches a maximum at ~50% $SrSO_4$ (Fig. 294).

Distinguishing features

Baryte is not easily distinguished from celestine except by its greater density, which also helps to distinguish it from other minerals, e.g. aragonite, albite, calcite and gypsum. In addition, albite is harder than baryte, gypsum is softer, and calcite effervesces whereas baryte is insoluble in dilute HCl; baryte gives a green flame coloration. The cleavages of minerals in the baryte group are characteristic, and are distinct from the three orthogonal cleavages of anhydrite. Baryte and celestine have lower refringence and birefringence than anglesite.

Paragenesis

Baryte is the most common barium mineral, occurring mainly as a gangue mineral in metalliferous

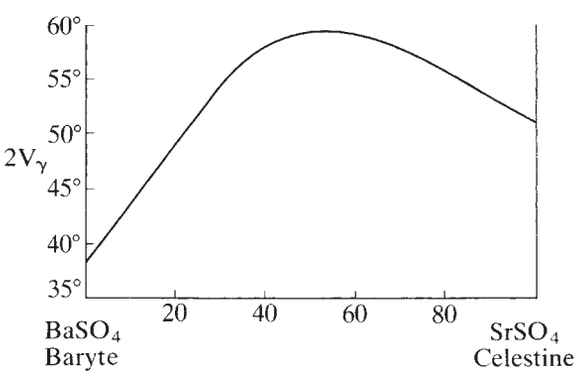


Fig. 294. Variation of 2Vγ with composition (mol.%) in the baryte–celestine series (after Burkhard, A., 1978, *Schweiz. Min. Petr. Mitt.*, **58**, 1–96).

Downloaded from https://pubs.geoscienceworld.org/books/chapter-pdf/3763660/9780903056434_ch100.pdf
by guest

hydrothermal veins, and as veins or cavity-filling concretions in limestones, sandstones, shales and clays. In addition to vein deposits, baryte occurs as surface deposits as a residual product of limestone weathering, and it may also occur in association with hot springs. The possible sources of Ba^{2+} and SO_4^{2-} leading to the formation of baryte are varied. In the baryte in hydrothermal veins and fissures, or in sedimentary baryte, SO_4^{2-} can be derived from sulphides in the cap rock or in other adjacent sulphur-bearing strata, or from sea-water. The solubility of baryte in aqueous solutions is very low (~2 mg/l) rising to ~40 mg/l at 500ºC, indicating that $BaSO_4$ is not itself carried appreciably in hydrothermal solutions. Precipitation of baryte can occur by the oxidation of reduced sulphur species to sulphate in solutions carrying barium, or by the mixing of barium-rich fluids with sulphate in surface waters. The barium may also originate in micas and feldspars in granite or other igneous rock, in dolomites or limestones, or clays and shales.

The minerals commonly associated with baryte are lead and zinc minerals, pyrite, quartz, carbonates and fluorite. Baryte and fluorite can show regional zonal relationships in low-temperature hydrothermal systems.

Further reading

Blount, C.W. (1977) Barite solubilities and thermodynamic quantities up to 300ºC and 1400 bars. *American Mineralogist*, **62**, 942–957.

Claypool, G.E., Holser, W.T., Kaplan, I.R., Sakai, H. and Zak, I. (1980) The age curves of sulfur and oxygen isotopes in marine sulfate and their mutual interpretation. *Chemical Geology*, **28**, 199–260.

Colville, A.A. and Staudhammer, K. (1967) A refinement of the structure of barite. *American Mineralogist*, **52**, 1877–1880.

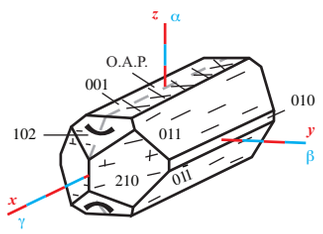
Dunham, K.C. (1990) Geology of the Northern Pennine orefield. (2nd ed.) *Memoir of the Geological Survey of Great Britain*.

Downloaded from https://pubs.geoscienceworld.org/books/chapter-pdf/3763660/9780903056434_ch100.pdf
by guest

Celestine $SrSO_4$

Orthorhombic (+)

α	1.619–1.622
β	1.622–1.624
γ	1.630–1.632
δ	~0.009
$2V_\gamma$	50°
Orientation	α = *z*, β = *y*, γ = *x*; O.A.P. (010)
D (g/cm^3)	~3.98
H	3–3½
Cleavage	{001} perfect, {210} very good, {010} good
Twinning	Very rare
Colour	Blue, orange, reddish, greenish, yellow, yellow-brown, colourless; colourless in thin section
Pleochroism	Blue crystals weakly pleochroic; indigo, lavender-blue, blue-green, violet; absorption γ > β > α
Unit cell	*a* 8.36 Å, *b* 5.35 Å, *c* 6.87 Å Z = 4; space group *Pnma*



Celestine, $SrSO_4$, is a member of the baryte group of minerals and is the principal source of strontium. The crimson flame coloration produced by strontium makes it an important constituent in the manufacture of fireworks and flares, for which purpose it is converted into the nitrate. Strontium is also used in its carbonate form for special glasses, and for ferrite magnets. Celestine itself is used as a filler for white and coloured paints.

The structure of celestine is similar to that of baryte, with Sr taking the place of Ba. There is a complete solid-solution series between $BaSO_4$ and $SrSO_4$, but solid solution of $CaSO_4$ in $SrSO_4$ is limited. Natural specimens, however, rarely contain more than 2 or 3% of the Ba or Ca component. Alteration products from celestine, some of which may be pseudomorphous, include strontianite, calcite, witherite, quartz, chalcedony, baryte and sulphur.

Celestine occurs in fibrous or rounded aggregates and also as well-formed crystals with tabular {001} habit. The colours of celestine specimens are mostly caused by impurities, but the blue of some is probably produced by irradiation. Celestine is similar to baryte in many respects but its density and refractive indices are lower; in the solid solution series, $2V_\gamma$ is at a maximum of 59° at about 50% $SrSO_4$ [baryte 37°, celestine 50° (Fig. 294, p. 442)]. Gypsum is softer and calcite effervesces with dilute HC1; celestine gives a crimson flame coloration. The cleavages of minerals in the baryte group are characteristic, and are distinct from the three orthogonal cleavages of anhydrite.

Celestine occurs mainly in sedimentary rocks, particularly dolomites, dolomitic limestones, and marls, either as a direct precipitate from aqueous solutions or, more usually, by the interaction of gypsum or anhydrite with Sr-rich waters. Beds of celestine are therefore found immediately above or below gypsum or anhydrite deposits. A well known occurrence of celestine in the UK is that at Yate, near Bristol, where large nodules are found in Triassic marl. Celestine can occur also as a primary mineral in hydrothermal veins.

Further reading

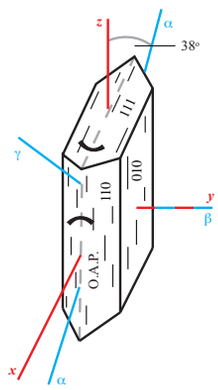
Nickless, E.F.P., Booth, S.J. and Mosley, F.N. (1975) Celestite deposits of the Bristol area. *Transactions of the Institution of. Mining and Metallurgy (Section B: Applied Earth Science)*, **84**, 62–64.

Wood, M.E.W. and Shaw, R.F. (1976) The geochemistry of celestites from the Yate area near Bristol (UK). *Chemical Geology*, **17**, 179–193.

Downloaded from https://pubs.geoscienceworld.org/books/chapter-pdf/3763710/9780903056434_ch101.pdf
by guest

Monoclinic (+)

α	1.519–1.521
β	1.523–1.526
γ	1.529–1.531
δ	0.010
$2V_\gamma$	~58º
Orientation	γ:*z* ~ 52º; O.A.P. (010); inclined dispersion of bisectrix
D (g/cm^3)	2.30–2.37
H	2
Cleavage	{010} perfect, {100} and {011} distinct
Twinning	Very common on {100}; less common {$\bar{1}$01}
Colour	Usually white or colourless, also grey, red, yellow, brown, blue; colourless in thin section
Unit cell	*a* 5.68 Å, *b* 15.18 Å, *c* 6.29 Å, β 113.8º Z = 4; space group *A*2/*a*



Morphological setting

Gypsum is the most abundant sulphate mineral, it occurs in extensive masses of great thickness in association with limestones and shales and in evaporite deposits. It is used as one of the standard minerals (H = 2) for the Mohs' scale of hardness. An important commercial use of gypsum is in the manufacture (by its partial dehydration) of plaster (plaster of Paris) and plasterboard. It is used also as a fertilizer, a filler in paper and paint, in muds for oil well drilling, and as a retarding agent in cement.

Structure

Euhedral crystals of gypsum commonly adopt the habit depicted above, and in most morphological studies the clinodome is taken to be the form {111} and prism {110}; this description yields axial ratios 0.6910:1:0.4145, and β 98º58′. The Bravais lattice of gypsum is illustrated in Fig. 295, which shows also six different ways in which two out of the four shortest vectors in the (010) plane may be chosen for the parameters *a* and *c*. The repeat distance perpendicular to (010) is 15.18 Å (= *b*), and this coincides in direction with the diad axis. The cell containing the smallest

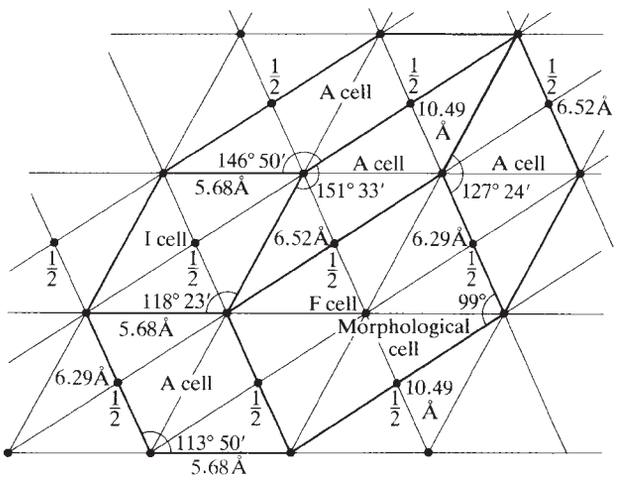


Fig. 295. The Bravais lattice of gypsum projected on (010), showing the six ways of choosing unit cells defined by two out of the four shortest vectors (Deer *et al*., 1992, *An Introduction to the Rock-Forming Minerals*, Longman, UK).

Downloaded from https://pubs.geoscienceworld.org/books/chapter-pdf/3763712/9780903056434_ch102.pdf
by guest

vectors is *A*-centred and has *a* 5.68 Å, *b* 15.18 Å, *c* 6.29 Å, β 113º51′. The morphological sketch and axial ratios, however, correspond with the *F*-cell.

The crystal structure of gypsum is illustrated in Fig. 296, which shows that CaO_8 polyhedra (Ca bonded to six oxygens of SO_4 tetrahedra and two of water molecules) are linked to each other by shared corners and to SO_4 tetrahedra by shared edges to form bands parallel to (010). Water molecules are located in the planes between bands and each is hydrogen-bonded to two of the oxygens of a Ca–O polyhedron.

The channels of water molecules in gypsum give it a somewhat zeolitic character and perhaps also facilitate the formation of anhydrite as a secondary mineral. Perfect (010) cleavage is consistent with the layered nature of the structure, and furthermore the direction of strongest linkages [001] corresponds with the fibre axis in the satin spar variety of gypsum.

Chemistry

Gypsum shows very little variation in chemical composition, and the main point of interest in its chemistry concerns the products of its dehydration. Three principal phases occur in the system calcium sulphate–water: $CaSO_4.2H_2O$ (gypsum), $CaSO_4.½H_2O$ (bassanite), and $CaSO_4$ (anhydrite). There is also another form (γ-$CaSO_4$) which may be regarded as dehydrated bassanite. When heated in air, gypsum is converted slowly to bassanite at about 70ºC or below, and rapidly at 90ºC and above; heating gypsum above about 200ºC produces anhydrite, and this change is irreversible.

Of the four principal phases in the system $CaSO_4$–H_2O, two, bassanite and γ-$CaSO_4$, exist only metastably. Thus at equilibrium the reaction:

$$\text{gypsum} \rightleftharpoons \text{anhydrite} + \text{water}$$

occurs without the formation of intermediate compounds. The temperature of transition of gypsum to anhydrite in pure water is 44ºC but gypsum may persist metastably above this temperature. The temperature of the transition is lowered considerably, however, by the presence of NaCl, and it is also reduced by increasing pressure; it is also affected by the presence of Na, Mg and K sulphates and their hydrates.

The isotopic composition of the structural water in gypsum is a sensitive diagnostic tool for determining mode of formation (i.e. by evaporation from brine, by hydration of anhydrite or by oxidation of sulphides). Gypsum is initially formed in isotopic equilibrium with the mother brine but exchange of water may subsequently occur fairly rapidly; in some arid conditions the primary isotopic record is preserved. There are also variations in the $^{34}S/^{32}S$ ratio in gypsum, with $\delta^{34}S$ in marine gypsum at around +20‰ but varying with stratigraphic age.

The DTA curves of gypsum show a double endothermic peak between 100 and 200ºC, the first representing the loss of 1½ molecules of water and the second peak the loss of the remaining water. Plaster of Paris consists largely of bassanite which has been produced by heating gypsum to about 170ºC over a period of one to three hours. If water is added to plaster of Paris, the dihydrate is reformed, and the mass sets hard through the formation of interlocking crystals of gypsum.

Optical and physical properties

Gypsum commonly occurs as euhedral transparent crystals, in which form it is known as selenite. Crystals of selenite commonly adopt a tabular habit {010}, showing the additional forms {120}, {$\bar{1}$11}, {011}; in some cases a lenticular appearance results from the presence of curved faces, the formation of which is probably influenced by the presence of impurities such as NaCl. Another distinctive habit is that of translucent fibrous aggregates (fibres parallel to the *z* axis), the

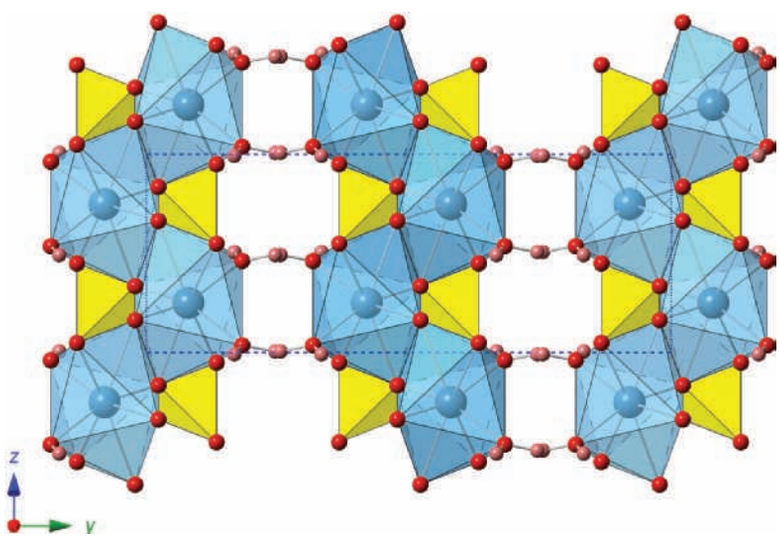


Fig. 296. Projection on (001) of the crystal structure of gypsum. Red: oxygen; yellow: sulphur; blue: calcium; pink: hydrogen (CrystalMaker image).

Downloaded from https://pubs.geoscienceworld.org/books/chapter-pdf/3763712/9780903056434_ch102.pdf
by guest

surfaces of which show a pearly sheen; this variety is known as satin spar. Most gypsum occurs as massive rock gypsum; when this is fine-grained and white or lightly coloured it finds use as an ornamental stone known as alabaster, but it is often darkened by impurities of clays, iron oxides and other minerals.

The perfect {010} cleavage of crystalline gypsum results in platy cleavage fragments which, because of further cleavages on {100} and {011}, commonly show a lozenge-shaped outline (angle 114º) with edges parallel to those of the two smallest *a* and *c* lattice parameters (Fig. 295). Contact twins on (100) are common; their appearance gives rise to the names 'swallow tail' or 'arrowhead'.

Dispersion of 2V with temperature is large for gypsum, 2V decreasing with temperature; at constant temperature and varying wavelength, dispersion of 2V ($r > v$) is also strong.

Distinguishing features

Gypsum is easily distinguished from anhydrite as the latter has higher refringence and birefringence: in addition anhydrite has characteristic pinacoidal cleavages and a higher density.

Paragenesis

The main occurrences of gypsum are as sedimentary deposits associated with limestones, shales, marls and clays, and in evaporite deposits. Sea-water contains about 3.5 wt.% of dissolved solids, 80% of which is sodium chloride and about 4% calcium sulphate. The usual sequence of deposition of salts from sea-water has been shown experimentally to be: calcium carbonate–calcium sulphate–sodium chloride–sulphates and chlorides of magnesium–sodium bromide and potassium chloride. If all the salt of a 1000 m column of water were precipitated it would make only 15 m of evaporite deposits of which about 0.4 m would be calcium sulphate, 11.6 m halite and the remainder potassium and magnesium-bearing salts.

In evaporites the calcium sulphate may be gypsum or anhydrite and the two minerals commonly occur together. It appears that in general anhydrite is a secondary mineral produced by the dehydration of gypsum, a reaction which involves a decrease in volume of the solid phase; in some cases halite fills the resultant voids and a halite-anhydrite assemblage results. The water released by the dehydration of gypsum may result in the local solution, redistribution and deposition of the soluble salts of the surrounding evaporites. In many areas gypsum has been dissolved in percolating waters (the solubility is increased by the presence of NaCl or $CaCO_3$), which in the dry season are drawn to the surface by capillary action, are evaporated, and leave gypsum as crystals, sometimes in aggregates described as 'desert roses'. Large gypsum deposits are also found in saline lakes and salt pans.

Whereas anhydrite is usually secondary, gypsum can be either primary or secondary. Gypsification of anhydrite occurs frequently along contacts of evaporites with carbonate rocks, and it proceeds along anhydrite cleavages, the textures showing that the gypsum is secondary. If large volumes of anhydrite have been altered to gypsum by hydration, masses of gypsum are found with relict nodules of anhydrite.

Gypsum is sometimes produced by the action of sulphuric acid solution on the calcium in the rocks through which it is moving. In clays and marls the acid solution may be produced by the weathering of sulphides, and in metalliferous veins by the oxidation of sulphides. Gypsum is also found in deposits of native sulphur and it is produced in volcanic regions by the action of sulphurous vapours on calcium-bearing minerals. Among the minerals which may be found in association with gypsum are halite, celestine, calcite, aragonite, dolomite, pyrite, sulphur and quartz.

Much use has been made of the determination of sulphur ($^{34}S/^{32}S$) and oxygen ($^{18}O/^{16}O$) isotope ratios in tracing the various modes of formation of gypsum.

Further reading

Claypool, G.E., Holser, W.T., Kaplan, I.R., Sakai, H. and Zak, I. (1980) The age curves of sulfur and oxygen isotopes in marine sulfate and their mutual interpretation. *Chemical Geology*, **20**, 199–260.

Cole, W.F. and Lancucki, C.J. (1974) A refinement of the crystal structure of gypsum $CaSO_4.2H_2O$. *Acta Crystallographica*, **B30**, 921–929.

Hawthorne, F.C., Krivovichev, S.V. and Burns, P.C. (2000) The crystal chemistry of sulphate minerals. Pp. 1–112 in: *Sulfate Minerals – Crystallography, Geochemistry, and Environmental Significance* (C.N. Alpers, J.L. Jambor and D.K. Nordstrom, editors). Reviews in Mineralogy and Geochemistry, **40**, Mineralogical Society of America & Geochemical Society, Washington, D.C.

Kushnir, J. (1980) The coprecipitation of strontium, magnesium, sodium, potassium and chloride ions with gypsum. An experimental study. *Geochimica et Cosmochimica Acta*, **44**, 1471–1482.

Putnis, A., Winkler, B. and Fernandez-Diaz, L. (1990) *In situ* IR spectroscopic and thermogravimetric study of the dehydration of gypsum. *Mineralogical Magazine*, **54**, 123–128.

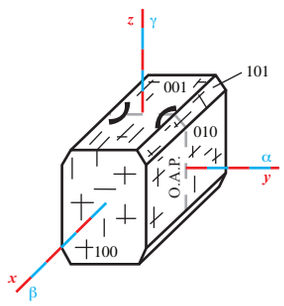
Sofer, Z. (1978) Isotopic composition of hydration water in gypsum. *Geochimica et Cosmochimica Acta*, **42**, 1141–1149.

Downloaded from https://pubs.geoscienceworld.org/books/chapter-pdf/3763712/9780903056434_ch102.pdf
by guest

Anhydrite $CaSO_4$

Orthorhombic (+)

α	1.567–1.574
β	1.574–1.579
γ	1.609–1.618
δ	~0.04
$2V_\gamma$	42–44°
Orientation	α = *y*, β = *x*, γ = *z*; O.A.P. (100)
D (g/cm^3)	2.9–3.0
H	3–3½
Cleavage	{010} perfect, {100} very good, {001} good
Twinning	Simple or repeated {011}
Colour	White or colourless when pure; often grey and more rarely bluish mauve, red or brown; colourless in thin section
Unit cell	*a* 6.99 Å, *b* 7.00 Å, *c* 6.24 Å Z = 4; space group *Amma*



Anhydrite is one of the principal minerals of evaporite deposits, and is also found as an accessory mineral in some dolomites and limestones. It is used in the manufacture of ammonia, and of ammonium sulphate for sulphuric acid production, and is the main constituent of certain plasters and cements. Anhydrite is so named because in contrast to gypsum it is a sulphate of calcium that contains no water.

Structure

The unit cell of anhydrite has two edges of nearly equal length, but the structure (Fig. 297) is not pseudotetragonal. The Ca is surrounded by eight oxygens which form a distorted triangular dodecahedron. This and the SO_4 tetrahedra link together to form alternating edge-sharing chains parallel to the *z* axis. Sulphur atoms (which are at the centres of tetrahedra of oxygens) and calcium atoms lie on the lines of intersection of mirror planes (100) and (010). These two planes contain approximately evenly spaced Ca and SO_4 ions, whereas layering is not so well defined parallel to (001); thus the (001) cleavage is not as perfect as those on (100) and (010).

Chemistry

Chemical analyses of anhydrite show only minor variations. Small amounts of Sr and Ba may replace Ca; other elements recorded are probably present as impurities, and H_2O if present is mainly due to the presence of gypsum. Anhydrite is soluble in acids but in water its solubility is slight, decreases with increasing temperature and increases with higher pressure. Crystals of anhydrite may be prepared by slowly cooling fusions of $CaSO_4$ with $CaCl_2$, $BaCl_2$ or NaCl, or of $CaCl_2$ with K_2SO_4, and also by heating gypsum with NaCl or $CaCl_2$ solution in a closed tube. Fine-grained anhydrite may be prepared by precipitating $CaSO_4$ from a solution containing a high concentration of $MgCl_2$ or $CaCl_2$ at room temperatures; gypsum is obtained at lower concentrations and at lower temperatures.

The alteration of anhydrite to gypsum by hydration is accompanied by deformation and an increase in volume. On heating, anhydrite undergoes transformation to a high-temperature trigonal form at about 1200°C, and beyond this transformation decomposition occurs:

$$2\,CaSO_4 \rightarrow 2\,CaO + 2\,SO_2 + O_2.$$

Among the minerals which may be found as pseudomorphs after anhydrite are quartz, siderite, calcite, dolomite, gypsum and marcasite.

Downloaded from https://pubs.geoscienceworld.org/books/chapter-pdf/3763717/9780903056434_ch103.pdf
by guest

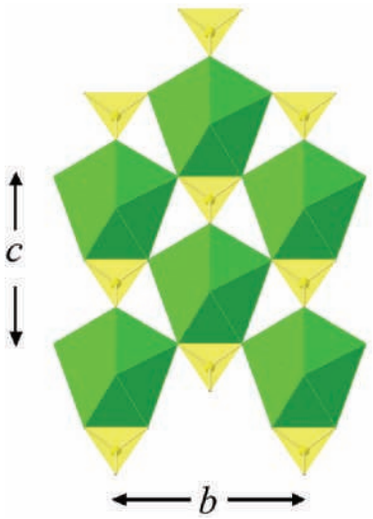


Fig. 297. Polyhedral representation of the anhydrite structure, viewed down the *x* axis. Alternating edge-sharing chains (parallel to *z*) of Ca dodecahedra (green) and S tetrahedra (yellow) link along *y* by corner-sharing between polyhedra (after Hawthorne, F.C. & Ferguson, R.B., 1975, *Can. Min.*, **13**, 289–92).

Optical and physical properties

Anhydrite usually occurs in massive aggregates of varying grain size, sometimes as groups of parallel or radiating fibres. Crystals, if they occur, usually have a thick tabular habit on pinacoidal faces, and may be elongated parallel to *x* or *z*: the crystals show three pinacoidal cleavages of which {010} is the best. Perfect crystals of pure anhydrite are transparent but specimens are often white, or coloured red, grey or brown by iron oxides. Some anhydrite is blue or violet, and this colour disappears on heating and reappears on exposure to radium radiation: thus the colour is thought to be a natural radiation colour, the source of radiation being either external, or present as an impurity within the anhydrite.

Distinguishing features

Anhydrite may be distinguished from baryte by its lower density, and in thin section by its pinacoidal cleavages. It is harder and more dense than gypsum and has higher relief and birefringence, and it is more dense than calcite.

Paragenesis

The principal occurrences of anhydrite are as a constituent of evaporites and as a product of hydrothermal alteration of limestone and dolomite rocks. In evaporite deposits, anhydrite or gypsum may occur, and the two minerals are commonly found together. According to the results of experiments on the solubility of anhydrite and gypsum, anhydrite should be deposited directly by the evaporation of sea-water above 49ºC, or at a lower temperature from a more saline solution: at lower temperatures and lower salinities gypsum should be deposited. Gypsum can, however, persist metastably above its transition temperature. Other experimental results indicate that the primary precipitation of anhydrite from sea-water is improbable, and that anhydrite is nearly always a secondary mineral produced by the dehydration of gypsum. Anhydrite does, however, form a primary precipitate at 'black smoker' systems. Anhydrite also occurs in salt plugs and domes. In metalliferous veins it is sometimes produced through the oxidation of sulphides.

Anhydrite is the most common sulphate in igneous rocks, occurring either as phenocrysts or as a product of alteration.

Further reading

Blount, C.W and Dickson, F.W. (1973) Gypsum-anhydrite equilibria in systems $CaSO_4$–H_2O and $CaSO_4$–NaCl–H_2O. *American Mineralogist*, **58**, 323–331.

Hawthorne, F.C. and Ferguson, R.B. (1975) Anhydrous sulphates II. Refinement of the crystal structure of anhydrite. *The Canadian Mineralogist*, **13**, 289–292.

Holser, W.J. (1970) Mineralogy of evaporites. In *Marine Minerals.* Mineralogical Society of America, Short Course Notes, **6** 231–294.

Innorta, G., Rabbi, E. and Tomaddin, L. (1980) The gypsum-anhydrite equilibrium by solubility measurements. *Geochimica et Cosmochimica Acta*, **44**, 1931–1936.

Luhr, J.F., Carmichael, I.S.E. and Varekamp, J.C. (1984) The 1982 eruptions of El Chichón Volcano, Chiapas, Mexico: mineralogy and petrology of the anhydrite-bearing pumices. *Journal of Volcanology and Geothermal Research*, **23**, 69–108.

Stewart, F.H. (1951) The petrology of the evaporites of the Eskdale no. 2 boring, east Yorkshire. Part II. The Middle Evaporite bed. Part III. The Upper Evaporite bed. *Mineralogical Magazine*, **29**, 445–475, 557–572.

Downloaded from https://pubs.geoscienceworld.org/books/chapter-pdf/3763717/9780903056434_ch103.pdf
by guest

Carbonates

The carbonates are a group of minerals in which the essential structural unit is the $(CO_3)^{2-}$ ion. Although there are approximately 250 known carbonate minerals many of them are comparatively rare, and some of the less common species are hydrated, contain hydroxyl or halogen ions, or are compounds with silicate, sulphate or phosphate radicals. The more common rock-forming carbonate minerals, and the properties of the pure end-members, are listed in Table 54.

The minerals of the carbonate group here considered include the species tabulated below together with ankerite, $Ca(Mg,Fe^{2+},Mn)(CO_3)_2$, which is related to dolomite, and huntite, $Mg_3Ca(CO_3)_4$, an alteration product of dolomite- or magnesite-bearing rocks.

Calcium carbonate is polymorphous and exists in at least five modifications. The two polymorphs commonly found in nature are calcite and aragonite. In addition, two synthetic forms known only at high pressures are calcite II and calcite III. Vaterite (μ-$CaCO_3$) is a metastable hexagonal form which crystallizes at ordinary temperatures and pressures. It is optically positive, as distinct from the negative optical character of most carbonates; its refractive indices have been reported to be ω 1.550, ε 1.660; density 2.54 g/cm^3. Vaterite has been recorded from the shells of certain young gasteropods and, in a geological environment, from a calc-silicate rock at Ballycraigy, Northern Ireland. Various calcium carbonate hydrates have been reported, several of which occur as natural minerals.

Although X-ray diffraction is commonly used, simple staining techniques may be used on grains of carbonates or on uncovered thin sections to distinguish calcite from dolomite and to distinguish ferroan from non-ferroan carbonates (Table 55). The dyes are dissolved in a weak acid solution, which also helps to distinguish dolomite from calcite, as dolomite does not react with cold dilute HCl whereas calcite does, producing a contrast in relief between the two minerals. The dye Alizarin Red S is used to differentiate calcite from dolomite and potassium ferricyanide is used to differentiate ferroan and non-ferroan minerals, these two reagents often being mixed together in some tests.

Other carbonates of fairly common occurrence in hydrothermal veins or in association with ore deposits, which are not further considered here, include cerussite, malachite, azurite and smithsonite (Table 56).

Table 54. Properties of the more common rock-forming carbonate minerals.

Name	Formula	System	ε	ω		
			α	β	γ	$2V_\alpha$
Calcite	$CaCO_3$	Trigonal	1.486	–	1.658	–
Magnesite	$MgCO_3$	Trigonal	1.509	–	1.700	–
Rhodochrosite	$MnCO_3$	Trigonal	1.597	–	1.816	–
Siderite	$FeCO_3$	Trigonal	1.635	–	1.875	–
Dolomite	$CaMg(CO_3)_2$	Trigonal	1.500	–	1.679	–
Aragonite	$CaCO_3$	Orthorhombic	1.530	1.680	1.685	18º
Strontianite	$SrCO_3$	Orthorhombic	1.517	1.663	1.667	8º
Witherite	$BaCO_3$	Orthorhombic	1.529	1.676	1.677	16º

Name	D (g/cm^3)	a (Å)	b (Å)	c (Å)	a_{rh} (Å)	α	Z_{rh}
Calcite	2.72	4.990	–	17.061	6.37	46º08′	2
Magnesite	2.98	4.632	–	15.012	5.675	48º10′	2
Rhodochrosite	3.70	4.777	–	15.66	5.91	47º43′	2
Siderite	3.96	4.69	–	15.37	5.77	47º43′	2
Dolomite	2.86	4.807	–	16.00	6.015	47º10′	1
Aragonite	2.94	4.96	7.97	5.74	–	–	4
Strontianite	3.72	5.11	8.42	6.03	–	–	4
Witherite	4.30	5.26	8.84	6.56	–	–	4

Downloaded from https://pubs.geoscienceworld.org/books/chapter-pdf/3763721/9780903056434_ch104.pdf
by guest

Table 55. Stain tests for carbonates.

Mineral	Effect of acid etching	Stain colour with Alizarin Red S	Stain colour with potassium ferricyanide	Stain colour with combined dyes
Calcite (non-ferroan)	Considerable (relief reduced)	Pink to red-brown	None	Pink to red-brown
Calcite (ferroan)	Considerable (relief reduced)	Pink to red-brown	Pale to deep blue depending on iron content	Mauve to blue
Dolomite (non-ferroan)	Negligible (relief maintained)	None	None	Colourless
Dolomite (ferroan)	Negligible (relief maintained)	None	Very pale blue	Very pale blue (turquoise or greenish in thin section)

Table 56. Properties of the less common carbonate rock-forming minerals.

	Formula	System	α	β	γ	2V	D (g/cm^3)	Colour
Cerussite	$PbCO_3$	Orthorhombic	1.803	2.074	2.076	8½°(−)	6.57	White
Nyerereite	$Na_2Ca(CO_3)_2$	Orthorhombic	1.513	1.533	1.534	29°(−)	2.417	Colourless
Malachite	$Cu_2(OH)_2CO_3$	Monoclinic	1.655	1.875	1.909	43°(−)	4.05	Green
Azurite	$Cu_3(OH)_2(CO_3)_2$	Monoclinic	1.730	1.758	1.838	68°(+)	3.80	Blue
			ε		ω			
Smithsonite	$ZnCO_3$	Trigonal	1.625		1.850		4.4	White
Huntite	$Mg_3Ca(CO_3)_4$	Trigonal	~1.615		2.696			White
Ankerite	$Ca(Fe^{2+},Mg,Mn)(CO_3)_2$	Trigonal	1.51−1.55		1.69−1.75		2.93−3.1	White

Further reading

Adams, A.E., MacKenzie, W.S. and Guilford, C. (1984) *Atlas of Sedimentary Rocks under the Microscope*. Longman, 104 pp.

Chang, L.L.Y., Howie, R.A. and Zussman, J. (1996) *Rock-Forming Minerals:* **5B,** *Sulphates, Carbonates, Phosphates and Halides*, 95−294, Longman.

Dickson, J.A.D. (1965) A modified staining technique for carbonates in thin section. *Nature*, **205**, 587.

Ogino, T., Suzuki, T. and Sawada, K. (1987) The formation and transformation mechanism of calcium carbonate in water. *Geochimica et Cosmochimica Acta*, **51**, 2757−2767.

Reeder, R.J. (editor) (1983) *Carbonates: Mineralogy and Chemistry*. *Reviews in Mineralogy*, **11**, Mineralogical Society of America, Washington, D.C., 394 pp.

Schneidermann, N. and Harris, P.M. (editors) (1985) *Carbonate Sediments*. Tulsa (Society of Economic Paleontologists and Mineralogists, Special Publication **36**), 379 pp.

Downloaded from https://pubs.geoscienceworld.org/books/chapter-pdf/3763721/9780903056434_ch104.pdf
by guest

Trigonal (−)

ε	1.486[a]−(1.550)
ω	1.658−(1.740)
δ	0.172−(0.190)
D (g/cm^3)	2.715−(2.94)
H	3
Cleavage[b]	$\{10\bar{1}1\}$ perfect
Twinning	$\{01\bar{1}2\}$ lamellar, very common; {0001} common; $\{10\bar{1}1\}$ not common
Colour	Colourless or white, but also grey, yellow and pale shades of pink, green or blue; colourless in thin section
Unit cell	a_{hex} 4.990 Å, c_{hex} 17.061 Å a_{rh} 6.37 Å, α 46.08° Z_{hex} = 6; Z_{rh} = 2; space group $R\bar{3}c$
Special features	Easily dissolves with brisk effervescence in cold dilute HCl

Calcite is very common and is the most abundant mineral in most limestones. It occurs also in metamorphic rocks and in some igneous rocks. It is the most stable form of $CaCO_3$ and is abundant in veins and alteration products. Its relative softness (H 3) and perfect rhombohedral cleavage are distinctive.

Structure

The structure of calcite can be described by analogy with that of halite: Na and Cl ions are replaced by Ca and $(CO_3)^{2-}$ ions, respectively and the unit cell is distorted by compression along a triad axis to give a face-centered rhombohedral cell with a_{rh} 6.42 Å, α 101.92° (Fig. 298). The distortion of the cube is necessary to accommodate the large planar (CO_3) groups which contain a carbon atom at the centre of an equilateral triangle of oxygens. This cell thus contains 4 $CaCO_3$ corresponding with the 4 NaCl in the cubic unit cell of halite; it is not however, a true cell of the rhombohedral Bravais lattice as successive (CO_3) triangles along the rhomb edge point in opposite directions. A true face-centred rhombohedral cell thus has a_{rh} 2×6.42 Å, α 101.92° and contains 32 $CaCO_3$. The rhombohedron with α 101.92° corresponds with the common cleavage rhomb of calcite which is usually indexed as {100} using Miller indices (Miller-Bravais $\{10\bar{1}1\}$).

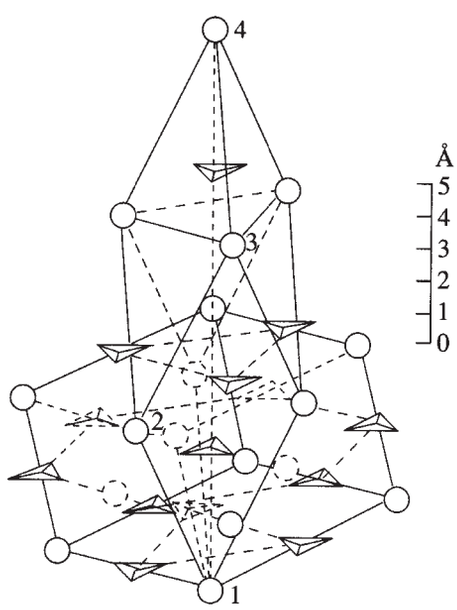


Fig. 298. Face-centred rhombohedral unit cell of calcite containing four $CaCO_3$. Open circles represent Ca atoms and triangles represent CO_3 groups. The elongated rhombohedral unit cell contains two $CaCO_3$ (after Lippmann, 1973, *Sedimentary Carbonate Minerals*, New York, Springer-Verlag).

[a] Value for pure calcite: higher values are due to the substitution of other ions for Ca

[b] Indices for cleavage and twinning, refer to the hexagonal cell with a ~ 20 Å (see Table 57).

Downloaded from https://pubs.geoscienceworld.org/books/chapter-pdf/3763722/9780903056434_ch105.pdf
by guest

Table 57. Calcite unit cells.

		X-ray smallest cell	Cleavage rhomb pseudocell	Cleavage rhomb true cell
Rhombohedral axes	a_{rh} (Å)	6.37	6.42	12.85
	α_{rh}	46.05°	101.92	101.92
	Z_{rh}	2	4	32
	Cleavage rhomb indices	{211}	{100}	{100}
Hexagonal axes	a_{hex} (Å)	~5	~10	~20
	c_{hex} (Å)	~17	~8.5	~17
	Z_{hex}	6	12	96
	Cleavage rhomb indices	{10$\bar{1}$4}	{10$\bar{1}$1}	{10$\bar{1}$1}

A smaller rhombohedral cell can be chosen to describe the lattice however, with parameters a_{rh} 6.37 Å, α 46.08°; this is a primitive cell containing 2 $CaCO_3$ and if the faces of this cell are taken as {100} those of the cleavage rhomb become {211} (Miller-Bravais {10$\bar{1}$4}). The relationship between the morphological (cleavage rhomb) pseudocell and the primitive elongated unit cell is shown in Fig. 298, and data for the various cells are listed in Table 57.

The percentage of calcite in a calcite–dolomite rock or in a calcite–aragonite rock can be determined by measuring the relative intensities of suitable X-ray powder diffraction lines in a series of mixtures of known proportions and applying these results to samples of unknown composition.

Table 58. Carbonate analyses.

	1	2	3	4	5	6	7	8	9
FeO	0.00	0.56	1.0	58.81	0.22	12.06	–	–	–
MnO	tr.	0.12	59.1	2.86	0.00	0.77	–	–	–
MgO	0.04	46.62	0.8	0.20	21.12	12.85	0.03	–	–
CaO	55.92	0.43	0.7	0.08	31.27	29.23	55.96	0.08	7.26
SrO	–	–	–	–	–	–	–	0.68	60.17
BaO	–	–	–	–	–	–	–	77.15	0.31
CO_2	43.95	51.93	38.7	38.08	47.22	44.70	43.95	22.50	31.33
Total	99.91	99.66	100.3	100.03	99.97	100.23	100.07	100.41	99.12
ε	1.488	1.5145	–	1.633	–	1.515	1.5296(α)	–	–
ω	1.661	1.7044	–	1.873	1.6801	1.710	1.6849(γ)	–	–
D	2.720	3.015	–	3.927	2.86	2.97	2.936	4.31	3.63
	Numbers of ions on the basis of 6 O								
Mg	0.002	1.963	0.045	0.011	0.973	0.626	0.001		–
Fe^{2+}	–	0.013	0.032	1.892	0.006	0.330	–		–
Mn	–	0.003	1.895	0.093	–	0.022	–		
Ca	1.997	0.013	0.028	0.003	1.036	1.024	1.999	0.006	0.363
Sr	–	–	–	–	–	–		0.026	1.631
Ba	–	–	–	–	–	–		1.968	0.006

1 Calcite, Mariatrost, Austria (Schoklitsch, K., 1935, *Z. Krist.*, **90**, 433–45).
2 Magnesite, Serra das Eguas, Bahia, Brazil (Fornaseri, M., 1941, *Rend. Soc. Min. Ital.* **I**, 60–5).
3 Rhodochrosite, Oe mine, south-west Hokkaido, Japan (Kojima, S. & Sugaki, A., 1980, *J. Min. Soc. Japan*, **14** (Spec. Issue 3), 27–38). Probe analysis.
4 Siderite, Ivigtut, Greenland (Sundius, N., 1925, *Geol. För. Förh.*, Stockholm, **47**, 269–70).
5 Dolomite, Haley, Ontario, Canada (Harker, R.I. & Tuttle, O.F., 1955, *Amer. J. Sci.*, **253,** 209–24). Includes SiO_2 0.12, H_2O- 0.02.
6 Ankerite, Oak Colliery, Oldham, Lancashire, UK (Broadhurst, F.M. & Howie, R.A., 1958, *Geol. Mag.*, **95**, 397–402). Includes SiO_2 0.15, $A1_2O_3$ 0.28, Fe_2O_3 0.10, Na_2O 0.06, K_2O 0.01, H_2O- 0.02.
7 Aragonite, Matsushiro, Iwami Prov., Japan (Yamaguchi, K., 1927, *J. Geol. Soc. Japan*, **34**, 159–74). β 1.6804, $2V_\alpha$ 18°15′; includes insol. 0.13.
8 Witherite, Anglezarke Moor, Lancashire, UK (Baldasari, A. & Speer, A.J., 1979, *Amer. Min.*, **64**, 742–7).
9 Strontianite, Faylor Quarry, Winfield, Union Co., Pennsylvania, USA (Lapham, D.M. & Geyer, A.R., 1972, *Penn. Geol. Surv. Bull.*, **G-33**). Includes PbO 0.05.

Downloaded from https://pubs.geoscienceworld.org/books/chapter-pdf/3763722/9780903056434_ch105.pdf
by guest

Chemistry

Although various divalent cations may partially replace Ca in calcite, many calcite specimens are relatively free from other ions and are fairly close in composition to pure $CaCO_3$ (e.g. Table 58, analysis 1).

Substitutions which commonly occur include that of Mg. The stability field for magnesian calcites is shown in Fig. 299, but solubilities of higher amounts of as much as 20 mol% $MgCO_3$ are metastable at low temperatures. There is almost neglible solubility of $CaCO_3$ in magnesite, however, this difference reflecting the relative difficulty of substituting the rather large Ca^{2+}ion on a small site in magnesite compared with substituting the smaller Mg^{2+} ion on a larger site as in magnesian calcite. The solid solution of $MgCO_3$ in calcite is one of the most important carbonate solid solutions in nature. The exsolution of dolomite in natural calcite is sometimes observed.

Manganese-bearing calcites are known with up to 42 mol% $MnCO_3$, and experimental work indicates that calcite with up to 50 mol % $MnCO_3$ can exist. The substitution of Fe^{2+} for some Ca is also fairly common, though iron-bearing calcites are less common than iron-bearing dolomites and members of the ankerite series. In natural samples up to 5–10 mol% $FeCO_3$ has been reported.

Small amounts of Sr commonly substitute for Ca, though Sr is less abundant in calcites than in aragonites, the larger Sr^{2+} ion being more acceptable in the aragonite structure. The recrystallization of aragonite to calcite probably only takes place when much of the Sr has been removed. Barium, cobalt and zinc may also occur partially replacing Ca.

The calcite–aragonite polymorphism is brought about by the fact that the radius of the calcium ion is very close to the limiting value for the transition from the rhombohedral carbonate structure type to that of the orthorhombic carbonates. Calcite is the low-pressure polymorph (see aragonite, p. 468 and Fig. 309, p. 469) it can be transformed to aragonite by grinding at room temperature for a few hours. Experimental work shows that calcite melts incongruently to liquid and vapour at 1310 ± 10ºC at 0.1 GPa pressure. In the presence of water vapour at 0.1 GPa, calcite begins to melt at 740ºC. In the system CaO–CaO–H_2O at this pressure, univariant equilibria CaO + $Ca(OH)_2$ + calcite + liquid and calcite + $Ca(OH)_2$ + liquid + vapour occur at 683ºC and 675ºC, respectively (Fig. 300): the development of liquid at moderate temperatures and pressures has important petrological implications.

The terrestrial abundance of the stable isotopes of oxygen and carbon are in the relative ratios $^{16}O/^{17}O/^{18}O$ = 99.763:0.0375:0.1905, respectively, and $^{12}C/^{13}C$ = 99.89:1.11. However fractionation occurs analogous to trace element partitioning, and in particular $\delta^{18}O$ is sensitive to variation in temperature. Determinations of $\delta^{13}C/\delta^{18}O$ ratios have indicated that four genetic calcite groups have specific isotope ratios and occupy their own fields. In calcite of ore-mineral associations, $\delta^{13}C$ falls in the range 0 to −18.1‰; calcite from metamorphic stringers in Jurassic limestone has $\delta^{18}O$ +18.6 to +29‰, which overlaps the range for the limestone (+25.3 to +29.1‰); calcite stalactites have another different set of ratios. For marbles, extrapolation of the calcite–dolomite fractionation expressions to 20ºC indicates that dolomite is enriched in ^{18}O by ~5‰ and in ^{13}C by ~2–3‰.

The solubility of calcite in water increases with increasing CO_2 pressure and decreasing temperature. The precipitation of $CaCO_3$ from $CaCl_2$ and Na_2CO_3 in solution produces calcite at below 35ºC, but mixtures of calcite and aragonite, and also vaterite (μ-$CaCO_3$), are precipitated at higher temperatures.

The dissociation temperature of calcite at atmospheric pressure (0.1 MPa) is 894.4ºC; at 7 and 3.5 MPa CO_2 pressure it is 985ºC and 1100ºC, respectively.

The alteration of calcite is accomplished mainly by solution and replacement, due to its ease of solution in slightly acid waters.

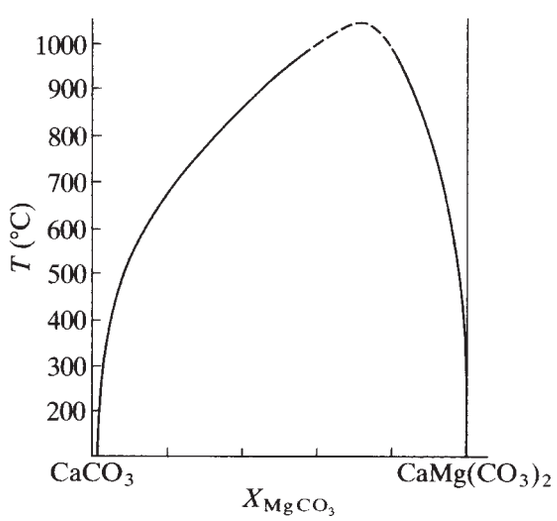


Fig. 299. The calcite–dolomite solvus (after Anovitz, L.M. & Essene, E.J., 1987, *J. Petrol.*, **28**, 389–414).

Downloaded from https://pubs.geoscienceworld.org/books/chapter-pdf/3763722/9780903056434_ch105.pdf
by guest

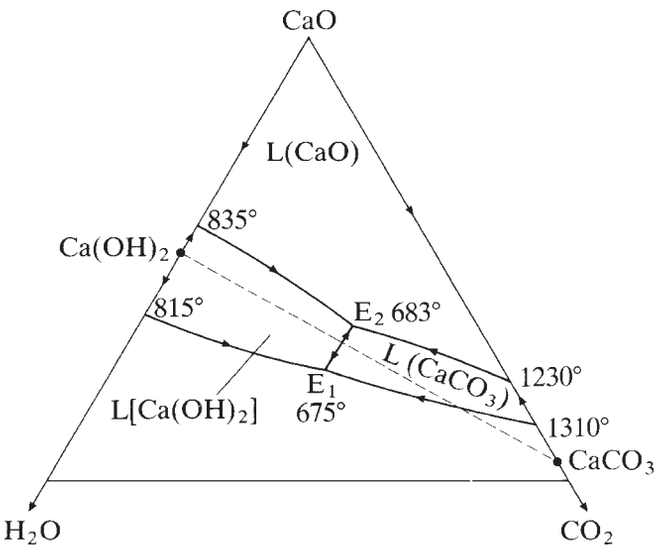


Fig. 300. Enlarged and distorted view of the liquidus field boundaries in the system $CaO-CO_2-H_2O$ at 1 kbar. L(CaO), $L(CaCO_3)$ and $L[Ca(OH)_2]$ are liquidus surfaces with CaO, $CaCO_3$ and $Ca(OH)_2$ respectively as crystalline phases (after Wyllie, P.J. & Tuttle, O.F., 1960, *J. Petrol.*, **1**, 1–46).

Optical and physical properties

Calcite is uniaxial and optically negative with extreme birefringence (Fig. 301). The substitution of other ions for Ca raises the refractive indices: a chart correlating ω with composition for the common rhombohedral carbonates is given in Fig. 302. The strong birefringence ($\omega - \varepsilon = 0.172$) is ascribed to the particular configuration of the (CO_3) groups in the crystal structure. The three oxygen atoms lying in a plane and surrounding a carbon atom are more strongly polarized by an electric field parallel to the plane than by a field perpendicular to it: thus light travels more slowly (i.e. the refractive index is greater) if the electric vector is perpendicular to the *z* axis.

The composition of biogenic and inorganic magnesian calcites are usually determined by X-ray powder diffraction; the *d* spacing of the $10\bar{1}4$ reflection varies nearly linearly with Mg concentration from pure calcite to about 20 mol% $MgCO_3$.

Although most calcite is colourless or white, natural varieties in yellow, pale blue, violet, red or green are known. The entry of appreciable manganese into the structure usually introduces a pale pink to rose-red colour. Many specimens of calcite show luminescence including cathodoluminescence and thermoluminescence, and in ultraviolet radiation many calcites show a weak-to-strong fluorescence at various wavelengths. The phenomena differ for specimens from different localities and have been ascribed to various trace elements: the indiscriminate use of fluorescence for mineral identification can thus give misleading results. The technique of cathodoluminescence petrography often reveals, by

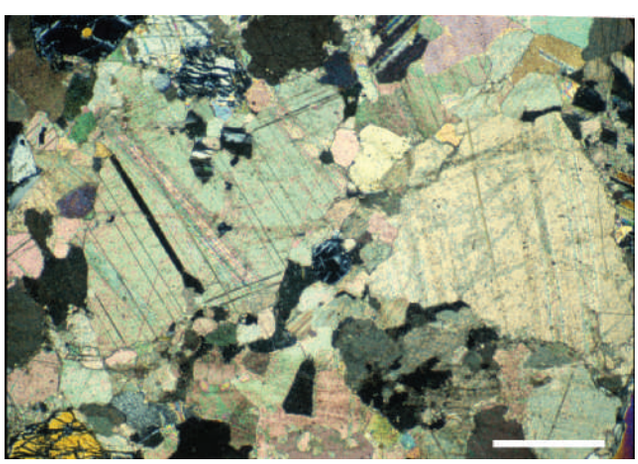


Fig. 301. Calcite in diopside forsterite marble, Loch Duich, Scotland (crossed polars, scale bar 0.5 mm), showing high order interference colours, approaching high-order white (W.S. MacKenzie collection, courtesy of Pearson Education).

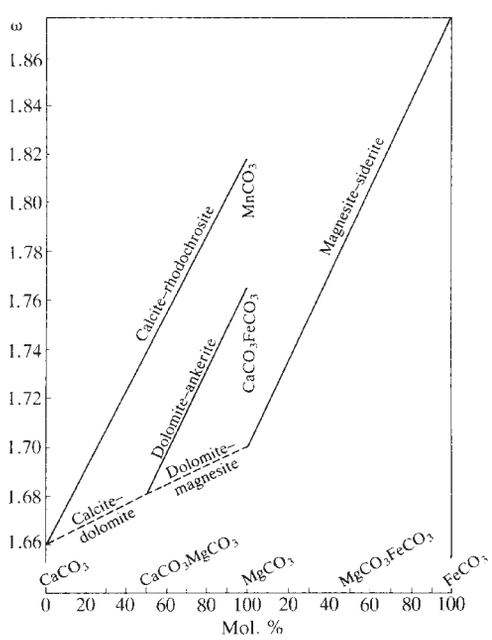


Fig. 302. Variation of ω with composition in the rhombohedral carbonates (after Kennedy, G.C., 1947, *Amer. Min.*, **32**, 561–73).

Downloaded from https://pubs.geoscienceworld.org/books/chapter-pdf/3763722/9780903056434_ch105.pdf
by guest

zoned colour variations, sequential stages of crystal growth.

The density of calcite, like the refractive indices, is raised by any of the usual substituent ions entering the structure. The hardness is 3 on Mohs' scale, but varies from 2½ on {0001} to about 3 on a surface parallel to the *z* axis.

The main lamellar twinning in calcite is that on $\{01\bar{1}2\}$, which gives rise to striae parallel to the edges and to the long diagonal of the cleavage rhomb. This type of twinning can be produced artificially by subjecting calcite to deformation, in which case in addition to twin gliding on $\{01\bar{1}2\}$, there is commonly translation gliding on $\{10\bar{1}1\}$; translation gliding on $\{02\bar{2}1\}$ is also known. The mechanical twinning of calcite can be demonstrated by pressing a knife-blade into one edge of a cleavage rhombohedron: a wedge-shaped opening of constant angle develops and part of the rhombohedron is displaced, the contact or twin plane being $\{01\bar{1}2\}$.

Distinguishing features

Calcite may be recognized as a rhombohedral carbonate by its effervescence with dilute HCl, its perfect $\{10\bar{1}1\}$ cleavage, and its extremely high birefringence. It may be distinguished from the other rhombohedral carbonates by various chemical and physical properties. The refractive indices of calcite are lower than for the other carbonates, with the ε index considerably less than that of the standard mounting medium. The glide twins, which may be particularly evident in calcite of metamorphic rocks, are on $\{10\bar{1}2\}$ rather than on $\{02\bar{2}1\}$ as in dolomite; thus in a cleavage rhombohedron of calcite the twin lamellae lie parallel to the long diagonal of the rhomb (but not to the short diagonal as in dolomite), and other sets are parallel to the rhombohedral edges (see p. 465, Fig. 307). The density of calcite is considerably less than that of dolomite and the other rhombohedral carbonates.

Staining techniques, as applied to hand specimens or thin sections, may be of considerable use in the distinction of calcite from other carbonates (see Table 55, p. 452). In general, organic dyes stain calcite in acid solutions, and dolomite and magnesite in basic solutions: two different stains, Alizarin Red S and potassium ferricyanide, may be used for differentiating calcite, high-magnesium calcite, dolomite, aragonite, gypsum and anhydrite. Other stains specific for calcite are Harris' haematoxylin and copper nitrate (see also p. 465).

Paragenesis

Calcite is one of the most ubiquitous minerals, and in addition to being an important rock-forming mineral in sedimentary environments, it also occurs in metamorphic and igneous rocks and is a common mineral of hydrothermal and secondary mineralization.

In sedimentary rocks calcite is the principal constituent of most limestones. It occurs both as a primary precipitate and in the form of fossil shells. Calcite is the stable form of $CaCO_3$ and although approximately equal numbers of organisms make their shells of calcite and aragonite (or, as for some of the mollusca, of both), the aragonite eventually undergoes recrystallization to calcite. The Chalk of western Europe, although at one time considered to be chemically precipitated $CaCO_3$, has now been shown to consist of up to 80% organic debris, though on a much finer scale than in other fossiliferous limestones.

Low-temperature magnesian calcites are important constituents in biological materials and are particularly common in calcareous sponges, echinoids, crinoids, brachiopods and calcareous algae. They are also found in marine magnesian calcite cements and in some fresh-water tufas.

Precipitated calcite in sediments occurs in the calcrete of surface limestones, and in travertine deposits where, in limestone regions, underground streams may carry considerable quantities of calcium in solution as calcium bicarbonate. On reaching the surface the rise in temperature brings about a release of CO_2, and the growth of mosses and reeds at the exit may extract further CO_2 from the solution, leading to the precipitation of $CaCO_3$ as calcite. The precipitation of $CaCO_3$ in fresh-water lake marls and in marine conditions is generally in the form of aragonite, giving rise to aragonite muds or to aragonite ooliths: in time, however, many of these recrystallize giving rise to calcite mudstones and to an oolitic rock composed of calcite ooliths.

Calcite also occurs in sedimentary rocks as a secondary deposit acting as a cementing medium, as in some oolites and other calcareous rocks, and also in sandstones. A particular form of the latter may occur in which large crystals of calcite contain many thousands of sand grains, a famous example being the sand-calcite of the Fontainebleau district in the Paris basin: in other cases the calcite occurs in crystals of up to 1 cm across, which cause the rock to break preferentially along the calcite cleavage planes giving rise to a phenomenon known as lustre mottling, as each crystal unit gives a more or less brilliant reflection when viewed from an appropriate angle. Veins of fibrous calcite, known as 'beef', occur in some shales, and have the fibres parallel to *z*: the veins may show cone-in-cone structure due to the sensitivity of the rhombohedral cleavage of the fibres to shear.

When sedimentary calcite in limestone undergoes metamorphism a relatively small amount of overburden is sufficient to prevent its breakdown and the escape of CO_2, and in the normal course of events the calcite merely recrystallizes to form a marble. Calcite is thus a relatively common mineral in calcareous sediments

Downloaded from https://pubs.geoscienceworld.org/books/chapter-pdf/3763722/9780903056434_ch105.pdf
by guest

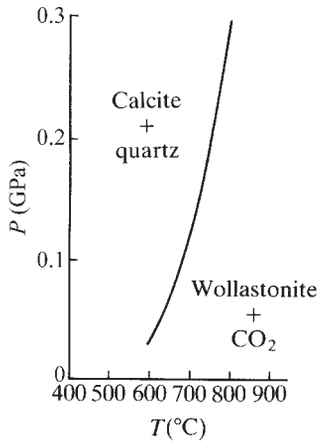


Fig. 303. The experimentally determined univariant $P_{CO_2}-T$ curve for the reaction $CaCO_3 + SiO_2 \rightleftharpoons CaSiO_3 + CO_2$ (after Harker, R.I. & Tuttle, O.F., 1956, *Amer. J. Sci.*, **254**, 239–56).

which have been thermally or regionally metamorphosed. If the original sediments contained other material in addition to $CaCO_3$, or if metasomatic introduction of other elements occurs during the metamorphism, the calcite may react and give rise to various mineral assemblages. Where, in addition to $CaCO_3$, SiO_2 is present, the reaction $CaCO_3 + SiO_2 \rightleftharpoons CaSiO_3 + CO_2$ may take place, with the formation of wollastonite. The disappearance of the calcite–quartz assemblage to give rise to wollastonite is thus of considerable interest as a geothermometer (Fig. 303). In certain circumstances the CO_2 pressure may be effectively reduced, however, either by a dilution by some other volatile component or by the escape of CO_2 through fissures, and the calcite may then react at somewhat lower temperatures: thus it is probable that a decarbonation reaction will proceed more readily in an impure wet limestone than in a pure dry one. In both thermally and regionally metamorphosed impure limestones calcite may be found in association with such calc-silicate minerals as diopside, tremolite, vesuvianite and grossular garnet, and also with forsterite.

Calcite commonly crystallizes in the later stages of hydrothermal deposition, in veins and cavities. Well formed crystals may be found in amygdales in basic igneous rocks, where calcite is commonly associated with zeolites or with quartz. One of the best-known localities in Iceland for the Iceland spar variety of calcite is at Helgustadir, where crystals of optical quality occur associated with quartz, heulandite and stilbite. In many hydrothermal veins calcite is associated with fluorite, baryte, dolomite, quartz and sulphides.

Calcite also occurs in certain alkaline igneous rocks, notably the carbonatites, lamprophyres, kimberlites and some nepheline syenites. It had been suggested that the association of carbonates with alkaline rocks was due to the contamination of a magma with carbonate rock. The experimental work on the system $CaO-CO_2-H_2O$, however, offers strong evidence in favour of a true magmatic origin for carbonatites either as a primary magma or by liquid immiscibility between carbonate-rich and silicate-rich melts. The low-temperature liquids in this system can be regarded as simplified carbonatite magmas in which CaO represents the basic oxides with CO_2 and H_2O representing the volatile constituents, and in this system it has been shown that the high melting temperature of calcite is lowered markedly by the addition of CO_2 and H_2O under pressure.

Further reading

Ferrill, D.A., Morris, A.P., Evans, M.A., Burkhard, M., Groshong, R.H. and Onasch, C.M. (2004) Calcite twin morphology: a low-temperature deformation geothermometer. *Journal of Structural Geology*, **26**, 1521–1529.

Friedman, M. (1959) Identification of carbonate minerals by staining methods. *Journal of Sedimentary Petrology*, **29**, 87–90.

Friedman, I. and O'Neil, J.R. (1977) Compilation of stable isotope fractionation factors of geochemical interest. *Data of Geochemistry*, 6th edition, US Geological Survey Professional Paper 440 KK.

Goldsmith, J.R. (1983) Phase relations of rhombohedral carbonates. Pp. 49–76 in: *Carbonates*: *Mineralogy and Chemistry* (R.J. Reeder, editor). Reviews in Mineralogy, **11**, Mineralogical Society of America, Washington, D.C.

Goldsmith, J.R. and Newton, R.C. (1969) P–T–X relations in the system $CaCO_3-MgCO_3$ at high temperatures and pressures. *American Journal of Science*, **267A**, 160–190.

Mackenzie, F.T., Bischoff, W.D., Bishop, F.C., Loijens, M., Schoonmaker, J. and Wollast, R. (1983) Magnesian calcites: low-temperature occurrence, solubility and solid-solution behavior. Pp. 97–144 in: *Carbonates: Mineralogy and Chemistry* (R.J. Reeder, editor). Reviews in Mineralogy, **11**, Mineralogical Society of America, Washington, D.C.

Reeder, R.J. (1983) Crystal chemistry of the rhombohedral carbonates. Pp. 1–47 in: *Carbonates: Mineralogy and Chemistry* (R.J. Reeder, editor). Reviews in Mineralogy, **11**, Mineralogical Society of America, Washington, D.C.

Wyllie, P.J. and Tuttle, O.F. (1960) The system $CaO-CO_2-H_2O$ and the origin of carbonatites. *Journal of Petrology*, **1**, 1–46.

Downloaded from https://pubs.geoscienceworld.org/books/chapter-pdf/3763722/9780903056434_ch105.pdf
by guest

Magnesite $MgCO_3$

Trigonal (−)

ε	1.509[a]−(1.563)
ω	1.700−(1.782)
δ	0.190−(0.218)
D (g/cm^3)	2.98−(3.48)
H	3½− 4½
Cleavage[b]	{10$\bar{1}$1} perfect
Twinning	Translation gliding may occur on {0001} in the direction [10$\bar{1}$1]
Colour	White or colourless, but the iron-bearing varieties may be yellow or brown; colourless in thin section
Pleochroism	Rare; in coloured varieties the absorption may be ε < ω
Unit cell	a_{hex} 4.632 Å, c_{hex} 15.012 Å Z = 6 a_{rh} 5.675 Å, α 48.10° Z = 2; space group $R\bar{3}c$
Special features	Slightly soluble in cold dilute HCl; soluble with effervescence in warm HCl.

The structure of magnesite is similar to that of calcite but with a slightly smaller cell due to the smaller size of the magnesium ion.

Pure end-member magnesite has the composition $MgCO_3$, and there appears to be a complete solid-solution series between magnesite and siderite, $FeCO_3$. The ferroan variety, breunnerite, extends from 5 to 50 mol% $FeCO_3$. The substitutions of Mn for Mg and of Ca for Mg are both limited (Table 58, analysis 2). Experimental work shows evidence of slight solid solution of calcite in magnesite (Fig. 304). Magnesite is an important raw material for basic refractories: after heating and sintering, the product known as 'dead-burned magnesite' is produced which has the composition MgO (periclase).

The refractive indices and birefringence of magnesite increase linearly with the substitution of Fe^{2+} or Mn for Mg (see Fig. 302, p. 456).

Magnesite resembles dolomite in being only slightly soluble in cold dilute HCl, but it dissolves with effervescence in warm acid. It differs from dolomite and calcite in usually showing no twin lamellae, and in having higher refractive indices.

The most common occurrence of magnesite is as an alteration product of various magnesium-rich igneous and metamorphic rocks. Peridotites commonly become transformed to serpentinites and if such rocks undergo low- or medium-grade metamorphism under conditions in which CO_2 is available magnesite may be formed. The presence of monomineralic deposits of magnesite associated with talc and chlorite in Shetland has been ascribed to localized shearing movements, assisted by the penetration of hydrothermal fluids. It also occurs in evaporite deposits and as the result of Mg metasomatism of pre-existing sediments.

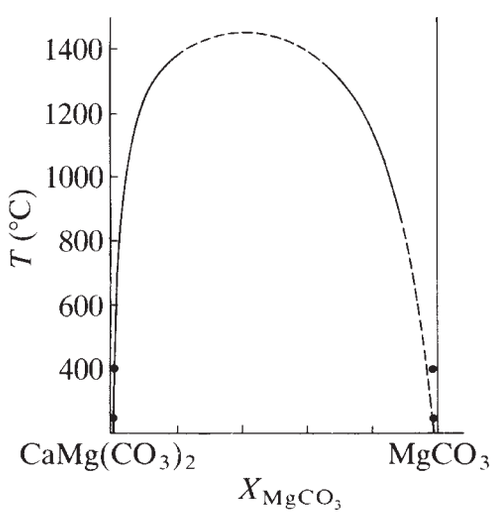


Fig. 304. The magnesite−dolomite solvus (after Anovitz, L.M. & Essene, E.J., 1987, *J. Petrol.*, **28**, 389−415).

[a] Pure magnesite: higher values are due to the substitution of Mg by other ions.

[b] Indices for cleavage and twinning, refer to the hexagonal cell with $a = 4a_{hex}$ (see Table 57, p. 454).

Downloaded from https://pubs.geoscienceworld.org/books/chapter-pdf/3764120/9780903056434_ch106.pdf
by guest

Further reading

Byrnes, A.P. and Wyllie, P.J. (1981) Subsolidus and melting relations for the join $CaCO_3$–$MgCO_3$ at 10 kbar. *Geochimica et Cosmochimica Acta*, **45**, 321–328.

Zhang, R.Y. and Liou, J.G. (1994) Significance of magnesite paragenesis in ultrahigh-pressure metamorphic rocks. *American Mineralogist*, **79**, 397–400.

Downloaded from https://pubs.geoscienceworld.org/books/chapter-pdf/3764120/9780903056434_ch106.pdf
by guest

Trigonal (−)

ε	(1.575)−1.635[a]
ω	(1.782)−1.875
δ	(0.207)−0.240
D (g/cm^3)	(3.5)−3.96
H	4− 4½
Cleavage[b]	{10$\bar{1}$1} perfect
Twinning	Occasional lamellar twinning on {01$\bar{1}$2}, rare twins on {0001}
Colour	Yellowish brown, brown or dark brown; colourless to yellowish brown in thin section
Unit cell	a_{hex} 4.69−4.73 Å, c_{hex} 15.37−15.46 Å Z_{hex} = 6 a_{rh} 5.77−5.84 Å, α 47.43° Z_{rh} = 2; space group $R\bar{3}c$.
Special features	Slowly soluble in cold dilute HCl; dissolves with effervescence in hot acid. On heating, CO_2 is driven off leaving an iron oxide.

Siderite occurs in bedded sedimentary iron ores, usually massive, but also in botryoidal and globular forms and in earthy masses. It is found also in hydrothermal sulphide veins and in some metamorphic deposits, such as banded iron formations. The term 'sphaerosiderite' is used for the spherulites of siderite sometimes found in clay ironstones.

Structure

The structure of siderite is similar to that of calcite, but with smaller cell parameters due to the smaller ionic radius of Fe^{2+} as compared with Ca.

Chemistry

Substitution of Fe^{2+} by other metallic ions is common in siderite and the mineral is rarely found as pure $FeCO_3$. Both Mn and Mg commonly substitute for Fe^{2+} (e.g. Table 58, p. 454, analysis 4), and there is complete solid solution between siderite and rhodochrosite and between siderite and magnesite. Magnesian siderite has been described using the names sideroplesite (5−30 mol% $MgCO_3$) or pistomesite (30−50 mol% $MgCO_3$) but these are now obsolete. The substitution of Ca for Fe^{2+} appears to be limited to 10−15% $CaCO_3$, probably due to the appreciable difference in size of these ions (Fig. 305).

Siderite may be produced artificially by heating $(NH_4)_2CO_3$ with $FeCl_2$. It decomposes at about 580ºC and the resultant FeO oxidizes at about 600ºC.

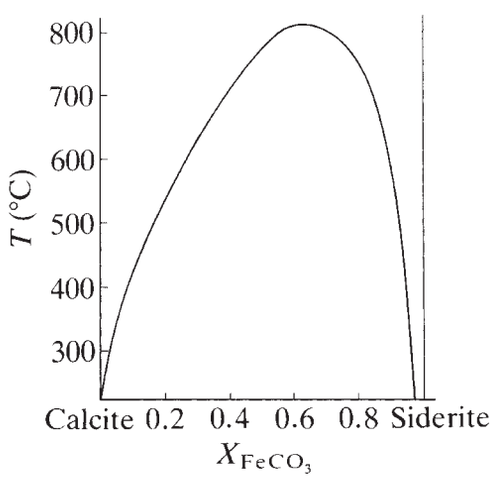


Fig. 305. The calcite–siderite solvus (after Anovitz, L.M. & Essene, E.J., 1987, *J. Petrol.*, **28**, 389−415).

[a] Value for pure siderite: lower values are due to the substitution of Fe by other ions.
[b] Indices for cleavage, twinning, etc., refer to the hexagonal cell with a ~ 19 Å (see Table 57, p. 454).

Downloaded from https://pubs.geoscienceworld.org/books/chapter-pdf/3764153/9780903056434_ch107.pdf
by guest

The most common alteration product of siderite is a hydrous ferric oxide, which is commonly described as limonite (p. 417). It may also alter to hematite and magnetite.

Optical and physical properties

For pure end-member, $FeCO_3$, the extrapolated refractive indices are ε 1.635, ω 1.875, with a density of 3.96 g/cm^3. With the substitution of Mn for Fe^{2+} the refractive indices, birefringence and density are reduced, and the substitution of Mg for Fe^{2+} reduces the values of these properties to an even greater extent (Fig. 302, p. 456).

Distinguishing features

Within the group of trigonal carbonates, siderite differs from calcite in its relative insolubility in cold dilute HCl, and from magnesite in its fairly common lamellar twinning. Its refractive indices are always greater than that of the normal mounting medium whereas for calcite, dolomite and magnesite $\varepsilon < 1.54$. Its density is considerably higher than that of any other common rhombohedral carbonate, though smithsonite ($ZnCO_3$) has a density of 4.0–4.4 g/cm^3. On heating, siderite forms a black iron oxide which may be magnetic. It may be distinguished from minerals of other groups by its well-developed rhombohedral cleavage and high birefringence.

Paragenesis

The most common occurrence of siderite is in banded iron formations (BIFs); it is the chief iron-bearing mineral in clay ironstones. Banded iron formations are known from every Precambrian continental region; they are often very abundant and an important source of iron. In the oolitic Jurassic ironstones of the English Midlands it is one of the principal ore minerals, together with chamosite and hydrated iron oxides. The origin of these deposits is not entirely certain but it is generally assumed that the iron was derived from continental sources by the normal processes of weathering, being transported as the bicarbonate and precipitated when CO_2 was not present in sufficient amount to maintain all the iron as the soluble bicarbonate. Much siderite results from carbonation of chamosite, and it may also be formed by the penecontemporaneous replacement of calcite by $FeCO_3$.

Siderite also occurs as a hydrothermal mineral in metallic veins, where it may be manganoan: the iron-rich carbonates of the Coeur d'Alene district of Idaho are associated with Pb, Ag and Zn sulphide orebodies. Its occurrence in the Ivigtut cryolite deposit is well known (Table 58, analysis 4), where it is considered to be of pegmatitic–pneumatolytic origin.

Further reading

James, H.L. (1954) Sedimentary facies of iron-formation. *Economic Geology*, **49**, 235–293.

Klein, C. (2005) Some Precambrian banded iron-formations (BIFs) from around the world: their age, geologic setting, mineralogy, metamorphism, geochemistry, and origin (Presidential Address). *American Mineralogist*, **90**, 147–199.

Smythe, J.A. and Dunham, K.C. (1947) Ankerites and chalybites from the northern Pennine orefield and the north-east coalfield. *Mineralogical Magazine*, **28**, 53–74.

Trendall, A.F. (1973) Precambrian iron-formations of Australia. *Economic Geology*, **68**, 1032–1034.

Downloaded from https://pubs.geoscienceworld.org/books/chapter-pdf/3764153/9780903056434_ch107.pdf
by guest

Dolomite $CaMg(CO_3)_2$

Trigonal (−)

ε	1.500[a]−(1.520)
ω	1.679−(1.703)
δ	0.179−(0.185)
D (g/cm^3)	2.86−(2.93)
H	3½− 4
Cleavage[b]	{10$\bar{1}$1} perfect
Twinning	Common on {0001}, {10$\bar{1}$0}, {11$\bar{2}$0}, rare on {10$\bar{1}$1}; glide twinning {02$\bar{2}$1}
Colour	Colourless or white, often tinged with yellow or brown; colourless in thin section
Unit cell	a_{hex} 4.807 Å, c_{hex} 16.00 Å Z_{hex} = 3 a_{rh} 6.015 Å, α 47.10° Z_{rh} = 1; space group $R\bar{3}$
Special features	Soluble with difficulty in cold dilute HCl.

Dolomite is common in sedimentary rocks, where it is formed mostly as a diagenetic product in limestones. It occurs also in marbles and other metamorphic rocks, and in evaporites. Carbonatites may contain dolomite as an igneous mineral. The majority of dolomites have a composition close to $CaMg(CO_3)_2$; it is common, however, for the Mg to be partly replaced by Fe and/or Mn to produce ferroan dolomite or ankerite $Ca(Fe,Mg,Mn)(CO_3)_2$.

Structure

The structure of dolomite resembles that of calcite but has a slightly lower symmetry. The diads in calcite which intersect in the carbon atom and on which the oxygens lie are not present in dolomite, and neither are the glide planes {11$\bar{2}$0}; the symmetry of dolomite thus consists of only a triad axis and a centre of symmetry. It is best considered as combining one layer of $CaCO_3$ from calcite and one layer of $MgCO_3$ from magnesite. The replacement of some Mg by Fe^{2+} has the effect of increasing the size of the unit cell; most sedimentary dolomites also have unit cells expanded relative to ideally ordered single-crystal dolomites.

Chemistry

Although the composition is normally fairly close to pure $CaMg(CO_3)_2$, many dolomites contain small amounts of Fe^{2+} replacing Mg, giving the mineral a brownish tinge in hand specimen: among the purest dolomites is that of Table 58, analysis 5 (p. 454), and the water-clear dolomite from Gabbs, Nevada. There is a continuous replacement of Mg by Fe^{2+}, through ankerite towards $CaFe(CO_3)_2$: the term dolomite is here restricted to material with Mg/Fe > 4. Manganese also commonly replaces Mg and although dolomite with more than about 3% MnO is rare a continuous series to kutnohorite, $CaMn(CO_3)_2$, may exist. Zinc- and lead-rich dolomites are also known. For the ordered $Ca^{2+}R^{2+}(CO_3)_2$ compounds the relative stabilities appear to be R^{2+} = Mg >> Mn > Zn > Fe > Co > Ni. Dolomites from carbonatites may contain appreciable Sr and also rare earths, with Ce more abundant than La. The $\delta^{18}O$ value of dolomite at near-surface temperatures is about 3−6‰ heavier than for cogenetic calcite and decreases with increasing temperature. For ^{13}C, sedimentary dolomites have δ values about 2−3% heavier than their cogenetic calcites. There is also some evidence for the existence of natural dolomite with up to 5 mol% excess structural $CaCO_3$.

A typical morphological feature which is commonly present on well crystallized dolomites is the occurrence of curved or distorted faces giving a saddle shape. Electron microscopy has revealed profuse coherent laths

[a] Value for pure dolomite.
[b] Indices for cleavage, twinning, etc., refer to the hexagonal cell with $a = 4a_{hex}$ (see Table 57, p. 454).

Downloaded from https://pubs.geoscienceworld.org/books/chapter-pdf/3764177/9780903056434_ch108.pdf
by guest

of calcitic material, explaining the characteristic excess Ca found in most saddle dolomites. Because the lattice spacings of calcite are 4–6% larger than those of dolomite, these calcitic ribbons cause local microscopic distortion and are probably the source of distortion seen on the macroscopic scale.

The use of coexisting calcite and dolomite as a geothermometer involves determining the mol% $MgCO_3$ once dissolved in calcite equilibrated with dolomite (Fig. 299, p. 455). This has been extensively used to evaluate conditions of metamorphism, as it is independent of fluid composition and any pressure correction is small. It is not suitable for temperatures higher than about 650ºC and is not well constrained below 400ºC. The iron correction, for extension to the system $CaCO_3$–$MgCO_3$–$FeCO_3$, has also been established (Fig. 306), but the entry of any appreciable Mn gives erratic results. Carbonate geothermometry is thus best suited to greenschist to middle-amphibolite facies terranes.

Artificial dolomite has never been directly precipitated in the laboratory from solutions at ordinary temperatures and pressures. Its field of stability for moderate temperatures and high CO_2 pressures has been determined (Fig. 299): this confirms the small deviation from the ideal 1:1 Ca/Mg ratio of dolomite, in the direction of excess Ca, for material in equilibrium with magnesian calcite at high temperature. In experimental runs at low temperatures rather calcium-rich dolomite-like materials, or protodolomites, are produced, and it may be that the necessity for obtaining an ordered arrangement of Ca and Mg at relatively rapid rates of crystallization is responsible for the difficulty of producing dolomite at ordinary temperatures. Ions other than Ca, Mg and (CO_3) may be important in the precipitation of dolomite; for example, synthetic dolomite can be precipitated from a solution of $MgCl_2$, $CaCl_2$ and urea at slightly elevated pressures (above 0.2 or 0.3 MPa) and at 220ºC, but the presence of 6–7% NaCl in the solution extends the temperature range over which dolomite can be precipitated down to as low as 150ºC. The presence of sulphates has also been suggested as an essential condition for the low-temperature precipitation of dolomitic carbonates.

The thermal dissociation of dolomite takes place in two steps:

$$CaMg(CO_3)_2 \rightarrow CaCO_3 + MgO + CO_2$$

at around 800ºC, followed by the breakdown of the calcite component,

$$CaCO_3 \rightarrow CaO + CO_2$$

at just over 900ºC.

The thermal stability of dolomite in the system $CaCO_3$–$CaMg(CO_3)_2$ was investigated by Goldsmith and Heard (1961), and extended to high pressures by Irving and Wyllie (1975) and Byrnes and Wyllie (1981).

Commercially, dolomite is of considerable importance as a refractory, for which purpose it is calcined at about 1500ºC, resulting in a sintered mixture of MgO (periclase) and CaO. It is also used in the extraction of magnesia from sea-water.

Optical and physical properties

In transmitted light pure dolomite is colourless with ε 1.500, ω 1.679; the substitution of Fe^{2+} for Mg, however, increases the refractive indices (see Fig. 302, p. 456) and also the birefringence. The substitution of Mn for Mg has a similar though smaller effect. Glide twinning occurs on $\{02\bar{2}1\}$ giving lamellar twins. The experimental deformation of dolomite rock has shown that after being subjected to 0.3 GPa pressure at 380ºC a cylinder of dolomite had shortened by 9.4% and had twin gliding on $\{02\bar{2}1\}$ and translation gliding on {0001}.

Dolomite when pure is colourless or pearly white but the small amount of Fe^{2+}, which often substitutes for

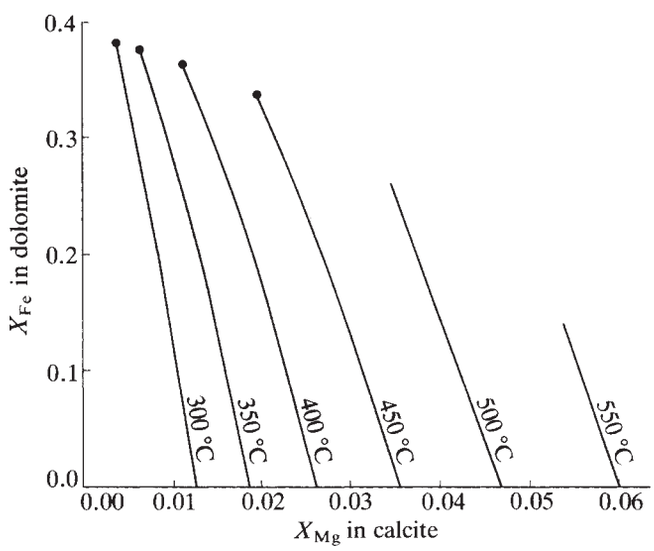


Fig. 306. A plot of the mol fraction of iron in dolomite *vs.* the mol fraction of magnesium in calcite for temperatures of 300–550ºC for equilibrium between calcite and dolomite; ●, compositions for the three-phase assemblage calcite–siderite–dolomite (after Powell *et al.*, 1984).

Downloaded from https://pubs.geoscienceworld.org/books/chapter-pdf/3764177/9780903056434_ch108.pdf
by guest

Mg, commonly gives it a yellow or brown colour. The more iron-rich dolomites commonly weather to a darker brown. The presence of appreciable Mn gives rise to a rose-pink colour. Dolomite appears mostly as a fine to coarse cleavage aggregate; euhedral crystals are, however, rather common as simple rhombohedra often with markedly curved faces. The latter, called saddle or baroque dolomite, is widely associated with high fluid temperature (>60ºC), as also is zebra dolomite which consists of alternating layers of dark replacement and light void-filling saddle or sparry dolomite.

Distinguishing features

Dolomite may be distinguished as a rhombohedral carbonate by its extremely high birefringence in conjunction with its perfect $\{10\bar{1}1\}$ cleavage. It shows a rhombohedral form, the rhombohedral faces commonly being slightly curved. The distinction of dolomite from the other rhombohedral carbonates may be made by various physical and chemical tests. Dolomite is denser than calcite (2.86 compared with 2.72 g/cm^3), and has higher refractive indices. Glide twinning occurs on $\{02\bar{2}1\}$ rather than on $\{01\bar{1}2\}$ as in calcite; thus in a cleavage rhombohedron of dolomite the glide twin lamellae lie parallel to the short diagonal of the rhomb as well as parallel to the long diagonal as in calcite (in which other sets of twin lamellae lie parallel also to the rhombohedral edge). Twinned grains may be distinguished from calcite by their extinction angle measured between the fast direction ε′ and the trace of the twin lamellae. Suitable sections cut the twin lamellae at high angles, showing them sharply defined; these sections are inclined at low angles to the optic axis, and show a pronounced change in relief on rotation in plane-polarized light. The angle between ε′ and the trace of the twin lamellae is greater than 55º in calcite and usually between 20º and 40º in dolomite. Also, if one grain shows two sharply defined sets of twin lamellae, ε′ (the direction of lower refractive index) lies in the acute angle for dolomite, whereas for calcite it lies in the obtuse angle of intersection (Fig. 307).

Using an X-ray diffractometer, a scan between 28 and 32º2θ (Cu-$K\alpha$) will establish the position of the very strong $10\bar{1}4$ reflection at d = 2.886 Å (~30.96º) for dolomite and d = 3.035 Å (~29.42º) for calcite.

Dolomite, unlike calcite, is only slowly soluble in cold dilute acids, and does not effervesce: freshly powdered dolomite does react, and dissolves readily with effervescence in warm acids. Treatment with copper nitrate solution and fixing with ammonia gives a deep blue colour on calcite but not on dolomite. If carbonate chips are boiled with copper nitrate alone, aragonite or calcite develops a pale (Cambridge) blue colour after boiling for up to five minutes: dolomite is unaffected in this period. With a 0.1% solution of Alizarin Red S in M/15 HCl, calcite takes a reddish stain whereas dolomite is unaffected (see also pp. 452 and 457). A direct test for Mg may be made by covering the section except for the sample grain, adding a drop of dilute H_2SO_4 and warming slightly; after effervescence has ceased moisten with ammonium carbonate $[(NH_4)_2CO_3]$ solution, place a drop of microcosmic salt solution near by, warm the slide and gently unite the two drops: orthorhombic crystals of magnesium ammonium phosphate indicate the presence of Mg. Dolomite may be distinguished from magnesite by heating to about 550ºC for one hour; magnesite changes to periclase which can be readily distinguished microscopically from the unaltered dolomite.

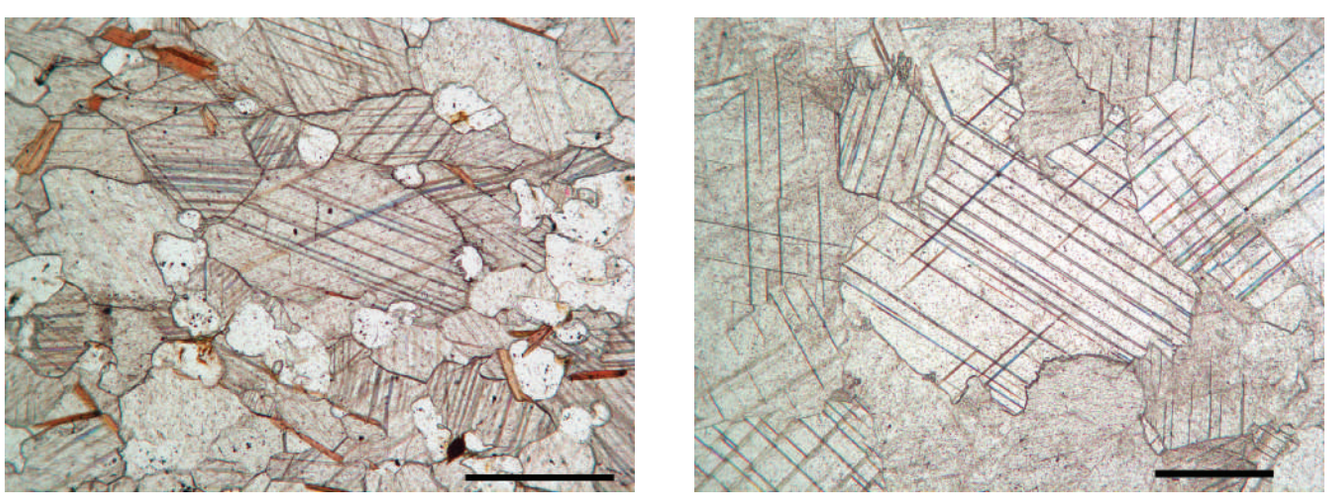


Fig. 307. (*left*) Calcite, quartz-biotite-calcite schist, Perthshire, Scotland, showing two sets of multiple twinning intersecting at a moderately low angle (ppl, scale bar 0.5 mm). (*right*) Dolomite, marble, Qadda, Saudi Arabia (ppl, scale bar 0.2 mm), showing two sets of twins intersecting at ~80º. Both carbonates show high relief and large variation in relief with orientation, due to high bireferingence. (courtesy of G.T.R. Droop)

Downloaded from https://pubs.geoscienceworld.org/books/chapter-pdf/3764177/9780903056434_ch108.pdf
by guest

Paragenesis

Dolomite occurs typically as a mineral of sedimentary environments, though there are important occurrences in metamorphic and hydrothermal metasomatic deposits. A few sedimentary deposits are thought to have contained dolomite initially, having precipitated directly from highly saline solutions such as isolated marine waters or saline lakes, and include dolomite associated with evaporite deposits, as in the Permian evaporites of north-east England. A thin bed of nearly pure unconsolidated dolomite occurs ~0.3 m below the surface of the Great Salt Lake Desert, west of Knolls, Utah, and is believed to have been precipitated from a saline lake left isolated from Great Salt Lake. In the sabkha of the Trucial Coast, Arabian Gulf, crystals of dolomite are precipitated within the supratidal zone, a metre or so beneath the surface.

Dolomite is important both as a metasomatic replacement and as a 'void filling' mineral.

Dolomite formation is thermodynamically favoured in solutions with low Ca^{2+}/Mg^{2+} and low Ca^{2+}/CO_3^{2-} (or Ca^{2+}/HCO_3^-) ratios and high temperatures. Chemical conditions conducive to dolomitization include alkaline environments, temperatures above 50ºC and salinity above saturation with respect to dolomite. Shallow, hypersaline subtidal environments favour massive replacement dolostones*.

The percentage of dolomite in dolomitic carbonate rocks in various Phanerozoic depositional environments throughout North America shows a distinct bimodal distribution with modes at 97% (dolostones) and 20% (dolomitic limestones). These data may indicate that two separate processes occurred, dolomitic limestones originating in diagenetically closed systems during magnesian calcite dissolution and precipitation of calcite and dolomite, and dolostones originating in diagenetically open systems during the dissolution of $CaCO_3$ precursors in the presence of allochthonous Mg ions. Most dolostones consist of stoichiometric dolomite whereas most dolomitic limestones contain rhombs of calcian dolomite.

Dolomite formed from limestone by metasomatic alteration can be divided into two classes. One occurs over relatively wide areas at one horizon and was formed very soon after deposition of the limestone, the dolomitization having probably occurred while the sediment was in an unconsolidated condition on the sea floor, this being referred to as penecontemporaneous dolomitization. In the other type of occurrence the dolomite formed much later than the lithification of the limestone, the magnesian solutions having entered through faults and joints. Dolomitization is a very selective process, in some cases replacing only the matrix or even only shell fragments, depending partly on whether recrystallization has taken place and whether the $CaCO_3$ is present as calcite or aragonite. The magnesium for dolomitization must have been derived from sea-water but the mechanism involved is not clear: the necessity for obtaining an ordered arrangement of Ca and Mg in the structure of dolomite may imply that at normal temperatures the time factor may be of considerable importance.

The present-day formation of dolomitic sediments in a number of saline lakes and in a shallow inlet of the sea has been ascribed to elevated pH caused by plant growth in shallow saline water.

There is some evidence that dolomitization can only take place at low dissolved sulphate concentrations and insubstantial contemporaneous silica diagenesis. Common sites for dolomitization are areas where dissolved sulphate is reduced by microbial sulphate reduction. Dolomite formation may be inhibited by the transformation of amorphous silica (opal-A) to opal-CT, but subsequent transformation to quartz favours the formation of dolomite, possibly by the production of nuclei with Mg^{2+} and OH^- from the opal-CT structure. It has also been suggested that some post-compactional dolomite is the result of the diagenesis of smectite to illite, similarly releasing Mg (and Si).

Well crystallized dolomite occurs in hydrothermal veins, associated with ores of lead, zinc and copper, and with fluorite, baryte, calcite, siderite and quartz. A dolomite-rich alkaline intrusive dyke has been recorded cutting the Permian evaporite deposits of New Mexico, and consists of sodic plagioclase phenocrysts, dolomite rhombs, and small amygdales of dolomite and natrolite set in a groundmass of orthoclase, biotite and ilmenite. Dolomitic or dolomitic–sideritic carbonatites are known from many carbonatite complexes. Dolomite is also typically associated with altered ultrabasic igneous rocks where it may occur with magnesite in serpentinites and talc-bearing rocks.

In metamorphic rocks dolomite occurs chiefly in contact or regionally metamorphosed magnesian or dolomitic limestones where it may recrystallize to form a dolomitic marble. At a higher grade of metamorphism the dolomite may break down in two stages:

$$CaMg(CO_3)_2 \rightarrow CaCO_3 + MgO + CO_2$$
$$MgO + H_2O \rightarrow Mg(OH)_2$$

thus leading to the formation of periclase and later brucite, giving the rock types pencatite, or with more abundant calcite, predazzite. In the progressive metamorphism of siliceous dolomite-bearing limestones the dolomite enters into the formation of talc, tremolite, forsterite and periclase, and may itself be temporarily reformed by the reaction:

$$2\ \text{talc} + 3\ \text{calcite} \rightarrow 1\ \text{tremolite} + 1\ \text{dolomite} + CO_2 + H_2O$$

* The term *dolomite* is used by many to describe a rock composed mainly of dolomite, but *dolostone* was introduced in order to avoid ambiguity with dolomite used as a mineral name.

Downloaded from https://pubs.geoscienceworld.org/books/chapter-pdf/3764177/9780903056434_ch108.pdf
by guest

The exsolution of dolomite in calcite has been recorded in marbles associated with granulite-facies metamorphism and from carbonate rocks almost completely engulfed in a quartz-bearing pyroxene diorite: from the subsolidus relations between $CaCO_3$ and $CaMg(CO_3)_2$ a calcite host is to be expected for such exsolution intergrowths. The term dedolomitization is used for dolomite solution and concurrent precipitation of calcite.

Further reading

Anovitz, L.M. and Essene, E.J. (1987) Phase equilibria in the system $CaCO_3$–$MgCO_3$–$FeCO_3$. *Journal of Petrology*, **28**, 389–414.

Bogosch, R., Magaritz, M. and Michard, A. (1986) Dolomite of possible mantle origin, southeast Sinai. *Chemical Geology*, **56**, 281–288.

Botz, R.W. and Von der Borth, C.C. (1984) Stable isotope study of carbonate sediments from the Coorong area, South Australia. *Sedimentology*, **31**, 837–849.

Byrnes, A.P. and Wyllie, P.J. (1981) Subsolidus and melting relations for the join $CaCO_3$–$MgCO_3$ at 10 kbars. *Geochimica et Cosmochimica Acta*, **45**, 321–328.

Davies, G. and Smith, L. (2006) Structually controlled hydrothermal dolomite reservoir facies: an overview. *AAPG Bulletin*, **90**, 1641–1690.

Goldsmith, J.R. and Heard, H.C. (1961) Subsolidus phase relations in the system $CaCO_3$–$MgCO_3$. *Journal of Geology*, **69**, 45–74.

Howie, R.A. and Broadhurst, F.M. (1958) X-ray data for dolomite and ankerite. *American Mineralogist*, **43**, 1210–1214.

Irving, A.J. and Wyllie, P.J. (1975) Subsolidus and melting relationships for calcite, magnesite and the join $CaCO_3$–$MgCO_3$ to 36 kbars. *Geochimica et Cosmochimica Acta*, **29**, 35–53.

Kretz, R. (1982) A model for the distribution of trace elements between calcite and dolomite. *Geochimica et Cosmochimica Acta*, **46**, 1979–1981.

Land, L.S. (1983) The application of stable isotopes to studies of the origin of dolomite and to problems of diagenesis in clastic sediments. Pp. 4.1–4.22 in: *Stable Isotopes in Sedimentary Geology* (M.A. Arthur and T.F. Anderson, editors). Short Course 10. Society of Economic Paleontologists and Mineralogists.

Pokrovsky, G.S., Golubev, S.V. and Schott, J. (2005) Dissolution kinetics of calcite, dolomite and magnesite at 25ºC and 0 to 50 atm pCO_2. *Chemical Geology*, **217**, 239–55.

Powell, R., Condliffe, D.M. and Condliffe, E. (1984) Calcite-dolomite geothermometry in the system $CaCO_3$–$MgCO_3$–$FeCO_3$: an experimental study. *Journal of Metamorphic Geology*, **2**, 33–41.

Radke, B. and Mathis, R. (1980) On the formation and occurrence of saddle dolomite. *Journal of Sedimentary Petrology*, **50**, 1149–1168.

Reeder, R.J. and Sheppard, C.E. (1984) Variation of lattice parameters in some sedimentary dolomites. *American Mineralogist*, **69**, 520–527.

Sheppard, S.M.F. and Schwarz, H.P. (1970) Fractionation of carbon and oxygen isotopes and magnesium between coexisting metamorphic calcite and dolomite. *Contributions to Mineralogy and Petrology*, **26**, 161–198.

Sibley, D. and Gregg, J. (1987) Classification of dolomite rock textures. *Journal of Sedimentary Petrology*, **57**, 967–975.

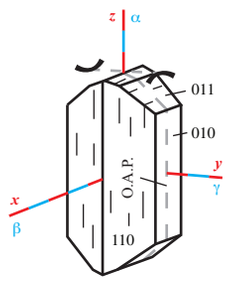
Warren, J. (2000) Dolomite: occurrence, evolution and economically important associations. *Earth Science Reviews*, **52**, 1–81.

Downloaded from https://pubs.geoscienceworld.org/books/chapter-pdf/3764177/9780903056434_ch108.pdf
by guest

Aragonite $CaCO_3$

Orthorhombic (−)

α	1.530−1.531
β	1.680−1.681
γ	1.685−1.686
δ	0.155−0.156
$2V_\alpha$	18−18.5°
Orientation	$\alpha = z$, $\beta = x$, $\gamma = y$; O.A.P. (100)
D (g/cm^3)	2.94−2.95
H	3½− 4
Cleavage	{010} imperfect, {110} poor
Twinning	Common, twin plane {110}, giving lamellar twins parallel to *z*, or repeated or mimetic twins leading to pseudohexagonal groups
Colour	Typically colourless or white; colourless in thin section
Unit cell	*a* 4.96 Å, *b* 7.97 Å, *c* 5.74 Å *Z* = 4; space group *Pmcn*
Special features	Effervesces with dilute HCl. When immersed in hot $Co(NO_3)_2$ solution, aragonite chips or grains become lilac-coloured.



Aragonite is one of the three naturally occurring polymorphs of $CaCO_3$, the other two being calcite and vaterite. It occurs in marine sediments, and the shells of some marine organisms are made of aragonite. It is found also in amygdales in basalt and andesite, and in the oxidized zone of some ore deposits. Aragonite is also a characteristic mineral of high-pressure, low-temperature metamorphism.

Structure

In the crystal structure of aragonite layers of Ca ions parallel to (001) lie approximately in the positions of hexagonal close packing which has been deformed by compression perpendicular to the layers. This is in contrast with the deformed cubic close-packed arrangement of Ca in calcite and explains the pseudo-hexagonal symmetry of aragonite. In calcite the triangular (CO_3) groups occur halfway between Ca layers, and each oxygen has two Ca as nearest neighbours, whereas in aragonite the (CO_3) groups do not lie midway between Ca layers and are rotated 30° to right or left so that each oxygen atom has three neighbouring Ca atoms. As a consequence successive (CO_3) groups along *z* point alternately to the $+y$ and $-y$ directions (Fig. 308): thus although the Ca ions are in a hexagonal array, the arrangement of the (CO_3) groups lowers the symmetry to orthorhombic. The Ca atom is slightly displaced from the plane of carbonate oxygens.

In general terms the structures of the carbonate group of minerals are governed by the radius of the metallic ion: if this exceeds about 1.0 Å the aragonite-type structure is preferred to that of calcite. As the calcium ion is close to this critical value, $CaCO_3$ is dimorphous, and can adopt either structure.

Chemistry

Most aragonites are relatively pure and conform to the ideal formula (e.g. Table 58, p. 454, analysis 7). Many aragonites contain small but appreciable amounts of strontium, the ionic radii of Sr and Ca being fairly similar. Lead also substitutes for Ca, and the varietal name tarnowitzite has been given to this plumbian aragonite.

Aragonite can be readily synthesized by mixing carbonate solutions with solutions containing calcium ions under conditions of controlled temperature and ageing. With the addition of sodium polyphosphate, $CaCO_3$ precipitated from sodium chloride and carbonate solutions is largely or wholly aragonite. In general the crystallization of aragonite is favoured by temperatures of 50−80°C, and by the presence of salts of Sr, Pb or

Downloaded from https://pubs.geoscienceworld.org/books/chapter-pdf/3764350/9780903056434_ch109.pdf
by guest

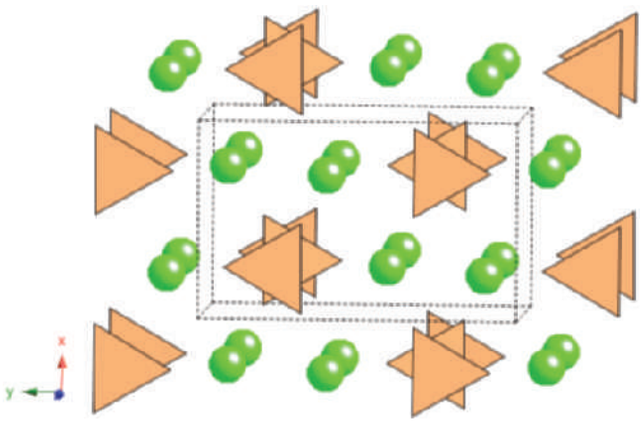


Fig. 308. Perspective view from a direction near the *z* axis of the crystal structure of aragonite (based on data from Speer, J.A., 1983, *Reviews in Mineralogy*, Min. Soc. Amer., **11**, p. 148). Green: Ca; triangles: approximately planar CO_3 groups.

Ba, or of $CaSO_4$, in solution. The $P-T$ curve defining the stability fields of calcite and aragonite has been determined experimentally (Fig. 309), confirming that aragonite is metastable at room temperature and at atmospheric pressure.

Although the oxygen isotope fractionation between aragonite and water appears to be independent of temperature (unlike the calcite–water system) it has been found that $\delta^{13}C$ of biogenic aragonite is temperature-dependent: relative to dissolved inorganic carbon, the $\delta^{13}C$ values of aragonitic foraminifera and molluscs decrease with temperature and can provide a sensitive palaeothermometer.

Aragonite commonly alters to calcite. It has been found that in some corals the aragonite portion contains about twice as much Sr as does the calcite portion, and it has been suggested that Sr inhibits the alteration of aragonite to calcite under natural conditions and that only when much of the Sr is removed may the alteration take place.

Optical and physical properties

Aragonite is biaxial and optically negative, with a 2V of ~18º. Except for varieties rich in Sr or Pb, the range of optical properties of aragonite is small; the substitution of Sr for Ca lowers the refractive indices and optic axial angle whereas Pb has the opposite effect. The strong birefringence, as for calcite, is a resuilt of the orientation of the (CO_3) group in the structure. Repeated twinning on the twin plane {110}, with composition plane also {110}, gives pseudohexagonal aggregates; in basal sections these show a distribution of twinned individuals in sectors, with the optic axial plane of each of the six sectors arranged at approximately 60º to that of the neighbouring sectors (Fig. 310).

Distinguishing features

Although the X-ray powder diffraction pattern is distinctive, other identification methods may prove useful. Aragonite may be distinguished from calcite by its greater density (2.94 compared with 2.71 g/cm^3 for calcite and 2.86 for dolomite): it sinks in bromoform whereas calcite and dolomite float. Aragonite lacks the perfect rhombohedral cleavage of calcite and dolomite, and has higher refractive indices than calcite. Meigen's reaction is commonly used as a chemical test for aragonite: if grains or a powder of the mineral are boiled for a few minutes with a solution of $Co(CO_3)_2$ a lilac or violet colour rapidly appears, staining the mineral. Calcite remains colourless or becomes slightly blue only after prolonged boiling. A neutral solution of a mixture of manganese and silver sulphates when used in the cold on calcite or aragonite gives a far more rapid reaction with the latter, with deposition of black MnO_2

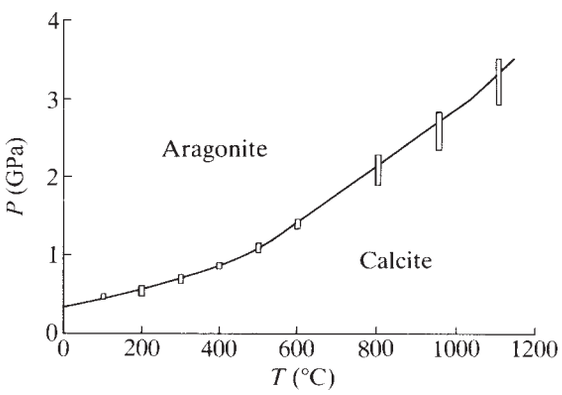


Fig. 309. The equilibrium curve for aragonite–calcite (based on data from Carlson, W.D., 1983, *Reviews in Mineralogy*, Min. Soc. Amer., **11**, p. 191).

Downloaded from https://pubs.geoscienceworld.org/books/chapter-pdf/3764350/9780903056434_ch109.pdf
by guest

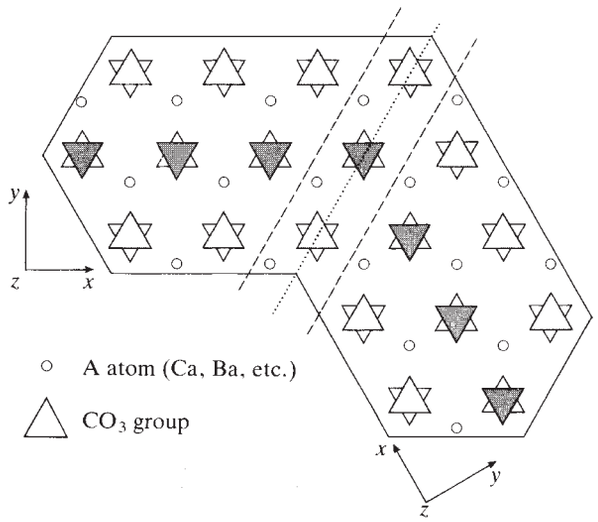


Fig. 310. Idealized structural model of the (110) twinning in orthorhombic carbonates (cf. Fig. 308). The twinning is on a glide plane (dotted line) parallel to (110), gliding in the [001] direction. The structure between the dashed lines conforms to the structure of both twin members (after Speer, J.A., 1983, *Reviews in Mineralogy*, Min. Soc. Amer., **11**, p. 153).

and Ag: the reaction is sufficiently localized to reveal intimate intergrowths of calcite and aragonite. Aragonite differs from the zeolites and other white or colourless minerals, other than the carbonates, by effervescing in acid. The other members of the aragonite group may be distinguished by their higher densities and by the distinctive flame tests for Ba, Sr or Pb.

Paragenesis

Aragonite is less common than calcite; at normal temperatures and pressures it is metastable and fairly readily inverts to calcite. Many organisms with calcareous skeletons build their shells of aragonite: in certain molluscs (e.g. in many bivalves) calcite and aragonite may occur in separate layers in the same shell, while in the cephalopods, aragonite and calcite are segrated in different parts of the skeleton, e.g. the ammonite shell consists of aragonite whereas the aptychus is made of calcite. The aragonite of fossil shells is gradually converted into calcite, although at a much slower rate than for synthetic material; under suitable conditions of burial, shells as old as the latter half of the Mesozoic may still contain aragonite. It is the normal material of pearls.

Primary precipitation of $CaCO_3$ from sea-water also occurs as aragonite, giving rise to aragonite muds, and under suitable conditions to aragonite ooliths. Aragonite is also found associated with gypsum or celestine in marls or clays, and in pisolites or sinter deposits from geysers and hot springs: it may form stalactites in caves in limestone districts, and some 'cave-pearls' occurring in pools in such caves have been shown to have layers of very fine-grained aragonite.

Aragonite occurs as a secondary mineral in cavities in volcanic rocks, chiefly andesites and basalts, and may be associated with zeolites. It is also found pseudomorphous after other minerals such as gypsum, and as a secondary mineral in altered dolomite. In the oxidized zone of ore deposits aragonite may occur together with limonite, malachite, calcite and other minerals.

Aragonite is a widespread metamorphic mineral along the Pacific margin of North America. Its occurrence in the Franciscan blueschists of California, and its rarity in other blueschist terranes, have been taken to suggest that the Franciscan metamorphic assemblage either reached lower maximum temperatures (120–190ºC), or was more rapidly uplifted than other blueschists. The low geothermal gradients needed (perhaps less than 12ºC/km) are consistent with a subduction zone origin. Partial inversion to calcite is common. Aragonite cannot survive in the presence of a fluid phase for appreciable geological time or in dry rocks if they are subjected to temperatures greater than 300ºC.

Further reading

Brown, W.H., Fyfe, W.S. and Turner, F.J. (1962) Aragonite in Californian glaucophane schists, and the kinetics of the aragonite–calcite transformation. *Journal of Petrology*, **3**, 565–585.

De Villiers, J.P.R. (1971) Crystal structure of aragonite, strontianite, and witherite. *American Mineralogist*, **56**, 758–767.

Grossman, E.L. and Ku, T.-L. (1986) Oxygen and carbon isotope fractionation in biogenic aragonite: temperature effects. *Chemical Geology (Isotope Geoscience Section)*, **59**, 59–74.

Jarosch, D. and Heger, G. (1986) Neutron diffraction refinement of the crystal structure of aragonite. *Tschermaks Mineralogische und Petrographische Mitteilungen*, **35**, 127–31.

Sandberg, P. (1985) Aragonite cements and their occurrence in ancient limestones. In *Carbonate Cements*, (SEPM, Special. Publication 36), 33–57.

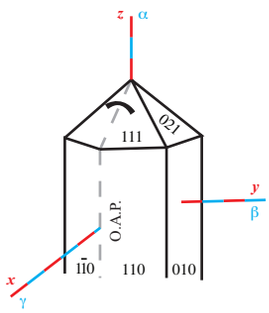
Speer, J.A. (1983) Crystal chemistry and phase relations of orthorhombic carbonates. Pp. 145–190 in: *Carbonates: Mineralogy and Chemistry* (R.J. Reeder, editor). Reviews in Mineralogy, **11**, Mineralogical Society of America, Washington, D.C.

Yoshioka, S., Ohde, S., Kitano, Y. and Kanamori, N. (1986) Behaviour of magnesium and strontium during the transformation of coral aragonite to calcite in aquatic environments. *Marine Chemistry*, **18**, 35–48.

Downloaded from https://pubs.geoscienceworld.org/books/chapter-pdf/3764350/9780903056434_ch109.pdf
by guest

Orthorhombic (−)

α	1.517−1.520
β	1.663−1.667
γ	1.667−1.669
δ	0.149−0.150
$2V_\alpha$	7−10°
Orientation	α = *z*, β = *y*, γ = *x*; O.A.P. (010)
D (g/cm^3)	~3.76
H	3½
Cleavage	{110} good, {021} and {010} poor
Twinning	Common on {110}, single, repeated and lamellar twins
Colour	Colourless, white, yellow, greenish or brownish; colourless in thin section
Unit cell	*a* 5.11 Å, *b* 8.42 Å, *c* 6.03 Å Z = 4; space group *Pmcn*
Special features	Soluble in dilute HCl. When moistened with HCl it gives an intense red colour to a flame.



Strontianite occurs mostly as a low-temperature hydrothermal mineral found typically in veins, cavities and concretions in limestone and calcareous clays. It may be found also as a gangue mineral in hydrothermal metalliferous deposits and is known from carbonatites.

The structure of strontianite is similar to that of aragonite, but with slightly larger cell parameters due to the strontium ion being larger than that of calcium. Some calcium is generally present substituting for strontium and in natural material the Ca/Sr ratio may reach approximately 1:4 (e.g. Table 58, analysis 9, p. 454). The intermediate composition $CaSr(CO_3)_2$ has been synthesized and has cell dimensions between those of strontianite and aragonite. Barium may also substitute for strontium in the natural mineral, and a complete synthetic series $SrCO_3$−$BaCO_3$ has been prepared.

Substitution of Ca for Sr causes an increase in refractive indices and a decrease in the density (Fig. 311). The d_{132} X-ray peak gives an indirect determination of composition:

mol% $SrCO_3$ in strontianite = $-2116.24 + 1162.84d_{132}$ (Å)

The solubility in HC1, and the intense red colour imparted to a flame, are diagnostic.

Strontianite most commonly occurs as fibrous masses in veins in limestones and marls and in hydrothermal vein deposits, but it is also known from igneous rocks, possibly as an alteration of celestine. Strontianite-rich rocks have been found in association with carbonatites in Malawi, Poland, the Kola Peninsula and Colorado, and strontianite has been found as a secondary mineral in kimberlites. It is often associated with witherite, baryte, celestine, fluorite and lead-bearing minerals, and is named after the Strontian, Argyllshire, locality, where

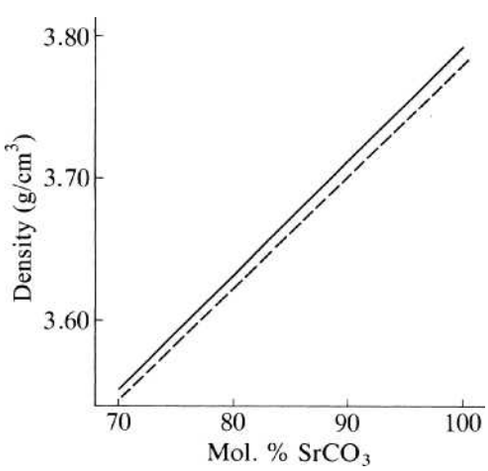


Fig. 311. Calculated values of density plotted against mol% $SrCO_3$ content in $(Sr,Ca)CO_3$. Upper line for natural strontianites, lower line for synthetic strontianites (after Speer & Hensley-Dunn, 1976).

Downloaded from https://pubs.geoscienceworld.org/books/chapter-pdf/3764355/9780903056434_ch110.pdf
by guest

it occurs in association with lead mineralization. Witherite, the barium analogue of strontianite, is commonly found in low-temperature hydrothermal veins.

Further reading

Armbrustmacher, T.J. (1979) Replacement and primary magmatic carbonatites from the Wet Mountains area, Fremont and Custer Counties, Colorado. *Economic Geology*, **74**, 888–901.

Morgan, D.J. and Milodowski, A.E. (1982) Thermal investigations of members of the strontianite–calciostrontianite series. Pp. 642–649 in: *Thermal Analysis*: *Proceedings of the 7th International Conference on Thermal Analysis*, **Vol 1**, (B. Miller, editor). Wiley.

Speer, J.A. and Hensley-Dunn, M.L. (1976) Strontianite composition and physical properties. *American Mineralogist*, **61**, 1001–1004.

Downloaded from https://pubs.geoscienceworld.org/books/chapter-pdf/3764355/9780903056434_ch110.pdf
by guest

Phosphates

Apatite $Ca_5(PO_4)_3(OH,F,Cl)$

Hexagonal (−)

ε	1.624−1.666
ω	1.629−1.667
δ	0.001−0.007
D (g/cm^3)	3.1−3.35
H	5
Cleavage	{0001} and {10$\bar{1}$0}, poor
Colour	Green, white, yellow, blue, brown; generally colourless in thin section
Pleochroism	Coloured varieties may show weak to moderate pleochroism, with absorption ε > ω
Unit cell	*a* 9.32−9.64 Å, *c* 6.78−6.90 Å
	Z = 2; space group $C6_3/m$
Special features	Soluble in HNO_3 or HCl

Members of the apatite group are common accessory minerals in almost all igneous rocks and are also found in sedimentary and metamorphic rocks. They are the most abundant phosphorus-bearing minerals; the most common varieties are represented by the isomorphous series with end-members:

Fluorapatite	**$Ca_5(PO_4)_3F$**
Chlorapatite	**$Ca_5(PO_4)_3Cl$**
Hydroxylapatite	**$Ca_5(PO_4)_3OH$**

Fluorapatite is by far the most common apatite-group mineral, and the term apatite is used synonymously with fluorapatite. The apatites are common accessory minerals in many rock types and are the most abundant phosphorus-bearing minerals and thus are of considerable economic interest if they are found in abundance, as in phosphorites.

Structure

The crystal structure of apatite is illustrated in Fig. 312. There are two sets of calcium atoms, one in seven-fold coordination, shown as Ca–O polyhedra (blue) and another in nine-fold coordination shown as sets of six blue spheres. The polyhedra share faces to form columns parallel to *z*, and six such columns form a circle, at the centre of which there is a line of fluorine atoms (green) repeating in the *z* direction at intervals of *c*/2. They are surrounded by planar triangles of Ca atoms (blue) which repeat at the same intervals along *z* but with successive rotations of sixty degrees, and are linked to oxygens of PO_4 tetrahedral groups (triangular in projection), all forming a structure with hexagonal symmetry.

The differing sizes of the monovalent anions in apatite lead to a variation in the cell parameters: the values for the end-member compositions are shown in Table 59.

Table 59. Cell parameters for end-members of the apatite group.

	a (Å)	*c* (Å)	c/*a*
Fluorapatite	9.39	6.88	0.73
Chlorapatite	9.60	6.78	0.71
Hydroxylapatite	9.42	6.87	0.73

Downloaded from https://pubs.geoscienceworld.org/books/chapter-pdf/3764358/9780903056434_ch111.pdf
by guest

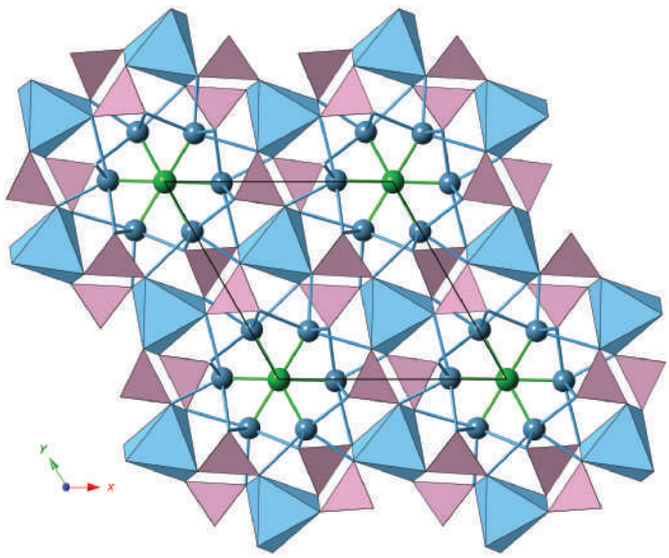


Fig. 312. Part of the structure of fluorapatite, $Ca_5(PO_4)_3F$, viewed along *z* (CrystalMaker image). Blue spheres and blue polyhedra: Ca; green: F; lavender: PO_4 groups. Oxygens at corners of polyhedra and tetrahedra are not shown.

Chemistry

In the formula $Ca_5(PO_4)_3(OH,F,Cl)$, fluorine, chlorine and the hydroxyl ion can mutually replace each other to form the almost pure end-members. Complete solid solution is obtained in synthetic preparations and it is possible that there is a complete isomorphous range in natural apatites, though there may be a miscibility gap between OH-F-apatite with up to 10 mol% Cl-apatite and the relatively pure end-member chlorapatite. Analyses of several apatites are given in Table 60, where formulae have been calculated on the basis of 26(O,OH,F,C1). Calcium may be partially replaced by Mn (analysis 4), and an Mn/Ca ratio of 1:8 is not uncommon. Strontium or the rare earths, predominantly Ce, may also replace Ca to a considerable extent and fluorapatites with Sr as a major component are known.

The analyses of some apatites show appreciable CO_2 (up to 6 or 7 wt.%): the term francolite has been applied to apatite containing both appreciable CO_2 and more than 1 mol% of fluorine, whereas dahllite has been applied to apatite with abundant CO_2 but with a small content of fluorine. Neither of these names is accepted as a mineral species in the modern sense; they are carbonate-rich varieties of fluorapatite and hydroxyl-apatite, respectively. After earlier uncertainty it now seems accepted that the CO_2 is not present as calcite or aragonite impurities, but is part of the apatite structure. Its exact role in the structure remains somewhat problematical, but the commonest substitution is that of $(CO_3^{2-} + F^-)$ for PO_4^{3-} on virtually a 1:1 basis. The commonest substituents for Ca are trace amounts of Sr and rare earths; the Y group generally predominate but the lighter rare earths may be important in apatite of alkaline rocks and carbonatites.

Microscopic defects and tracks that occur in some apatites represent radiation damage caused primarily by the fission of ^{238}U impurities: their study and analysis have been used as a method of dating. Their lengths have been used to study the degree of annealing of induced fission tracks and hence to establish 'closure temperatures', nominal temperatures below which the radiogenic fission tracks are effectively retained. Experimental work has shown, however, that the tracks are extremely sensitive to the three parameters pressure, temperature and stress, leading to some uncertainty concerning the extrapolation of fission track data to geological time scales. Recent apatite age determinations using (U-He)/He ratios have also been reported.

Fluorapatite may be synthesized by the fusion of $Ca_3(PO_4)_2$ with CaF_2, whereas hydroxylapatite is most readily obtained by precipitation from solutions of calcium salts with the addition of ammoniacal phosphate solutions. Chlorapatite has been prepared by passing phosphorus trichloride vapour over red-hot lime. Various other elements and radicals have been substituted in synthetic apatites, including Sr, Pb, Ba, Y, Si and SO_4. Carbonate-fluorapatites have been prepared by the treatment of $CaCO_3$ by alkaline phosphate solutions, the carbonate-fluorapatite thus formed being due to incomplete replacement of CO_3^{2-} by PO_4^{3-}.

Optical and physical properties

Apatite is optically negative and is normally uniaxial, though biaxial varieties with an optic axial angle of up to 20º are known: the carbonate-bearing apatites in particular have anomalous optics, e.g. the carbonate-fluorapatite of Table 60, analysis 6.

The large variations in composition within the apatite group make the accurate correlation of optical data difficult. In general, however, the refractive indices are highest for chlorapatite and are reduced by the substitution of (OH) and still more by the substitution of F (Fig. 313). The partial replacement of P by C also brings about a general reduction of refractive indices: the entry of Mn increases the refractive indices and also increases the density. The substitution of Sr for Ca does

Downloaded from https://pubs.geoscienceworld.org/books/chapter-pdf/3764358/9780903056434_ch111.pdf
by guest

Table 60. Apatite analyses.

	1	2	3	4	5	6
Fe_2O_3	tr.	–	0.03	–	–	0.25
FeO	–	–	–	0.26	0.32	–
MnO	–	0.07	0.01	5.32	0.02	–
MgO	–	0.10	0.02	0.04	0.05	0.53
CaO	53.40	55.84	55.88	50.31	55.08	54.84
SrO	–	–	–	–	0.03	–
Na_2O	–	–	–	0.00	0.04	0.20
K_2O	–	–	–	–	0.01	–
P_2O_5	41.20	42.05	42.00	41.50	42.40	35.01
F	0.13	0.16	3.72	3.41	1.63	5.60
Cl	6.20	–	0.00	–	0.2	0.03
H_2O+	0.09	1.86	0.05	0.25	0.98	1.51
H_2O-	–	–	0.00	0.03	0.08	0.16
CO_2	–	–	–	–	–	4.43
	101.02	100.23	101.80	101.47	100.84	102.66
$-O \equiv F$, Cl	1.45	0.07	1.57	1.44	0.72	2.36
Total	99.57	100.16	100.23	100.03	100.12	100.30
ε	α 1.665	1.644	1.630	1.6411	–	–[a]
ω	β 1.667	1.651	1.633	1.6459	1.642	
D (g/cm^3)	3.181	3.21	–	3.22	3.14	3.116
	Numbers of ions on the basis of 26 (O,OH,F,Cl)[b]					
P	6.039	5.953	5.962	5.980	6.014	4.930
C	–	–	–	–	–	1.006
Fe^{3+}	–	–	0.004	–	–	0.031
Mg	–	0.025	0.005	0.010	0.012	0.131
Fe^{2+}	–	–	–	0.037	0.045	–
Mn	–	0.010	0.001	0.767	0.003	–
Na	–	–	–	–	0.012	0.064
Ca	9.905	10.004	10.040	9.175	9.887	9.774
Sr	–	–	–	–	0.003	–
	9.91	10.04	10.07[c]	9.99	9.96[d]	10.00
F	0.071	0.084	1.979	1.835	0.868	2.946
OH	0.104	2.074	0.056	0.284	1.098	1.671
Cl	1.819	–	–		0.056	0.008
	1.99	2.16	2.03	2.12	2.03	4.63

1 Pinkish white, monoclinic chlorapatite, actinolite-diopside-calcite marble, Bob's Lake, southeast Ontario, Canada (Hounslow, A.M. & Chao, G.Y., 1970, *Can. Min*. **10**, 252–9). *a* 9.606, *c* 6.705 Å.
2 Yellow hydroxylapatite, Holly Springs, Georgia, USA (Mitchell, L. *et al*., 1943, *Amer. Min*., **28**, 356–77). Includes insol. 0.15.
3 Fluorapatite, stilpnomelane-calcite vein, near Dolgellau, North Wales, UK (Matthews, D.W. & Scoon, J.H., 1964, *Mineral. Mag*., **33**, 1032–7). Includes $A1_2O_3$ 0.08%, Sr 430 ppm, Y 140 ppm.
4 Bluish green manganapatite, pegmatite, Varuträsk, Sweden (Quensel, P., 1937, *Geol. För. Förh*, **59**, 257–61). Includes insol. 0.35.
5 Yellowish white hydroxyl-fluorapatite, two-pyroxene granulite, Hitterö, Norway (Howie, R.A., 1964, *Indian Geophys. Union*, Krishnan vol., 297–307).
6 Francolite, altered lava, Namaqualand, South Africa (Villiers, J.E. de., 1942, *Amer. J. Sci*., **240**, 443–7). Includes insol. 0.10.

[a] α 1.614–1.617, β 1.627, γ 1.627–1.630, $2V_\alpha$ 0–36°.
[b] Numbers of ions for the carbonate-apatite (anal. 6) calculated on the basis of 10 (Ca,Mg, etc.).
[c] Includes Al 0.016.
[d] Includes K 0.002.

not appreciably alter the refractive indices, though the density is considerably increased. The birefringence also varies with the substitution in the (OH,F,Cl) group, being lowest for chlorapatite (0.001), intermediate for fluorapatite (around 0.004) and highest for hydroxylapatite (0.007). The birefringence of some carbonate-fluorapatites may be even stronger, e.g. that of analysis 6 (Table 60) is 0.013. The cryptocrystalline variety of apatite, collophane, may appear isotropic or show only weak birefringence: this is due to the aggregate polarization effect produced by a mass of superimposed submicroscopic crystallites.

The colour of apatite is extremely variable. The intensity of the colour increases with an increase in Mn content of the apatite, but the colour itself depends on the state of oxidation of the manganese: thus Mn^{2+} produces pale pink and blue tones, Mn^{3+} blue, and Mn^{7+} violet. Ferric and ferrous iron together produce a green

Downloaded from https://pubs.geoscienceworld.org/books/chapter-pdf/3764358/9780903056434_ch111.pdf
by guest

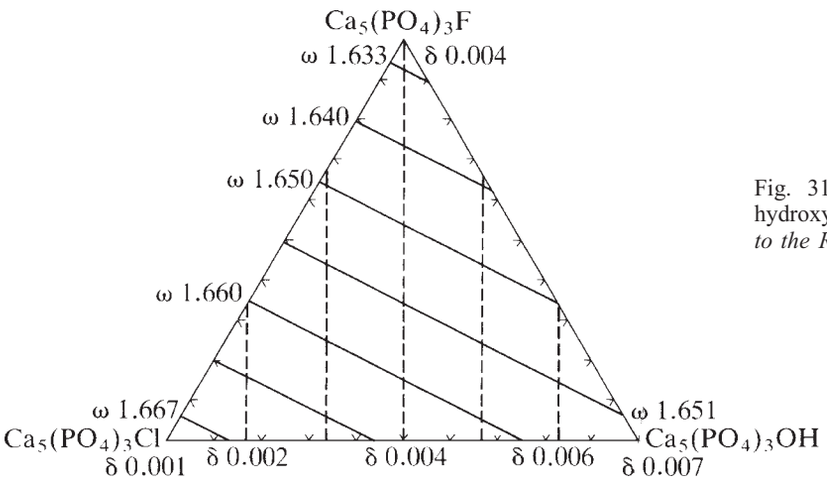


Fig. 313. Optical properties of the fluor-, chlor- and hydroxylapatite series (Deer *et al*., 1992, *An Introduction to the Rock-Forming Minerals*, Longman, UK).

colour in both synthetic and natural apatites: some other colours may be due to rare earths. Some apatites show a yellow or a pale violet fluorescence. The coloured varieties of apatite may, in thick sections, show moderate pleochroism with absorption ε > ω; blue apatite, for example, may have ε greenish blue, ω light blue. Zonal distribution of the colour is also known, particularly for the blue pegmatitic manganapatites.

Distinguishing features

The high relief and low birefringence of apatite serve to distinguish it from most light-coloured minerals. Its straight extinction and the absence of a good cleavage help to distinguish it from sillimanite and melilite. Topaz is optically positive as well as being biaxial, eudialyte has a more distinct cleavage and, in general, lower refractive indices. Vesuvianite and zoisite have considerably higher relief and may show anomalous interference colours. The coloured slightly pleochroic varieties may be distinguished from tourmaline by having absorption ε > ω, tourmaline having ω >> ε. The addition of a drop of nitric acid followed by some ammonium molybdate will confirm the presence of a phosphate by giving a yellow precipitate of ammonium phosphomolybdate.

Paragenesis

Apatite is a common accessory mineral in many types of rock and is the most abundant phosphorus-bearing mineral. It occurs as an accessory mineral in almost all igneous rocks from basic to acid, and in some may amount to as much as 5% by volume, though 0.1–1% is the more normal range. In most igneous apatites, the fluorapatite molecule is dominant, with appreciable OH in addition, giving a hydroxyl-fluor-apatite. Apatite is a fairly common mineral of granitic pegmatites where the bluish manganese-bearing varieties commonly occur, e.g. Table 60, analysis 4: they may be associated with lithium minerals such as lepidolite and spodumene, and with beryl. Apatite also occurs in hydrothermal veins and cavities (e.g. Table 60, analysis 1) and is found in Alpine-type veins, with quartz, adularia, chlorite and titanium oxides.

Carbonatites generally contain appreciable apatite. There are several apatite-rich areas in the Khibina tundra, Kola Peninsula, Russia, where apatite–nepheline rocks occur and form the world's largest apatite deposit. Apatite forms about 3% of the Palabora shonkinite, in the Transvaal, South Africa, and locally apatite–diopside rock and apatite rock have up to 96% phosphate. Carbonate-fluorapatite also occurs in the calcitic carbonatites (alvikites) of the Alnö alkaline complex, and may amount to 13% in the sövites.

Apatite occurs in both contact and regionally metamorphosed rocks. Fluorapatite is a common associate of chondrodite and phlogopite in metasomatized calc-silicate rocks and impure limestones, whereas chlorapatite may occur associated with scapolite in such rocks which have undergone chlorine metasomatism: carbonate-fluorapatite is also known from contact-metamorphosed rocks, as at Magnet Cove, Arkansas. The intrusion of igneous sills and dykes into the Permian phosphate-bearing beds of Montana has converted collophane and carbonate-fluorapatite to colourless fine-grained apatite, sometimes giving quartz-apatite veins. The hydroxylapatite (Table 60, analysis 2) in talc schist and the fluor-hydroxylapatite in chlorite schist, both from a serpentinite near Holly Springs, Georgia, USA, are considered to be metamorphic in origin, the hydrous environment being essential for their formation.

Apatite is not uncommon in sedimentary rocks where it occurs both as a detrital mineral and as a primary deposit. Deposits containing appreciable vertebrate remains are usually highly phosphatic, and fish scales or bones may act as nuclei for the secondary concentration of calcium phosphate to form nodules. In some areas phosphatic deposits are developed on a vast scale, constituting independent formations covering a wide area. For example, in the Permian Phosphoria

Downloaded from https://pubs.geoscienceworld.org/books/chapter-pdf/3764358/9780903056434_ch111.pdf
by guest

Formation of western North America, beds containing up to 80% phosphate are interbedded with phosphatic shales and impure limestones: such phosphate-rich strata are termed phosphorites. The mineralogy of phosphorites is complex, the phosphate occurring as a cryptocrystalline, often concretionary, virtually isotropic material. The name 'collophane' has been applied to the cryptocrystalline mineral component, and as in the case of 'limonite' (p. 417) it is of use only when the apatite-like phase cannot be definitely identified. Most phosphorites are of marine origin and contain carbonate-rich fluorapatite as the main phosphate mineral. The maximum substitution of CO_3^{2-} in francolite appears to be about 6% CO_2; other substitutions in carbonate-fluorapatite include Na, Sr, Mg for Ca and SO_4 for PO_4.

True coprolites are a relatively uncommon constituent of sediments but may include cryptocrystalline collophane.

Further reading

Barbarand, J., Hurford, T. and Carter, A. (2003) Variation in fission-track measurement: implications for thermal history modelling. *Chemical Geology*, **198**, 77–106.

Boyce, J.W. and Hervig, R.L. (2009) Apatite as a monitor of late-stage magmatic processes at Volcan Irazu, Costa Rica. *Contributions to Mineralogy and Petrology*, **157**, 135–145.

Hansen, E.C. and Harlov, D.E. (2007) Whole rock, phosphate, and silicate compositions across an amphibolite- to granulite-facies transition, Tamil Nadu, India. *Journal of Petrology*, **48**, 1641–1680.

Harlov, D.E., Wirth, R. and Förster, H.-J. (2005) An experimental study of dissolution-reprecipation in fluorapatite: fluid infiltration and the formation of monazite. *Contributions to Mineralogy and Petrology*, **150**, 268–286.

Hughes, J.M. and Rakovan, J. (2002) The crystal structure of apatite, $Ca_5(PO_4)_3(F,OH,Cl)$. Pp. 1–12 in: *Phosphates: Geochemical, Geobiological, and Materials Importance* (M.L. Kohn, J. Rakovan and J.M. Hughes, editors). Reviews in Mineralogy and Geochemistry, **48**, Mineralogical Society of America and Geochemical Society, Washington, D.C.

Mason, H.E., McCubbin, F.M., Smirnov, A. and Phillips, B.L. (2009) Solid-state NMR and IR spectroscopic investigation of the role of structural water and F in carbonate-rich fluorapatite. *American Mineralogist*, **94**, 507–516.

Piccoli, P.M. and Candela, P.A. (2002) Apatite in igneous systems. Pp. 255–292 in: *Phosphates: Geochemical, Geobiological, and Materials Importance* (M.L. Kohn, J. Rakovan and J.M. Hughes, editors). Reviews in Mineralogy and Geochemistry, **48**, Mineralogical Society of America and Geochemical Society, Washington, D.C.

Schettler, G., Gottschalk, M. and Harlov, D.E. (2011) A new semi-micro wet chemical method for apatite analysis and its application to the crystal chemistry of fluorapatite-chlorapatite solid solutions. *American Mineralogist*, **96**, 138–152.

Spear, F.S. and Pyle, J.M. (2002) Apatite, monazite, and xenotime in metamorphic rocks. Pp. 293–336 in: *Phosphates: Geochemical, Geobiological, and Materials Importance* (M.L. Kohn, J. Rakovan and J.M. Hughes, editors). Reviews in Mineralogy and Geochemistry, **48**, Mineralogical Society of America and Geochemical Society, Washington, D.C.

Stormer, J.C., Pierson, M.J. and Tacker, R.C. (1993) Variation of F and Cl X-ray intensity due to anisotropic diffusion of apatite during electron microprobe analyses. *American Mineralogist*, **78**, 641–648.

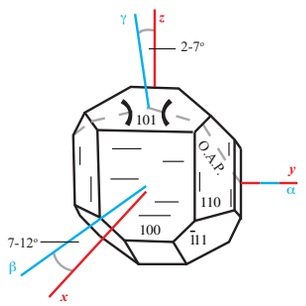
Webster, J.D., Tappen, C.M. and Mandeville, C.W. (2009) Partitioning behavior of chlorine and fluorine in the system apatite-melt-fluid. II: Felsic silicate systems at 200 MPa. *Geochimica et Cosmochimica Acta*, **73**, 559–581.

Downloaded from https://pubs.geoscienceworld.org/books/chapter-pdf/3764358/9780903056434_ch111.pdf
by guest

Monazite (Ce,La,Th)PO_4

Monoclinic (+)

α	1.774–1.800
β	1.777–1.801
γ	1.828–1.851
δ	0.045–0.075
$2V_\gamma$	10–26°
Orientation	γ:*z* = 2–7°; O.A.P. ⊥(010)
D (g/cm^3)	5.0–5.3
H	5
Cleavage	{100} moderate, {001} variable
Twinning	Twin plane {001}, common: also rare lamellar twinning on {001}
Colour	Yellow or reddish brown; yellow or colourless in thin section
Pleochroism	Very weak, light yellow to very light yellow
Unit cell	*a* 6.75–6.84 Å, *b* 6.96–7.04 Å, *c* 6.44–6.58 Å, β 104°
	Z = 4; space group $P2_1/n$
Special features	Slowly decomposed by acids



Monazite occurs as a pale yellow accessory mineral in granites and is found as a detrital mineral in beach sands. It is an important source of thorium and rare earth elements (*REE*).

The structure of monazite contains chains of alternating PO_4 tetrahedra and edge-sharing *REE*–O polyhedra running parallel to the *z* axis. The chains are linked laterally by shared edges of adjacent *REE* polyhedra. The *RE* atoms are coordinated by nine oxygens, and each oxygen is bonded to one P and two *RE* atoms. There is a systematic decrease in cell dimensions with the substitution of Ca and Th for Ce and La.

The most common varieties of monazite have 4–12 mol% ThO_2, though Th-free monazite is known; the variety cheralite has around 30 mol% ThO_2. Minor amounts of the other rare earths, and of U, Al and Fe^{3+}, may also occur. The isotope ratios $^{238}U/^{206}Pb$, $^{235}U/^{207}Pb$, $^{207}Pb/^{206}Pb$ and $^{232}Th^{208}Pb$ in monazite have been extensively used for determining the absolute ages of monazite-bearing pegmatites. Huttonite, $ThSiO_4$, is isostructural with monazite, and there may be a continuous series between the two minerals, with the coupled substitution $Th^{4+} + Si^{4+} \leftrightarrow Ce^{3+} + P^{5+}$. Rock and mineral sources of *rare earth elements* are important economic resources, since these elements are essential in many modern electronic devices, particularly those involved in communications and alternative energy systems.

Millimetric ellipsoidal monazite nodules in Lower Palaeozoic sedimentary rocks in Britain, France, Africa, Alaska and elsewhere are characterized by a pronounced zonation of light and heavy *REE*, low Th content and an inclusion fabric of low-grade metamorphic minerals indistinguishable from the host rock. This monazite is greyish in colour, brown and opaque in thin section; it is distinguishable from igneous monazite in having more than 0.5% Eu.

Monazite is typically light yellow or yellowish brown in thin section or in grains, but rarely shows any appreciable pleochroism. The refractive indices are high and are increased by the entry of Th. Partly metamict monazite has been reported, however, with a low birefringence and *n* 1.79. Zircon is uniaxial and has higher refractive indices, titanite has higher birefringence, staurolite is more strongly pleochroic, and both olivine and epidote have a larger 2V.

Monazite occurs as an accessory in granites, syenitic and granitic pegmatites, in most grades of metapelitic and metabasic rocks, and in dolomitic marbles. It also occurs as a low-grade diagenetic mineral in sedimentary rocks and is commonly concentrated as a detrital mineral in stream and beach sands. These concentrates are one of the chief economic sources for Th and the light *REE*.

Downloaded from https://pubs.geoscienceworld.org/books/chapter-pdf/3764363/9780903056434_ch112.pdf
by guest

Further reading

Cherniak, D.J. and Pyle, J.M. (2008) Th diffusion in monazite. *Chemical Geology*, **256**, 52–61.

Finger, F. and Krenn, E. (2007) Three metamorphic monazite generations in a high-pressure rock from the Bohemian Massif and the potentially important role of apatite in stimulating polyphase monazite growth along a PT loop. *Lithos*, **95**, 103–115.

Harlov, D.E., Wirth, R. and Hetherington, C.J. (2011) Fluid-mediated partial alteration of monazite: the role of coupled dissolution-reprecipitation in element redistribution and mass transfer. *Contributions to Mineralogy and Petrology*, **162**, 329–348.

Ni, Y., Hughes, J.M. and Mariano, A.N. (1995) Crystal chemistry of the monazite and xenotime structures. *American Mineralogist*, **80**, 21–26.

Rasmussen, B. and Muhling, J.R. (2007) Monazite begets monazite: evidence for dissolution of detrital monazite and reprecipitation of syntectonic monazite during low-grade regional metamorphism. *Contributions to Mineralogy and Petrology*, **154**, 675–689.

Read, D., Cooper, D.C. and McArthur, J.M. (1987) The composition and distribution of nodular monazite in the Lower Palaeozoic rocks of Great Britain. *Mineralogical Magazine*, **51**, 271–280.

Williams, M.L., Jercinovic, M.J. and Hetherington, C.J. (2007) Microprobe monazite geochronology: understanding geologic processes by integrating composition and chronology. *Annual Review Earth and Planetary Science*, **35**, 137–175.

Downloaded from https://pubs.geoscienceworld.org/books/chapter-pdf/3764363/9780903056434_ch112.pdf
by guest

Halides

Fluorite CaF_2

Cubic

n	1.433–1.435
Dispersion	Weak
D (g/cm^3)	3.18
H	4
Cleavage	{111} perfect
Twinning	{111}, commonly as interpenetrant cubes
Colour	Extremely variable: colourless, white, yellow, green, blue and purple varieties are the most common; colourless, pale green or pale violet in thin section
Unit cell	*a* 5.463 Å Z = 4; space group *Fm*3*m*
Special features	Soluble in H_2SO_4 with evolution of HF; slightly soluble in HCl

Fluorite occurs typically as late-stage accessory mineral in granites and greisens, and is also found as a product of hydrothermal mineralization in limestones.

Structure

The calcium ions in fluorite are arranged on a cubic face-centred lattice, while each fluorine ion is at the centre of one of the smaller cubes obtained by dividing the unit cube into eight parts (Fig. 314). Each Ca is thus coordinated by eight F ions and each F is surrounded by four Ca ions arranged at the corners of a regular tetrahedron. This is the simplest of the structures commonly assumed by AX_2 compounds and represents the highest possible coordination (8:4), the radius ratio condition being that $R_A:R_X > 0.732$.

Chemistry

Most fluorite is at least 99% CaF_2, and the small amounts of Si, Al and Mg reported are probably due to impurities or inclusions. The chief substitutions which can occur are the replacement of part of the Ca by Sr or by Y and Ce: in the variety yttrofluorite, $(Ca,Y)F_{2-3}$, the YF_3 component may amount to 10–20% with minor amounts of CeF_3. Some fluorites are reported to contain free fluorine, and on grinding these specimens may give a strong odour of ozone and HF: this variety is sometimes known as antozonite. Some dark purple fluorite may contain hydrocarbons, and in particular the Blue John fluorite from Treak Cliff, Castleton, Derbyshire, has yielded as much as 0.27% carbon. Dark purple fluorites have also been reported to be relatively rich in strontium, containing up to 1% Sr.

Fluorite can be prepared artificially by the evaporation of a solution of CaF_2 in HCl. Large synthetic crystals for optical purposes have been obtained by fusing precipitated CaF_2 in a graphite crucible in a vacuum furnace; PbF_2 may be added to act as a scavenger for impurities. The name is derived from the Latin *fluo*, I flow, in allusion to its readily fusible nature and its commercial use as a flux in smelting.

Optical and physical properties

The low refractive index, small dispersion and isotropic nature make colourless fluorite a suitable material for optical use. For fluorite with substantial substitution of Y for Ca, the refractive index is considerably increased.

The problem of colour in fluorite has been extensively discussed. The theories put forward include

Downloaded from https://pubs.geoscienceworld.org/books/chapter-pdf/3764375/9780903056434_ch113.pdf
by guest

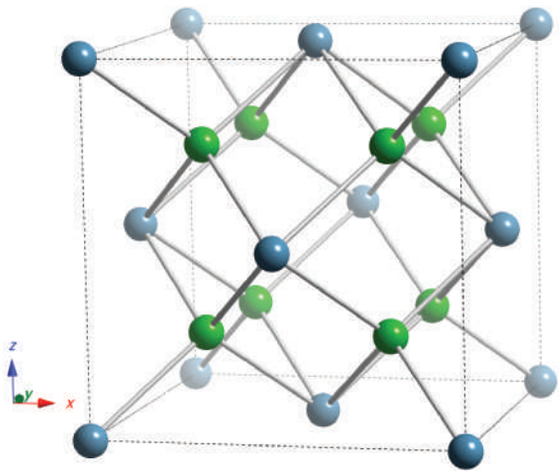


Fig. 314. The crystal structure of fluorite (CrystalMaker image). Blue: calcium; green: fluorine.

physical defects in the crystal structure, radioactive inclusions or emanations from nearby radioactive material, traces of rare earths, and the presence of inclusions of carbonaceous material or MnO_2. Purple fluorite found in association with radioactive minerals becomes colourless on heating above about 175ºC: the colour is associated with an increase in refractive index and a decrease in density.

Recent studies have shown that complex 'centres' involving rare-earth ions and/or oxygen give rise to many of the various colours observed. These include yttrium-associated *F* centres (blue), coexisting yttrium- and cerium-associated *F* centres (yellowish green), the YO_2 centre (rose) and the ionized O_2 molecule (O_3^-) (yellow), cf. halite colours p. 483. Divalent rare-earth ions also contribute to the coloration as in green fluorite (Sm^{2+}). Strong irradiation of the crystals with ionizing radiation leads to coagulation of colour centres and to precipitation of metallic Ca colloids which may be responsible for the deep blue colour of Blue John-type fluorite. The fluorescence (a phenomenon which derives its name from fluorite) is commonly strong and has been correlated with relatively high contents of the rare earths Eu, La and Ce (Fig. 315); Y and Sm may also be important in the green varieties.

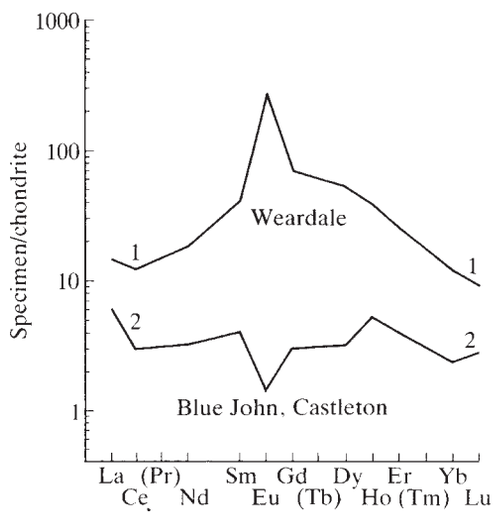


Fig. 315. Chondrite-normalized plots of *REE* in (1) fluorescent green fluorite from Weardale and (2) Blue John fluorite, Castleton, Derbyshire (after Howie, R.A., Pegram, E. & Walsh, J.N., 1982, *J. Russell Soc.*, **1**, 22–5).

Distinguishing features

In hand specimen fluorite may be distinguished by its perfect octahedral cleavage, its vitreous lustre and its cubic habit. The colour is so variable as to be of little help, but varying shades of purple and violet are common colours, as are green and yellow, and the colourless material is not rare. Fluorite is relatively soft, does not effervesce with acid as calcite does, but is attacked by H_2SO_4. Under the microscope its isotropic character and very low refractive index are characteristic: purple varieties often have sufficient depth of colour to remain purple or violet in thin section. Cryolite (Na_3AlF_6) has an even lower relief, is very weakly birefringent, and has a pseudocubic {001} cleavage. Halite has a perfect {001} cleavage and a higher refractive index.

Paragenesis

In igneous rocks fluorite may occur as a late-crystallizing, mainly hydrothermal product, especially in granites, syenites and greisen: it is a rather common accessory mineral in some granitic pegmatites. Examination of liquid inclusions in pegmatite fluorites by the decrepitation method has given a range of crystallization temperatures of 450–550ºC. It is found in the Alnö Island alkaline complex where it occurs in calcite–fluorite dykes, and has been reported from nepheline syenite, and from apatite-rich deposits in alkaline rocks in the Transvaal where it occurs in economically important quantities. Some Newfoundland deposits, in granite, consist of veins 1.5–6 m thick,

Downloaded from https://pubs.geoscienceworld.org/books/chapter-pdf/3764375/9780903056434_ch113.pdf
by guest

containing 75–95% CaF_2. Fluorite has also been recorded in the drusy cavities of blocks ejected from volcanoes, and as a volcanic sublimate. In these igneous occurrences associated minerals include cassiterite, topaz, apatite and lepidolite for the pneumatolytic deposits, and calcite, pyrite and apatite for the hydrothermal product.

Fluorite is commonly found associated with typical hydrothermal minerals not known to be directly related to any igneous body. Such hydrothermal vein deposits may also carry baryte, sphalerite, galena, calcite and chalcedony or quartz. In the English Pennines purple and green fluorite occur towards the centre of the fluorite zone whereas in the outer portion yellow fluorite is found, and it is commonly associated with baryte. Homogenization studies on primary fluid inclusions in hydrothermal fluorite from the North Pennine (Pb,Zn,Ba)–fluorite deposits indicate depositional temperatures of 92–220ºC; the fluids are highly saline with 15–25 equivalent wt.% NaCl. The ore-forming fluid was probably a concentrated (Na,Ca,K)-chloride brine similar to modern oilfield waters found at depth in sedimentary basins; at a flow rate of 0.5–1.0 cm/s, the formation of a typical vein might take 1000 years. The Illinois-Kentucky fluorite deposits are epigenetic and include vein deposits and bedding replacement deposits: physical guides were structural and stratigraphical. Dilution of mineralizing fluids by groundwater, and the change in temperature gradient on contact with excess groundwater, are considered to be the major chemical factors governing the formation of these fluorite deposits.

Fluorite is sometimes found as a cementing material in sandstone: violet grains of fluorite are fairly common as a detrital mineral in sands, being derived from acid igneous rocks and hydrothermal deposits. The mineral is known from geodes, with calcite, baryte and sphalerite in limestone, where it is probably hydrothermal in origin. The variety of fluorite known as Blue John occurs in spheroidal nodular masses with a radiating crystalline structure, and contains blue bands of varying intensity arranged concentrically, parallel to the nodular surface, and between these, colourless, yellow or paler blue bands: this variety is virtually restricted to an area near Castleton, Derbyshire.

Further reading

Allen, R.D. (1952) Variations in chemical and physical properties of fluorite. *American Mineralogist*, **37**, 910–930.

Bill, H. and Calas, G. (1978) Color centers, associated rare-earth ions and the origin of coloration in natural fluorites. *Physics and Chemistry of Minerals*, **3**, 117–131.

Braithwaite, R.S.W., Flowers, W.T. Hazeldine, R.N. and Russell, M. (1973) The cause of the colour of Blue John and other purple fluorites. *Mineralogical Magazine*, **39**, 401–411.

Naldrett, D.L., Lachaine, A. and Naldrett, S.N. (1987) Rare earth elements, thermal history, and the colour of natural fluorites. *Canadian Journal of Earth Sciences*, **24**, 2082–2088.

Nordstrom, D.K. and Jenne, E.A. (1977) Fluorite solubility equilibria in selected geothermal waters. *Geochimica et Cosmochimica Acta*, **41**, 175–188.

Rogers, P.J. (1978) Fluid inclusion studies on fluorite from the Askrigg Block. *Transactions of the Institution of Mining & Metallurgy (Section B: Applied Earth Science)*, **87**, 125–131.

Downloaded from https://pubs.geoscienceworld.org/books/chapter-pdf/3764375/9780903056434_ch113.pdf
by guest

Halite NaCl

Cubic

n	1.544
D (g/cm^3)	2.16–2.17
H	2½
Cleavage	{100} perfect
Twinning	On {111}, for synthetic crystals
Colour	Colourless or white when pure, more typically orange or red due to inclusions of iron compounds, and may also be grey, yellow or blue; colourless in thin section
Unit cell	*a* 5.639 Å Z = 4; space group *Fm*3*m*
Special features	Salty taste. Colours a flame deep yellow.

Halite is an evaporite mineral which begins to be precipitated when sea-water has been reduced to around 10% of its original volume.

The structure of halite was the first to be determined by X-ray diffraction. The cubic unit cell shown in Fig. 316 contains chlorine atoms at its corners and face centres, and sodium atoms at the mid-points of cell edges and at its centre. A description with an alternative choice of origin would reverse these assignments. The structure is based on planes of chlorine atoms parallel to {111} in the ...ABCABC.... arrangement of cubic close packing; both sodium and chlorine atoms are in octahedral coordination, and the $NaCl_6$ octahedra share all twelve edges with adjacent octahedra.

Carefully purified halite contains over 99% NaCl; massive rock salt, however, may contain admixed clay, iron oxides and gypsum. There is little replacement of Na by K, although sylvite (KCl) is isomorphous. Large single crystals used for making lenses for ultraviolet or infrared spectroscopes, etc., are prepared by the slow cooling of the fused salt for seven to ten days.

Halite is normally colourless, but material which is deeply coloured in hand specimen may show a faint colour in thin section. Although the reddish colours in some rock salt are due to iron compounds, certain yellow and blue halites owe their colour to the presence of *F* centres, i.e. structural sites where an electron is held in an anion vacancy. In hand specimen the perfect cubic cleavage, salty taste, solubility and relative softness are characteristic. In thin section the isotropic nature and the low relief are distinctive: sylvite has a refractive index (*n* 1.490) less than that of the standard mounting medium.

Halite occurs chiefly in sedimentary rocks where it has been deposited by evaporation from sea-water or salt lakes: associated minerals commonly include gypsum, anhydrite, carnallite and sylvite. NaCl represents 77.6% of the salts evaporated from present day sea-water: on evaporation, halite begins to crystallize when the sea-water has been reduced to about 10% of its original volume. Deformation of stratified rocks with interbedded halite deposits may produce upthrusting of massive salt domes. The latter are usually circular in cross-section and may be several kilometres in diameter; in oil-

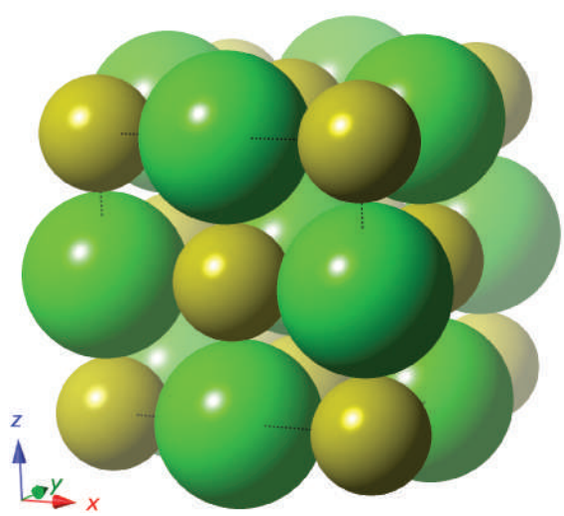


Fig. 316. The structure of halite (CrystalMaker image). Yellow: sodium; green: chlorine.

Downloaded from https://pubs.geoscienceworld.org/books/chapter-pdf/3764378/9780903056434_ch114.pdf
by guest

bearing strata, they act as oil and gas traps. Halite also occurs as a volcanic sublimate and as a surface efflorescence in arid regions.

Halite is of widespread occurrence as a daughter mineral in fluid inclusions from veins and crystalline rocks. The first such occurrence was noted by Sorby in 1858, in an Aberdeenshire granite. Halite is also now known from Martian meteorites. Dissolved salt in deep crustal waters plays a fundamental role in raising the solubility of many ore metals, primarily through chloride complexing, and high salinity also modifies the solubility of silicate minerals.

Further reading

Bridges, J.C. and Grady, M.M. (2000) Evaporite mineral assemblages in the nakhlite (martian) meteorites. *Earth and Planetary Science Letters*, **176**, 267–279.

Eastoe, E., Long, A., Land, L.S. and Kyle, J.R. (2001) Stable chlorine isotopes in halite and brine from the Gulf Coast basin: genesis and evolution. *Chemical Geology*, **176**, 343–360.

Siemann, M.G. (2003) Extensive and rapid changes in seawater chemistry during the Phanerozoic: evidence from Br contents in basal halite. *Terra Nova*, **15**, 243-248.

Sorby, H.C. (1858) On the microscopic structure of crystals, indicating the origin of minerals and rocks. *Quarterly Journal of the Geological Society of London*, **14**, 453–500.

Warren, J.K. (2006) *Evaporites: Sediments, Resources and Hydrocarbons*. Springer, Berlin, 1036 pp.

Worley, N.E. (2005) The occurrence of halite in the Permian A Bed Evaporite, Kirkby Thore, Cumbria. *Proceedings of the Yorkshire Geological Society*, **55**, 199–203.

Downloaded from https://pubs.geoscienceworld.org/books/chapter-pdf/3764378/9780903056434_ch114.pdf
by guest

Appendix 1

Calculation of a chemical formula from a mineral analysis

Magnesiohornblende analysis

	1 Wt.% of oxides	2 Molecular proportion of oxides	3 Atomic proportion of oxygen from each molecule	4 No. of anions on basis of 24 (O,OH) i.e. col. 3×8.3735		5 No. of ions in formula	
SiO_2	51.63	0.8594	1.7188	14.392	Si	7.196	8.00
						0.804	
Al_2O_3	7.39	0.0725	0.2175	1.821	Al	1.214	
						0.410	
Fe_2O_3	2.50	0.0157	0.0471	0.394	Fe^{3+}	0.263	5.07
FeO	5.30	0.0738	0.0738	0.618	Fe^{2+}	0.618	
MnO	0.17	0.0024	0.0024	0.020	Mn	0.020	
MgO	18.09	0.4489	0.4489	3.759	Mg	3.759	
CaO	12.32	0.2197	0.2197	1.840	Ca	1.840	2.00
Na_2O	0.61	0.0098	0.0098	0.082	Na	0.164	
H_2O+	2.31	0.1282	0.1282	1.073	OH	2.146	2.15
Total	100.32		2.8662				

$$\frac{24}{2.8662} = 8.3735$$

The procedure for calculating a chemical formula is described by means of the above example, a magnesiohornblende.

Column 1 lists the composition of the mineral expressed in the usual manner as weight percentages of oxides.

Column 2 is derived by dividing each column 1 entry by the molecular weight of the oxide concerned (see Appendix 2). The figures so obtained therefore express the molecular proportions of the various oxides.

Column 3 is derived from column 2 by multiplying by the number of oxygen atoms in the oxide concerned. It thus gives a set of numbers proportional to the numbers of oxygen atoms associated with each of the elements concerned. At the foot of column 3 is its total (T).

If we require the amphibole formula based upon 24 oxygen atoms (this represents half the content of the unit cell) we need to re-cast the oxygen atom proportions so that they total 24. This is done by multiplying all of them by 24/T and the results are given in Column 4.

Column 5 gives the number of cations associated with the oxygens in column 4. Thus for SiO_2 there is one silicon for two oxygens so the column 4 entry is divided by 2. For $A1_2O_3$ there are two aluminiums for every three oxygens so the column 4 entry is multiplied by $\frac{2}{3}$. For divalent ions the column 5 value is the same as that of column 4, and for monovalent ions (including hydrogen) the latter is doubled in column 5.

The numbers of ions on the basis of 24 oxygens given in column 5 can be grouped as shown to conform to a structural formula. In the present example it is assumed that the tetrahedral sites which are not filled by Si are occupied by Al, and the remaining Al atoms are in octahedral coordination.

It should be noted that a chemical analysis in itself can give only the ratios of atoms in the formula, and that the actual numbers of atoms given depends on an assumption about the actual number of one of them or of a group of them. A check of the correctness of the formula can be made if the cell volume and density are accurately known, since a calculated density can then be compared with that measured.

A check of charge balance, made by adding positive and negative charges in the formula, is a check only on

Downloaded from https://pubs.geoscienceworld.org/books/chapter-pdf/3764380/9780903056434_app1.pdf
by guest

Appendix 1

arithmetic and not on the quality of the analysis. This is because any analysis expressed in terms of neutral oxides must lead to numbers of cations and oxygens which balance electrically.

In many silicates, as in the example above, the only anion in the mineral is oxygen (or OH). Each element is expressed (and generally directly determined) as a weight percentage of oxide, even though the oxides do not exist as such in the mineral. The calculation procedure outlined is justifiable, as each element can be thought of as associated with its appropriate share of the oxygen atoms in the crystal structure.

If oxygen is not the only anion present the calculation is somewhat more complicated, and an example (a fluorphlogopite) is shown below.

Here fluorine is shown, as well as the oxides of all the cations, as a weight percentage. We may assume for simplicity that the fluorine atoms in the structure are bonded to magnesium atoms only, and yet the same atoms of magnesium are recorded as combined with oxygen in MgO. Thus an excess of oxygen is recorded and the total will exceed 100%. To obtain a real total (which is a measure to some extent of the accuracy of the data), an oxygen equivalent of the fluorine atoms must be subtracted.

One excess oxygen atom is recorded for each two atoms of fluorine present, so that the oxygen equivalent of a fluorine by weight is obtained by multiplying the fluorine content by the factor

$$\frac{\text{atomic weight of oxygen}}{2 \times \text{atomic weight of fluorine}}, \text{ i.e. } \frac{16}{38}$$

The oxygen equivalent of the fluorine weight is subtracted from the total of column 1 to give a true total.

The procedure for obtaining column 2 is as before, the fluorine content being divided by 19, the atomic weight of fluorine. For column 3 the number of fluorine atoms is inserted along with the oxygens and the total is again too high. It is necessary to subtract the oxygen equivalent of the fluorine atoms, i.e. half their number, to give a true total.

In the case of fluorphlogopite, the number of anions (O,OH,F) assumed is 24, so that the total of column 3 is divided into 24 to give the multiplying factor which is applied to produce column 4. Column 5 is derived as before.

Many modern analyses are carried out by use of an electron microprobe and this method does not yield values for H_2O and does not differentiate between Fe^{2+} and Fe^{3+}.

If H_2O has not been determined or is thought to be unreliable the mineral formula can be calculated on an anhydrous basis assuming the (OH) content to be ideal. Thus for the magnesiohornblende example above, instead of using 24(O,OH) to derive the scaling factor, 23(O) equivalents [i.e. 22(O) + 2(OH)] can be assumed as associated with all the cations apart from hydrogen.

If Fe^{3+} has not been determined, total iron is usually presented as an FeO equivalent. There are many ways of gaining an estimate of Fe^{3+} and Fe^{2+}, most of which are referred to by Droop (1987). The most appropriate method depends upon the mineral concerned. Some methods re-assign Fe to Fe_2O_3 and FeO in the way which gives the ideal total for all the cations or for particular groups. Some adjust Fe so that trivalent ions in octahedral sites balance the Al replacing Si in tetrahedra. All methods depend on assumptions which may or may not be warranted and all may give only an approximate result.

Fluorphlogopite analysis

	1 Wt.% of oxides	2 Molecular proportion of oxides	3 Atomic proportion of oxygen from each molecule	4 No. of anions on basis of 24 (O,OH) i.e. col. (3) × 8.500		5 No. of ions in formula
SiO_2	41.18	0.6854	1.3708	11.651	Si	5.826
Al_2O_3	12.52	0.1228	0.3684	3.131	Al	2.088
TiO_2	0.99	0.0124	0.0248	0.211	Ti	0.105
FeO	0.30	0.0041	0.0041	0.034	Fe	0.034
MnO	0.04	0.0005	0.0005	0.004	Mn	0.004
MgO	27.32	0.6779	0.6779	5.762	Mg	5.762
Na_2O	0.88	0.0142	0.0142	0.121	Na	0.241
K_2O	11.93	0.1266	0.1266	1.076	K	2.152
H_2O+	1.06	0.0588	0.0588	0.500	OH	1.000
F	6.74	0.3547	0.3547	3.113	F	3.113
	102.96		3.015			
$-O \equiv F$	2.84		$-0.1773 = \frac{1}{2}7 \times 0.3547$			
Total	100.12		2.8235			

$$\frac{24}{2.8235} = 8.500$$

Downloaded from https://pubs.geoscienceworld.org/books/chapter-pdf/3764380/9780903056434_app1.pdf
by guest

Further reading

Droop, G.T.R. (1987) A general equation for estimating Fe^{3+} concentrations in ferromagnesian silicates and oxides from microprobe analyses using stoichiometric criteria. *Mineralogical Magazine*, **51**, 431–435.

Appendix 2

Atomic and molecular weights for use in calculations of mineral formulae from chemical analyses.

Al_2O_3	101.96	H_2O	18.015	S	32.06
B	10.81	HfO_2	210.49	SO_3	80.06
B_2O_3	69.62	K_2O	94.20	Sc_2O_3	137.91
BaO	153.33	La_2O_3	325.81	SiO_2	60.08
BeO	25.01	Li_2O	29.88	SnO	134.71
CO_2	44.01	MgO	40.30	SrO	103.62
CaO	56.08	MnO	70.94	Ta_2O_5	441.89
CeO_2	172.12	MnO_2	86.94	ThO_2	264.04
Ce_2O_3	328.24	Mn_3O_4	228.81	TiO_2	79.87
Cl	35.45	Na_2O	61.98	UO_2	270.03
CoO	74.93	NiO	74.69	U_3O_8	842.08
Cr_2O_3	151.99	Nb_2O_5	265.81	V_2O_5	181.88
CuO	79.55	P_2O_5	141.94	Y_2O_3	225.81
F	19.00	PbO	223.20	ZnO	81.38
FeO	71.84	Rb_2O	186.94	ZrO_2	123.22
Fe_2O_3	159.69				

Downloaded from https://pubs.geoscienceworld.org/books/chapter-pdf/3764380/9780903056434_app1.pdf
by guest

Further reading

Droop, G.T.R. (1987) A general equation for estimating Fe^{3+} concentrations in ferromagnesian silicates and oxides from microprobe analyses using stoichiometric criteria. *Mineralogical Magazine*, **51**, 431–435.

Appendix 2

Atomic and molecular weights for use in calculations of mineral formulae from chemical analyses.

Al_2O_3	101.96	H_2O	18.015	S	32.06
B	10.81	HfO_2	210.49	SO_3	80.06
B_2O_3	69.62	K_2O	94.20	Sc_2O_3	137.91
BaO	153.33	La_2O_3	325.81	SiO_2	60.08
BeO	25.01	Li_2O	29.88	SnO	134.71
CO_2	44.01	MgO	40.30	SrO	103.62
CaO	56.08	MnO	70.94	Ta_2O_5	441.89
CeO_2	172.12	MnO_2	86.94	ThO_2	264.04
Ce_2O_3	328.24	Mn_3O_4	228.81	TiO_2	79.87
Cl	35.45	Na_2O	61.98	UO_2	270.03
CoO	74.93	NiO	74.69	U_3O_8	842.08
Cr_2O_3	151.99	Nb_2O_5	265.81	V_2O_5	181.88
CuO	79.55	P_2O_5	141.94	Y_2O_3	225.81
F	19.00	PbO	223.20	ZnO	81.38
FeO	71.84	Rb_2O	186.94	ZrO_2	123.22
Fe_2O_3	159.69				

Downloaded from https://pubs.geoscienceworld.org/books/chapter-pdf/3764384/9780903056434_app2.pdf
by guest

Appendix 3

End-member calculations

For some purposes it can be useful to express the formula of a mineral which can show a range of compositions between specified end-members, in terms of the percentages of these end-members. There is no single procedure for the required calculation as different assumptions are needed for different minerals and different purposes. In general a relatively small number of 'major' constituent end-members are specified. In the olivines, for example, Mg_2SiO_4(Fo) and Fe_2SiO_4(Fa) may suffice, but the Mn_2SiO_4 (tephroite end-member) could also be calculated. If the Mn content is low it is usually included with Fe as part of the Fa component. For a minor constituent the decision needs to be taken as to whether to ignore it or include it as proxying for a major element, and if so, for which element.

The examples given below help to indicate the kinds of procedures adopted.

Olivine

Ideal formula $(Mg,Fe)_2SiO_4$.
End-members: Mg_2SiO_4(Fo)–Fe_2SiO_4(Fa).
Example formula on basis of 4(O):

$$(Si_{0.97}Al_{0.03})_{1.00}(Ti_{0.02}Fe^{3+}_{0.01}Mg_{1.91}Fe^{2+}_{0.04}Mn_{0.01})_{1.99}$$

End-member percentages:

$100Mg/(Mg + Fe^*) = 191/1.96 = 97.4\%$
$100Fe^*/(Mg + Fe^*) = 5/1.96 = 2.6\%$
(where $Fe^* = Fe^{2+} + Fe^{3+}$) } $Fo_{97.4}Fa_{2.6}$

If $Fe^* = Fe^{2+} + Fe^{3+} + Mn$. Fo = 191/1.97 = 96.9%: $Fo_{96.9}Fa_{3.1}$

Augite

Ideal formula $(Ca,Mg,Fe)_2(Si,Al)_2O_6$.
End-members: $Mg_2Si_2O_6$(En)–$Fe_2Si_2O_6$(Fs)–$Ca_2Si_2O_6$(Wo).
Example formula on basis of 6(O):

$$(Si_{1.94}Al_{0.06})_{2.00}(Al_{0.01}Fe^{3+}_{0.03}Ti_{0.02}Mg_{0.21}Fe^{2+}_{0.87}Mn_{0.02}Ca_{0.82}Na_{0.02})_{2.00}$$

End-member percentages:

$100Mg/(Mg + Fe^* + Ca) = 21/1.95 = 10.77\%$

$100Fe^*/(Mg + Fe^* + Ca) = 92/1.95 = 47.18\%$

$100Ca/(Mg + Fe^* + Ca) = 82/1.95 = 42.05\%$

(where $Fe^* = Fe^{2+} + Fe^{3+} + Mn$); i.e. $En_{10.77}Fs_{47.18}Wo_{42.05}$
Alternative including end-member $NaFe^{3+}Si_2O_6$(Ac)

$100Na/(Mg + Fe^* + Ca + Na) = 2/1.97 = 1.02\%$

leaving 21/1.97(En), 92/1.97(Fs) and 82/1.97(Wo), i.e. $En_{10.66}Fs_{46.70}Wo_{41.62}Ac_{1.02}$

Downloaded from https://pubs.geoscienceworld.org/books/chapter-pdf/3764385/9780903056434_app3.pdf
by guest

Garnet

Ideal formula $(Mg,Fe^{2+},Mn,Ca)_3(Al,Fe^{3+},Cr)_2(Si,Al)_3O_{12}$.
End-members: Mg_3Al_2 pyrope; $Fe_3^{2+}Al_2$ almandine; Mn_3Al_2 spessartine; Ca_3Al_2 grossular; $Ca_3Fe_2^{3+}$ andradite; Ca_3Cr_2 uvarovite
Example formula on basis of 24(O):

$$(Si_{5.98}Al_{0.02})_{6.00}(Al_{3.91}Fe^{3+}_{0.13}Cr_{0.03})_{4.07}(Mg_{3.58}Fe^{2+}_{1.55}Mn_{0.04}Ca_{0.73})_{5.90}$$

End-member percentages

pyrope 358/5.90 = 60.68%, andradite 13/4.07 = 3.19%

almandine 155/5.90 = 26.27%, uvarovite 3/4.07 = 0.74%

spessartine 4/5.90 = 0.67%, Σ(and + uv) 16/4.07 = 3.93%

gro + and + uv = 73/5.90 = 12.37%

gro = 12.37 − Σ(and + uv) = 12.37 − 3.93 = 8.44%

Result: $py_{60.7}alm_{26.3}gro_{8.4}and_{3.2}uv_{0.7}sp_{0.7}$

Feldspar

Plagioclase feldspar: as for olivine but use

100Ca/(Ca + Na) = An

100Na/(Ca + Na) = Ab

Alkali feldspar: as for olivine but use

100Na/(Na + K) = Ab

100K/(Na + K) = Or

Ternary feldspar: as for augite but use

100Ca/(Ca + Na + K) = An

100Na/(Ca + Na + K) = Ab

100K/(Ca + Na + K) = Or

Downloaded from https://pubs.geoscienceworld.org/books/chapter-pdf/3764385/9780903056434_app3.pdf
by guest

Appendix 4

Use of optical identification tables

The birefringence (δ) exhibited by a crystal varies with orientation, but the maximum birefringence shown by crystals of a mineral (of specific composition) in a range of orientations is characteristic of that mineral. 'Maximum birefringence' might also, however, be taken to mean the highest characteristic value shown by the members of a chemical series, e.g. forsterite (Mg_2SiO_4)–fayalite (Fe_2SiO_4). Use of birefringence diagnostically needs to take account of both meanings, the former to determine a meaningful value, and the latter to allow for the possible 'chemical range' when using that value to suggest a mineral name.

The petrological use of the polarising microscope can be treated at different levels according to the needs of different student groups. At one level would be the practical observation of the colours of a mineral in thin section between crossed polars and relating these to birefringence (δ)[a]. This relationship is presented here in Table A for use with a thin section of standard thickness, 0.03 mm. (The presence of twinning is also best observed between crossed polars, and isotropic minerals could be noted). In Table A alongside each δ value are the minerals that possibly match but, mainly because of chemical variation, those somewhat lower in the chart need also to be considered. The possibilities should be readily narrowed by observation of other properties using Table B as suggested below.

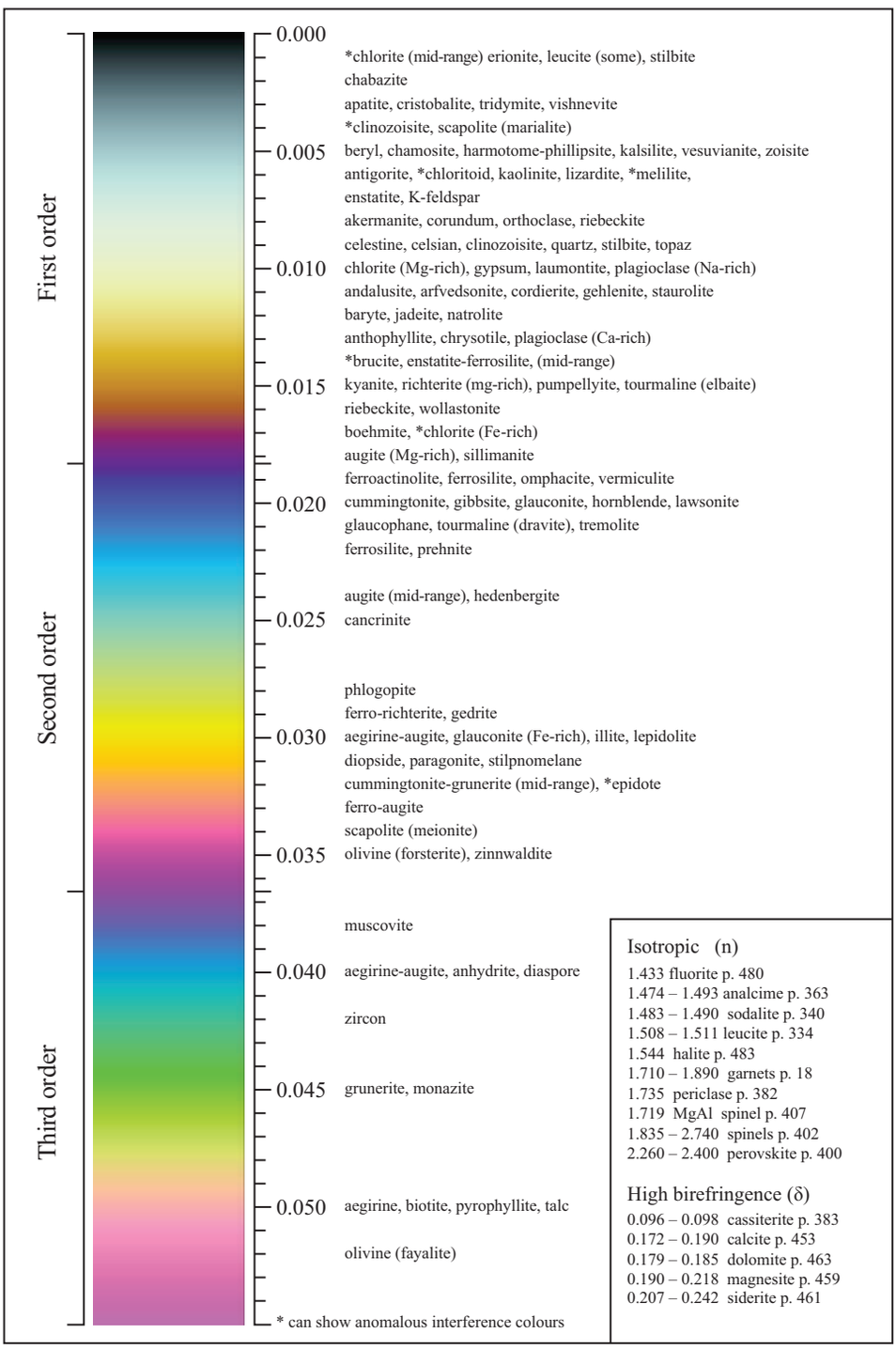
Also at a fairly basic level of investigation would be some (mostly qualitative) observations in plane polarized light, including prominent cleavage(s), pleochroism and 'relief' (high, moderate or low). A further level would involve observing interference figures in convergent light to determine whether a mineral is uniaxial or biaxial, and using a testing instrument, to determine optic sign. The above properties are listed in that order in Table B. For each mineral treated in the present text, this Table gives the range of δ that results from chemical variation, and the minerals are listed in numerical order according to the low birefringence end of that range.

For more detail and for quantitative data such as optical orientation, extinction angles and values of the optic axial angle (2V), Table B gives the starting page reference for each mineral. More general properties (colour, hardness, density, etc.) are also listed there. In addition, the text for each main mineral contains a section headed 'Distinguishing features' which helps discriminate between that mineral and a selection of others with which it might be confused.

[a] Similar colours in different 'orders' can be distinguished by gradually inserting a quartz wedge testing instrument to 'compensate' those colours , and observing the gradual changes of colours as the net birefringence is reduced to zero.

Downloaded from https://pubs.geoscienceworld.org/books/chapter-pdf/3764396/9780903056434_app4.pdf
by guest

Table A. Birefringences and Michel-Lévy interference colours (0.03 mm thin section) for the most common rock-forming minerals (colour strip (calculated) kindly provided by Professor Takenori Kato, Nagoya University, Japan (http://www.nendai.nagoya-u.ac.jp/gsd/sicc/).



Downloaded from https://pubs.geoscienceworld.org/books/chapter-pdf/3764396/9780903056434_app4.pdf
by guest

Appendix 4

Table B. Optical properties of common minerals in order of increasing birefringence.

Relief: L low, M moderate, H high, VH very high; all with R.I >1.54 (standard mounting medium). L−, M−, negative relief. (R.I. <1.54).
Cleavage: * one cleavage commonly visible. ** two intersecting cleavages.
Pleochroic: * can show pleochroism.
U: uniaxial, B: biaxial, +: positive, −: negative, (+ −): either positive or negative.

Birefringence	Relief	Cleavage	Pleochroic	U	B	+	−	(+ −)	Page
0.00−0.01 chlorite (mid-range)	M	*	*		*			*	208
0.001−0.005 chabazite	M−				*			*	374
0.001−0.007 apatite	M		*	*			*		473
0.001−0.009 vesuvianite	H			*			*		28
0.001−0.013 melilite	M	*	*	*				*	72
0.002−0.004 vishnevite	L−	*		*			*		345
0.002−0.004 α-tridymite	M−				*	*			311
0.005−0.020 approx. cancrinite	L−	*		*			*		345
0.003 α cristobalite	M−			*			*		311
0.003−0.004 clinoptilolite	M−	*			*			*	372
0.003−0.005 erionite	M−			*				*	355
0.003−0.005 nepheline	L−			*			*		325
0.003−0.008 zoisite	H	*			*	*			53
0.003−0.009 heulandite	M−	*			*			*	372
0.003−0.010 phillipsite	M−				*	*			368
0.004−0.005 mordenite	M−	*			*	*		*	377
0.004−0.005 scapolite (marialite)	L	**		*			*		349
0.004−0.007 antigorite	L	*			*		*		216
0.004−0.009 beryl	L			*			*		76
0.004−0.015 clinozoisite	H	*			*	*			56
0.005−0.006 kalsilite	L−			*			*		325
0.005−0.008 harmotome	M−				*	*			368
0.005−0.010 hyalophane	L−	**			*		*		291
0.005−0.022 chloritoid	H	*	*		*			*	47
0.006−0.008 lizardite	L	*		*			*		216
0.006−0.010 K-spar−Na-spar	L−	**			*			*	253
0.006−0.016 riebeckite	H	**	*		*			*	162
0.006−0.021 jadeite	H	**	*		*	*			125
0.006 approx. kaolinite	L	*			*			*	227
0.007−0.021 katophorite	H	**	*		*		*		167
0.007−0.016 enstatite	H	**	*		*			*	102
0.008 approx. microcline	L−	**			*		*		253
0.008−0.009 corundum	H		*	*			*		384
0.008−0.011 topaz	M	*	*		*	*			44
0.008−0.018 cordierite	L	*	*		*			*	80
0.008 approx. åkermanite	M			*		*			72
0.009 α-quartz	L			*		*			311
0.009−0.010 stilbite	L−	*			*		*		335
0.009−0.012 andalusite	M	*			*		*		33
0.009−0.013 celsian	M	**			*	*			291
0.009 approx. celestine	M	**	*		*	*			444
0.01−0.04 smectite	L	*			*		*		234
0.010−0.012 arfvedsonite	H	**	*		*		*		169
0.010−0.012 laumontite	L−	**			*		*		370
0.010−0.020 pumpellyite	H	**	*		*			*	68
0.010 approx. albite	L−	**			*	*			253
0.010 approx. gypsum	L−	*			*	*			445
0.011−0.014 staurolite	H	*	*		*	*			39
0.011 approx. gehlenite	H			*					72
0.012−0.016 kyanite	H	*	*		*		*		36
0.012 approx. natrolite	M−	*			*	*			366
0.012 approx. baryte	M	**			*	*			441
0.013−0.014 wollastonite	M	**			*		*		132
0.013−0.017 chrysotile	L								216
0.013−0.020 eckermannite	H	**	*		*		*		169

Downloaded from https://pubs.geoscienceworld.org/books/chapter-pdf/3764396/9780903056434_app4.pdf
by guest

Table B (*contd*.)

Birefringence	Relief	Cleavage	Pleochroic	U	B	+	−	(+ −)	Page
0.013−0.021 anthophyllite	M	**			*			*	144
0.013−0.036 allanite	H		*		*			*	63
0.013 approx. anorthite	L	**			*		*		292
0.014−0.020 brucite	M	*		*		*			409
0.014−0.027 spodumene	H	**			*	*			131
0.012−0.028 omphacite	H	**	*		*	*			122
0.015−0.020 boehmite	M				*	*			414
0.015−0.022 kosmochlore	H	**	*		*		*		125
0.015−0.022 Mg-richterite	H	**	*		*		*		167
0.015−0.051 epidote	H	*	*		*		*		56
0.016−0.022 ferrosilite	H	**	*		*			*	102
0.017−0.021 tourmaline (elbaite)	M		*	*			*		86
0.018−0.022 sillimanite	H	*	*		*	*			30
0.018−0.025 augite	H	**	*		*	*			116
0.018−0.035 lepidolite	L	*		*	*		*		195
0.019−0.021 lawsonite	H	**			*	*			65
0.02−0.03 glauconite	M	*			*		*		188
0.02−0.03 vermiculite	L	*	*		*		*		239
0.02 approx gibbsite	L	*			*	*			410
0.02 approx hornblende	H	**	*		*			*	154
0.020−0.032 cummingtonite	H	**			*	*			147
0.021−0.029 gedrite	H	**	*		*			*	144
0.021−0.029 tourmaline (dravite)	M		*	*			*		86
0.022−0.017 ferro-actinolite	H	**	*		*		*		150
0.022−0.029 johannsenite	H	**			*	*			112
0.022−0.029 Fe-richterite	H	**	*		*		*		167
0.022−0.051 prehnite	M	*			*	*			244
0.023−0.020 glaucophane	M	**	*		*		*		162
0.023−0.029 pigeonite	H	**	*		*	*			109
0.025−0.073 piemontite	H	*	*		*	*			61
0.025−0.033 ferro-augite	H	**			*	*			116
0.025−0.035 tourmaline (schorl)	H		*	*		*			86
0.027−0.022 tremolite	M	**			*		*		150
0.028−0.024 hedenbergite	H	**	*		*	*			112
0.028−0.047 kaersutite	H	**	*		*		*		160
0.028−0.07 phlogopite-biotite	M	*	*		*		*		189
0.03−0.11 stilpnomelane	H	*	*		*		*		199
0.03 approx. illite	L	*			*		*		230
0.030−0.045 aegirine-augite	H	**	*		*			*	128
0.034−0.028 diopside	H	**			*	*			112
0.032−0.045 grunerite	H	**	*		*		*		147
0.024−0.034 scapolite (meionite)	L			*			*		349
0.035 forsterite	H				*	*			5
0.035 approx. zinnwaldite	L	*	*		*		*		198
0.035−0.042 muscovite	M	*			*		*		181
0.04−0.05 diaspore	H	*			*	*			412
0.04 approx. anhydrite	L	**			*	*			448
0.040−0.060 aegerine	H	**	*		*		*		128
0.042−0.065 zircon	H			*		*			12
0.045−0.075 monazite	H	*		*		*			478
0.050 approx. pyrophyllite	M	*			*		*		202
0.050 approx. talc	M	*			*		*		204
0.052 olivine (fayalite)	H		*		*		*		5
0.073 approx. anatase	H	**		*			*		396
0.096−0.098 cassiterite	H			*		*			383
0.100−0.192 titanite	H	*	*		*	*			15
0.117−0.158 brookite	H				*	*			398
0.138−0.140 goethite	H	*	*		*		*		418

Downloaded from https://pubs.geoscienceworld.org/books/chapter-pdf/3764396/9780903056434_app4.pdf
by guest

Appendix 4

Table B (*contd.*)

Birefringence	Relief	Cleavage	Pleochroic	U	B	+	−	(+ −)	Page
0.149−0.150 strontianite†	L,H	*			*		*		471
0.155−0.156 aragonite†	L,H	*			*		*		468
0.172−0.190 calcite†	L,H	*		*			*		453
0.179−0.185 dolomite†	L,H	*		*			*		463
0.182−0.202 ankerite†	L,H	*		*			*		456
0.190−0.218 magnesite†	L,H	*		*			*		459
0.207−0.242 siderite	H	*		*			*		461
0.28 approx. hematite	VH			*			*		387
0.286−0.296 rutile	VH	*		*		*			393
0.57 approx. lepidocrocite	H	*	*		*		*		420

† Relief changes markedly on rotating polariser

Isotropic minerals (*n*)									
1.433 fluorite	H−	*							480
1.479−1.493 analcime	M−								363
1,483−1.490 sodalite	M−								340
1.508−1.511 leucite	L−								334
1.544 halite	L	*							483
1.71−1.89 garnets	H								18
1.735 periclase	H	*							382
1.719−2.74 spinels	H								402
2.30−2.38 perovskite	H								400

Downloaded from https://pubs.geoscienceworld.org/books/chapter-pdf/3764396/9780903056434_app4.pdf
by guest

Appendix 1

Calculation of a chemical formula from a mineral analysis

Magnesiohornblende analysis

	1 Wt.% of oxides	2 Molecular proportion of oxides	3 Atomic proportion of oxygen from each molecule	4 No. of anions on basis of 24 (O,OH) i.e. col. 3×8.3735		5 No. of ions in formula	
SiO_2	51.63	0.8594	1.7188	14.392	Si	7.196	8.00
Al_2O_3	7.39	0.0725	0.2175	1.821	Al	1.214 (0.804 / 0.410)	
Fe_2O_3	2.50	0.0157	0.0471	0.394	Fe^{3+}	0.263	5.07
FeO	5.30	0.0738	0.0738	0.618	Fe^{2+}	0.618	
MnO	0.17	0.0024	0.0024	0.020	Mn	0.020	
MgO	18.09	0.4489	0.4489	3.759	Mg	3.759	
CaO	12.32	0.2197	0.2197	1.840	Ca	1.840	2.00
Na_2O	0.61	0.0098	0.0098	0.082	Na	0.164	
H_2O+	2.31	0.1282	0.1282	1.073	OH	2.146	2.15
Total	100.32		2.8662				

$$\frac{24}{2.8662} = 8.3735$$

The procedure for calculating a chemical formula is described by means of the above example, a magnesiohornblende.

Column 1 lists the composition of the mineral expressed in the usual manner as weight percentages of oxides.

Column 2 is derived by dividing each column 1 entry by the molecular weight of the oxide concerned (see Appendix 2). The figures so obtained therefore express the molecular proportions of the various oxides.

Column 3 is derived from column 2 by multiplying by the number of oxygen atoms in the oxide concerned. It thus gives a set of numbers proportional to the numbers of oxygen atoms associated with each of the elements concerned. At the foot of column 3 is its total (T).

If we require the amphibole formula based upon 24 oxygen atoms (this represents half the content of the unit cell) we need to re-cast the oxygen atom proportions so that they total 24. This is done by multiplying all of them by 24/T and the results are given in Column 4.

Column 5 gives the number of cations associated with the oxygens in column 4. Thus for SiO_2 there is one silicon for two oxygens so the column 4 entry is divided by 2. For $A1_2O_3$ there are two aluminiums for every three oxygens so the column 4 entry is multiplied by $\frac{2}{3}$. For divalent ions the column 5 value is the same as that of column 4, and for monovalent ions (including hydrogen) the latter is doubled in column 5.

The numbers of ions on the basis of 24 oxygens given in column 5 can be grouped as shown to conform to a structural formula. In the present example it is assumed that the tetrahedral sites which are not filled by Si are occupied by Al, and the remaining Al atoms are in octahedral coordination.

It should be noted that a chemical analysis in itself can give only the ratios of atoms in the formula, and that the actual numbers of atoms given depends on an assumption about the actual number of one of them or of a group of them. A check of the correctness of the formula can be made if the cell volume and density are accurately known, since a calculated density can then be compared with that measured.

A check of charge balance, made by adding positive and negative charges in the formula, is a check only on

Downloaded from https://pubs.geoscienceworld.org/books/chapter-pdf/3764459/9780903056434_backmatter.pdf
by guest

Appendix 1

arithmetic and not on the quality of the analysis. This is because any analysis expressed in terms of neutral oxides must lead to numbers of cations and oxygens which balance electrically.

In many silicates, as in the example above, the only anion in the mineral is oxygen (or OH). Each element is expressed (and generally directly determined) as a weight percentage of oxide, even though the oxides do not exist as such in the mineral. The calculation procedure outlined is justifiable, as each element can be thought of as associated with its appropriate share of the oxygen atoms in the crystal structure.

If oxygen is not the only anion present the calculation is somewhat more complicated, and an example (a fluorphlogopite) is shown below.

Here fluorine is shown, as well as the oxides of all the cations, as a weight percentage. We may assume for simplicity that the fluorine atoms in the structure are bonded to magnesium atoms only, and yet the same atoms of magnesium are recorded as combined with oxygen in MgO. Thus an excess of oxygen is recorded and the total will exceed 100%. To obtain a real total (which is a measure to some extent of the accuracy of the data), an oxygen equivalent of the fluorine atoms must be subtracted.

One excess oxygen atom is recorded for each two atoms of fluorine present, so that the oxygen equivalent of a fluorine by weight is obtained by multiplying the fluorine content by the factor

$$\frac{\text{atomic weight of oxygen}}{2 \times \text{atomic weight of fluorine}}, \text{ i.e. } \frac{16}{38}$$

The oxygen equivalent of the fluorine weight is subtracted from the total of column 1 to give a true total.

The procedure for obtaining column 2 is as before, the fluorine content being divided by 19, the atomic weight of fluorine. For column 3 the number of fluorine atoms is inserted along with the oxygens and the total is again too high. It is necessary to subtract the oxygen equivalent of the fluorine atoms, i.e. half their number, to give a true total.

In the case of fluorphlogopite, the number of anions (O,OH,F) assumed is 24, so that the total of column 3 is divided into 24 to give the multiplying factor which is applied to produce column 4. Column 5 is derived as before.

Many modern analyses are carried out by use of an electron microprobe and this method does not yield values for H_2O and does not differentiate between Fe^{2+} and Fe^{3+}.

If H_2O has not been determined or is thought to be unreliable the mineral formula can be calculated on an anhydrous basis assuming the (OH) content to be ideal. Thus for the magnesiohornblende example above, instead of using 24(O,OH) to derive the scaling factor, 23(O) equivalents [i.e. 22(O) + 2(OH)] can be assumed as associated with all the cations apart from hydrogen.

If Fe^{3+} has not been determined, total iron is usually presented as an FeO equivalent. There are many ways of gaining an estimate of Fe^{3+} and Fe^{2+}, most of which are referred to by Droop (1987). The most appropriate method depends upon the mineral concerned. Some methods re-assign Fe to Fe_2O_3 and FeO in the way which gives the ideal total for all the cations or for particular groups. Some adjust Fe so that trivalent ions in octahedral sites balance the Al replacing Si in tetrahedra. All methods depend on assumptions which may or may not be warranted and all may give only an approximate result.

Fluorphlogopite analysis

	1 Wt.% of oxides	2 Molecular proportion of oxides	3 Atomic proportion of oxygen from each molecule	4 No. of anions on basis of 24 (O,OH) i.e. col. (3) × 8.500		5 No. of ions in formula
SiO_2	41.18	0.6854	1.3708	11.651	Si	5.826
Al_2O_3	12.52	0.1228	0.3684	3.131	Al	2.088
TiO_2	0.99	0.0124	0.0248	0.211	Ti	0.105
FeO	0.30	0.0041	0.0041	0.034	Fe	0.034
MnO	0.04	0.0005	0.0005	0.004	Mn	0.004
MgO	27.32	0.6779	0.6779	5.762	Mg	5.762
Na_2O	0.88	0.0142	0.0142	0.121	Na	0.241
K_2O	11.93	0.1266	0.1266	1.076	K	2.152
H_2O+	1.06	0.0588	0.0588	0.500	OH	1.000
F	6.74	0.3547	0.3547	3.113	F	3.113
	102.96		3.015			
$-O \equiv F$	2.84		$-0.1773 = \frac{1}{2}7 \times 0.3547$			
Total	100.12		2.8235			

$$\frac{24}{2.8235} = 8.500$$

Downloaded from https://pubs.geoscienceworld.org/books/chapter-pdf/3764459/9780903056434_backmatter.pdf
by guest

Further reading

Droop, G.T.R. (1987) A general equation for estimating Fe^{3+} concentrations in ferromagnesian silicates and oxides from microprobe analyses using stoichiometric criteria. *Mineralogical Magazine*, **51**, 431–435.

Appendix 2

Atomic and molecular weights for use in calculations of mineral formulae from chemical analyses.

Al_2O_3	101.96	H_2O	18.015	S	32.06
B	10.81	HfO_2	210.49	SO_3	80.06
B_2O_3	69.62	K_2O	94.20	Sc_2O_3	137.91
BaO	153.33	La_2O_3	325.81	SiO_2	60.08
BeO	25.01	Li_2O	29.88	SnO	134.71
CO_2	44.01	MgO	40.30	SrO	103.62
CaO	56.08	MnO	70.94	Ta_2O_5	441.89
CeO_2	172.12	MnO_2	86.94	ThO_2	264.04
Ce_2O_3	328.24	Mn_3O_4	228.81	TiO_2	79.87
Cl	35.45	Na_2O	61.98	UO_2	270.03
CoO	74.93	NiO	74.69	U_3O_8	842.08
Cr_2O_3	151.99	Nb_2O_5	265.81	V_2O_5	181.88
CuO	79.55	P_2O_5	141.94	Y_2O_3	225.81
F	19.00	PbO	223.20	ZnO	81.38
FeO	71.84	Rb_2O	186.94	ZrO_2	123.22
Fe_2O_3	159.69				

Downloaded from https://pubs.geoscienceworld.org/books/chapter-pdf/3764459/9780903056434_backmatter.pdf
by guest

Appendix 3

End-member calculations

For some purposes it can be useful to express the formula of a mineral which can show a range of compositions between specified end-members, in terms of the percentages of these end-members. There is no single procedure for the required calculation as different assumptions are needed for different minerals and different purposes. In general a relatively small number of 'major' constituent end-members are specified. In the olivines, for example, Mg_2SiO_4(Fo) and Fe_2SiO_4(Fa) may suffice, but the Mn_2SiO_4 (tephroite end-member) could also be calculated. If the Mn content is low it is usually included with Fe as part of the Fa component. For a minor constituent the decision needs to be taken as to whether to ignore it or include it as proxying for a major element, and if so, for which element.

The examples given below help to indicate the kinds of procedures adopted.

Olivine

Ideal formula $(Mg,Fe)_2SiO_4$.
End-members: Mg_2SiO_4(Fo)–Fe_2SiO_4(Fa).
Example formula on basis of 4(O):

$$(Si_{0.97}Al_{0.03})_{1.00}(Ti_{0.02}Fe^{3+}_{0.01}Mg_{1.91}Fe^{2+}_{0.04}Mn_{0.01})_{1.99}$$

End-member percentages:

$100Mg/(Mg + Fe^*) = 191/1.96 = 97.4\%$
$100Fe^*/(Mg + Fe^*) = 5/1.96 = 2.6\%$
(where $Fe^* = Fe^{2+} + Fe^{3+}$) } $Fo_{97.4}Fa_{2.6}$

If $Fe^* = Fe^{2+} + Fe^{3+} + Mn$. Fo = 191/1.97 = 96.9%: $Fo_{96.9}Fa_{3.1}$

Augite

Ideal formula $(Ca,Mg,Fe)_2(Si,Al)_2O_6$.
End-members: $Mg_2Si_2O_6$(En)–$Fe_2Si_2O_6$(Fs)–$Ca_2Si_2O_6$(Wo).
Example formula on basis of 6(O):

$$(Si_{1.94}Al_{0.06})_{2.00}(Al_{0.01}Fe^{3+}_{0.03}Ti_{0.02}Mg_{0.21}Fe^{2+}_{0.87}Mn_{0.02}Ca_{0.82}Na_{0.02})_{2.00}$$

End-member percentages:

$100Mg/(Mg + Fe^* + Ca) = 21/1.95 = 10.77\%$

$100Fe^*/(Mg + Fe^* + Ca) = 92/1.95 = 47.18\%$

$100Ca/(Mg + Fe^* + Ca) = 82/1.95 = 42.05\%$

(where $Fe^* = Fe^{2+} + Fe^{3+} + Mn$); i.e. $En_{10.77}Fs_{47.18}Wo_{42.05}$
Alternative including end-member $NaFe^{3+}Si_2O_6$(Ac)

$100Na/(Mg + Fe^* + Ca + Na) = 2/1.97 = 1.02\%$

leaving 21/1.97(En), 92/1.97(Fs) and 82/1.97(Wo), i.e. $En_{10.66}Fs_{46.70}Wo_{41.62}Ac_{1.02}$

Downloaded from https://pubs.geoscienceworld.org/books/chapter-pdf/3764459/9780903056434_backmatter.pdf
by guest

Garnet

Ideal formula $(Mg,Fe^{2+},Mn,Ca)_3(Al,Fe^{3+},Cr)_2(Si,Al)_3O_{12}$.
End-members: Mg_3Al_2 pyrope; $Fe_3^{2+}Al_2$ almandine; Mn_3Al_2 spessartine; Ca_3Al_2 grossular; $Ca_3Fe_2^{3+}$ andradite; Ca_3Cr_2 uvarovite
Example formula on basis of 24(O):

$$(Si_{5.98}Al_{0.02})_{6.00}(Al_{3.91}Fe^{3+}_{0.13}Cr_{0.03})_{4.07}(Mg_{3.58}Fe^{2+}_{1.55}Mn_{0.04}Ca_{0.73})_{5.90}$$

End-member percentages

pyrope 358/5.90 = 60.68%, andradite 13/4.07 = 3.19%

almandine 155/5.90 = 26.27%, uvarovite 3/4.07 = 0.74%

spessartine 4/5.90 = 0.67%, Σ(and + uv) 16/4.07 = 3.93%

gro + and + uv = 73/5.90 = 12.37%

gro = 12.37 − Σ(and + uv) = 12.37 − 3.93 = 8.44%

Result: $py_{60.7}alm_{26.3}gro_{8.4}and_{3.2}uv_{0.7}sp_{0.7}$

Feldspar

Plagioclase feldspar: as for olivine but use

100Ca/(Ca + Na) = An

100Na/(Ca + Na) = Ab

Alkali feldspar: as for olivine but use

100Na/(Na + K) = Ab

100K/(Na + K) = Or

Ternary feldspar: as for augite but use

100Ca/(Ca + Na + K) = An

100Na/(Ca + Na + K) = Ab

100K/(Ca + Na + K) = Or

Downloaded from https://pubs.geoscienceworld.org/books/chapter-pdf/3764459/9780903056434_backmatter.pdf
by guest

Appendix 4

Use of optical identification tables

The birefringence (δ) exhibited by a crystal varies with orientation, but the maximum birefringence shown by crystals of a mineral (of specific composition) in a range of orientations is characteristic of that mineral. 'Maximum birefringence' might also, however, be taken to mean the highest characteristic value shown by the members of a chemical series, e.g. forsterite (Mg_2SiO_4)–fayalite (Fe_2SiO_4). Use of birefringence diagnostically needs to take account of both meanings, the former to determine a meaningful value, and the latter to allow for the possible 'chemical range' when using that value to suggest a mineral name.

The petrological use of the polarising microscope can be treated at different levels according to the needs of different student groups. At one level would be the practical observation of the colours of a mineral in thin section between crossed polars and relating these to birefringence (δ)[a]. This relationship is presented here in Table A for use with a thin section of standard thickness, 0.03 mm. (The presence of twinning is also best observed between crossed polars, and isotropic minerals could be noted). In Table A alongside each δ value are the minerals that possibly match but, mainly because of chemical variation, those somewhat lower in the chart need also to be considered. The possibilities should be readily narrowed by observation of other properties using Table B as suggested below.

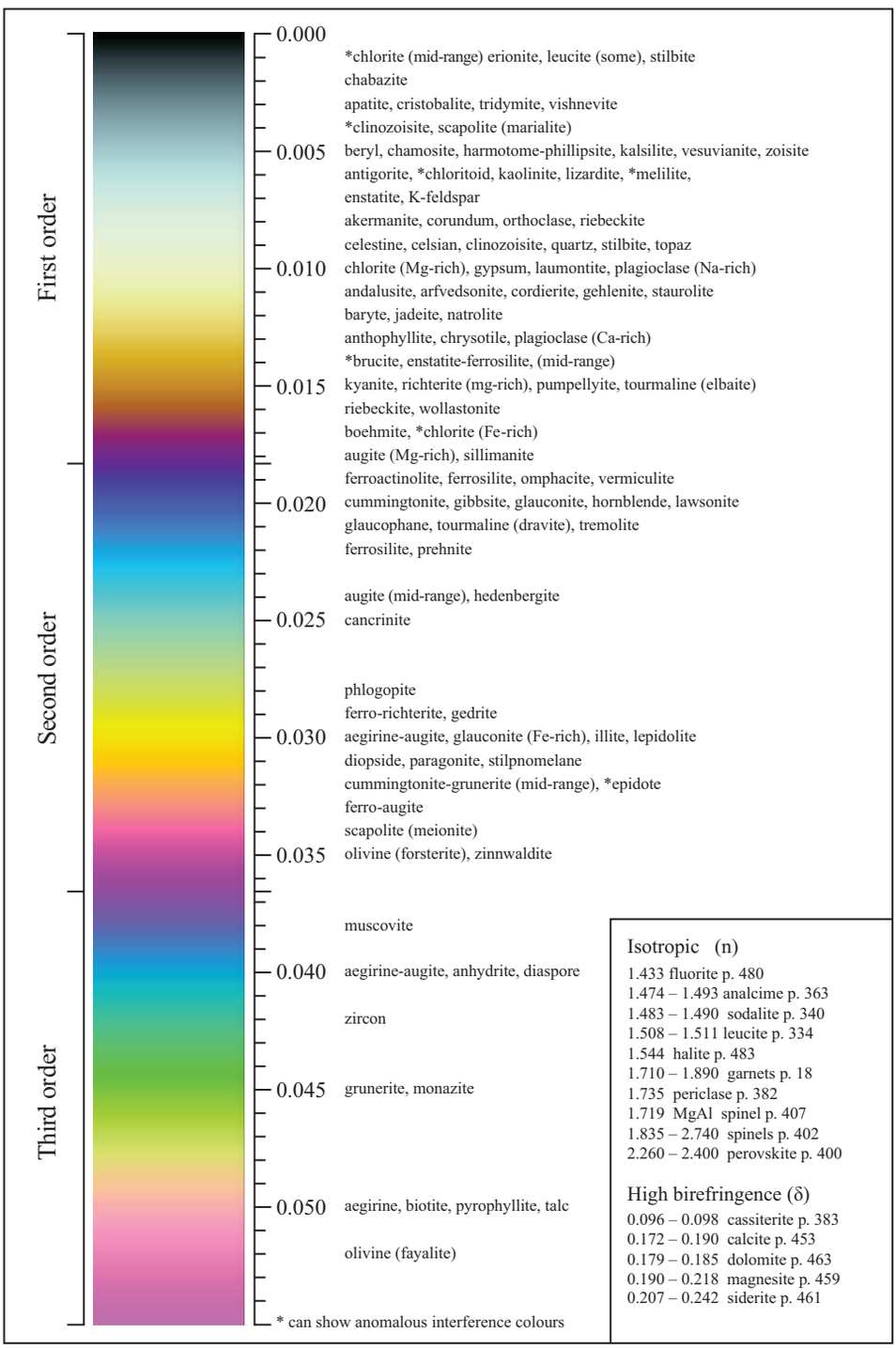
Also at a fairly basic level of investigation would be some (mostly qualitative) observations in plane polarized light, including prominent cleavage(s), pleochroism and 'relief' (high, moderate or low). A further level would involve observing interference figures in convergent light to determine whether a mineral is uniaxial or biaxial, and using a testing instrument, to determine optic sign. The above properties are listed in that order in Table B. For each mineral treated in the present text, this Table gives the range of δ that results from chemical variation, and the minerals are listed in numerical order according to the low birefringence end of that range.

For more detail and for quantitative data such as optical orientation, extinction angles and values of the optic axial angle (2V), Table B gives the starting page reference for each mineral. More general properties (colour, hardness, density, etc.) are also listed there. In addition, the text for each main mineral contains a section headed 'Distinguishing features' which helps discriminate between that mineral and a selection of others with which it might be confused.

[a] Similar colours in different 'orders' can be distinguished by gradually inserting a quartz wedge testing instrument to 'compensate' those colours , and observing the gradual changes of colours as the net birefringence is reduced to zero.

Downloaded from https://pubs.geoscienceworld.org/books/chapter-pdf/3764459/9780903056434_backmatter.pdf
by guest

Table A. Birefringences and Michel-Lévy interference colours (0.03 mm thin section) for the most common rock-forming minerals (colour strip (calculated) kindly provided by Professor Takenori Kato, Nagoya University, Japan (http://www.nendai.nagoya-u.ac.jp/gsd/sicc/).



Downloaded from https://pubs.geoscienceworld.org/books/chapter-pdf/3764459/9780903056434_backmatter.pdf
by guest

Appendix 4

Table B. Optical properties of common minerals in order of increasing birefringence.

Relief: L low, M moderate, H high, VH very high; all with R.I >1.54 (standard mounting medium). L−, M−, negative relief. (R.I. <1.54).
Cleavage: * one cleavage commonly visible. ** two intersecting cleavages.
Pleochroic: * can show pleochroism.
U: uniaxial, B: biaxial, +: positive, −: negative, (+ −): either positive or negative.

Birefringence	Relief	Cleavage	Pleochroic	U	B	+	−	(+ −)	Page
0.00−0.01 chlorite (mid-range)	M	*	*		*			*	208
0.001−0.005 chabazite	M−				*			*	374
0.001−0.007 apatite	M		*	*			*		473
0.001−0.009 vesuvianite	H			*			*		28
0.001−0.013 melilite	M	*	*	*				*	72
0.002−0.004 vishnevite	L−	*		*			*		345
0.002−0.004 α-tridymite	M−				*	*			311
0.005−0.020 approx. cancrinite	L−	*		*			*		345
0.003 α cristobalite	M−			*			*		311
0.003−0.004 clinoptilolite	M−	*			*			*	372
0.003−0.005 erionite	M−			*				*	355
0.003−0.005 nepheline	L−			*			*		325
0.003−0.008 zoisite	H	*			*	*			53
0.003−0.009 heulandite	M−	*			*			*	372
0.003−0.010 phillipsite	M−				*	*			368
0.004−0.005 mordenite	M−	*			*	*		*	377
0.004−0.005 scapolite (marialite)	L	**		*			*		349
0.004−0.007 antigorite	L	*			*		*		216
0.004−0.009 beryl	L			*			*		76
0.004−0.015 clinozoisite	H	*			*	*			56
0.005−0.006 kalsilite	L−			*			*		325
0.005−0.008 harmotome	M−				*	*			368
0.005−0.010 hyalophane	L−	**			*		*		291
0.005−0.022 chloritoid	H	*	*		*			*	47
0.006−0.008 lizardite	L	*		*			*		216
0.006−0.010 K-spar−Na-spar	L−	**			*			*	253
0.006−0.016 riebeckite	H	**	*		*			*	162
0.006−0.021 jadeite	H	**	*		*	*			125
0.006 approx. kaolinite	L	*			*			*	227
0.007−0.021 katophorite	H	**	*		*		*		167
0.007−0.016 enstatite	H	**	*		*			*	102
0.008 approx. microcline	L−	**			*		*		253
0.008−0.009 corundum	H		*	*			*		384
0.008−0.011 topaz	M	*	*		*	*			44
0.008−0.018 cordierite	L	*	*		*			*	80
0.008 approx. åkermanite	M			*		*			72
0.009 α-quartz	L			*		*			311
0.009−0.010 stilbite	L−	*			*		*		335
0.009−0.012 andalusite	M	*			*		*		33
0.009−0.013 celsian	M	**			*	*			291
0.009 approx. celestine	M	**	*		*	*			444
0.01−0.04 smectite	L	*			*		*		234
0.010−0.012 arfvedsonite	H	**	*		*		*		169
0.010−0.012 laumontite	L−	**			*		*		370
0.010−0.020 pumpellyite	H	**	*		*			*	68
0.010 approx. albite	L−	**			*	*			253
0.010 approx. gypsum	L−	*			*	*			445
0.011−0.014 staurolite	H	*	*		*	*			39
0.011 approx. gehlenite	H			*					72
0.012−0.016 kyanite	H	*	*		*		*		36
0.012 approx. natrolite	M−	*			*	*			366
0.012 approx. baryte	M	**			*	*			441
0.013−0.014 wollastonite	M	**			*		*		132
0.013−0.017 chrysotile	L								216
0.013−0.020 eckermannite	H	**	*		*		*		169

Downloaded from https://pubs.geoscienceworld.org/books/chapter-pdf/3764459/9780903056434_backmatter.pdf
by guest

Table B (*contd*.)

Birefringence	Relief	Cleavage	Pleochroic	U	B	+	−	(+ −)	Page
0.013−0.021 anthophyllite	M	**			*			*	144
0.013−0.036 allanite	H		*		*			*	63
0.013 approx. anorthite	L	**			*		*		292
0.014−0.020 brucite	M	*		*		*			409
0.014−0.027 spodumene	H	**			*	*			131
0.012−0.028 omphacite	H	**	*		*	*			122
0.015−0.020 boehmite	M				*	*			414
0.015−0.022 kosmochlore	H	**	*		*		*		125
0.015−0.022 Mg-richterite	H	**	*		*		*		167
0.015−0.051 epidote	H	*	*		*		*		56
0.016−0.022 ferrosilite	H	**	*		*			*	102
0.017−0.021 tourmaline (elbaite)	M		*	*			*		86
0.018−0.022 sillimanite	H	*	*		*	*			30
0.018−0.025 augite	H	**	*		*	*			116
0.018−0.035 lepidolite	L	*		*	*		*		195
0.019−0.021 lawsonite	H	**			*	*			65
0.02−0.03 glauconite	M	*			*		*		188
0.02−0.03 vermiculite	L	*	*		*		*		239
0.02 approx gibbsite	L	*			*	*			410
0.02 approx hornblende	H	**	*		*			*	154
0.020−0.032 cummingtonite	H	**			*	*			147
0.021−0.029 gedrite	H	**	*		*			*	144
0.021−0.029 tourmaline (dravite)	M		*	*			*		86
0.022−0.017 ferro-actinolite	H	**	*		*		*		150
0.022−0.029 johannsenite	H	**			*	*			112
0.022−0.029 Fe-richterite	H	**	*		*		*		167
0.022−0.051 prehnite	M	*			*	*			244
0.023−0.020 glaucophane	M	**	*		*		*		162
0.023−0.029 pigeonite	H	**	*		*	*			109
0.025−0.073 piemontite	H	*	*		*	*			61
0.025−0.033 ferro-augite	H	**			*	*			116
0.025−0.035 tourmaline (schorl)	H		*	*		*			86
0.027−0.022 tremolite	M	**			*		*		150
0.028−0.024 hedenbergite	H	**	*		*	*			112
0.028−0.047 kaersutite	H	**	*		*		*		160
0.028−0.07 phlogopite-biotite	M	*	*		*		*		189
0.03−0.11 stilpnomelane	H	*	*		*		*		199
0.03 approx. illite	L	*			*		*		230
0.030−0.045 aegirine-augite	H	**	*		*			*	128
0.034−0.028 diopside	H	**			*	*			112
0.032−0.045 grunerite	H	**	*		*		*		147
0.024−0.034 scapolite (meionite)	L			*			*		349
0.035 forsterite	H				*	*			5
0.035 approx. zinnwaldite	L	*	*		*		*		198
0.035−0.042 muscovite	M	*			*		*		181
0.04−0.05 diaspore	H	*			*	*			412
0.04 approx. anhydrite	L	**			*	*			448
0.040−0.060 aegerine	H	**	*		*		*		128
0.042−0.065 zircon	H			*		*			12
0.045−0.075 monazite	H	*		*		*			478
0.050 approx. pyrophyllite	M	*			*		*		202
0.050 approx. talc	M	*			*		*		204
0.052 olivine (fayalite)	H		*		*		*		5
0.073 approx. anatase	H	**		*			*		396
0.096−0.098 cassiterite	H			*		*			383
0.100−0.192 titanite	H	*	*		*	*			15
0.117−0.158 brookite	H				*	*			398
0.138−0.140 goethite	H	*	*		*		*		418

Downloaded from https://pubs.geoscienceworld.org/books/chapter-pdf/3764459/9780903056434_backmatter.pdf
by guest

Appendix 4

Table B (*contd.*)

Birefringence	Relief	Cleavage	Pleochroic	U	B	+	−	(+ −)	Page
0.149−0.150 strontianite†	L,H	*			*		*		471
0.155−0.156 aragonite†	L,H	*			*		*		468
0.172−0.190 calcite†	L,H	*		*			*		453
0.179−0.185 dolomite†	L,H	*		*			*		463
0.182−0.202 ankerite†	L,H	*		*			*		456
0.190−0.218 magnesite†	L,H	*		*			*		459
0.207−0.242 siderite	H	*		*			*		461
0.28 approx. hematite	VH			*			*		387
0.286−0.296 rutile	VH	*		*		*			393
0.57 approx. lepidocrocite	H	*	*		*		*		420

† Relief changes markedly on rotating polariser

Isotropic minerals (*n*)									
1.433 fluorite	H−	*							480
1.479−1.493 analcime	M−								363
1,483−1.490 sodalite	M−								340
1.508−1.511 leucite	L−								334
1.544 halite	L	*							483
1.71−1.89 garnets	H								18
1.735 periclase	H	*							382
1.719−2.74 spinels	H								402
2.30−2.38 perovskite	H								400

Downloaded from https://pubs.geoscienceworld.org/books/chapter-pdf/3764459/9780903056434_backmatter.pdf
by guest

Index

Mineral names in **bold** type are those described in detail; page numbers in **bold** type refer to the principal descriptions or definition of the mineral. Entries other than mineral names are in *italic* type, t refers to a table.

Acmite 128
Actinolite 140t
Adularia 250, 282, 288
Aegirine-augite **128–30**
Aegirine 99t, **128–30**
Aenigmatite 133
Agate 318
Akaganéite 417
Åkermanite **72–5**
Al hydroxides and oxyhydroxides **409–15**
Alabaster 447
Alamosite 133
Albite 248, 253, 256, 258–9, 261, 264, 268, 272, 292, 299t, 309
Albite: authigenic 309
Albite: twins 265–7, 304–5
Alexandrite 385
Alkali Feldspar **248–90**
  analyses 270
  electron microscopy 280–2
  order–disorder 272
  relationships in magmas 283
  solvus curves 274–6
  system Ab–Or–Q–H_2O 273
Allanite 58t, **63–4**
Almandine 18, 20, 22
Altaite 439
Aluminotschermakite 141t
Amblygonite 196
Amesite 210, 216, 222
Amethyst 317
Amosite 149
Amphibole structure 137
Amphibole Group **137–71**
Analcime 355, 357, **363–5**, 364t
Anatase **396–7**
Andalusite **33–35**, 37t
Andesine 250, 393
Andradite 18, 20
Anglesite 440–1
Anhydrite **448–9**
Ankerite 451, 452, 454t, 463
Annite 179t, 180t, **189–94**
Anorthite **292–4**
Anorthoclase 268–9, 277–8, 282, 287
Anorthosite 307
Anthophyllite 139t, **144–6**
Antigorite 216, 219, 220, 221t
Antiperthite 260, 297
Antozonite 480
Apatite **473–7**, 475t
Aquamarine 78–9
Aragonite 451, 454t, **468–70**
Arfvedsonite 142t, **169–71**
Arsenopyrite 424
Asbestiform 145, 149, 151, 164
Asbestos 164–5, 216, 221
Asterism 192
Augite–Ferro-augite 98t, **116–21**
Authigenic albite 309
Aventurescence 352
Aventurine feldspar 280, 306
Azurite 452

Baddeleyite 394
Baileychlore 210, 211
Barium Feldspars **291**
Barroisite 139, 167
Baryte **441–3**
'Basic' sodalite 341
Bassanite 446
Bastite 106
Bauxite 411, 414
Baveno twins 265–7
Bayerite 329
'*Beef' (calcite)* 457
Behaviour diagrams 258–60, 275
Beidellite 225, 235, 237
Berthierine 210, 216, 222
Beryl **76–9**, 78t
Biotite 177t, 179t, **189–94**
Biotite-vermiculite 183
Blue John fluorite 481, 482
Boehmite **414–5**, 420
Bøggild intergrowths 249, **294–5**, 306, 308
Bowlingite 8
Braid perthite 263, 279–81, 288
Brammallite 187, 231
Bravoite 424
Brazilian 'ruby' 45
Breunnerite 459
Brewsterite 357
Brewsterlinite 45
Brookite **398–9**
Brucite **409**
Buddingtonite 270
Buergerite 88–9
Bustamite 132
Bytownite 250, 393

Calciocelsian 291
Calcite 451, **453–8**, 454t
Calderite 21
Californite 28
Cancrinite 347
Cancrinite–Vishnevite **345–8**
Carbonates **451–72**
Carlsbad twins 265–6, 298
Carnegieite 325
Cassiterite **383**
Cation exchange 224, 231, 236, 240
Cattierite 424
Ce-perovskite 400
Cebollite 74
Celadonite 177, 188
Celestine 441, **444**
Celsian 291
Cerussite 440, 452
Chabazite series 355, 356–7, **374–6**
Chalcedony 312, 318
Chalcocite 433
Chalcopyrite **432–4**
Chalcopyrite disease 433
Chamosite **208–15**, 211t, 222
Cheralite 478
Chert 318
Chiastolite 34
China clay 229
Chlorapatite 473, 475
Chlorite 211t
Chlorite Group **208–15**
Chloritoid **47–51**
Chlorophaeite 8
Chondrodite 4, 9
Chrome-pyrope 19, 25–6
Chromite 402, 406, 408
Chromite series 406
Chrysoberyl 77
Chrysotile 7, **216–21t**
Citrine 317
Clausthalite 439
Clay Minerals **224–43**
Cleavelandite habit 298
Clinochlore **208–15**, 211t,
Clinochrysotile 216, 220
Clinoenstatite 102–3
Clinoferrosilite 103
Clinohumite 4, 10
Clinoptilolite-K 372
Clinoptilolite series 355, **372–3**
Clinozoisite–epidote **56–60**
Clintonite 177
Coesite 312, 315, 322
Coherent/incoherent intergrowth 260
Collophane 475
Convergent/non-convergent ordering 257, 261

Downloaded from https://pubs.geoscienceworld.org/books/chapter-pdf/3764459/9780903056434_backmatter.pdf
by guest

Cookeite 210
Cordierite **80–5**, 81t
Corrensite 210
Corundum **384–6**, 385t
Cristobalite 311, **313–5**, 317, 319, 321
Crocidolite 164–5
Cronstedtite 210, 216
Cryolite 481
Cryptoperthite 249, 263
Crystallinity index 231
Cummingtonite–Grunerite 140t, **147–9**
Cyprine 28

Dachiardite 357
Dahlite 474
Dannemorite 148
Datolite 245
Demantoid 22, 26
Desert rose 442, 447
Diaspore **412–3**
Dickite **227–8**
Differential thermal analysis 202, 211, 220, 228, 231, 236, 241
Digenite 433
Dioctahedral chlorite 210
Diopside–Hedenbergite 98t, **112–5**
Distribution coefficient
biotite/garnet 192
pyroxenes 104
Dolomite 451, 454t, **463–7**
Donbassite 213, 215
Donpeacorite 95, 103
Dravite **86–92**, 90t

Eastonite **189–94**
Eckermannite 139, 142, 169
Eckermannite–Arfvedsonite **169–71**
Edenite-Ferro-edenite 139t, **154–5**
Edingtonite 366
Elbaite **86–92**, 90t
Emerald 77–9
Enantiomorphism 317
Enstatite–Ferrosilite **102–8**, 98t
Epidote Group **52–64**
Epidote **56–60**, 58t
Epistilbite 357
Erionite 355, 357–8, 374
Esseneite 95
Eucryptite 131
Europium anomaly 298
Exfoliation 239–40
Extinction angle (plagioclase) 304–6

Faujasite 357
Fayalite **8–11**
Fe-Mg distribution coefficient 24
Feldspar twin laws 265
Feldspar Group **248–309**
Feldspar
system Ab–Or–H_2O 271
system Ab–Or–Q–H_2O 272–3
system $KAlSi_3O_8$–H_2O 271
system Ab–Or–An
solvus curtves 250, 275–6
system Ab–Or–An–Q 284
Feldspathoids **325–54**
Fe oxyhydroxides **417–21**
Feroxyhyte 417
Ferrierite 357
Ferrihydrite 417, **421**
Ferripyrophyllite 202
Ferristilpnomelane 199–201
Ferro-actinolite 140t, **150–3**
Ferroan talc 205
Ferro-augite 98t, **116–21**
Ferrobrucite 409
Ferrobustamite 113, 117, 132
Ferro-edenite **154–9**
Ferroglaucophane 142t, 163
Ferrohornblende **154–9**
Ferrohortonolite 7
Ferrokaersutite **160–1**
Ferropargasite **154–9**
Ferropericlase 382
Ferrorichterite **167–8**
Ferrosaponite 236
Ferrosilite 98t, 100, **102–8**
Ferrostilpnomelane 199–201
Ferrotschermakite **154–9**
Fibrolite 30
Film perthite 279–81
Flint 318
Fluid inclusion 281, 318
Fluor-dravite 86
Fluor-elbaite 86
Fluor-olenite 86
Fluor-schorl 86
Fluor-uvite 86
Fluorapatite 473, 475
Fluorite **480–2**
Foitite 88
Forsterite 8
Framboidal texture (pyrite) 426
Francolite 474, 475
Franklinite 402, 405, 408
Fuchsite 182
Fuller's earth 236–7

Gahnite 402, 404, 407
Galaxite 402, 404
Galena **439-40**
Garnet Group **18–27**
Gedrite 139t, **144–6**
Gehlenite **72–5**, 73t
Geikielite 391
Geothermometry 24, 104
Gibbsite **410–1**
Gismondine 355, 357
Glauconite **188**, 231
Glaucophane 139t, 141t, **162–6**
Glycerol 235, 239, 241
Glycol 226, 228, 230, 239
Gmelinite 355, 357
Goethite 388, **418–9**
Goldmanite 21
Gonnardite 366
Goslarite 437
Granophyric texture 289
Greenalite 201
Greigite 426
Grossmanite 95
Grossular 18, 20
Grothite 16
Groutite 418
Grunerite 140t, **147–9**
Gypsum **445–7**

Hackmanite 341, 342, 343
Hafnon 13
Halides **480–4**
Halite **483–4**
Halloysite-10Å 227
Halloysite-7Å 227
Halloysite **225–6**, 229
Hancockite 57
Harmotome **355–7**
Hastingsite 141t, **154**
Hauerite 424
Haüyne **340–4**, 342t
Hectorite 235, 237
Hedenbergite 98t, **112–5**
Heliodor 78
Helvite 79
Hematite **387–9**
Hepatite 441
Hercynite **402–5, 407**
Hessonite 22
Heulandite-Ca 372
Heulandite series 355–7, **372–3**
Hexagonal pyrrhotite 429
HF etching (feldspars) 280
Hibschite 18, 21
Hiddenite 131
High albite **253–4**
High sanidine **253–4**, 278
Holmquistite 146
Hornblende 140t, **154–9**
Hortonolite 7, 8
Hour-glass structure 221, 244
Hourglass zoning 129
Humite 4, 10
Humite Group 4
Huntite 451, 452
Hüttenlocher intergrowths 249, **294–6**, 306, 308
Huttonite 478
Hyacinth 13
Hyalophane 291
Hyalosiderite 7
Hydroandradite 21
Hydrogarnet 19, 21
Hydrogrossular 18, 22
Hydromuscovite 183
Hydrosodalite 340
Hydroxyl-fluorapatite 475
Hydroxylapatite 473, 475

Iceland spar 458
Iddingsite 8
Illite Group 225t, **230–3**
Ilmenite **390–2**, 391t
Indialite 80
Indicolite 89
Interlayer molecules 236
Inverse spinel 403

Downloaded from https://pubs.geoscienceworld.org/books/chapter-pdf/3764459/9780903056434_backmatter.pdf
by guest

Iridescence
anthophyllite 145
perthite 249, 280
plagioclase 306
Iron-åkermanite 73
Iron-gehlenite 73

Jacobsite 402, 405
Jade 151
Jadeite 99t, **125–7**
Jargoon 13
Jasper 318
Jervisite 95
Johannsenite 95, 98t, **112–5**
Julgoldite 69

Kaersutite–Ferrokaersutite 141, 158, **160–1**
Kaliophilite 327
Kalsilite **325–33**, 329
Kammererite 211
Kanoite 95, 103, 108
Kanonaite 34
Kaolinite Group 225t, **227–9**
Kataphorite **167–8**
Katoite 21
Keatite 131, 315, 317
Keilhauite 16
Kidney ore 387
Kimzeyite 21
Knebelite 8
Knorringite 19
Kôzulite 170
Kosmochlor 99t, **125–7**
Kunzite 131
Kushiroite 95
Kutnohorite 463
Kyanite **36–8**

Labradorescence 306
Labradorite 250, 393
Lapis lazuli 342
Larnite 75
Larvikite 280
Latrappite 400
Laumontite 355, 357, **370–1**
Lawsonite **65-7**, 244
Lazurite 340, 342
Lechatelierite 312
Leonhardite 370
Lepidocrocite 417, **420**
Lepidolite 177t, 179t, 190, **195–7**
Lepispheres 312
Leucite **334–9**, 336t
Leucoxene 391
Lévyne 357, 374
Liddicoatite 88
Lithian muscovite 184, 190
Lithium micas 180
Lizardite 216, 219, 221t
Löllingite 424
Loparite-(Ce) 400
Low microcline 256
Lueshite 400
Lusakite 40

Macfallite 68
Mackinawite 426
Macroperthite 249
Maghemite 387, 402, 405, 408
Magnesian ilmenite 392
Magnesioarfvedsonite 170
Magnesiochloritoid 48–9
Magnesiochromite 402, 406, 408
Magnesioferrite 402, 404, 407
Magnesiohastingsite–Hastingsite **154–9**
Magnesiohornblende–Ferrohornblende 141t, **154–9**
Magnesiokataphorite 142t
Magnesiokatophorite–Katophorite 167
Magnesioriebeckite–Riebeckite 141t, **162–6**
Magnesiostaurolite 42
Magnesiotaramite 168
Magnesiowüstite 382
Magnesite 451, 454t, **459**
Magnetite 402, 404, 407
Malachite 452
Malayaite 16–7
Manebach twinning 265–6, 298
Manganapatite 475
Manganocummingtonite 148
Manganogrunerite 148
Manganorichterite 142t
Marcasite 424
Margarite 177
Marialite **349**
Martite 387
Maskylenite 309
Masutomilite 198
Meionite **349**
Melanite 21, 22, 26
Melilite Group **72–5**
Melnikovite 426
Merwinite 75
Mesh structure 221
Mesolite 355, 366
Mesoperthite 249, 260, 262
Metakaolin 228
Metamict state 13, 14, 63, 478
Mica structure 174–6
Mica Group **174–98**
Microcline 249, **253–9**
Microperthite 249, 262
Microsommite 347
Minnesotaite 204
Mogánite 312
Molecular sieve 356, 358
Monalbite 250, 258–9
Monazite **478–9**
Monoclinic pyrrhotite 429
Montasite 149
Monticellite 4, 8
Montmorillonite 225, 235, 237
Mordenite 355, **377–8**
Morganite 78
Morphology and twinning feldspars 249, 264, 297–8
Mukhinite 57, 61
Mullite 37
Muscovite 177t, 179t, **181–6**
Myrmekite texture 289, 321

Nacrite 227–8
Namansilite 95
Natalyite 95
Natrolite 355, 357, **366–7**
Nb-perovskite 400
Nemalite 409
Nepheline **325–33**, 329t
Nephrite 151
Niccolite 429
Nimite 210, 213
Nontronite 225, 235, 237, 238
Norbergite 4
Normal spinel 403
Nosean **340-4**, 342t
Nyerereite 452

Obliquity (microcline) 249
Offretite 357
Olenite **86–92**, 90
Oligoclase 250, 393
Olivine Group **4–11**
Olivine, serpentinization 9
Omphacite 99, 100, 117, **122–4**
Opal 312, 319
Opalescence 319
Orthochrysotile 216
Orthoclase feldspar 256, 265, 270, 275, 278
Orthopyroxene 94, **102–8**
Ottrelite 48, 49
Oxides **382–408**
Oxo-hornblende 156, 159

Palygorskite 224
Panunzite 326
Parachrysotile 218
Paragonite 177t, **187**
Pargasite–Ferropargasite 139t, **154–9**
Parsettensite 200
Patch perthite 279, 281
Pearl 470
Pecoraite 220
Pectolite 132
Peg structure 74–5
Pennantite 210, 211, 213
Pentlandite 431
Percussion figure 178, 192
Periclase **382**
Pericline twins 265–6, 268–9, 298
Peristerite 249, 306, 308
Peristerite intergrowths 249, **294–5**, 306
Perovskite **400-1**
Perthite(s) 249, 260, 262, 287
Petedunnite 95, 113
Phenakite 77
Phengite 179, 183
Phillipsite–Harmotome **368–9**
Phillipsite 355
Phlogopite 177t, 179t, **189–94**
Phosphates **473–9**
Picotite 404
Piemontite 58t, **61–2**
Piezoelectric and pyroelectric properties (tourmaline) 87
Pigeonite 98t, **109–11**
Pinite 81

Downloaded from https://pubs.geoscienceworld.org/books/chapter-pdf/3764459/9780903056434_backmatter.pdf
by guest

Pistomesite 461
Plagioclase Feldspar **292–309**
analyses 299t
extinction angles 304–5
iridescence 306
structure 354–9
Plagioclase alteration 302
Plaster of Paris 445
Plasticity of clays 229
Pleochroic haloes 14, 192, 213
Pleonaste 403
Pollucite 334, 357
Polygonal serpentine 218, 219
Polylithionite 195–6
Povondraite 88
Prehnite **244–6**, 245t
Protoenstatite 100, 102-103, 105
Pseudobrookite 399
Pseudoleucite 289, 334, 336
Pseudowollastonite 133, 135
Pumpellyite **68–71**, 69t
Pyrite **424–8**
Pyromorphite 440
Pyrope 18–20
Pyrophanite 390–1
Pyrophyllite **202–3**, 235
Pyroxene Group **94–131**
Pyroxene geothermobarometry 104
Pyroxmangite 133
Pyrrhotite **429–31**

Quartz **311–3**, **315–8**, 320
twin laws 317
rotary polarization 317

Rectorite 235
Reedmergnerite 271
Reidite 13
Rhodochrosite 451, 454t
Rhodonite 120, 133
Rombic section; feldspar 266–8
Richterite–Ferrorichterite 142t, **167–8**
Riebeckite 142t, **162–6**
Rose quartz 317
Rose muscovite 182, 184, 196
Rossmanite 88
Rubellite 89, 91
Rubicline 270
Ruby 384
Rutile **393–5**, 394t

Sanidine twinning **253–8**, **270t**, **282**, **287**
Saponite 225, 235, 237
Sapphire 384–5
Sapphirine 133, 386
Satin spar 447
Sauconite 234, 235, 237, 238
Scapolite 26, **349–53**, 352t
Schiller 280, 306
Schorl **86–92**, 90t
Schorlomite 20, 21, 22, 26
Scolecite 366
Sector twinning 22, 83, 119
Seifertite 312, 320
Sekaninaite 81
Selenite 446
Sepiolite 224
Sericite 231
Sericitization 232
Serpentine **216–23**
Serpentinization of olivine 9
Shearing transformation 274
Shirozulite 190
Si–Al ordering: orthoclase 256
Siderite 451, 454t, **461–2**
Siderophyllite **189–94**
Sideroplesite 461
Silica polymorphs 315
Silica minerals **311–23**
Silicalite 358
Sillimanite **30–2**, 37t
Silvialite 353
Smectite 226, 230
Smectite Group **234–8**
Smithsonite 452
Smoky quartz 317
Soda melilite 72-73
Sodalite Group **340-4**, 342t
Sodium amphiboles 162
Sodium feldspars 259, 268, 299t, 306, 309
Specularite 387
Spessartine 18, 20, 22
Sphaerosiderite 461
Sphalerite **435-8**
Spinel twin law 403, 406
Spinel Group **402–8**, 405t
Spinel (*sensu stricto*) 403–4, 406–7
Spinodal decomposition 276
Spodumene 99t, **131**
Spurrite 75
Staining technique 451–2, 457
Staining potassium feldspar 282
Star-sapphires 385
Staurolite **39–43**
Stilbite **355–7**
Stilpnomelane **199–201**
Stishovite 312, 315, 320
Strüverite 394
Strontianite 454t, **471–2**
Sudoite 211, 213
Sulphates **441–9**
Sulphur 444, 447
Sulphides **423–40**
Sursassite 68
Sylvite 483

Talc **204–7**, 235
Tanzanite 54
Taramite 139, 167–8
Tarnowitzite 468
Tartan twinning (alkali feldspar) 248, 259, 266, 268, 288
Tawmawite 53, 57
Tephroite 8
Tetraferriannite 190
Tetraferriphlogopite 190
Tetrakalsilite 326, 328
Thomsonite **355–6**
Thulite 53–4, 61
Tirodite 148
Titanite **16–7**
Titanohematite 388
Topaz **44–6**
Topazolite 22, 26
Tosudite 235
Tourmaline **86–92**, 90t
Tremolite–Ferro-actinolite 139–40t, **150–3**
Trevorite 402, 405
Tridymite **311–21**
Trikalsilite 326, 328
Trilithionite 195–6
Trioctahedral chlorite 209
Triple point: Al_2SiO_5 31, 36
Troilite 429
Tschermakite–Ferrotschermakite 139t, **154–9**
‘*Tschermak’ component* 101
Turbidity (feldpars) 277, 280–1
Tweed microstructure 250, 257, 272, 288
Twin laws (feldspars) 264–6
Two feldspar geothermometer 251

Ugrandite 21
Ultramarine 342
Ulvöspinel 402, 405
Undulatory extinction 317
Uralite 153, 159
Uvarovite 18, 20, 21, 22
Uvite **86–92**, 90t

Vaesite 424
Vaterite 451
Verdelite 89
Vermiculite 225–6, 230, **239–41**
Vesuvianite **28–9**
Viridine 34, 35, 37
Vishnevite **345–8**

Wairakite 357, 363–4
Willemseite 204
Wiluite 28
Winchite 139, 167
Withamite 61
Witherite 451, 454t, 472
Wollastonite **132–5**
Wood tin 383
Wurtzite 435–8
Wüstite 382

Xonotlite 28, 133

Yttrofluorite 480
Yttrotitanite 16

Zeolite Group **355–79**
analyses 359
structures 357
Zinnwaldite 177, 195, 198
Zircon **12–4**
Zoisite **53–5**, 58t

Downloaded from https://pubs.geoscienceworld.org/books/chapter-pdf/3764459/9780903056434_backmatter.pdf
by guest